

REPORT DOCUMENTATION PAGE				Form Approved OMB No. 0704-0188	
<p>The public reporting burden for this collection of information is estimated to average 1 hour per response, including the time for reviewing instructions, searching existing data sources, gathering and maintaining the data needed, and completing and reviewing the collection of information. Send comments regarding this burden estimate or any other aspect of this collection of information, including suggestions for reducing the burden, to Department of Defense, Washington Headquarters Services, Directorate for Information Operations and Reports (0704-0188), 1215 Jefferson Davis Highway, Suite 1204, Arlington, VA 22202-4302. Respondents should be aware that notwithstanding any other provision of law, no person shall be subject to any penalty for failing to comply with a collection of information if it does not display a currently valid OMB control number.</p> <p>PLEASE DO NOT RETURN YOUR FORM TO THE ABOVE ADDRESS.</p>					
1. REPORT DATE (DD-MM-YYYY)		2. REPORT TYPE		3. DATES COVERED (From - To) 01/26/2004 - 07/25/04	
4. TITLE AND SUBTITLE Physics and Simulation of Optoelectronic Devices XII			5a. CONTRACT NUMBER W911NF-04-1-0039		
			5b. GRANT NUMBER 2004 AIG 24		
			5c. PROGRAM ELEMENT NUMBER		
			5d. PROJECT NUMBER PW 1604		
6. AUTHOR(S) Marek Osinski, Hiroshi Amano, Fritz Henneberger			5e. TASK NUMBER 8:09		
			5f. WORK UNIT NUMBER		
7. PERFORMING ORGANIZATION NAME(S) AND ADDRESS(ES) Society of Photo-Optical Instrumentation Engineers 1000 20th St Bellingham, WA 98225				8. PERFORMING ORGANIZATION REPORT NUMBER Volume 5349	
9. SPONSORING/MONITORING AGENCY NAME(S) AND ADDRESS(ES) U.S. Army Research Office ATTN: AMSRD-ARL-RO P.O. Box 12211 Research Triangle Park, NC 27709-2211				10. SPONSOR/MONITOR'S ACRONYM(S) ARO	
				11. SPONSOR/MONITOR'S REPORT NUMBER(S) 45856.1-EL-CF	
12. DISTRIBUTION/AVAILABILITY STATEMENT Approved for Public Release					
13. SUPPLEMENTARY NOTES ISBN 0-8194-5257-2				20040914 027	
14. ABSTRACT Papers on Novel Nanostructures and Optoelectronic Devices, Physics of Quantum Dot Lasers, Simulation of Fiber Devices and Optical Waveguides, Optical Communications, Diode Laser Simulation, VCSels and Resonant-Cavity Photodiodes, Physics of Low Dimensional Structures and Devices, Chaos Synchronization in Diode Lasers, Diode Lasers with Optical Feedback and Wide Bandgap/Visible Materials and Devices.					
15. SUBJECT TERMS Optoelectronic Devices, Lasers					
16. SECURITY CLASSIFICATION OF:			17. LIMITATION OF ABSTRACT SAR	18. NUMBER OF PAGES 486	19a. NAME OF RESPONSIBLE PERSON Janice Gaines Walker
a. REPORT Nonclassified	b. ABSTRACT	c. THIS PAGE			19b. TELEPHONE NUMBER (Include area code) (360) 676-3290

BEST AVAILABLE COPY

PROCEEDINGS OF SPIE



SPIE—The International Society for Optical Engineering

Physics and Simulation of Optoelectronic Devices XII

**Marek Osiński
Hiroshi Amano
Fritz Henneberger**
Chairs/Editors

**26–29 January 2004
San Jose, California, USA**

Sponsored by
SPIE—The International Society for Optical Engineering

Cosponsored by
U. S. Army Research Office

DISTRIBUTION STATEMENT A
Approved for Public Release
Distribution Unlimited



Volume 5349



PROCEEDINGS OF SPIE
SPIE—The International Society for Optical Engineering

Physics and Simulation of Optoelectronic Devices XII

**Marek Osiński
Hiroshi Amano
Fritz Henneberger**
Chairs/Editors

**26–29 January 2004
San Jose, California, USA**

Sponsored and Published by
SPIE—The International Society for Optical Engineering

Cosponsored by
U.S. Army Research Office



Volume 5349

SPIE is an international technical society dedicated to advancing engineering and scientific applications of optical, photonic, imaging, electronic, and optoelectronic technologies.



The papers included in this volume were part of the technical conference cited on the cover and title page. Papers were selected and subject to review by the editors and conference program committee. Some conference presentations may not be available for publication. The papers published in these proceedings reflect the work and thoughts of the authors and are published herein as submitted. The publisher is not responsible for the validity of the information or for any outcomes resulting from reliance thereon.

Please use the following format to cite material from this book:

Author(s), "Title of Paper," in *Physics and Simulation of Optoelectronic Devices XII*, edited by Marek Osinski, Hiroshi Amano, Fritz Henneberger, Proceedings of SPIE Vol. 5349 (SPIE, Bellingham, WA, 2004) page numbers.

ISSN 0277-786X
ISBN 0-8194-5257-2

Published by
SPIE—The International Society for Optical Engineering
P.O. Box 10, Bellingham, Washington 98227-0010 USA
Telephone 1 360/676-3290 (Pacific Time) • Fax 1 360/647-1445
<http://www.spie.org>

Copyright © 2004, The Society of Photo-Optical Instrumentation Engineers

Copying of material in this book for internal or personal use, or for the internal or personal use of specific clients, beyond the fair use provisions granted by the U.S. Copyright Law is authorized by SPIE subject to payment of copying fees. The Transactional Reporting Service base fee for this volume is \$15.00 per article (or portion thereof), which should be paid directly to the Copyright Clearance Center (CCC), 222 Rosewood Drive, Danvers, MA 01923. Payment may also be made electronically through CCC Online at <http://www.copyright.com>. Other copying for republication, resale, advertising or promotion, or any form of systematic or multiple reproduction of any material in this book is prohibited except with permission in writing from the publisher. The CCC fee code is 0277-786X/04/\$15.00.

Printed in the United States of America.

Contents

ix *Conference Committee*

SESSION 1 NOVEL NANOSTRUCTURES

- 1 **Theory of electronic states and optical absorption in carbon nanotubes (Keynote Address)** [5349-01]
T. Ando, Tokyo Institute of Technology (Japan)
- 11 **Epitaxial single-crystalline inorganic nanowires and nanowalls: growth morphogenesis and applications in nano-optoelectronics** [5349-02]
H. T. Ng, P. Nguyen, Y. P. Chen, A. Mao, J. Han, M. Meyyappan, NASA Ames Research Ctr. (USA)
- 18 **From nanowire lasers to quantum wire lasers** [5349-03]
P. Yang, Univ. of California/Berkeley (USA)
- 24 **Modal properties of semiconductor nanowires for laser applications** [5349-05]
A. V. Maslov, C. Z. Ning, NASA Ames Research Ctr. (USA)

SESSION 2 PHYSICS OF QUANTUM DOT LASERS

- 31 **Long-wavelength (1.3 to 1.5 μm) quantum dot lasers based on GaAs (Invited Paper)** [5349-06]
A. R. Kovsh, Nanosemiconductor GmbH (Germany), A.F. Ioffe Physico-Technical Institute (Russia), and Industrial Technology Research Institute (Taiwan); N. N. Ledentsov, Nanosemiconductor GmbH (Germany), A.F. Ioffe Physico-Technical Institute (Russia), and Technische Univ. Berlin (Germany); S. S. Mikhlin, Nanosemiconductor GmbH (Germany) and A.F. Ioffe Physico-Technical Institute (Russia); A. E. Zhukov, A.F. Ioffe Physico-Technical Institute (Russia); D. A. Livshits, N. A. Maleev, A.F. Ioffe Physico-Technical Institute (Russia) and Industrial Technology Research Institute (Taiwan); M. V. Maximov, V. M. Ustinov, A. E. Gubenko, I. M. Gadjiev, E. L. Portnoi, A.F. Ioffe Physico-Technical Institute (Russia); J. S. Wang, J. Chi, Industrial Technology Research Institute (Taiwan); D. Ouyang, D. Bimberg, Technische Univ. Berlin (Germany); J. A. Lott, Air Force Institute of Technology (USA)
- 46 **Shell model of semiconductor quantum dots** [5349-07]
P. G. Eliseev, CHTM/Univ. of New Mexico (USA) and P.N. Lebedev Physical Institute (Russia); D. P. Popescu, CHTM/Univ. of New Mexico (USA); T. V. Torchynska, Instituto Politécnico Nacional (Mexico); A. Stintz, K. J. Malloy, CHTM/Univ. of New Mexico (USA)
- 54 **Quantum well to quantum dot phonon-assisted tunneling** [5349-08]
S.-W. Chang, S.-L. Chuang, N. Holonyak, Jr., Univ. of Illinois/Urbana-Champaign (USA)
- 63 **Energy distributions of carriers in quantum dot laser structures** [5349-09]
S. Osborne, P. Blood, P. Smowton, J. Lutti, Cardiff Univ. (United Kingdom); Y. C. Xin, A. Stintz, D. Huffaker, L. F. Lester, CHTM/Univ. of New Mexico (USA)

SESSION 3 PHYSICS OF LOW-DIMENSIONAL STRUCTURES AND DEVICES

- 69 **Internal optical loss and threshold characteristics of semiconductor lasers with a reduced-dimensionality active region** [5349-10]
L. V. Asryan, SUNY/Stony Brook (USA) and A.F. Ioffe Physico-Technical Institute (Russia);
S. Luryi, SUNY/Stony Brook (USA)
- 81 **On pattern-effects-free operation of QD SOAs for high-speed applications** [5349-11]
A. V. Uskov, National Microelectronics Research Ctr. (Ireland) and P.N. Lebedev Physical
Institute (Russia)
- 90 **Theory for intersubband absorption in quantum dots** [5349-12]
E. H. Hoffman, S.-L. Chuang, Univ. of Illinois/Urbana-Champaign (USA)
- 95 **Microscopic theory and simulation of quantum well intersubband absorption: a three-subband model** [5349-13]
J. Li, C. Z. Ning, NASA Ames Research Ctr. (USA)
- 103 **Si photonic wire components and microfilters on SOI substrate** [5349-14]
T. Fukazawa, F. Ohno, T. Baba, Yokohama National Univ. (Japan)

SESSION 4 PHYSICS AND SIMULATION OF FIBER DEVICES

- 112 **Thermal analysis of packaging device with metal-coated fiber Bragg grating** [5349-16]
B. Xu, W. He, L. Ng, M. Liu, G. Yuan, H. Yuan, C. An, T. Chong, Data Storage Institute/
National Univ. of Singapore (Singapore)
- 117 **Simultaneous mode-locked operation of a fiber laser at two wavelengths** [5349-17]
H. Dong, G. Zhu, Q. Wang, N. K. Dutta, Univ. of Connecticut (USA)

SESSION 5 PHYSICS AND SIMULATION OF OPTICAL WAVEGUIDES

- 122 **Waveguide optical polarization splitter using microprism consisting of dielectric multilayer** [5349-19]
K. Baba, Sendai National College of Technology (Japan); Y. Sone, M. Miyagi, Tohoku Univ.
(Japan)
- 132 **Split-step nonparaxial beam propagation method** [5349-20]
A. Sharma, A. Agrawal, Indian Institute of Technology/Delhi (India)
- 143 **Improved imaginary-distance beam propagation method for full-vectorial eigenmode analysis of optical waveguides** [5349-21]
Y. He, F. G. Shi, Univ. of California/Irvine (USA)
- 151 **Parameters affecting the performance of a perfectly matched layer for beam propagation methods** [5349-22]
A. Sharma, A. Agrawal, Indian Institute of Technology/Delhi (India)
- 163 **Closed-form modal field expressions in diffused channel waveguides** [5349-23]
G. Jain, A. K. Taneja, E. K. Sharma, Univ. of Delhi (India)

SESSION 6 NOVEL OPTOELECTRONIC DEVICES

- 172 **Simulations of $\chi^{(2)}$ nonlinear optical devices with comparisons to laboratory performance (Invited Paper)** [5349-24]
A. V. Smith, D. J. Armstrong, Sandia National Labs. (USA); W. J. Alford, Coherent Technologies, Inc. (USA); M. S. Bowers, Aculight Corp. (USA)
- 176 **Monolithically integrated InP-based tunable wavelength conversion** [5349-25]
J. M. Hutchinson, Intel Corp. (USA); J. S. Barton, M. L. Mašanović, M. N. Sysak, J. A. Henness, L. A. Johansson, D. J. Blumenthal, L. A. Coldren, Univ. of California/Santa Barbara (USA)
- 185 **3D simulation of an integrated wavelength converter** [5349-26]
J. Piprek, N. Trenado, Univ. of California/Santa Barbara (USA); J. Hutchinson, Univ. of California/Santa Barbara (USA) and Intel Corp. (USA); J. Henness, L. A. Coldren, Univ. of California/Santa Barbara (USA)
- 197 **Analysis of InGaAs metal-semiconductor-metal OE mixers** [5349-27]
P. H. Shen, K. Aliberti, B. Stann, P. G. Newman, Army Research Lab. (USA); R. Mehandru, F. Ren, Univ. of Florida (USA)

SESSION 7 COMPONENTS FOR OPTICAL COMMUNICATION

- 206 **Low-threshold high- T_0 high-efficiency 1300-nm and 1500-nm lasers with AlInGaAs active region grown by MOCVD (Invited Paper)** [5349-28]
A. Tandon, D. P. Bour, Y. Chang, C. Lin, S. W. Corzine, M. R. Tan, Agilent Technologies (USA)
- 218 **Two-color semiconductor lasers (Invited Paper)** [5349-29]
S. Hoffmann, M. R. Hofmann, Ruhr-Univ. Bochum (Germany)
- 228 **Modeling, simulating, and characterizing performance in optical switching networks** [5349-30]
J. N. Kutz, Univ. of Washington (USA); B. Small, W. Lu, K. Bergman, Columbia Univ. (USA)
- 236 **Ultrasmall-footprint silica-on-silicon WDM based on holographic Bragg reflectors** [5349-32]
D. Iazikov, C. Greiner, T. W. Mossberg, LightSmyth Technologies, Inc. (USA)

SESSION 8 SEMICONDUCTOR LASER DYNAMICS

- 247 **Anticompetition of laser modes in semiconductor lasers** [5349-33]
C.-C. Huang, C.-F. Lin, National Taiwan Univ. (Taiwan); Y.-C. Yu, Y.-X. Lin, Industrial Technology Research Institute (Taiwan)
- 255 **Timing jitter measurement and its reduction for gain-switched DFB lasers** [5349-35]
Q. Wang, G. Zhu, H. Dong, N. K. Dutta, Univ. of Connecticut (USA)
- 262 **Analysis of self-pulsation in a distributed Bragg reflector laser based on four-wave mixing** [5349-36]
P. Landais, Dublin City Univ. (Ireland); J. Renaudier, P. Gallion, Ecole Nationale Supérieure des Télécommunications (France); G.-H. Duan, Alcatel Research and Innovation (France)

- 271 **Radio-frequency spectra of long-cavity diode lasers under CW pumping** [5349-37]
C. Liu, H. Cao, M. Benavidez, H. Ling, H. Su, CHTM/Univ. of New Mexico (USA); G. M. Peake, Sandia National Labs. (USA); P. G. Eliseev, CHTM/Univ. of New Mexico (USA) and P.N. Lebedev Physical Institute (Russia); M. Osiński, CHTM/Univ. of New Mexico (USA)

SESSION 9 CHAOS SYNCHRONIZATION IN DIODE LASERS

- 282 **Synchronization in chaotic vertical-cavity surface-emitting semiconductor lasers** [5349-38]
N. Fujiwara, J. Ohtsubo, Shizuoka Univ. (Japan)
- 290 **A fiber optics setup for experiments on chaos synchronization and chaotic cryptography** [5349-39]
V. Annovazzi-Lodi, M. Benedetti, S. Merlo, M. Norgia, Univ. degli Studi di Pavia (Italy)
- 298 **Chaotic synchronous modulation of semiconductor lasers subject to optical injection** [5349-40]
H. F. Chen, J. M. Liu, Univ. of California/Los Angeles (USA)

SESSION 10 NONLINEAR DYNAMICS OF MUTUALLY COUPLED AND OPTICALLY INJECTED SEMICONDUCTOR LASERS

- 307 **Simple interpretation of the dynamics of mutually coupled semiconductor lasers with detuning** [5349-41]
R. Vicente, J. Mulet, Univ. de les Illes Balears (Spain); M. Sciamanna, Faculté Polytechnique de Mons (Belgium); C. R. Mirasso, Univ. de les Illes Balears (Spain) and Univ. of California/Los Angeles (USA)
- 319 **Experimentally observed dynamical characteristics of mutually coupled semiconductor lasers with or without optoelectronic feedback** [5349-42]
S. Tang, M. C. Chiang, J. M. Liu, Univ. of California/Los Angeles (USA); R. Vicente, C. R. Mirasso, Univ. de les Illes Balears (Spain) and Univ. of California/Los Angeles (USA)
- 331 **Dynamics of mutually coupled VCSELs** [5349-43]
R. Vicente, Univ. de les Illes Balears (Spain); C. R. Mirasso, Univ. de les Illes Balears (Spain) and Univ. of California/Los Angeles (USA)
- 339 **Period-one oscillations in optically injected semiconductor lasers** [5349-44]
S. K. Hwang, National Chung Cheng Univ. (Taiwan); J. M. Liu, Univ. of California/Los Angeles (USA); J. K. White, Bookham Technology (Canada)

SESSION 11 DIODE LASERS WITH OPTICAL FEEDBACK

- 348 **Dynamics of lasers with ultrashort optical feedback (Invited Paper)** [5349-45]
O. Ushakov, Humboldt-Univ. zu Berlin (Germany); S. Bauer, O. Brox, Fraunhofer-Institut für Nachrichtentechnik (Germany); H.-J. Wünsche, Humboldt-Univ. zu Berlin (Germany) and Fraunhofer-Institut für Nachrichtentechnik (Germany); F. Henneberger, Humboldt-Univ. zu Berlin (Germany)

- 358 **Instability and dynamic characteristics of self-pulsating semiconductor lasers with optical feedback** [5349-47]
H. Koshio, J. Ohtsubo, Shizuoka Univ. (Japan)

SESSION 12 PHYSICS AND SIMULATION OF VCSELS AND RESONANT-CAVITY PHOTODIODES

- 366 **High-power single-mode 1330- and 1550-nm VCSELS bonded to silicon substrates (Invited Paper)** [5349-48]
V. M. Robbins, S. D. Lester, D. Bour, J. N. Miller, F. Mertz, Agilent Technologies (USA)
- 375 **Design and optimization of high-performance 1.3- μ m VCSELS** [5349-49]
J. Piprek, M. Mehta, V. Jayaraman, Univ. of California/Santa Barbara (USA)
- 385 **Resonant coupled-cavity effects in VCSELS with annular ring contacts** [5349-50]
G. A. Smolyakov, V. A. Smagley, W. Chen, M. Osiński, CHTM/Univ. of New Mexico (USA)

SESSION 13 WIDE BANDGAP/VISIBLE MATERIALS AND DEVICES

- 397 **Molecular-beam epitaxy of III-N on novel ZrB₂ substrates (Invited Paper)** [5349-52]
J. Suda, Kyoto Univ. (Japan)
- 408 **Optical and electrical properties of interdigitated InGaN/GaN green light-emitting diodes** [5349-54]
J. Lee, CHTM/Univ. of New Mexico (USA); P. G. Eliseev, CHTM/Univ. of New Mexico (USA) and P.N. Lebedev Physical Institute (Russia); M. Osiński, CHTM/Univ. of New Mexico (USA); D.-S. Lee, J. C. Ramer, D. I. Florescu, E. A. Armour, Veeco TurboDisc Operations (USA)
- 416 **Color-dependent degradation of high-brightness AlGaInP LEDs** [5349-55]
P. Altieri, A. Jaeger, R. Windisch, N. Linder, P. Stauss, R. Oberschmid, K. Streubel, OSRAM Opto Semiconductors GmbH (Germany)
- 426 **Effect of oxygen on the electronic band structure of II-O-VI alloys** [5349-56]
W. Shan, W. Walukiewicz, K. M. Yu, J. W. Ager III, J. Wu, J. Beeman, Lawrence Berkeley National Lab. (USA); M. A. Scapulla, O. D. Dubon, E. E. Haller, Lawrence Berkeley National Lab. (USA) and Univ. of California/Berkeley (USA); Y. Nabetani, Univ. of Yamanashi (Japan); P. Becla, Massachusetts Institute of Technology (USA)

SESSION 14 DIODE LASER SIMULATION

- 435 **Essex distributed time-domain model (eDTDM) for complex laser modeling (Invited Paper)** [5349-57]
S. P. Higgins, A. J. Vickers, Univ. of Essex (United Kingdom)

POSTER SESSION

- 446 **Design optimization of InGaAlAs/GaAs single and double quantum well lasers emitting at 808 nm** [5349-59]
M. Zbrozczyk, M. Bugajski, Institute of Electron Technology (Poland)

- 454 **Temperature dependence of photoluminescence in noncrystalline silicon** [5349-64]
A. Serpengüzel, T. Bilici, I. Inanç, A. Kurt, Koç Univ. (Turkey); J. Carey, E. Mazur, Harvard Univ. (USA)
- 463 **Multilayered grating diffraction graphical-user-interfaced simulation toolbox in the MATLAB environment** [5349-65]
M. Auslender, A. Bergel, N. Pinhas, S. Hava, Ben-Gurion Univ. of the Negev (Israel)
- 475 *Author Index*

Conference Committee

Symposium Chair

Nasser Peyghambarian, University of Arizona (USA)

Symposium Cochair

Gernot Pomrenke, Air Force Office of Scientific Research (USA)

Conference Chairs

Marek Osinski, CHTM/University of New Mexico (USA)

Hiroshi Amano, Meijo University (Japan)

Fritz Henneberger, Humboldt-Universität zu Berlin (Germany)

Program Committee

Michael J. Adams, University of Essex (United Kingdom)

Toshihiko Baba, Yokohama National University (Japan)

Peter Blood, Cardiff University (United Kingdom)

David P. Bour, Agilent Technologies (USA)

Weng W. Chow, Sandia National Laboratories (USA)

Shun-Lien Chuang, University of Illinois/Urbana-Champaign (USA)

Silvano Donati, Università degli Studi di Pavia (Italy)

Guang-Hua Duan, OPTO+, Alcatel Research and Innovation (France)

Athanasios Gavrielides, Air Force Research Laboratory (USA)

Ortwin G. Hess, DLR (Germany) and University of Surrey (United Kingdom)

Mark S. Hybertsen, Agere Systems (USA)

Stephan W. Koch, Philipps-Universität Marburg (Germany)

Fumio Koyama, Tokyo Institute of Technology (Japan)

Nikolai N. Ledentsov, Technische Universität Berlin (Germany) and
A.F. Ioffe Physico-Technical Institute (Russia)

Hai-Feng Liu, Photonics Technology Operation/Intel Corporation (USA)

Luigi A. Lugiato, Università dell'Insubria (Italy)

Claudio R. Mirasso, Universitat de les Illes Balears (Spain)

Cun-Zheng Ning, NASA Ames Research Center (USA)

Joachim Piprek, University of California/Santa Barbara (USA)

Paul Hongen Shen, U.S. Army Research Laboratory (USA)

Yuzo Yoshikuni, NTT Photonics Laboratories (Japan)

Session Chairs

- 1 Novel Nanostructures

Cun-Zheng Ning, NASA Ames Research Center (USA)

- 2 Physics of Quantum Dot Lasers

Shun-Lien Chuang, University of Illinois/Urbana-Champaign (USA)

- 3 Physics of Low-Dimensional Structures and Devices
 Peter Blood, Cardiff University (United Kingdom)
- 4 Physics and Simulation of Fiber Devices
 Hai-Feng Liu, Photonics Technology Operation/Intel Corporation (USA)
- 5 Physics and Simulation of Optical Waveguides
 Joachim Piprek, University of California/Santa Barbara (USA)
- 6 Novel Optoelectronic Devices
 Toshihiko Baba, Yokohama National University (Japan)
- 7 Components for Optical Communication
 Jean-Claude Bouley, OPTO+, Alcatel Research and Innovation (France)
- 8 Semiconductor Laser Dynamics
 Anthony J. Vickers, University of Essex (United Kingdom)
- 9 Chaos Synchronization in Diode Lasers
 Claudio R. Mirasso, Universitat de les Illes Balears (Spain)
- 10 Nonlinear Dynamics of Mutually Coupled and Optically Injected
 Semiconductor Lasers
 Fritz Henneberger, Humboldt-Universität zu Berlin (Germany)
- 11 Diode Lasers with Optical Feedback
 Athanasios Gavrielides, Air Force Research Laboratory (USA)
- 12 Physics and Simulation of VCSELs and Resonant-Cavity Photodiodes
 Paul Hongen Shen, U.S. Army Research Laboratory (USA)
- 13 Wide Bandgap/Visible Materials and Devices
 Hiroshi Amano, Meijo University (Japan)
- 14 Diode Laser Simulation
 Marek Osiński, CHTM/University of New Mexico (USA)

Theory of electronic states and optical absorption in carbon nanotubes

Tsuneo ANDO

Department of Physics, Tokyo Institute of Technology
2-12-1 Ookayama, Meguro-ku, Tokyo 152-8551, Japan

ABSTRACT

A brief review is given of electronic and optical properties of carbon nanotubes mainly from a theoretical point of view. The topics cover an effective-mass description of electronic states, Aharonov-Bohm effects, and optical absorption including interaction effects on the band structure gap and excitonic effects.

Keywords: graphite, effective-mass approximation, exciton, Aharonov-Bohm effect, band-gap renormalization

1. INTRODUCTION

Carbon nanotubes (CNs) are quasi-one-dimensional materials made of sp^2 -hybridized carbon networks¹ and have been a subject of an extensive study. In particular, the electronic structure of a single CN has been studied theoretically, which predicted that CN becomes either metallic or semiconducting depending on its chiral vector, i.e., boundary conditions in the circumference direction.²⁻¹¹ These predictions have been confirmed by Raman experiments¹² and direct measurements of local density of states by scanning tunneling spectroscopy.¹³⁻¹⁵ The purpose of this paper is to give a brief review of recent theoretical study on electronic and optical properties of carbon nanotubes.

In understanding electronic properties of nanotubes, a $\mathbf{k}\cdot\mathbf{p}$ method or an effective-mass approximation¹¹ is quite powerful. It has been used successfully in the study of wide varieties of electronic properties of CN. Some of such examples are magnetic properties¹⁶ including the Aharonov-Bohm effect on the band gap, optical absorption spectra,¹⁷ exciton effects,¹⁸ lattice instabilities in the absence^{19,20} and presence of a magnetic field,²¹ magnetic properties of ensembles of nanotubes,²² effects of spin-orbit interaction,²³ effects of lattice vacancies,^{24,25} and electronic properties of nanotube caps.²⁶ Long wavelength phonons and electron-phonon scattering have also been studied.²⁷ In this paper, we shall discuss electronic states and optical spectra obtained mainly in this $\mathbf{k}\cdot\mathbf{p}$ scheme.

2. ENERGY BANDS

2.1. Neutrino on cylinder surface

Figure 1 shows the lattice structure and the first Brillouin zone of a two-dimensional (2D) graphite together with the coordinate systems. A unit cell contains two carbon atoms denoted by A and B. A nanotube is specified by a chiral vector $\mathbf{L} = n_a \mathbf{a} + n_b \mathbf{b}$ with integer n_a and n_b and basis vectors \mathbf{a} and \mathbf{b} ($|\mathbf{a}| = |\mathbf{b}| = a = 2.46 \text{ \AA}$). In the coordinate system fixed onto the graphite sheet, we have $\mathbf{a} = (a, 0)$ and $\mathbf{b} = (-a/2, \sqrt{3}a/2)$. For convenience we introduce another coordinate system where the x direction is along the circumference \mathbf{L} and the y direction is along the axis of CN. The direction of \mathbf{L} is denoted by the chiral angle η . It should be noted that there is another convention of choosing the basis vectors \mathbf{a}_1 and \mathbf{a}_2 instead of \mathbf{a} and \mathbf{b} such that $\mathbf{a}_1 = \mathbf{a} + \mathbf{b}$ and $\mathbf{a}_2 = \mathbf{b}$.

A graphite sheet is a zero-gap semiconductor in the sense that the conduction and valence bands consisting of π states cross at K and K' points of the Brillouin zone, whose wave vectors are given by $\mathbf{K} = (2\pi/a)(1/3, 1/\sqrt{3})$ and $\mathbf{K}' = (2\pi/a)(2/3, 0)$.^{28,29} Electronic states near a K point of 2D graphite are described by the $\mathbf{k}\cdot\mathbf{p}$ equation:^{11,30}

$$\gamma(\vec{\sigma} \cdot \hat{\mathbf{k}})\mathbf{F}(\mathbf{r}) = \epsilon\mathbf{F}(\mathbf{r}), \quad \mathbf{F}(\mathbf{r}) = \begin{pmatrix} F_A(\mathbf{r}) \\ F_B(\mathbf{r}) \end{pmatrix}, \quad (1)$$

E-mail: ando@phys.titech.ac.jp URL: <http://www.stat.phys.titech.ac.jp/ando/>

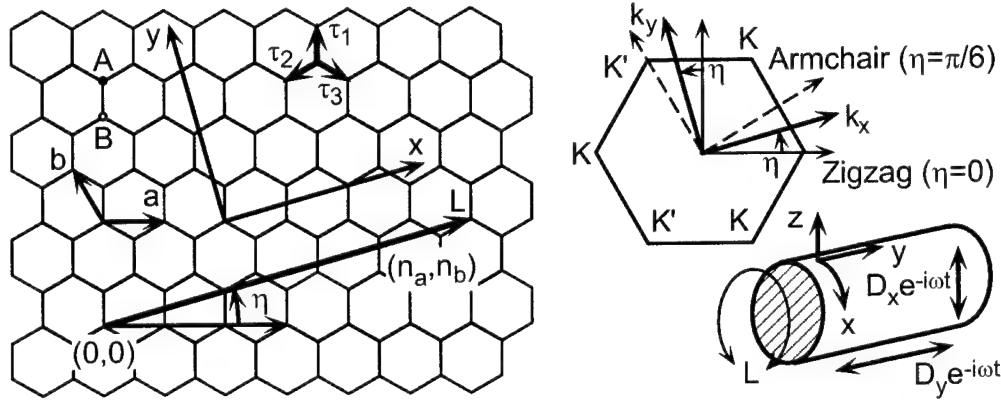


Figure 1. Left: Lattice structure of two-dimensional graphite sheet. η is the chiral angle. The coordinates are chosen in such a way that x is along the circumference of a nanotube and y is along the axis. Right-top: The first Brillouin zone and K and K' points. Right-bottom: The coordinates for a nanotube.

where γ is the band parameter, $\hat{\mathbf{k}} = (\hat{k}_x, \hat{k}_y)$ is a wave-vector operator, ε is the energy, and σ_x and σ_y are the Pauli spin matrices. Equation (1) has the form of Weyl's equation for neutrinos, i.e., relativistic Dirac electrons with vanishing rest mass. Figure 2 shows the energy dispersion and the density of states schematically.

The electronic states in a nanotube can be obtained by imposing the periodic boundary condition in the circumference direction $\Psi(\mathbf{r}+\mathbf{L})=\Psi(\mathbf{r})$ except for extremely thin CNs. The Bloch functions at a K point change their phase by $\exp(i\mathbf{K}\cdot\mathbf{L})=\exp(2\pi i\nu/3)$, where ν is an integer defined by $n_a+n_b=3M+\nu$ with integer M and can take 0 and ± 1 . Because $\Psi(\mathbf{r})$ is written as a product of the Bloch function and the envelope function, i.e., the neutrino wave function, this phase change should be canceled by that of the envelope functions and the boundary conditions become $\mathbf{F}(\mathbf{r}+\mathbf{L})=\mathbf{F}(\mathbf{r})\exp(-2\pi i\nu/3)$. The extra phase can be regarded as a fictitious Aharonov-Bohm flux passing through the cross section of CN.

Energy levels in CN for the K point are obtained by putting $k_x=\kappa_\nu(n)$ with $\kappa_\nu(n)=(2\pi/L)[n-(\nu/3)]$ and $k_y=k$ in the above $\mathbf{k}\cdot\mathbf{p}$ equation as $\varepsilon_\nu^{(\pm)}(n,k)=\pm\gamma\sqrt{\kappa_\nu(n)^2+k^2}$,¹¹ where $L=|\mathbf{L}|$, n is an integer, and the upper (+) and lower (-) signs represent the conduction and valence bands, respectively. The Hamiltonian and the boundary condition for the K' point are obtained by replacing \hat{k}_y by $-\hat{k}_y$ and ν by $-\nu$. This shows that CN becomes metallic for $\nu=0$ and semiconducting with gap $E_g=4\pi\gamma/3L$ for $\nu=\pm 1$. Figure 3 shows a schematic illustration of the bands for $\nu=0$ and $+1$ in the vicinity of the K point.

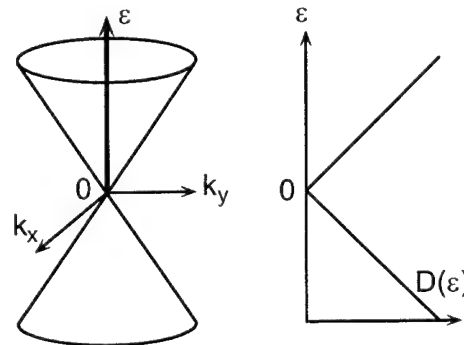


Figure 2. The energy dispersion and density of states in the vicinity of K and K' points obtained in a $\mathbf{k}\cdot\mathbf{p}$ scheme

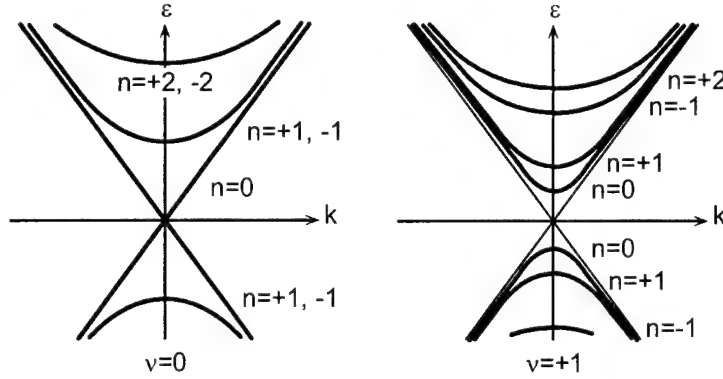


Figure 3. Energy bands of a nanotube obtained in the effective-mass approximation for $\nu=0$ (left) and $\nu=+1$ (right)

2.2. Aharonov-Bohm effect

In the presence of a magnetic flux ϕ passing through the cross section of CN, the boundary condition changes into $\Psi(\mathbf{r}+\mathbf{L}) = \Psi(\mathbf{r}) \exp(2\pi i\varphi)$ with $\varphi = \phi/\phi_0$, where $\phi_0 = ch/e$ is the magnetic flux quantum. Consequently, $\kappa_\nu(n)$ is replaced by $\kappa_{\nu\varphi}(n)$ with

$$\kappa_{\nu\varphi}(n) = \frac{2\pi}{L} \left(n + \varphi - \frac{\nu}{3} \right). \quad (2)$$

The corresponding result for the K' point is again obtained by the replacement $\nu \rightarrow -\nu$. The band gap exhibits an oscillation between 0 and $2\pi\gamma/L$ with period ϕ_0 as is shown in Fig. 4.^{11,31} This giant Aharonov-Bohm (AB) effect on the band gap is a unique property of CN's. The AB effect appears also in a tunneling conductance across a finite-length CN.³²

This AB effect was shown to be responsible for observed oscillation of the resistance in multi-wall nanotubes.³³ Quite recently, splitting of the band gap in semiconducting tubes in the presence of magnetic flux was observed directly in optical absorption spectra of single-wall CN's.³⁴

2.3. Topological singularity and absence of backward scattering

The wave function in the 2D graphite is written explicitly as

$$\mathbf{F}_{s\mathbf{k}} = \frac{1}{\sqrt{2}} \begin{pmatrix} e^{i\theta(\mathbf{k})} \\ s \end{pmatrix} \exp(i\mathbf{k} \cdot \mathbf{r}), \quad (3)$$

where $\theta(\mathbf{k})$ is the direction angle of \mathbf{k} and $s = +1$ and -1 for the conduction and valence band, respectively. This wave function acquires Berry's phase $-\pi$ when the wave vector \mathbf{k} is rotated around the origin $\mathbf{k} = 0$, although it looks continuous as a function of \mathbf{k} .^{35,36} In fact, when \mathbf{k} is rotated once in the anticlockwise direction adiabatically as a function of time t for a time interval $0 < t < T$ with $\mathbf{k}(T) = \mathbf{k}(0)$, the wavefunction $\mathbf{F}_{s\mathbf{k}}$ is changed into $\mathbf{F}_{s\mathbf{k}} \exp(-i\psi)$, where ψ is Berry's phase given by

$$\psi = -i \int_0^T dt \left\langle s\mathbf{k}(t) \left| \frac{d}{dt} \right| s\mathbf{k}(t) \right\rangle = -\pi. \quad (4)$$

This is equivalent to the well-known signature change of the spinor wave function or a spin rotation operator under a 2π rotation.

It should be noted that $\psi = -\pi$ when the closed contour encircles the origin $\mathbf{k} = 0$ but $\psi = 0$ when the contour does not contain $\mathbf{k} = 0$. Further, the wave function at $\mathbf{k} = 0$ depends on the direction of \mathbf{k} and its "spin" direction is undefined. These facts show the presence of a topological singularity at $\mathbf{k} = 0$. The nontrivial Berry's phase leads to the unique property of a metallic carbon nanotube that there exists no backscattering and the tube is a perfect conductor even in the presence of scatterers.^{35,37} In fact, it has been proved that the Born series for

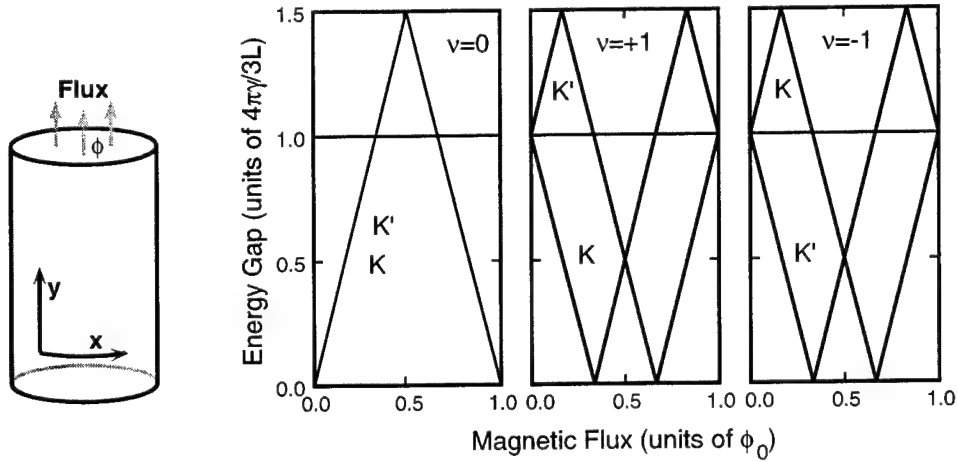


Figure 4. A schematic illustration of magnetic flux passing through a tube cross section (left) and energy gap versus the flux for metallic ($\nu=0$) and semiconducting ($\nu=\pm 1$) CN (right).

backscattering vanish identically and the conductance calculated exactly for finite-length nanotubes containing many impurities has shown to be given by $2e^2/\pi\hbar$ independent of length.³⁷ The absence of backscattering has been confirmed also by numerical calculations in a tight binding model.³⁸

Backscattering corresponds to a rotation of the \mathbf{k} direction by $\pm\pi$. In the absence of a magnetic field, there exists a time reversal process corresponding to each backscattering. This process corresponds to a rotation by $\pm\pi$ in the opposite direction. The scattering amplitudes of these two processes are same in the absolute value but have opposite signatures because of Berry's phase. As a result, the backscattering amplitude cancels out completely. In semiconducting nanotubes, on the other hand, backscattering appears because the symmetry is destroyed by a nonzero Aharonov-Bohm magnetic flux. The singularity causes also the appearance of a perfectly conducting channel and makes the conductivity infinite even in the presence of several bands at the Fermi level.³⁹ It gives rise to various zero-mode anomalies in transport properties of 2D graphite.^{40, 41}

3. OPTICAL ABSORPTION, BAND GAPS, AND EXCITONS

3.1. Polarization and selection rules

The optical absorption is described by a dynamical conductivity obtained in a linear response theory.¹⁷ We first expand electric field $E_\alpha(\theta, \omega)$ and induced current density $j_\alpha(\theta, \omega)$ into a Fourier series:

$$E_\alpha(\theta, \omega) = \sum_l E_\alpha^l(\omega) \exp(il\theta - i\omega t), \quad j_\alpha(\theta, \omega) = \sum_l j_\alpha^l(\omega) \exp(il\theta - i\omega t), \quad (5)$$

with $\alpha = x, y$ and $\theta = 2\pi x/L$. It is quite straightforward to show that the induced current has the same Fourier component as that of the electric field, i.e., $j_\alpha^l(\omega) = \sigma_{\alpha\alpha}^l(\omega) E_\alpha^l(\omega)$. The dynamical conductivity is given by

$$\sigma_{\alpha\alpha}^l(\omega) = \sum_{nk} \frac{|(n, k, +|j_\alpha^l|n+l, k, -)|^2}{iLA[\varepsilon_n^{(+)}(k) - \varepsilon_{n+l}^{(-)}(k)]} \frac{f[\varepsilon_{n+l}^{(-)}(k)](1 - f[\varepsilon_n^{(+)}(k)])2\hbar^2\omega}{[\varepsilon_n^{(+)}(k) - \varepsilon_{n+l}^{(-)}(k)]^2 - (\hbar\omega)^2 - i\hbar^2\omega/\tau}, \quad (6)$$

where A is the length of the nanotube, the current-density operator is given by $j_\alpha^l = -(e\gamma/\hbar)\sigma_\alpha e^{-il\theta}$, a phenomenological relaxation time τ has been introduced, and $f(\varepsilon)$ is the Fermi distribution function.

When external electric field \mathbf{D} is polarized along the CN axis, the Fourier components of a total field are $E_y^l = D_y \delta_{l,0}$ and the absorption is proportional to $\text{Re}\sigma_{yy}(\omega)$ with $\sigma_{yy}(\omega) = \sigma_{yy}^{l=0}(\omega)$. It can be seen from Eq. (6) that transitions occur between valence and conduction bands with the same band index n . At a band edge

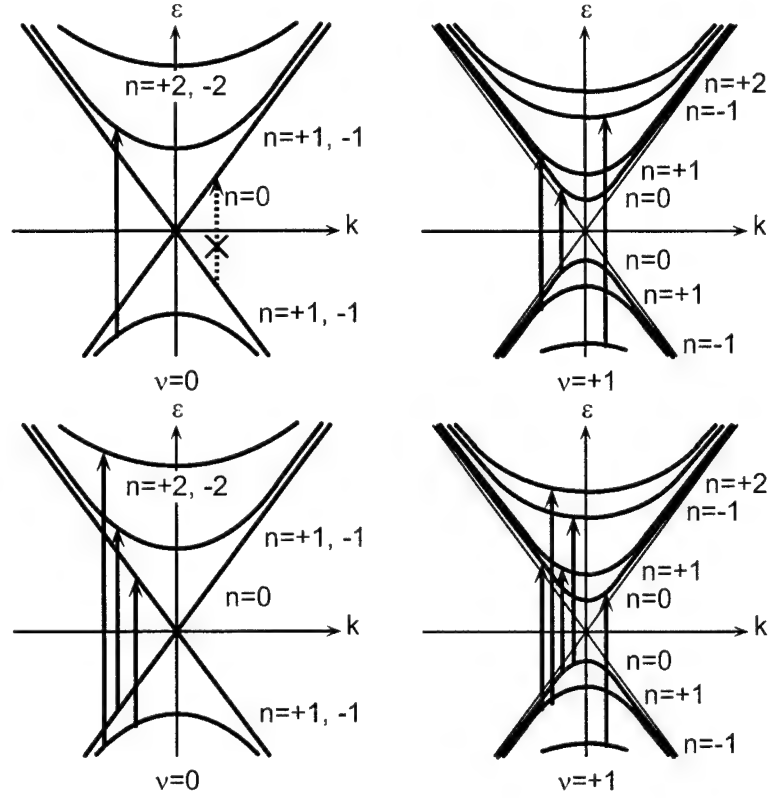


Figure 5. The band structures of a metallic and semiconducting CN. The allowed optical transitions for the parallel polarization are denoted by arrows in the upper figure and those for the perpendicular polarization in the lower figure.

$k=0$, in particular, the envelope function is given by an eigenvector of a Pauli matrix σ_x . Because the current operator j_y is proportional to σ_y , the transitions at their edges are all allowed.

The situation becomes much more complicated when an external electric field is polarized in the direction perpendicular to the CN axis. In this case, effects of an electric field induced by the polarization of nanotubes should be considered. This depolarization effect can be calculated also in the $\mathbf{k} \cdot \mathbf{p}$ scheme.

Suppose an external electric field $D_x^l e^{i l \theta - i \omega t}$ is applied in the direction normal to the tube axis and let j_x^l be the induced current. Then, the corresponding induced charge density localized on the cylindrical surface is calculated as $\rho^l = (2\pi/L)(l/\omega)j_x^l$ with the use of the equation of continuity. This charge leads to potential $\phi^l = (L/\kappa|l|)\rho^l$ or electric field $E_x^l = -i(2\pi/\kappa L)l\phi^l$. The static dielectric constant κ describes polarization of states (σ and π bands) except those lying in the vicinity of the Fermi level. It is expected to be in the range $1 < \kappa < 10$, but its exact value is not known. Thus, the total electric field becomes $E_x^l = D^l - i|l|(4\pi^2/\kappa L\omega)j_x^l$, which leads with the use of $j_x^l = \sigma_{xx}^l E_x^l$ to $j_x^l = \tilde{\sigma}_{xx}^l D_x^l$, where

$$\tilde{\sigma}_{xx}^l = \sigma_{xx}^l \left(1 + i|l| \frac{4\pi^2}{\kappa L\omega} \sigma_{xx}^l \right)^{-1}. \quad (7)$$

For the light-polarization perpendicular to the tube axis, its field is written as $\mathbf{D} = (D_x \sin \theta, 0)$. The absorption in a unit area is then proportional to $\text{Re}(j_x E_x^*) \propto \text{Re} \tilde{\sigma}_{xx}(\omega)$ with $\tilde{\sigma}_{xx} = \tilde{\sigma}_{xx}^{l=1} = \tilde{\sigma}_{xx}^{l=-1}$. According to Eq. (6) the absorption occurs between the valence band with index n and the conduction bands with $n \pm 1$.

Let us consider a spectral edge corresponding to $k=0$, for which the eigenstates are those of a Pauli matrix σ_x . Because the current operator is proportional to σ_x , transitions between valence- and conduction-band states become allowed only when $\kappa_{\nu\varphi}(n)$ and $\kappa_{\nu\varphi}(n \pm 1)$ have a sign opposite to each other. This leads to the conclusion

in a metallic CN, for example, that transitions from $n=0$ to $n=-1$ and from $n=-1$ to $n=0$ are allowed as shown in Fig. 5. When the depolarization effect is included, however, these peaks disappear almost completely because most of their intensity is transferred to interband plasmons with much higher energy.¹⁷ Therefore, interband optical transitions among valence and conduction bands near the Fermi level is observable only for polarization parallel to the tube axis.

3.2. Band gap renormalization and excitons

One important problem is a many-body effect on the band structure and optical absorption spectrum. In fact, band gaps are likely to be influenced strongly by electron-electron interactions. Further, the exciton binding energy becomes infinite in the limit of an ideal one-dimensional electron-hole system.^{42, 43} This means that the exciton effect can be quite important and modify the absorption spectra drastically. The band-gap renormalization and optical spectra with exciton effects have been calculated in the conventional screened Hartree-Fock approximation within a $\mathbf{k}\cdot\mathbf{p}$ scheme.¹⁸

The strength of the Coulomb interaction is specified by $(e^2/\kappa L)/(2\pi\gamma/L)$, which turns out to be independent of the circumference length L . In the $\mathbf{k}\cdot\mathbf{p}$ scheme, therefore, all physical quantities become almost universal if the length is scaled by L and the energy by $2\pi\gamma/L$. This parameter is estimated as $(e^2/\kappa L)(2\pi\gamma/L)^{-1} = 0.3545 \times \kappa^{-1}$ for $\gamma = 6.46 \text{ eV}\cdot\text{\AA}$, which corresponds to $\gamma = \sqrt{3}a|\gamma_0|/2$ with $\gamma_0 = -3.03 \text{ eV}$ and $a = 2.46 \text{ \AA}$.

Figure 6 shows some examples of calculated exciton energy levels for a semiconducting CN ($\nu=1$) versus the strength of the Coulomb interaction in the left hand side. With the increase of the interaction, the number of exciton bound states increases and their energy levels are shifted to the higher energy side in spite of the fact that their binding energy increases. The reason is in the considerable enhancement of the band gap due to the Coulomb interaction. It is interesting to notice that the energy of the lowest excitonic state varies very little as a function of the strength of the Coulomb interaction.

Figure 6 shows calculated absorption spectra in a semiconducting CN for $(e^2/\kappa L)/(2\pi\gamma/L) = 0.1$ in the right hand side. The energy levels of excitons are denoted by vertical straight lines. The considerable optical intensity is transferred to the lowest exciton bound states. For a sufficiently larger strength of the Coulomb interaction, transitions to exciton excited states become appreciable.

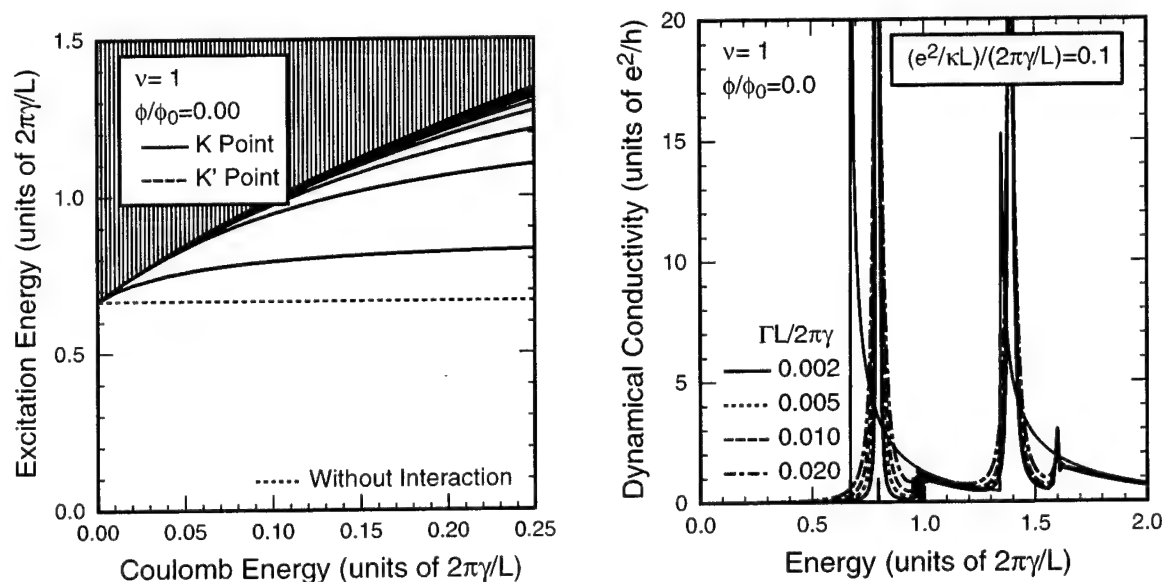


Figure 6. Interband excitation spectra calculated in a screened Hartree-Fock approximation (left) and examples of interband optical absorption spectra in the presence of electron-electron interaction (right).

In addition to excitons associated with the highest valence and the lowest conduction bands ($n=0$), exciton effects are important for transitions to excited bands. In fact, the exciton binding energy and the intensity transfer is larger for the transition to the higher conduction band ($n=1$) than those with $n=0$. This arises because the effective mass along the axis direction for the conduction and valence bands with $n=1$ is twice as large as that of the lowest conduction band and the highest valence band with $n=0$.

It turned out that interaction effects on the band gap are almost independent of $n=0$ and $n=1$ and the exciton energy is almost as large as the band-gap renormalization for the bands with larger optical gap $n=1$. As a result, the absorption peak stays almost at the corresponding band gap in the absence of interaction for $n=1$ and exciton effects independent of the interaction strength and the energy difference between the absorption peaks for $n=0$ and $n=1$ becomes smaller than that in the absence of interactions.

Optical absorption spectra of thin film samples of single-wall nanotubes were observed quite recently and analyzed by assuming a distribution of their chirality and diameter.⁴⁴ Careful comparison of the observed spectrum with calculated in a simple tight-binding model suggested the importance of excitonic effects.⁴⁵ In fact, comparing the observed spectrum with the calculated one in the fundamental absorption region, the observed absorption band for $n=0$ lies at an energy higher than half of the band for $n=1$. The results can roughly be explained by the theoretical result for $(e^2/\kappa L)/(2\pi\gamma/L) \sim 0.05$. This strongly suggests that the exciton effect together with the band-gap renormalization plays an important role in the optical transition near the fundamental absorption edge in semiconducting nanotubes.

3.3. Interaction effects on band structure

In the screened Hartree-Fock approximation discussed above, a dielectric function appearing in the self-energy is replaced by the static one and therefore dynamical effects such as coupling with charge density excitations are not taken into consideration explicitly. Quite recently, calculations were performed in a full dynamical random-phase approximation (RPA),^{46, 47} often called the GW approximation,⁴⁸

In RPA, the Coulomb interaction appearing in the self-energy diagram $\Sigma_{ns}(k, \varepsilon)$ is screened by the dynamical dielectric function $\varepsilon_{n-m}(q, \omega)$. The self-energy diverges logarithmically and therefore a cutoff function $g_0(\varepsilon) = \varepsilon_c^{\alpha_c} / (|\varepsilon|^{\alpha_c} + \varepsilon_c^{\alpha_c})$ is introduced so as to exclude contributions from states far away from the Fermi level. The cutoff energy ε_c is of the order of the width of the π bands in 2D graphite.

The single-particle energy $E_{ns}(k)$ is calculated by $E_{ns}(k) = \varepsilon_n^{(s)}(k) + \Sigma_{ns}(k, \varepsilon_n^{(s)}(k))$ with $s = \pm$. Originally, it is determined by the equation obtained from the above by the replacement of $\Sigma_{ns}(k, \varepsilon_n^{(s)}(k))$ by $\Sigma_{ns}(k, E_{ns}(k))$. However, the present procedure is known to give more accurate results if the self-energy is calculated only in the lowest order.^{49, 50} Using the single-particle energy, we evaluate the band gap Δ_n which is defined by the energy difference at $k=0$ between conduction and valence bands of the same index n as $\Delta_n = E_{n+}(0) - E_{n-}(0)$. The cutoff parameters are chosen as $\varepsilon_c/(2\pi\gamma/L) = 5$ and $\alpha_c = 4$.

Figure 7 gives the gap of the first parabolic band in a metallic CN and the first and second band gap for a semiconducting CN. In the regime of very weak interaction $(e^2/\kappa L)/(2\pi\gamma/L) < 0.05$, the band gap increases with the interaction strength in both metallic and semiconducting CN's. With the further increase of the interaction, however, the gap in a metallic CN starts to decrease after taking a maximum at around $(e^2/\kappa L)/(2\pi\gamma/L) \approx 0.15$, while that in a semiconducting CN continues to increase.

In the weak interaction regime $(e^2/\kappa L)/(2\pi\gamma/L) < 0.2$, dynamical effects on the band gap are small and the static RPA works well. When the interaction is stronger, the difference between the dynamical and static RPA becomes larger in a metallic CN than in a semiconducting CN. The shift in the gaps of a semiconducting CN is nearly independent of the band. This shows that the interaction effects cannot be absorbed into a simple renormalization of the band parameter γ .

Figure 8 shows the band gaps for a semiconducting CN for different cutoffs, $\varepsilon_c/(2\pi\gamma/L) = 2.5, 5.0$, and 10 . The band gap scaled by $2\pi\gamma/L$ increases logarithmically with the increase of the cutoff energy. This logarithmic cutoff dependence means that the band-gap enhancement increases slightly (logarithmically) with the increase of the CN diameter if being scaled by $2\pi\gamma/L$. Unfortunately, experimental measurements of band gaps have not been accurate enough to make detailed comparison possible so far. Note that such logarithmic dependence

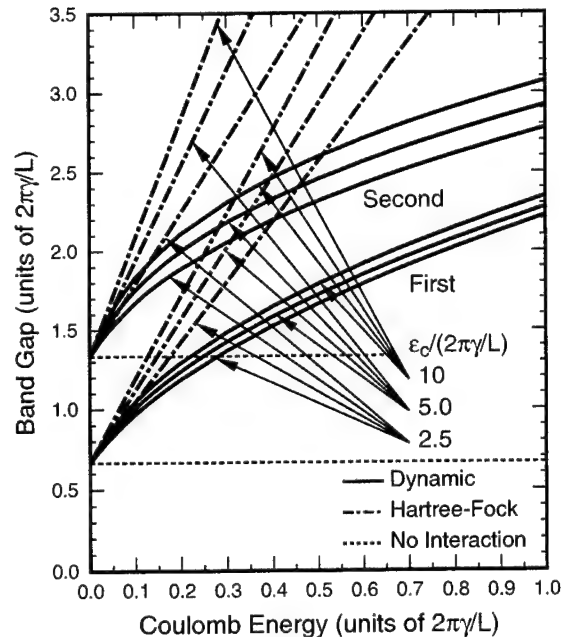
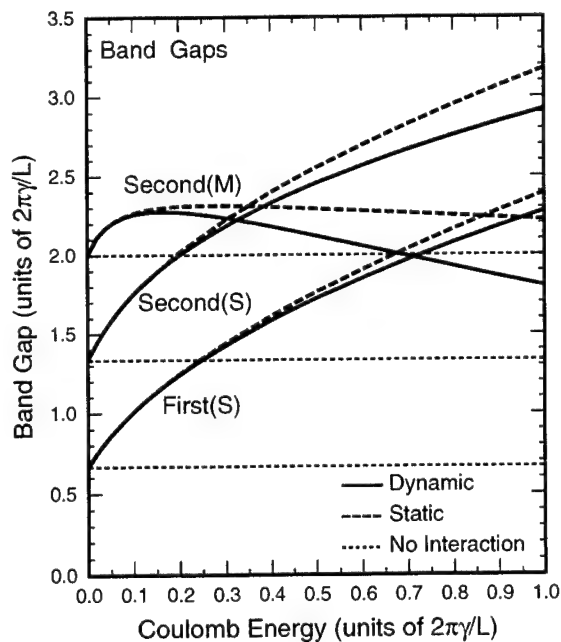


Figure 7. (Left) Calculated gap of a parabolic bands ($n = \pm 1$) in a metallic CN (M) and first and second gaps of a semiconducting CN (S) versus the effective strength of the Coulomb interaction.

Figure 8. (Right) The cutoff-energy dependence of the gap in a semiconducting nanotube. The gap increases logarithmically with the thickness after being scaled by $2\pi\gamma/L$.

on the diameter cannot be reproduced in the conventional local-density approximation used in first-principles calculations.

If we employ the same scheme, we can calculate the self-energy for the linear bands with $n = 0$ in metallic CN's, giving a gapless linear band with a renormalized velocity. In fact, although each term of perturbation expansion of the self-energy is known to exhibit a divergence, the RPA self-energy itself does not diverge because of the cancellation of a divergent polarization function. This result is in clear contradiction with the fact that only a charge-density and a spin-density excitation can exist and there are no well-defined quasi-particle excitations in systems with a linear dispersion,^{51,52} leading to the breakdown of the Fermi liquid picture.

This apparent inconsistency arises from the way of determining the quasi-particle energy from the self-energy. Even in RPA, the spectral function (the imaginary part of the Green's function) exhibits double sharp peaks in a system with only metallic linear bands as shown in Fig. 9. This peak splitting, into charge-density and spin-density excitations presumably, is a result of the divergent behavior of the polarization function and qualitatively in agreement with that of the spectral function for a Tomonaga-Luttinger liquid reported in refs. 53 and 54. For the parabolic bands both in semiconducting and metallic CN's, no singular behavior appears in the polarization function and therefore quasi-particle states are expected to give a good picture of their low-energy excitations.

4. SUMMARY AND CONCLUSION

In summary, an electron in a nanotube is a massless neutrino on a cylinder surface with a fictitious Aharonov-Bohm flux determined by its structure. A nanotube becomes a metal or a semiconductor, depending on whether the amount of the flux vanishes or not. In the presence of an external magnetic flux, the band structure changes due to a large Aharonov-Bohm effect. One important feature of the neutrino equation is the presence of a topological singularity at the origin of the wave-vector space, leading to the absence of backward scattering and the presence of a perfectly conducting channel even in the presence of scatterers.

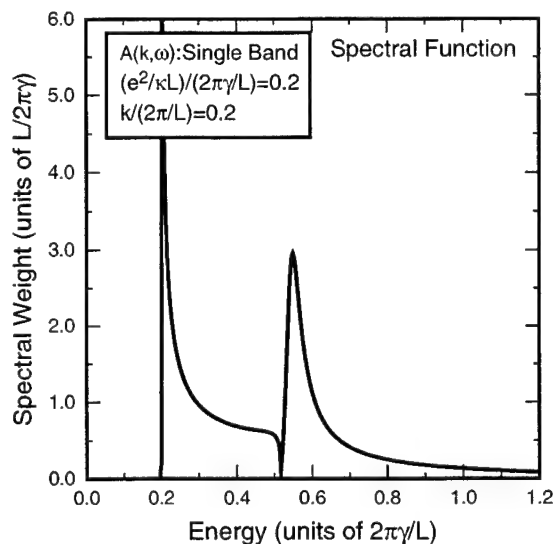


Figure 9. An example of the spectral function in a single linear-band model calculated in RPA. The energy of the first peak corresponds well to the spin-density excitation and the second to the charge-density excitation.

Optical absorptions are appreciable only for polarization parallel to the axis. Because of the dimensionality of a nanotube, excitonic effects are expected to play important roles in optical spectra. Explicit calculations of the band structure with the inclusion of effects of electron-electron interactions in several approximation schemes demonstrate a considerable band-gap enhancement depending on the strength of a dimensionless interaction parameter. Calculations of optical excitation spectra show that excitonic effects can also be important.

ACKNOWLEDGMENTS

This work was supported in part by a 21st Century COE Program at Tokyo Tech "Nanometer-Scale Quantum Physics" and by Grants-in-Aid for Scientific Research and for COE (12CE2004 "Control of Electrons by Quantum Dot Structures and Its Application to Advanced Electronics") from Ministry of Education, Culture, Sports, Science and Technology Japan. Numerical calculations were performed in part using the facilities of the Supercomputer Center, Institute for Solid State Physics, University of Tokyo.

REFERENCES

1. S. Iijima, *Nature (London)* **354**, 56 (1991).
2. N. Hamada, S. Sawada, and A. Oshiyama, *Phys. Rev. Lett.* **68**, 1579 (1992).
3. J. W. Mintmire, B. I. Dunlap, and C. T. White, *Phys. Rev. Lett.* **68**, 631 (1992).
4. R. Saito, M. Fujita, G. Dresselhaus, and M. S. Dresselhaus, *Phys. Rev. B* **46**, 1804 (1992); *Appl. Phys. Lett.* **60**, 2204 (1992).
5. M. S. Dresselhaus, G. Dresselhaus, and R. Saito, *Phys. Rev. B* **45**, 6234 (1992).
6. R. A. Jishi, M. S. Dresselhaus, and G. Dresselhaus, *Phys. Rev. B* **47**, 16671 (1993).
7. K. Tanaka, K. Okahara, M. Okada and T. Yamabe, *Chem. Phys. Lett.* **191**, 469 (1992).
8. Y. D. Gao and W. C. Herndon, *Mol. Phys.* **77**, 585 (1992).
9. D. H. Robertson, D. W. Brenner, and J. W. Mintmire, *Phys. Rev. B* **45**, 12592 (1992).
10. C. T. White, D. C. Robertson, and J. W. Mintmire, *Phys. Rev. B* **47**, 5485 (1993).
11. H. Ajiki and T. Ando, *J. Phys. Soc. Jpn.* **62**, 1255 (1993).
12. A. M. Rao, E. Richter, S. Bandow, B. Chase, P. C. Eklund, K. W. Williams, M. Menon, K. R. Subbaswamy, A. Thess, R. E. Smalley, G. Dresselhaus, and M. S. Dresselhaus, *Science* **275**, 187 (1997).

13. C. H. Olk and J. P. Heremans, *J. Mater. Res.* **9**, 259 (1994).
14. J. W. Wildoer, L. C. Venema, A. G. Rinzier, R. E. Smalley, and C. Dekker, *Nature (London)* **391**, 59 (1998).
15. A. Hassanien, M. Tokumoto, Y. Kumazawa, H. Kataura, Y. Maniwa, S. Suzuki, and Y. Achiba, *Appl. Phys. Lett.* **73**, 3839 (1998).
16. H. Ajiki and T. Ando, *J. Phys. Soc. Jpn.* **62**, 2470 (1993). [Errata, *J. Phys. Soc. Jpn.* **63**, 4267 (1994).]
17. H. Ajiki and T. Ando, *Physica B* **201**, 349 (1994); *Jpn. J. Appl. Phys. Suppl.* **34-1**, 107 (1995).
18. T. Ando, *J. Phys. Soc. Jpn.* **66**, 1066 (1997).
19. N. A. Viet, H. Ajiki, and T. Ando, *J. Phys. Soc. Jpn.* **63**, 3036 (1994).
20. H. Suzuura and T. Ando, *Proceedings of 25th International Conference on the Physics of Semiconductors*, edited by N. Miura and T. Ando (Springer, Berlin, 2001), p. 1525.
21. H. Ajiki and T. Ando, *J. Phys. Soc. Jpn.* **64**, 260 (1995); **65**, 2976 (1996).
22. H. Ajiki and T. Ando, *J. Phys. Soc. Jpn.* **64**, 4382 (1995).
23. T. Ando, *J. Phys. Soc. Jpn.* **69**, 1757 (2000).
24. T. Ando, T. Nakanishi, and M. Igami, *J. Phys. Soc. Jpn.* **68**, 3994 (1999).
25. M. Igami, T. Nakanishi, and T. Ando, *J. Phys. Soc. Jpn.* **70**, 481 (2001).
26. T. Yaguchi and T. Ando, *J. Phys. Soc. Jpn.* **70**, 3641 (2001); *ibid* **71**, 2224 (2002).
27. H. Suzuura and T. Ando, *Physica E* **6**, 864 (2000); *Mol. Cryst. Liq. Cryst.* **340**, 731 (2000); *Phys. Rev. B* **65**, 235412 (2002).
28. P. R. Wallace, *Phys. Rev.* **71**, 622 (1947).
29. G. S. Painter and D. E. Ellis, *Phys. Rev. B* **1**, 4747 (1970).
30. J. C. Slonczewski and P. R. Weiss, *Phys. Rev.* **109**, 272 (1958).
31. J. P. Lu, *Phys. Rev. Lett.* **74**, 1123 (1995).
32. W. -D. Tian and S. Datta, *Phys. Rev. B* **49**, 5097 (1994).
33. A. Fujiwara, K. Tomiyama, H. Suematsu, M. Yumura, and K. Uchida, *Phys. Rev. B* **60**, 13492 (1999).
34. S. Zaric, G. N. Ostojic, J. Kono, X. Wei, M. S. Strano, V. C. Moore, R. H. Hauge, and R. E. Smalley, *Proceedings of 6th International Symposium on New Phenomena in Mesoscopic Structures, Maui, USA, 2003* (in press).
35. T. Ando, T. Nakanishi, and R. Saito, *J. Phys. Soc. Jpn.* **67**, 2857 (1998).
36. M. V. Berry, *Proc. Roy. Soc. London* **A392**, 45 (1984).
37. T. Ando and T. Nakanishi, *J. Phys. Soc. Jpn.* **67**, 1704 (1998).
38. T. Nakanishi and T. Ando, *J. Phys. Soc. Jpn.* **68**, 561 (1999).
39. T. Ando and H. Suzuura, *J. Phys. Soc. Jpn.* **71**, 2753 (2002).
40. N. H. Shon and T. Ando, *J. Phys. Soc. Jpn.* **67**, 2421 (1998).
41. T. Ando, Y. Zheng, and H. Suzuura, *J. Phys. Soc. Jpn.* **71**, 1318 (2002).
42. R. Loudon, *Am. J. Phys.* **27**, 649 (1959).
43. R. J. Elliot and R. Loudon, *J. Phys. Chem. Solids* **8**, 382 (1959); **15**, 196 (1960).
44. H. Kataura, Y. Kumazawa, Y. Maniwa, I. Umez, S. Suzuki, Y. Ohtsuka and Y. Achiba, *Synth. Met.* **103**, 2555 (1999).
45. M. Ichida, S. Mizuno, Y. Tani, Y. Saito, and A. Nakamura, *J. Phys. Soc. Jpn.* **68**, 3131 (1999).
46. H. Sakai, H. Suzuura, and T. Ando, *J. Phys. Soc. Jpn.* **72**, 1698 (2003).
47. H. Sakai, H. Suzuura, and T. Ando, *Physica E* (in press).
48. L. Hedin, *Phys. Rev.* **139**, A796 (1965); A. W. Overhauser, *Phys. Rev. B* **3**, 1888 (1971); L. Hedin and S. Lundqvist, *Solid State Physics*, ed. F. Seitz, D. Turnbull and H. Ehrenreich (Academic, New York, 1969) Vol. 23, p. 1.
49. T. M. Rice, *Ann. Phys. (N.Y.)* **31**, 100 (1965).
50. D. F. Du Bois, *Ann. Phys. (N.Y.)* **7**, 174 (1959).
51. S. Tomonaga, *Prog. Theor. Phys.* **5**, 544 (1950).
52. J. M. Luttinger, *J. Math. Phys.* **4**, 1154 (1963).
53. J. Voit, *Phys. Rev. B* **47**, 6740 (1993).
54. V. Meden and K. Schonhammer, *Phys. Rev. B* **46**, 15753 (1992).

Epitaxial single crystalline inorganic nanowires and nanowalls: growth morphogenesis and applications in nano-optoelectronics

Hou T. Ng*, Pho Nguyen, Yi P. Chen, Aaron Mao, Jie Han, M. Meyyappan
Center for Nanotechnology, NASA Ames Research Center, Moffett Field, CA, USA 94035

ABSTRACT

Inorganic single crystal nanowires and nanowalls which exhibit rich growth morphogenesis are shown. More specifically, these were grown on lattice-matched substrates, which facilitate their specific growth directions with respect to the substrates' planes. Structural and optical characterizations suggest high single crystallinity of these nanostructures and possible applications in nano-optoelectronics are discussed.

Keywords: nanowires, nanowalls, inorganic, directional growth, zinc oxide, indium oxide, tin oxide, metal oxide, resonance Raman spectroscopy, photoluminescence spectroscopy

1. INTRODUCTION

Wide band gap metal oxides such as ZnO, ZrO₂, SnO₂, In₂O₃, and CdO have important roles in numerous applications ranging from energy storage/conversion¹, liquid crystal displays², gas sensors³ to microelectronics⁴. In particular, the single crystalline form of these materials has been explored recently in nanoscale science and technology. More recently, research and development have been conducted on metal oxide nanostructures, predominantly in the form of nanowires, for potential applications in high-sensitivity sensor, optoelectronic, field-emission, electronic, and memory devices.⁵⁻⁷

Various synthesis approaches have been demonstrated, which include vapor transport⁸ and laser ablation⁹ on a variety of substrates. However, common to other nanowire syntheses, growth directionality control (with respect to the substrate) and direct integration (on the same substrate) into functional devices remain as two significant challenges. To realize and maximize the true potential of these nanostructures for advanced applications in nanoelectronics and optoelectronics, reproducible synthesis of 1-dimensional (D) nanowires with controlled directionality and morphology is critical. Equally important, a means of providing ideal and direct electrical interface to the nanowires without disrupting their structural integrity would facilitate subsequent nanoscale device integration and help achieving good device performance.

To avoid the usual pick-and-place methods of manipulating and aligning horizontally lying nanowires to fabricate prototype testing platforms,^{10,11} a proposed solution is to grow single crystalline nanowires epitaxially on a lattice-matched substrate with the major nanowire growth direction orthogonal to the substrate plane and to use this integrated platform for direct device fabrication. Ideally, the substrate should be electrically conductive.

In this work, we show the controlled synthesis of directional metal oxide nanowires on single crystal or well-defined substrates. By tweaking the growth conditions, quasi-3D nanostructures, for example a matrix consisting of ZnO nanowires and nanowalls, can be obtained on these substrates easily and reproducibly. The structural and optical properties of the nanowires were characterized to reveal their high single crystallinity.

2. EXPERIMENTAL

In the synthesis of the metal oxide nanowires, carbothermal reduction followed by catalyst-mediated heteroepitaxial growth was used¹². In general, powdered metal oxide was pulverized and mixed thoroughly with graphite powder (99.99% purity) in a 1:1 weight ratio. The mixture was then placed upstream of a substrate inside a horizontal tube furnace. The substrate was coated with 2 nm thickness of catalyst, for example gold via ion beam sputtering. Uniform nanowire growth was achieved at respective temperatures with argon (Ar, 99.999%) as the carrier gas.

Field-emission scanning electron microscopy (SEM) analysis was performed using a field emission Hitachi S4000 while transmission electron microscopy (TEM) analysis was performed using a Phillips CM20 with an accelerating voltage of 200 kV.

In the photoluminescence spectroscopy, the photoluminescence signals of the nanowires at room temperature were generated in the backscattering geometry by excitation with the 325 nm line of a He-Cd laser and were dispersed by a 1m double-grating monochromator before being detected by a GaAs detector.

UV resonant Raman scattering was performed with a Renishaw microspectrometer with a 3600 grooves/mm grating in the backscattering configuration. A He-Cd laser ($\lambda = 325$ nm) was used as the excitation source. The spectrum was taken with 60 s accumulation from a $2 \mu\text{m}^2$ spot.

3. RESULTS AND DISCUSSION

Using a combination of carbothermal reduction and catalyzed-assisted heteroepitaxial deposition approach, a variety of metal oxide nanowires such as ZnO, SnO_2 and In_2O_3 can be obtained successfully. Figure 1 shows a typical SEM image of as-grown ZnO nanowire arrays on a *m*-sapphire substrate. A majority of the nanowires grow into regular and yet intricate arrays, with their longitudinal axes making an angle of ~ 30 degrees with the substrate normal. From the corresponding top view, the arrays present themselves in a relatively well-aligned geometry, with the end planes exhibiting either regular or distorted hexagonal facets. When an α -sapphire substrate or highly oriented pyrolytic graphite (HOPG) are used, vertical ZnO nanowires are obtained as shown in Fig. 2, due to the ideal lattice-match between the epitaxial (0001) plane of ZnO and that of the substrates.^{12,13}

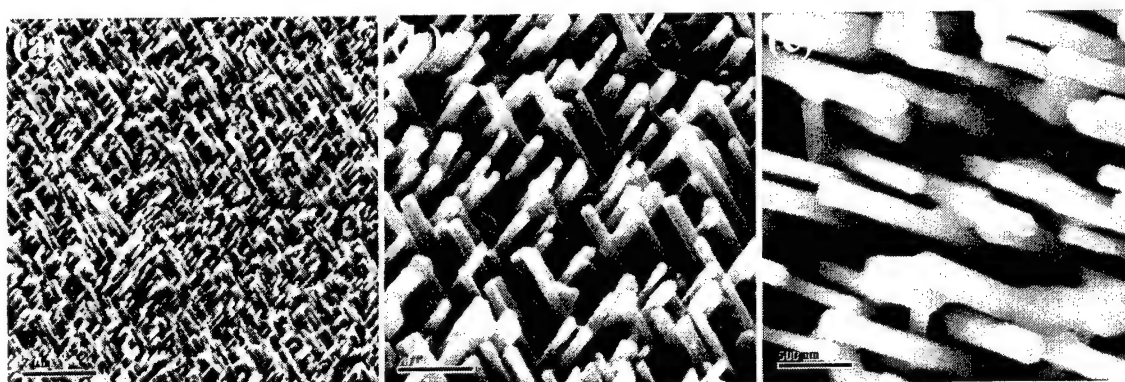


Fig. 1. FE-SEM images of ZnO nanowire arrays on *m*-sapphire substrates. (a) Perspective (45°) SEM image; (b) A zoom-in SEM image and (c) a top view SEM image, showing the characteristic hexagonal cross-section of the nanowires.

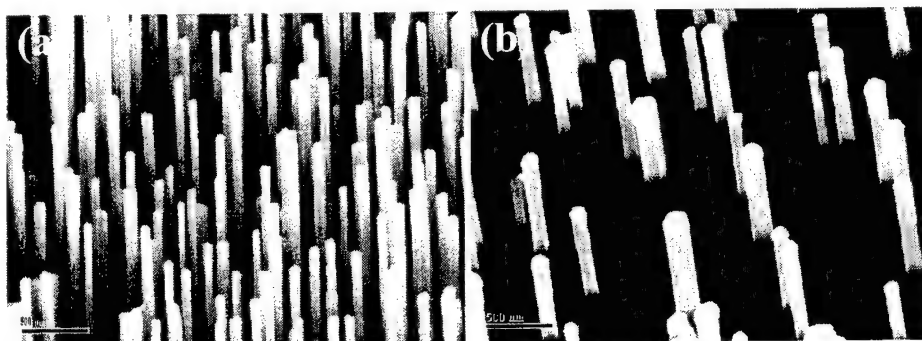


Fig. 2. FE-SEM images of vertically aligned (with respect to substrate plane) ZnO nanowire arrays. (a) Perspective SEM images of ZnO nanowires on α -sapphire substrate and (b) on HOPG substrate. The catalysts at the terminating growth front of the nanowires could be clearly observed in (b).

Further evidences of interfacial effect on the directional growth of nanowires could also be observed in the case of In-doped SnO_2 nanowires. Representative SEM images (top views) of mesh-like In- SnO_2 nanowire networks are shown in

Fig. 3a and b. These networks present complex 3D structures comprising of individual nanowires; in contrast with previous SnO networks which involve a different growth mode¹⁴, leading to structurally connected junctions.

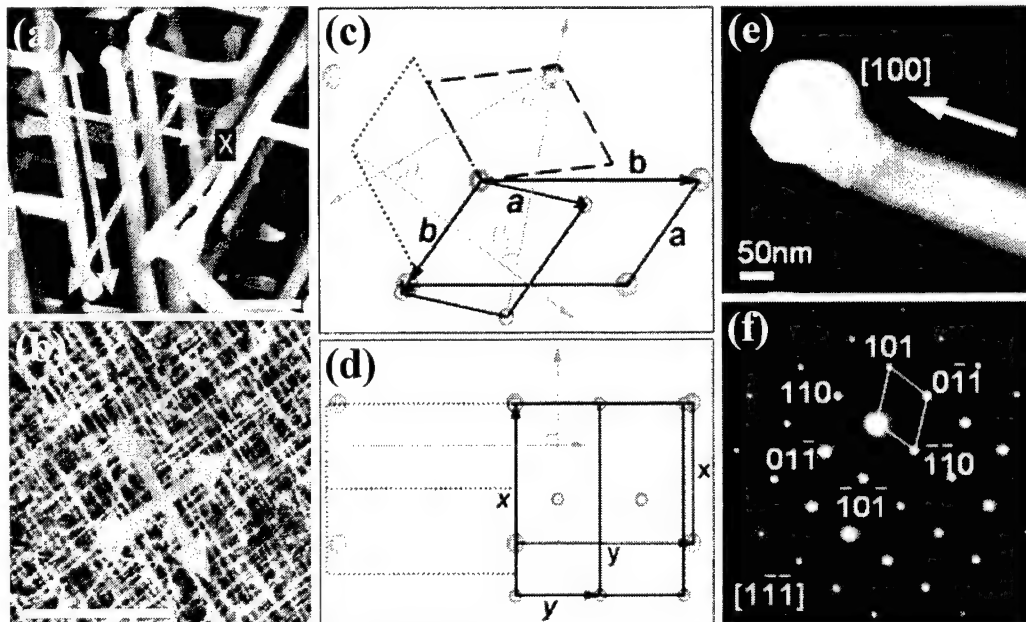


Fig. 3. (a) Top view SEM image of In-SnO₂ nanowires on *a*-sapphire. (b) Top view SEM image of similar nanowires on *m*-sapphire. (c) Epitaxial relationship of a unit cell of (110) SnO₂ with that of *a*-sapphire and (d) on *m*-sapphire. Red circles represent the oxygen atoms of sapphire while those in solid grey refer to the tin atoms of SnO₂. (e) A TEM image showing the catalytic head at the terminating front of the nanowire. (f) A selective-area electron diffraction pattern of the nanowire.

The nanowires are observed to project at ~ 45 degrees with respect to the substrate normal. Pseudo three- and four-fold symmetries, as indicated respectively by green arrows, are observed. Since the In-SnO₂ nanowires possess a tetragonal rutile structure with preferred growth direction along the [100] direction (see Fig. 3 (e)), minimum epitaxial lattice mismatch with (110) (*a* face) of optical sapphire could be achieved with its (110) plane as shown in Fig. 3(c). The unit cell of (110) SnO₂, represented by the grey Sn atoms with lattice constants *a* and *b*, is found to match reasonably well along three different directions (also the directions of (100) plane with respect to (110)) with that of the *a*-sapphire (lattice constants *a* and *b*) and found to agree with the experimental values.

Lattice mismatches between *ba*, *ca* and *aa* are calculated to be $\sim 6.03\%$, $\sim 6.03\%$ and $\sim 8.92\%$ respectively with $\theta_1 = \theta_2$ ($\sim 64.56^\circ$) and $\theta_3 \sim 50.88$. These geometrical angles agree well with the experimental values. Due to mirror images of the unit cell, nanowires can be grown in opposite directions along each *x*, *y* and *z* directions. On (100) sapphire (*m* face), however, preferred lattice matches with SnO₂ (110) are found only along two major directions which are orthogonal to each other. Lattice mismatches between *2yy* and *xy* are $\sim 1.89\%$ and $\sim 3.14\%$, comparatively lower than on *a*-sapphire. This evidently explains the different directional growth phenomena and the more favorable growth leading to higher nanowire density in the latter. The angle between (110) and (100) of SnO₂ is calculated to be exactly 45° , which coincides well with the nanowires' projected angles. The high single crystallinity of the In-SnO₂ nanowire can be indirectly inferred from the well-defined selective-area electron diffraction pattern as shown in Fig. 3 (f), taken perpendicular to the core of the nanowire.

By tweaking the growth conditions, an electrical contact to the nanowire can be introduced *in-situ* during the growth process prior to the nanowire growth. This is achieved in the case of In₂O₃ nanowires, as shown in Fig. 4. An SEM image of the nanowires reveals a general structure consisting of a square columnar vertical body and a pyramidal base. Each nanowire is observed to taper gradually towards the growth front and terminate with a nano-sized Au catalyst.

Uniform coverage of the nanowires is typically observed on the entire substrate where the Au catalysts are present. A uniform buffer layer of In_2O_3 resided under the nanowires. Each as-synthesized nanowire resembles a pillar having “nanothreads” cladding it. These nanothreads reside along the nanowire main growth axis and resemble regularly spaced well-faceted triangular nano-wedges.¹⁵

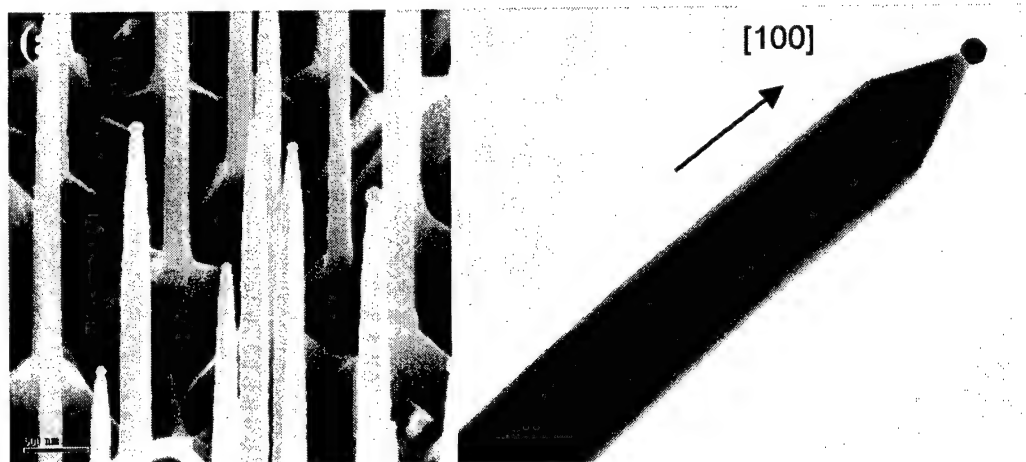


Fig. 4. (a) An SEM image showing regular arrays of In_2O_3 nanowires grown from a buffer layer of itself. (b) A TEM image of a In_2O_3 nanowire, showing a well-defined Au catalyst at the tip of the nanowire.

Besides 1D nanowires, intricate 2D and quasi-3D nanostructures can also be obtained by varying the growth conditions and catalyst configurations. In the ZnO system, when the thickness of the Au film (acting as the catalyst) is maintained above the threshold limit of 15 Å, highly intricate quasi-3D nanostructures (Fig. 5a) which comprise of an array of vertical 1D ZnO nanowires on top of a 2D network of intricate nanowalls are obtained. SEM image further reveals a random honeycomb-like pattern, resembling typical structures observed from anodization of thin film aluminum. The nanowires are observed to grow from the ‘nodes’ of the nanowalls. The average diameters of the nanowires and the thickness of the nanowalls are of the same order of magnitude (~ 80 nm). By controlling specifically the growth time, 2D network of nanowalls can be obtained otherwise (Fig. 5b).

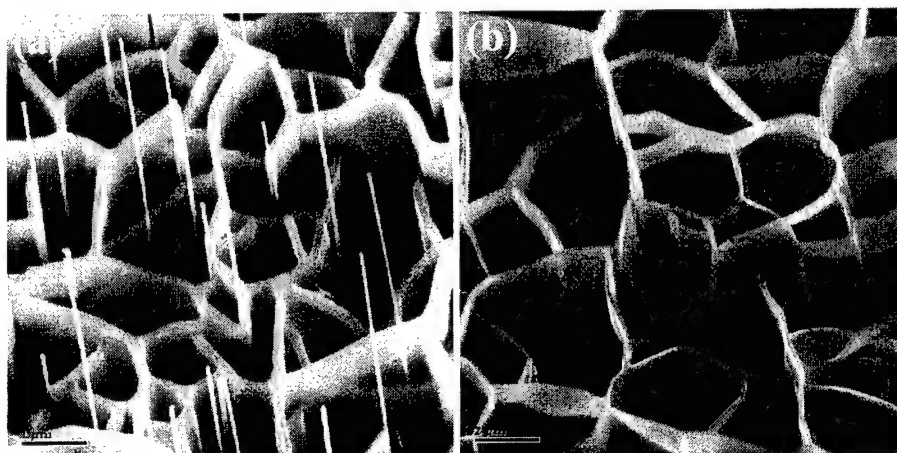


Fig. 5. (a) Perspective SEM image of quasi- 3D nanostructures on α -sapphire. (b) Perspective SEM image of 2D nanowalls on α -sapphire.

An understanding of the optical properties of nanowires is important for their successful applications in optoelectronics and photonics. Photoluminescence (PL) and resonance Raman spectroscopy are used to investigate the fundamental optical properties of these metal oxide nanowires. Figure 6 shows PL measurement of ZnO nanowires. The mean

diameter of the nanowires is ~ 100 nm. We observed strong emission at ~ 380 nm (3.26 eV) for the nanowires and a faint blue-green emission at ~ 490 nm. The former is in good agreement with the typically reported free exciton peak position^{16,17} and could be attributed to UV near band-edge emission while the latter to singly ionized oxygen vacancy in the ZnO nanowires.¹⁸ Although it is known¹⁹ that presence of Cu^+ and Cu^{2+} ions in trace amounts in ZnO thin film could provide the green luminescence via either donor-acceptor pair or donor-hole recombination, we have ruled out such a possibility since high purity ZnO and graphite powder (both 99.999% purity) were used and elemental analysis confirmed absence of Cu.

The PL full width at half maximum (FWHM) values at ~ 380 nm was calculated to be ~ 0.13 eV. These are better than that observed in ZnO powders (0.22 eV) and comparable to high-quality undoped ZnO thin films (0.11 eV) and ZnO nanowires (0.12 eV). The narrow FWHM indeed suggests a narrow size distribution of the nanowires, as also evident from the SEM images.

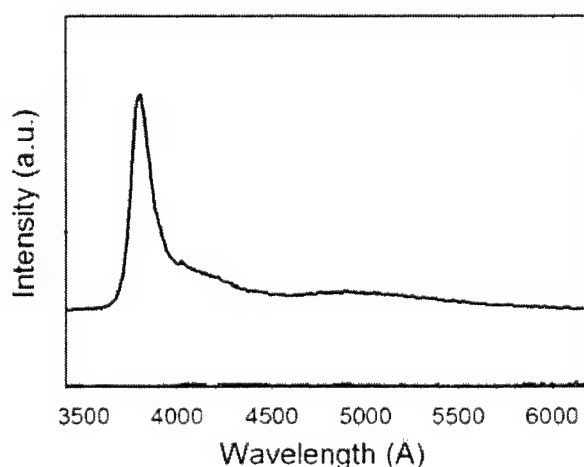


Fig. 6. A PL spectrum of ZnO nanowires on α -sapphire substrate.

Figure 7 shows a resonant Raman spectrum of the ZnO nanowires. Four major bands, centred at 577, 1152, 1734 and 2319 cm^{-1} , with bandwidths at 30, 46, 55, 53 cm^{-1} respectively are observed. They are attributed to the Raman longitudinal optical (LO) phonon scattering and its overtones.²⁰⁻²² The zone center optical phonons of wurtzite ZnO are: $A_1 + 2E_2 + E_1$. Since the exciting photon energy is in resonance with the electronic interband transition energy, polar symmetry A_1 and E_1 are the dominant modes. Such multiphonon scattering processes have also been reported for single crystalline bulk ZnO²². The Lorentzian curve fitting results show that the first-order LO mode consists mostly of A_1 mode. The necessity to include A_1 LO fitting suggests that the ZnO nanowires exhibit phonon quantum confinement effect.

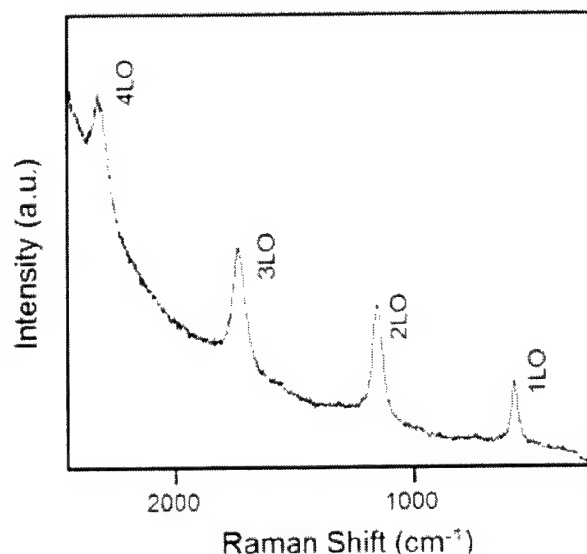


Fig. 7. A resonant Raman spectrum of ZnO nanowires.

4. CONCLUSION

In summary, we have shown the importance of substrate engineering and growth conditions in obtaining well-aligned nanowires and other intricate nanostructures. High quality single crystal nanowires were characterized structurally and optically. An understanding of these properties is crucial and allows fine-tuning of the desirable structures for future nanoscale optoelectronics and photonics applications.

REFERENCES

1. J. McBreen, S. Srinivasan, A. C. Khandkar, B. V. Tilak *Electrode Materials and Process for Energy Conversions and Storage*, Electrochemical Society, 1997.
2. V. G. Chigrinov, *Liquid Crystal Devices: Physics and Applications*, Artech House, London, 1999.
3. A. Mandelis, C. Christofides, *Physics Chemistry and Technology of Solid State Gas Sensor Devices*, Wiley-Interscience, 1993.
4. M. J. Madon, *Fundamentals of Microfabrication: The Science of Miniaturization*, CRC Press, 2002.
5. C. Li, D. Zhang, X. Liu, S. Han, T. Tang, J. Han, C. Zhou, *Appl. Phys. Lett.* 82, 1613, 2003.
6. H. Jia, Y. Zhang, X. Chen, J. Shu, X. Luo, Z. Zhang, D. Yu, *Appl. Phys. Lett.* 82, 4146, 2003.
7. D. Zhang, X. Liu, S. Han, T. Tang, C. Zhou, W. Fan, J. Koehne, J. Han, M. Meyyappan, A. M. Rawlett, D. W. Price, J. M. Tour, *Appl. Phys. Lett.* 82, 645, 2003.
8. X. C. Wu, J. M. Hong, Z. J. Han, Y. R. Tao, *Chem. Phys. Lett.* 373, 28, 2003.
9. C. Li, D. Zhang, S. Han, X. Liu, T. Tang, C. Zhou, *Adv. Mater.* 15, 143, 2003.
10. X. Duan, Y. Huang, R. Agarwal, C. M. Lieber, *Nature* 421, 241, 2003.
11. B. Messer, J. H. Song, P. Yang, *J. Am. Chem. Soc.* 122, 10232, 2000.
12. H. T. Ng *et al.* *Appl. Phys. Lett.* 82, 2023, 2003.
13. H. T. Ng, J. Li, M. Smith, P. Nyugen, A. Cassell, J. Han, M. Meyyappan, *Science* 300, 1249, 2003.
14. Z. L. Wang, Z. Pan, *Adv. Mater.* 14, 1029, 2002.
15. P. Nguyen, H. T. Ng, T. Yamada, M. K. Smith, J. Li, J. Han, M. Meyyappan, *Nano Letters* 4, 651, 2004.
16. M. H. Huang, Y. Wu, H. Feick, N. Tran, E. Weber and P. Yang, *Adv. Mater.* 13, 113, 2001.
17. Y. Chen, D. M. Bagnall, H. J. Koh, K. T. Park, K. Hiraga, Z. Zhu and T. Yao, *J. Appl. Phys.* 84, 3912, 1998.

18. S. Bethke, H. Pan and B. W. Wessels, *Appl. Phys. Lett.* 52, 138, 1998.
19. N. Y. Garces, L. Wang, L. Bai, N. C. Giles, L. E. Halliburton and G. Cantwell, *Appl. Phys. Lett.* 81, 622, 2002.
20. M. Tzolov, N. Tzenov, D. Dimova-Malinovska, M. Kalitzova, C. Pizzuto, G. Vitali, G. Zollo and I. Ivanov, *Thin Solid Films* 379, 28, 2000.
21. M. Tzolov, N. Tzenov, D. Dimova-Malinovska, M. Kalitzova, C. Pizzuto, G. Vitali, G. Zollo and I. Ivanov, *Thin Solid Films* 396, 274, 2001.
22. J. Scott, *Phys. Rev. B* 2, 1209, 1970.

From Nanowire Lasers to Quantum Wire Lasers

Peidong Yang
Department of Chemistry
University of California, Berkeley, California 94720

Abstract

Vapor-liquid-solid epitaxy process has been developed to synthesize high quality semiconductor nanowire arrays. The nanowires generally are single crystalline and have diameters of 10-200 nm and aspect ratios of 10-100. There is much current interest in the optical properties of these semiconductor nanowires, as the cylindrical geometry and strong two-dimensional confinement of electrons, holes, and photons makes them particularly attractive as potential building blocks for nanoscale electronics and optoelectronics devices. We recently reported the first study of laser action and nonlinear optical mixing in individual zinc oxide (ZnO) and GaN nanowires, demonstrating the potential of these structures as room temperature nanoscopic coherent light sources and frequency converters. These efforts further led to the demonstration of ZnO nanoribbon laser as well as GaN-based quantum wire lasers.

Keywords: Nanowires, lasers, quantum wires.

1. Introduction

Nanoscale one-dimensional (1D) materials have stimulated great interest due to their importance in basic scientific research and potential technology applications¹. A lot of unique and fascinating properties have been proposed and demonstrated for this class of materials, such as metal-insulator transition, superior mechanic toughness, higher luminescence efficiency, enhancement of thermoelectric figure of merit and lowered lasing threshold¹. 1D materials can also be used as building blocks to construct new generation of nanoscale electronic circuits and photonics. Below, we briefly summarize our work on the optical property study of these semiconductor nanowires, particularly those of ZnO and GaN.

One of the most important techniques for nanowire growth is the vapor-liquid-solid (VLS) process². It is further possible to apply the conventional epitaxial crystal growth technique into this VLS process to achieve orientation control. By choosing suitable substrate whose lattice constants match with the desired nanowire crystal structure, the growth direction can be dictated by the choosing substrate orientation. This technique, vapor-liquid-solid epitaxy (VLSE), is particularly powerful in controlled synthesis of high quality nanowire arrays. Nanowires generally have preferred growth direction. For example, ZnO prefer to grow along $\langle 001 \rangle$ direction. ZnO nanowires grow epitaxially on *a*-plane (110) sapphire substrate³. ZnO nanowires have wurtzite structure with lattice constant $a=3.24 \text{ \AA}$ and $c=5.19 \text{ \AA}$. ZnO *a* axis and sapphire *c* axis are related almost by a factor of 4 (mismatch less than 0.08% at room temperature). Fig. 1 shows vertical ZnO nanowire arrays on *a*-plane sapphire substrate. Their diameters range from 70-200 nm and lengths can be adjusted between 2-10 microns. Similar level of growth control can be achieved for the GaN system (Fig. 1)⁴.

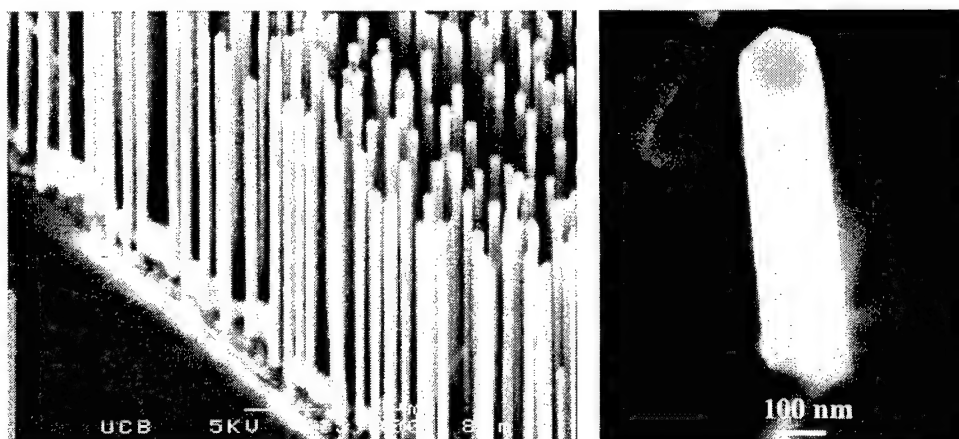


Fig. 1 Scanning electron microscopy images of (a) ZnO nanowire arrays on a plane sapphire wafer and (b) GaN nanowire.

In addition to these pure semiconductor nanowires, coaxial nanowire is an important class of nanowire heterostructures that are both fundamentally interesting and have significant technological potential. Coaxial structures can be fabricated by coating an array of nanowires with a conformal layer of a second material. The coating method chosen should allow excellent uniformity and control of the sheath thickness. Cladding nanowires with amorphous layers of SiO_2 or carbon is synthetically facile and routinely demonstrated in the literature. A more exciting and difficult task, with greater technological import, is to form heterostructures of two single-crystalline semiconductor materials. We reported the synthesis of $\text{GaN}/\text{Al}_{0.75}\text{Ga}_{0.25}\text{N}$ core-sheath structures using a chemical vapor transport method (Fig. 2)⁵. It is important to point out that the choice of appropriate core and sheath materials with similar crystallographic symmetries and lattice constants is essential to achieve the deposition of single-crystalline epitaxial thin film sheath structures, thereby producing high quality materials.

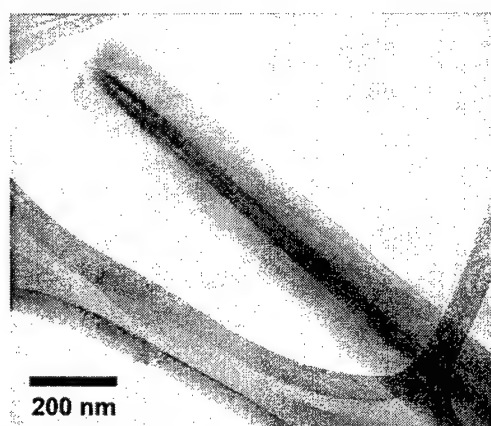


Figure 2. Transmission electron microscopy image of a GaN/AlGaIn core-sheath nanowire. [Reprinted with permission from Ref. 5, Copyright American Chemical Society, 2003]

2. Nanowire Lasing

Nanowires with flat end facets can be exploited as optical resonance cavities to generate coherent light on the nanoscale. Room temperature UV lasing has been demonstrated in our laboratory for the ZnO and GaN nanowire systems with epitaxial arrays³, combs⁶, ribbons⁷ and single nanowires^{8,9,10}(Fig. 3). ZnO and GaN are wide bandgap semiconductors (3.37, 3.42 eV) suitable for ultraviolet-blue optoelectronic applications. The large binding energy for excitons in ZnO (~60 meV) permits lasing via exciton-exciton recombination at low excitation conditions, while GaN is known to support an electron-

hole plasma (EHP) lasing mechanism. In a series of studies, we have applied far-field imaging and near-field scanning optical microscopy (NSOM) to understand photon confinement in these small ($d \leq \lambda$, where d is the nanowire diameter and λ is the wavelength) cavities.

Well-faceted nanowires with diameters from 100 nm to 500 nm support predominantly axial Fabry-Perot waveguide modes (separated by $\Delta\lambda = \lambda^2/[2Ln(\lambda)]$, where L is the cavity length and $n(\lambda)$ is the group index of refraction) due to the large diffraction losses suffered by transverse trajectories. Diffraction prevents smaller wires from lasing; PL is lost instead to the surrounding radiation field. ZnO and GaN nanowires produced by VLS growth are cavities with low intrinsic finesse (F) due to the low reflectivity (R) of their end faces¹¹ (~19%) (where $F = \pi R^{1/2}/(1-R)$), such that the confinement time for photons is short and photons travel an average of one to three half-passes before escaping from the cavity. Far-field imaging indicates that PL and lasing emission are localized at the ends of nanowires, which suggests strong waveguiding behavior that is consistent with axial Fabry-Perot modes (Fig. 3).

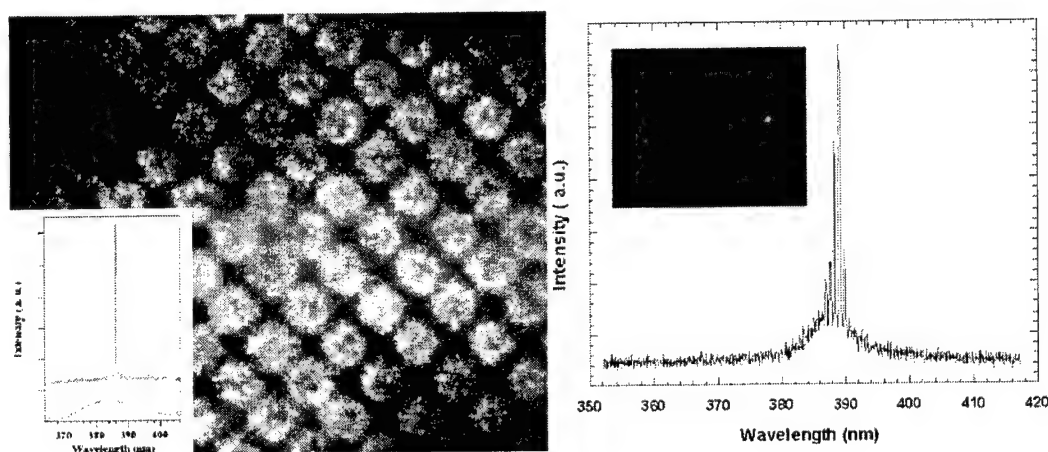


Fig. 3. (Left). Far-field optical image of patterned lasing ZnO nanowire arrays. Inset is typical emission spectrum below and above lasing threshold. (Right). Lasing spectrum from an individual ZnO nanoribbon, inset is the far-field optical image of the waveguiding ZnO nanoribbon.

The transition from spontaneous PL to optical gain is achieved by exciting a high density of carriers via pulsed UV illumination. The dependence of nanowire emission on pump power typically shows three regimes¹⁰, corresponding to (I) spontaneous emission, followed by (II) stimulated emission (lasing) above a certain threshold fluence and (III) saturation due to gain-pinning at high pump power. The lasing thresholds observed in nanowires vary across several orders of magnitude as a consequence of differing nanowire dimensions, quality of the particular nanowire cavities, and coupling to the substrate (the lowest threshold observed for ZnO is $\sim 70 \text{ nJ cm}^{-2}$; for GaN, $\sim 500 \text{ nJ cm}^{-2}$). The simultaneous appearance of narrow cavity modes (line widths 0.25 – 1.0 nm) spaced in agreement with cavity dimensions confirms the lasing behavior. The spectral position of the ZnO gain profile is typically nearly independent of pump power at the moderate pumping intensities that correspond to exciton-exciton lasing, but exhibits significant red-shift near saturation as band filling and charge screening induce an exciton-to-EHP transition. GaN nanowires, on the other hand, show a consistent red-shift from threshold to saturation due to band-gap renormalization. Polarization of the various modes has also been studied¹⁰.

Recent work in our labs has focused on two aspects of lasing in one-dimensional ZnO structures: its ultrafast dynamics in nanowires and its manipulation in nanoribbons⁷. Time-resolved second-harmonic generation (TR-SHG) and transient photoluminescence spectroscopy were used¹² to probe carrier relaxation dynamics near the lasing threshold as well as under gain saturation conditions. Above the lasing threshold, a bi-exponential decay of the PL was observed, with a fast component ($\sim 10 \text{ ps}$) corresponding to exciton-exciton lasing and a slow component ($\sim 70 \text{ ps}$) due to free exciton spontaneous emission. The fast process shifted to shorter times with increased pumping power, reflecting the

increasing influence of EHP dynamics at higher carrier densities (Fig. 4). The SHG transient, which monitors the overall repopulation of the valence bands after excitation, showed a fast component with a decay time that decreased from 5 ps to ~ 1 ps from threshold to saturation due to a multi-body scattering process consisting of both radiative and nonradiative events.

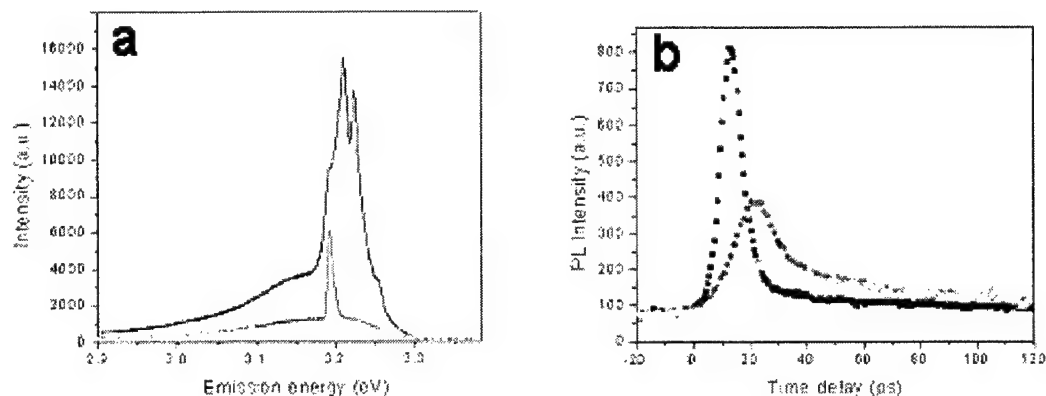


Figure 4: (a) PL/lasing spectra of single ZnO nanowire near the lasing threshold (excitation $\sim 1 \mu\text{J}/\text{cm}^2$) and (b) transient PL response. Long decay component is 70 ± 7 ps and short component is 9 ± 0.8 ps (red) and 4.0 ± 0.3 ps (black). [Reprinted with permission from Ref. 12, Copyright American Chemical Society, 2004]

3. Quantum Wire Lasers

Beyond the nanowire lasers, confined core-sheath nanowire heterostructures provide a unique geometry for applications in optoelectronics. We recently demonstrated UV lasing from optically pumped GaN/ $\text{Al}_x\text{Ga}_{1-x}\text{N}$ core-sheath quantum wires (Fig.5)⁵. Phase separation during the VLS process leads to cylindrical GaN cores with diameters as small as 5 nm cladded by a 50-100 nm layer of $\text{Al}_{0.75}\text{Ga}_{0.25}\text{N}$. Normally, GaN nanowires with diameters less than ~ 100 nm are too leaky to sustain laser cavity modes. Surrounding slender GaN wires with a material of larger bandgap and smaller refractive index creates a structure with simultaneous exciton and photon confinement (waveguiding). When optically pumped, the core provides a gain medium while the sheath acts as a Fabry-Perot optical cavity (Fig. 6). We found that PL and lasing emission was blueshifted from the bulk, with lasing thresholds roughly ten times higher than those of larger, unclad GaN nanowire lasers.

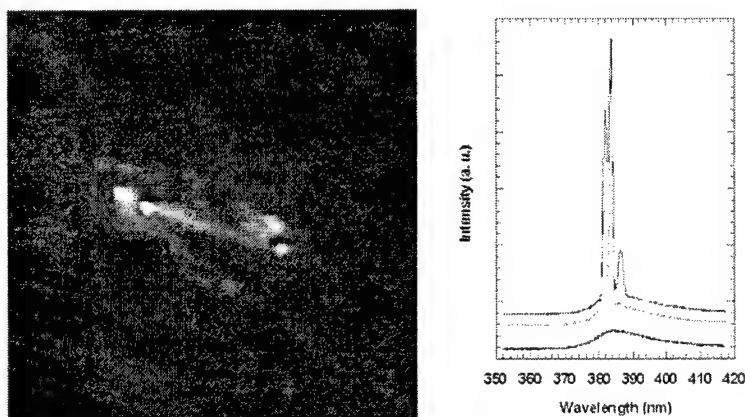


Fig 5: (Left). Far-field optical image of a GaN/AlGaIn core-sheath based quantum wire laser. (Right). Spectra of light emission from GaN/AlGaIn core-sheath nanowires below, near and above threshold (about $2\text{-}3 \mu\text{J}/\text{cm}^2$). [Reprinted with permission from Ref. 5, Copyright American Chemical Society, 2003]

These core-sheath GaN/AlGaIn nanowires (Fig. 2) provide unique model systems for the study of simultaneous photon and carrier confinement (Fig. 6). The GaN core size is comparable to the Bohr radius of the exciton for GaN (11 nm). The band gap of the core (GaN, 3.42 eV) is smaller than that of the sheath ($\text{Al}_{0.75}\text{Ga}_{0.25}\text{N}$, 5.25 eV), i.e., a type-I band-offset alignment. Both factors would lead to effective carrier/exciton confinement within such unique core-sheath nanostructures. To test this hypothesis, the photoluminescence (PL) of single heterostructured nanowires was characterized. Significantly, blue-shifted PL, which is a signature of the quantum confinement effect, was observed. Moreover, in coaxial heterostructures nanowires, modulation doping of larger band-gap material will allow spatial separation of ionized dopants and free carriers, and, thus, higher mobilities could be achieved.

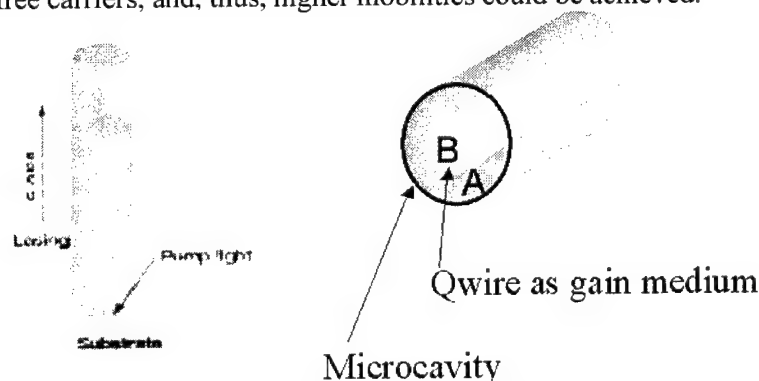


Fig 6: Schematic illustrations for nanowire laser and quantum wire laser. Note the gain medium volume is significantly reduced from nanowire to quantum wire.

In addition to the carrier/excitonic confinement within the GaN core region, there are two additional characteristics of the nanostructures that would allow us to examine the nature of photonic confinement (waveguiding and amplification) within such structures. First, the refractive index of the sheath (2.25 for $\text{Al}_{0.75}\text{Ga}_{0.25}\text{N}$) is smaller than that of the core region (2.54 for GaN). The core-sheath structure essentially resembles a properly index-engineered optical fiber. Indeed, with this arrangement of refractive index and size, the nanostructure would behave as a single-mode optical fiber for UV light. Second, the entire core-sheath structure has well-defined end surfaces (which become natural mirrors for the optical fiber and form an optical cavity). Hence, this structure is an ideal quantum-wire-in-optical-fiber (Qwof) nanostructure, which would, for the first time, allow us to examine the possibility of simultaneous confinement of the exciton and the photon (followed by their possible amplification) within the same chemically synthesized nanostructure. To examine this possibility, individual core-sheath nanostructures were optically pumped and their power-dependent PL was collected. The localization of bright emission near the nanowire ends indicates stimulated emission from the nanowires. Figure 5 shows a series of far-field spectra taken as a function of the pump fluence on these nanowires. Below the lasing threshold, the PL spectrum is broad and featureless. Near and above the threshold (at $\sim 2\text{--}3 \mu\text{J}/\text{cm}^2$), sharp features that are centered at $\sim 384 \text{ nm}$ ($\sim 3.2 \text{ eV}$) appear in the spectrum, indicating the onset of lasing emission from the GaN core of nanowires. Power-dependent lasing spectra near the threshold reflects the typical lasing action of a wide band-gap semiconductor.

4. Conclusion

The most useful applications for nanowire lasers require that they be integrated in circuits and activated by electron-injection rather than optical pumping. Lieber and co-workers have made progress in this direction by assembling n-type CdS nanowire Fabry-Perot cavities on p-Si wafers to form the required heterojunction for electrically driven lasing¹³. More robust assembly methods appropriate to a larger variety of materials will enable the use of injection nanolasers in sensing¹⁴, optical communications¹⁵ and probe microscopy.

Acknowledgement

This work was supported by National Science Foundation and Department of Energy.

References

- 1) Y. Xia, P. Yang et al. *Adv. Mater.* **15**, pp353, 2003.
- 2) Y. Wu, P. Yang, *J. Am. Chem. Soc.* **123**, pp 3165, 2001.
- 3) M. Huang, S. Mao, H. Feick, H. Yan, Y. Wu, H. Kind, E. Weber, R. Russo, P. Yang, *Science*, **292**, pp1897, 2001.
- 4) T. Kuykendall, P. Pauzauskie, S. K. Lee, Y. Zhang, P. Yang, *Nano. Lett.* **3**, pp1063, 2003.
- 5) H. Choi, J. Johnson, R. He, S. Lee, R. Saykally, P. Yang, *J. Phys. Chem. B*, **107**, pp8721, 2003.
- 6) H. Yan, R. He, P. Yang, *J. Am. Chem. Soc.*, **125**, pp4728, 2003.
- 7) H. Yan, J. Justin, M. Law, R. Saykally, P. Yang, *Adv. Mater.* **15**, pp1904, 2003.
- 8) J. Johnson, H. J. Choi, K. P. Knutsen, R. D. Schaller, P. Yang, R. J. Saykally, *Nature Materials*, **1**, pp101, 2002.
- 9) J. Johnson, H. Yan, R. Schaller, R. Saykally, P. Yang, *J. Phys. Chem. B*, **105**, pp11387, 2001
- 10) J. Johnson, H. Yan, P. Yang, R. J. Saykally *J. Phys. Chem. B* **107**, pp8816, 2003.
- 11) A. V. Maslov, C. Z. Ning, *Appl. Phys. Lett.* **83**, pp1237, 2003.
- 12) J. C. Johnson, K. P. Knutsen, H. Yan, M. Law, P. Yang, R. J. Saykally *Nano Lett.* **4**, pp197, 2004.
- 13) X. Duan, Y. Huang, R. Agarwai, C. M. Lieber, *Nature* **421**, pp241, 2003.
- 14) H. Kind, H. Yan, B. Messer, M. Law, P. Yang, *Adv. Mater.* **14**, pp158, 2002.
- 15) J. C. Johnson, H. Yan, R. D. Schaller, P. B. Peterson, P. Yang, R. J. Saykally, *Nanolett*, **2**, pp279, 2002.

Modal properties of semiconductor nanowires for laser applications

A. V. Maslov and C. Z. Ning

Center for Nanotechnology, NASA Ames Research Center
Mail Stop 229-1, Moffett Field, California 94035

ABSTRACT

We review the basic electromagnetic properties of semiconductor nanowires which are required to evaluate their performance as lasers. These properties include the dispersions for guided modes, mode spacing, reflectivities from the nanowire facets, directionality and polarization of far fields, and confinement factors. We also discuss features that distinguish nanowire lasers from the usual heterostructure lasers.

Keywords: lasers, nanowires, guided waves, far-field diagram, confinement factors

1. INTRODUCTION

The recent demonstration of lasing in ZnO,¹ GaN,² and CdS³ nanowires has introduced semiconductor nanowires as potential competitors of presently prevailing heterostructure lasers. Experimental near-field images of lasing nanowires provide a strong evidence that lasing occurs into the modes which are guided by the nanowire and propagate along its axis. This ability to support guided modes and to provide gain to the modes is a remarkable feature of nanowires and it leads to a significant reduction of laser size and simplification in fabrication. The typical radii of semiconductor nanowires are in the 20-200 nm range; the length can be up to about 50 μm .

Despite the experimental evidence of lasing in nanowires¹⁻³ and other optical characterizations,⁴ very little theoretical work exists that would provide insight into the details of the lasing mechanism and predict possible performance of nanowires as lasers. The purpose of this paper is to review our recent work⁵⁻⁷ on the electromagnetic properties of nanowires.

The paper is organized as follows. We start with a discussion of guided modes which can be supported by nanowires and into which lasing can occur. Next in Sec. 3 we discuss the reflectivity from the ends of nanowires. In Sec. 4 we show typical far-field diagram of laser emission. Finally, we calculate the confinement factors for nanowires in Sec. 5 and draw our conclusion in Sec. 6.

2. GUIDED MODES

To find the electromagnetic properties of a free-standing nanowire, we model it as a dielectric cylinder of radius R that stands on a substrate and is surrounded by air. In our calculations we take the dielectric constant $\epsilon = 6$ which is typical for GaN, ZnO, and CdS at lasing frequencies. It is well known that a dielectric cylinder can support guided electromagnetic waves that propagate along the axis and decay with the distance from the cylinder surface.¹⁰ The fields of the guided modes can be found by solving Maxwell's equations inside and outside of the cylinder and then matching the tangential components of the fields at the interface. The matching procedure gives the dependence of the wave vector k_z for the guided modes as a function of frequency ω . The guiding mechanism in nanowires (i.e., total internal reflection from the interface) is identical to that in the usual optical fibers. However, the refractive index contrast between the nanowire and air is very large compared to the core/cladding index contrast in fibers. This allows nanowires to achieve a much stronger confinement of light. A large refractive index contrast between the waveguiding material and surrounding air is also used for guiding light in recently developed silica wires.⁸

A.V.M.: E-mail: amaslov@nas.nasa.gov, Telephone: 1 (605) 604-3986

C.Z.N.: E-mail: cning@mail.arc.nasa.gov, Telephone: 1 (650) 604-3983

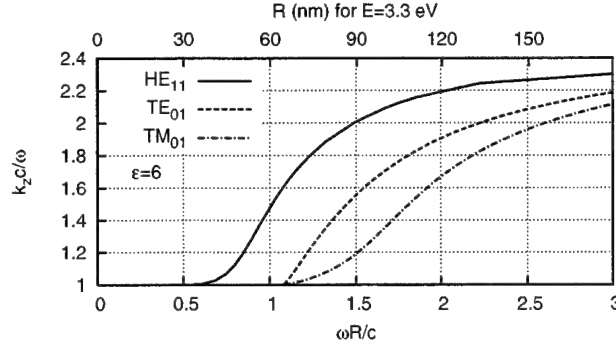


Figure 1. Ratio of the propagation wave vector to frequency for the first three guided modes of a nanowire with $\epsilon = 6$ surrounded by air. The top axis shows the nanowire radius for a typical bandgap energy of 3.3 eV for GaN.

Typical dispersions curves for several lowest order modes guided by nanowires are shown in Fig. 1. The nanowire can support transverse electric (TE_{0m}), transverse magnetic (TM_{0m}) modes, which have only three field components and no dependence on the angle ϕ , and hybrid modes (HE_{nm} and EH_{nm}), which have all six field components with $\cos n\phi$ and $\sin n\phi$ dependence. The index m denotes the radial dependence of the fields, n denotes angular symmetry. All modes except HE_{11} have low-frequency cutoffs. The cutoff frequency is $\omega_c R/c = x_{11}/\sqrt{\epsilon-1} \approx 1.71$ for HE_{12} and EH_{11} , $\omega_c R/c = x_{01}/\sqrt{\epsilon-1} \approx 1.08$ for TE_{01} and TM_{01} , and $\omega_c R/c = x_{02}/\sqrt{\epsilon-1} \approx 2.47$ for TE_{02} and TM_{02} , where x_{kl} is the l th zero of the Bessel function $J_k(x)$, $k = 0, 1$. The cutoff for HE_{21} mode is $\omega_c R/c \approx 1.47$.⁹

The nanowires lase at energies about 3.26 eV for ZnO,¹ at 3.31 eV for GaN,² and at 2.43 eV for CdS.³ In Fig. 1 we label the top axis with radius that corresponds to the typical lasing energy $E = 3.3$ eV in GaN. For small radii, $R < 64$ nm, only HE_{11} exists and thus most likely it was the mode observed in narrow nanowires.¹⁻³ However, in ZnO and GaN nanowires with $R > 64$ nm several different modes can lase.¹ Near the cutoff, the TE_{01} mode is likely to dominate over TM_{01} mode due to its much stronger localization.

All field components of the guided modes decay with the distance from the surface of the nanowire. In particular, the z -components of all guided modes outside of the nanowire vary according to the modified Bessel functions of the second kind, $K_n(\beta\rho)$, where n is the angular index and $\beta = \sqrt{k_z^2 - \omega^2/c^2} = (\omega/c)\sqrt{(k_z c/\omega)^2 - 1}$ determines the mode extension in the air. The larger β is, the better the mode is confined in the transverse direction. For a given nanowire radius, as the frequency increases, the field becomes confined closer and closer to the nanowire. Even though the HE_{11} mode does not have a cutoff, in thin nanowires ($\omega R/c \lesssim 0.7$) the field extends for a considerable distance beyond the surface, making the mode poorly confined and thus, not suitable for single nanowire lasers. However, in an array of nanowires the long tails of the guided mode may provide coupling between the nanowires and lead to lasing in the array. The other modes also extend far away from the surface at the frequencies just above the cutoff frequency.

Given the dispersion properties, one can easily calculate the spacing between the modes of a fixed type due to a finite length of the nanowire L . The spacing between the modes $\Delta\omega$ is given by

$$\Delta\omega = \frac{2\pi}{2\frac{\partial k_z}{\partial \omega}L + \frac{\partial \phi_1}{\partial \omega} + \frac{\partial \phi_2}{\partial \omega}} \approx \frac{2\pi}{2\frac{\partial k_z}{\partial \omega}L} = \frac{\pi v_{gr}}{L} \quad (1)$$

where $\phi_{1,2}$ are the phases of the reflection coefficients from the nanowire ends, $v_{gr} = \partial\omega/\partial k_z$ is the group velocity for the guided wave. For long nanowires, the terms which depend on the reflection phases can be neglected and thus the spacing becomes proportional to the group velocity. Figure 2 shows the group velocity and energy spacing between the modes. With increase in $\omega R/c$, the ratio c/v_{gr} initially increases, reaches a maximum, and then starts to decrease. Asymptotically at $\omega R/c \rightarrow \infty$, $c/v_{gr} \rightarrow \sqrt{\epsilon}$. It is important that the mode spacing depends not only on the length of the nanowire but also on its radius. We also mention that even though Eq. (1) is exact, the dispersion itself $k_z(\omega)$ was calculated assuming a frequency independent $\epsilon = 6$. The variation of the dielectric constant with frequency can also contribute to the change of dispersion and thus, the mode spacing.

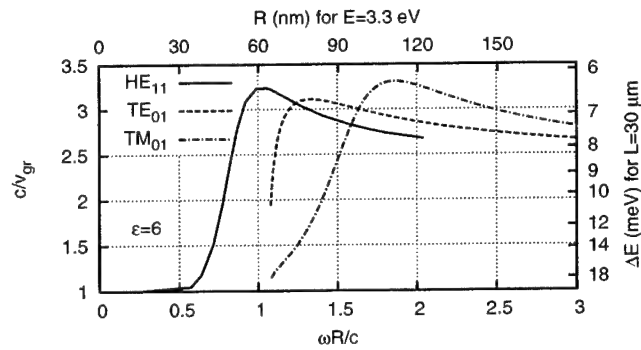


Figure 2. Ratio of the speed of light to the group velocity for the three lowest order modes. The top axis shows the nanowire radius for a typical bandgap energy of 3.3 eV for GaN. The right axis shows the mode spacing $\Delta E = \hbar\Delta\omega$ for a $L = 30 \mu\text{m}$ long nanowire.

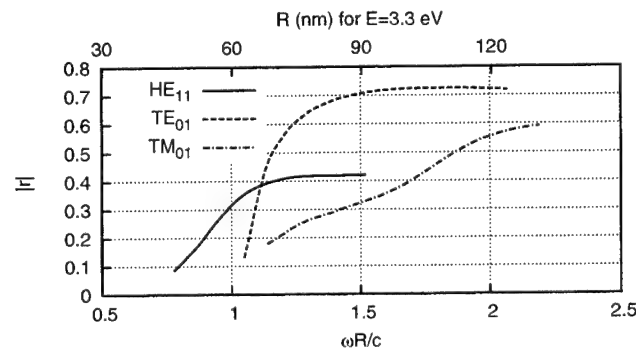


Figure 3. Absolute value of the reflection coefficient for the first three guided modes from the open end (top facet) of the nanowire.

3. REFLECTIVITIES FROM THE FACETS

The reflection coefficients for the guided modes from the nanowire ends determine the threshold gain, i.e., the gain which is required to compensate all losses. In the usual heterostructure lasers, waveguiding is achieved because of a small dielectric mismatch between the active medium and the surrounding semiconductor. This results in the transverse size of the guided mode being significantly larger than the wavelength. In such a case, the reflection coefficient from the laser facets is approximately equal to the one for a plane wave incident on the semiconductor/air interface. For nanowires, the situation is much more complicated because the parts of the mode outside and inside the nanowire experience different dielectric constant mismatches. To find the reflection coefficients for a guide wave from the ends one has to solve a typical diffraction problem. We addressed this problem using the finite-difference time-domain method (FDTD).⁵ In the simulations, we initially create a guided wave packet that propagates towards one of the ends. After the wave packet reaches the end, a part of it forms outgoing radiation, the remaining part is reflected. Using the reflected wave packet and taking a Fourier transformation we can directly calculate the reflection coefficient. We also note that in general an incident wave packet can produce several reflected guided wave packets. These wave packets should have the same frequencies as the incident wave but different wave numbers. However, in thin nanowires only one reflected wave packet of the same type as the incident one can exist because the nanowire is thinner than the cutoff radii for the other modes.

In Fig. 3 we plot the reflection coefficient from the open end (top facet) of the nanowire for different guided modes. A common feature of the reflection coefficient for all modes is its growth with frequency and thus with the mode confinement. However, because of different polarizations of the modes, the reflection coefficients take quite different values. The results of Fig. 3 can be compared to the reflection of a plane wave at dielectric/air interface

when the reflection coefficient varies from zero (at Brewster's angle) to unity (for total internal reflection); at normal incidence it is $(n - 1)/(n + 1) = 0.42$. Interestingly, in the regime of strong confinement for the HE_{11} mode the reflection approaches the value for the normal incidence on an infinite dielectric/air interface. However this does not happen for TE_{01} or TM_{01} modes. The reflectivity of guided modes is always less than unity in the frequency range of interest because of diffraction losses. The reflection from the bottom end has a more complicated frequency dependence compared to the one from the top.⁵

4. POLARIZATION AND DIRECTIONALITY OF FAR FIELDS

We now turn to the discussion of the fields that are emitted from the top of a free-standing nanowire. While near the end the fields can have quite complicated behavior because of diffraction, their distribution in the far-field zone is what we are mostly interested in. In the far-field region, the radiation emitted in the direction specified by the unit vector $\hat{\mathbf{r}}$ can be represented as a superposition of two locally plane waves. If $\hat{\theta}$ and $\hat{\phi}$ are the usual basis vectors orthogonal to $\hat{\mathbf{r}}$, one plane wave has its electric field in the $\hat{\theta}$ direction, the other – in the $\hat{\phi}$ direction. Thus, the far-field emission is completely characterized by its polarization and the energy density $S(\hat{\mathbf{r}}, \omega)$ emitted in the unit solid angle in the direction $\hat{\mathbf{r}}$ per unit time.

The polarization properties of the far fields can be deduced from the symmetry of the modes. We focus on the lowest order modes (HE_{11} , TM_{01} , and TE_{01}); their dispersion properties are shown in Fig. 2.¹⁰ The transverse modes TM_{01} and TE_{01} produce far fields that are independent of ϕ -coordinate, i.e., $S(\hat{\mathbf{r}}, \omega) = S(\theta, \omega)$. The TM_{01} mode has only E_ρ , E_z , and H_ϕ components. Thus, the far-field radiation produced by the TM_{01} mode will have only E_θ component; $E_\phi = 0$ everywhere. By the same token, the far fields of the TE_{01} mode will have only E_ϕ component; $E_\theta = 0$ everywhere. The HE_{11} mode has all six components and it is degenerate, i.e., two possible angular dependencies exist. Let us consider one situation when the components E_z , E_ρ , $H_\phi \sim \cos \phi$, while H_z , H_ρ , $E_\phi \sim \sin \phi$. It follows from the assumed angular dependencies that the far fields behave like $E_\theta \sim \cos \phi$ and $E_\phi \sim \sin \phi$. Thus, unlike the TE_{01} and TM_{01} modes, the far fields of the HE_{11} mode depend not only on θ but also on ϕ . Using the assumed angular dependence for the HE_{11} mode we can write the energy density of the generated far fields as

$$S(\hat{\mathbf{r}}, \omega) = [S_\theta(\hat{\mathbf{r}}, \omega) \cos^2 \phi + S_\phi(\hat{\mathbf{r}}, \omega) \sin^2 \phi],$$

where the subscripts θ and ϕ denote polarization of the corresponding plane waves. In a typical experimental situation, the HE_{11} modes with the two possible polarizations are excited and thus, the intensity of the emitted radiation does not have any ϕ -dependence.

Figure 4 shows the energy density of the emitted radiation for the HE_{11} mode as a function of θ . The intensity was normalized so that

$$\int_0^{2\pi} d\phi \int_0^\pi d\theta \sin \theta S(\hat{\mathbf{r}}, \omega) = 1.$$

At $\omega R/c = 1.0$, the emission at small θ is quite pronounced and is independent of polarization. As $\omega R/c$ increases, the emission in the forward direction decreases while the emission in the backward direction increases. This broadening of the emission angle with growth of $\omega R/c$ can be attributed to the decrease of the transverse extent of the mode for larger $\omega R/c$. The difference of the intensities between the θ - and ϕ -polarized components also increases with $\omega R/c$. A strong maximum in the backward direction develops for the θ -polarized component. The most directional emission with a strong maximum at $\theta = 0$ is achieved in thin nanowires where $\omega R/c$ is small. This is simply because the guided mode is weakly localized in thin nanowires. However, in this regime the reflection coefficient from the top facet is very small. This leads to a high values of the threshold gain. Thicker nanowires can provide lower threshold gain but their emission has very broad angular distribution.

The emission diagram for the transverse TE_{01} and TM_{01} modes is quite different from that for the HE_{11} mode.⁶ The main difference is the complete absence of emission at $\theta = 0$. This absence follows directly from the symmetry of the transverse modes. Indeed, the far field emitted at $\theta = 0$, if present, must have the electric and magnetic components perpendicular to the nanowire axis. Such components can not be produced by the transverse modes which are independent of the angle ϕ .

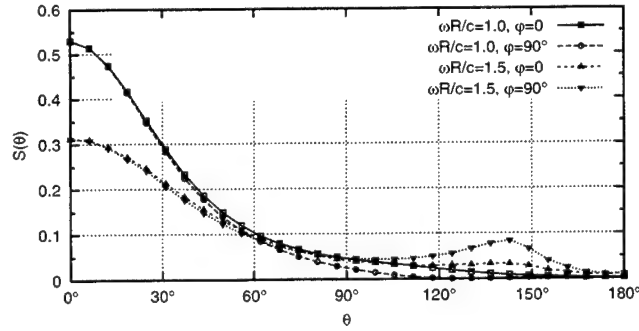


Figure 4. Normalized intensity $S(\hat{\mathbf{r}}, \omega)$ of the far fields as a function of θ for HE_{11} mode.

5. CONFINEMENT FACTORS

In order to have lasing, the gain experienced by the mode should reach its threshold value which can be directly calculated from the facet reflectivities. Let us now calculate the modal gain. If $I(z)$ is the power of the guided mode (i.e., the energy which crossed an infinite plane perpendicular to the nanowire axis per unit time), then it obeys the rate equation

$$\frac{dI(z)}{dz} = GI(z). \quad (2)$$

The coefficient G is the modal gain:

$$G = - \frac{2 \int_{\rho < \infty} d\rho \sigma |\tilde{\mathbf{E}}(\rho)|^2}{\frac{c}{4\pi} \int_{\rho < \infty} d\rho [\tilde{\mathbf{E}}(\rho) \times \tilde{\mathbf{H}}^*(\rho) + \tilde{\mathbf{E}}^*(\rho) \times \tilde{\mathbf{H}}(\rho)] \cdot \hat{\mathbf{z}}} \quad (3)$$

where $\tilde{\mathbf{E}}(\rho)$, $\tilde{\mathbf{H}}(\rho)$ are the complex fields of the mode, ρ is the transverse coordinate, and σ is the optical conductivity that provides gain. The description of gain using the bulk conductivity σ holds for the presently used GaN and ZnO nanowires where quantization effects are absent due to their large radii. For simplicity we assume here the conductivity σ to be isotropic although it is a bad approximation for GaN, especially near the bandedge.⁷ We can relate the modal gain G to the material gain $G^0 = -(4\pi\sigma)/(c\sqrt{\varepsilon})$ (with ε the dielectric constant of the nanowire):

$$G = \Gamma G^0. \quad (4)$$

where Γ is the so-called confinement factor:

$$\Gamma = \frac{2\sqrt{\varepsilon} \int_{\text{active region}} d\rho |\tilde{\mathbf{E}}(\rho)|^2}{\int_{\rho < \infty} d\rho [\tilde{\mathbf{E}}(\rho) \times \tilde{\mathbf{H}}^*(\rho) + \tilde{\mathbf{E}}^*(\rho) \times \tilde{\mathbf{H}}(\rho)] \cdot \hat{\mathbf{z}}}. \quad (5)$$

The knowledge of the confinement factors allows one to obtain the modal gain from the material gain of the active medium. The material gain has to be calculated using a microscopic theory for the given semiconductor and carrier density.

Figure 5 shows the confinement factors for several lowest order modes of a nanowire. The confinement factors initially grow as functions of $\omega R/c$ as the modes become more confined. In the limit $\omega R/c \rightarrow \infty$ the confinement factors reach unity. An interesting feature of the confinement factors is that they can exceed unity. This is somewhat unusual and does not occur in heterostructure lasers. The large values of the confinement factors can be explained by small values of the group velocity for the guided modes compared to the group velocity for a plane wave in the active material (see Fig. 2).

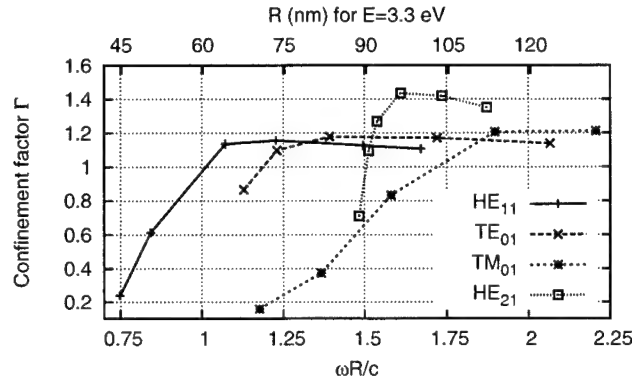


Figure 5. Confinement factor as a function of the dimensionless parameter $\omega R/c$. The top axis shows the nanowire radius for a typical lasing frequency of 3.3 eV for GaN.

6. CONCLUSION

We have discussed the electromagnetic properties of semiconductor nanowires in which lasing was recently demonstrated. Our focus was on the properties that distinguish them from the usual heterostructure lasers. Let us summarize some key feature of nanowires. First, free-standing nanowires can function both as an active material and a waveguide. The strong waveguiding is achieved due to a very large refractive index contrast between the nanowire and surrounding air. Second, the reflectivities from the nanowire facets are rather complicated functions of the radius and frequency. Third, the far-field radiation generated by the HE_{11} mode in a thin nanowire can be rather directional. This is because the mode has a very large transverse size which makes it similar to the guiding regime in a heterostructure laser. However, unlike the case of a heterostructure laser, the mode experiences very little reflection as it reaches the top end. This leads to a very large threshold gain. The modes of wide nanowires can have rather high reflection coefficients, however, the far fields are emitted into a very large cone and even in the backward direction. Forth, the confinement factors in nanowires can be large and even exceed unity because the modes can have small group velocities. Another aspect of nanowires that we would like to emphasize is that, unlike heterostructure lasers, nanowire lasers do not require a semiconductor barrier to confine the carriers. This may be very useful for making lasers operating in the deep ultraviolet range where it is difficult to find a semiconductor with sufficiently large bandgap to be used as the barrier.

ACKNOWLEDGMENTS

Work of AVM was supported in part by the NASA Ames Research Center Director's Discretionary Fund (DDF) and by a NASA contract to ELORET Corporation.

REFERENCES

1. J. C. Johnson, H. Yan, R. D. Schaller, L. H. Haber, R. J. Saykally, and P. Yang, "Single nanowire lasers," *J. Phys. Chem. B* **105**, 11387-11390 (2001).
2. J. C. Johnson, H. J. Choi, K. P. Knutsen, R. D. Schaller, P. Yang, and R. J. Saykally, "Single gallium nitride nanowire lasers," *Nature Materials* **1**, 106-110 (2002).
3. X. Duan, Y. Huang, R. Agarval, and C. M. Lieber, "Single-nanowire electrically driven lasers," *Nature* **421**, 241-244 (2003).
4. H. T. Ng, B. Chen, J. Li, J. Han, M. Meyyappan, J. Wu, S. X. Li, and E. E. Haller, "Optical properties of single-crystalline ZnO nanowires on *m*-sapphire," *Appl. Phys. Lett.* **82**, 2023-2025 (2003).
5. A. V. Maslov and C. Z. Ning, "Reflection of guided modes in a semiconductor nanowire laser," *Appl. Phys. Lett.* **83**, 1237-1239 (2003).
6. A. V. Maslov and C. Z. Ning, "Far-field emission of a semiconductor nanowire laser," *Optics Letters*, accepted.

7. A. V. Maslov and C. Z. Ning, "Modal gain in a semiconductor nanowire laser with anisotropic bandstructure," submitted for publication.
8. L. Tong, R. R. Gattass, J. B. Ashcom, S. He, J. Lou, M. Shen, I. Maxwell, and E. Mazur, "Subwavelength-diameter silica wires for low-loss optical wave guiding," *Nature* **426**, 816-819 (2003).
9. A. Yariv, *Optical electronics* (CBS College Publishing, New York, 1985).
10. R. E. Collin, *Field theory of guided waves* (IEEE Press, Piscataway, NJ, 1991), p. 721.

Long-wavelength (1.3 -1.5 micron) quantum dot lasers based on GaAs

A.R.Kovsh^{1,2,3}, N.N.Ledentsov^{1,2,4}, S.S.Mikhrin^{1,2}, A.E.Zhukov², D.A.Livshits^{2,3}, N.A.Maleev^{2,3},
M.V.Maximov², V.M.Ustinov², A.E.Gubenko², I.M.Gadjiev², E.L.Portnoi²,
J.S. Wang³, J.Chi³, D.Ouyang⁴, D. Bimberg⁴, and J.A.Lott⁵

¹ NSC-Nanosemiconductor-GmbH, 44227, Dortmund, Germany

² A.F.Ioffe Physico-Technical Institute, 194021, St.Petersburg, Russia

³ Industrial Technology Research Institute, 310, Hsinchu, Taiwan, ROC

⁴ Technical University of Berlin, 10623, Berlin, Germany

⁵ Air Force Institute of Technology, 2950, Ohio, USA

ABSTRACT

The molecular beam epitaxy of self-assembled quantum dots (QDs) has reached a level such that the principal advantages of QD lasers can now be fully realized. We overview the most important recent results achieved to date including excellent device performance of 1.3 μm broad area and ridge waveguide lasers ($J_{\text{th}} < 150 \text{ A/cm}^2$, $I_{\text{th}} = 1.4 \text{ mA}$, differential efficiency above 70%, CW 300 mW single lateral mode operation), suppression of non-linearity of QD lasers, which results to improved beam quality, reduced wavelength chirp and sensitivity to optical feedback. Effect of suppression of side wall recombination in QD lasers is also described. These effects give a possibility to further improve and simplify processing and fabrication of laser modules targeting their cost reduction. Recent realization of 2 mW single mode CW operation of QD VCSEL with all-semiconductor DBR is also presented. Long-wavelength QD lasers are promising candidate for mode-locking lasers for optical computer application. Very recently 1.7-ps-wide pulses at repetition rate of 20 GHz were obtained on mode-locked QD lasers with clear indication of possible shortening of pulse width upon processing optimization. First step of unification of laser technology for telecom range with QD-lasers grown on GaAs has been done. Lasing at 1.5 μm is achieved with threshold current density of 0.8 kA/cm^2 and pulsed output power 7W.

Keyword: quantum dots, diode lasers, beam quality, vertically surface emitting lasers, short pulses

1. Introduction

Heterostructure diode lasers [^{1,2}] have revolutionized many areas of the human being. They have made possible such great applications as optical storage and fiber telecommunications. Huge potential accumulated in these fields can be applied to other directions, for example to computer optical clocking and interconnects including chip to chip and intra-chip optical data links. In high volume a marriage between silicon leading in electronic applications and III-Vs leading in optoelectronics can only happen if the cost structures and form factors are synchronized. Here, development of cost-efficient laser diodes providing an opportunity of high-speed operation ($> 10 \text{ Gb/s}$) in a wavelength-controlled single-mode regime is a precondition for penetration of optoelectronic devices into the mainstream semiconductor market.

There exists an opinion that today's semiconductor lasers have already approached a high level of perfection and further progress is hardly possible. In this paper we will present results of recent development of Quantum Dot (QD) diode lasers. These results show QD technology as a fast developing technology moving from academic frame to production stage with clear potential for further improvement of semiconductor lasers.

It is also argued that semiconductor lasers suitable for applications in high-speed data- and telecommunications will always remain costly and their practical application in computer interconnects is unlikely. The reasons of this controversy are related to some general properties of semiconductor lasers and their fabrication process, including single frequency temperature stable device.

Concept of on-wafer processing of Vertically Surface Emitting Lasers (VCSELs) with inherent stabilization of lasing wavelength is a current direction for cost-reduction of wavelength stabilized devices. Commercial success of 850 nm VCSEL is an example. In this case an important for conventional 850 nm edge-emitting lasers and quite expensive technological operation such as facet protection is excluded. However, this spectral range is beyond one for

Corresponding author : A.R.Kovsh, e-mail: alexey.kovsh@nanosemiconductor.com

standard telecom/advanced datacom applications (1.25 – 1.7 μm). The fact that 0.85 μm VCSEL was successful is directly related to the unique properties of the lattice matched GaAs-AlAs heterojunction, which provides high refractive index difference suitable for DBR fabrication. GaAs and AlAs additionally provide high thermal conductivity important for high power operation, and a technology of selective oxidation of AlAs layers allows fabrication of small oxide-confined buried current apertures without the need of expensive lithography and overgrowth. A completely different situation occurs for VCSELs grown on InP substrates which are traditionally used for 1.3-1.55 μm -range devices. The need of lattice matching restricts the choice of materials for making the Bragg mirrors and only certain compositions of the alloy are allowed. For workable combinations of materials the resulting refractive index is not much different. To compensate, lots of layers, or a few hundred per mirror, are needed to achieve high reflectivity making the technology very complex. The situation becomes even more difficult, as the thermal conductivity of In-based alloys lattice matched to InP is low (20-30 times lower than for GaAs-AlAs DBRs) and the heat dissipation is much less efficient.

Successful realization of cost-effective long wavelength VCSELs on GaAs substrates with parameters close or better than those for 0.85 μm devices is one of the most challenging and promising task of modern semiconductor optoelectronics. As it will be shown in this paper InAs QDs grown on GaAs substrates is a very promising candidate to fulfill this task.

A remarkable progress has been achieved in the understanding of universal phenomena of self-organization of epitaxial nanostructures at crystal surfaces over last decade. Significant technical improvements of epitaxial techniques, including Molecular Beam Epitaxy (MBE), such as improved initial quality of materials, reduced residual pressure in MBE reactors, better reproducibility of growth regimes from run to run, better uniformity and lower defect density have been also done. This is a solid basement for further fascinating device development which is expected for QD material.

Besides VCSEL application, the overwhelming part of potential advantages of QDs has been verified today for other types of devices [^{3,4}] and new previously unexpected advantages have been demonstrated. It has appeared, for example, that the use of QDs in diode lasers has also several decisive technological advantages:

- (i) Largely extended wavelength control by QD size and composition on a given substrate. Lasing wavelengths at 1.3 μm and 1.5 μm spectral range are realized. This gives a chance for creation of unified technology of GaAs-based lasers for spectral ranges important for telecom, datacom, automotive datacom and optical wireless applications.
- (ii) Carrier confinement in narrow gap QDs placed in a wide gap matrix can prevent nonequilibrium carrier spreading and nonradiative recombination. This improves radiation hardness [⁵], suppresses side wall recombination in devices etched through the active region [⁶] and suppresses the facet overheating, increasing the catastrophic optical mirror damage (COMD) level [^{7,8}].
- (iii) In many cases, QDs advantages are still not even well understood. Quite surprisingly semiconductor optical amplifiers (SOAs) (*which are not addressed in this paper*) based on QD GaAs show remarkable promise to outperform InGaAsP bulk and QW SOAs as in the case of lasers since QD SOAs show gain recovery times of 140 fs, 4-7 times faster than classical ones [⁹].

2. Design and MBE growth of 1.3 μm QDs for active media of diode lasers

The need in high optical gain makes the surface density of QDs be one of the key parameters when choosing the most promising among existing approaches to the growth of 1.3- μm QDs, provided that all of them offer about the same level of size distribution. InAs QDs embedded into InGaAs layer, which were proposed for 1.3- μm lasers almost simultaneously by several research groups [^{10,11,12}], have the highest surface density compared to the other growth techniques like atomic layer deposition [¹³] or low-rate growth deposition [¹⁴].

The maximum gain can be increased by improving size distribution of QDs. Promising results in this direction were presented very recently in [¹⁵], however reported technique of “leveling and rebuilding” was applied to InGaAs QDs emitting at a shorter wavelength. Using QDs of first layer as seeding centers is also a possible way to improve gain characteristics of QDs of the next layer through their improved uniformity [¹⁶] or increased surface density [¹⁷]. Although accumulation of high strain in 1.3- μm QDs limits the flexibility of design and growth condition, a careful adaptation of mentioned methods to these QDs could be aimed. The multiple stacking of QDs with relatively thick spacer layers is currently most developed and commonly used method to increase gain of QD lasers.

Previously, we have demonstrated 1.3- μm VCSEL with highly-reflective AlO/GaAs distributed Bragg reflectors (DBR) based on three layers of these QDs [18]. Further increase in the number of QD planes aiming increment in modal gain typically led to degradation of laser characteristics [19], until very recently a breakthrough in the technology of multiple stacking of 1.3- μm QDs was achieved by several groups [20, 21, 22]. 5 layers of QD layers placed in *p*-type doped $\text{Al}_{0.05}\text{Ga}_{0.95}\text{As}/\text{Al}_{0.85}\text{Ga}_{0.15}\text{As}$ waveguide demonstrated extremely high characteristic temperature (T_0) of 232 K [20].

QDs formed in Stranski-Krastanow growth mode by deposition of 2.5-3 monolayers (ML) of InAs emit around 1.2 μm . To obtain 1.3- μm emission they have to be either placed in the middle of InGaAs QW or deposited directly on GaAs and then covered by InGaAs layer. In this case the surface density of QDs equals to about $3\div 5 \times 10^{10} \text{ cm}^{-2}$. There are a few possible reasons of the red shift of emission in this case. The most obvious is the decrease of band-gap of surrounding material. However, our experiments showed that when InGaAs layer was substituted for InAlAs layer with band gap closed to GaAs the "red shift" could be even stronger [23]. Another reason is the strain reduction in QDs, when they are covered with InGaAs layer [10]. Also, the presence of In in covering material can reduce In out-diffusion from QDs. It results in the sharper heterointerface and, in turn, in deeper position of energy levels in QDs. However, we believe that the phase separation of the covering layer has the most significant effect on the observed red shift of emission [24]. Once the dots are covered by the InGaAs alloy, it is energetically favorable for InAs molecules to nucleate at the elastically relaxed islands. It leads to the increase in the volume of strained islands, as it can be clearly seen in Figure 1.

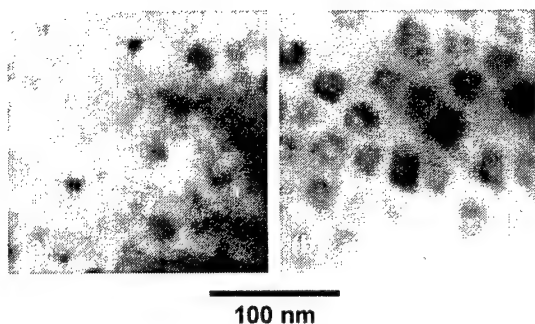


Fig.1. Plan-view transmission electron microscopy image of single layer of QDs formed by (a) 2.5 ML InAs deposition followed by GaAs overgrowth and (b) 2.5 ML InAs deposition followed by overgrowth with a 5-nm-thick $\text{In}_{0.15}\text{Ga}_{0.85}\text{As}$ layer prior to GaAs deposition

deposition of 2.5 ML of InAs at the growth rate of 0.083 ML/sec and then covered with 5-nm thick $\text{In}_{0.15}\text{Ga}_{0.85}\text{As}$ layer (Fig.1). *In situ* defect-reduction technique proposed in [26] can be applied to selectively eliminate dislocations and defect dipoles, which may be formed simultaneously with formation of QDs.

Another parameter, which needs to be optimized, is the thickness of spacer layer between QD stacks. High strain accumulated in each QD layer requires relatively thick spacer layers. At the same time a large distance between QD layers reduces contribution of side layers to the modal gain. We found that the GaAs spacer of around 30 nm thickness provides a possibility to grow up to 10 QD layers without any noticeable degradation in optical properties [21].

3. Performance of broad area QD lasers

The lasers presented in this paper were grown by solid source MBE in different apparatus: Riber 32P, which is a machine of laboratory scale (one 2 inch or 3 inch wafer per growth run), Riber Epineat, which is a semi-production system (three 2 inch wafers or one 4 inch wafer at once), and in a system Riber MBE49, which is a production machine for optoelectronic needs (five 3 inch wafers per growth run). It allowed us to accommodate knowledge about influence of epitaxial equipment on QD technology and work out valuable recommendations for configuration and design of MBE chamber optimized for growth of QD lasers.

Different numbers of layers ($N=2, 5, 10$) with QDs in GaAs matrix formed as described in the previous chapter were used in an active region of lasers in study. The typical laser design is as follows. Waveguide of total thickness of 0.5 μm consists of GaAs core layer with QDs, about 10 periods of short-period 2nm/2nm $\text{Al}_{0.27}\text{Ga}_{0.73}\text{As}/\text{GaAs}$ superlattices and 50-nm-thick $\text{Al}_{0.27}\text{Ga}_{0.73}\text{As}-\text{Al}_{0.7}\text{Ga}_{0.3}\text{As}$ graded layers on both sides. 1.5 μm -thick *Si*- and *Be*-doped $\text{Al}_{0.7}\text{Ga}_{0.3}\text{As}$ layers were used as *n*- and *p*-type cladding layers.

3.1 Pulsed operation (Threshold, differential efficiency)

For pulsed measurements, aiming evaluation of internal properties of active region such as transparency current and internal loss, the lasers were processed into 100- μm -wide stripes (broad area devices) of different cavity length with as-cleaved facets. Measurements of threshold current density and differential efficiency were performed in pulsed operation regime (2 μs , 2 kHz).

Fig.2 shows the dependence of output power on drive current of the 1.5-mm-long laser based on 10 layers of QDs along with electroluminescence spectra recorded at different drive currents. The lasing proceeds in the maximum of ground-state emission. High output power (5W) operation considerably widens the lasing spectrum. The threshold current is 220 mA and slope efficiency is 0.78 W/A, corresponding to the threshold current density (J_{th}) of 147 A/cm² and η_D of 80%.

Dependences of the threshold current density, lasing wavelength, and external differential efficiency on the cavity length (L) are summarized in Fig.3 for diodes operating at ground state. For the 5-QD- and 10-QD-lasers the threshold current density is in the 100-200 A/cm² range for L longer than 1 mm. Stronger dependence of J_{th} on L and shorter emission wavelength of 2-QD-laser are caused by the lower value of maximum optical gain in this structure. Nevertheless, we would like to emphasize that this structure demonstrate GS lasing even in the diode of 675 μm length. Lasers based on 5 and 10 QD layers demonstrate GS lasing in shorter cavity diodes down to 500 μm . Diodes with even shorter L oscillate via excited state (ES) at about 1.18 μm .

It can be seen that J_{th} increases significantly for diodes shorter than 1 mm. This is accompanied by the blue shift of the lasing wavelength and by steep decrease of differential efficiency in the shortest diodes. Such a behavior indicates that position of electron and hole Fermi levels at lasing threshold is different for different L . It means that population of matrix states and free carrier absorption in waveguide are higher for shorter L . Thus, internal loss (α_i) of laser diode becomes cavity-length dependent. In this case the determination of α_i and η_i by linear fit of $1/\eta_D$ - L dependence, which is commonly used for QW lasers [27], is not really applicable for our QD diodes. Nevertheless, we would like to mention here that linear extrapolation for 10-QD lasers gives value of internal loss below 2 cm⁻¹ and internal quantum efficiency above 95%.

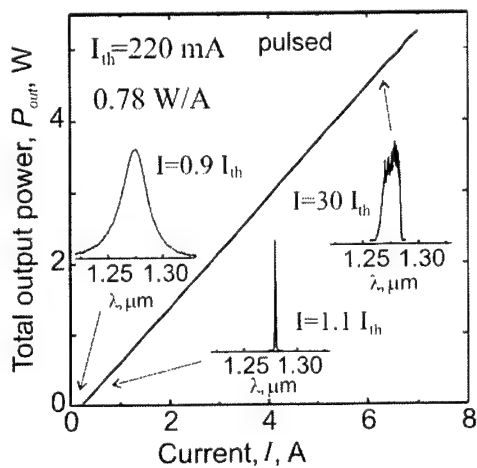


Fig.2. Pulsed RT L-I curve for the laser diode based on 10 layers of QDs (100- μm -wide and 1.5 -mm-long diode with as cleaved facets). Spectra at different currents are shown on inserts.

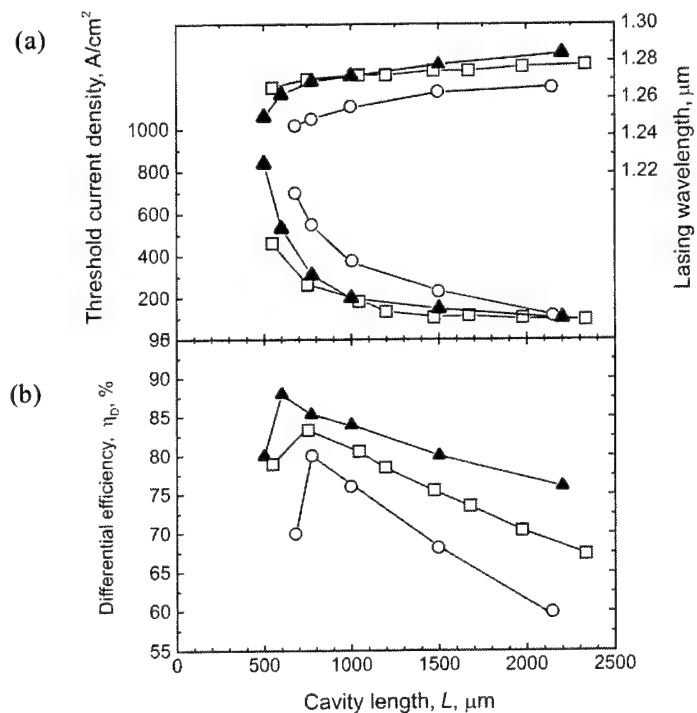


Fig.3. Dependences of (a) the threshold current density, J_{th} , lasing wavelength, λ , and (b) the differential efficiency, η_D , on the cavity length, L , for lasers based on 2 (open circles), 5 (open squares) and 10 (solid triangles) layers of QDs. Lines are shown for eye-guidance.

As it follows from Fig.3(b) the higher number of QD layers in the active region provides higher value of the differential efficiency. Increase in the number of QD planes has been shown to prevent the carrier pile-up in the waveguide and hence to lower α_i in QD lasers of a shorter wavelength [28]. It results in increasing η_D for the diodes of the same L . This effect in the combination with the extended range of the GS lasing (shorter diodes) leads to the improved maximum external differential efficiency, which is equal to 80, 84 and 88% for 2-, 5- and 10-QD lasers.

3.2 Temperature stability of threshold current density

Temperature dependences of J_{th} and lasing wavelength of 1.5 mm long diodes based on 2, 5 and 10 QD layers are presented in Fig.4. There are two distinct regions in J_{th} temperature behavior. T_0 is 130-150 K below 50°C, whereas at higher observation temperature it is considerably lower. The laser with 5 stacks of QDs has demonstrated the highest T_0 of 150 K in 20-50°C. For the lasers based on 2 and 10 QD layers T_0 were equal to 140 K and 130 K, respectively. Degradation of differential efficiency from 20 to 80°C was found to be only about 10%.

As was mentioned in the introduction, p -type doping of the matrix can provide T_0 more than 200 K [20], however, there is a "trade off" of T_0 and η_D in this approach. We believe that further reduction of defects associated with growth of highly strained material can be the key to further improve temperature stability of threshold current. Recent unpublished temperature behavior of QD lasers is shown in Fig.5. The region of high temperature stability is enhanced to higher temperature as compared with previous results. Threshold current density is still below 400 A/cm² at 150°C.

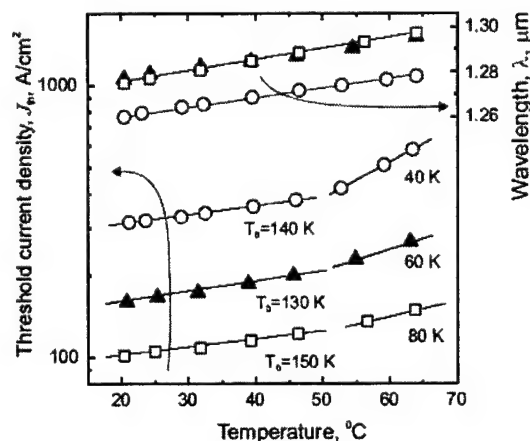


Fig.4. Temperature dependences of J_{th} and wavelength of 1.5-mm-long lasers based on 2 (open circles), 5 (open squares) and 10 (solid triangles) QD stacks.

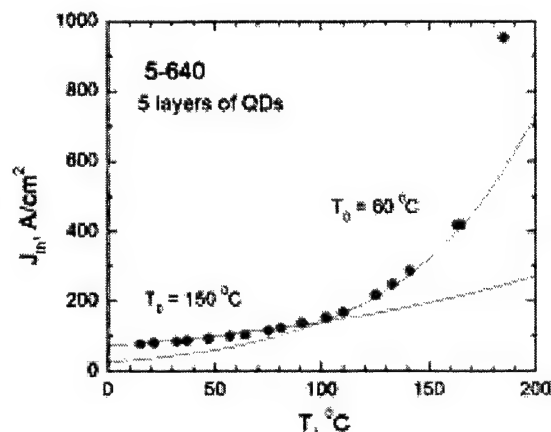


Fig.5. Temperature dependences of J_{th} for 4-cleaved facets laser based on 5 layers of QDs grown with special technique to reduce defect density. (unpublished result)

3.3 CW operation of broad area lasers

To realize high power out of diode laser in CW operation regime a special attention has to be paid to series resistance. Specially designed QD laser was grown with improved doping profile to check high current operation of QD devices. Laser structure contained 5 layers of QDs. The laser design was chosen to be similar as described above with slightly higher doping of cladding and graded layers. 100-μm-wide 1.6 mm-long diodes were bonded on a heatsink after HR/AR coating.

Fig.6 shows CW operation at heatsink temperature of 15°C. Lasing spectra at different drive currents are in Fig6(b). Lasing spectra get broader and shifts toward longer wavelength with increasing of drive current. CW power reaches level of 3W without any noticeable thermal rollover. This value is limited by power supply. The wall plug efficiency reaches 30% at 2A and remains higher than 20% at high drive current. The threshold current density is below 200A/cm² and differential efficiency is higher than 65% in CW operation. These values are superior to InP-based counterparts.

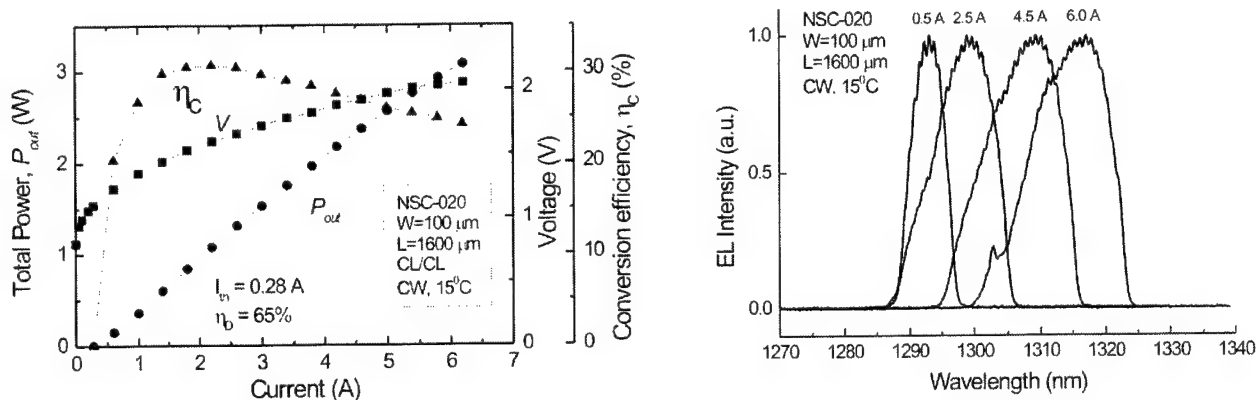


Fig.6. CW operation of broad area QD laser based of 5-layers of QDs with reduced series resistance. No significant thermal rollover is observed up to high currents. Lasing spectra were recorded at different drive currents.

4 Performance of narrow ridge-waveguide single lateral mode diodes

The QD laser wafers were used for the fabrication of ridge waveguide lasers with a stripe width of 2.7 or 4.5 μm . Fig. 7 shows a scanning electron micrograph of the typical laser cross section. The ridge profile was formed by plasmachemical etching in a Cl_2/Ar gas mixture in a high-density plasma regime. The etching depth was monitored by laser interferometer. The process was terminated at the boundary between the upper emitter and the waveguide layer. The insulating layer of SiN_x was formed by plasma-activated vapor deposition. A window in the insulating layer for the Ti/Pt/Au p -contact deposition was made using the self-matched mask technique. In order to provide for a reliable electric contact, the p -side of the structure was galvanically coated with an 0.5- μm -thick gold film. The lasers were fixed with the p -side up by soldering onto metallized AlN ceramic substrates with a thermal conductivity coefficient of 1.7 $\text{W}/(\text{mK})$ and mounted in standard TO46 cases.

4.1 Low threshold diode

To demonstrate ability of QD laser as an extremely low threshold device laser diode with cavity length of 600 μm was fabricated from 2-QD laser structure. The front and rear cleaved mirror facets were coated with electron beam deposited high-reflection (HR) interference films comprising three and four $\text{Al}_2\text{O}_3/\text{Si}$ bilayers respectively. Fig.8 shows

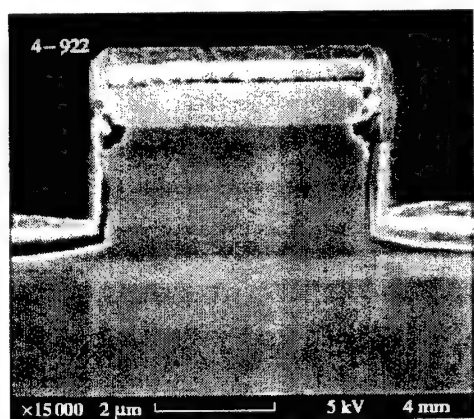


Fig.7 SEM cross section image of QD laser

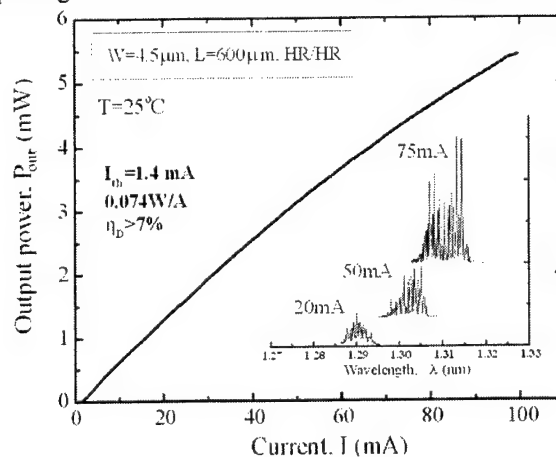


Fig.8 CW operation of ridge waveguide laser based on 2 QD sheets. Lasing spectra at different currents are shown in the insert.

the typical output power–drive current characteristic of such a laser measured in CW regime. A minimum threshold current reached in such laser diodes 1.4 mA. This is a record value for ridge waveguide lasers. Lower thresholds reported in the literature were obtained only in lasers with the cavity design ensuring localization of charge carriers in the mesa region, such as quantum-well lasers with regrown mesa [29] and QD lasers with oxidized aperture [30]. Despite the HR coating on the front (output) facet, this device still has a reasonable external slope efficiency of 0.074 W/A and an output power of 5.5 mW at a drive current of 100 mA. Such a low CW threshold current is explained by low internal optical losses in the heterostructures (about 1.5 cm^{-1} , as determined from the dependence of the differential efficiency on the cavity length) and by a small number of the carrier states in the active region of a laser with two QD layers, determining low transparency current. The inset in Fig.8 shows the lasing spectra measured for various drive currents (10, 40, and 90 mA). In the whole range of drive currents, lasing involves only the ground state of the QD array.

4.2 High power CW operation

To obtain high differential efficiency HR/AR coating was used for structures containing higher number of QD layers. For example, 75% differential efficiency at CW operation was achieved in the ridge-waveguide laser diode based on 5 layers of QDs of 1-mm-long cavity [31]. The threshold current was still as low as 4.5 mA. One can see that depending of practical application laser parameters can be adjusted in a wide range by means of design of active region and design of output loss in a laser diode.

Fig.9 shows recent unpublished result. The CW output power (from both uncoated facets) with single lateral mode as high as 300 mW is achieved. To the best of our knowledge this is the highest value reported for $1.3 \mu\text{m}$ GaAs based single lateral mode lasers. Regardless clear practical application of $1.3 \mu\text{m}$ laser with such a high power this result indicates that QD devices show excellent performance under high current density. No current induced transition between ground state and excited state, which can be caused by insufficient fast carrier capture into ground state at high photon flux, was observed.

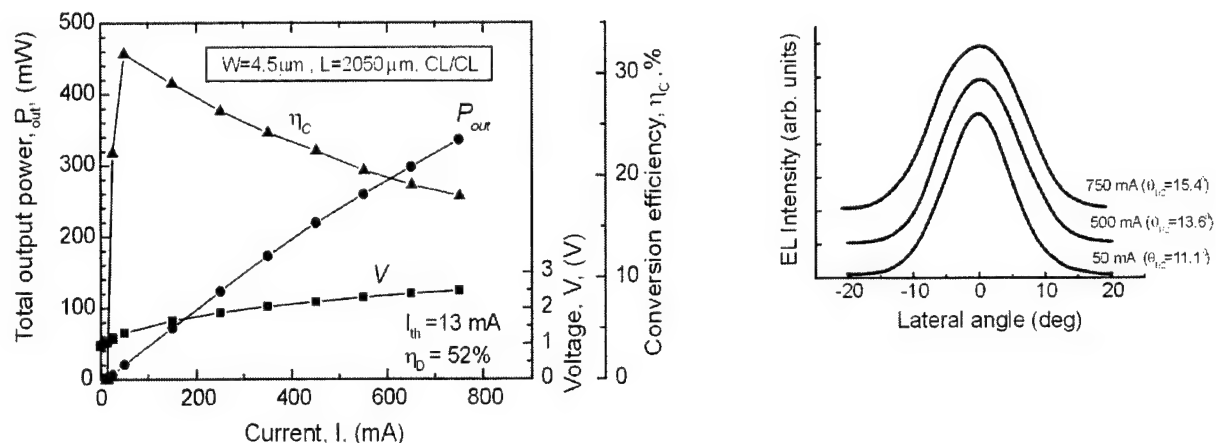


Fig.9 Dependence of CW output power, voltage and wall-plug efficiency on drive current for ridge-waveguide QD laser based on 5 layers of QDs with as-cleaved facets. Slow axis far field patterns prove single lateral mode operation up to high currents.

5. Suppression of non-linear effects in QD lasers

5.1 Reduced linewidth enhancement factor

In semiconductor lasers a change in the injection current causes a modification of the gain/absorption curve and, according to the Kramers-Kronig equations, the respective change in the resonant component of the refractive index. In QW lasers the spectral range of the most significant change in the refractive index coincides with the lasing wavelength, which is typically placed on a longer wavelength side of the initial absorption onset due to the electron-hole plasma-induced band-gap narrowing effect. Consequently, a significant change in the wavelength of the Fabry-Pérot modes occurs with current injection. A similar effect occurs also in distributed feedback (DFB) QW devices.

As opposite, as the ground state absorption or the gain peak of the QD laser can be highly symmetric, the lasing energy appears to be close to the gain maximum. In such a situation the resonant component of the refractive index and

the linewidth enhancement factor responsible for the wavelength shift (α -factor) should be close to zero, as it is shown schematically in Fig. 10. (In reality, gain spectra of QD lasers may be quite different from the idealized case depending on the impact of the homogeneous broadening and the relative energy spacing between the inhomogeneously-broadened ground and the excited state QD exciton energy levels.)

For example, long-wavelength ($>1.25 \mu\text{m}$) MBE QD lasers typically demonstrate well-resolved symmetric ground state QD gain peak as it is shown in Fig. 11 for the case of $1.28 \mu\text{m}$ edge-emitting laser based on 3-fold stacked InAs QDs [32]. This symmetric shape of the gain spectrum together with relatively low modal gain can be, indeed, responsible for the remarkably weak wavelength chirp in QD lasers [33].

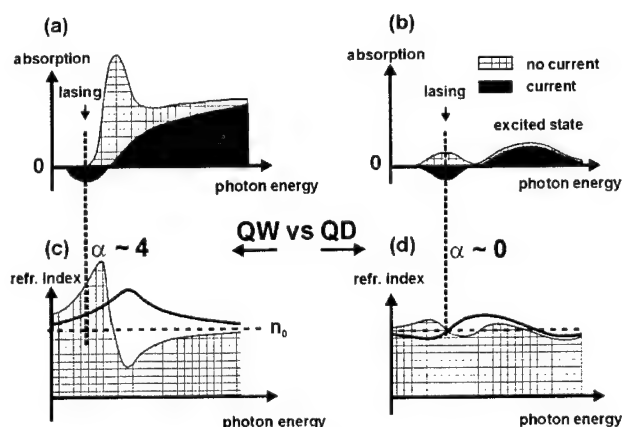


Fig.10: Schematic illustration of difference in gain spectra and refractive index modulation in quantum well and quantum dot lasers. Note that lasing in QD lasers takes place near the ground state gain maximum.

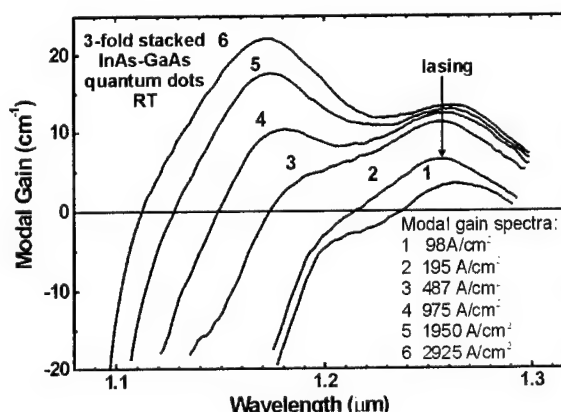


Fig.11: Gain spectra of long-wavelength QD GaAs laser. Note symmetric ground state gain peak at currents near the lasing threshold (70 A/cm^2 for 2 mm cavity length).

Reduced linewidth enhancement factor is indeed serious advantage of QD lasers against QW based counterparts.

Another feature of QD laser which is probably caused by the same reason of reduced non-linearity is reduced sensitivity of external optical feedback. This fact is not presented in this paper and is to be described and discussed in the proceedings of another presentation at the conference [34]. This fact is of very high practical importance, since such a feature may allow laser module fabrication without optical isolator. In addition to the absence of TE-cooling element for $1.3 \mu\text{m}$ QD lasers it may considerably reduce the cost of transceiver module.

Further investigation of these issues will follow to fully clarify the physical reasons and identify the dependence of α -factor and reduced sensitivity of QD laser to optical feedback on laser operation regime.

5.2. Reduced beam filamentation

Reduced α -factor also results in the reduced beam filamentation in QD lasers. The beam filamentation effect arises from the refractive index dependence on the injection current fluctuations. As it was just mentioned, the change in the injection current may cause significant change in the gain spectrum affecting the resonant component of the refractive index of the active media. At the lasing wavelength this modulation is far less important for QD devices than for QW devices. Furthermore, the areas with local fluctuations of the refractive index capable of confining the light, exhibit a higher rate of stimulated emission and should be faster refilled by injected nonequilibrium carriers. In QWs additional currents can be channeled into these regions from the nearby regions causing a positive feedback effect called "current filamentation". Carrier localization in QDs suppresses this effect and may reduce the beam filamentation further.

In Fig. 12 we show near-field patterns of GaAs-based QW and QD lasers grown in a similar design and processed in a similar ridge stripe geometry [35]. The QW laser (MOCVD) emits at $1.1 \mu\text{m}$, and the QD lasers emit at $1.1 \mu\text{m}$ (grown by MOCVD) or at $1.3 \mu\text{m}$ (MBE). First, it is clearly seen from Fig. 12 that in spite of the similar lasing wavelength ($\sim 1.1 \mu\text{m}$), the similar epitaxial and processing designs and the same growth equipment used (MOCVD) the near field of the QW device is much more extended in the lateral direction as compared to both the geometrical stripe width

(6 μm) and the QD laser near-field pattern. This is a direct consequence of the pronounced nonequilibrium carrier spreading in QWs, absent for QD devices.

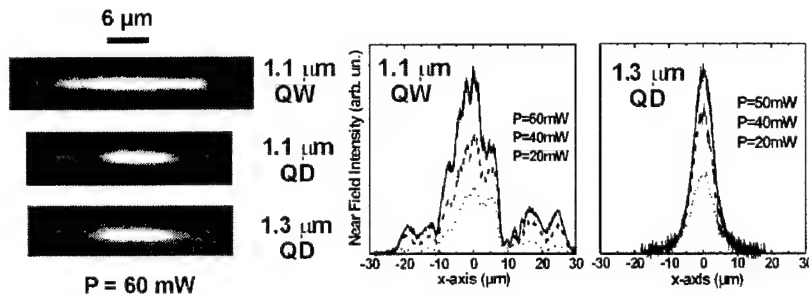


Fig.12: Comparison of the near-field patterns of QW and QD lasers grown in similar waveguide geometry. Note clearly resolved beam filamentation (2-3 μm) in the case of the QW device.

found to be the best and remained remarkably high with M^2 values close to unity [35] up to high powers and maximum stripe widths studied (9 μm) at which high-order transverse modes appear. More efficient suppression of nonequilibrium carrier diffusion in deeper QDs and a lower α -factor due to the influence of the excited QD and continuum states are responsible for the improved performance of long-wavelength MBE QD GaAs lasers [35].

5.3 Longitudinal Mode Grouping in QD Lasers

It was found that lasing spectra of ridge-stripe QD lasers may demonstrate a strong tendency towards longitudinal mode grouping evidenced as multiple quasi-equidistant peaks in the lasing spectrum [36, 37, 38].

Detailed studies of the dependence of the characteristic separation between the valleys in the lasing spectrum on the ridge stripe width of QD lasers was done in [39]. It was clearly shown that the mode group spacing strongly increases with decrease in the ridge stripe width, evidencing the impact of the transverse cavity effect. It was concluded that the transverse cavity and the respective partial transverse holeburning effect in the inhomogeneously-broadened QD gain spectrum affects the lasing in the longitudinal direction.

One should also additionally stress, that the observation of the transverse cavity mode groups up to high currents and stripe widths (50 μm) is only possible, when the device exhibits no beam filamentation. Otherwise the curved beam filaments, which make the optical field distribution nonuniform and provide extra reflections at the filament boundaries, would mask the transverse cavity resonator. This fact additionally stresses the major difference of the QD lasers with respect to the QW devices.

Mode grouping effect can be either enhanced or avoided depending on the laser stripe design. Shallow stripe QD lasers do not show pronounced mode grouping, while the devices where the etching is terminated just at the waveguide layer demonstrate remarkably strong mode-grouping with intensity modulation in the lasing spectra exceeding three orders of magnitude. This potentially allows achieving simple and cost-efficient wavelength stabilization of the device.

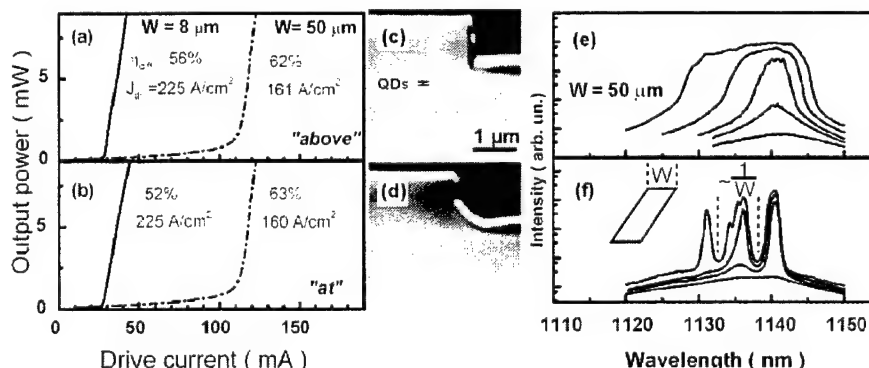
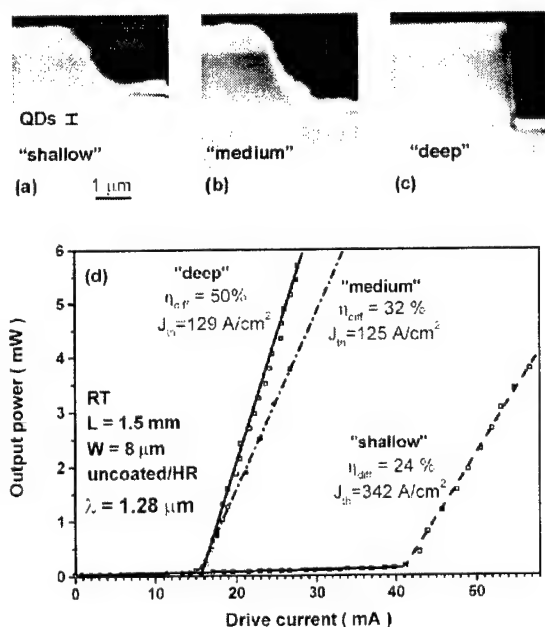


Fig. 13: $L-I$ curves (a, b) of QD lasers fabricated in shallow (c) or deep (d) mesa geometry. The emission spectra are presented for 50- μm -wide stripes at different currents between 0.8 and 4 I_{th} . The spectra (e) and (f) correspond to the devices with etching profiles revealed in scanning electron microscopy images (c) and (d), respectively.

5.4 Suppression of Surface Recombination in QD Lasers

Potential of optical mode and wavelength control in QDs lasers, originating from the reduced α -factor and suppressed beam filamentation, can be further extended by fabrication of *etched-through-waveguide* laser structures, which keep



exceptionally-good device performance. 1.3 μm-range narrow-stripe (8 μm) MBE quantum dot (QD) lasers processed in deep mesa geometry etched through the waveguide demonstrate high differential efficiency (50%), stable ground-state lasing and low threshold current density (<130 A/cm²) [55]. This observation opens a new way for cost-efficient fabrication of distributed feedback and photonic crystal QD devices. As opposite, QW devices fabricated in the same *etched-through-waveguide* design demonstrated no lasing due to the strong impact of the surface recombination of nonequilibrium carriers at the open mesa sidewalls.

Fig. 14: Scanning electron microscopy images (a-c) and *L-I* curves (d) of 1.3 μm QD devices fabricated in shallow (a) or deep (b, c) mesa geometry with termination of the etching before (a, b) or after (c) the waveguide layer. Worse performance of the shallow mesa device is due to significant current spreading.

6. 1.3 μm intracavity-contacted QD VCSEL with all-semiconductor DBR

Previously we reported on CW operation of QD VCSEL with AlO/GaAs DBR [18]. This design with low output loss was chosen to ensure vertical lasing since only three layers of QDs were used in the active region. In spite of low output loss we demonstrated differential efficiency of 40% due to very low round trip loss. The highest output CW power approached 1.25 mW for 8 μm aperture [40] and maximum wall-plug efficiency approached 15%. QD VCSEL appeared to be quite robust to degradation. Operation lifetime in excess of 5000 h at 50°C was demonstrated.

Improvement of technology of multiple stacking of QDs recently allowed us to achieve 1.3 μm single mode CW operation with average device power of 1.5 mW ("hero" device up to 2 mW) at room temperature in intracavity contacted VCSEL with all-semiconductor DBR. [41].

VCSEL heterostructures consist of a 2λ -thick GaAs microcavity containing three sets of triple-stacked InAs/InGaAs quantum dot sheets. A schematic of this arrangement is shown in Fig.15(a), from which it can be observed that each group of three vertically stacked quantum dots is placed at an antinode of the standing wave (electric-field intensity) within the 2λ -thick GaAs microcavity. The microcavity is surrounded by two $\sim\lambda/4$ -thick Al_{0.98}Ga_{0.02}As layers (step-graded from GaAs to Al_{0.98}Ga_{0.02}As over ~ 24 nm, with 6-nm-thick steps of Al_xGa_{1-x}As with $x=0.1, 0.25, 0.6$, and 0.8) which are later selectively oxidized to form both current and tapered waveguide apertures. These Al_{0.98}Ga_{0.02}As layers are followed by 1.75λ -thick intracavity contact/current spreading layers which are followed by undoped and ungraded Al_{0.9}Ga_{0.1}As/GaAs distributed Bragg reflectors (DBR) with 29 periods in the top (light emitting) DBR and 35.5 periods in the bottom (highly reflecting) DBR. The 1.75λ -thick intracavity contact layer is doped with Be to 1×10^{18} cm⁻³ and includes $\lambda/8$ -thick Be doping spikes to 1×10^{19} cm⁻³ centered at the two standing wave nodes closest to the top DBR. Similarly, the lower n-doped 1.75λ -thick intracavity contact layer is doped with Si to 1.5×10^{18} cm⁻³ and includes $\lambda/8$ -thick Si doping spikes to 4×10^{19} cm⁻³ centered at the two standing wave nodes closest to the bottom DBR.

In addition to the all-semiconductor QD VCSELs described above, other similar QD active region test structures, bottom-emitting QD VCSELs, resonant-cavity enhanced light emitting diodes (RC LED) were grown for design/optimization studies. The active structures RC LED are identical to the QD VCSELs described above except that the GaAs substrate is n-type, the bottom DBR consists of only 12.5 periods of ungraded $\lambda/4$ thick AlAs/GaAs layers all n-doped with Si to 1.5×10^{18} cm⁻³, and a top DBR is not included. The room temperature normalized electroluminescence

(EL) intensity from QD RC LED test device with an AlGaO-current aperture as a function of forward bias current is given in the semi-log plot of Fig.15(c). We obtained a peak in the EL spectra near 1280 nm, corresponding to the RC LED resonance and close to the desired peak emission wavelength from the ensemble of QDs in the microcavity.

After epitaxial growth, the QD VCSELs are fabricated into electrically-injected devices as shown schematically in Fig.15(b). Two mesa patterns are defined on the wafer surface using Cl_2 and BCl_3 gas in an inductively coupled plasma etching system and in-situ laser diode reflectance monitoring. Next, the AlGaAs aperture layers are selectively oxidized at 5 Torr in water vapor (at a flow of 500 sccm) at 400°C . Finally, intracavity metal contacts are deposited by e-beam evaporation in a lift-off process. A plot of the output light power-current-voltage (L-I-V) characteristic for a QD VCSEL ("hero" device) with a $12\text{ }\mu\text{m}$ -diametre current aperture is given in Fig.15(d). With a threshold current of 2.2 mA, a threshold voltage of ~ 1.9 Volts, and a slope efficiency over 0.3 W/A , the overall efficiency of this QD device approached 5%.

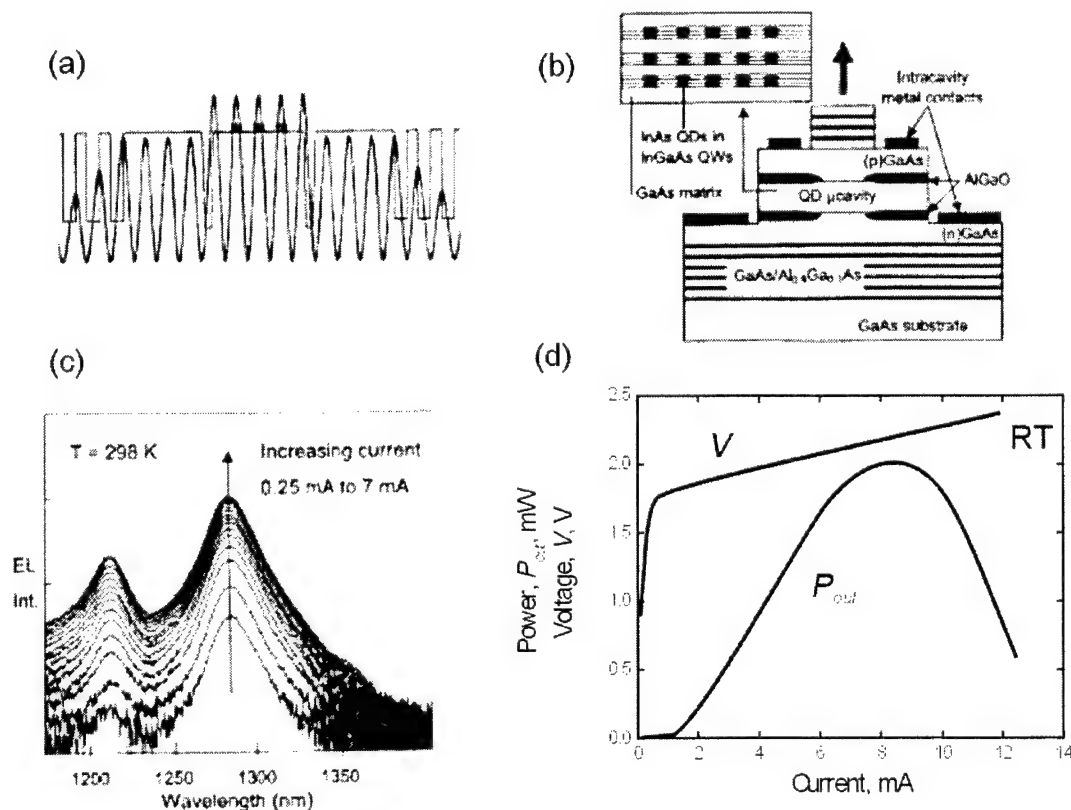


Fig.15. CW operation of QD VCSEL at $1.3\text{ }\mu\text{m}$. (a)Schematic of the E-field intensity and refractive index profile of the QD VCSEL around microcavity; (b) Schematic of a fabricated intracavity-contacted VCSEL; (c)Normalized EL intensity from a QD RC LED test structure; (d)L-I-V curves of the best QD VCSEL. 2 mW CW single mode operation is achieved.

7. Passive Mode-locking QD lasers

Upon receiving excellent DC characteristics of QD laser more and more interest is appearing for direct modulation of QD lasers, data transmission and generation of short pulses. An application of edge-emitting lasers and VCSEL for computer optical clocking and interconnects is a next fascinating milestone in development of diode laser technology.

First results of error-free data modulation and transmission with $1.3\text{ }\mu\text{m}$ QD laser at 5 Gb/s at elevated temperatures will be presented in the proceedings of another paper of this conference⁴². In this chapter we present recent results of passive mode-locking QD lasers with very a record short pulses of 1.7 ps. Mode-locking is the ideal process for optical clocking in computers because of much lower jitter as compared with other pulse generation techniques such as gain or Q-switching.

Long-wavelength QDs offer the following advantages. The wavelength is transparent for Si. If low repetition frequency is targeted (<10 GHz) long-cavity diodes (> 4 mm) must be used for monolithical cavity design. In this case high differential efficiency is provided by very low internal in QD diodes. Since QDs demonstrates lower linewidth enhancement factor, the negative effect of wavelength chirp on pulse width is expected to be suppressed. In this case Fourier-limited pulses can be generated in mode-locked QD lasers. Reduced instability caused by external feedback is among of other advantages of QD lasers for mode-locking pulse generation. Potentially QDs medium gain spectrum is broad enough for subpicosecond pulse generation.

Double-sectional passively mode-locked QD lasers have previously shown 17 ps FWHM light pulses duration [43]. This value is considerably larger in comparison with analogous QW LDs [44]. Moreover the mode-locking regime existed in relatively narrow range of parameters. Careful optimization of growth and device processing was done to widen range of mode-locking and to demonstrate possibility to achieve very short pulses in QD lasers. The detailed results will be published in a separate communication [45], whereas here we present the shortest pulses achieved so far.

The fabricated devices have a tandem two-section structure with a 20 μm gap in the top p-type contact metals. An isolation resistance of 5-10 k Ω is achieved between these two sections by using dry etching to remove the heavily doped cap layer in the gap region. The lengths of the gain and absorber sections were varied by proper cleaving. Shallow mesa was formed for both current and light confinement within the region of 5-7 μm in width, so as the lasers operate in a single lateral mode. No coating is applied to the cleaved facets. The devices were mounted on the copper heat sink with the p-side up, and were tested at room temperature.

CW lasing and bistable operation is observed under unconnected absorber section. Mode-locking appears when absorber section is zero or reverse DC biased. The pulse width is characterized by background-free intensity autocorrelation function. Measurements under various driving conditions show that both pumping current decreasing and also absorber reverse bias increasing lead to the shortening of mode-locked pulses. Mode-locking regime with the shortest pulses is shown on the Fig. 16. It was measured under pumping current of 80 mA (2 mA over the switching-off threshold) and absorber reverse bias of 6V.

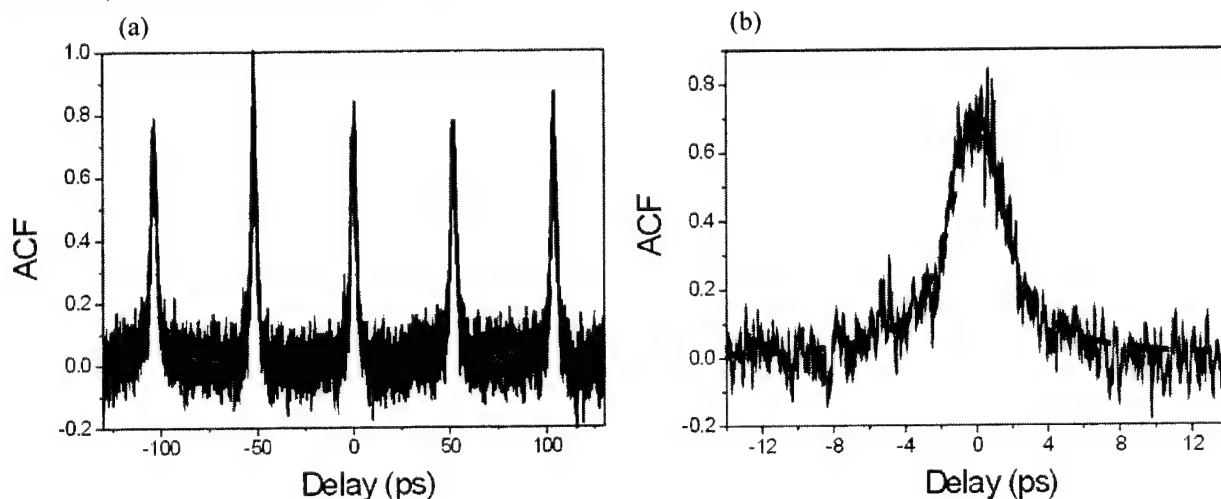


Fig 16. Measured autocorrelation trace (a) and its central spike, which is fitted by Lorentzian curve (b). Autocorrelation trace width 3.4 ps corresponds to the light pulse duration of 1.7 ps.

Thus, as short as 1.7 ps pulses have been achieved by passive mode-locking under pumping at the threshold vicinity and reverse absorber section bias. Uncorrelated jitter was estimated to be below 1 ps. We have clear indication that further optimization of fabrication of two-sectional devices will result to shorten of pulse width.

8. Extension of wavelength range of QD GaAs lasers to 1.5 μm

Further extension of the wavelength in QD lasers is possible by using metamorphic (relaxed) InGaAs layers with incorporated InAs QDs grown on GaAs substrates [46]. In case when the threading dislocations can be avoided in the active region, a high-performance operation with quantum efficiency exceeding 60-70% is realized (Figs.17(a) and (b)). Threshold current density of 0.8 kA/cm^2 is achieved for 4-facet cleaved diodes.

High-temperature operation of the device is realized (Fig.17(c)) up to temperatures above 80°C and the emission wavelength approaches wavelengths $>1.515 \mu\text{m}$.

Total output powers up to 7 W were demonstrated in 2-mm long unmounted devices in a pulsed mode (Fig.17(d)).

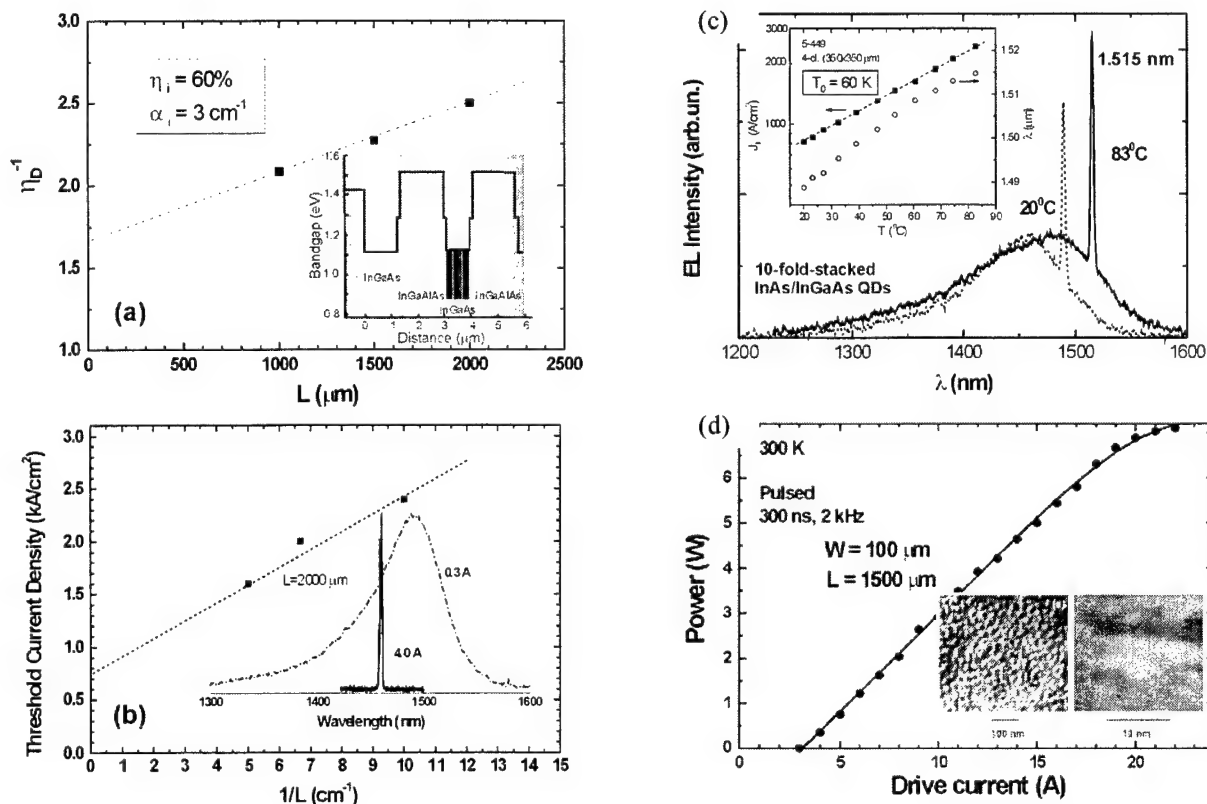


Fig.17. Performance of the broad area ($W=100 \mu\text{m}$) QD lasers grown on metamorphic InGaAs/GaAs buffer.

(a) Dependence of reciprocal differential efficiency on cavity length.

(b) Dependence of threshold current density on reciprocal cavity length. The secondary electron microscopy image of the typical MM structure and the emission spectra are shown in the insets of (a) and (b), respectively.

(c) Spectra of EL slightly above threshold at different temperatures. Insert shows dependence of lasing wavelength and threshold current density on temperature

(d) L-I curve of 1.5 μm QD laser. Differential efficiency as high as 52% is achieved. Inset shows plan-view and cross-section of TEM image for QDs grown on metamorphic buffer. The areal density of QDs is as high as $2 \times 10^{11} \text{ cm}^{-2}$.

8. Conclusion

Combined nanoapproaches for QD formation and defect engineering powered by excessive experience and know-how in MBE technology appeared to be of crucial importance for the success in the field of development of QD lasers.

Excellent laser parameters such threshold current density ($<100 \text{ A/cm}^2$), differential efficiency ($>70\%$), internal loss ($<2 \text{ cm}^{-1}$), CW power (3W for multimode operation and 300 mW for single mode device), temperature stability of threshold current ($T_0 > 100\text{K}$) have been demonstrated.

1.3 μm VCSEL with 2 mW single mode CW operation is realized with all-semiconductor DBR.

Further work will concentrate on system application of QD devices, based on their unique properties, such as reduced beam filamentation, wavelength chirp, and optical feedback sensitivity.

QD lasers are shown to be perspective for generation of ultra-short pulses targeting application of diode lasers in computing.

GaAs "unified" laser technology is shown to be feasible to cover the whole telecom wavelength range by realization of 1.5 μm QD laser.

References:

- ¹ Zh.I. Alferov, "The history and future of semiconductor heterostructures," in Proceedings of 99th Nobel Symposium, Arild, June 4-8, 1996, *Physica Scripta*, vol. T68, pp. 32-45, 1996.
- ² I. Hayashi, "Heterostructure lasers," *IEEE Transaction on Electron Devices*, vol. 31, 1630-1645, 1984.
- ³ N.N. Ledentsov and V.A. Shchukin "Novel concepts for injection lasers" *SPIE Optical Engineering*, vol. 41, pp. 3193-3203, 2002.
- ⁴ for a review: N.N. Ledentsov "Long-wavelength quantum-dot lasers on GaAs substrates: from media to device concepts", *IEEE J. Sel. Top. Quantum Electron.*, Vol. 8, pp. 1015-1024, 2002.
- ⁵ C. Ribbat, R. Sellin, M. Grundmann, D. Bimberg, N.A. Sobolev, and M.C. Carmo "Enhanced radiation hardness of quantum dot lasers to high energy proton irradiation," *Electron. Lett.*, vol. 37, pp. 174-175, 2001.
- ⁶ D. Ouyang, N. N. Ledentsov, D. Bimberg, A. R. Kovsh, A. E. Zhukov, S. S. Mikhlin and V. M. Ustinov, High performance narrow stripe quantum-dot lasers with etched waveguide, *Semicond. Sci. Technol.* 18 (2003) L53-L54
- ⁷ A.R.Kovsh, A.E.Zhukov, D.A.Livshits, A.Yu.Egorov, V.M.Ustinov, M.V.Maximov, Yu.G.Musikhin, N.N.Ledentsov, P.S.Kop'ev, Zh.I.Alferov, and D.Bimberg, "3.5 W CW operation of quantum dot laser", *Electron. Lett.*, 1999, 35, pp.1161-1163
- ⁸ J. Tomm, R. Sellin, C. Ribbat, D. Bimberg, to be published.
- ⁹ P. Borri, W. Langbein, J.M. Hvam, F. Heinrichsdorff, M.-H. Mao, D Bimberg, *IEEE J. Sel. Top. Quantum Electronics*, vol. 6, pp. 544-551, 2000.
- ¹⁰ K. Nishi, H. Saito, S. Sugou, J.-S. Lee, *Appl. Phys. Lett.* 74 (8) (1999) 1111.
- ¹¹ L.F. Lester, A. Stinz, H. Li, T.C. Newell, E.A. Pease, B.A. Fuchs, K.J. Malloy, *IEEE Photon. Technol. Lett.* 11 (8) (1999) 931.
- ¹² A.E. Zhukov, A.R. Kovsh, A.Yu. Egorov, N.A. Maleev, V.M. Ustinov, B.V. Volovik, M.V. Maximov, A.F. Tsatsul'nikov, N.N. Ledentsov, Yu.M. Shernyakov, A.V. Lunev, Yu.G. Musikhin, N.A. Bert, P.S. Kop'ev, Zh.I. Alferov, *Semiconductors* 33 (2) (1999) 153.
- ¹³ D.L. Huffaker, D.G. Deppe, *Appl. Phys. Lett.* 73 (4) (1998) 520.
- ¹⁴ J.W. Gray, D. Childs, S. Malik, P. Sivers, C. Roberts, P.N. Stavrinou, M. Whitehead, R. Murray, G. Party, *Electron. Lett.* 35 (1999) 242.
- ¹⁵ Q. Gong, R. Notzel, G.J. Hamhuis, T.J. Eijkemans, J.H. Wolteret, *Appl. Phys. Lett.* 81 (2002) 1887.
- ¹⁶ I. Mukhametzhano, Z. Wei, R. Heitz, A. Madhukar, *Appl. Phys. Lett.* 75 (1999) 85.
- ¹⁷ A.R. Kovsh, A.E. Zhukov, A.Yu. Egorov, V.M. Ustinov, Yu.M. Shernyakov, M.V. Maximov, B.V. Volovik, A.F. Tsatsul'nikov, Yu.V. Musikhin, N.N. Ledentsov, P.S. Kop'ev, D. Bimberg, Zh.I. Alferov, *J. Crystal Growth* 201/202 (1999) 1117.
- ¹⁸ J.A. Lott, N.N. Ledentsov, V.M. Ustinov, N.A. Maleev, A.E. Zhukov, A.R. Kovsh, M.V. Maximov, B.V. Volovik, Zh.I. Alferov, D. Bimberg, *Electron. Lett.* 36 (16) (2000) 1384.
- ¹⁹ N.N. Ledentsov, M. Grundmann, F. Heinrichsdorff, D. Bimberg, V.M. Ustinov, A.E. Zhukov, M.V. Maximov, Zh.I. Alferov, J.A. Lott, *IEEE J. Sel. Top. Quantum Electron.* 6 (3) (2000) 439
- ²⁰ O.B. Shchekin, D.G. Deppe, *Appl. Phys. Lett.* 80 (18) (2002) 3277
- ²¹ A.R. Kovsh, N.A. Maleev, A.E. Zhukov, S.S. Mikhlin, A.P. Vasil'ev, Yu.M. Shernyakov, M.V. Maximov, D.A. Livshits, V.M. Ustinov, Zh.I. Alferov, N.N. Ledentsov, D. Bimberg, *Electron. Lett.* 38 (19) (2002) 1104
- ²² J.S. Wang, R.S. Shiao, G. Lin, L. Wei, Y.T. Wu, J.Y. Chi, A.R. Kovsh, N.A. Maleev, A.V. Sakharov, D.A. Livshits, Second International Conference on QDs Tokyo Japan, 30 September-3 October 2002.

- ²³ B.V.Volovik, A.F.Tsatsul'nikov, D.A.Bedarev, A.Yu.Egorov, A.E Zhukov, A.R.Kovsh, N.N.Ledentsov, M.V.Maximov, N.A. Maleev, Yu.G.Musikhin, A.A.Suvorova, V.M.Ustinov, P.S.Kop'ev, Zh.I.Alferov, D.Bimberg, P.Werner, *Semiconductors* 33 (1999) 901
- ²⁴ M.V. Maximov, A.F. Tsatsul'nikov, B.V. Volovik, D.S. Sizov, Yu.M. Shernyakov, I.N. Kaiander, A.E. Zhukov, A.R. Kovsh, S.S. Mikhlin, V.M. Ustinov, Zh.I. Alferov, R. Heitz, V.A. Shchukin, N.N. Ledentsov, D. Bimberg, Yu.G. Musikhin, W. Neumann, *Phys. Rev. B* 62(24) 16671.
- ²⁵ V.M. Ustinov, N.A. Maleev, A.E. Zhukov, A.R. Kovsh, A.Yu. Egorov, A.V. Lunev, B.V. Volovik, I.L. Krestnikov, Yu.G. Musikhin, N.A. Bert, P.S. Kop'ev, Zh.I. Alferov, N.N. Ledentsov, D. Bimberg, *Appl. Phys. Lett.* 74 (19) (1999) 2815.
- ²⁶ N.N. Ledentsov, M.V. Maximov, D. Bimberg, T. Maka, C.M. Sotomayor Torres, I.V. Kochnev, I.L. Krestnikov, V.M. Lantratov, N.A. Cherkashin, Yu.M. Musikhin, Zh.I. Alferov, *Semicond. Sci. Technol.* 15 (2000) 604.
- ²⁷ P.M. Smowton and P. Blood, *IEEE J. of Sel. Top. in Quantum Electronics*, 3 (1997) 491
- ²⁸ A.E. Zhukov, V.M. Ustinov, Zh.I. Alferov, in: *Advances in semiconductor lasers and applications to optoelectronics*, Vol. 16, WorldScientific, Singapore, 2000, pp. 263–292
- ²⁹ T.R.Zhen, B. Zhao, Y. H. Zhuang, and A. Yariv, *Appl. Phys. Lett.* 60, (1992), 1782.
- ³⁰ D. L. Huffaker, G. Park, Z. Zou, *et al.*, *IEEE J. Sel. Top. Quantum Electron.* 6, 452 (2000).
- ³¹ A.R.Kovsh, D.A.Livshits, N.A.Maleev, A.E.Zhukov, V.M.Ustinov, J.S.Wang, R.S.Hsiao, G.Lin, J.Y.Chi, and N.N.Ledentsov, "1.3 micron single lateral mode lasers based on InAs QDs and InGaAsN quantum wells", 12th North American Conference on MBE, Keystone, Colorado, USA, Sept.28-Oct.2, 2003
- ³² M.V. Maximov, L.V. Asryan, Yu.M. Shernyakov, A.F. Tsatsul'nikov, I.N. Kaiander, V.V. Nikolaev, A.R. Kovsh, S.S. Mikhlin, V.M. Ustinov, A.E. Zhukov, Zh.I. Alferov, N.N. Ledentsov, D. Bimberg, "Gain and threshold characteristics of longwavelength lasers based on InAs/GaAs quantum dots formed by activated alloy phase separation," *IEEE J. Quantum Electron.*, vol. 37, pp. 676-683, 2001.
- ³³ T.C. Newell, D.J. Bossert, A. Stintz, B. Fuchs, K.J. Malloy and L.F. Lester, "Gain and linewidth enhancement factor in InAs quantum-dot laser diodes," *IEEE Photonics Technol. Lett.*, vol. 11, pp. 1527-1529, 1999.
- ³⁴ G. Huyet, D. O'Brien, S. P. Hegarty, J. G. McInerney, Univ. College Cork (Ireland); D. Bimberg, C. Ribbat, Technische Univ. Berlin (Germany); V. M. Ustinov, A. E. Zhukov, S. S. Mikhlin, A. R. Kovsh, Reduced sensitivity to external optical feedback in quantum dot lasers, to be presented at Pwotonic West 2004, 24-29 January, San Jose, California, USA, *paper # 5361-04*.
- ³⁵ Ch. Ribbat, R.L. Sellin, I. Kaiander, F. Hopfer, N.N. Ledentsov, D. Bimberg, A.R. Kovsh, V.M. Ustinov, A.E. Zhukov, and M.V. Maximov, "Complete suppression of filamentation and superior beam quality in quantum-dot lasers," *Appl. Phys. Lett.*, vol. 82, pp. 952-954, 2003.
- ³⁶ D. Bhattacharyya, E. A. Avrutin, A. C. Bryce, J. H. Marsh, D. Bimberg, F. Heinrichsdorff, V. M. Ustinov, S. V. Zaitsev, N. N. Ledentsov, P. S. Kop'ev, Zh. I. Alferov, A. I. Onischenko, and E. P. O'Reilly, "Spectral and dynamic properties of InAs-GaAs self-organized quantum dot lasers," *IEEE J. Select. Topics Quantum Electron.*, vol. 5, pp. 648-657, 1999.
- ³⁷ L. Harris, A.D. Ashmore, D.J. Mowbray, M.S. Skolnick, M. Hopkinson, G. Hill, and J. Clark "Gain characteristics of InAs/GaAs self-organized quantum-dot lasers" *Appl. Phys. Lett.*, vol. 75, pp. 3512-3514, 1999.
- ³⁸ M. Sugawara, K. Mukai, Y. Nakata, H. Ishikawa, and A. Sakamoto, "Effect of homogeneous broadening of optical gain on lasing spectra in self-assembled In_{0.15}Ga_{0.85}As/GaAs quantum dot lasers," *Phys. Rev.*, vol. B 61, pp. 7595-7603, 2000.
- ³⁹ D. Ouyang, R. Heitz, N.N. Ledentsov, S. Bognár, R.L. Sellin, Ch. Ribbat, and D. Bimberg, "Lateral-cavity spectral hole burning in quantum-dot lasers" *Appl. Phys. Lett.*, vol. 81, pp. 1546-1548, 2002
- ⁴⁰ D. Bimberg, N.N. Ledentsov, and J.A. Lott, "Quantum-Dot Vertical-Cavity Surface-Emitting Lasers," *MRS Bulletin*, vol. 27, pp. 531-538, 2002
- ⁴¹ J.Lott, N.Ledentsov, A.Kovsh, V.Ustinov, D.Bimberg, Multiple stacks of InAs/InGaAs Quantum Dots for GaAs-based 1.3 mm Vertical Surface Cavity Lasers, *LEOS*, Tucson, AZ, USA, October 26-30,2003
- ⁴² D. H. Bimberg, High power single and multimode quantum dot lasers with superior beam profile (Invited Paper), to be presented at Pwotonic West 2004, 24-29 January, San Jose, California, USA, *paper # 5365-06*
- ⁴³ X.Huang, A. Stintz, Hua Li, L. F. Lester, Julian Cheng, and K. J. Malloy, "Passive mode-locking in 1.3 mm two-section InAs quantum dot lasers," *Appl. Phys. Lett.* 78(19), 2001 pp. 2825-2827.
- ⁴⁴ E.A.Avrutin, J.H.Marsh, and E.L.Portnoi, *IEE Proc.: Optoelectron.* 147, 251 (2000).
- ⁴⁵ A.E.Gubenko et al. *to be published*
- ⁴⁶ N.N.Ledentsov, A.R.Kovsh, A.E.Zhukov, N.A.Maleev, S.S.Mikhlin, A.P.Vasil'ev, E.S.Semenova, M.V.Maximov, Yu.M.Shernyakov, N.V.Kryzhanovskaya, V.M.Ustinov and D.Bimberg, High performance quantum dot laser on GaAs substrates operating in 1.5 μ m range. *Electronics Lett.* 39, 1126 (2003)

Shell model of semiconductor quantum dots

P. G. Eliseev^{*a,b}, D. P. Popescu^a, T. V. Torchynska^c, A. Stintz^a, K. J. Malloy^a,

^a Center for High Technology Materials, Uni. of New Mexico, Albuquerque, NM

^b also P. N. Lebedev Physics Institute, Moscow, Russia

^c Material Science Department, Faculty of Physics and Mathematics, National Polytechnic Institute, Mexico D.F., 07738, Mexico

ABSTRACT

Model consideration is given to explain observed multi-shell emission spectra from InAs quantum dots embedded in GaAs or InGaAs. The shell model is based on the quantization of kinetic energy of lateral motion of carrier in the dot. 2-D oscillator is calculated on the basis of effective mass approximation. Profiles of inter-level separation are classified into categories that are connected with the lateral confining potential. Comparison is carried with experimental data on InAs/InGaAs quantum dot structures of the DWELL type (dot-in-a-well).

Keywords: semiconductor quantum dots, energy spectra, modeling, multi-shell emission

1. INTRODUCTION

Quantum-dots (QDs) are in focus of numerous investigations motivated by their advantageous properties for optoelectronic devices. DWELL InAs/InGaAs QD structures are successfully applied to semiconductor lasers with ultra-low threshold current density at room temperature [1,2]. Usually, the emission spectra of QD ensembles contain several spectral bands corresponding to the *ground* and *excited* states of carriers captured into dots. The spectral width and separation between these bands are important characteristics of QDs because these parameters influence the performance of lasers. The lowest lasing threshold is achievable in the ground-state band whereas occupation of excited states is not desirable. From another point of view, for wider tuning of the lasers, involvement of excited states is favorable.

An atom-like QD is challenging quantum-mechanical many-particle object. For a comparison, in atom the confining potential is the Coulomb one with a screening by electrons at inner shells. In nucleus there are nuclear short-distance interaction defining the nuclear structure. These many-particle systems are treated in terms of shell model. For example, electronic shell is a fundamental category of atomic physics to understand atomic spectra and all basic chemistry of atoms. In semiconductor QDs, the confining potential is associated with several factors, namely, the composition, shape and size of dots that all influence the energy band diagram with a modification produced by misfit stress. Thus the confining potential is not universal but it is sensitive to growth and annealing parameters, for example it is subjected to significant change by thermal intermixing. There are developed theoretical approaches to treat different QDs to find their basic electron structure [3-10]. Nevertheless the comparison with experimental results is not always satisfactory. There are different interpretations of spectral bands emitted by QD ensembles and nature of optical transitions. Particular issue is how many electron states are involved in optical transitions. In modeling of the QD spectra, some authors yield to a point of only electron level take a part, whereas others consider equal number of electron and hole levels with proper selection rules between them to provide known multi-shell spectral distributions.

In this paper we present data on multi-shell emission from semiconductor epitaxial structures containing ensembles of self-formed quantum dots. A short review is also given on related data in literature. We propose an attempt to come a model consideration into agreement with experiments on InAs dots in different matrices.

*eliseev@chtm.unm.edu; phone 1 505 272 7807

2. REVIEW OF MULTI-SHELL EMISSION SPECTRA OF QDs

2.1. Shell definition and spectral parameters

At first, we specify our subject as optical spectra of QD ensemble in contrast with spectra from individual dot. The ensemble spectra are result of summation of individual spectra over a large number of dots scattered by their size and composition. The inhomogeneous broadening due to fluctuation of dot parameters is the main contribution into the spectral width of shell band. Typically the bandwidth of 20-40 meV is characteristic for particular shells, and the spectral shape is roughly close to the Gaussian. In numerous papers the multi-shell behavior had been reported of self-formed QDs [10-15]. Spectroscopy of emission from individual dots yields narrow lines (~ 1 meV wide) that can be interpreted in terms of states of localized excitons subjected to some splitting due to dot irregularities and other factors [16]. These lines are grouped around some centers that associated with centers of shell bands in the ensemble spectra.

The concept of shells proved to be rather fruitful in atomic and nuclear physics. It is based on a fact that the energy levels of particles in many-body systems are determined primarily by quantization of their kinetic energy in the confining potential. In spite of substantial interaction between confined particles, these levels can be roughly determined by the single-particle approach whereas many-body effects should be included for correction. A shell is defined as a single or several levels with quite close energy that allows one to distinguish this shell from other shells. It is reasonable to use this concept if the energy parameters of shells have a trend to be invariant under variable occupation of the dot. Experimentally, the peak position in the multi-shell observations from self-formed QDs is of this invariant type. It suggests that the main part of the total energy is consisted by quantization of the energy in confinement potential, and capture of many particles does not change this energy substantially. An example of multi-shell spectrum is shown in Fig. 1 for photoluminescence of the DWELL-type InAs QDs at 12 K [10]. The variation of the pumping rate had been of 50 times. Detailed analysis shows that spectral peak position is not much sensitive to the intensity (the ground state peak red-shifts only about 2.1 meV over the whole range of pumping rate. The broadening is dependent also weakly: the Gaussian bandwidth parameter of the ground-state shell increases from ~ 15 to 20.7 meV.

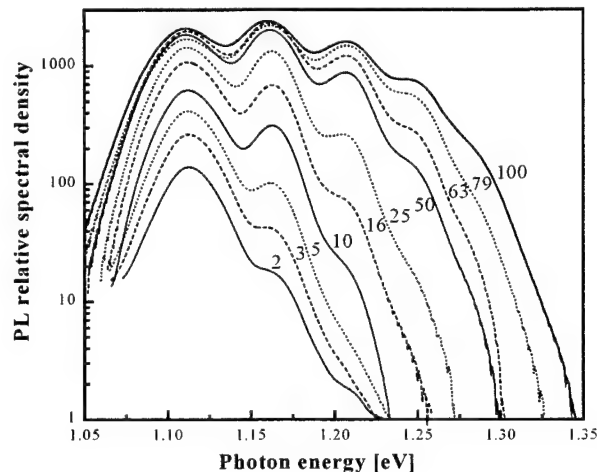


Fig. 1. Power dependent PL spectra of QD-heterostructure at 12 K. The pumping power is indicated in percent of maximum power of 600W/cm^2 [10]

2.2. Effect of growth and annealing parameters

In Ref. [12] it had been clearly demonstrated that in a particular case of MBE growth technique (at fixed growth temperature of 480°C) the amount of deposited InAs determines the spectra obtained from QD ensembles. The growth occurs in a Stranski-Krastanov mode. It is characteristic that the equivalent amount of ~ 1.5 monolayers (ML) of InAs is consumed to obtain an uniform layer of InAs ("wet layer") closely corresponding to the critical thickness of InAs epilayer with the lattice misfit of $\sim 7.2\%$ (in respect to the GaAs substrate and matrix material). Up to ~ 1.81 ML only the

wet layer emission is detected by PL measurements. With the increase of deposited InAs, the part that is not consumed for the wet layer, coagulates into 3-D islands. These islands become dots when the matrix material (GaAs, InGaAs or AlGaAs) is grown over them. In the range from 1.81 to 1.88 ML, there are well-defined sets of 4-5 spectral peaks (shells) between photon energies of 1.03 and 1.30 eV (at 77 K), quite below the absorption edge of GaAs matrix. The density of dots was just near 10^{10} cm^{-2} . At further increase of the deposited InAs, the dot density overcomes $\sim 10^{10} \text{ cm}^{-2}$ and the ground-state blue-peak shifts to $\sim 1.12 \text{ eV}$ at 2 ML. The shell structure disappears and the QD emission becomes a broad band ($> 100 \text{ meV}$).

This evolution of the QD emission spectra reflects the formation of electronic shells in the dots along with increase of their size. Notice that a very small 3D-confinement potential has no localized states (in contrast to a QW, where the confined state exists formally for any depth and size). So, probably, dots formed at an amount of deposited InAs between 1.5 and 1.8 ML are too small to form deep levels. The levels appear between 1.8 and 2 ML and then the average size of the dots begins to decrease (producing the blue shift of the ground state emission) simultaneously with the increase of the dot density. Further increase of the amount of deposited InAs leads to the formation of multiple defects associated with a large lattice misfit and a decrease in the emission from the epilayer. Another example of spectral evolution is produced by the diffusion intermixing of the dot and matrix material [13]. Rapid thermal annealing (typically around 30 seconds long) at temperatures between 800 and 850°C transforms the QD emission spectrum because the ground state shifts toward blue, separation between shells decreases and some narrowing takes place. But ultimately, the emission weakens and degrades into one bell-shaped band. The intermixing-produced blue shift can be as large as 200-300 meV [13,14]. From the aforementioned data it is seen that QD-structures can be quite flexible in their properties for different functions and different wavelengths. It is also important to develop adequate understanding of these properties.

2.3. Two types of shell "profiles".

In Fig. 2 we show the first type of shell profiles represented by the dependence of the interlevel spacing on the number of lower states (consequently with the energy increase). Profile 1 shown in Fig. 2 is for InAs QDs in GaAs matrix grown at 540°C [17], and profile 2 is for similar dot layers grown at 530°C [13]. It has a saw-like shape that is also seen in the calculated profile 2D-RO for oscillator with rectangular potential. Profile 3 is the same wafer as 2 but after atomic intermixing induced by a rapid thermal annealing procedure at 850°C. The variation of the spacing is reduced here as the potential profile approaches one similar to a harmonic oscillator.

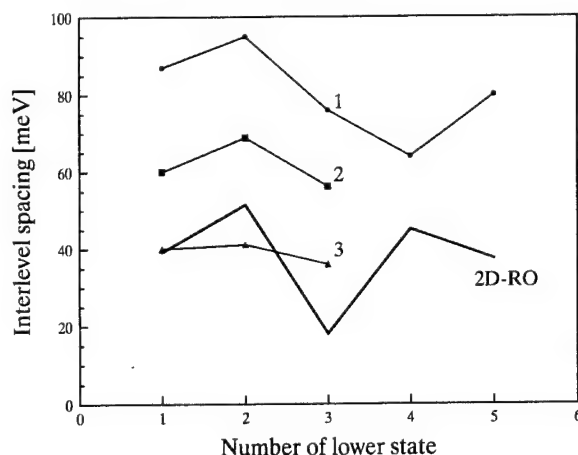


Fig. 2. Profile of interlevel spacing: 1)[17]; 2)[13]; 3) [13, after intermixing]; also calculated profile is shown (2D-RO) for 2-D rectangular oscillator

Second type of profiles is shown in Fig. 3. Profile 1 is for InAs QDs in InGaAs QW [10] with monotone decrease of the interlevel spacing. Dots had been grown by MBE at 510°C. This characteristic is also seen in other profiles of Fig. 3. Lines 2 and 3 relate to InGaAs dots in GaAs matrix [11,15]. Growth temperature was 530°C (2) and 512°C (3). In the last case, the spacing changes very little so the spectrum could be assumed to correspond to a harmonic oscillator. Lines 4 and 5 are data for the samples B and C of Ref. [13] that had been grown at 515°C and $\sim 480^\circ\text{C}$, respectively. Thus we

see some correlation between the type of the profile and the growth temperature. Namely, higher temperature provides sharper potential well shape. We can speculate that the potential shape in formed dots is close to rectangular at higher growth temperatures (530-540°C), whereas at lower temperatures (480-530°C) the shape evolves toward an anharmonic oscillator well profile. As for the intermixing procedure, it changes the type I profile to HO or to type II profile (simultaneously with a decrease of the first spacing).

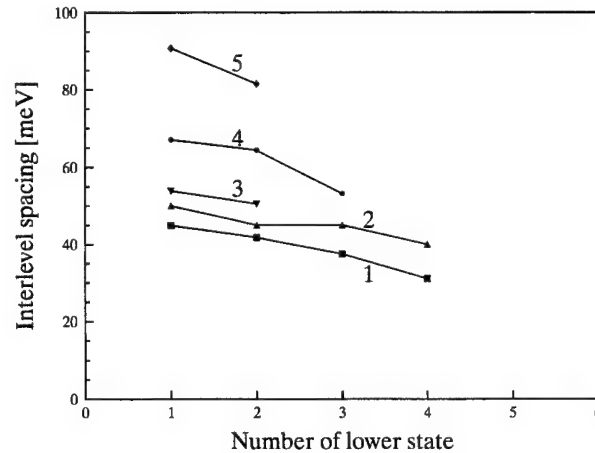


Fig. 3. Profile of interlevel spacing: 1) [10]; 2) [11]; 3)[15]; 4, 5) [13].

4. SHELL MODEL

4.1. Preliminary comments

We had discussed above on experimental evidence in favor of the shell model. We have to present some theoretical reasons here. In multi-electron atoms, the unfilled shell is considered as an independent system moving in the effective field created by a nucleus and by electrons of another shells. In nuclear physics, the interaction between particles is of quite different nature as compared with atomic systems. Nevertheless the shell model appeared to be suitable to explain properties of nucleus and their magic numbers. As applied to semiconductors nanostructures, the validity of the shell concept is discussed in terms of comparison between the confining energy of electron and hole in the dot and their Coulomb interaction energy. It is concluded in Ref. [3] that in small QDs (diameter of 20-40 nm), the ratio of single-particle excitation energy and the Coulomb energy is similar to that ratio in many-electron atoms. This allows one to specify shells by rules known in atomic physics, but with usage of other confining potential than the screened Coulomb one in atoms. Particularly, this means that the ground and near excited states are well determined by quantization of single-particle motion in a confining potential. As it occurs in atoms, particles in QD would fill up single-particle states according to the Pauli exclusion principle. This gives a basis to construct the multi-shell model for QD with a single-particle energy spectrum as a first approximation followed by many-body corrections.

4.2. Approximations

The essence of effective mass approach (EMA) is an usage of a single effective mass for each type of particle under consideration [3,6,9,10]. There is a technical advantage of EMA to utilize an extensive experience of quantum mechanical treatment of spectra in different regions of physics (molecular, atomic and nuclear spectra). The reconstruction of the confining potential from data on the energy spectrum is one of typical goals in the quantum mechanics (see, for example [18]). There are a wide variety of solvable potentials allowing us to use easily analytic solution as a possible approximation. Solvable potentials in connection with a super-symmetry principle had been analyzed systematically (see, for example, [19,20]). The effective mass of electron in InAs is $0.022m_0$. In InAs QD, the energy bands are affected by significant strain. It provides some modification of the effective mass. In Ref. [8], the effective mass is estimated as $0.04 m_0$. The energy of localization (zero-point energy) at a dot of 10-nm size is by order of value ~ 100 meV. The separation between few lower levels is of the same order. For a typical well depth of ~ 300 meV, there are a room for 1-2 levels. The heavy-hole mass in InAs is substantially anisotropic with $\sim 0.33m_0$ along a height of dot and $\sim 0.57m_0$ as averaged for in-plane directions. The localization energy is ~ 10 meV. This difference suggests the multi-shell appearance of (4-5 bands) is associated with a set of hole levels rather than with electron ones.

4.3. One-dimensional case

The 1D case is suitable to demonstrate the influence of the confining potential shape on the relative position of energy levels of bound states. We consider three characteristic potentials as shown in Fig. 4 in the frames of EMA. Namely, these are the "rectangular oscillator" (RO), harmonic oscillator (HO) and anharmonic oscillator (AHO) with a potential of $sech^2$ -type known as the modified Poeschl-Teller potential [20]. Corresponding spectra are shown in Fig. 5. According to the 1D assumption, the energy levels are dependent on only one quantum number, n . In the RO case the inter-level spacing increases along with an increase of n , whereas in the HO-case the spacing is almost constant (some anharmonicity associated with a finite depth of the well is negligible for most deep levels). In the AHO case, the levels are not equidistant anymore, and the spacing decreases along with increase of n , that correlates with the smoothened profile of the potential at the peripheral distance. Thus the relative position of energy levels correlates with the shape of confining potential. It is useful to notice that for rectangular and parabolic well, analytic solutions are available for infinite depth. When finite well depth is considered, the level position is affected into side to lower energy in the extend depending on level position to the upper edge of truncated potential: the shift is larger as close to the upper edge (that is edge of continuum). The shift can be rather small for deep levels. In the HO, the first order perturbation approximation is satisfactory.

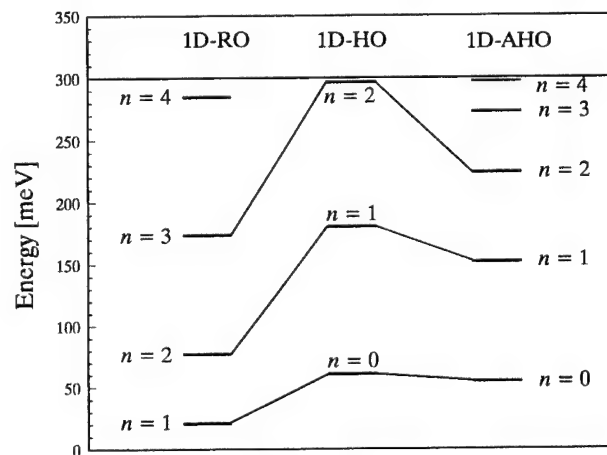


Fig. 4. Energy levels of 1-D oscillators: rectangular oscillator (RO), truncated harmonic oscillator (HO), anharmonic oscillator (AHO). Notice different notation of quantum numbers n .

4.4. Circular oscillator

In 2D and 3D cases additional quantum numbers appears to influence the energy of confined states. We consider here the 2D case that seems to be applicable to "quantum disks" and to quantum dots with a large ratio of lateral diameter to dot height (most self-assembled QDs are of this sort). The circular oscillator is described in a two-coordinate space: radial distance r and azimuth angle ϕ . The motions along these coordinates are represented by the radial quantum number n and by the orbital quantum number m . Remembering that an actual QD is a 3D object, we have to specify the motion in vertical z direction. By separation of variables, we assume the confined vertical motion as an independent coordinate with a quantization that provides only a ground state with zero-point energy E_z . Calculated energy levels are shown in Fig. 5 for two-dimensional oscillators with a well of finite depth (300 meV). The left column represents levels in the rectangular-profile potential well (2D-RO). There are two series, $1s$ - $1f$ and $2s$, $2p$ corresponding to different radial quantum numbers, among the six lower states. It is seen that the interlevel spacing increases with orbital number inside the first series (49, 64, 75,... meV), however the $2s$ level that is 133 meV above $1s$. The $2s$ level falls between $1d$ and $1f$ levels and the monotonic increase of the spacing is violated by the overlapping of two series. The medium column represents the levels in the truncated parabolic potential (parabolic well of finite depth). Because of a so-called accidental degeneracy, the energies of the $1d$ and $2s$ states coincide as well as the energies of some other states starting from the third level. The finite depth of the harmonic oscillator well has a small influence, so these levels are almost equidistant. Severe anharmonicity included in the calculation of right column 2D-AHO. It relate to the potential of $sech^2$ type. In fact, the profile is known as analytically solvable at least for the s -states, however there are no available results in literature for the 2D case.

and Φ_h are the eigenfunctions resulting from solving the Schrödinger equation for an electron or for a hole in the EMA approximation. Distinct spatial volume units are given in terms of $d\vec{r}_e$ and $d\vec{r}_h$ for electron and hole, respectively. Because of the cylindrical geometry characteristic to a dot, the electron-hole distance has to be expanded in cylindrical coordinates as follows:

$$\frac{1}{|\vec{r}_e - \vec{r}_h|} = \frac{4}{\pi} \int_0^\infty dk \cos[k(z_e - z_h)] \left\{ \frac{I_0(kr_<)K_0(kr_>)}{2} + \sum_{s=1}^\infty \cos[s(\theta_e - \theta_h)] I_s(kr_<)K_s(kr_>) \right\}. \quad (2)$$

I_0 and K_0 are the zero-th order Bessel functions, k is the wave-vector corresponding to the spatial decomposition, z_e and z_h are the position coordinates along the growth direction (z -axis), ϕ_e and ϕ_h are the angles between the z -axis and vectors \vec{r}_e and \vec{r}_h , s is an integer variable used for summation. Quantity $r_>$ ($r_<$) represents the larger (smaller) absolute value when comparing the magnitudes of vectors \vec{r}_e and \vec{r}_h .

At first, we show in Table 1 how the Coulomb correction depends on size and effective mass of carriers captured into the dot. We consider the correction to the energy of ground-state transition (from level 1s of electron to level 1s of holes). Variable parameter is a quantity $(m/m_0)^{1/2}R$, where m is hole effective mass and R is radius of dot with a rectangular potential. For electrons, this parameter is taken to be 1 nm. It is seen how the correction decreases along with increase of the dot size or hole effective mass. Such calculation is also useful to determine the contribution of the Coulomb interaction into the spectral broadening associated with size fluctuations of dots.

Table 1. Variation of the Coulomb energy of interaction between an electron and a hole trapped into quantum dot with a rectangular potential.

Parameter $(m/m_0)^{1/2}R$ [nm]	2.5	3.0	3.5	4.0	4.5	5
The Coulomb correction [meV]	-22.0	-20.5	-19.0	-18.0	-18.0	-17.0

Another set of calculated data is shown in Table 2. There are the Coulomb corrections for several (ground-state and excited-state) transitions in the case of the harmonic oscillator. Parameters are the same as for data presented in Fig. 5. The correction to the ground-state transition energy is about -12 meV in this particular case. It is seen that the Coulomb interaction produces some splitting of transitions to 1d and 2s states. However such splitting is much smaller than the bandwidth of the shell. Therefore these levels will be integrated in the same shell. Also, it is important, the correction appears to be weakly dependent on the states involved in the transition. This allows us to conclude that the mutual position of energy shells would not change after accurate correction for Coulomb attraction between electron and hole captured into QD. The type of interlevel separation profile would not change as well.

Table 2. Calculated transition energy for QD with parabolic 2-D confinement potential

Electron state	1s	1s	1s	1s
Hole state	1s	1p	1d	2s
Correction due to the Coulomb interaction, meV	-11.7	-11.3	-8.2	-9.6

5. CONCLUSIONS

We presented here an attempt to find relationship between optical spectra of semiconductor quantum-dot structures and their properties. A survey of multi-shell emission spectra is given. Theoretical consideration for multi-shell dots is based on circular oscillator model with different lateral confining potential. The many-body corrections to the optical spectrum are calculated for some particular cases. It is shown that these corrections comparable or smaller than the

typical inhomogeneous broadening in the quantum-dot ensembles. Therefore, the shell model seems to be valid for these structures.

In conclusion:

- 1) Model considerations are given on the multi-shell emission from structures with quantum dots (QDs). The shell model can be based on the energy quantization of the single-particle motion in the dot.
- 2) Satisfactory fit is obtained for InAs/InGaAs QDs with a two-dimensional anharmonic oscillator model. The relative position of shells is shown to correlate with a shape of the confining potential. The Coulomb attraction correction is calculated. It is shown to do not influence relative position of shell bands.
- 3) Two types of interlevel spacing profiles are identified in multi-shell spectra of QD structures fabricated in different conditions (InAs/GaAs, InGaAs/GaAs, and InAs/InGaAs). The sharper potential is characteristic for structures grown at higher temperature.

6. REFERENCES

1. G. T. Liu, A. Stintz, H. Li, K. J. Malloy, L. F. Lester, *Electron. Lett.*, 35 (14), 1163-1165 (1999).
2. P. G. Eliseev, H. Li, A. Stintz, G. T. Liu, T. C. Newel, K. J. Malloy, L. F. Lester, *Appl. Phys. Lett.*, 77 (2), 262-264 (2000).
3. L. Jacak, P. Hawrylak, A. Wojs, *Quantum dots*, Springer-Verlag, Berlin, 1998, Ch. 8.2 (1998).
4. D. Bimberg, M. Grundmann, N. N. Ledentsov, *Quantum Dot Heterostructures*, Wiley & Sons, Chichester, 1999.
5. O. Stier, M. Grundmann, D. Bimberg, *Phys. Rev.*, B, 59, 5688 (1999).
6. S. -S. Li, J.-B. Xia, Z. L. Yuan, Z. Y. Xu, W. Ge, X. R. Wang, Y. Mang, J. Wang, L. L. Chang, *Phys. Rev.*, B, 54 (16), 11575-11581 (1996).
7. A. Wojs, P. Hawrylak, S. Fafard, L. Jacak, *Phys. Rev.*, B, 54 (8), 5604-5608 (1996).
8. C. Pryor, *Phys. Rev.*, B 57 (12), 7190-7195 (1998).
9. F. Gelbard, K. J. Malloy, *Proc. SPIE*, 4283, 178-189 (2001).
10. P. G. Eliseev, K. J. Malloy, A. Stintz, T. V. Torchynska, H. M. Alfaro Lopez, R. Pena Sierra, *Proc. SPIE*, 4986, 21-28 (2003).
11. S. Raymond, S. Fafard, P. J. Poole, A. Wojs, P. Hawrylak, S. Charbonneau, D. Leonard, R. Leon, P. M. Petroff, J. M. Merz, *Phys. Rev.*, B 54, 11548-11554 (1996).
12. S. Fafard, Z. R. Wasilievski, and M. Spanner, Evolution of the energy levels in quantum dot ensembles with different densities, *Appl. Phys. Lett.*, 75 (13), 1866-1868 (1999).
13. S. Fafard, C. N. Allen, *Appl. Phys. Lett.*, 75 (16), 2374-2376 (1999).
14. J. J. Dubowski, C. N. Allen, and S. Fafard, *Appl. Phys. Lett.*, 77 (22), 3583-3585 (2000).
15. D. G. Deppe, D. L. Huffaker, S. Csutak, Z. Zou, G. Park, O. B. Shchekin, *IEEE J. Quant. Electron.*, 35 (8), 1238-1246 (1999).
16. D. Gammon, Al. L. Efros, T. A. Kennedy, M. Rosen, D. S. Katzer, D. Park, S. W. Brown, V. L. Korenev, I. A. Merkulov, *Phys. Rev. Lett.*, 86 (22), 5176-5179 (2001, May 28).
17. F. Adler, M. Geiger, A. Bauknecht, F. Scholz, H. Schweizer, M. H. Pilkuhn, B. Ohnesorge, A. Forchel, *J. Appl. Phys.*, 80 (7), 4019-4026 (1996).
18. A. S. Davydov, *Quantum Mechanics*, Pergamon, Oxford, 1968; Ch. 6. There is the level nomenclature for general oscillator that we follow in this paper; namely, the first digit relates to radial quantum number, the letter (s,p,d,...) relates to orbital quantum number. Therefore levels exist like 1p, 1d, etc. In atomic physics another system is used where first digit relates to principal quantum number (there are no levels 1p, 1d). Usage of that in the case of general oscillator seems to be not suitable.
19. L. E. Gendenshtein, *JETP Lett.*, 38 (6), 356-359 (1983).
20. J. W. Dabrowska, A. Khare, U. P. Sukhatme, *J. Phys. A: Math. Gen.*, 21, L195-L200 (1988).
21. G. Poeschl, E. Teller, *Z. Phys.*, 83, 143 (1933).
22. P. G. Eliseev, H. Li, G. T. Liu, A. Stintz, T. C. Newel, L. F. Lester, K. J. Malloy, *IEEE J. Select. Topics Quant. Electron.*, 7 (2), 135-142 (2001).

Quantum-Well to Quantum-Dot Phonon-Assisted Tunneling

Shu-Wei Chang, Shun-Lien Chuang, and Nick Holonyak, Jr.

Department of Electrical and Computer Engineering,
1406 West Green Street, Urbana, IL, USA

ABSTRACT

There have been great interests on semiconductor quantum dot (QD) due to its novel physical properties and potential applications such as semiconductor lasers with high gain and narrow linewidth. The collection of carriers by the QDs is a critical issue for efficient gain of QD lasers. A tunneling injection quantum-dot laser has been researched recently. Direct, photon-, phonon-, and Auger-assisted tunneling are all possible mechanisms for carrier transfer from QW to QD. In this talk, we present a theoretical model for the phonon-assisted tunneling from a quantum well (QW) state to the QD ground state in the conduction band. We assume a quantum-disk model and use its analytical wave functions to calculate the tunneling rate based on Fermi's Golden rule. The single-LO-phonon-emission and absorption processes are modeled by Frölich Hamiltonian. The dependence of the tunneling rate on the QW carrier density, temperature, barrier width between QW and QD, and energy difference between the QW state and the QD states are studied. The tunneling time ranging from several to a few tens of picoseconds are possible depending on the thickness of the barrier and the energy spacing between the QW and QD states.

Keywords: Phonon, tunneling, quantum dot, Fermi's golden rule, semiconductor lasers.

1. INTRODUCTION

Research on semiconductor quantum dots (QDs) has attracted a lot of attention recently not only due to their atomic-like properties but also on the potential application in high-performance semiconductor lasers.¹⁻⁵ However, the carrier collection and relaxation in QDs are critical issues on the high performance of the semiconductor lasers. Although the discrete density of states of QDs potentially provides high gain and low threshold for laser operation, it nevertheless restricts the fast phonon-assisted relaxation mechanism for efficient and sufficient supply of carriers. This difficulty is the so-called phonon bottleneck.⁶⁻⁸ The slow relaxation of carriers from the excited QD states to the lasing ground state reduces the efficiency of lasing.

Recently, a tunneling injection quantum well (QW) coupled to QD laser structure has been proposed to overcome the difficulty of carrier relaxation.⁹⁻¹² A QW adjacent to QDs serves as a collector of the injected carriers. The carriers in the QW then diffuse laterally and tunnel into the QDs. Experiments have shown reduced threshold current density in this QW coupled QD structure.¹⁰ In this QW-QD coupled structure, many possible tunneling mechanisms may exist depending on the relative QW and QD energy levels. If the QD states lie in the continuum of the QW, the carriers in the QW states with identical energy to those of the QD states can tunnel coherently into QDs by energy conservation. This direct tunneling mechanism has been discussed by Chuang and Holonyak.¹³ Carriers in QW states with different energies from those of QDs can also tunnel into the QDs with the aid of the interactions between photons, phonons, and so on. A QW carrier can tunnel into the QD by emitting a photon. This photon-assisted tunneling process has been analyzed by Chuang et al.¹⁴ Two carriers in a QW can also interact with each other via Coulomb interaction. One of them gains energy and is excited to a high-energy QW state while the other loses energy and tunnels into QDs. Similar Auger-assisted processes have been discussed by Magnusdottir et al.¹⁵ and Uskov et al.^{16,17} to describe the relaxation of the carriers from the wetting layer to QDs.

Phonon-assisted tunneling was observed by Holonyak et al.¹⁸ as an inelastic process in heavily-doped silicon p-n junctions at 4.2 K. The successful growth of QDs has extended the phonon-related issue to QDs mainly because of phonon bottleneck.⁶⁻⁸ Magnusdottir et al.¹⁹ have calculated the one-phonon and two-phonon assisted

Further author information: (Send correspondence to Shun-Lien Chuang. E-mail: s-chuang@uiuc.edu)

processes for spherical QDs embedded in three-dimensional continuum. In their calculation, relaxation times of the order of picosecond are possible for both mechanisms. For the QW-QD structure, Bhattacharya et al.²⁰ have experimentally obtained a phonon-assisted capture time of 1.7 ps by the differential transmission spectrum in similar structures.

In this paper, we will present the model for phonon-assisted tunneling process in this QW-QD coupled structure. Fermi's golden rule will be used to calculate the capture rate and average tunneling time. The numerical calculation shows a phonon-assisted capture time in the same order of magnitude as the experimental result from Bhattacharya et al.²⁰

2. MODEL FOR PHONON-ASSISTED TUNNELING IN QW-QD COUPLED SYSTEM

Fig. 1 shows the scheme of phonon-assisted tunneling. Carriers are first collected in the QW layer. After lateral diffusion and thermalization in the QW, carriers in the QW spontaneously emit a longitudinal-optical (LO) phonon and tunnel into QDs. In our model, the LO-phonon interaction is modeled by the Fröhlich Hamiltonian using bulk modes. It has been shown that in QD-related scattering problems, the differences between phonon confined and bulk modes is not significant.²¹ For the electronic parts, the effective-mass approximation for a single band is adopted to calculate the envelope wave functions for QW and QD states. In the evaluation of the Fröhlich matrix elements, the difference between the Bloch periodic parts of the wave functions in the QW and the QD states is neglected.

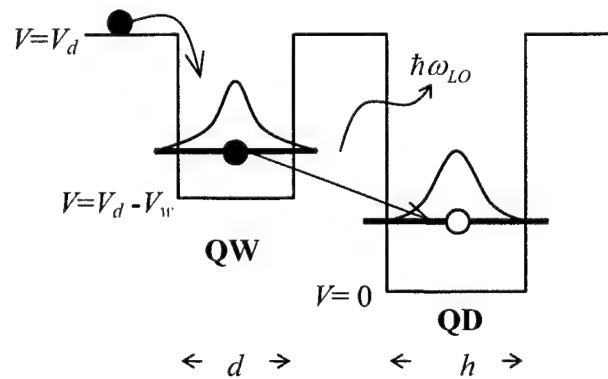


Figure 1. (a) The QW to QD LO-phonon-assisted tunneling. The carriers in the QW emit an LO phonon and tunnel into the QD.

The zero energy reference is set at the bottom of the QD, as shown in Fig. 1. The QD is modeled as a quantum disk with a height h and a radius ρ_0 , and its potential depth is denoted as V_d . We approximate the QD envelope wave function as a product of the growth-direction (z) and the in-plane components, namely:

$$\begin{aligned}\phi_{\tilde{N}}(\mathbf{r}) &= \phi_{lmn}(\mathbf{r}) \\ &= \Psi_{lm}(\rho)\varphi_n(z) \\ &= R_{lm}(\rho)\frac{e^{im\phi}}{\sqrt{2\pi}}\varphi_n(z)\end{aligned}\quad (1)$$

where \tilde{N} represents the quantum numbers (l, m, n), which are in-plane radial quantum number, magnetic quantum number, and the growth-direction quantum number, respectively. This approximation works for the QD bound states with a good carrier confinement, especially the ground state, which will be our main concern in the calculation. The growth-direction and in-plane parts of the QD wave functions are then obtained by matching

the boundary conditions at the interfaces of the barrier and QD region. The growth direction component of the wave function will be described as sinusoidal functions in the QD region and exponential functions in the barrier region. Similarly, the in-plane component will be modeled by Bessel functions of the first kind in the QD region and modified Bessel functions of the second kind in the barrier region.

The QW states are quasi two-dimensional (2D) plane waves in the transverse direction and a bound state in the z direction:

$$\phi_{\mathbf{k}}(\mathbf{r}) = \frac{e^{i\mathbf{k}\cdot\boldsymbol{\rho}}}{\sqrt{A}}\Phi_w(z) \quad (2)$$

where \mathbf{k} is a 2D wave vector of the plane wave, A is the area of the QW, and $\Phi_w(z)$ is the quantized wave function in the growth direction. The z dependence of the envelope wave function is described as sinusoidal functions in the QW region and exponential functions in the barrier regions.

In principle, tunneling from excited subbands in the QW can also be included. However for simplicity, we will not consider this process since the electrons in the QW accumulate mostly in the first conduction subband.

We use Fermi's golden rule to calculate the net capture rate based on these models' wave functions. The net capture rate of the QD state $|\bar{N}\rangle$ for each spin is as follows:

$$W_{w\rightarrow\bar{N}}^{\text{phonon}} = \frac{2\pi}{\hbar} \sum_{\mathbf{k},\mathbf{p}} |M_{\bar{N},\mathbf{k}}(\mathbf{p})|^2 [(n_{LO} + 1)f_k(1 - f_{\bar{N}}) - n_{LO}(1 - f_k)f_{\bar{N}}] \delta(E_w + \frac{\hbar^2 k^2}{2m_w^{xy*}} - E_{\bar{N}} - \hbar\omega_{LO}) \quad (3)$$

where $M_{\bar{N},\mathbf{k}}(\mathbf{p})$ is the Fröhlich matrix element; \mathbf{p} is the wave vector of the LO phonon; $n_{LO} = 1/[\exp(\hbar\omega_{LO}/k_B T) - 1]$ is the Bose-Einstein occupation number of the LO phonon; f_k and $f_{\bar{N}}$ are the occupation numbers of the QW state labeled by the wave vector \mathbf{k} and the QD state labeled by quantum number \bar{N} , respectively; E_w is the first subband edge energy of the QW, i.e., the energy of the QW state with zero wave vector; m_w^{xy*} is the in-plane effective mass, and $E_{\bar{N}}$ is the energy of the QD state $|\bar{N}\rangle$. The LO phonon is assumed to be dispersionless.

The matrix element of Fröhlich Hamiltonian is written as

$$M_{\bar{N},\mathbf{k}}(\mathbf{p}) = i(\frac{e^2\hbar\omega_{LO}}{2\varepsilon_0 V_{ol}})^{1/2} [\frac{1}{\varepsilon_{\infty}} - \frac{1}{\varepsilon_s}]^{1/2} \frac{1}{p} \langle \bar{N} | e^{i\mathbf{p}\cdot\mathbf{r}} | \mathbf{k} \rangle \quad (4)$$

where V_{ol} is the volume of the bulk; \mathbf{p} and ω_{LO} are the wave vector and angular frequency of an LO phonon; ε_{∞} and ε_s are the high-frequency and static dielectric constants, respectively. We note that the Fröhlich matrix element contains the form factor $\langle \bar{N} | e^{i\mathbf{p}\cdot\mathbf{r}} | \mathbf{k} \rangle$. If we expand the in-plane component of the state $|\bar{N}\rangle$ as a superposition of the plane wave states, the form factor $\langle \bar{N} | e^{i\mathbf{p}\cdot\mathbf{r}} | \mathbf{k} \rangle$ is proportional to the magnitude of the plane wave $e^{i(\mathbf{p}_{\perp} + \mathbf{k})\cdot\boldsymbol{\rho}}$ where \mathbf{p}_{\perp} is the component of the LO phonon wave vector perpendicular to the growth direction. If there is no confinement in the QW plane, the in-plane QD wave function will be replaced by two-dimensional plane wave, too. The form factor is then proportional to a delta function in momentum space, which represents momentum conservation. Therefore, the form factor is actually another representation of momentum conservation. Only the plane wave component of the QD in-plane wave function which satisfies momentum conservation will be selected.

Equation (3) can be simplified as a two-dimensional integration. For detailed calculations, please refer to Ref. 22. Here, we present the final results only. The functions $X(q)$, $Y(q)$, and $U(q)$ are defined below as

$$X(q) = \int_{-\infty}^{\infty} dz \varphi_n^*(z) e^{iqz} \Phi_w(z) \quad (5)$$

$$Y(q) = |X(q)|^2 \quad (6)$$

$$U(q) = \left| \int_0^{\infty} d\rho \rho R_{lm}^*(\rho) J_m(q\rho) \right|^2 \quad (7)$$

where J_m is the m th Bessel function of the first kind. The net capture rate then can be written as

$$W_{w-\bar{N}}^{\text{phonon}} = \frac{m_w^{xy*} e^2 \hbar \omega_{LO}}{2\pi \hbar^3} \left(\frac{1}{\epsilon_\infty} - \frac{1}{\epsilon_s} \right) [(n_{LO} + 1)f_Q(1 - f_{\bar{N}}) - n_{LO}(1 - f_Q)f_{\bar{N}}] \\ \times \int_0^\infty dq \int_{-1}^1 dt \frac{q^2 Y(qt) U(q\sqrt{1-t^2})}{\sqrt{(q+Q)^2(q-Q)^2 + (2Qqt)^2}} \quad (8)$$

where the quantity Q is a parameter due to energy conservation:

$$Q = \frac{\sqrt{2m_w^{xy*}(E_{\bar{N}} + \hbar\omega_{LO} - E_w)}}{\hbar} \quad (9)$$

Equation (9) target the occupation of the QD state $|\bar{N}\rangle$ for each spin. Here, the average time constant for carriers in the QW to tunnel into the QD is of greater interests. Denote the surface density of QDs as N_D . The surface density of carriers in QW is given explicitly as follows:²³

$$n_w = \frac{2}{A} \sum_{\mathbf{k}} f_k \\ = \frac{m_w^{xy*} k_B T}{\pi \hbar^2} \ln[1 + e^{(E_{Fw} - E_w)/k_B T}] \quad (10)$$

where E_{Fw} is the quasi-Fermi level of the carriers in the QW. If the initial occupation of the QD state is zero, the conservation of particle numbers enables us to define the average tunneling time constant $\tau_{Av}^{\text{phonon}}$, which depends on the surface carrier density in the QW:

$$\frac{n_w}{\tau_{Av}^{\text{phonon}}(n_w)} \equiv 2N_D W_{w-\bar{N}}^{\text{phonon}}|_{f_{\bar{N}}=0} \quad (11)$$

where a factor of two is used to account for the spin degeneracy. Similar to equation (11), we can also define the total tunneling rate per unit volume $R(n_w)$ for the carriers in the QW, which represents the number of carriers leaving the QW per unit time per unit volume:

$$R(n_w) \equiv \frac{1}{d} \frac{n_w}{\tau_{Av}^{\text{phonon}}(n_w)} \\ = \frac{2}{d} N_D W_{w-\bar{N}}^{\text{phonon}}|_{f_{\bar{N}}=0} \quad (12)$$

3. THEORETICAL RESULTS FOR PHONON-ASSISTED CAPTURE RATES

We use the following parameters to calculate the physical quantities of interests in phonon-assisted tunneling. In the barrier, QW, and QD regions, the electron effective masses are $0.067 m_0$, $0.0522 m_0$, and $0.0495 m_0$, respectively, where m_0 is the free electron mass. The barrier heights of the QW (V_w) and the QD (V_d) are 175 meV and 215 meV at room temperature. The energy of the first quantized subband in QW (E_w) is 62 meV above the bottom of the QW potential, which is at an energy $E_w + V_d - V_w = 102$ meV measured from the bottom of the QD potential. The QW width and the QD height are 60 and 100 Å, respectively. The QD radius is 100 Å. The energy difference between the QW subband edge and the QD state is around one phonon energy if a biased electric field is absent. The LO phonon energy is 35.9 meV. The surface density of QD is set as 10^{10} cm^{-2} unless otherwise mentioned. Only the ground state of the QD in conduction band will be considered. The occupations of the QD states are assumed to be empty initially.

Fig. 2(a) shows the net capture rate $W_{w-\bar{N}}^{\text{phonon}}$ of the QD ground state as a function of the QD ground-state energy. If we apply an electric field bias, the energy difference between the QW subband edge and the QD ground state will change. In this case, the QW subband edge is fixed, and the energy shift of the QD ground state due

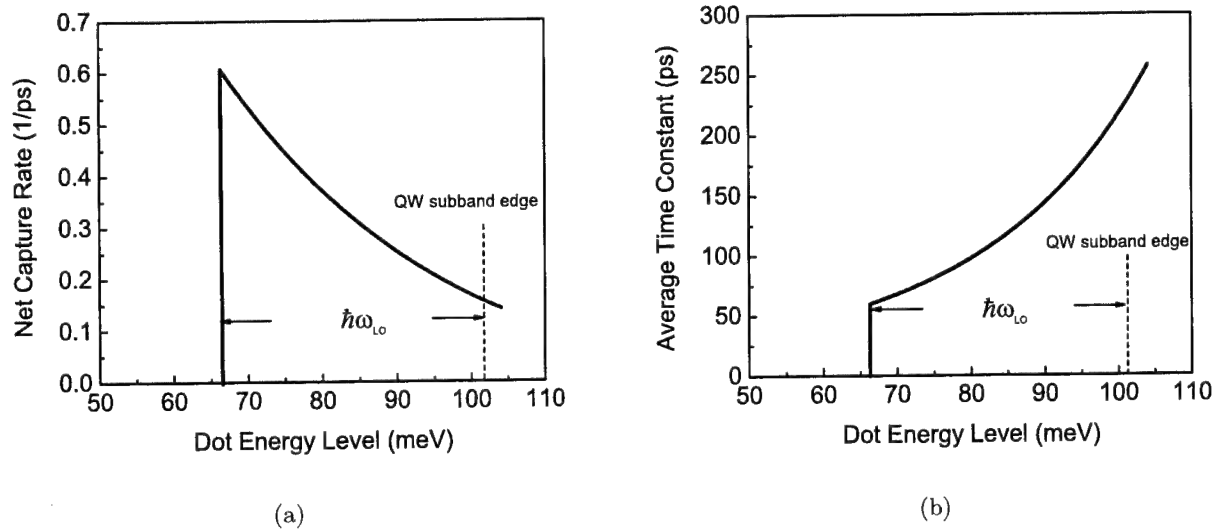


Figure 2. (a) The net capture rate due to phonon-assisted tunneling processes, $W_{w \rightarrow \bar{N}}^{\text{phonon}}$ using equation (3), as a function of QD energy level. (b) The average tunneling time constant, $\tau_{\text{Av}}^{\text{phonon}}(n_w)$ using equations (11). The parameters used are: $d = 60 \text{ \AA}$; $h = 100 \text{ \AA}$; barrier width = 20 \AA ; $\rho_0 = 100 \text{ \AA}$; $N_D = 10^{10} \text{ cm}^{-2}$; $n_w = 7.25 \times 10^{11} \text{ cm}^{-2}$; and $T = 300 \text{ K}$. The QW subband edge is at 102 meV measured from the bottom of the QD at zero bias.

to the biased electric field is referenced from the bottom of the unperturbed QD potential. In Fig. 2(b), the average tunneling time constant $\tau_{\text{Av}}^{\text{phonon}}(n_w)$ using equation (11) is plotted as a function of the energy shift of the QD ground state. The quasi-Fermi level is set to be 25 meV above the QW subband edge at 300 K , which corresponds to a surface carrier density of $7.25 \times 10^{11} \text{ cm}^{-2}$; the barrier width is set at 20 \AA . Since the energy of the LO phonon is a constant, the difference between the energy of the QD ground state and the QW subband edge must be smaller than one LO phonon energy for the first-order phonon-assisted process to occur. Thus, the applied biased electric field must increase the energy of the QD ground state so that the energy difference between the QW subband edge and the QD ground state lies within one LO phonon energy.

From Fig. 2(a), the net capture rate reaches a maximum value when the energy difference between the QW subband edge and the energy of the QD ground state is exactly one LO phonon energy. The minimum tunneling time constant $\tau_{\text{Av}}^{\text{phonon}}(n_w)$ at this energy difference shown in Fig. 2(b) also reflects the trend in Fig. 2(a). This maximum capture rate is due to two factors. First, since the carrier distribution in the QW is modeled as Fermi-Dirac statistics, the occupation of the low-energy QW states will be higher than that of the high-energy QW states. Due to energy conservation, if the energy difference between the QW subband edge and the QD ground state is narrower, the QW states participating in the first-order interaction will be those with higher energies. Because the net capture rate is proportional to the occupation of the initial QW states, the lower occupations of the high-energy QW states will decrease the capture rate. Second, high-energy QW states have higher momentum than the low-energy QW states. If we view the in-plane component of the QD ground state wave function as a superposition of the two-dimensional plane waves, the high-momentum states tend to sense the plane waves with large wave vectors. This is a result of the momentum conservation between the plane wave components, low-momentum LO phonon, and the QW states. For the QD ground state, the magnitudes of the plane wave components with small wave vectors are more significant than those with large wave vectors. This is another reason why the high momentum states have less contribution to the tunneling process and result in lower net capture rate when the energy difference between the QW subband edge and the QD ground state is within one LO phonon energy.

From Figs. 3-5, the dependence of the tunneling rates on the QW surface carrier density is considered. The

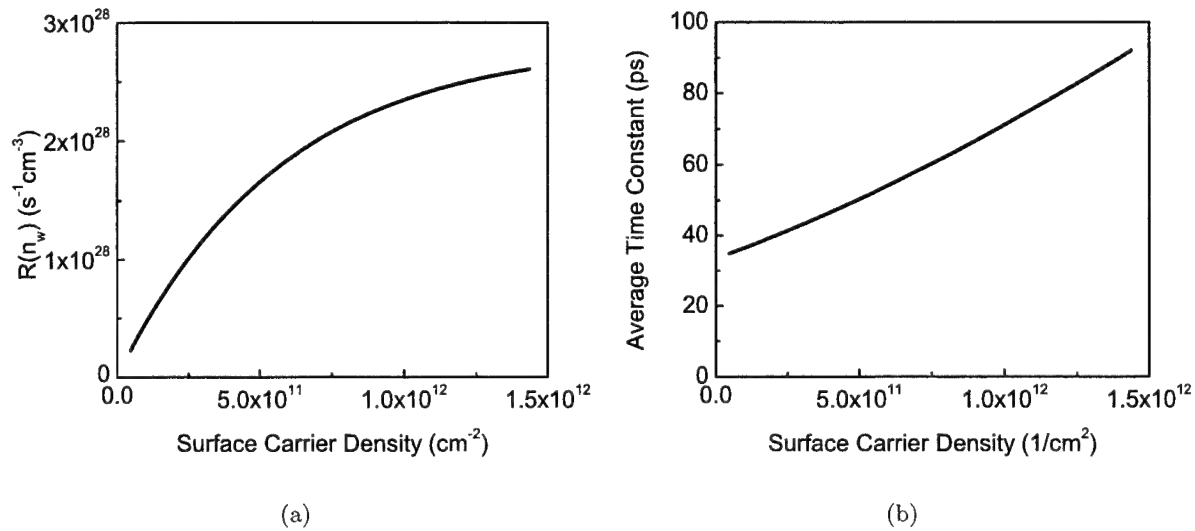


Figure 3. (a) The total tunneling rate per unit volume, $R(n_w)$ using equation (12), due to phonon-assisted processes as a function of QW surface carrier density. (b) The average tunneling time constant $\tau_{\text{Av}}^{\text{phonon}}(n_w)$ using equation (11). The parameters used are: $d = 60 \text{ \AA}$; $h = 100 \text{ \AA}$; barrier width = 20 \AA ; $\rho_0 = 100 \text{ \AA}$; $E_w - E_N \approx 35.9 \text{ meV}$; $N_D = 10^{10} \text{ cm}^{-2}$; and $T = 300 \text{ K}$.

biased electric field is set to zero. In Fig. 3(a), the total tunneling rate per unit volume $R(n_w)$ is plotted as a function of the QW surface carrier density. The corresponding average tunneling time constant $\tau_{\text{Av}}^{\text{phonon}}(n_w)$ is plotted in Fig. 3(b). The barrier width is still set as 20 \AA . From Fig. 3(a), the total tunneling rate per unit volume $R(n_w)$ is saturated as the QW surface carrier density is increased. The saturation of the quantity $R(n_w)$ is due to the saturation of the occupations of the low-energy QW states as the number of the QW carriers increases. On the other hand, from Fig. 3(b), the average tunneling time constant $\tau_{\text{Av}}^{\text{phonon}}(n_w)$ increases as the QW surface carrier density is increased. Since the number of the QDs for the QW carriers to tunnel through is fixed, only a fixed number of the QW carriers can participate in the tunneling process under energy conservation. Other carriers will only accumulate in the QW. Thus, the average tunneling time constants will become longer as the surface carrier density increases. A rule of thumb is that an increased QW surface density will enhance the net carrier capture rate in the QD, but slowdown the tunneling of the carriers in the QW.

Fig. 4 shows the total tunneling rate per unit volume $R(n_w)$ as a function of the surface carrier density under different barrier widths. We use the same parameters as those in the calculations of Fig. 3 except for the barrier widths. The barrier widths are set at 20 , 40 , and 60 \AA . Longer barrier width reduces the overlap between the z-dependent wave functions of the QW and QD ground states, and the magnitude of the Fröhlich matrix element. For efficient carrier injection by phonon-assisted tunneling, the barrier has to be thin enough so that fast tunneling process can take place.

Fig. 5 shows the total tunneling rate per unit volume $R(n_w)$ of the carriers in the QW for different surface QD densities. We use the same parameters as those used in the simulations for Fig. 3 except for the QD surface density. The QD surface densities are set to be 2×10^9 , 10^{10} , and $5 \times 10^{10} \text{ cm}^{-2}$. If the number of the QDs is increased, the number of QDs for the QW carriers to tunnel into will increase. Thus, fast tunneling of the QW carriers into QDs will be achieved.

Bhattacharya et al.²⁰ measured a 1.7-ps phonon-assisted capture time for the occupation of the QD ground state at low temperature. In their structure, the QD ground state is designed to have eigenenergy below the QW subband edge by about one phonon energy. Although the structure we consider is not the same as that in Ref. 20, the two structures are similar in nature. In this paper, we perform the calculation at room temperature.

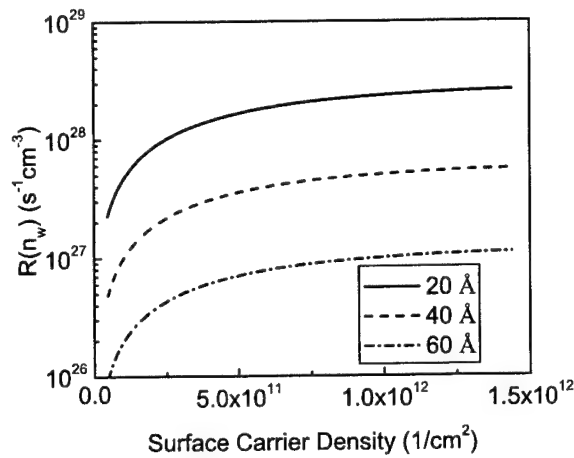


Figure 4. The total tunneling rate per unit volume, $R(n_w)$ using equation (12), as a function of QW surface carrier density for different barrier widths. The parameters used are: $d = 60 \text{ Å}$; $h = 100 \text{ Å}$; $\rho_0 = 100 \text{ Å}$; $E_w - E_{\bar{N}} \approx 35.9 \text{ meV}$; $N_D = 10^{10} \text{ cm}^{-2}$; and $T = 300 \text{ K}$.

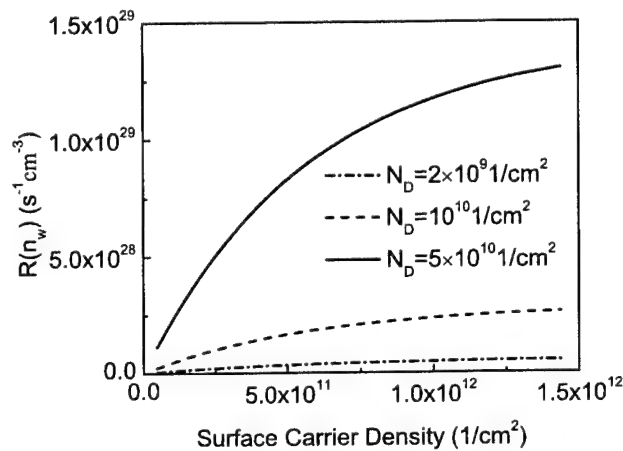


Figure 5. The total tunneling rate per unit volume, $R(n_w)$ using equation (12), as a function of QW surface carrier density for different QD densities. The parameters used are: $d = 60 \text{ Å}$; $h = 100 \text{ Å}$; barrier width = 20 Å ; $\rho_0 = 100 \text{ Å}$; $E_w - E_{\bar{N}} \approx 35.9 \text{ meV}$; and $T = 300 \text{ K}$.

However, the stimulated emission rate for LO phonon does not significantly change the order of the magnitude of the phonon-assisted net capture rate as the temperature is raised. From Fig. 2(a), the inverse of the net capture rate, which is the physical quantity they measured, is in the same order of magnitude as our theoretical calculation. Our model agrees generally well with the experimental results.

4. CONCLUSION

We have calculated the phonon-assisted tunneling rate in this QW-QD coupled system. The typical net capture time, depending on the barrier width, range from less than one picosecond to a few hundred seconds. The energy

difference between the QW subband energy and QD state energy has to be less than one phonon energy for efficient tunneling to take place. For the QD ground state, larger magnitudes of the low momentum components make the tunneling process most efficient when the energy difference between the QW subband edge and QD ground state is about one LO phonon energy. In laser or detector applications, a thin barrier between the QD and QW and a properly designed energy scheme must be employed so that the adjacent QWs can provide an efficient supply of carriers into the QDs.

ACKNOWLEDGMENTS

The work was supported by MURI-ARO program under grant number DAAD19-01-1-0591 and DARPA under grant number AFSA3631-22549.

REFERENCES

1. P. Bhattacharya and S. Ghosh, "Tunnel injection $\text{In}_{0.4}\text{Ga}_{0.6}\text{As}/\text{GaAs}$ quantum dot lasers with 15 ghz modulation bandwidth at room temperature," *Appl. Phys. Lett.* **80**(19), p. 3482, 2002.
2. L. Harris, D. J. Mowbray, M. S. Skolnick, M. Hopkinson, and G. Hill, "Emission spectra and mode structure of InAs/GaAs self-organized quantum dot lasers," *Appl. Phys. Lett.* **73**(7), p. 969, 1998.
3. H. Shoji *et al.*, "Temperature dependent lasing characteristics of multi-stacked quantum dot lasers," *Appl. Phys. Lett.* **71**(2), p. 193, 1997.
4. D. Bimberg, M. Grundmann, and N. N. Ledentsov, *Quantum Dot Heterostructures*, John Wiley and Sons Ltd., 1st ed., 1999.
5. M. Sugawara, J. C. Bean, and Willardson, *Self-Assembled $\text{InGaAs}/\text{GaAs}$ Quantum Dots*, Academic Press, 1st ed., 1999.
6. R. Heitz *et al.*, "Existence of a phonon bottleneck for excitons in quantum dots," *Phys. Rev. B* **64**, p. 241305, 2001.
7. J. Urayama, T. B. Norris, J. Singh, and P. Bhattacharya, "Observation of phonon bottleneck in quantum dot electronic relaxation," *Phys. Rev. Lett.* **86**(21), p. 4930, 2001.
8. K. Mukai, N. Ohtsuka, H. Shoji, and M. Sugawara, "Phonon bottleneck in self-formed $\text{In}_x\text{Ga}_{1-x}\text{As}/\text{GaAs}$ quantum dots by electroluminescence and time-resolved photoluminescence," *Phys. Rev. B* **54**(8), p. 5243, 1996.
9. G. Walter, N. Holonyak, Jr., J. H. Ryou, and R. D. Dupuis, "Room-temperature continuous photopumped laser operation of coupled InP quantum dot and InGaP quantum well $\text{InP-InGaP-In(AlGa)P-InAlP}$ heterostructures," *Appl. Phys. Lett.* **79**(13), p. 1956, 2001.
10. G. Walter, N. Holonyak, Jr., J. H. Ryou, and R. D. Dupuis, "Coupled InP quantum-dot InGaP quantum well $\text{InP-InGaP-In(AlGa)P-InAlP}$ heterostructure diode laser operation," *Appl. Phys. Lett.* **79**(20), p. 3215, 2001.
11. T. Chung, G. Walter, and N. Holonyak, Jr., "Coupled strained-layer InGaAs quantum-well improvement of an InAs quantum dot $\text{AlGaAs-GaAs-InGaAs-InAs}$ heterostructure laser," *Appl. Phys. Lett.* **79**(27), p. 4500, 2001.
12. G. Walter, T. Chung, and N. Holonyak, Jr., "High-gain coupled InGaAs quantum well InAs quantum dot $\text{AlGaAs-GaAs-InGaAs-InAs}$ heterostructure diode laser operation," *Appl. Phys. Lett.* **80**(7), p. 1126, 2002.
13. S. L. Chuang and N. Holonyak, Jr., "Efficient quantum well to quantum dot tunneling: Analytical solutions," *Appl. Phys. Lett.* **80**(7), p. 1270, 2002.
14. S. L. Chuang, P. Littlewood, G. Walter, and N. Holonyak, "Spontaneous emission and optical gain due to quantum-well to quantum-dot photon-assisted tunneling," in *Conference on Lasers and Electro-Optics/Quantum Electronics and Laser Science Conference*, (Baltimore Convention Center, Baltimore), June 2003.
15. I. Magnusdottir, S. Bischoff, A. V. Uskov, and J. Mork, "Geometry dependence of auger carrier capture rates into cone-shaped self-assembled quantum dots," *Phys. Rev. B* **67**, p. 205326, 2003.
16. A. V. Uskov *et al.*, "Auger carrier capture kinetics in self-assembled quantum dot structures," *Appl. Phys. Lett.* **72**(1), p. 58, 1998.

17. A. V. Uskov, F. Adler, H. Schweizer, and M. H. Pilkuhn, "Auger carrier relaxation in self-assembled quantum dots by collisions with two-dimensional carriers," *J. Appl. Phys.* **81**(12), p. 7895, 1997.
18. N. Holonyak, Jr., I. A. Lesk, R. N. Hall, J. J. Tiemann, and H. Ehrenreich, "Direct observation of phonons during tunneling in narrow junction diodes," *Phys. Rev. Lett.* **3**(4), p. 167, 1959.
19. I. Magnusdottir *et al.*, "One- and two-phonon capture processes in quantum dots," *J. Appl. Phys.* **92**(10), p. 5982, 2002.
20. P. Bhattacharya *et al.*, "Carrier dynamics and high-speed modulation properties of tunnel injection InGaAs-GaAs quantum-dot lasers," *IEEE. J. Quantum Electron.* **39**(8), p. 952, 2003.
21. U. Bockelmann and G. Bastard, "Phonon scattering and energy relaxation in two-, one-, and zero-dimensional electron gases," *Phys. Rev. B* **42**(14), p. 8947, 1990.
22. S. W. Chang, S. L. Chuang, and N. Holonyak, Jr., "Phonon- and Auger-assisted tunnelings from quantum well to quantum dot." *Phys. Rev. B*, submitted.
23. S. L. Chuang, *Physics of Optoelectronic Devices*, John Wiley and Sons, New York, 1st. ed., 1995.

Energy distributions of carriers in quantum dot laser structures

Simon Osborne, Peter Blood, Peter Smowton, Julie Lutti
Department of Physics and Astronomy, Cardiff University,
PO Box 913, Cardiff CF24 3YB, UK.

and

Y C Xin, A Stintz, D Huffaker, and L F Lester
Centre for High technology Materials, University of New Mexico,
Albuquerque, NM 87106, US.

ABSTRACT

Using the segmented contact method, we have measured the passive modal absorption, modal gain and spontaneous emission spectra of an InAs “dot-in-well” (DWELL) system where the inhomogeneous broadening is sufficiently small that the ground and excited state transitions can be spectrally resolved. The modal optical gain from the ground state saturates with current at a maximum value of one third of the magnitude of the measured absorption. The population inversion factor spectrum, obtained from the measured gain and emission spectra, shows that the carrier distributions cannot be described by a single global Fermi distribution. However, the inversion factor spectrum can be described by a system where the ground state and excited state occupancies are each described by a Fermi distribution but with different quasi-Fermi energy separations.

Keywords: quantum dots, quantum dot lasers, optical gain, gain saturation.

1. INTRODUCTION

With careful design, it is possible to use quantum dot structures to make semiconductor diode lasers with very low threshold current densities. The maximum modal gain which can be obtained from a fully inverted dot system is small compared with quantum wells and lies in the region of 3 to 10 cm⁻¹ per layer depending on the dot density (typically in the range 10¹⁰ to 10¹¹ cm⁻²) and the low thresholds are achieved by minimising the optical waveguide loss (α_i) and the distributed mirror loss, and by using several layers of dots. Further refinements such as the use of “dot-in-well” (DWELL) structures have led to threshold current densities as low as $J_{th} = 26 \text{ Acm}^{-2}$ at a lasing wavelength of 1.25 μm ¹ using long cavity devices (7.8mm).

Despite this progress, the manner in which the localised dot states are occupied by electrons under lasing conditions is not well understood. It has been shown that in some cases at room temperature the occupation of dot states of different energy can be described by Fermi Dirac probability distribution in energy with a global Fermi level², possibly because of the strong interaction of the dot states with the extended states of the wetting layer. From this standpoint the wetting layer may play a valuable role in maintaining a spatially uniform dot state occupancy. On the other hand, there is evidence that the high density of states at higher energies, associated with excited states or the wetting layers, itself serves to make it difficult to populate fully the ground state of the dot system³, even under quasi-equilibrium conditions. An understanding of the energy distribution of electrons is important in obtaining the maximum available gain from a system of dots.

We have investigated these effects at room temperature in a DWELL structure using the segmented contact method to measure the passive modal absorption, the modal gain, inversion factor and spontaneous emission spectrum. These measurements enable us to compare the magnitude of the passive modal absorption with the magnitude of the modal gain and by combining gain and spontaneous emission spectra the population inversion factor spectrum can be determined and compared with that predicted for a thermal distribution giving insight into the energy distribution of carriers. In the structures used the ground and excited states can be clearly distinguished even under high injection conditions, due to the low inhomogeneous broadening and reasonably deep confining potential.

2. EXPERIMENTAL DETAILS

The sample was grown by MBE and comprised layers of InAs dots embedded in a $\text{In}_{0.15}\text{Ga}_{0.85}\text{As}$ well of thickness 9.6nm and surrounded by un-doped GaAs to provide a waveguide core of total thickness 230nm⁴. The cladding layers were $\text{Al}_{0.7}\text{Ga}_{0.3}\text{As}$. The material was processed into 100 μm wide oxide-isolated devices with the contact separated into segments each 293 μm long in a device of overall length 3mm. These devices were mounted onto copper heatsinks. The contact segments were driven separately with pulses of 1 μs duration at a duty cycle of 0.1%. The amplified spontaneous emission was collected from the facet of the structure and detected using a grating spectrometer and a Hamamatsu cooled photomultiplier sensitive out to a wavelength of 1.4 μm .

The method by which the modal absorption, modal gain and spontaneous emission spectra are obtained from analysis of edge-emitted amplified spontaneous emission (ASE) spectra is given in ref⁵. The passive absorption of the gain material is measured by observing emission when the first and second segments are driven separately, the light from the second segment being passively absorbed by the first segment before being detected. The gain is measured by driving section one, then section one and two together and so on, to replicate a stripe-length determination of modal gain⁶. All measurements are for light polarised in the plane of the layers of the structure (TE).

3 RESULTS

The measured passive net modal absorption spectrum for light propagating along the waveguide containing the layer of dots, measured with a drive current through the exciting segment of 100mA, is shown in figure 1. Absorption at photon energies below the main absorption edge is due to scattering losses in the waveguide which amount to about 5 \pm 1 cm^{-1} . This is a larger value than that obtained from an analysis of the differential efficiency as a function of cavity length⁷. The absorption peaks at 1.02eV and 1.08eV are due to the ground and excited states of the dot system and the modal absorption at each peak attributable to the dots is 30 \pm 1 cm^{-1} and 56 \pm 1 cm^{-1} respectively (ie. after correction for the waveguide loss).

The net modal TE gain is shown in figure 2 for currents per segment between 20mA and 200mA; the passive absorption spectrum is also shown. The "gain" at low photon energy below the absorption edge tends to a similar value to the absorption spectrum, confirming the value obtained for the waveguide loss. As the current is increased the ground state gain tends toward saturation at currents above about 100mA (340 Acm^{-2}) and the ground state peak modal gain (after correction for the waveguide loss) is about 8 \pm 1 cm^{-1} . The modal gain determined from measurements of threshold current as a function of cavity length is about 12.5 cm^{-1} ^{1,4} for a current density of 200 Acm^{-2} . In both cases the maximum ground state gain is significantly less than the measured ground state absorption, by a factor 2 or 3.

The uncalibrated experimental data for true spontaneous emission spectra in fig 3 show four transitions below the transition energy of the well at 1.25 eV. The ground state emission saturates with increasing current at a value of about 160 mA.

Figure 4 shows uncalibrated data for the population inversion factor obtained as the measured modal gain (G) divided by the uncalibrated spontaneous emission (I_{spont}) at each photon energy:

$$P_F(h\nu) = \frac{G(h\nu)}{I_{\text{spont}}(h\nu)} \quad (1)$$

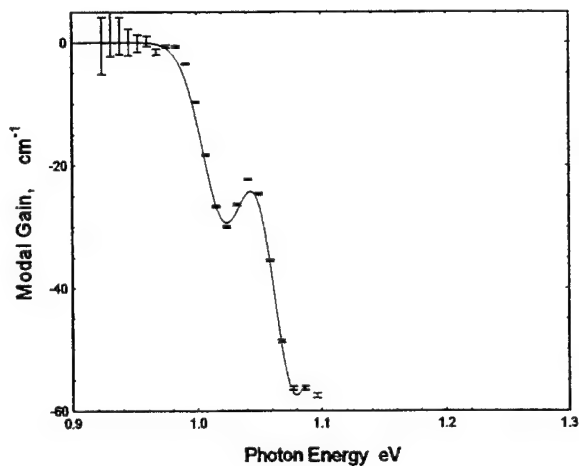


Figure 1. Measured modal absorption spectrum (being negative gain). (Corrected for waveguide loss)

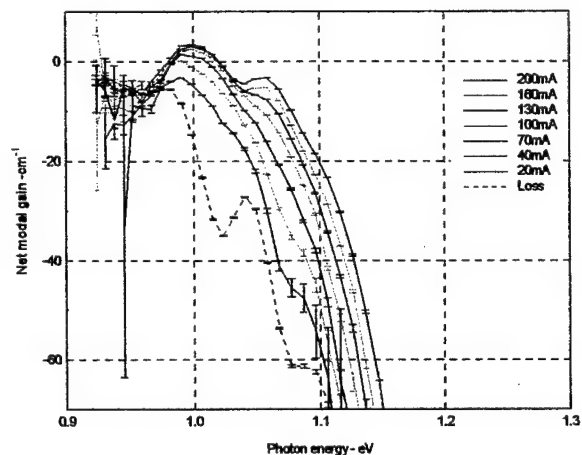


Figure 2. Measured modal gain spectra for drive currents per segment from 20mA to 200mA.

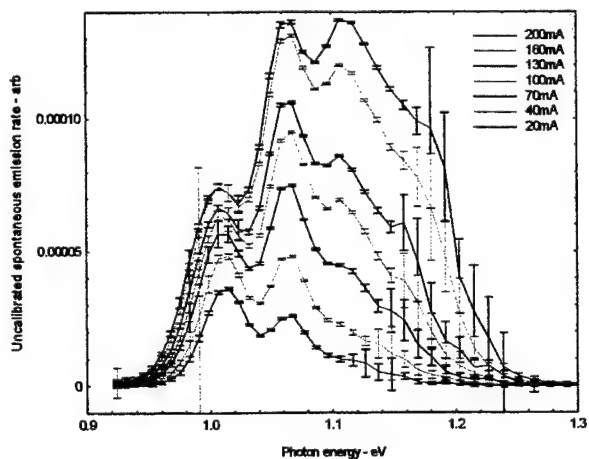


Figure 3. True spontaneous emission spectra derived from analysis of edge emitted ASE spectra.

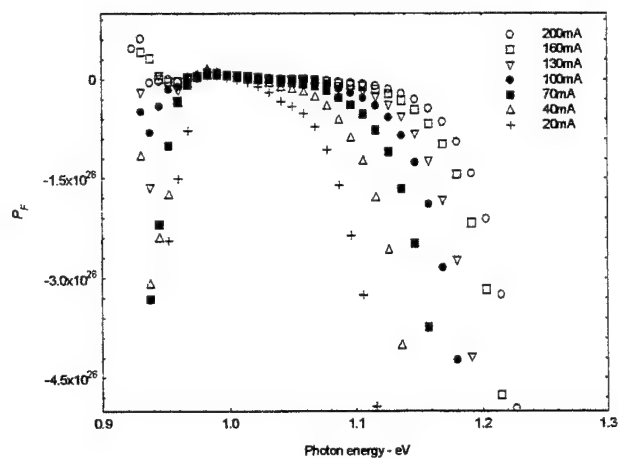


Figure 4 Spectra of the measured population inversion factor obtained from experimental data using equation (1).

4 ANALYSIS OF INVERSION FACTOR

The population inversion factor is related to probabilities of occupation by electrons of the upper and lower energy states (f_1 and f_2 respectively) which participate in a transition at photon energy $h\nu$:

$$P_F(h\nu) \propto \frac{f_1 - f_2}{f_1(1 - f_2)} \quad (2)$$

The constant of proportionality includes an unknown calibration factor for the measured spontaneous emission rate. The inversion factor tends to $-\infty$ at high photon energy where the upper state is empty and the lower state full, and to $+1$ at small photon energy where the system is fully inverted such that the upper state is completely full ($f_1 = 1$) and the lower state completely empty ($f_2 = 0$). P_F also tends to $+1$ when, either $f_1 = 1$ or $f_2 = 0$, with the other respective occupation factor taking any value between 0 and 1. P_F crosses zero at the transparency point.

Although the experimental data is in arbitrary units, these features are apparent in the spectra in figure 4, where P_F decreases with increasing photon energy and increases with increasing drive current. We also observe that the values of P_F for different drive currents converge to a common value at low photon energy and this is to be expected when the system becomes fully inverted, or when the occupation of one or both states saturates before reaching their limiting values. At the ground state gain peak (1 eV) the gain saturates with current above 100mA, as does the spontaneous emission within the error bars, so we conclude that above this current the occupation factors have saturated for the ground state, though comparison of absorption and gain spectra shows that the ground state is not fully inverted. We conclude that either $f_1 < 1$ and $f_2 = 0$, or $f_1 = 1$ and $f_2 > 0$, or the system saturates with both f_1 and f_2 constant at values between 0 and 1. In the first two cases equation (2) takes the value unity, but is undetermined in the third case.

These remarks apply to any pair of occupation factors for the upper and lower states which can be globally defined throughout the sample as a function of energy. In the specific case that the system adopts a quasi-equilibrium distribution defined by a global Fermi-Dirac (F-D) function the inversion factor becomes:

$$P_F \propto \left\{ 1 - \exp\left(\frac{h\nu - \Delta E_f}{kT}\right) \right\} \quad (3)$$

where ΔE_f is the separation of the quasi-Fermi levels specifying the occupancy of the upper and lower states. Figure 5 shows equation (3) superimposed on the experimental data of figure 4 where the quasi-Fermi level separations have been chosen to correspond to the transparency points of the experimental data. The data has been scaled such that P_F tends to unity at low photon energy (though this may not actually be the case). There is good agreement between equation (3) and the data at low current where only the ground state is populated, however at 100mA this agreement only extends to a photon energy of about 1.03eV and at higher values, where the excited state begins to contribute, the measured P_F is greater than the F-D value. At 200mA there is only agreement at low photon energy where the gain is saturated.

Equation (2) is based upon a simple two-level model, however it can be shown that even when more than one transition contributes to the gain and emission, the behaviour of the inversion factor follows that of equation (3) when all states are in quasi-equilibrium defined by a common quasi-Fermi level separation. Thus contributions from multiple transitions in a system which is in overall equilibrium does not explain why our data does not match the Fermi-Dirac expression (3) and we conclude from figure 5 that this dot system cannot be described by a universal Fermi-Dirac distribution. However, an inspection of the spectra in figures 4 and 5 suggests that in regions where only one transition is dominant the data can be represented by a Fermi-Dirac distribution with equation (3).

To verify that the data can be represented in this way we have calculated the inversion factor for inhomogeneously broadened ground and excited state distributions with different quasi-Fermi energy separations using inhomogeneous broadening parameters obtained from the passive absorption spectrum. The parameters used in the calculations were those for InAs where the matrix element, M , is given by $2|M|^2/m_0 = 21.1\text{eV}$, and the overlap envelope integrals in the

dots were taken as unity. We assumed that the inhomogeneous broadening (given by a Gaussian distribution, B) is much greater than the homogeneous broadening (given by a Lorentzian, L) and obtained a good description of the absorption spectrum with a Lorentzian linewidth of $\Lambda=21\mu\text{eV}$, (corresponding to a 200ps dephasing time), an inhomogeneous linewidth of the ground state of $\sigma=16\text{ meV}$ and $\sigma=18\text{meV}$ for the excited state. This increase in σ was necessary to fit the absorption edge of the 1st excited state and is expected for higher dot states, as they are more sensitive to variations of size and composition⁸.

We have calculated the population inversion spectrum for three transitions assuming that the occupancy of states within the ground state distribution and those within the excited state distribution are each independently described by a Fermi-Dirac function but with different quasi-Fermi energy separations:

$$P_F(h\nu) = \frac{\sum_{j=1-3} \int |M|^2 B(E_i, \sigma_j) L(h\nu - E_i, \Lambda) [f_1(E_i, \Delta E_{ff}) - f_2(E_i, \Delta E_{ff})] dE_i}{\sum_{j=1-3} \int |M|^2 B(E_i, \sigma_j) L(h\nu - E_i, \Lambda) [1 - f_2(E_i, \Delta E_{ff})] dE_i} \quad (4)$$

To determine the Fermi functions it is necessary to assign values to the two individual quasi-Fermi energies and this was done by setting the quasi Fermi energies such that the lower state is empty of electrons, ie $f_2=0$, assuming that it is the upper states which are not full populated achieve complete inversion at high injection. (The inverse situation, ie the upper states fully populated and the lower states partially empty, gives very similar results.) The values of quasi Fermi energy separation used to match the spectrum measured at 200mA were 1.04 eV for the ground state, 1.06eV and 1.10eV for the first and second excited states respectively. The agreement between the calculation from equation (4) and experimental results shown in figure 6 is very good.

We conclude that in this dot system, the ground state and excited state carrier populations are not in quasi equilibrium with each other, but they can be individually described by Fermi-Dirac distributions with the quasi-Fermi energy separation for the first excited state being 20 meV greater than for the ground state.

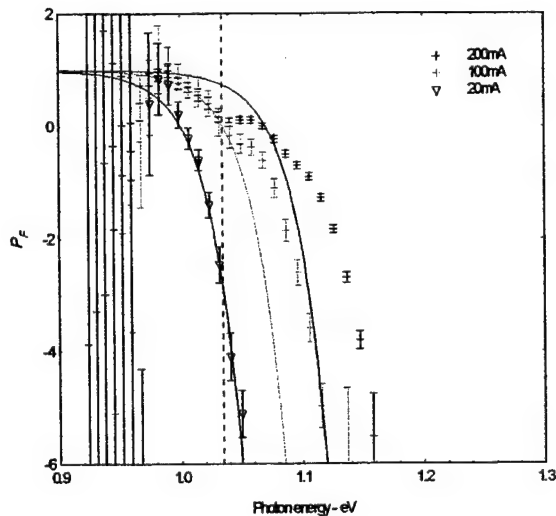


Figure 5. Experimental data for the inversion factor compared with calculated spectra assuming a Fermi Dirac distribution.

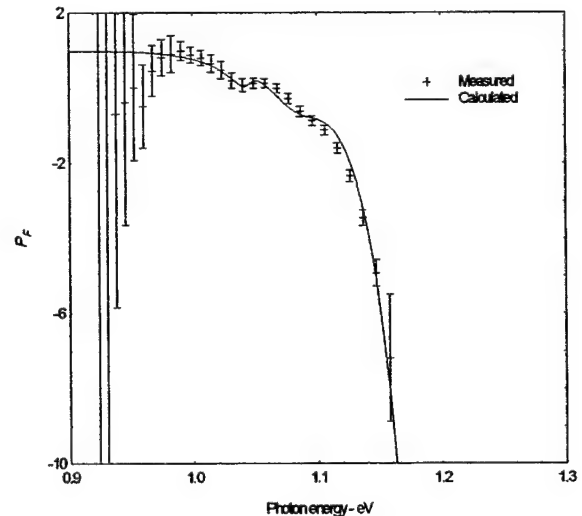


Figure 6. Measured and calculated (equation 4) inversion factor spectra for a current of 200mA per segment.

5. DISCUSSION

Figure 6 shows that the carrier distribution in this *particular* quantum dot system can be *described* by a model in which the occupancies of the ground and excited states are not in overall equilibrium but can each be described by a quasi-equilibrium Fermi-Dirac distribution with different appropriate Fermi energy separations. If this is indeed the case, the occupation of the localised, spatially-separated states within the inhomogeneous distribution of *ground* states are in global quasi-equilibrium and the occupation of spatially-separated states within the inhomogeneous distribution of *excited* states are similarly in global quasi-equilibrium. It may be that photon mediation between dots is important in establishing this particular situation because in these structures the inhomogeneous distributions of ground state and excited state transitions hardly overlap so there is little photon interaction between them though the ground and excited states can individually interact within the homogeneous linewidth.

6 SUMMARY

We have measured the passive modal absorption, modal gain and spontaneous emission spectra in a quantum dots system where the inhomogeneous broadening is sufficiently small that the ground and excited state transitions can be spectrally resolved. The optical gain from the ground state saturates with current at a value which is about one third of the magnitude of the measured ground state absorption. The measured population inversion factor cannot be described by a single global Fermi distribution. However, we find that the inversion factor can be described by a system where the ground state and excited state occupancies are each described by a Fermi distribution but with different quasi-Fermi energy separations.

ACKNOWLEDGEMENTS

We thank the Engineering and Physical Sciences Research Council in the UK for financial support for SWO and some of the equipment used in this work. We have had valuable discussions with Huw Summers.

REFERENCES

- ¹ G. T. Liu, A. Stintz, H. Li, K. J. Malloy, L. F. Lester, *Electron. Letts.*, **35**, 1163 (1999)
- ² H D Summers, J D Thomson, P M Smowton, P Blood and M Hopkinson, *Semic Sci and Technol* **16** (2001) 1-4.
- ³ D R Matthews, H D Summers, P M Smowton, and M Hopkinson, *Appl Phys Letts* **81** (2002) 4904-06
- ⁴ P. G. Eliseev, H. Li, G. T. Liu, A. Stintz, T. C. Newell, L. F. Lester, K. J. Malloy, *IEEE J. S. T. Quan. Elec.*, **7**, 135 (2001).
- ⁵ Peter Blood, Gareth M Lewis, Peter Smowton, Huw Summers, John Thomson, and Julie Lutti, *Journal of Special Topics in Quantum Electron.* Accepted for publication.
- ⁶ J D Thomson, H D Summers, P J Hulyer, P M Smowton and P Blood. *Appl Phys Letts* **75** (1999) 2527-2529
- ⁷ G T Liu, S Stintz, H Li, T C Newell, A L Gray, P M Varangis, K J Malloy and L F Lester *Journ Quantum Electron* **36** (2000) 1272-1279
- ⁸ D. Bimberg, M. Grundmann, N. N. Ledentsov, *"Quantum Dot Heterostructures"*, Wiley, New York (1998).

Internal optical loss and threshold characteristics of semiconductor lasers with a reduced-dimensionality active region

Levon V. Asryan^{§¶} and Serge Luryi[§]

[§] State University of New York at Stony Brook, Stony Brook, NY 11794-2350, USA

[¶] Ioffe Physico-Technical Institute, St Petersburg 194021, Russia

ABSTRACT

We develop a general approach to including the internal optical loss in the description of semiconductor lasers with a quantum-confined active region. We assume that the internal absorption loss coefficient is linear in the free-carrier density in the optical confinement layer and is characterized by two parameters, the constant component and the net cross-section for all absorption loss processes. We show that the free-carrier-density dependence of internal loss gives rise, in general, to the existence of a second lasing threshold above the conventional threshold. Above the second threshold, the light-current characteristic is two-valued up to a maximum current at which the lasing is quenched. We show that the presence of internal loss narrows considerably the region of tolerable structure parameters in which the lasing is attainable; for example, the minimum cavity length is significantly increased. Our approach is quite general but the numerical examples presented are specific for quantum dot (QD) lasers. Our calculations suggest that the internal loss is likely to be a major limiting factor to lasing in short-cavity QD structures.

Keywords: Quantum dots, quantum wires, quantum wells, heterojunctions, semiconductor lasers, internal loss

1. INTRODUCTION

Internal optical loss is present in all types of semiconductor lasers. It adversely affects their operating characteristics — increasing the threshold current density and decreasing the differential efficiency.¹

In general, several mechanisms can contribute to the internal loss, such as free-carrier absorption in the optical confinement layer (OCL) and in the cladding layers (emitters),² intervalence band absorption (hole photoexcitation into the split-off subband),^{3–6} carrier absorption in the quantum-confined active region itself, and scattering at rough surfaces and imperfections of the waveguide. Determination of the absorption coefficient for each of these processes is very important because, depending on their relative strengths and the structure design parameters, the net absorption loss coefficient can be as low as 1.4 cm^{-1} (see Ref.⁷) or as high as 20 cm^{-1} (see Ref.⁸), and even higher.⁹

Due to the variety of possible mechanisms, one hardly expects a first-principle evaluation of the net internal loss coefficient. Formally, however, all different processes can be grouped into two categories, one dependent on the injection carrier density (such as free-carrier absorption in the OCL), the other insensitive to this density (such as scattering at rough interfaces).

Leaning upon this fact, we develop here a general phenomenological approach to the inclusion of the effect of internal loss on threshold characteristics in semiconductor lasers. We show that the injection-carrier-density dependence of internal loss coefficient gives rise to the existence of a second lasing threshold above the conventional threshold; above the second threshold, the light-current characteristic is two-valued. We also show that the presence of internal loss narrows considerably the region of tolerable structure parameters in which the lasing is attainable.

E-mail: asryan@ece.sunysb.edu

E-mail: Serge.Luryi@sunysb.edu

The total net internal loss coefficient (which we shall refer to as the internal loss) is presented as the sum of a constant α_0 and a component linear in the carrier density in the OCL n

$$\alpha_{\text{int}} = \alpha_0 + \sigma_{\text{int}} n \quad (1)$$

where σ_{int} can be viewed as an effective cross-section for all absorption loss processes.

The assumption of a linear dependence on the free-carrier density in the waveguide is justified in most situations of practical interest. For example, intervalence band absorption increases proportionally to hole density³⁻⁵; free-carrier absorption also increases linearly with n (see Ref.²).

The carrier densities in the cladding layers, being mainly defined by the doping levels there, remain practically unchanged and close to their built-in values as the injection current varies. For this reason, the free-carrier and the intervalence band absorption loss due to the optical mode penetration into the cladding layers are both lumped into the constant component α_0 of the internal loss.

2. LASING THRESHOLD CONDITION

With (1), the lasing threshold condition [balance between the modal gain $g = g^{\text{max}}(f_n + f_p - 1)$ and the total loss $\beta + \alpha_{\text{int}}$] becomes

$$g^{\text{max}}(f_n + f_p - 1) = \beta + \alpha_0 + \sigma_{\text{int}} n \quad (2)$$

where g^{max} is the maximum (saturation) value of the modal gain and $\beta = (1/L) \ln(1/R)$ is the external (mirror) loss, L being the cavity length, R the mirror reflectivity.

In (1) and (2), α_{int} is the weighted average of the internal loss across the optical mode shape.¹

For quantum well (QW) or quantum wire (QWR) lasers, f_n and f_p are occupancies of the electron and hole subband-edge levels, between which the lasing transitions occur. For a quantum dot (QD) laser, f_n and f_p are occupancies of the discrete electron and hole levels. The maximum value g^{max} of the modal gain g is obtained at full occupancies $f_n = f_p = 1$ and the minimum $g = -g^{\text{max}}$ at zero occupancies.

For QW or QWR lasers, the right-hand sides of (1) and (2) should also contain a term for absorption in the active region, which is linear in the 2D or 1D carrier density, respectively. However, at high injection currents (or high temperatures – see Refs.^{10,11}), this term will be small compared to absorption in the OCL.

In a QD laser, the process analogous to free-carrier absorption is carrier photoexcitation from the QD levels to states in the continuous spectrum.^{12,13} The absorption coefficient for this process is linear in the confined-carrier level occupancy in a QD and, generally, it should also be included into the right-hand sides of (1) and (2). However, this contribution is typically less than about 0.1 cm^{-1} (see Refs.^{12,13}).

In general, in the right-hand sides of (1) and (2) one should use separate terms for electrons and holes, since they have different cross-sections σ_{int}^n and σ_{int}^p . For simplicity, we will use the lasing threshold condition in the form of (2) having left understood that σ_{int} refers to the cross-section corresponding to the carrier type dominant in absorption.

We assume equal electron and hole occupancies in a quantum-confined active region ($f_n = f_p$). At relatively high temperatures and below the lasing threshold, the thermal equilibrium holds and f_n is given by the Fermi-Dirac distribution function with the quasi-Fermi level determined by the pumping. The carrier density n in the waveguide (OCL) is related to f_n as follows¹²:

$$n = n_1 \frac{f_n}{1 - f_n} \quad (3)$$

where $n_1 = N_c^{\text{OCL}} \exp(-E_n/T)$ is a quantity characterizing the intensity of thermally excited escape of carriers from a reduced-dimensionality active region to the OCL, with $N_c^{\text{OCL}} = 2(m_c^{\text{OCL}} T / 2\pi\hbar^2)^{3/2}$, E_n is the carrier excitation energy from an active region and the temperature T is measured in units of energy.

The threshold condition is then written as follows:

$$g^{\text{max}}(2f_n - 1) = \frac{1}{L} \ln \frac{1}{R} + \alpha_0 + \sigma_{\text{int}} n_1 \frac{f_n}{1 - f_n}. \quad (4)$$

It is illustrated in Fig. 1(a) where the modal gain $g = g^{\max} (2f_n - 1)$ and the internal loss $\alpha_{\text{int}} = \alpha_0 + \sigma_{\text{int}} n_1 f_n / (1 - f_n)$ are shown as functions of the level occupancy f_n . Though the theoretical approach developed here is general and applies equally to semiconductor lasers with a quantum-confined active region of an arbitrary dimensionality, our numerical examples, including those in Figs. 1–7, are specific for QD lasers; the simulation parameters are given in Section 5.1.

With (3), the level occupancy in the active region and the modal gain can be expressed in terms of the carrier density in the OCL as follows:

$$f_n = \frac{n}{n + n_1} \quad (5)$$

$$g = g^{\max} \frac{n - n_1}{n + n_1}. \quad (6)$$

The threshold condition becomes

$$g^{\max} \frac{n - n_1}{n + n_1} = \frac{1}{L} \ln \frac{1}{R} + \alpha_0 + \sigma_{\text{int}} n. \quad (7)$$

Fig. 1(b, top axis), showing the modal gain and the internal loss as functions of the carrier density in the OCL n [given by eqs. (6) and (1), respectively], illustrates the threshold condition of the form (7).

In the absence of lasing, the injection current density j is related to the level occupancy in the active region f_n as follows^{12,14}:

$$j = j_{\text{spon}}^{\text{active}} + ebBn^2 = j_{\text{spon}}^{\text{active}}(f_n) + ebBn_1^2 \frac{f_n^2}{(1 - f_n)^2} \quad (8)$$

where b is the OCL thickness and B is the radiative constant for the OCL. A relation between the spontaneous recombination current density in a quantum-confined active region $j_{\text{spon}}^{\text{active}}$ and the level occupancy can be found in Ref.¹⁹.

With the functional relationship (8) between the level occupancy f_n and the injection current density j , both the modal gain and the internal loss can be calculated as functions of j [shown in Fig. 1(b, bottom axis)].

3. SOLUTIONS OF THE THRESHOLD CONDITION: TWO LASING THRESHOLDS

For $\sigma_{\text{int}} \neq 0$, eq. (4) is a quadratic equation in the confined-carrier level occupancy in the active region f_n ; the roots are (see Fig. 1 for a graphic illustration to the solutions)

$$f_{n\text{-th1}, n\text{-th2}} = f_{n\text{-th}}^{\text{crit}} \mp \sqrt{(f_{n\text{-th}}^{\text{crit}})^2 - f_{n0} - \frac{1}{2} \frac{\alpha_0}{g^{\max}}} \quad (9)$$

where

$$f_{n\text{-th}}^{\text{crit}} = \frac{1}{2} \left(1 + f_{n0} + \frac{1}{2} \frac{\alpha_0}{g^{\max}} - \frac{1}{2} \frac{\sigma_{\text{int}} n_1}{g^{\max}} \right) \quad (10)$$

is the “critical” solution [corresponding to the case when a structure parameter attains its critical tolerable value – see eq. (17) in Section 5], and

$$f_{n0} = \frac{1}{2} \left(1 + \frac{\beta}{g^{\max}} \right) = \frac{1}{2} \left(1 + \frac{L_0^{\min}}{L} \right) \quad (11)$$

is the level occupancy in the active region at the lasing threshold in the absence of internal loss ($\alpha_0 = 0$, $\sigma_{\text{int}} = 0$), L_0^{\min} being the minimum tolerable cavity length in the absence of internal loss given as

$$L_0^{\min} = \frac{1}{g^{\max}} \ln \frac{1}{R}. \quad (12)$$

For L shorter than the minimum tolerable cavity length, the lasing is unattainable in the structure. We discuss the minimum cavity length in detail in Section 5.2.

In general, the following inequalities hold for $f_{n\text{-th1}}$ and $f_{n\text{-th2}}$ [Fig. 1(a)]:

$$\frac{1}{2} \leq f_{n0} \leq f_{n\text{-th1}} \leq f_{n\text{-th}}^{\text{crit}} \leq f_{n\text{-th2}} < 1. \quad (13)$$

The value $1/2$ is the level occupancy at the transparency threshold [when the modal gain is zero: $g^{\max}(2f_n - 1) = 0$].

Both solutions (9) are physically meaningful and describe two distinct lasing thresholds. The first solution, $f_{n,th1}$, is the conventional threshold, similar to f_{n0} but modified by the internal loss. The second solution, $f_{n,th2}$, appears purely as a consequence of the carrier-density-dependent component of the internal loss in the OCL.

As σ_{int} decreases, the first threshold, $f_{n,th1}$, decreases and the second threshold, $f_{n,th2}$, increases. At $\sigma_{int} = 0$, the only solution of (4) is

$$f_{n,th1} = f_{n0} + \frac{1}{2} \frac{\alpha_0}{g^{\max}} = \frac{1}{2} \left(1 + \frac{\beta + \alpha_0}{g^{\max}} \right). \quad (14)$$

Clearly $f_{n,th1} = f_{n0}$ when both α_0 and σ_{int} are zero.

Thus, when the internal loss depends on carrier density, there are, in general, two solutions of the threshold condition, $f_{n,th1}$ and $f_{n,th2}$, and hence we have two lasing thresholds.

We shall refer to the injection current densities corresponding to $f_{n,th1}$ and $f_{n,th2}$, respectively, as the lower threshold current density j_{th1} and the upper threshold current density j_{th2} . These threshold current densities are given by (8) wherein one substitutes either $f_n = f_{n,th1}$ or $f_n = f_{n,th2}$.

The existence of a second lasing threshold stems from the nonmonotonic dependence of the difference between the modal gain and the internal loss on the level occupancy in a quantum-confined active region [the solid curve in Fig. 1(a)], or, equivalently, on the carrier density in the OCL [the solid curve in Fig. 1(b, top axis)], or on the injection current density [the solid curve in Fig. 1(b, bottom axis)]. The point is that the modal gain $g = g^{\max}(2f_n - 1)$ increases linearly with f_n [the dotted line in Fig. 1(a)] and saturates at its maximum value g^{\max} as $f_n \rightarrow 1$ [which corresponds to $n \rightarrow \infty$ and $j \rightarrow \infty$ - see (3), (8) and Fig. 1(b)]. At the same time, α_{int} is superlinear in f_n [see (1) and (3) and the dashed curve in Fig. 1(a)] and increases infinitely as $f_n \rightarrow 1$. At a certain f_n [see (23)], i.e., at a certain j , the rate of increase in α_{int} with j will inevitably equal that of increase in g , and hence the difference $g - \alpha_{int}$ will peak. Any further increase of the injection current density will decrease the difference $g - \alpha_{int}$ [the solid curve in Fig. 1(b)]. This corresponds to the so-called "loss-multiplication" regime, discussed in Refs.^{10,11} for InGaAsP/InP-based strained-layer multiple-QW lasers and attributed to the pileup of carriers due to electrostatic band-profile deformation.^{15,16} In the context of QD lasers, the loss-multiplication regime was discussed in Refs.^{17,18}. As evident from our analysis, this regime and the second lasing threshold are inherent to all structures where the internal loss depends on the carrier density in the OCL.

Due to bimolecular (quadratic in n) spontaneous recombination in the OCL, the injection current density j is superlinear in n [quadratic at high n - see (8)] and hence the internal loss (being linear in n) is strongly sublinear in j [increases as \sqrt{j} at high j - see the dashed curve in Fig. 1(b)]. [Also the modal gain is strongly sublinear in both n and j - see (6), (8) and the dotted curve in Fig. 1(b)]. In Ref.¹⁷, a linear relation between α_{int} and j was however assumed, which is justified for only monomolecular (linear in n) recombination in the OCL, such as recombination via nonradiative centers. At high injection levels, bimolecular and then Auger (cubic in n) recombination dominate and j becomes superlinear in n and hence α_{int} sublinear in j .

4. TWO-VALUED CHARACTERISTICS: GAIN-CURRENT AND LIGHT-CURRENT

In a continuous-wave (CW) operation, increasing j from zero, one reaches the first lasing threshold j_{th1} . Above this threshold, the difference between the gain and the internal loss is pinned at the value of the mirror loss β and hence Fig. 1 (which is valid for determining the positions of both thresholds) no longer applies. What actually happens above j_{th1} is shown in Fig. 2, derived in Ref.¹⁹ by rigorously solving the rate equations in the presence of light generation. In a steady state, the rate equation for photons reduces to our eq. (2), where now the quantities f_n , f_p and n are calculated in the presence of light generation.

As a consequence of the non-instantaneous carrier capture from the OCL into the quantum-confined active region, the free-carrier density n in the OCL does not pin and increases above threshold. A quantitative theoretical study of this effect was given in Ref.¹⁴. The effect has also been seen experimentally, see Ref.² and numerous references cited in Ref.¹⁴. To simplify the consideration, the carrier-density-dependent component of the internal loss [the last term in the right-hand side of (2)] was neglected in Ref.¹⁴; with that assumption, the confined-carrier level occupancy f_n in the active region is pinned above threshold at a value given by (14), as is evident from (2).

As is also evident from eq. (2), the carrier-density-dependent component of the internal loss in the OCL couples the confined-carrier level occupancy f_n in the active region and the free-carrier density n in the OCL; the equation relating these quantities is [we assume equal electron and hole occupancies ($f_n = f_p$)]

$$f_n = \frac{1}{2} \left(1 + \frac{\beta + \alpha_0 + \sigma_{\text{int}} n}{g^{\text{max}}} \right). \quad (15)$$

As seen from (15), when $\sigma_{\text{int}} \neq 0$, the confined-carrier level occupancy f_n is no longer pinned in the presence of light generation.

Above the second threshold $j_{\text{th}2}$ and up to a maximum pump current j_{max} , there are two solutions of the rate equations. The injection-current-density dependence of the confined-carrier level occupancy f_n corresponding to the first solution (conventional lasing regime) and the second solution (anomalous new regime) is shown by the solid and dashed curves, respectively, in Fig. 2(a) (right axis). The intersections of these curves with the dotted curve for f_n in the absence of lasing determine the first and the second lasing thresholds (the abscissae determine $j_{\text{th}1}$ and $j_{\text{th}2}$, the ordinates determine $f_{n-\text{th}1}$ and $f_{n-\text{th}2}$). Since the light intensity is zero at the threshold points, the two solutions for f_n of the rate equations in the presence of light generation go (as they should) into $f_{n-\text{th}1}$ and $f_{n-\text{th}2}$ determined from (4) and given by (9).

Above the second threshold $j_{\text{th}2}$, both the gain-current dependence [Fig. 2(a), left axis] and the light-current characteristic (LCC) [Fig. 2(b)] are two-valued. At $j = j_{\text{max}}$, the two branches merge in both characteristics.

As seen from (2), in the presence of carrier-density-dependent component of the internal loss too the difference between the gain and the internal loss is pinned at the value of the mirror loss β , though both the internal loss $\alpha_{\text{int}} = \alpha_0 + \sigma_{\text{int}} n$ and the gain $g = g^{\text{max}}(2f_n - 1)$ [Fig. 2(a), left axis] change with the injection current. As α_{int} increases with the current above the conventional threshold $j_{\text{th}1}$ in the first (conventional) lasing regime, the gain strictly follows it so as to maintain the stable generation condition $g - \alpha_{\text{int}} = \beta$. An increase of $\alpha_{\text{int}} = \alpha_0 + \sigma_{\text{int}} n$, caused by increasing free-carrier density n in the OCL, is compensated by an increase in $g = g^{\text{max}}(2f_n - 1)$, ensured by increasing confined-carrier level occupancy f_n above the conventional threshold in the first lasing regime [the solid curve in Fig. 2(a)]. This continues up to the maximum pump current j_{max} at which the lasing is quenched.

At this time, we cannot propose a definite experimental technique to access the second lasing regime (the upper branch of the gain-current characteristic [the dashed curve in Fig. 2(a)] and the lower branch of the LCC [the dashed curve in Fig. 2(b)]). Analysis of the stability of the second lasing regime will be published elsewhere.

Other mechanisms, such as carrier heating and modal gain compression, can also lead to the second lasing threshold. Thus, due to the increase in carrier temperature with the injection current^{20-23, 16} the modal gain itself can become nonmonotonic with j , decreasing at high currents.²² Such mechanisms can further enhance the effect of internal loss. The effect of internal loss in the presence of other mechanisms is a matter of a separate study. This study will show the relative importance of different mechanisms involved and how to discriminate them from each other. Here, it is however worth noting that the internal loss will remain present in temperature-stabilized devices, in which the heating effects are strongly suppressed.

5. CRITICAL TOLERABLE PARAMETERS

The lasing in a structure is only possible in a certain region of values of the structure parameters. This multi-dimensional region of tolerable parameters is given by the existence condition of real positive roots $f_{n-\text{th}1}$ and $f_{n-\text{th}2}$ [see (9)] of (4). This condition is of the form

$$\sqrt{1 + \frac{\beta + \alpha_0}{g^{\text{max}}}} + \sqrt{\frac{\sigma_{\text{int}} n_1}{g^{\text{max}}}} \leq \sqrt{2}. \quad (16)$$

In the absence of internal loss, (16) reduces to the inequality $g^{\text{max}} \geq \beta$ discussed earlier.^{12,24}

The limiting case when the inequality (16) becomes equation, yields the critical tolerable value for any one of the parameters, other parameters being fixed. These critical tolerable parameters are α_0^{max} , $\sigma_{\text{int}}^{\text{max}}$ (Section 5.1) and L^{min} (and, equivalently, β^{max}) (Section 5.2). In QD lasers, two more critical parameters are N_S^{min} and δ^{max} .^{12,24}

When the equality in (16) holds, there is only one solution of the threshold condition. The curve for $g^{\max}(2f_n - 1) - \alpha_{\text{int}}$ is tangent at its maximum to the horizontal line for the mirror loss β (Fig. 1). This happens as L or α_0 (affecting the constant component of the total loss), or σ_{int} (affecting the carrier-density-dependent component of the internal loss), or, in the context of QD lasers, N_S or δ [affecting g^{\max} – see (20)] tend to their critical tolerable values. In this case,

$$f_{n,\text{th}1} = f_{n,\text{th}2} = f_{n,\text{th}}^{\text{crit}} = \sqrt{\frac{1}{2} \left(1 + \frac{\beta + \alpha_0}{g^{\max}} \right)} = 1 - \sqrt{\frac{1}{2} \frac{\sigma_{\text{int}} n_1}{g^{\max}}} \quad (17)$$

[see eq. (10) for $f_{n,\text{th}}^{\text{crit}}$].

5.1. Critical tolerable values of α_0 and σ_{int}

The loss parameters α_0 and σ_{int} are not directly controllable variables as they are determined by the specific loss processes involved. Nevertheless, it is instructive to determine the 2D-region of tolerable values of α_0 and σ_{int} where lasing can be attained (the hatched region in Fig. 3) for given structure parameters. This procedure becomes even more appealing in view of the wide scatter of reported data for α_{int} , even for similar structures. For example, $\alpha_{\text{int}} = 1.2 \text{ cm}^{-1}$ (Ref.²⁵) and $\alpha_{\text{int}} = 11 \text{ cm}^{-1}$ (Ref.²⁶) was reported in structures with InGaAs QDs based on GaAs substrates (in the wavelength ranges $\lambda_0 = 1.25\text{--}1.29 \mu\text{m}$ and $1\text{--}1.1 \mu\text{m}$, respectively). In Ref.²⁶, the internal loss was unaffected by the number of QD layers, which indicates that the carrier-density-dependent component of α_{int} was negligible; hence the measured value of 11 cm^{-1} can be attributed solely to α_0 . The estimated value of σ_{int} is $1.3 \times 10^{-17} \text{ cm}^2$ in Ref.⁴ while it is in the range of $2.1 \pm 0.3 \times 10^{-17} \text{ cm}^2$ in Ref.⁸ for GaInAsP/InP double heterostructure lasing at $\lambda_0 = 1.3 \mu\text{m}$. For GaInAsP/InP double heterostructure lasing at $\lambda_0 = 1.6 \mu\text{m}$, $\sigma_{\text{int}} = 2.5 \times 10^{-17} \text{ cm}^2$ in Ref.⁴ and $\sigma_{\text{int}} = 4 \times 10^{-17} \text{ cm}^2$ in Refs.^{3,5}.

The solid curve [given by the equality in (16)] in Fig. 3 bounds the region of tolerable values of α_0 and σ_{int} for a given mirror loss $\beta = 10 \text{ cm}^{-1}$; the dashed curve is the corresponding upper bound, obtained by assuming an infinitely long cavity ($\beta = 0$). Each point on the solid (dashed) curve presents the maximum tolerable value of σ_{int} at a fixed α_0 and given L (at $L = \infty$); and vice versa, maximum tolerable value of α_0 at a fixed σ_{int} .

At $L = \infty$ and $\alpha_0 = 0$,

$$\sigma_{\text{int}}^{\max} = (3 - 2\sqrt{2}) \frac{g^{\max}}{n_1} \approx 0.17 \frac{g^{\max}}{n_1} \quad (18)$$

(see the intersection of the dashed curve and the vertical axis in Fig. 3).

At $L = \infty$ and $\sigma_{\text{int}} = 0$, the equation for α_0^{\max} is obvious:

$$\alpha_0^{\max} = g^{\max} \quad (19)$$

(see the tangent point of the dashed curve and the horizontal axis in Fig. 3).

All the above equations apply equally to QD, QWR and QW lasers. One specifies the type of laser by substituting the relevant expression for g^{\max} and relation between $j_{\text{spon}}^{\text{active}}$ and f_n [see (8) and (??)–(??)].

Our general approach is illustrated below by detailed calculations for QD lasers. The saturation value of the modal gain is given by^{12,27}

$$g^{\max} = \frac{\xi}{4} \left(\frac{\lambda_0}{\sqrt{\epsilon}} \right)^2 \frac{1}{\tau_{\text{QD}}} \frac{\hbar}{(\Delta\epsilon)_{\text{inhom}}} \frac{\Gamma}{a} N_S \quad (20)$$

where $\xi = 1/\pi$ and $\xi = 1/\sqrt{2\pi}$ for the Lorentzian and the Gaussian QD-size distributions, respectively, λ_0 is the lasing wavelength, ϵ is the dielectric constant of the OCL, a is the mean size of QDs, and Γ is the optical confinement factor in a QD layer (along the transverse direction in the waveguide). The inhomogeneous line broadening caused by fluctuations in QD sizes is $(\Delta\epsilon)_{\text{inhom}} = (q_n \epsilon_n + q_p \epsilon_p) \delta$, where ϵ_n and ϵ_p are the quantized energy levels of an electron and a hole in a mean-sized QD, $q_{n,p} = -(\partial \ln \epsilon_{n,p} / \partial \ln a)$ and δ is the root mean square (RMS) of relative QD size fluctuations.

For illustration, we consider room-temperature operation of a GaInAsP/InP heterostructure similar to that assumed in Refs.^{12–14}. Throughout the paper, we assume the following structure parameters, unless otherwise specified: $\delta = 0.05$ (10% QD-size fluctuations); as-cleaved facet reflectivity at both ends ($R = 0.32$) and $L =$

1.139 mm, which correspond to the mirror loss $\beta = 10 \text{ cm}^{-1}$; $N_S = 6.11 \times 10^{10} \text{ cm}^{-2}$, which, in the absence of internal loss, is the optimum N_S minimizing the threshold current density at the above values of δ and β . At these parameters, $g^{\max} = 29.52 \text{ cm}^{-1}$. At $T = 300 \text{ K}$, $n_1 = 5.07 \times 10^{16} \text{ cm}^{-3}$.

We see from (18)–(20) that $\sigma_{\text{int}}^{\max}$ and α_0^{\max} increase indefinitely with either $N_S \rightarrow \infty$ or $\delta \rightarrow 0$. Hence making the QD ensemble denser or improving the QD-size uniformity is a direct way to alleviate the limitations on lasing imposed by the internal loss in QD structures.

5.2. Critical tolerable values of L and β

The minimum cavity length is readily obtained from (11) and (16) and is given by:

$$L^{\min} = \frac{L_0^{\min}}{\left(\sqrt{2} - \sqrt{\frac{\sigma_{\text{int}} n_1}{g^{\max}}}\right)^2 - 1 - \frac{\alpha_0}{g^{\max}}} \quad (21)$$

where L_0^{\min} is the minimum cavity length in the absence of internal loss [see (12)].

The equation for the critical tolerable parameters [equality in (16)] can be rewritten as follows:

$$\beta^{\max} = \left(\sqrt{2g^{\max}} - \sqrt{\sigma_{\text{int}} n_1}\right)^2 - g^{\max} - \alpha_0 \quad (22)$$

where $\beta^{\max} = (1/L_{\min}) \ln(1/R)$ is the maximum tolerable mirror loss. Eq. (22) has an evident meaning. The right-hand side is simply the peak value of the difference between the modal gain and the internal loss (Fig. 1); this value is obtained when the level occupancy in the active region is

$$f_n = 1 - \sqrt{\frac{\sigma_{\text{int}} n_1}{2g^{\max}}} \quad (23)$$

[see also the last equation in (17)]. When the mirror loss approaches this peak value, the critical condition (22) is met. The peak value of the difference between the modal gain and the internal loss can be considerably lower than the saturation value g^{\max} of the modal gain itself; in addition, in contrast to g^{\max} , it is temperature-dependent [through the T -dependence of the quantity n_1 characterizing the intensity of the thermal escape of carriers from an active region, cf. eq. (3)].

Equations (21)–(23) hold true for QD, QWR and QW lasers.

For QD lasers, using eq. (20) for g^{\max} and eq. (12), we have²⁴

$$L_0^{\min} = \frac{4}{\xi} \left(\frac{\sqrt{\epsilon}}{\lambda_0}\right)^2 \tau_{\text{QD}} \frac{a}{\Gamma} \frac{(q_n \epsilon_n + q_p \epsilon_p) \delta}{\hbar} \frac{1}{N_S} \ln \frac{1}{R}. \quad (24)$$

Fig. 4 shows L^{\min} as a function of σ_{int} calculated using (21) and (24). As evident from the figure, depending on α_0 and σ_{int} , the restriction L^{\min} can be considerably increased compared to its value L_0^{\min} in the absence of internal loss. This is consistent with the discussion in Refs.^{17,18}, concerning the limitation of L^{\min} for the QD-ground-state lasing posed by a steep increase in α_{int} with decreasing cavity length (due to loss-multiplication^{10,11}).

Throughout the paper, we chose $\alpha_0 = 3 \text{ cm}^{-1}$ and $\sigma_{\text{int}} = 2.67 \times 10^{-17} \text{ cm}^{-1}$ (unless otherwise specified), so that L^{\min} , β^{\max} , N_S^{\min} and δ^{\max} are equal to 1.139 mm, 10 cm^{-1} , $6.11 \times 10^{10} \text{ cm}^{-2}$ and 0.05, respectively. At these plausible α_0 and σ_{int} , the internal loss is within a typical range from several to above ten cm^{-1} (the solid curve and the left axis in Fig. 7). The minimum cavity length is hence almost threefold increased compared to its value in the absence of internal loss $L_0^{\min} = 386 \mu\text{m}$. Thus, our theory shows that the absence of lasing often observed in short-cavity QD structures can be attributed to internal loss. Another possible reason that limits lasing via the ground-state transition at short (under a millimeter) cavity lengths can be a small overlap integral of the electron and hole wave functions in low-symmetry QDs; this was discussed in Ref.²⁸.

When the denominator of the right-hand side in (21) is zero, then $L^{\min} \rightarrow \infty$, i.e. the lasing is unattainable at a finite cavity length. This situation at a high internal loss may be somewhat alleviated by using high-reflectivity mirrors. Indeed, when $R \rightarrow 1$, then $L_0^{\min} \rightarrow 0$ [see (24)] and L^{\min} can be kept finite.

6. THRESHOLD CURRENT DENSITIES AGAINST STRUCTURE PARAMETERS

The confined carrier level occupancies in the active region at both the lower and the upper lasing thresholds, f_{n_th1} and f_{n_th2} , calculated using (9) are shown in Fig. 5 (solid and dashed curves, respectively). The lower and the upper threshold current densities, j_{th1} and j_{th2} , are shown by the solid and the dashed curves, respectively, in Fig. 6. To illustrate how strong the effect of internal loss can be, the level occupancy and the threshold current density in the absence of internal loss, f_{n0} and j_{th0} , respectively, are also shown in Figs. 5 and 6 (dotted curves).

In the absence of internal loss, the level occupancy in a quantum-confined active region tends to unity ($f_{n0} \rightarrow 1$) when any structure parameter approaches its critical tolerable value [see (11) and the dotted curve in Fig. 5]; hence the threshold current density in the absence of internal loss increases infinitely ($j_{th0} \rightarrow \infty$) – see the dotted curve in Fig. 6.

As the structure parameter equals its critical tolerable value in the presence of carrier-density-dependent internal loss ($\sigma_{int} \neq 0$), the two solutions of the threshold condition (the solid and the dashed curves in Fig. 5) merge together at a value given by (17). Hence the lower threshold current density j_{th1} (the solid curve in Fig. 6) and the upper threshold current density j_{th2} (the dashed curve in Fig. 6) merge together at a finite value. The derivatives of f_n , and hence of n and j_{th} , with respect to the structure parameter are infinitely high at a critical point (Figs. 5–7). This is a consequence of $\partial(g - \alpha_{int})/\partial f_n = 0$ at this point – see Fig. 1. Immediately behind the critical point, the lasing is unattainable. Hence, the curve for j_{th1} joins smoothly the vertical line at the critical point (Fig. 6). In contrast, when only the constant component of the internal loss is present ($\sigma_{int} = 0$), the curve for j_{th1} approaches only asymptotically the vertical line at the critical point, much as the curve for j_{th0} does [dotted curve in Fig. 6].

It is evident from Fig. 6 that the internal loss can have a strong effect on the lower threshold current density j_{th1} , especially near the critical point, when j_{th1} may increase by several times compared to its value j_{th0} in the absence of internal loss.

Fig. 7 shows the free-carrier density in the OCL (right axis) and the internal loss (solid curve, left axis) at the lower lasing threshold against L . The dotted curve shows the free-carrier density in the OCL in the absence of internal loss (right axis). As seen from the figure, the free-carrier density can be considerably increased due to the internal loss.

7. CONCLUSIONS

We have carried out a theoretical analysis of the threshold behavior of semiconductor lasers with a reduced-dimensionality active region taking a general account of the internal optical loss.

When the internal loss depends on the free-carrier density in the OCL, we predict the existence of a second (upper) lasing threshold. Above the second threshold, two physically distinct lasing regimes exist; correspondingly, the gain-current characteristic and the LCC are two-valued up to a maximum current at which the lasing is quenched.

Due to the internal loss, the region of tolerable values of the structure parameters is strongly narrowed, and both the free-carrier density outside the active region and the confined-carrier level occupancy in the active region at the lasing threshold are increased; thus the threshold current density is increased.

Presented analysis, exemplified in the context of QD lasers, can be used for their further optimizing, especially for lowering the threshold current density in short-cavity structures.

ACKNOWLEDGMENTS

This work was supported in part by the AFOSR MURI under Grant F49620-00-1-0331 and the New York State Center for Advanced Sensor Technology. The work of L. V. Asryan was also supported by the RFBR and by the Russian Program "Physics of Solid State Nanostructures."

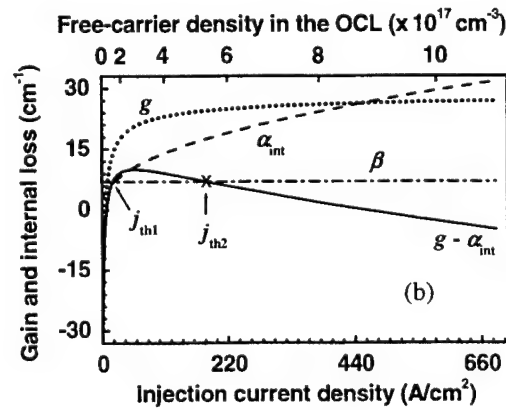
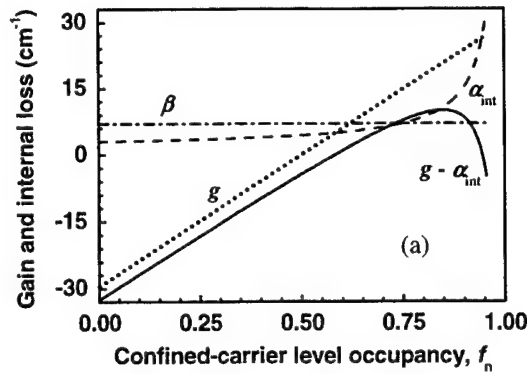


Fig. 1. Illustration of the threshold condition (4) and of the two lasing thresholds. Modal gain g [dotted line in (a) and dotted curve in (b)], internal loss α_{int} (dashed curve) and difference of modal gain and internal loss (solid curve) against confined-carrier-level occupancy in the active region f_n (a), free-carrier density in the OCL n (b, top axis) and injection current density j (b, bottom axis). The intersections of the solid curve and the horizontal dash-dotted line for the mirror loss β are the solutions (9) of (4) [in (a)], the free-carrier densities in the OCL at the lower and the upper thresholds [in (b, top axis)], and the lower and the upper threshold current densities, j_{th1} and j_{th2} , respectively [in (b, bottom axis)]. The dependences on n and j in (b) are easily converted from those in (a) using (3) and (8). Throughout the paper, a GaInAsP/InP-based QD-heterostructure lasing near $1.55 \mu\text{m}$ (see Refs. ¹²⁻¹⁴) is considered for illustration. In Figs. 1 and 2, the mirror loss $\beta = 7 \text{ cm}^{-1}$; otherwise, $\beta = 10 \text{ cm}^{-1}$. Parameters α_0 and σ_{int} are plausibly taken as 3 cm^{-1} and $2.67 \times 10^{-17} \text{ cm}^{-1}$, respectively.

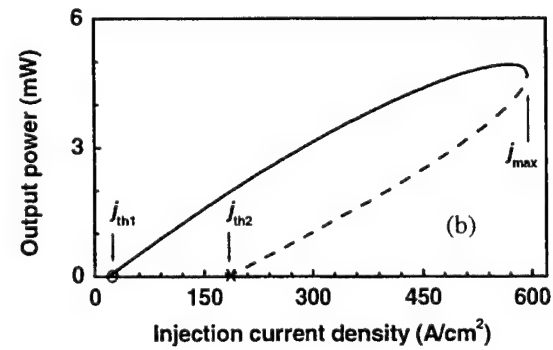
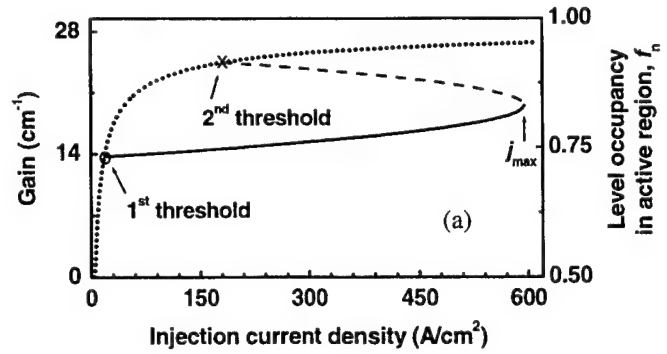


Fig. 2. Two-valued lasing characteristics: gain-current (a, left axis) and light-current (b). The branches corresponding to the first (conventional) and the second (anomalous) regimes (solid and dashed curves, respectively) merge together at the point j_{max} , which defines the maximum operating current. At $j > j_{\text{max}}$, the lasing is quenched. The dotted curve in (a) is the gain-current dependence for a nonlasing regime. Since $g = g^{\text{max}}(2f_n - 1)$, the same curves in (a) show the confined-carrier level occupancy f_n in the active region (right axis): solid and dashed curves — for the first and the second lasing regimes, respectively, dotted curve — for a nonlasing regime. The intersections of the solid and dashed curves for the first and the second lasing regimes with the dotted curve for nonlasing regime determine the first and the second lasing thresholds (the abscissae determine j_{th1} and j_{th2} , the ordinates determine $f_{n\text{-th1}}$ and $f_{n\text{-th2}}$). In (b), the assumed stripe width $W = 2 \mu\text{m}$.

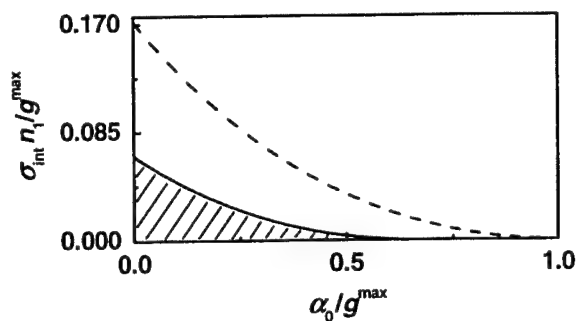


Fig. 3. 2D-region of tolerable values of the normalized internal loss parameters α_0/g^{max} and $\sigma_{int}n_i/g^{max}$ given by (16) (the hatched region below the solid curve); the ratio $\beta/g^{max} = 0.34$, which corresponds to $\beta = 10 \text{ cm}^{-1}$ and $g^{max} = 29.52 \text{ cm}^{-1}$ for the structure considered. The tolerable region for the case $\beta = 0$ is the region below the dashed curve. The boundary (the solid or the dashed curve at $\beta/g^{max} = 0.34$ or $\beta/g^{max} = 0$, respectively) represents the maximum tolerable value of σ_{int} , σ_{int}^{max} , versus α_0 ; and vice versa, the maximum tolerable value of α_0 , α_0^{max} , versus σ_{int} if the functional relationship between the abscissa and the ordinate is interchanged.

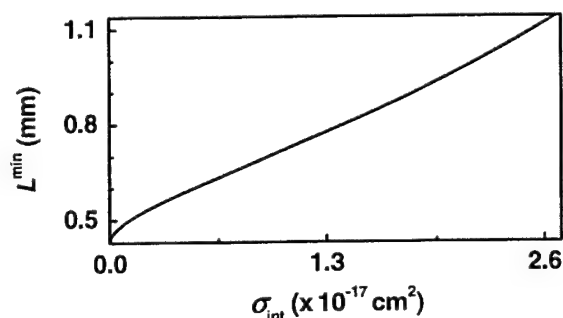


Fig. 4. Minimum cavity length L^{min} against absorption loss cross-section σ_{int} . L^{min} is calculated using (21). The same curve can be viewed as representing σ_{int}^{max} versus the cavity length L .

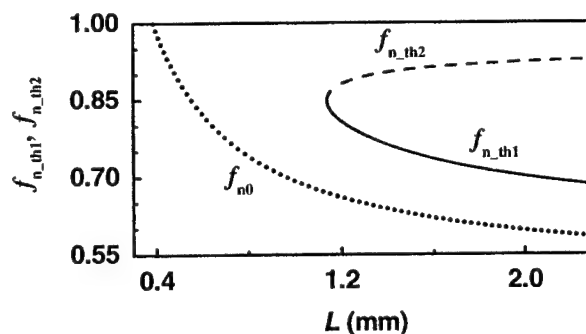


Fig. 5. Confined-carrier level occupancy in the active region at the lower (solid curve) and upper (dashed curve) lasing thresholds, $f_{n,th1}$ and $f_{n,th2}$ [see (9)], against L . The dotted curve shows the level occupancy f_{n0} at the lasing threshold in the absence of internal loss.

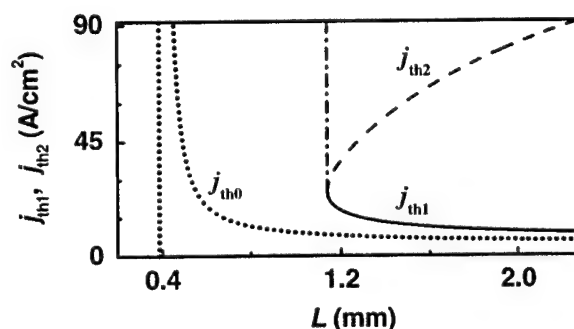


Fig. 6. The lower and the upper threshold current densities (solid and dashed curves, respectively), j_{th1} and j_{th2} , against L . The curve for j_{th1} joins smoothly the vertical dash-dotted line at the critical point. The dotted curve and the vertical dotted lines show the threshold current density j_{th0} and its asymptote at the critical point in the absence of internal loss.

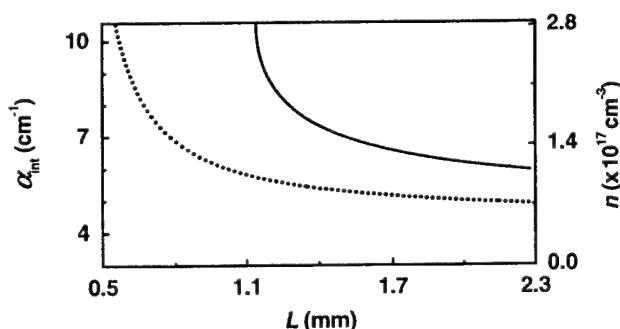


Fig. 7. Free-carrier density in the OCL (right axis) and internal loss (left axis) at the lower lasing threshold against L . The dotted curve shows n in the absence of internal loss.

REFERENCES

1. L. A. Coldren and S. W. Corzine, "Diode lasers and photonic integrated circuits," New York: John Wiley & Sons, 1995, 594 p.
2. D. Z. Garbuzov, A. V. Ovchinnikov, N. A. Pikhtin, Z. N. Sokolova, I. S. Tarasov, and V. B. Khalfin, "Experimental and theoretical investigations of singularities of the threshold and power characteristics of InGaAsP/InP separate-confinement double-heterostructure lasers ($\lambda = 1.3\mu\text{m}$)," Sov. Phys. Semicond., vol. 25, no. 5, pp. 560-564, May 1991.
3. M. Asada, A. R. Adams, K. E. Stubkjaer, Y. Suematsu, Y. Itaya, and S. Arai, "The temperature dependence of the threshold current of GaInAsP/InP DH lasers," IEEE J. Quantum Electron., vol. 17, no. 5, pp. 611-619, May 1981.
4. C. H. Henry, R. A. Logan, F. R. Merritt, and J. P. Luongo, "The effect of intervalence band absorption on the thermal behavior of InGaAsP lasers," IEEE J. Quantum Electron., vol. 19, no. 6, pp. 947-952, June 1983.
5. M. Asada, A. Kameyama and Y. Suematsu, "Gain and intervalence band absorption in quantum-well lasers," IEEE J. Quantum Electron., vol. 20, no. 7, pp. 745-753, July 1984.
6. N. A. Gun'ko, V. B. Khalfin, Z. N. Sokolova, G. G. Zegrya, "Optical loss in InAs-based long-wavelength lasers," J. Appl. Phys., vol. 84, no. 1, pp. 547-554, July 1998.
7. J. J. Lee, L. J. Mawst, and D. Botez, "MOCVD growth of asymmetric 980 nm InGaAs/InGaAsP broad-waveguide diode lasers for high power applications," J. Cryst. Growth, vol. 249, nos. 1-2, pp. 100-105, Feb. 2003.
8. D. A. Ackerman, G. E. Shtengel, M. S. Hybertsen, P. A. Morton, R. F. Kazarinov, T. Tanbun-Ek, and R. A. Logan, "Analysis of gain in determining T_0 in $1.3\mu\text{m}$ semiconductor lasers," IEEE J. Sel. Top. Quantum Electron., vol. 1, no. 2, pp. 250-63, June 1995.
9. G. L. Belenky, C. L. Reynolds, D. V. Donetsky, G. E. Shtengel, M. S. Hybertsen, M. A. Alam, G. A. Baraff, R. K. Smith, R. F. Kazarinov, J. Winn, L. E. Smith, "Role of p-doping profile and regrowth on the static characteristics of $1.3\mu\text{m}$ MQW InGaAsP-InP lasers: Experiment and modeling," IEEE J. Quantum Electron., vol. 35, no. 10, pp. 1515-1520, Oct. 1999.
10. S. Seki, H. Oohasi, H. Sugiura, T. Hirono, and K. Yokoyama, "Dominant mechanisms for the temperature sensitivity of $1.3\mu\text{m}$ InP-based strained-layer multiple-quantum-well lasers," Appl. Phys. Lett., vol. 67, no. 8, pp. 1054-1056, Aug. 1995.
11. S. Seki, H. Oohasi, H. Sugiura, T. Hirono, and K. Yokoyama, "Dominant mechanism for limiting the maximum operating temperature of InP-based multiple-quantum-well lasers," J. Appl. Phys., vol. 79, no. 5, pp. 2192-2197, Mar. 1996.
12. L. V. Asryan and R. A. Suris, "Inhomogeneous line broadening and the threshold current density of a semiconductor quantum dot laser," Semicond. Sci. Technol., vol. 11, no. 4, pp. 554-567, Apr. 1996.
13. L. V. Asryan and R. A. Suris, "Carrier photoexcitation from levels in quantum dots to states of the continuum in lasing," Semicond., vol. 35, no. 3, pp. 343-346, Mar. 2001.
14. L. V. Asryan, S. Luryi and R. A. Suris, "Internal efficiency of semiconductor lasers with a quantum-confined active region," IEEE J. Quantum Electron., vol. 39, no. 3, pp. 404-418, Mar. 2003.
15. S. Seki and K. Yokoyama, "Electrostatic deformation in band profiles of InP-based strained-layer quantum-well lasers," J. Appl. Phys., vol. 77, no. 10, pp. 5180-5184, May 1995.
16. L. V. Asryan, N. A. Gun'ko, A. S. Polkovnikov, G. G. Zegrya, R. A. Suris, P.-K. Lau, and T. Makino, "Threshold characteristics of InGaAsP/InP multiple quantum well lasers," Semicond. Sci. Technol., vol. 15, no. 12, pp. 1131-1140, Dec. 2000.
17. A. E. Zhukov, A. R. Kovsh, V. M. Ustinov and Zh. I. Alferov, "Loss multiplication in a quantum dot laser," Laser Phys., vol. 13, no. 3, pp. 319-323, Mar. 2003.
18. A. R. Kovsh, N. A. Maleev, A. E. Zhukov, S. S. Mikhlin, A. P. Vasil'ev, E. A. Semenova, Yu. M. Shernyakov, M. V. Maximov, D. A. Livshits, V. M. Ustinov, N. N. Ledentsov, D. Bimberg, and Zh. I. Alferov, "InAs/InGaAs/GaAs quantum dot lasers of $1.3\mu\text{m}$ range with enhanced optical gain," J. Cryst. Growth, vol. 251, nos. 1-4, pp. 729-736, Apr. 2003.
19. L. V. Asryan and S. Luryi, "Two lasing thresholds in semiconductor lasers with a quantum-confined active region," Appl. Phys. Lett., vol. 83, no. 26, pp. 5368-5370, Dec. 2003.

20. P. G. Eliseev, "Introduction to the physics of injection lasers," Moscow: Nauka, 1983, 294 p. (in Russian).
21. V. B. Gorfinkel, S. Luryi and B. Gelmont, "Theory of gain spectra for quantum cascade lasers and temperature dependence of their characteristics at low and moderate carrier concentrations," *IEEE J. Quantum Electron.*, vol. 32, no. 11, pp. 1995-2003, Nov. 1996.
22. V. Gorfinkel, M. Kisin and S. Luryi, "Hot electrons and curves of constant gain in long wavelength quantum well lasers," *Optics Express*, vol. 2, no. 4, pp. 125-130, Feb. 1998.
23. L. V. Asryan, N. A. Gun'ko, A. S. Polkovnikov, R. A. Suris, G. G. Zegrya, B. B. Elenkrig, S. Smetona, J. G. Simmons, P.-K. Lau, and T. Makino, "High-power and high-temperature operation of InGaAsP/InP multiple quantum well lasers," *Semicond. Sci. Technol.*, vol. 14, no. 12, pp. 1069-1075, Dec. 1999.
24. L. V. Asryan and R. A. Suris, "Longitudinal spatial hole burning in a quantum-dot laser," *IEEE J. Quantum Electron.*, vol. 36, no. 10, pp. 1151-1160, Oct. 2000.
25. S. S. Mikhlin, A. E. Zhukov, A. R. Kovsh, N. A. Maleev, A. P. Vasil'ev, E. S. Semenova, V. M. Ustinov, M. M. Kulagina, E. V. Nikitina, I. P. Soshnikov, Yu. M. Shernyakov, D. A. Livshits, N. V. Kryzhanovskaya, D. S. Sizov, M. V. Maksimov, A. F. Tsatsul'nikov, N. N. Ledentsov, D. Bimberg, and Zh. I. Alferov, "High efficiency ($\eta_D > 80\%$) long wavelength ($\lambda > 1.25 \mu\text{m}$) quantum dot diode lasers on GaAs substrates," *Semicond.*, vol. 36, no. 11, pp. 1315-1321, Nov. 2002.
26. P. M. Smowton, E. Herrmann, Y. Ning, H. D. Summers, P. Blood, M. Hopkinson, "Optical mode loss and gain of multiple-layer quantum-dot lasers," *Appl. Phys. Lett.*, vol. 78, no. 18, pp. 2629-2631, Apr. 2001.
27. L. V. Asryan and R. A. Suris, "Charge neutrality violation in quantum dot lasers," *IEEE J. Select. Topics Quantum Electron.*, vol. 3, no. 2, pp. 148-157, Apr. 1997.
28. L. V. Asryan, M. Grundmann, N.N. Ledentsov, O. Stier, R.A. Suris, and D. Bimberg, "Effect of excited-state transitions on the threshold characteristics of a quantum dot laser," *IEEE J. Quantum Electron.*, vol. 37, no. 3, pp. 418-425, March 2001.

On pattern-effects-free operation of QD SOAs for high speed applications

Alexander V. Uskov *

National Microelectronics Research Center, Lee Maltings, Prospect Row, Cork, Ireland;
Lebedev Physical Institute, Leninsky pr.53, 119991, Moscow, Russia

ABSTRACT

We have developed a theory of high-speed operation of quantum dot (QD) semiconductor optical amplifiers (SOAs), and showed that pattern-effect-free amplification of pulse trains, cross gain modulation (XGM) and cross phase modulation (XPM) can take place in QD SOA in the regime with maximum gain. Formulas, which relate the maximum bit-rate for the pattern-effect-free operation and the average SOA output power to the SOA pump current density, were derived. XGM without pattern effect can be realized in the regime with maximum gain due to spectral hole burning effects. Possibility of ultrafast frequency conversion and demultiplexing of data pulse streams through this nonlinearity is illustrated. Expression for the nonlinear refractive index η_{nl} due to spectral hole burning in QD structure was obtained. The value of η_{nl} in QD SOAs can be by 4-5 orders larger than η_{nl} in silica; and efficient ultrafast XPM without pattern effects can be carried out in QD SOA through this nonlinearity. In whole, usage of the regime with maximum gain in QD SOAs can lead to development of new generation of high-speed devices for ultrafast optical processing and communications.

Keywords: Semiconductor optical amplifiers, quantum dots, high-speed optical processing

1. INTRODUCTION

Quantum Dot (QD) technologies already have demonstrated their great possibilities in the realization of semiconductor lasers with record parameters [1]. At present, interest is growing rapidly in QD semiconductor optical amplifiers (SOAs), due to the unique potential that they possess for applications in high-speed optical communications and optical processing [2-9]. The first experimental results showing pattern-effect-free (PEF) operation of a QD SOA at 10 GHz were presented by Akiyama *et al* in [2]. In [3], QD SOA with an extremely-high penalty-free output power of 20 dBm at 40 Gb/s were presented. Numerical simulation of QD SOAs [4-5] allowed Sugawara *et al* to conclude that the PEF operation can be realized in QD SOA at 160 Gb/s. It was shown in [6] that the pattern-effect-free amplification can occur in SOA in the regime with maximum (constant) linear gain.

The goal of the presented work has been to develop a theory of pattern-effect-free operation of QD SOAs, and in particular, and to identify the conditions, under which pattern effects are suppressed, and to compare QD SOAs with quantum well and bulk SOAs for realization of the pattern-effect-free operation. In Section 2 of the paper, the model for carrier dynamics in QD SOA is presented, and PEF amplification in SOA is considered. High-speed cross-gain-modulation (XGM) without pattern-effects in QD SOAs is described in Section 4. Section 5 describes briefly PEF cross-phase-modulation (XPM). Section 5 is Conclusions.

2. PULSE TRAIN AMPLIFICATION WITHOUT PATTERN EFFECTS

The propagation of a pulse train in an SOA along the z-axis is described with the propagation equation for the photon density $S=S(z, t)$

$$\frac{\partial S(z, t)}{\partial z} + \frac{1}{v_g} \frac{\partial S(z, t)}{\partial t} = (g_{\text{mod}} - \alpha_{\text{abs}}) \cdot S(z, t) \quad (1)$$

* auskov@nmrc.ie or alexusk@sci.lebedev.ru; phone +353 21 4904178; fax +353 21 4904058;
<http://www.nmrc.ie/research/sfi/index.html>

where $v_g = c/\eta_{gr}$ is the group velocity, η_{gr} is the group refractive index, α_{abs} is the absorption coefficient, and g_{mod} is the modal gain for the pulses of the frequency ω . Propagation of pulse trains in QD SOAs depends strongly on carrier dynamics over energy levels in QD structure, which is described by the appropriate rate equations for the QD level populations and the Wetting Layer (WL) carrier density [4-5, 7, 10]. In consideration of carrier dynamics in QD structures, two time scales are of particular importance: namely the pulse duration τ_p , and the characteristic relaxation time τ_{rel} in which the working QD levels ground state return to equilibrium due to carrier capture, escape and relaxation processes in the QD structure. Experimentally, relaxation times τ_{rel} ranging from hundreds of femtoseconds to tens of picoseconds have been observed; see, for instance, [8-9]. In this paper, we consider only the case when the pulse duration, τ_p , is much longer than the characteristic relaxation time τ_{rel} :

$$\tau_p \gg \tau_{rel} \quad (2)$$

In this case, the gain g_{mod} can then be written as a function of the total areal carrier density n in the QD structure (QD layer and Wetting Layer) and of the photon density S [10],

$$g_{mod} = g_{mod}(n, S) \quad (3)$$

At low photon densities S ($\varepsilon S \ll 1$), the gain (3) can be written as [10]

$$g_{mod} = g_{mod}(n, S) = g_{mod}^{lin}(n) \cdot (1 - \varepsilon S) \quad (4)$$

where $g_{mod}^{lin} = g_{lin}(n)$ is the linear modal gain (i.e. the gain at $S \approx 0$). The nonlinear gain coefficient ε describes "spectral hole burning" (SHB) in the QD structure (i.e. the change of the carrier distribution in the inhomogeneously broadened QD ensemble and WL, due to stimulated carrier recombination). The nonlinear gain coefficient can be evaluated approximately as [10]

$$\varepsilon \approx \pi \tau_{rel} \nu_g \sigma_{res} \quad (5)$$

where

$$\sigma_{res} = \frac{2\mu^2 \omega}{c \eta_{bg} \varepsilon_0 \hbar \gamma_{hom}} \quad (6)$$

is the resonant cross-section of the carrier-photon interaction; μ is the dipole moment of the working optical transition in the QD; η_{bg} is the nonresonant background refractive index. Fig. 1 shows the dependence of the linear gain g_{mod}^{lin} in QD SOA (solid line) on the dimensionless total carrier density $x = n/2N_D$ (N_D is the areal density of the QDs in one QD layer). The linear gain fast achieves its maximum value g_{max} , and then at $x > x_c$ it remains *approximately* constant, having reached complete population inversion of the ground electron and hole QD levels. Experimentally, such a behavior of the modal gain has been observed, for instance, in [11-12]. The maximum modal gain due to transitions between the ground electron and hole QD levels can be evaluated as

$$g_{max} = l \frac{2N_D}{t_{wg}} \sqrt{\pi \ln 2} \frac{\gamma_{hom}}{\gamma_{inhom}} \sigma_{res} \quad (7)$$

(see, for instance [13]), where l is the number of QD layers in the SOA, t_{wg} is the effective optical thickness of the SOA waveguide, and γ_{inhom} is the inhomogeneous linewidth of the QD ensemble. The characteristic carrier density $n_c = 2N_D x_c$, at which the gain reaches approximately its maximum, is defined by the QD sizes, the material parameters of the QD structure and the temperature. As shown below, the regime with constant (maximum) gain is the key to achieve PEF operation in QD SOA. For comparison, Fig. 1 shows the dependence of the modal gain on the dimensionless carrier density x also for QW and bulk. For QW and bulk, $x = n_{2D}/\bar{n}_{2D}$ and $x = n_{3D}/\bar{n}_{3D}$, correspondingly, where n_{2D} (n_{3D}) is the two (three) – dimensional carrier density in QW (bulk), and \bar{n}_{2D} (\bar{n}_{3D}) is the two (three) – dimensional density of states for the QW (bulk). One sees that in QW and bulk SOAs the gain also tends to maxima, but the maxima are achieved at much higher pumps.

The dynamics of the total carrier density n is given by the rate equation

$$\frac{dn}{dt} = \frac{n - n_J}{\tau_s} - \nu_g \frac{t_{wg}}{l} g_{mod}^{lin}(n) (1 - \varepsilon S) S \quad (8)$$

where $1/\tau_s$ is the interband carrier relaxation rate; $n_j = J\tau_s/ql$, and J is the pump current density in the SOA. Below we consider pulse train amplification using Eq.(8), which works if the condition (2) is satisfied.

One should stress that PEF operation is not restricted by the condition (2). This operation can take place also under other relations between the pulse duration τ_p and the characteristic relaxation time τ_{rel} . In particular, PEF amplification for $\tau_p \ll \tau_{rel}$ has been analyzed in detail in [14].

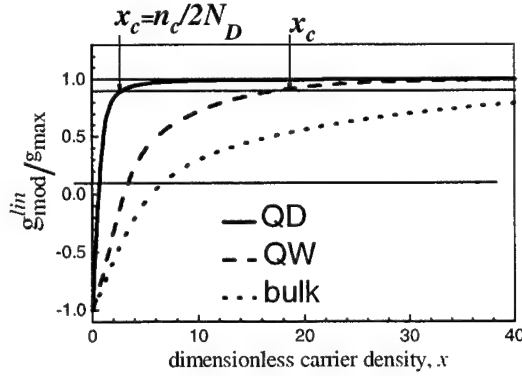


Fig. 1. Dependence of the linear gain g_{lin} on the dimensionless carrier density x for QD (solid), QW (dashed) and bulk (dotted) SOA.

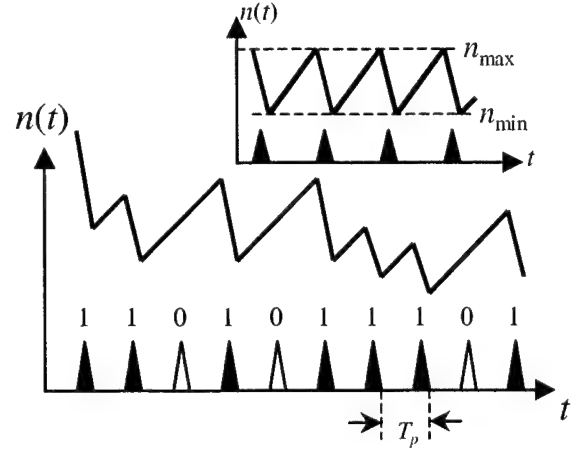


Fig.2. Carrier density dynamics (solid line) in a SOA upon amplification of a data pulse train with a random distribution of pulses. T_p is the bit-period in the train. Black triangles are pulses ("1"); light triangles are empty positions in the data pulse train ("0"). Inset shows the carrier dynamics in the case of a periodic pulse train.

If a pulse train propagates through the SOA, the carrier density decreases during the passage of the pulse, and then recovers between pulses (Fig.2). From Eq.(8), a characteristic recovery time can be defined for the carrier density after each pulse by the carrier lifetime τ_s (~ 1 ns). If the pulse train has a *random* distribution of pulses, and the bit-period T_p in this bit stream (Fig.2) is less than the carrier lifetime τ_s , then such a pulse train will lead to *random* variations of the carrier density, as in Fig. 2. Since the gain in Eq.(4) depends, in general, on the carrier density n , this results in random changes of the gain. Such random gain dynamics can cause pattern effects in the operation of SOA-based devices for optical processing [15]. This situation, where the random carrier dynamics leads to pattern effects, is typical for bulk and QW SOAs [15]. However, if the carrier density n is larger than the characteristic carrier density n_c , $n(t) > n_c$ (see Fig.1), then the linear gain will remain approximately constant, despite the strong carrier dynamics in the SOA. The constancy of the linear gain, $g_{lin} \approx g_{max}$, provides absence of pattern effects during amplification of random pulse train. Indeed, if for instance $\epsilon S \ll 1$, the modal $g_{mod} \approx g_{max} = \text{const}$ [see Eq.(4)], so that arbitrary pulse in the train is amplified linearly (without any saturation of amplification) with the linear SOA gain

$$G_{lin} = G_{lin}(L) = \exp[(g_{max} - \alpha_{abs})L] \quad (9)$$

[see Eq.(1)], where L is the SOA length. This implies the PEF amplification of random pulse trains. But if even the condition $\epsilon S \ll 1$ is not satisfied, PEF amplification also occurs. In the regime with maximal linear gain, we have for the modal gain

$$g_{mod} = g_{max} \cdot (1 - \epsilon \cdot S) \quad (10)$$

From Eq.(10), the modal gain is changed instantaneously with change of the photon density S in the amplified pulse itself. It means that *identical* pulses in random pulse train are amplified equally, and pattern effects are absent in amplification of random pulse train consisting of identical pulses.

The propagation equation (1) can be easily integrated, when the gain is given by Eq.(10). The output photon density are given by

$$S_{out} = S_{out}(z=L, t) = S_{in}(\tau) \cdot G(L, \tau) \quad (11)$$

where the SOA gain $G(L, \tau)$ is given by

$$G(L, \tau) = \frac{(g_{\max} - \alpha_{\text{abs}}) \cdot G_{\text{lin}}}{g_{\max} - \alpha_{\text{abs}} + (G_{\text{lin}} - 1) g_{\max} \varepsilon S_{\text{in}}(\tau)} \quad (12)$$

where $S_{\text{in}}(t) = S(z=0, t)$ is the input photon density, $\tau = t - L/v_g$. One can see from the solution (11)-(12), that the pulses in train, which do not overlap each other, do not affect amplification of each other; this means PEF amplification of random pulse trans. The pulse gain $G_{\text{pulse}} = E_{\text{out}}/E_{\text{in}}$, where E_{out} (E_{in}) is the output (input) pulse energy, depends on pulse shape. For rectangular pulses of the duration τ_p , we have from Eqs.(11)-(12)

$$G_{\text{pulse}} = \frac{G_{\text{lin}}}{1 + E_{\text{in}}/E_{\text{in}}^{\text{sat}}} \quad (13)$$

where

$$E_{\text{in}}^{\text{sat}} = \frac{\hbar \omega v_g A_{\text{wg}} \tau_p (g_{\max} - \alpha_{\text{abs}})}{\varepsilon \cdot (G_{\max} - 1) g_{\max}}$$

is the input saturation pulse energy due to the SHB gain nonlinearity, A_{wg} is the optical cross-section of the SOA waveguide. Eq.(13) shows that the gain G_{pulse} is saturated with increasing input pulse energy E_{in} due to the SHB effects. One should stress again that PEF amplification takes place in the maximum linear gain regime despite of the gain saturation due to SHB.

The condition when the linear modal gain $g_{\text{mod}}^{\text{lin}} = g_{\text{mod}}^{\text{lin}}(n)$ can be taken as constant can be obtained as follows. For a given bit-period T_p (see Fig. 2), and the output pulse energy E_{out} in the data stream, the minimal carrier densities occur at SOA output for the most dense data stream (...11111...), i.e. for a periodic pulse train. In this case, the carrier density has a periodic dynamic variation, changing between n_{\min} and n_{\max} ; as illustrated by the inset in Fig.2. We assume that the pulse duration τ_p in this train is much shorter than the bit-period T_p between pulses and also than the carrier lifetime τ_s ($\tau_p \ll T_p, \tau_s$). Each pulse can then be approximated by a δ -function [15]. In this case, assuming $n \geq n_c$ (i.e. the linear gain is equal to its maximum, $g_{\text{mod}}^{\text{lin}} \approx g_{\max}$), one can obtain from Eq.(7) values for n_{\max} and n_{\min} . Integrating (8) over pulses and between them, we find

$$n_{\max} - n_{\min} = \frac{t_{\text{wg}} g_{\max}}{l \hbar \omega A_{\text{wg}}} E_{\text{out}} (1 - E_{\text{out}}/E_{\text{SHB}}) \quad (14)$$

$$n_{\max} = n_j + (n_{\min} - n_j) \cdot \exp(-T_p/\tau_s) \quad (15)$$

where $E_{\text{out}} = \hbar \omega v_g A_{\text{wg}} \int_{\text{pulse}} dt S(L, t)$ is the output pulse energy, $E_{\text{SHB}} = \tau_p \hbar \omega v_g A_{\text{wg}} / (\xi \varepsilon)$ is the saturation parameter due to SHB, and ξ is a numerical coefficient, which depends on the pulse shape; $\xi \sim 1$. In the derivation of Eq.(14), we used the relation: $\int dt [S(L, t)]^2 = \xi \cdot \left[\int dt S(L, t) \right]^2 / \tau_p$. Finding n_{\min} from (14)-(15), and requiring that $n_{\min} \geq n_c$, we obtain the condition for the linear gain to be constant as:

$$n_j \geq n_c + \frac{t_{\text{wg}} g_{\max}}{l \cdot \hbar \omega A_{\text{wg}}} \frac{E_{\text{out}} (1 - E_{\text{out}}/E_{\text{SHB}})}{[1 - \exp(-T_p/\tau_s)]} \quad (16)$$

If $T_p \ll \tau_s$ (for high-speed modulation), the condition in Eq.(16) can be rewritten as

$$P_{\text{out}}^{\text{avr}} \leq (n_j - n_c) \cdot l \hbar \omega A_{\text{wg}} / t_{\text{wg}} g_{\max} \tau_s \quad (17)$$

where $P_{\text{out}}^{\text{avr}} = E_{\text{out}}/T_p$ is the average power at SOA output. We note that Eq.(17) is obtained from (16) by ejecting the terms involving E_{SHB} , so that Eq.(17) is therefore an even stronger condition than Eq.(16). Both Eqs. (16) and (17) show that increasing the SOA pump carrier density n_j will increase the range of bit-rates, pulse energies and powers for which the linear gain can be kept at its maximum. For $P_{\text{avr}}=40\text{mW}$, $g_{\max} = 3 \cdot 10^3 \text{m}^{-1}$, $l=5$, we require from Eq.(17) that

$(n_j - n_c) \geq 4 \cdot 10^{16} \text{ m}^{-2}$. Assuming that $n_j \gg n_c$, we estimate the corresponding pump current density as $J \geq 6 \text{ kA/cm}^2$, which is quite reasonable for a QD SOA [2-5, 8-9, 11-12].

From Eq.(17), one can conclude on superiority of QD SOAs for realization PEF amplification in comparison with QW and bulk SOAs. At first, the maximum gain regime (complete population of working levels) in QDs is achieved at lower pumps than in QWs and bulk (the dimensionless carrier density x_c is smaller for QDs than for QW and bulk, see Fig. 1). At second, the maximum gain g_{\max} is lower in QD SOA than in QW and bulk, in particular, because the carrier-photon interaction cross-section σ_{res} in QDs is lower than in QWs and bulk due to imperfect overlap of the electron and hole wavefunctions in QDs [13]. As result, PEF amplification can be realized in QD SOAs at higher bit-rates and average powers in pulse train, and at lower pump current densities than in QW and bulk SOAs.

As noted above, the modal gain can be written as a function of the total carrier density n and the photon density [see, Eq.(3)-(4)], if the pulse duration τ_p is much longer than the population relaxation time τ_{rel} : $\tau_p \gg \tau_{rel}$. In above analysis, we also assume that the bit-period T_p in the amplified pulse train is much longer than the pulse duration τ_p , $T_p \gg \tau_p$. That is, the relation $T_p \gg \tau_p$ must be satisfied for validity of above results. Thus, if for instance the time τ_{rel} is of the order of 0.1-1ps, and if the SOA is pumped sufficiently strongly so that Eq.(17) is satisfied, then the pattern-effect-free amplification of pulse trains of given power P_{out}^{avr} can take place up to frequencies of 0.1–1 THz.

3. PATTERN-EFFECT-FREE CROSS-GAIN MODULATION

The cross-gain modulation is described using the propagation equations for the photon density $S_0 = S_0(z, t)$ of a *controlling* (modulating, pump) signal at the frequency ω_0 , and the photon density $S_1 = S_1(z, t)$ of a *controlled* (modulated, probe) signal at the frequency ω_1 , propagating along the z-axis in the SOA:

$$\frac{\partial S_i(z, t)}{\partial z} + \frac{1}{v_g} \frac{\partial S_i(z, t)}{\partial t} = (g_{modi} - \alpha_{abs}) S_i(z, t) \quad (18)$$

($i=0,1$) g_{modi} is the modal gain for signal i . Eqs.(18) are solved with the boundary conditions:

$$\begin{aligned} S_0(z=0, t) &= S_{0,in}(t) \\ S_1(z=0, t) &= S_{1,in}(t) \end{aligned} \quad (19)$$

The functions $S_{0,in}(t)$ and $S_{1,in}(t)$ in (19) depend on the XGM-based functionality, given by (18)-(19). For demultiplexing, the input controlling signal $S_{0,in}(t)$ is a periodic clock, $S_{0,in}(t + T_p) = S_{0,in}(t)$, where T_p is the bit-period; and the input controlled signal $S_{1,in}(t)$ is a data pulse train. For frequency conversion, the input controlling (modulating) signal $S_{0,in}(t)$ is a data pulse train, and the input controlled (modulated) signal $S_{1,in}$ is continuous wave (cw), $S_{1,in} = \text{const}$. Note that in the description of XGM with the model (18)-(19), we neglect four-wave mixing between signals in the SOA. That is valid, in particular, if the controlling and controlled signals have orthogonal polarizations [16]. For parallel polarizations of the signals, the inclusion of four-wave mixing effects should not modify our main conclusion concerning XGM without pattern effect in QD SOAs. We assume the difference between the signal frequencies ω_0 and ω_1 is much less than the homogeneous linewidth $\gamma_{\text{hom}} = 2/T_2$ (T_2 is the dephasing time), $|\omega_0 - \omega_1| \ll \gamma_{\text{hom}}$. In this case, one can consider that the modal gains coincide to each other, $g_{mod0} \approx g_{mod1} \equiv g_{\text{mod}}$, since photons of the two signals interact with the same QDs in the inhomogeneously broadened QD ensemble. We consider that the pulse durations, τ_p , in the signals is much longer than the characteristic relaxation time τ_{rel} , so that Eqs. (3)-(4) for the modal gain are applicable where $S = S_0 + S_1$ is the total photon density.

In the regime with maximum gain [see Eq.(10)], modulation of the gain is possible only if the nonlinear gain coefficient \mathcal{E} is nonzero, and that the gain is altered instantaneously as the photon density S is varied. As a result, pattern-effect-free XGM may be achieved in a QD SOA. Eqs.(18) can be easily integrated with the boundary conditions of Eq.(19), when the gain is given by Eq.(10). The output photon densities are given by

$$S_{i,out} = S_{i,out}(L,t) = S_{i,in}(\tau) \cdot G_{XGM}(L,\tau) \quad (20)$$

The SOA gain $G_{XGM}(L,\tau)$ is given in this case by

$$G_{XGM}(L,t) = \frac{(g_{max} - \alpha_{abs}) \cdot G_{lin}}{g_{max} - \alpha_{abs} + (G_{lin} - 1) g_{max} \varepsilon [S_{0,in}(\tau) + S_{i,in}(\tau)]} \quad (21)$$

In Fig. 3 and 4 below, which illustrate the solution of (20)-(21), we use the following device and material parameters: the optical cross-section of the SOA waveguide is taken as $A_{wg} = 0.2 \mu m \times 2 \mu m$; the photon energy $\hbar\omega = 1 \text{ eV}$; the maximal modal gain $g_{max} = 3 \cdot 10^3 \text{ m}^{-1}$; the absorption coefficient $\alpha_{abs} = 500 \text{ m}^{-1}$; and the nonlinear gain coefficient $\varepsilon = 4.3 \cdot 10^{-23} \text{ m}^3$. This value of ε was calculated from Eq.(5) with $\tau_{rel} = 1 \text{ ps}$ and $\sigma_{res} = 1.6 \cdot 10^{-19} \text{ m}^2$, and is in accordance with experimental data [9].

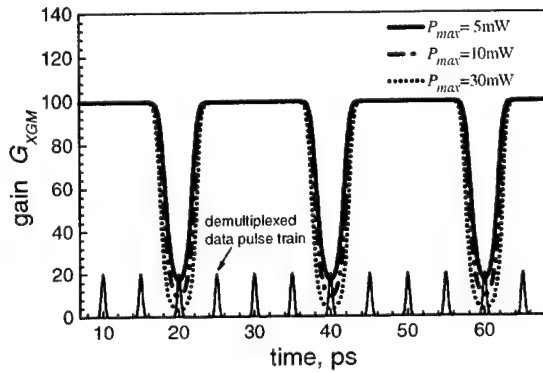


Fig.3. Gain modulation by a controlling pulse train with a bit-rate of 50 GHz and with different maximum input power values of $P_{max} = 5, 10, 30 \text{ mW}$. The controlled data pulse train with a bit-rate of 200 GHz is shown by the thin solid line.

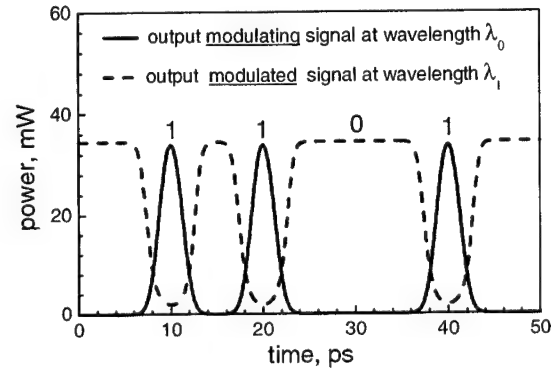


Fig. 4. Frequency conversion: modulation of a signal at wavelength λ_1 (dash) by a data pulse train (1101) at wavelength λ_0 (solid).

Fig. 3 shows the modulation of the SOA gain G_{XGM} with a periodic pulse train used as the controlling signal. We assume the SOA to have length $L = 1.84 \text{ mm}$ and a linear gain of 20 dB. In this calculation, we neglect any saturation of the SOA by the controlled signal, $S_{i,in} \rightarrow 0$ in Eq.(21). The bit-rate in this controlling pulse train is 50 GHz ($T_p = 20 \text{ ps}$), the pulse duration is $\sim 3 \text{ ps}$, the maximum power in the input pulses is assumed as $P_{max} = 5$ (solid), 10 (dash-dot), 30 mW (dot). One can see strong saturation of the SOA gain due to the modulating pulses: during the passage of the pulses the SOA gain is decreased by a factor of 5-20 times compared with the linear (unsaturated) value. The depth of the gain modulation is enhanced by increasing the power of the controlling (modulating) pulses. This gain modulation can be used to demultiplex data pulse trains. As example, in Fig.3, if the bit-rate in the data pulse train is 200 GHz, then pulses in the data stream which do not coincide in time with the controlling pulses (see Fig.3), get high amplification. By contrast, data pulses which overlap the controlling signal will experience a much lower gain.

Fig.4 demonstrates the modulation of a signal at wavelength λ_1 by a data pulse train at wavelength λ_0 . The SOA length is taken as $L = 2.5 \text{ mm}$, and the linear gain as 25 dB. The λ_1 -signal at input is cw with power 0.1 mW; the maximum power of the modulating data pulses at input is 5 mW. It is seen that almost complete modulation occurs with "dips" in the λ_1 -signal, corresponding to pulses in the λ_0 -signal.

The condition, when the linear gain is constant, is given again by Eq.(17); and in this XGM case, the average power P_{out}^{avr} is the average power at SOA output including both the averaging powers of modulating and modulated signals at SOA output.

Note that similarly to PEF amplification, this purely nonlinear-gain-based, pattern-effect-free XGM can take place also up to frequencies of 0.1–1 THz in modulating (saturating) pulse trains.

4. NONLINEAR REFRACTIVE INDEX AND CROSS-PHASE MODULATION

In this section, we consider the propagation of two pulse trains through a QD SOA: the pump (modulating) train of strong pulses with the photon density $S_0(z, t)$ and the frequency ω_0 , and the probe (modulated) pulse train $S_1(z, t)$ with the frequency ω_1 . The interaction of the pump pulses with QD carriers leads to changes in distribution of carriers over levels in QD structure (spectral hole burning), and the modal gain $g_{\text{mod}1}$ for the probe pulses becomes to be dependent on the photon density S_0 of the pump pulse train:

$$g_{\text{mod}1} = g_{\text{mod}1}(n, S_0) = g_{\text{mod}1}^{\text{lin}}(n) \cdot (1 - \varepsilon_1 S_0) \quad (22)$$

Similarly, the modal refractive index at the frequency ω_1 of the probe pulses can be written as

$$\eta_1 = \eta_{\text{lin}1} + \eta_{\text{nl}1} \cdot I_0 \quad (23)$$

where $I_0 = v_g \hbar \omega_0 S_0$ is the light intensity in the pump pulses. The “linear” refractive index $\eta_{\text{lin}1}$ depends on the total carrier density n in QD structure and the frequency ω_1 : $\eta_{\text{lin}1} = \eta_{\text{lin}1}(n, \omega_1)$. The “nonlinear” $\eta_{\text{nl}1}$ refractive index depends not only on n and ω_1 , but also on the frequency detuning $\Delta = \omega_1 - \omega_0$ between the pump and probe pulses: $\eta_{\text{nl}1} = \eta_{\text{nl}1}(n, \omega_1, \Delta)$. Fig.5 shows an example of the calculated dependences of the linear index $\eta_{\text{lin}1}$ (dashed line) and nonlinear index $\eta_{\text{nl}1}$ (solid line) indices on the carrier density n . Dotted line in the figure illustrates behavior of the linear gain $g_{\text{mod}1}^{\text{lin}} = g_{\text{mod}1}^{\text{lin}}(n)$. One can see that similarly to the linear gain, the indices fast achieve their maximum or minimum values, and then at $n > n_c$ they remain approximately constant, having reached complete population inversion of the electron and hole QD levels. Thus, in the regime with maximum gain, which we have considered above, the refractive index (23) are changed instantaneously with changing pump pulses. This implies an opportunity of pattern-effect-free phase modulation of probe pulses by pump pulses.

One can show that in the maximum gain regime, the nonlinear refractive $\eta_{\text{nl}1}$ can be estimated with the expression

$$\eta_{\text{nl}1} = -\frac{\lambda g_{\text{max}} \cdot \varepsilon}{4\pi^2 v_g \hbar \omega} \cdot \frac{(\omega_1 - \omega_0) \gamma_{\text{hom}}}{\gamma_{\text{hom}}^2 + (\omega_1 - \omega_0)^2} \quad (24)$$

where $\lambda = 2\pi c / \omega_1 = 2\pi c / \omega_0$ is the pulse wavelength; $\omega = \omega_1 \approx \omega_0$; and the nonlinear gain coefficient ε is given by Eq.(5). One sees from Eq.(24) that $\eta_{\text{nl}1} = 0$, if $\omega_1 = \omega_0$. Thus, for the ultrafast phase modulation, the probe and pump pulses must be detuned from each other ($\omega_1 \neq \omega_0$), and the optimal detuning is $|\omega_1 - \omega_0| \sim \gamma_{\text{hom}}$. It is worth to note that in QD SOAs the homogeneous broadening $\hbar \gamma_{\text{hom}} \sim 10 - 20 \text{ meV}$ [17], so the XPM bandwidth (see below) $|\lambda_1 - \lambda_0|$ can be of order of 50-100 nm. Estimation of the nonlinear refractive index at $|\omega_1 - \omega_0| \sim \gamma_{\text{hom}}$ from Eq.(24) gives $\eta_{\text{nl}1} \approx 3 \cdot 10^{-16} \text{ m}^2/\text{W}$ which is 4 orders larger than the nonlinear refractive index in silica [15].

The nonlinear refractive index $\eta_{\text{nl}1}$ can be used for XPM of the probe pulse and for XPM based optical switching. The nonlinear phase shift $\Delta\Phi_{\text{nl}}$ of the probe pulse due the change in the refractive index excited by the pump pulse S_0 is given by

$$\Delta\Phi_{\text{nl}1} = \frac{2\pi}{\lambda} \cdot (\eta_{\text{nl}1} I_0) \cdot L = \frac{2\pi}{\lambda} \cdot \left(\eta_{\text{nl}1} \frac{P_0}{A_{\text{wg}}} \right) \cdot L \quad (25)$$

(see, for instance [15]). Assuming the wavelength $\lambda = 1.3 \mu\text{m}$, the nonlinear refractive index $\eta_{\text{nl}1} = 3 \cdot 10^{-16} \text{ m}^2/\text{W}$, the power $P_0 = 50 \text{ mW}$ in the switching pump pulse, the optical cross-section of the SOA waveguide $A_{\text{wg}} = 0.2 \mu\text{m} \times 2 \mu\text{m}$, we obtain from (25) the phase shift $\Delta\Phi_{\text{nl}1} \sim \pi$ for the SOA length $L = 10 - 20 \text{ mm}$. Thus, using the nonlinearity in the refractive index caused by SHB effects, one can realize effective XPM in QD SOA, and correspondingly, ultrafast optical switching in QD SOA based nonlinear interferometers. Since this XPM and optical switching are accomplished in the regime with maximum gain, these XPM and optical switching are free of pattern effect.

The condition for realization of the maximum gain regime and the pattern-effect-free XGM is given by Eq.(17), where in this case P_{out}^{avr} is the average power of the pump (modulating) pulse train at SOA output.

Note that similarly to PEF amplification and XGM, this purely nonlinear-refractive-index-based, pattern-effect-free XPM can take place up also to frequencies of 0.1–1 THz.

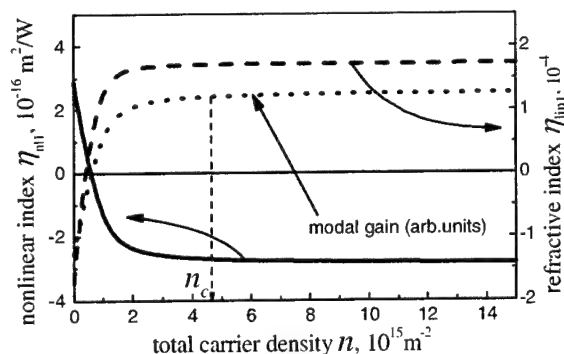


Fig. 5. The linear η_{lin} (solid) and η_{nl} (dashed) nonlinear refractive indices as functions of the total carrier density n . For comparison, dotted curve shows behavior of the modal gain with increasing n .

5. CONCLUSION

It has been shown that in the regime with maximum gain, which achieved in QD SOAs at much lower pumps than in bulk and QW SOAs, one can obtain amplification of pulse trains without pattern effects. In this regime, pattern-effect-free XGM and XPM through gain and refractive index nonlinearities due to spectral hole burning effects can be realized. This pattern-effect-free operation can take place in QD SOAs up to frequencies of 0.1–1 THz. Operating in the regime with maximum gain in QD SOAs offers the opportunity to develop new generation of high-speed devices for ultrafast optical processing and communications.

ACKNOWLEDGMENTS

The work was supported, in particular, by Science Foundation Ireland, RFBR (No. 01-02-17330), INTAS (No. 2001-0571) and the Russian Federal Program "Integration" (No. A0155).

REFERENCES

1. D. Bimberg, M. Grundmann, N.N. Ledentsov, *Quantum Dot Heterostructures*, Wiley & Sons, 1999.
2. T. Akiyama, N. Hatori, Y. Nakata, H. Ebe, M. Sugawara, *Electron. Lett.*, **8**, 1139 (2002).
3. T. Akiyama, K. Kawaguchi, M. Sugawara, H. Sudo, M. Ekawa, H. Ebe, A. Kuramata, K. Otsubo, K. Morito, and Y. Arakawa, *ECOC'2003*, post-deadline paper Th.4.4.3, 21-25 Sept. 2003, Rimini, Italy.
4. M. Sugawara, N. Hatori, T. Akiyama, Y. Nakata, H. Ishikawa, *Jpn. J. Appl. Phys.*, **40** (Part 2), L488 (2001).
5. M. Sugawara, T. Akiyama, N. Hatori, Y. Nakata, H. Ebe, and H. Ishikawa, *Meas. Sci. Technol.*, **13**, 1683 (2002).
6. A. V. Uskov, T. W. Berg, and J. Mørk, *CLEO/Europe-EQEC'2003*, EA5-4, 22-27 June, 2003, Munich, Germany.
7. T. W. Berg, S. Bischoff, I. Magnusdottir, and J. Mørk, *IEEE Photon. Technol. Lett.*, **13**, 541 (2001).
8. P. Borri, W. Langbein, J. M. Hvam, F. Heinrichsdorf, M.-H. Mao, D. Bimberg, *IEEE Photon. Technol. Lett.*, **12**, 594 (2000).
9. T. Akiyama, H. Kuwatsuka, T. Simoyama, Y. Nakata, K. Mukai, M. Sugawara, O. Wada, and H. Ishikawa, *IEEE J. Quantum Electron.*, **37**, 1057 (2001).
10. A. V. Uskov, Y. Boucher, J. Le Bihan, and J. McInerney, *Appl. Phys. Lett.*, **73**, 1499 (1998).
11. P. G. Eliseev, H. Li, G. T. Liu, T. C. Stintz, T. C. Newell, L. F. Lester, and K. J. Malloy, *Quantum Electron.*, **30**, 664 (2000).

12. P. Borri, W. Langbein, S. Schneider, U. Woggon, R. L. Sellin, D. Ouyang, D. Bimberg, *IEEE J. Select. Topics Quantum Electron*, **8**, 984 (2002).
13. L. A. Asryan, M. Grundmann, N. N. Ledentsov, O. Stier, R. A. Suris, and D. Bimberg, *J. Appl. Phys.*, **90**, 1666 (2001).
14. A. V. Uskov, T. W. Berg, and J. Mørk, *IEEE J. Quantum Electron.*, in press.
15. R. J. Manning, A. D. Ellis, A. J. Poustie, K. L. Blow, *J. Opt. Soc. Am. B* **14** (1997) 3204-3216.
16. A. Uskov, J. Mørk, J. Mark, *IEEE J. Quantum Electron.*, **30**, 1769 (1994).
17. P. Borri, W. Langbein, J. Mørk, J. M. Hvam, F. Heinrichsdorff, M.-H. Mao, and D. Bimberg, *Phys. Rev. B* **60**, 7784 (1999).

Theory for Intersubband Absorption in Quantum Dots

Erik H. Hoffman and Shun-Lien Chuang

Department of Electrical and Computer Engineering, University of Illinois
at Urbana-Champaign, 1406 W. Green Street, Urbana, IL 61801

ABSTRACT

Quantum-dot infrared photodetectors (QDIPs) have been researched intensively because normal incidence absorption of the quantum dot layer is possible, unlike quantum-well infrared photodetectors (QWIPs) which require a grating coupled structure or an off-normal incidence configuration to satisfy the polarization selection rules. In this paper, we present a theoretical model for the band structure of a strained quantum dot, modeled as a quantum disk, and the intersubband absorption. We first present analytical expressions for the polarization-dependent optical dipole moments and then calculate the absorption spectra for various carrier densities and temperatures. The effects of carrier density, temperature, and inhomogeneous broadening will be discussed.

Keywords: Quantum dots, intersubband absorption, infrared, photodetectors.

1. INTRODUCTION

Quantum-dot infrared photodetectors (QDIPs) have been widely investigated due to the potential advantages of normal incidence detection and higher operating temperature.¹ The detection mechanism in QDIPs is based on intersubband transitions in the conduction band, where absorption of normally incident light is a direct consequence of the three dimensional quantum confinement of carriers in a quantum dot (QD). Normal incidence absorption does not take place in quantum-well infrared photodetectors (QWIPs) because of polarization selection rules.²

We discuss a simple method of calculating the electronic band structure of a QD, modeled as a quantum disk. Our treatment is based on the effective index (EI) method used in dielectric waveguide theory.³⁻⁵ Lamouche and Lépine used an approach similar to EI to calculate the ground state energy in a quantum disk.⁴ This method leads to a good approximation of the electronic levels and wave functions when the confinement is large. We then present analytical expressions for the polarization-dependent optical dipole moments, which allow us to determine the absorption spectra for various carrier densities and temperatures.

2. THE MODEL

Our treatment models the QD as a small disk of radius a and height h surrounded by finite transverse and longitudinal barriers (Fig. 1). The origin of this system lies in the center of the disk and the z axis is chosen along the rotation axis. The potential inside the QD is $V_d = 0$ and the potential in the barrier is V_b . The effective mass inside the dot (m_d^*) and in the barrier (m_b^*) is assumed to be isotropic. In cylindrical coordinates (ρ, ϕ, z) , the Hamiltonian may be written

$$\hat{H} = \begin{cases} -\frac{\hbar^2}{2m_d^*} \left[\frac{1}{\rho} \frac{\partial}{\partial \rho} \left(\frac{1}{\rho} \frac{\partial}{\partial \rho} \right) + \frac{1}{\rho^2} \frac{\partial^2}{\partial \phi^2} + \frac{\partial^2}{\partial z^2} \right], & \text{inside the QD} \\ -\frac{\hbar^2}{2m_b^*} \left[\frac{1}{\rho} \frac{\partial}{\partial \rho} \left(\frac{1}{\rho} \frac{\partial}{\partial \rho} \right) + \frac{1}{\rho^2} \frac{\partial^2}{\partial \phi^2} + \frac{\partial^2}{\partial z^2} \right] + V_b, & \text{outside the QD} \end{cases} \quad (1)$$

The wave function can be obtained by solving the Schrödinger equation under the effective mass approximation. Solutions take the form

$$\Psi(\mathbf{r}) = R_{mn}(\rho) \frac{e^{im\phi}}{\sqrt{2\pi}} \varphi_\ell(z). \quad (2)$$

Further author information: (Send correspondence to Shun-Lien Chuang. E-mail: s-chuang@uiuc.edu)

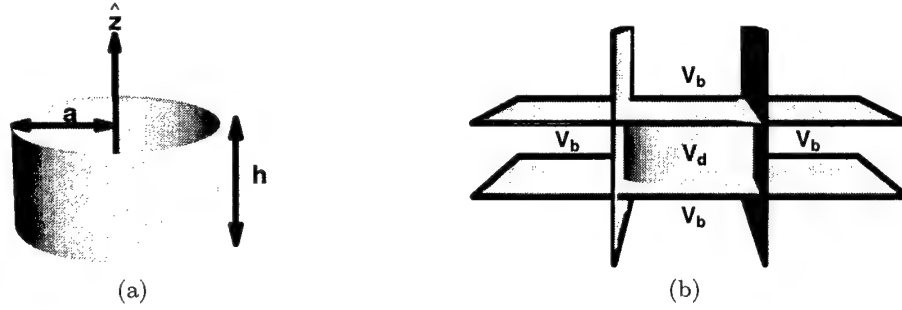


Figure 1. Schematic representation of the quantum disk with radius a and height h (a) surrounded by finite transverse and longitudinal barriers (b).

where

$$R_{mn}(\rho) = C_{mn} \begin{cases} J_m(p\rho) & \rho \leq a \\ \frac{J_m(pa)}{K_m(qa)} K_m(q\rho) & \rho \geq a \end{cases} \quad (3)$$

and $\varphi_\ell(z)$ is the well-known solution for the finite square well. Each state is characterized by three integral quantum numbers (n, m, ℓ) such that n and m correspond to the ρ - ϕ (transverse) dependence and ℓ corresponds to the z (longitudinal) dependence. Observe that $\Psi(r)$ has a Bessel function transverse dependence (similar to the LP_{mn} mode of a step-index optical fiber), where $J_m(p\rho)$ and $K_m(q\rho)$ are the Bessel function of the first kind and the modified Bessel function of the second kind, respectively, and a sinusoidal longitudinal dependence.

The optical dipole moment for bound-to-bound transitions in the conduction band is

$$\begin{aligned} \mu_{fi} &= \langle \Psi_f | e\mathbf{r} | \Psi_i \rangle \\ &= \begin{cases} -e\hat{z} \int_{-\infty}^{\infty} z \varphi_{\ell_f}^* \varphi_{\ell_i} dz, & m_f = m_i, n_f = n_i, \text{ and } \ell_f - \ell_i = \text{odd} \\ -e\frac{1}{2}\hat{x} \int_0^\infty \rho^2 R_{m_f n_f}^* R_{m_i n_i} d\rho \pm e\frac{i}{2}\hat{y} \int_0^\infty \rho^2 R_{m_f n_f}^* R_{m_i n_i} d\rho, & m_f - m_i = \pm 1 \text{ and } \ell_f = \ell_i \\ 0, & \text{otherwise} \end{cases} \end{aligned} \quad (4)$$

which can be evaluated analytically. The integral for the longitudinal dipole moment is given by

$$\begin{aligned} \int_{-\infty}^{\infty} z \varphi_{\ell_f}^* \varphi_{\ell_i} dz &= C_{\ell_f} C_{\ell_i} \left[CS(k_f h/2) CS(k_i h/2) \frac{2 + h(\alpha_f + \alpha_i)}{(\alpha_f + \alpha_i)^2} + (-1)^{\ell_f} \frac{h \cos[(k_f - k_i)h/2]}{2(k_f - k_i)} \right. \\ &\quad \left. - \frac{h \cos[(k_f + k_i)h/2]}{2(k_f + k_i)} - (-1)^{\ell_f} \frac{\sin[(k_f - k_i)h/2]}{(k_f - k_i)^2} + \frac{\sin[(k_f + k_i)h/2]}{(k_f + k_i)^2} \right] \end{aligned} \quad (5)$$

where k is the wave number inside the QD, α is the decaying constant in the barrier, and $CS(x)$ is defined as $\cos x$ or $\sin x$ when ℓ is odd or even, respectively. The integral for the transverse dipole moment is given by

$$\int_0^\infty \rho^2 R_{m_f n_f}^* R_{m_i n_i} d\rho = C_{m_f n_f} C_{m_i n_i} \left[F(p_f, p_i, m_f) + \frac{J_{m_f}(p_f a)}{K_{m_f}(q_f a)} \frac{J_{m_i}(p_i a)}{K_{m_i}(q_i a)} G(q_f, q_i, m_f) \right] \quad (6)$$

where we have made use of the following identities:

$$F(u, v, m) = \mp \frac{dP(u, x, m)}{dx} \Big|_{x=v} + \frac{m}{v} P(u, v, m) \quad (7)$$

$$G(u, v, m) = -\frac{dQ(u, x, m)}{dx} \Big|_{x=v} \pm \frac{m}{v} Q(u, v, m) \quad (8)$$

$$P(u, v, m) = \int_0^a J_m(u\rho) J_m(v\rho) \rho d\rho = \frac{a[uJ_{m-1}(ua)J_m(va) - vJ_{m-1}(va)J_m(ua)]}{v^2 - u^2} \quad (9)$$

$$Q(u, v, m) = \int_a^\infty K_m(u\rho) K_m(v\rho) \rho d\rho = \frac{a[vK_{m-1}(va)K_m(ua) - uK_{m-1}(ua)K_m(va)]}{v^2 - u^2} \quad (10)$$

The polarization-dependent absorption coefficient for intersubband transitions can be written as⁵

$$\alpha(\hbar\omega) = \left(\frac{\omega}{n_r c \epsilon_o} \right) \frac{2}{V} \sum_{a,b} \frac{|\hat{e} \cdot \mu_{ba}|^2 (\Gamma/2)}{(E_b - E_a - \hbar\omega)^2 + (\Gamma/2)^2} (f_a - f_b), \quad (11)$$

where n_r is the average refractive index, V is the QD volume (prefactor of two accounts for spin degeneracy), \hat{e} is the unit vector indicating the polarization of incident radiation, Γ is the full width at half maximum (FWHM), and f is the Fermi-Dirac distribution function. For simplicity, we assume a Lorentzian line shape for both homogeneous and inhomogeneous broadening.

3. RESULTS AND DISCUSSION

We now apply our model to a planar array of InAs QDs grown on a GaAs substrate, assuming the parameters of Ref. 6 ($m_d^* = 0.023m_o$, $m_b^* = 0.067m_o$, $V_b = 513.41$ meV) and an areal density of $3 \times 10^{10} \text{ cm}^{-2}$. Arrays of QDs are typically grown under the Stranski-Krastanov growth mode, which leads to a large variation in dot sizes. Inhomogeneous broadening caused by the random size distribution is considerably larger than homogeneous broadening.⁷

Consider a QD of radius 10 nm and height 4 nm with four bound states in the conduction band (Fig. 2). There are four distinct energy levels with three allowed transitions: $(1,0,1) \rightarrow (1,\pm 1,1)$, $(1,\pm 1,1) \rightarrow (1,\pm 2,1)$, and $(1,\pm 1,1) \rightarrow (2,0,1)$; which have optical dipole moments $29.8\text{e}\text{\AA}(i\hat{y} - \hat{x})$, $36.4\text{e}\text{\AA}(i\hat{y} - \hat{x})$, and $-21.0\text{e}\text{\AA}(\hat{x} + i\hat{y})$, respectively. All the dipole moments are transverse because the QD is relatively flat and has only one longitudinal bound state ($\ell = 1$). Transitions are either allowed or suppressed depending on the temperature and the carrier density, since temperature decides the sharpness of the Fermi-Dirac distribution function and carrier density dictates the average number of electrons per dot. Fig. 3 shows the effects of these variables on the normal incidence absorption coefficient in the absence of inhomogeneous broadening. The homogeneous linewidth is taken to be 0.5 meV at 77 K and 5 meV at 300 K. The two-dimensional carrier densities required to obtain 1, 2, 3, and 4 electrons per dot are $3 \times 10^{10} \text{ cm}^{-2}$, $6 \times 10^{10} \text{ cm}^{-2}$, $9 \times 10^{10} \text{ cm}^{-2}$, and $1.2 \times 10^{11} \text{ cm}^{-2}$, respectively. Among these values, it is clear that absorption is highest when there are 4 electrons per dot. Then, $(1,0,1) \rightarrow (1,\pm 1,1)$ is suppressed while $(1,\pm 1,1) \rightarrow (1,\pm 2,1)$ and $(1,\pm 1,1) \rightarrow (2,0,1)$ are allowed. The peak absorption coefficients at 77 and 300 K are 5.2×10^5 and $4.3 \times 10^4 \text{ cm}^{-1}$, respectively.

In a large ensemble of QDs grown under the Stranski-Krastanov growth mode, inhomogeneous broadening is dominant. The absorption spectra shown in Fig. 4 account for homogeneous and inhomogeneous broadening, where the inhomogeneous linewidth is temperature independent and assumed to be 30 meV. These spectra are much broader than those in Fig. 3 and the linewidth does not change much with temperature. This effect also results in a significant reduction in peak absorption coefficient, which falls to 8700 and 6400 cm^{-1} at 77 and 300 K, respectively.

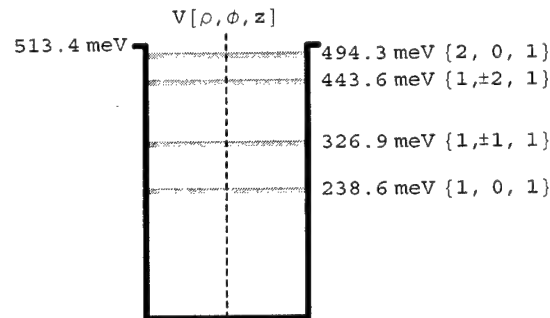


Figure 2. Electronic levels in the conduction band of an InAs QD with radius 10 nm and height 4 nm, grown on a GaAs substrate.

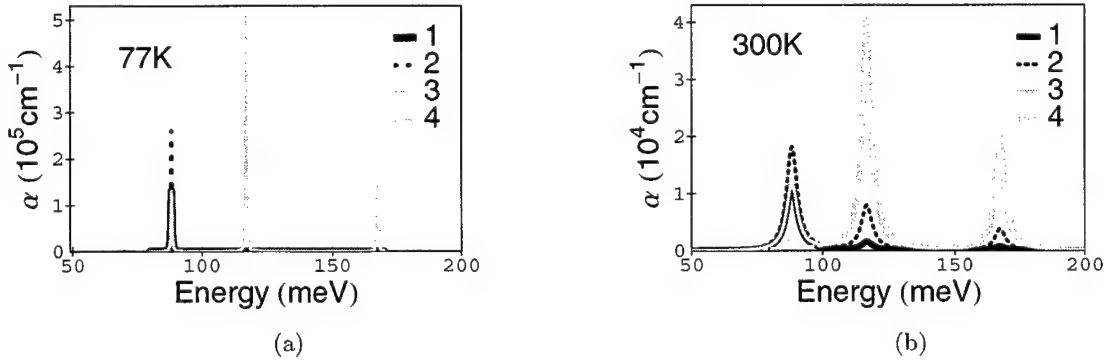


Figure 3. Homogeneously broadened absorption coefficient at (a) 77 K and (b) 300 K for a planar array of InAs QDs grown on a GaAs substrate with 1, 2, 3, and 4 electrons per dot. The dots have radius 10 nm and height 4 nm and an areal density of $3 \times 10^{10} \text{ cm}^{-2}$.

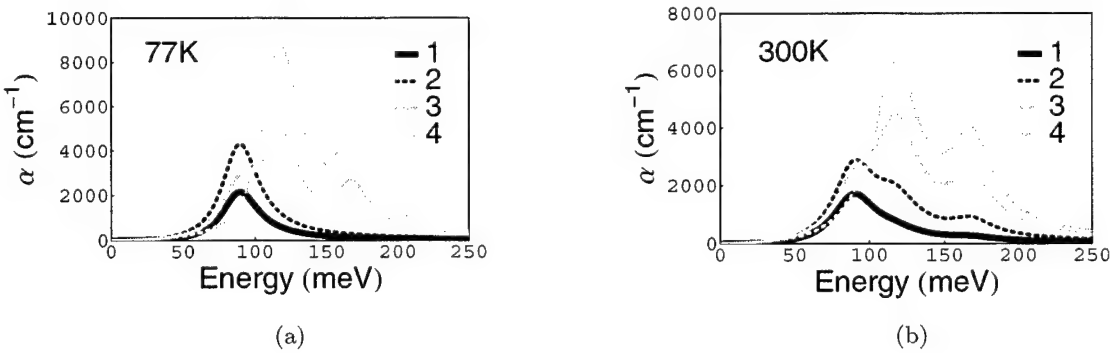


Figure 4. Inhomogeneously broadened absorption coefficient at (a) 77 K and (b) 300 K for a planar array of InAs QDs grown on a GaAs substrate with 1, 2, 3, and 4 electrons per dot. The dots have radius 10 nm and height 4 nm and an areal density of $3 \times 10^{10} \text{ cm}^{-2}$.

4. CONCLUSION

We have presented a theoretical model for the band structure of a QD that allows us to obtain analytical expressions for the polarization-dependent optical dipole moment. We calculated absorption spectra for several carrier densities at 77 and 300 K, and discussed the effects of these variables on the shape and magnitude of the absorption spectrum. Our results show the suppression and enhancement of allowed transitions as the carrier density within the QDs changes, as well as the effects of inhomogeneous broadening on the intersubband absorption coefficient. Research on comparing our theoretical results with experimental data is in progress, using Fourier Transform Infrared (FTIR) Spectroscopy and InAs/InP QDs.

ACKNOWLEDGMENTS

This work was funded by the MURI-ARO program under grant number DAAD 19-01-1-0591.

REFERENCES

1. E. Towe and D. Pan, "Semiconductor quantum-dot nanostructures: their application in a new class of infrared photodetectors," *J. Selected Topics Quantum Electron.* **6**, pp. 408–421, 2000.
2. B. F. Levine, "Quantum-well infrared photodetectors," *J. Appl. Phys.* **74**, pp. R1–R81, 1993.
3. G. B. Hocker and W. K. Burns, "Mode dispersion in diffused channel waveguides by the effective index method," *Appl. Opt.* **16**, pp. 113–118, 1977.
4. G. Lamouche and Y. Lépine, "Ground state of a quantum disk by the effective-index method," *Phys. Rev. B* **51**, pp. 1950–1953, 1995.
5. S. L. Chuang, *Physics of Optoelectronic Devices*, Wiley, New York, 1995.
6. S. S. Li, J. B. Xia, Z. L. Yuan, Z. Y. Xu, W. Ge, X. R. Wang, Y. Wang, J. Wang, and L. L. Chang, "Effective-mass theory for InAs/GaAs strained coupled quantum dots," *Phys. Rev. B* **54**, pp. 11 575 – 11 581, 1996.
7. B. Kochman, A. D. Stiff-Roberts, S. Chakrabarti, J. D. Phillips, S. Krishna, J. Singh, and P. Bhattacharya, "Absorption, carrier lifetime, and gain in InAs/GaAs quantum-dot infrared photodetectors," *IEEE J. Quantum Electron.* **39**, pp. 459–467, 2003.

Microscopic Theory and Simulation of Quantum-Well Intersubband Absorption: A Three-Subband Model

Jianzhong Li and C. Z. Ning

Center for Nanotechnology and NASA Advanced Supercomputing Division
NASA Ames Research Center, Mail Stop N229-1, Moffett Field, CA 94035-1000

ABSTRACT

We study the linear intersubband absorption spectra of a 15 nm InAs quantum well using the intersubband semiconductor Bloch equations with a three-subband model and a constant dephasing rate. We demonstrate the evolution of intersubband absorption spectral line shape as a function of temperature and electron density. Through a detailed examination of various contributions, such as the phase space filling effects, the Coulomb many-body effects and the nonparabolicity effect, we illuminate the underlying physics that shapes the spectra.

Keywords: Intersubband transition, linear absorption, semiconductor heterostructure, InAs quantum well

1. INTRODUCTION

Intersubband optical phenomena attract great attention for their applications in communications, sensing, imaging, and “finger printing” molecules in the infrared regime.^{1–3} The advantages of an intersubband transition (ISBT)-based device include bandgap-independent design rules, large dipole matrix elements and ultrafast dynamic response.^{4–7} Particularly, antimonide-based quantum well (QW) heterostructures, such as InAs/AlSb with a conduction band offset as deep as 2 eV, provide attractive design flexibilities.

We have investigated effects of bandstructure, Coulomb interaction, electron-longitudinal optical (LO) phonon interaction, and other material-related issues on ISBTs within a two-subband model.^{8–11} The analysis is based on density matrix formalism. In this paper, linear intersubband absorption spectra in a 15 nm InAs quantum well are studied in the same framework—the intersubband semiconductor Bloch equations approach—but under a three-subband model and dephasing rate approximation. We demonstrate the evolution of intersubband absorption line shape as temperature and carrier density are changed. Through a detailed examination of various contributions, such as phase space filling effects and Coulomb interaction-induced many-body effects, we elucidate the underlying physics that shapes the spectra.

Theoretical treatment of intersubband transitions typically involves two steps. The first step is to compute the bandstructure, while the second step is to formulate light-semiconductor interaction on the basis of this obtained bandstructure. The first step is sometimes called determination of the ground state, while the second step treats the excitations of the system by external light field. In the present model study, we model the bandstructure with different effective masses for the three parabolic subbands, whereas the density matrix theory^{12, 13} is adopted to treat the light-semiconductor heterostructure interaction. By explicitly formulating the two-point correlation functions, such as the intersubband polarization, the set of the so-called intersubband semiconductor Bloch equations (iSBEs) is derived. Within this approach, it is known that the exchange interaction leads to a self-energy renormalization (exchange self-energy, or XSE) to the single particle energy and a nonlocal vertex (excitonlike in the case of interband transitions) term that couples the other intersubband polarizations to each individual \mathbf{k} -transition, whereas the direct (Hartree) interaction contributes the so-called depolarization field term that describes the dynamic screening of the charge carriers to the external exciting field, which is of collective nature and modifies the local field that each individual carrier feels. This paper examines in detail the case of a 15 nm InAs quantum well within a three-subband model and illustrates how different contributions help shape the ISBTs as a function of temperature and carrier density.

Further author information: Both authors are employees of Computer Sciences Corporation.

J.L.: E-mail: jianzhng@nas.nasa.gov, Telephone: (650) 604 4410

C.Z.N.: E-mail: cning@mail.arc.nasa.gov, Telephone: (650) 604 3983

This paper is organized as follows: In the second section, we summarize our theoretical considerations with a minimum set of equations; we present simulated ISBT spectra for the InAs quantum well in Sec. 3; and then we conclude the paper with a summary.

2. THEORETICAL CONSIDERATIONS

As mentioned above, the microscopic theory consists of two steps: the static description of the subband dispersions and kinetic description for the intersubband optical transitions. We describe the energy dispersions in an approximate manner in this work, or more specifically, different effective masses are used for the three subbands. The focus of our work is on the kinetic description of the ISBTs.

To treat the light-semiconductor heterostructure interaction, we consider the following expectation values of the bilinear combination of creation ($c_{n\mathbf{k}}^\dagger$) and annihilation ($c_{n\mathbf{k}}$) operators among the same \mathbf{k} (the in-plane electron wavevector) states within a three-subband model (subband labeled by index $n = 1, 2, 3$): ground subband population $f_{1\mathbf{k}} \equiv \langle c_{1\mathbf{k}}^\dagger c_{1\mathbf{k}} \rangle$, lower excited subband population $f_{2\mathbf{k}} \equiv \langle c_{2\mathbf{k}}^\dagger c_{2\mathbf{k}} \rangle$, upper excited subband population $f_{3\mathbf{k}} \equiv \langle c_{3\mathbf{k}}^\dagger c_{3\mathbf{k}} \rangle$, intersubband polarization $p^{12}(\mathbf{k}) \equiv \langle c_{1\mathbf{k}}^\dagger c_{2\mathbf{k}} \rangle$ between subband 1 and 2, $p^{23}(\mathbf{k}) \equiv \langle c_{2\mathbf{k}}^\dagger c_{3\mathbf{k}} \rangle$ between subband 2 and 3, $p^{13}(\mathbf{k}) \equiv \langle c_{1\mathbf{k}}^\dagger c_{3\mathbf{k}} \rangle$ between subband 1 and 3, and their corresponding Hermitian conjugates. Following the quantum kinetic approach, the semiclassical kinetic equations for the above dynamic variables are derived as a limiting case.¹³ The derivation is extensive and will not be given here. Under linearization with respect to the incident light field amplitude, some plausible assumptions, and the rotating wave approximation, the resultant equations for intersubband polarizations are found as follows:

$$[\hbar(\omega + i\gamma_p^{mn}) - (\varepsilon_{n\mathbf{k}} - \varepsilon_{m\mathbf{k}})]p_{\mathbf{k}}^{mn} = (\mathbf{d}_{\mathbf{k}}^{mn} \cdot \mathbf{E}_0 + \varepsilon_{\mathbf{k}}^{mn})(f_{m\mathbf{k}} - f_{n\mathbf{k}}) - \sum_{j,q} f_{j\mathbf{k}+\mathbf{q}} (V_{\mathbf{q}}^{njlj} p_{\mathbf{k}}^{ml} - V_{\mathbf{q}}^{ljmj} p_{\mathbf{k}}^{ln}) , \quad (1)$$

where ω is the angular frequency of the incident light of amplitude \mathbf{E}_0 , γ_p^{mn} is the dephasing rate, $\mathbf{d}_{\mathbf{k}}^{mn}$ is the dipole matrix element, and $l \neq m, l \neq n$. $f_{m\mathbf{k}}$ is taken as the Fermi distribution function in the linear absorption calculation and $p_{\mathbf{k}}^{mn}$ is the amplitude of the intersubband polarization $p^{mn}(\mathbf{k})$. The renormalized single particle energy ($\varepsilon_{m\mathbf{k}}$) by the Coulomb self-energy and the *local field* correction term ($\varepsilon_{\mathbf{k}}^{mn}$) are, respectively, given by

$$\varepsilon_{m\mathbf{k}} = E_{m\mathbf{k}}^{(0)} - \sum_{l,q} V_{\mathbf{q}}^{mlml} f_{l\mathbf{k}+\mathbf{q}} , \quad (2)$$

$$\varepsilon_{\mathbf{k}}^{mn} = - \sum_{j \neq l, q} V_{\mathbf{q}}^{njml} p_{\mathbf{k}+\mathbf{q}}^{jl} + \sum_{j \neq l, q} V_{\mathbf{0}}^{njlm} p_{\mathbf{q}}^{jl} . \quad (3)$$

The *local field* correction consists of a Fock (first) term that gives rise to a type of collective excitation called repellon and a Hartree (second) term that stimulates another type of collective excitation called the intersubband plasmons (ISPs).^{10, 14} We mention that the first term is responsible for the Fermi-edge singularity effect, whereas the second term leads to the depolarization effect, as described in detail in our earlier work. Their effects have been known from previous studies and play the same roles as well within the present three-subband model. The Coulomb matrix elements ($V_{\mathbf{q}}^{njml}$'s) are defined as in Ref. 9. The static single plasmon-pole approximation¹² has been used for screening the exchange interaction by the intrasubband processes in the present work. The iSBEs are solved numerically by a matrix inversion for the intersubband polarization functions. We note that the last term in Eq. (1) is unimportant in this work.

The linear absorption coefficient is defined by

$$\alpha(\omega) \equiv \frac{\omega}{\varepsilon_0 n(\omega) c} \text{Im}\{\epsilon(\omega)\} \approx \frac{\omega}{n(\omega) c} \text{Im}\{\chi(\omega)\} , \quad (4)$$

with $n(\omega)$ being the background index of refraction (slowly varying in frequency), $\epsilon(\omega)$ the dielectric function, and c the speed of light *in vacuo*. The susceptibility, $\chi(\omega)$, is given by

$$\chi(\omega) \equiv P/\varepsilon_0 E_0 , \quad (5)$$

$$P = 2S/[(2\pi)^2\mathcal{V}] \sum_{m \neq n} \int d\mathbf{k} \{d_{\mathbf{k}}^{mn}\}^* p_{\mathbf{k}}^{mn}. \quad (6)$$

where P is the total intersubband polarization, ϵ_0 is the electric constant, S is the QW area, and \mathcal{V} is the QW volume. $\mathcal{V} = WS$, and W is the QW thickness. Finally, the absorbance of the semiconductor heterostructure is given by $2W\alpha(\omega)$ (per bounce at TM polarization).

3. NUMERICAL RESULTS

Table I lists the bandstructure-related parameter values that were used in the numerical simulation. All the values were obtained using a spurious-state-free 8-band $\mathbf{k} \cdot \mathbf{p}$ Hamiltonian under the envelope function approximation,^{9,15} with the exception of the depolarization factors; their values are the quantum box results of the same QW thickness. The calculated subband populations are presented in Table II, which help understand the simulated spectra, as shown later.

Table I. Parameters used in simulations

subband effective mass	m_i (m_e)	0.0336 (1)	0.049 (2)	0.0715 (3)
subband separation	E_{ij} (meV)	131.065 (12)	150.92 (23)	281.985 (13)
dipole matrix element	d^{ij} (e·Å)	30.0 (12)	35.0 (23)	0.0 (13)
depolarization factor	D^{jlmn} (W)	0.1222 (1122)	0.1146 (2233)	0.0343 (1133) 0.1101 (1232)

m_e : free electron mass; e : absolute electron charge. Numbers in parenthesis behind entry values indicate subband indices. See Ref. 14 for the definition of the depolarization factor.

The effective masses were found after a least square fitting to the $\mathbf{k} \cdot \mathbf{p}$ subbands; the subband separation is the energy difference at the Γ point ($\mathbf{k} = \mathbf{0}$) between the $\mathbf{k} \cdot \mathbf{p}$ subbands; the dipole matrix elements are found to be weakly dependent on the wavevector so that their values at the Γ point were used in the simulation. We mention that the depolarization factor is a measure of the contributing strength of the Hartree term to the *local field*, which in turn determines the strength of the ISPs.^{10,14} Note that a value of the order of 0.1, in the unit of the QW thickness (W), means a rather strong depolarization effect; the total strength of the depolarization effect is proportional to the product of the QW thickness and the density difference between the subbands. Furthermore, coherent Coulomb effects due to the coupling of ISPs associated with individual ISBTs are important, and the results will be presented elsewhere.

Table II. Calculated subband populations

electron density (10^{12} cm^{-2})	temperature (K)	n_1	n_2	n_3
1.00	12	1.00	0.00	0.00
	80	1.00	2.41×10^{-5}	1.09×10^{-14}
	300	9.58×10^{-1}	4.16×10^{-2}	1.84×10^{-4}
2.50	12	2.11	3.92×10^{-1}	0.00
	80	2.10	3.95×10^{-1}	9.91×10^{-10}
	300	2.00	4.96×10^{-1}	3.49×10^{-3}
5.00	12	3.13	1.87	0.00
	80	3.13	1.87	3.77×10^{-5}
	300	3.09	1.84	6.78×10^{-2}
7.50	12	4.06	3.23	2.10×10^{-1}
	80	4.04	3.21	2.49×10^{-1}
	300	3.93	3.06	5.10×10^{-1}

n_i : Electron density in Subband i .

Shown in Fig. 1 are the energy dispersions of the three conduction subbands (left panel) considered and the single-particle absorption spectrum (right panel) of the 15 nm InAs QW. Owing to a nonparabolicity in the bulk InAs conduction band, dispersions for the three subbands are different so that the subband separations

are k -dependent. The rather strong nonparabolicity of InAs leads to a large value range of the intersubband separation. In a single-particle picture, this introduces an inhomogeneous broadening and an accompanying low frequency tailing to the absorption spectrum. All these are reflected in the figure. Note that we did not consider the temperature dependence of the subband structure in this model study. As a comparison, we also show in the figure the case of a vanishing nonparabolicity (dashed curves with upward arrows): The spectrum consists of sharp resonances without any inhomogeneous broadening.

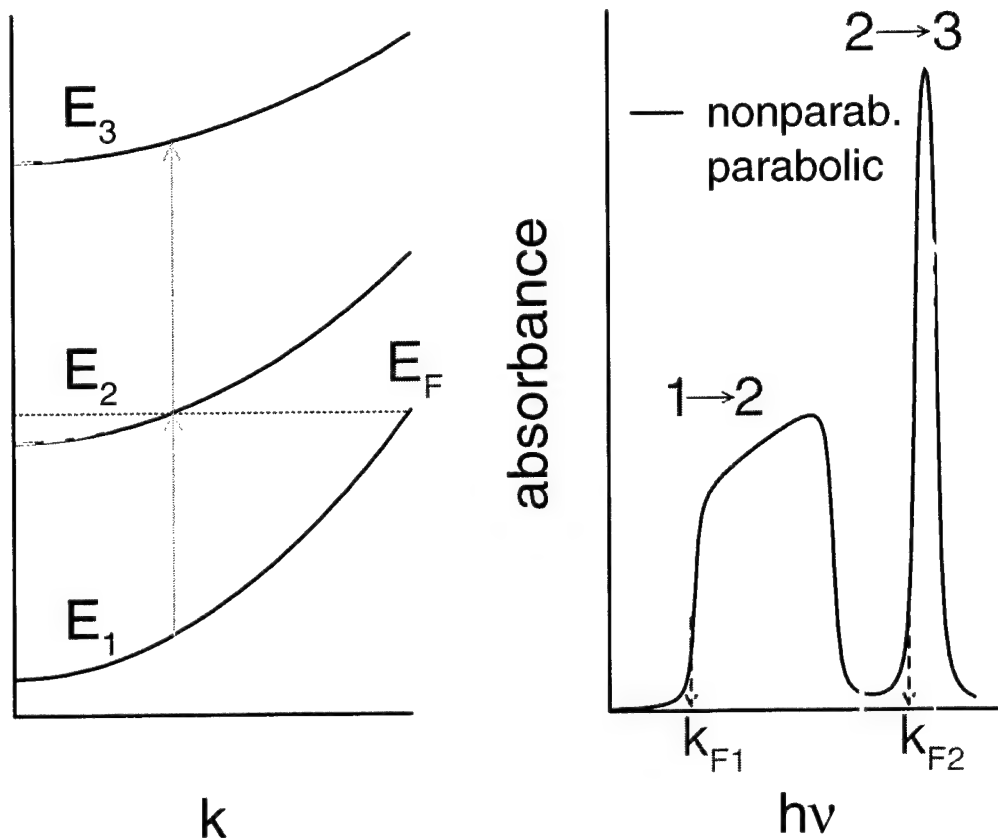


Figure 1. Schematic of subband dispersions (left panel) and single-particle intersubband absorption spectrum for a 15 nm InAs quantum well. The decreasing intersubband separation with increasing k represents the result of a nonparabolicity in InAs conduction band, which is consequently reflected by the broadened absorption spectrum.

Next, we study the effects of Coulomb many-body and collective effects. We first show how the absorbance changes as a function of temperature at different electron densities in Fig. 2. Since the two-subband results have been understood rather well,^{10, 14} we thus emphasize density range where a three-subband model is warranted, that is when the lower excited subband 2 starts to be populated. We have chosen four densities, as denoted in the figures as well as in Table II. At the lowest one, the second subband is only thermally populated at 300 K, as witnessed by the appearance of the weak resonance from the lower excited subband 2 to the upper excited subband 3 ($2 \rightarrow 3$) near 150 meV. Otherwise, only a single, inhomogeneously broadened resonance ($1 \rightarrow 2$) is present. Expectedly, it is further weakened and broadened thermally, as electrons increasingly populate higher energy states that have smaller transition energies, as displayed in Fig. 1. Increase in electron density strengthens resonance $2 \rightarrow 3$ because the amplitude of the resonance is roughly proportional to the density difference of the two subbands, $n_2 - n_3$. This dependence on the density difference also provides an explanation for the reduction in resonance strength as temperature rises at all the four densities, which tends to diminish the difference. This is a phase space filling effect. Its another manifestation is seen in the red shift of resonance $1 \rightarrow 2$ —more distinctly

in Fig. 3—as a function of density. On the other hand, note that at a certain density, *e.g.*, $5 \times 10^{12} \text{ cm}^{-2}$ in Fig. 2, resonance 2→3 is temperature insensitive. As we understand it now, ISBT is a collective phenomenon associated with the intersubband plasmon under normal circumstances, which could be a robust response, depending upon how strong the plasmon couples to the decay channels, possibly through Landau damping as argued by Warburton *et al.*¹⁶ It is worth mentioning that in this model study, we have set the dephasing rate to 1 meV and no particular dephasing physics is considered. Furthermore, temperature dependence of ISBTs is a strong function of nonparabolicity, as shown later in Fig. 4.

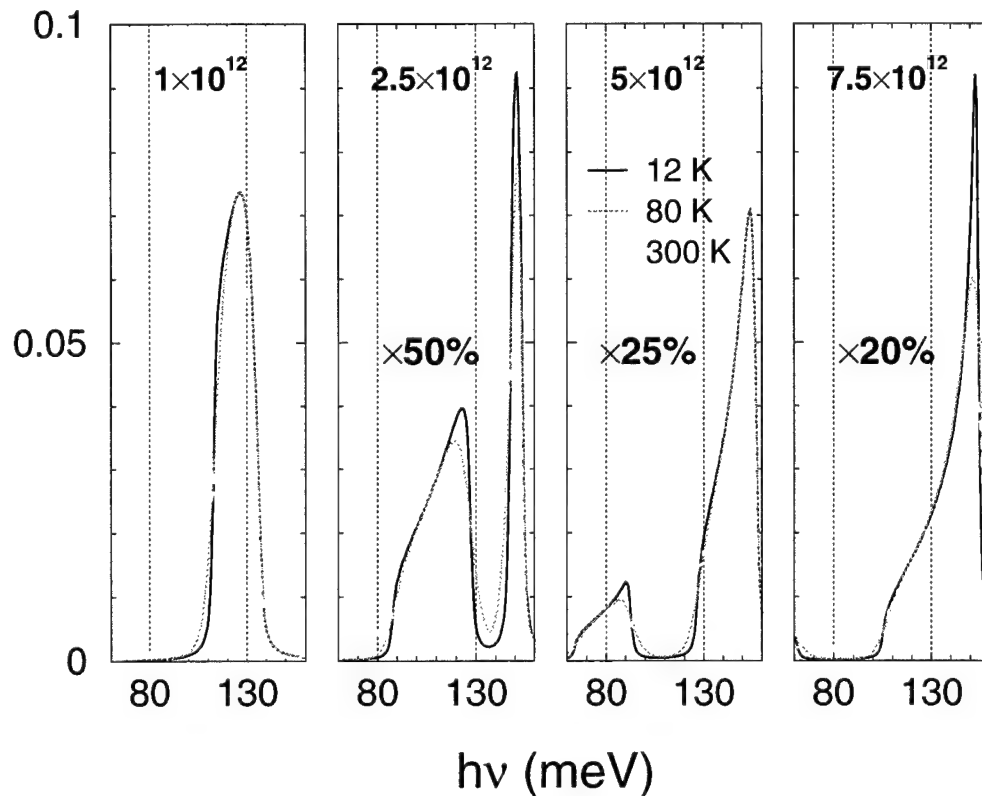


Figure 2. Absorbance dependence on temperature at different electron densities. At low density, only the ground subband 1 is occupied and thus only single resonance (1→2) is observed at low temperature. Thermal population of the lower excited subband 2 (see Table II) is revealed by the presence of a second resonance (2→3). This resonance grows as density increases. Accordingly, the first resonance is weakened and redshifted, as a consequence of phase space filling. Note that at certain density, *e.g.*, $5 \times 10^{12} \text{ cm}^{-2}$, the second resonance is temperature insensitive.

The same results as in Fig. 2 are further presented as a function of electron density at different temperatures in Fig. 3 to illustrate all the effects from a different perspective. The phase space filling effects are more directly demonstrated in this case. First, at this particular QW thickness (15 nm), the first resonance line shape at the lowest chosen density of $1 \times 10^{12} \text{ cm}^{-2}$ is single-particle-like, or a spectrum reflecting the constant 2D joint density of states as a result of the interplay of collective excitations.¹⁰ Increase in electron density has two consequences: starting populating the higher subband(s) and thus redistributing the oscillator strengths. As seen from resonance 1→2, a larger density broadens its line shape further, collects the oscillator strength in favor of the high-frequency side, and redshifts the spectrum. All these are indications that the ISPs play a more dominant role in the interplay, which is expected for higher density cases. Then the resonance is gradually diminished as further increase in electron density actually decreases the density difference of the two subbands, $n_1 - n_2$. As a result, more redshift of the spectrum is observed. On the other hand, resonance 2→3 starts to appear below a density of $2 \times 10^{12} \text{ cm}^{-2}$ and takes a symmetric line shape at low temperature. This is changed as either the temperature or the density increases, as seen in the figure. Within the present three-subband

model, further increase in electron density first blueshifts the spectrum before the upper subband begins to be populated, because the self-energy renormalization of the populated subband increases the effective intersubband separation—similar to the two-subband model results.¹⁰ However, as expected, continuing increasing the electron density will start to populate the upper subband 3 (see Table II). Then, the oscillator strength will eventually decrease and the spectrum will redshift, just like resonance 1→2. Ultimately, we need to consider resonance(s) from subband 3 to even higher one(s). Note that we have not explicitly presented simulation results for resonance 1→3, which lies at higher energy that is beyond the scope of our interested spectral range, but its physics is fundamentally the same as what we have discussed with regard to the other two resonances.

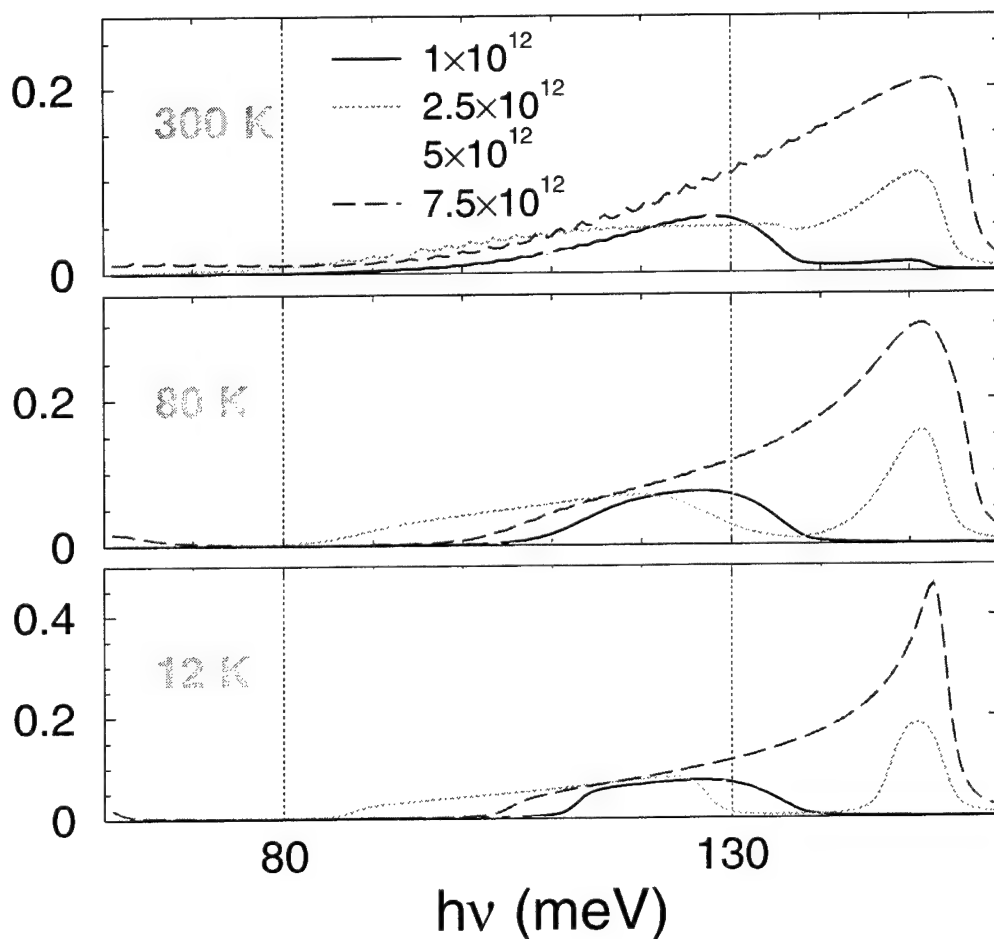


Figure 3. Same absorbance data as in Fig. 2, but presented at different electron densities for a given temperature in each panel. Clearly seen is the phase space filling effects: Occupancy of the lower excited subband 2 introducing the second resonance (2→3) and adding to its oscillator strength as density increases; the enhancement of the plasmon peak at low temperature (12 K); redshifting both resonances as lower k states are occupied. Note the anomalous decrease at 300 K of the second resonance—a reflection of the robustness of the plasmon excitation at $5 \times 10^{12} \text{ cm}^{-2}$, as discussed earlier.

What has not been touched upon till now is the nonparabolicity effect, and this is the focus of Fig. 4. To demonstrate that, we choose an extreme case, that is to set the effective mass (m_3) of the upper excited subband equal to that (m_2) of the lower excited subband. In other words, there is no nonparabolicity effect, to the lowest order, for resonance 2→3. Furthermore, the intersubband separation E_{23} is set to 173 meV, which bears no particular meaning other than to avoid the subject of the coupling of intersubband plasmons, which is the topic of a future paper. Not surprisingly, resonance 1→2 behaves as what have been shown previously. Furthermore, as expected, we observe narrow and symmetric Lorentzian line shape for resonance 2→3. Two features are worth

noting: (i) an anomalous temperature dependence of the resonance at $2 \times 10^{12} \text{ cm}^{-2}$ and (ii) the temperature insensitivity of this resonance at higher density. On the first feature, the resonance is strongly enhanced when temperature rises. This turns out to be a manifestation of the phase space filling effects: At low temperature, the second subband is populated with a rather small electron density. As the temperature increases, more electrons are thermally excited from the ground subband into the second one. As a result of this, the number of electrons available for absorbing incident photons at resonance 2 \rightarrow 3 increases as well. Thanks to zero nonparabolicity, the temperature rise does not broaden the line shape, in contrast to a large nonparabolicity case as discussed already. Therefore, the anomalous temperature dependence of the resonance at the density of $2 \times 10^{12} \text{ cm}^{-2}$ is observed. Following the same line of thinking, the second feature of temperature insensitivity at higher density is easily understood. That is to say, under normal circumstances, the ISBTs are robust if without nonparabolicity. In this sense, temperature insensitivity of an ISBT in a material with large nonparabolicity is accidental, as shown in Figs. 2–3. Finally, the blueshift of the resonance with increase in electron density reflects an effect of the Hartree contribution in Eq. (3). It is often called the depolarization shift in literature^{17,18} as, in the present case of zero nonparabolicity, it acts similar to a depolarization field.

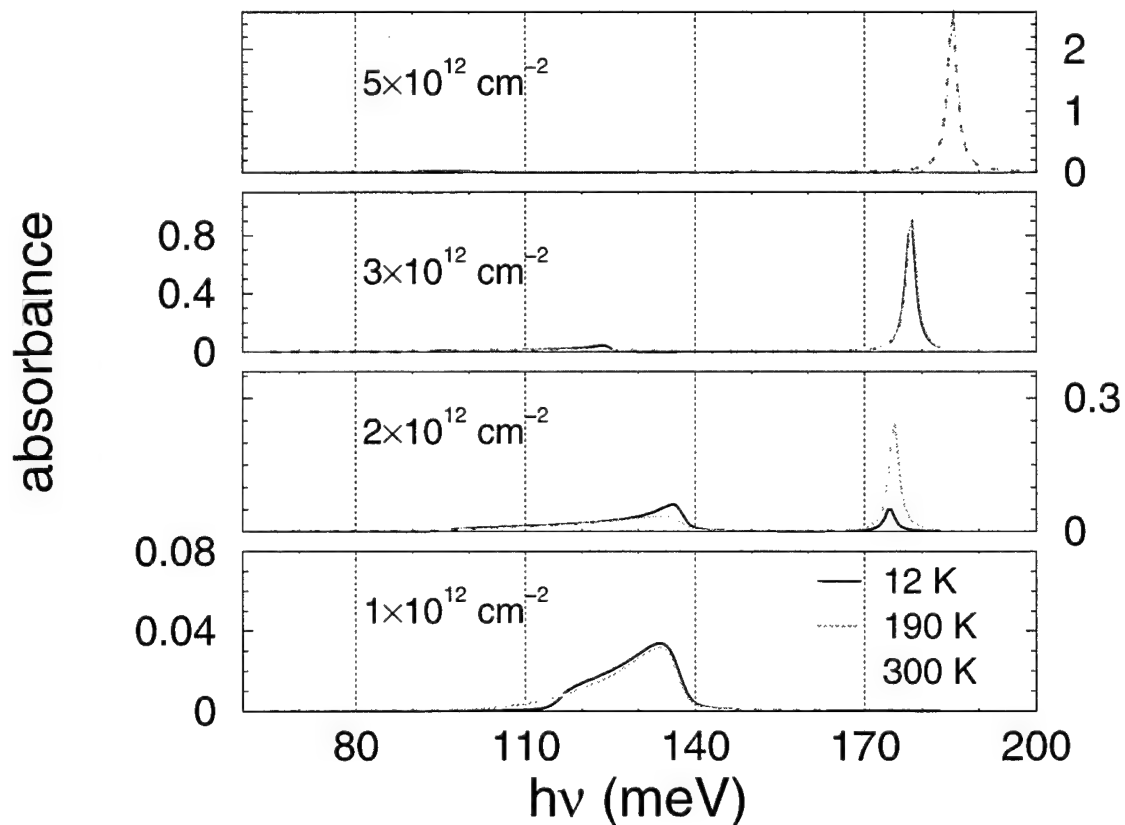


Figure 4. Absorbance evolution similar to Fig. 2, but depicting the nonparabolicity effect as the effective mass of the upper excited subband was set to equal that of the lower excited subband. The intersubband separation E_{23} is set to 173 meV. Two features are worth noting regarding the second resonance: (i) anomalous temperature dependence at $2 \times 10^{12} \text{ cm}^{-2}$ and (ii) its temperature insensitivity at higher density.

4. SUMMARY

In conclusion, we present a microscopic theoretical approach to intersubband optical resonances, similar to the semiconductor Bloch equations approach to interband transitions. This approach is applied to a 15 nm InAs quantum well case that is representative of materials with large conduction band nonparabolicity. The evolution

of intersubband resonances as a function of the temperature and the electron density is presented and discussed in detail. We demonstrate the importance of the phase space filling effects and Coulomb many-body effects in understanding the underlying physics of intersubband resonances. Finally, we show that the nonparabolicity effect is instrumental in shaping the spectra of intersubband resonances.

ACKNOWLEDGMENTS

The work is supported by the NASA Advanced Supercomputing Division under Task Order A61812D (ITOP Contract DTTS59-99-D-00437/TO #A61812D) with Advanced Management Technology Incorporated (AMTI), DARPA-AFOSR and NASA-NCI.

REFERENCES

1. H. C. Liu and F. Capasso, eds., *Intersubband Transitions in Quantum Wells: Physics and Device Application I*, vol. 62 of *Semiconductors and Semimetals*, Academic Press, San Diego, 2000.
2. H. C. Liu and F. Capasso, eds., *Intersubband Transitions in Quantum Wells: Physics and Device Application II*, vol. 66 of *Semiconductors and Semimetals*, Academic Press, San Diego, 2000.
3. R. Q. Yang, "Infrared laser based on intersubband transition in quantum well," *Superlattices Microstruct.* **17**, pp. 77–83, 1995.
4. O. Gauthier-Lafaye, P. Boucaud, F. H. Julien, S. Sauvage, S. Cabaret, J.-M. Lourtioz, V. Thierry-Mieg, and R. Planel, "Long-wavelength ($\approx 15.5 \mu\text{m}$) unipolar semiconductor laser in GaAs quantum wells," *Appl. Phys. Lett.* **71**, pp. 3619–3621, 1997.
5. I. Lyubomirsky, Q. Hu, and M. R. Melloch, "Measurement of far-infrared intersubband spontaneous emission from optically pumped quantum wells," *Appl. Phys. Lett.* **73**, pp. 3043–3045, 1998.
6. A. Liu and C. Z. Ning, "Near-infrared laser pumped intersubband THz laser gain in InGaAs-AlAsSb-InP quantum wells," *Appl. Phys. Lett.* **76**, pp. 1984–1986, 2000.
7. K. T. Lai, M. Missous, R. Gupta, and S. K. Haywood, "Intersubband absorption in strain-compensated InAlAs/AsAs/ $\text{In}_x\text{Ga}_{(1-x)}\text{As}$ ($x \sim 0.8$) quantum well grown on InP," *J. Appl. Phys.* **93**, pp. 6065–6067, 2003.
8. J. Li, K. I. Kolokolov, C. Z. Ning, D. C. Larrabee, G. A. Khodaparast, J. Kono, K. Ueda, Y. Nakajima, S. Sasa, and M. Inoue, "Intersubband transitions in InAs/AlSb quantum wells," in *Progress in Semiconductors II: Electronic and Optoelectronic Applications*, B. Weaver, M. O. Manasreh, C. Jagdish, and S. Zollner, eds., *Proceedings of Materials Research Society* **744**, p. 571, 2003.
9. J. Li, K. I. Kolokolov, and C. Z. Ning, "Microscopic modeling of intersubband optical processes in type ii semiconductor quantum wells: Linear absorption," *Proc. SPIE* **4986**, p. 255, 2003.
10. J. Li and C. Z. Ning, "Interplay of collective excitations in quantum-well intersubband resonances," *Phys. Rev. Lett.* **91**, p. 097401, 2003.
11. J. Li, K. I. Kolokolov, C. Z. Ning, D. C. Larrabee, G. A. Khodaparast, J. Kono, K. Ueda, Y. Nakajima, S. Sasa, and M. Inoue, "Microscopic modeling of intersubband resonances in InAs/AlSb quantum wells," *Physica E*, 2003 (in press).
12. H. Haug and S. W. Koch, *Quantum Theory of the Electrical and Optical Properties of Semiconductors*, World Scientific, Singapore, 1994.
13. T. Kuhn, "Density matrix theory of coherent ultrafast dynamics," in *Theory of Transport Properties of Semiconductor Nanostructures*, E. Schöll, ed., Chapman & Hall, London, 1998. Chap. 6.
14. D. E. Nikonov, A. Imamoğlu, L. V. Butov, and H. Schmidt, "Collective intersubband excitations in quantum wells: Coulomb interaction versus subband dispersion," *Phys. Rev. Lett.* **79**, pp. 4633–4646, 1997.
15. K. I. Kolokolov, J. Li, and C. Z. Ning, "k.p hamiltonian without spurious-state solutions," *Phys. Rev. B* **68**, p. 161308(R), 2003.
16. R. J. Warburton, K. Weillhammer, C. Jabs, J. P. Kotthaus, M. Thomas, and H. Kroemer, "Collective effects in intersubband transitions," *Physica E* **7**, pp. 191–199, 2000.
17. T. Ando, A. B. Fowler, and F. Stern, "Electronic properties of two-dimensional systems," *Rev. Mod. Phys.* **54**, pp. 437–672, 1982.
18. M. Zalužny, "Intersubband absorption line broadening in semiconductor quantum wells: Nonparabolicity contribution," *Phys. Rev. B*, pp. 4511–4514, 1991.

Si photonic wire components and microfilters on SOI substrate

Tatsuhiko Fukazawa, Fumiaki Ohno and Toshihiko Baba

Department of Electrical and Computer Engineering, Yokohama National University
79-5 Tokiwadai, Hodogaya-ku, Yokohama, Kanagawa Japan 240-8501

ABSTRACT

We designed and fabricated some components and devices by using Si photonic wire waveguides on SOI substrate. Because of the very high index contrast between the core and claddings, the waveguide allows a μ -bend. We applied this bend to form a μ -branch and μ -intersection, which exhibited a loss of less than 0.3 dB in the experiment. The H-tree optical signal distribution circuit, the Mach-Zehnder interferometer, and the arrayed waveguide grating demultiplexer were demonstrated by this waveguide, for the first time. Although a more careful design and precise fabrication technologies are necessary for future high performance, this waveguide is expected to miniaturize any kind of conventional silica based devices by a factor over 10000 and realize more sophisticated functions by the dense integration of devices.

Keywords: photonic wire, silicon photonics, SOI, optical waveguide, PLC, integrated optics

1. INTRODUCTION

The conventional optical circuit based on silica waveguides occupies 1 – 100 cm² area because of large bends of mm- to cm-order radius. A compact waveguide with micro-bends (μ -bends) will allow flexible optical wirings and reduce the size of the optical circuit to less than 1 mm². Such a μ -bend requires a waveguide with the strong optical confinement. An ultra-high Δ waveguide is suitable for this purpose, where Δ is the relative refractive index difference defined as $(n_1^2 - n_2^2)/2n_1^2$ for core index n_1 and cladding index n_2 .

The commercially available silicon-on-insulator (SOI) substrate is usable for such a high- Δ waveguide [1-7]. The Si slab processed into the submicron size rectangular channel is used as a core and the SiO₂ layer is used as a cladding in the transparent wavelength range of 1.3 – 1.6 μ m. Such a waveguide is sometimes called photonic wire. The SOI wafer is also used for electronic circuits, so it is expected to be a platform of functional optoelectronic circuits. In our previous study, we fabricated the photonic wire waveguide, and demonstrated the singlemode propagation at a wavelength λ of 1.55 μ m and a low loss μ -bend with a radius less than 3 μ m [2].

In this paper, we review other two μ -components, i.e. a branch and an intersection, which will be widely used in dense optical circuits. We propose and demonstrate the bend-waveguide-type branch [3] and the elliptical intersection [4], which simultaneously realize the compactness and low loss. As applications of the branch, we show the series connection of branches, an H-tree optical distribution signal circuit [5], and a simple Mach-Zehnder interferometer (MZI) [6]. Finally, we demonstrate an arrayed-waveguide-grating filter (AWG) [6] whose size is 200 – 250000 times smaller than conventional ones.

2. ANALYSIS, DESIGN AND FABRICATION

In this study, the 3-dimensional (3-D) finite-difference time-domain (FDTD) analysis was frequently used for the design of the waveguide and devices. Most calculations assumed $\lambda = 1.55$ μ m, the polarization having the (major) electric field component parallel to the 2-D plane (TE-like polarization), and Si (refractive index $n = 3.45$) and SiO₂ ($n = 1.44$) layers of 0.32 μ m and 1.0 μ m thickness, respectively. The air above the Si core and Si substrate below the SiO₂ layer were also included in the analysis. One side of the cubic Yee cell Δx was 40 nm, and the time step is 0.06 fs. Figure 1 shows calculated dispersion characteristics. The single mode condition is satisfied for a waveguide width w of < 0.5 μ m in the SOI-type and $w < 0.38$ μ m in the airbridge-type. As first indicated in [2], the large structural dispersion can provide a group index of typically 4.5 – 5.0, which is higher than the index of the core material.

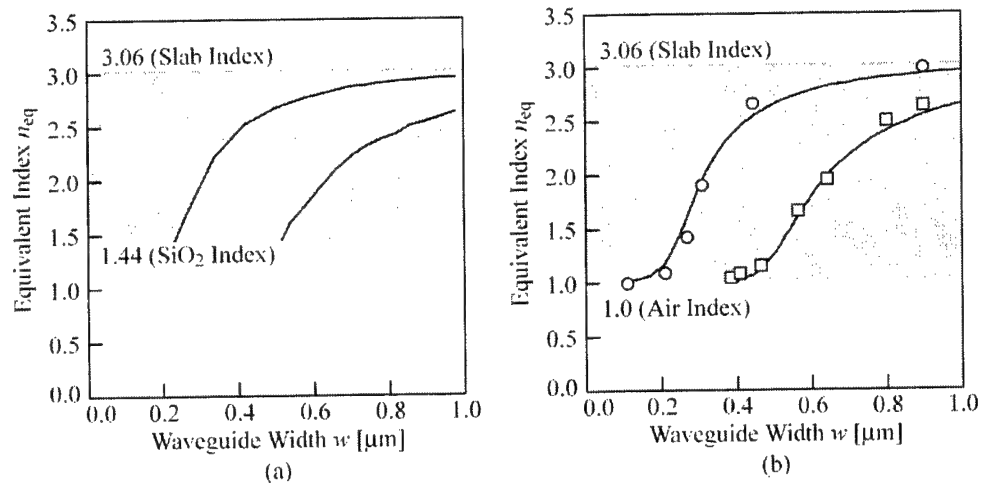


Fig. 1 Dispersion curves of 0th and 1st order modes as a function of waveguide width w . (a) SOI-type waveguide, which were calculated by 3-D FDTD method. (b) Air-bridge-type waveguide. The solid curves and plots were calculated by equivalent index method and 3-D FDTD method with the periodic boundary condition, respectively.

In overall experiments in this paper, a unibond-type SOI substrate was used, which has Si and SiO₂ layers with thicknesses assumed in the calculation. In the fabrication process, the waveguide pattern was formed into a positive resist ZEP520 (Zeon Corp.) by electron beam lithography. The pattern was transferred to Ni or Cr mask by the lift-off technique. Then, the Si layer and partly SiO₂ layer were etched down by CF₄/Xe inductively coupled plasma etching. The typical sidewall angle was 85 – 90°. The structure formed in this way was directly used as an SOI-type waveguide. But for the demonstration of a small intersection, we fabricated an air-bridge-type waveguide as well. Here, the SiO₂ layer beneath the core was removed by HF. For all the waveguides, the input end facet was formed by cleavage. The output end was also formed by cleavage or terminated in the drawn pattern on the substrate. In the measurement, laser light from a tunable source was polarization-controlled to TE or TM, focused to 1 μm spot diameter by a couple of objective lenses, and directly inserted into the input end facet. The light output was observed from the top and the side using vidicon camera with a lens system, and measured in both directions by optical power meters. Light intensity detected from the top was sufficiently strong, because the radiation pattern of light output from such a small waveguide has a very wide solid angle over 2π . Figure 2 shows the scanning electron micrograph (SEM) of fabricated waveguide and the near field pattern (NFP) of light output observed from the side. As seen in the NFP, clear single lobe mode profile is observed. The propagation loss was measured by comparing the light output for waveguides with various lengths. The result has some fluctuations in different process cycles. The typical value is 10 dB/mm and the best one is 2 – 3 dB/mm for both polarizations. The origin of the loss is considered to be the light scattering by the roughness of processed sidewalls.

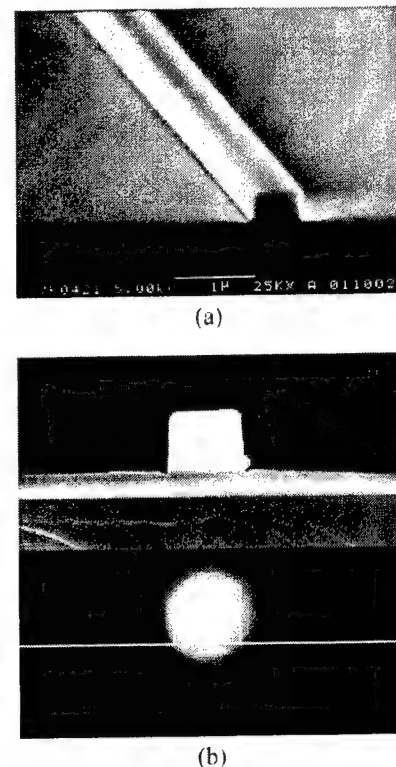


Fig. 2 Scanning electron microscope (SEM) view of fabricated waveguide, and NFP of light output.

3. BEND-WAVEGUIDE-TYPE BRANCH

The branch or splitter is used for many devices such as an optical signal distribution device and an MZI. In silica-based devices, the input waveguide is divided into two by a very slow taper. This is the reason that the branch becomes a long component. However, only such a taper cannot suppress the excess loss. For the loss reduction, another modification of the structure is necessary for the control of wavefronts in the branch so that light power is smoothly split into two.

In this study, the FDTD analysis was carried out for some candidate structures of μ -branches. We finally found that the bend-waveguide-type branch, as shown in Fig. 3, achieves a low excess loss [3]. In this structure, two bend waveguides are directly connected to the input waveguide. At the connected part, the waveguide width is suddenly expanded. This wide waveguide continues by length g and then it is divided into two bend waveguides with radius of r . The branching ratio and excess loss are dependent on the length g and the position shift of input waveguide Δw , as shown in Fig. 4. For $g \leq 0.7 \mu\text{m}$, $P_{\text{out1}}/P_{\text{out}}$ decreases as $\Delta w/w$ increases. For example, $P_{\text{out1}}/P_{\text{out}}$ is 43% for $\Delta w/w = 10\%$. On the other hand, for $g > 0.8 \mu\text{m}$, it increases as $\Delta w/w$ increases. The critical point that gives $P_{\text{out1}}/P_{\text{out}} = 0.5$ for any $\Delta w/w$ is expected for $g = 0.75 \mu\text{m}$. On the other hand, loss takes its minimum value of 0.2 dB at $g = 0.6 \mu\text{m}$, but the sensitivity is not so strong.

Figure 5 shows the NFP of light output from the bend-waveguide-type branch with $r = 2.75 \mu\text{m}$. As expected from the FDTD calculation, light passes through the branch with no irregular scattering and is extracted from two output ends. The excess loss at the branch was specified by comparing the output power from a simple bent waveguide and that from the branch, as plotted in Fig. 4(b). Here, g is changed. The loss takes the minimum value of 0.3 dB for $g = 0.4 \mu\text{m}$. This result almost agrees with the calculation.

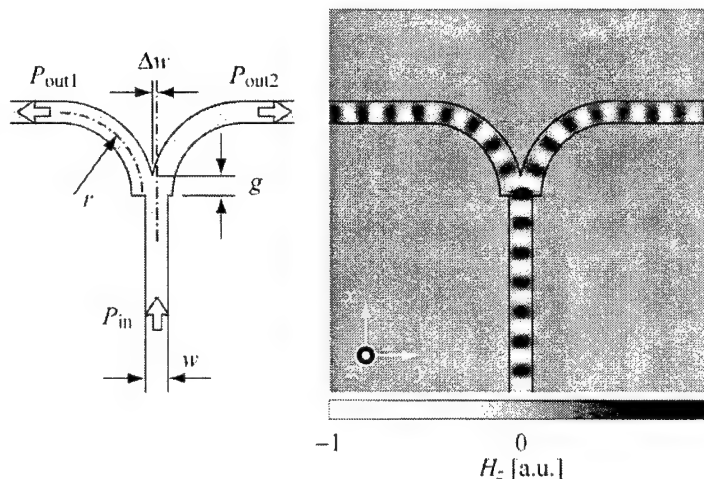


Fig. 3 Schematic of bend-waveguide-type branch and magnetic field profile of TE-like mode at $\lambda = 1.55 \mu\text{m}$ for $r = 1.78 \mu\text{m}$, $w = 0.44 \mu\text{m}$, $g = 0.28 \mu\text{m}$ and $\Delta w = 0 \mu\text{m}$.

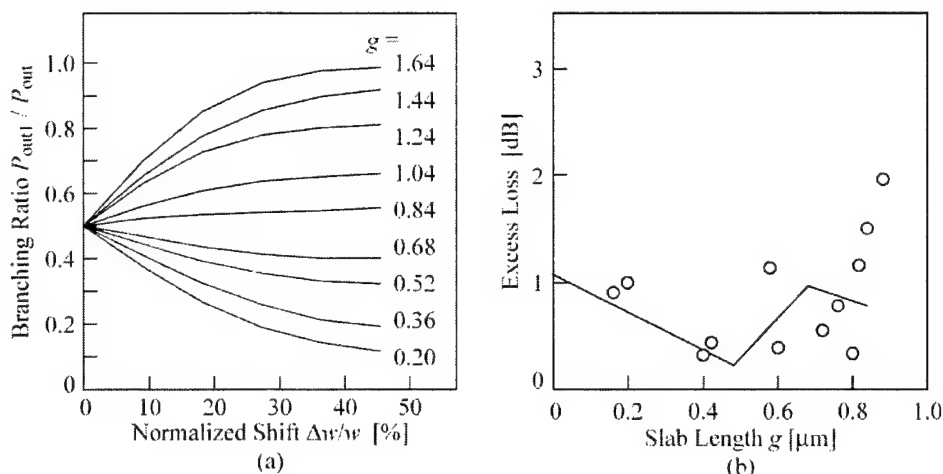


Fig. 4 (a) Branching ratio calculated with normalized shift $\Delta w/w$ of input waveguide. (b) Solid curve and plots indicate calculated and measured excess loss with slab length g , respectively.

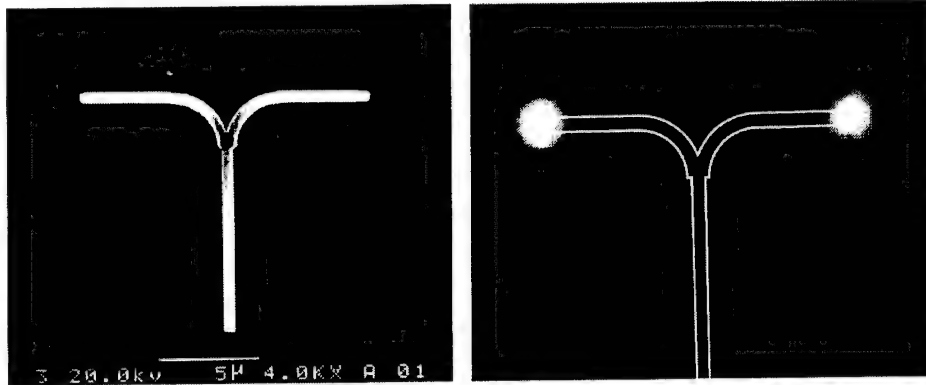


Fig. 5 SEM view of fabricated branch and NFP of light output at $\lambda = 1.55 \mu\text{m}$.

4. ELLIPTICAL INTERSECTION

A low loss and low crosstalk intersection is important for the simplification of optical wiring and the reduction in waveguide loss in dense optical circuits. In addition, a series of intersections are useful as mechanical suspensions of the airbridge-type waveguide, when they are integrated with an airbridge-type photonic crystal waveguide. Thus far, a resonant-type intersection has been theoretically studied for the Si photonic wire waveguide [7]. An insertion loss of < 0.2 dB was calculated by a 2-D calculation. However, the transmission band was as narrow as ~ 10 nm at $\lambda \sim 1.55 \mu\text{m}$. On the other hand, a low crosstalk was theoretically calculated for an intersection with mode expanders in standard low- Δ waveguides [8]. This type of intersection is expected to have a broad transmission band. In this study, we designed the mode-expander-type intersection for the Si photonic wire waveguide and experimentally demonstrated a low loss [4,6].

The light propagation characteristics of the proposed intersection was compared with that of the standard intersection in the 3-D FDTD simulation. In the standard intersection, the insertion loss and the crosstalk were estimated to be 1.4 dB and -9.2 dB, respectively, when the width of the crossing waveguide is equal to that of the input waveguide. (Here, the crosstalk is determined for one crossing waveguide.) In a parabolic shape mode expander, the guided mode is expanded without any excitation of higher order modes [9]. As the expanded mode has a narrow angular spectrum, the crosstalk is suppressed. In this study, we employed an elliptical instead of parabolic shape for the mode expansion and shrinkage, because of the easy fabrication. As the first step, one elliptical region was modeled along the direction of the input waveguide. Then, light smoothly expands and shrinks in the elliptical region, and passes through the intersection, as shown in Fig. 6(b). For $1.5 \mu\text{m} \times 7.2 \mu\text{m}$ elliptical region, the insertion loss and crosstalk were estimated to be < 0.1 dB and < -30 dB, respectively, in the wide spectral range of $\lambda = 1.51 - 1.57 \mu\text{m}$. In the four fold symmetric intersection using two $1.6 \mu\text{m} \times 10.4 \mu\text{m}$ elliptical regions, the insertion loss was slightly higher, i.e. 0.4 dB.

In the experiment, the crossing waveguide, which was used as a suspension of the airbridge waveguide, was $5 \mu\text{m}$ in length on each side. Figure 7 shows NFPs at $\lambda = 1.55 \mu\text{m}$ for the standard and elliptical intersections of the airbridge-type waveguide. For the standard intersections, strong light scattering and decrease in guided intensity were observed. On the other hand, they were negligibly observed for the elliptical intersections. We estimated the loss of one intersection by comparing the output intensity from a waveguide with a series of inter-

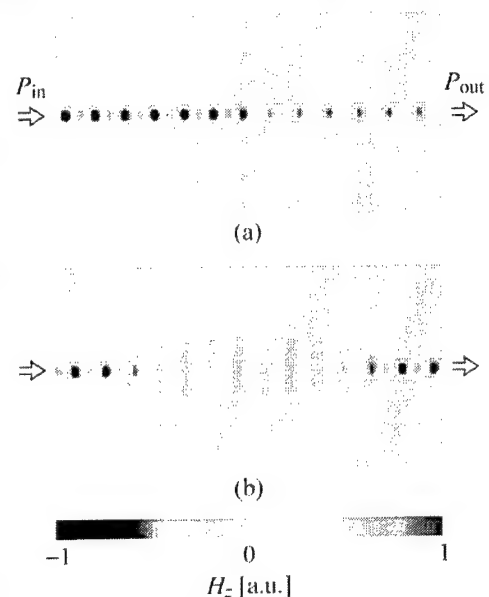


Fig. 6 Magnetic field profiles of TE-like mode at $\lambda = 1.55 \mu\text{m}$. (a) Standard intersection. (b) Elliptical intersection.

sections and from a simple straight waveguide. Figure 8 shows measured loss for various long axes a of the elliptical region. Experimental plots agreed well with theoretical lines. For $a = 7.2 \mu\text{m}$, the average loss and crosstalk were $< 0.1 \text{ dB}$ and $< -25 \text{ dB}$, respectively. (These values were mostly determined from the background noise level.) For the four fold symmetric elliptical intersection, the loss was 1.2 dB . For this type of intersection, more careful optimizations of the structure, e.g., a balance between the long and short axes, may be necessary.

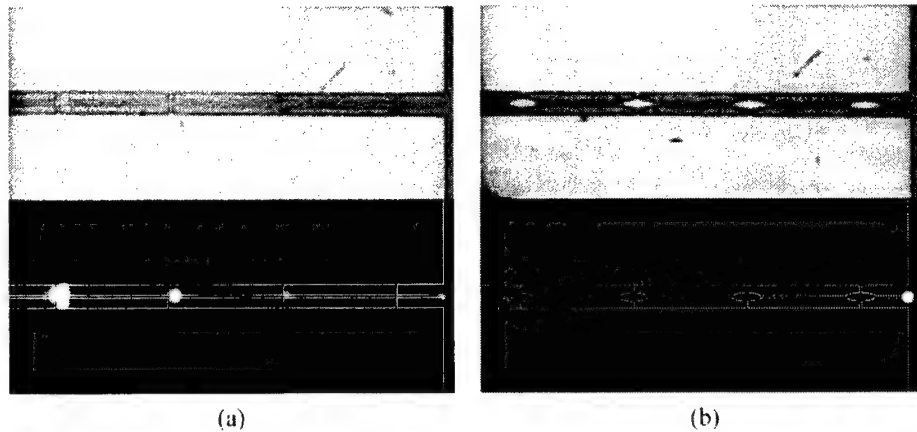


Fig. 7 Top view of fabricated intersections and NFP of light output at $\lambda = 1.55 \mu\text{m}$. Each intersection was placed with $25 \mu\text{m}$ interval.

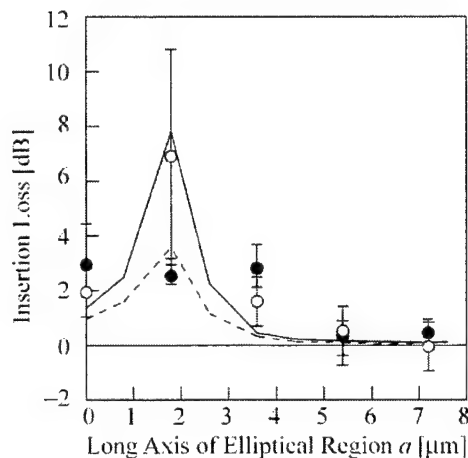


Fig. 8 Insertion loss with long axis of the elliptical region. Solid and dashed curves denote theoretical results by the 3-D FDTD method, and open and closed plots denote experimental results for SOI-type and air-bridge-type waveguides, respectively.

5. H-TREE OPTICAL SIGNAL DISTRIBUTION CIRCUIT

To solve the signal skew problem in an LSI chip, the intra-chip optical interconnection has been discussed. The most fundamental target is the H-tree circuit, which distributes the clock signal to all output ports via waveguides of the same length. Such H-tree circuit has not been realized yet, except for a large prototype composed of a polymer waveguide with millimeter-size branches and bends [10]. For the drastic miniaturization of this circuit, the Si photonic wire waveguide is effective, and the bend-waveguide-type branch discussed in Section 3 is useful. We demonstrated an ultra small H-tree circuit by using this branch [5].

We designed a $35\ \mu\text{m} \times 25\ \mu\text{m}$ circuit with eight output ports. It included a total of seven branches, so that light successively passed through three branches between the input port and one output port. In the branches, $r = 2.75\ \mu\text{m}$, which sufficiently suppressed the bend loss. The length g of the wide waveguide region was designed to be $0.8\ \mu\text{m}$ to obtain a stable $0.5 : 0.5$ branching ratio. Each of the two branches was connected by a straight waveguide of $5\ \mu\text{m}$ length. Each output port was terminated by a straight waveguide of $3\ \mu\text{m}$ length. Figure 9 shows a SEM view of the fabricated circuit and the NFP (TM-like polarization) at $\lambda = 1.55\ \mu\text{m}$. Clear outputs are observed from all ports without any significant scattering at the branches. Figure 10 shows transmission spectra. Here, the intensity includes a calculated coupling loss of 6 dB at the input end, experimental waveguide losses of 1.2 dB and 1.6 dB for TE and TM polarizations, respectively, an experimental total excess loss of 2 dB at the branches and a calculated reflection loss of 3 dB at the output end. On the other hand, it excludes the loss in the optical setup and the intensity attenuation by power distribution of 9 dB. The intensity fluctuation of 7–8 dB is primarily caused by the Fabry-Perot resonance either between input and output ends of waveguides, between a waveguide end and a branch, or between two branches. This resonance is not a serious problem, since it is easily removed by tapered waveguide ends and/or anti-reflection coatings. Except for this resonance, there still remain intensity fluctuations among eight ports of $\sim 5\ \text{dB}$ for TE polarization and $\sim 2\ \text{dB}$ for TM polarization. It is caused by the unstable branching ratio, which arises from the asymmetric corner shape at each branch.

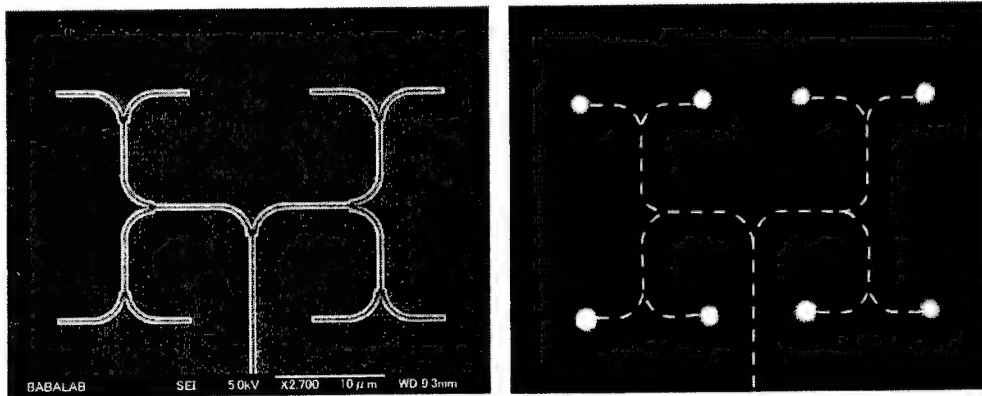


Fig. 9 SEM view of H-tree circuit (left) and NFP of light output for TM-polarized light at $\lambda = 1.55\ \mu\text{m}$ (right).

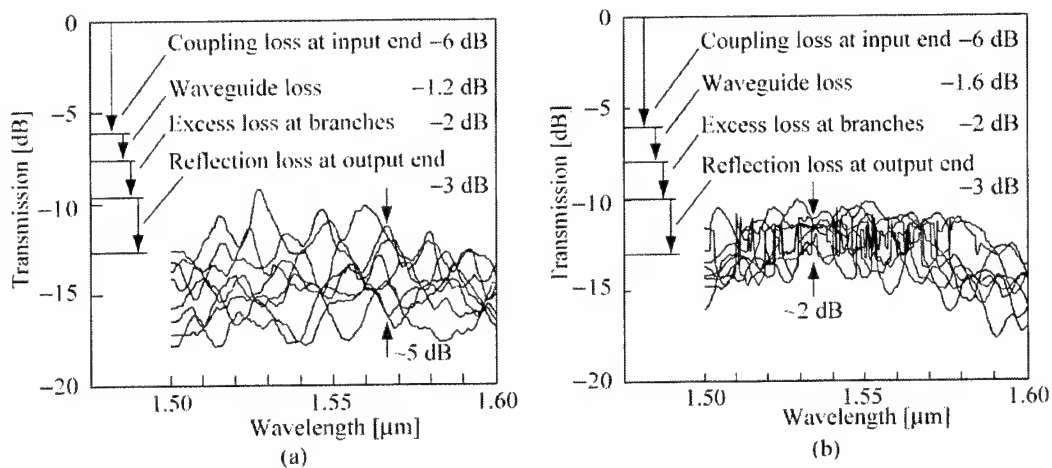


Fig. 10 Transmission spectra for eight ports. (a) TE polarization. (b) TM polarization. Fast oscillation seen in one output port in (b) is not due to the waveguide but due to the unstable condition of the optical power meter.

6. MACH-ZEHNDER INTERFEROMETER (MZI)

The MZI is one of the most popular interferometer, which is used for modulators, switches, filters, and so forth. To switch the output on and off by changing the phase condition, 3 dB directional couplers are commonly used. But in the photonic wire waveguide, it is still difficult to control the space between a directional coupler as it is of $0.1\text{ }\mu\text{m}$ order. In this study, we applied a couple of two bend-waveguide-type branched to construct the MZI, and showed the preliminary interference characteristics [6]. As shown in Section 3, this branch provides low excess loss. In addition, its branching characteristic is less sensitive to the wavelength, which is desired for the MZI.

Figure 11 shows a SEM view and the NFP of light output. At each branch, $r = 3\text{ }\mu\text{m}$. The difference between two waveguide lengths was $28.7\text{ }\mu\text{m}$. Clear light output was observed without any irregular scattering at the branches. (Background noisy light was caused by the uncoupled light at the input end of the waveguide.) The total loss at the branches and the bends was 1.0 dB. Figure 12 shows the transmission spectrum exhibiting a clear resonance. The fine structure in the spectrum arises from the Fabry-Perot resonance between input and output ends of the waveguide. The maximum peak to bottom ratio was 14 dB. The free spectral range (FSR) of $\sim 16\text{ nm}$ well agrees with the theoretical value calculated for a group index of 4.6.

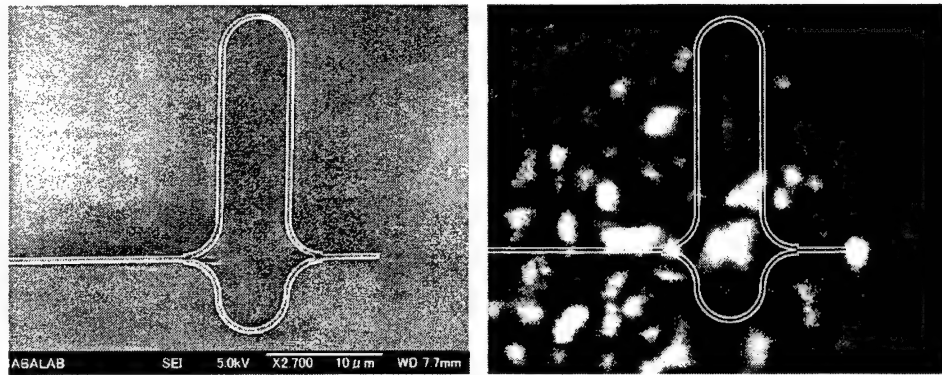


Fig. 11 SEM view of MZI (left) and NFP of light output for TE-polarized light at $\lambda = 1.57\text{ }\mu\text{m}$ (right).

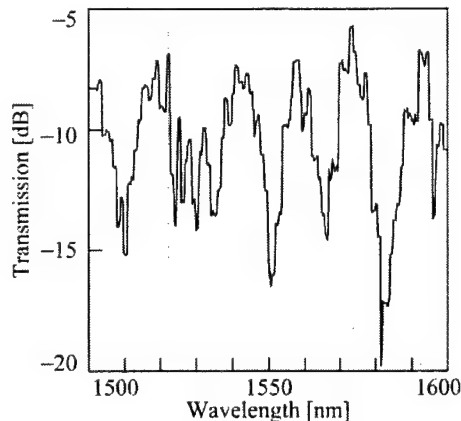


Fig. 12 Measured transmission spectrum. Vertical lines denote the Fabry-Perot resonance peaks

7. ARRAYED-WAVEGUIDE-GRATING (AWG)

The silica-based AWG demultiplexer is widely used as a key device for wavelength-division-multiplexing (WDM) systems at $\lambda = 1.5 - 1.6\text{ }\mu\text{m}$ due to its narrow channel spacing, low crosstalk and low insertion loss. Various functionalities

such as add/drop multi/demultiplexing, channel selection, multiwavelength modulation, and so on, which are realized by integrating multiple AWGs. are additional attractive features. However, due to the large bend radius of the silica waveguide, the smallest AWG still has a size of cm^2 order [11]. A more advanced structure is the III-V based AWG with high mesa waveguides [12]. The waveguide has a standard semiconductor/semiconductor structure in the vertical direction, while has a semiconductor/air structure in the lateral direction. It allows a bend radius of $100\text{ }\mu\text{m}$ order, which is restricted by the vertical leakage loss at the bend. The total size of the AWG can be of several mm^2 order. This size is remarkably small compared with silica ones, but still not small enough as an individual device in a future more sophisticated functional circuit. In addition, this device requires a complex dry etching process in the formation of several- μm -high mesas. Particularly, a high aspect ratio of > 20 is ideally required for narrow grooves between neighboring arrayed waveguides at connection parts with slab waveguides. An insufficient aspect ratio causes an excess loss in transmission characteristics.

As for filter applications of the photonic wire waveguide, microring filters [13-15] and a lattice filter [16] have been demonstrated, but the AWG has never been reported yet. Here, we do not discuss an AWG with low mesa rib-type waveguides on SOI substrate, since it does not have advantages of the ultrahigh- Δ waveguide. It rather has the size compatibility to silica AWGs, which is out of interest in this study. The μ -bend of the photonic wire waveguide expands the design flexibility of the AWG and allows the drastic miniaturization of the total device size to of $(100\text{ }\mu\text{m})^2$ order. As the typical core height of the photonic wire waveguide is $0.3\text{ }\mu\text{m}$, the etching process is much easier and more precise than for the high mesa type. In this study, we designed and fabricated such a compact AWG, and observed a clear demultiplexing characteristic, for the first time, in $1.50 - 1.57\text{ }\mu\text{m}$ wavelength range.

We designed a horseshoe-shape AWG with 34 arrayed waveguides and two slab waveguides, as shown in Fig. 13. The arrayed waveguides are composed of 90° bends and straight waveguides. The total size is $100 \times 93\text{ }\mu\text{m}^2$. A half-elliptical taper of $3.5 \times 1.5\text{ }\mu\text{m}^2$ was placed between the input waveguide and the slab waveguide to smoothly excite a Gaussian beam in the slab waveguide. Similarly, $1.5\text{ }\mu\text{m} \times 0.8\text{ }\mu\text{m}$ tapers were placed between the slab waveguides and other channel waveguides to reduce the joint loss. Each two elliptical tapers were separated by grooves of $\sim 10\text{ nm}$ end width. Figure 14 shows transmission spectra for TE-polarized input light. Here, the vertical axis excludes input and output coupling losses between the device and the measurement setup. The clear spectral peak appeared and linearly shifted among 17 output waveguides. The fine structure in the peak was caused by the Fabry-Perot resonance inside the device. The peak interval was 3 nm , which well agreed with the designed value. However, the full width at half maximum (FWHM) of each peak was $\sim 6\text{ nm}$. Therefore, the number of fully separated channels was nine. The average sidelobe level was -5 dB of the main peak intensity. The FWHM and the sidelobe level will also be improved by optimizing the tapers and the focal length f to form a high quality Gaussian beam in the slab waveguides. In each spectrum, another main peak was not observed over the measured wavelength range of 100 nm . The free spectral range (FSR) was wider than 90 nm .

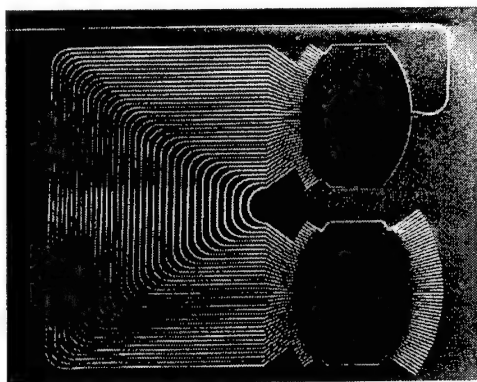


Fig. 13 SEM view of fabricated AWG.

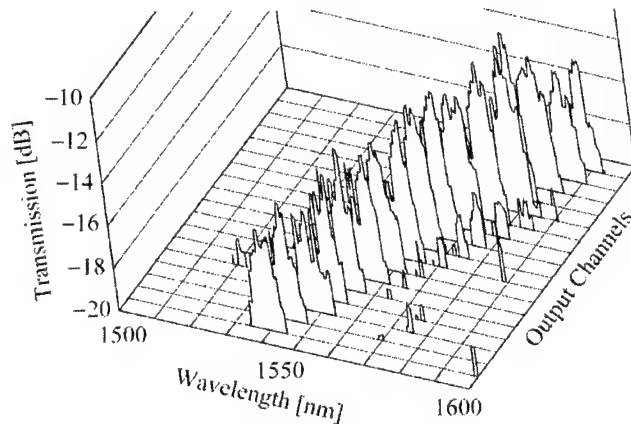


Fig. 14 Transmission spectra for 17 output waveguides.

8. CONCLUSIONS

We demonstrated the μ -branch and the μ -intersection of Si photonic wire waveguide, which showed a low loss of < 0.3 dB and < 0.1 dB, respectively, and the wavelength insensitive characteristics in the experiment. As applications of the μ -branch, we fabricated the H-tree optical signal distribution circuit with eight output ports and the simple MZI. For the H-tree circuit, the clear light distribution was observed with an intensity fluctuation of 2 dB. For the MZI, the typical frequency response was observed with an attenuation ratio of 14 dB. Finally, we demonstrated the AWG of $\sim (100 \mu\text{m})^2$ size. The demultiplexing function was observed with a spectral width of 6 nm for nine channels and an FSR of 90 nm.

Now, we can fabricate any conventional devices by the Si photonic wire waveguides. To obtain high performance, we have to clarify crucial points of design and fabrication for such a high index contrast system. However, we expect to achieve them in the near future, owing to the complete 3-D FDTD calculation of lightwaves and the fine fabrication process so far developed for not only this purpose but also more complex photonic crystal waveguides.

REFERENCES

1. K. K. Lee, D. R. Lim, H-C Luan, A. Agarwal, J. Foresi and L. C. Kimerling, "Effect of size and roughness on light transmission in a Si/SiO₂ waveguide: Experiments and model," *Appl. Phys. Lett.*, **77**, pp. 1617-1619, 2000.
2. A. Sakai, G. Hara and T. Baba, "Propagation characteristics of ultrahigh Δ optical waveguide on silicon-on-insulator substrate," *Jpn. J. Appl. Phys.*, **40**, pp. L383-L385, 2001.
3. A. Sakai, T. Fukazawa and T. Baba, "Low loss ultra-small branches in a silicon photonic wire waveguide," *IEICE Trans. Electron.*, **E85-C**, pp. 1033-1037 2002.
4. T. Fukazawa, T. Hirano, F. Ohno and T. Baba, "Low loss intersection of Si photonic wire waveguides," *Jpn. J. Appl. Phys.*, (to be published).
5. T. Fukazawa, A. Sakai and T. Baba, "H-tree-type optical clock signal distribution circuit using a Si photonic wire waveguide," *Jpn. J. Appl. Phys.*, **41**, pp. L1461-L1463, 2002.
6. T. Fukazawa, T. Hirano and T. Baba, "Ultrasmall filters and low loss intersection by Si photonic wire waveguides," *Proc. CLEO PR*, THC-(16)-5, 2003.
7. C. Manolatou, S. G. Johnson, S. Fan, P. R. Villeneuve, H. A. Haus and J. D. Joannopoulos, "High-density integrated optics," *J. Lightwave Technol.*, **17**, pp. 1682-1692, 1999.
8. T. Kato and Y. Kokubun, "Loss reduction of cross grid intersection for large-scale micro-ring filter integrated circuit," *Proc. Spring Meet. IEICE*, C-3-851, 2002.
9. W. K. Burns, A. F. Milton and A. B. Lee, "Optical waveguide parabolic coupling horns," *Appl. Phys. Lett.*, **30**, pp. 28-30, 1977.
10. L. Wu, B. Bihari, J. Gan and R. T. Chen, *Proc. Top. Meet. Integrated Photonics Research*, pp. 282, 1998.
11. e.g., M. Ishii, Y. Hibino, Y. Hida, A. Kaneko, M. Itoh, T. Goh, A. Sugita, T. Saida, A. Himeno, and Y. Ohmori, "Low-loss and compact silica-based 16 channel arrayed waveguide grating multiplexer module with higher index difference," *Proc. ECOC 2000*, **3**, pp. 27-28, 2000.
12. M. Kohtoku, H. Sanjoh, S. Oku, Y. Kadota, Y. Yoshikuni and Y. Shibata, "InP-based 64-channel arrayed waveguide grating with 50 GHz channel spacing and up to -20 dB crosstalk," *Electron. Lett.*, **33**, pp. 1786-1787, 1977.
13. B. E. Little, J. S. Foresi, G. Steinmeyer, E. R. Thoen, S. T. Chu, H. A. Haus, E. P. Ippen, L. C. Kimerling and W. Greene, "Ultra-compact Si-SiO₂ microring resonator optical channel dropping filters," *IEEE Photonics Technol. Lett.*, **10**, pp. 549-551, 1998.
14. A. Vörckl, M. Münster, W. Henschel, P. H. Bolivar and H. Kurz, "Asymmetrically coupled silicon-on-insulator microring resonator for compact add-drop multiplexers," *IEEE Photonics Technol. Lett.*, **15**, pp. 921-923, 2003.
15. P. Dumon, W. Bogaerts, J. V. Campenhout, V. Wiaux, J. Wouters, S. Beckx and R. Baets, "Low-loss, single-mode photonic wires and ring resonators in silicon-on-insulator," *Proc. LEOS 2003*, **1**, pp. 289-291, 2003.
16. K. Yamada, T. Shoji, T. Tsuchizawa, T. Watanabe, J. Takahashi and S. Itabashi, "Silicon-wire-based ultrasmall lattice filters with wide free spectral range," *Opt. Lett.*, **28**, pp. 1663-1664, 2003.

Thermal Analysis of Packaging Device with Metal-Coated Fiber Bragg Grating

Baoxi Xu, Wanxun He*, Lungtat Ng,
Mingyu Liu, Gaoqiang Yuan, Hongxing Yuan, Chengwu An, Towchong Chong
Data Storage Institute, 5 Engineering Drive 1,
(Off Kent Ridge Crescent, NUS), SINGAPORE 117608

ABSTRACT

The three-dimensional model of the packaging device is established based on ANSYS simulation platform. The thermal properties such as time response, axial and radial temperature distributions at different applied voltages are exhibited. With aids of Real Time Optical Spectrum Analyzing System and IR Camera System, time response of the device and axial temperature distribution along the coated fiber with intracore FBG are both demonstrated. Temperature responses to different applied voltages are achieved after measuring voltage induced wavelength shift and temperature dependent wavelength shift. Simulation shows results in agreement with those of experiment. Finally, regulations on length of the metal coating, size of the package, power consumption and tuning properties of the packaging device are discussed.

Key Words: Packaging device, fiber Bragg grating (FBG), temperature distribution, time response

1. INTRODUCTION

Optical fiber coated with micros of resistively heating layer has attracted more attentions in the past few years. Such an electrically regulated component is promising for its merits such as small size, low power consumption and low cost. Imprinted with intra-core Fiber Bragg Grating (FBG), the component can find applications such as tunable filtering or sensing components used in fields of optical communications or sensing technologies. Till now it has been proposed to be used as wavelength modulator [1], tunable dispersion compensator for single channel in WDM or long haul transmission systems [2][3] and sensing element for electrical current [4].

With approximations of the coated fiber as two-layered structure and one-dimensional model in axial direction, thermal distribution at steady-state has been computed by nonlinear finite element modeling method [2]. Regarding the coated fiber as one-layered structure and also one-dimensional model in axial direction, heat flow along the axis of fiber has been analyzed and thermal characteristics such as temperature response and spatial distribution has been discussed in detail [5]. Only considering heat flow from coated fiber to ambient air in radial direction, another one-dimensional model has been proposed to discuss thermal response of the component [6]. Upon one-dimensional model of the coated fiber, one can discuss thermal characteristics such as time response and axial temperature distribution. However, in some cases such as package's design for the coated fiber, temperature distributions of ambient air in two or three dimensions beyond the coated fiber are greatly desired in order to optimize the package's size. Furthermore, in building the theoretical models and subsequent analysis mentioned above, many assumptions and approximations have been made. This will undoubtedly weaken the suitability of the models and add some errors compared with results of experiment.

Based on finite element analysis method and with the help of commercial simulation software ANSYS, three-dimensional model for a packaging device with metal-coated FBG is established in this paper. Based on simulation result, thermal analysis such as temperature response and spatial distributions in radial and axial directions are conducted. The establishment of the model on ANSYS is more attractive due to its easiness and intuitiveness. Moreover, thermal analysis based on this method can extend temperature distributions in multiple directions and temperature responses at dynamic and steady states at the same time. Because of consideration of temperature dependent material parameters, more accurate simulation result should be expected.

*he_wanxun@dsi.a-star.edu.sg; phone +65 6874 8412; fax +65 6777 8517; dsi.a-star.edu.sg

In the following section 2, simulation and experiment are described. Then results are demonstrated and discussed. In last section several conclusions are listed.

2. SIMULATION&EXPERIMENT

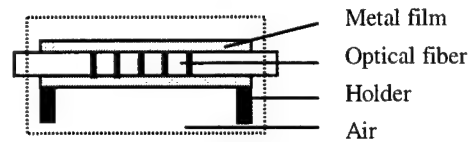


Fig. 1 Schematic description of packaging device to be modeled

The modeled packaging device consists of four parts (shown in fig. 1): FBG based optical fiber with $125\mu\text{m}$ in diameter and 70mm in length, a metal film with $3\mu\text{m}$ in thickness and 60mm in length, which is coated around the fiber, two fused quartz based fiber holders with V-grooves curved on top surfaces and size of $15\times 4\times 2\text{mm}^3$, $2\mu\text{m}$ -thick gold film covered on top surfaces of the holders for electrical contact, all the parts are surrounded by air.

The 3-dimensional model of the packaging device was established on ANSYS platform. The material's parameters used in the modeling are listed in tab. 1.

Optical fiber
Density: 2203Kg/m^3 , thermal conductivity: $1.38\text{W/m}\cdot\text{K}$, heat capacity: $703\text{W}\cdot\text{S/Kg}\cdot\text{K}$.
Metal film
Density: 8900Kg/m^3 , thermal conductivity: 91.3, 90.5, 80.1, 72.1 and $66.0\text{W/m}\cdot\text{K}$ at 293.15, 300, 400, 500 and 600K, heat capacity: $444\text{W}\cdot\text{S/Kg}\cdot\text{K}$, film resistivity: 67.5 and $69\mu\Omega\cdot\text{cm}$ at 295.75K and 573.5K.
Holder
Fused quartz: density: 2203Kg/m^3 , thermal conductivity: $1.38\text{W/m}\cdot\text{K}$, heat capacity: $703\text{W}\cdot\text{S/Kg}\cdot\text{K}$.
Gold: density: 19300Kg/m^3 , thermal conductivity: 317, 311, 304 and $296\text{W/m}\cdot\text{K}$ at 300, 400, 500 and 600K, heat capacity: $129\text{W}\cdot\text{S/Kg}\cdot\text{K}$, film resistivity: $22.2\mu\Omega\cdot\text{cm}$.
Air
Density: 1.1774Kg/m^3 , thermal conductivity: $0.02624\text{W/m}\cdot\text{K}$, heat capacity: $1005.7\text{W}\cdot\text{S/Kg}\cdot\text{K}$.

Tab. 1 Material parameters used for modeling of packaging device

Most of them were taken from reference [7]. Some temperature dependent parameters were obtained by interpolation. The film resistivity of metal layer was estimated by measuring electrical resistance at different temperatures and its geometrical size.

Solid lines in fig. 2 show the time responses of the simulated device at different applied voltages. The temperatures increase nonlinearly at starting phase. They will reach stable values after 2 seconds and keep constants of 510K, 435K and 330K at voltages of 5V, 4V and 2V. It's likely to conclude that applied voltage will not affect rising time of the packaging device, although it can affect temperature values at constant phase.

Temperature distributions of the packaging device along coated fiber are shown in fig. 3. Three curves represent those when the packaging device is applied with voltages of 5V, 4V and 2V. Temperature rising span at coating's end is nearly 10mm for all cases. In central portion of coated fiber, temperature keeps constant in span of 30mm. It's likely to conclude that the length of temperature rising span at the end relates less to applied voltage.

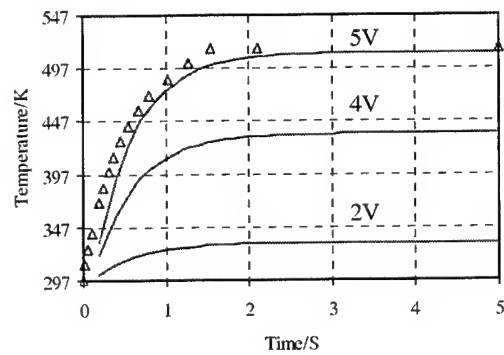


Fig. 2 Time response of packaging device at starting phase

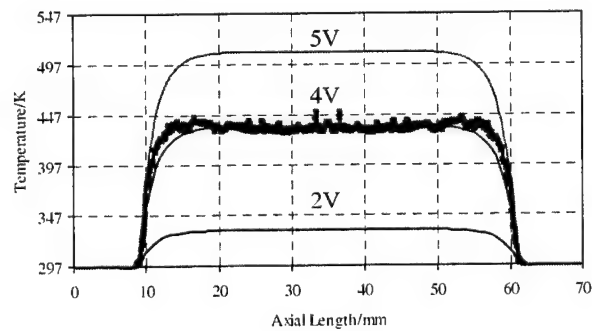


Fig. 3 Temperature distribution of packaging device along fiber's axis

Fig. 4 demonstrates radial temperature distribution of the packaging device in the central part. Inside coated fiber temperature keeps constant value. In ambient air beyond coated fiber, temperature decreases sharply first, then slowly and gradually to ambient temperature.

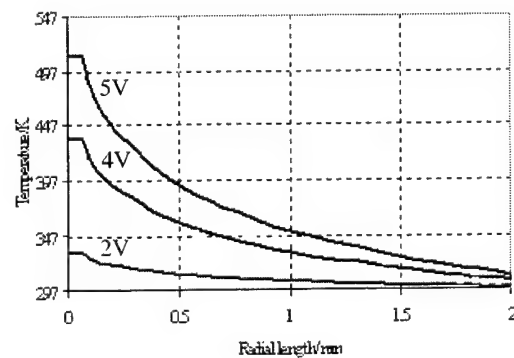


Fig. 4 Temperature distribution of packaging device in radial direction

Solid curve in fig. 5 illustrates the packaging device's temperature relationship with applied voltage. At low voltage it increases slowly. Gradually it becomes rapid and reaches 510K at voltage of 5V.

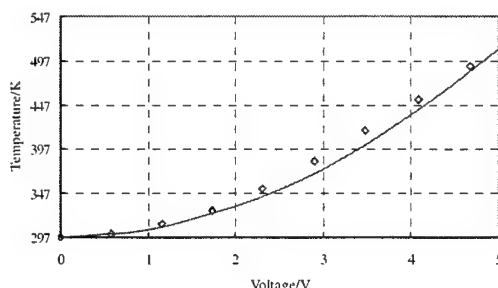


Fig. 5 Voltage-induced temperature variation at fiber's center

In order to experimentally acquire center's temperature of the coated fiber, FBG was taken use to imprint in fiber's core. By means of measuring Bragg wavelength's response at starting phase and wavelength shifts at differently applied voltages, and with reference of temperature dependent wavelength shift at steady state, temperature response of the packaging device and relationship of temperature variation and applied voltage could be achieved. The setup used for measuring wavelength response could be described as: the light beam from a broadband light source (Super Laser Diode) was first guided into the packaging device through a circulator, then reflected and went through the circulator again, finally measured by a Real Time Optical Spectrum Analyzing System (RTOSAS, Hamamatsu). In order to measure wavelength shifts at different voltages, Optical Spectrum Analyzer (OSA) instead of RTOSAS was used. Also an external heating/cooling platform was used as temperature controller to calibrate the dependence of wavelength shift on temperature. Measured result showed very good linearity of temperature dependent wavelength shift. The slope's value was 1.171nm/100K. The packaging device's time response is demonstrated in fig. 2 ('Δ' symbols). At starting phase, temperature increases quickly to 515K at time of 1.7seconds, and then keeps constant. Symbols '◇' in fig. 5 show voltage induced temperature variation. Temperature increases from room temperature to about 490K with voltages increasing from 0 to 4.67V. Both curves agree with simulation results very well.

In order to measure temperature distribution along the fiber, IR Camera System (AVIO, TVS600) was introduced. Setting material's emissivity of 0.1, retrieved data (solid square symbols) were demonstrated in fig. 3 (4V). Temperature rising span at the end of fiber's coating is about 7mm. The curve agrees well with that at fiber's center in simulation.

Based on achievements of thermal analysis, together with consideration of heating sinking of sensor structure on coated fiber [8], the length of fiber coating is optimized to 65mm. For the sake of operativity of assembling fiber into package, the package we designed for the packaging device is proposed with the size of 84x20x8mm³.

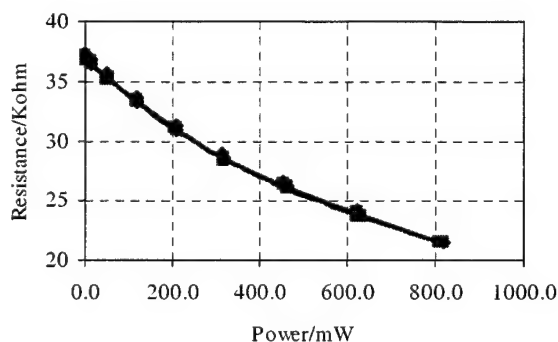


Fig. 6 Sensor's response to electrical power applied on coated fiber

For fear of working wavelength shifting with environmental variations, temperature measuring and controlling module has been designed. Sensitive profile of the miniature sensor we used to measure temperature is exhibited in fig. 6. When coated fiber is supplied with electrical power of 0.82W, the sensor's resistance decreases from 36.9 to 21.5Kohm. With the setup of temperature sensor and control circuit, wavelength tuning profile of the packaging device is demonstrated in fig. 7 (one curve denotes that in ascending order, the other in descending order). Tuning range more than 3nm can be expected with voltage applied as large as 8V. To increase tuning range of the packaging device, larger voltage can be applied. However, it is found that metal coating will be seriously damaged at higher voltage close to 10V.

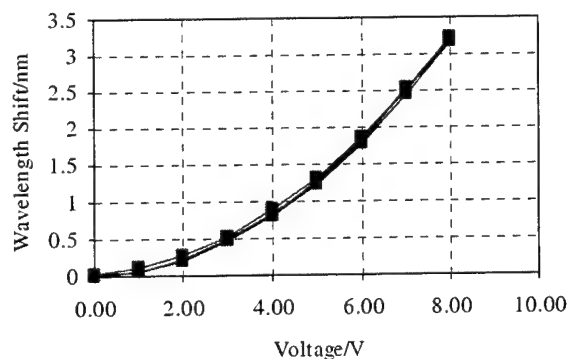


Fig. 7 Wavelength tuning profile of packaging device

3. CONCLUSIONS

3-dimensional model has been presented to analyze thermal characteristics of the packaging device with metal-coated FBG. Rising time of the device and temperature rising span at the end of the metal coating are nearly 2seconds and 10mm, respectively, which have less relation with applied voltage. Length of the metal coating is optimized to 65mm. The packaging device can enable a tuning range more than 3nm. It is potentially a low cost fiber-based tunable filter.

REFERENCES

- [1] H. G. Limberger, Nguyen Hong Ky, D. M. Costantini and R. P. Salathe, "Efficient miniature fiber-optic tunable filter based on intracore Bragg grating and electrically resistive coating," *IEEE Photonics Technol. Lett.*, **10**, 361-363, 1998.
- [2] J. A. Rogers, B. J. Eggleton, J. R. Pedrazzani and T. A. Strasser, "Distributed on-fiber thin film heaters for Bragg gratings with adjustable chirp", *Applied Physics Lett.*, **74**, 3131-3133, 1999.
- [3] B. J. Eggleton, A. Ahuja, P. S. Westbrook and J. A. Rogers, "Integrated tunable fiber gratings for dispersion management in high-bit rate systems", *J. Lightwave Technol.*, **18**, 1418-1432, 2000.
- [4] P. M. Cavaleiro, F. M. Araujo and A. B. Lobo Ribeiro, "Metal-coated fibre Bragg grating sensor for electric current metering", *Electronics Lett.*, **34**, 1133-1135, 1998.
- [5] J. A. Rogers, P. Kuo, A. Ahuja and B. J. Eggleton, "Characteristics of heat flow in optical fiber devices that use integrated thin-film heaters", *Applied Optics*, **39**, 5109-5115, 2000.
- [6] L. Li, J. X. Geng, L. Zhao and G. Chen, "Response characteristics of thin-film-heated tunable fiber Bragg gratings", *IEEE Photonics Technol. Lett.*, **15**, 545-547, 2003.
- [7] M. A. James, *Handbook of electronic materials*, NY: IFI/Plenum, 1971.
- [8] W. X. HE, B. X. XU, L. T. NG, "Influence of sensor structure on thermal characteristics of metal-coated optical fiber based component", *ICOON'03*, Bangalore, INDIA, 2003.

Simultaneous mode locked operation of a fiber laser at two wavelengths

H. Dong, G. Zhu, Q. Wang, N. K. Dutta

Department of Physics, University of Connecticut, Storrs, CT 06269

ABSTRACT

We demonstrate simultaneous stabilized operation of a mode locked ring fiber laser at two wavelengths. At one of the wavelengths the mode locked operation is at 10 GHz and it is at 40 GHz at the second wavelength. The laser has an intracavity LiNbO₃ modulator driven at 10 GHz. The 40 GHz pulses are obtained by rational harmonic mode locking. Pulses with widths in 5 to 8 ps range are obtained.

Keywords: harmonic mode-locking, phase locked loop

1. INTRODUCTION

Ultra short pulse trains with high-repetition-rate at multiple wavelengths may be required in high-bit-rate optical communication. Recently actively mode-locked Er-doped fiber lasers have been used for the simultaneous generation of high-repetition picosecond pulses at multiple wavelengths¹⁻³. Li et al.³ generated the pulses at 2.5 and 5 GHz respectively with pulse widths of 17.7 and 13 ps respectively. However, due to the fluctuation of laser cavity and dual-mode competition, stability was limited.

In this paper, using a modulation frequency $f_m=10$ GHz, we achieve stable optical pulse trains at the repetition rate of 10 and 40 GHz with pulse widths of 8ps and 5ps respectively. The instability has been reduced considerably using an intracavity semiconductor optical amplifier (SOA) and a phase locked loop (PLL) associated with the optical cavity.

2. MODE LOCKING

The schematic of a ring fiber laser with an SOA in the optical cavity is shown in Figure 1. The Erbium doped fiber amplifier (EDFA) is pumped with a 980nm pump laser. The wavelength selective element employed in the cavity is a pair of multiplier/demultiplier (MUX/DMUX), which has 4 channels with the bandwidth of 1.5 nm each. By tuning the delay line, the total optical cavity length (which determines the round-trip time of the optical pulse in the cavity) is varied. A 10/90 output coupler is placed after the MUX. The LiNbO₃ electro optical modulator is driven by modulation signal, which is controlled by the voltage-controlled oscillator (VCO); the modulation frequency f_m is ~10GHz. The pulses are observed using an autocorrelator.

Figure 2(a) and (b) show the pulse trains with repetition of 40GHz and 10GHz. The 10 GHz pulse train is mode locked at the drive frequency of the modulator and the 40 GHz pulse train is locked at 4 times the drive frequency. The harmonic mode-locking happens when the modulation frequency $f_m = Nf_{c1}$, where N is an integer, f_m is the modulation frequency provided by VCO, and f_{c1} the fundamental cavity round trip frequency for channel 1, (one of the lasing wavelengths). These quantities could be expressed as follows:

$$f_m = N f_{c1} = N \frac{c}{n_{eff} L_1} \quad (1)$$

Here c is the speed of light in vacuum, n_{eff} is the effective refractive index of the ring cavity and L_1 is the total length of the ring cavity. Since L_1 is more than 50 m, the fundamental cavity frequency f_{c1} is only several MHz.

Figure 2(b) shows the 10 GHz pulse train generated in channel 1, corresponding to the $\lambda_1 = 1546\text{nm}$. It shows a

pulse width of 8ps. For the second wavelength, the rational harmonic mode locking is observed when drive modulation frequency f_m is set at $(N+1/p)$ multiple of the cavity round trip time, i.e.

$$f_m = (N+1/p) \frac{c}{n_{eff} L_2} \quad (2)$$

Where p is integer and L_2 is the cavity length of corresponding to the second wavelength. Since f_m in equations (1)

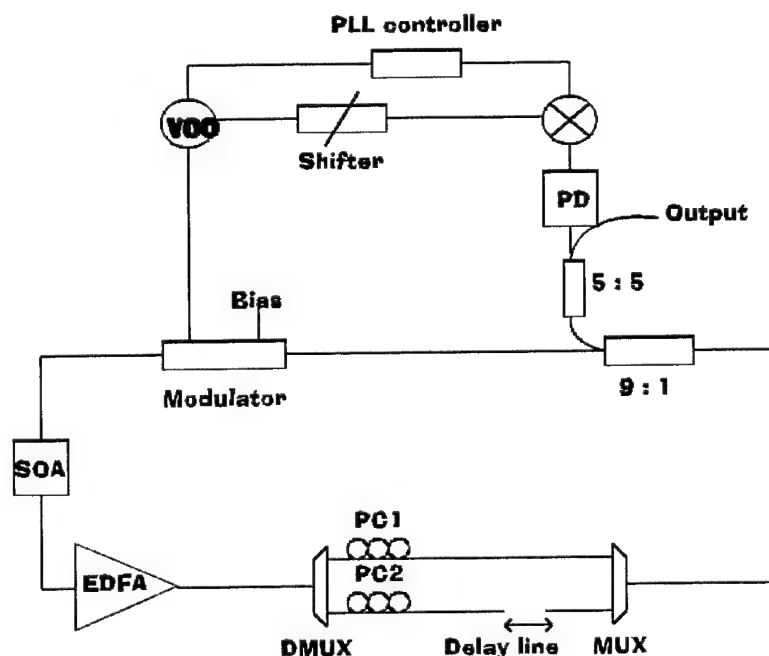


Fig. 1. Schematic of two-wavelength fiber ring laser.

and (2) are identical, L_2 should be adjusted (using the delay line) so that $p=4$ satisfies equation (2) for the second wavelength. Since the drive frequency is the same, from (1) and (2),

$$N \frac{c}{n_{eff} L_1} = (N+1/p) \frac{c}{n_{eff} L_2} \quad (3)$$

or

$$Np \Delta L = L_1 \quad (4)$$

where $\Delta L = L_2 - L_1$,

From (1), we have

$$\frac{L_1}{N} = \frac{c}{n_{eff} f_m} = 100 \text{ ps} \quad (5)$$

Using (4) and (5) for $p=4$,

$$\Delta L = \frac{L_1}{4N} = 25 \text{ ps} \quad (6)$$

Thus, the cavity length difference for the two wavelengths is ~ 25 ps. Figure 2(a) shows the 40 GHz pulse train observed by autocorrelator, the pulse width is ~ 5 ps.

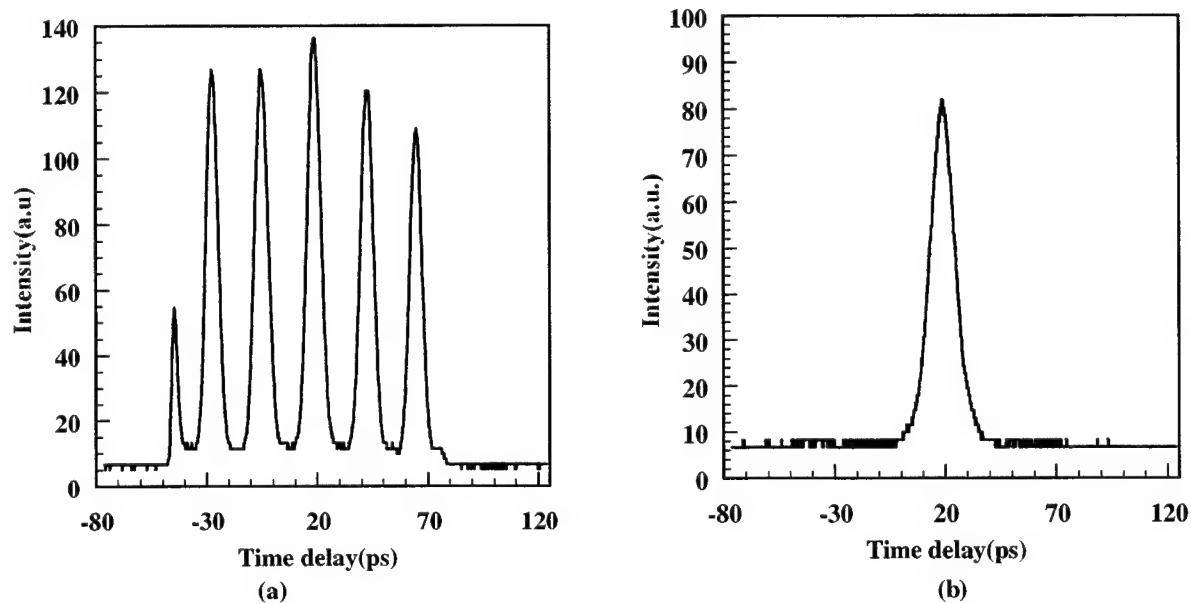


Fig.2. Pulse trains observed by autocorrelator. (a) 40GHz pulse train with pulse width of 5ps (b) 10GHz pulse train with pulse width of 8ps

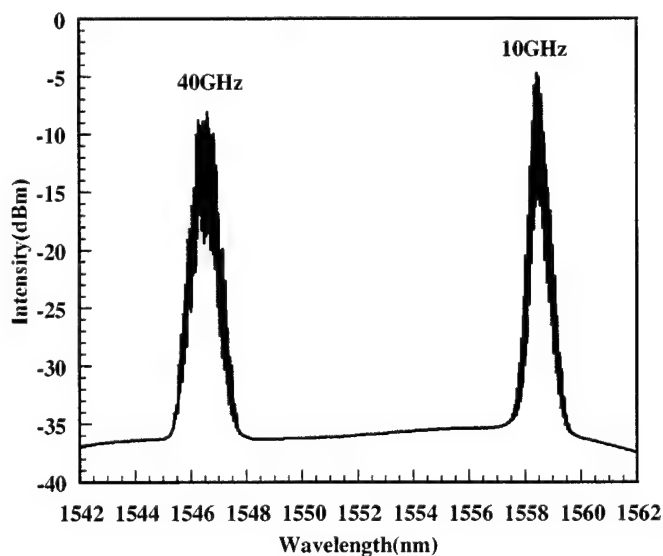


Fig.3. Spectrum of the pulses at wavelength of 1546 nm (40 GHz) and 1558nm (10 GHz) respectively

Figure 3 shows the optical spectrum of the pulses. The width of optical spectrum of 10 GHz pulse train is narrower than that of the 40GHz pulse train.

3. STABILIZATION

The stability of the pulse trains is important for practical applications. Generally, for the pulses generated by mode-locked operation from fiber lasers, two main factors contribute to the pulse instability: 1) Fluctuation of the cavity length due to mechanical vibrations or temperature fluctuations. 2) Competition between modes in the laser cavity.

As is known, for the harmonic mode locked fiber laser, 10GHz pulse train can be generated in the ring cavity configuration when the modulation frequency f_m is adjusted with high precision to nf_c , while 40GHz pulse train is generated when the modulation frequency f_m is adjusted with high precision to $(n+1/4)f_c$. Both sets of train are generated at two wavelengths at the same drive frequency (f_m) when the cavity round trip time for the two wavelengths differ by ~ 25 ps. However, due to the environmental influence, the cavity length may drift off the mode-locking conditions. For this reason, we introduce phase locked loop (PLL) in the cavity to maintain the mode locking condition. The key components of the PLL are a 10 GHz mixer, a phase locked loop controller and a voltage-controlled oscillator (VCO). The mixer detects the phase difference between the

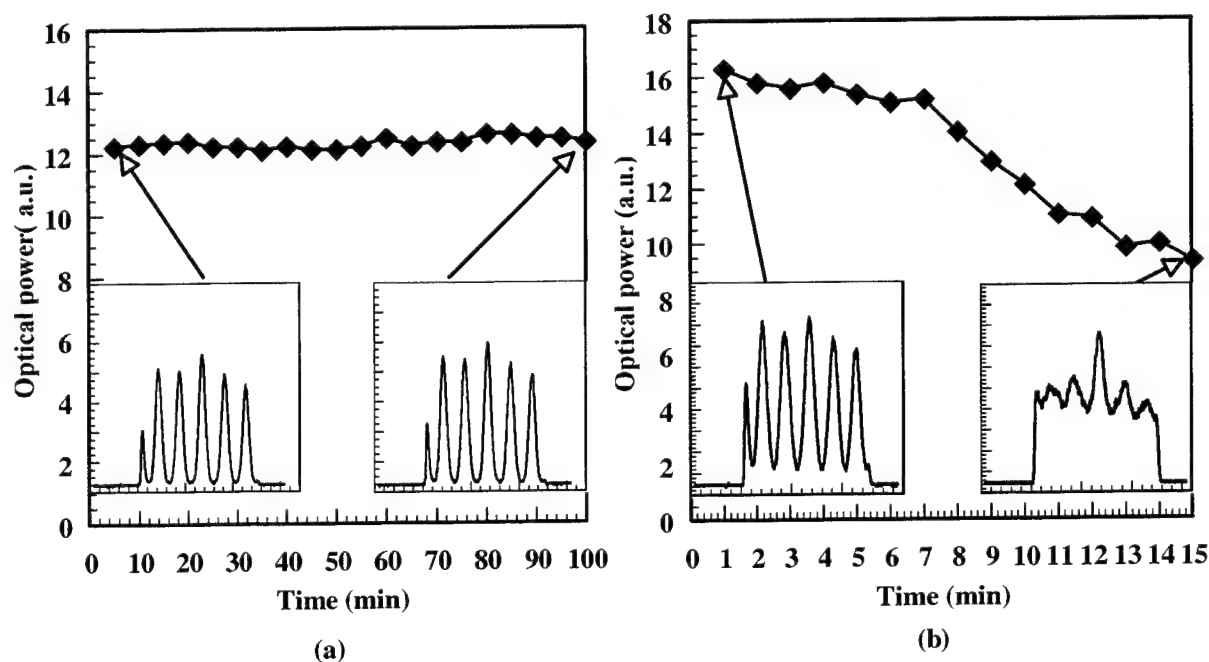


Fig.4. Stability of pulse train (a) intensity and pulse form of 40 GHz pulse train with SOA and PLL in the fiber ring. (b) Intensity and pulse form of 40 GHz pulse train without SOA and PLL in the fiber ring.

photodiode output and the VCO, the output of the mixer is then sent back to the PLL controller, which will have an output of $v_{bias} - \int v_{mixer} dt$. Thus through negative feedback, the circuit continuously adjusts the modulation frequency to the mode-locking frequency, assuring long-term stability of 10GHz pulse train in the operation.

As shown in the above section, the 10GHz and 40GHz pulse trains can be generated simultaneously only if we adjust the cavity length difference to 25ps. Therefore, to stabilize both sets of wavelength pulses, the drift of

cavity length difference must be minimized. To satisfy this requirement, we make the fiber lines between DMUX and MUX as short as possible.

The semiconductor optical amplifier (SOA) in the cavity reduces the instability due to mode-competition as observed previously⁴. In the two-wavelength mode-locking scheme, two pulses will compete for the available population inversion in the laser. Consequently, any oscillation of one pulse will possibly suppress another⁵. Pulses at two wavelengths can exist simultaneously at certain stable points, and the intensities of two pulses will reach equilibrium. However, any perturbation of intensity will break such equilibrium. The SOA is operated in a saturated regime that stabilizes any fluctuations.

Figure 4 shows the measurements of intensity of 40GHz pulse train vs. time. For the two cases: (i) PLL and SOA in the fiber laser configuration and (ii) without PLL and SOA. Stable performance is obtained with the phase locked loop and SOA in the cavity.

4. SUMMARY

We have demonstrated simultaneous stabilized operation of a mode locked ring fiber laser at two wavelengths. At one of the wavelengths the mode locked operation is at 10 GHz and it is at 40 GHz at the second wavelength. The laser has an intracavity LiNbO₃ modulator driven at 10 GHz. The 40 GHz pulses are obtained by rational harmonic mode locking. Pulses with widths in 5 to 8 ps range are obtained.

REFERENCES

1. Z. Ahned and N. Onodera, "High repetition rate optical pulse generation by frequency multiplication in actively mode-locked fiber ring lasers," *Electron. Lett.*, vol. 32, p. 455, 1996.
2. C. Wu and N. K. Dutta, "High-repetition-rate optical pulse generation using a rational harmonic mode-locked fiber laser", *IEEE J. Quant. Electron.*, vol. 36, No. 2, p. 145, 2000.
3. Z. Li et al., "A dual-wavelength and dual-repetition -rate actively mode-locked fiber ring laser," *Opt. Commun.* 185, p. 381-385, 2000.
4. H. Chen, G. Zhu, N. K. Dutta, "Suppression of Self-Pulsing Behavior in Erbium-Doped Fiber Lasers with a Semiconductor Optical Amplifier", *Applied Optics*, vol. 41, 3511-3516, 2002.
5. Anthony E. Siegman, *Lasers*, University Science Books, 1986.

Waveguide Optical polarization splitter using micropism consisting of dielectric multilayer

Kazutaka Baba^{*a}, Yoshiaki Sone^b, Mitsunobu Miyagi^b

^aSendai National College of Technology, ^bTohoku University, Sendai, JAPAN

ABSTRACT

A new type of waveguide optical polarization splitter is proposed and investigated theoretically. The waveguide optical polarization splitter is composed of a Y branch waveguide and a micropism consisting of a dielectric periodic multilayer. As the dielectric periodic multilayer has large birefringence, the TM (x) - and TE (y) - polarized propagating waves are refracted with different angle each other at the micropism. This is the principle of the proposed waveguide polarization splitter. First we have designed the waveguide polarization splitters. An asymmetric Y branch, in which one output port is a straight waveguide for an input waveguide and the other is an abruptly bending waveguide, is used for the design. The refractive indices of the core and cladding (substrate) are 1.51 and 1.509, respectively. The dielectric periodic multilayer for the micropism has been designed so as the effective refractive index for the x-polarization become equal to the refractive index of the substrate. Therefore the x-polarized wave propagates for the output port consisting of the straight waveguide with low loss. The prism has been designed by using the method for the microorism-type of bending waveguide proposed by C. T. Lee and J. M. Hsu so as the y-polarized wave can propagate for the port consisting the abruptly bending waveguide with low loss. Finally we have calculated optical losses for the x- and y-polarizations by using a beam propagating method. The insertion losses of the typically designed waveguide optical polarization splitter for the x- and y-polarizations are 0.14 dB and 0.2 dB, respectively. It has also been confirmed that the crosstalks are <-35 dB for both polarizations.

Keywords: Optical polarization splitter, dielectric periodic multilayer, micropism, integrated optics

1. INTRODUCTION

An optical polarization splitter is one of important devices for various optical systems. In "bulk" polarization splitters, the most typical one is a polarization beam splitter (PBS) cube based on the Brewster's angle. The PBS cube consists of dielectric multilayer sandwiched between two 45° glass prisms and is widely used for an optical pick-up system in an optical disc player. A crosstalk of the PBS cube is about -40 dB and insertion loss is negligibly low. As for "waveguide" polarization splitters for integrated optics, many types of splitter have been proposed and investigated¹⁻¹¹, although it seems that most splitters have not been used practically from any drawback. The waveguide polarization splitters would be classified into three groups, that is, 1) directional coupler-type¹⁻⁴, 2) interferometer-type⁵⁻⁶, and 3) Y branch-type⁷⁻¹¹ waveguide polarization splitters. As the directional coupler-type and interferometer-type waveguide polarization splitters are based on the polarization-dependent coupling properties and the polarization-dependent phase changes, respectively, the polarization splitting characteristics are sensitive to the waveguide parameters, including refractive indices of core and substrate, etc. Therefore, the fabricating tolerance is severe and some control means for the waveguide parameters are required. On the other hand, the Y branch-type

^{*} baba@cc.sendai-ct.ac.jp; phon: +81-22-391-5588; fax: +81-22-391-6144

waveguide polarization splitters are based on the polarization-dependent branching properties induced by the birefringence in LiNbO₃ waveguides⁷, semiconductor waveguides⁹, polymeric waveguides¹⁰⁻¹¹, and Langmuir-Blodgett cladding layer loaded on the core⁸. It seems that the Y branch-type waveguide polarization splitters are more useful for practical use as the fabricating tolerance is not severe.

In this paper, we propose a novel type of Y branch-type waveguide optical polarization splitter. In the proposed splitter, a microprism consisting of dielectric periodic multilayer with large birefringence is buried at the Y branch. In this work, we do not use the LiNbO₃ or semiconductor substrates with birefringence since we guess that those expensive substrates should be used for active optical devices. As the polarization splitter is just a passive optical device, we use glass substrate, which can be connected to optical fibers with low coupling loss. Therefore, the used Y branch waveguide does not have the polarization-dependent branching properties. The x- and y-polarized propagating waves are split by the polarization-dependent angle of refraction in the microprism, where polarizations normal and parallel to the surface of substrate are defined as x- and y-polarizations, respectively. In the conventional Y branch-type waveguide optical polarization splitters⁷⁻¹¹, a branching angle between two output waveguides is usually less than 0.5° as the insertion loss increases and the crosstalk decreases with the branching angle. However, in the Y branch type optical devices, large branching angle is strongly required in order to realize compact device size. In the proposed waveguide polarization splitter, the large branching angle of 9° can be realized as the microprism is used.

In this paper, first we describe the principle of the proposed waveguide polarization splitter. Next we design the waveguide optical polarization splitter consisting of an asymmetric Y branch, in which one output port is a straight waveguide for an input waveguide and the other is an abruptly bending waveguide. The prism has been designed so as the y-polarized wave propagates for the port consisting the abruptly bending waveguide with low loss by using the method proposed for a microprism-type bending waveguide by C. T. Lee and J. M. Hsu¹². Finally we have calculated optical losses for the x- and y-polarizations by using a 2-dimensional (2D) beam propagating method (BPM)¹³. The insertion losses of the typically designed waveguide optical polarization splitter for the x- and y-polarizations are 0.14 dB and 0.2 dB, respectively. It has also been confirmed that the crosstalks are <-35 dB.

2. PRINCIPLE

In this section we describe the principle of the proposed waveguide polarization splitter. Figure 1 shows the basic configuration of the waveguide polarization splitter to be investigated in this work. A rectangular core with cross section of $T \times T$ and refractive index n_g is formed at the surface of a glass substrate with refractive index n_s . We assume that a cover layer with thickness d_f and refractive index n_c is fabricated on the substrate since it is necessary to use the effective refractive index method for 2D BPM. The waveguide optical polarization splitter consists of an asymmetric Y branch, in which one output port is a straight waveguide for an input waveguide and the other is an abruptly bending waveguide. The branching angle between those output waveguides represents θ . At the Y branch, a microprism consisting of dielectric periodic multilayer is buried.

The periodic dielectric multilayer is one of artificial anisotropic media and exhibits large birefringence. Here, we consider the periodic multilayer consisting of ultra-thin layers of dielectric-1 with the refractive index n_1 and thickness d_1 and dielectric-2 with the refractive index n_2 and thickness d_2 . When those dielectric layers are thinner than wavelength λ , the effective refractive indices n_{px} and n_{py} of the periodic dielectric multilayer for the x- and y-polarizations are approximately expressed¹⁴ as

$$n_{px} = n_1 n_2 / \sqrt{q n_1^2 + (1-q) n_2^2} \quad (1)$$

$$n_{py} = \sqrt{(1-q) n_1^2 + q n_2^2} \quad (2)$$

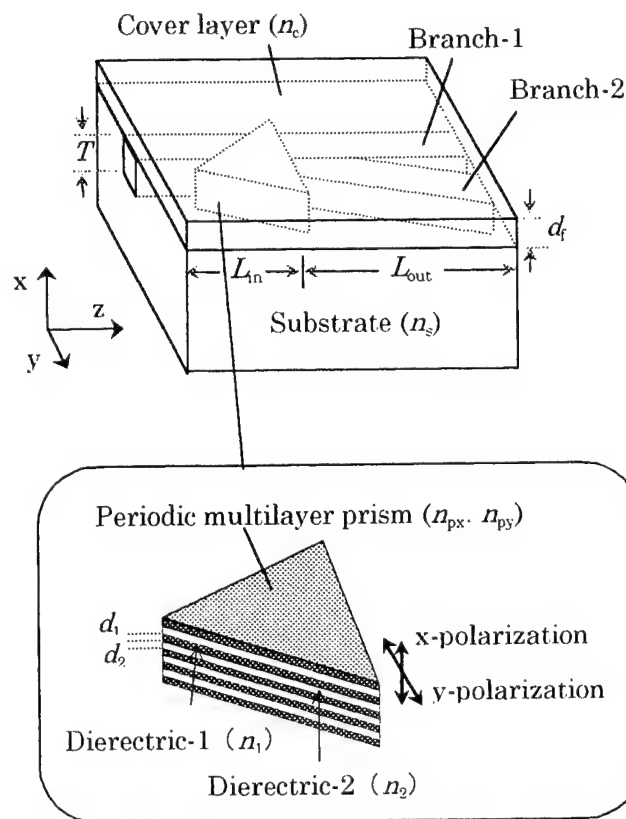


Fig.1 Configuration of waveguide polarization splitter using periodic dielectric multilayer.

where q is a fill fraction of dielectric-2 defined as

$$q = d_2 / (d_1 + d_2). \quad (3)$$

In the periodic dielectric multilayer, the effective refractive indices for both polarization is between the refractive index of dielectric-1 and that of dielectric-2. The theoretical effective refractive indices n_{px} and n_{py} of the periodic multilayer using alumina ($n_1=1.579^{15}$) and silica ($n_2=1.453^{15}$) are shown in Fig.2 as a function of q . It is confirmed that the effective refractive index for the x-polarization n_{px} is less than that for the y-polarization n_{py} .

The dielectric periodic multilayer for the microprism is designed so as the effective refractive index for the x-polarization become nearly equal to the refractive index of the substrate. As the angle of refraction for the x-polarization is very small in the microprism, the x-polarized light propagates for the output port consisting of the straight waveguide (branch-1) with low loss. The prism is designed so as the y-polarized wave can propagate for the port consisting the abruptly bending waveguide (branch-2). Therefore, in the designed waveguide polarization splitter, the x-polarized light comes out from the branch-1, while the y-polarized light exits from the branch-2. As the microprism is used, the large branching angle of 9° can be realized with low loss in comparison with conventional Y branch-type waveguide polarization splitter.

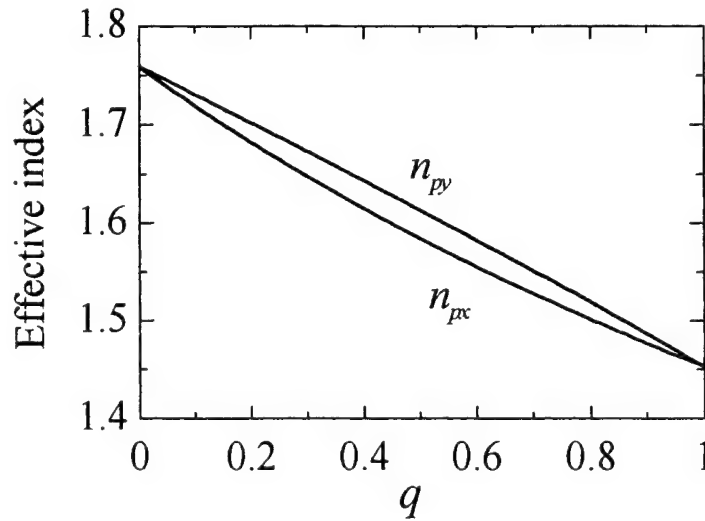


Fig.2 Calculated effective refractive index of an alumina-silica periodic multilayer at the wavelength of 850 nm as a function of fill fraction q of silica.

3.DESIGN

In this Section, we design the Y blanch-type waveguide polarization splitter for the wavelength of 850 nm. We chose BK7 glass, which had been often used for glass integrated optics, as a substrate. We assumed that the refractive index of the substrate n_s is 1.509, which is the refractive index of the BK7 glass at 850 nm. For the core, we assumed that the refractive index profile is step-index and the cross-section is rectangular for simplification. The refractive index of core n_g is 1.510 and the core size (width & depth) T is 5 μm so as to obtain the singlemode waveguide. We also assumed that the refractive index of cover layer n_c is assumed to be equal to that of the core (1.510) and the thickness layer d_f is 2 μm .

In this work, we use alumina-silica periodic multilayer for a microprism as the refractive index of the substrate n_s of 1.509 is between the refractive indices of dielectric materials consisting the periodic multilayer (alumina : 1.579 and silica : 1.453). As described in Sec.2, we design the periodic multilayer so as to obtain the effective refractive index for the x- polarization nearly equal to the refractive index of the substrate. As we describe in details in Sec.4, when $n_{px} = n_s$, insertion loss for the x-polarized light propagating for the output port consisting of the straight waveguide (blanch-1) becomes minimum as the angle of refraction for the x-polarization is very small in the microprism. From Eq.(1), it is derived that the condition $n_{px} = n_s$ ($=1.509$) is satisfied when q is 0.771. The effective refractive index for the y-polarization n_{py} of the alumina-silica periodic multilayer with $q = 0.771$ is calculated to be 1.529 from Eq.(2).

Finally, we design the microprism consisting of the alumina-silica periodic multilayer with $q = 0.771$ for the Y blanch waveguides with various blanching angles θ . The microprism is designed so as the y-polarized wave propagates for the port consisting the abruptly bending waveguide with low loss by using the method proposed for the microprism-type bending waveguide by C. T. Lee and J. M. Hsu¹². In this work, we apply this method to the Y blanch waveguide instead of the bending waveguide. We consider the structure of the waveguide polarization splitters schematically shown in Fig.3. In this method, the parameters for the size and position of microprism are W_a , W_p , and L_p , which are defined in Fig.3. Lee and Hsu proposed to evaluate these parameters from following equations¹²,

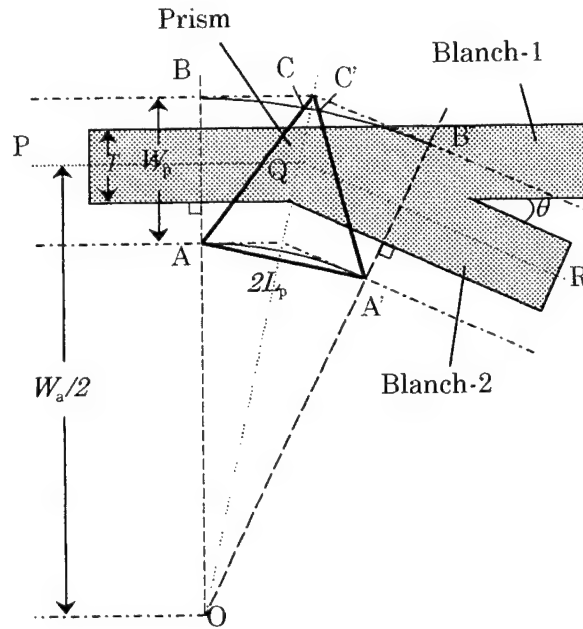


Fig. 3 Schematic views of the proposed Y branch polarization splitter for design of microprism.

$$W_p = 2 \left(T + \frac{2}{\sqrt{\beta^2 - k_0^2 n_s^2}} \right), \quad (4)$$

$$(n_{py} - n_s) \frac{(W_a - W_p)}{2} \left[\frac{\cos(\theta/2) - m \cos^2(\theta/2)}{1 - m \cos^2(\theta/2)} \right] = n_{eff} W_p, \quad (5)$$

$$L_p = \frac{W_a - W_p}{2} \sin(\theta/2), \quad (6)$$

$$\text{where } m = (W_a - W_p) / (W_a + W_p).$$

where $m = (W_a - W_p) / (W_a + W_p)$, k_0 is wave number of light in free space, β and n_{eff} represent the phase constant and effective refractive index of the waveguide, respectively.

4. THEORETICAL CHARACTERISTICS

To evaluate the theoretical characteristics of the designed Y branch waveguide polarization splitter, we calculated the field distributions in the waveguide polarization splitter for x- and y-polarizations by using a BPM¹³. For calculations, we used the commercially available BPM software provided by Optiwave Corporation. For simplification, we used 2D-BPM and calculate the effective refractive index of the slab structure in the x-direction for each part of the waveguide polarization splitter. We have assumed that the microprism is fully thick and the effective refractive indices for the x- and y-polarizations are equal to n_{px} and n_{py} , respectively. We have assumed that an incident wave on the input waveguide of the Y branch is a fundamental mode. The optical losses have been evaluated from the calculation of overlap integral between the field distributions of the fundamental mode and the propagated wave calculated by the BPM. We have assumed that the length between an input end of the splitter and the point Q defined in Fig.3 (i.e., the

starting point of Y branch) L_{in} is 0.5 mm and the length between the point Q and the output point of the branch-1 L_{out} is 4.5 mm.

We have designed the Y branch waveguide polarization splitters with various blanching angle θ between 1° and 10° by using Lee & Hsu' method. Figure 4 shows the calculated optical losses for the x-polarization in the branch-1 and for the y-polarization in the branch-2, which correspond to insertion losses of the waveguide polarization splitters, as a function of blanching angle. For the waveguide polarization splitters with the blanching angle between 2° and 7° , the insertion losses are less than 0.5dB for both polarizations. The insertion loss for the y-polarization in the branch-2 becomes greater with the blanching angle when $\theta > 8^\circ$. Figure 5 shows the calculated optical losses for the y-polarization in the branch-1 and for the x-polarization in the branch-2, which correspond to crosstalks of the waveguide polarization splitters, as a function of blanching angle. The crosstalks become smaller (that is, the losses for the polarizations to be extinct become larger) with the blanching angle. The blanching angle of $>5^\circ$ is required for the crosstalk less than -30 dB.

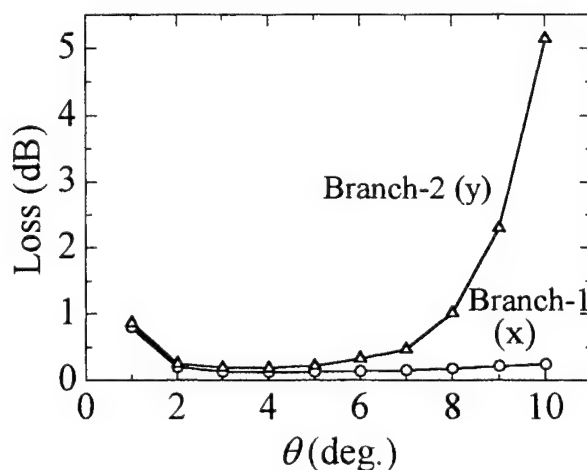


Fig.4 Calculated insertion losses (losses for the x-polarization in the branch-1 and for the y-polarization in the branch-2) of the designed waveguide polarization splitters as a function of blanching angle.

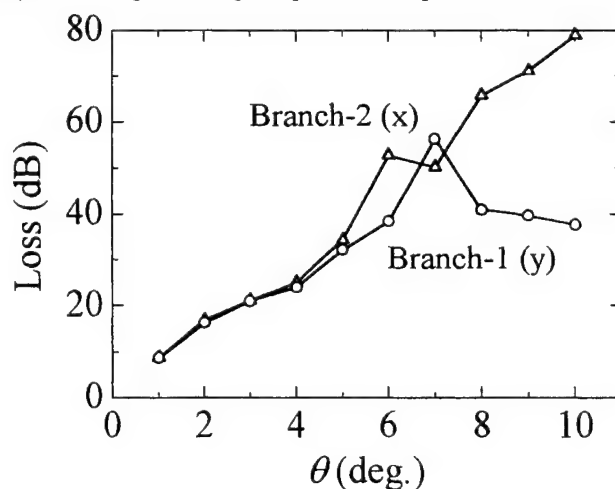


Figure 5 Calculated crosstalks (losses for the y-polarization in the branch-1 and for the x-polarization in the branch-2) of the waveguide polarization splitters as a function of blanching angle.

Next, to check the accuracy of the microprism design based on the Lee & Hsu's method, we calculated the insertion losses (that is, optical losses for the x-polarization in the branch-1 and for the y-polarization in the branch-2) for the waveguide polarization splitter using the microprism designed for the blanching angle of 10° as a function of θ . Figure 6 shows the calculated results. The insertion loss for the x-polarization in the branch-1 is slightly changed with the blanching angle. On the other hand, the insertion loss for the y-polarization in the branch-2 becomes minimum at the blanching angle of 9° . Therefore, it seems that any corrections for the design of the microprism is necessary to realize the waveguide polarization splitters with higher polarization-splitting characteristics. We guess that the cause of error in the design of the microprism is application of the design method for the bending waveguide to the design of the Y branch. Figure 7 shows the calculated insertion losses for the y-polarization in the branch-2 of the waveguide polarization splitters with optimized blanching angle as a function of θ . It is seen that the insertion losses greatly decrease in the waveguide polarization splitters with large blanching angle by the optimization.

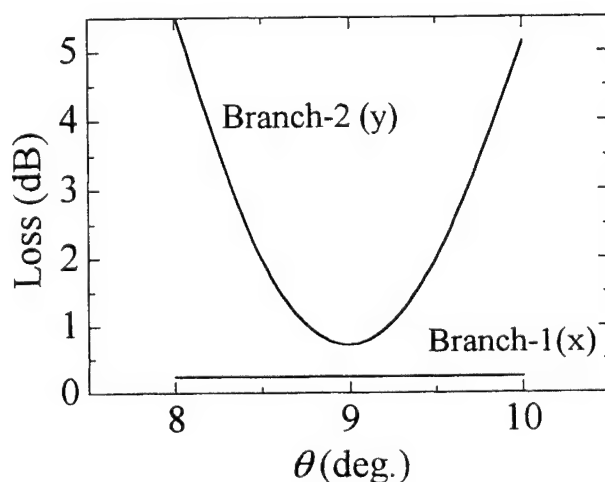


Fig.6 Calculated insertion losses (optical losses for the x-polarization in the branch-1 and for the y-polarization in the branch-2) for the waveguide polarization splitter using the microprism designed for the blanching angle of 10° as a function of blanching angle.

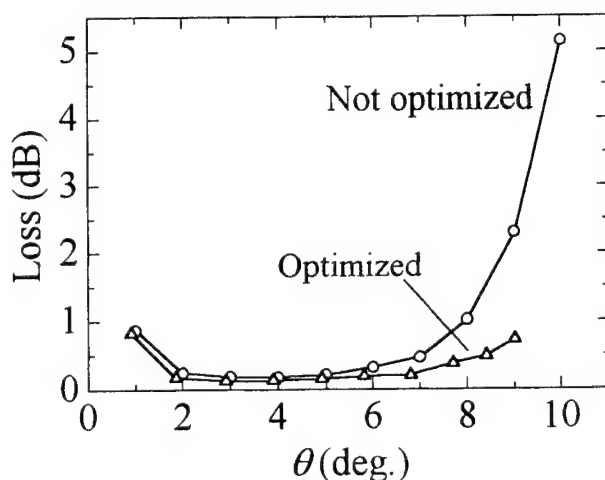


Fig.7 Calculated insertion losses for the y-polarization in the branch-2 of the waveguide polarization splitters with optimized blanching angle.

Next, we describe the optimum effective refractive index of periodic dielectric multilayer for the microprism for the x-polarization n_{px} . Figure 8 shows the insertion losses for the x-polarization in blanch-1 in the waveguide polarization splitters design for the blanching angle of 5° and 10° as a function of n_{px} . In both waveguide polarization splitters, the insertion loss becomes minimum when n_{px} is 1.509 equal to the refractive index of the substrate. It is also seen that the insertion loss of the waveguide polarization splitter with large blanching angle is drastically changed with n_{px} . Figure 9 shows the optical losses for the x-polarization in blanch-2, corresponding to the crosstalk, in the waveguide polarization splitters design for the blanching angle of 5° and 10° as a function of n_{px} . From this figure, it is seen that the crosstalk is slightly depend on n_{px} and smaller than -30 dB. Therefore, we can conclude the optimum effective refractive index of periodic dielectric multilayer for the x-polarization n_{px} is equal to the refractive index of the substrate n_s .

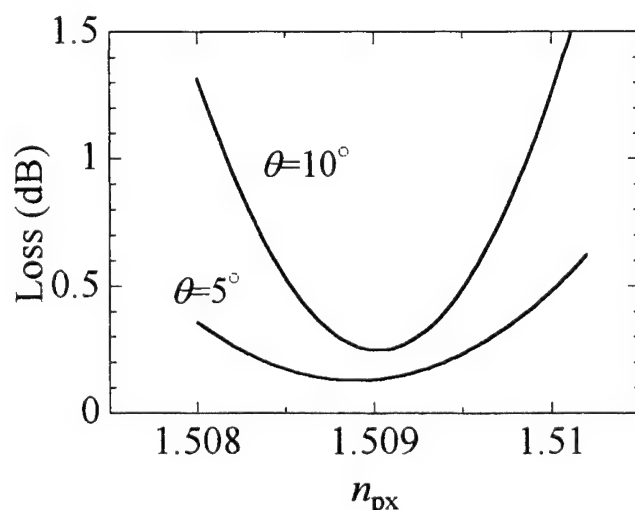


Fig.8 Insertion losses for the x-polarization in blanch-1 in the waveguide polarization splitters design for the blanching angle of 5° and 10° as a function of n_{px} .

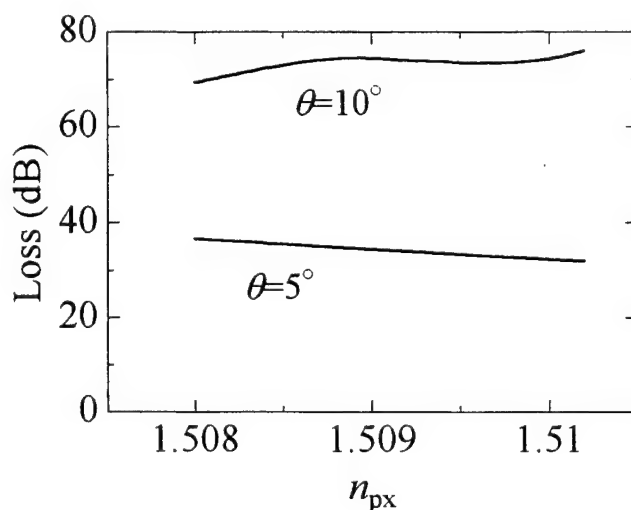


Fig.9 Optical losses for the x-polarization in blanch-2, corresponding to the crosstalk, in the waveguide polarization splitters design for the blanching angle of 5° and 10° as a function of n_{px} .

Finally, we show the structural parameters and optical characteristics of typically designed Y branch waveguide polarization splitter. For the waveguide polarization splitter with the blanching angle with 5.8° , the most optimum structural parameters are as follows; for the alumina-silica periodic multilayer, the fill fraction q of 0.771 ($n_{px}=1.509$ and $n_{py}=1.529$), for the microprism, W_a of 6.86 mm, W_p of $40.3 \mu\text{m}$ and L_p of $172 \mu\text{m}$, respectively. As summarized in Table 1, the optical losses are 0.14 dB for the x-polarization in the branch-1 and 0.20 dB for the y-polarization in the branch-2, which correspond to insertion losses. For the crosstalks, the optical losses are 50 dB for the x-polarization in the branch-2 and 38 dB for the y-polarization in the branch-1. In addition, we also show the field distributions in the designed waveguide polarization splitter in Fig. 10.

Table 1 Optical losses of the typically designed waveguide polarization splitter with the blanching angle with 5.8° .

Polarization	Loss (dB)	
	Branch-1	Branch-2
x	0.14	50
y	38	0.20

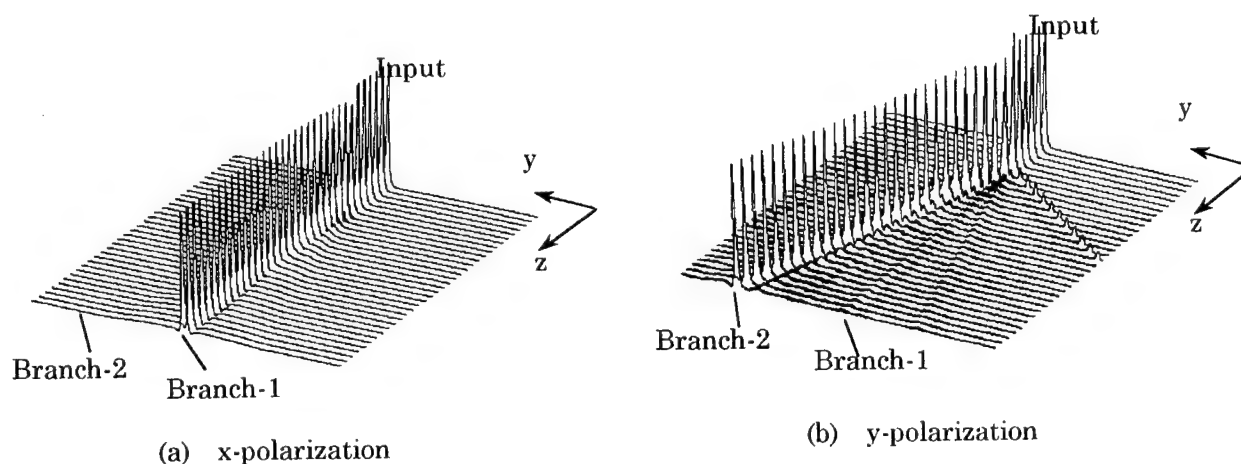


Fig.10 Field distributions in the designed waveguide polarization splitter calculated 2D BPM.

5. CONCLUSION

We have proposed and theoretically investigated a new type of waveguide optical polarization splitter. The waveguide optical polarization splitter is composed of Y branch waveguide and a microprism consisting of dielectric periodic multilayer. As the dielectric periodic multilayer has large birefringence, the x- and y-polarized propagating waves are refracted with different angle at the microprism. An asymmetric Y branch, in which one output port is a straight waveguide for an input waveguide and the other is an abruptly bending waveguide, is used for the design. In the waveguide, the refractive indexes of the core and substrate (cladding) are 1.51 and 1.509, respectively. The

dielectric periodic multilayer for the microprism has been designed so as the effective refractive index for the x-polarization become equal to the refractive index of the substrate. Therefore the x-polarized wave propagates for the output port consisting of the straight waveguide with low loss. The prism has been also designed by using the method for the microprism-type of bending waveguide proposed by C. T. Lee and J. M. Hsu so as the y-polarized wave propagates for the port consisting the abruptly bending waveguide with low loss. The insertion losses of the typically designed waveguide optical polarization splitter with the blanching angle of 5.8° for the x- and y-polarizations are 0.14 dB and 0.2 dB, respectively. It has also been confirmed that the crosstalks are <-35 dB.

ACKNOWLEDGEMENTS

This research has been supported by a Scientific Research Grant-in-Aid (14550341) from the ministry of Education, Science, Sports, and Culture of Japan.

REFERENCES

1. O. Mikami, "LiNbO₃ coupled-waveguided TE/TM mode splitter," *Appl. Phys. Lett.* **36**, pp. 491-493, 1980.
2. P. Albrecht, M. Hamacher, H. Heidrich, D. Hoffmann, H. P. Nolting, C. M. Weinert, "TE/TM mode splitters on InGaAsP/InP," *IEEE Photo. Technol. Lett.* **2**, pp. 114-115, 1990.
3. A. N. Miliou, R. Srivastava, R. V. Ramaswamy, "A 1.3- μ m directional coupler polarization splitter by ion exchange," *J. Lightwave Technol.* **11**, pp. 220-225, 1993.
4. M. Okuno, A. Sugita, K. Jinguji, M. Kawachi, "Birefringence control of silica waveguide on Si and its application to polarization-beam splitter/switch," *J. Lightwave Technol.* **12**, pp. 625-633, 1994.
5. D. Yap, L. M. Johnson, G. W. Pratt, Jr, "Passive Ti:LiNbO₃ channel waveguide TE-TM mode splitter," *Appl. Phys. Lett.* **44**, pp. 583-585, 1984.
6. A. Neyer, "Low-crosstalk passive polarization splitters using Ti:LiNbO₃ waveguide crossings," *Appl. Phys. Lett.* **55**, pp. 927-929, 1989.
7. N. Goto, G. L. Yip, "A TE-TM mode splitter in LiNbO₃ by proton exchange and Ti diffusion," *J. Lightwave Technol.* **7**, pp. 1567-1574, 1989.
8. T. Mizumoto, N. Iwakiri, T. Kaneko, Y. Naito, "Analytical and experimental study of waveguide optical polarization splitter with Langmuir-Blodgett cladding layer," *J. Lightwave Technol.* **12**, pp. 1807-1813, 1992.
9. Y. Suzuki, H. Iwamura, T. Miyazawa, and O. Mikami, "A novel waveguide polarization mode splitter using refractive index changes induced by superlattice disordering," *IEEE J. Quantum Electron.* **30**, pp. 1794-1800, 1994.
10. M. Oh, M. Lee, H. Lee, "Polymeric waveguide polarization splitter with a buried birefringent polymer," *IEEE Photo. Technol. Lett.* **11**, pp. 1144-1146, 1999.
11. S. Garner, V. Chuyanov, S. Lee, A. Chen, W. H. Steier, L. R. Dalton, "Vertically integrated waveguide polarization splitters using polymer," *IEEE Photo. Technol. Lett.* **11**, pp. 842-844, 1999.
12. C. T. Lee and J. M. Hsu, "Systematic design of microprism-type low-loss step-index bent waveguide," *Appl. Opt.* **37**, pp. 3948-3953, 1998.
13. For example, P. Liu, B. Li, "Semivectorial beam-propagation method for analyzing polarized modes of rib waveguide," *IEEE J. Quantum Electron.* **28**, pp. 778-781, 1992.
14. M. Born, E. Wolf, *Principles of Optics*, 5th ed., Pergamon, Oxford, 1975.
15. E. D. Parik, *Handbook of Optical Constants of Solids*, Academic, Orlando, 1985.

Split step non-paraxial beam propagation method

Anurag Sharma and Arti Agrawal

Department of Physics, Indian Institute of Technology Delhi, New Delhi, India 110016

ABSTRACT

A new method for solving the wave equation is presented, which, being non-paraxial, is applicable to wide-angle beam propagation. It shows very good stability characteristics in the sense that relatively larger step-sizes can be used. It is both faster and easier to implement. The method is based on symmetrized splitting of operators, one representing the propagation through a uniform medium and the other, the effect of the refractive index variation of the guiding structure. The method can be implemented in the FD-BPM, FFT-BPM and collocation schemes. The method is stable for a step size of 1 micron in a graded index waveguide with accuracy better than 0.001 in the field overlap integral for 1000-micron propagation. At a tilt angle of 50° , the method shows an error less than 0.001 with 0.25-micron step. In the benchmark test, the present method shows a relative power of ~ 0.96 in a 100 micron long waveguide with 1000 propagation steps and 800 sample points, while FD-BPM with Padé(2,2) approximation gives a relative power of 0.95 with 1000 sample points and 2048 propagation steps. Thus, the method requires fewer points, is easier to implement, faster, more accurate and highly stable.

Keywords: BPM-Beam Propagation Method. Padé approximant. collocation, wide-angle propagation.

1. INTRODUCTION

Non-paraxial beam propagation techniques have become very important in modeling of optical waveguides and photonic devices as these lead to more accurate modeling of beams propagating at large angles with respect to the direction of propagation, and are capable of handling large changes in the refractive index. Some wide-angle schemes are capable of handling reflections and bi-directional propagation as well.¹⁻¹³ Non-paraxial propagation involves solution of the wave equation, which contains a second order partial derivative with z (the general direction of propagation) as against the first order partial derivative in the paraxial wave equation. Most methods for non-paraxial beam propagation discussed in the literature approach this problem iteratively, in which a numerical effort equivalent to solving the paraxial equation several times is involved. The actual number of iterations depends on the desired accuracy and the obliquity of the beam. Many of these methods neglect the backward propagating components and solve the one-way wave equation; but even methods that deal with bi-directional propagation employ special techniques either to suppress or to model evanescent modes, which are a source of instability in these methods.⁸⁻¹⁰ In all these methods, the square root of the propagation operator involved in the wave equation is approximated in various ways. One of the approximations used is based on the Padé approximants.¹⁻¹¹ In some recent results, we have shown that a direct numerical solution (DNS) of the scalar wave equation gives very good accuracy and is also numerically efficient.¹⁴ The method is non-paraxial and hence, is applicable to wide-angle as well as to bi-directional propagation. We used the collocation method¹⁵⁻¹⁷ to formulate our equations. Here, we present a new method to solve the non-paraxial wave equation using symmetrized splitting of the operators. Examples show that this method is more tolerant to larger step sizes than other methods including the DNS.¹⁴

2. THEORY

2.1 Mathematical Outline

In this section we present the mathematical outline of the technique and its implementation. We discuss here the solution of the two-dimensional scalar wave equation which can be represented by the Helmholtz equation:

$$\frac{\partial^2 \psi}{\partial x^2} + \frac{\partial^2 \psi}{\partial z^2} + k_0^2 n^2(x, z) \psi(x, z) = 0, \quad (1)$$

where $\psi(x, z)$ represents one of the Cartesian components of the electric field (generally referred to as the scalar field) and $n^2(x, z)$ defines the refractive index distribution of the medium. The time dependence of the field has been assumed to be $e^{i\omega t}$ and $k_0 = \omega/c$ is the free space wave number.

Equation 1 can be rewritten as

$$\frac{\partial \Phi}{\partial z} = \mathbf{H}(z) \Phi(z), \quad (2)$$

where

$$\Phi(z) = \begin{bmatrix} \psi \\ \frac{\partial \psi}{\partial z} \end{bmatrix}, \quad \mathbf{H}(z) = \begin{bmatrix} 0 & 1 \\ -\nabla_r^2 - k_0^2 n^2 & 0 \end{bmatrix}. \quad (3)$$

The operator \mathbf{H} can be written as a sum of two operators, one representing the propagation through a uniform medium of index, say n_r , and the other representing the effect of the index variation of the guiding structure; thus,

$$\mathbf{H}(z) = \mathbf{H}_1 + \mathbf{H}_2(z) \quad (4)$$

$$= \begin{bmatrix} 0 & 1 \\ -\nabla_r^2 - k_0^2 n_r^2 & 0 \end{bmatrix} + \begin{bmatrix} 0 & 0 \\ k_0^2 (n_r^2 - n^2) & 0 \end{bmatrix}$$

A formal solution of Eq. 2, after using the symmetrized splitting of summation of operators as in Eq. 4, can be written as

$$\Phi(z + \Delta z) = \mathbf{P} \mathbf{Q}(z) \mathbf{P} \Phi(z) + O((\Delta z)^3) \quad (5)$$

$$\mathbf{P} = e^{\frac{1}{2} \mathbf{H}_1 \Delta z}, \quad \mathbf{Q}(z) = e^{\mathbf{H}_2 \Delta z}. \quad (6)$$

The operator \mathbf{P} represents propagation in the uniform medium n_r over a distance of $\Delta z/2$, and hence, can be evaluated using any method like the collocation, finite-difference or FFT methods. The operator $\mathbf{Q}(z)$ can also be easily evaluated due to the specific form of the matrix and it can be easily seen that

$$\mathbf{Q}(z) = \begin{bmatrix} 1 & 0 \\ k_0^2 (n_r^2 - n^2) \Delta z & 1 \end{bmatrix}, \quad (7)$$

since,

$$(\mathbf{H}_2)^m = \mathbf{0}, \quad m \geq 2 \quad (8)$$

due to the special form of the matrix \mathbf{H}_2 . It may be noted that for lossless propagation the matrix \mathbf{P} would be Hermitian, while the matrix \mathbf{Q} always has a determinant value equal to unity. We discuss below the implementation of this procedure in the collocation method.

In the collocation method, the wave equation is converted to a matrix ordinary differential equation using the representation of the field $\psi(x, z)$ as a linear combination of a set of orthogonal basis functions, $\phi_n(x)$:

$$\psi(x, z) = \sum_{n=1}^N c_n(z) \phi_n(x) \quad (9)$$

where $c_n(z)$ are the expansion coefficients, n is the order of the basis functions and N is the number of basis functions used in the expansion. The choice of $\phi_n(x)$ depends on the boundary conditions and the symmetry of the guiding structure. The coefficients of expansion, $c_n(z)$, are unknown and represent the variation of the field with z . In the collocation method,¹⁵⁻¹⁷ these coefficients are effectively obtained by requiring that the differential equation, Eq. 1, be satisfied *exactly* by the expansion, Eq. 9, at N collocation points $x_j, j = 1, 2, \dots, N$, which are chosen such that these are the zeroes of $\phi_{N+1}(x)$. Thus, using this condition and with some algebraic manipulations,¹⁵⁻¹⁷ one converts the wave equation, Eq. 1, into a matrix ordinary differential equation:

$$\frac{d^2 \Psi}{dz^2} + [S_0 + k_0^2 n_r^2 \mathbf{I} + \mathbf{R}(z)] \Psi(z) = 0 \quad (10)$$

with

$$\Psi(z) = \begin{bmatrix} \psi(x_1, z) \\ \psi(x_2, z) \\ \vdots \\ \psi(x_N, z) \end{bmatrix}, \quad \mathbf{R}(z) = k_0^2 \begin{bmatrix} \Delta n^2(x_1, z) & 0 & \cdot & 0 \\ 0 & \Delta n^2(x_2, z) & \cdot & \cdot \\ \cdot & \cdot & \cdot & 0 \\ 0 & \cdot & 0 & \Delta n^2(x_N, z) \end{bmatrix}, \quad (11)$$

where $\Delta n^2(x_m, z) = n^2(x_m, z) - n_r^2$, $m = 1, 2, \dots, N$, and S_0 is a constant known matrix defined by the basis functions.¹⁵⁻¹⁷ We refer to Eq. 10 as the *collocation equation*. In deriving this equation from the wave equation, Eq. 1, no approximation has been made except that N is finite and Eq. 10 is exactly equivalent to Eq. 1 as $N \rightarrow \infty$. Thus, the accuracy of the collocation method improves indefinitely as N increases. The collocation equation is a matrix ordinary differential equation and can be solved as an initial value problem using any standard method such as the Runge-Kutta method as we have done in the DNS.¹⁴ Here we solve this equation using the split step procedure.

We have chosen here a set of sinusoidal functions as the basis functions^{16,17} and following the symmetrized splitting of operators procedure, we obtain the formal solution of Eq. 10 as in Eq. 5, with the operators \mathbf{P} and \mathbf{Q} , and the field function Φ now being block matrices:

$$\Phi(z) = \begin{bmatrix} \Psi \\ \frac{d\Psi}{dz} \end{bmatrix}, \quad \mathbf{P} = \exp \left\{ \frac{\Delta z}{2} \begin{bmatrix} \mathbf{0} & \mathbf{I} \\ -(\mathbf{S}_0 + k_0^2 n_r^2 \mathbf{I}) & \mathbf{0} \end{bmatrix} \right\}, \quad \mathbf{Q}(z) = \begin{bmatrix} \mathbf{I} & \mathbf{0} \\ -\mathbf{R}(z) & \mathbf{I} \end{bmatrix}, \quad (12)$$

where \mathbf{I} and $\mathbf{0}$ the unit and null matrices, respectively. The operator \mathbf{P} represents propagation in uniform medium of index n_r over a distance of $\Delta z/2$ and can be easily obtained as a constant square matrix using the basis functions and their properties.¹⁷ \mathbf{P} has to be evaluated only once. Each propagation step thus requires only simple matrix multiplications. A further advantage in using the sinusoidal basis functions in the collocation method is that no FFT, matrix inversion or matrix diagonalization need be done for propagation through uniform medium and all matrices involved are obtained analytically; the details are given in the section below.

2.2 Evaluation of \mathbf{P}

The operator \mathbf{P} amounts to a solution of the collocation equation, Eq. 10, without the $\mathbf{R}(z)$ term, i.e., propagation in a medium of uniform refractive index, n_r , over a distance of Δz . That is, solution of the equation:

$$\frac{d^2 \Psi}{dz^2} + \mathbf{S} \Psi(z) = 0 \quad (13)$$

where $\mathbf{S} = \mathbf{S}_0 + k_0^2 n_r^2 \mathbf{I}$ is a constant matrix. Equation 13 can also be written as

$$\frac{\partial \Phi}{\partial z} = \mathbf{H}_1 \Phi(z) \quad (14)$$

where $\Phi(z)$ is defined in Eq. 12, and

$$\mathbf{H}_1 = \begin{bmatrix} \mathbf{0} & \mathbf{I} \\ -\mathbf{S} & \mathbf{0} \end{bmatrix}$$

is a constant matrix and has to be evaluated just once. A formal solution Eq. (14) can be written:

$$\Phi(z + \Delta z) = e^{\mathbf{H}_1 \Delta z} \Phi(z). \quad (15)$$

The evaluation of $e^{\mathbf{H}_1 \Delta z}$ can be done by diagonalization of \mathbf{H}_1 which may involve complex matrix algebra. A simpler and more elegant method is by eigenvalue decomposition utilizing the special properties of the sinusoidal basis functions.

As Eq. 13 represents propagation in a uniform medium, the propagation can be obtained by eigenvalue decomposition method. Thus, the solution of Eq. 13 over a single step can be written as

$$\Psi(z + \Delta z) = \cos(\sqrt{\mathbf{S}} \Delta z) \Psi(z) + \frac{1}{\sqrt{\mathbf{S}}} \sin(\sqrt{\mathbf{S}} \Delta z) \Psi'(z) \quad (16)$$

$$\Psi'(z + \Delta z) = -\sqrt{\mathbf{S}} \sin(\sqrt{\mathbf{S}} \Delta z) \Psi(z) + \cos(\sqrt{\mathbf{S}} \Delta z) \Psi'(z). \quad (17)$$

Using this solution in Eq. 15 gives

$$e^{\mathbf{H}_1 \Delta z} = \begin{pmatrix} \cos(\sqrt{\mathbf{S}} \Delta z) & \frac{1}{\sqrt{\mathbf{S}}} \sin(\sqrt{\mathbf{S}} \Delta z) \\ -\sqrt{\mathbf{S}} \sin(\sqrt{\mathbf{S}} \Delta z) & \cos(\sqrt{\mathbf{S}} \Delta z) \end{pmatrix} \quad (18)$$

In order to evaluate the functions of the matrices involved in Eq. 18, we use the diagonalization procedure. Thus, let $\mathbf{S} = \mathbf{V} \mathbf{\Lambda} \mathbf{V}^{-1}$ where \mathbf{V} and $\mathbf{\Lambda}$ are the eigenvectors and eigenvalues of \mathbf{S} , respectively. Then, we have

$$\sqrt{\mathbf{S}} \Delta z = \mathbf{V} (\sqrt{\mathbf{\Lambda}} \Delta z) \mathbf{V}^{-1} \quad \text{with} \quad \sqrt{\mathbf{\Lambda}} = \text{diag}(\sqrt{\lambda_i}), \quad (19)$$

and

$$\cos(\sqrt{\mathbf{S}} \Delta z) = \mathbf{V} \cos(\sqrt{\mathbf{\Lambda}} \Delta z) \mathbf{V}^{-1} \quad (20)$$

$$\sin(\sqrt{\mathbf{S}} \Delta z) = \mathbf{V} \sin(\sqrt{\mathbf{\Lambda}} \Delta z) \mathbf{V}^{-1} \quad (21)$$

Thus

$$e^{\mathbf{H}_1 \Delta z} = \begin{pmatrix} \mathbf{V} & 0 \\ 0 & \mathbf{V} \end{pmatrix} \begin{bmatrix} \cos(\sqrt{\Lambda} \Delta z) & \frac{1}{\sqrt{\Lambda}} \sin(\sqrt{\Lambda} \Delta z) \\ -\sqrt{\Lambda} \sin(\sqrt{\Lambda} \Delta z) & \cos(\sqrt{\Lambda} \Delta z) \end{bmatrix} \begin{pmatrix} \mathbf{V}^{-1} & 0 \\ 0 & \mathbf{V}^{-1} \end{pmatrix}. \quad (22)$$

The operator \mathbf{P} in Eq. 12 is thus given by Eq. 22 with Δz replaced by $\Delta z/2$.

In the case of sinusoidal basis functions in the collocation method,¹⁶ the form of \mathbf{S} is such that the eigenvalue decomposition required as per Eq. 19 is simply done analytically. In this case, we choose the basis functions as

$$\begin{aligned} \phi_n(x) &= \cos(v_n x) & \text{for } n = 1, 3, 5, \dots, N-1 \\ &= \sin(v_n x) & \text{for } n = 2, 4, 6, \dots, N \end{aligned} \quad (23)$$

where $v_n = n\pi/2L$, with computation window being from $-L$ to L . The collocation points are at

$$x_j = \left(\frac{2j}{N+1} - 1 \right) L, \quad j = 1, 2, 3, \dots, N. \quad (24)$$

The matrix \mathbf{S} in this case is then given by^{16,17}

$$\mathbf{S} = \mathbf{A} \mathbf{G} \mathbf{A}^{-1} + k_o^2 n_r^2 \mathbf{I} = \mathbf{A} (\mathbf{G} + k_o^2 n_r^2 \mathbf{I}) \mathbf{A}^{-1} \quad (25)$$

where \mathbf{A} is a constant square matrix with elements as $A_{ij} = \phi_j(x_i)$ and the matrix \mathbf{G} is given by

$$\mathbf{G} = \text{diag.} (v_1^2 \quad v_2^2 \quad v_3^2 \cdots v_N^2). \quad (26)$$

Thus, we have

$$\mathbf{V} = \mathbf{A} \quad \text{and} \quad A_i = k_o^2 n_r^2 v_i^2 \quad (27)$$

Further, it can be shown that

$$\mathbf{V}^{-1} = \mathbf{A}^{-1} = \left(\frac{2}{N+1} \right) \mathbf{A}^T \quad (28)$$

Thus, no matrix eigenvalue equation need be solved. With these values of \mathbf{V} and \mathbf{A} , one obtains from Eq. 22:

$$e^{\mathbf{H}_1 \Delta z} = \left(\frac{2}{N+1} \right) \begin{pmatrix} \mathbf{A} & 0 \\ 0 & \mathbf{A} \end{pmatrix} \begin{bmatrix} c_1 & 0 & \cdots & 0 & s_1 & 0 & \cdots & 0 \\ 0 & c_2 & \cdots & 0 & 0 & s_2 & \cdots & 0 \\ \vdots & \vdots & \ddots & \vdots & \vdots & \vdots & \ddots & \vdots \\ 0 & 0 & \cdots & c_N & 0 & 0 & \cdots & s_N \\ \tilde{s}_1 & 0 & \cdots & 0 & c_1 & 0 & \cdots & 0 \\ 0 & \tilde{s}_2 & \cdots & 0 & 0 & c_2 & \cdots & 0 \\ \vdots & \vdots & \ddots & \vdots & \vdots & \vdots & \ddots & \vdots \\ 0 & 0 & \cdots & \tilde{s}_N & 0 & 0 & \cdots & c_N \end{bmatrix} \begin{pmatrix} \mathbf{A}^T & 0 \\ 0 & \mathbf{A}^T \end{pmatrix} \quad (29)$$

where

$$c_i = \cos(\sqrt{A_i} \Delta z), \quad s_i = \frac{1}{\sqrt{A_i}} \sin(\sqrt{A_i} \Delta z) \quad \text{and} \quad \tilde{s}_i = -\sqrt{A_i} \sin(\sqrt{A_i} \Delta z).$$

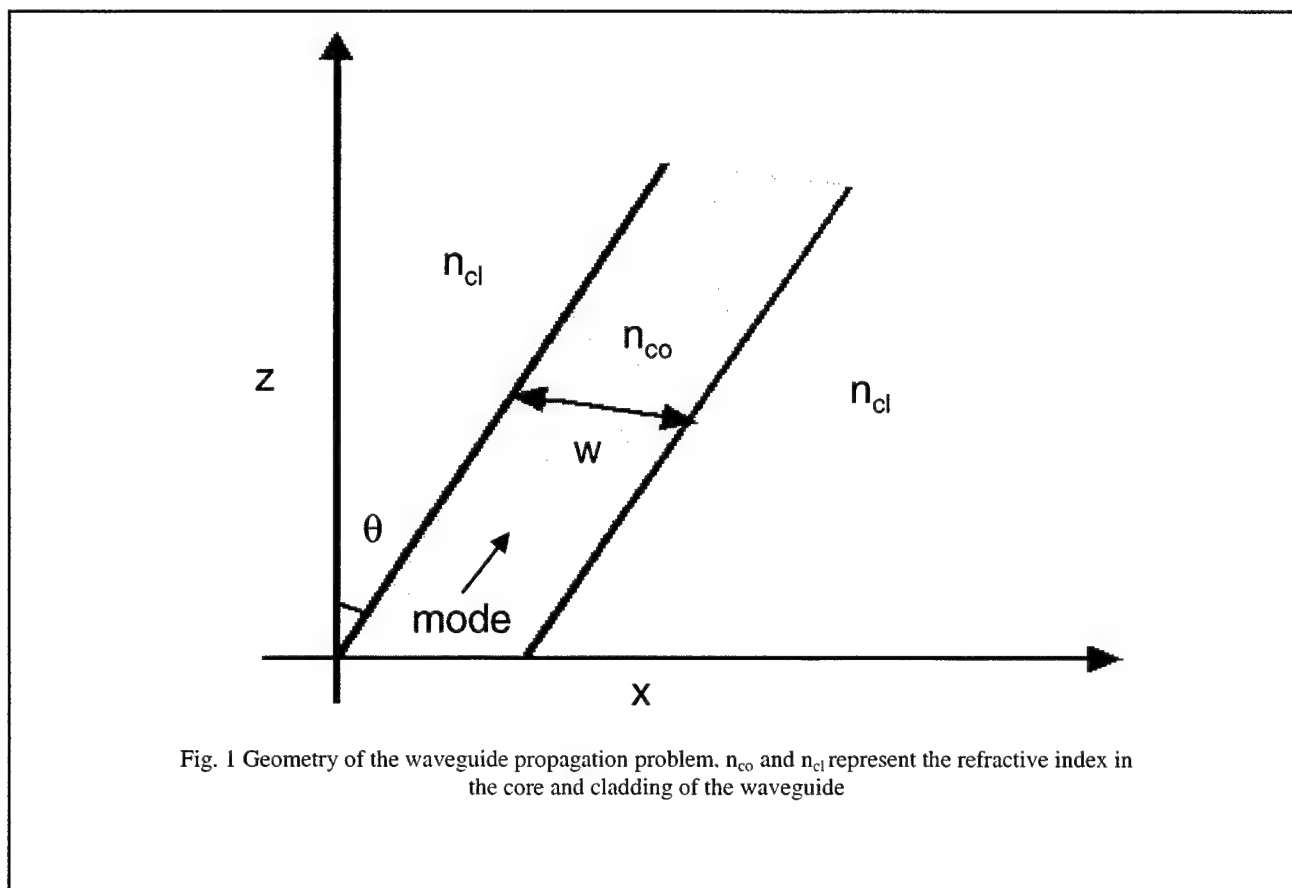
In cases, where A_i is imaginary [see Eq. 27], the quantities c_i , s_i and \tilde{s}_i remain real and sine and cosine functions are evaluated through the corresponding hyperbolic functions.

3. NUMERICAL TESTS AND RESULTS

In order to test the performance of the method, we include here some examples. We consider the propagation of a mode in a tilted waveguide. Figure 1 shows the geometry of the test problem. The mode is launched into the tilted waveguide and after the mode has propagated to a distance of $100 \mu\text{m}$, the overlap integral between the input field and the calculated field is calculated. More exactly, we define a Correlation Factor (CF):

$$CF = \frac{\left| \int \psi_{exact}^* \psi_{cal} dx \right|}{\sqrt{\left\{ \int |\psi_{inp}|^2 dx \right\} \left\{ \int |\psi_{exact}|^2 dx \right\}}} \quad (30)$$

This factor measures both loss in power of the propagating mode as well as loss of shape of the mode. A value of unity for the correlation factor implies perfect propagation, without loss in either power or shape. Therefore error is defined as $1 - CF$.



In the first example we consider the propagation of the fundamental mode of a graded index waveguide⁵, with index profile given by $n^2(x) = n_s^2 + 2n_s \Delta n \operatorname{sech}^2(2x/w)$, $n_s = 2.1455$, $\Delta n = 0.003$, $w = 5 \mu\text{m}$ and $\lambda = 1.3 \mu\text{m}$. The

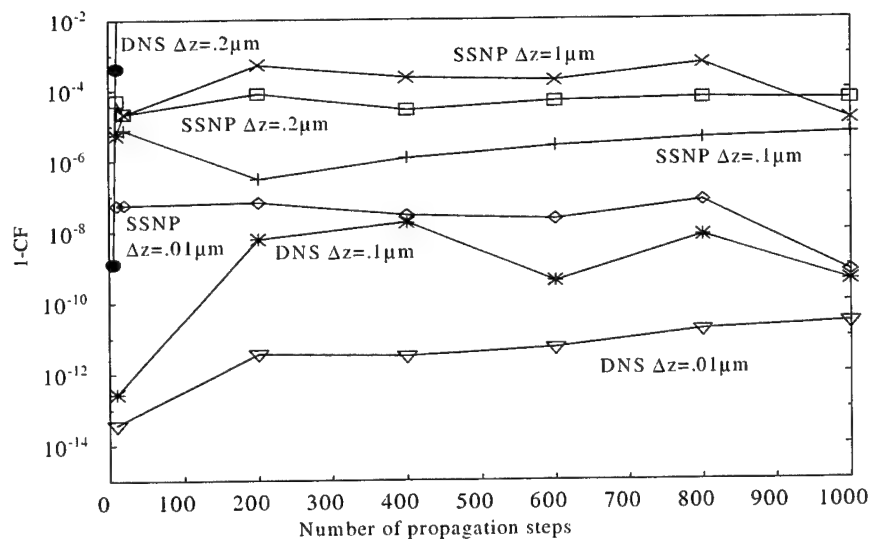


Fig. 2 Error in propagation as a function of the number of propagation steps with Δz for the graded index waveguide.⁵

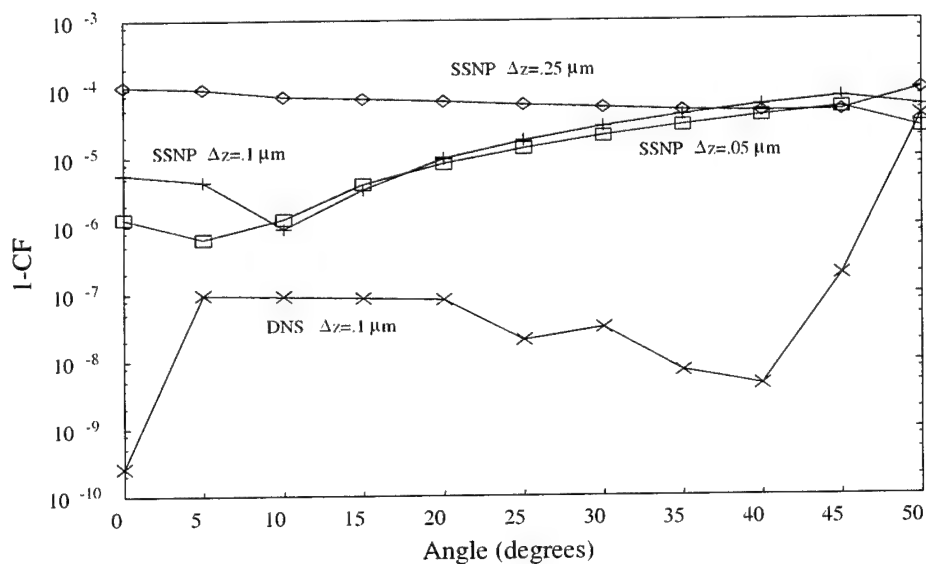


Fig. 3 Error in propagation with the tilt angle of the graded-index waveguide⁵ for propagation up to $100 \mu\text{m}$.

computation was done with 530 collocation points and the width of the numerical window was about $185 \mu\text{m}$. Figure 2 shows the performance of the method in respect of stability of the method for relatively larger values of Δz . The direct numerical solution (DNS) based on the Runge-Kutta solution of the collocation equation¹⁴ becomes unstable for $\Delta z > 0.1 \mu\text{m}$, whereas the SSNP method remains stable even for $1 \mu\text{m}$. In Fig.3, we have plotted the error in propagation, $1-CF$, as a function of the tilt angle. The figure shows that the SSNP method gives accuracy of the order of 10^{-4} even with a step size of $0.25 \mu\text{m}$, which is much better than those obtained by Shibayama *et al.*⁵ To illustrate the point, let us consider the error for a tilt angle of 50° . The error in the best results reported by Shibayama *et al.*⁵ for the 3-

step GD scheme is about 0.04 with $\Delta z = 0.05 \mu\text{m}$, whereas in our method the error is less than 0.001 with $\Delta z = 0.25 \mu\text{m}$. This would thus mean much faster and accurate propagation. Of course, one gets better accuracy with the DNS as the single step error in the Runge-Kutta method (used in the DNS) is $O((\Delta z)^5)$ as against $O((\Delta z)^3)$ in the SSNP method, but then the computation effort is significantly reduced with the latter method.

For numerically more intensive tests we consider the propagation of the TE_1 mode in step index waveguides. Fig. 4 shows a plot of $1-\text{CF}$ as a function of the number of propagation steps for the step index waveguide⁶ with $n_{co}=1.002$, $n_{clad}=1.000$, $\lambda=1.0 \mu\text{m}$, $w=15.092 \mu\text{m}$. Even with a step size as large as $0.4 \mu\text{m}$, the propagation is extremely stable and highly accurate. Fig. 5 shows performance with variation in tilt angle of the waveguide. We can see that the present method and DNS¹⁴ curves are very close, except for SSNP method with step size $0.4 \mu\text{m}$ at 0° where error is higher. However, the error value even with $0.4 \mu\text{m}$ step size is better than that reported by Yamauchi *et al.*⁶ at 50° . The SSNP method gives better accuracy with twice the step size used by Yamauchi *et al.*⁶ and in DNS;¹⁴ in fact,

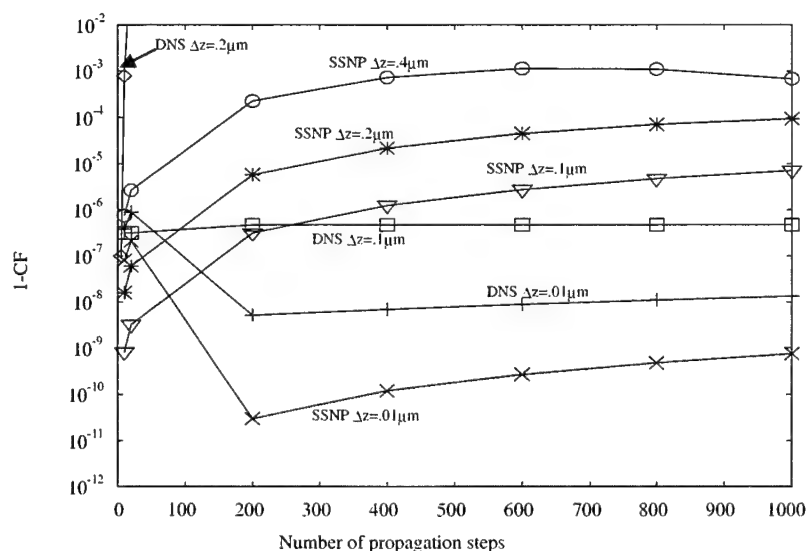


Fig. 4 Error in propagation as a function of the number of propagation steps with Δz for the step index waveguide.⁶

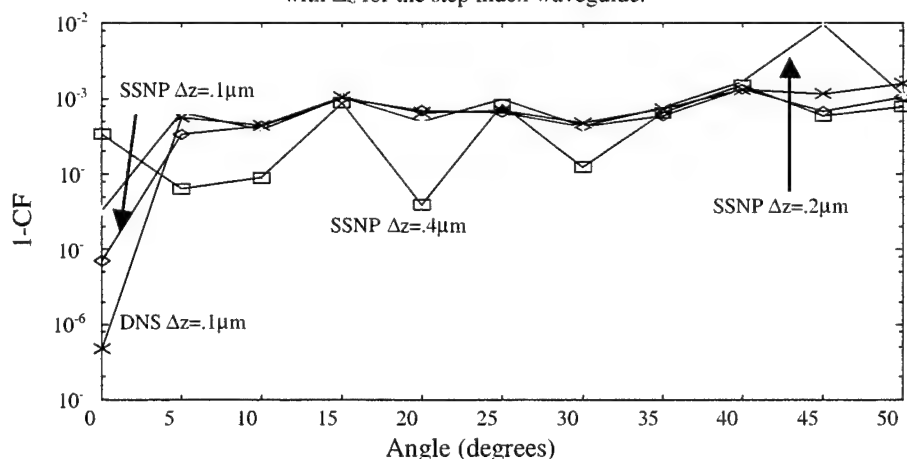


Fig. 5 Error in propagation with the tilt angle of the step-index waveguide⁶ for propagation up to $100 \mu\text{m}$.

only 500 computation points are required as against 1800 by Yamauchi *et al.*⁶

Figures 6 and 7 show performance of the method for the TE₁ mode in the benchmark waveguide¹⁹ with $n_{co}=3.3$, $n_{clad}=3.17$, $\lambda=1.55\ \mu\text{m}$, $w=8.8\ \mu\text{m}$. As the refractive index change from core to cladding is very large here, only small step sizes can be taken, yet the SSNP method is stable for a step size of $0.2\ \mu\text{m}$, as shown in Fig. 6. In fact, the performance at large tilt angles with $0.2\ \mu\text{m}$ is quite close to that for the DNS,¹⁴ as shown in Fig. 7.

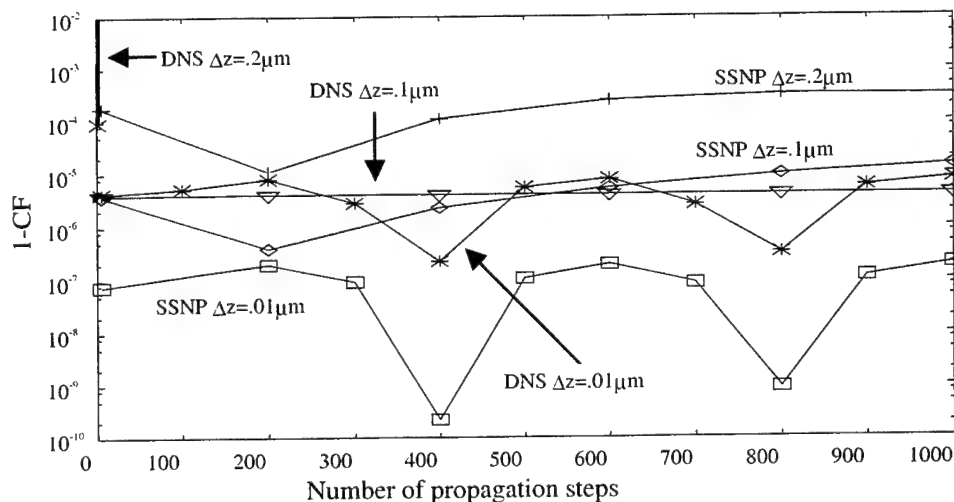


Fig. 6 Error in propagation as a function of the number of propagation steps with Δz for the benchmark step-index waveguide¹⁹.

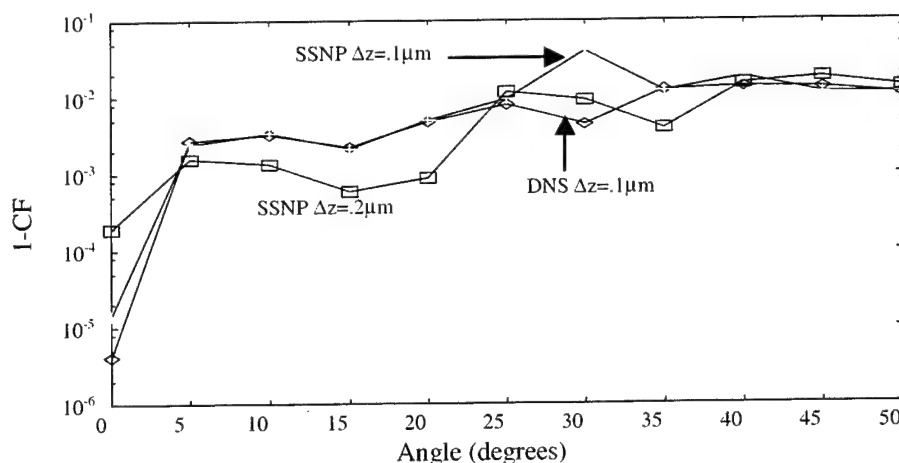


Fig. 7 Error in propagation with the tilt angle of the benchmark step-index waveguide¹⁹ for propagation up to $100\ \mu\text{m}$.

We also discuss the results for propagation of the TE₁₀ mode in the benchmark waveguide and compare the results for power loss in propagation of the mode after $100\ \mu\text{m}$ at 20° , designated as the benchmark test,¹⁹ the results are summarized in Table 1. N_x represents the number of points in the transverse direction and N_z , the number of longitudinal or propagation steps. It is quite obvious that the most accurate method would be the one, which shows highest power in the mode after the propagation. The present method requires fewer number of computation points, 800, as against 1311

and 2048 in AMGO¹⁹ and FD2BPM¹⁹ respectively, while still yielding higher power. This clearly shows that even for the most stringent tests, the split step procedure performs better than most other methods.

Table 1: Comparison of error/power loss in propagation to 100 μm in the benchmark¹⁹ step index waveguide for TE₁₀ mode using different methods.

Method	N _z	N _x	Power in waveguide at 20°
SSNP	1000	800	~0.96
DNS ¹⁴	1000	800	~0.90
AMIGO ¹⁹	1429	1311	~0.95
FD2BPM ¹⁹	1000	2048	~0.95
FTBPM ¹⁹	1000	256	~0.55
LETI-FD ¹⁹	200	1024	~0.15

4. SUMMARY AND CONCLUSIONS

We have presented the split step non-paraxial (SSNP) method, a wide-angle propagation method, based on symmetrized splitting of the propagation operator. We have described the implementation of this method in the collocation method, however it can be implemented using other methods such as the FD-BPM and the FFT-BPM, as well. The strength of this method lies in that the beam propagation is done mathematically by simple matrix multiplication and that no numerical matrix diagonalization or inversion is required. The method is highly stable and even with large step sizes, for which other methods become unstable, the method allows stable and accurate beam propagation. The method is faster and easier to implement and is more efficient than other methods. The numerical examples comparing the present method with those reported in the literature show clearly the advantages of the present method.

ACKNOWLEDGEMENTS

This work was partially supported by a grant (No. 03(0976)/02/EMR-II) from the Council of Scientific and Industrial Research (CSIR), India. One of the authors (AA) is a CSIR research fellow.

REFERENCES

1. D. Yevick and M. Glasner, "Forward wide-angle light propagation in semiconductor rib waveguides", *Opt. Lett.* **15**, 174-176, 1990.
2. G.R. Hadley, "Multistep method for wide-angle beam propagation", *Opt. Lett.* **17**, 1743-1745, 1992.
3. Y. Chung and N. Dagli, "A wide-angle propagation technique using an explicit finite-difference scheme", *IEEE Photon. Technol. Lett.* **6**, 540-542, 1994.
4. W.P. Huang and C.L. Xu, "A wide-angle vector beam propagation method", *IEEE Photon. Technol. Lett.* **4**, 1118-1120, 1992.
5. J. Shibayama, K. Matsubara, M. Sekiguchi, J. Yamauchi and H. Nakano, "Efficient nonuniform scheme for paraxial and wide-angle finite difference beam propagation methods", *J. Lightwave Technol.*, **17**, 677-683, 1999.
6. J. Yamauchi, J. Shibayama, M. Sekiguchi and H. Nakano, "Improved multistep method for wide-angle beam propagation", *IEEE Photon. Technol. Lett.* **8**, 1361-1363, 1996.
7. Y. Tsuji, M. Koshihara and T. Tanabe, "A wide-angle beam propagation method based on a finite element scheme", *IEEE Trans. Magnetics* **33**, 1544-1547, 1997.
8. H. Rao, M.J. Steel, R. Scarmozzino and R. Osgood, "Complex propagators for evanescent waves in bidirectional beam propagation method", *J. Lightwave Technol.*, **18**, 1155-1160, 2000.
9. H. El-Refaei, I. Betty and D. Yevick, "The Application of complex Padé approximants to reflection at optical waveguide facets", *IEEE Photon. Technol. Lett.*, **12**, 158-160, 2000.
10. Y.Y. Lu and S.H. Wei, "A new iterative bidirectional beam propagation method", *IEEE Photon. Technol. Lett.* **14**, 1533-1535, 2002.

11. C. Vassallo, "Limitations of the wide-angle beam propagation method in non-uniform systems", *J. Opt. Soc. Am. A* **13**, 761-770, 1996.
12. R.P. Ratowsky, J.A. Fleck, Jr., and M.D. Feit, "Accurate solution of the Helmholtz equation by Lanczos orthogonalization for media with loss or gain", *Opt. Lett.* **17**, 10-12, 1992.
13. Q. Luo and C.T. Law, "Discrete Bessel-based Arnoldi method for nonparaxial wave propagation", *IEEE Photon. Technol. Lett.*, **14**, 50-52, 2002.
14. A. Sharma and A. Agrawal, "Wide angle and bi-directional beam propagation using the collocation method for the non-paraxial wave equation", *Opt. Commun.* **216**, 41-45, 2003.
15. A. Sharma and S. Banerjee, "Method for propagation of total fields or beams through optical waveguides", *Opt. Lett.* **14**, 94-96, 1989.
16. A. Taneja and A. Sharma, "Propagation of beams through optical waveguiding structures: comparison of the beam propagation method (BPM) and the collocation method", *J. Opt. Soc. Am. A* **10**, 1739-1745, 1993.
17. A. Sharma, "Collocation method for wave propagation through optical waveguiding structures" in *Methods for Modeling and Simulation of Guided-Wave Optoelectronic Devices*, W.P. Huang, ed. (EMW Publishers, Cambridge, Mass., 1995), pp. 143-198.
18. I. Ilić, R. Scarmozzino and R. Osgood, "Investigation of the Padé approximant-based wide-angle beam propagation method for accurate modeling of waveguiding circuits", *J. Lightwave Technol.*, **14**, 2813-2822, 1996.
19. H.-P. Nolting and R. März, "Results of benchmark tests for different numerical BPM algorithms", *J. Lightwave Technol.* **13**, 216-224, 1995.

Improved imaginary-distance beam propagation method for full-vectorial eigenmode analysis of optical waveguides

Yongzhi He and Frank G. Shi

Optoelectronics Integration & Packaging Lab

Henry Samueli School of Engineering, University of California, Irvine, CA 92697-2575

E-mail address: yzhe2002@hotmail.com, fgshi@uci.edu

ABSTRACT

Two schemes are developed to improve the computational accuracy of the full-vectorial imaginary-distance beam propagation method (FV-ID-BPM). In the first scheme, the cross-coupling terms (CCTs) demanded for the FV analysis are expressed in explicit forms, which are independent of specific types of waveguides, by using an improved finite-difference formula. In the second one, the generalized Douglas (GD) scheme is adopted for discretizing the second-order partial derivatives in the FV-ID-BPM equations. A detailed comparative study between the two schemes in improving the computational accuracy is performed by taking a strongly-guiding rib waveguide as a testing example. The highest accuracy is demonstrated in case of the combination of the two schemes. Nevertheless, the improved FD formula for the CCTs is proved to play a much more significant role than the GD scheme in improving the computational accuracy. Moreover, the effectiveness of the GD scheme diminishes as the FD grid is refined.

Index terms: imaginary-distance beam propagation method; cross-coupling term; the generalized Douglas scheme.

I. INTRODUCTION

The imaginary-distance beam propagation method (ID-BPM), based on the finite-difference (FD) scheme, has been widely used for computing eigenmodes of arbitrary-shaped index-guiding optical waveguides [1-3]. In the imaginary propagation context, the fundamental mode always dominates after a sufficiently long propagation since it has the largest effective index, hence the largest amplification coefficient among all modes [1]. As a result, the fundamental mode can be extracted spontaneously, while the higher order modes can only be computed by subtracting the previously obtained lower order modes at each numerical propagation step [1].

The accuracy of the ID-BPM strongly depends on the discretization schemes for the cross-coupling terms (CCTs) and the second-order partial derivatives, if for the full-vectorial analysis purpose, in the BPM equations. A direct discretization for the CCTs has been proved to result in poor convergence behavior [4-5]. On the other hand, the simple three-point formula for the second-order partial derivatives does not ensure the second-order truncation error due to the discontinuity of electric fields at optical interfaces [6]. Therefore, there have been some attempts to develop improved formulas for discretizing the CCTs and the second-order partial derivatives to restore the truncation error [6-9]. In one of our attempts, the CCTs are treated by a short form for mixed partial derivatives, which has been proposed for modeling of seismic wave propagation [10]. Unlike the improved formula developed in [7], the present one is expressed in explicit forms and does not rely on specific types of waveguides, thus makes the FVBPM programming much easier. In the other one of our attempts, the second-order partial derivatives are treated by the generalized Douglas (GD) scheme, which has

been demonstrated to dramatically improve the computational accuracy in the scalar-wave or semivector mode analysis [8-9]. The numerical experiments, in which a strongly-guiding rib waveguide is taken as a testing example, are then performed to test the effectiveness of the two schemes.

II. THE FV-ID-BPM FORMULATION

Considering the paraxial approximation for the FV-BPM, the propagation of the electromagnetic wave is governed by the following two coupled equations with \hat{E}_x and \hat{E}_y defined as the x and y polarized electric fields, respectively,

$$\sigma \frac{\partial}{\partial z} \begin{bmatrix} \hat{E}_x \\ \hat{E}_y \end{bmatrix} = \begin{bmatrix} \tilde{D}_{xx} + D_{yy} + \gamma & D_{xy} \\ D_{yx} & D_{xx} + \tilde{D}_{yy} + \gamma \end{bmatrix} \begin{bmatrix} \hat{E}_x \\ \hat{E}_y \end{bmatrix} \quad (1)$$

where

$$\tilde{D}_{\alpha\alpha} \hat{E}_\alpha = \frac{\partial}{\partial \alpha} \left[\frac{1}{n^2} \left(\frac{\partial}{\partial \alpha} (n^2 E_\alpha) \right) \right] \quad (2)$$

$$D_{\alpha\alpha} \hat{E}_\beta = \frac{\partial^2 E_\beta}{\partial \alpha^2} \quad (3)$$

$$D_{\alpha\beta} E_\beta = \frac{\partial}{\partial \alpha} \left[\frac{1}{n^2} \left(\frac{\partial}{\partial \beta} (n^2 \hat{E}_\beta) \right) - \frac{\partial \hat{E}_\beta}{\partial \beta} \right] \quad (4)$$

with $\alpha, \beta \in \{x, y\}$, $\sigma = 2jk_0 n_0$, and $\gamma = k^2 [n(x, y, z)^2 - n_0^2]$, in which k_0 , n_0 , and $n(x, y, z)$ denote the free-space wavenumber, the reference index, and the index profile, respectively.

After discretizing with the Crank-Nicholson (CN) scheme and adopting the alternating direction implicit (ADI) method, (1) becomes [11]

$$\begin{bmatrix} \hat{E}_x \\ \hat{E}_y \end{bmatrix}^{n+1} = \frac{\left(1 + \frac{\Delta z}{2\sigma} \begin{bmatrix} D_{yy} + \gamma/2 & 0 \\ D_{yx} & \tilde{D}_{yy} + \gamma/2 \end{bmatrix} \right) \left(1 + \frac{\Delta z}{2\sigma} \begin{bmatrix} \tilde{D}_{xx} + \gamma/2 & D_{xy} \\ 0 & D_{xx} + \gamma/2 \end{bmatrix} \right)}{\left(1 - \frac{\Delta z}{2\sigma} \begin{bmatrix} \tilde{D}_{xx} + \gamma/2 & D_{xy} \\ 0 & D_{xx} + \gamma/2 \end{bmatrix} \right) \left(1 - \frac{\Delta z}{2\sigma} \begin{bmatrix} D_{yy} + \gamma/2 & 0 \\ D_{yx} & \tilde{D}_{yy} + \gamma/2 \end{bmatrix} \right)} \begin{bmatrix} \hat{E}_x \\ \hat{E}_y \end{bmatrix}^n \quad (5)$$

which results in two tridiagonal systems of linear equations and can be solved efficiently. The idea behind the ADI method is that the propagation is split into two half-steps, i.e., $(z \rightarrow z + \Delta z/2)$ and $(z + \Delta z/2 \rightarrow z + \Delta z)$. We only discuss the first half-step since the treatment regarding the two half-steps is the same. For the first half-step, \hat{E}_x and

\hat{E}_y are governed by

$$\left(\sigma \frac{\partial \hat{E}_x}{\partial z}\right)^n = 2(\tilde{D}_{xy} \hat{E}_x + D_{xy} \hat{E}_y)^n + \gamma \hat{E}_x^n \quad (6)$$

$$\left(\sigma \frac{\partial \hat{E}_x}{\partial z}\right)^{n+1/2} = 2(D_{yy} \hat{E}_x)^{n+1/2} + \gamma \hat{E}_x^{n+1/2} \quad (7)$$

$$\left(\sigma \frac{\partial \hat{E}_y}{\partial z}\right)^n = 2(D_{xy} \hat{E}_y)^n + \gamma \hat{E}_y^n \quad (8)$$

$$\left(\sigma \frac{\partial \hat{E}_y}{\partial z}\right)^{n+1/2} = 2(\tilde{D}_{yx} \hat{E}_y + D_{yx} \hat{E}_x)^{n+1/2} + \gamma \hat{E}_y^{n+1/2} \quad (9)$$

in which (6) and (8) can be explicitly solved, while (7) and (9) result in two tridiagonal matrices and should be solved implicitly.

The standard FV-BPM formulation described above can be turned into an efficient mode solver by simply replacing z by $i\tau$, where i denotes the imaginary symbol and τ is the propagation distance [1].

III. NOVEL FD FORMULA FOR THE CROSS-COUPLED TERMS

Instead of the direct discretization, we treat the CCTs $D_{\alpha\beta} E_\beta$ as shown in (4) by a short form for mixed partial derivatives, which has been proposed for modeling of seismic wave propagation [10]. In a general case, a short form of a mixed partial derivative, expressed by $\frac{\partial}{\partial \alpha} \left(a \frac{\partial f}{\partial \beta} \right)$, can be approximated by a FD form as

$$\frac{\partial}{\partial \alpha} \left(a \frac{\partial f}{\partial \beta} \right) \cong \frac{1}{4d\alpha d\beta} \left[\frac{a_{0,1} + a_{0,0}}{2} (f_{1,0} + f_{1,1} - f_{-1,0} - f_{-1,1}) - \frac{a_{0,-1} + a_{0,0}}{2} (f_{1,0} + f_{1,-1} - f_{-1,0} - f_{-1,-1}) \right] \quad (10)$$

As a result, the cross coupling terms can be expressed by

$$\begin{aligned}
\delta_{\alpha\beta} \hat{E}_\beta = & \frac{1}{8n_0 k \Delta \alpha \Delta \beta} \left\{ \left[\frac{2n^2(m+1, n+1, l)}{n^2(m+1, n, l) + n^2(m, n, l)} - 1 \right] \cdot \hat{E}_\beta(m+1, n+1) \right. \\
& - \left[\frac{2n^2(m+1, n-1, l)}{n^2(m+1, n, l) + n^2(m, n, l)} - 1 \right] \cdot \hat{E}_\beta(m+1, n-1) - \\
& \left[\frac{2n^2(m-1, n+1, l)}{n^2(m-1, n, l) + n^2(m, n, l)} - 1 \right] \cdot \hat{E}_\beta(m-1, n+1) \\
& + \left[\frac{2n^2(m-1, n-1, l)}{n^2(m-1, n, l) + n^2(m, n, l)} - 1 \right] \cdot \hat{E}_\beta(m-1, n-1) + \\
& \left[\frac{2n^2(m, n+1, l)}{n^2(m+1, n, l) + n^2(m, n, l)} - \frac{2n^2(m, n+1, l)}{n^2(m-1, n, l) + n^2(m, n, l)} \right] \hat{E}_\beta(m, n+1) - \\
& \left. \left[\frac{2n^2(m, n-1, l)}{n^2(m+1, n, l) + n^2(m, n, l)} - \frac{2n^2(m, n-1, l)}{n^2(m-1, n, l) + n^2(m, n, l)} \right] \hat{E}_\beta(m, n-1) \right\}
\end{aligned} \tag{11}$$

where $\delta_{\alpha\beta}$ denotes the difference operator representing $D_{\alpha\beta}$, $\alpha = m\Delta\alpha$, $\beta = n\Delta\beta$, $z = l\Delta z$, and $n(m, n, l)$ denotes the index distribution, in which m , n , and l are integers. In comparison with the direct discretization shown in [4], the numerators corresponding to the dielectric constant in each term of the present formulas are the average value of two adjacent grid points, e.g., $n^2(m+1, n, l)$ is replaced by $[n^2(m+1, n, l) + n^2(m, n, l)]/2$, and as a result, two more grid points corresponding to electric fields are added on the right side of each equation. The present formula takes more adjacent grid points for electric fields and index distribution into account than the direct discretization forms, which leads to a substantial improvement in accuracy.

IV. FORMULATION OF THE GENERALIZED DOUGLAS SCHEME

The application of the GD scheme to (7) and (8) is trivial as the Taylor's series expansion regarding $D_{\alpha\alpha} \hat{E}_\beta$ can be approximated by [8-9]

$$D_{\alpha\alpha} \hat{E}_\beta = \delta_{\alpha\alpha} \hat{E}_\beta - \frac{1}{12} \delta_{\alpha\alpha} \left(\sigma \frac{\partial \hat{E}_\beta}{\partial z} - \gamma \hat{E}_\beta \right) \tag{12}$$

where $\delta_{\alpha\alpha}$ denotes the difference operator used to replace $D_{\alpha\alpha}$.

Unfortunately, it is not simple to apply the GD scheme to (6) and (9) due to the existence of $D_{\alpha\beta} \hat{E}_\beta$ and the index

term in $\tilde{D}_{\alpha\alpha}\hat{E}_\alpha$. In the semivector analysis, $\tilde{D}_{\alpha\alpha}\hat{E}_\alpha$ is expanded by the analogy with (12) based on the Stern's expression for $\tilde{\delta}_{\alpha\alpha}$ defined as the difference operator to replace $\tilde{D}_{\alpha\alpha}$ [9]

$$\tilde{D}_{\alpha\alpha}\hat{E}_\alpha = \tilde{\delta}_{\alpha\alpha}\hat{E}_\alpha - \frac{1}{12}\delta_{\alpha\alpha}\left(\sigma\frac{\partial\hat{E}_\alpha}{\partial z} - \gamma\hat{E}_\alpha\right) \quad (13)$$

Although (13) is not mathematically guaranteed, the numerical experiments still show that it results in substantial improvement in accuracy as compared with the conventional CN scheme [9]. The philosophy behind this can be understood by decomposing $\tilde{D}_{\alpha\alpha}$ into

$$\tilde{D}_{\alpha\alpha}\hat{E}_\alpha = D_{\alpha\alpha}\hat{E}_\alpha + \frac{\partial}{\partial\alpha}\left(\frac{1}{n^2}\frac{\partial n^2}{\partial\alpha}\hat{E}_\alpha\right). \quad (14)$$

(13) is effective once the second term on the right side of (12) is much smaller than $D_{\alpha\alpha}\hat{E}_\alpha$. It is also a common knowledge that the CCTs contribute very little to mode computation in comparison with the second-order partial derivatives for most of the optical waveguides currently used or proposed, which ensures us to apply the GD scheme to (6) and (9) by the analogy with (13),

$$\tilde{D}_{\alpha\alpha}\hat{E}_\alpha + D_{\alpha\beta}\hat{E}_\beta = \tilde{\delta}_{\alpha\alpha}\hat{E}_\alpha + \delta_{\alpha\beta}\hat{E}_\beta - \frac{1}{12}\delta_{\alpha\alpha}\left(\sigma\frac{\partial\hat{E}_\alpha}{\partial z} - \gamma\hat{E}_\alpha\right) \quad (15)$$

Consequently, (6-9) can be efficiently solved by substituting (12) and (15) into them. It is noteworthy that $\hat{E}_x^{n+1/2}$ should be formally obtained by (6-7) to solve (8-9).

V. NUMERICAL SIMULATIONS

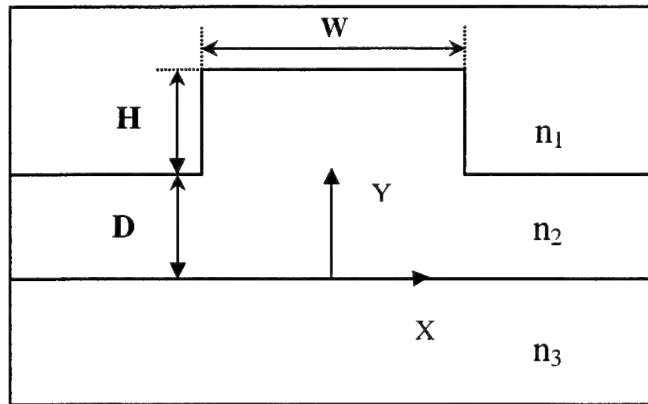


Fig. 1 Rib waveguide geometry.

To verify the effectiveness of the two schemes developed, a comparative study is performed among four methods i.e., Method 1 – the direct discretization for the CCTs plus the conventional CN scheme, Method 2 – the direct discretization for the CCTs plus the GD scheme, Method 3 – (11) plus the conventional CN scheme, and Method 4 – (11) plus the GD scheme. The numerical experiments are performed by taking a strongly-guiding rib waveguide as illustrated in Fig.1, which has been used as a classical benchmark, as the testing example [7,11]. The structural parameters are

set as follows: $n_1 = 1.0$, $n_2 = 3.44$, $n_3 = 3.4$, $W = 3\mu\text{m}$, and $D = H = 0.5\mu\text{m}$. The wavelength is taken to be $1.55\mu\text{m}$. The effective indexes of the two fundamental modes, i.e., the quasi-TE and quasi-TM modes, are computed by Methods 1-4. The effective indexes obtained by the shifted inverse power method (SIPM) in [11] are taken to be the standard for comparison as the SIPM was proved to provide guided mode solution with high accuracy [11]. In the subsequent simulations, a technique of updating the reference index at each numerical step is employed by following [12] to get better convergence behavior. The propagation step size Δz is fixed to be $0.1\mu\text{m}$ and the transverse grid size $\Delta = \Delta x = \Delta y$.

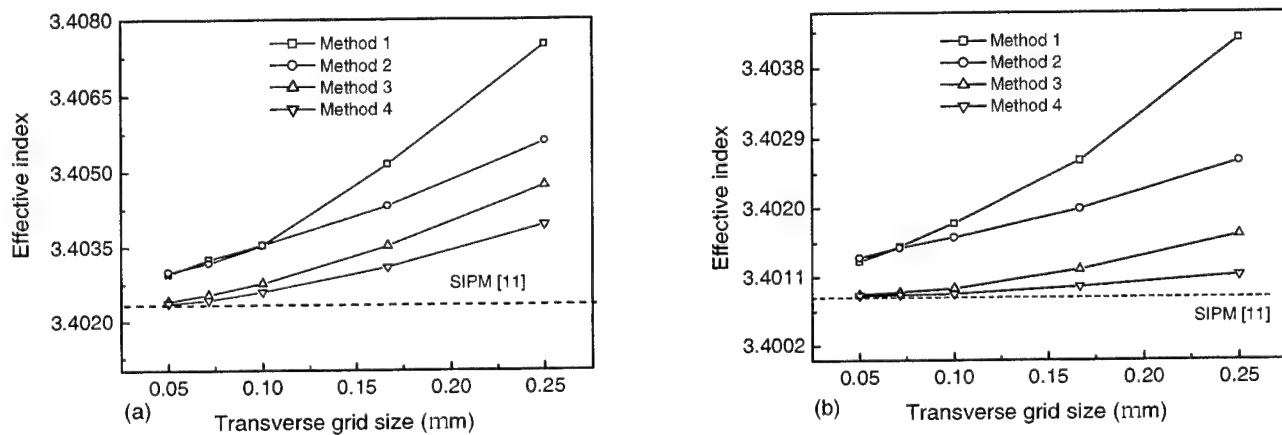


Fig. 2 Convergence of the effective indexes versus the transverse grid size. (a) quasi-TE mode; (b) quasi-TM mode. Method 1 – the direct discretization for the CCTs plus the conventional CN scheme. Method 2 – the direct discretization for the CCTs plus the GD scheme, Method 3 – (11) plus the conventional CN scheme, and Method 4 – (11) plus the GD scheme.

Fig. 2 presents the convergence behavior of the quasi-TE and quasi-TM modes as a function of the transverse grid size (Δ). Comparison between Method 1 and 2 or between Method 3 and Method 4 demonstrates that the GD scheme presented in section II evidently improves the computational accuracy when a relatively coarse grid is used. Comparison between Method 1 and 3 or between Method 2 and Method 4 shows that the novel formulas for the CCTs also greatly improve the computational accuracy. Moreover, it can be seen that the introduction of (11) plays a much more important role in improving the computational accuracy than the GD scheme if a further comparison is made between Method 2 and 3. The results by Method 3 and Method 4 or Methods 1 and 2 almost converge with each other as the transverse grid size is sufficiently small, demonstrating that under the present condition the effectiveness of the GD scheme is not apparent and the convergence behavior is almost governed by the FD formulas for the CCTs. The best convergence behavior can be obtained once both the GD scheme and the novel FD formulas for the CCTs expressed by (11) are employed in the FV-ID-BPM. Table I shows the comparison of effective indexes obtained by Methods 1-4 and the SIPM, when the transverse grid size is $0.05\mu\text{m}$. It is evident that the results by Method 3 and Method 4 remarkably agree with

the ones obtained by the SIPM, and the difference is on the order of 10^{-5} , which is much smaller than Methods 1-2. The difference between Method 3 and Method 4 is very small, demonstrating the GD scheme is not necessary to be combined with (11) in the FV-ID-BPM when a fine enough grid is used.

Method	Quasi-TE	Difference (Quasi-TE)	Quasi-TM	Difference (Quasi-TM)
SIPM [11]	3.4023129	0	3.4008152	0
Method 1	3.4029487	0.0006358	3.4012857	0.0004705
Method 2	3.4029664	0.0006535	3.4013485	0.0005333
Method 3	3.4024076	0.0000947	3.4008678	0.0000526
Method 4	3.4023695	0.0000566	3.4008456	0.0000304

Table I Comparison of effective indexes for the rib waveguide case obtained by Methods 1-4 and the SIPM. Here $\Delta = 0.05 \mu m$ and the results obtained by the SIPM are used as the reference to calculate the effective index difference.

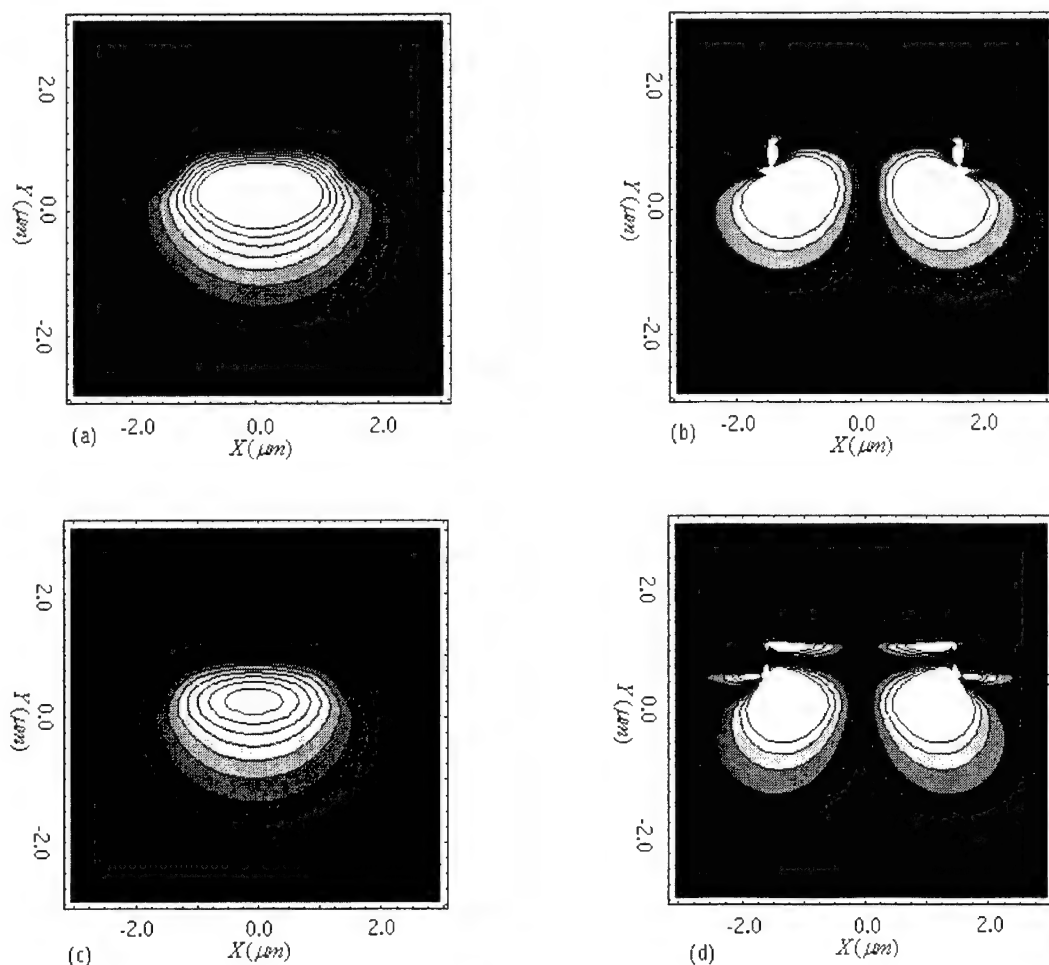


Fig.3 Contour plots of the calculated major and minor fields of the quasi-TE and TM modes. (a) major field of the quasi-TE mode, (b) minor field of the quasi-TE mode, (c) major field of the quasi-TM mode, (d) minor field of the quasi-TM mode.

The contour plots of the major and minor fields of the quasi-TE and TM modes obtained by Method 4 are presented in Fig. 3 (a-d) after the propagation reaches the convergence in case of $\Delta = 0.05 \mu\text{m}$. The discontinuities of the fields at the optical interfaces are clearly shown. It is also evident that the major fields of the two fundamental modes have almost the similar shape, whereas the two minor fields are greatly different from each other.

VI. CONCLUSION

Two schemes, i.e., an improved FD formula for the CCTs and the GD scheme, have been developed and demonstrated to dramatically improve the computational accuracy of the FV-ID-BPM. The highest accuracy is demonstrated in case of the combination of the two schemes. Nevertheless, the improved FD formula for the CCTs is proved to play a much more significant role than the GD scheme in improving the computational accuracy. Moreover, the effectiveness of the GD scheme diminishes as the FD grid is refined.

REFERENCE

- [1] Y.Z. He and F.G. Shi, "Finite-difference imaginary-distance beam propagation method for modeling of the fundamental mode of photonic crystal fibers", *Opt. Commun.*, vol. 225, pp. 151-156, 2003.
- [2] S. Jüngling and J.C. Chen, "A study and optimization of eigenmode calculations using the imaginary-distance beam-propagation method", *IEEE J. Quantum Electron.*, vol. 30, pp. 2098-2105, 1994.
- [3] J.C. Chen and S. Jüngling, "Computation of higher-order waveguide modes by the imaginary-distance beam propagation method", *Optical and Quantum Electron.*, vol. 26, pp. S199-S205, 1994.
- [4] W. P. Huang and C. L. Xu, "Simulation of three-dimensional optical waveguides by a full-vector beam propagation method", *IEEE J. Quantum Electron.*, vol. 29, pp. 2639-2649, 1993.
- [5] J. Yamauchi, G. Takahashi, and H. Nakano, "Full-vectorial Beam propagation method based on the Mckee-Mitchell scheme with improved finite-difference formulas", *J. Lightwave Technol.*, vol. 16, no. 12, pp. 2458-2464, Dec., 1998.
- [6] C. Vassallo, "Interest of improved three-point formulas for finite-difference modeling of optical devices", *J. Opt. Soc. Am. A*, vol. 14, no. 12, pp. 3273-3284, Dec., 1997.
- [7] J. Yamauchi, G. Takahashi, and H. Nakano, "Full-vectorial Beam propagation method based on the Mckee-Mitchell scheme with improved finite-difference formulas", *J. Lightwave Technol.*, vol. 16, no. 12, pp. 2458-2464, Dec., 1998.
- [8] J. Yamauchi, J. Shibayama, M. Sekiguchi, and H. Nakano, "Finite-difference beam propagation method based on the generalized Douglas scheme for a nonuniform grid", *IEEE Photon. Technol. Lett.*, vol. 9, no. 1, pp. 67-69, Jan., 1997.
- [9] J. Yamauchi, J. Shibayama, O. Saito, O. Uchiyama, and H. Nakano, "Improved finite-difference beam-propagation method based on the Generalized Douglas scheme and its application to semivectorial analysis", *J. Lightwave Technol.*, vol. 14, no. 10, pp. 2401-2406, Oct., 1996.
- [10] I. Oprsal and J. Zahradnik, "Elastic finite-difference method for irregular grids", *Geophysics*, vol. 64, no. 1, pp. 240-250, 1999.
- [11] Y. L. Hsueh, M. C. Yang, and H. C. Chang, "Three-dimensional noniterative full-vectorial beam propagation method based on the alternating direction implicit method", *J. Lightwave Technol.*, vol. 17, no. 11, pp. 2389-2397, Nov., 1999.
- [12] J. Shibayama, M. Sekiguchi, J. Yamauchi, and H. Nakano, "Eigenmode analysis of optical waveguides by an improved finite-difference imaginary-distance beam propagation method," *IEICE Trans.*, vol. J81-C-I, no. 1, pp. 9-16, 1998.

Parameters affecting the performance of a perfectly matched layer for beam propagation methods

Anurag Sharma and Arti Agrawal

Department of Physics, Indian Institute of Technology Delhi, New Delhi, India 110016

ABSTRACT

In numerical wave propagation methods, the perfectly matched layer (PML) boundary condition is employed to prevent spurious reflections. However, PML takes additional resources in number of computation points and time. In this study, the PML performance is examined with change in the distribution of sampling points and PML absorption profile with a view to optimizing its efficiency. We have used the collocation method in our examples. We have found that equally spaced field sampling points give better absorption of beams under both optimal as well as non-optimal conditions for lower PML widths. While at higher PML widths, unequally spaced basis points may be more advantageous. The behavior of different absorption profiles varies with point spacing. For numerical tests, Gaussian beam propagation in a homogeneous medium is considered. Comparing different profiles, we find that a new profile \sin^p with $p = 4$ and quartic profiles are the best in equally spaced points, while \sin^2 and square profiles are the best in unequally spaced points.

Keywords: PML – Perfectly Matched Layer, boundary condition, absorption profile, sampling points

1. INTRODUCTION

Numerical methods for beam propagation, which propagate the total field, have become very important for optical waveguide and device simulation. These methods directly give the total picture of the field as it propagates through a waveguide, which may have a very complicated structure involving several branches and variations in physical characteristics. Examples of some the important methods used include the FFT-BPM¹, the FD-BPM² and the collocation method.³⁻⁷

A major problem afflicting all beam propagation methods is that the infinite transverse extent has to be represented by a finite domain bounded by numerical boundaries. In these methods, the numerical boundary is represented by the extreme points, on which the field is sampled. Since the whole numerical scheme is generally lossless the total energy within the numerical window remains the same and hence, any wave, which in reality should leave the numerical window region is directed back into the numerical window thereby representing an unreal phenomenon. The conventional way to reduce the effect of this problem is to put a strongly absorbing medium of appropriate thickness at the edge of the window thereby imposing the so-called absorbing boundary condition (ABC).⁸⁻¹¹ Another way is to use the so called transparent boundary condition (TBC)¹²⁻¹⁴ in which the wave parameters near the edge of the window are so modified for a given angle of incidence that it represents an outgoing plane wave at that angle. Both these methods have been successful to a limited extent. Some time back, Berenger¹⁵ introduced the concept of a perfectly matched layer (PML) for application with finite-difference (FD) methods. This has been found to be very effective for applications to optical wave propagation using the finite difference time domain (FDTD) methods.^{11,16-18} In the PML method, a layer of a specially designed anisotropic medium is put at the edge of the window. The absorption profile in this window can be arbitrarily chosen subject to certain conditions.

In any implementation of the PML method (or any other method), one seeks to increase the absorption of the undesired reflections as well as to keep the thickness of the layer as small as possible so as not to increase the computation effort significantly. In this respect, the design of the absorption profile of the PML assumes significance. Further, in the numerical beam propagation methods, the points on which the field is sampled are generally taken equally spaced. However, in a number of cases unequally spaced points have also been tried with distinct computational

advantage. In this paper, we have implemented the PML method in the collocation method of beam propagation and have found it very effective. Using this implementation, we have investigated the effect of distribution of sample points on the PML performance. We have also investigated influence of different absorption profiles in the PML, including a new type of absorption profile.

2. THEORY

In this section, we describe the perfectly matched layer (PML) boundary condition and its implementation in the collocation method. We give details of the collocation method and describe the mathematical formulation in defining the two sets of sampling points- equally spaced and unequally spaced, along with their properties. We also define the different PML absorption profiles used.

2.1 The perfectly matched layer (PML) boundary condition

In the PML technique, a layer of an artificial anisotropically absorbing medium which strongly absorbs the waves propagating along the x -direction, but does not absorb at all the waves propagating along the z -direction (which is the general direction of propagation) is introduced at the edge of the numerical window.^{11, 15} Further, the layer is matched perfectly at the interface with the real window, so that there are no reflections from there. The perfectly matched layer is implemented as a variable transformation in which the transverse coordinate x becomes complex with the imaginary part increasing gradually as one moves into the layer.¹¹ Thus, we introduce a transformation (see Fig.1)

$$x = h(\sigma) \quad (1)$$

with

$$h(\sigma) = \sigma \quad \sigma < x_p$$

$$= x_p + \int_{x_p}^{\sigma} [1 - ip(\xi)] d\xi \quad x_p < \sigma < x_b \quad (2)$$

where $\xi = \sigma - x_p$; x_p being the edge of the real medium and x_b is the edge of the numerical window. The absorption profile function $p(\xi)$ should be such that $p(0) = 0 = p'(0)$ for perfect matching at $x = x_p$. The region upto x_p is termed as the real window while the region between x_p and x_b is the PML.

A variety of profiles have been used in the literature.^{18, 19} These are all power law profiles including square, cubic and quartic profiles:

$$p(\xi) = p_o \xi^q, \quad q = 2, 3, 4, \dots, \quad (3)$$

It has been shown that for finite difference time domain (FDTD) schemes the quartic profile is better than the usual square profile.^{18, 19} However, for continuous wave propagation problems generally square profile has been used. We have investigated various power-law profiles for the wave propagation problems. We have also investigated a new profile:

$$p(\xi) = p_o \sin^q(\pi\xi / 2\delta), \quad q = 2, 3, 4, \dots, \quad (4)$$

where δ is the width of the PML layer and q defines the shape of the profile. By choosing the power q , the strength, p_o and the width, $\delta = x_b - x_p$, of the PML, the wave can be absorbed to a desired level to reduce reflections into the computation window.

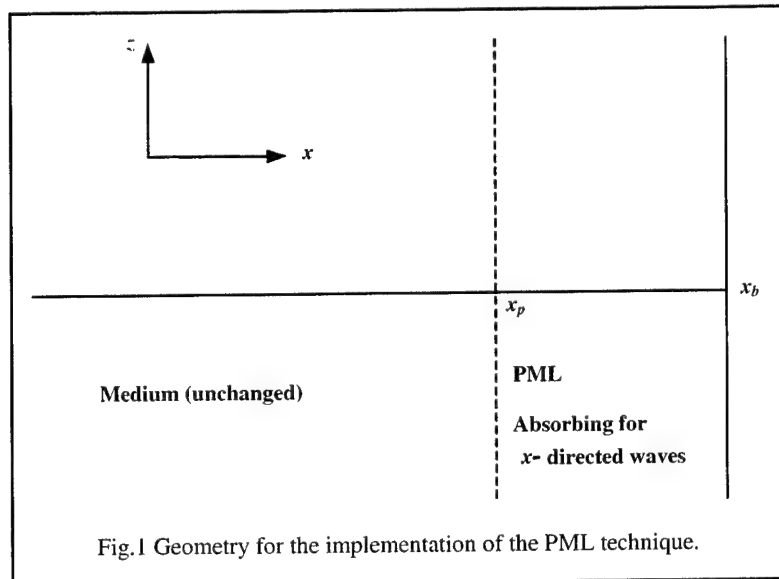


Fig.1 Geometry for the implementation of the PML technique.

2.2 The collocation method

We discuss here two-dimensional waveguides only; however, the method discussed can be extended to three-dimensional structures. A 2-D waveguide structure is defined by its refractive index distribution $n^2(x, z)$. The electromagnetic fields that propagate through such a dielectric structure must satisfy Maxwell's equations. However, in a majority of practical waveguiding structures (we will confine our discussion to such cases), the relative variation of the refractive index is sufficiently small to allow the scalar wave approximation. Then, it suffices to consider instead a much simpler Helmholtz equation:

$$\frac{\partial^2 \Psi}{\partial x^2} + \frac{\partial^2 \Psi}{\partial z^2} + k_0^2 n^2(x, z) \Psi(x, z) = 0, \quad (5)$$

where $\Psi(x, z)$ represents one of the Cartesian components of the electric field (generally referred to as the scalar field). The time dependence of the field has been assumed to be $e^{i\omega t}$ and $k_0 = \omega/c$ is the free space wave number.

In the collocation method, we express the unknown field as a linear combination over a set of orthogonal basis function, $\phi_n(x)$:

$$\Psi(x, z) = \sum_{n=1}^N c_n(z) \phi_n(x) \quad (6)$$

where $c_n(z)$ are the expansion coefficients, n is the order of the basis functions and N is the number of basis functions used in the expansion. The choice of $\phi_n(x)$ depends on the boundary conditions and the symmetry of the guiding structure. The coefficients of expansion $c_n(z)$ are unknown and represent the variation of the field with z . In the collocation method, these coefficients are effectively obtained by requiring that the differential equation, Eq. 5, be satisfied *exactly* by the expansion, Eq. 6, at N collocation points $x_j, j = 1, 2, \dots, N$, which are chosen such that these are the zeroes of $\phi_{N+1}(x)$. Thus, using this condition and with some algebraic manipulations,³⁻⁶ one converts the wave equation, Eq. 5, into a matrix ordinary differential equation:

$$\frac{d^2 \Psi}{dz^2} + [S_0 + R(z)] \Psi(z) = 0 \quad (7)$$

where

$$\Psi(z) = \begin{bmatrix} \Psi(x_1, z) \\ \Psi(x_2, z) \\ \vdots \\ \Psi(x_N, z) \end{bmatrix}, \quad R(z) = k_0^2 \begin{bmatrix} n^2(x_1, z) & 0 & \cdot & 0 \\ 0 & n^2(x_2, z) & \cdot & \cdot \\ \cdot & \cdot & \cdot & 0 \\ 0 & \cdot & 0 & n^2(x_N, z) \end{bmatrix} \quad (8)$$

and S_0 is a constant known matrix defined by the basis functions. We refer to Eq. 7 as the *collocation equation*. In deriving this equation from the wave equation, Eq. 5, no approximation has been made except that N is finite, and Eq. 7 is exactly equivalent to Eq. 5 as $N \rightarrow \infty$. Thus, the accuracy of the collocation method improves indefinitely as N increases.

In the collocation method, one can either solve the collocation equation directly or invoke the paraxial approximation, if valid, to obtain the equation for the envelope:

$$\frac{d\chi}{dz} = \frac{1}{2ik} [S_0 + R(z) - k^2 I] \chi(z) \quad (9)$$

where $\chi(z) \equiv \Psi(z) e^{ikz} = \text{col}[\chi(x_1, z) \ \chi(x_2, z) \ \cdots \ \chi(x_N, z)]$ and I is a unit matrix. This equation can be solved directly using, e.g., the Runge-Kutta method, or using the operator method like in the case of FFT-BPM. The latter procedure has been shown to be unconditionally stable numerically⁶.

A unique feature of the collocation method is that one obtains an equation as a result which can be solved or modified in a variety of ways. It can be solved as an initial value problem using any standard method such as the Runge-Kutta method³⁻⁵ or the predictor-corrector method. In the paraxial form, it can also be solved using matrix operator methods based on the approach of symmetrized splitting of the sum of two non-commutating operators⁶. One could also use a suitable transformation of the independent and/or dependent variable to an advantage. Indeed, it has been shown⁷ that a transformation could be used to redistribute the collocation points (which are the field sampling points in the transverse cross-section) in such a way that the density of points increases in and around the guiding region, and the transverse extent, covered by the sampled field, also increases.

2.2.1 Sampling point distribution: Equally spaced sample points

The electric field can be expressed in terms of plane waves that can further be expressed in terms of sinusoidal functions. These sinusoidal functions are solutions of the Helmholtz equation for a homogeneous medium. These functions oscillate even at $x \rightarrow \infty$, in order that the field vanishes at large distances; we assume an artificial boundary at $\pm L$ where the field is assumed to vanish. With these boundary conditions the Helmholtz equation for a homogeneous medium gives solutions that vary as:

$$\begin{aligned}\phi_n(x) &= \cos(v_n x) & \text{for } n = 1, 3, 5, \dots, N-1 \\ \phi_n(x) &= \sin(v_n x) & \text{for } n = 2, 4, 6, \dots, N\end{aligned}\tag{10}$$

where $v_n = n\pi/2L$. The collocation points are then the equally spaced zeroes of $\cos(v_{N+1}x)$ for an even N ; thus,

$$x_j = \left(\frac{2j}{N+1} - 1 \right) L, \quad j = 1, 2, 3, \dots, N.$$

In this case, the matrix S_0 is given by

$$S_0 = A H A^{-1}\tag{11}$$

where

$$A = \begin{pmatrix} \phi_1(x_1) & \phi_2(x_1) & \dots & \phi_N(x_1) \\ \phi_1(x_2) & \phi_2(x_2) & \dots & \phi_N(x_2) \\ \dots & \dots & \ddots & \vdots \\ \phi_1(x_N) & \phi_2(x_N) & \dots & \phi_N(x_N) \end{pmatrix} \text{ and } H = \begin{pmatrix} -v_1^2 & 0 & \dots & 0 \\ 0 & -v_2^2 & \dots & 0 \\ \vdots & \vdots & \ddots & \vdots \\ 0 & 0 & \dots & -v_N^2 \end{pmatrix}.$$

Thus, the collocation equation, Eq. 9, is fully defined and can be solved numerically for a given $n^2(x, z)$.

The sample points, in this case, are equally spaced and we can vary the spacing between them by choosing the values of L and N appropriately. This allows one to define an equi-spaced grid which has a desired density of sampling points. Depending on the geometry of the structure and complexity of the field being propagated, we can choose a finer or coarser grid while still maintaining equal spacing between the grid points.

2.2.2 Sampling point distribution: Unequally spaced sample points

In this case, we choose the expansion functions to be the Hermite Gauss functions such that

$$\phi_n(x) = N_{n-1} H_{n-1}(\alpha x) \exp\left(-\frac{1}{2}\alpha^2 x^2\right)\tag{12}$$

where N_{n-1} is the normalization constant and α is an adjustable parameter. The collocation points are now given by:

$$H_N(\alpha x_j) = 0, \quad j = 1, 2, \dots, N\tag{13}$$

The Hermite polynomial, H_N , defined above has N distinct zeroes which are unequally spaced. The matrix S_0 in this case is given by

$$S_0 = D_1 - A D_2 A^{-1} \quad (14)$$

where

$$D_1 = \alpha^4 \times \begin{pmatrix} -x_1^2 & 0 & \cdots & 0 \\ 0 & -x_2^2 & 0 & 0 \\ \vdots & \vdots & \ddots & \vdots \\ 0 & 0 & \cdots & -x_N^2 \end{pmatrix}, \quad D_2 = \alpha^2 \times \begin{pmatrix} 1 & 0 & \cdots & 0 \\ 0 & 3 & 0 & 0 \\ \vdots & \vdots & \ddots & \vdots \\ 0 & 0 & \cdots & 2N-1 \end{pmatrix}, \quad (15)$$

$$\text{and} \quad A = \begin{pmatrix} \phi_1(x_1) & \phi_2(x_1) & \cdots & \phi_N(x_1) \\ \phi_1(x_2) & \phi_2(x_2) & \cdots & \phi_N(x_2) \\ \cdots & \cdots & \ddots & \vdots \\ \phi_1(x_N) & \phi_2(x_N) & \cdots & \phi_N(x_N) \end{pmatrix}$$

The sample points are now no longer equally spaced, in fact the spacing between them varies such that the points near the origin are more closely spaced and the points towards the window extremity are farther apart.

2.3 Variable transformation in the collocation method: PML implementation

By applying a variable transformation in the collocation method, it is possible to redistribute the sample points to suit the nature and demands of the problem.⁷ It is, for example, possible to use transformations that concentrate the sample points more closely in a region where the field variations are rapid and distribute them far apart where the field is slowly varying. It is also possible to implement transformations where the variables can be made complex. In fact, that is the essence of the PML implementation in the collocation method. We have thus implemented the PML technique using the variable transformation, given in Sec. 2.1 in the Collocation method. The formalism is outlined here.

The PML is implemented by transforming Eq.5 using

$$x = h(\sigma) \\ \psi(x, z) = \sqrt{h'(\sigma)} U(\sigma, z) \quad (16)$$

where $h(\sigma)$ is defined in Eq. 2. Equation 5 then becomes

$$\frac{\partial^2 U}{\partial z^2} + f(\sigma) \frac{\partial^2 U}{\partial \sigma^2} + [g(\sigma) + k_o^2 n^2(\sigma, z)] U(\sigma, z) = 0 \quad (17)$$

where

$$f(\sigma) = [h'(\sigma)]^{-2} \quad (18)$$

$$g(\sigma) = \frac{1}{2h'^4} (h'''h' - \frac{3}{2}h''^2) \quad (19)$$

where prime denotes differentiation with respect to σ . Equation 17 is similar to Eq. 5 in form except for a factor $f(\sigma)$ in the second term. We can therefore use the collocation method of Sec. 2.2 to convert Eq. 17 into a matrix equation⁷

$$\frac{d^2 \mathbf{U}}{dz^2} + [\hat{\mathbf{S}}_0 + \mathbf{R}(z)] \mathbf{U}(z) = 0 \quad (20)$$

The vector $\mathbf{U}(z) = \{U_j : U_j = U(\sigma_j)\}$ denotes the values of the transformed field at the collocation points and the matrix $\hat{\mathbf{S}}_0$ is given by

$$\hat{\mathbf{S}}_0 = \mathbf{F} \mathbf{D}_1 - \mathbf{F} \mathbf{A} \mathbf{D}_2 \mathbf{A}^{-1} + \mathbf{G} \quad (21)$$

where $\mathbf{F} = \{F_j : F_j = f(\sigma_j)\}$, $\mathbf{G} = \{G_j : G_j = g(\sigma_j)\}$ and \mathbf{A} , \mathbf{D}_1 , \mathbf{D}_2 are defined as earlier after Eq.14, except that now x is replaced by σ . Using the paraxial approximation for the envelope $\hat{\chi}(z) \equiv \mathbf{U}(z) e^{ikz}$, we obtain the equation

$$\frac{d\hat{\chi}}{dz} = \frac{1}{2ik} [\hat{\mathbf{S}}_0 + \mathbf{R}(z) - k^2 \mathbf{I}] \hat{\chi}(z) \quad (22)$$

Eq.22 can be solved as an initial value problem using any standard method such as the Runge-Kutta method or the predictor-corrector method. We have used the fourth order Runge-Kutta method in our examples. It may be noted that in the real window, the field $U(\sigma)$ and $\psi(x)$ are identical and hence, $\hat{\chi}$ directly gives χ , which is the quantity of interest.

3. RESULTS

The PML performance depends on factors such as PML width, absorption profile and sample point distribution. In this section, we outline and discuss numerical examples that test the PML performance on each of these parameters. Based on these results, we suggest ways to improve PML effectiveness and decrease the computational burden.

For a test problem we have considered at the absorption of a Gaussian beam of width $4 \mu\text{m}$ launched towards the PML layer at different angles. The refractive index of the homogeneous medium is taken to be 1.4472. As a measure of the energy reflected from the PML, we calculate the fractional energy remaining in the real window at a point exactly above the starting point in the computation window where the beam would have reached after reflection from the edge. We have chosen a window of total width $44.6 \mu\text{m}$ and the number of sample points is $N=100$. This fractional energy is designated as E_R .

Figure 2 shows a plot of E_R versus the PML width for a beam tilted at 25° for both the sampling point distributions discussed Section 2.2. The PML layer has a square absorption profile and the layer is optimized in both cases for maximum absorption by choosing a suitable value of p_0 . We can see that E_R decreases with increasing PML width for both the distributions. However, in equally spaced points, E_R is much lower, by about three orders of magnitude at the smallest PML width as compared to unequally spaced points. For other widths also the absorption is better for equally spaced sample points, though for larger PML widths both equally spaced points and unequally spaced points perform nearly equally well.

Figure 3 shows the results for a non-optimal case. We have optimized the layer for absorption at 22.5° and then we obtain the absorption at angles larger and smaller than 22.5° , for the square profile. It can be seen that for unequally spaced points, as angle deviates from 22.5° , E_R increases rapidly. But in equally spaced points, even as angle increases, E_R varies much less. Thus with equally spaced points, the PML can better absorb beams at angles other than the one for which the layer is optimized. Figure 4 shows the results for another non-optimal test case. Here the layer is optimized for absorption at 22.5° again, however we make incident simultaneously two beams, one at 15° and the other at 30° . The figure shows fractional energy remaining in the real window, E_z , as a function of z for the two sampling point distributions when the layer width is $6.7 \mu\text{m}$ which is 15% of the total window (dashed curves) and $3.5 \mu\text{m}$, i.e., 8% of the total window (continuous curves). The beam tilted at 30° hits the PML first and gets absorbed first so that we see a decrease in E_z and then it becomes somewhat constant, while the second beam still continues to travel in the real window for some time. When the 15° beam also hits the PML, E_z again starts decreasing. The important point to note is that for smaller PML width (continuous curves), E_z is lower by almost 3 orders of magnitude in the equally spaced basis, while performance is comparable in both cases at larger PML width. The figure also shows that the PML

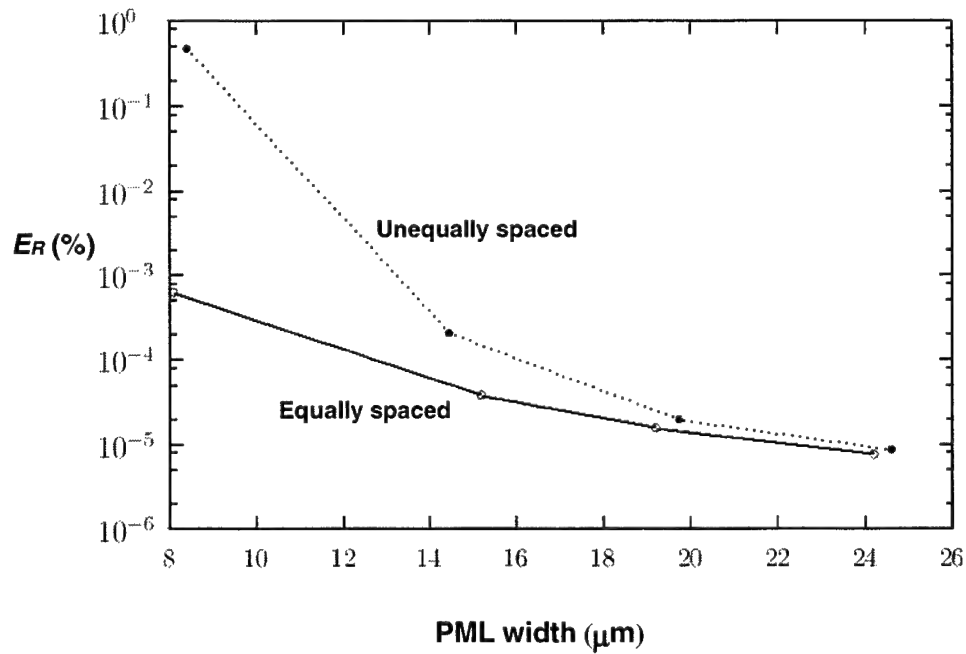


Fig.2 Energy remaining in the real window, E_R , (in %) as function of the PML width for the square profile with the unequally spaced and equally spaced distribution of sample points.

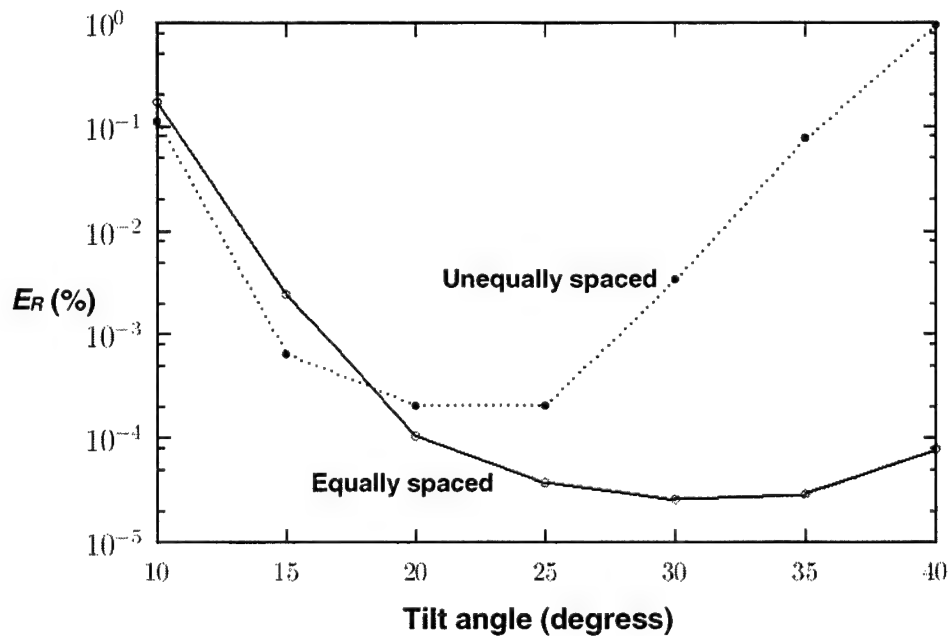


Fig.3 Energy remaining in the real window, E_R , (in %) as function of beam tilt angle for the square profile with the unequally spaced and equally spaced distribution of sample points

absorptivity is much more sensitive to width when the points are unequally spaced, while with equally spaced points, the PML performance is not affected as much with change in width. Thus, with smaller PML width, using equally spaced basis has a very distinct advantage in reducing reflected energy under optimum as well as non-optimum conditions. For larger widths, the PML performance for the two types of point distributions is comparable.

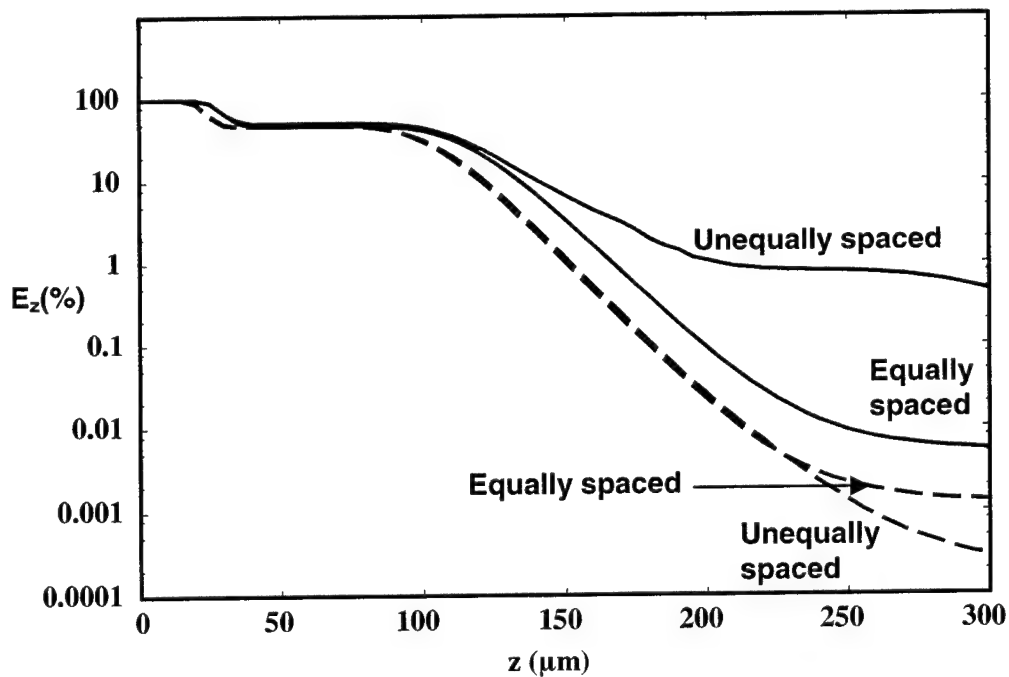


Fig.4 Energy remaining in the real window, E_z , (in %) as function of propagation distance z . The results are shown for square profile with the unequally spaced and equally spaced distribution of sample points. The PML width is $3.5 \mu\text{m}$ (8% of the total window) for the continuous curves and $6.7 \mu\text{m}$ (15% of the total window) for the dashed curves.

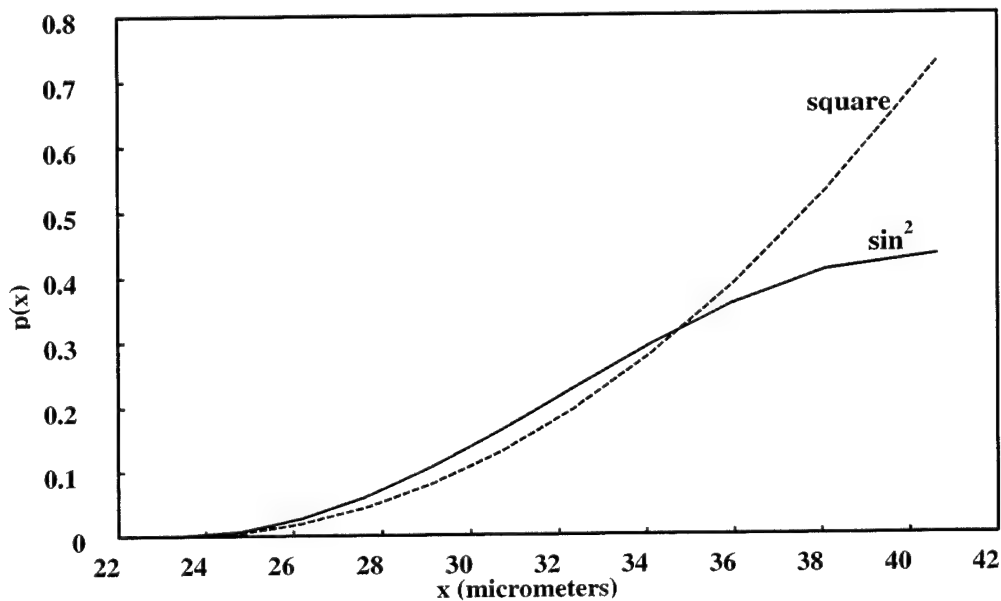
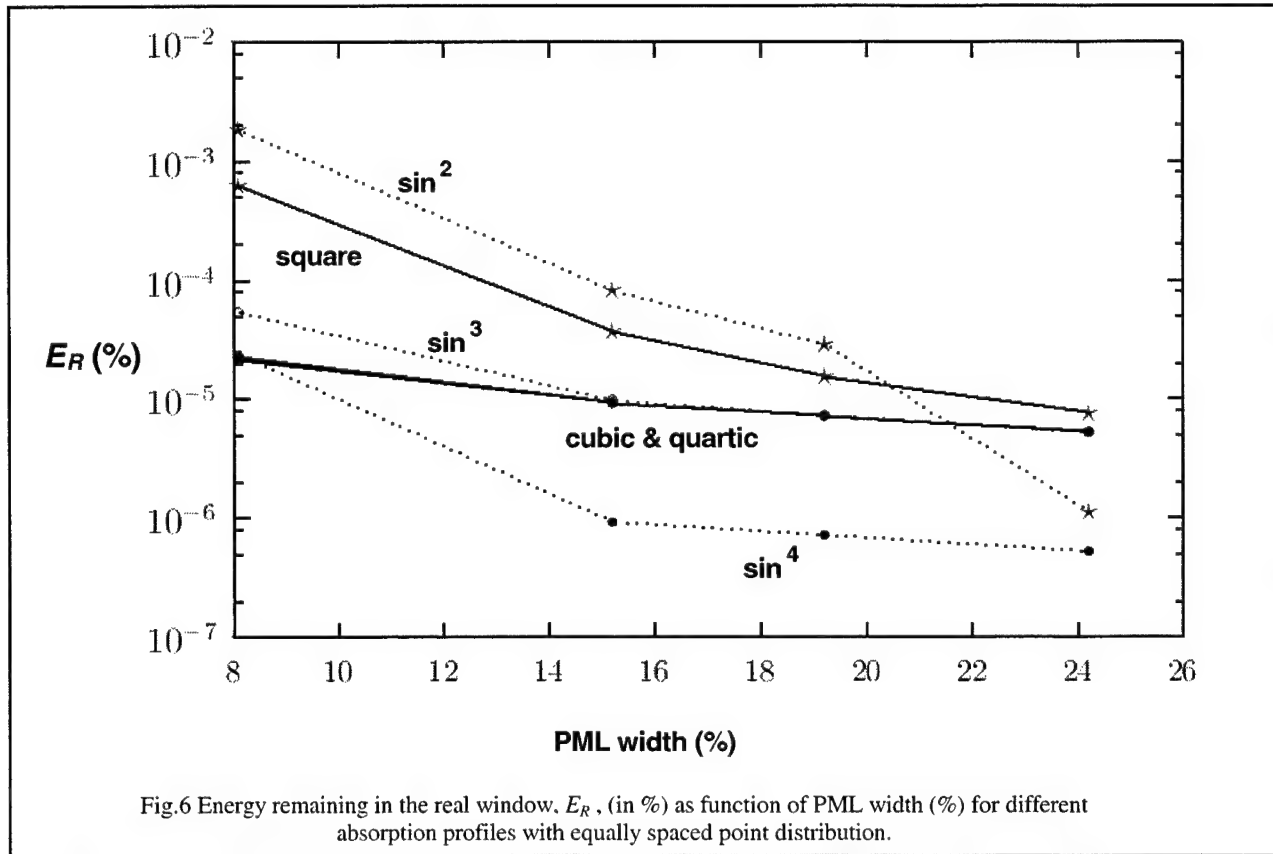


Fig.5 Absorption profile variation for the square and \sin^2 profiles in equally spaced point distribution.

Fig. 5 shows the square and \sin^2 absorption profiles. The main difference between the two is that the square profile has a steep increase in slope while the \sin^2 profile gets flattened near the window end. To compare the effect of the two different set of profiles, consider E_R as a function of the PML width for different profiles for equally spaced



points (Fig. 6), as well as for unequally spaced points (Fig. 7). In the case of equally spaced points, the \sin^4 profile is by far the best, at all widths. The cubic, quartic and the \sin^3 perform similarly, and square and \sin^2 are by far the worst. On the other hand, with unequally spaced points, quartic and \sin^4 are the worst at lower width, square and \sin^2 being best. At higher widths, all the profiles show E_R values saturated to nearly the same value in the case of unequally spaced points. Comparing these two figures, we can conclude that for all profiles, at lower width, equally spaced basis is better, and with this point distribution a steeper profile \sin^4 is the best among all the profiles investigated

The above results show that for smaller widths of the PML, it is important to choose a correct point distribution, which is equally spaced at least for the example we have chosen, and an appropriate absorption profile, which is \sin^4 for our example. Of course, one could choose a large (20-25%) PML width and not worry about the specifics of the point distribution and the absorption profile; however, the penalty would be larger computation window and larger computational effort. For repetitive computations, as in the case of a typical design exercise, it would pay to follow the first option of using a lower PML width with appropriately chosen point distribution and absorption profile.

Another aspect that we found advantageous in the sine profiles was that it is possible to add extra sections of uniform absorption layers to the existing PML, at the end of the PML, that is beyond x_b and extend the boundary when required. This increase in PML width does increase the computation, but leads to large improvement in the absorption as can be seen in Fig. 8, which shows how the energy remaining in the real window decreases as additional uniform absorption sections (containing 1, 2, 3, or 4 extra points) are added at the end of the existing PML layer. While it would be better to optimize the larger layer, but if the time required to optimize the now larger layer is not available, simply adding the constant absorption sections, is an attractive way to decrease E_r without too much effort. A similar approach cannot be followed with power law profiles due to discontinuity at the interface between the existing PML and the additional PML sections.

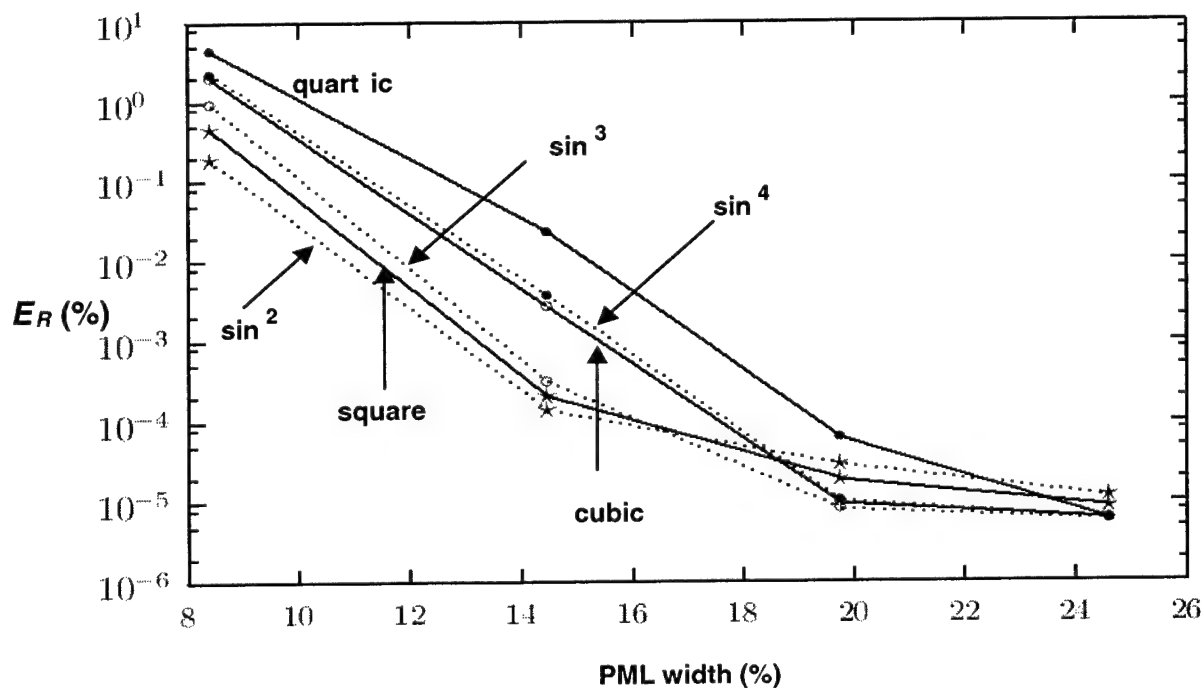


Fig.7 Energy remaining in the real window, E_R , (in %) as function of PML width (%) for different absorption profiles with unequally spaced point distribution.

4. SUMMARY AND CONCLUSIONS

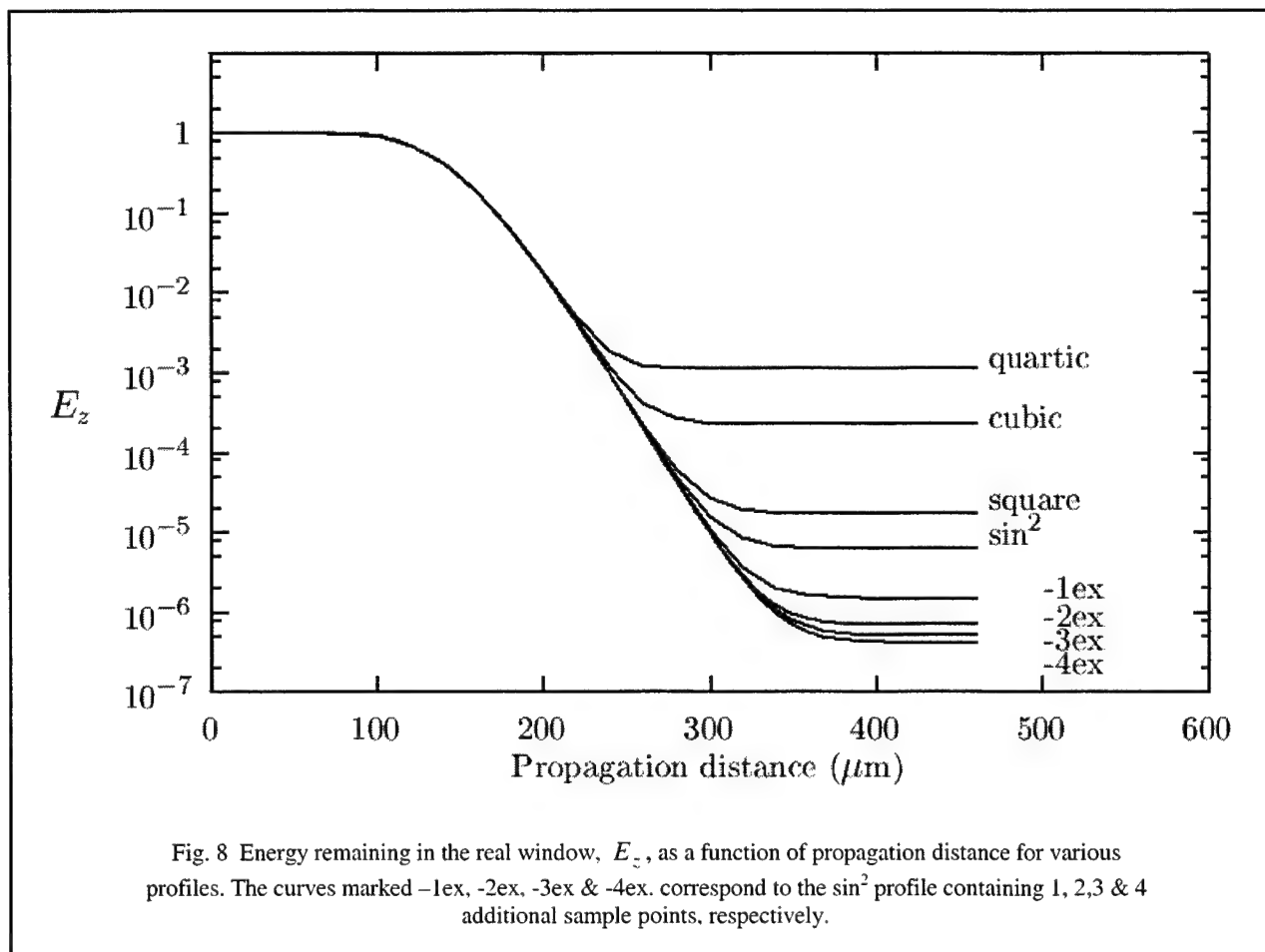
The PML boundary condition has been implemented in the collocation method for equally spaced and unequally spaced distribution of sample points. We have then studied the performance of the PML as an absorbing layer for a Gaussian beam as a test case. The effect of different distributions of sample points and of different PML absorption profiles on PML performance has thus been studied. We found that equal spacing between points leads to better absorption of beams under both optimal as well as non-optimal conditions for smaller PML widths. While for larger PML widths, both unequally spaced and equally spaced points perform equally well. The PML performance is a strong function of the absorption profile for smaller (and hence, numerically more efficient) PML widths, while for larger widths, the nature of absorption profile matters much less. For smaller widths, a newly suggested \sin^4 absorption profile with equally spaced points gives the best PML performance. For better numerical efficiency, one would like to use smaller PML widths and for optimized performance of the PML, it would be important choose appropriate point distribution and absorption profile.

ACKNOWLEDGEMENTS

This work was partially supported by a grant (No. 03(0976)/02/EMR-II) from the Council of Scientific and Industrial Research (CSIR), India. One of the authors (AA) is a CSIR research fellow.

REFERENCES

1. M.D. Feit and J.A. Fleck, Jr., "Light propagation in graded-index optical fibers," *Appl. Opt.* **17**, 3990-3998, 1978.
2. C.L. Xu and W.P. Huang, "Finite-difference beam propagation methods for guided-wave optics", in *Methods for Modeling and Simulation of Optical Guided-Wave Devices*, (Guest editor: W.Huang) of series *Prog. Electromagnet. Res.*, vol. **11**, pp. 1-49, 1995 [EMW Publishing, Cambridge, Mass., USA]



3. A. Sharma, "Collocation method for wave propagation through optical waveguiding structures", *ibid* pp. 143-198, 1995.
4. S. Banerjee and A. Sharma, "Propagation characteristics of optical waveguiding structures by direct solution of the Helmholtz equation for total fields," *J. Opt. Soc. Am. A*, **6**, 1884-1894, 1989.
5. A. Sharma and S. Banerjee, "Method for propagation of total fields or beams through optical waveguides," *Opt. Lett.* **14**, 94-96, 1989.
6. A. Sharma and A. Taneja, "Unconditionally stable procedure to propagate beams through optical waveguides using the collocation method," *Opt. Lett.* **16**, 1162-1164, 1991.
7. A. Sharma and A. Taneja, "Variable-transformed collocation method for field propagation through waveguiding structures," *Opt. Lett.* **17**, 804-806, 1992.
8. E.L. Lindman, "Free space boundary conditions of the time dependant wave equation", *J. Comp. Phy.* **18**, 66-78, 1975.
9. B. Engquist and A. Majda, "Absorbing boundary conditions for the numerical simulation of waves," *Math. Computation*, **31**, 629-651, 1977.
10. G. Mur, "Absorbing boundary condition for the finite-difference approximation of the time-domain electromagnetic-field equations," *IEEE Tran. Electromag. Compat.* **EMC-23**, 377-382, 1981.
11. C. Vasallo and F. Collino, "Highly efficient absorbing boundary conditions for the beam propagation method," *J. Lightwave Technol.* **14**, 1570-1577, 1996.

12. G.R. Hadley, "Transparent boundary condition for beam propagation," *Opt. Lett.* **16**, 624-626, 1991.
13. G.R. Hadley, "Transparent boundary condition for the beam propagation method," *Opt. Lett.* **28**, 624-626, 1992.
14. G.R. Hadley, "Transparent boundary condition for the beam propagation method," *IEEE J. Quant. Electron.* **QE-28**, 363-370, 1992.
15. J.P. Berenger, "A perfectly matched layer for the absorption of electromagnetic waves," *J. Computational Phys.* **114**, 185-200, 1994.
16. W.P. Huang, C.L. Xu, W. Lui and K. Yokoyama, "The perfectly matched layer (PML) boundary condition for the beam propagation method," *IEEE Photon. Technol. Lett.* **8**, 649-651, 1996.
17. W.P. Huang, C.L. Xu, W. Lui and K. Yokoyama, "The perfectly matched layer boundary condition for modal analysis of optical waveguides: leaky mode calculations," *ibid*, 652-654, 1996.
18. D. Zhou, W.P. Huang, C.L. Xu, D.G. Fang and B. Chen, "The perfectly matched layer boundary condition for scalar finite-difference time-domain method," *IEEE Photon. Technol. Lett.* **13**, 454-456, 2001.
19. J.C. Chen and K. Li, "Quartic perfectly matched layers for dielectric waveguides and gratings," *Microwave Opt. Technol. Lett.* **10**, 319-323, 1995.

Closed form modal field expressions in Diffused Channel Waveguides

Geetika Jain, Ashmeet Kaur Taneja, Enakshi Khular Sharma*

Department of Electronic Science
University of Delhi South Campus
New-Delhi-110021, India

ABSTRACT

We present accurate closed form expressions for modal fields and propagation constant of the fundamental mode in diffused channel waveguides using a scalar variational approach. The results have been compared with those obtained by use of the Optiwave BPM_CAD software package. The closed form fields have been shown to be useful in optimizing fiber to waveguide coupling and evaluating gain in Erbium doped waveguides.

Keywords: Channel Waveguides, Closed form modal fields, Titanium diffused LiNbO₃ waveguides

1. INTRODUCTION

Design of integrated optical devices using diffused channel optical waveguides demands a sufficiently accurate knowledge of their modal properties. Since, in general, analytical solutions are not possible for diffused channel waveguides, one has to use either approximate method like Effective-Index method or numerically intensive methods like finite difference, finite element or Beam propagation techniques. In all these methods, modal fields are obtained as numerical data and not as closed form expressions useful for device design. In this paper we present, accurate closed form expressions for the modal fields and propagation constant based on scalar variational procedure [1]. The variational approach is based on maximizing a stationary expression for the propagation constant with respect to various parameters in a judiciously chosen trial field where accuracy depends on the functional form of the chosen field and the number of parameters [2,3]. We have taken three, four and five parameter trial fields and have compared our results with results obtained by use of the BPMCAD Simulator [4].

To illustrate the applications of our analytical modal fields, we have used them for the optimization of fiber waveguide coupling and to estimate the gain and loss characteristics of an Erbium-Doped LiNbO₃ waveguide [5], which is an emerging component of amplifying integrated circuits.

2. VARIATIONAL APPROACH

The typical refractive index profile of a diffused channel waveguide can be described as

$$\begin{aligned} n^2(x, y) &= n_s^2 + 2n_s \Delta n \exp\left(-x^2/w^2\right) \exp\left(-y^2/h^2\right) & y > 0 \\ &= n_c^2 & y < 0 \end{aligned} \quad (1)$$

where n_s and n_c are the substrate and cover layer indices, w and h are the half width and penetration depth of the index variation of diffused waveguide. Δn , w and h depend on material and process parameters.

For the two dimensional refractive index profile $n(x, y)$ the stationary scalar variational expression for the effective index of the fundamental mode of the channel waveguide is given as [6]

$$n_e^2 = \iint \psi_r(x, y) |\Delta \psi_r(x, y)|^2 dx dy + \iint n^2(x, y) |\psi_r(x, y)|^2 dx dy \quad (2)$$

* enakshi@bol.net.in

where ψ_t is an approximation to the modal field sought as solution to the propagation problem with three, four or five variational parameters with respect to which right hand side of the above expression is maximized. The trial field is assumed to be normalized, $\int_{-\infty}^{\infty} |\psi_t(x, y)|^2 dx dy = 1$.

We will approximate the trial field to be separable, i.e.,

$$\psi_t(x, y) = \chi(x)\phi(y) \quad (3)$$

Substituting the suitably chosen field forms into the stationary expression we obtain closed form expressions for the normalized effective index $b = (n_e^2 - n_s^2)/2n_s \Delta n$ in terms of the variational parameters, a normalized V parameter in y direction $V_y = k_0 h \sqrt{2n_s \Delta n}$, a normalized V number in x direction, $V_x = k_0 w \sqrt{2n_s \Delta n}$, and the asymmetry parameter, $p = (n_s^2 - n_c^2)/2n_s \Delta n$, where $k_0 = 2\pi/\lambda_0$ is the free space wave number. Maximizing the expression for normalized effective index by standard routines available [7] e.g. Powell's method, gives the optimized values of the variational field parameters.

2.1 Three Variable Trial Field

A suitable normalized trial field consists of a two variable evanescent Hermite Gauss function [2] in the asymmetric y direction and a Gaussian function in the symmetric x direction

$$\begin{aligned} Y(y) &= A_y \left(1 + \gamma_y \frac{y}{h} \right) \exp \left(-\alpha_y^2 \frac{y^2}{h^2} \right) & y > 0 \\ &= A_y \exp \left(\gamma_y \frac{y}{h} \right) & y < 0 \\ X(x) &= A_x \exp \left(-\alpha_x^2 \frac{x^2}{w^2} \right) & \text{for all } x \end{aligned} \quad (4)$$

where A_y and A_x are the normalization constants. There are three variational parameters γ_y and α_y defining the field in y direction and α_x gives the width of the Gaussian field in x direction. Substituting this field into the stationary expression we obtained a closed form expression for normalized effective index b in terms of the variational parameters.

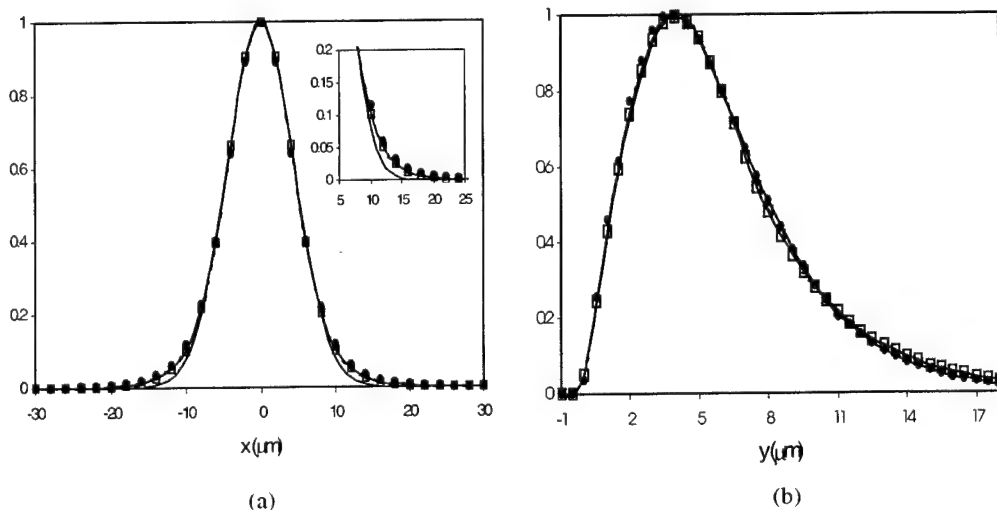


Fig. 1. The closed form variational field at wavelength of 1532nm (a) x-variation at $y=4.0\mu\text{m}$. (b) y-variation at $x=0.0\mu\text{m}$. The points correspond to the numerical results obtained by the OPTIWAVE BPM_CAD 3D-simulator, continuous line to three variable fields, rectangles to four variable x-improved field in (a) and four variable y-improved field in (b), dashed lines to five variable modal field.

In order to illustrate the procedure we carried out calculations for the TE mode of a typical waveguide [8] fabricated by indiffusion (1030°C, 9hrs) of a 7µm wide, 95nm thick Titanium stripe into z-cut LiNbO₃ substrate for use at 1532nm. The substrate index is taken as 2.297. Assuming the typical values of diffusion constants for horizontal and vertical directions as 0.023cm²/sec with a temperature coefficient of 30300⁰K and simulating the diffusion process, the actual waveguide parameters are obtained as $h=6.5\mu\text{m}$, $w=7.5\mu\text{m}$ and $\Delta n=0.0048$. The modal fields obtained by the closed form expression are compared with those obtained by the BPM_CAD Simulator from Optiwave [4] as shown in Figs. 1(a) and (b). The three variable optimized fields (3V) are in good agreement with simulated results except for small deviations in tail regions in both x and y directions. The values of the three parameters and corresponding effective index obtained, for the waveguide described above, are given in Table I.

2.2 Four Variable Trial Field- improvement in y direction

Fig. 1(a) and (b) show that the variational field matches the exact field quite well in the region where the field is maximum, but in the evanescent tail it falls off very rapidly. An additional exponential function in the evanescent tail region in the $y/h > a_y$ further increases the accuracy.

The trial field with y improvement is described as:

$$\begin{aligned}
 Y(y) &= A_y \left(1 + \gamma_y a_y\right) \exp\left(\alpha_y^2 a_y^2 - \frac{\gamma_y a_y}{1 + \gamma_y a_y}\right) \exp\left(-\left(2\alpha_y^2 a_y - \frac{\gamma_y a_y}{1 + \gamma_y a_y}\right) \frac{y}{h}\right) & y/h > a_y \\
 &= A_y \left(1 + \gamma_y \frac{y}{h}\right) \exp\left(-\alpha_y^2 \frac{y^2}{h^2}\right) & y/h < a_y \\
 &= A_y \exp\left(\gamma_y \frac{y}{h}\right) & y < 0 \\
 X(x) &= A_x \exp\left(-\alpha_x^2 \frac{x^2}{w^2}\right) & \text{for all } x
 \end{aligned} \tag{5}$$

Now there are four variational parameters γ_y , α_y , α_x and a_y . Closed form expression for b is obtained. The maximization gives the optimized variational parameters and hence, the optimized field. Fig. 1(b) shows comparison of y variation of closed form modal fields with those obtained by the BPM Simulator. There is no significant change in the field in x direction, while the field variation in the y direction has significantly improved. However, as shown in the Table I, there is a significant change in effective index for this field description which implies the effective index is sensitive to the field form in y direction.

2.3 Four Variable Trial Field- improvement in x direction

The actual field form in the x direction is also not a Gaussian but penetrates deeper into the width. This evanescent tail plays an important part in evanescently coupled adjacent waveguides. Hence, we included an exponential tail in the Gaussian function for a more accurate description of transverse field in x direction in the following form:

$$\begin{aligned}
 Y(y) &= A_y \left(1 + \gamma_y \frac{y}{h}\right) \exp\left(-\alpha_y^2 \frac{y^2}{h^2}\right) & y > 0 \\
 &= A_y \exp\left(\gamma_y \frac{y}{h}\right) & y < 0 \\
 X(x) &= A_x \exp\left(-\alpha_x^2 \frac{x^2}{w^2}\right) & |x/w| < a_x \\
 &= A_x \exp(\alpha_x^2 a_x^2) \exp\left(-2\alpha_x^2 a_x \frac{x}{w}\right) & |x/w| > a_x
 \end{aligned} \tag{6}$$

where γ_y and α_y are the two variational parameters in $\phi(y)$ and two variational parameters a_x and α_x in $\chi(x)$. Again a closed form expression for b can be obtained and its maximization gives us the optimized variational parameters. The

corresponding x improved field is plotted in Fig. 1(a). There is, however, no improvement in the effective index as shown in Table I, which implies that effective index is more sensitive to the y -field description. However, the improvement in the field forms obtained in the x direction is essential for studying laterally coupled structures such as directional couplers.

2.4 Five Variable Trial Field

We can also use a complete five variable trial field which has an exponential tail in both x and y directions. The trial field is now described as

$$\begin{aligned}
 Y(y) &= A_y \left(1 + \gamma_y a_y\right) \exp\left(\alpha_y^2 a_y^2 - \frac{\gamma_y a_y}{1 + \gamma_y a_y}\right) \exp\left(-\left(2\alpha_y^2 a_y - \frac{\gamma_y a_y}{1 + \gamma_y a_y}\right) \frac{y}{h}\right) & y/h > a_y \\
 &= A_y \left(1 + \gamma_y \frac{y}{h}\right) \exp\left(-\alpha_y^2 \frac{y^2}{h^2}\right) & y/h < a_y \\
 &= A_y \exp\left(\gamma_y \frac{y}{h}\right) & y < 0 \\
 X(x) &= A_x \exp\left(-\alpha_x^2 \frac{x^2}{w^2}\right) & |x/w| < a_x \\
 &= A_x \exp(\alpha_x^2 a_x^2) \exp\left(-2\alpha_x^2 a_x \frac{x}{w}\right) & |x/w| > a_x
 \end{aligned} \tag{7}$$

The field is now a combination of improved fields in x as well as y direction. The closed form expression can be obtained for b , which is maximized to get the five variational parameters. The comparison of the five variable modal fields with simulated fields in Figs 1(a) and (b) show that the two exactly match with each other. It is important to note from Table I that α_y in five parameter field is the same as in the four parameter y -improved field and α_x is same as the four parameter x -improved field.

Fortunately, the variation of a_y is not much for Gaussian profile over the entire single mode region. Hence, it is possible to fix the value of the a_y parameter at $a_y=1.04$. Similarly the variation in a_x is not significant, so we can even fix the a_x parameter at $a_x=0.87$ to reduce our analysis with exponential tails to a three parameter variational form. The new improved three parameter fields gives accurate analytical description of the modal field as shown in figs. 2(a) and (b).

TABLE I

Variational parameters for channel waveguide with
 $n_s=2.297$, $n_c=1.0$, $\Delta n=0.0048$, $h=6.5\mu\text{m}$, $w=7.5\mu\text{m}$, $\lambda=1532\text{nm}$

Method	γ	α_y	α_x	a_y	a_x	n_{eff}
3-variable	47.46	1.099	1.188	-	-	2.29807
4-variable (y)	53.30	1.138	1.186	1.041	-	2.29817
4-variable (x)	52.31	1.098	1.206	-	0.8749	2.29807
5-variable	51.92	1.137	1.204	1.043	0.8755	2.29817
New 3-variable	52.00	1.137	1.204	1.040	0.87	2.29817

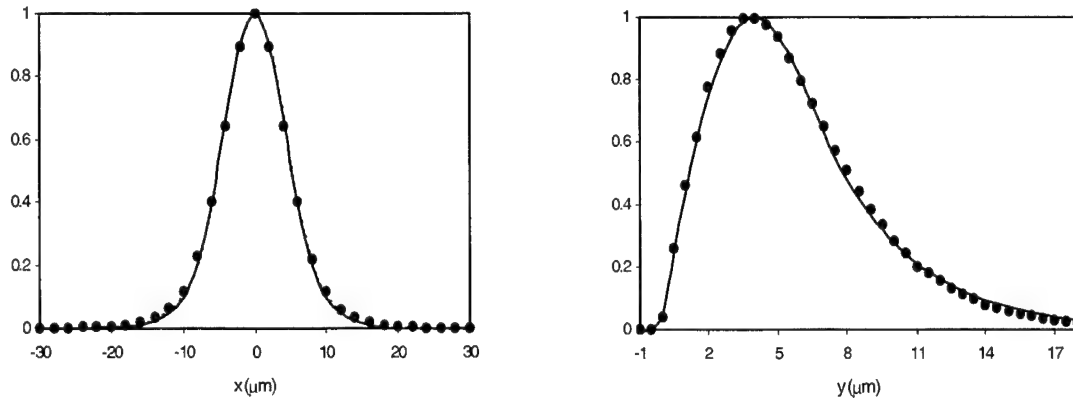


Fig. 2. The closed form variational field at wavelength of 1532nm (a) x-variation at $y=4.0\mu\text{m}$. (b) y-variation at $x=0.0\mu\text{m}$. The points correspond to the numerical results obtained by the OPTIWAVE BPM_CAD 3D-simulator and continuous line to the new three variable fields .

3. APPLICATIONS

We illustrate the use of the closed form expressions in two important applications, namely, fiber to waveguide coupling and estimation of gain in rare-earth doped waveguides. The closed form field expression leads to a closed form expression for fiber to waveguide coupling. The closed form field expressions also facilitates the estimation of gain and loss characteristics of an Erbium-Doped LiNbO_3 waveguide, which is an emerging component of amplifying integrated circuits.

3.1 Fiber Waveguide Coupling

In the optical systems that contain integrated optical components, coupling efficiency between the fundamental mode of the waveguides of an integrated optical circuit and the optical fiber that is connected to the circuit plays an important role in power loss considerations. In an optimization process the computations have to be repeated a large number of times [9]. With the closed form expressions the process of obtaining optimum waveguide parameters becomes very simplified. The coupling efficiency is given by

$$\eta = \int \psi_1(x, y) \psi_2(x, y) dx dy \quad (8)$$

here $\psi_1(x, y)$ is the normalized waveguide modal field and $\psi_2(x, y)$ is the normalized modal field of the fiber . The maxima of three parameter waveguide the modal field of Eq. 4 is at $x=0$ and $y = \xi_0$ where ξ_0 is given by

$$\xi_0 = \frac{-\alpha_y + \sqrt{\alpha_y^2 + 2\gamma_y^2}}{2\alpha_y\gamma_y/h}$$

For a fiber placed at $(0, \xi)$, the fiber field can be well approximated to a Gaussian, written as

$$\psi_2(x, y) = \sqrt{\frac{2}{\pi}} \frac{1}{\omega_f} \exp\left(-\frac{[x^2 + (y - \xi)^2]}{\omega_f^2}\right) \quad (9)$$

where ω_f is the spot size of the fiber and is typically a function of V number and radius of the fiber. Since both the fields are separable in x and y , the coupling efficiency can be written as a product

$$\eta = \eta_x \eta_y \quad (10)$$

Using the optimized three parameter fields, we get analytical expressions for the coupling efficiency as

$$\eta_x = \frac{I^2}{w\omega_f d_x} \sqrt{\frac{2}{\pi}} \quad (11)$$

$$\eta_y = \frac{J^2}{h\omega_f d_y} \sqrt{\frac{2}{\pi}} \quad (12)$$

here I is given by

$$I = \frac{\sqrt{\pi}}{\sqrt{\frac{1}{\omega_f^2} + \frac{\alpha_x^2}{w^2}}} \quad (13)$$

and J for the three variable fields is

$$J = \frac{\exp\left(-\frac{\xi^2}{\omega_f^2}\right) \left[\exp(k_1^2) \left\{ \sqrt{\pi} k_2^2 (1 + \operatorname{erf}(k_1)) + h\sqrt{\pi} \gamma_y \xi (1 + \operatorname{erf}(k_1)) \right\} + k_2 \omega_f \gamma_y \right]}{\frac{2k_2^3}{h\omega_f}} \quad (14)$$

with $k_1 = \frac{\xi}{\sqrt{\frac{\alpha_y^2}{h^2} + \frac{1}{\omega_f^2}}}$ and $k_2 = \sqrt{h^2 + \alpha_y^2 \omega_f^2}$

For optimizing the position of the fiber $(0, \xi)$, we have to maximize the coupling efficiency with respect to ξ , or obtain $\xi = \xi_m$, which is the value of ξ at which $\frac{d\eta_y}{d\xi} = 0$. This leads to the following transcendental equation, the

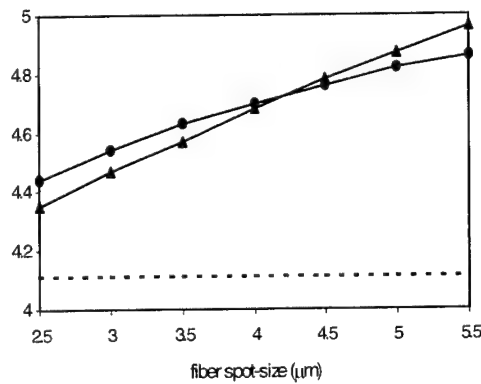


Fig. 3. Variation of optimal position of fiber (ξ_m) with spot-size. Triangles correspond to 5V modal field and points to the three 3V modal field of the waveguide; dashed line corresponds to the value of ξ_0 .

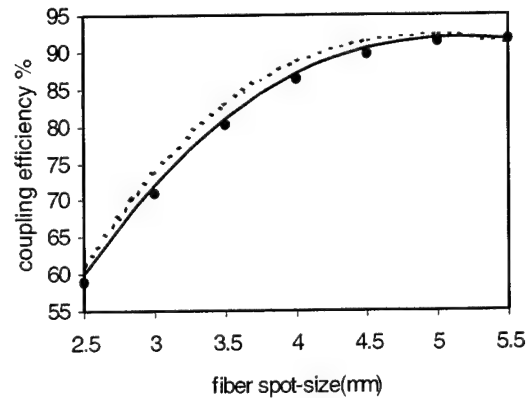


Fig. 4. Variation of Fiber to Waveguide Coupling Efficiency with Fiber spot-size. The points correspond to the numerical results obtained by the OPTIWAVE BPM_CAD 3D-simulator; continuous line correspond to the 5V modal field and dashed line to the 3V modal field of the waveguide.

solution of which gives ξ_m

$$a1(\xi) + a2(\xi) + a3(\xi) = 0 \quad (15)$$

where

$$\begin{aligned} a1(\xi) &= \frac{-\xi h}{\omega_f k_2^3} \left[\exp(k_1^2) \left\{ \sqrt{\pi} k_2^2 + h \sqrt{\pi} \gamma_y \xi \right\} (1 + \operatorname{erf}(k_1)) \right] + k_2 \omega_f \gamma_y \\ a2(\xi) &= \frac{h \omega_f}{k_2^4} \left[\frac{\xi}{\omega_f^4} \exp(k_1^2) \left\{ \sqrt{\pi} k_2^2 + h \sqrt{\pi} \gamma_y \xi \right\} (1 + \operatorname{erf}(k_1)) \right] \\ a3(\xi) &= \frac{h \omega_f}{k_2^3} \left[\frac{2}{\omega_f^4 k_2^2 h^2} (k_2^2 + h \xi \gamma_y) \exp(-k_1^2) + \left\{ h \sqrt{\pi} \gamma_y \xi (1 + \operatorname{erf}(k_1)) \right\} \right] \end{aligned}$$

The variation of ξ_m with fiber spot size is shown in Fig. 3. The position of the waveguide field maxima ξ_0 is also marked. It is important to note that the maximum power transfer is not obtained when fiber center is placed at $y = \xi_0$, where the waveguide modal field is maximum but at a different value $y = \xi_m$. As shown in the figure, the difference in the two values is considerable and varies with the spot-size of the fiber. The corresponding results for coupling efficiency have also been compared with those obtained by BPM_CAD [4] and are shown in Fig. 4.

3.3 Estimation of Gain and Loss in Optical Amplifier Waveguides

In general an amplifying media can be described by a complex refractive index $n = n_r + in_i$ and hence, the intensity variation can be written as $\frac{dI}{dz} = \frac{4\pi}{\lambda_0} n_i I$. An Er-doped LiNbO₃ waveguide, pumped at 1484nm, is an amplifying waveguide for signals in the wavelength region of 1530nm. For such a waveguide using the laser rate equations [8] for the doped waveguide, one can define an imaginary part for the index profile [10] describing the signal amplification and pump attenuation as

$$\begin{aligned} n_i(\text{signal}) &= \frac{\lambda_s}{4\pi} \sigma_a(\lambda_s) \frac{(\eta_s - \eta_p) \tilde{q} \psi_p^2(x, y) - 1}{1 + (\eta_s + 1) \tilde{p} \psi_s^2(x, y) + (\eta_p + 1) \tilde{q} \psi_p^2(x, y)} \rho(x, y) \\ n_i(\text{pump}) &= -\frac{\lambda_p}{4\pi} \sigma_a(\lambda_p) \frac{(\eta_s - \eta_p) \tilde{p} \psi_s^2(x, y) - 1}{1 + (\eta_s + 1) \tilde{p} \psi_s^2(x, y) + (\eta_p + 1) \tilde{q} \psi_p^2(x, y)} \rho(x, y) \quad (16) \end{aligned}$$

here $\tilde{p} = P_s(z)/I_{s0}$, $\tilde{q} = P_p(z)/I_{p0}$ are signal and pump power normalized to their respective saturation intensities defined as $I_{s0, p0} = \frac{\hbar \omega_{s, p}}{\sigma_a(\lambda_{s, p}) \tau}$, τ is the fluorescence lifetime of the Erbium ions corresponding to the transitions from level 2 to level 1, σ_a is the absorption cross-section, $\eta_{s, p}$ is the ratio of emission to absorption cross-sections, $\psi_{s, p}$ is the normalized modal field of signal (s) and pump (p) and $\rho(x, y)$ is the total erbium ion density profile. We consider the typical Erbium ion doping profile in the waveguide to be a planar Gaussian, i.e., $\rho = \rho_0 \exp(-y^2/h_{er}^2)$ as reported in [8], with $h_{er} = 5.12 \mu\text{m}$ and peak erbium ion concentration $\rho_0 = 6.6 \times 10^{25} \text{ m}^{-3}$. The emission and absorption coefficients corresponding to TE polarization are also obtained from the figures in [8] and are tabulated in Table II.

TABLE II
Absorption and emission cross-section at various wavelengths [8]

$\lambda(\text{nm})$	$\sigma_{abs}(m^2)$	$\sigma_{ems}(m^2)$
1484	5.9×10^{-25}	2.0×10^{-25}
1532	25.5×10^{-25}	24.1×10^{-25}
1546	8.46×10^{-25}	10.7×10^{-25}
1563	4.6×10^{-25}	8.0×10^{-25}

The complete complex index profile can be written as

$$n^2(x, y) = n_s^2 + 2n_s \Delta n \exp(-x^2/w^2) \exp(-y^2/h^2) + 2in_s n_i(x, y) \quad (17)$$

For the Erbium doped waveguide with the complex refractive index defined above the complex propagation constant can be written as $\beta(z) = \beta_r + i\beta_i(z)$ with β_i calculated by considering $2in_s n_i(x, y)$ as a small perturbation [11] in the real index profile, given by

$$2\beta_{is} = \frac{n_s}{n_{es}} \sigma_a(\lambda_s) \iint \frac{(\eta_s - \eta_p) \tilde{q} \psi_p^2(x, y) - 1}{1 + (\eta_s + 1) \tilde{p} \psi_s^2(x, y) + (\eta_p + 1) \tilde{q} \psi_p^2(x, y)} \rho(x, y) \psi_s^2(x, y) dx dy$$

$$2\beta_{ip} = -\frac{n_s}{n_{ep}} \sigma_a(\lambda_p) \iint \frac{(\eta_s - \eta_p) \tilde{p} \psi_s^2(x, y) - 1}{1 + (\eta_s + 1) \tilde{p} \psi_s^2(x, y) + (\eta_p + 1) \tilde{q} \psi_p^2(x, y)} \rho(x, y) \psi_p^2(x, y) dx dy \quad (18)$$

here n_{es} and n_{ep} are the effective indices corresponding to signal and pump wavelengths in the absence of gain or loss. The closed form expressions for modal fields and facilitates the estimation of the RHS in the above equation. Hence, the evolution of signal or pump power can be written as:

$$\begin{aligned} \tilde{p}(z + \Delta z) &= \tilde{p}(z) \exp[\gamma(z) \Delta z] \\ \tilde{q}(z + \Delta z) &= \tilde{q}(z) \exp[-\alpha(z) \Delta z] \end{aligned} \quad (19)$$

where $\gamma = 2\beta_{is}$ and $\alpha = 2\beta_{ip}$. The procedure can be used to estimate the signal gain or pump loss for a given length of waveguide by a beam propagation type of procedure in which total length of waveguide is divided into segments and propagation is considered in terms of local mode through each segment. We carried out calculation of gain across a 5 cm length of the waveguide for different pump power levels by dividing the total length into small sections (typically 10) and estimated the gain by using the appropriate complex propagation constant in each section.

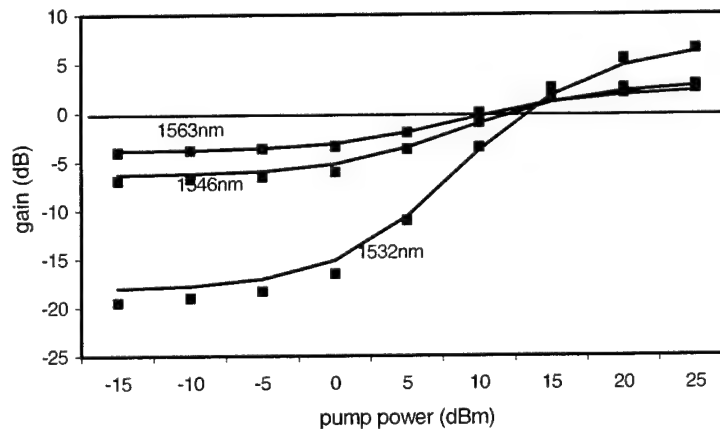


Fig. 5. Variation of gain with pump power a 5cm length of Er doped LiNbO₃ waveguide at different wavelengths: comparison of calculated (continuous lines) and experimental (rectangles) results.

Fig.5 shows a comparison of the variation of gain for a 5cm length of the waveguide with pump power for different wavelengths. The results agree with the experimental results of Dinand and Sohler [8] shown as rectangles. An additional attenuation of 0.16dB/cm due to scattering loss has also been included in the calculations. The results also show that a threshold pump power of 20mW is necessary to obtain gain.

4. CONCLUSION

In conclusion, we have presented accurate closed form field expressions for the modal field in single mode Titanium diffused LiNbO₃ channel waveguides. The closed form field form have been shown to be useful for optimization of fiber to waveguide coupling and estimation of gain in pumped Erbium doped LiNbO₃ waveguides.

REFERENCES

- [1] Woo-Hu Tsai, Shih-Chieh-Chao, and Mu-Shiang Wu, "Variational Analysis of Single Mode Inhomogeneous Planar Optical Waveguides," *J. Lightwave Technol.*, **Vol. 10**, 1992, pp. 747-756.
- [2] Anurag Sharma and Pushpa Bindal, "Analysis of Diffused Planar and Channel Waveguides," *IEEE J. Quantum Electron.*, **29**, 1993, pp 150-153.
- [3] Ashmeet K. Taneja, Sangeeta Srivastava and Enakshi Khular Sharma, "Closed form expression for propagation characteristics of diffused planar optical waveguides," *Microwave and Opt. tech. Lett.* **Vol. 15**, 1997, pp. 305-310.
- [4] BPM_CAD: Waveguide Optics Modeling Software Systems, Version 4.0; Optiwave Corporation, Canada.
- [5] I. Bauman, S. Bosso, R. Brinkmann, R. Corsini, M. Dinand, A. Greiner, K. Schäfer, J. Söchtig, H. Suche and R. Wessel, "Er-doped integrated optical devices in LiNbO₃," *IEEE J. Selected Topics Quantum Electron* **Vol. 2**, 1996, pp. 355-365.
- [6] Adams. M. J. *An Introduction to Optical Waveguides*, Wiley Interscience, New York.
- [7] William H. Press, Saul A. Teukolsky, William T. Vetterling and Brian P. Flannery, *Numerical Recipes in Fortran*, (Cambridge University Press).
- [8] Manfred Dinand, Wolfgang Sohler, "Theoretical modeling of optical amplification in Er-doped Ti: LiNbO₃ waveguide," *IEEE J. Quantum Electron* **30**, 1994, pp. 1267-1276.
- [9] Shih-Chieh-Chao, Mu-Shiang Wu, Woo-Hu Tsai, "Variational Analysis of Modal Coupling Efficiency between Graded Index Optical Waveguide," *J. Lightwave Technol.*, **Vol. 12**, 1994, pp. 1543-1549.
- [10] Sunanda and Enakshi Khular Sharma, "Field variational analysis for modal gain in Erbium-doped fiber amplifier," *J. Opt. Soc. Am. B* **16**, 1999, pp. 1344-1347.
- [11] Snyder, A.W. Love, J.D. *Optical Waveguide Theory*, Chapman and Hall, London.

Simulations of $\chi^{(2)}$ nonlinear optical devices with comparisons to laboratory performance

A. V. Smith and D. J. Armstrong
Sandia National Laboratories
Dept. 1118, Albuquerque, NM 87185-1423

W. J. Alford
Coherent Technologies, Inc.
135 Taylor Dr., Louisville, CO 80026

M. S. Bowers
Aculight Corporation
11805 N. Creek Parkway, Bothell, WA 98011

Abstract

We have developed public domain numerical models of nonlinear three-wave mixing in birefringent crystals that include diffraction and dispersion. They are suitable for detailed and realistic modeling of mixing for both a single crystal pass and for multiple passes appropriate for a crystal in a resonant cavity. We routinely compare our models with laboratory devices, usually achieving excellent agreement.

Crystals that lack inversion symmetry have a small quadratic response to optical fields. The polarization induced by the electric field of an optical wave is given by

$$P = \chi^{(1)}E + \chi^{(2)}E^2$$

The nonlinear polarization described by the second term has Fourier frequencies at all possible sum and differences of the driving wave(s). If a freely propagating wave at one of these frequencies has the same phase velocity as the polarization, energy can be efficiently coupled to it, making possible substantial energy transfer from the driving waves to the driven wave. Perhaps the simplest example is second harmonic generation in which a wave of frequency ω enters the crystal and waves at frequency ω and 2ω exit. More generally, the crystal mediates sum- and difference-frequency mixing in which waves of frequencies ω_1 and ω_2 enter and frequencies $(\omega_3 = \omega_1 + \omega_2)$ and $(\omega_3 = \omega_1 - \omega_2)$ are generated. In the case of difference-frequency generation, the two redder waves both experience gain at the expense of the blue wave. This gain can be exploited to make an optical parametric oscillator by placing the crystal between mirrors for feedback of one or both of the red waves.

Good numerical models of these mixing processes address several needs. First, there are 50 or more nonlinear crystals from which to choose, each with different properties that

impact their performance. It is crucial to choose a crystal for each application with the proper transmission range, walkoff, and nonlinearity, among other properties. And of course it must be possible to achieve phase matching. A good database of crystal properties coupled to functions for calculating refractive indices and phase matching is invaluable to this task. A second function of models is design optimization. Crystals and related optics are expensive, often costing \$10k or more for a simple parametric oscillator, so it is important to test the expected performance to avoid expensive design mistakes. A third function is to develop new design concepts for nonlinear devices. I will give some examples later. Another function is to validate the performance of a laboratory device. It is not unusual to encounter problems in the quality of the crystal and optics. If a numerical model is to be useful to the community of device builders rather than just to professional modelers, it is necessary to make it user friendly and adaptable. It is also a good idea to make the source code public domain.

The somewhat simplified form of the equations that describe propagation and mixing of three paraxial waves in a crystal are of the form

$$\left[\frac{\partial}{\partial z} - \frac{i}{2k_j} \nabla_{\perp}^2 + \tan \rho_j \frac{\partial}{\partial x} + \frac{1}{v_j} \frac{\partial}{\partial t} + \underline{i\alpha_j} \frac{\partial^2}{\partial t^2} \right] \underline{\varepsilon_j(x, y, z, t)} = P_j(x, y, z, t) e^{\pm i\Delta k z}$$

where P_j is the nonlinear polarization driving the j^{th} wave and Δk is the phase mismatch. The terms underlined once account for walkoff at the angle ρ and diffraction in the plane normal to propagation. Terms underlined twice describe the translation of short time structures with group velocity v and the evolution of time structure due to group velocity dispersion.

The equations can be integrated numerically using various methods but we find that the well known split-step, Fourier method is fast and robust. In the split-step method the integration over one z step is split into two separate alternating steps, one being the propagation in the absence of the polarization terms, and the second being nonlinear mixing in the absence of the propagation terms. The propagation is handled in $\{\omega, k\}$ space and the mixing is handled in $\{t, x\}$ space. Similar models have been widely published and are included in packages such as the commercial physical optics code GLAD¹ and in laser/nonlinear optics packages such as Miro^{2,3}.

There are two types of devices to model; a single pass of the crystal, or multiple passes in cases where the crystal is in a resonant cavity. Examples of cavity devices include cavity enhanced second harmonic generation where the fundamental wave is resonated to build up its intensity, and optical parametric oscillators where one or two or even all three waves are resonated. Integrating the full propagation equations with both diffraction and dispersion can be demanding in processor time and memory, particularly for cavity devices, but this is often unnecessary. If the difference in group velocities leads to temporal walkoff among the three waves that is less than the duration of the finest time structure, it is usually not necessary to include the dispersion terms. Similarly, if the

spatial walkoff and diffraction is small compared with the finest spatial structure it is not necessary to include the diffractive terms. Our package of models includes several such simplified versions. However, if both diffraction and dispersion are needed it is still possible in most cases to model the device on a desktop computer with run times ranging from a few seconds for femtosecond or picosecond pulse devices to a few hours for broadband, large-beam, nanosecond optical parametric oscillators. More detail is given in references 3-8.

Reference 6 provides an example of a new device concept developed using these models. We noticed in our models of nanosecond OPO's that the quality of the signal beam generated by a ring cavity OPO with birefringent walkoff between the signal and idler waves was better in the walkoff direction than in the other transverse direction. This led to the idea that rotating the image of the signal beam on each pass of the optical cavity could provide good beam quality in both transverse dimensions. We verified this idea using the models, and we also optimized the image rotating cavity design based on the models, with the result that the laboratory device worked well on the first try.

A second example of the utility of the models is as a diagnostic for a 1500 nm nanosecond OPO based on KTA crystals. In comparisons between predicted and laboratory performance we noted a large difference in thresholds and efficiencies. They could be reconciled by reducing the nonlinear coefficient of the crystal by 40%, indicating that either the crystal was defective or the reported values of the nonlinear coefficient were in error.

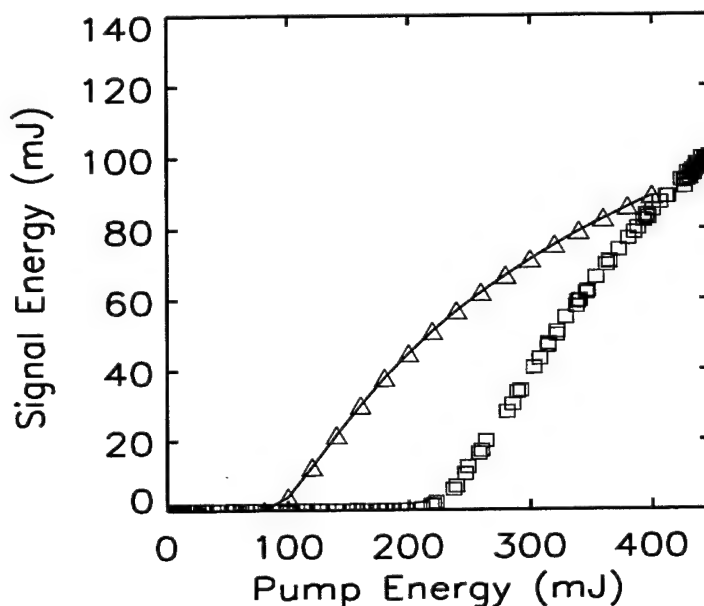


Fig. 1 Comparison of model and experiment for a KTP OPO showing that the crystal is defective or the nonlinear coefficient is incorrect.

Our public domain software SNLO and related source codes can be downloaded without charge at <http://www.sandia.gov/imrl/XWEB1128/xxtal.htm>.

Acknowledgement

Sandia is a multiprogram laboratory operated by Sandia Corporation, a Lockheed Martin Company for the United States Department of Energy's National Nuclear Security Administration under contract DE-AC04-94AL85000.

References

1. GLAD (General Laser Analysis and Design Software), Applied Optics Research.
2. O. Morice, X. Ribeyre, and V. Rivoire, "Broad-band computations using the *Miro* software," in *Proc. third international conf. on solid state lasers and application to inertial confinement fusion*, W. H. Lowdermilk, ed., SPIE **3492**, 832-838 (1999).
3. O. Morice, "Miro: complete modeling and software for pulse amplification and propagation in high-power laser systems," *Opt. Eng.* **42**, 1530-1541 (2003).
4. A. V. Smith, D. J. Armstrong, M. C. Phillips, R. J. Gehr, and G. Arisholm, "Degenerate type I nanosecond optical parametric oscillators," *J. Opt. Soc. Am. B* **20**, 2319-2328 (2003).
5. A. V. Smith and D. J. Armstrong, "Generation of vortex beams by an image-rotating optical parametric oscillator," *Opt. Exp.* **11**, 868-873 (2003).
6. A. V. Smith and D. J. Armstrong, "Nanosecond optical parametric oscillator with 90° image rotation: design and performance," *J. Opt. Soc. Am. B* **19**, 1801-1814 (2002).
7. W. J. Alford, R. J. Gehr, R. L. Schmitt, A. V. Smith, and G. Arisholm, "Beam tilt and angular dispersion in broad-bandwidth, nanosecond optical parametric oscillators," *J. Opt. Soc. Am. B* **16**, 1525-1532 (1999).
8. A. V. Smith, W. J. Alford, T. D. Raymond, and M. S. Bowers, "Comparison of a numerical model with measured performance of a seeded, nanosecond KTP optical parametric oscillator," *J. Opt. Soc. Am. B* **12**, 2253-2267 (1995).

Monolithically integrated InP-based tunable wavelength conversion

John M. Hutchinson^{*1}, Jonathon S. Barton, Milan L. Mašanović, Matthew N. Sysak, Jeffrey A. Henness, Leif A. Johansson, Daniel J. Blumenthal, Larry A. Coldren

¹Intel Corporation, MS FM6-30, 1900 Prairie City Rd. Folsom, CA 95630-9598;
University of California, ECE Dept, Santa Barbara, CA 93106

ABSTRACT

In this work, we describe tunable wavelength converters based on a photodiode receiver integrated with a tunable laser transmitter. Devices are fabricated on a robust InP ridge/InGaAsP waveguide platform. The photodiode receiver consists of an integrated SOA pre-amplifier and a PIN diode to improve sensitivity. The laser transmitter consists of a 1550 nm widely tunable SGDBR laser modulated either directly or via an integrated modulator outside the laser cavity. An SOA post-amplifier provides high output power. The integrated device allows signal monitoring, transmits at 2.5 GB/s, and removes the requirements for filtering the input wavelength at the output. Integrating the SGDBR yields a compact wavelength agile source that requires only two fiber connections, and no off-chip high speed electrical connections. Analog and digital performance of directly and externally modulated wavelength converters is also described.

Keywords: Optoelectronics, Indium Phosphide, Wavelength Conversion, Tunable lasers

1. INTRODUCTION

Tunable wavelength converters represent a novel class of highly sophisticated photonic integrated circuits that are crucial in the functions or functioning or for functions of future optical networks[1]. They allow for the manipulation of wavelengths in WDM optical switches, routers and add/drop multiplexers. Many different implementations of non-tunable wavelength converters have been proposed: using cross phase modulation (XPM) in semiconductor optical amplifiers (SOAs), and fiber [2,3], and cross absorption modulation (XAM) in EAMs[4]. In our previous work, we have demonstrated tunable photocurrent driven wavelength converters utilizing a photodiode driving a laser or a modulator[5, 6]. High-speed integrated photodiodes and electroabsorption modulators suitable for wavelength conversion have also been proposed by other groups [7, 8]. Many of these architectures have been demonstrated to perform the significant feature of digital signal regeneration – including improvements in extinction ratio, signal to noise ratio, pulse width control, etc. Monolithically integrated, widely-tunable all-optical wavelength converters (TAO-WC)[9] have been demonstrated and have shown promise to allow for the conversion of one wavelength to another without requiring the signal to pass through electronics. In this paper, we will describe our work on *tunable* photocurrent driven WC's, and compare them against one another as well as against the TAO-WC approach pursued at UCSB.

2. PHOTOCURRENT DRIVEN TUNABLE WAVELENGTH CONVERSION

The simplest photocurrent-driven wavelength converter (PD-WC) consists of a photodiode receiver directly modulating a laser diode (Figure 1 left). Optical input is incident upon a reverse biased photodiode, which generates a photocurrent directly modulating the gain section of an integrated laser. The laser, and therefore the wavelength converter, can be made tunable by embedding the gain section within tunable mirrors such as implemented in the sampled-gating distributed Bragg reflector (SGDBR) laser [10]. A separate DC electrode connected to the gain section can bias the laser to a level suitable for high output extinction. Above laser threshold, the design affords linear operation, which is of importance for application in analog links. In the direct mod. approach, the extinction ratio of the converted output is proportional to the photocurrent and the laser differential efficiency. In order to improve the extinction ratio, we implement integrated optical pre-amplifiers with on-chip SOAs to generate increased photocurrent.

Modulation bandwidth of the directly modulated PD-WC is ultimately limited by the relaxation resonance frequency of the laser, typically ~ 6GHz in SGDBRs. External modulation of the laser, via an electro-absorption modulator (EAM)

or a Mach-Zehnder modulator (MZM), represents a second important class of tunable photocurrent-driven wavelength converter approaches (Figure 1 right). In these configurations, the photocurrent generates a voltage via a load resistor, which in turn, modulates the transmission of the light through an EAM or MZM. Utilizing either EAMs or MZMs may lower the photocurrent requirements, and offers reduced (and perhaps tunable) chirp suitable for higher data rates.

The semiconductor optical amplifier Mach-Zehnder interferometer (SOA-MZI) wavelength converter is another important class of tunable integrated wavelength converters that also implements the significant feature of digital signal regeneration. Instead of being photocurrent driven, the SOA-MZI WC is based upon the cross-phase modulation, where all of the light interaction between the original data and the new signal takes place in the one arm of an MZI. The monolithically integrated SOA-MZI WC consists of an InP SGDBR laser integrated with a MZI (Figure 2). The laser and the interferometer are connected via a multimode interference (MMI) splitter. The input signal is coupled onto the chip through a tapered input waveguide, and then amplified by an 800 μm long input semiconductor optical amplifier. The same MMI splitter/combiner design is used to connect the data input waveguide with one of the interferometer's SOAs, as well as to combine the light from the two branches at the interferometer output. Waveguides in Mach-Zehnder branches are of the same width and length, hence, with no external stimuli the signal traversing the two interferometer arms will experience no phase change, compared to each other, and thereby add constructively at the output.

All of the designs described in this section have the significant capability for electronic signal monitoring which is a key function required for high speed data networks.

3. DEVICE DESIGN

3.1. Device structure design

Tunable PD-WC's consist of a receiver stage, which collects, amplifies, absorbs and converts the light into a photocurrent, and a transmitter stage which has a tunable laser and perhaps a modulator. Our designs are fabricated on a robust exposed InP ridge platform with a quarternary InGaAsP waveguide. SOAs are used for optical pre-amplification of the input signal, and to boost the converted output signal. Photodiodes are all waveguide type utilizing either Franz-Keldysh (no QWs) or quantum confined stark effect (QW) absorption. SOAs are typically 3 μm wide by 500 to 800 μm long. Photodiode ridges are 3 μm wide by 50 to 100 μm long.

The transmitter stage consists of a SGDBR laser, tunable over the entire C-band. The exposed ridge waveguide laser consists of 5 sections: front and rear SGDBR mirror sections, phase section, gain section and a backside absorber. The Laser output wavelength tuning is achieved by current injection into the SGDBR front and rear mirrors that utilize the vernier effect to select dominant lasing mode. The front mirror consists of 5 4 μm wide burst on a 68.5 μm pitch. The rear mirror consists of 12 6 μm wide bursts on a 68.5 μm pitch. The gain section is 550 μm long and the phase section is 75 μm long.

3.2. Device fabrication and testing

The devices are fabricated on an exposed ridge strip design with a single blanket P-type InP regrowth. The layer structure consists of a 350 nm thick 1.4Q quarternary waveguide with seven compressively strained (1%) 1.55 μm quantum-well active regions grown on top, separated by a thin InP etch stop layer (Figure 3). Epi growth is performed in a Thomas Swan near-atmospheric MOCVD reactor using tertiary-butyl phosphine and tertiary-butyl arsine for the group V precursors, and diethylsilane and diethylzinc for the dopants. Passive sections, such as SGDBR mirrors, phase and franz-keldysh modulators/detectors are formed by selectively etching off the quantum wells in a wet etch process. The sampled grating DBR laser mirrors are defined using a two-step lithography/holography process and etched directly into the top of the waveguide using a $\text{CH}_4/\text{H}_2/\text{Ar}$ RIE process. Blanket regrowth of a thick p-InP cladding and an InGaAs cap. 3 μm wide exposed ridges are formed after regrowth lithographically using a combined dry-wet etch process to provide smooth sidewalls and minimize scattering loss. E-beam evaporated Ni/AuGe/Ni/Au metal is used to contact the N-type semiconductor and Ti/Pt/Au is used to contact the P-type semiconductor. Selectively removing the regrown P-type InGaAs and implanting protons provides carrier confinement between adjacent device sections. The

temperature of the N-type contact anneal is $\sim 430^\circ\text{C}$, which significantly repairs the proton induced damage used for section isolation, requiring that N-metal formation and anneal occur prior to proton implant. The implant is designed to penetrate through the p-InP cladding and stop just above the waveguide to avoid creating defects in the intrinsic region that would lead to increased optical loss. In order to reduce the capacitance, a multiple layer dielectric stack of PECVD silicon nitride and biscyclobutene (Dow Chemical Cyclotene 4024) is used to separate the semiconductor from the pad metallization. Following Ti/Pt/Au P-type metallization and anneal, devices are lapped back to 100 μm thickness, cleaved into bars and AR coated. Working devices are mounted on probable AlN carriers with Pb/Sn/Ag solder.

Figure 4 shows a schematic of the experimental arrangement. An Agilent 70841A 2.5 Gbps pseudo-random bit sequencer (PRBS) was used to drive an Agilent 83433A optical transmitter. The modulated optical signal was amplified and coupled into the wavelength converter. Flextronics conical tip lensed fibers mounted on Melles Griot piezo-electric three axis stages were used to couple the light onto and off of the wavelength converters. Wavelength converters were mounted on AlN carriers on top of a thermoelectric cooler to provide temperature stabilization. The output power of the wavelength converter is controlled by an optical attenuator before it is received by an Agilent 83434A optical receiver, connected to an Agilent 70842B 2.5 Gbps bit error rate tester (BERT). The received eye could also be directly observed in an Agilent 86100A high-speed oscilloscope. The amplified monitor signal from the OEIC-WC device could also be observed in the oscilloscope. For back-to-back testing, i.e. without wavelength conversion, the optical transmitter was directly connected to the optical receiver via an optical attenuator.

4. WAVELENGTH CONVERTER COMPONENT RESULTS

Crucial to the operation of photocurrent driven wavelength converters is a high efficiency receiver. Two types of photodiodes have been investigated: Franz-Keldysh and QW absorbers. Figure 5 (left) shows the detected photocurrent of an optically pre-amplified QW photodiode of 50 and 100 μm length. Current saturation is observed and is due to both power saturation in the SOA, and QW band filling. An improved photodetector can be fabricated using Franz-Keldysh absorption. Figure 5 (right) shows the detected photocurrent vs. reverse bias for different fiber optical power levels for such a device without any optical pre-amplification on chip. No saturation is observed up to photocurrents of at least 30 mA. Others using the same structure have observed even higher saturation currents, up to 70 mA [11]. Coupling efficiency from the lensed fiber to the waveguide mode was $\sim 25\%$.

Figure 6 shows the modulation bandwidth of the directly modulated SGDBR tunable laser. The relaxation resonance frequency of the laser limits the modulation bandwidth to a few GHz. To obtain a flat bandwidth response to above 2.5 GHz, the laser must be DC biased at least to 100 mA. For directly modulated wavelength converters, the resulting extinction ratio is limited by the available photocurrent from the receiver

Externally modulated wavelength converters utilize a DC biased SGDBR laser with an additional EAM or MZM modulator. The potential used to drive the modulator is developed across a 50 Ω load resistor connected in parallel. As discrete components, the crucial figure of merit for modulators is modulation efficiency in dB/Volt. Figure 7 (left) shows the extinction of a bulk franz-Keldysh EAM and Figure 7 (right) shows the extinction vs. bias for a MZM. The maximum obtained EAM efficiency, for a 10 dB transmission loss is ~ 10 dB/V at 1530 nm, and the efficiency drops as the wavelength moves away from the waveguide absorption edge. Higher modulation efficiencies can be obtained by operating at larger DC biases, at the expense of overall transmission. The MZM exhibits an increased ~ 20 dB/V modulation efficiency, at the expense of device area and complexity compared to the EAM.

5. WAVELENGTH CONVERTER MODULATION RESULTS

All of the wavelength converter implementation were successfully fabricated and were tested using the setup described in Figure 4 previously. Figure 8 shows input and output eye diagrams at 2.5 GB/s for the directly modulated WC, the MZM WC and the SOA-MZI WC. All three demonstrated clearly open eyes at 2.5 GB/s data rates across at least a 20 nm SGDBR laser tuning range. Extinction ratio for the directly modulated WC was ~ 3 dB as the photocurrent was limited in fully integrated devices due to a fabrication error resulting in higher than expected contact resistance. Extinction ratio for both MZM-WC and SOA-MZI WC was greater than ~ 8 dB.

All of the wavelength converter approaches fabricated demonstrated error-free operation at 10^{-9} BER with a 2.5 GB/s 2^{31} -1 PRBS signal (Figure 9). Power penalties were 8 dB, 1-2 dB and <1 dB for the direct mod WC, MZM and SOA-MZI WC respectively. The larger power penalty for the direct mod WC was due to the lower than expected extinction.

6. CONCLUSIONS

We described tunable wavelength converters based on a photodiode receiver integrated with a tunable laser transmitter. Devices are fabricated on a robust InP ridge/InGaAsP waveguide platform. The photodiode receiver consists of an integrated SOA pre-amplifier and a PIN diode to improve sensitivity. The laser transmitter consists of a 1550 nm widely tunable SGDBR laser modulated either directly or via an integrated modulator outside the laser cavity. An SOA post-amplifier provides high output power. The integrated device allows signal monitoring, transmits at 2.5 GB/s, and removes the requirements for filtering the input wavelength at the output. Integrating the SGDBR yields a compact wavelength agile source that requires only two fiber connections, and no off-chip high speed electrical connections. Analog and digital performance of directly and externally modulated wavelength converters is also described.

7. ACKNOWLEDGEMENTS

The financial support of Intel Corporation, DARPA CS-WDM and NSF IGERT is gratefully acknowledged. Tom Mates (Materials Department, UCSB) provided SIMS.

REFERENCES

1. S. J. B. Yoo, "Wavelength Conversion Technologies for WDM Network Applications", IEEE J. Lightwave Technology, 14, 944-966 (1996).
2. L.H. Spiekman, U. Koren, M.D. Chien, B.I. Miller, J.M. Wiesenfeld, J.S. Perino, "All-Optical Mach-Zehnder Wavelength Converter with Monolithically Integrated DFB Probe Source", IEEE Photonics Technology Letters, 9, IEEE, 1349-51. (1997)
3. B.-E. Olsson, P. Ohlen, L. Rau, D. J. Blumenthal, "A simple and robust 40-Gb/s wavelength converter using fiber cross-phase modulation and optical filtering", IEEE Photonics Technology Letters, 12, IEEE, 846-848 (2000)
4. N. Edagawa, M. Suzuki, S. Yamamoto, "Novel wavelength converter using an electroabsorption modulator," IEICE Trans. Electron., E81-C, 1251-1257 (1998).
5. J. M. Hutchinson, J. A. Henness, L. A. Johansson, J. S. Barton, M. L. Masanovic, "2.5 Gb/sec wavelength conversion using monolithically-integrated photodetector and directly modulated widely-tunable SGDBR laser," IEEE LEOS 2003 Annual meeting proceedings, WU4, 6 50-651 (2003).
6. J. S. Barton, M. L. Mašanović, M. N. Sysak, J. M. Hutchinson, E. J. Skogen, D. J. Blumenthal, L. A. Coldren, "A novel monolithically-integrated widely-tunable wavelength converter based on a SGDBR-SOA-MZ transmitter and integrated photodetector" Photonics in Switching proceedings, Versailles France (2003).
7. H. Demir, V. Sabnis, O. Fidaner, S. Latif, J. Harris, D. A. B. Miller, J. Zheng, "Novel optically controlled optical switch based on intimate integration of surface-normal photodiode and waveguide electroabsorption modulator for wavelength conversion," IEEE LEOS 2003 Annual Meeting proceedings, WU1, 644-645, (2003).
8. H. Takeuci, T. Saotoh, H. Ito, "High-speed electroabsorption modulators with traveling-wave electrodes," OFC 2002 Technical Digest, 336-338 (2002).
9. M. L. Masanovic, V. Lal, J. S. Barton, E. J. Skogen, D. J. Blumenthal, L.A. Coldren, "Monolithically Integrated Mach-Zehnder Interferometer wavelength converter and widely-tunable laser in InP", IEEE Photonics Technology Letters, 15, 1117-1119 (2003)
10. B. Mason, G. A. Fish, J. Barton, L. A. Coldren, S. P. DenBaars, "Design of sampled grating DBR lasers with integrated semiconductor optical amplifiers", IEEE Photonics Technology Letters, 12, 762-764 (2000).
11. L.A. Johansson, Y.A. Akulova, G.A. Fish, L.A. Coldren, "High optical power electroabsorption waveguide modulator," Electron. Lett., 39, 364-365 (2003).

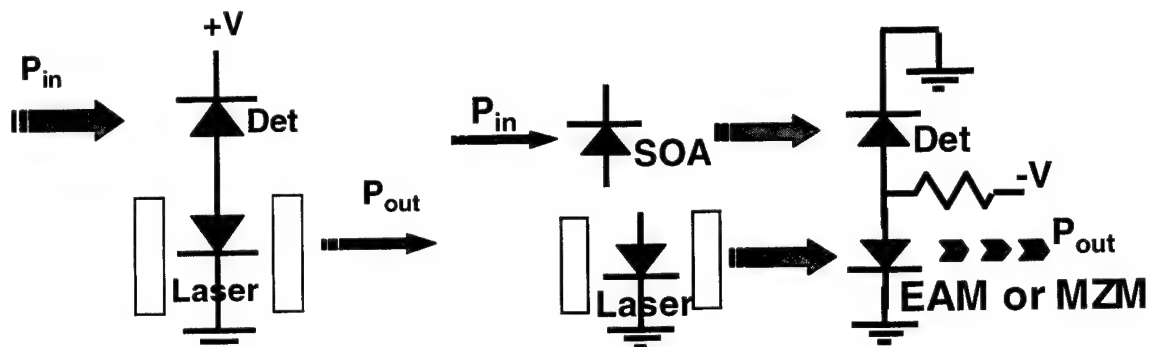
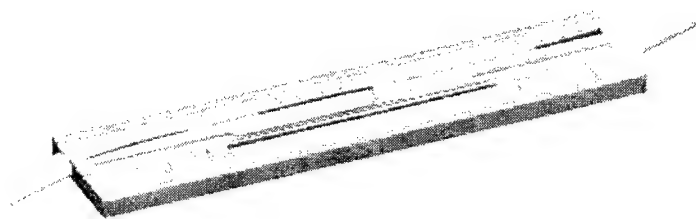
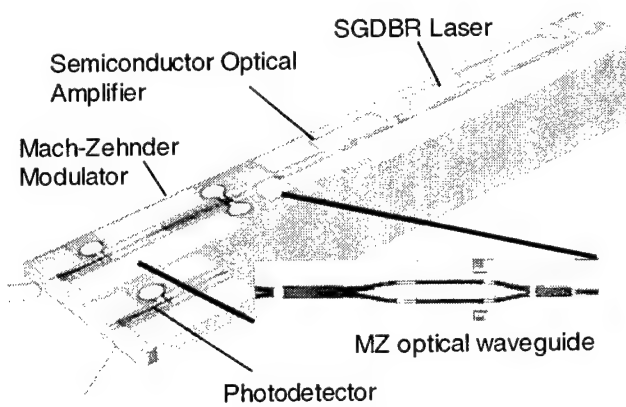


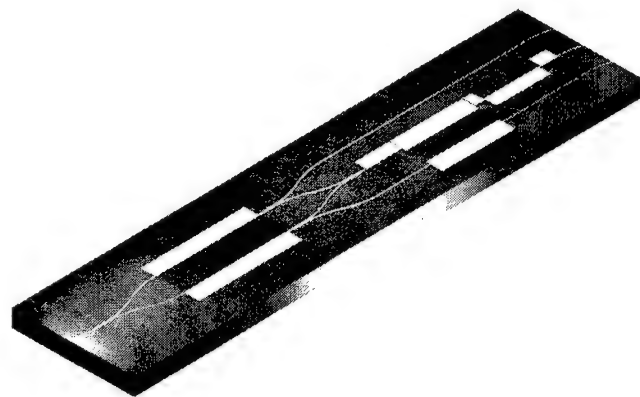
Figure 1. Left: Equivalent circuit of directly modulated wavelength converter
Right: Equivalent circuit of externally modulated wavelength converter



(a)



(b)



(c)

Figure 2. Schematic of three different wavelength converters based on a common InP SGDBR laser process, (a) directly modulated, (b) MZM modulated and (c) SOA-MZI all-optical

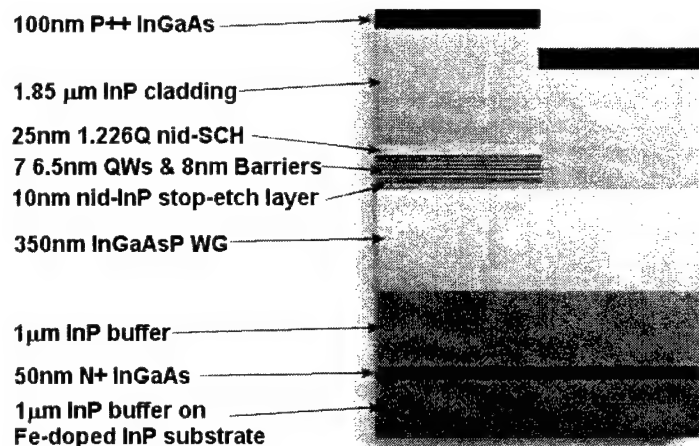


Figure 3. InP MOCVD epitaxial structure of directly modulated WC.

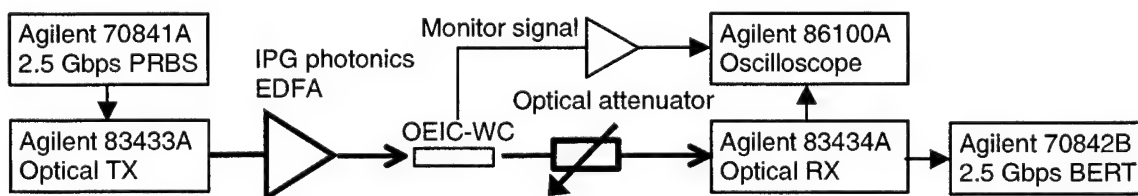


Figure 4. Experimental arrangement for 2.5 Gbps wavelength conversion demonstration. Thick line indicates optical path while thin line indicated electrical path.

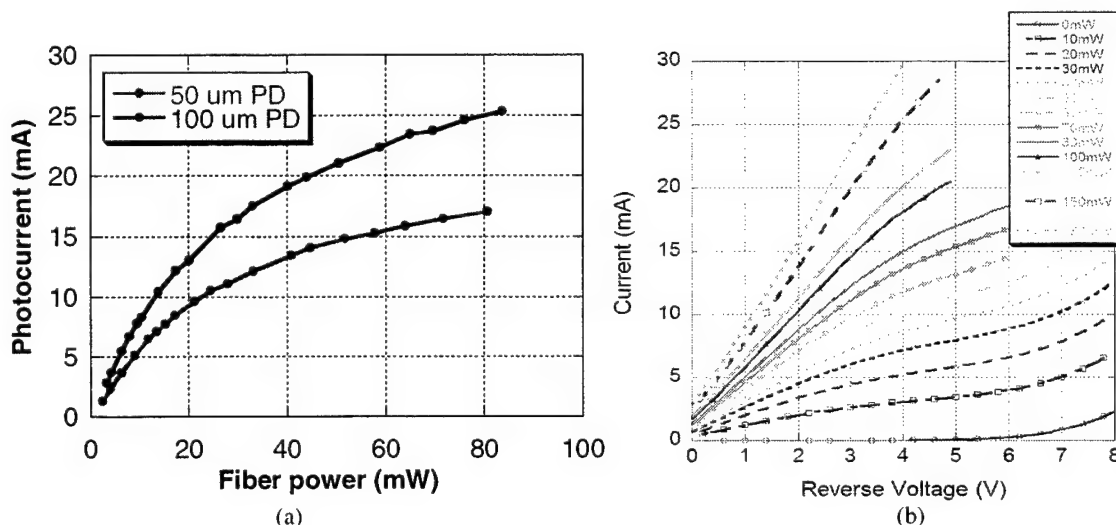


Figure 5. (a) QW absorber photodiode I-L response and (b) Franz-Keldysh absorber photodiode I-V.

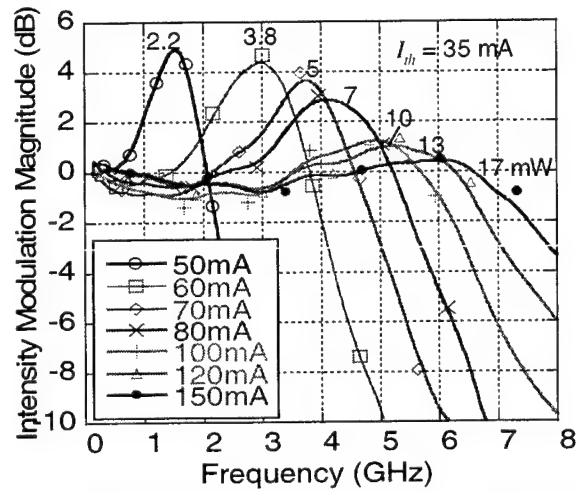


Figure 6. Modulation bandwidth of an SGDBR laser as a function of gain section bias current. Optical power output is labeled on individual curves.

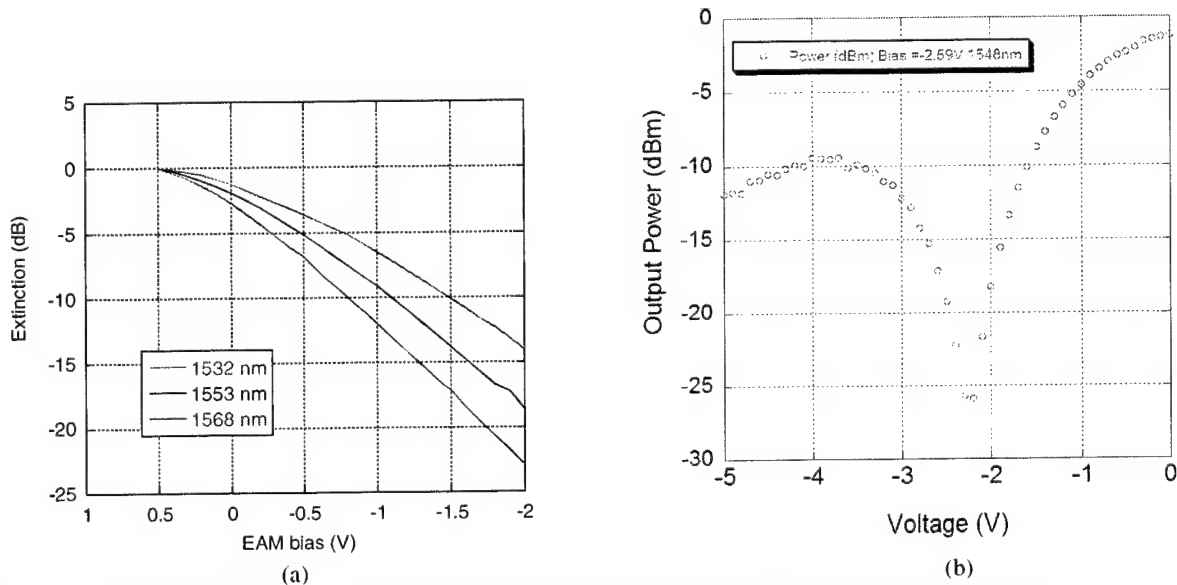


Figure 7. Optical Extinction vs. Voltage for (a) 600 um long EAM and (b) Mach-Zender modulator

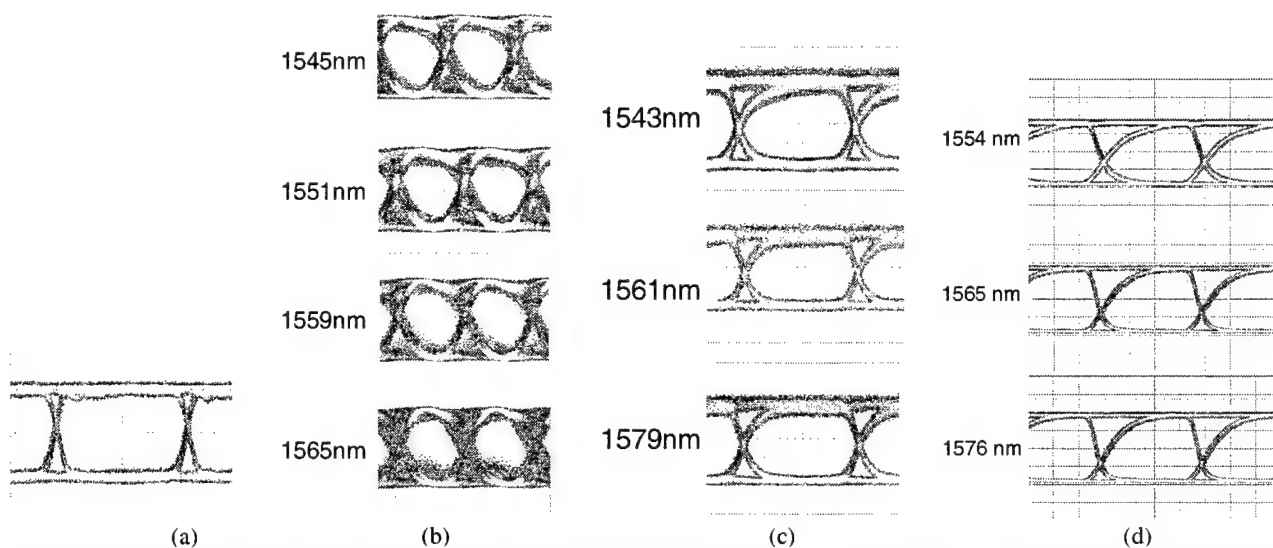


Figure 8. 2.5 Gb/s optical eyes, $2^{31}-1$ NRZ pattern, (a) input signal, (b) directly modulated WC output eye, (c) MZM WC output eye and (d) SOA-MZI all-optical output eyes.

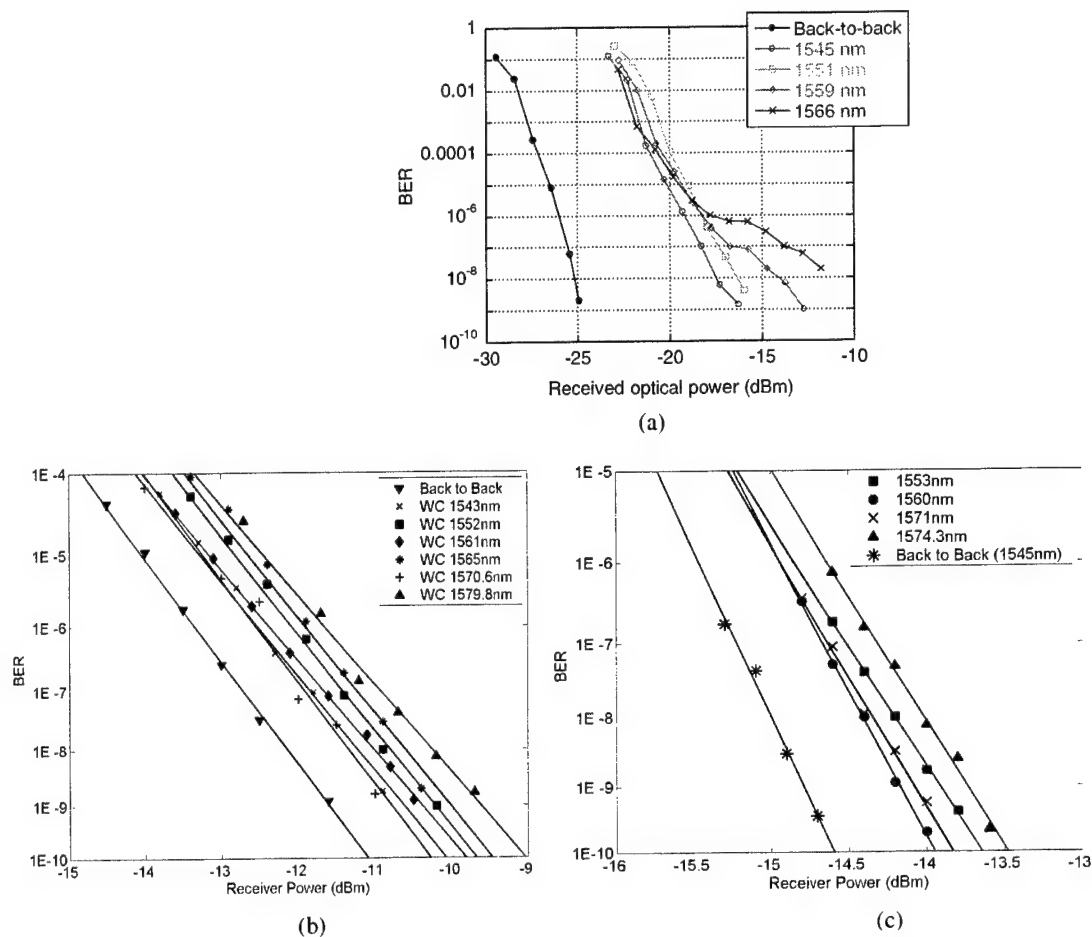


Figure 9. 2.5 GB/s bit-error rates as a function of received optical power for (a) directly modulated WC, (b) MZM WC and (c) all-optical SOA-MZI WC.

3D Simulation of an Integrated Wavelength Converter

Joachim Piprek,ⁱ Nicolas Trenado, John Hutchinson,^a Jeffrey Henness, and Larry A. Coldren

Electrical and Computer Engineering Department,
University of California, Santa Barbara, CA 93106

^a also with Intel Corporation, Portland, OR

ABSTRACT

In this paper, we present three-dimensional (3D) simulation results for an integrated wavelength converter which monolithically combines a pre-amplifying receiver with a post-amplified sampled-grating distributed Bragg reflector tunable laser diode. The self-consistent physical model used in the simulation takes into account gain and absorption in the quantum wells, carrier drift and diffusion, and optical wave-guiding. In order to validate and calibrate the model, we compare the results to available experimental data. Microscopic physical processes inside the converter components are revealed and analyzed, such as receiver saturation effects.

Keywords: Optoelectronic integrated circuits, OEIC, wavelength converter, numerical simulation

1. INTRODUCTION

Our wavelength converter electrically couples an optical receiver for any input wavelength of the C band, e.g., $\lambda_{in} = 1530$ nm, with an optical transmitter for any other output wavelength of the C band, e.g., $\lambda_{out} = 1550$ nm (Fig. 1). The receiver integrates signal pre-amplification by a 500 μm long semiconductor optical amplifier (SOA) and signal detection by a 50 μm long waveguide photodiode (WPD). The optical signal is converted into an electrical signal that directly modulates a sampled-grating distributed-Bragg-reflector (SGDBR) laser diode which is integrated with a semiconductor optical amplifier (SOA) for signal enhancement.¹ The SGDBR laser can be tuned to emit at any wavelength of the C band.

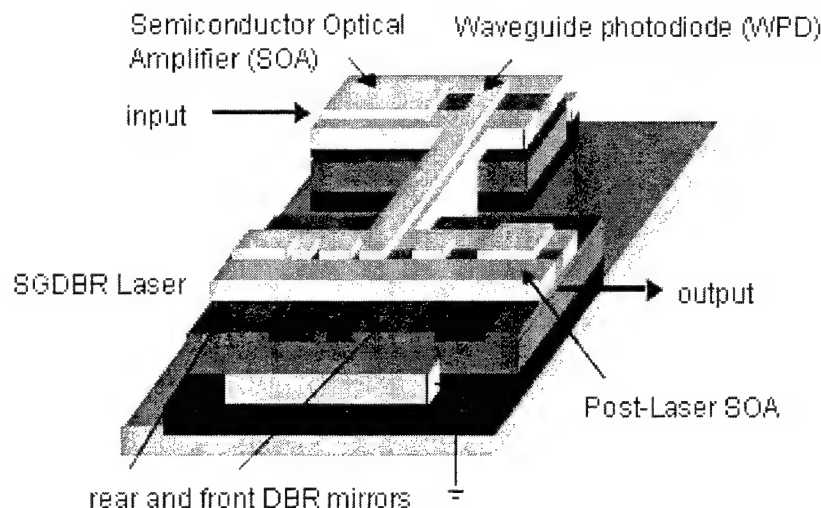


Fig. 1: Schematic view of the InP-based integrated wavelength converter.

ⁱ Corresponding author, e-mail: piprek@icce.org

The structure of the different components is very similar as all are based on the same epitaxial growth (Tab. 1). An offset multi-quantum-well (MQW) active region is grown on top of the waveguide region. A ridge waveguide structure is etched through the MQW region. Passive device sections are formed by etching off the MQWs completely.

Layer	Material	Thickness nm	Doping 10^{18} cm^{-3}	Refractive index
p-contact	InGaAs	100	30 (p)	3.72
upper cladding	InP	1600	1 (p)	3.167
upper cladding	InP	200	0.3 (p)	3.167
doping setback	InP	50	-	3.167
quantum barrier (8x)	$\text{In}_{0.735}\text{Ga}_{0.265}\text{As}_{0.513}\text{P}_{0.487}$	8	-	3.396
quantum well (7x)	$\text{In}_{0.735}\text{Ga}_{0.265}\text{As}_{0.845}\text{P}_{0.155}$	6.5	-	3.616
etch stop	InP	10	-	3.167
waveguide	$\text{In}_{0.612}\text{Ga}_{0.338}\text{As}_{0.728}\text{P}_{0.272}$	350	0.1 (n)	3.455
lower cladding	InP	1400	1 (n)	3.167
etch stop / n-contact	InGaAs	100	1 (n)	3.72
Buffer	InP	1000	-	3.167

Tab. 1 Epitaxial layer sequence of the devices simulated.

The self-consistent numerical simulation² includes band-structure and gain calculations for the strained quantum wells, carrier transport, optical waveguiding, and Bragg reflection. Field effects on MQW gain and absorption (quantum confined Stark effect) are considered as well as free-carrier and intervalence band absorption. InGaAsP material parameters are adjusted based on recent publications.³

The next section discusses 2D simulation results and general device physics. The following section addresses the specifics of each device based on 3D simulation. Section 4 compares simulation results to available receiver measurements and discusses parameter calibration issues.

2. TWO-DIMENSIONAL SIMULATION

2.1 Optical Waveguiding

The software solves the scalar Helmholtz equation in two dimensions to obtain the intensity of the fundamental mode $W_0(x,y)$. The vertical profile $W_0(0,y)$ is plotted in Fig. 2 together with the refractive index profile. The unsymmetrical index profile results in an optical confinement factor for the quantum wells of $\Gamma=0.06$. The 2D mode profile is given in Fig. 3. It is well confined by the p-InP ridge. In agreement with experimental results, fundamental mode operation is assumed here. Near $1.55\mu\text{m}$ wavelength, optical losses are mainly caused by intervalence band absorption (IVBA). The IVBA coefficient is considered proportional to the local hole density, i.e., it is only relevant within the quantum wells and within p-doped regions. The total local absorption coefficient is calculated as

$$\alpha(x,y) = \alpha_b + k_n n + k_p p \quad (1)$$

with the background loss α_b , the electron density n and the hole density p . The hole coefficient $k_p = 25 \times 10^{-18} \text{ cm}^2$, the electron coefficient $k_n = 1 \times 10^{-18} \text{ cm}^2$, and the background value $\alpha_b = 10 \text{ cm}^{-1}$ are employed in our calculations.

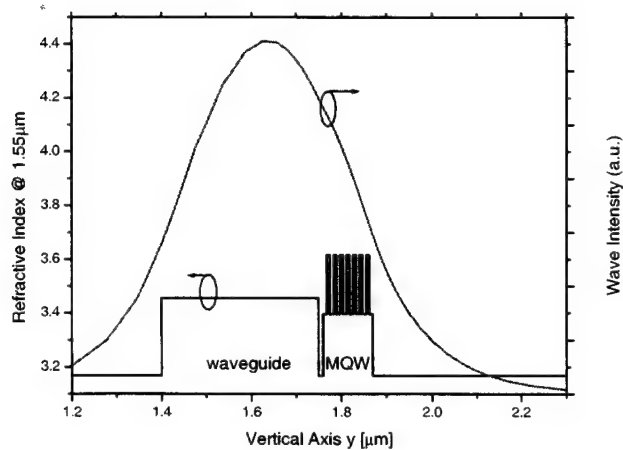


Fig. 2: Vertical profile of refractive index and optical intensity of the fundamental mode.

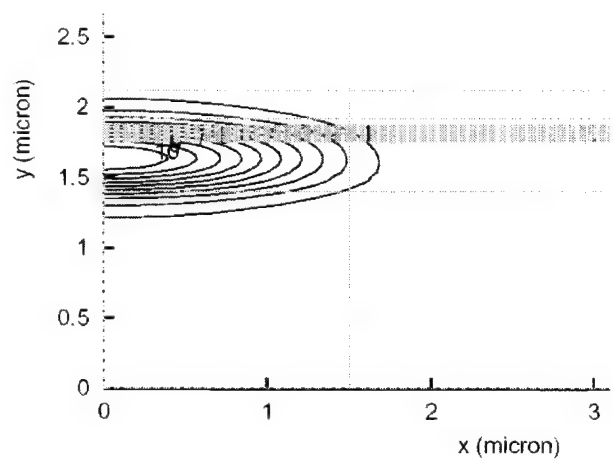


Fig. 3: 2D intensity profile of the fundamental waveguide mode for half the device (y - symmetry plane, ridge width = 3 μm).

2.2 Multi-Quantum Well Active Region

The energy band diagram of the multi-quantum well active region is plotted in Fig. 4. The etch stop layer is needed for longitudinal integration of different devices, however, it constitutes a barrier for electron injection into the MQW which requires thermionic emission of electrons from the waveguide layer. The common conduction band edge offset ratio $\Delta E_c / \Delta E_g = 0.4$ is employed at all interfaces (E_c - conduction band edge, E_g - band gap). On the other hand, the etch stop layer also generates a barrier in the valence band, which helps to prevent holes from escaping the MQW.

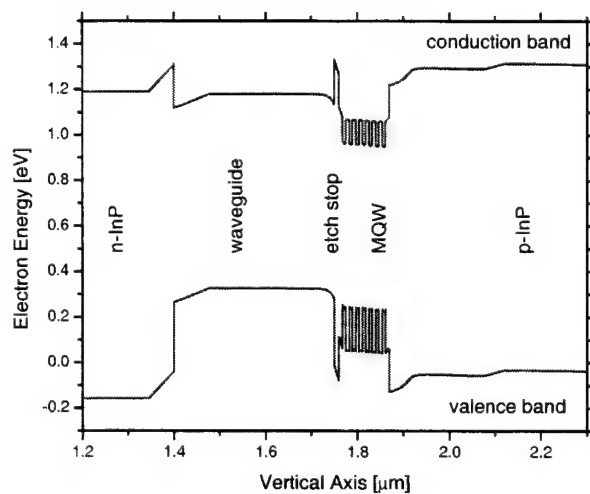


Fig. 4: Energy band diagram of the active region.

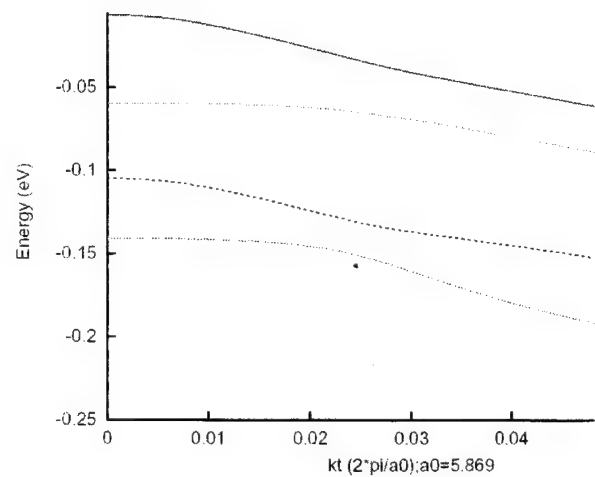


Fig. 5: Energy vs. transversal wavenumber for the quantum well valence subbands (from top: HH1, HH2, LH1, HH3).

For the quantum wells, compressive strain of 0.88% is calculated. The tensile strain in the barrier is -0.2%. The conduction bands are assumed parabolic with an in-plane effective mass of 0.0447. The non-parabolic valence bands are calculated using the popular 4x4 $\mathbf{k}\mathbf{p}$ method including valence band mixing (Fig. 5). Three heavy hole (HH) levels and one light hole (LH) level are found. The relevant top level has an effective HH mass of 0.3 at the Γ point.

2.3 Carrier Transport

The drift and diffusion of electrons and holes is calculated by solving the semiconductor transport equations.³ For forward bias operation (95 mA) of amplifier or laser, Fig. 6 gives the vertical carrier density profile in the center of the device. The average quantum well carrier density is about $2 \times 10^{18} \text{ cm}^{-3}$. The lateral carrier density profile reveals relatively strong lateral carrier diffusion away from the waveguide ridge. The corresponding lateral profiles of the recombination rates are plotted in Fig. 7. Stimulated recombination is restricted to the fundamental optical mode profile (cf. Fig. 3). The strongest carrier loss is caused by the Auger recombination rate

$$R_{\text{Aug}} = n p (C_n n + C_p p) \quad (2)$$

with the preliminary Auger parameters $C_n=0$ and $C_p = 8 \times 10^{-29} \text{ cm}^6/\text{s}$. Those parameters can later be adjusted to fit experimental characteristics. Spontaneous emission is calculated by integrating the spontaneous emission rate, it is proportional to the square of the carrier density. Shockley-Read-Hall (SRH) recombination at crystal defects and interfaces is inversely proportional to the SRH lifetime of the carriers. We here assume a uniform SRH lifetime of 20 ns for electrons and holes throughout the device. This value is longer than the total (measured) lifetime which includes all recombination mechanisms.

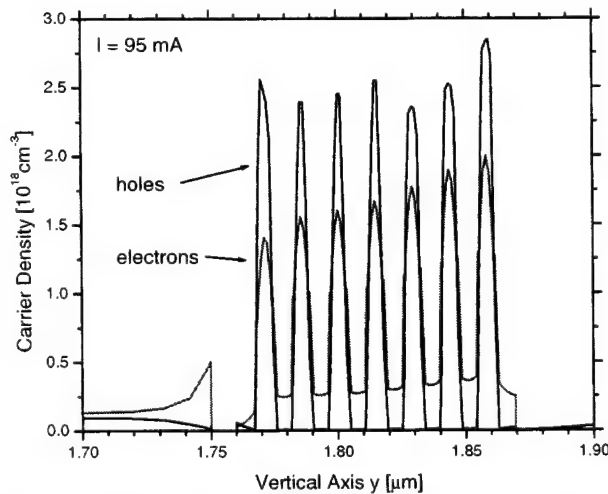


Fig. 6: Vertical carrier density profile in the center of the device.

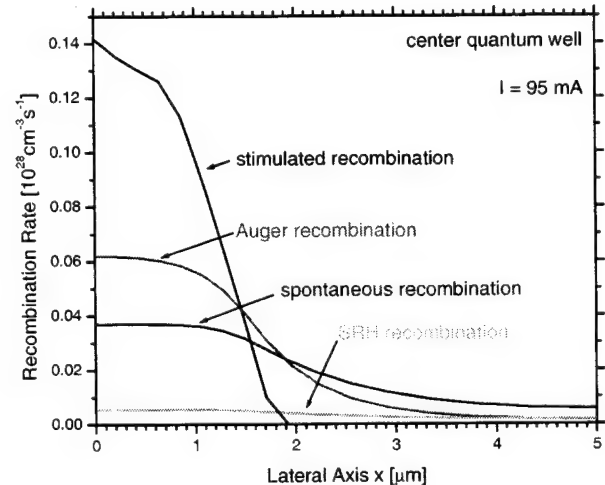


Fig. 7: Lateral profile of the quantum well recombination rates.

2.4 Quantum Well Gain and Absorption

Calculated gain spectra are shown in Fig. 8 under flat-band condition (zero field) using a free carrier model including Lorentz broadening with 0.1 ps intraband relaxation time. The gain peak wavelength blue-shifts slightly due to band filling, however, it is close to the target wavelength of 1550 nm. Figure 9 plots calculated quantum well absorption spectra for different reverse bias conditions of the photodetector. Higher reverse bias gives a stronger internal field which moves the absorption edge towards longer wavelength (quantum confined Stark effect). At the same time, the maximum possible absorption is reduced. At 2V reverse bias, our quantum well shows an absorption edge near 1610 nm. It absorbs light almost uniformly from 1500nm to 1600nm wavelength.

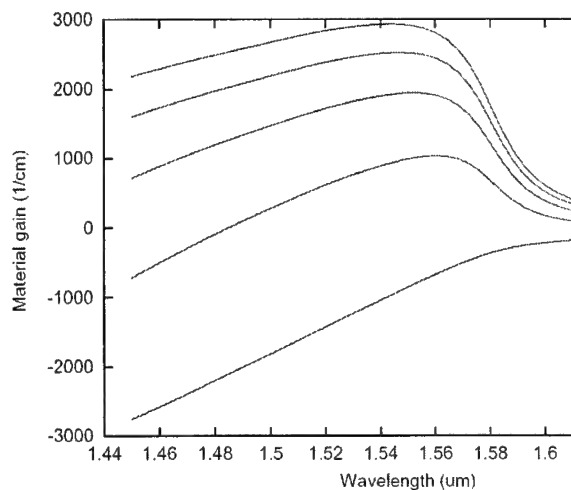


Fig. 8: Flat-band quantum well gain spectra for different carrier densities (from bottom: 1, 2, 3, 4, and 5 $\times 10^{18} \text{cm}^{-3}$).

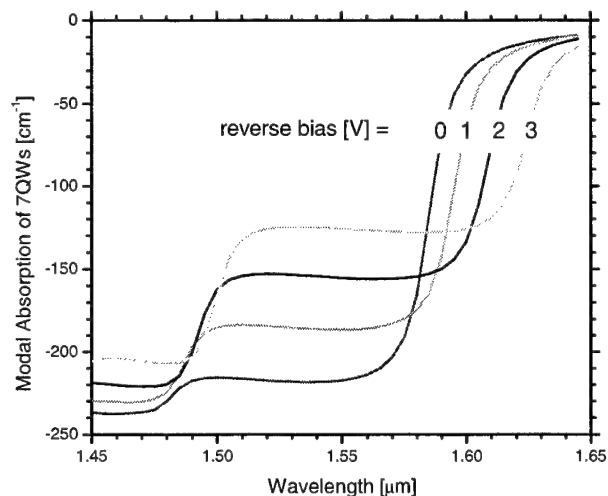


Fig. 9: Quantum well absorption spectrum at different bias.

3. THREE-DIMENSIONAL SIMULATION

3.1 Waveguide Photodetector

Figure 10 shows a 3D plot of the optical intensity calculated for the fundamental mode with 0.01 mW input power. The optical power decays exponentially in travel direction (z) and it is almost completely absorbed at the other end.

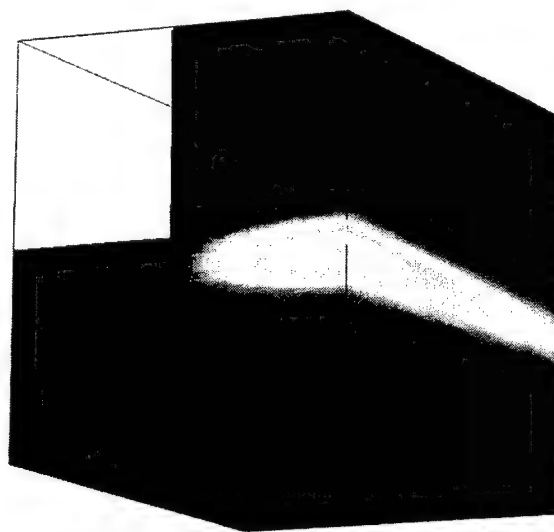


Fig. 10: Fundamental optical mode intensity for half the photodetector.

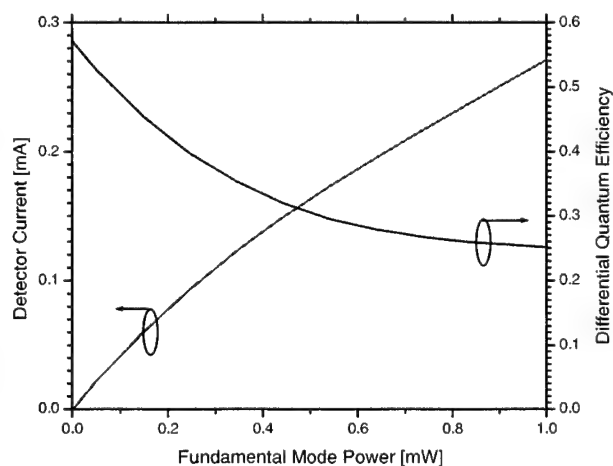


Fig. 11: Photocurrent and quantum efficiency vs. input power.

Photocurrent and quantum efficiency are given in Fig. 11. The calculation considers a front facet reflectance of $R=0.29$, which reduces the maximum possible quantum efficiency to 71%. At low input power, the calculated quantum efficiency is 58%, due to the incomplete absorption of the lightwave. With higher input power, the efficiency decays and it is only 25% at 1 mW. The decay in efficiency is reflected by the non-linear current-power characteristic in Fig.

11. The non-linear response of the photodetector is mainly attributed to the reduction of the quantum well absorption with increasing carrier density. The photon density is highest at the input facet. With increasing power, it generates an increasing number of electron-hole pairs in the quantum wells (QWs). The average QW carrier density is shown in Fig. 12 for different input power. Due to band filling, higher carrier density leads to lower absorption (Fig. 13) which affects the decay of the optical power along the waveguide (Fig. 14). With higher input power, the detection is less efficient, i.e., a larger part of the input power remains undetected. While the intensity decays by a factor of about 14 for low input power, it only decays by a factor of 5 for 1 mW input power in Fig. 14. This mechanism is the main reason for the non-linear photocurrent response shown in Fig. 11. The photocurrent is non-uniform in longitudinal direction (Fig. 15).

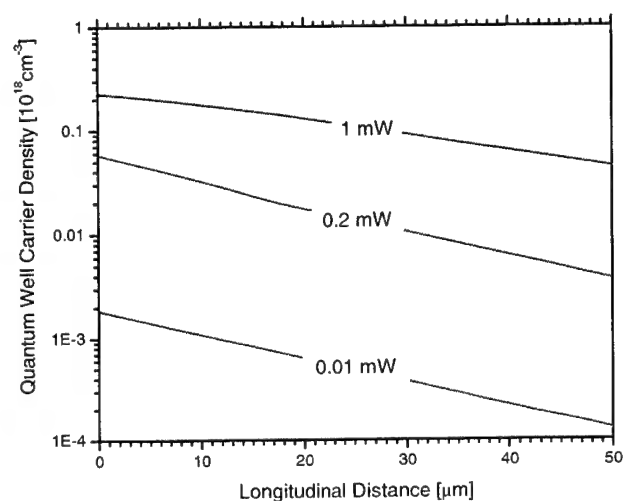


Fig. 12: Longitudinal profile of the quantum well carrier density at different input power.

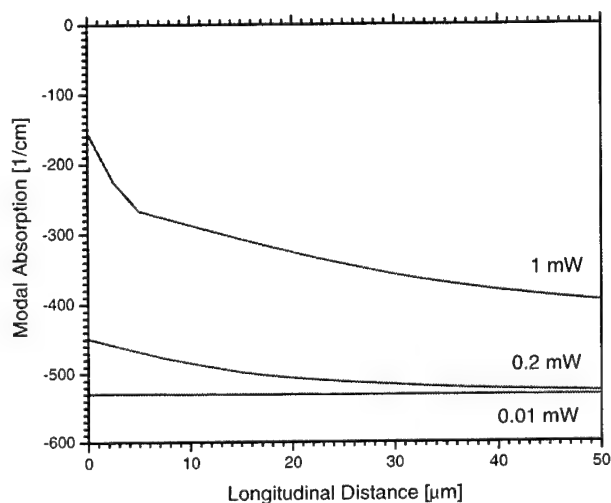


Fig. 13: Longitudinal profile of the modal absorption at different input power (1550 nm).

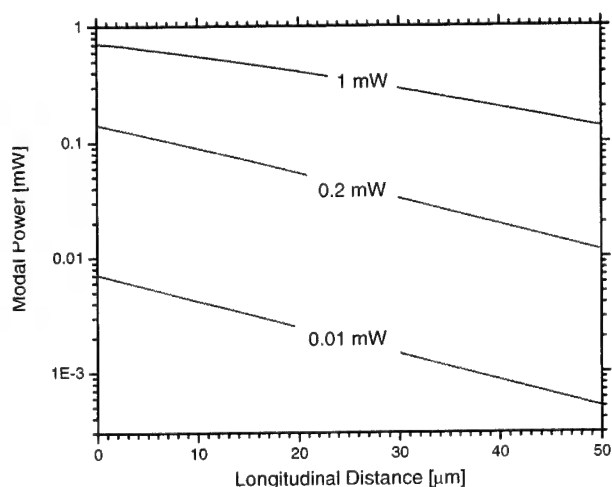


Fig. 14: Longitudinal decay of the modal power at different input power.

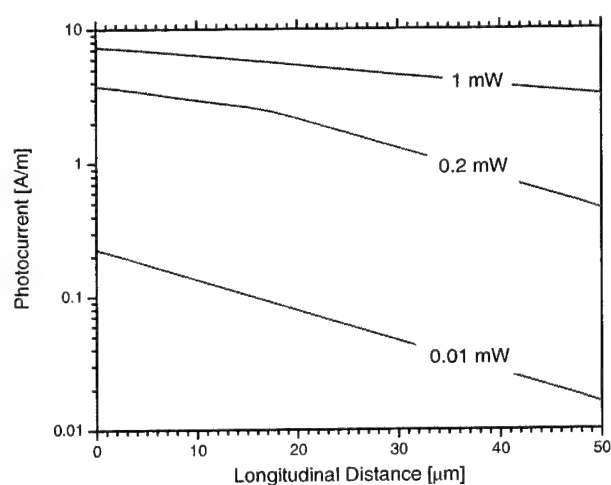


Fig. 15: Non-uniform distribution of the photocurrent at different input power.

However, it needs to be mentioned that PICS3D simulations are not truly 3D since carriers cannot move in longitudinal z direction. The device is rather sliced up into many 2D sections (x,y) within which the device equations are solved self-consistently. The only difference between all the 2D sections is the photon density $S(z)$ which varies in longitudinal direction (Fig. 10). Thus, the quantum well carrier density $N(x,y)$ varies among the 2D sections. Iteratively, a balance between $S(z)$ and $N(x,y)$ is achieved by the software which can be called quasi-3D solution.

3.2 Integrated Receiver

The optical gain of the MQW active region depends on the applied bias: if it is positive, the gain is positive and the region is an amplifying region, if the bias is negative, the gain is negative and the region is an absorbing region. The energy bands of the SOA region are plotted in Figure 16. The bands are flat due to presence of the doping region and the fact that a forward bias is applied to the SOA. In this case, the overlap between electron and hole wave function is optimum and the modal gain is positive (cf. Fig. 8). The energy bands of the WPD region are shown in Figure 17. A reverse bias is applied so that the bands are not flat and the absorption is dominant (cf. Fig. 9). The modal gain is positive for the SOA region and negative for the WPD region (Fig. 18). Accordingly, the wave intensity in Fig. 19 is increasing within the SOA region and decreasing within the WPD region.

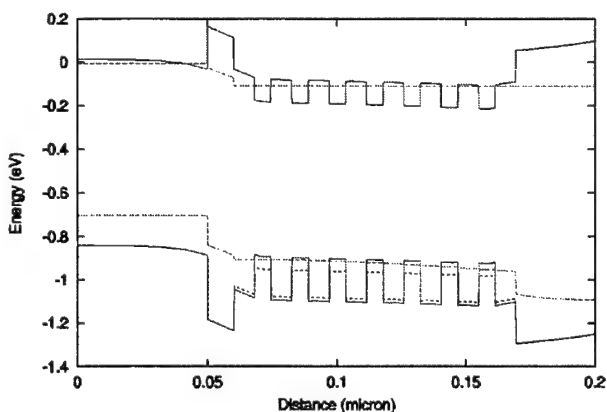


Fig. 16: Conduction (upper) and valence (lower) bands in the SOA region along the vertical y direction (dashed: quasi-Fermi levels)

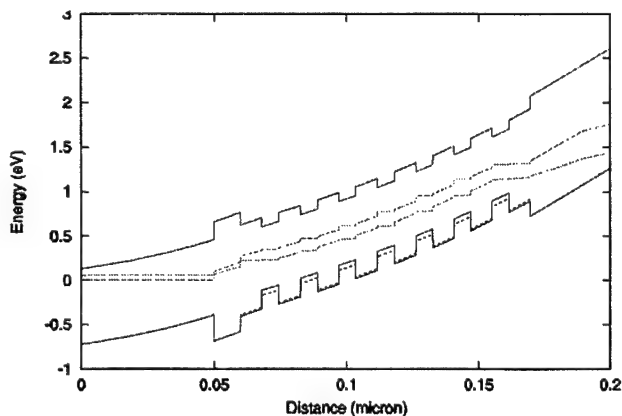


Fig. 17: Conduction (upper) and valence (lower) bands in the WPD region along the vertical y direction (dashed: quasi-Fermi levels)

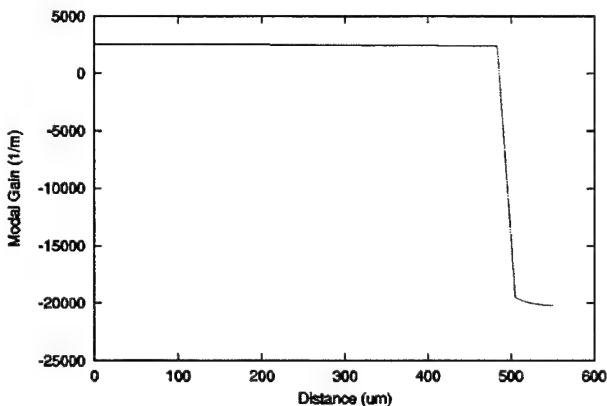


Fig. 18: Receiver modal gain along the longitudinal propagation direction z .

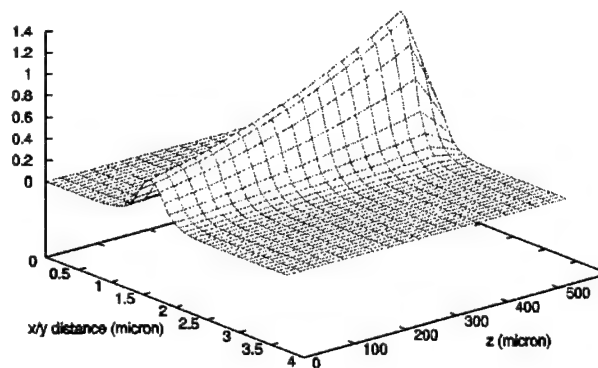


Fig. 19: Wave intensity surface plot (a.u.) within the vertical symmetry plane of the receiver ($x=0$).

3.3 Integrated Transmitter

Simulation of the sampled-grating DBR laser diode⁴ is the most challenging part of this project. The laser includes five longitudinal sections (Tab. 2). Optical gain is provided in the active section of the laser as well as in the amplifier. For this example simulation, both mirrors are tuned to exhibit reflectivity peaks at 1550 nm (Fig. 20). Laser emission is therefore at the same wavelength (Fig. 21). A 3D plot of the calculated wave intensity is shown in Fig. 22. In this case, the laser is biased well above threshold (25 mA). The amplifier current of 20 mA gives additional photon multiplication, resulting in a strong enhancement of the optical intensity towards the right facet of the emitter. The same situation is shown in Fig. 23 as longitudinal intensity profile, comparing two different amplifier currents. Within the SGDBR sections, each grating burst reflects part of the wave and gives a stepwise change in wave intensity. At low amplifier current (5 mA), the SOA region exhibits net optical loss and the optical intensity decays as the light approaches the right facet. SOA transparency is obtained at 16.5 mA. At higher SOA current net amplification is achieved.

The corresponding light-current (LI) characteristic is given in Fig. 24. Lasing threshold is calculated at about 14 mA. At first, the amplifier current is kept constant at 5 mA and the laser current is ramped up to 25 mA. The slope of the LI curve is 0.043 W/A which corresponds to a differential quantum efficiency of only 5% for the right facet, due to the photon losses in the amplifier. Second, the SOA current is ramped up to 20 mA keeping the laser current constant at 25 mA. The SOA slope efficiency is 0.23 W/A. At the SOA current of 20 mA, the laser slope efficiency would be 0.273 W/A, which translates into 34% differential quantum efficiency of the laser. At higher SOA currents, more than 100% differential quantum efficiency can be achieved this way, i.e., each electron injected into the laser above threshold leads to more than one emitted photon, due to the photon multiplication in the SOA region. The side mode suppression ratio is only about 20 dB (Fig. 21) and it decreases with higher amplifier current (Fig. 25).

Section name	Length [μm]	κ [1/cm]	DBR Sampled Grating
Left mirror	552	250	12 x 6 μm grating bursts with 46 μm period
Phase tuning	75	-	-
Active	500	-	-
Gain lever	100	-	-
Right mirror	307.5	250	5 x 4 μm grating bursts with 61.5 μm period
Amplifier	500	-	-

Tab. 2 Longitudinal sections of the integrated transmitter (κ – optical coupling coefficient).

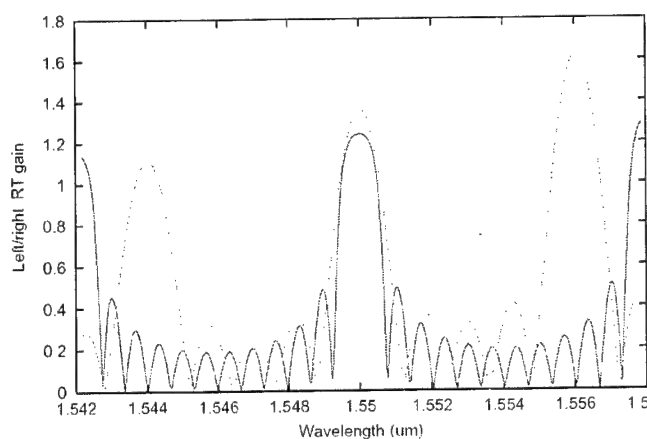


Fig. 20: Round trip gain spectra for left mirror (dashed) and right mirror (solid).

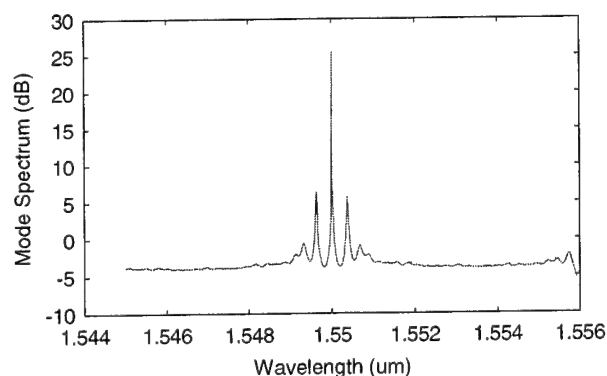


Fig. 21: Calculated mode spectrum (laser current = 25 mA, SOA current = 20 mA).

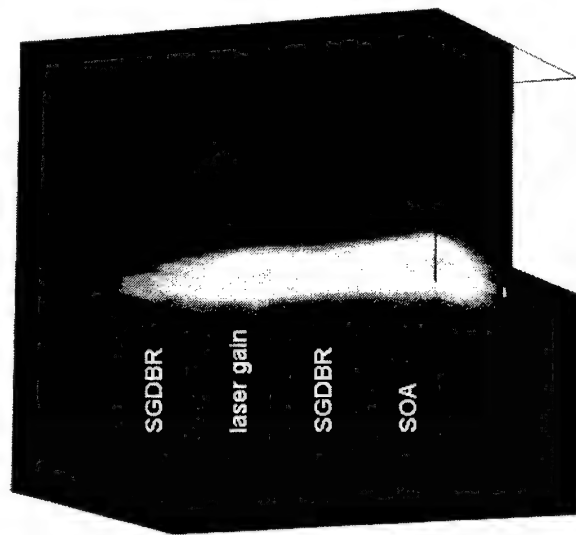


Fig. 22: 3D visualization of the internal light intensity for half the device (laser current = 25 mA, amplifier current = 20 mA).

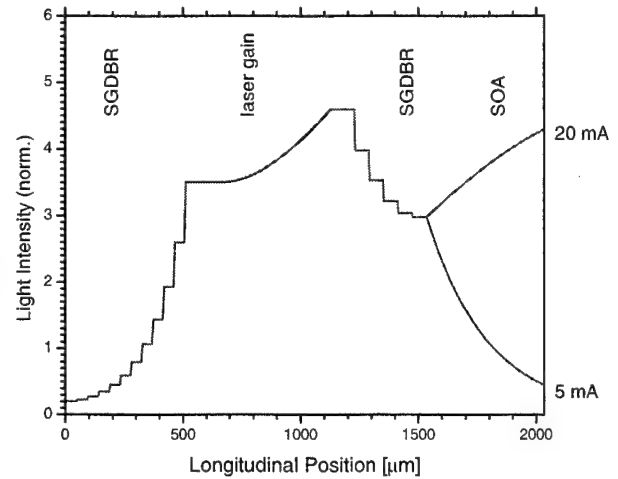


Fig. 23: Longitudinal light intensity profile with 25 mA laser current and with the amplifier current given as parameter.

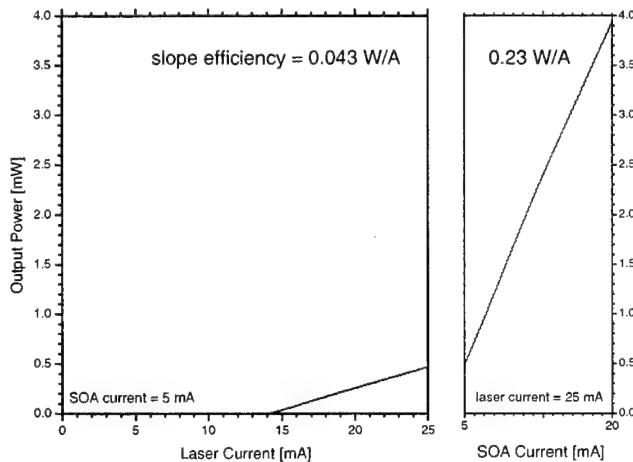


Fig. 24: Calculated light-current characteristics.

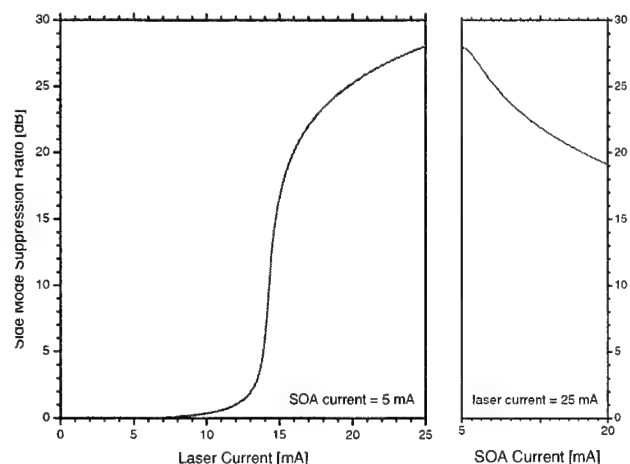


Fig. 25: Calculated side mode suppression ratio vs. current.

4. COMPARISON TO MEASUREMENTS AND PARAMETER CALIBRATION

In this section, we compare our results to the first available receiver measurements in order to validate the model and to calibrate critical material parameters. First, X-ray and photoluminescence (PL) measurements are utilized to adjust MQW parameters. Slight variations from the intended numbers (Tab. 1) are unavoidable during the growth process. For both the quantum wells and the barriers, we extract a slightly lower Ga mole fraction of 0.2367. In addition, the width of both layers is smaller than intended (well: 56.8 Å, barriers: 70.4 Å). Quantum well band-gap renormalization (BGR) is taken into account in order to find agreement with the measured PL peak wavelength (Fig. 26). BGR leads to

decreasing band gap energy with higher carrier density (spectral shift to longer wavelength). The formula used to express BGR is

$$\Delta E_g = A_x \left(\frac{n+p}{2} \right)^{1/3} \quad (3)$$

with $A_x = 0.8 \times 10^{-10}$ eV/m. The difference to the PL measurement at high energies (low wavelengths) is attributed to the fact that the common free carrier model is currently considered in our gain calculation. Many-body models are expected to correctly reproduce the entire gain spectrum.

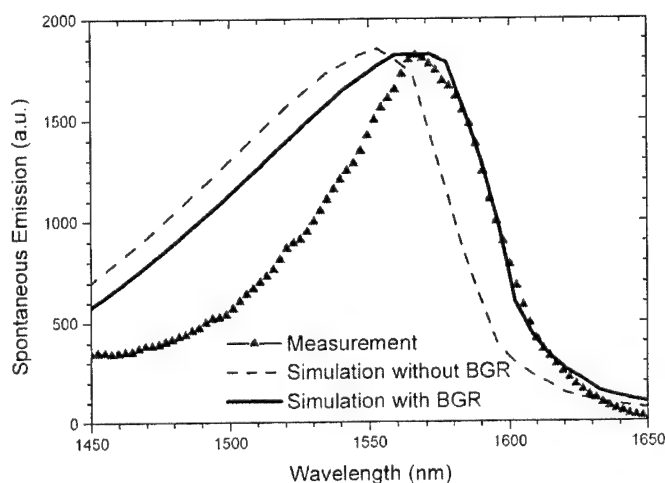


Fig. 26: Comparison between MQW photoluminescence measurement (triangles) and calculated spontaneous emission spectra with and without band-gap renormalization (BGR).

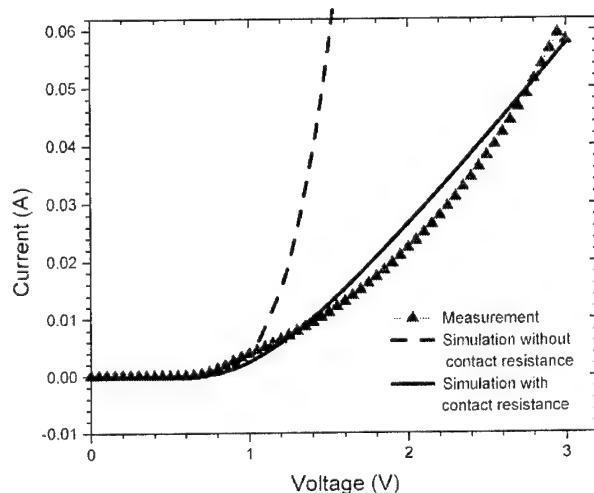


Fig. 27: Dark current versus voltage curve for a 300 μm long SOA.

The measurement of the dark current of a 300 μm long SOA is shown and compared to our simulation in Figure 27. This curve depends on the mobility of the carriers. The mobility depends on the composition of the layer and the doping. Since exact numbers for doping and mobility are unknown, we use 2200 cm^2/Vs for the electron mobility and 70 cm^2/Vs for the hole mobility in all layers. The resulting current-voltage (IV) curve is much steeper than measured (dashed line in Fig. 27). The inclusion of an additional contact resistance of 52 Ω in the simulation gives a much better agreement with the measurement (solid line in Fig. 27). Future measurements of the contact resistance will allow us to adjust the mobility values.

The contact resistance is known to vary from device to device. IV curves for a 500 μm long SOA are shown in Fig. 28 for different input light power. Here, a contact resistance of 8.5 Ω is extracted from the fit. Another crucial input parameter is the optical coupling factor between fiber and SOA. Best agreement with the measurements in Fig. 28 is obtained when a coupling factor of 0.163 is assumed for this measurement. With ideal fiber adjustment, a maximum coupling factor of 0.25 is estimated. Thus, less than one quarter of the light power is coupled into our receiver waveguide.

Figure 29 compares the calculated receiver photocurrent to the measurement. In this measurement, the ideal fiber coupling factor of 0.25 was achieved. In order to fit the measurement, gain and absorption need to be scaled down by a factor of 0.5 (dip_factor). This indicates significant inaccuracies of the free carrier model used for gain and absorption calculation.

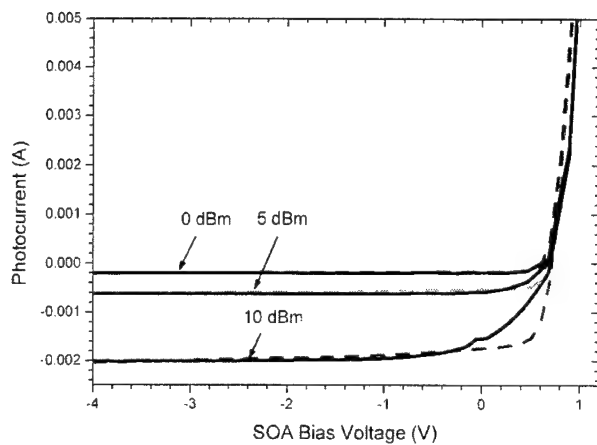


Fig. 28: Photocurrent versus applied reverse voltage for a 500 μm long SOA at different light power in the fiber (dashed: measurement, solid – simulation).

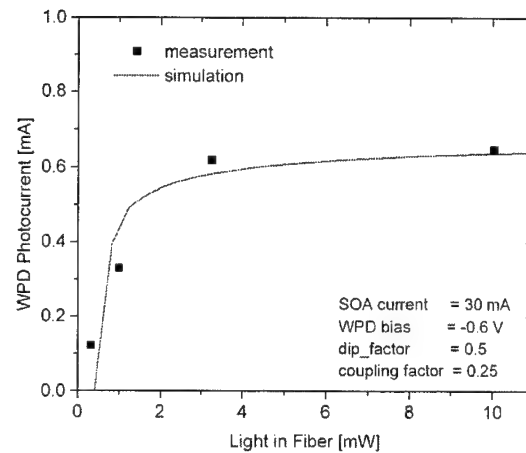


Fig.29: Receiver photocurrent vs. fiber input power.

Finally, light vs. current (LI) measurements on broad-area Fabry-Perot laser structures are compared to simulations in Fig. 30. The main fit parameters are the Auger recombination coefficient $C = 10^{-28} \text{ cm}^6/\text{s}$ and the modal loss parameter $\alpha_i = 24 \text{ cm}^{-1}$, which is larger than expected and attributed to an overestimation of the quantum well gain within the free carrier model. The corresponding recombination rates are plotted in Fig. 31. Auger recombination is by far the dominating mechanism, spontaneous photon emission and defect related SRH recombination are less important.

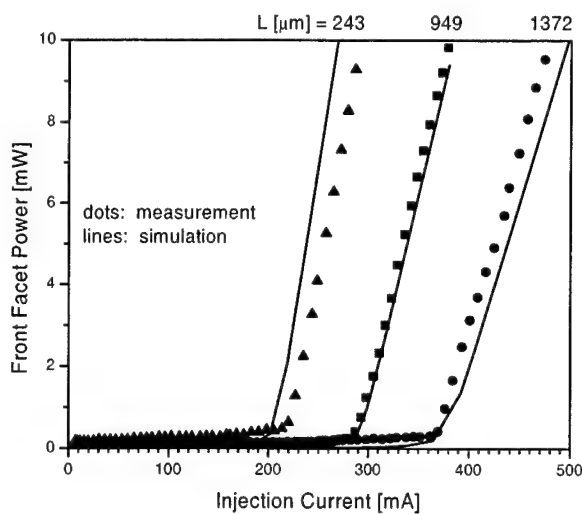


Fig.30: Light-current characteristics for 50 μm wide Fabry-Perot lasers of different length L .

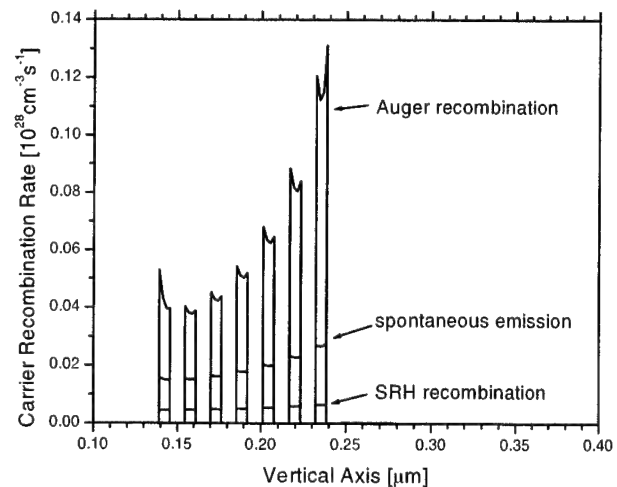


Fig.31: Quantum well recombination rate at 380 mA ($L=949 \mu\text{m}$).

5. SUMMARY

We have presented first results on the self-consistent numerical simulation of an InP-based integrated wavelength converter that monolithically combines optical amplifier, waveguide photodetector, and sampled-grating DBR laser diode. Comparison to available measurements reveals crucial parameters such as the contact resistance, the fiber coupling efficiency, and the Auger coefficient. The free carrier model used for quantum well gain and absorption calculations is found to be not accurate enough to achieve good agreement with measurements and to predict the device performance. More advanced models will be employed in future simulations.

ACKNOWLEDGEMENT

This research project is sponsored by the Semiconductor Research Corporation (Award 2001-NJ-968) and by Intel.

REFERENCES

1. B. Mason, J. Barton, G. A. Fish, L. A. Coldren, S. P. Denbaars, "Design of sampled grating DBR lasers with integrated semiconductor optical amplifiers," *IEEE Phot. Techn. Lett.*, vol. 12, pp. 762-764 (2000).
2. PICS3D by Crosslight Software, 2003.
3. J. Piprek, *Semiconductor Optoelectronic Devices – Introduction to Physics and Simulation*, Academic Press, San Diego, 2003.
4. V. Jayaraman, A. Mathur, L. A. Coldren, and P. D. Dapkus, "Theory, design, and performance of extended tuning range in sampled grating DBR lasers," *IEEE J. Quantum Electron.*, vol. 29, pp. 1824-1834, 1993.

Analysis of InGaAs Metal-Semiconductor-Metal OE Mixers

H. Shen^a, K. Aliberti^a, B. Stann^a, P. G. Newman^a, R. Mehandru^b and F. Ren^b

^aUS Army Research Laboratory, 2800 Powder Mill Road, Adelphi, MD 20783

^bDepartment of Chemical Engineering, University of Florida, Gainesville, FL 32611

ABSTRACT

We analyze the optoelectronic mixing characteristics of InAlAs, Schottky-enhanced, InGaAs-based, metal-semiconductor-metal photodetectors. For devices with Schottky-enhancement layers (SELs) of about 500 Å, the measured frequency bandwidth is less than that of a corresponding photodetector. The mixing efficiency decreases with decrease in optical power, decreases with increase in local oscillator frequency and decreases with decrease in mixed signal frequency. We attribute this behavior to the band-gap discontinuity associated with the SEL. For devices with thinner SELs (≈ 100 Å), the mixing characteristics are greatly improved: the bandwidth of the optoelectronic mixer (OEM) is similar to that of a corresponding photodetector and the mixing efficiency decreases only slightly with decrease in optical power. We attribute these results to the enhancement of thermionic/tunneling current through the thinner SEL. We also present a circuit model of the Schottky-enhanced, InGaAs-based OEM to explain the experimental results.

Keywords: Optoelectronic mixers, InGaAs photodetectors, Schottky enhancement layers

1. INTRODUCTION

Interdigitated-finger, metal-semiconductor-metal photodetectors (MSM-PDs) are widely used for high-speed optoelectronic (OE) applications and are also used as OE mixers (OEMs) to generate radio-frequency subcarriers in fiber-optic microwave links.^{1,2} Recently, GaAs MSM-PDs have been successfully utilized as OEMs in an incoherent laser radar (LADAR) system where a backscattered intensity-modulated light signal (RF) and a bias voltage [local oscillator (LO) voltage] (0.1-1.0 GHz) are mixed to recover an intermediate frequency (IF) signal (0.1-1.0 MHz).^{3,4}

InGaAs MSM-PDs would allow LADAR operation at eye-safe wavelengths. Unfortunately, the Schottky barrier height on InGaAs is quite low (~ 0.1 - 0.2 eV)⁵ leading to high dark current and, hence, low signal-to-noise ratio. To reduce dark current, various methods of "enhancing" the Schottky barrier are used. The most commonly used method employs a high-band-gap lattice-matched InP⁶ or InAlAs^{7,8} Schottky enhancement layer (SEL). Detectors using SELs yield low dark current, high responsivity, and high bandwidths.

In this paper we analyze the optoelectronic mixing effect in InAlAs, Schottky-enhanced, InGaAs-based MSM-PDs. We show that conventional Schottky-enhanced, InGaAs-based MSM-PDs with SELs of approximately 500 Å do not operate well as OEMs. The frequency bandwidth of such a mixer is much less than that of a corresponding photodetector and the mixing responsivity of the OEM is found to depend on the RF and LO signals and decreases non-linearly with decrease in optical power. The behavior of the InGaAs-based MSM-PD OEM is attributed to the large band-gap discontinuity associated with the SEL. By reducing the SEL thickness to 100 Å, the mixing characteristics are found to improve: The bandwidth of the optoelectronic mixer is similar to that of a corresponding photodetector and the mixing response decreases only slightly with decrease in optical power. We present a circuit model of the Schottky-enhanced, InGaAs-based OEM to explain the experimental results.

2. EXPERIMENT

The InAlAs, Schottky-enhanced, InGaAs-based MSM-PD OEM structure, grown via molecular-beam epitaxial technology, is shown in Figure 1. The structure consists of an InAlAs SEL, a 250-Å In(Ga,Al)As graded layer, a 1.0- μ m

InGaAs absorption layer, and a 3000-Å InAlAs buffer layer with a semi-insulating InP:Fe substrate. The InAlAs SEL is 500 Å for device A and 100 Å for device B. The electrodes consist of Ti/Au Schottky contacts deposited via electron-beam evaporation. The electrodes have 3-μm finger widths and spacings. The contact pads and electrode tips of the 60×60-μm² MSM-PD are insulated from the InAlAs SEL to further reduce dark current.⁹

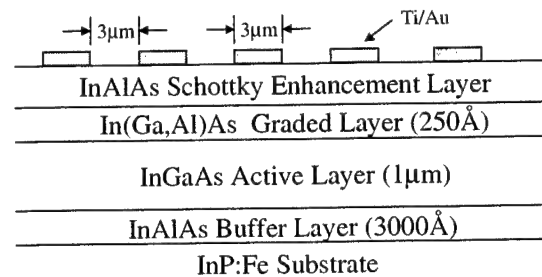


Figure 1. Cross-section of MSM-PD OEM structure.

Mixing characteristics were measured (see Figure 2) with light from an amplitude-modulated, 1.55-μm, 10-Gb/s, fiber-pigtailed laser. Optical power was adjusted via a continuously-variable, in-line, fiber-coupled attenuator and focused on the MSM-PD OEM. The LO bias (3.97 V_{rms}) was applied to one electrode, shunted with a 50-ohm termination, and the down-converted mixed signal (IF) was recovered from the other electrode, which was connected to a spectrum analyzer through a low-pass filter.

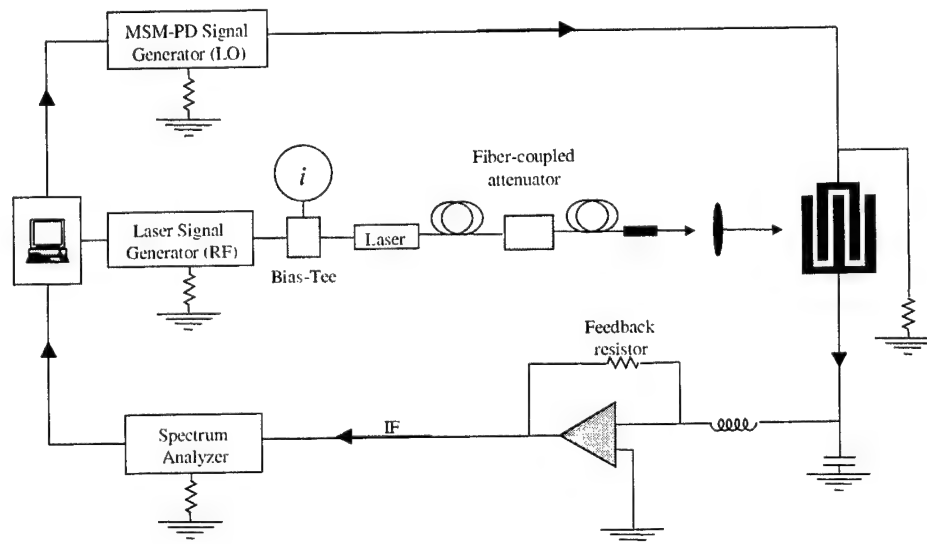


Figure 2. Schematic of MSM-PD OEM test setup.

3. EXPERIMENTAL RESULTS

In Figure 3 we plot the IV characteristics of device A for optical powers of 7.0 μW and 0.7 mW. Both curves exhibit a region where dI/dV transitions from a low value to a high value: this is referred to as a “knee”. InGaAs MSM-PDs without SELs do not exhibit knee-like features. The knee voltage is defined as the bias voltage where the photocurrent equals 5% of the value at the second region, where dI/dV is low. This knee has been reported in the literature^{8,10-11} and is usually attributed to complete depletion of the InGaAs absorption layer. The increase in knee voltage with optical power is usually attributed to interface trap states or space charges.^{10,11} The inset of Figure 3 shows the knee voltage as a function of the optical power. We find that there is a logarithmic relation between the knee voltage and optical power that suggests a thermionic emission and/or tunneling related process.

The mixing efficiency of the MSM-PD OEM is defined as the ratio of the responsivity of the detector at the IF frequency to its ideal dc responsivity. When both the RF and LO frequencies are low, the quasi-steady (QS) mixing efficiency can be calculated using the steady state IV characteristics. Figure 4 shows the measured mixing efficiency as a function of LO frequency for optical powers of 5.0 to 24 μW. The RF and LO frequencies were displaced by 10.0 kHz.

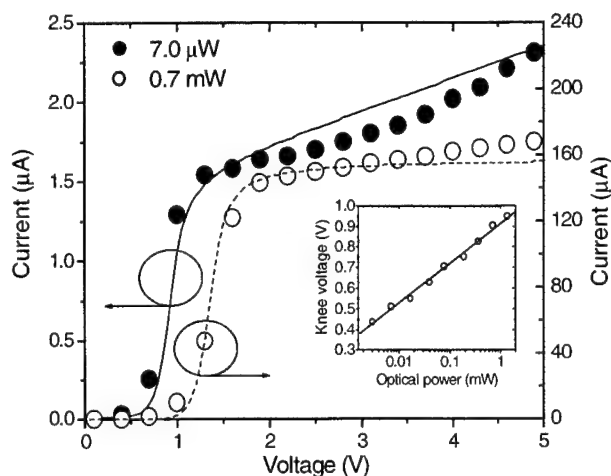


Figure 3. IV characteristics of device A. Inset shows the knee voltage as a function of optical power.

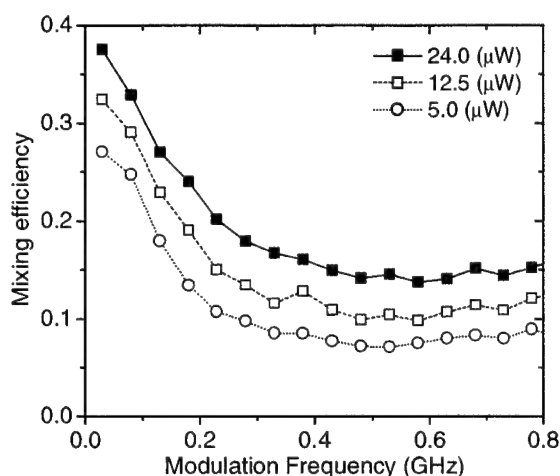


Figure 4. Measured mixing efficiency, as a function of LO frequency, for different optical powers for device A.

The measured mixing efficiency is less than the calculated QS value and cuts off at about 0.2 GHz. Moreover, the mixing efficiency increases with optical power and approaches the QS value for high optical powers (not shown). The same device operated as a photodetector has a flat frequency response with a 3.0-dB cut off at 3.0 GHz (Figure 5). In addition, the photodetector responsivity is independent of optical power except for powers above 4.0 mW, where screening effects cause a slight decrease.

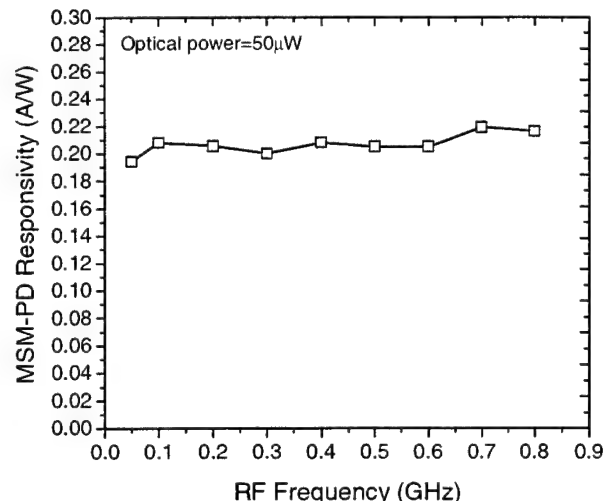


Figure 5. Measured MSM-PD responsivity of device A as a function of light modulation frequency.

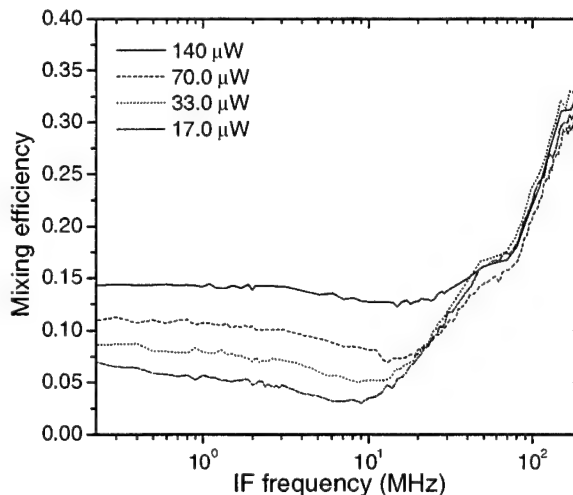


Figure 6. Measured mixing efficiency as a function of IF frequency at different incident light intensities for device A.

Figure 6 plots the measured mixing efficiency of device A, as a function of IF frequency, for optical powers of 17.0 to 140 μW . Here, the RF frequency was at 500 MHz, while the LO frequency was varied from 500.1 to 715 MHz, yielding IF frequencies from 0.1 to 215 MHz. The mixing efficiency is flat with IF frequency from 0.1 to 30 MHz beyond which an increase occurs. For high IF frequencies, the mixing efficiency approaches the QS value, whereas for low IF frequencies the mixing efficiency is significantly lower than the QS value and decreases as optical power decreases. We compared the sum-frequency signal to the difference-frequency signal and found that the sum signal is close to its

calculated QS value. It is expected that, since the difference signal is at low frequency, an OEM operating at the difference frequency would work better than or equal to a photodetector or a mixer operating at the sum frequency. Our results suggest a restriction of the low frequency signal for an InGaAs mixer with a SEL.

To compare the behavior of MSM-PD OEMs with differing SEL thickness, we plot the IV characteristics of device A and B in Figure 7. The knee voltage of device B is significantly smaller than that of device A. In addition, the knee voltage of device B also exhibits a logarithmic relation with optical power (not shown).

Figure 8 compares mixing efficiency as a function of RF frequency, for devices A and B. There is a marked improvement in the mixing efficiency for device B (100-Å SEL). In addition, the bandwidth of device B extends beyond 0.8 GHz (not shown) while the corresponding bandwidth of device A is about 200 MHz.

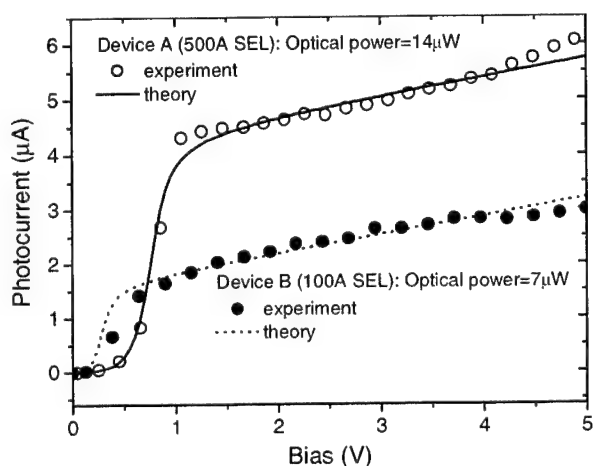


Figure 7. Comparison of DC IV characteristics of device A and device B.

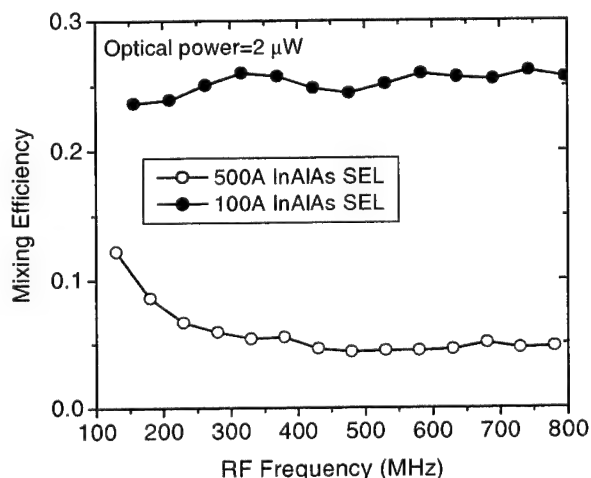


Figure 8. Mixing efficiency, as a function of RF frequency, for device A (open circles) and device B (solid circles).

Figure 9 compares mixing efficiency, as a function of IF frequency, for the devices A and B. Here, the RF light modulation was set to 500 MHz while the LO was varied from 500.1 to 715 MHz. This yields IF frequencies from 0.1 to 215 MHz. Again we observed a significant improvement in the mixing efficiency for device B. In addition, the mixing efficiency of device B is flat for both low and high IF frequencies and does not vary with optical power.

Figure 10 shows the mixing efficiency, as a function of optical power, for devices A and B. Here, the RF light modulation is set to 500 MHz and the LO bias frequency is set to 500.1 MHz (i.e., the IF frequency is at 10.0 kHz). The mixing efficiency for device A is very low and decreases significantly (and non-linearly) with decrease in optical power while the mixing efficiency for device B only slightly decreases with optical power.

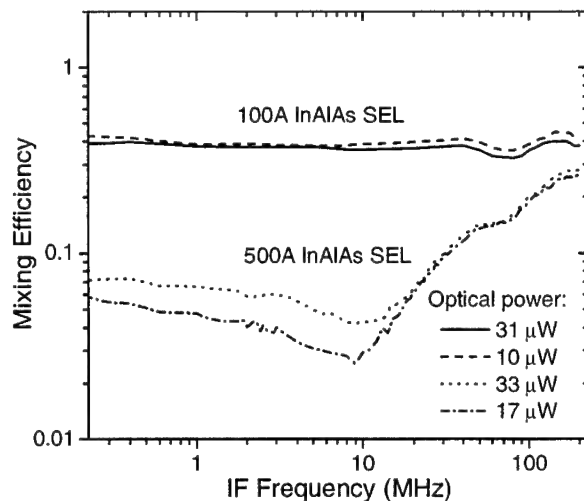


Figure 9. Mixing efficiency, as a function of IF frequency, for devices A and B at two different optical powers.

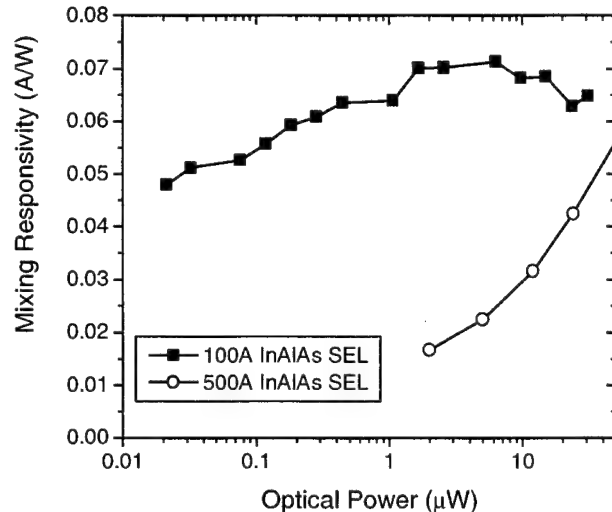


Figure 10. Mixing efficiency, as a function of optical power, for devices A and B.

4. MODELING AND DISCUSSION

We have used a 2-D finite-volume based drift-diffusion model to simulate the InGaAs MSM-PDs. We find a knee in the photocurrent that only exists when a SEL is utilized. In addition the knee voltage is dependent on optical power: It increases when optical power increases, following a logarithmic relation. Moreover, the knee voltage decreases drastically with decrease in SEL thickness. Details of the drift-diffusion model are beyond the scope of this paper and will be published elsewhere. In this paper, we only present a simplified circuit model to describe the behavior of the MSM-PDs.

In the circuit model, we divide the device into three regions (see Figure 11(a)). Regions A and C include the contact metal, the InAlAs SEL, and the InAlAs/InGaAs interface. The InGaAs absorption layer is included in region B. When the bias is above flat band, the electric field in each layer is uniform, except for small band bending at the location of the 2-D gas. In region B, the generated photocurrent is given by⁸

$$I_{ph} = \frac{g}{g+w} (1-R)(1-e^{-\alpha d}) \frac{\eta_i q}{h\nu} P, \quad (1)$$

where g is the interdigitated finger spacing, w is the finger width, R is the semiconductor reflectivity, α is the absorption coefficient, d is the InGaAs thickness, η_i is the intrinsic quantum efficiency, $h\nu$ is the photon energy, and P is the incident optical power. Photo-generated electrons and holes move toward the anode and cathode, respectively. Under low bias, the electron and hole currents are limited by the potential barriers. Therefore, some of the photo-generated carriers will recombine before the electrons and holes are completely separated. From the diffusion-drift model, we found that the field in region B is almost uniform, therefore we can calculate the

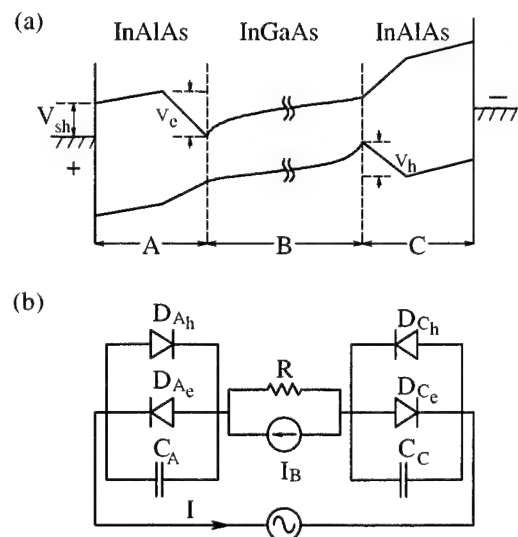


Figure 11. (a) 1-D illustration of the band structure for an InAlAs Schottky-enhanced InGaAs-based MSM-PD. (b) Circuit model of the MSM-PD OEM.

drift time for electrons and write the current in this region as

$$I_B(V_B) = I_{ph}e^{-t/\tau} = I_{ph}e^{-d^2/2\mu V_B\tau}, \quad (2)$$

where t is the average transient time for electrons, μ is the electron mobility, V_B is the voltage drop in region B and τ is the recombination lifetime. In regions A and C, light is not absorbed and the current is due to thermionic emission and/or tunneling. Depending on the bias polarity, either the electron or hole current will dominate. The hole current is limited by the valence band offset V_h while the electron current is limited by the Schottky barrier height V_{sh} , as well as the conduction band offset V_e . Therefore we can write the current in region A as

$$I_A = \begin{cases} A_{el}^* T^2 e^{-eV_{sh}/kT} (e^{eV_A/n_{el}kT} - 1) & V_A > 0 \\ -A_{hole}^* T^2 e^{-eV_h/kT} (e^{-eV_A/n_{hole}kT} - 1) & V_A < 0, \end{cases} \quad \begin{matrix} 3(a) \\ 3(b) \end{matrix}$$

where A_{el}^* and A_{hole}^* are the effective Richardson constants for electrons and holes, respectively, V_A is the voltage drop across region A, k is the Boltzmann constant, T is the device temperature, and n_{el} and n_{hole} are the ideality factors for electrons and holes, respectively. Similar equations can be given for the current in region C.

Figure 11(b) is a circuit model of the OEM. Equations 3(a) and (b) represent diodes D_{Ae} and D_{Ah} which model, respectively, the electron and hole currents in region A. Region C is similarly modeled by diodes D_{Ce} and D_{Ch} . Equation (2) is represented by the current source in region B, and the dark current is modeled by a resistor R, equal to $(dI/dV)^{-1}$ at large bias. The drop of the valence band barrier under bias depends on the structure. For example, in device A, only 1/3 of the total voltage across region A (or C) drops across the 250-Å In(Ga,Al)As graded layer. Therefore, we let $n_{hole}=3$. The ideality factor for electrons n_{el} is extracted from the photocurrent curves as a free parameter. All other parameters can be found in the literature. Using these values, with $\eta_i=100\%$ and $n_{el}=3.5$, the simulated photocurrent is shown in Figure 3, by solid and dotted lines, for optical powers of 7.0 μ W, and 0.7 mW, respectively. The agreement is very good.

Using the parameters obtained from fitting the DC IV characteristics, we simulate the mixing efficiency for device A (Figure 12). We add two capacitors ($C_A=C_C$) to the circuit. Due to the 2-D nature of the device, the values of $C_{A,C}$ are difficult to determine. The capacitance for the whole device, calculated using the conformal mapping technique, is 7.0 fF. We use 10.0 fF in our simulation. Figure 12 shows the simulated mixing efficiency as a function of LO frequency, for optical powers of 4.5 to 22.0 μ W. The RF and LO frequencies were displaced by 10.0 kHz. The simulated mixing efficiency decreases as LO frequency increases and cuts off at about 0.2 GHz. Figure 13 shows the simulated mixing efficiency as a function of IF frequency. Here, the modulation frequency was at 501 MHz, while the LO frequency was varied from 501.2 to 701 MHz, yielding IF frequencies from 0.2 to 200 MHz. The mixing efficiency is flat with IF frequency from 0 to 10 MHz beyond which an increase occurs. In both figures, the mixing efficiency increases with optical power. Considering the simplicity of our model and the fact that parasitic components are not included in the simulation, the general agreement with the experimental results is good. We also simulated the device as a photodetector (Figure 14). The frequency response is almost flat and slightly decreases (<5% and 0.1% for optical powers of 0.1 and 10 μ W, respectively) at low frequency. In addition, the responsivity is almost independent of optical power.

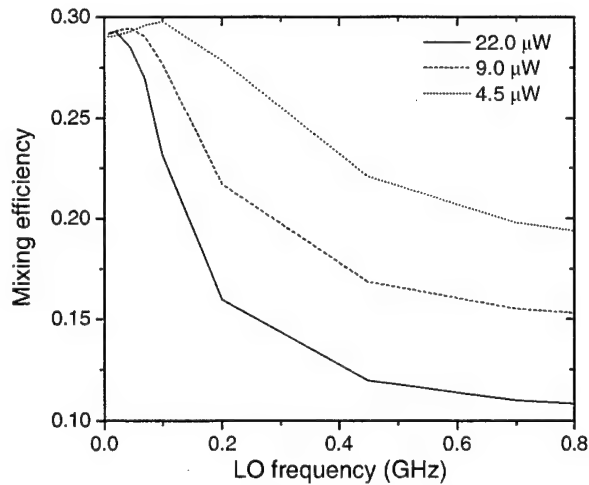


Figure 12. Simulated mixing efficiency as a function of LO frequency for device A at different optical powers.

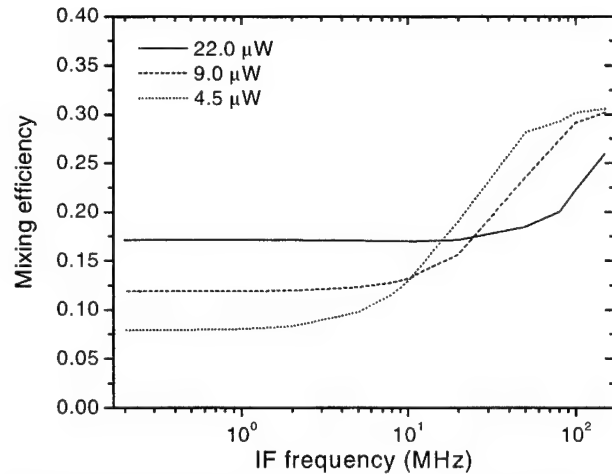


Figure 13. Simulated mixing efficiency as a function of IF frequency for device A at different optical powers.

These results can be explained as follows. When operated as a photodetector, a significant DC voltage drops across the SEL (V_A, V_C), the differential resistance of the forward-biased diode is low and, since Equation 3 shows that the current is limited by the forward-biased diode, the detector responsivity is almost unaffected by the SEL. When operated as an OE mixer, however, the LO bias on the SEL is frequency dependent due to the capacitors in the circuit. The capacitors in the circuit effectively reduce the LO bias on the diodes as the LO frequency increases and, hence, the differential resistance of the diodes increases. The mixing efficiency, therefore, decreases with increase in LO frequency (see Figure 12). This is especially true at low IF frequencies because the only signal path is through the diodes. However, increasingly higher IF signals pass through the two capacitors, and the mixing efficiency increases (see Figure 13). As optical power increases, the differential resistance of the absorption region decreases, V_A and V_C increase, and the differential resistance of the diodes decreases. As a result, the mixing efficiency increases with optical power (see Figures 12 and 13).

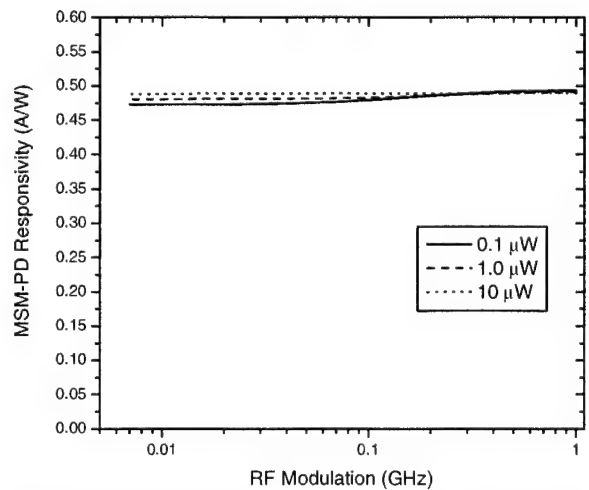


Figure 14. Simulated MSM-PD responsivity as a function of light modulation frequency for device A at different incident light intensities.

We have used the same parameters to model device B, except that the ideality factors, n_{hole} and n_{el} , have been modified according the structure. Since the SEL has been reduced to 100-Å in device B, the voltage drop across the 250-Å In(Ga,Al)As graded layer is 5/7 of the total voltage across regions A and C. Therefore, we let $n_{hole}=1.4$. The best fit to the experimental IV data is shown by the dashed line in Figure 7, with $n_{el}=1.8$. Figures 15 and 16 show the simulated mixing efficiency as a function of LO and IF frequency, respectively, for devices A and B. The simulated mixing efficiency for device B is improved and it is less dependent on the RF and IF frequencies.

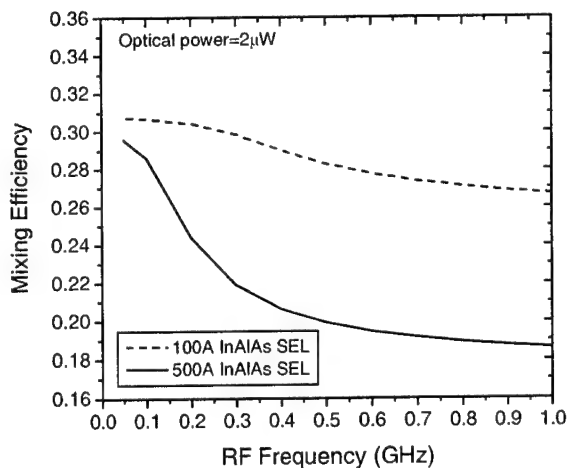


Figure 15. Simulated mixing efficiency, as a function of LO frequency, for devices A and B.

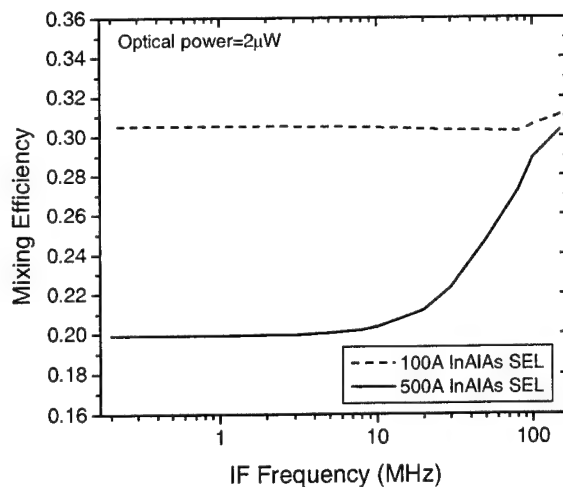


Figure 16. Simulated mixing efficiency, as a function of IF frequency, for devices A and B.

A detailed analysis of the model shows that the improvement of the mixing efficiency in device B is mainly due to the enhancement of the majority carrier (electron) current in Equation 3(a). A thinner SEL enhances the thermionic/tunneling current resulting in a reduction in the knee voltage and an improvement in the mixing efficiency.

5. CONCLUSION

The optoelectronic mixing characteristics of InAlAs, Schottky-enhanced, InGaAs-based metal-semiconductor-metal photodetectors have been studied. The mixing efficiency of MSM-PD OEMs depends on the thickness of the InAlAs Schottky-enhancement layer. For thick SELs ($\approx 500 \text{ \AA}$), the bandwidth of a MSM-PD OEM is much less than that of a corresponding MSM-PD. In addition, the mixing efficiency depends on the RF, LO, and IF frequencies, and decreases nonlinearly with decrease in optical power. Decreasing the thickness of the SEL to $\approx 100 \text{ \AA}$ improves the mixing characteristics of the MSM-PD OEM. The bandwidth of the OEM is similar to that of a corresponding photodetector and the mixing efficiency is found to decrease only slightly with decrease in optical power.

ACKNOWLEDGMENTS

The work in UF is supported by an ARO grant (DAAD 19-01-1-0756, monitored by Dr. M. D. Gerhold).

REFERENCES

1. Q. Z. Liu and R. I. MacDonald, Controlled nonlinearity monolithic integrated optoelectronic mixing receiver, *IEEE Photon Technol Lett*, Vol. 5, (1993), 1403-1406.
2. T. E. Darcie, S. Obrein, G. Raybon, and C. A. Burrus, Subcarrier multiplexing for multiple-access lightwave networks, *J Lightwave Technol*, Vol. 5, (1987), 1103-1110.
3. B. L. Stann *et al.*, "Research progress on a focal plane array lidar system using chirped amplitude modulation," in *Proc. of SPIE Vol. 5086 Laser Radar Technology and Applications VIII*, edited by Gary W. Kamerman, (SPIE, Bellingham, WA) pp. 47-57, 2003.

4. W. Ruff, K. Aliberti, J. Dammann, M. Giza, P. Shen, B. Stann, "Performance of an FM/cw prototype ladar using a 32-element linear self-mixing detector array," in Proc. of SPIE Vol. 5086 *Laser Radar Technology and Applications VIII*, edited by Gary W. Kamerman, (SPIE, Bellingham, WA) pp. 58-69, 2003.
5. K. Kajiyama, Y. Mizushita, and S. Sakata, Schottky barrier height of $n\text{-In}_x\text{Ga}_{1-x}\text{As}$ diodes," Appl Phys Lett, Vol. 23, (1973), 458-459.
6. K. C. Song, M. A. Martin, B. Robinson, J. G. Simmons, D. A. Thompson, and P. Mascher, High performance InP/InGaAs-based MSM photodetector operating at 1.3-1.5 μm , Solid-State Electron, Vol. 39, (1996), 1283-1287.
7. H. T. Griem, S. Ray, J. L. Freeman, and D. L. West, Long-wavelength (1.0-1.6 μm) $\text{In}_{0.52}\text{Al}_{0.48}\text{As}/\text{In}_{0.53}(\text{Ga}_x\text{Al}_{1-x})\text{As}/\text{In}_{0.53}\text{Ga}_{0.47}\text{As}$ metal-semiconductor-metal photodetector, Appl Phys Lett, Vol. 56, (1990), 1067-1068.
8. J. B. D. Soole and H. Schumacher, InGaAs metal-semiconductor-metal photodetectors for long wavelength optical communications, IEEE J of Quantum Electron, Vol. 27, (1991), 737-752.
9. W. A. Wohlmuth, P. Fay, C. Caneau and I. Adesida, Low dark current, long wavelength metal-semiconductor-metal photodetectors, Electronics Letters, Vol. 32, (1996), 249-250.
10. A. Xiang, W. Wohlmuth, P. Fay, S. M. Kang and I. Adesida, Modeling of InGaAs MSM photodetector for circuit-level simulation, J Lightwave Technol, Vol. 14, (1996) 716-723.
11. J. H. Kim, H. T. Griem, R. A. Friedman, E. Y. Chan, and S. Ray, IEEE Photon Technol Lett, High-performance back-illuminated InGaAs/InAlAs MSM photodetector with a record responsivity of 0.96 A/W, Vol. 4, (1992), 1241-1244.

Low threshold, high T_0 and high efficiency 1300nm and 1500nm lasers with AlInGaAs active region grown by MOCVD

Ashish Tandon, David. P. Bour, Ying-lan Chang, Chaokun Lin, Scott W. Corzine, Michael R. Tan
Agilent Laboratories, 3500 Deer Creek Road, Palo Alto, CA, USA 94304

ABSTRACT

We report results for broad area edge emitting lasers having AlInGaAs active regions that exhibit low thresholds, high T_0 and T_1 and high efficiencies. The lasers were grown on InP substrates using MOCVD. This paper analyzes the effects of doping, epilayer design, wavelength dependence and number of QWs on device performance. Our results show that the concentration and offset of zinc doping in the p-cladding layer plays a major role in carrier confinement and hence high temperature performance. The difference in surface mobility of Al adatoms (as compared to In or Ga) poses some challenges in the growth of AlInGaAs.

1. INTRODUCTION

AlInGaAs-based lasers exhibit better high temperature performance, improved efficiencies and enhanced differential gain than their InGaAsP-based counterparts. This is attributed to improved carrier confinement resulting from a higher conduction band offset [1-10]. It has also been observed that the ratio of radiative to non-radiative recombination is also higher in the AlInGaAs system [5]. These improved properties have been used in the development of InP-based long wavelength VCSELs [6,7].

2. METHODOLOGY

Epitaxial growths were performed by low pressure metalorganic chemical vapor deposition (MOCVD), in H_2 carrier gas with precursors arsine, phosphine, trimethyl- group III alkyls, triethylgallium, and for doping disilane (0.01% in H_2) and diethylzinc. Growth was initiated by heating an InP:S substrate wafer in PH_3 to the growth temperature, growing a 0.2 μm InP:Si buffer layer, then depositing an AlInGaAs layer or heterostructure. The substrate orientation was either exact (100), or vicinal, with a misorientation of 2-6° toward $\langle 111 \rangle A$. The growth temperature was varied between 640C and 750C, the group-V to group-III molar ratios were 50-120, and the growth rate was typically 0.4-0.5 nm/sec. Two reactor configurations were compared: a Thomas Swan 3 x 2-inch reactor with close-coupled showerhead, and an Aixtron AIX2000 5x2-inch reactor with radial injector and planetary rotation. However, no significant differences were observed in the native material characteristics, heterostructure properties or device performance, for AlInGaAs grown under optimum conditions in these two very different reactors.

The MOCVD growth of compound semiconductors whose constituent elements include both aluminum and indium is challenging because of the tradeoffs associated with the choice of growth temperature. Low growth temperatures are favored for indium-containing alloys, as this condition avoids evaporation from the surface, which leads to difficulty controlling the alloy stoichiometry. On the other hand, high growth temperatures are better suited for alloys containing aluminum, since this encourages surface mobility for smooth film growth, and also suppresses oxygen contamination. Compared to the mobility of indium or gallium atoms on a III-V surface, the surface mobility of Al atoms is significantly lower. As a result, the optimum growth window for AlInAs as well as AlInGaAs is much narrower than the range of growth temperatures available for InGaAs growth, which is only limited by dissociation at high growth temperatures.

The band offsets occurring at the interfaces in semiconductor heterostructures are of interest from both a fundamental standpoint and for the design and understanding of the optoelectronic device characteristics. In order to determine the band offsets in the AlInGaAs material system, a simple MQW test structure, consisting of lattice matched InGaAs QWs confined by lattice matched AlInAs barriers, was grown on an InP (100) substrate. X-ray diffraction confirmed the

existence of the periodic structure, specifically characterizing the MQW as being formed from two discrete alloys with abrupt interfaces between them (i.e., no significant alloy intermixing between QW and barriers). To examine the family of allowed optical transitions, Fourier transform infrared spectroscopic (FTIR) measurements were made on this sample both at room temperature and liquid helium (5K) temperature. Absorption spectroscopy techniques such as FTIR, photoluminescence (PL) excitation, or photocurrent absorption are especially useful because they permit observation of the higher energy transitions that are not active in emission spectroscopy such as standard PL. To evaluate the band offset, the measured transition energies were fit by simulating the affect of space quantization, by using sub--band calculations, which assumed 70Å QWs, 70Å barriers and a conduction band offset ratio Q_c of 0.7. The effective mass ratios (m^*/m_0) for the QW were taken to be 0.37, 0.041, and 0.042 for the heavy hole, light hole, and electron, respectively, while the corresponding values for the barrier were 0.40, 0.046, and 0.083. Figs. 1 (a) and (b) show that for this Q_c value the calculated transition energies match well with the experimental data, thereby confirming the generally-accepted bandgap and Q_c values.

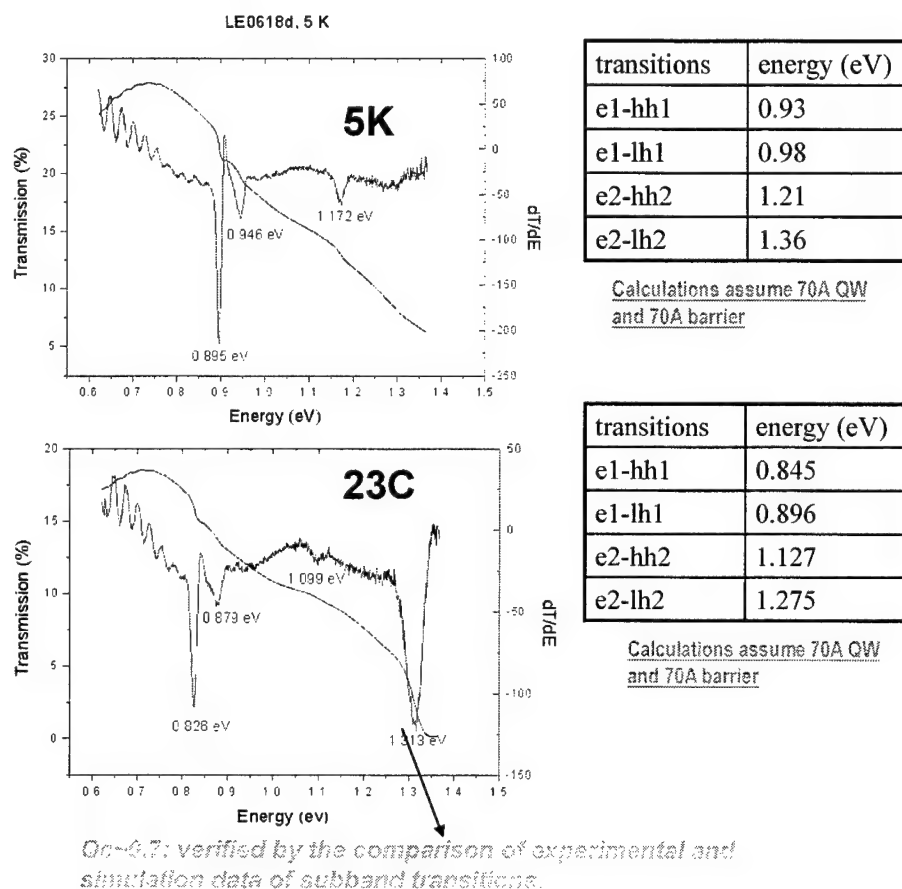


Fig. 1 (a) Low temperature (5K) FTIR spectra for InGaAs/AlInAs MQW. The transition energy in the spectra match well with the calculated values shown in the table; (b) Room temperature FTIR spectra for InGaAs/AlInAs active region. Here again, the transition energy in the spectra agree well with the calculated values shown in the table.

Based on this determination of the band offsets, the band structure of AlInGaAs diode laser structures was constructed. For example, Figs 2 (a) and (b) outline the band diagram for AlInGaAs active region in a laser under forward bias. These two cases illustrate the impact of p-type doping on carrier confinement, by comparing two zinc doping profiles. First, we examined low zinc doping together with a large set back, as is often used to avoid zinc diffusion and to reduce free-carrier and intervalence band absorptions. However, this represents a tradeoff, since the confinement potential for injected electrons may be enhanced with higher zinc doping. Accordingly, the second case corresponds to a more aggressive zinc doping profile. The simulations for the biased condition were performed using CROSSLIGHT software. It can be seen from the modeling results that increasing the p-doping level along with moving the p-doping close to the

active region (Figure 2b), leads to better confinement for the electrons which are being injected into the active region from the n-cladding. Such a change in band structure decreases carrier leakage from the QWs and should therefore lead to improved characteristic temperatures as well as higher internal quantum efficiencies.

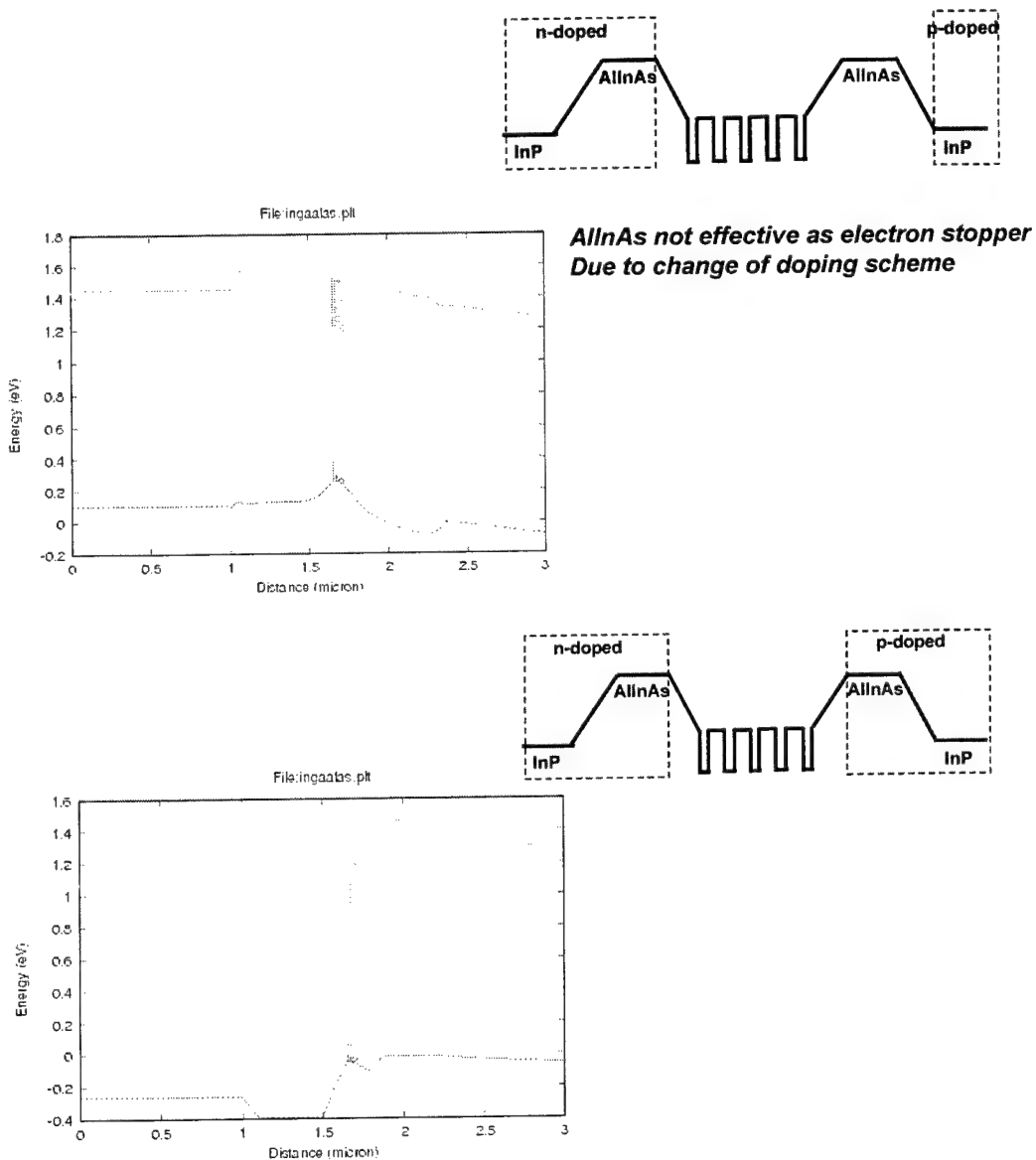


Fig. 2 (a) Band diagram for AlInGaAs laser with low and recessed p-doping; (b) Band diagram for AlInGaAs laser where p-doping is higher and moved closer to the active region.

3. DEVICE RESULTS AND DISCUSSION

A. 1300nm edge emitting lasers

In order to experimentally validate the effect of the p-type doping profile on laser performance, two 1300 nm AlInGaAs laser structures were compared. The AlInGaAs separate confinement heterostructure (SCH) layers were 120 nm thick, Si doped on the n-side, and with set back zinc doping on the p-side. The active region consisted of 5 x 70 Å AlInGaAs

QWs with 1.4% compressive strain and 70 Å unstrained AlInGaAs barriers. This basic structure is illustrated in Fig. 3. This structure provides a total (all five QWs) optical confinement factor of about 18.3%. The only difference in the two structures was the concentration level and initiation point for the Zn doping. Figs 4 (a) and (b) show the zinc acceptor profiles measured by secondary ion mass spectroscopy (SIMS) analysis for the two samples, clearly illustrating the Zn doping concentrations and setbacks.

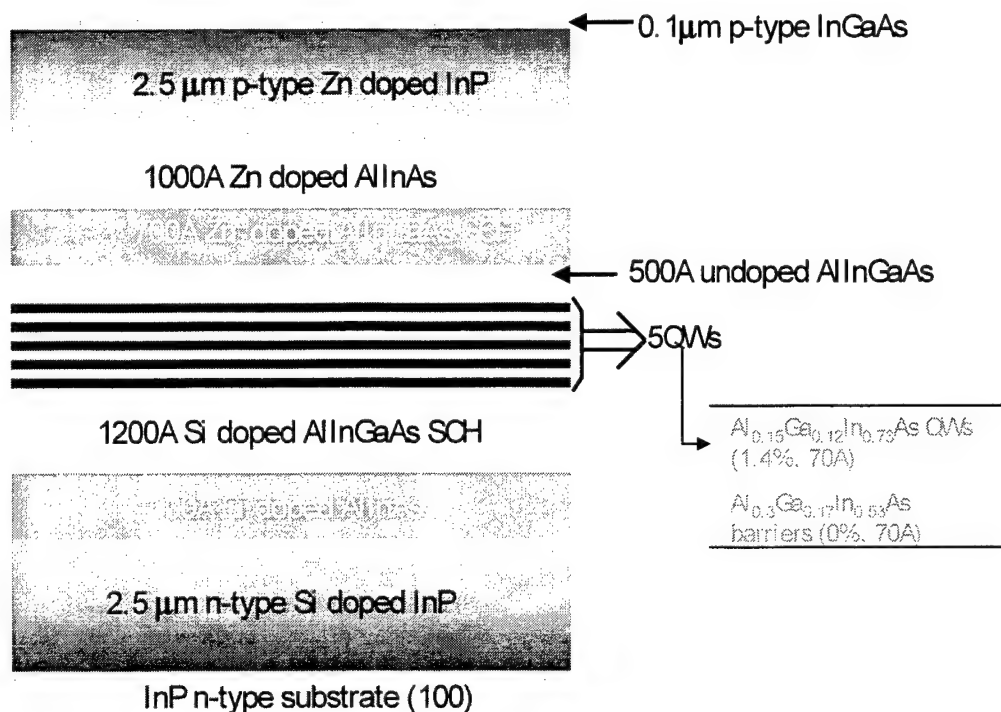
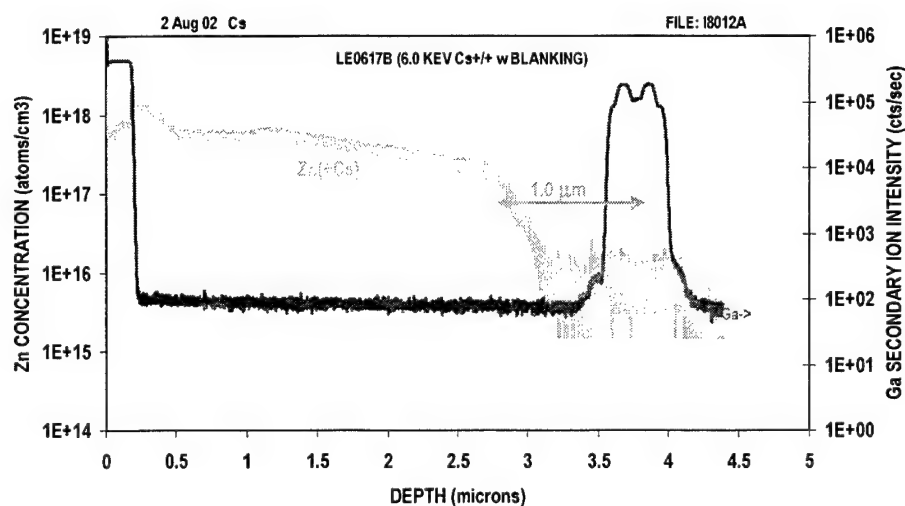


Fig. 3 Epitaxial layer structure for AlInGaAs edge emitting laser.



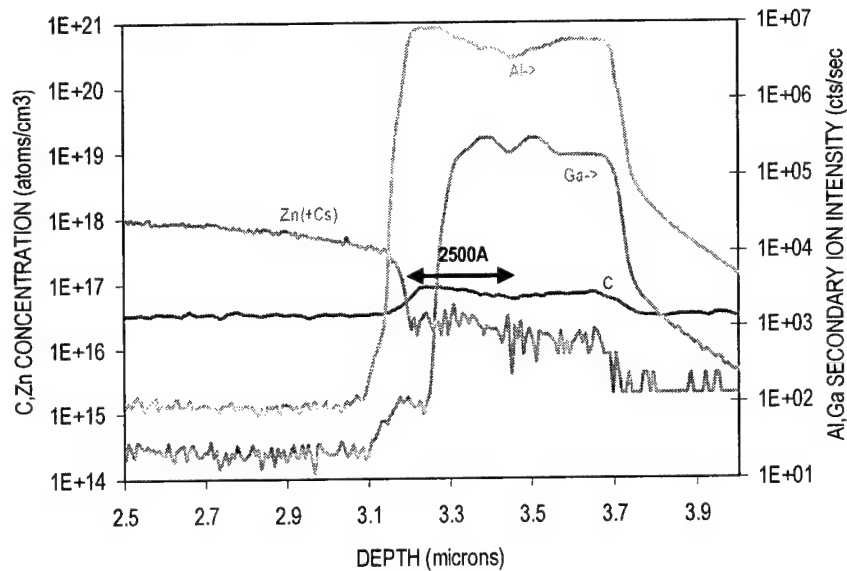


Fig. 4 (a) SIMS data for AlInGaAs laser where p-doping is recessed from the active region. The Zn profile falls below a concentration of 1×10^{17} at a distance of $1.0 \mu\text{m}$ from the QWs; (b) SIMS data for AlInGaAs laser where p-doping is both higher and extended closer to the active region. The Zn profile falls below a concentration of 1×10^{17} at a distance of 2500 \AA from the QWs.

From these two AlInGaAs laser wafers, broad area edge emitting lasers with stripe width of $50 \mu\text{m}$, varying stripe lengths and cleaved facets were fabricated and tested under pulsed conditions at various temperatures. Figs 5 (a) and (b) illustrate the room temperature and over-temperature light-current (L-I) characteristics for the two device structures. These data show that while the thresholds for the two structures are fairly comparable, there is a pronounced difference in the temperature dependence of their threshold currents and differential quantum efficiencies, whose exponential change with respect to temperature are characterized by the temperatures T_0 and T_1 , respectively. For instance, for a cavity length of $1000 \mu\text{m}$, the room-temperature (RT) threshold current density is about 610 A/cm^2 for the laser with the low and set back zinc doping, but this improves modestly to about 480 A/cm^2 for the laser whose zinc doping is moved closer to the active region. However, the differential quantum efficiency at room temperature demonstrates a much greater improvement when the zinc doping profile is optimized, increasing from $\sim 20\%$ to about 60% . Likewise, the characteristic temperatures T_0 and T_1 are improved to $T_0 \sim 80\text{K}$ and $T_1 \sim 200\text{K}$ for the structure with an optimized zinc doping profile. This benefit presumably accrues from the greater electron confinement associated with the high p-doping.

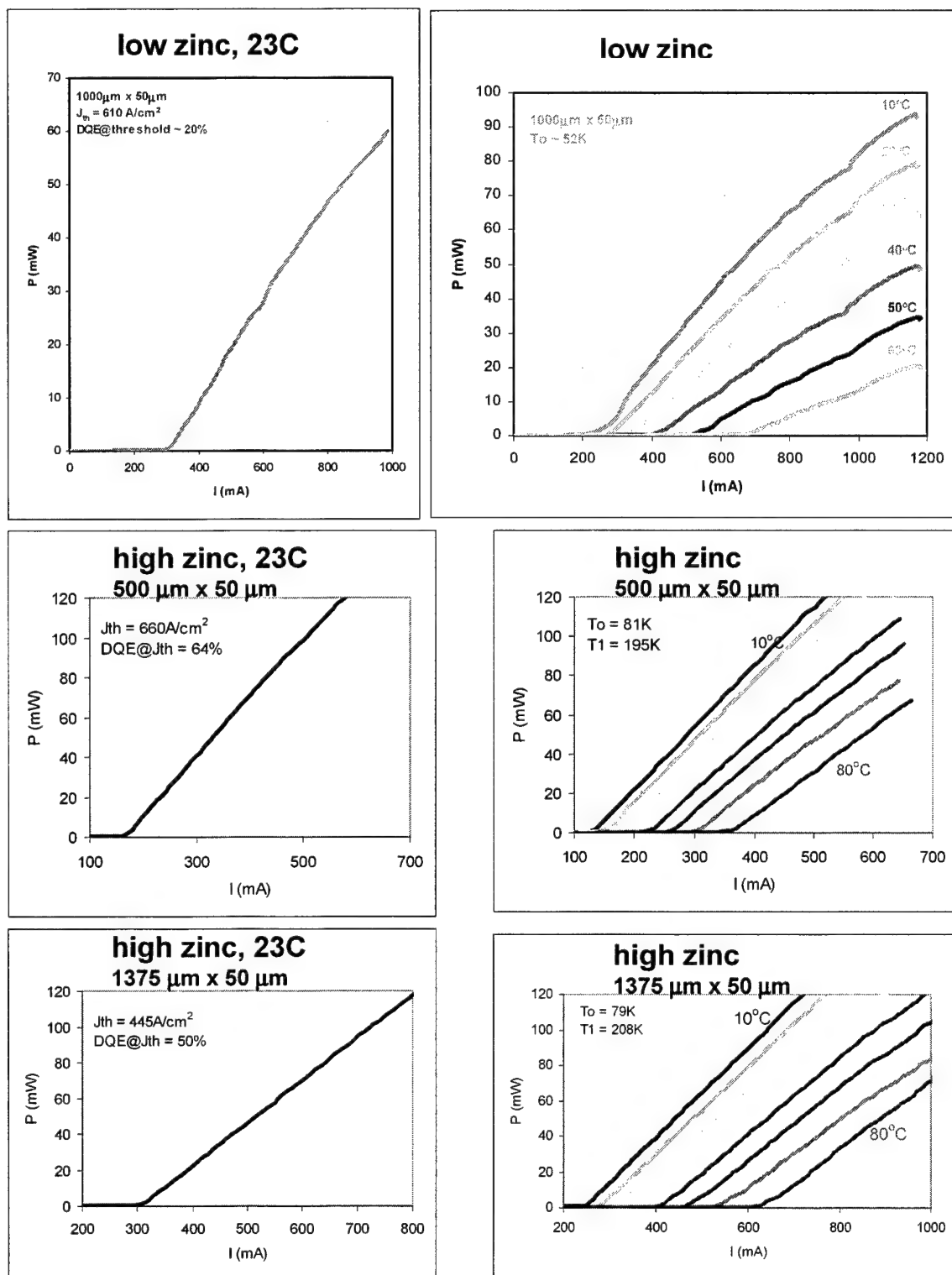


Fig. 5 (a) Room and high temperature L-I characteristics of broad-area ($w=50\mu\text{m}$) AlInGaAs lasers that had Zn doping recessed from the active region. (b) Room and high temperature LIV results from edge emitting AlInGaAs lasers that had higher Zn doping, moved closer to the active region. These edge emitters had low thresholds combined with high efficiency and high T_0 . ($\lambda \sim 1300 \text{ nm}$).

Based on the L-I characteristics obtained from laser bars of different cavity lengths (L), we extracted the distributed loss (α_i) and internal quantum efficiency (η_i) values, by fitting the inverse of the measured differential quantum efficiencies (η_i^{-1}) to a straight-line dependence with respect to L , in the standard manner. These trends are illustrated in Figs 6 (a) and (b) for room temperature and for 50°C. Both the internal efficiency and the distributed loss are degraded with higher temperature due to carrier leakage and intervalence band absorption, respectively. The optical spectrum for a typical laser bar at room temperature is shown in Fig. 7.

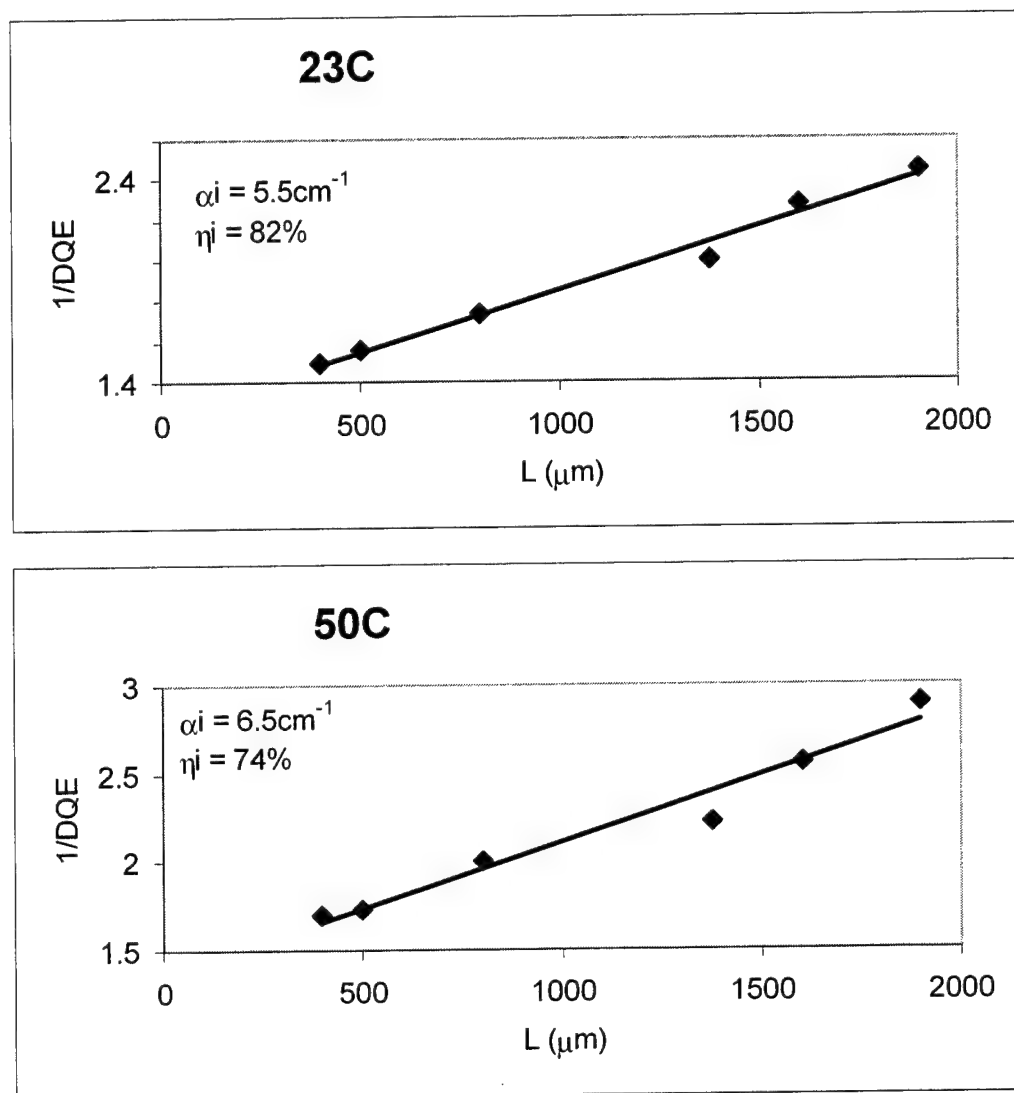


Fig. 6: Room temperature (a) and high temperature (b) efficiency data for AlInGaAs lasers of different cavity lengths, and with optimized zinc doping profile.

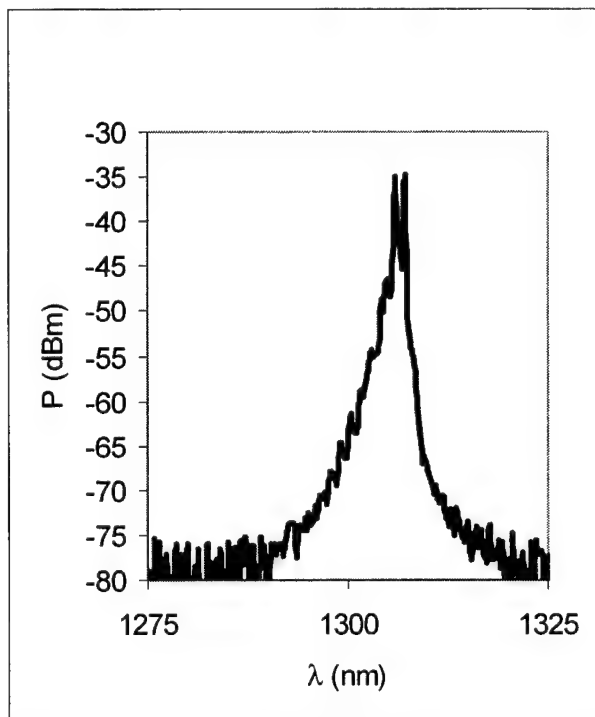


Fig. 7 Room temperature emission spectra from AlInGaAs lasers with optimized Zn doping profile.

B. 1500nm edge emitting lasers

At 1500 nm wavelength, it is expected that Auger recombination rather than carrier leakage will most limit the high-temperature laser performance. Nevertheless, the improved carrier confinement offered by AlInGaAs heterostructures may still contribute some performance benefit at this longer wavelength. The 1500 nm AlInGaAs lasers grown here are very similar to the 1300 nm structures, with modification to the quantum wells (QWs), barriers, and separate confinement heterostructure (SCH), as appropriate for extending the operation to 1500 nm. The target photoluminescence wavelength was 1480 nm.

Similar to the 1300 nm MQW lasers, the 1500 nm structures also incorporate 100 nm AlInAs surrounding the SCH. For maximum carrier confinement, the n- and p-type doping are included in these AlInAs layers. Similar to the 5-QW 1300 nm structures, we chose 1.0% compression for the QWs. On the other hand, rather than using unstrained barriers (that we used in the case of 1300nm lasers), we instead incorporated strain-compensating barriers with 0.5% tensile strain. This choice was made because we anticipated using larger numbers of QWs, for better performance at longer wavelength where the Auger recombination rate is greater. The SCH comprises 45 nm undoped, lattice-matched $(\text{Al}_{0.5}\text{Ga}_{0.5})_{0.5}\text{In}_{0.5}\text{As}$ while the QWs are 85 Å $(\text{Al}_{0.31}\text{Ga}_{0.69})_{0.32}\text{In}_{0.68}\text{As}$, which experiences 1.0% compression. The barriers are 70 Å thick, 0.5% tensile-strained $(\text{Al}_{0.5}\text{Ga}_{0.5})_{0.55}\text{In}_{0.45}\text{As}$. The bandgap wavelength of this alloy is approximately 1.0 μm. Both 5- and 9-QW structures were grown for comparison. Likewise, similar structures with conventional InGaAsP active regions, both 5- and 9-QW, were also grown. In this case the QWs were 85 Å $\text{In}_{0.75}\text{Ga}_{0.25}\text{As}_{0.75}\text{P}_{0.25}$ (0.7% compression), while the barriers were 80 Å thick, and tensile strained to compensate the QW compression. The SCH comprised a stepped-index waveguide, with 30 nm each of 1.0 μm and 1.05 μm InGaAsP quaternary layers around both sides of the MQW.

Generally, the 1500 nm AlInGaAs lasers exhibited good performance, and in some cases they appeared superior to the InGaAsP lasers. For example, the cavity-length dependence of threshold current density for 5-QW InGaAsP and AlInGaAs broad-area lasers of width 50 μm compared in Figure 8a. Both devices have an emission wavelength of 1500-

1510 nm, as expected for a nominal PL wavelength of 1480 nm. The threshold currents at 22C are nearly identical, around 550 A/cm^2 for $500 \mu\text{m}$ long lasers, and dropping to 425 A/cm^2 for $1000 \mu\text{m}$ cavity lasers. A slight difference was apparent, however, in the temperature dependence of threshold current density, shown in Figure 8b. Over the temperature range 10-80C, the threshold is less temperature-sensitive for the AlInGaAs lasers, with a characteristic temperature $T_0=64\text{K}$, compared to a value of 49K for the InGaAsP lasers (both lasers have length $L=530 \mu\text{m}$). Similarly, the differential quantum efficiency is also less temperature sensitive for AlInGaAs lasers, as indicated in Figure 9. The T_1 values, characteristic of the exponential drop in quantum efficiency with temperature, are 139K and 101K for AlInGaAs and InGaAsP 5-QW active regions, respectively.

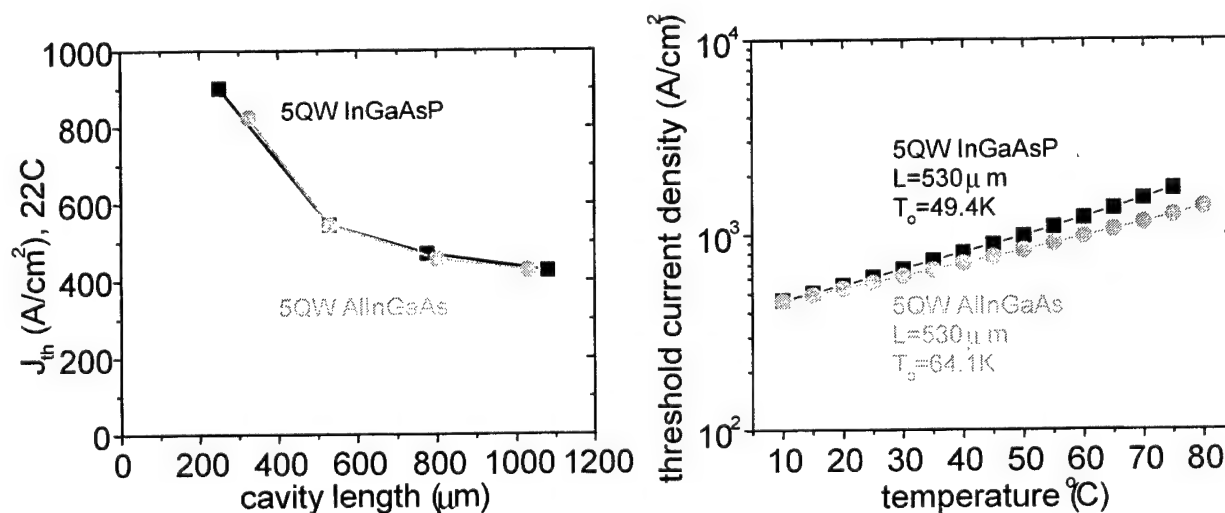


Fig. 8 Comparison of threshold current densities (J_{th}) of 5-QW, 1500nm AlInGaAs and InGaAsP lasers: (a) cavity length dependence of J_{th} ; and (b) temperature dependence of J_{th} .

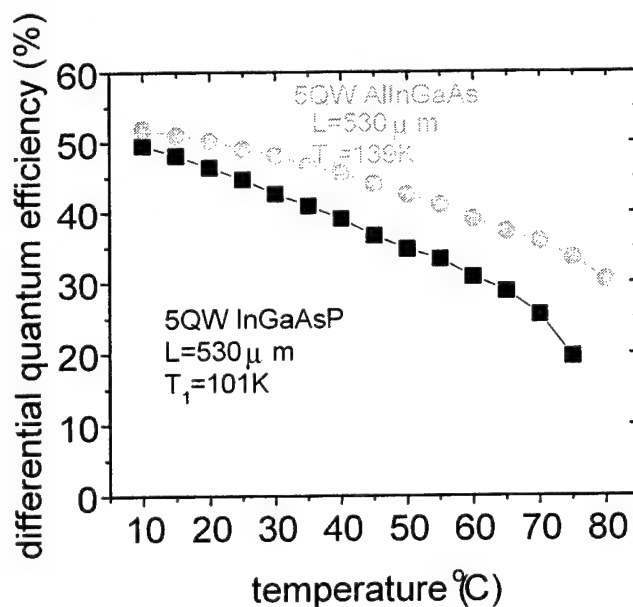


Fig. 9 Comparison of temperature dependence of the external differential quantum efficiency of 5-QW, 1500nm AlInGaAs and InGaAsP lasers

Oftentimes, nonradiative recombination associated with oxygen-related defects in AlInGaAs causes the characteristic temperature to appear artificially high, because this nonradiative component of the total threshold current is not so

temperature-sensitive. In these cases, however, the room-temperature threshold current is typically higher than for InGaAsP lasers, and the quantum efficiency lower. Here, in contrast, over the entire range of temperatures tested (10–80°C), the threshold is similar or lower and the efficiency higher for the 5-QW AlInGaAs devices. This suggests that the performance improvement is genuine, accruing from the some fundamental property of the AlInGaAs heterostructures, for example favorable band offsets, lower Auger recombination, etc.

Broad-area lasers of various cavity lengths (L) were examined, to determine the internal quantum efficiency (η_i) and distributed loss (α) in the standard manner. These results are shown in Fig. 10a, which compares the cavity-length dependence of efficiency for 5- and 9-QW AlInGaAs lasers. The internal quantum efficiency extrapolates to $\eta_i \sim 80\%$, while the distributed loss is $\alpha = 14 \text{ cm}^{-1}$ for the 5QW lasers and $\alpha = 31 \text{ cm}^{-1}$ for the 9-QW laser. The disproportionately high distributed loss for the 9-QW laser may be a result of a nonuniform carrier distribution among the more numerous QWs. This trend was also observed when the 5- and 9-QW InGaAsP lasers were compared, with $\alpha = 14$ and 39 cm^{-1} , respectively, as indicated in Fig. 10b.

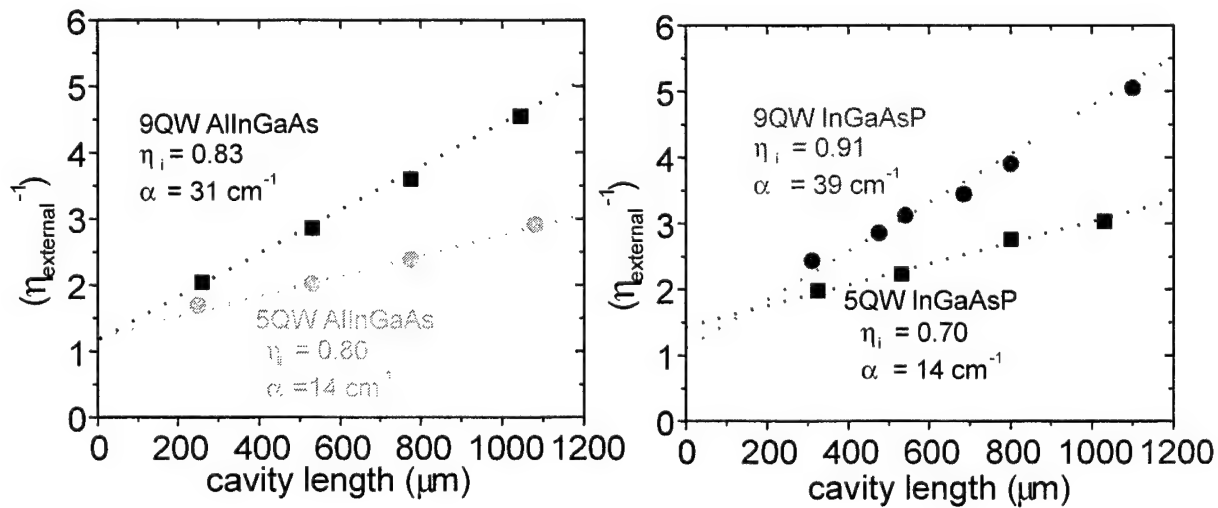


Fig. 10 Comparison of the differential quantum efficiency of 5 and 9 QW 1500nm lasers: (a) AlInGaAs: and (b) InGaAsP active regions

Although the room-temperature threshold current density is higher for the 9-QW lasers compared to the 5-QW lasers, the 9-QW devices generally exhibit less temperature sensitivity (higher T_0 and T_1 values) than 5-QW devices. This tendency is expected, since the gain per QW (and therefore the carrier density) is lowered as more QWs are added to the active region. This is illustrated in Fig. 11, comparing the temperature-dependence of threshold current density for 5- and 9-QW AlInGaAs lasers of length $530 \mu\text{m}$. However, the injected carrier distribution may also become more uniform at elevated temperatures, since a larger fraction of injected carriers are not confined to the QWs. In this situation, increasing the available thermal energy can promote a more uniform distribution, which may also contribute to the higher T_0 .

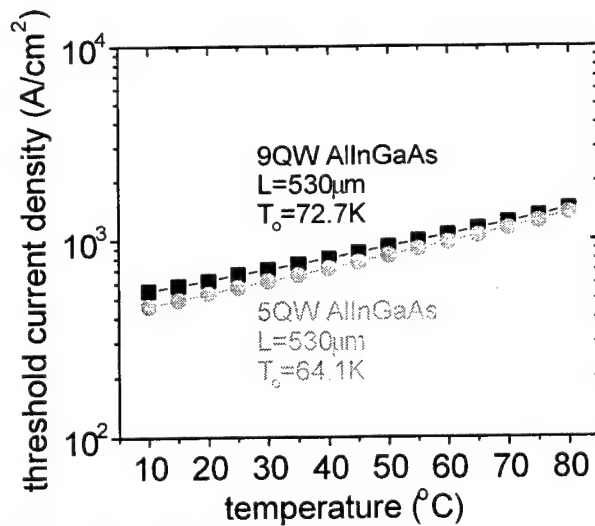


Fig. 11 Comparison of J_{th} of 5 and 9 QW, 1500nm AlInGaAs lasers

In order to better understand the source of the decrease in differential quantum efficiency at elevated temperatures, the cavity length studies were also performed at a higher temperature of 60C. The observed reduction in efficiency could be caused by a combination of lower internal quantum efficiency, or a higher distributed loss. If only the internal quantum efficiency was reduced at higher temperature (by carrier leakage, for example), the intercept of the η^{-1} vs. L curve would change, but the slope would remain unchanged. Alternatively, if the distributed loss was increased at high temperature, the slope would increase but the intercept stay unchanged. Generally, from the high-temperature cavity-length studies, it appeared that the lower efficiency was predominantly associated with an increase in the distributed loss with temperature, rather than any sizeable decrease in the internal quantum efficiency. This is represented in Fig. 12a for the 9-QW AlInGaAs laser; also shown are the temperature dependence of threshold current density and quantum efficiency for this device (Fig. 12b), with $T_0 = 72.7K$ and $T_1 = 152K$. Similar trends were observed for all laser samples, InGaAsP and AlInGaAs alike.

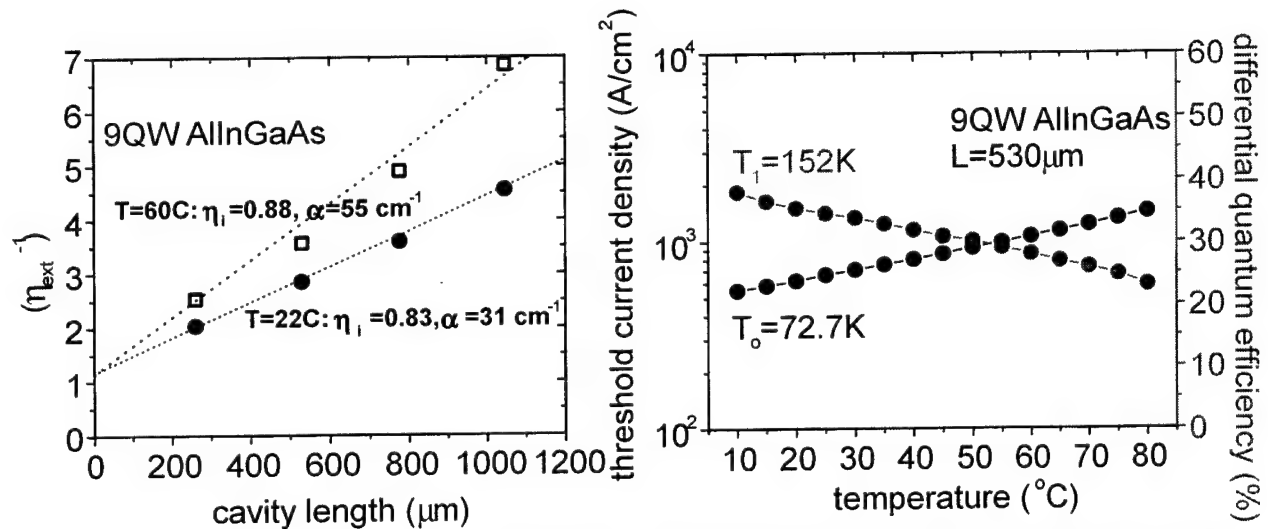


Fig. 12(a) Cavity length dependence of $1/\eta_{ext}$, measured at room temperature and 60C for 9QW 1500nm AlInGaAs lasers; and (b) temperature dependence of threshold current density (J_{th}) and DQE (η_{ext}).

The performance improvements associated with AlInGaAs are often attributed to greater band offsets that better confine injected carriers and suppress leakage. Nevertheless, Auger recombination also plays a strong role in determining T_0 , especially in 1500-nm band lasers. The absence of a significant decrease in the internal quantum efficiency when the temperature increases from 22C to 60C (Figure 12a), indicates that carrier leakage can be minimized in the AlInGaAs structures.

4. CONCLUSIONS

Edge emitting lasers with excellent thresholds, efficiencies and high temperature performance were demonstrated at 1300nm and 1500nm. These lasers had an AlInGaAs active region and exhibit significantly improved performance over their counterparts that use the more conventional InGaAsP active region. The growth of AlInGaAs active regions by MOCVD poses certain challenges and calls for careful optimization of growth conditions. The doping levels and offsets in the active region and cladding layers play a significant role in device performance.

REFERENCES

- [1] P.A. Andrekson, R.F. Kazarinov, N.A. Olsson, T. Tanbun-Ek, and R.A. Logan, "Effect of thermionic electron emission from the active layer on the internal quantum efficiency of InGaAsP lasers operating at 1.3 μ m", IEEE J. Quantum Electronics, vol. 30, pp. 219-221, 1994.
- [2] J.W. Pan and J.I. Chyi, "Theoretical study of the temperature dependence of 1.3 μ m AlInGaAs-InP multiple quantum well lasers", IEEE J. Quantum Electronics, vol. 32, pp. 2133-2138, 1996.
- [3] S.J. Bae, S.H. Park and Y.T. Lee, "Bandgap effects of quantum well active layer on threshold current density, differential gain and temperature characteristics of 1.3 μ m InGaAlAs/InP quantum well lasers", Jpn. J. Appl. Phys. Vol. 41, pp. 1354-1358, 2002.
- [4] S.R. Selmic, T.M. Chou, J.P. Sih, J.B. Kirk, A. Mantie, J.K. Butler, D. Bour, and G.A. Evans, "Design and characterization of 1.3 μ m AlInGaAs-InP multiple quantum well lasers", IEEE Journal on selected topics in quantum electronics, vol. 7, no. 2, pp. 340-349, 2001.
- [5] T. Higashi, S.J. Sweeney, A.F. Phillips, A.R. Adams, E.P. O'Reilly, T. Uchida and T. Fujii, "Observation of reduced nonradiative current in 1.3 μ m AlInGaAs-InP strained MQW lasers", IEEE Photonics Tech. Lett., vol. 11, no. 4, pp. 409-411, 1999.
- [6] D.A. Buell, A.S. Huntington, R. Koda, E. Hall, S. Nakagawa, M. Reddy, L.A. Coldren, "InP-based 1310-1550 nm lattice-matched VCSELs", Lasers and Electro-Optics Society, 2001. LEOS 2001. The 14th Annual Meeting of the IEEE, vol. 2, pp. 447-448, 2001.
- [7] R. Shau, M. Ortsiefer, J. Rosskopf, G. Bohm, F. Kohler and M.C. Amann, "Vertical cavity surface emitting laser diodes at 1.55 μ m with large output power and high operation temperature", Electron. Lett., vol. 37, no. 21, pp. 1295-1296, 2001.
- [8] Chuang, Optical properties of III-V compounds (1995)
- [9] D. Olego, T.Y. Chang, E. Silberg, E.A. Caridi, A. Pinzuck, "Compositional dependence of band-gap energy and conduction-band effective mass of $In_{1-x-y}Ga_xAl_yAs$ lattice matched to InP", Applied Physics Letters, Vol.41, no. 5, pp. 476-478, 1982
- [10] M. Gurden and J. Piprek, "Material Parameters of Quaternary III-V Semiconductors for Multilayer Mirrors at 1.55 μ m Wavelength", Modelling and Simulation in Materials Science and Engineering, vol. 4, pp349-357, 1996

Two-color semiconductor lasers

S. Hoffmann* and M.R. Hofmann

AG Optoelektronische Bauelemente und Werkstoffe, University of Bochum, IC2/156, D-44780 Bochum, Germany

ABSTRACT

The emission spectrum of a two-color semiconductor laser is analyzed. We find four-wave mixing sidebands for difference frequencies up to 4 THz. The appearance of four-wave mixing signals is a clear sign for a modulation of the carrier plasma at the corresponding difference frequency. We prove experimentally that this difference frequency is also directly emitted out of the laser diode and suggest a new simple concept for the generation of tunable coherent THz-radiation.

Keywords: Terahertz, THz, four-wave-mixing, FWM, external cavity, semiconductor laser, nonlinear dynamics

1. INTRODUCTION

Semiconductor lasers are widely used in spectroscopy, metrology and telecommunications. Their main advantages are spectral tunability, low cost, compact design and their low power consumption. The best performance with respect to tuning range and linewidth are achieved by the combination of semiconductor laser diodes with external cavities. Common realizations like the Littmann¹ or Littrow² configuration use the movement of a grating or mirror to tune the wavelength of the laser emission.

In the last years the application of external cavity semiconductor lasers for the generation of cw-THz-radiation has been intensively discussed. In most approaches, the outputs of two separate stabilized lasers are superimposed and focused on a photoconducting antenna³. When the emission frequency of both lasers is slightly different (detuned by several GHz or THz) the difference frequency is generated in and emitted out of the antenna⁴. The effort of generating THz Radiation could be considerably reduced using only one laser system emitting two colors simultaneously. This idea has been demonstrated by⁵ using a complex and expensive cw-Titan-Sapphire laser system. Using diode lasers as light source would considerably reduce the cost, footprint and complexity of such systems. Unfortunately simultaneous emission of two frequencies is neither possible in the Littrow nor in the Littmann configuration. But the external cavity used in this work, the so called Fourier-Transform External Cavity Laser (FTECAL) – geometry offers the unique opportunity to emit two colors simultaneously⁶. This system has been used previously to generate THz-Radiation⁷. Also the first cw-THz imaging system described in section 3 has been demonstrated using this laser system. The dynamics of such a Two Color Laser (TCL) is crucial for the THz generation and is therefore analyzed in this work.

Semiconductor lasers and amplifiers in general are well known to show a rich dynamic behavior due to the interaction of the complex carrier dynamics in the semiconductor with the light field. The corresponding nonlinear effects have been extensively studied in pump-probe^{8,9} and four-wave mixing^{10,11} experiments using semiconductor laser amplifiers. The subpicosecond gain dynamics found in femtosecond pump-probe experiments could be explained by spectral hole burning¹² and carrier heating¹³. Even faster coherent dynamics were found with a heterodyne four-wave-mixing experiment¹⁴, other effects like free carrier absorption¹⁵ and two photon absorption¹⁶ are still controversially discussed. It has been shown that these ultrafast nonlinearities¹⁷ lead to nondegenerate four-wave mixing (FWM) up to difference frequencies above 4 THz. Four-Wave-Mixing in a two color semiconductor laser has to our knowledge not been reported, yet.

* Stefan.Hoffmann@ruhr-uni-bochum.de

2. EXPERIMENTAL SETUP

The FTECAL setup for the laser cavity used in this work is similar to the Littman configuration. But in addition to the Littman setup, a Fourier transformation in the cavity is exploited. This laser cavity is extensively discussed in Reference ^{6,7}, in ¹⁸ a similar cavity is used for modelocking and pulse shaping of semiconductor lasers. The setup is shown in Fig. 1. The emission of an antireflexion coated semiconductor laser diode (LD) is collimated with lens (L1) and then diffracted by an optical grating (G). The diffracted light is collected by a second lens (L2) and focused onto the external mirror (M). The distances between mirror and lens on one hand and the grating and the lens on the other equal the focal length of (L2). So the different frequencies diffracted from the grating into different directions are focused onto different sections of the mirror. This corresponds to a Fourier transformation performed by the grating (G) and the lens (L2). An unstructured end mirror would reflect the whole spectrum back into the cavity such that each spectral component is back reflected in itself. A selection of the lasing frequency can be achieved by introducing an aperture directly in front of the mirror between (M) and (L2). In our case we used a laterally structured mirror in order to select two frequencies for simultaneous feedback. It consists of a glass-substrate on which a V-shaped gold stripe is evaporated. The difference frequency can be selected by vertical translation of the end mirror [14]. Different center frequencies can be achieved by lateral translation of the end mirror.

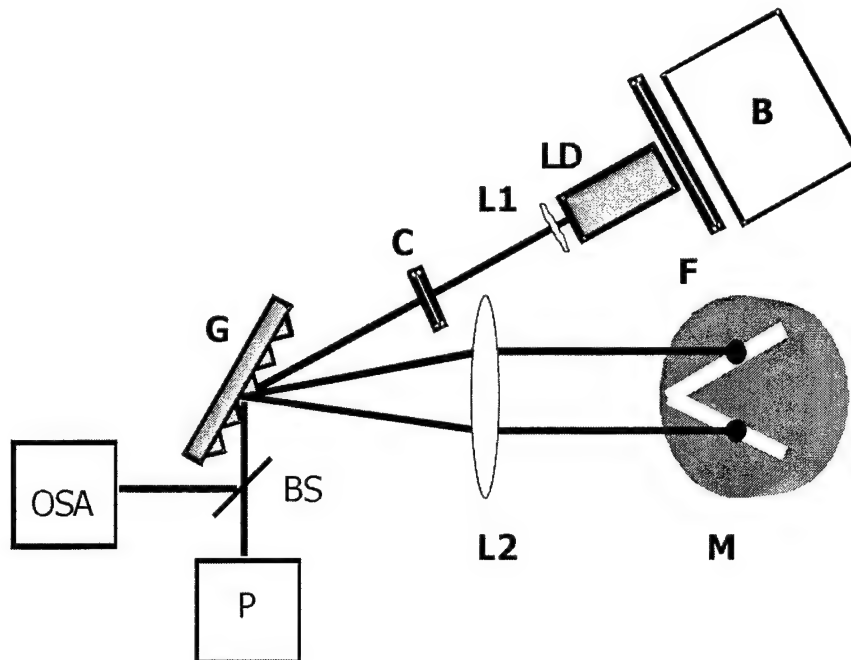


Fig. 1: Schematic setup of the FTECAL: The optical emission of the laserdiode (LD) is collimated with lens L1 and directed to a grating (G) via a chopper wheel (Ch). The spectrally dispersed light is focused onto the end mirror (M) by a lens (L2). Two spectral modes are selected by the V-striped endmirror. The difference frequency is tuned by a vertical translation of M. The NIR emission of the laser is split by a beamsplitter (BS) and monitored by a powermeter (P) and an optical spectrum analyzer (OSA) simultaneously. The THz emission out of the back facet of the laser is measured with a bolometer (B). A small bandwidth bandpass filter (F) can be inserted between LD and B.

Light is coupled out of the laser by utilizing the 0-order (reflection) of the grating. The optical emission is analyzed with an Optical Spectrum Analyzer (OSA) and a power meter (P). A chopper wheel (C) could also be included in the cavity

to use lock-in technique for the detection. For the measurement of electromagnetic frequencies in the THz-regime a bolometer (B) and filters (F) were used as described in section 5.

In our FWM experiments and THz emission experiments we used a ridge waveguide laser diode (Eagleyard Photonics, Type RWE-0805). The device is 750 μm long and the active region contains one single 9 nm thick InGaAsP quantum well grown on GaAs. The device is mounted on a c-mount carrier.

3. TWO-COLOR OPERATION

The laser system described above has been successfully used as a laser source in a THz-imaging system operating with continuous wave terahertz radiation¹⁹. A sketch of the imaging system is shown in figure 2. The two-color optical output is generated in the laser system described above. The emitted radiation is focussed onto a photoconducting antenna in which the difference frequency in the THz regime is generated by photomixing. The THz radiation is focussed onto a sample, the transmitted signal is detected by a bolometer. By scanning the sample in two directions, a THz transmission picture is obtained.

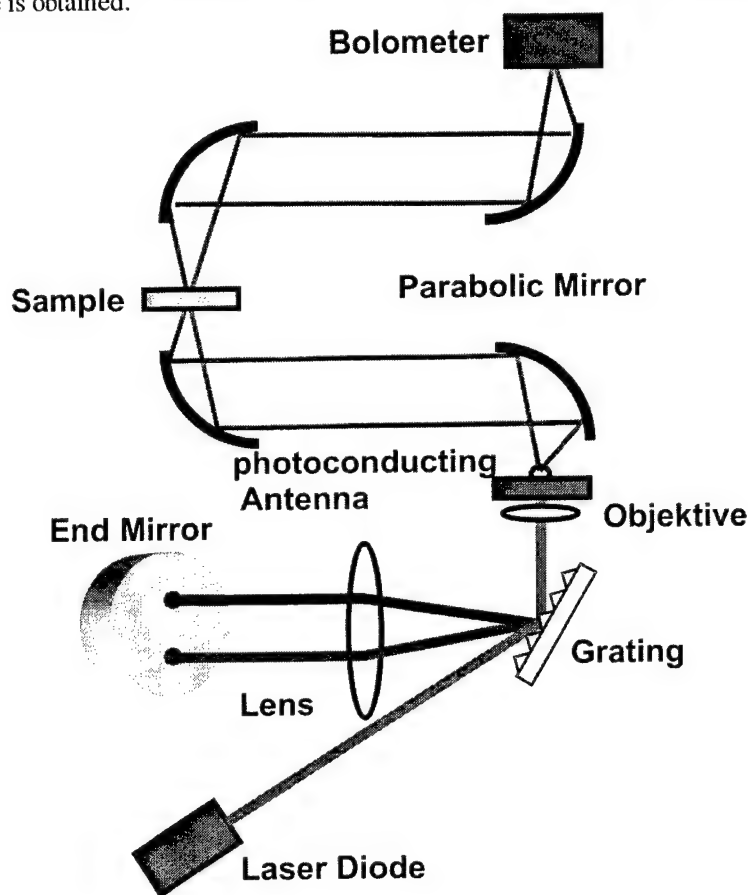


Fig. 2: Setup for THz imaging using Two-color laser

For this application, the synchronicity of the two laser modes is crucial. Typical emission spectra of the TCL are shown in Figure 3. However, from these time-integrated spectra it cannot be concluded, that the laser is emitting on both lines simultaneously. The simultaneity of the emission in this configuration was recently demonstrated by upconverting the emission of the laser in a nonlinear LiTaO₃-crystal⁶. Upconversion of the spectra plotted in Figure 3 yields the spectra plotted in figure 4. Assuming that the laser is emitting the frequencies f_1 and f_2 , we find the second harmonics $2f_0$ and $2f_1$ and, in addition, the mixing product f_0+f_1 when the two frequencies are emitted at least partially synchronously. So

the appearance of a contribution at f_0+f_1 in the spectrum is an unambiguous proof that both colors are at least temporarily simultaneously emitted.

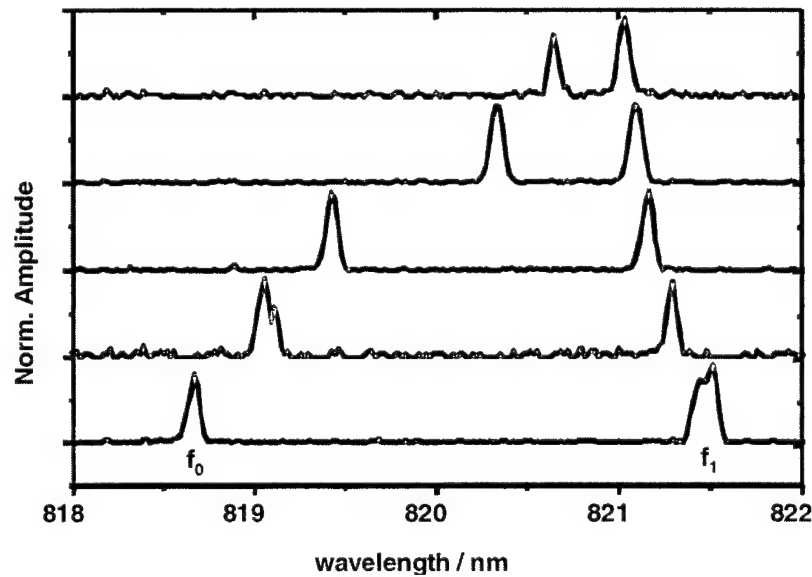


Fig. 3: Two color emission

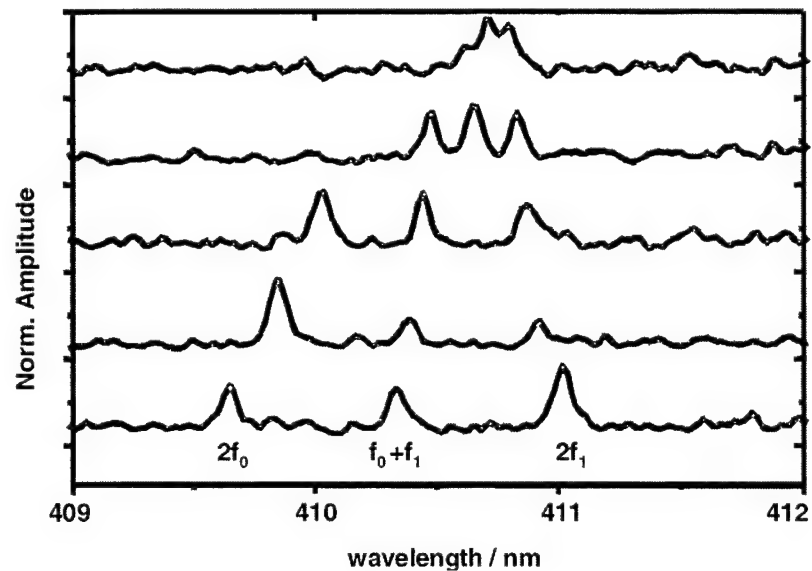


Fig. 4: Graph of the frequency doubled spectrum of the FTECAL emission spectrum shown in Fig. 3, together with the upconversion mixing-product.

Theoretical modeling of this laser system provided a rich temporal dynamics²⁰ and showed that perfect synchronization of the two modes is not easy to achieve. Since synchronous operation is crucial for applications as the THz imaging system shown above, it is important to monitor the synchronicity of the modes to achieve optimum performance of the system. But the above described concept using mixing in a nonlinear crystal introduces too much complexity and an easier approach to control the two-color emission is highly desirable.

4. FOUR-WAVE-MIXING

As mentioned in section 1, semiconductor lasers are highly nonlinear media themselves. Nondegenerate four-wave mixing experiments with two different wavelengths injected into a semiconductor laser amplifier were extensively investigated in the literature (see e.g. Refs. ^{10,11}). Synchronous operation of the FTECAL on two colors is similar to this approach and accordingly FWM sidebands can be expected, too, when the two modes are synchronous. We inspected the emission spectra of our TCL. Emission spectra recorded with high sensitivity and 50 pm resolution are plotted in Figure 5. Side modes due to FWM are clearly visible in the optical spectrum and so prove the synchronicity of the two colors. Further, we find that FWM is not limited to a well selected central wavelength in the gain spectrum. As shown in Figure 5, the occurrence of sidebands does not critically depend on the positions of the two modes within the gain spectrum.

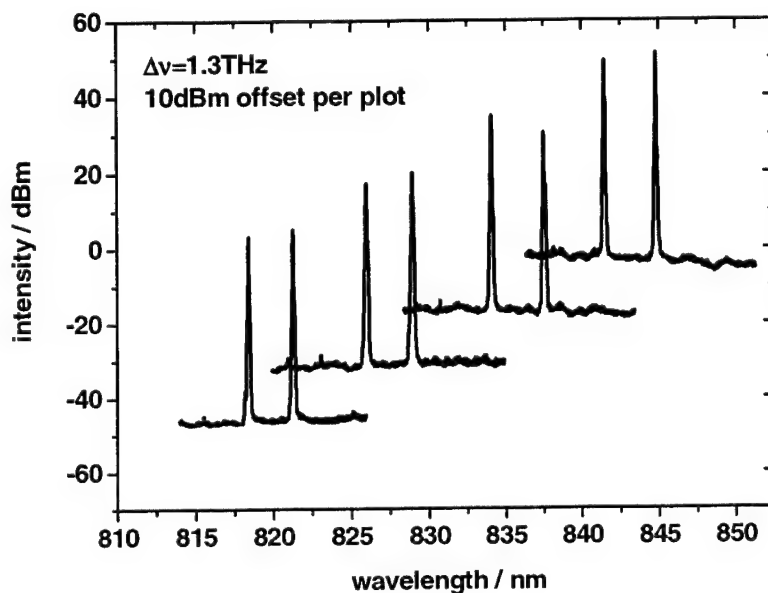


Fig. 5: FWM spectra for different central frequencies

We further investigated our system for different difference frequencies. Emission spectra for difference frequencies between 0.37 THz and 2.51 THz are shown in Figure 6. Four-wave mixing sidebands are detectable on the high-energy side of the two modes over the entire range. In all cases the high energy FWM sideband $2\omega_1 - \omega_2$ is stronger than the low energy sideband at the frequency $2\omega_2 - \omega_1$. We attribute this to the higher differential gain at the high energy side of the gain spectrum. The FWM intensity decreases with increasing difference frequency. This is a consequence of the modulation response of the laser diode which obviously drops at frequencies above 2 THz.

Four-wave mixing sidebands at even higher difference frequencies could be achieved by modelocking the semiconductor laser. For that purpose, the laser diode current is modulated synchronously to the roundtrip time in the external cavity. As shown in Figure 7, FWM with difference frequencies up to 4.2 THz could be achieved with this scheme. This value is as high as the record value by nondegenerate FWM experiments reported in ¹⁷.

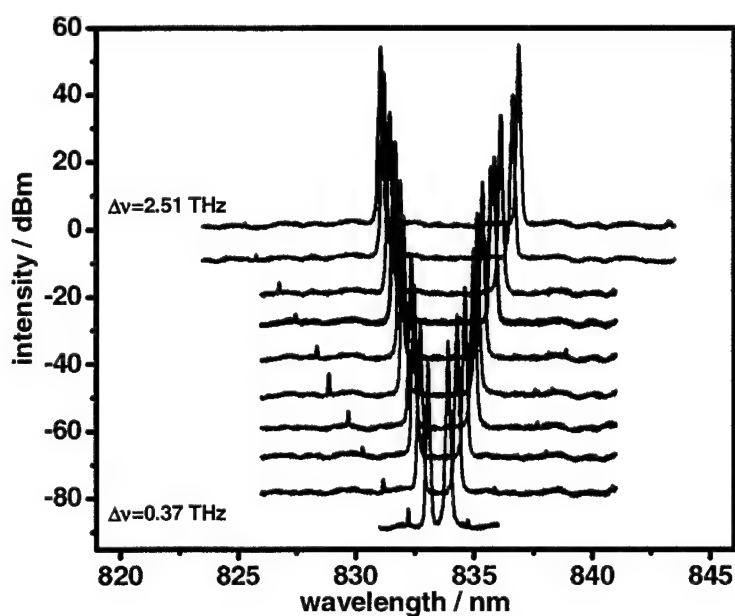


Fig. 6: The FWM signal for a range of difference frequencies with the laser operated in cw-mode is shown in this plot. An offset of 10 dBm is added to each curve.

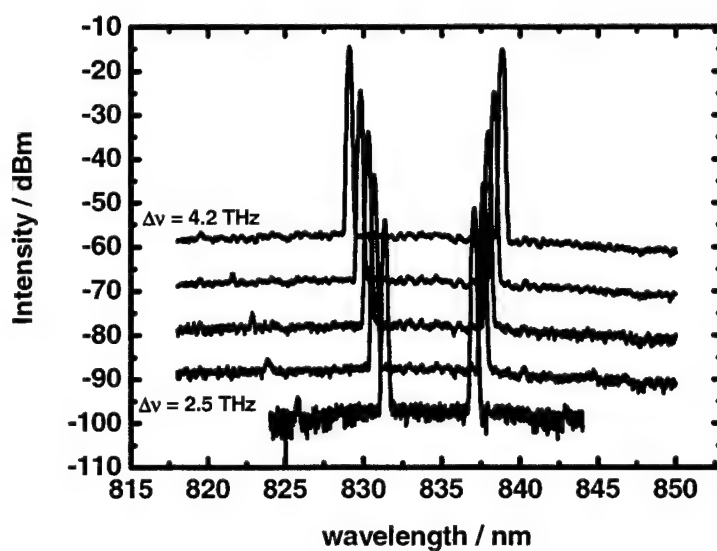


Fig. 7: The FWM signal for a range of difference frequencies with the laser operated in modelocked-mode is shown in this plot. An offset of 10 dBm is added to each curve.

5. DIRECT THZ EMISSION

The presence of the FWM-sidebands indicates that there is an oscillation of the carrier plasma in the semiconductor with the difference frequency of the two colors. Since the third order non-linear effect FWM is so easy to observe in the optical spectrum, we expect that difference frequency generation as a second-order nonlinear process might be strong enough to support direct THz emission out of the semiconductor laser itself.

To check this prediction experimentally²¹, we analyzed the output of the laser diode with a bolometer positioned behind the facet opposite to the external cavity (Fig. 1). The experiments were performed at room temperature. We used a magnetically enhanced InSb bolometer (QMC Instruments QFI/2BI) cooled to 4K. This instrument is sensitive for THz radiation in a broad detection window between 0.3 and 1.5 THz.

Since we used a standard semiconductor laser without modifications for the THz emission we had to take particular care to isolate the signal due to direct THz emission from background noise.

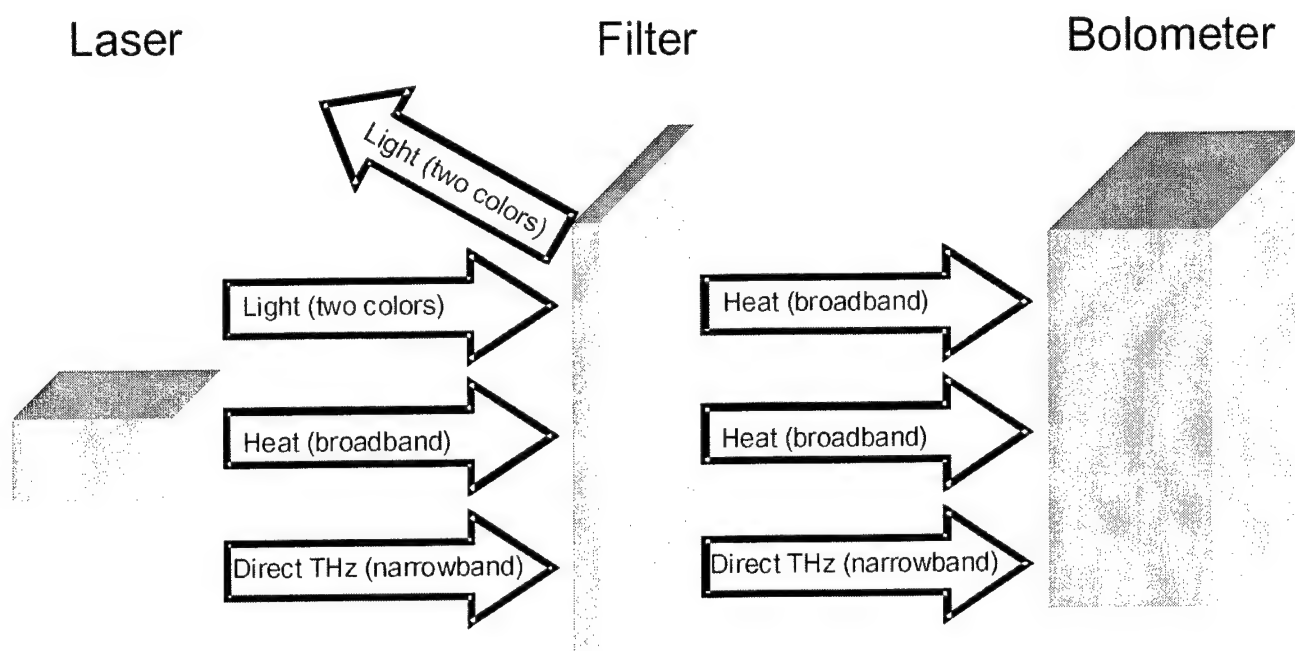


Fig. 8: Detection of direct emission and background

All measurements are performed using a lock-in amplifier connected to the bolometer output. A chopper wheel is positioned in the external laser cavity. So the bolometer is only sensitive for signals modulated with the chopper frequency. Then the principal contributions to the bolometer signal are: the narrow-bandwidth THz signal we expect from our laser in two-color mode, residual light hitting the bolometer, heat radiation caused by light absorbed in the entrance window of the bolometer, and heat radiation originating directly from the laser. In contrast to the desired THz signal the heat radiation has a broadband spectrum. To illustrate this, Fig. 8 shows the signals detected with the bolometer in our experiment.

Since the heat radiation due to light absorbed by the bolometer entrance window and the residual light hitting the detector lead to an undesired background bolometer signal two orders of magnitude higher than the direct THz emission signal, we introduced a filter composed of several layers of paper between laser and bolometer. While THz-emission in the detection window is passing the filter only with an attenuation of approximately 50%, optical light is attenuated by more than 99.97%²². Most of the light is scattered and reflected from the filter. But again, the light absorbed in the filter is leading to a modulated background of broadband heat radiation and we observed that the background of

modulated heat radiation is proportional to the optical output power of the laser. This is accounted for by normalizing all measured bolometer signal by the optical power for each measurement. To reduce the influence from further heat sources to the measured signal, the normalized bolometer signal for the operation on one color only²³ is subtracted from the two-color signal to extract the specific contribution due to two-color operation. This normalized difference frequency is measured for a range of difference frequencies as shown in Fig. 9 (a).

To discriminate whether the direct THz emission really coincides with the difference frequency of the laser, we inserted a THz bandpass filter²⁴ with sharp transmission characteristics between filter and bolometer. The transmission characteristics of the filter is shown in Fig. 9 (b) as a dotted line together with the normalized THz emission with the filter inserted. The THz emission is only observed when the chosen difference frequency of the laser is in the detection window defined by the filter. Since we measure the THz signal as a function of the difference frequency, this unambiguously confirms, that the THz emission is centered at the difference frequency of the laser.

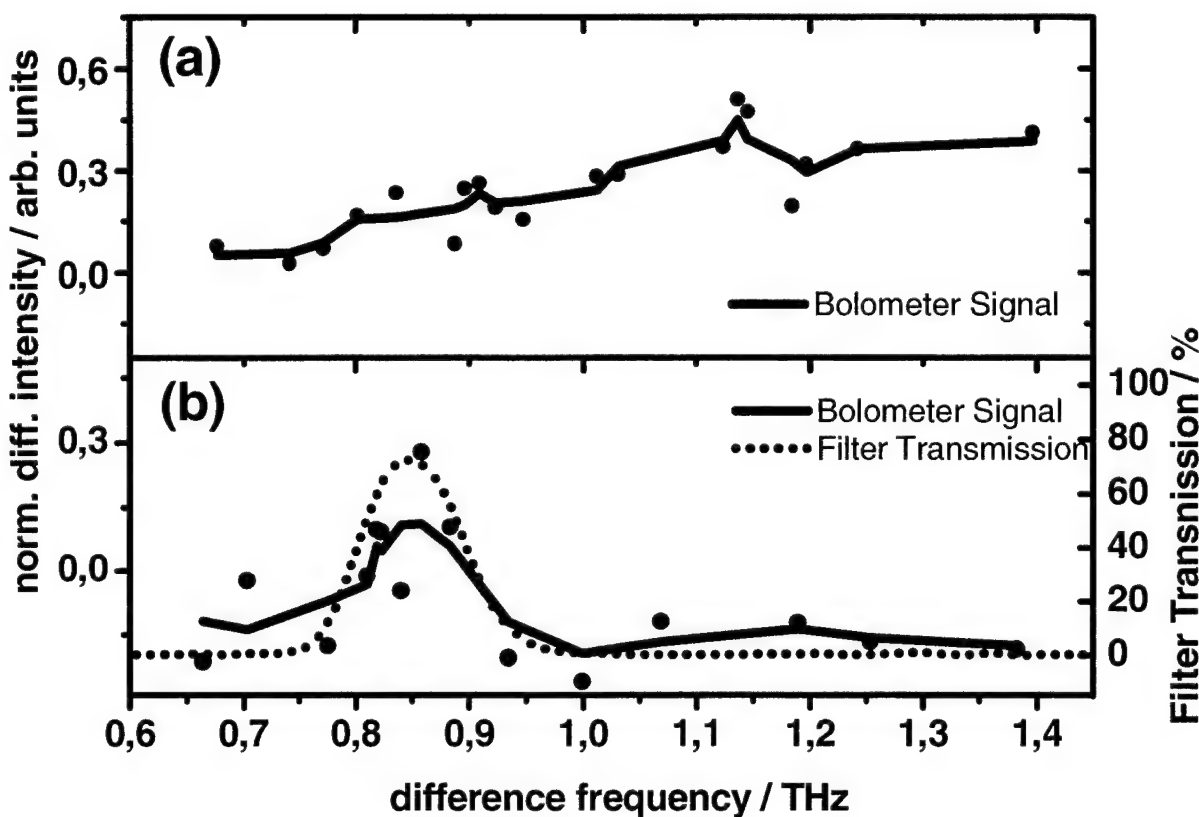


Fig. 9: Direct THz Emission

The detected THz-power in these experiments is low (in the sub - nW range), but it can be increased to application relevant levels by using laser diodes with higher intensity and by modifying the geometry of the laser diode to provide wave guiding not only for the optical but also for the THz wave. The outcoupling efficiency of the laser can also be increased by adding an antenna structure to the laser diode to provide impedance matching between semiconductor and surrounding air.

6. CONCLUSIONS

In conclusion, we have analyzed FWM sidebands in two color semiconductor lasers. Four-wave mixing sidebands were observed for difference frequencies up to 2.5 THz in CW operation. Sideband spacings up to 4.2 THz were achieved with a modelocked two color laser. Moreover, we could show that the corresponding difference frequency in the THz-regime is emitted directly out of the laser diode. With a few improvements our system promises to become a simple tunable coherent THz source at room temperature competitive to more complex approaches as, e.g. difference frequency generation of two stabilized lasers by photomixing²⁵ or THz-quantum cascade lasers²⁶.

7. ACKNOWLEDGEMENT

We thank E. Bründermann, N.C. Gerhardt and M. Breede for the stimulating discussions; S.W.Koch, M. Kira, M. Matus and J.V. Moloney for the theoretical support, S. Saito and K.Sakai for lots of information and clues in the generation of THz-radiation; M. Koch and T. Kleine-Ostmann for the cooperation in the THz-Imaging system.

8. REFERENCES

1. M.G. Littmann, *Opt. Lett.* **3** (1978) 138.
2. T. W. Hänsch, *Appl. Opt.*, **11** (1972) 895.
3. P. Chen et.al., *Appl. Phys. Lett.*, **71**, 1601 (1997)
4. K.A. McIntosh, E.R. Brown, K.B. Nichols, O.B. McMahon, W.F. DiNatale and T.M. Lyszczarz, *Appl. Phys. Lett.*, **67**, 3844 (1995)
5. E.R. Brown, K.A. McIntosh, F. W. Smith, K. B. Nichols, M. J. Nichols, M. J. Manfra, C. L. Dennis and J. P. Dennis, *Appl. Phys. Lett.*, **64**, 3311 (1994)
6. M. Breede, S. Hoffmann, J. Zimmermann, J. Struckmeier, M. Hofmann, T. Kleine-Ostmann, P. Knobloch, M. Koch, J.P. Meyn, M. Matus, S.W. Koch, and J.V. Moloney, *Opt. Commun.* **207**, 261 (2002).
7. M. Tani, P. Gu, M. Hyodo, K. Sakai, and T. Hidaka, *Optical and Quantum Electron.* **32**, 503 (2000) and references therein.
8. M.S. Stix, M.P. Kesler, and E.P. Ippen, *Appl. Phys. Lett.* **48**, 1722 (1986).
9. K.L. Hall, G. Lenz, A.M. Darwish, and E.P. Ippen, *Opt. Commun.* **111**, 589 (1994).
10. S. Murata, A. Tomita, J. Shimizu, M. Kitamura, and A. Suzuki, *Appl. Phys. Lett.* **58**, 1458 (1991).
11. A. D'Ottavi, A. Mecozzi, S. Scotti, F. Cara Romeo, F. Martelli, P. Spano, R. Dall'Ara, J. Eckner, and G. Guekos, *Appl. Phys. Lett.* **67**, 2753 (1995).
12. K. Henneberger, F. Herzel, S.W. Koch, R. Binder, A.E. Paul, and D. Scott, *Phys. Rev. A* **45**, 1853 (1992);
13. M. P. Kesler, C.S. Harder, and E.E. Latta, *Appl. Phys. Lett.* **59**, 2775 (1991).
14. M. Hofmann, S.D. Brorson, J. Mörk, and A. Mecozzi, *Appl. Phys. Lett.* **68**, 3236 (1996).
15. A. Haug, *Semicond. Sci. Technol.* **7**, 373 (1992).
16. J. Moerk, J. Mark, and C.P. Seltzer, *Appl. Phys. Lett.* **64**, 2206 (1994).
17. A. D'Ottavi, E. Iannone, A. Mecozzi, S. Scotti, P. Spano, R. Dall'Ara, G. Guekos, and J. Eckner, *Appl. Phys. Lett.* **65**, 2633 (1994).
18. S.Gee, G. A. Alphonse, J.C. Connolly, C. Barty, and P.J. Delfyett, *IEEE J. Quantum. Electron.*, **36**, 1035 (2002).
19. T. Kleine-Ostmann, P. Knobloch, M. Koch, S. Hoffmann, M. Breede, M. Hofmann, G. Hein, K. Pierz, M. Sperling, and K. Donhuijsen, *Electronics Letters* **37**, 1461-1463 (2001).
20. M. Matus et. al. submitted to *IEEE J. Quantum. Electron.*
21. S. Hoffmann, M. Hofmann, E. Bründermann, M. Havenith, M. Matus, J.V. Moloney, A. Moskalenko, M. Kira, S.W. Koch, S. Saito and K. Sakai submitted to *Appl. Phys. Lett.*
22. Pulsed THz radiation generated by ultrashort pulses in photoconducting antennas was used for the transmission measurements.
23. All other parameters (e.g. optical power, temperature, current) are kept constant.
24. Filter type: BPF 851 by QMC Instruments
25. K.J. Siebert, H. Quast, R. Leonhardt, T. Löffler, M. Thomson, T. Bauer, H.G. Roskos and S. Czasch, *Appl. Phys. Lett.*, **80**, 3003 (2001).

26. R. Köhler, A. Tredicucci, F. Beltram, H. E. Beere, E.H. Linfield, A.G. Davies, and D.A. Richie, Opt. Lett. **28**, 810 (2003).

Modeling, Simulating, and Characterizing Performance in Optical Switching Networks

J. Nathan Kutz^a, B. Small^b, W. Lu^b, and K. Bergman^b

^aDepartment of Applied Mathematics, University of Washington, Box 352420, Seattle, 98195-2420, USA

^bDepartment of Electrical Engineering, Columbia University, 1312 S. W. Mudd, 500 W. 120th Street, New York, NY 10027 USA

ABSTRACT

Photonic packet switching for all-optical networks is a rapidly developing technology since it circumvents many of the traditional bottlenecks created by the use of electronics. All-optical networking has application to both long-haul communications systems and high-performance computing systems. In each case, all-optical technologies are responsible for the routing, switching and logic decisions of the network. Characterizing the performance of a network includes calculating the latency and scalability of a given architecture assuming ideal behavior of its physical components. However, the physical layer ultimately determines the feasibility of data transmission. Thus accurately calculating the accumulated bit-error-rate (BER) is fundamental to evaluating the optical network as a whole, regardless of the network architecture. A new simulation technique, which is based upon experimental findings, is introduced which characterizes the physical layer performance of a given network architecture known as the Data Vortex. Experiments show that almost all the physical layer penalty is generated by the nodes which are used for switching and routing. Specifically, at each node data packets are amplified by a semiconductor optical amplifier so that coupling and routing losses are compensated. In this process, the data packets receive a noise penalty which results primarily from amplified spontaneous emission and in small part from spectral broadening. By using a phenomenological approach to modeling the noise penalties, the performance of the network nodes can be characterized. The modeling allows for a comprehensive understanding of the network and is a highly efficient computational tool for evaluating performance when compared to conventional time-domain techniques.

Keywords: all-optical network, photonic switching

1. INTRODUCTION

Basic technologies for realizing all-optical networking configurations are rapidly being developed. The impetus for such efforts results from the ultra-high speeds possible when circumventing traditional electronic technologies and their inherent latency. All-optical networking has application to both long-haul communications systems and high-performance computing systems. In each case, all-optical technologies are responsible for the routing, switching and logic decisions of the network. Characterizing the performance of a network is a two-fold process. First the network architecture is itself evaluated. This includes calculating the latency and scalability of a given network assuming ideal behavior of its physical components. The second characterization involves the integration of the physical layer and its performance penalties. The physical layer ultimately determines the feasibility of data transmission. Thus accurately calculating the Q-factor and accumulated bit-error-rate (BER) is fundamental to evaluating the optical network as a whole, regardless of the network architecture. This aim of this paper is to characterize the physical layer performance of a given network architecture known as the *Data Vortex*.¹⁻³ To this end, simulation and modeling are used to calculate the cumulative Q and BER so that a comprehensive evaluation of the data vortex network is achieved.

Physical layer modeling of all-optical networks is an important aspect of characterizing a given network topology. In many respects, a physical layer performance evaluation is independent of the methods used to evaluate a

Further author information: (Send correspondence to J. N. Kutz)

J.N.Kutz: E-mail: kutz@amath.washington.edu, Telephone: 1 206 685 3029

given network architecture. Thus, once a viable network is chosen for in-depth study due to its high scalability and low latency properties, physical layer modeling provides insight into the true behavior of the network due to physical limitations and penalties of the all-optical devices and components responsible for processing the flow of data. Extensive evaluations of optical networks have been performed for long-haul transmission systems for which large penalties are incurred in optical fibers. These penalties are primarily generated from chromatic dispersion, self-phase and cross-phase modulation, polarization mode dispersion, amplified spontaneous emission (ASE) noise, and periodic attenuation and amplification. Numerical modeling is heavily utilized to quantify the penalties arising from these physical effects and characterize the performance of national and international long-haul systems. In contrast, we are considering the all-optical network for high-performance computing applications.¹⁻³ Thus the length of optical fibers used is limited to meters and the propagation penalties in the fiber are virtually non-existent. For this case, almost all the physical layer penalty is generated by the network nodes which are used for switching and routing. The modeling here will focus on the penalties incurred from the node only and will ignore any propagation penalties since they are orders of magnitude smaller over the meters of fiber used for propagating around the network.

2. MODELING THE NETWORK

The model to be described here is based upon the experimental performance of the node structures responsible for switching and routing. The bulk of the transmission penalty comes from the semiconductor optical amplifier (SOA) which offsets the attenuation of the propagating optical signal from the routing, switching and logic operations. Thus the node penalties will accumulate as data is propagated through the Data Vortex structure. This section will outline how the network architecture is dealt with along with calculating the transmission penalties.

2.1. Network Architecture

Although the analysis here does not provide a performance evaluation of the network architecture, it is the architecture which ultimately determines the mean-time a data stream propagates in the network and accumulates penalties from the node structures. The Data Vortex architecture¹⁻³ is free of optical buffers and enables simple routing logic for large scale, low latency packet switch fabrics.¹ The hierarchical system employs a synchronous timing and distributed control signaling to avoid packet contention and to achieve simplicity, scalability, and high throughput.

The Data Vortex architecture, illustrated in Fig. 1, is characterized by the parameters A and H which represent the corresponding nodes lying along the "angle" and "height" dimension respectively of the cylindrical geometry. The number of cylinders, C , in the architecture scales as $C = \log_2(H) + 1$. The data packets are processed synchronously within the switch fabric in a parallel manner. Within each time slot, every packet progresses forward by one angle ($a = a + 1$) by either staying on the same cylinder (solid line, $c = c$) or by moving toward an inner cylinder (dashed line, $c = c + 1$).

Data packets are inserted at nodes on the outermost cylinder ($c = 0$) and are propagated to the output ports on the innermost cylinder ($c = C - 1$). The packets are self-routed and proceed along the "angle" dimension until the appropriate output port has been reached. Along with the data payload, which is a collection of wavelength division multiplexed (WDM) channels each operating at 10 gigabits per second, there are two separate channels for header information and timing frame which are modulated at a slower rate. A testbed for studying the traffic control and WDM routing in the Data Vortex is presented in Ref.³ The Data Vortex network is shown to have low-latency, high scalability, and requires no optical buffering: ideal qualities for all-optical networking applications.

2.2. Node Structure and Penalties

The nodes of the optical Data Vortex serve the purpose of routing input data streams towards their output destinations. Each routing node (see Fig 2) consists of two SOAs. The packet comes from either North or West port. A small amount of optical power ($\approx 10\%$) is tapped off for the header reading and routing purpose. Optical delay lines need to be inserted in the packet path to compensate for the delay associated with tap off and routing processor. Since the header and frame information is WDM encoded, simple, fixed band-pass filters are used

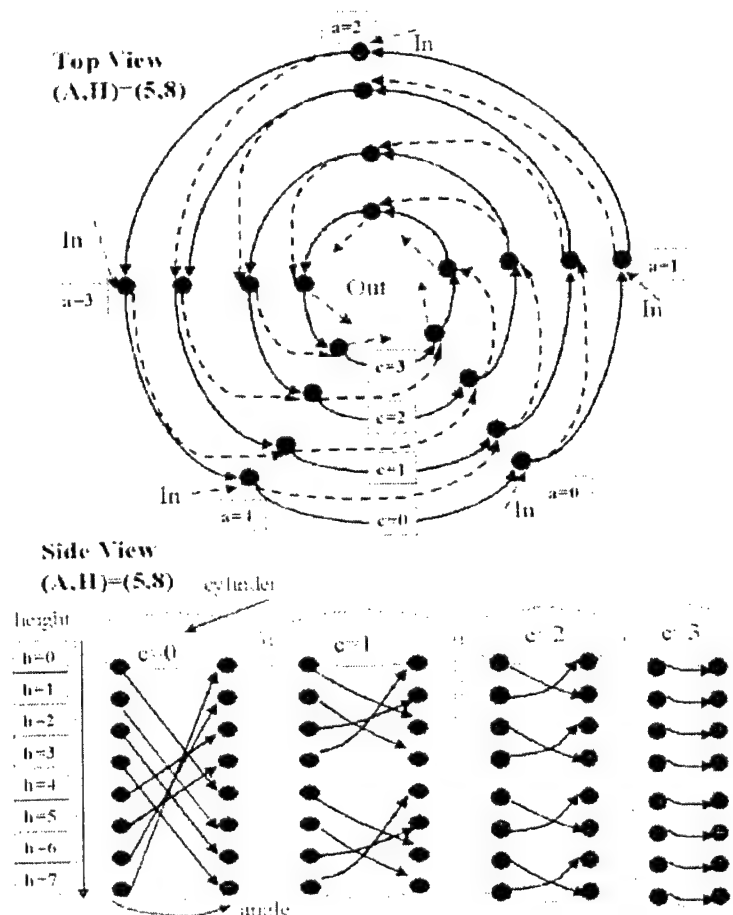


Figure 1. Data Vortex topology with the parameters $(A, H) = (5, 4)$ and nodes labeled by (a, c, h) where $0 < a < A$, $0 \leq c < C$ and $0 \leq h < H$. The routing tours are seen from the top and side. Information is input on the outermost cylinder ($c = 0$) and is propagated to the appropriate output port on the innermost cylinder ($c = C - 1$).

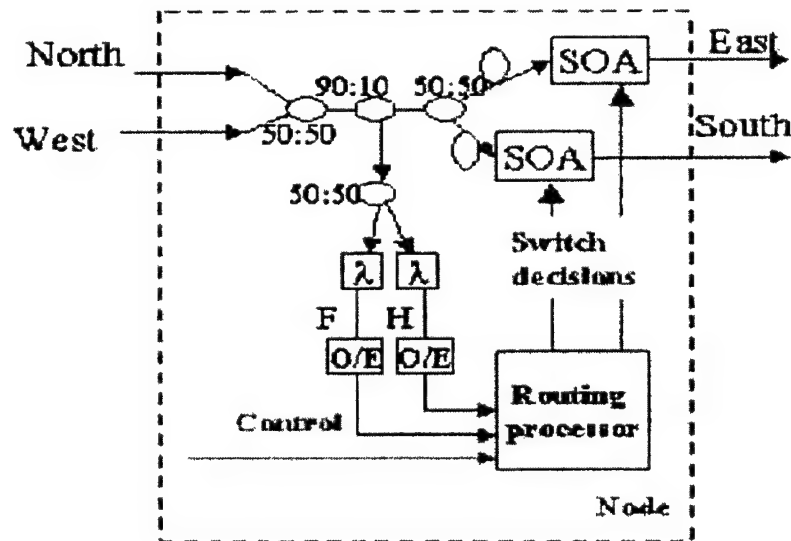
to retrieve the bit-per-wavelength encoded routing bits. All the nodes located on one cylinder would have the same setup of decoding filters since they all process the same specific bit wavelength. The routing information runs at rather low packet rates. Therefore it can be converted into electronics by low cost detectors prior to the routing processor. The routing processor also needs to examine the control signal, which may be transmitted through either optical links or electronic lines depending on the implementation choice. The routing processor thus output switching decision that control SOAs on or off. The truth table for the routing processor is simple and is included in Fig. 2.

2.3. The SOA

Ordinarily utilized as amplifiers in long-haul lightwave systems, SOAs are also extraordinarily useful as the active switching elements within numerous lightwave systems.⁴ Because high extinction ratios and reasonable switching times can be achieved, SOAs are often utilized in switching architectures.^{5,6}

Fabricated from III-V semiconductor materials, contemporary SOAs utilize the electronic transition from the conduction band to the valence band as a radiation source. Population inversion is achieved through the introduction of a pump current. This current can be modulated, effectively turning the amplifier on and off. Ideally, the switching speed is only limited by the carrier lifetimes. Moreover, the electronic transitions generally occur only when stimulated by incoming radiation, thereby functioning as an amplifying device.

However, as in all laser systems, unwanted spontaneous emissions can occur. These emissions may be amplified as they propagate through the length of the devices, and are often termed amplified spontaneous emissions (ASE).⁷



F	H	C	Switch-E	Switch-S
0	0	0/1	0	0
1	0	0	1	0
1	1	0	1	0
1	1	1	0	1

Figure 2. Routing node structure and its associated truth table. Note that the bulk of transmission penalties are incurred from amplification through the SOAs.

Fortunately though, this contribution is predictable and well-behaved: the noise figure is additive, accumulating in the spectrum as an increase in the noise floor.⁸ Other minor nonlinear effect also occur due to homogeneous and inhomogeneous nonuniformities. All of these nonidealities together contribute to signal degradation in lightwave systems that rely on SOAs as amplifying or as switching elements.

3. PHYSICAL LAYER NETWORK MODELING

Transmission penalties leading to degradation of the Q-factor and BER are due primarily to the accumulated ASE noise from the SOAs. Experiments show the SOAs have two primary noise contributions. The first is the expected white-noise (broadband) contribution from ASE of the amplification process. The second is a colored noise component of a Lorentzian shape centered around the individual WDM channels. By incorporating these two dominant physical effects into our penalty model, a rough guide to the propagation efficiency can be numerically calculated. More sophisticated modeling requires the calculation of errors due to other physical effects such as time-domain cross-talk. For the present, only noise penalties will be considered as they are the dominant contributions to transmission degradation.

The physical layer node penalties can be incorporated into a network model by considering a data stream packet propagating from its input node to its output node. Each data packet will traverse a statistically deter-

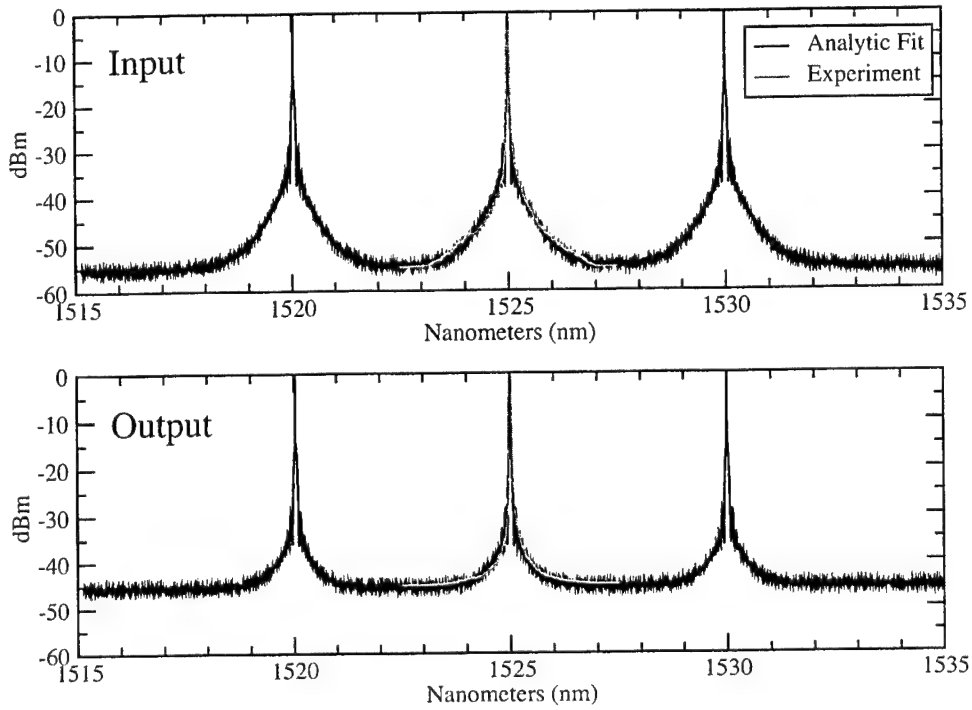


Figure 3. Analytic fit, using A , B , and C , to the experimentally measured noise penalties due to white-noise and a Lorentzian contribution. The analytic data corresponds to (1) where 500 realizations have been averaged over. Three channels have been used in the experimental fit with a channel spacing large enough so that no noticeable overlap occurs between neighboring Lorentzian contributions.

mined number of nodes which is determined by the size of the Data Vortex.^{1,2} The model simply requires the mean number of nodes traversed and the associated variance in number of nodes. The algorithm developed for the network model then considers a large number of WDM data stream realizations each of which propagates through the network a statistically determined number of nodes. The eye diagrams, along with the calculation of Q-factor and BER, are then determined from the total set of data streams propagated through the network at the various WDM channels. Thus the model relies on accurate qualitative and quantitative accounting for the penalties incurred at each node.

To consider modeling the noise penalties, a single WDM channel is first considered. The pulse stream profile is assumed to be given by $u(t, z)$ where in optics coordinates z gives the distance propagated and t gives the temporal profile of a 10 gigabit per second, pseudo-random, non-return-to-zero (NRZ) data stream. Fourier transforming gives the spectral representation $\hat{u}(\omega, z)$ of the data. The white-noise and Lorentzian noise penalties are then incorporated into transmission via

$$\hat{u}(\omega, t)_+ = \hat{u}(\omega, t)_- + A(\eta_1 + i\eta_2) + B(\eta_3 + i\eta_4) \frac{1}{1 + C(\omega - \omega_0)^2} \quad (1)$$

where $\hat{u}(\omega, t)_\pm$ represents a given spectral component before ($-$) and after ($+$) an SOA. Here the η_i are normally distributed random variables with mean zero and unit variance, the parameter A determines the strength of the white noise, and B and C measure the strength and width associated with the Lorentzian noise contribution which is centered at the WDM frequency ω_0 .

The parameters A , B , and C are determined from fitting to experimental measurements. Figure 3 depicts a fit of these three parameters to an experimentally measured input and output relationship of an SOA. In order

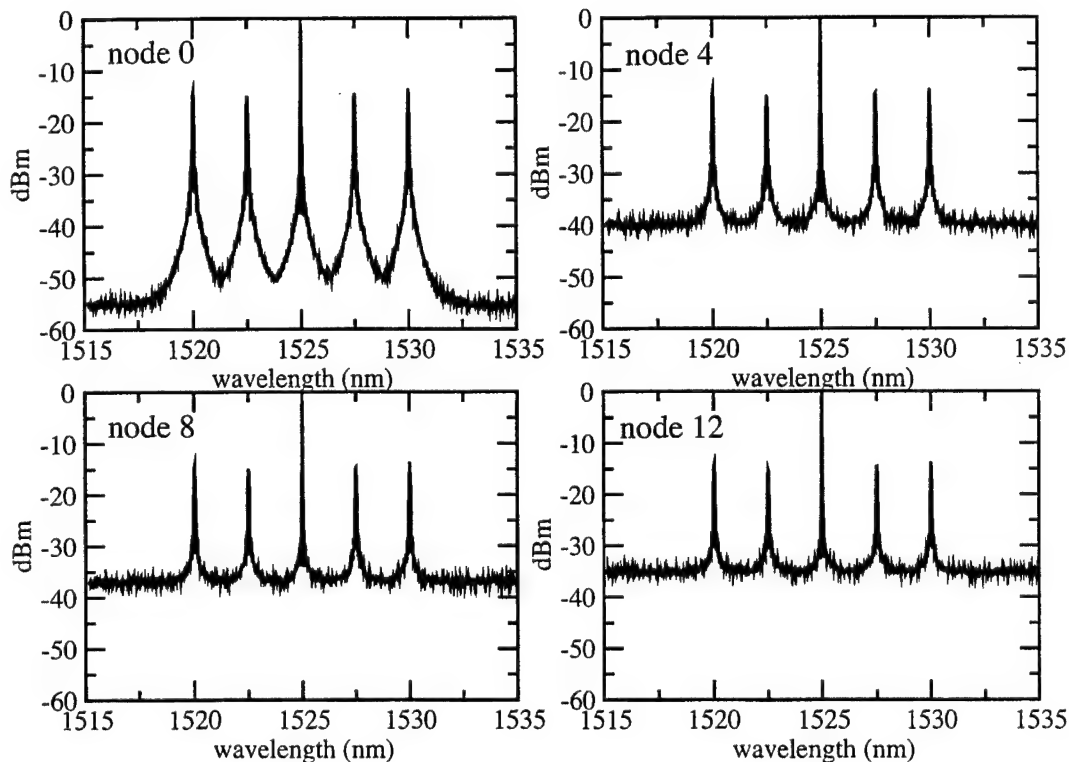


Figure 4. Evolution of the spectrum of five WDM channels spaced 2 nm apart over 12 SOAs (nodes). The transmission penalties at each node are derived from (1) with the parameters fit to Fig. 3. Two hundred realizations have been simulated.

for the analytic curve to be smooth as depicted in the figure, 2000 realizations of (1) were averaged together to produce the otherwise noisy fit. Further, the output was normalized to the same peak power as the input in order to preserve the correct signal-to-noise ratio.

To illustrate the penalties incurred from cascading SOAs together, we consider the penalty as modeled by (1) with the parameters A , B , and C fit according to Fig. 3. As a specific example, five WDM channels are transmitted, each with a 32-bit random data sequence. It is assumed that the only penalties are those generated by the SOA, i.e. perfect splicing and transmission through a fiber from one SOA to another SOA are assumed. Figure 4 shows the spectral evolution of the WDM channels over 12 cascaded SOAs. The simulation is performed using the penalties (1) with the parameters A , B , and C derived from the fit in Fig. 3. It is clear from this figure that the noise shelf is increased significantly with the number of SOAs (nodes) traversed.

A more formal way of calculating the transmission penalty is to construct the eye diagrams associated with Fig. 4. The statistics of the ones and zeros then allow for the calculation of the Q-factor and BER of transmission.⁸ Figure 5 illustrates how the eye diagram closes as the number of SOAs is cascaded. Depending on network performance restrictions, the number of nodes physically possible for transmission can be calculated. For instance, the cascaded SOAs considered here allow for the transmission over five nodes with a BER below 10^{-9} . A BER rate of 10^{-12} can be maintained through four nodes and over eight nodes can be cascaded with a BER below 10^{-6} . Figure 6 depicts the drop in Q-factor and increase in bit-error as the data propagates through the cascaded SOA chain.

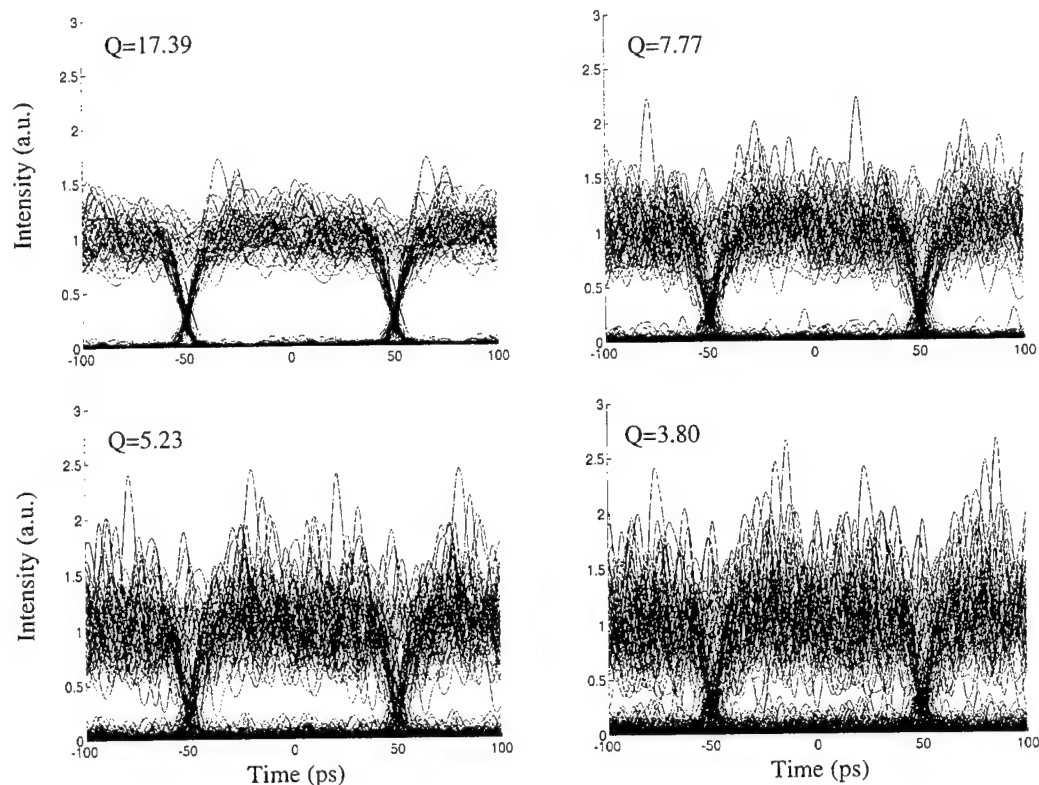


Figure 5. Evolution of the eye diagram for five WDM channels spaced 2 nm apart over 12 cascaded SOAs (nodes). The transmission penalties at each node are derived from (1) with the parameters fit to Fig. 3. Note that this is only a single realization of the data and noise.

4. CONCLUSIONS AND DISCUSSION

Network characterization can be accomplished through a qualitative modeling process which captures the primary physical sources of penalties. Experiments show that the growth of ASE noise is one of the primary sources for generating propagation penalties. The ASE noise has both a white-noise component and Lorentzian noise contribution. By fitting, the BER and Q-factor can be calculated for a data stream propagating through a given network.

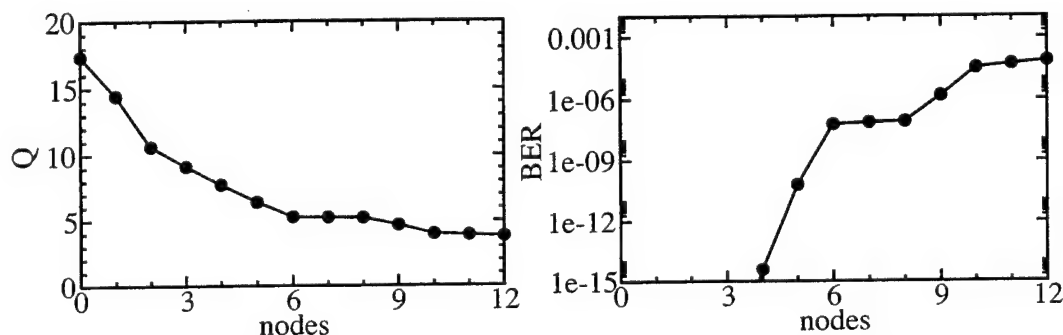


Figure 6. Q factor and BER for five WDM channels spaced 2 nm apart over 12 cascaded SOAs (nodes). The transmission penalties at each node are derived from (1) with the parameters fit to Fig. 3. Note that this is only a single realization of the data and noise.

Additional penalties can also be considered. Of most significant is the gain recovery and saturation dynamics in the SOA. These effects along with four-wave mixing penalties can all be considered within this qualitative model. Thus a realistic modeling tool can be created which significantly reduces the computational time of evaluating the optical switching network.

Additionally, the modeling results suggest how to improve network performance by illustrating the significant level of penalties incurred by various physical effects. Recently, several improvements have been made to greatly improve the number of hops achievable in the optical network architecture.

REFERENCES

1. C. Reed, "Multiple level minimum logic network," U. S. Patent 5996020, Nov. 30, 1999.
2. Q. Yang, K. Bergman, F. G. Johnson, and G. D. Hughes, "WDM packet routing for high capacity data networks," *J. Light. Tech.* **19**, 1420-1426 (2001).
3. Q. Yang and K. Bergman, "Traffic Control and WDM Routing in the Data Vortex Packet Switch," *IEEE Pho. Tech. Lett.* **14**, 236-238 (2002).
4. N.A. Olsson, "Lightwave Systems with Optical Amplifiers," *J. Lightwave Technol.* **7**, 1071-1082 (1989).
5. Evankow, Thompson, "Photonic switching modules designed with laser diode amplifiers," *IEEE J. Select. Areas Commun.* **6**, 1087-1095 (1988).
6. Papadimitriou, Papazoglou, Pomportsis, "Optical Switching: Switch Fabrics, Techniques, and Architectures," *J. Lightwave Technol.* **21**, 384-405 (2003).
7. M. J. Adams, J. V. Collins, and I. D. Henning, "Analysis of semiconductor laser optical amplifiers," *Inst. Elec. Eng. Proc. Part J.* **132**, 58-63 (1985).
8. G. P. Agrawal, *Fiber-Optic Communication Systems*, 2nd Ed., (Wiley, New York, 1997).

Ultra-small footprint silica-on-silicon WDM based on Holographic Bragg Reflectors

D. Iazikov, C. Greiner*, and T. W. Mossberg

LightSmyth Technologies, Inc., 860 W. Park St., Ste 250, Eugene, OR 97041

ABSTRACT

We report on wavelength-division-multiplexing (WDM) based on lithographically-fabricated slab-waveguide-contained planar holographic Bragg reflectors (HBRs). Partial HBR diffractive contour writing and contour displacement are successfully demonstrated to enable precise bandpass engineering of multiplexer transfer functions and make possible compact-footprint devices based on hologram overlay. Four and eight channel multiplexers with channel spacings of ~ 50 and ~ 100 GHz, improved sidelobe suppression and flat-top passbands are demonstrated. When a second-order apodization effect, comprising effective waveguide refractive index variation with written contour fraction, and the impact of hologram overlap on the hologram reflective amplitude are included in the simulation, excellent agreement between predicted and observed spectral passband profiles is obtained. With demonstrated simulation capability, the ability to fabricate general desired passband profiles becomes tractable.

Keywords: Integrated Optics, Photonic Crystals, Fiber Optics, Distributed Bragg Reflector, Planar Lightwave Circuit, Photonic Bandgap, Apodization, Lithography, Silica-on-Silicon, Holography, Wavelength Division Multiplexing.

1. INTRODUCTION

Planar holographic Bragg reflectors (HBRs) [1-4] are two-dimensional lithographically-scribed volume holograms contained within a planar slab waveguide. In the slab waveguide, optical signals are free to propagate without constraints in two dimensions – a geometry that enables 2D Bragg structures to provide powerful spectral and spatial holographic functions. A single HBR can simultaneously spatially image an input signal to an output port (or from one point within an integrated photonic circuit to another) while at the same time providing spectral filtering of the signal. Unlike fiber and channel-waveguide gratings, where separation of the counter-propagating input and output signals typically requires additional elements, planar HBRs provide spatially distinct and thus easily accessed outputs. HBRs constitute the building blocks of unique integrated photonic circuits that operate entirely without wire-analog channel waveguides, being based on HBR-mediated signal transport where signals freely overlap as they are imaged from active element to active element. The HBR approach marries the power of free-space optics and volume holography with a fully integrated environment. The powerful volume-holographic function provided by HBR structures provides, via computer-generated complex-shaped diffractive contours, fully-optimized spatial mapping of an arbitrary complex input field wavefront to an output field mode tailored to match the chosen output means. This broad *in-plane* spatial wavefront transformation capability contrasts with previously discussed 2D distributed Bragg reflectors intended for *out-of-plane* applications such as laser feedback and outcoupling [5-7] and free-space to slab-waveguide beam coupling [8,9]. HBR spatial wavefront transformation, due to its holographic nature, is generally more powerful than that provided by simple conic section DBRs [10], whose focusing power degrades when input and output optics deviate from the point source limit.

* e-mail: cgreiner@lightsmyth.com; phone: (541)-431-0026; fax: (541)-284-5607

Recently [3], we demonstrated that photolithographic fabrication of HBRs in silica-on-silicon allows the highly accurate placement of constituent diffractive contours as evidenced by fabrication of fully coherent centimeter-scale planar holographic structures. Additionally, a robust and fabrication-friendly method to control the reflective amplitude of diffractive element contours via partial writing of the latter was presented [4]. Together, precise feature placement and partial contour writing provide control over the phase and amplitude of diffractive elements on an individual line basis. This is enabling to 2D Bragg reflector design for two reasons. *Spectrally*, it offers a pathway to unprecedented precision and flexibility in the design of HBR transfer functions via the tailoring of the diffractive element arrangement. *Spatially*, partial contour writing and displacement allows the overlay of several planar holograms on the same substrate – thus making it possible to design high-resolution (de)multiplexing devices for multi-wavelength signals with very compact footprint. In the present paper, we demonstrate, for the first time, the application of these concepts to the spectral (bandpass) and spatial engineering of multiplexing devices based on holographic Bragg reflectors. We furthermore identify an important coupling between partial contour writing and the effective waveguide index that must be accounted for when using amplitude apodization based on fractional contour writing.

2. RESULTS AND DISCUSSION

Figure 1 is a schematic of a simple four-channel HBR device fabricated to explore the general potential of the HBR approach for spectral multiplexing and to characterize basic device performance. The top view of Figure 1a illustrates the device operational principle. An input signal is coupled into the planar device via an input channel waveguide (IN) from whose endpoint the input beam expands into a slab region. Through interaction with the multiplexer sections in the slab region the input signal is spectrally filtered and spatially directed to one of the four wavelength-specific outputs. The HBR multiplexer consists of four stacked, 5-mm-long holographic Bragg gratings whose vacuum resonance wavelengths, λ_1 through λ_4 , increase with distance from the input port in increments of ~ 0.35 nm, corresponding to about 50 GHz. The precise multiplexer channel spacings and center wavelengths depend on the core thickness and

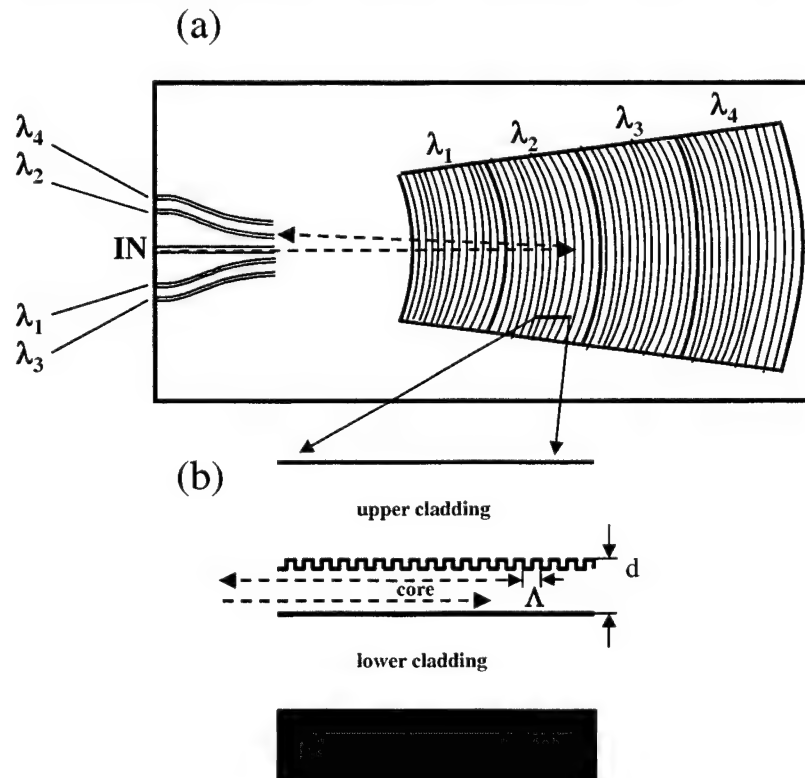


Figure 1. Four-channel wavelength-division multiplexer based on planar holographic Bragg reflectors. 1a, Cross-sectional view; 1b, Top view.

refractive index of the specific waveguide in which the device is lithographically realized. Consistent with our objective to first examine basic device operation and performance no apodization was applied to the grating sections in this initial design. The multiplexer's wavelength-to-output port assignment follows the layout shown in Figure 1a. The HBR diffractive contours, represented in Figure 1a by thin solid lines, can be designed individually to match the back-diffracted input field to the output port. For the devices described here, the diffractive contours were not optimized to provide maximal output coupling. In these early stage devices, contours are configured as circular arcs concentric about the point midway between the end of the input channel waveguide and the beginning of the corresponding output channel waveguide. Fully optimized holographic contours will improve input-output coupling by more effectively coupling to the mode of the output waveguide.

Figure 1b is a partial device cross section. The multiplexers discussed here are based on silica-on-silicon slab waveguides that consist of a central silica core with thickness $d = 2\ \mu\text{m}$ or $4\ \mu\text{m}$ and bilateral $15\text{-}\mu\text{m}$ -thick cladding layers. For all the devices, the waveguide core exhibits a $+0.8\%$ index contrast with respect to its claddings. Also depicted at the upper core-cladding interface are cross-sections of representative lithographically-scribed grating diffractive contours. The diffractive contours, with depth $\sim 450\ \text{nm}$, for all devices, consist of trenches etched into the core and filled with cladding material. All gratings operate in first order with a contour spacing, Λ , of about $500\ \text{nm}$, i.e. one half of the in-medium wavelength of resonant light. In the schematic cross-section of Figure 1b light enters the device from the left side and is coherently backscattered to the left by the diffractive elements.

The multiplexer's input-output channel waveguide manifold (Figure 1a) exhibits an interchannel spacing of $30\ \mu\text{m}$ at the input side to the HBR slab region. Here, all waveguides have a design width of $12.7\ \mu\text{m}$, adiabatically increased from $6\ \mu\text{m}$ at the die edge via a $1\ \text{mm}$ -long taper. The output waveguides are angled with respect to the input waveguide. The angle of a given output waveguide is given by $0.1575^\circ/(30\ \mu\text{m}) \times l$, where l is the distance (in microns) between the end point of the input guide and the given output guide. The radius of the HBR's diffractive arc closest to the center of curvature is $3.5\ \text{mm}$. All devices discussed here occupy die areas of only about $1.7\ \text{cm}^2$ including access channel waveguides. All multiplexers reported on in this paper were fabricated from a laser-written reticle employing a DUV optical stepper and standard etching, deposition, and annealing processes.

Figure 2a depicts the designed spectral transfer functions of the four multiplexer channels (band pass profiles). The transfer functions are calculated from the spatial design data using an extensive Fresnel-Huygens diffraction calculation and assuming weak overall device reflectivity. The relatively high adjacent side lobes in the design spectral transfer functions are a direct consequence of the fact that this initial multiplexer design employs grating structures that are unapodized. The adjacent sidelobe suppression seen is essentially dictated by Fourier transform theory. For comparison, the transform-limited sidelobe suppression provided by a uniform grating is shown by the two bars on the right side of Figure 2a. In multiplexer designs discussed below, grating apodization is demonstrated to significantly improve sidelobe suppression. Figure 2b shows the measured spectral transfer functions of the four multiplexer output channels of the fabricated multiplexer for TE-polarized input light. The device was realized in a slab waveguide with $d = 4\ \mu\text{m}$. The results shown in Figure 2b comprise the first successful implementation of a photolithographically-written HBR-based device for spectral multiplexing and indicates an excellent coherent realization of the design structure. The average insertion loss, measured through coupled fibers, was found to be about $-3\ \text{dB}$ which implies a HBR insertion loss of about $-2\ \text{dB}$. Measured channel bandpass functions are broadened and adjacent sidelobes are stronger than seen in the simulation – as expected at the achieved reflectivity levels. The longer wavelength channels ($\lambda_2 - \lambda_4$) are seen to exhibit passband shapes slightly different from the λ_1 -channel. These are believed to arise from input depletion caused by signal travel through spatially preceding and partially resonant grating structures. Grating designs incorporating appropriate apodization acting to remove sidelobes of preceding gratings that are spectrally coincident with primary bandpasses of subsequent ones are expected to provide mitigation of this effect.

An inherent advantage of the HBR technology is its capability to address multiplexing needs in a broad range of networks, including those based on hyperfine, dense, and coarse WDM. Specifically, the approach provides for both the ability to implement almost arbitrary channel spacings (both uniform and non-uniform) as well as channel passbands that may be tailored to a very high degree. To demonstrate these properties we have fabricated an eight-channel HBR multiplexer with a channel spacing about twice that of the previous device (i.e., about $100\ \text{GHz}$) wherein channel transfer functions are designed to exhibit

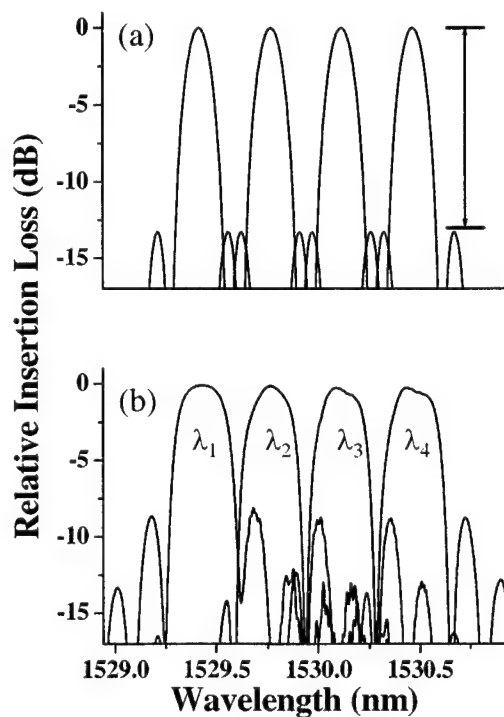


Figure 2. Four-channel multiplexer spectral throughput. 2a, simulated throughput; 2b, Measured response (for TE-polarization). The arrow indicates the transform-limited sidelobe suppression provided by a uniform (unapodized) 1D grating.

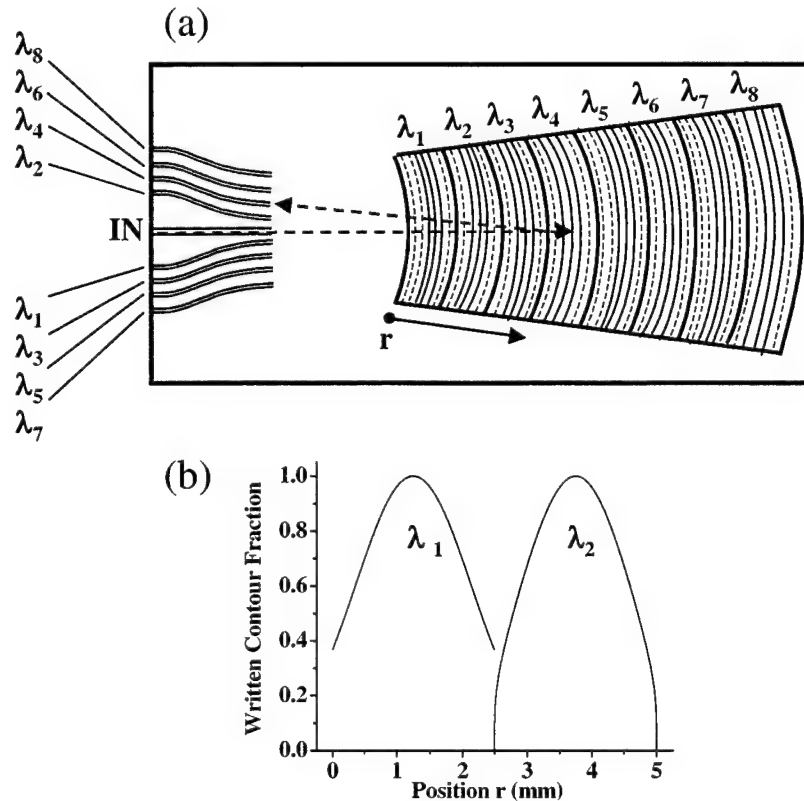


Figure 3. 3a, Schematic top view of eight-channel HBR-based multiplexer; 3b, Apodization profiles for odd (λ_1) and even (λ_2) multiplexer channels.

improved adjacent sidelobe suppression compared to Figure 2. The device layout is shown in Figure 3a.

The multiplexer consists of eight stacked, 2.5-mm-long apodized holographic Bragg gratings. Again, the individual channel-gratings were spatially ordered so that their resonance wavelength increased with distance from the device input side. For the 8-channel multiplexer of Figure 3a, $d = 4 \mu\text{m}$. Engineering of the multiplexer's bandpass employs the fact that the grating spectral transfer function is determined by the detailed contour spacing and relative reflective amplitude of the diffractive contours as a function of position along the input direction. Specifically, in the limit of weak device reflectivity, the transfer function is proportional to the spatial Fourier transform of the amplitude distribution of diffracted light along that direction [1]. In the devices of concern here, diffractive contour amplitude and phase apodization is achieved via partial contour writing and positional displacements, respectively [4]. Two different, amplitude-only adpodization profiles, shown in Figure 3b, and based on the partial-fill method were employed in the device of Figure 3a. All gratings with an even (odd) channel number are designed with the apodization function used for the λ_1 - (λ_2) channel. All parameters of the access waveguide manifold of the device shown in Figure 3a are the same as for the device of Figure 1a.

Figure 4a depicts the designed spectral transfer function of the eight multiplexer channels. Note the improved suppression ($> 20\text{dB}$) of sidelobes immediately adjacent to the main channel passband compared to that evident in the designed bandpass of the unapodized four-channel device of Figure 2a. Figure 4b gives the measured spectral transfer function of the eight channels of the fabricated device for TE-polarized input light. Agreement between measured and designed performance is good except for the unexpectedly high side lobes on the long wavelength side of each primary passband. The device average intrinsic insertion loss (due to weak reflection) was found to be about -7 dB . The long-wavelength sidelobes in the measured multiplexer response are found to arise from a second-order apodization effect, detailed below,

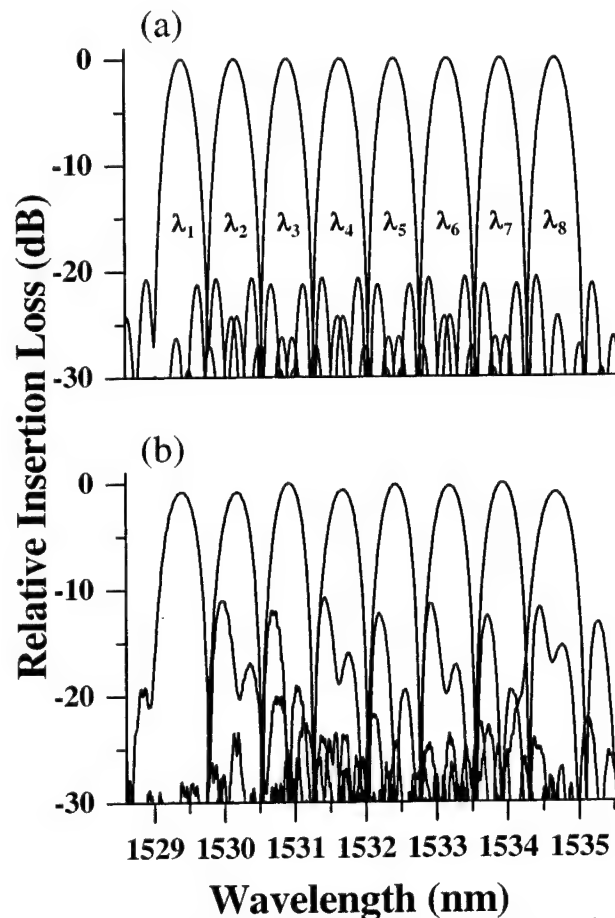


Figure 4. Eight-channel multiplexer spectral throughput (core thickness $d = 4 \mu\text{m}$). 4a, Multiplexer design spectral transfer function, simulated with constant refractive index; 4b, Measured spectral response (for TE-polarization).

that was unaccounted for in the device designs. The second-order effect comprises an effective refractive index variation inadvertently introduced by using partial contour fill to effect amplitude apodization. Note that the spectral transfer functions of the channels to the very left (λ_1) and right (λ_8) in Figure 4b are seen to exhibit slightly higher insertion losses and broader bandpasses than all other channels of the same respective apodization function. This effect was caused by a photolithographic fabrication error wherein 10% (20%) of the originally designed length of the λ_1 - (λ_8) grating was not written.

In the present multiplexer design, apodization of the reflective amplitude of HBR diffractive contours is achieved through partial contour writing [4]. Nominally continuous diffractive contours are written fractionally, with the written contour fraction determining the contour's reflective amplitude. Contour writing occurs through etching (and filling with cladding material) of trenches into the core. Variations in the written trench fraction due to amplitude apodization lead to differences in waveguide morphology that cause variations in the slab waveguide effective refractive index and consequently the Bragg resonance condition. Measurements performed on various test grating structures, each having diffractive contours of fixed written fraction, show a small and approximately linear variation of effective waveguide refractive index with written trench fraction. The fractional effective index difference between a waveguide without a grating and one with a Bragg reflector employing fully written, first-order trenches was found to be $-2 \times$

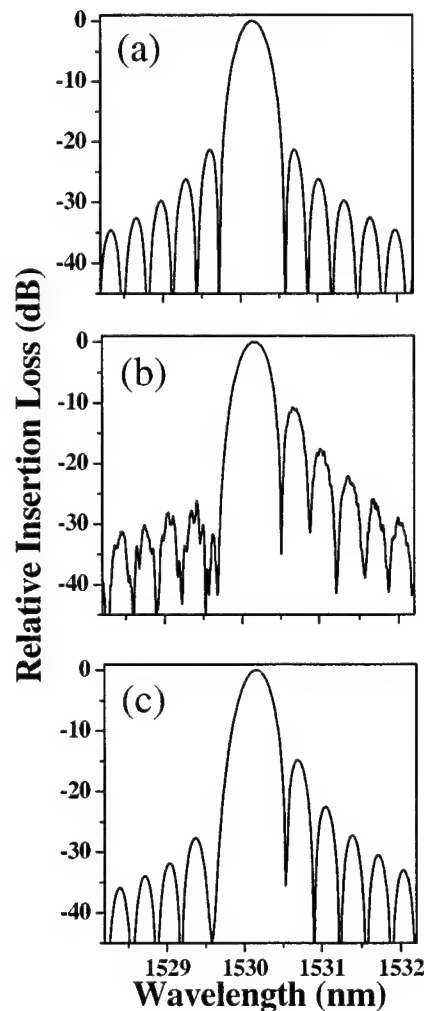


Figure 5. Detail of the passband function for the second multiplexer channel (λ_2). 5a, Simulated throughput, calculated with constant effective index; 5b, Measured throughput (for TE-polarization); 5c, Simulated throughput, calculated with account for apodization-induced effective index changes.

10^{-4} with slab waveguide core thickness $d = 4 \mu\text{m}$ and $\sim 450 \text{ nm}$ deep diffractive trenches.

In Figure 5 we explore the impact of the apodization-induced resonance shifts on the multiplexer spectral transfer function. Figure 5a is a blow up of the original design passband function for the second multiplexer channel (λ_2) calculated with constant effective slab waveguide refractive index. Figure 5b shows the detailed measured spectral response for the same channel. Figure 5c shows the passband profile simulated including the effect of measured apodization-induced effective refractive index changes. A comparison of Figures 5b and 5c shows that the simulation now clearly reproduces all features of the fabricated device. The center wavelengths of the simulations (Figure 5a and 5c) were adjusted to coincide with the measured center wavelength (Fig 5b) to facilitate comparison.

Lithographically-enabled partial writing (amplitude apodization) and displacement (phase shifts) of contours not only makes possible the precise bandpass engineering of multiplexer spectral transfer functions but also enables the overlay of planar holograms [1] on the same substrate providing for very compact footprint devices. We apply this concept to the design of a 4-channel $\sim 100 \text{ GHz}$ channel-spacing HBR-based multiplexer with designed flat-top channel passbands. Figure 6a is a top view schematic of an overlain HBR device. The device comprises apodized individual-channel HBRs that are staggered along the input beam direction but are heavily overlapping as well. Each hologram is realized with a maximum written trench fraction of 0.65 which ensures that the aggregate (summed over all holograms) written trench fraction at any given position in the multiplexer does not exceed unity significantly (< 1.1). The multiplexer is based on a $2\text{-}\mu\text{m}$ thick slab waveguide. Parameters of the input/output waveguide manifold are the same as for the device of Figure 1. Figure 6b depicts the apodization profile of the λ_1 - channel. Negative portions in the apodization function correspond to π phase shifts of the reflected field and were realized by spatially offsetting the diffractive contours of the corresponding grating sections by $\lambda/4$ spatial

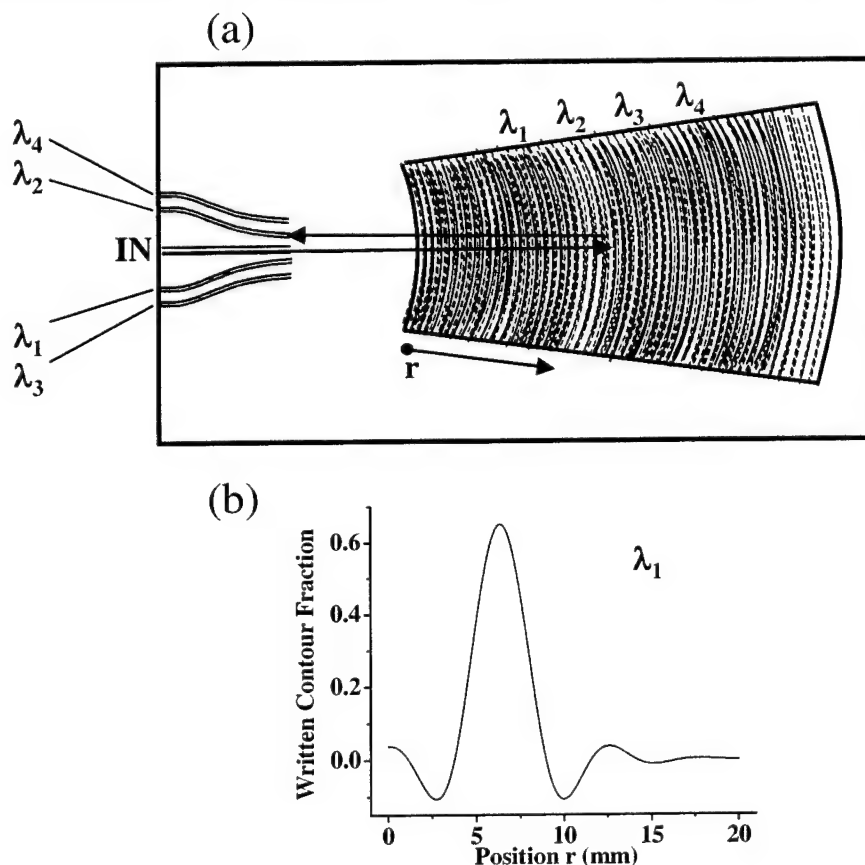


Figure 6. 6a. Schematic top view of four-channel flat-top HBR-based multiplexer based on overlain planar holograms; 6b. Apodization profile for leftmost (λ_1) multiplexer channel.

shifts with respect to the positive grating sections.

Figure 7a (7b) depicts the simulated (measured) spectral transfer functions of the various multiplexer channels for TE-polarized input light. The measured passbands clearly show the designed flat passband and channel spacing. The multiplexer's adjacent channel isolation exceeds -22 dB. This is excellent for a first iteration design. The absolute multiplexer insertion loss through coupled fibers was about -6 dB implying a -5 dB device intrinsic loss, primarily caused by low device reflection. Discrepancies between measured and designed channel transfer functions such as the long-wavelength shoulder of the measurement arise principally from two factors. First, apodization-induced effective index changes are not compensated for in the present multiplexer design. Second, in designing the device, the various individual-channel HBRs were overlaid without taking detailed precaution to avoid overlap of diffractive contours belonging to different holograms. Due to the present constant-etch-depth multiplexer layout, the overall device reflective strength at a given position is not a linear sum of all contributing diffractive contours at that location. Rather, portions of a given hologram that coincide with diffractive contours of a different grating exhibit a reflective amplitude that is reduced from its design value. Consequently, the actual apodization of a planar hologram is altered from the original design value through two position-dependent effects, i.e. (1) variations in slab waveguide effective refractive index and (2) variations in expected reflective amplitude. Both effects must be accounted for to correctly predict the bandpass function of the fabricated multiplexers. Consideration of these same effects at the design stage allows for precisely crafted bandpass engineering.

Figure 8 explores the impact of the above described phenomena on the spectral transfer function of the λ_1 multiplexer channel. Figure 8a is a blow up of the original design passband function calculated with constant effective index and without account for the reduction of reflective amplitude caused by hologram overlap. Figure 8b shows the detailed measured TE-polarized spectral response for the same channel.

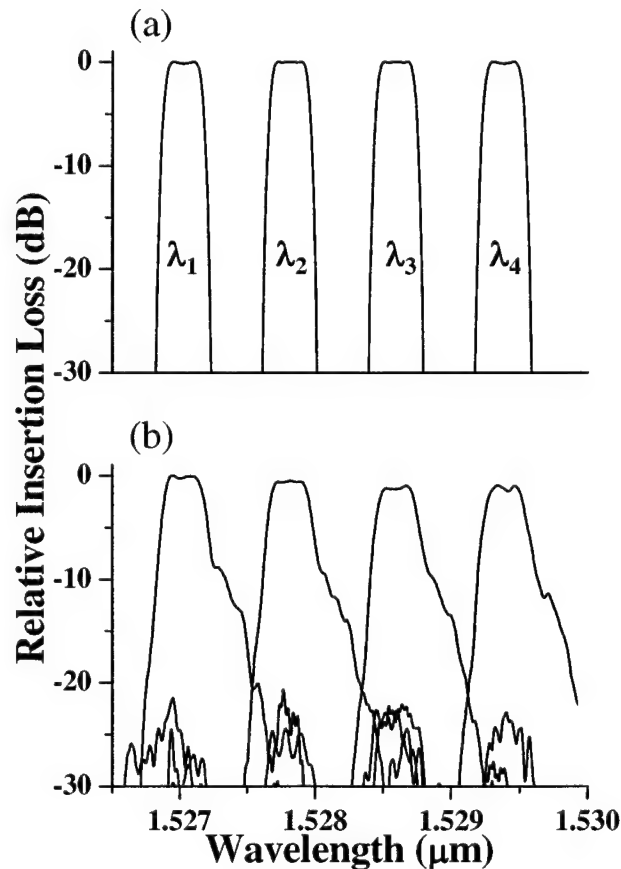


Figure 7. 7a, Multiplexer spectral transfer function simulated with constant effective index; 7b, Measured multiplexer spectral transfer function (for TE-polarization).

Figure 8c shows the passband profile simulated with both the spatially varying effective refractive index and reflective amplitude changes accounted for as described below.

The apodization and overlap effects lead to a position-dependent effective waveguide refractive index which we model as

$$n_{eff}(r) = n_o (1 - 6 \times 10^{-4} (1 - R(r))),$$

where $R(r)$ is the unetched (no written trenches) fraction of slab waveguide at each position, r , within the device and n_o is the effective index of the slab waveguide in the absence the HBR contours. $R(r)$ was calculated according to

$$R(r) = \prod_{i=1}^N (1 - \alpha_i \times G_i(r)),$$

where $G_i(r)$ is the written diffractive contour fraction of the i th planar grating at position r and α_i is its duty cycle. The summation runs over all HBRs written. In the present multiplexer design all gratings operate in the first grating order, thus $\alpha_i = 0.5$ for $i = 1, \dots, N$.

The reflective amplitude of the j th planar hologram as modified by grating superimposition is written as

$$A_j(r) = A'_j(r) \prod_{i=1, i \neq j}^N (1 - \alpha_i \times G_i(r)),$$

where $A'_j(r)$ is the apodization function that pertains in the absence of overlap. The sum runs over all HBRs except for the j th. As comparison of Figures 8b and 8c shows the simulation now clearly reproduces all features of the fabricated device. The simulated passbands shown in Figure 8 were adjusted to exhibit coincident center wavelengths to facilitate straight-forward profile comparison. Overall, the results shown in Figure 7 and 8 demonstrate both the feasibility of spectral passband engineering and the ability to construct devices based on overlaid HBRs.

The agreement between the simulation of Fig. 8c and the measured bandpass spectrum of Fig. 8b is quite excellent. It is apparent from this agreement that the photolithographic fabrication method employed reproduced the design set of grating elements with great precision. The multiplexers studied here were designed without consideration of the effective refractive index variation with amplitude apodization and the impact of hologram overlay on reflective amplitude. Multiplexer designs can be simply corrected for the effect of apodization-induced effective refractive index changes by scaling the separation between grating lines to keep optical path distances constant. Overlay-induced reflective amplitude reduction may be avoided by employing higher grating orders or lower peak fill fractions and implementing a design algorithm wherein spatially overlapping contour elements are displaced to avoid overlap. Alternatively, overlap effects may simply be added to the design algorithm. It should be noted that the HBR overlap multiplicity is constrained by the required reflective strength. For fixed diffractive contour index contrast and waveguide dimensional parameters the net reflective strength per unit surface area is subject to constraints. Evaluation of the details of these constraints is beyond the scope of the present work, but it appears that overlay has advantages over spatial stacking when, for example, spectral resolution necessitates structures that extend spatially beyond the device length required to obtain adequate reflectivity. In this case, overlay of spatially extended but locally weakly reflecting (low partial fill) structures can provide a pathway to high-resolution multiplexers in an overall footprint that is smaller than that necessitated by spatially separated HBR structures.

The measurements shown in this work employ TE-polarized input signals. For TM-input polarization, the grating bandpass functions were observed to shift by approximately +0.65 nm (+0.72 nm) for devices with a core thickness $d = 2 \mu\text{m}$ ($d = 4 \mu\text{m}$). Measurements of other HBR devices have indicated that polarization-dependent wavelength shifts originate from residual slab waveguide birefringence [3]. No (about 0.3 dB of) polarization-dependent loss (PDL) was measured for multiplexers implemented in the 4- μm (2- μm) thick slab waveguides. For $d = 2 \mu\text{m}$, the observed PDL is consistent with magnitudes expected to arise from access channel waveguides, either through propagation loss or fiber-to-waveguide coupling.

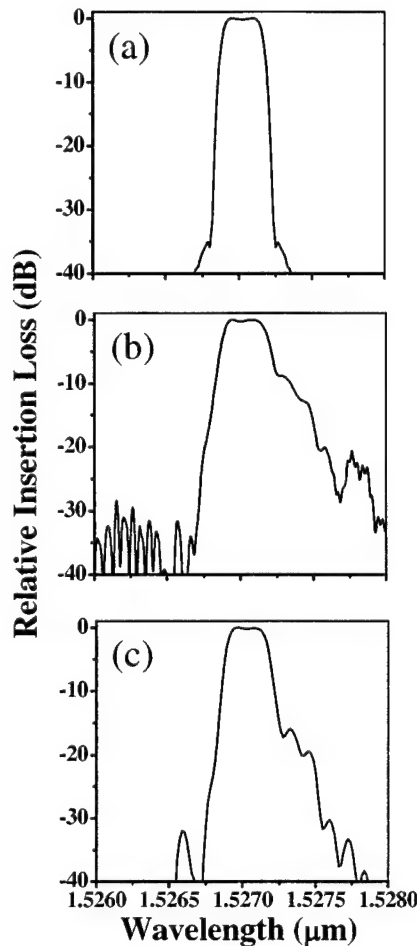


Figure 8. Blow-up of the leftmost multiplexer channel. 8a. Constant effective index simulation; 8b, Measured passband; 8c. Multiplexer throughput calculated including apodization-induced effective index variations and reflective amplitude reduction due to hologram overlay.

This was corroborated by independent measurement of the latter. In the limit of strong grating reflectivity, the reflective bandwidth ratio for TE and TM polarization, γ , is directly proportional to that of the TE and TM amplitude reflection coefficients and can be used to estimate the latter. From test results for $d = 2$, we find $\gamma = 1.018$. Based on this value we estimate the weak-reflectivity ($R \approx 10\%$) PDL inherent to the HBR to be about 0.15 dB and correspondingly less for more strongly reflecting devices as is the case with the multiplexers reported on here.

As constructed, the present HBR-based multiplexers operate at low to moderate reflectivity. Detailed calculations, to be presented elsewhere [11], indicate that achievable alterations in diffractive structure geometry and refractive-index contrast will lead to HBRs of centimeter-scale having strong reflectivity and thus low insertion loss over an aggregate bandwidth as large as several hundred nanometers, i.e. broad enough to support a 16-channel CWDM multiplexer with 13-nm-wide flat-top passbands. Furthermore, a wide range of HBR internal designs is possible providing even broader reflection bands and fully consistent with low loss at the fiber-to-die interface. It appears entirely feasible to integrate much of the functionality currently attributed to discrete-component based thin-film filters into the fully integrated environment. We note also that waveguide-sampled HBR structures [4] offer a pathway to mitigation of polarization dependent wavelength shifts.

III. CONCLUSIONS

In summary, we have demonstrated the viability of planar holographic Bragg reflectors as powerful building blocks for wavelength-division multiplexers. Our present results demonstrate, for the first time, 1) the application of the simultaneous spectral and spatial processing capability of photolithographically-written HBR structures to spectral multiplexing, 2), the successful bandpass engineering of HBR-based multiplexers via fractional writing and positional displacements of constituent diffractive contours and 3), the spatial overlay of multiple HBR structures to create high resolution multiport integrated photonic devices of compact footprint. From a more general point of view, the powerful spectral and spatial beam control inherent to the planar volume-holographic approach offers the possibility of channel-waveguide-free integrated photonic circuits wherein signal routing and processing occurs entirely through interaction with distributed diffractive structures like the HBR. Furthermore, as planar surface-relief structures, HBRs promise consistency with low-cost, mass-production, nanoreplication techniques such as hot embossing or nanoimprint lithography. In embossed/stamped formats, HBR's present an economic route to volume production of high performance optical communications components for datacom and access networks.

REFERENCES

1. T. W. Mossberg, "Planar holographic optical processing devices", *Opt. Lett.* 26, 414-416 (2001).
2. T. W. Mossberg, "Lithographic holography in planar waveguides", *SPIE Holography Newsletter* 2, 1 and 8 (2001).
3. C. Greiner, D. Iazikov, and T. W. Mossberg, "Lithographically-fabricated planar holographic Bragg reflectors", *J. Lightwave Technol.*, accepted for publication.
4. D. Iazikov, C. Greiner, and T. W. Mossberg, "Effective gray-scale in lithographically-scribed planar holographic Bragg reflectors", *Appl. Opt.*, accepted for publication.
5. T. Erdogan and D. G. Hall, "Circularly symmetric distributed feedback laser: coupled mode treatment of TE vector fields," *J. Quant. Electron.* 28, 612-623 (1992).
6. R. H. Jordan, D. G. Hall, O. King, G. Wicks, and S. Rishton, "Lasing behavior of circular grating surface emitting semiconductor lasers," *J. Opt. Soc. Am. B* 14, 449-453 (1997).
7. S. Kristjansson, N. Eriksson, A. Larsson, R. S. Penner, and M. Fallahi, "Observation of stable cylindrical modes in electrically pumped circular grating-coupled surface-emitting lasers," *Appl. Opt.* 39, 1946-1953 (2000).
8. M. Li, B. S. Luo, C. P. Grover, Y. Feng, and H. C. Liu, "Waveguide grating coupler with a tailored spectral response based on a computer-generated waveguide hologram," *Opt. Lett.* 24, 655-657 (1999).
9. J. Backlund, J. Bengtsson, C. Carlstrom, and A. Larsson, "Input waveguide grating couplers designed for a desired wavelength and polarization response," *Appl. Opt.* 41, 2818-2825 (2002).
10. C. H. Henry, R. F. Kazarinov, Y. Shani, R. C. Kistler, V. Pol, and K. J. Orlowsky, "Four-channel wavelength division multiplexers and bandpass filters based on elliptical Bragg reflectors", *J. Lightwave Technol.* 8, 748-755 (1990).
11. D. Iazikov, C. Greiner, and T. W. Mossberg, "Apodizable integrated filters for coarse WDM and FTTH-type applications", submitted to *J. Lightwave Technol.*

Anti-competition of laser modes in semiconductor lasers

Chi-Chia Huang ^a, Ching-Fuh Lin ^{a, b}, Yu-Chen Yu ^c and Yi-Xiong Lin ^c

^a Graduate Inst. of Electron-Optical Engr., National Taiwan Univ., Taiwan

^b Dept. of Electrical Engr. and Graduate Inst. of Electronics Engr., National Taiwan Univ., Taiwan

^c Industrial Technology of Research Institute, Chutung, Hsinchu, Taiwan

ABSTRACT

Anti-competition of laser modes is observed in dual-wavelength semiconductor lasers with single gain medium. Under anti-competition, the increase of intensity of one lasing mode could enhance the intensity of another mode, which is opposite to the usual mode competition. In our experiment, anti-competition can be observed for wavelength separation larger than 111 nm, and gradually disappears for wavelength separation less than 100 nm. Besides, anti-competition can also be influenced by the intensity and the wavelength position of both modes. A simple theoretical analysis shows that anti-competition is due to the physics similar to optical pumping.

Keywords: mode competition, anti-competition, two-mode semiconductor laser, nonidentical multiple quantum wells, broadband semiconductor optical amplifier.

1. INTRODUCTION

Mode competition is a well-known phenomenon in lasers. Soon after the invention of lasers, competition of laser modes has been observed and analyzed [1]. In a multi-mode laser system, different modes will in general have different gains, losses and saturation parameters, and will compete for the available population inversion in the laser. Since the total gain of a laser system is constant under fixed external pumping level, oscillation in one mode will generally reduce the gain available for another mode, and in some situations may suppress the other mode entirely [2]. Under strong coupling condition, competition can lead to bistability of the two lasing modes [3], which has been analyzed through perturbation stability analysis [2]. Competition can also lead to tristability [4, 5] and even chaotic behaviors [6, 7]. Those phenomena are found useful for optical switching, optical logic, data encryption [8, 9], and so on. Competition dynamics is also an important phenomenon in injection locking [10], mode locking [11-13], and cross gain modulation in optical amplifiers [14]. For many years, the appearance of competition has been taken for granted among laser modes, and is thought to be inevitable. However, we have discovered a behavior opposite to competition between lasing modes. That is, the increase of the oscillation intensity in one lasing mode was found to enhance the intensity of another mode. This behavior is what we called anti-competition of laser modes.

In this work, we will demonstrate that anti-competition can be observed at wavelength separation larger than 111 nm. Besides, the larger the wavelength separation is, the more apparent anti-competition can be observed. Some other influential factors of anti-competition will also be demonstrated, including the intensity and the wavelength position of the two oscillating modes. A simple theoretical analysis will be given, which shows that anti-competition is due to the physics similar to optical pumping.

2. EXPERIMENT

2.1 Broadband gain medium design

Since anti-competition can be observed only when the WS is larger than 111 nm, a broadband laser gain medium is necessary. Quantum-well (QW) engineering is a convenient, widely used approach to broaden the bandwidth of semiconductor superluminescent diodes (SLDs). This scheme includes using a single QW with simultaneous transitions of $n = 1$ and $n = 2$ states [15,16], and using nonidentical QWs [17-20]. Because the simultaneous transitions of $n = 1$ and $n = 2$ energy states in identical QWs rely strongly on the device lengths [15,16], nonidentical multiple quantum wells (MQWs) were recently been widely used for broadband purposes.

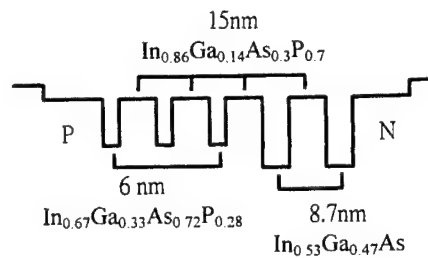


Fig. 1. Designed QW structure.

However, theoretically analysis has predicted that carrier distribution among the MQWs is nonuniform [17, 18]. Experimental evidence of this phenomenon was also indirectly obtained from the characteristics of laser diodes [19, 20]. Nonuniform carrier distribution means that each QW of the MQW structure accumulates a different number of carriers, so their corresponding emission intensities are not equal. Thus, the overlap of the individual spectrum from each type of QW, weighed by its corresponding emission intensity, does not directly result in a broadband spectrum. Investigation on the influential factors of the nonuniform carrier distribution in order to achieve broadband characteristics is thus important [19-21]. With proper design of the nonidentical QW structure, extremely broad bandwidth of the gain medium of the semiconductor lasers/amplifiers is possible [22].

The designed QW structure is shown in Fig.1. A separate confinement heterostructure (SCH) is formed in connection with the wells. The SCH layer has a thickness of 120 nm. The wells are separated by 15-nm-wide $\text{In}_{0.86}\text{Ga}_{0.14}\text{As}_{0.3}\text{P}_{0.7}$ barriers. Three 6.0-nm $\text{In}_{0.67}\text{Ga}_{0.33}\text{As}_{0.72}\text{P}_{0.28}$ QWs are placed near the n-cladding layer, and two 8.7-nm $\text{In}_{0.53}\text{Ga}_{0.47}\text{As}$ QWs are placed near the p-cladding layer. The emission energies of the 6.0-nm $\text{In}_{0.67}\text{Ga}_{0.33}\text{As}_{0.72}\text{P}_{0.28}$ QW and 8.7-nm $\text{In}_{0.53}\text{Ga}_{0.47}\text{As}$ QW were calculated using the Luttinger-Kohn method [23]. Table I shows the emission wavelengths corresponding to the calculated energy levels. $\text{In}_{0.67}\text{Ga}_{0.33}\text{As}_{0.72}\text{P}_{0.28}$ QWs and $\text{In}_{0.53}\text{Ga}_{0.47}\text{As}$ QWs have three and two quantized energy levels, respectively.

For this QW structure, emission at low injection current occurs at the wavelength corresponding to the $n = 1$ transition in the 8.7-nm $\text{In}_{0.53}\text{Ga}_{0.47}\text{As}$ QWs, which are close to the n-cladding layer. When the injection current increases, the emission spectrum is broadened owing to the simultaneous transitions of $n = 1$ and $n = 2$ states. The emission contribution from the 6.0-nm $\text{In}_{0.67}\text{Ga}_{0.33}\text{As}_{0.72}\text{P}_{0.28}$ QWs is obvious only when the injection current is very large. In our experiment, we use laser diodes (LDs) with straight waveguide. This is because, compared with the tilt or bent waveguide superluminescent diodes (SLDs), the straight-waveguide LD has lower loss and lower threshold current. This can facilitate the tuning of the modes above 1500 nm because those modes are very loss-sensitive. The length of the device was about 300 μm . No facet coatings were applied to the device. The measured emission spectrum of the LD is shown in Fig. 2. The bandwidth of the emission spectrum is limited by the Fabry-Perot resonance of the straight waveguide LD. The operation temperature and current are 22.7 $^{\circ}\text{C}$ and 146 mA, respectively. The operation current is only 3 mA larger than the threshold current of the Fabry-Perot mode, so the oscillation of the Fabry-Perot mode is still negligible.

TABLE I. Calculated Transition Wavelengths Corresponding to the Bounded Energy States of the Nonidentical MQWs of the Designed SLD

n	8.7-nm $\text{In}_{0.53}\text{Ga}_{0.47}\text{As}$ Double QW (μm)	6.0-nm $\text{In}_{0.67}\text{Ga}_{0.33}\text{As}_{0.72}\text{P}_{0.28}$ Triple QW (μm)
1	1.54	1.3
2	1.46	1.24
3	1.18	Unbounded

2.2 Experimental setup and steps

Our experimental setup is shown in Fig. 3. The external cavity is of reflected-type grating telescope configuration. Two collimators with $f = 4.5$ mm and $NA = 0.55$ are used to collimate the light beams emitted from two facets of the LD. The coupling efficiency of the collimators is about 70%. The grating is 600 lines/mm and is Au-coated. Its efficiency is about 80%. A lens with $f = 10$ cm is placed at 10 cm from both the grating and the mirror M2. The insertion of the mirror M1 and two physically separated mirrors for the mirror M2 are for the purpose of broadband tuning range. A double-slit is used for selecting the short-wavelength mode (SWM) and the long-wavelength mode (LWM), and a ND filter is put in front of each slit to control the light power of each mode at the same time.

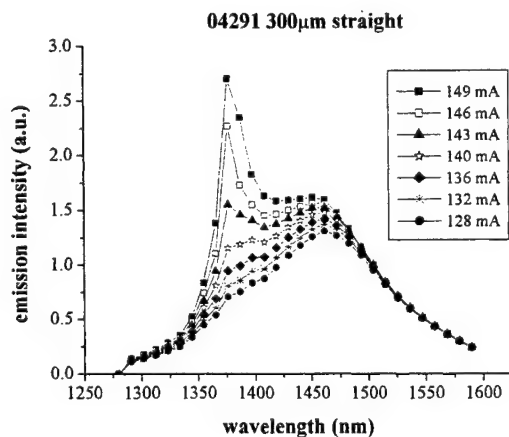


Fig. 2. Measured emission spectrum of the SLD.

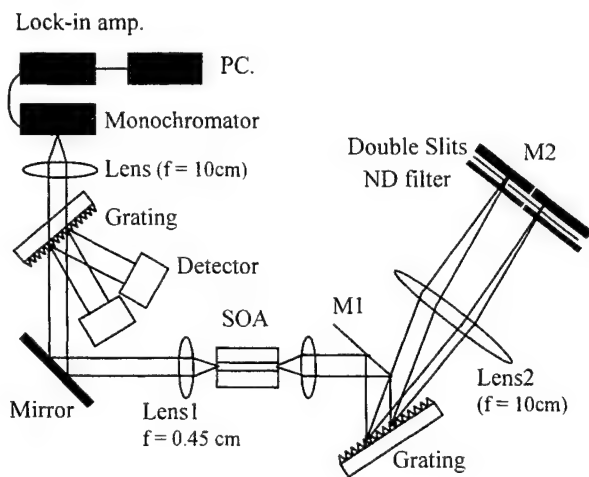


Fig. 3. Experimental setup.

By varying the loss of the ND filter in front of the slit, we can change the intensity of the controlled mode. When the intensity of either mode is changed, the intensity of the other mode also varies due to the competition or anti-competition. Plotting out the variation of the power of those modes, we can obtain several curves on the power plane, where the two axes represent the power of the SWM and the LWM, respectively. Moreover, if the vertical axis represents the power of the LWM, then the external loss introduced to the LWM must be kept constant throughout the measurement, and vice versa. The experiment for obtaining the curve with the vertical axis representing the power of the LWM goes through as follows. First, we choose the double-slit of certain mode spacing. The grating at the output

diffracts the two oscillation wavelengths chosen by the double-slit, and their light power is measured through two detectors and an oscilloscope. Next, we tune the left ND filter (the one corresponding to the SWM) to a certain value of loss, and again measure the light power of both modes. Because the holding stage of the optical components in the external cavity is not very stable, the ND filter of the LWM is tuned for keeping the external loss a constant if necessary. This step is repeated until we have tuned the ND filter to its maximum loss, and the light power of the SW mode is about to vanish. After that, we have obtained a curve with certain external loss, or say, certain initial power of the LWM. Then, we tune the ND filter of the LWM to change the external loss, and follow the steps mentioned above to obtain another curve with this new external loss and initial power of the LWM. Finally, we remove the grating and the detectors and use the monochromator to measure the spectrum. For obtaining the curves with vertical axis represents the power of the SWM, the experimental steps are similar to that described above.

2.3 Experimental results and discussion

Our experimental result for wavelength separation 18 nm is shown in Fig. 4 (a). We see that, under this wavelength separation, the curves are of negative gradient. That is, the light power of the LWM decreases with the increasing of the light power of the SWM. This is the same as the well-known mode competition. However, when the wavelength separation is increased to 111 nm (see Fig. 4 (b)), a curve with positive gradient appears on the plane. That is, increasing the light power of the SWM leads to the increase of the light power of the LWM. This behavior is opposite to mode competition, so we call it mode anti-competition. Some experimental results for larger wavelength separation are shown

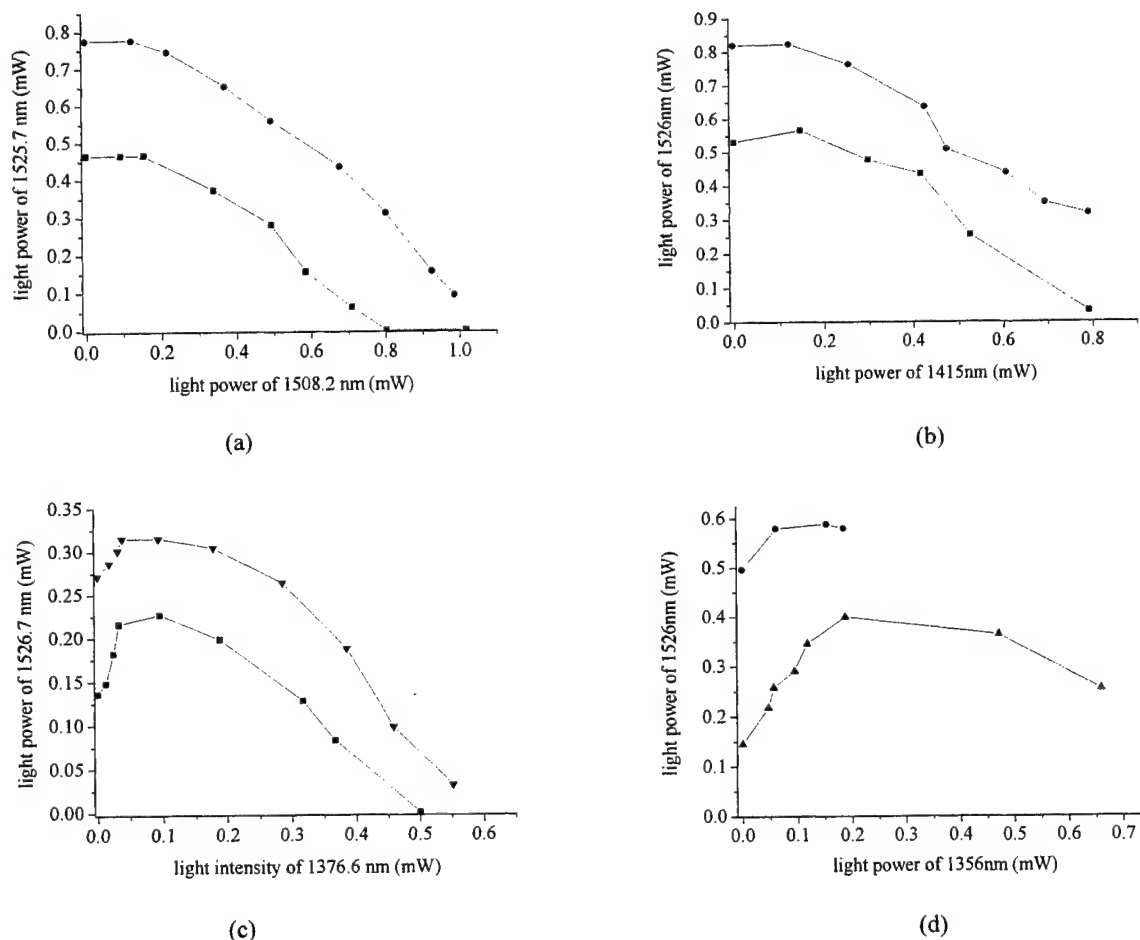


Fig. 4. Variation of the light power of the LWM to that of the SWM at wavelength separation of: (a) 18 nm, (b) 111 nm, (c) 150 nm, (d) 168 nm.

in Fig. 4 (c), (d).

Next, some influential factors of anti-competition are investigated. The first one is wavelength separation of the two modes. From Fig. 4, we can see that at larger wavelength separation, the slope of the positive-gradient curve is steeper, and the maximum power the LWM can reach under fixed initial power is larger. That is, the larger the wavelength separation is, the severer anti-competition is. For example, when the initial power of the LWM (the power of the LWM when the power of the SWM is zero) is fixed to about 0.14 mW, anti-competition can cause the light power of the LWM to increase to about 0.23 mW and 0.4 mW at wavelength separation 150 nm and 168 nm, respectively (see Fig. 4 (c), (d)). In addition, for those two curves, the slopes of the positive gradient region are about 1.5 and 1.8 at wavelength separation of 150 nm and 168 nm, respectively.

The second influential factor is the light power of the SWM. From Fig. 4, we see that no matter which wavelength separation is, anti-competition can exist only when the light power of the SWM is below certain level. For example, at wavelength separation of 150 nm and 168 nm (see Fig. 4 (c), (d)), anti-competition can exist only when the light power of the SWM is below 0.1 mW and 0.2 mW, respectively. Above this level, anti-competition disappears, and the interaction between these two modes gradually turns into competition. In general, this power level, or say, the existing range of a anti-competition, is larger at large wavelength separation. During the transition from anti-competition to competition, region exists where the variation of the SWM power has no influence on the LWM power. The existing range of anti-competition seems larger at wavelength separation 111 nm than at 150 nm. This is because, at wavelength separation 111 nm, we only sample two points when the power of the short-wavelength mode increases from 0 mW to 0.18 mW (see Fig. 4 (b)). Therefore, in Fig. 4 (b), the maximum power of the long-wavelength mode (or say, the end point of anti-competition) should have appeared prior to our second sample point, but that point was missed.

The third influential factor is the initial power of the LWM. In general, anti-competition is severer when the initial power of the LWM is smaller. This can be verified from Fig. 4 (b), (c), (d).

The last influential factor of anti-competition is the wavelength position of the two modes. As shown in Fig. 5, anti-competition at fixed wavelength separation 160 nm can have different behaviors because of different wavelength positions. When both modes reside in the longer wavelength region, anti-competition is severer. The same phenomenon can be observed for wavelength separation larger than 140 nm. When the wavelength separation is smaller than 140 nm, a phenomenon behaves in the opposite way appears. That is, when both modes reside in the longer wavelength region, anti-competition is less obvious.

2.4 Reasons for anti-competition

The reasons for anti-competition are as follows. First, as discussed above, the emission spectrum of the laser gain medium is the overlap of the emission spectra of two different QWs. Since in our experiment, the wavelength position of the LWM is always above 1510 nm (see Fig. 4, 5), most of the carriers for the oscillation of the LWM are mostly

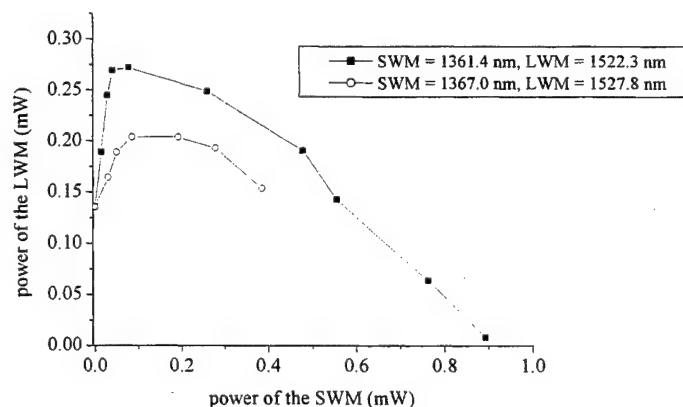


Fig. 5. Power of the LWM – power of the SWM curve with wavelength separation fixed to 160 nm.

contributed from the $n = 1$ state of the 8.7-nm $\text{In}_{0.53}\text{Ga}_{0.47}\text{As}$ QWs. However, the wavelength position of the SWM ranges from 1356 nm to 1415 nm at wavelength separation ranging from 168 nm to 111 nm. Therefore, both the 6.0-nm $\text{In}_{0.67}\text{Ga}_{0.33}\text{As}_{0.72}\text{P}_{0.28}$ QWs and the $n = 2$ state of the 8.7-nm $\text{In}_{0.53}\text{Ga}_{0.47}\text{As}$ QWs contribute to the carriers for the oscillation of the SWM. The ratio of the carrier contribution from these two types of QWs to the SWM depends on the wavelength position of the SWM. If the SWM is located near 1300 nm, the $\text{In}_{0.67}\text{Ga}_{0.33}\text{As}_{0.72}\text{P}_{0.28}$ QWs have more contribution to the gain, and vice versa. Therefore, at wavelength separation 111 nm (see Fig. 4 (b)), the two wavelengths are nearly contributed from the $\text{In}_{0.53}\text{Ga}_{0.47}\text{As}$ QWs. On the other hand, at wavelength separation 168 nm (see Fig. 4 (d)), the SWM and LWM are nearly contributed from the $\text{In}_{0.67}\text{Ga}_{0.33}\text{As}_{0.72}\text{P}_{0.28}$ QWs and the $\text{In}_{0.53}\text{Ga}_{0.47}\text{As}$ QWs, respectively. Therefore, competition at wavelength separation 168 nm is weaker than at 111 nm (as shown in Fig. 4) because the carrier transportation between different QWs is a relatively slow process, compared with the intraband relaxation in the same well.

The second reason is, because the photon energy of the short-wavelength QWs is larger than that of the long-wavelength QWs, some of the emitted short-wavelength photons will be absorbed by the long-wavelength QWs. This can provide the long-wavelength QWs with some optical gain, and is somewhat similar to optical pumping. At larger wavelength separation, the photon energy difference is larger, so stronger optical pumping and thus severer anti-competition occurs. In addition, if the initial power of the LWM is large, there are already plenty carriers for the oscillation of LWM. Therefore, optical pumping and anti-competition is weak at large LWM initial power. Moreover, the gain spectrum of the $\text{In}_{0.53}\text{Ga}_{0.47}\text{As}$ QW has one peak at 1480 nm [24]. That is, the gain at 1522.3 nm is larger than at

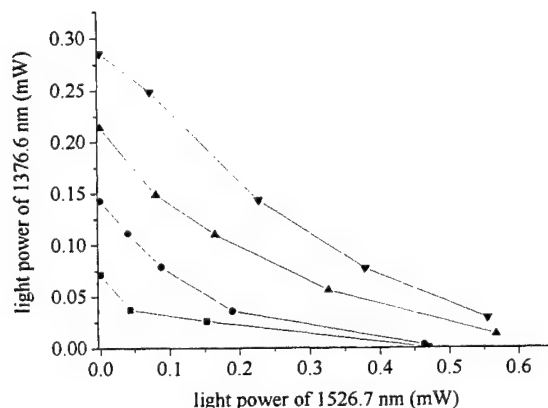


Fig. 6. Variation of the light power of the SWM to that of the LWM at wavelength separation of 150 nm. The wavelength positions of the two modes are the same as in Fig. 4 (c).

1527.8 nm, and thus 1527.8 nm has fewer carriers. This results in that 1527.8 nm has stronger “optical consumption ability” of the short-wavelength photons. Therefore, LWM at 1527.8 nm will have less apparent anti-competition behavior than LWM at 1527.8 nm under fixed wavelength separation, as shown in Fig. 5.

Since anti-competition is due to the physics similar to optical pumping, it can exist only at the LWM. For the SWM, increasing the light power of the LWM will only decrease its light power, as shown in Fig. 6 for the same two modes as in Fig. 4 (c). Note that although both Fig. 4 (a) and Fig. 6 are curves with competition, their behaviors are different. For example, the curves in Fig. 4 (a) are curving downward, whereas those in Fig. 6 are curving upward.

3. ANALYSIS

Previous models of competition usually use the following rate equations to describe the gain saturation: [5]

$$\frac{dI_1}{dt} = \left(\frac{g_{10}}{1 + S_1 I_1 + C_{12} I_2} - l_1 \right) I_1, \quad (1a)$$

$$\frac{dI_2}{dt} = \left(\frac{g_{20}}{1 + S_2 I_2 + C_{12} I_1} - l_2 \right) I_2, \quad (1b)$$

where the first term in parentheses [Eq. (1a)] represents the gain with self- and cross-saturation; g_{10} and g_{20} are the unsaturated gains of the modes I_1 and I_2 , respectively; l_1 and l_2 are losses of the modes I_1 and I_2 , respectively. In reality, the denominators in Eqs. (1a) and (1b) are not linear functions of I_1 and I_2 . The rate equations can be put into more general forms:

$$\frac{dI_1}{dt} = [G_1(I_1, I_2) - l_1] I_1, \quad (2a)$$

$$\frac{dI_2}{dt} = [G_2(I_1, I_2) - l_2] I_2, \quad (2b)$$

with $G_1(I_1, I_2)$ and $G_2(I_1, I_2)$ representing general relations of the gains and the intensities I_1 and I_2 . In the steady state, $dI_1/dt = dI_2/dt = 0$. Equations (2a) and (2b) can then be written as

$$[G_1(I_1, I_2) - l_1] I_1 = 0, \quad (3a)$$

$$[G_2(I_1, I_2) - l_2] I_2 = 0, \quad (3b)$$

where $G_1(I_1, I_2) - l_1 = 0$ and $G_2(I_1, I_2) - l_2 = 0$ represent two curves on the I_1 - I_2 phase plane.

Let's define I_1 and I_2 as the intensity of the LWM and SWM, respectively. The saturation effect causes the gain to decrease with the intensity, so the self-saturation leads to $\partial G_2 / \partial I_2 < 0$. The competition is due to cross-saturation [2,3], so $\partial G_2 / \partial I_1 < 0$. Thus, for competition situation, the gain curve $G_2(I_1, I_2) - l_2 = 0$ should have the slope $dI_1/dI_2 < 0$, which is the case for Fig. 4 (a) and for previous experiments [2,6]. For the case of anti-competition shown in Fig. 4 (b)-(d), $dI_1/dI_2 > 0$. Because self-saturation still gives $\partial G_2 / \partial I_2 < 0$, it must be that $\partial G_2 / \partial I_1 > 0$. As a result, the power-series expansion of $G_2(I_1, I_2)$ consists of a term $(\partial G_2 / \partial I_1) I_1 (= \gamma I_1 > 0)$, which means the condition like optical pumping. That is, the short-wavelength mode gives away its optical power to the long-wavelength mode. However, the two-mode operation is not exactly the same as optical pumping. As shown in Fig. 4 (b)-(d), some regime of competition still exists, indicating that the cross-saturation plays an important role again for certain intensity of I_1 .

4. CONCLUSION

Anti-competition of laser modes is observed in semiconductor laser with nonidentical MQWs. In this behavior, the oscillation intensity of the long-wavelength mode can be enhanced by that of the short-wavelength mode, which is opposite to the well-known mode competition. The phenomenon of anti-competition can be observed as long as the wavelength separation is larger than 111 nm, and is even more prominent for wavelength separation up to 168 nm. The influential factors of anti-competition includes the wavelength separation, the power of both modes and the wavelength position. Theoretical analysis shows that anti-competition is due to the physics similar to optical pumping.

REFERENCES

- [1] W. E. Lamb, "Theory of an optical maser," *Phys. Rev. A* **134**, 1429 (1964)
- [2] A. E. Siegman, *Lasers* (University Science Books, 1986).
- [3] K. Shimoda, *Introduction to Laser Physics* (Springer, Berlin, 1984), p.187.
- [4] M. Watanabe, H. Itoh, S. Mukai, and H. Yajima, "Optical tristability using a twin-stripe laser diode," *Appl. Phys. Lett.* **50**, 427 (1987).

- [5] C.-F. Lin and P.-C. Ku, "Analysis of stability in two-mode laser system," *IEEE J. Quantum Electron.* **32**, 1377 (1996).
- [6] H. Kawaguchi, *Bistability and Nonlinearities in Laser Diodes* (Artech House, Norwood, MA, 1994), p. 199.
- [7] S. Sivaprakasam, P. S. Spencer, P. Rees, and K. A. Shore, "Regimes of chaotic synchronisation in external cavity laser diodes," *IEEE J. Quantum Electron.* **38**, 1155 (2002).
- [8] H. Kawaguchi and I. S. Hidayat, "Gigahertz all-optical flip-flop operation of polarisation-bistable vertical-cavity surface emitting lasers," *Electron. Lett.* **31**, 1150 (1995).
- [9] G. D. VanWiggeren and R. Roy, *Science* (Washington, DC, U.S.) **279**, 1198 (1998).
- [10] X. Jin and S. L. Chuang, "Relative intensity noise characteristics of injection-locked semiconductor lasers," *Appl. Phys. Lett.* **77**, 1250 (2000).
- [11] H. Statz and C. L. Tang, *J. Appl. Phys.* **36**, 3923 (1965).
- [12] L. E. Hargrove, R. L. Fork, and M. A. Pollack, "Locking of He-Ne Laser Modes Induced by Synchronous Intracavity Modulation," *Appl. Phys. Lett.* **5**, 4 (1964).
- [13] P. W. Smith, *Proc. IEEE* **58**, 1342 (1970).
- [14] I. White, R. Penty, M. Webster, Y. J. Chai, A. Wonfor, and Sadegh Shahkooh, "Wavelength switching components for future photonic networks," *IEEE Communications Magazine* **40**, 74 (2002).
- [15] H. S. Gingrich, D. R. Chumney, S.-Z. Sun, S. D. Hersee, L. F. Lester, and S. R. Brueck, "Broadly-tunable external cavity laser diodes with staggered thickness multiple quantum wells," *IEEE Photon. Technol. Lett.* **9**, 155 (1997).
- [16] C.-F. Lin and B.-L. Lee, "Extremely broadband AlGaAs/GaAs superluminescent diodes," *Appl. Phys. Lett.* **71**, 1598 (1997).
- [17] N. Tessler and G. Eisenstein, "On carrier injection and gain dynamics in quantum well lasers," *IEEE J. Quantum Electron.* **29**, 1586 (1993).
- [18] R. Nagarajan, T. Fukushima, S. W. Corzine, and J. E. Bowers, "Effects of carrier transport on high-speed quantum well lasers," *Appl. Phys. Lett.* **59**, 1835 (1991).
- [19] H. Yamazaki, A. Tomita, M. Yamaguchi, and Y. Sasaki, "Evidence of nonuniform carrier distribution in multiple quantum well lasers," *Appl. Phys. Lett.* **71**, 767 (1997).
- [20] B.-L. Lee, C.-F. Lin, J.-W. Lai, and W. Lin, "Experimental evidence of nonuniform carrier distribution in multiple-quantum well laser diodes," *Electron. Lett.* **34**, 1230 (1998).
- [21] D. Ban and E. H. Sargent, "Influence of nonuniform carrier distribution on the polarization dependence of modal gain in multi-quantum-well lasers and semiconductor optical amplifiers," *IEEE J. Quantum Electron.* **36**, 1081 (2000).
- [22] C.-F. Lin, B.-R. Wu, L.-W. Lai, and T.-T. Shih, "Sequence influence of nonidentical InGaAsP quantum wells on broadband characteristics of semiconductor optical amplifiers-superluminescent diodes," *Optics Lett.* **26**, 1099 (2001).
- [23] D. Ahn and S. L. Chuang, "Optical gain and gain suppression of quantum-well lasers with valence band mixing," *IEEE J. Quantum Electron.* **26**, 13 (1990).
- [24] C.-S. Chang and S. L. Chuang, "Modeling of strained quantum-well lasers with spin-orbit coupling," *IEEE Journal of Selected topics in Quantum Electronics* **1**, 218 (1995).

Timing Jitter Measurement and its Reduction for Gain-Switched DFB Laser

Q. Wang, G. Zhu, H. Dong, N. K. Dutta

Department of Physics, University of Connecticut, Storrs, CT 06269

Abstract

We present two methods for timing jitter measurement. The first method uses the spectral content of the noise, and, the second method uses autocorrelation and cross correlation of the pulsed output. For a distributed feedback (DFB) laser gain switched at 1 GHz, the timing jitter is about 3-4 ps. When an external CW laser injected into the DFB laser, the timing jitter can be reduced to 1-1.5 ps.

Introduction

Gain-switched laser diodes have been extensively used to generate the pico-second optical pulses needed by the high-bite-rate transmission systems[1]-[3]. As the pulse width becomes shorter, pulse to pulse timing jitter impairs the system performance when such a laser is used in a transmission system. Studies of timing jitter have concentrated on determining the correlated timing jitter from the phase noise. The root-mean-square (RMS) correlated jitter of both mode locked diodes and gain-switched laser diodes has been measured to be < 1 ps [4]. For gain-switched laser diodes, due to the spontaneous character of the onset of the lasing process, there is uncorrelated timing jitter. Previous authors have reported uncorrelated jitter of ~ 1.7 to 14 ps for pulse width of ~ 30 ps [6].

This paper describes measurement of timing jitter for distributed feedback (DFB) laser diodes with and without external injection.

Measurements

The experimental setup is shown in Fig. 1.,

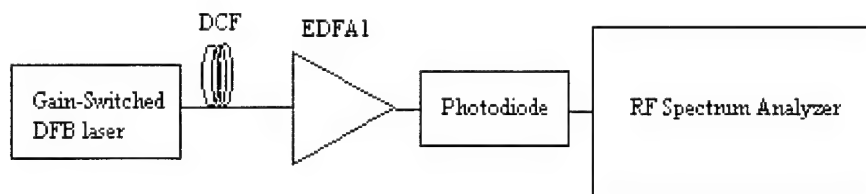


Figure 1. Schematic diagram of experimental setup for timing jitter measurement using RF spectrum analyzer

The DFB laser was gain switched at 5 GHz generated by synthesized sweeper (HP 8340B). After the pulse compression, the pulse width is about 10 ps. The pulses are detected using a high speed photodiode connected to a RF spectrum analyzer.

The pulse to pulse jitter (relative positions of the pulses in time domain) of a short optical pulse train can be measured by analyzing the power spectrum of the pulse train obtained using a high speed photodiode. The root-mean-square (RMS) value of the correlated and uncorrelated timing jitter are given by [4-6]

$$\sigma_c = \frac{1}{2\pi f} \sqrt{\frac{P_n \Delta f}{P_c RB}}$$

$$\sigma_{uc} = \frac{1}{2\pi \sqrt{n^2 + 1/12} f} \sqrt{\frac{P_n f}{P_c RB}}$$

where n is the harmonic number, f is the pulse repetition frequency, P_c and P_n are respectively the powers of the n th harmonics and the maximum of the phase noise centered on the harmonics, Δf is the noise bandwidth (full width at half maximum FWHM), and RB is the resolution bandwidth of the RF spectrum analyzer used.

The measured uncorrelated and correlated timing jitter obtained using the above equations are shown in Fig. 2. The uncorrelated jitter is about 3 ps and the correlated jitter is much smaller, less than 200 fs.

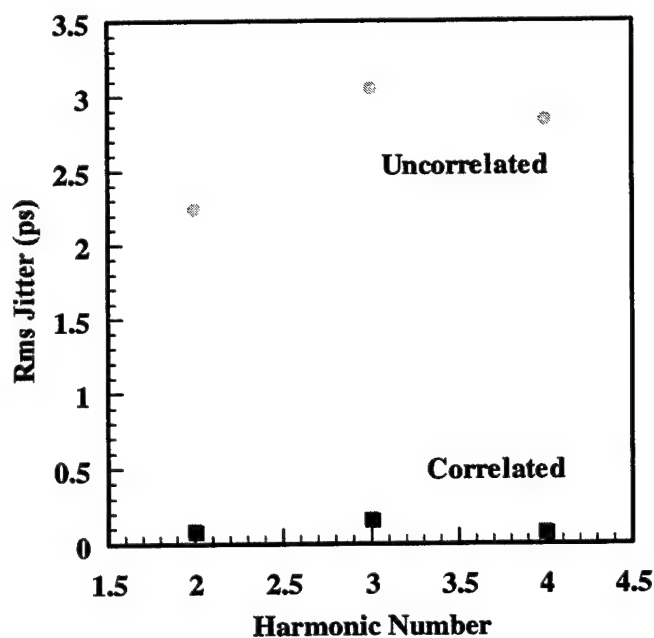


Figure 2: Timing Jitter as a function of harmonic number

Thus for gain-switched DFB lasers, the timing jitter mainly consists of uncorrelated jitter. The second method for timing jitter measurement that we have used utilizes optical cross correlation and autocorrelation. The experimental setup is in Fig. 3.,

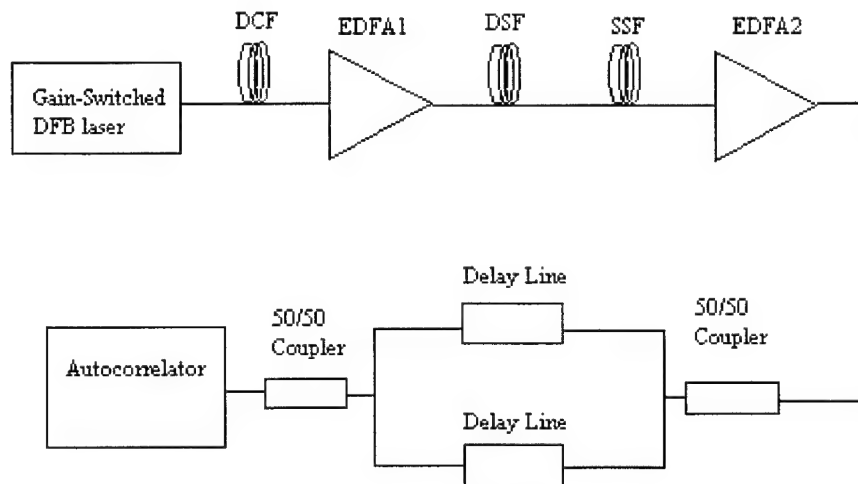


Figure 3: Schematic diagram of experimental setup for timing jitter measurement using autocorrelation and cross correlation

The DFB laser was gain switched at 1GHz. The pulse width was ~ 30 ps. After propagation through a dispersion compensating fiber (DCF), the pulses are compressed to ~ 7 ps. Then the pulse train is amplified by a erbium doped fiber amplifier (EDFA) and propagated through the dispersion shifted fiber (DSF) and standard single mode fiber (SSF) of suitable lengths. The pulse width was further reduced to 3.5 ps using this scheme.

Using the delay lines, two sets of pulses were multiplexed so that a dual set of pulses are produced. The dual pulses in each set are separated by ~ 40 ps, which is within the delay range of the autocorrelator. These dual set of pulses produces three peaks on the autocorrelator output as shown in Figure 4. This allows simultaneous measurement of the autocorrelation and cross correlation pulse-width.

The RMS timing jitter is given by[7]

$$\sigma_{pp} = \sqrt{\sigma_{XC}^2 - \sigma_{AC}^2}$$

σ_{pp} is the pulse to pulse variance, σ_{XC} , σ_{AC} are the standard deviation of the cross correlation and autocorrelation of the laser pulse.

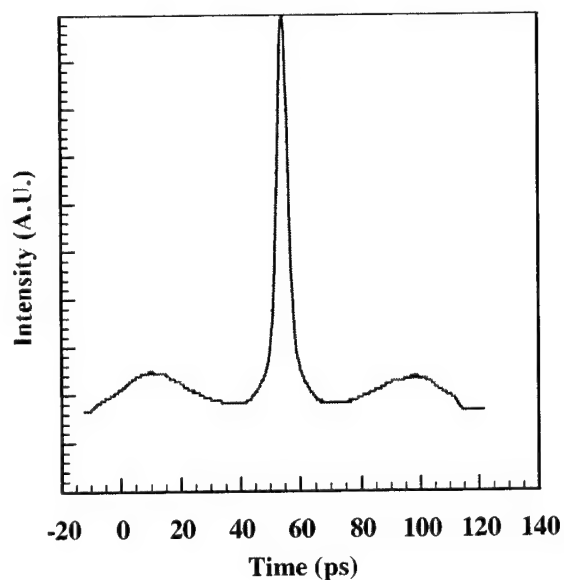


Figure 4: A typical trace from the autocorrelator for the dual set of pulses.

Reduction of timing jitter using external CW injection

Self or external injection seeding has been used to reduce the timing jitter[8]. We used the experimental setup shown below (Fig. 5) for our measurements.

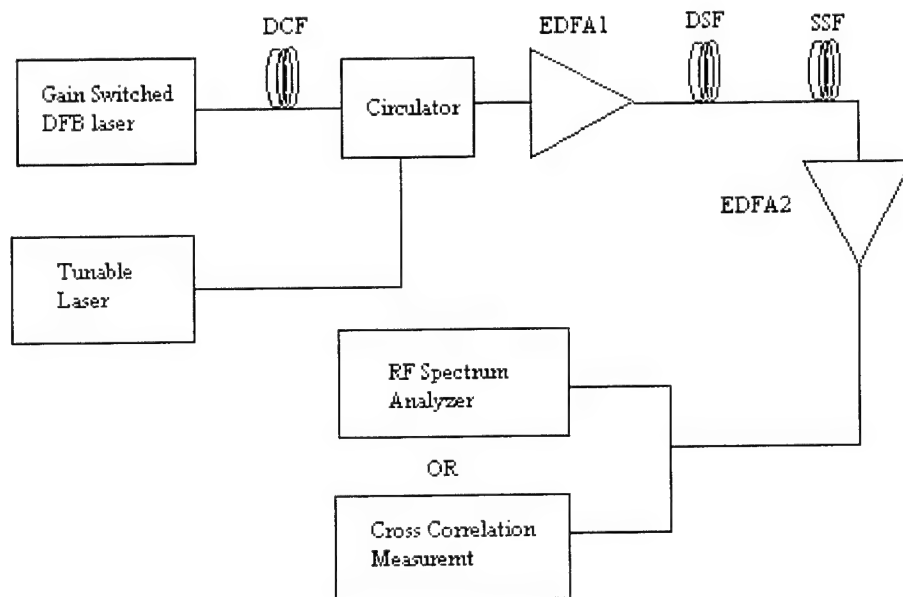
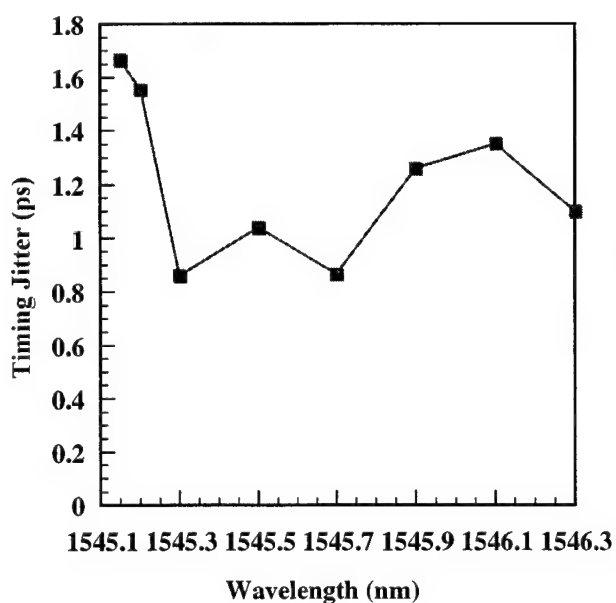
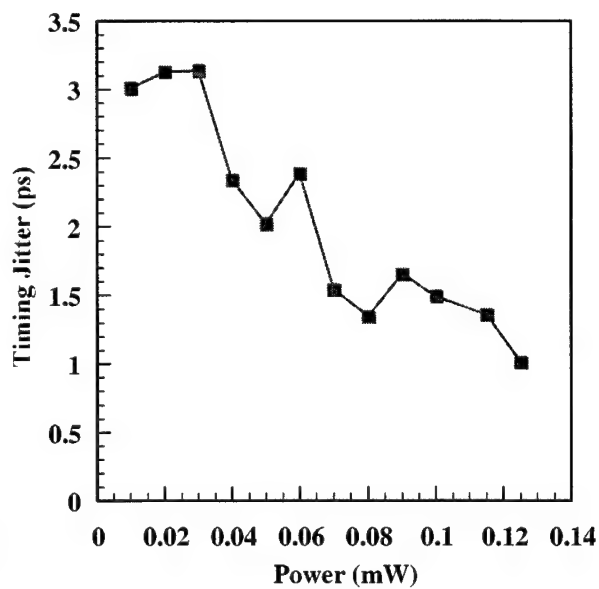


Figure 5: Schematic diagram of experimental setup of external injection seeding

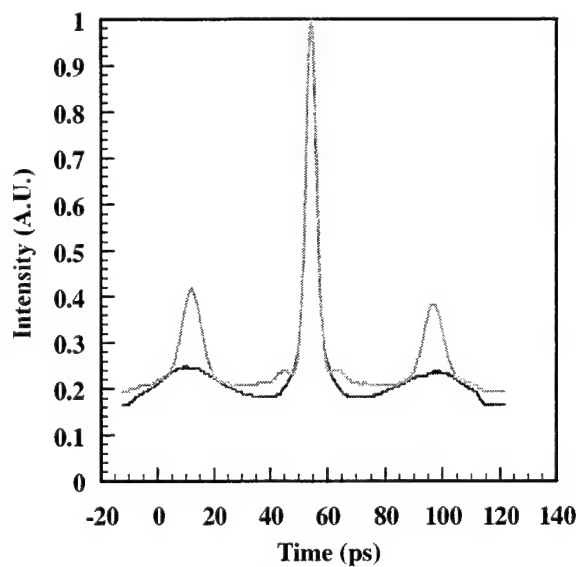
The results are shown in Figures 6 and 7.



(a)

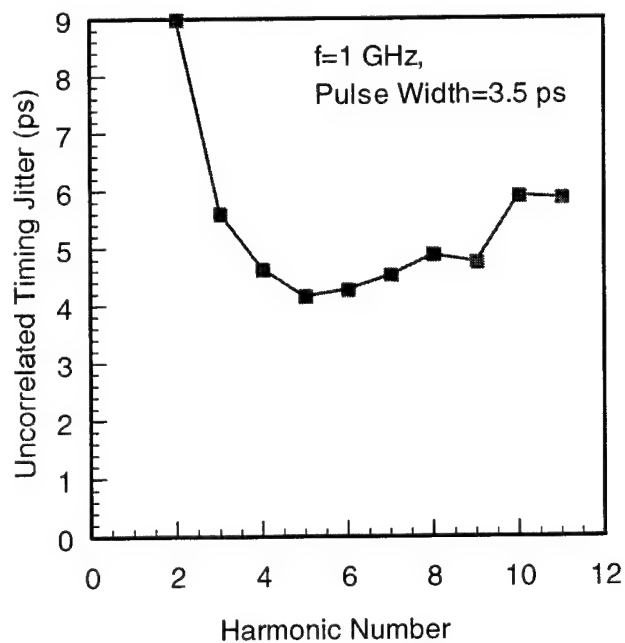


(b)

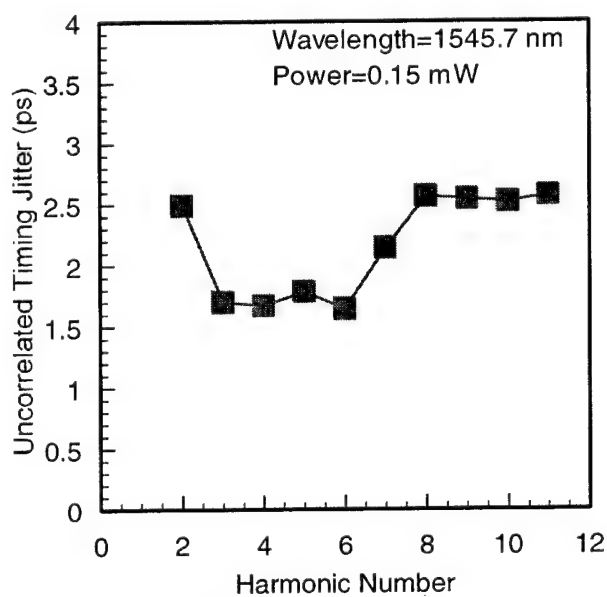


(c)

Figure 6: The results using cross and auto correlation (a) Timing jitter as a function of injection seeding wavelength. The power is 0.05 mW. (b) Timing jitter vs injection seeding power. (c) Comparing the autocorrelator results of injection and no injection



(a)



(b)

Figure 7: The results using spectrum analyzer (a) Uncorrelated timing jitter vs harmonic number without external injection. Repetition rate 1 GHz and pulse width 3.5 ps (b) Uncorrelated timing jitter vs harmonic number with external injection. The power is 0.15 mW and wavelength is 1547.7 nm. The DFB is lasing at 1545.8 nm

Summary

We present two methods for timing jitter measurement. The first method uses the spectral content of the noise, and, the second method uses autocorrelation and cross correlation of the pulsed output. For a

distributed feedback (DFB) laser gain switched at 1 GHz, the timing jitter is about 3-4 ps. When an external CW laser injected into the DFB laser, the timing jitter can be reduced to 1-1.5 ps.

References

1. P.W. Juodawlkis, J.C. Twichell, G.E. Betts, J.J. Hargreaves, R.D. Younger, J.L. Wasserman, F.J. O'Donnell, K.G. Ray, and R.C. Williamson, "Optically sampled analog-to-digital converters". IEEE Trans. Microwave Theory Tech., vol. 49, pp. 1840-1853, Oct. 2001
2. S. A. Crooker, F.D. Betz, J. Levy, and D.D. Awschalom, "Femtosecond synchronization of two passively mode-lock Ti:sapphire lasers", Rev. Sci. Instrum., vol. 67, no. 6, pp. 2068-2071, June 1996
3. S. Kawanish and M. Saruwatari, "New-type phase-locked loop using travelling-wave laser-diode optical amplifier for very high-speed optical transmission", Electron. Lett., vol. 24, pp. 1452-1453, 1988
4. Masahiko Jinno, "Correlated and uncorrelated timing jitter in gain-switched laser diodes", IEEE Photonics Technol. Lett. vol. 5, No. 10, pp. 1140-1143, Oct. 1993
5. P. J. Delfyett, D.H. Hartman, and S.Z. Ahmad, "Optical clock distribution using a mode-locked semiconductor laser diode system", J. Lightwave Technol., vol.9, pp. 1646-1649, 1991
6. D. von der Linde, "Characterization of the noise in continuously operating mode-locked lasers", Appl. Phys. B. 39, 201-217, 1986
7. L. A. Jiang, S.T. Wong, M.E. Grein, E.P. Ippen, and H.A. Haus, "Measuring timing jitter with optical cross correlations", IEEE J. Quantum Electron., vol. 38, No. 8, August 2002
8. Dong-Sun Seo, D.Y. Kim, and Hai-Feng Liu, "Timing jitter reduction of gain-switched DFB laser by external injection-seeding", Electron. Lett. Vol. 32, no. 1, pp. 44-45, Jan. 1996

Analysis of self-pulsation in a distributed Bragg reflector laser based on four-wave mixing

P. Landais^a, J. Renaudier^b, P. Gallion^b and G.-H. Duan^c

^aSchool of Electronic Engineering, Dublin City University,
Glasnevin, Dublin 9, Ireland

^bDépartement Communications et Electronique,
Ecole Nationale Supérieure des Télécommunications,
46 rue Barrault,
75634 Paris Cedex 13, France

^c Alcatel Research & Innovation,
Route de Nozay, 91460 Marcoussis, France

ABSTRACT

All-optical regeneration at 40 Gbit/s and beyond is a crucial element for future transparent networks. One solution to achieve the regeneration is an all-optical clock recovery element combined with a Mach-Zehnder interferometer. Among the different approaches investigated so far to accomplish the clock recovery function, a scheme based on a single self-pulsating distributed Bragg reflector laser is of particular interest from practical and cost viewpoints. In this structure at least two longitudinal modes beat together, generating power oscillation even though the laser is DC biased. The oscillation frequency is given by the free spectral range of the structure. In order to optimize the clock recovery performance of such a laser, a model based on four-wave-mixing has been developed. It takes into account the evolution of the amplitude and the phase of the complex electric field of each longitudinal mode. From this model, a stability analysis is derived through the adiabatic approximation. The spectral density of the correlated phases of these modes is calculated and compared to the uncorrelated spectral density of each mode.

Keywords: Distributed Bragg reflector, self-pulsating laser, clock recovery, four-wave mixing and phase correlation.

1. INTRODUCTION

In order to improve the transmission distance, transparency, capacity and speed of optical networks, practical means for all-optical treatment of the data, such as all-optical digital logic functions and 3R (re-amplify, re-time, and re-shape) regeneration are of particular interest¹⁻³. For example, all-optical clock recovery would supersede the complicated optoelectronic schemes including a high speed photo-receiver, a high-Q filter, a power amplifier and a high speed laser or an integrated laser modulator. Among the different approaches investigated so far, a scheme based on a single self-pulsating distributed Bragg reflector (SP DBR) laser is of particular interest from practical and cost viewpoints. In such a structure, under certain bias conditions, the beating between the longitudinal modes generates a power oscillation even though the laser is DC biased. The non-linearities and characteristic

Further author information: (Send correspondence to P. Landais)

P. Landais: E-mail: landaisp@eeng.dcu.ie, Telephone: +353-1-7008044

times of semiconductor devices lead to oscillation in the radio-frequency (RF) domain. It has been demonstrated that such a SP DBR laser is able to synchronize its self-pulsation to the bit-rate of an incoming data signal, acting as an all-optical clock recovery device⁴. The optical field generated inside the laser cavity can be expressed as a monochromatic wave with a slowly time varying amplitude:

$$E_k(z, t) = A_k(t) \exp(-j(\omega_k t + \phi_k(t)) \cdot Z_k(z), \quad (1)$$

where A_k is the amplitude of the k^{th} mode, $\omega_k = 2\pi\nu_k$ its angular frequency with ν_k the optical frequency, Z_k its longitudinal dependence and ϕ_k its instantaneous phase fluctuation. In the case of a laser with M longitudinal modes, the beating between these modes leads to a quadratic temporal average of the total electric field with the following expression:

$$\langle |E_T|^2 \rangle = \sum_{k=1}^M \langle |E_k|^2 \rangle + \sum_{k=1}^M \sum_{j \neq k}^M 2 \langle E_k E_j \cos(\Omega_{kj}t + (\phi_j(t) - \phi_k(t))) \rangle, \quad (2)$$

where the pulsation frequency between two adjacent modes, Ω_{kj} , is given by $(\omega_j - \omega_k)$. For example, for a laser with two uncorrelated modes, a RF signal at the frequency $\Omega_{kj}/2\pi$ can be observed by a photodiode, with a spectral linewidth corresponding to the sum of the two modes' spectral linewidths. However, in the case of a SP laser, the RF signal linewidth is smaller, benefiting from the phase correlation of the optical modes through the non-linear effects. Indeed, the four-wave-mixing (FWM) results in a modulation of the carrier population, leading to a nonlinear gain and refractive index modulation, affecting both the amplitude and the phase of the lasing modes. Based on a four-wave mixing formalism, we present in this paper a study of the origin of the RF oscillation in a SP DBR laser with 3 longitudinal modes. The paper is organized as follows: in Part 2 the equations describing the behavior of a multimode DBR SP laser are described including the FWM nonlinearity, in Part 3 the stability analysis of this equation system is performed and the solutions are established. The power spectral density for the modes of the DBR SP laser are calculated and compared with the spectral power density of uncorrelated modes. Part 4 presents and discusses the simulation results based on our model. Finally conclusions are drawn in Part 5.

2. FOUR WAVE MIXING IN A SELF-PULSATING DBR LASER

There are five non-linear effects generating four-wave mixing (FWM) in a semiconductor components: the carrier density modulation (CDM), the carrier heating, the spectral hole burning, the two-photon absorption and the Kerr effect. These last four effects can be neglected when the free spectral range between the modes involved is of the order of 40 GHz⁵, so that only CDM will be taken into account. For the sake of simplicity and clarity, only three longitudinal modes ($M = 3$) propagating in the SP DBR are considered in our approach. The time evolution of the electric field is given by:

$$\begin{aligned} \frac{dE_k}{dt} = & \frac{1}{2}(1 - j\alpha_H)(G - \gamma_k)E_k \\ & + \frac{1}{2}(1 - j\alpha_H)\frac{\Gamma v_g a}{V} \left(\sum_{m=1}^{M-1} (\Delta N_m E_{k-m} + \Delta N_m^* E_{k+m}) \right) \\ & - j(\omega_k - \omega_k^i)E_k + F_k(t), \end{aligned} \quad (3)$$

where α_H represents the phase-amplitude coupling factor, γ_k the cavity loss for the k^{th} mode. The instantaneous fluctuations of the electric field due to the spontaneous emission are given by Langevin source term, $F_k(t)$. $(\omega_k - \omega_k^i)$ represents the detuning of the angular frequency ω_k of the k^{th} lasing

mode from its initial cavity resonance one ω_k^i . The gain, G , is assumed constant over the spectral range of the three modes. G is given by $\Gamma v_g g$ where Γ is the optical confinement, v_g the group velocity and g is equal as $a(N_0 - N_{tr})/V$, where a is the differential gain, V the volume of the active layer, N_{tr} the carrier number at transparency and N_0 the average carrier number, satisfying, the carrier rate equation given by:

$$\frac{dN_0}{dt} = \frac{I}{e} - \frac{N_0}{\tau_e} - GP_t, \quad (4)$$

where P_t is the total photon number and is equal, in this study, to $|E_1|^2 + |E_2|^2 + |E_3|^2$. ΔN_m represents the m^{th} order of the carrier modulation. Its dependence on the frequency is given by⁶:

$$\Delta N_m = -(N_0 - N_{tr}) \cdot \frac{\sum_{i=1}^M E_k E_{i-m}^*}{P_t + P_s - jm\Omega\tau_e P_s} \quad (5)$$

with the photon saturation number, P_s equal to $V/(\Gamma v_g a \tau_e)$, and τ_e is the carrier lifetime. Since $\Omega_{sp}\tau_e \gg 1$, the contribution to the carrier modulation of $(1 + P_t/P_s)$ can be neglected. By separating real and imaginary parts of Eq. (4), six rate equations are obtained, describing the time evolution of both the amplitude A_k and the phase ϕ_k of the k^{th} mode. Based on the approximation that $A_2^2/(\Omega_{sp}\tau_e P_s) \ll 1$, the contribution to the non-linear gain corresponding only to a transfer of energy between modes is neglected, whereas the other contribution introducing a transfer of phase is kept. We consider as well, that the amplitude of mode 2 is larger than that of mode 1, which is larger than that of mode 3, in accord with some previous experimental investigations⁴. We achieve for the amplitude and the phase the following equations :

$$\frac{dA_1}{dt} = \frac{1}{2} \left((G - \gamma_1) + \frac{G}{\Omega_{sp}\tau_e} \frac{A_2^2}{P_s} \frac{A_3}{A_1} \sqrt{1 + \alpha_H^2} \sin(\psi + \arctan \alpha_H) \right) A_1 + F_{A_1} \quad (6)$$

$$\frac{dA_2}{dt} = \frac{1}{2} (G - \gamma_2) A_2 + F_{A_2} \quad (7)$$

$$\frac{dA_3}{dt} = \frac{1}{2} \left((G - \gamma_3) - \frac{G}{\Omega_{sp}\tau_e} \frac{A_2^2}{P_s} \frac{A_1}{A_3} \sqrt{1 + \alpha_H^2} \sin(\psi + \arctan \alpha_H) \right) A_3 + F_{A_3}, \quad (8)$$

$$\frac{d\phi_1}{dt} = \frac{\alpha_H}{2} (G - \gamma_1) - \frac{1}{2} \frac{G}{\Omega_{sp}\tau_e} \frac{A_2^2}{P_s} \frac{A_3}{A_1} \sqrt{1 + \alpha_H^2} \cos(\psi + \arctan \alpha_H) - (\omega_1 - \omega_1^i) + F_{\phi_1} \quad (9)$$

$$\frac{d\phi_2}{dt} = \frac{\alpha_H}{2} (G - \gamma_2) - (\omega_2 - \omega_2^i) + F_{\phi_2} \quad (10)$$

$$\frac{d\phi_3}{dt} = \frac{\alpha_H}{2} (G - \gamma_3) + \frac{1}{2} \frac{G}{\Omega_{sp}\tau_e} \frac{A_2^2}{P_s} \frac{A_1}{A_3} \sqrt{1 + \alpha_H^2} \cos(\psi + \arctan \alpha_H) - (\omega_3 - \omega_3^i) + F_{\phi_3}, \quad (11)$$

where F_{A_k} and F_{ϕ_k} represent the instantaneous fluctuation of the amplitude and the phase respectively; and ψ is equal to $2\phi_2 - \phi_1 - \phi_3$. The equations (6)-(11) are similar to those describing an injection-locked laser. The time-rate of change of the mode consists of a classical contribution involving the phase amplitude coupling factor and the gain, but also a term of injection with a phase difference given by $\psi + \arctan(\alpha_H)$. If we introduce the injection rate terms, ρ_1 and ρ_3 , such that:

$$\rho_1 = \frac{G}{\Omega_{sp}\tau_e} \frac{A_2^2}{P_s} \frac{A_3}{A_1} \sqrt{1 + \alpha_H^2} \quad (12)$$

$$\rho_3 = \frac{G}{\Omega_{sp}\tau_e} \frac{A_2^2}{P_s} \frac{A_1}{A_3} \sqrt{1 + \alpha_H^2}, \quad (13)$$

we can express Eqs.(6)-(11) as:

$$\frac{dA_1}{dt} = \frac{1}{2} \left((G - \gamma_1) + \rho_1 \cos(\psi + \arctan \alpha_H - \frac{\pi}{2}) \right) A_1 + F_{A_1} \quad (14)$$

$$\frac{dA_2}{dt} = \frac{1}{2} (G - \gamma_2) A_2 + F_{A_2} \quad (15)$$

$$\frac{dA_3}{dt} = \frac{1}{2} \left((G - \gamma_3) + \rho_3 \cos(\psi + \arctan \alpha_H - \frac{\pi}{2}) \right) A_3 + F_{A_1} \quad (16)$$

$$\frac{d\phi_{21}}{dt} = \frac{1}{2} \left(\alpha_H (\Delta G_2 - \Delta G_1) - \rho_1 \sin(\psi + \arctan \alpha_H - \frac{\pi}{2}) \right) - \Delta\omega_{21}^i + F_{\phi_{21}} \quad (17)$$

$$\frac{d\phi_{32}}{dt} = \frac{1}{2} \left(\alpha_H (\Delta G_3 - \Delta G_2) - \rho_3 \sin(\psi + \arctan \alpha_H - \frac{\pi}{2}) \right) - \Delta\omega_{32}^i + F_{\phi_{32}}, \quad (18)$$

where $\Delta\omega_{jk}^i = (\omega_k^i - \omega_j^i)$, represents the cavity resonance frequency detuning between modes k and j , $\Delta G_k = G - \gamma_k$, $\phi_{21} = \phi_2 - \phi_1$ and $\phi_{32} = \phi_3 - \phi_2$, represent the relative phases.

3. ANALYSIS

3.1. Steady state condition

In order to determine the validity limit of this system of differential equations, the time-rate of change and the amplitude and phase noise sources terms are set to zero. A quadratic equation is then obtained:

$$\frac{1 + \alpha_H^2}{4} X^2 - \alpha_H \Delta\omega^i X + (\Delta\omega^i)^2 - \frac{1}{4} (\rho_3 - \rho_1)^2 = 0, \quad (19)$$

where X is equal to $(2\Delta G_2 - \Delta G_1 - \Delta G_3)$ and the spectral detuning between the modes, $\Delta\omega^i$ is given by $\Delta\omega_{21}^i - \Delta\omega_{32}^i$. This equation has a real root only if its discriminant is positive. This implies that:

$$|\Delta\omega^i| \leq \frac{\sqrt{1 + \alpha_H^2}}{2} |\rho_3 - \rho_1| = \Delta\omega_l. \quad (20)$$

Eq. (20) relates the maximal value of $\Delta\omega^i$ to the intermodal half-locking bandwidth⁷, $\Delta\omega_l$. While $|\Delta\omega^i|$ is smaller than $\Delta\omega_l$, the system converges towards a steady state solution in the injected regime. Alternatively, if $|\Delta\omega^i|$ is larger than $\Delta\omega_l$, the system does not produce a stable solution since the modulation lateral bandwidths are not sufficiently close to the mode frequencies to realize injection-locking. It is worth noticing that $\Delta\omega_l$ is function of the injection rate, related to the amplitude ratio of modes 1 and 3. As the discrepancy between A_1 and A_3 increases, $\Delta\omega_l$ increases. A self-pulsating behavior is achieved when the main mode is surrounded by asymmetric modes, as previously demonstrated.⁴

3.2. Small-signal analysis

Small perturbation analysis is performed within the steady state condition defined in Eq. (20). In order to simplify this calculation, we assume that the intensity of the electric field of each mode instantaneously follows any changes in the gain and refractive index of the cavity. This implies that fluctuation in the phase and amplitude is exclusively caused by the spontaneous emission coupled to the modes. This will affect the amplitude and the phase of each mode. Consequently, the adiabatic

approximation allows us to consider the fluctuations at frequencies around the self-pulsation frequency. The small signal analysis of the Eqs. (17) and (18) leads to the following equations for the relative phases:

$$\frac{d\delta\phi_{21}}{dt} = \frac{\alpha_H}{2} (\delta(\Delta G_2) - \delta(\Delta G_1)) - \frac{1}{2}\rho_1 \cos(\bar{\theta}) \cdot (\delta\phi_{21} - \delta\phi_{32}) + F_{\phi_{21}} \quad (21)$$

$$\frac{d\delta\phi_{32}}{dt} = \frac{\alpha_H}{2} (\delta(\Delta G_3) - \delta(\Delta G_2)) - \frac{1}{2}\rho_3 \cos(\bar{\theta}) \cdot (\delta\phi_{21} - \delta\phi_{32}) + F_{\phi_{32}}, \quad (22)$$

where the static phase, $\bar{\theta}$ is equal to $(\psi^0 + \arctan \alpha_H - \frac{\pi}{2})$. If we applied the adiabatic approximation to the rate equation of the photon number for the k^{th} mode, it is possible to substitute $\delta(\Delta G_k)$ by the ratio between the photon noise source, F_{P_k} and the photon number, P_k where $P_k = A_k^2$. The rate of change of the fluctuation of the relative phases with respect to time can then be written as:

$$\frac{d\delta\phi_{21}}{dt} = \frac{\alpha_H}{2} \left(\frac{F_{P_1}}{P_1} - \frac{F_{P_2}}{P_2} \right) - \frac{1}{2}\rho_1 \cos(\bar{\theta}) \cdot (\delta\phi_{21} - \delta\phi_{32}) + F_{\phi_{21}} \quad (23)$$

$$\frac{d\delta\phi_{32}}{dt} = \frac{\alpha_H}{2} \left(\frac{F_{P_2}}{P_2} - \frac{F_{P_3}}{P_3} \right) - \frac{1}{2}\rho_3 \cos(\bar{\theta}) \cdot (\delta\phi_{21} - \delta\phi_{32}) + F_{\phi_{32}}. \quad (24)$$

These equations show that the evolution of the phase detuning between modes 2 and 1 is linked to the one between modes 3 and 2, and also to the ratio of the amplitude of modes 3 and 1, through ρ_1 and ρ_3 .

3.3. Relative phase noise power spectra

The above system of differential equations can be easily solved in the frequency domain using the Fourier transformation. The relative phases fluctuations are expressed as a function of the electrical analysis frequency, Ω' , where $\Omega' = \Omega - \Omega_{sp}$. In the frequency domain, Eqs. (23) and (24) are expressed as follows:

$$\widetilde{\delta\phi_{21}}(\Omega') = \frac{j\Omega' (\widetilde{\delta\phi_2^0} - \widetilde{\delta\phi_1^0}) + \frac{\rho_1}{2} \cos(\bar{\theta}) \widetilde{\delta\phi_{32}}}{j\Omega' + \frac{\rho_1}{2} \cos(\bar{\theta})} \quad (25)$$

$$\widetilde{\delta\phi_{32}}(\Omega') = \frac{j\Omega' (\widetilde{\delta\phi_3^0} - \widetilde{\delta\phi_2^0}) + \frac{\rho_3}{2} \cos(\bar{\theta}) \widetilde{\delta\phi_{21}}}{j\Omega' + \frac{\rho_3}{2} \cos(\bar{\theta})}, \quad (26)$$

where $\widetilde{\delta\phi_k^0}$ is the Fourier transform of the phase fluctuation of the k^{th} mode in absence of four-wave mixing and is equal to $1/(j\Omega')(\bar{F}_{\phi_k} - \frac{\alpha_H}{2} \frac{\bar{F}_{P_k}}{P_k})^8$. Thus, it is now possible to express the noise power spectral density of the relative phases as a function of the spectral densities of the three uncorrelated modes. The spectral densities for ϕ_{21} and ϕ_{32} are expressed as follows:

$$S_{\phi_{21}}(\Omega') = (S_{\phi_2^0} + S_{\phi_1^0}) \frac{1}{1 + \left(\frac{\rho_1 \cos(\bar{\theta})}{2\Omega'} \right)^2} + S_{\phi_{32}} \frac{1}{1 + \left(\frac{2\Omega'}{\rho_1 \cos(\bar{\theta})} \right)^2} \quad (27)$$

$$S_{\phi_{32}}(\Omega') = (S_{\phi_3^0} + S_{\phi_2^0}) \frac{1}{1 + \left(\frac{\rho_3 \cos(\bar{\theta})}{2\Omega'} \right)^2} + S_{\phi_{21}} \frac{1}{1 + \left(\frac{2\Omega'}{\rho_3 \cos(\bar{\theta})} \right)^2}. \quad (28)$$

These expressions, obtained in the case of an adiabatic approach, demonstrate qualitatively the existence of a phase correlation between the different modes involved in our model. Indeed, the absence of phase correlation between modes leads theoretically to $S_{\phi_{ij}} = S_{\phi_i}^0 + S_{\phi_j}^0$, which is not the case here. Furthermore, Eqs. (27) and (28) give some information about the behavior of the spectral densities of the noise of the relative phases. Analysis at high frequencies shows, they behave as the sum of the spectral densities of the modes in absence of four-wave mixing. At lower frequencies, the contribution of the uncorrelated spectral densities vanishes and $S_{\phi_{21}}(\Omega')$ converges towards $S_{\phi_{32}}(\Omega')$. From Eqs. (27) and (28), it is also possible to express the sum $S_{\phi_{21}} + S_{\phi_{32}}$ as a function of $S_{\phi_1}^0$, $S_{\phi_2}^0$ and $S_{\phi_3}^0$.

$$S_{\phi_{21}} + S_{\phi_{32}} = 2S_{\phi_2}^0 + S_{\phi_1}^0 + S_{\phi_3}^0 + \frac{b^2 - a^2}{1 + a^2 + b^2} (S_{\phi_1}^0 - S_{\phi_3}^0) \quad (29)$$

with $a = \frac{\rho_1 \cos(\bar{\theta})}{2\Omega'}$ and $b = \frac{\rho_3 \cos(\bar{\theta})}{2\Omega'}$. Therefore, it can be proven that the sum of the spectral densities of the relative phases, $S_{\phi_{32}}$ and $S_{\phi_{21}}$, is smaller than the sum of the uncorrelated phases, $2S_{\phi_2}^0 + S_{\phi_1}^0 + S_{\phi_3}^0$. Indeed, this condition is always satisfied because $S_{\phi_1}^0$ is smaller, by definition, than $S_{\phi_3}^0$ when A_1 is greater than A_3 , and conversely. This relation shows that the phase correlation induced by FWM results in a reduction of the spectral linewidth of the self-pulsating signal.

4. NUMERICAL RESULTS

After linearization and Fourier transformation of Eqs. (4), (6)-(11), the following equation is achieved:

$$\begin{pmatrix} \tilde{F}_{A_1} \\ \tilde{F}_{A_2} \\ \tilde{F}_{A_3} \\ \tilde{F}_{\phi_1} \\ \tilde{F}_{\phi_2} \\ \tilde{F}_{\phi_3} \\ \tilde{F}_N \end{pmatrix} = (j\Omega' I - M) \cdot \begin{pmatrix} \delta \tilde{A}_1 \\ \delta \tilde{A}_2 \\ \delta \tilde{A}_3 \\ \delta \tilde{\phi}_1 \\ \delta \tilde{\phi}_2 \\ \delta \tilde{\phi}_3 \\ \delta \tilde{N}_0 \end{pmatrix}, \quad (30)$$

where M is 7×7 matrix and I the identity matrix. For any values of Ω' satisfying the condition that $\det(j\Omega' I - M) \neq 0$, we can express the phase fluctuations of the three modes as a function of the Langevin terms. With Q equal to the inverse matrix of $(j\Omega' I - M)$, the phase fluctuations are given directly by:

$$\delta \tilde{\phi}_1 = q_{4,1} \tilde{F}_{A_1} + q_{4,2} \tilde{F}_{A_2} + q_{4,3} \tilde{F}_{A_3} + q_{4,4} \tilde{F}_{\phi_1} + q_{4,5} \tilde{F}_{\phi_2} + q_{4,6} \tilde{F}_{\phi_3} + q_{4,7} \tilde{F}_N \quad (31)$$

$$\delta \tilde{\phi}_2 = q_{5,1} \tilde{F}_{A_1} + q_{5,2} \tilde{F}_{A_2} + q_{5,3} \tilde{F}_{A_3} + q_{5,4} \tilde{F}_{\phi_1} + q_{5,5} \tilde{F}_{\phi_2} + q_{5,6} \tilde{F}_{\phi_3} + q_{5,7} \tilde{F}_N \quad (32)$$

$$\delta \tilde{\phi}_3 = q_{6,1} \tilde{F}_{A_1} + q_{6,2} \tilde{F}_{A_2} + q_{6,3} \tilde{F}_{A_3} + q_{6,4} \tilde{F}_{\phi_1} + q_{6,5} \tilde{F}_{\phi_2} + q_{6,6} \tilde{F}_{\phi_3} + q_{6,7} \tilde{F}_N, \quad (33)$$

where $q_{i,j}$ are the elements of Q . Using the Eqs.(31)-(33) and the properties of the Langevin forces, the power spectral density of the phase noise of the k^{th} mode can be written as follows:

$$\begin{aligned} S_{\phi_k}(\Omega') &= |q_{k,1}|^2 \langle \tilde{F}_{A_1} \cdot \tilde{F}_{A_1}^* \rangle + |q_{k,2}|^2 \langle \tilde{F}_{A_2} \cdot \tilde{F}_{A_2}^* \rangle + |q_{k,3}|^2 \langle \tilde{F}_{A_3} \cdot \tilde{F}_{A_3}^* \rangle \\ &+ |q_{k,4}|^2 \langle \tilde{F}_{\phi_1} \cdot \tilde{F}_{\phi_1}^* \rangle + |q_{k,5}|^2 \langle \tilde{F}_{\phi_2} \cdot \tilde{F}_{\phi_2}^* \rangle + |q_{k,6}|^2 \langle \tilde{F}_{\phi_3} \cdot \tilde{F}_{\phi_3}^* \rangle \\ &+ |q_{k,7}|^2 \langle \tilde{F}_N \cdot \tilde{F}_N^* \rangle \end{aligned} \quad (34)$$

where the spectral densities of the Langevin forces are:

$$\langle \tilde{F}_{A_k} \cdot \tilde{F}_{A_k}^* \rangle = \frac{R_{sp}}{2}, \quad (35)$$

$$\langle \tilde{F}_N \cdot \tilde{F}_N^* \rangle = \frac{I}{e} \quad (36)$$

$$\langle \tilde{F}_{\phi_k} \cdot \tilde{F}_{\phi_k}^* \rangle = \frac{R_{sp}}{2A_k^0{}^2}, \quad (37)$$

where R_{sp} is the spontaneous emission rate. Fig.1 and Fig.2 show an example of calculation results obtained with three different modes such as $A_2 > A_1 > A_3$, for three different values of the cavity resonance frequency detuning $\Delta\omega^i = (2\omega_2^i - \omega_1^i - \omega_3^i) : 0, \frac{\Delta\omega_l}{2}, \Delta\omega_l$. The other parameters used for these calculations are listed in Table 1.

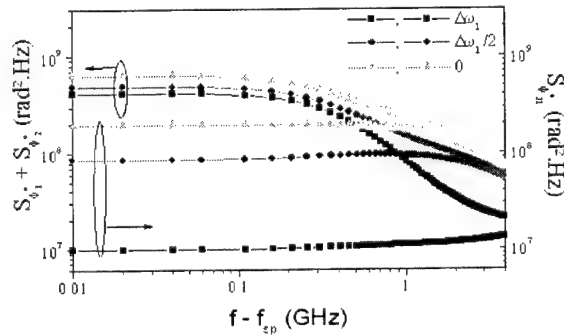


Figure 1. FM noise spectra of the relative phase ϕ_{21} and of the sum of the individual FM noise spectra of modes 1 and 2, in terms of analysis frequency.

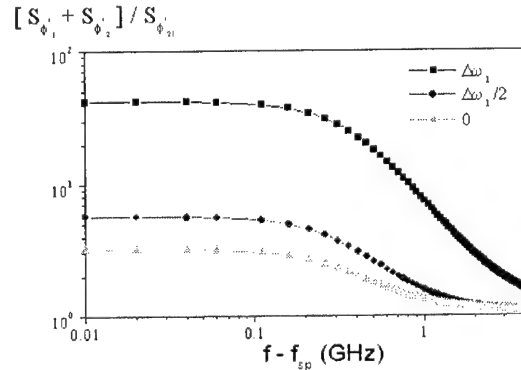


Figure 2. Ratio between FM noise spectral densities of the sum of the individual FM noise spectra of modes 1 and 2, and the ones of the relative phase ϕ_{21} , in terms of analysis frequency.

Fig.1 compares the FM noise spectra obtained for the relative phase ϕ_{21} with the sum of the individual FM noise spectra of modes 1 and 2, as a function of the analysis frequency around f_{sp} . Fig.2 represents the ratio, in a logarithmic scale. Firstly, Fig.1 shows that the FM noise spectra of the relative phase ϕ_{21} are different to that for the sum of the individual FM noise spectra of modes 1 and 2. They converge at high analysis frequencies, as expressed by Eq. (27). This demonstrates quantitatively the existence of phase correlation, as previously explained in section 3.3. Secondly, Fig.2 shows that the FM noise spectra of the relative phase ϕ_{21} are always smaller than the sum of the individual FM noise spectra of modes 1 and 2. This indicates that the FM noise spectra of ϕ_{21} have been drastically reduced through the non-linear FWM process in the vicinity of the self-pulsation frequency. So, it shows that FWM, by inducing a phase correlation between the modes, is responsible for the reduction of the spectral linewidth of the generated self-pulsating signal.

5. DISCUSSIONS AND CONCLUSIONS

Self-pulsation in DBR lasers have already been demonstrated. It is an oscillation of the output power due to the carrier modulation resulting from four-wave-mixing of adjacent longitudinal modes selected by the DBR mirror. Nevertheless, the phase correlation between modes inside the cavity, which is

Table 1. Parameter used for Fig.1 and Fig.2.

Parameters	Symbols	Values	Unit
Width and thickness	$w.d$	$0, 1.10^{-12}$	m^2
Length	L	1.10^{-3}	m
Volume	V	1.10^{-16}	m^3
Optical confinement	Γ	0.3	
Linewidth enhancement factor	α_H	5	
Speed of light	c	3.10^8	$m.s^{-1}$
Refractive index	n	3.4	
Group index	n_g	4	
Carrier lifetime	τ_e	2×10^{-9}	s
Photon lifetime	τ_p	2×10^{-12}	s
Spontaneous emission rate	R_{sp}	10^{12}	s^{-1}
Carrier number at transparency	n_{tr}	1×10^{24}	m^{-3}
Average carrier number	n_0	1.7×10^{24}	m^{-3}
Differential gain	a	3.2×10^{-20}	m^2
Mode 1 optical losses	γ_1	1.86×10^{11}	s^{-1}
Mode 2 optical losses	γ_2	1.70×10^{11}	s^{-1}
Mode 3 optical losses	γ_2	1.80×10^{11}	s^{-1}
Saturation power	P_{sat}	7×10^4	
Self-pulsation frequency	Ω_{sp}	40.10^9	Hz
Amplitude of mode 1	A_1	$A_2/2$	
Amplitude of mode 2	A_2	$3/2\sqrt{P_{sat}}$	
Amplitude of mode 3	A_3	$2A_2/5$	

necessary to the generation of self-pulsation, has not been previously clearly demonstrated. In this paper, a theoretical work based on the rate equations of three modes has been developed to study the time evolution of phases and amplitudes of the modes. From a steady-state analysis, it was possible to determine some criteria that the three modes have to fulfil in order to achieve self-pulsation. From a small-signal analysis, we were able to extract different phase noise spectral densities and to study the stability of our differential equation system. We also proved, qualitatively and quantitatively, that the phases of the different modes are partially correlated through the four-wave-mixing in this type of self-pulsating laser. Our analysis can satisfactorily explain the experimental results obtained from these lasers, and can be used to design high performance SP DBRs for clock recovery applications.

REFERENCES

1. M. J. O'Mahony, "The application of optical packet switching in future communication networks," *IEEE Communication Magazine* **19**, pp. 128-135, 2001.

2. A. Jourdan, "The perspective of optical packet switching in *ip* dominant backbone and metropolitan networks," *IEEE Communication Magazine* **39**, pp. 136–141, 2001.
3. B. Lavigne, P. Guerber, P. Brindel, E. Balmeffre, and B. Dagens, "Cascade of 100 optical 3R regenerators at 40 Gbit/s based on all-active Mach-Zehnder interferometer," *European Conference on Optical Communication*, pp. 290–291, 2001.
4. G.-H. Duan, C. Gosset, B. Lavigne, R. Brenot, B. Thedrez, J. Jacquet, and O. Leclerc, "40GHz all-optical clock recovery using polarization insensitive distributed Bragg reflector lasers," *Conference on Lasers and Electro Optics* **1898**, pp. 716–731, 2002.
5. G. P. Agrawal, "Highly nondegenerate four-wave mixing in semiconductor lasers due to spectral hole burning," *Appl. Phys. Letters* **5**, pp. 302–304, 1987.
6. G. R. Gray and G. P. Agrawal, "Importance of self-induced carrier-density modulation in semiconductor lasers," *IEEE Photon. Technol. Letters* **4**, pp. 1216–1219, 1992.
7. P. Gallion and G. Debarge, "Influence of amplitude-phase coupling on the injection locking bandwidth of a semiconductor laser," *Electronics Letters* **21**, pp. 264–266, 1985.
8. P. Gallion, H. Nakajima, C. Chabran, and G. Debarge, "Contribution of spontaneous emission to the linewidth of an injection-locked semiconductor laser," *Electronics Letters* **21**, pp. 626–628, 1985.

Radio-frequency spectra of long-cavity diode lasers under CW pumping

Chiyu Liu^a, Hongjun Cao^a, Marcita Benavidez^a, Hai Ling^a, Hui Su^a, Gregory M. Peake^b,
Petr G. Eliseev^{a,c}, and Marek Osinski^{a,*}

^aCenter for High Technology Materials, University of New Mexico, 1313 Goddard SE, Albuquerque, New Mexico 87106-4343

^bSandia National Laboratories, P.O. Box 5800, Albuquerque, New Mexico 87185

ABSTRACT

High-frequency spectra of free-running 5-mm-long triple-quantum-well graded-index separate-confinement heterostructure broad-area diode lasers emitting at $\sim 1\ \mu\text{m}$ are investigated in the range of 1–20 GHz using RF spectrum analyzer. The spectra reveal stable beat lines at ~ 8 and ~ 16 GHz, corresponding to single and double mode spacings between adjacent longitudinal modes. A current-dependent peak, varying from 0.6 to 2 GHz, is associated with the relaxation resonance. Measurements of mode beating spectra provide additional characterization of diode laser emission for coherent light applications.

Key words: Semiconductor lasers, quantum wells, mode beating

1. INTRODUCTION

High-frequency characterization of semiconductor lasers is an important topic in studies of high-speed modulation, mode locking, Q-switching, mode selection and tuning, *etc.* Beating between longitudinal modes in typical diode lasers occurs at frequencies too high to be measured directly, in the THz frequency range. Consequently, mode beating was initially investigated in external-cavity diode lasers [Bogatov 1979], [Bachert 1981], with mode spacings of ~ 100 MHz. More recently, beating between adjacent longitudinal modes was observed in lasers with 2–2.5-mm-long cavities [Lau 1985], [Sharfin 1994]. Here, we study mode beating spectra in diode lasers with cavity length of ~ 5 mm. For the first time, in addition to previously reported beat signals from adjacent longitudinal modes, we have observed beating between second-neighbor modes separated by double spacing.

2. CHARACTERIZATION OF LONG-CAVITY InGaAs/GaAs/AlGaAs GRIN-SCH DIODE LASERS

2.1 Device Structure

InGaAs/GaAs/AlGaAs triple-quantum-well graded-index separate-confinement heterostructure (GRIN-SCH) samples were grown by low-pressure MOCVD on *n*-type GaAs substrates with a (100) 2° (110) orientation. A schematic illustration of the layer sequence in fabricated laser devices is shown in Fig. 1. After a 1 μm Te-doped $\text{Al}_{0.3}\text{Ga}_{0.7}\text{As}$ *n*-cladding layer and a 1000 Å Te-doped $\text{Al}_x\text{Ga}_{1-x}\text{As}$ ($x = 0$ to 0.3) linearly graded index (GRIN) *n*-layer, the active region, consisting of five ~ 10 -nm-thick undoped GaAs barriers and three 10-nm-thick undoped $\text{In}_{0.2}\text{Ga}_{0.8}\text{As}$ wells, was grown. A 1000-Å-thick C-doped $\text{Al}_x\text{Ga}_{1-x}\text{As}$ ($x = 0$ to 0.3) linearly graded index (GRIN) *p*-layer capped the active region, followed by a 1- μm thick C-doped $\text{Al}_{0.3}\text{Ga}_{0.7}\text{As}$ *p*-cladding layer, and a 50 nm p^+ -GaAs contact layer. Long-cavity broad-area lasers emitting at $\sim 1\ \mu\text{m}$ were cleaved from a wafer with 50- μm -wide *p*-side stripe contacts.

*Contact author: Email: osinski@chtm.unm.edu; Telephone: (505) 272-7812; Fax: (505) 272-7801; <http://www.chtm.unm.edu>

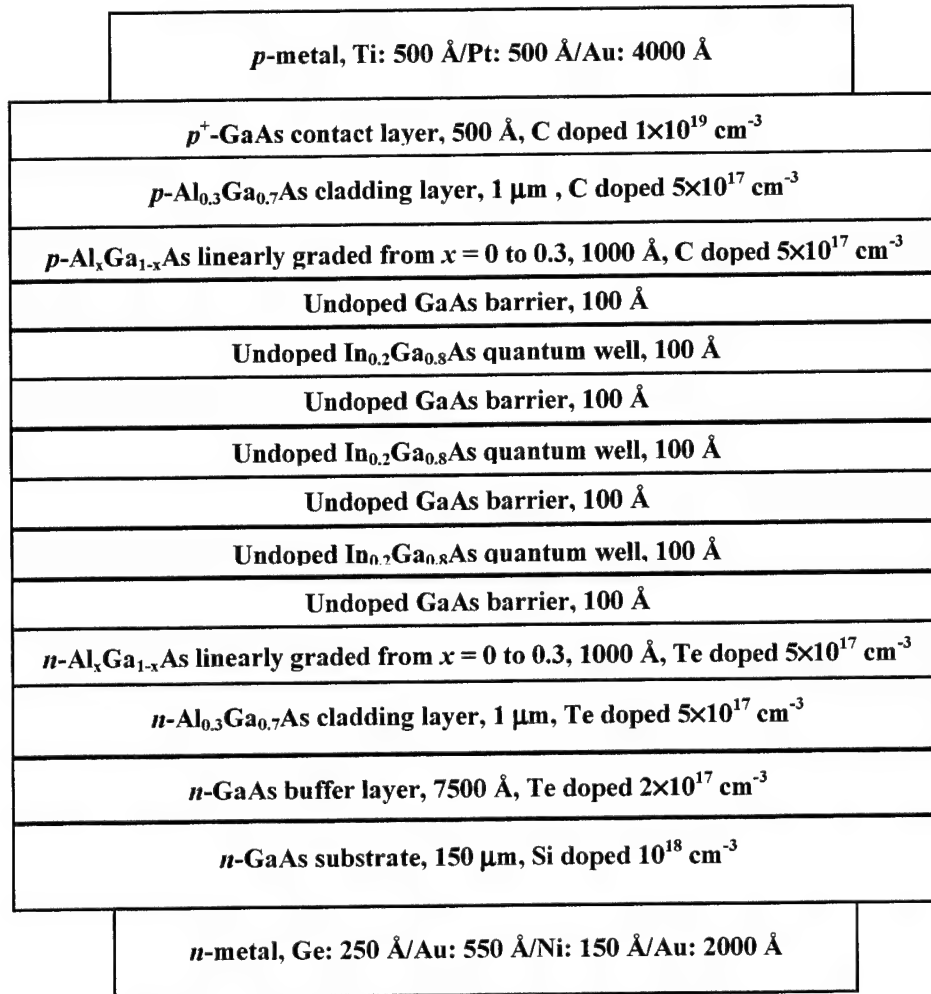


Fig. 1. Schematic structure of a laser fabricated from wafer EMC6979.

2.2. Electrical and Optical Characterization

Routine characterization data of I - V and L - I curves were collected. An ILX Lightwave modular laser controller LDC-3900 (CW) was used as current source for the lasers. A Keithley 200 multimeter was used to measure the voltage. An 1830-C power meter and an 818-Si-1035 detector were used to detect the light output from the laser facet. The data were assembled and processed by a computer running LabVIEW. The measurements were conducted in steps of 5 mA in the range from zero to 1000 A. The lasers were placed on a thermostabilized holder and a constant temperature of 10 °C was maintained during tests under dc bias.

Fig. 2 illustrates typical I - V and L - I characteristics of the long-cavity lasers. The threshold current is ~ 710 mA, as confirmed by a kink in the differential IdU/dI curve. The threshold current density at 10 °C is 270 A/cm^2 . The series resistance of the device, extracted from the differential IdU/dI characteristic, is 0.455Ω , and the junction voltage V_{pn} above threshold is 1.2458 V. The voltage saturation above the threshold is quite complete before kinks at L - I curve. Notice that the photon energy of laser emission is 1.238 eV, i.e. 7.2 meV lower than the quasi-Fermi-level separation in the active region.

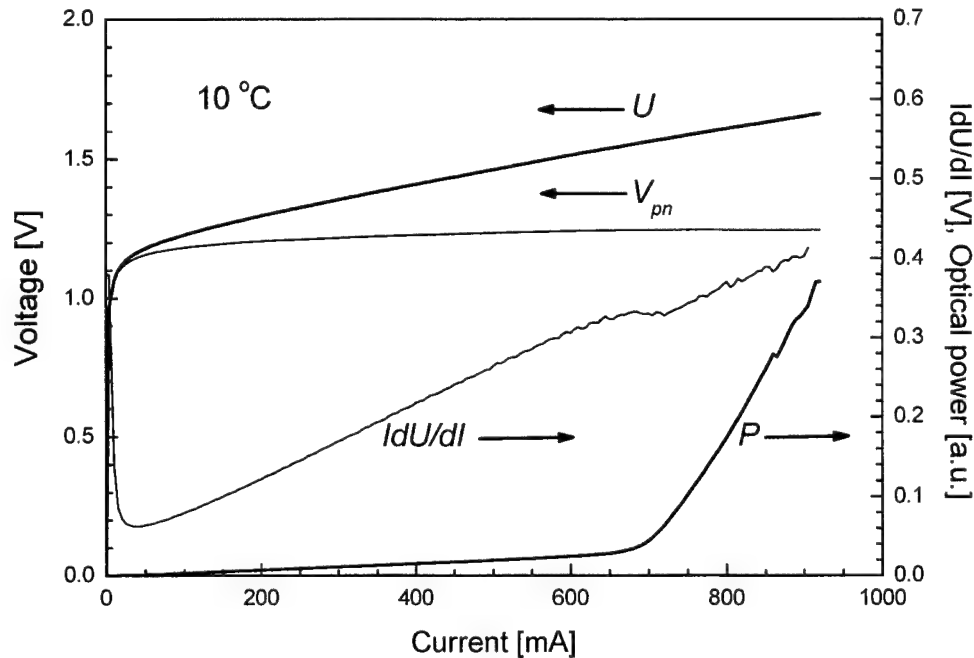


Fig. 2. Basic characterization data of a 4987- μm -long 50- μm -wide diode laser operating cw at 10 °C. P – optical power, U – diode voltage, I – current, V_{pn} – the junction voltage (after subtraction from U the voltage drop due to series resistance), dU/dI – differential I - V curve demonstrating a kink associated with lasing threshold at ~ 710 mA.

2.3. Optical Emission Spectra

The optical output from the laser was collected with a collimating lens and focused onto the entrance slit of a monochromator (CVI DK 480) with the maximum resolution of 0.03 nm. The scan step was 0.01 nm and the entrance and exit slits were set to 40 μm . As previously, the laser was placed on a thermostabilized holder and the temperature of 10 °C was maintained during measurements under dc current injection.

Using the known parameters such as central wavelength of 1 μm , cavity length of 5 mm and group index n_g of 3.9 (calculated from the spectra of a short cavity edge-emitting laser cleaved from the same bar), the longitudinal mode spacing for a 5-mm-long laser can be estimated as:

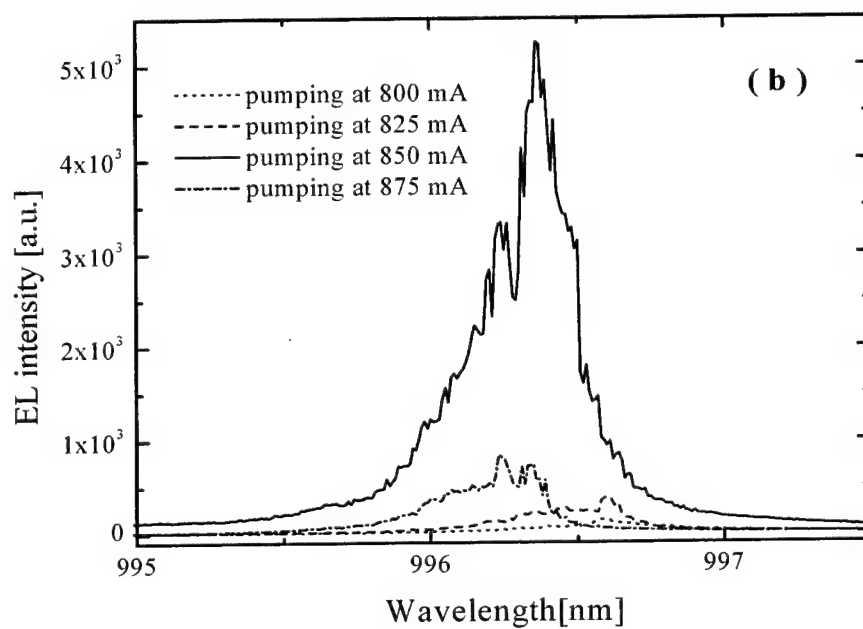
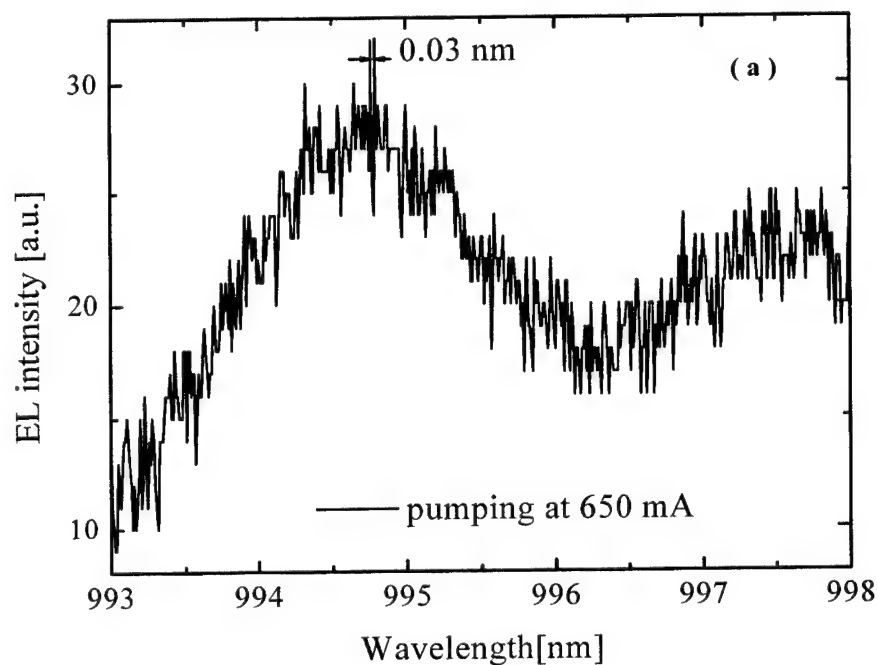
$$\Delta\lambda = \frac{\lambda^2}{c} \cdot \Delta\nu = \frac{\lambda^2}{c} \cdot \frac{c}{2n_g L} = \frac{\lambda^2}{2n_g L} = \frac{(1000 \text{ nm})^2}{2 \times 3.9 \times 5000 \times 10^3 \text{ nm}} = 0.0256 \text{ nm} , \quad (1)$$

$$\Delta\nu = \frac{c}{\lambda^2} \cdot \Delta\lambda = 7.69 \text{ GHz} . \quad (2)$$

As indicated by Eq. (1), the longitudinal mode spacing is smaller than the resolution of the monochromator. Therefore, we do not expect to be able to resolve the individual longitudinal modes.

Fig. 3(a) shows a spontaneous emission spectrum at an injection current lower than the lasing threshold. The spacing between the longitudinal modes shown in Fig. 3(a) is ~ 0.03 nm (limited by the monochromator resolution). Fig. 3(b) shows laser emission spectra at four values of injection current. It can be seen that the emission intensity increased when

the injection current was increased from 800 to 850 mA, but decreased when injection current reached 875 mA. We attribute this reduction in the output power to internal heating of the active region. The spectra shown in Fig. 3(c) were measured four times at intervals of about 10 minutes between scans, and demonstrate good long-term stability, as the successive scans could be superimposed on each other with no discernible changes of spectral features.



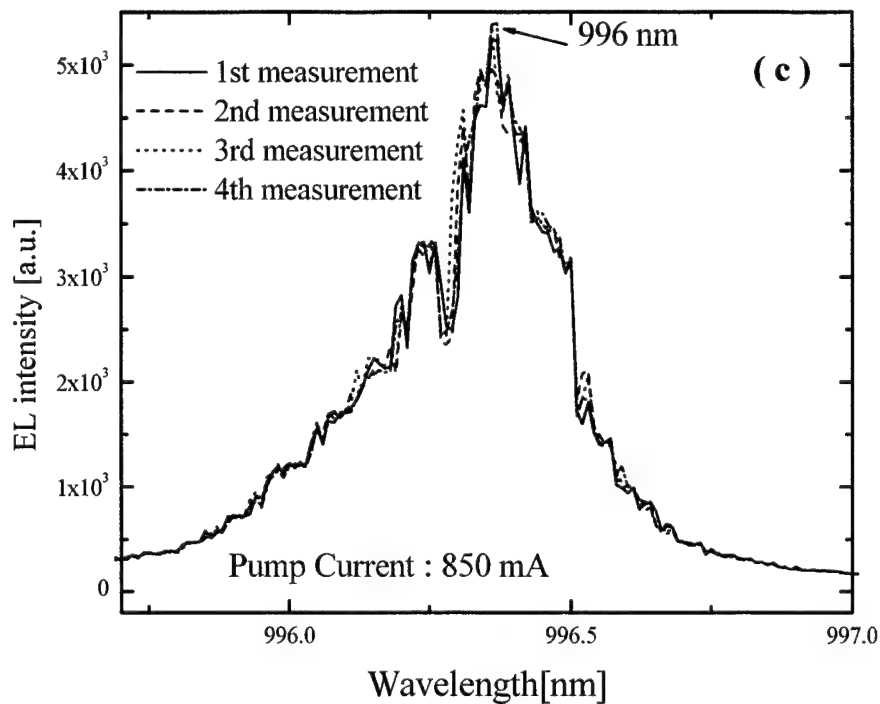


Fig. 3. Optical emission spectra from a 4987- μm -long 50- μm -wide diode laser operating cw at 10 °C.

- (a) Spontaneous emission spectrum taken at the pumping level of 650 mA;
- (b) Laser emission spectra taken at four values of injection current;
- (c) Laser emission spectra measured four times at intervals of about 10 min between scans at a fixed current of 850 mA.

2.3.1. FTIR Measurements

In order to resolve the multi-longitudinal-mode spectra, the optical output from the long-cavity lasers was analyzed using a Nicolet Magna-IR 760 Fourier Transform Infrared (FTIR) spectrometer with ~ 0.0125 nm resolution. The emission from the laser was collected with an objective lens and focused onto the entrance slit of the FTIR spectroscope. The laser was pumped by a quasi-cw current source with 95% duty cycle.

Typical optical emission spectra are shown in Fig. 4 for two different pumping levels. Multimode operation can be clearly seen, with periodic longitudinal mode spectral structure. The longitudinal mode spacing is ~ 0.026 nm, corresponding to the effective modal index of 3.83. The main emission line is slightly above 1001 nm, with ~ 60 subsidiary longitudinal modes spanning the range between 999.5 and 1001.3 nm.

The FFT analysis of optical spectra, shown in Fig. 5, gives the mode spacing frequency between adjacent longitudinal modes $\Delta\nu = 7.98$ GHz, and $2\Delta\nu = 15.9$ GHz.

3. DIRECT MEASUREMENTS OF MODE BEATING IN MICROWAVE SPECTRA

The experimental setup for beat frequency measurements is shown in Fig. 6. The measurements were performed by coupling the optical output via an optical fiber into a fast speed photodetector (Newport 1014). The output of the photodetector was amplified by two serially connected 30-dB electrical signal amplifiers, and then analyzed by a electrical spectrum analyzer (HP 7000 series). The combined bandwidth of the system was up to 22 GHz. The laser was placed on a thermostabilized holder and the temperature of 10 °C was maintained during tests under dc current injection.

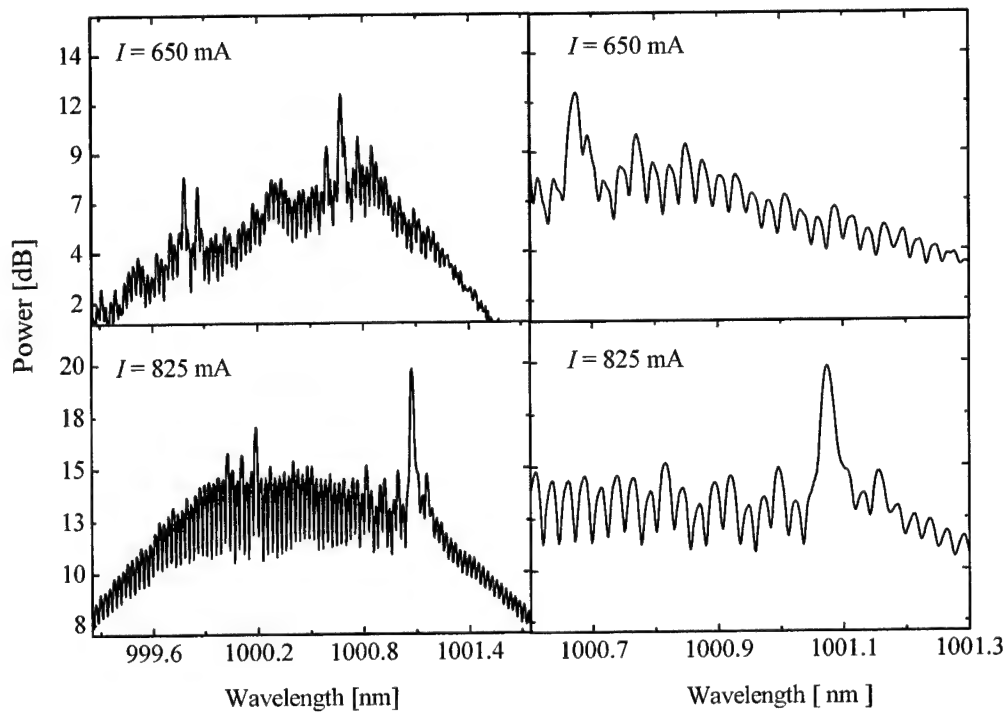


Fig. 4. Optical emission spectra from a 4987- μm -long 50- μm -wide diode laser obtained using Fourier-transform infrared spectrometer. Multiple longitudinal modes can be clearly seen, with the main emission line slightly above 1001 nm.

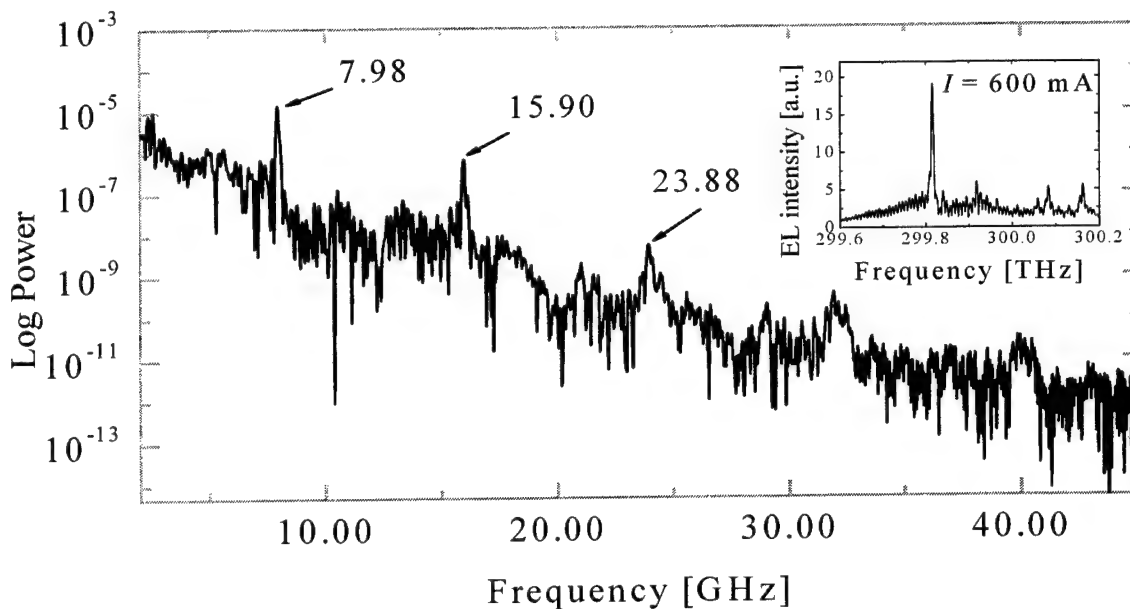


Fig. 5(a). The optical spectrum from a 4987- μm -long 50- μm -wide diode laser (insert) and its FFT at the pumping current of 600 mA.

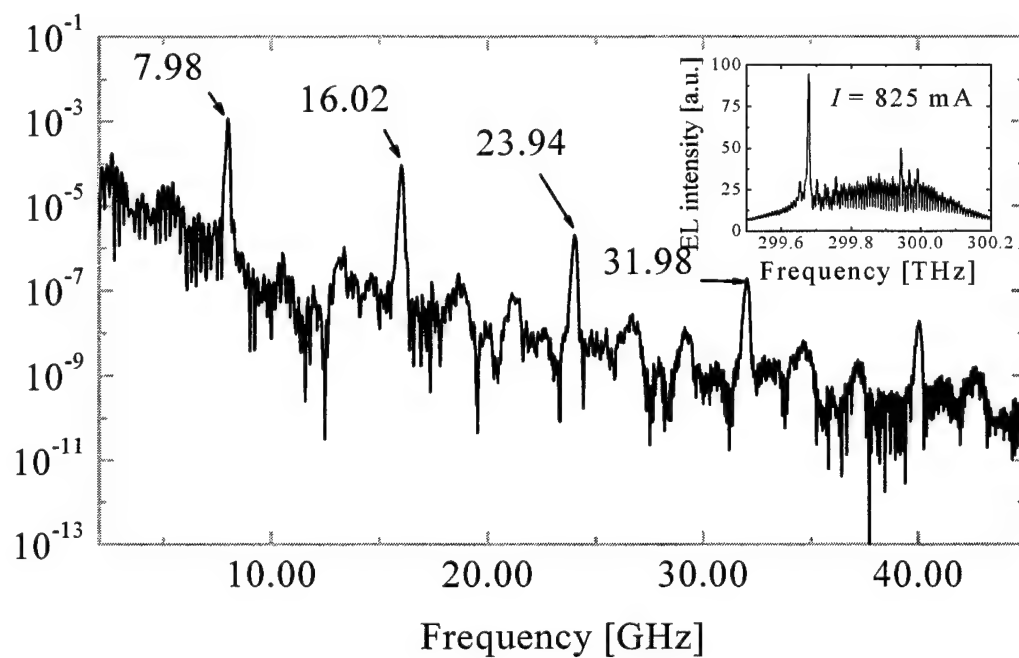


Fig. 5(b). The optical emission spectrum from a 4987- μm -long 50- μm -wide diode laser (insert) and its FFT at the pumping current of 825 mA.

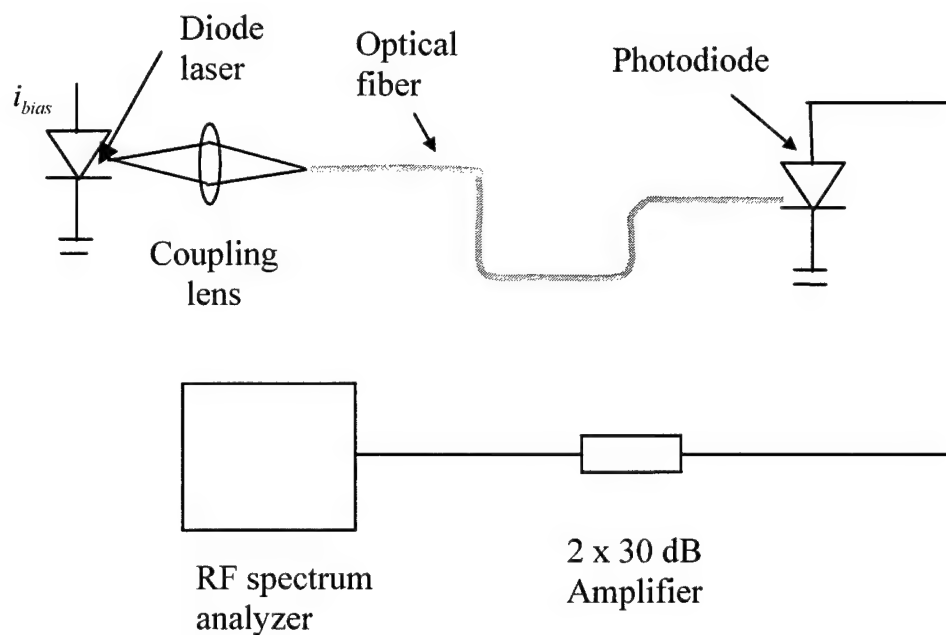


Fig. 6. Experimental setup for beat frequency measurements.

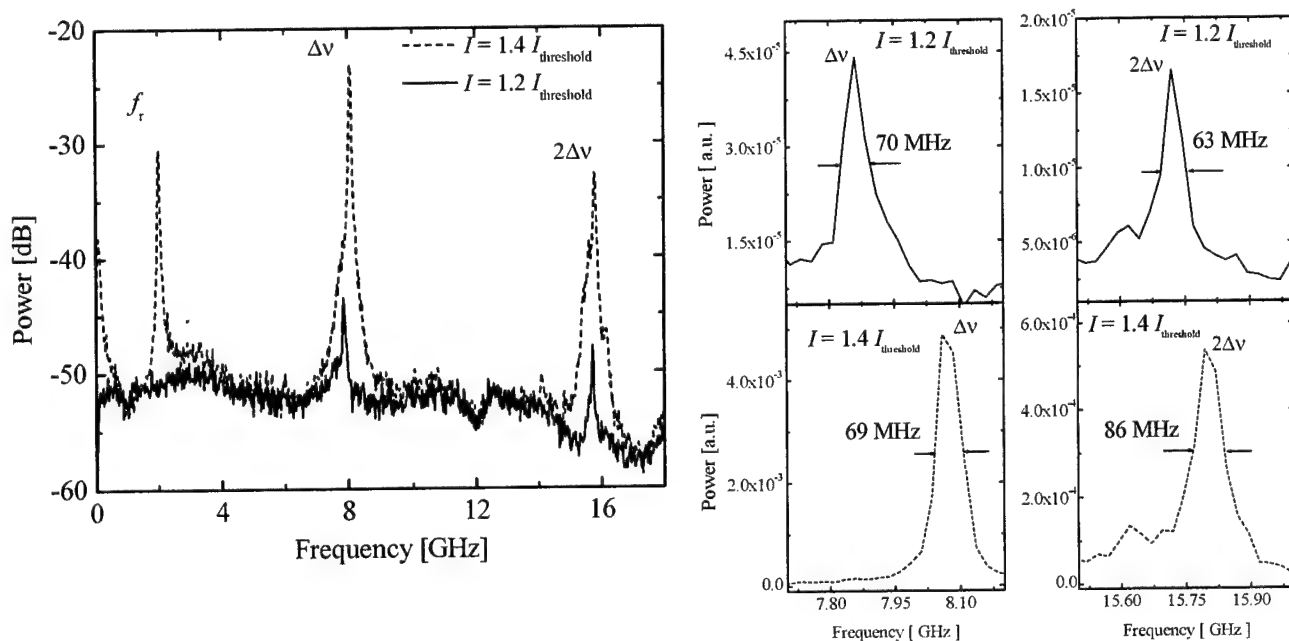


Fig. 7. Typical microwave spectra of the detected laser emission at different injection current. Stable mode beating peaks are seen near 8 and 16 GHz. A current-dependent peak at 1-2 GHz is due to the relaxation resonance in the laser.

The survey rf spectra are shown in Fig. 7. A current-dependent peak associated with relaxation oscillations in the laser appears above the pumping level of ~ 770 mA. The frequency f_r of this peak increase roughly in proportion with a square root of the optical power, in agreement with the rate equation analysis. It reaches ~ 2 GHz at the injection current of 1 A. Relatively stable peaks at ~ 8 and ~ 16 GHz are attributed to longitudinal mode beating, as they correspond very well with the output beam coupling into the fast detector is blocked. This proves that the 8 GHz signal and its second harmonic are not produced by electromagnetic interference from cell phone and decimeter TV communications.

Shifts of the rf spectrum peak positions with the pumping current are shown in Fig. 8. Table 1 contains numerical data about position and full width at half maximum (FWHM) of the observed peaks. The FWHM of mode beating peaks Δv and $2\Delta v$ at 1 A is 23 MHz and 63 MHz, respectively, while the FWHM of the relaxation oscillation peak is 69 MHz. The latter peak seems quite narrow, indicating a possibility of quasi-regular pulsations rather than random fluctuations. Some narrowing of the mode-beat linewidths with increasing current can be an indication of a self-induced beat-frequency locking [Lamb 1964].

Table 1. Peak positions and full width of half magnitude (FWHM) for oscillation and beat signal

Current [mA]	Relaxation oscillation frequency f_r		1 st beat frequency Δv		2 nd beat frequency $2\Delta v$	
	Peak position [GHz]	FWHM [GHz]	Peak position [GHz]	FWHM [GHz]	Peak position [GHz]	FWHM [GHz]
776	0.67	—	7.87	—	15.7	—
850	1.2	0.12	7.87	0.066	15.7	0.068
900	1.5	0.12	7.87	0.08	15.7	0.027
950	1.7	—	7.96	0.022	15.8	0.112
1000	2.05	0.069	8.1	0.023	15.8	0.063

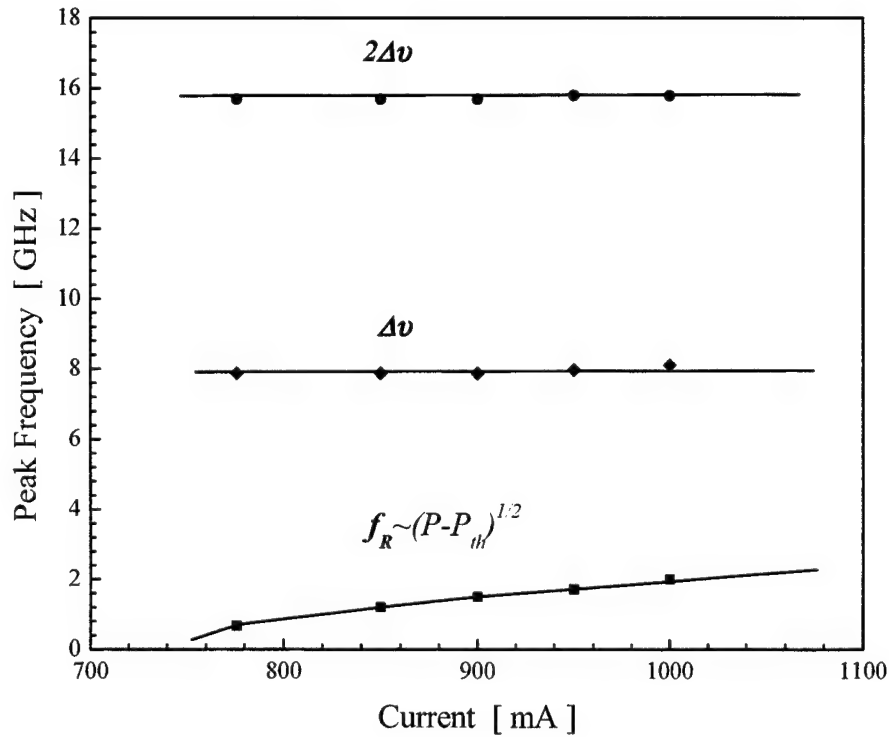


Fig. 8. RF spectral peak positions versus injection current: f_r is the relaxation oscillation peak, $\Delta\nu$ and $2\Delta\nu$ are longitudinal mode beating peaks for adjacent modes and for the next-nearest-neighbor modes, respectively. The relaxation oscillation frequency f_r is fitted by the square-root dependence on the optical power P minus the power P_{th} near the threshold, representing the power of spontaneous emission.

The relaxation oscillations are produced by non-stationary variations of the refractive index under the influence of varying carrier density. According to the rate equation analysis, the relaxation oscillation frequency f_r increases in proportion with the square root of $(I - I_{th})$, as given by the following equation:

$$f_r = 2\pi \left[\frac{\Gamma_v g a}{qV} \eta_i (I - I_{th}) \right]^{1/2} \quad (3)$$

In Fig. 9, the curve of relaxation oscillation peak positions versus injection current is shown and it is fitted by an expression corresponding to Eq. (3).

A simple structure of the mode-beating peaks and their relatively narrow linewidth indicate quite low dispersion of the group index in the active waveguide (especially since numerous modes are expected to contribute to the beating signal). The linewidth of the $\Delta\nu$ -peak can be narrower than the linewidth of the individual mode of lasing because fluctuations of the material optical parameters could affect the instantaneous frequency of the modes in the same manner. Therefore, they are eliminated in the integrated rf spectrum. For example, self-sustained pulsations result in a frequency chirp, thus broadening the dynamic linewidth of individual modes. The chirp is produced by non-stationary variations of the refractive index caused by variation in the carrier density [Eliseev 1979]. However, the longitudinal mode spacing can still remain quite constant, producing the narrow beat peak. The spectral resolution in the FTIR measurements of optical spectra is 0.0125 nm (3.75 GHz). Thus, the observed rf spectra indicate that the broadening due to the chirp has to be smaller than ~3.75 GHz.

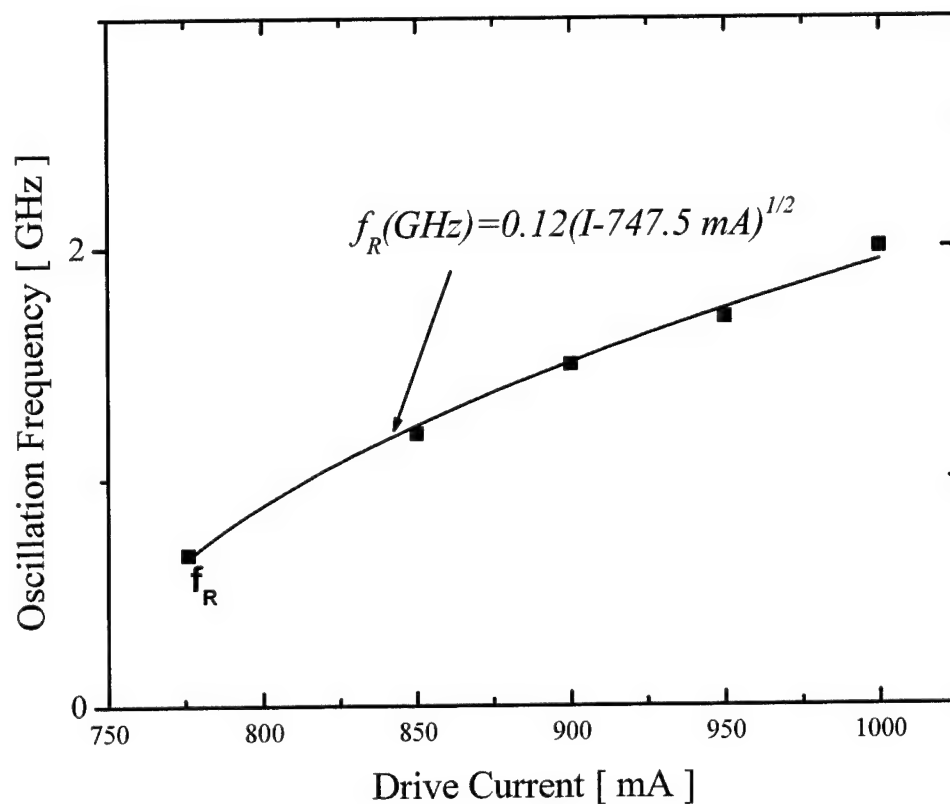


Fig. 9. The relaxation oscillation peaks versus drive current and its fit.

At currents exceeding 950 mA, the beat peaks drift slightly towards higher frequencies. This drift is smaller than 1% in the $2\Delta\nu$ -peak, and smaller than 3% in the $\Delta\nu$ -peak. Most likely it is caused by some heating of the active medium as the refractive index of semiconductor media at constant wavelength increases along with temperature rise.

4. CONCLUSIONS

In conclusion, we have observed mode beating spectra at frequencies $\Delta\nu$ and $2\Delta\nu$ in free-running long-cavity diode lasers and measured corresponding peak positions and linewidths. The beating frequency of adjacent longitudinal modes in a 5-mm long diode is ~ 8 GHz. The relaxation oscillation peak was also recorded. We believe this paper reports the first experimental observation of mode beating at doubled frequency spacing $2\Delta\nu$.

5. ACKNOWLEDGMENTS

This work was supported by the NASA Faculty Awards for Research program (NASA Research Grant NAG8-1664) and by the NASA Goddard Space Flight Center (NASA Grant NAG5-10372).

REFERENCES

- [Bachert 1981] H. Bachert, A. P. Bogatov, Yu. V. Gurov, P. G. Eliseev, O. G. Okhotnikov, G. T. Pak, M. P. Rakhvalski, and K. A. Khairtdinov, "Radio-frequency spectra of mode beating and intensity pulsing of injection laser with external dispersive cavity", *Sov. J. Quantum Electron.*, **8** (#9), pp. 1957-1962 (1981).
- [Bogatov 1979] A. P. Bogatov, Yu. V. Gurov, P. G. Eliseev, O. G. Okhotnikov, G. T. Pak, and K. A. Khairtdinov, "Low-frequency pulsations in the output intensity and multimode operation of GaAs-AlGaAs C.W. diode laser coupled to an external dispersive cavity", *Solid State & Electron Dev.* **3** (#3), pp. 72-74 (1979).
- [Eliseev 1979] P. G. Eliseev, "Interpretation of the frequency self-modulation of the injection laser emission", *Sov. J. Quantum Electron.*, **6** (#10), pp. 1443-1445 (1979).
- [Lamb 1964] W. E. Lamb, "Theory of an optical maser", *Phys. Rev.*, **A134**, pp. 1429-1450 (1964).
- [Lau 1985] K. Lau, I. Ury, and A. Yariv, "Passive and active mode locking of a semiconductor laser without an external cavity", *Appl. Phys. Lett.*, **46** (#12), pp. 1117-1119 (1985).
- [Sharfin 1994] W. F. Sharfin, J. Schlafer, and E. S. Koteles, "Observation of mode beating and self-frequency locking in a nearly single-mode semiconductor laser", *IEEE J. Quantum Electron.*, **30** (#8), pp. 1709-1712 (1994).

Synchronization in Chaotic Vertical-Cavity Surface-Emitting Semiconductor Lasers

Natsuki Fujiwara and Junji Ohtsubo

Faculty of Engineering, Shizuoka University, 3-5-1 Johoku, Hamamatsu, 432-8561 Japan

Abstract

Chaos synchronization in polarization selected mutually coupled vertical-cavity surface-emitting semiconductor lasers (VCSELs) is experimentally investigated in a low-frequency fluctuation regime. Two lasers synchronize in one of the orthogonal polarization modes selected for synchronization. The counterpart polarization components also show synchronized outputs due to anti-phase oscillations of VCSELs.

Keywords: VCSELs, chaos, injection locking, polarization

1. Introduction

Vertical-cavity surface-emitting lasers (VCSELs) have been studied extensively in the past decade because of several useful characteristics which make them very attractive for practical applications. Indeed, they show many advantages over ordinary edge-emitting semiconductor lasers, such as their small size, emission of circular beam, and the availability of a large-scale laser array sources. They exhibit very low laser threshold and have single longitudinal mode operation. Despite of their high facet reflectivity (more than 99%), VCSELs are also sensitive to external optical feedback and optical injection like edge-emitting semiconductor lasers.¹⁻³ Dynamics and instabilities of VCSELs due to optical feedback and optical injection have also been studied.

Meanwhile, chaos synchronization has been extensively investigated in semiconductor laser systems for its potential applications in chaotic secure communications.⁴⁻⁶ Also chaos synchronization in VCSELs has been demonstrated besides of systems of edge-emitting lasers. Up to now, the present authors have experimentally examined chaos synchronization under mutually coupled configurations of VCSELs in low-frequency fluctuation (LFF) regimes.⁷ We have observed chaotic synchronization in either x - or y -polarization component of the laser outputs, or even in both for the polarization components in VCSELs. Here, we define y -polarization mode as polarization direction along the optical axis of the laser material and x -polarization mode as the orthogonal direction to the y -component. In chaos synchronization in VCSELs, the polarization modes play an important role. Under the configuration of mutually coupled VCSELs both for the polarization components, we have observed three typical cases of synchronization. One is the case of chaos synchronization under x -polarization mode. In this case, the y -polarization components also synchronize with each other due to anti-phase oscillations, which are typical dynamic characteristics of VCSELs. The second case is the opposite case for the first and is chaos synchronization of y -polarization components. Then the x -polarization components synchronize by anti-phase oscillations. The third case is synchronization both for x - and y -polarization components. In the third case, both polarization modes are chaotically synchronized.

In the previous experiments,⁷ both of the polarization modes were mutually injected for synchronization. In this report, we experimentally investigate chaos synchronization in VCSELs for selected polarization components. The experimental configuration is almost the same as the previous one except for the use of a polarized beam splitter to select one of the polarization modes in VCSELs. We successfully observe chaos synchronization for selected polarization modes. Under the synchronization condition, the counterpart modes still synchronize due to anti-phase oscillations in VCSELs.

2. Experimental

The experimental setup is shown in Fig. 1. VCSELs (AXT VY-TI11-4FO1 VCSELs) used in the experiments were oscillated at a wavelength of 780 nm and a maximum optical power of 10 mW. The y -polarization oscillation is a dominant laser mode close to the threshold (y is the direction along the optical axis of laser material). The x -polarization mode is here defined as the counterpart oscillation perpendicular to the y -polarization mode. With the increase of the

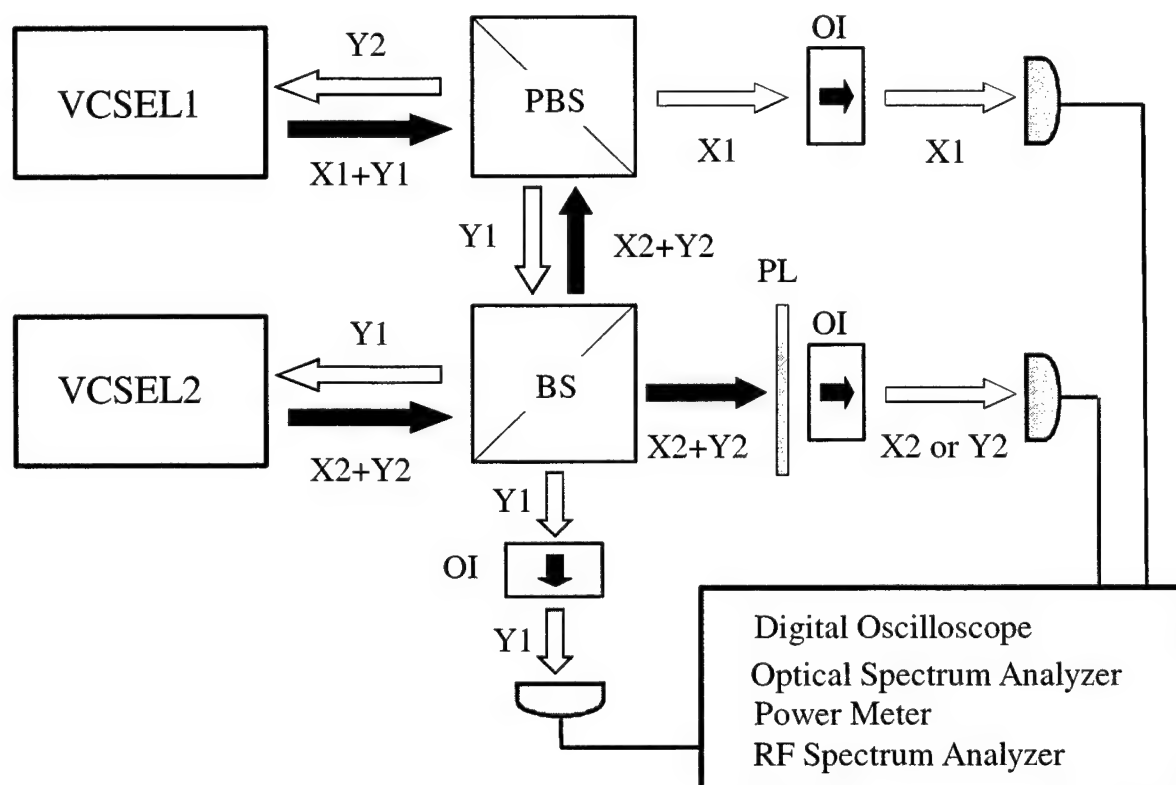


Fig. 1 Experimental setup. PBS: polarization beam splitter, BS: beam splitter, OI: optical isolator, PL: polarizer.

injection current, the output power of the x -polarization mode increased and had a comparable power with that of the y -polarization mode, although the light output of the x -polarization mode was always lower than that of the y -polarization mode. The two lasers were mutually coupled through a polarization beam splitter PBS to select a particular polarization mode, thus VCSEL1 was injected by VCSEL2 and VCSEL2 was also injected by VCSEL1 for the polarization oscillations. A neutral density filter NDF was used to control the injection strength. The bias injection currents of the two lasers were controlled by stabilized current source drivers, and the laser temperature was stabilized by automatic temperature control circuits. The two lasers used in our experiments had similar values of the device parameters with each other. In spite of the similar device parameters, each VCSEL showed quite different characteristics of the oscillation for the threshold injection current and the L-I characteristics including x - and y -polarization outputs.

The free-running threshold currents of VCSEL1 and VCSEL2 were 6.2 and 6.4 mA at temperature of 25.8 degree, respectively. The injection currents for VCSEL1 and VCSEL2 were biased slightly above the threshold currents. At the bias injection current, the output power of the x -polarization mode of VCSEL1 was very low and it oscillated at almost only y -polarization mode. On the other hand, comparable output power for the y - and x -polarization modes was observed in VCSEL2. Under these conditions, the lasers were oscillated at their lower order spatial modes (LP_{01} and LP_{11} modes). Each spatial mode was stable at solitary oscillation. The two lasers were separated 120 cm in space. Therefore, the coupling time of light between the two lasers was $\tau=4$ ns. The outputs from the two lasers were detected by a high-speed photo-detector (NEW FOCUS 1537M-LF: bandwidth of 6.0 GHz). Chaotic waveforms were analyzed by a RF spectrum analyzer (HP 8595E: bandwidth of 6.5 GHz) and a fast digital oscilloscope (HP 54845A: bandwidth of 1.5 GHz). Also, the optical outputs were analyzed by an optical spectrum analyzer (ADVANTEST Q8344A, maximum resolution of 0.05 nm), a wavelength meter (ADVANTEST QT8325, maximum resolution of 0.001 nm), and a Fabry-Perot spectrometer (free spectral range of 10GHz).

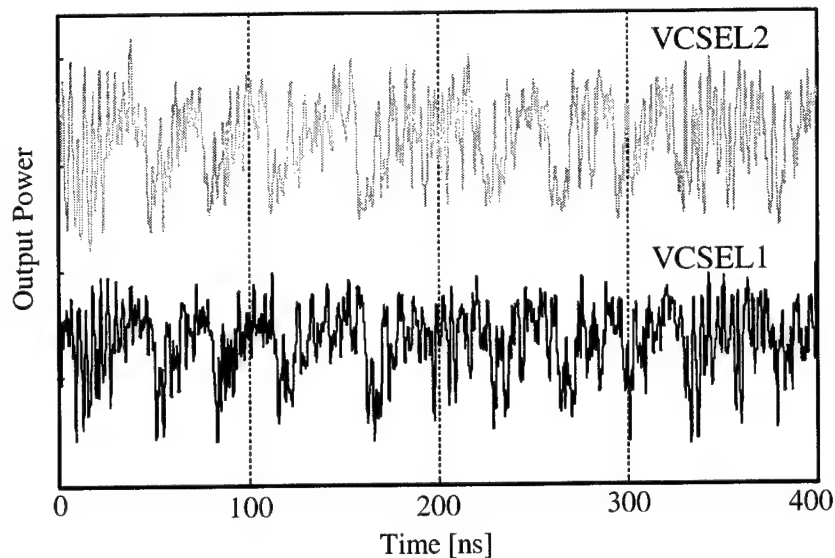


Fig. 2 Time series of y-polarization modes at synchronization..

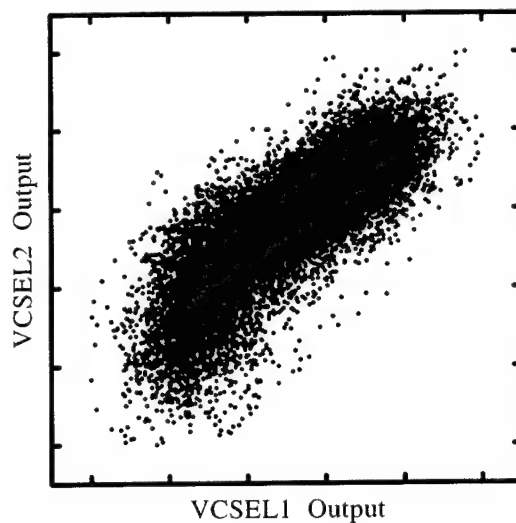


Fig.3 Correlation plot.

3. Results and discussion

We first show the results for mutually coupling of the y-polarization components at the bias injection currents of 6.9 mA ($1.11I_{th}$, where I_{th} is the laser threshold current) for the VCSEL1 and 7.1 mA ($1.15I_{th}$) for the VCSEL2, where the temperatures were fixed at 25.5 and 25.8 degrees, respectively. Figure 2 show time series of the two laser outputs for the y-polarization components. We can see low-frequency fluctuations (LFFs) in the waveforms, which have been

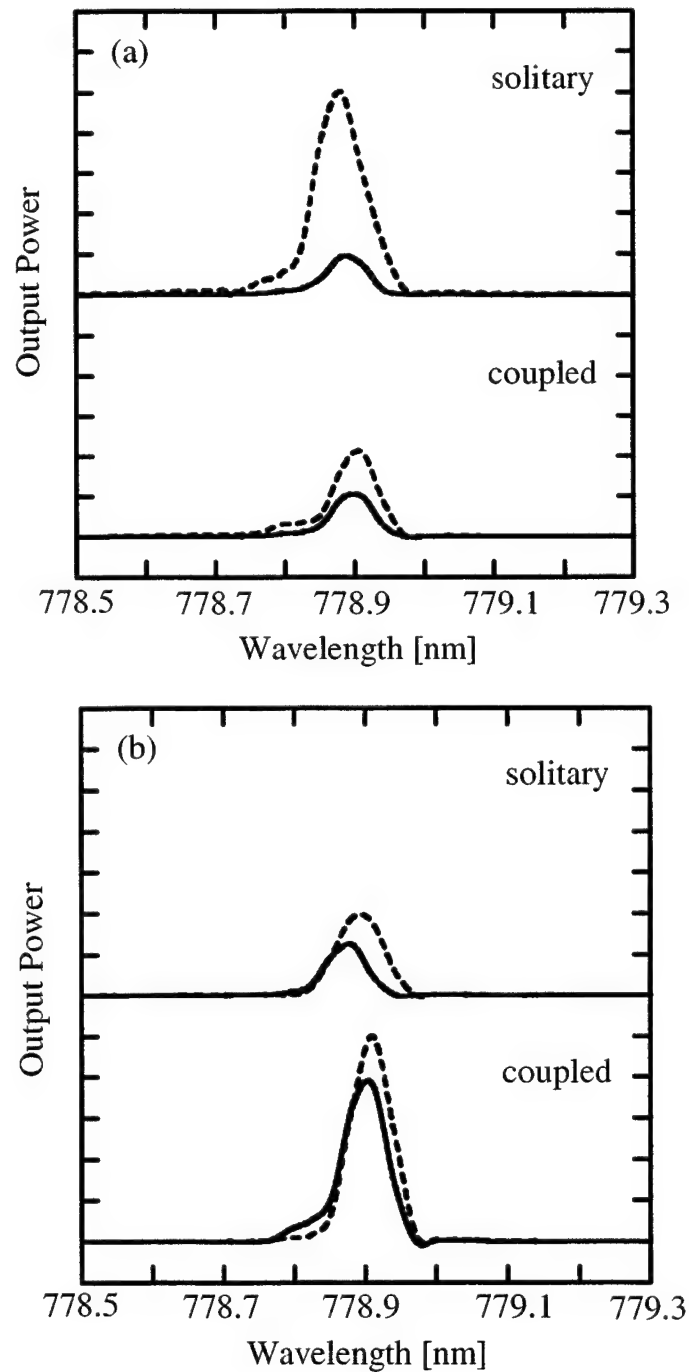


Fig. 4 Optical spectra of laser oscillation for (a) x - and (b) y -polarization modes.
Solid line: VCSEL1, broken line: VCSEL2

recently observed in VCSELs with optical feedback.² LFF is one of chaotic oscillations in semiconductor lasers and has sudden power dropouts and stepwise power recovery to the steady state following the dropout. The time duration of each step in the power recovery process is equal to the round-trip time 2τ of light in the mutual optical injection system. In this figure, VCSEL1 was a leader to VCSEL2 and the time lag between the waveforms was to be read 4 ns, which is

Table 1 Wavelength and output power

		VCSEL1	VCSEL2
X wavelength	solitary	778.884 [nm]	778.880
	coupled	778.902	778.914
Y wavelength	solitary	778.902	778.882
	coupled	778.911	778.911
X output power	solitary	17.33 [μ W]	92.24
	coupled	18.37	38.79
Y output power	solitary	146.07	223.63
	coupled	442.73	584.12

equal to the coupling time τ of light between the two lasers. Figure 3 is correlation plot between the two waveforms. The correlation coefficient was calculated to be 0.816. Since optical power of x -polarization components were too weak, we could not observe the time variations for that components by our detector. But we can expect that the x -polarization mode of each VCSEL was oscillated at out-of-phase with the y -polarization component. We will refer to this point in the following experiment.

Figure 4 shows the optical spectra of the output powers at solitary and mutually coupled oscillations observed by the optical spectrum analyzer. Table1 is a summary of the data analyzed by the wavelength meter and the power meter. These data correspond to the laser oscillations in Fig. 2. The upper and lower traces in Fig. 4 are the spectra at solitary and optically coupled oscillations, respectively. Peak optical powers of the observed spectra for each polarization component were normalized to the maximum intensity among the polarization components. After the optical coupling, the power of the y -component was amplified, while that of the x -polarization component was reduced. The wavelengths of the both lasers were shifted due to the mutual optical injection. After optical coupling, the oscillation wavelengths of the y -polarization components coincided with each other at 778.911 nm. The wavelengths of the y -polarization modes were locked at 778.911 nm by the mutual optical injection, while the x -components had different wavelengths. It is considered that the oscillation of the y -polarization mode of VCSEL2 was locked to that of VCSEL1 and the two lasers synchronized at that wavelength.

We also examined mutually coupling of the x -polarization oscillations. Synchronization of chaotic oscillations was obtained for the bias injection currents of 7.9 mA ($1.26I_{th}$) for the VCSEL1 and 7.6 mA ($1.19I_{th}$) for the VCSEL2, where the substrate temperatures were fixed at 25.5 and 25.8 degrees, respectively. From the observed optical spectra, it was judged that the two lasers chaotically synchronized at x -polarization components. However, the output powers for the x -polarization components were so low that we could not observed chaotic variations for the components. The optical powers of the x -polarization components were amplified by optical injection, but the optical powers were insufficiency to detect by our detector. Instead, we observed the output powers of the y -components. Figure 5 shows time series of the y -polarization components for the two laser outputs. We can see chaotic waveforms. The observed waveforms did not show clear low-frequency fluctuations, however it was still not a fully developed chaotic variations as observed from the waveforms. These oscillations are originated from anti-phase oscillations which are the typical feature of VCSELs. In this case, VCSEL2 was a leader to VCSEL1 and the time lag between the waveforms was to be read as 4 ns. The correlation coefficient was 0.677 (Fig. 6). Since the synchronization of the y -components was attained via anti-phase oscillations for chaotic synchronization of the x -components, the correlation coefficient was less than that calculated from Fig. 3.

Figure 7 shows the optical spectra at solitary and mutually coupled oscillations observed by the optical spectrum analyzer. Table2 is a summary of the data analyzed by the wavelength meter and the power meter. These data correspond to the laser oscillations in Fig. 5. Peak optical powers of the observed spectra were also normalized to the maximum intensity among the polarization modes. Before optical coupling, the output power for the x -polarization was very low but it showed significant power after optical injection. On the other hand, the output power of the y -polarization is reduced. The wavelengths of the y -components were shifted due to the mutual optical injection. There is

still a small wavelength difference between the x -polarization components at mutual coupling. It seemed that two spatial modes were oscillated simultaneously and the observed peak frequency of VCSEL1 was shifted toward higher wavelength. But it was still considered that the two lasers chaotically synchronized at the x -polarization modes and the x -polarization mode of VCSEL2 was locked to that of VCSEL1. On the other hand, the y -components had a significant difference of the wavelength and the wavelength difference was 0.035 nm.

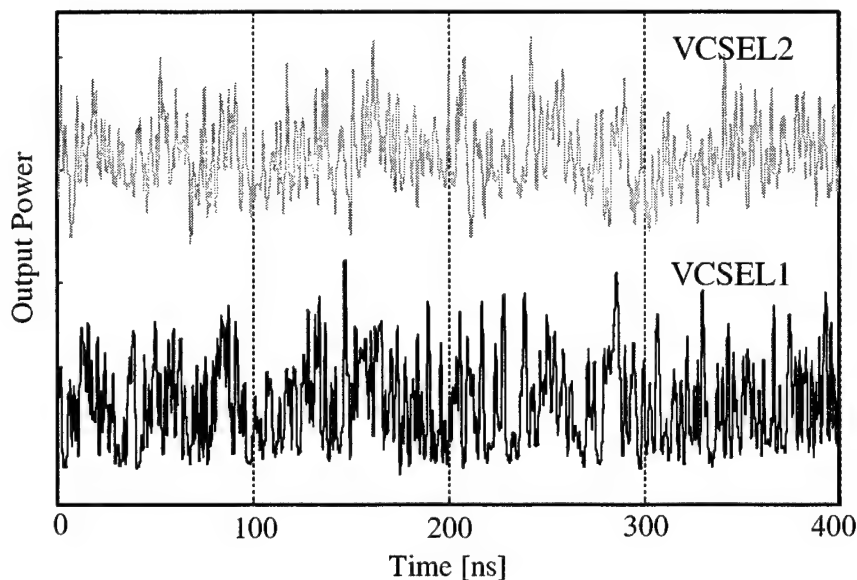


Fig. 5 Time series of y -polarization modes at synchronization.

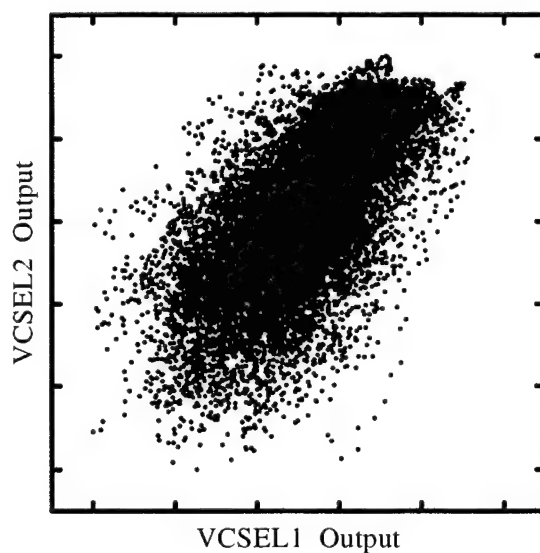


Fig. 6 Correlation plot.

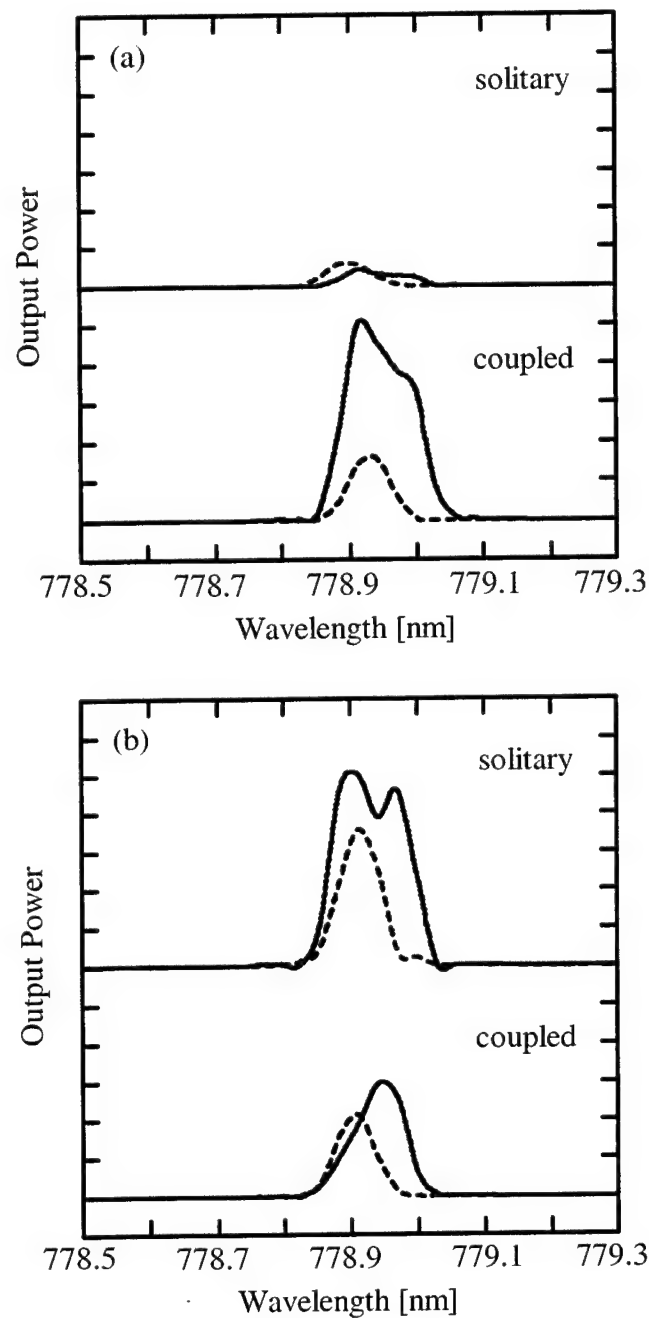


Fig. 7 Optical spectra of laser oscillation for (a) x - and (b) y -polarization modes.
Solid line: VCSEL1, broken line: VCSEL2

4. Conclusion

We have experimentally demonstrated synchronization of chaotic oscillations in polarization selected mutually coupled VCSELs. In chaos synchronization in VCSELs, the polarization modes play an important role. If y -polarization components are injected, chaos synchronization will occur in y -polarization components. As a result, the optical outputs of the y -polarization modes of both VCSELs are amplified. On the other hand, the outputs of the x -polarization mode decrease and they synchronize due to anti-phase oscillations. When x -polarization components are injected, the same

tendency were observed, namely, the x -polarization modes were injection-locked and the x -polarization modes were amplified accompanying the decrease of the output power in the y -polarization. The scheme of synchronization depends on the parameter conditions, such as device parameters, bias injection current, and other experimental configurations. They also determine a leading (master) or lagging (slave) laser in the synchronization system. Although we have focused on the operation under lower order spatial modes, chaos synchronization is expected to be occurred at multi-modes oscillations. We have only examined chaos synchronization at LFF regimes under low bias injection current. At higher bias injection current in VCSELs, we can still expect chaos synchronization with multi-mode oscillations of the spatial modes. There are a few studies of chaos synchronization in VCSELs, since it is not easy to realize chaos synchronization not only for polarization modes but also for spatial modes. But the study is very important for a viewpoint of practical applications, since VCSELs are the promising light sources for the future optical communications.

TABLE 2 Wavelength and output power

		VCSEL1	VCSEL2
X wavelength	solitary	778.982 [nm]	778.892
	coupled	778.922	778.916
Y wavelength	solitary	778.913	778.915
	coupled	778.941	778.906
X output power	solitary	30.32 [mW]	41.47
	coupled	366.96	115.02
Y output power	solitary	613.20	438.46
	coupled	263.84	258.18

References

- [1] J. Ohtsubo, *Progress in Optics* **44**, Chapter 1, Ed. E. Wolf, (Elsevier Science B. V., Amsterdam, 2002).
- [2] S. Jhian, Z. Pan, M. Dagenais, R. A. Morgan, and K. Kojima, *IEEE Photon. Technol. Lett.* **6**, 34 (1994).
- [3] N. Fujiwara, Y. Takiguchi, and J. Ohtsubo, *Opt. Lett.* **28**, 896 (2003).
- [4] J. Ohtsubo, *IEEE J. Quantum. Electron.* **38**, 1141 (2002).
- [5] M. Sondermann, H. Bohnet, and T. Ackemann, *Phys. Rev. E.* **67**, 021802(R) (2003).
- [6] J. Ohtsubo and P. Davis, *Unlocking Dynamical Diversity – Optical Feedback Effects on Semiconductor Lasers*, Chapter 10, Eds. D. Kane and K. A., Shore (Wiley, 2004) in press.
- [7] N. Fujiwara, Y. Takiguchi, and J. Ohtsubo, *Opt. Lett.* **28**, 1677 (2003).

J. Ohtsubo's e-mail address is tajohts@ipc.shizuoka.ac.jp.

A fiberoptics setup for experiments on chaos synchronization and chaotic cryptography

Valerio Annovazzi-Lodi*, Mauro Benedetti, Sabina Merlo, Michele Norgia**
Dipartimento di Elettronica, Universita' di Pavia, Via Ferrata 1, I-27100 Pavia, Italy

ABSTRACT

We have developed a fiberoptics setup which can be easily specialized with minor changes to implement different schemes of optical chaos generation and synchronization using semiconductor lasers. Long and short cavity, open and closed loop configurations have been compared, as well as various encoding/decoding methods for secure transmission based on chaotic carriers, such as CSK (Chaotic Shift Keying), ACM (Additive Chaotic Masking), CM (Chaos Modulation). Different transmission media, possibly including optical amplifiers, have been also tested.

Keywords: Chaos, synchronization, cryptography, injection, semiconductor laser

1. INTRODUCTION

In the last years, synchronization of chaotic semiconductor lasers has been proposed in several papers [1-8] as a method to implement secure data transmission on an optical link. Basically, this approach consists in hiding a message into the deterministic, yet very complex, waveform generated by a chaotic laser. In most schemes, chaos generation is based on delayed optical feedback from an external mirror [3-8] (Fig.1), since with this approach the amplitude and bandwidth of chaos can be easily controlled by acting on the mirror alignment. A suitable method for message encryption consists of simply adding it to chaos, as in Fig.2. The composite signal is then transmitted through the fiber link, and, if the signal is small enough, it is efficiently hidden both in the time and in the frequency domain. Message extraction is usually based on a master/slave synchronization scheme: another laser (the slave) is used at the receiver, whose parameters are matched with those of the transmitter laser (the master). The composite waveform (chaos + message) from the optical link is injected into the slave. Under suitable operating conditions, one can force the second laser to synchronize to the master chaos, (which means that it generates almost exactly the same chaotic waveform), without, however, synchronizing the message. Thus, the message can be extracted by making the difference between the received composite signal and the recovered chaotic waveform. The degree of matching required between master and slave for efficient synchronization is significantly high, which means, for example, that the lasers have to be selected from the same wafer. The laser couple thus represents the (hardware) cryptographic key.

The scheme outlined above is usually referred to as Additive Chaos Masking (ACM), and may be implemented by using a third laser modulated in amplitude by the analog or digital message, whose output is combined with the chaotic waveform. Such laser should be at the same wavelength as master and slave to prevent an eavesdropper from extracting the message by optical filtering. Other approaches are possible [5, 8], such as Chaos Shift Keying (CSK), where the message directly modulates the transmitter laser pump current, and Chaos Masking (CM), where the message is applied to the chaotic waveform by an external amplitude modulator.

Much theoretical and numerical work has been performed on such topic, usually based on the well-known Lang-Kobayashi model [9]; more advanced detection methods have been also proposed, such as those based on the Kapitaniak approach [6]. Also, chaos generation may use other schemes, such as a two-laser injection system [10].

However, delayed optical feedback for chaos generation, and direct injection of the master into the slave for synchronization, are by far much easier to implement than more advanced schemes, and have been used in virtually all experimental implementations reported in the literature. In this framework, two main cases may be considered, depending on the slave alone being intrinsically chaotic or stable. The first case is referred to as 'closed loop'; the second case, where the slave simply copies, because of injection, the master chaos, is referred to as 'open loop'.

Another important distinction is based on the length L of the external laser cavity, i.e., the distance between the laser

* valerio.annovazzi@unipv.it; phone +39 0382 505596; fax +39 0382 422583; optoele.unipv.it

** Michele Norgia is also with INFN, Italy.

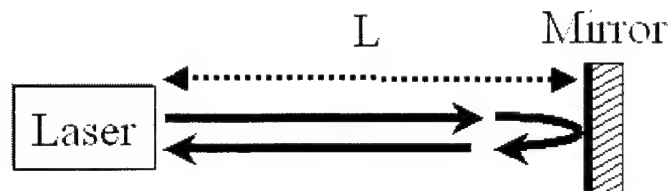


Fig.1 Delayed optical feedback on a laser from a remote mirror.

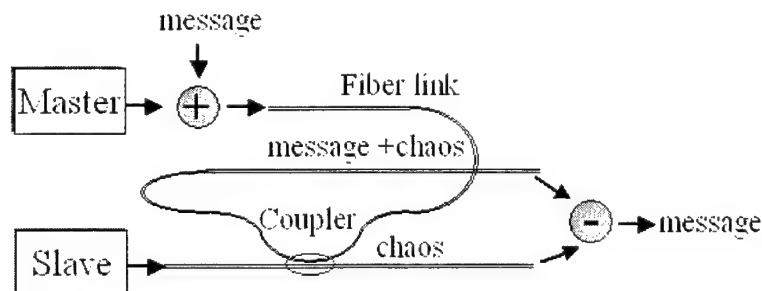


Fig.2 Basic ACM scheme: the master is a laser routed to chaos as in a); the slave may be a chaotic laser (closed loop) or a solitary laser (open loop).

facet and the external mirror (Fig.1). Defining $l = c/f_r$, where f_r is the laser relaxation frequency, if $L > l$ the laser is said to work in the 'long cavity' regime, while for $L < l$ it is said to work in the 'short cavity' regime. Both cases have been investigated in the literature, and both may be considered for cryptographic applications [4, 10-12]. In the following, we assume that the injected light is always polarized in the same direction as the laser emission, and, in addition, that L is shorter than the coherence length of the source. These assumptions are satisfied in most experiments reported in the literature. However, the incoherent case has been also investigated [13].

Experimental studies on cryptography based on chaotic lasers require to compare different encryption methods and detection schemes, each with a specific setup configuration. Also, the evaluation of the degree of matching required for efficient synchronization, a key issue for security, is based on testing of several device pairs. Though such work could be performed in a standard bulk optics setup, the alignment procedures would be very time consuming. For this reason, we have developed a fiber optics setup which can be easily specialized with minor changes to implement open and closed loop schemes with long and short cavities. Also, CSK, CM, ACM experiments, as well as transmission through fibers of different length (including splices, connectors, and optical amplifiers), can be performed simply by inserting or removing connectorized components. In the following we present our fiberoptics setup, and show some results that we have obtained for the case of the short cavity, closed loop configuration.

2. THE EXPERIMENTAL SETUP

The fiberoptics setup is shown in Fig.3. It includes two lasers connected in a master/slave configuration through an optical isolator which allows for one-way injection. The polarizer in front of the slave ensures coherent injection. Together with the birefringence controller, it also allows for trimming the injected power from the master into the slave. A fraction of the emission of each laser is supplied to an amplified photodiode (PD1, PD2), for both d.c. power detection (to be observed during the alignment procedures) and for RF modulation detection. The integrated indium phosphide photodiode/amplifier that we have selected (Optospeed HRXC10B, bandwidth $B=8$ GHz) is used also as a partial mirror, to reduce the setup complexity. Indeed, the reflected power from the gold contacts and the mass plane surrounding the photodiode, which comes on a chip carrier, is sufficient to drive a typical telecommunication laser to chaos; moreover, the feedback level can be easily varied by acting on the alignment.

(Fig.3). In this case, the delay line and the whole setup are trimmed for the best chaos cancellation. A RF spectrum analyzer gives an easy way of performing such job in real time over the whole chaos bandwidth.

Different fiber lengths and types may be inserted in the path between the two lasers, as well as splices and connectors, to simulate a real point-to-point connection. The effect of Erbium doped, and of semiconductor, optical amplifiers can be also tested. In Fig.3 the implementation of different encoding schemes (ACM, CSK and CM) is also shown.

In our laboratory, the fiber setup has been built on an optical table with pneumatic quenching. A special effort has been devoted to obtain two almost identical external cavities.

As already stated, a very accurate control of length L is required especially in short cavity experiments. To this purpose, an improvement of the basic setup consists in adding a built-in interferometric measurement of the laser-fiber distance on both master and slave. To avoid increasing the setup complexity, the lasers themselves are used as the optical sources of two interferometers. To this end, each laser source is operated in a non-chaotic regime by reducing backreflection by a small translation of the fiber tip in a direction orthogonal to its axis. The obtained configuration is the so-called feedback interferometer [14], which is suitable for measurement of distance and vibration amplitude on small targets, such as MEMS [15].

This configuration is compact and it does not need a reference arm. Its operating principle is based on the perturbation that the back-injected field from the target induces in the laser. Under suitable operating conditions, the photodetected current at a monitor photodiode has the form [14] of a typical interferometric signal and the target movement can be measured by fringe counting. In our case, since an absolute distance measurement is required on a standing target, a sweep in wavelength is given to the laser [14] by a slow linear variation of temperature, in order to develop fringes. In practical cases, where L is of the order of 30 mm, the distance is measured with a precision of a few tens of μm .

3. SYNCHRONIZATION WITH SHORT CAVITY, OPEN LOOP

In this section, we show experimental results obtained on a couple of Optospeed LSH1550-DFB in our fiberoptic setup. Such devices are standard DFB telecommunications laser working at a wavelength $\lambda=1550$ nm. They were operated at a current $I=7\text{--}20$ mA, for a maximum output power P of about 7mW. The two lasers were selected among devices built in close proximity on the same wafer, and, after being tuned at the same wavelength by temperature, they exhibited only 1% difference both in threshold current and in differential efficiency.

In the following, we focus on the short cavity, closed loop configuration, which represents a very promising approach for the practical implementation of optical chaos cryptography, because of its compactness, stability, high allowable data rate.

To align the setup, the master laser-fiber distance was first trimmed for the maximum chaos amplitude, which depends on the optical phase [12]. Then, accurate trimming of the phase of the slave was performed, since the synchronization quality is extremely sensitive to the relative phase of the laser cavities [4]. Finally, the injection level of the master into the slave was optimized.

The fiber path connecting the two lasers has been progressively increased in length, starting from about 2 m of single-mode standard fiber (SMR) of the isolator and coupler pigtails, then adding a piece of 500 m and finally another piece of 1300 m of fiber. Some joints were made by fusion splicing, others by using commercial connectors. Lossy splices were made by using short fiber pieces of different core diameters; additional losses were introduced by bending the fiber. Finally an EDFA amplifier was included to compensate for the overall loss. All added devices were positioned after the optical isolator, as shown in Fig.3, to avoid unwanted back-injection.

Figs.4 to 8 illustrate the synchronization quality of master and slave with the above described fiber connection, for a cavity length $L=30$ mm. It is interesting to observe that the performance was essentially the same as in the back to back experiments (pigtails only), as long as the optical amplification compensated for the fiber losses. The synchronization quality could be even improved when optical amplification increased the injection level from the master into the slave. Similar results were found by substituting the EDFA with a semiconductor optical amplifier.

Fig.4 shows a comparison of master and slave RF spectra in optimized conditions. A message at 3 GHz is also present. A relatively high amplitude has been selected in this experiment to make it visible in the master, so that the effect of selective synchronization of the slave can be appreciated. It must be pointed out that synchronization quality cannot be directly inferred from the diagrams of Fig.4, because it is not difficult to obtain almost identical spectra from similar lasers even with no injection. However, synchronization quality can be evaluated by a direct comparison of time series of the chaotic waveforms of master and slave in the time domain, as shown in Fig.5. From the time series, the master-slave correlation has been also computed as a function of the differential delay τ , and the result is plotted in Fig.6. A

correlation of more than 80% is found for zero differential delay. In Fig.7, a x-y oscilloscope plot, obtained in the same conditions, is shown.

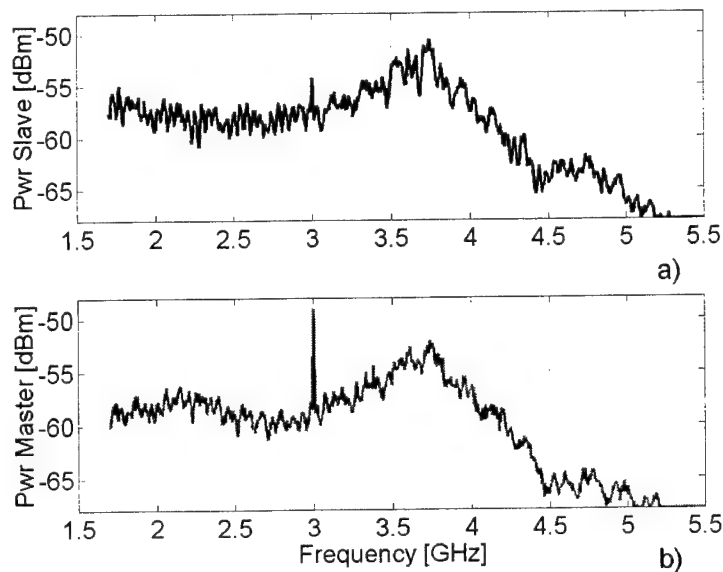


Fig.4 Typical short cavity ($L=30$ nm) RF spectra for two synchronized chaotic DFB laser at $\lambda=1550$ nm in the closed loop configuration (a: slave, b: master).

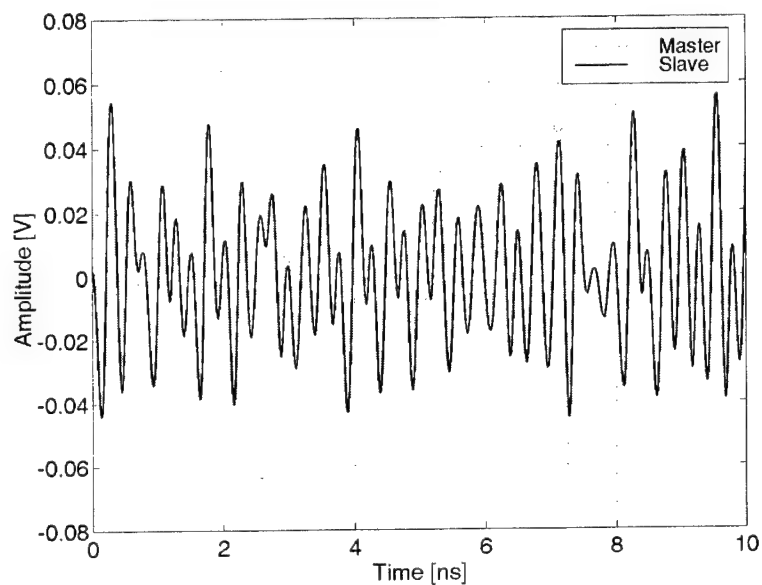


Fig.5 Time series showing master/slave synchronization in the time domain.

In the frequency domain, an interesting method to evaluate the synchronization quality is to select the length of the delay line so as to work with a relatively large differential path. In this case, different portions of the two chaos spectra have different relative phase difference, so that the spectrum of their combination exhibits several maxima (sum) and minima (difference), as shown in Fig.8. Thus, the system can be trimmed by maximizing the distance between such

maxima and minima, which is far easier than minimizing the signal difference only (possibly comparing it, at different times, with the master and slave chaos, or with their sum).

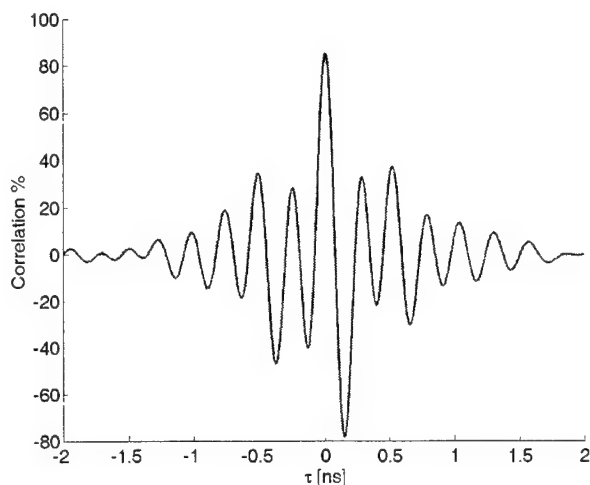


Fig.6 Correlation diagram of synchronized master and slave.

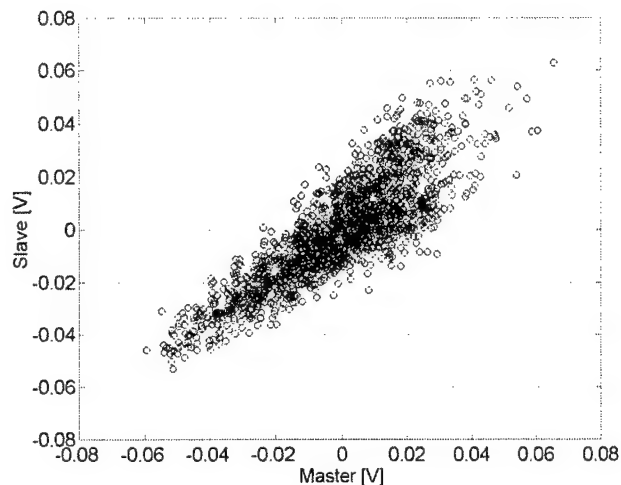


Fig.7 X-Y correlation diagram.

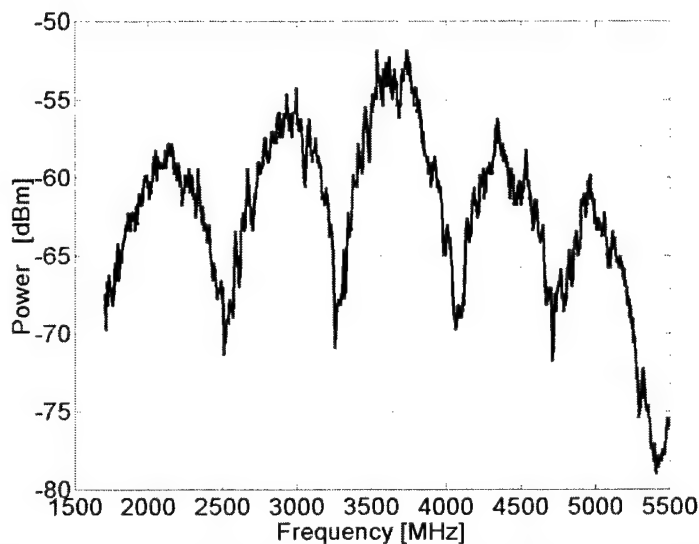


Fig.8 RF spectrum of the master/slave sum with uncompensated time delay in a short cavity, closed loop synchronization experiment.

4. SIGNAL TRANSMISSION

Transmission tests have been performed with the different methods shown in Fig.3, namely, CSK, ACM, CM. The first scheme was implemented by modulating the pump current of the laser; the second by using a third laser at the same wavelength as the master/slave couple; the third by a Lithium Niobate amplitude phase modulator, inserted after the

optical isolator. The fiber link between the master and the slave included different passive elements, as explained for the synchronization experiments, and possibly an optical amplifier.

The different methods for signal encoding have been studied theoretically and numerically and their peculiarities and performances have been pointed out [8]. From the experimental point of view a major issue determining the performances of all methods is chaos amplitude, which puts a limit to the signal amplitude which may be safely masked, and, thus, to the obtainable S/N ratio after detection. For example, an ACM transmission experiment is shown in Fig. 9: a sinusoidal signal is hidden within the master chaos (upper trace); the signal is then recovered by making the difference between the master and the synchronized slave outputs (lower trace). Very similar diagrams have been obtained in our setup with the other two encoding methods, since the maximum allowable amplitude, before the signal may be spotted by direct inspection of the spectrum, is always the same.

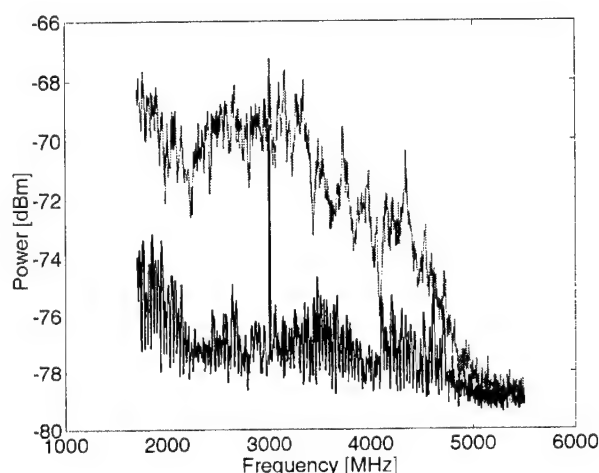


Fig.9 Example of message transmission and detection in the frequency domain: ACM scheme. Upper trace: master with hidden message; lower trace: master/slave difference with extracted message.

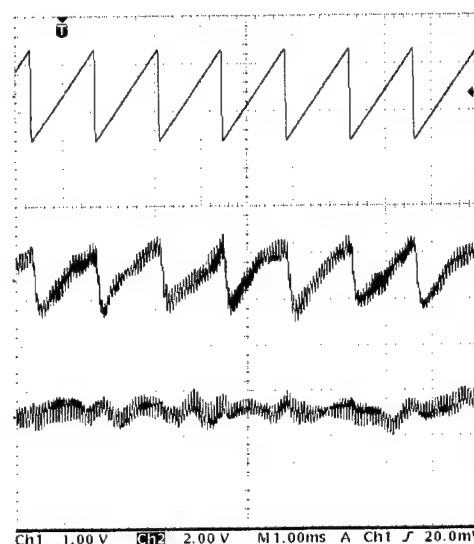


Fig.10 Example of message transmission and detection in the time domain: low frequency PM scheme. Transmitted message (upper trace) can be detected from master-slave superposition (middle trace); message cannot be detected from master alone (lower trace).

Still another possibility, which has not been shown in Fig.2, is phase modulation (PM) of chaos. It has been observed [4] that small variations of the external cavity length, around a suitable bias point, hardly affect the RF spectrum of chaos, so that an eavesdropper cannot detect a message which modulates the optical phase. However, the correlation degree between master and slave strongly depends on the relative phase: thus, a signal obtained by linear superposition of the master and of the slave outputs varies in amplitude allowing the authorized listener to extract the hidden signal at the receiver. To exploit such principle, a scheme was proposed where a relatively large digital signal switches the master/slave system from synchronization to de-synchronization (ON-OFF Chaos Phase Shift Keying [4]). Alternatively, transmission of a small analog signal may be considered.

The PM scheme has been implemented in our setup by inserting two electro-optical modulators between each laser and its fiber. The modulator of the master was used to transmit the message, while that of the slave was inserted just to work with identical external cavities at rest.

An example of application of such scheme is shown in Fig. 10 for a low amplitude, low frequency triangular-wave. The upper trace represents the transmitted message. The trace at the middle is the output of an envelop detector fed by the signal obtained by superposition of the synchronized master and slave outputs. For comparison, the lower trace represents the output of the envelop detector fed by the master output only, from which the signal cannot be extracted.

ACKNOWLEDGMENTS

This work was supported by the European Community under Contract ST 2000 29683 (OCCULT Project). The authors wish to thank Optospeed (CH) for supplying the selected laser couples, the amplified photodetectors and the semiconductor optical amplifier.

REFERENCES

1. S. Donati, C. R. Mirasso (eds.), "Feature Section on Optical Chaos and Applications to Cryptography", IEEE Journal of Quantum Electronics, 38-9, 1138-1196, 2002.
2. J.-P. Goedgebuer, P. Levy, L. Larger, C.-C. Chen, W.T. Rhodes, "Optical Communications with Synchronized Hyperchaos Generated Electrooptically", IEEE Journal of Quantum Electronics, 38-9, 1178-1183, 2002.
3. S. Sivaprakasam, P.S. Spencer, P. Rees, K. A. Shore, "Regimes of Chaotic Synchronization in External-Cavity Laser Diodes", IEEE Journal of Quantum Electronics, 38-9, 1155-1161, 2002.
4. T. Heil, J. Mulet, I. Fisher, C.R. Mirasso, M. Peil, P. Colet, W. Eilsasser, "ON/OFF Phase Shift Keying for Chaos-Encrypted Communication Using External-Cavity Semiconductor Lasers", IEEE Journal of Quantum Electronics, 38-9, 1162-1170, 2002.
5. J. Ohtsubo, "Chaos Synchronization and Chaotic Signal Masking in Semiconductor Lasers with Optical Feedback", IEEE Journal of Quantum Electronics, 38-9, 1141-1154, 2002.
6. V. Annovazzi-Lodi, S. Donati, A. Scire', "Synchronization of Chaotic Lasers by Optical Feedback for Cryptographic Applications", IEEE Journal of Quantum Electronics, 33-9, 1449-1454, 1997.
7. C. Mirasso, P. Colet, P. Garcia-Fernandez, "Synchronization of Chaotic Semiconductor Lasers: Application to encoded communication", IEEE Photonics Technology Letters, 8-2, 299-301, 1996.
8. J. Liu, H. Chen, S. Tang, "Synchronized Chaotic Optical Communications at high Bit Rates", IEEE Journal of Quantum Electronics, 38-9, 1184-1196, 2002.
9. R. Lang, K. Kobayashi, "External Optical Feedback Effects on Semiconductor Injection Laser Properties", IEEE Journal of Quantum Electronics, 16-3, 347-355, 1980.
10. V. Annovazzi-Lodi, S. Donati, A. Scire', "Synchronization of Chaotic Injected-Laser Systems and its Application to Optical Cryptography", IEEE Journal of Quantum Electronics, 32-6, 953-959, 1996.
11. V. Annovazzi-Lodi, S. Merlo, M. Norgia, A. Scire', "Characterization of a Chaotic Telecommunication Laser for Different Fiber Cavity Lengths", IEEE Journal of Quantum Electronics, 38-9, 1171-1177, 2002.
12. T. Heil, I. Fisher, W. Eilsasser, A. Gavrielides, "Dynamics of Semiconductor Lasers Subject to Delayed Optical Feedback", Physical Review Letters, 87-24, 243901/1-243901/4, 2001.
13. J. Houdian, G. Huyet, J. G. McInerney, "Dynamics of a Semiconductor Laser with Incoherent Optical Feedback", Optics Communications, 199, 175-179, 2001.
14. S. Donati, S. Merlo, "Applications of diode laser feedback interferometry", Journal of Optics, 23-3, 156-161, 1998.
15. V. Annovazzi Lodi, S. Merlo, M. Norgia, "Measurements on a Micromachined Silicon Gyroscope by Feedback Interferometry", IEEE Transactions on Mechatronics, 6-1, 1-6, 2001.

Chaotic synchronous modulation of semiconductor lasers subject to optical injection

H.F. Chen^a and J.M. Liu^b

^aDepartment of Electrical Engineering, University of California, Los Angeles
Los Angeles, California 90095-159410, USA;

^bDepartment of Electrical Engineering, University of California, Los Angeles
Los Angeles, California 90095-159410, USA

ABSTRACT

A direct experimental observation of chaotic synchronous scenarios, namely chaotic optical modulation, is demonstrated in a unidirectional chaotic-coupling semiconductor laser system. In this fully optical system, the channel signal is different from the output field of the transmitter laser by an additional monochromatic optical field. Different from the chaos synchronization explainable by theory of chaos synchronization, the output field of the receiver laser is not synchronized to that of the transmitter laser. Instead, it is synchronized to the channel signal. However, the optical frequency of the receiver is not locked to that of the transmitter. It is observed that not only is the intensity of the receiver output synchronized to that of the channel signal, but also the chaotic slowly-varying phase of the receiver. The synchronization of the slowly-varying phase is verified by optical interference between the output of the receiver and the channel signal, and the interference result is recorded through a photodetector.

Keywords: Chaotic Synchronization; Semiconductor lasers; Injection locking; Optical Modulation

1. INTRODUCTION

Optical chaos synchronization utilizing semiconductor lasers has attracted much attention for its potential application in high-speed private communications and spread spectrum communications.¹⁻⁶ Based on the mechanisms generating the chaotic optical waveform, the systems utilizing nonlinearity of semiconductor lasers to perform chaos synchronization can be classified as optical injection,^{7,8} optical feedback,⁹⁻¹² and optoelectronic feedback.^{13,14,6} Following the research in optical chaos synchronization, besides the rarely observed chaos synchronization, another synchronous phenomenon as chaotic driven oscillation is usually observed in optical feedback systems. The receiver duplicates the transmitter output in chaos synchronization, but duplicates the channel signal in chaotic driven oscillation. Nevertheless, both synchronous phenomena require the optical frequency of the receiver laser locked to that of the transmitter laser.^{10,11,15}

In this research, however, we report an experimentally observed synchronization of chaotic optical waveforms without the locking on the optical frequencies of the transmitter and the receiver. The chaotic waveform is generated by the high-speed nonlinearity of semiconductor lasers subject to optical injection.¹⁶ When this synchronous phenomenon occurs, it is possible that the channel signal as an optical field is duplicated by the receiver while the free-running oscillation mode of the receiver still exists. Therefore, the duplicated part of the receiver to the channel signal can be verified through the examination on the synchronization quality of the chaotic intensity after detectors and that on the optical interference between the channel signal and the receiver output. This synchronous phenomenon of the receiver to the channel signal without the locking on the optical frequency does not occur on the both sides of the receiver's oscillation mode though the receiver is operated as a free-running laser.

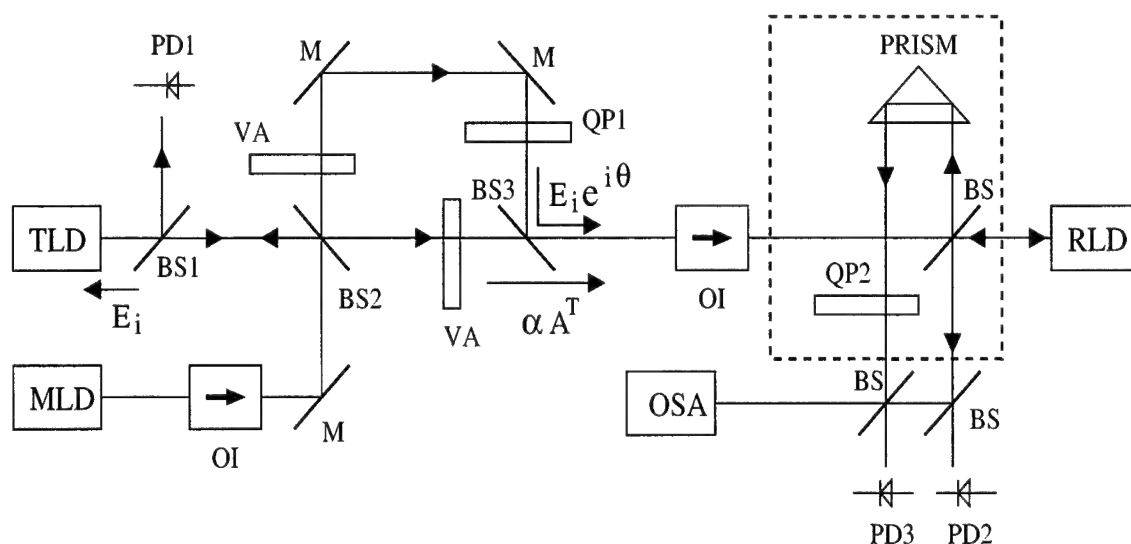


Figure 1. Schematic experimental setup. MLD: Master Laser, TLD: Transmitter Laser, RLD: Receiver Laser, M: Mirror, BS: Beam Splitter, PBS: Polarized beam splitter, VA: Variable Attenuator, PD: Photodetectors, QP: quartz plate, OSA: optical spectrum analyzer, $\lambda/2$: Half-wave Plate

2. SETUP AND DEVICES FOR EXPERIMENT

The schematic setup of the experiment is shown in Fig. 1. The output of the MLD is split into two beams through the beam splitter BS2: The one denoted by $E_i(t)$ is injected into the transmitter to drive the transmitter into chaotic states, and the other beam denoted by $E_i(t)e^{i\theta}$ is injected into the receiver together with the output of the transmitter at BS3. The existence of the relative optical phase θ can be realized from the fact that the optical field of the transmitter encounters the output field of the MLD twice. The first time occurs inside the transmitter laser, and the second time at BS3. The phase θ defines the optical phase difference between these two encounters for the same optical field of the transmitter.⁸ The phase θ is controlled by tilting QP1 in a small angle. Synchronization on the slowly-varying phase and the fast-varying phase is detected through the interferometer highlighted by the dashed box. When synchronization of both phases is achieved simultaneously, constructive interference or destructive interference can be detected by the detector PD3 by adjusting the relative optical phase between the transmitter output and the receiver output when they interfere with each other. This relative optical phase is adjusted by the quartz plate QP2. The detectors PD1 and PD2 are used to detect the transmitter output and the receiver output, respectively. Two two-stage optical isolators (OI) with 60-dB isolation are used in experiment.

The semiconductor lasers used in this setup are InGaAsP/InP single-mode DFB semiconductor lasers emitting at $1.295 \mu\text{m}$. They are all fabricated from the same wafer and selected by the close match of their intrinsic laser parameters that are found through experimental measurements.¹⁷ The photodetectors used to detect the outputs of the transmitter and the receiver are InGaAs photodetectors with a 3-dB bandwidth of 6 GHz. The electrical signal from the output of each detector is amplified by an HP 83006A microwave amplifier with a bandwidth covering the range from 0.01 GHz to 26.5 GHz and a gain of 23 dB. The output of the transmitter laser and that of the receiver laser after amplification are recorded in time domain by a Tektronix TDS 694C digitizing sampling oscilloscope that has a 3 GHz bandwidth and a sampling rate of 10 GS/s for four channels simultaneously. The power spectra of the laser outputs are taken with an HP E4407B spectrum analyzer with a bandwidth ranging

Further author information: (Send correspondence to H.F. Chen)

H.F. Chen: E-mail: howfoo@ucla.edu, Telephone: 1 310 825 8650

J.M. Liu: E-mail: liu@ee.ucla.edu, Telephone: 1 310 206 2097

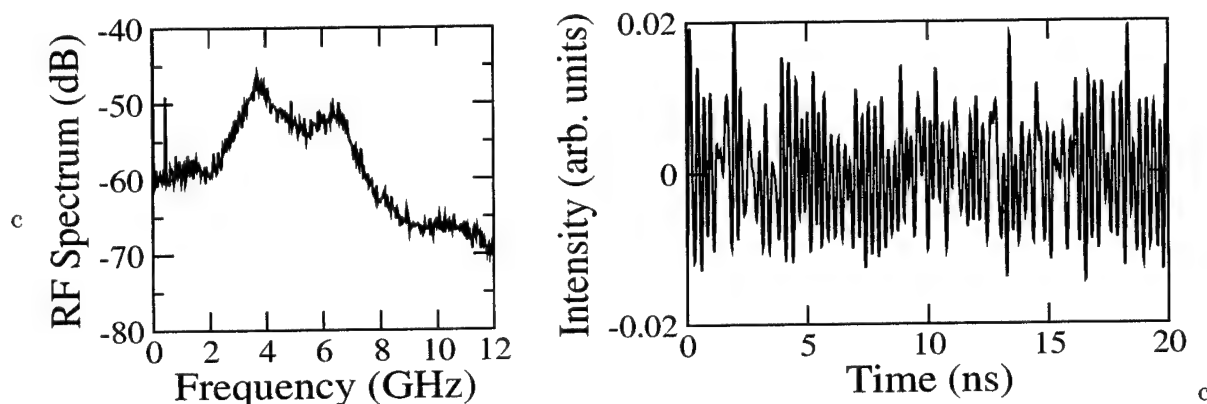


Figure 2. Experimental measurement of chaotic output of the transmitter: (a) is the power spectrum of the transmitter output, (b) is the intensity of waveform in time domain.

from 9 kHz to 26.5 GHz. The optical frequency and optical spectra of each laser is measured by an Advantest Q8347 optical spectrum analyzer with a resolution of 0.005 nm.

The synchronization quality is measured through the correlation coefficient, denoted by ρ^5 :

$$\rho = \frac{\langle [X(t) - \langle X(t) \rangle][Y(t) - \langle Y(t) \rangle] \rangle}{\langle |X(t) - \langle X(t) \rangle|^2 \rangle^{1/2} \langle |Y(t) - \langle Y(t) \rangle|^2 \rangle^{1/2}}, \quad (1)$$

where $X(t)$ and $Y(t)$ are the outputs of the transmitter and the receiver, respectively, and $\langle \cdot \rangle$ denotes the time average. The correlation coefficient is bounded as $-1 \leq \rho \leq 1$. A larger value for $|\rho|$ means a better synchronization quality. This correlation coefficient measures the similarity of the two attractors. In this paper, the examination of the similarity focuses on the intensity of the chaotic waveforms.

3. CHAOTIC SYNCHRONOUS SCENARIO

In the experiment, the transmitter laser is biased at $I^T = 2.38I_{th}^T$, where the threshold current of the transmitter is $I_{th}^T \simeq 21$ mA. The injection strength from the master laser to the transmitter is adjusted so that the transmitter is operated in a chaotic state. The power spectrum of the transmitter chaotic output is shown in Fig. 2(a), and the time series of that is shown in Fig. 2(b). The frequency detuning of the MLD from the transmitter in free-running condition is 2.73 GHz.

The frequency detuning of the receiver to the free-running transmitter is adjusted at 41.6 GHz. The optical frequency of the receiver is unlocked to that of the transmitter or the channel signal under this operating condition. However, desynchronization does not occur when the receiver becomes unlocked. Instead, significant degree of synchronization between the chaotic waveform of the transmitter and that of the receiver is observed. Opposite to a general believe that locking of optical frequency is a necessary condition of chaotic synchronous scenarios occurred in a fully optical system,¹⁰ the frequency locking is not required in this synchronous scenario.

Based on the understanding of chaos synchronization and chaotic driven oscillation observed in the experiment and theoretical analysis of optical feedback system,^{15,10} the output field of the receiver is synchronized to that of the transmitter when the optical feedback system performs chaos synchronization, and that of the receiver is synchronized to the channel signal when the system performs chaotic driven oscillation. For the synchronous phenomenon experimentally observed in the optical injection system, it is important to examine if the output field of the receiver is synchronized to that of the transmitter or the channel signal. Since the output field of the transmitter is different from the channel signal by an optical field $E_i(t)e^{i\theta}$ in this system, varying the relative optical phase θ can change the channel signal. Therefore, the synchronization quality of the observed synchronous scenario is measured at the operating conditions $\theta = 0$ and $\theta = \pi$.

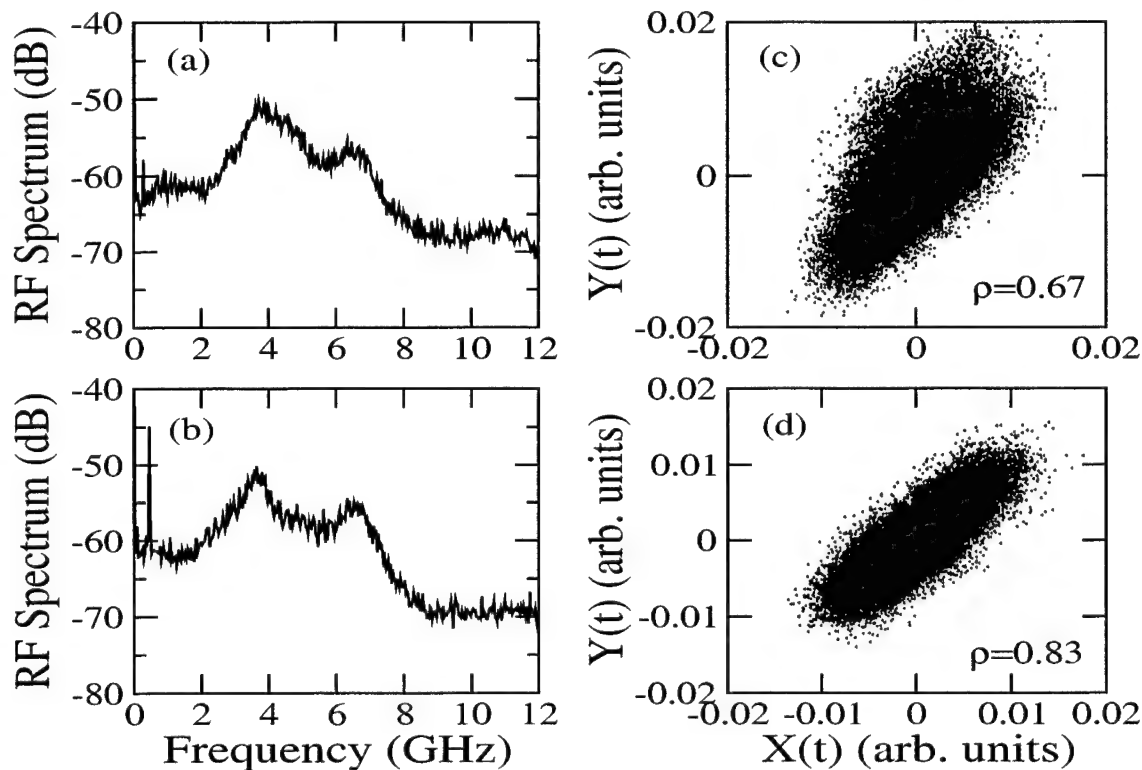


Figure 3. Experimental result when $\theta = 0$: (a) and (b) are power spectra of the receiver output and channel signal in respective; (c) correlation plot between the receiver output, $X(t)$, and the transmitter output, $Y(t)$; (d) correlation plot between the receiver output, $X(t)$, and the channel signal, $Y(t)$.

When $\theta = 0$, the power spectrum of the synchronized receiver is shown in Fig. 3(a). The power spectrum of the channel signal as the superposition of the transmitter output and the MLD output with $\theta = 0$ is shown in Fig. 3(b). The quality of the achieved synchronization is demonstrated through the synchronization of the intensity. The synchronization of the chaotic intensity is shown in Fig. 3(c) through the correlation plot between the intensities of the transmitter and receiver waveforms. The synchronization quality is measured to be $\rho \simeq 0.67$. The correlation between the channel signal and the receiver waveform is also measured, and is found to be $\rho \simeq 0.83$ as is shown in Fig. 3(d). Comparing the correlation plots in Fig. 3(c) and 3(d), we observed that the intensity of the receiver output is synchronized to that of the channel signal, but not that of the transmitter output.

When we gradually tune θ away from zero without changing other operating conditions, the channel signal and the response of the receiver change. The power spectrum of the receiver is shown in Fig. 4(a) when $\theta = \pi$. The power spectrum of the channel signal under the same operating condition is shown in Fig. 4(b). The correlation plot between the transmitter and the receiver is shown in Fig. 4(c), and $\rho \simeq 0.65$. The synchronization quality between the receiver and the channel signal is $\rho \simeq 0.81$, and the correlation plot is shown in Fig. 4(d). From the correlation plots shown in Fig. 4, we observed that the output field of the receiver is synchronized to the channel signal instead of that of the transmitter when $\theta = \pi$.

As is observed, the intensity of the receiver is synchronized to that of the channel signal but not that of the transmitter though the optical frequency of the receiver is not locked to that of either one. The experimental result also shows that this synchronous scenario in this system is not sensitive to the relative optical phase θ . Since the optical frequency of the receiver is not locked to that of the channel signal, the channel signal works as a strong optical modulation. Therefore, this chaotic synchronous scenarios is named as chaotic optical modulation.

As is observed, the intensity of the receiver output is synchronized to that of the channel signal, it is interesting

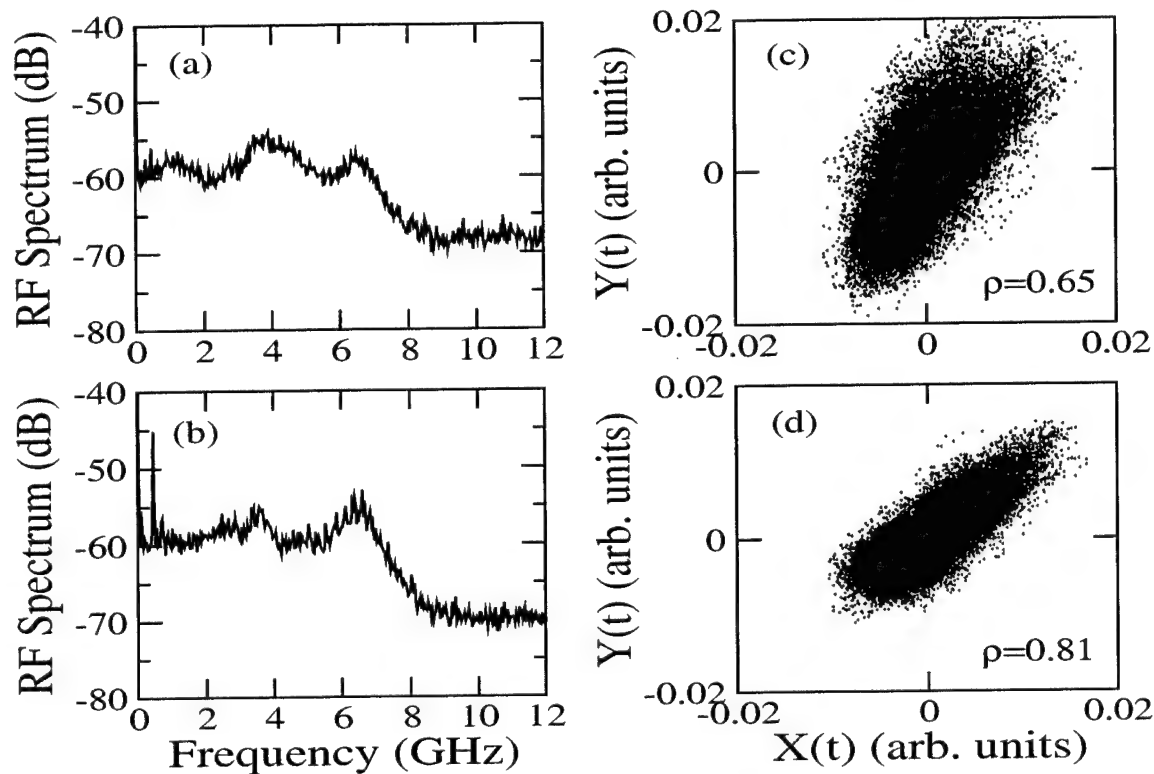


Figure 4. Experimental result when $\theta = \pi$: (a) and (b) are power spectra of the receiver output and channel signal in respective; (c) correlation plot between the receiver output, $X(t)$, and the transmitter output, $Y(t)$; (d) correlation plot between the receiver output, $X(t)$, and the channel signal, $Y(t)$.

to examine if their slowly-varying phases are also synchronized to each other. The synchronization of the slowly-varying chaotic phase is verified through optical interference with the result shown in Fig. 5. The result of this interference between the optical output of the receiver and the optical channel signal is detected by PD3 indicated in Fig. 1. The intensity of the constructive coherent interference is shown as the upper waveform in Fig. 5, and that of the destructive interference is shown as the lower waveform in Fig. 5. The intensity extinction ratio is between 3 and 4. Although the extinction ratio is not very high, it provides the evidence of the synchronization on the slowly-varying phases as well as on the amplitude. Since the optical frequency of the receiver is not locked to that of the transmitter, thus that of the channel signal, how this interference occur should be examined.

4. CHAOTIC OPTICAL MODULATION

Since this chaotic optical modulation occurs when the optical frequency of the receiver is not locked to that of the channel signal or the transmitter, but the intensity and the slowly-varying phase of the receiver are synchronized to those of the channel signal, it is interesting to examine the optical spectra of the channel signal and the receiver output for better understanding of this chaotic synchronous phenomenon. The optical spectra of the receiver output and the channel signal is examined when $\theta = 0$.

The optical spectrum of the channel signal is shown in Fig. 6(a). This optical spectrum cannot be distinguished from that of the transmitter output due to the very weak $E_i(t)$. The optical spectrum of the receiver is shown in Fig. 6(b). The sharp line with very narrow linewidth corresponds to the longitudinal mode of the free-running receiver indicated by RLD, and the much lower and wider part in the optical spectrum shown in Fig. 6(b) is the response of the receiver to the channel signal. This response of the free-running receiver to the channel signal is

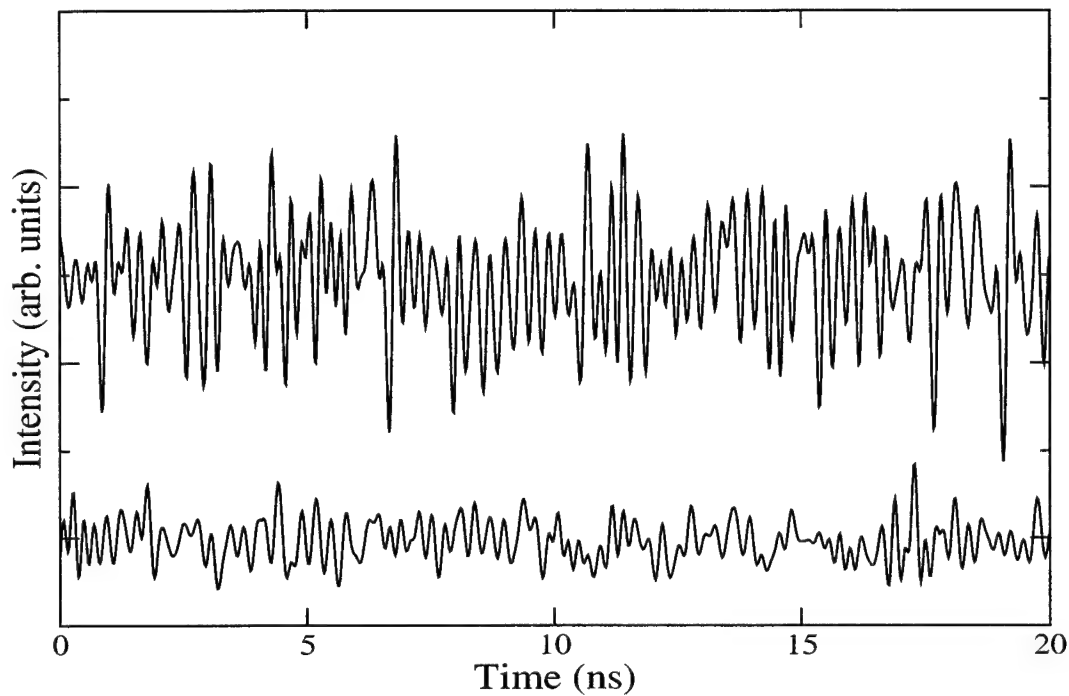


Figure 5. Optical interference of synchronized fields from the transmitter and the receiver: (a) constructive coherent interference, (b) destructive coherent interference.

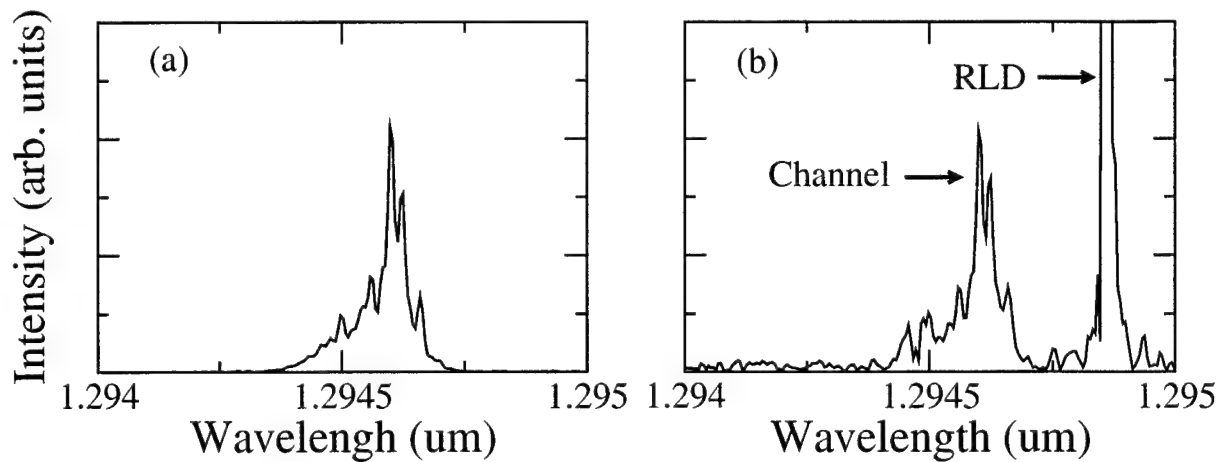


Figure 6. Optical spectra of (a) the channel signal, (b) the receiver output when $\Delta\omega_0 = 41.60$ GHz

indicated by Channel. For the convenience of comparison, the power of the optical spectrum of the receiver has been enlarged to make the response part comparable to the optical spectrum of the channel signal.

Based on the optical spectrum shown in Fig. 6(b), the power spectrum of the receiver shown in Fig. 3(a), and the correlation plot shown in Fig. 3(d), it is possible that the receiver reproduces the channel signal as the response to this strong optical channel signal. If this statement is true, the constructive and destructive optical interferences can be realized as the interferences between the channel signal and the response of the receiver to

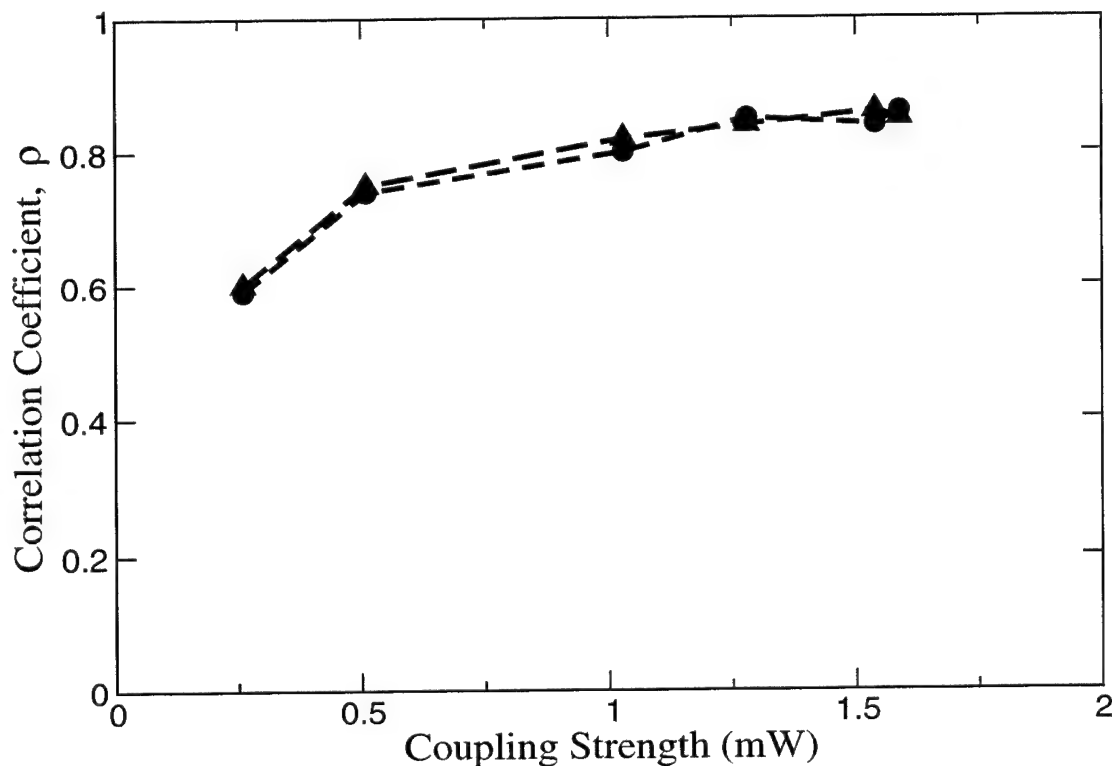


Figure 7. Experimental result of the correlation coefficient when the coupling strength varies: circle symbol indicates the value of ρ when $\theta = 0$; triangle symbol indicates the value of ρ when $\theta = \pi$.

the channel signal. Since the frequency detuning between the channel signal and the receiver is 41.6 GHz, and the bandwidth of the detector is around 6 GHz, the interference between the longitudinal mode of the receiver and the response of the receiver cannot be recorded in the oscilloscope. Therefore, the detector PD3 can only record the interference between the channel signal and the receiver response, indicated by Channel in Fig. 6(b). Based on the same reason, the synchronization of the intensity of the receiver to the intensity of the channel signal can be observed. Further experiment targeting at obtaining better synchronization quality and larger extinction ratio between the constructive interference and the destructive interference is under progress.

The synchronous response of the receiver to the channel signal is generated when the optical frequency of the channel signal or that of the transmitter is larger than that of the receiver. However, the synchronous phenomenon does not occur when the optical frequency of the receiver is still unlocked to that of the channel signal but its optical frequency is larger than that of the channel signal.

5. SYNCHRONIZATION QUALITY AS A FUNCTION OF COUPLING STRENGTH

It is important to notice that the power of the channel signal as the optical modulating signal is comparable to the output power of the receiver. Therefore, the observed chaotic optical modulation is different from small-signal optical modulation.¹⁸ In small-signal optical modulation of semiconductor lasers, because of the linewidth enhancement factor b , the output field of the modulated semiconductor laser is different from the modulating signal. Besides, large optical modulation provides distorted modulation response. This suggestion can be verified through the measure of the synchronization quality as a function of the coupling strength.

The correlation coefficient between the output of receiver and the channel signal as a function of coupling strength is shown in Fig. 7. The coupling strength is measured by the power of the channel signal injected into

the receiver. The synchronization quality of this chaotic synchronous phenomenon is measured when $\theta = 0$ and $\theta = \pi$. The synchronization quality of this chaotic optical modulation with $\theta = 0$ is indicated by the solid circles in Fig. 7. The synchronization quality of this chaotic optical modulation with $\theta = \pi$ is indicated by the solid triangle. The dashed lines to connect the same solid symbols serves for virtual guidance. As is shown, different θ does not contribute significant difference on the synchronization quality. The synchronization quality gradually deteriorates when the coupling strength decreases. It can be observed from the data shown in Fig. 10 that the chaotic optical modulation is different from the modulation response of small-signal optical modulation. The small-signal optical modulation has the advantage that the receiver does not generate a distorted response, but the weaker coupling strength does not provide better synchronization quality than the strong coupling strength.

6. CONCLUSION

In conclusion, we have experimentally demonstrated a new chaotic synchronous scenario, namely the chaotic optical modulation, occurred in a fully optical system, where the chaotic optical waveform is generated through the high-speed nonlinearity of semiconductor lasers subject to optical injection. The experimental observation shows that the chaotic intensity and the slowly-varying phase of the receiver optical output are synchronized to those of the channel signal. However, the optical frequency of the receiver is not locked to that of the channel signal. The comparison between the optical spectrum of the channel signal and that of the receiver output shows the possibility that the receiver just reproduced the channel signal. This synchronous scenario cannot be explained by small-signal optical modulation. Weaker coupling strength of the channel signal actually generates worse synchronization quality.

These experimental observations demonstrate that chaos synchronization and chaotic driven oscillation are not the only chaotic synchronous phenomena. There is another synchronous phenomenon. It also demonstrates that the lock of optical frequency is not a necessary condition to achieve chaotic synchronous phenomena.

7. ACKNOWLEDGMENT

This work is supported by the U. S. Army Research Office under contract No. DAAG55-98-1-0269.

REFERENCES

1. L.M. Pecora and T.L. Carroll, "Synchronization in chaotic systems," *Phys. Rev. Lett.*, vol. 64, no. 8, pp. 821-824, Feb. 1990.
2. "Special issue on applications of chaos in modern communication systems," *IEEE Trans. Circuits Syst. I*, vol. 48, Dec. 2001.
3. "Feature section on optical chaos and application to cryptography," *IEEE J. Quantum Electron.*, vol. 38, Sep. 2002.
4. G.D. VanWiggeren and R. Roy, "Optical communication with chaotic waveforms," *Phys. Rev. Lett.*, vol. 81, pp. 3547-3550, Oct. 1998.
5. J.M. Liu, H.F. Chen, and S. Tang, "Synchronized chaotic optical communications at high bit rates," *IEEE J. Quantum Electron.*, vol. 38, pp. 1184-96, Sep. 2002.
6. S. Tang and J.M. Liu, "Message encoding-decoding at 2.5 Gbits/s through synchronization of chaotic pulsing semiconductor lasers," *Opt. Lett.*, vol. 26, pp. 1843-1845, Dec. 2001.
7. T.B. Simpson, J.M. Liu, A. Gavrielides, V. Kovanis, and P.M. Alsing, "Period-doubling route to chaos in semiconductor lasers subject to optical injection," *Appl. Phys. Lett.*, vol. 64, pp. 3539-3541, Jun. 1994.
8. H.F. Chen and J.M. Liu, "Open-loop chaotic synchronization of injection-locked semiconductor lasers with gigahertz range modulation," *IEEE J. Quantum Electron.*, vol. 36, pp. 27-34, Jan. 2000.
9. M.W. Pan, B.P. Shi, and G.R. Gray, "Semiconductor laser dynamics subject to strong optical feedback," *Opt. Lett.*, vol. 22, pp. 166-168, Feb. 1997.
10. Junji Ohtsubo, "Chaotic synchronization and chaotic signal masking in semiconductor lasers with optical feedback," *IEEE J. Quantum Electron.*, vol. 38, pp. 1141-1154, Sep. 2002.
11. Y. Liu, Y. Takiguchi, P. Davis, T. Aida, S. Saito, and J.M. Liu, "Experimental observation of complete chaos synchronization in semiconductor lasers," *Appl. Phys. Lett.*, vol. 80, pp. 4306-4308, Jun. 2002.

12. Y. Liu, H.F. Chen, J.M. Liu, P. Davis, and T. Aida, "Communication using synchronization of optical-feedback-induced chaos in semiconductor lasers," *IEEE Trans. Circuits Syst. I*, vol. 48, pp. 1484-1489, Dec. 2001.
13. F.Y. Lin and J.M. Liu, "Nonlinear dynamics of a semiconductor laser with delayed negative optoelectronic feedback," *IEEE J. Quantum Electron.*, vol. 39, pp. 562-568, Apr. 2003.
14. S. Tang and J.M. Liu, "Synchronization of high-frequency chaotic optical pulses," *Opt. Lett.*, vol. 26, pp. 596-598, May 2001.
15. Y. Liu, P. Davis, Y. Takiguchi, T. Aida, S. Saito, and J.M. Liu, "Injection locking and synchronization of periodic and chaotic signals in semiconductor lasers," *IEEE J. Quantum Electron.*, vol. 39, pp. 269-278, Feb. 2003.
16. V. Kovanis, A. Gavrielides, T.B. Simpson, and J.M. Liu, "Instability and chaos in optically injected semiconductor lasers," *Appl. Phys. Lett.*, vol. 67, pp. 2780-2782, Nov. 1995.
17. J.M. Liu and T.B. Simpson, "Four-wave mixing and optical modulation in a semiconductor laser," *IEEE J. Quantum Electron.*, vol. 30, pp. 957-965, Apr. 1994.
18. T.B. Simpson, J.M. Liu, and A. Gavrielides, "Small-signal analysis of modulation characteristics in a semiconductor laser subject to strong optical injection," *IEEE J. Quantum Electron.*, vol. 32, pp. 1456-1468, Aug. 1996.

Simple Interpretation of the Dynamics of Mutually Coupled Semiconductor Lasers with Detuning

Raúl Vicente^a, Josep Mulet^a, Marc Sciamanna^b and Claudio R. Mirasso^{a,c}

^aDepartament de Física, Universitat de les Illes Balears, Crta. Valldemossa Km 7.5, E-07122, Palma de Mallorca, Spain;

^bFaculté Polytechnique de Mons, Service d'Electromagnétisme et de Télécommunications, Boulevard Dolez 31, B-7000, Mons, Belgium;

^cElectrical Engineering Department, University of California, Los Angeles, Los Angeles, CA, 90095-1594, USA

ABSTRACT

We investigate the synchronization properties of two mutually-coupled semiconductor lasers (SL) in a face to face configuration, when a non-negligible injection delay time is taken into account. Under the appropriate conditions, we derive a thermodynamic potential analog to the one studied by Mork et al.^{1,2} and by Lenstra³ for a semiconductor laser subject to an optical feedback. In this context, the role that noise and detuning play in the dynamics of the system is clearly identified. When operating in the Low Frequency Fluctuations (LFF) regime, the effect of the detuning on the leader-laggard operation is also analyzed. Finally, we focus on the short intercavity regime and we study the influence of the detuning and the propagation phase on the dynamics of each laser.

Keywords: Semiconductor Lasers, Delay, Instabilities in Diode Lasers, Bidirectional Coupling.

1. INTRODUCTION

The nonlinear dynamics and synchronization of mutually coupled oscillators have important applications in fields ranging from the high-power laser arrays⁴ to central issues in neuroscience.⁵ In fact, synchronization was first discovered in two mutually coupled oscillators.⁶ Despite of their inherent interest, only few studies have focused on the instabilities arising from the mutual coupling of two semiconductor lasers.⁷⁻¹² So far, the most studied configuration of mutually interacting laser systems is the evanescent coupling of solid-state lasers. However, due to the fundamental differences between the face-to-face and the evanescent coupling, new phenomena can be expected for the former. Moreover, the excellent controllability of semiconductor lasers in the laboratory make them ideal candidates for the experimental investigation of general phenomena in the theory of mutually coupled oscillators. In this context, besides the frequency and phase locking properties, oscillation death by delay,¹² localized synchronization⁷ and spontaneous symmetry-breaking⁸ among others effects, has been recently proved to occur in bidirectionally coupled semiconductor laser systems.

There are different options to mutually couple two edge-emitting semiconductor lasers. In the optoelectronic case,¹² the light coming from one laser facet is converted into electrical current that is added to the bias of the other laser. In the incoherent optical case,¹³ the TE mode of each laser output is 90 degrees rotated before entering into the other laser cavity. It is assumed that in this scheme, the injected fields act only on the carrier population and do not interact with the intracavity lasing fields. Finally, the richer option from the dynamical point of view, and the one in which we focus our attention, is the coherent optical mutual coupling. It represents the mutual injection of the TE mode of each laser into the other laser cavity. In this last case, the parameters controlling the dynamics of both lasers are the coupling strength, delay injection time and propagation phase. These quantities and the detuning between the free-running emission frequencies will be our main bifurcation parameters along this work.

Further author information: (Send correspondence to R.V.)

R.V.: E-mail: raulv@imedea.uib.es, Telephone: 34 971172505

Even in the case that rate equations models are used to describe the dynamics of the system under study, the complexity of the mathematical structure of the set of equations we are dealing with is huge. Consequently, a great advantage has been taken from the consideration of special limits where some approximations are fully justified. On the one hand, one can use the asymptotic analysis motivated from the very different time scales introduced by the photon lifetime, the carrier lifetime and the injection delay time.^{11,14} In particular, Ref.[11] analyzed the case of large distance between the two lasers. On the other hand, it is also common the study of the dynamics of a given system when the perturbation at which is subjected is small, with the hope that the complete understanding of this relatively simple situation will shed light into the interpretation of the more complex dynamics occurring for larger perturbation amplitudes. In this context, phase dynamics models are particularly popular and we will make use of one of them to describe the dynamics in the low coupling limit.

The paper is organized as follows. In Section 2 we present the rate equations describing two spatially-separated bidirectionally-coupled semiconductor lasers. Section 3 tackles the derivation of a phase model and the noise role in a potential picture of that model. Section 4 focuses on the role of the detuning in the dynamics of the system for both the short and long coupling delay time limits. Finally, Section 5 summarizes and points out the main conclusions of the paper.

2. THE MODEL

We consider our system consisting of two single-mode semiconductor lasers in a face to face configuration, where a moderate amount of coupling, arising from the mutual injection of their transverse electrical fields, is assumed. A rigorous derivation of the model that describes the system under consideration has been already presented in Ref.[9]. From that work, it turns out that the phenomenological model is valid when the coupling strength is weak enough. Since this is our case, we put forward the equations governing the evolution of the electrical fields and carriers in each one of the lasers as

$$\dot{E}_{1,2} = \mp i\Delta E_{1,2} + \frac{1}{2}(1 + i\alpha)[G_{1,2} - \gamma]E_{1,2} + \kappa e^{-i\Omega\tau}E_{1,2}(t - \tau) + \sqrt{2\beta N_{1,2}}\xi_{1,2} \quad (1)$$

$$\dot{N}_{1,2} = p \frac{J_{th}^{sol}}{e} - \gamma_e N_{1,2} - G_{1,2}|E_{1,2}|^2 \quad (2)$$

$$G_{1,2} \equiv \frac{g(N_{1,2} - N_t)}{1 + s|E_{1,2}|^2},$$

where both lasers are taken identical except for a possible detuning between their free-running frequencies ($\Delta = \frac{\omega_2 - \omega_1}{2}$, $\Omega_0 = \frac{\omega_2 + \omega_1}{2}$). The internal laser parameters used in our numerical simulations correspond to a realistic experimental situation where the linewidth enhancement factor is $\alpha = 3.5$, the cavity losses $\gamma = 240 \text{ ns}^{-1}$, the carrier decay rate $\gamma_e = 1.66 \text{ ns}^{-1}$, the differential gain $g = 3.2 \times 10^{-6} \text{ ns}^{-1}$, the carrier value at transparency $N_t = 1.5 \times 10^8$, the gain saturation parameter $s = 5 \times 10^{-7}$, the spontaneous emission rate $\beta = 10^{-5} \text{ ns}^{-1}$ and e is the electron charge. The solitary threshold current is $J_{th}^{sol} = 60 \text{ mA}$ and p is the injection current with respect to threshold. The rest of parameters will be varied through this paper and their particular values will be specified in each section.

Neglecting the Langevin noise sources in (1), the steady-states ($E_{1,2}(t) = \sqrt{P_{1,2}(t)}e^{i\varphi_{1,2}(t)}$; $\dot{P}_1 = \dot{P}_2 = 0$, $\dot{N}_1 = \dot{N}_2 = 0$, $\varphi_1(t) = \Omega t$, $\varphi_2(t) = \Omega t + \phi$) of the former six-dimensional set of equations can be found systematically with the algorithm presented in Appendix A. In absence of detuning, three types of fixed points can be distinguished: the in-phase symmetric ($\phi = 0$), anti-phase symmetric ($\phi = \pi$) and asymmetric solutions ($\phi \neq 0, \pi$). The structure and stability of these stationary solutions have been evaluated for the long distance limit and zero-detuning case in Ref.[11]. Figure 1a shows how these fixed points are typically arranged in the Inversion-Frequency plane ($N - N_{th}$ vs $\Omega\tau$) while Figure 1b illustrates how they bifurcate as increasing the coupling strength. Generically, after the saddle-node creation of the symmetric modes, the nodes loss their stability through a Hopf bifurcation while the asymmetric modes emerge and disappear from the symmetric solutions. As in the Lang-Kobayashi model for the case of optical feedback,¹⁵ for fixed κ , the symmetric solutions lie on an ellipse with a major semiaxis $C = \kappa\tau\sqrt{1 + \alpha^2}$. On the other hand, islands of asymmetric

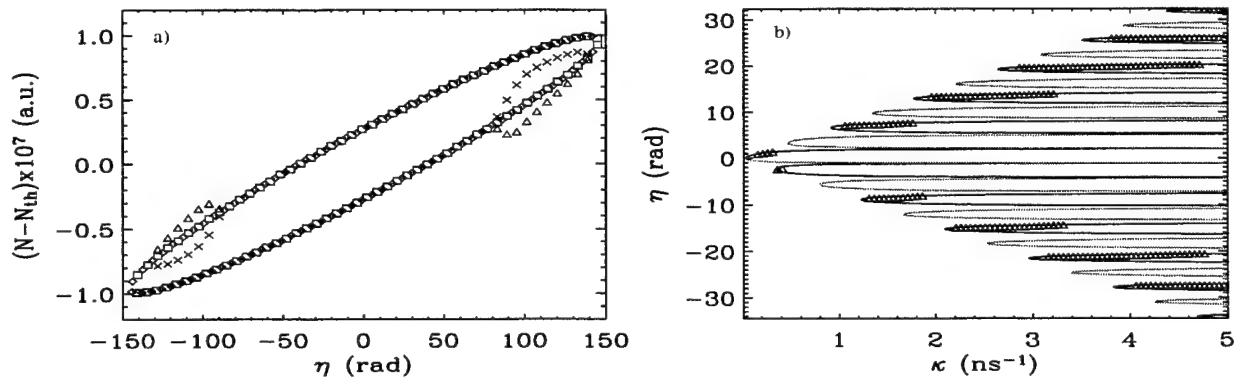


Figure 1. a) Steady-states of eqs. (1)-(2) in the Inversion-Frequency plane for $\kappa = 20 \text{ ns}^{-1}$. Squares and diamonds stand for in-phase and anti-phase solutions while crosses (triangles) represent asymmetric modes with positive (negative) phase difference ϕ . b) Evolution of the modes frequency as increasing the coupling level. Black (grey) solid lines indicate the in-phase (anti-phase) fixed points continuation while the triangles mark the asymmetric modes. In both cases, the pump level and the injection delay time have been set to $p = 1$ and $\tau = 2 \text{ ns}$.

solutions appear around the edges of the ellipse of symmetric states. However, it is worth mentioning that the number of asymmetric modes may change with the bias current whereas the symmetric ones remain unchanged. The modification of these structures under the presence of detuning or when decreasing the distance between lasers until entering in the short intercavity regime, will have important consequences on the dynamics of the system and they will be studied in Section 4.

The next section is devoted to investigate a reduced model based on the phase equations derived from eqs. (1-2), which we will see remains valid in the low coupling limit. From there, the effect of the spontaneous emission noise and locking regime borders will be predicted.

3. PHASE DYNAMICS

For a sufficiently weak coupling, where the relaxation oscillations are still damped, we can assume a constant light intensity and identical in both lasers by neglecting amplitude fluctuations ($E_{1,2}(t) = \sqrt{P_s} e^{i\varphi_{1,2}(t)}$). This approximation leads to the following coupled equations for the optical phases

$$\dot{\varphi}_{1,2}(t) = \mp \Delta - \kappa \sqrt{1 + \alpha^2} \sin(\varphi_{1,2}(t) - \varphi_{2,1}(t - \tau) + \Omega\tau + \arctan \alpha) + F_{\varphi_{1,2}}(t), \quad (3)$$

where the $F_{\varphi_{1,2}}(t)$ is the Langevin noise source associated to the each phase. Despite the important reduction that has been achieved, it still remains the difficulty of dealing with a system of delay differential equations (DDE). The next step is to assume a slow variation of the phases over a entire delay time by expanding $\varphi_{1,2}(t) \approx \varphi_{1,2}(t - \tau) + \tau \dot{\varphi}_{1,2}(t - \tau)$. It is worth noting that for DDE these kind of expansions may not lead to valid results. Surprisingly, for small delay τ the discarded term behaves like $1/\tau$ if the approximation is taken up to second order or beyond.¹⁶ Under these conditions, the resulting equations read¹⁷

$$\dot{\varphi}_{1,2} = \mp \Delta - \kappa \sqrt{1 + \alpha^2} \sin(\varphi_{1,2} - \varphi_{2,1} + \Phi) + F_{\varphi_{1,2}}(t), \quad (4)$$

$$\dot{\vartheta}_{1,2} = \frac{1}{\tau}(\varphi_{1,2} - \vartheta_{1,2}), \quad (5)$$

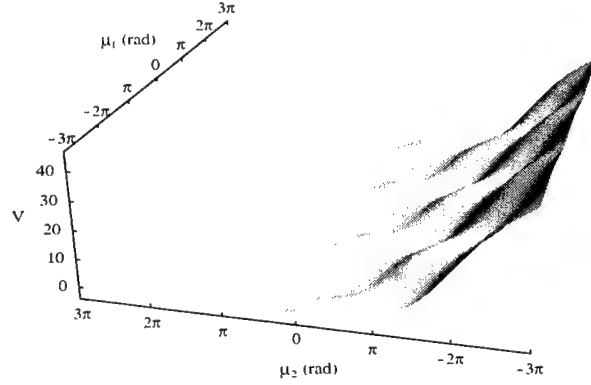


Figure 2. Potential function $V(\mu_1, \mu_2)$ computed for the following parameters: $\Delta = 0$, $\tau = 2$ ns, $\kappa = 0.5$ ns⁻¹ and $\Phi = 4.43$.

where $\vartheta_{1,2}(t) \equiv \varphi_{1,2}(t - \tau)$ and $\Phi \equiv \Omega\tau + \arctan \alpha \bmod 2\pi$. Now, defining $\mu_{1,2} \equiv \frac{1}{2}[(\varphi_1 - \vartheta_2) \mp (\varphi_2 - \vartheta_1)]$, i.e. the addition and difference of the injected phases, it is obtained that for these variables there exists a potential function V in terms of which the dynamics is written as

$$\dot{\mu}_{1,2} = -\frac{1}{\tau} \frac{\partial V(\mu_1, \mu_2)}{\partial \mu_{1,2}} + F_{\mu_{1,2}}(t), \quad (6)$$

$$V(\mu_1, \mu_2) = \tau\Delta\mu_1 + \frac{1}{2}\mu_2^2 - C \cos \mu_1 \cos(\Phi + \mu_2). \quad (7)$$

Figure 2 shows an example of the potential landscape where the relaxational gradient dynamics take place. Before continuing the analysis, it is worth mentioning that in the steady state operation (i.e. in a potential minima) the variable μ_1 represents the phase difference ϕ between both lasers while μ_2/τ accounts for the locked frequency Ω .

At this point, we numerically check the validity of our approximations by comparing the results obtained for the phase difference and frequency in the absence of noise, with the full model [eqs. (1)-(2)] and with the reduced model [eqs. (6)-(7)]. For the same parameters used in the Figure 2, the computation of these quantities with the full model provides, when the initial condition is in the neighborhood a steady-state, the values $\mu_1 = 0$, $\mu_2 = -1.009812$ while the model based on the potential description gives $\mu_1 = 0$, $\mu_2 = -1.009803$. It is then clear that the potential description is valid providing that the coupling values are small enough.

In absence of detuning, it is easy to demonstrate that the potential minima are generically located at coordinates where the μ_1 variable equals $n\pi$ with $n \in \mathbb{Z}$. Consequently, the absolute minimum of the potential at which the dynamics of the system approach in the long-time limit can be an in-phase or an anti-phase mode, its selection determined by Φ . In the presence of spontaneous emission noise, the interpretation of these steady-states is associated with the maxima of the probability density function given by the corresponding Fokker-Planck equation. The possible noise-induced mode hopping is illustrated in Figure 3. As consequence of the potential structure, each mode hopping or frequency slip is simultaneously accompanied by a phase slip. The correspondence of the mode hopping with the features of the potential landscape is clearly observed in the bottom panel of Figure 3, where the stochastic slips occur mainly through the saddles between different minima.

Although computation of Mean First Passage Time (MFPT) between potential wells is much more complicated to perform in several dimensions than in the simple one-dimensional case,¹⁸ there is still the inversely exponential dependence on the barrier height. Consequently, any increase of κ , τ or α maintained within the margins of validity of the approach here used will lead to the stabilization of the dynamics against the noise.

The role of the detuning on the potential is to break the periodicity in the μ_1 variable and to tilt the potential landscape. No in-phase or anti-phase states exist anymore, although for small positive (negative) detuning values

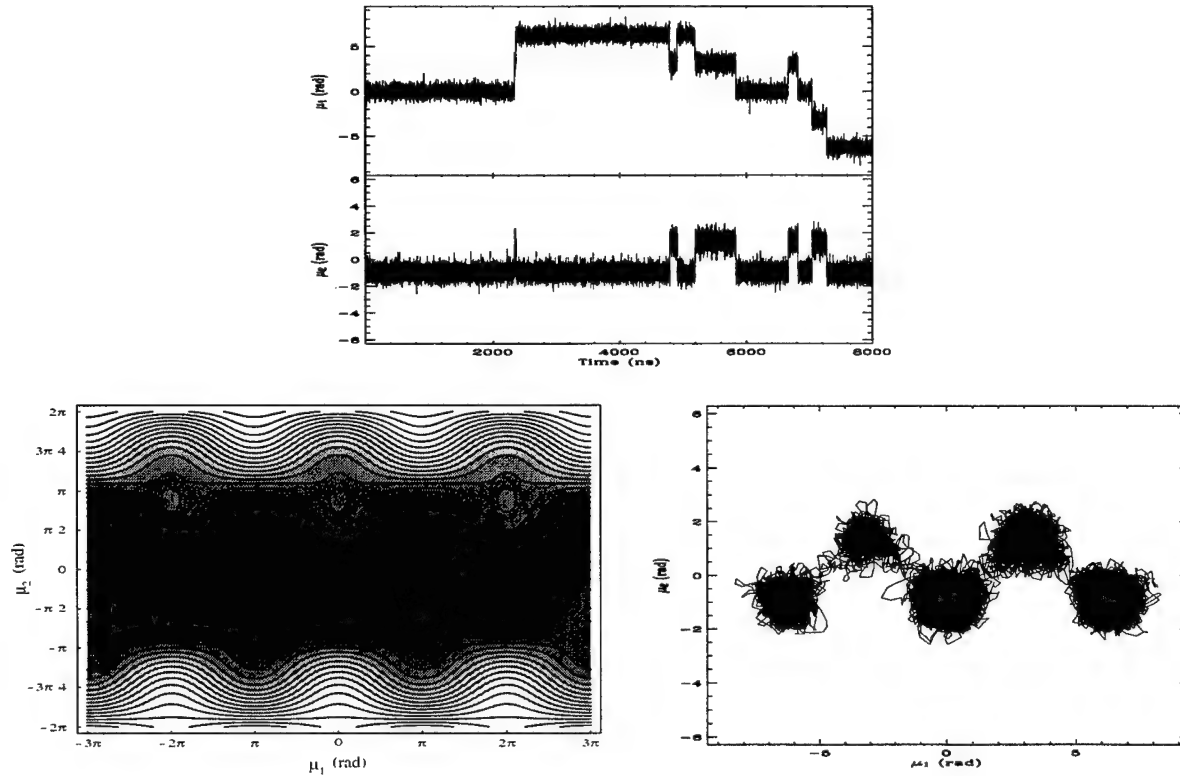


Figure 3. Top panel: Evolution of the phase difference and frequency. Bottom panel: Left graphic is the contour plot of the potential function. Right graphic contains the numerically simulated stochastic path followed by the system in the $\mu_1 - \mu_2$ plane. The parameters used are the same than those corresponding to Figure 2.

infinitely many minima with deeper wells are arranged in the direction of increasing (decreasing) phase difference. Then, in the absence of noise, both lasers would lock to a frequency and phase corresponding to one of these local minima. However, the presence of Gaussian noise (or any other unbounded noise) will make the system to continuously jump to deeper minima. If the detuning parameter exceeds a critical value, the potential becomes so tilted that it is unable to produce local minima. In this situation, both lasers cannot manage to lock and no steady-state can be reached. The border of this transition from locking to unlocking regime can be predicted by demanding the condition that the potential function presents a non-zero number of critical points. Eliminating μ_1 from the system of equations $\partial V/\partial \mu_1 = \partial V/\partial \mu_2 = 0$, it is obtained that μ_2 has to meet the following condition

$$\mu_2 + C \tan(\mu_2 + \Phi) \sqrt{\cos^2(\mu_2 + \Phi) - \frac{\tau^2 \Delta^2}{C^2}} = 0. \quad (8)$$

Consequently, in the $\kappa - \Delta$ plane, the Arnold tongue or locking regime area is determined by the region where real solutions for equation (8) exist. An important observation is the fact that changing the value of Φ , the size of the corresponding Arnold Tongue may suffer important modifications and that this effect occurs for both short and long injection delay times. For instance, in Figure 4, the locking limits for values of $\Phi = 0, \pi/4, \pi/2$ and $3\pi/4$ are represented.

Finally, it is worth to recall that the maximum coupling strength for which the former approach is valid (i.e. the maximum coupling for which the relaxation oscillations are still damped), is strongly dependent on the bias current level. Hence, if for $p = 1.1$ (10% above solitary threshold) $\kappa_{max} \approx 3 \text{ ns}^{-1}$, for $p = 1.5$ (50% above solitary threshold) $\kappa_{max} \approx 9 \text{ ns}^{-1}$ what represents a moderate amount of coupling level.

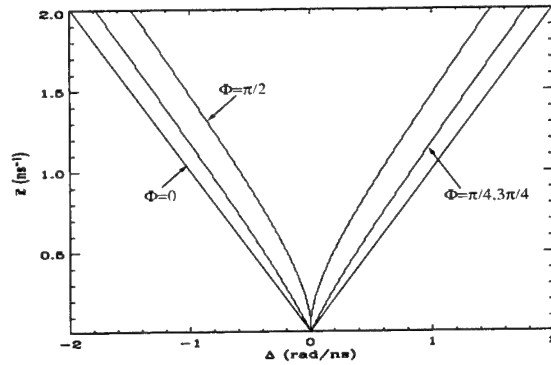


Figure 4. Synchronization regions or Arnold tongues for different values of the injection phase Φ . The modified coupling coefficient that appears in the vertical axis is defined as $\bar{\kappa} \equiv \kappa\sqrt{1+\alpha^2}$. The maximum locking size is achieved for $\Phi = n\pi$ while the minimum one is obtained for $\Phi = (2n+1)\pi/2$, $n \in \mathbb{Z}$.

4. DETUNING EFFECT ON THE DYNAMICS: THE SHORT AND LONG COUPLING DELAY TIME LIMITS

The detuning influence on the dynamics of unidirectionally coupled laser schemes has been extensively studied in the literature.¹⁹ In these works, the locking properties and their stability as well as multi-wave mixing processes in the non-locking area have been reported and analyzed. Chirp reduction and bandwidth increment are among the practical applications that benefited from the study of these Master-Slave (M-S) semiconductor lasers systems. However, the fundamental differences between an unidirectional and a mutually coupled scheme make clear the necessity of a separated study of the detuning effect on the dynamics of the system under consideration. Besides the mutual frequency pulling effects, there is the novelty that the propagation phase φ_0 between the lasers may act as an important parameter, unlike in the M-S case where it could be removed from the equations by a simple rescaling of the time variable.

First, we focus on the short intercavity regime by taking the distance between lasers $L = 6$ cm ($\tau = 0.2$ ns). The coupling strength has been chosen to be small ($\kappa = 5$ ns⁻¹), the pumping has been set close to the solitary threshold $p = 1$ and the propagation phase is fixed to $\varphi_0 = 0$. Figure 5 (left panel) displays the bifurcation diagram of the optical power of both lasers when the detuning parameter is continuously changed from 0 to 12 GHz. From the diagram, it is observed that for small detuning ($\Delta\nu < 0.5$ GHz) the lasers are still operating in the steady-state condition with a very similar optical power output, until they enter into a period-1 window (0.5 GHz $< \Delta\nu < 1.1$ GHz). In this regime, the optical power undergoes oscillations in anti-phase dynamics. After this regime, the dynamics enters into a more complex oscillatory regime (1.1 GHz $< \Delta\nu < 1.5$ GHz), before reaching a sequence of alternating periodic and constant states. For large detunings, it is observed that in the periodic windows, the relative phase between the optical powers depends specifically on the value of the detuning. The right panel of Figure 5 shows the optical spectra of both lasers for selected values of the detuning. Locking, non-locking states and multi-wave mixing phenomena are clearly identified from these graphics. For instance, graphics a) and e) are examples of the locking of both lasers to the most negative mode, while graphics d) and f) show a clear behavior of non-locking states. Interestingly, it is noticed that even when the system is unable to lock for $\Delta\nu = 4$ GHz, it is able to do so for the larger value of the detuning $\Delta\nu = 6$ GHz, although for larger values of the frequency mismatch it is again in an unlocked state. In these unlocked states for large detuning, the periodic oscillations of each laser have a frequency very similar to the detuning value $\Delta\nu$.

Steady-states and typical trajectories, after transients have died out, are plotted in Figure 6 for the same parameters as those used in the right panel of Figure 5. The phase space used to visualize the dynamics is as follows: a) both lasers lock to the most negative frequency plane. The description of each graphics is as follows: a) both lasers lock to the most negative frequency mode, which is stable for small values of the detuning, b) each laser is operating in different limit cycles located at different frequencies ranges, c) there is an increment of the complexity of the trajectory,

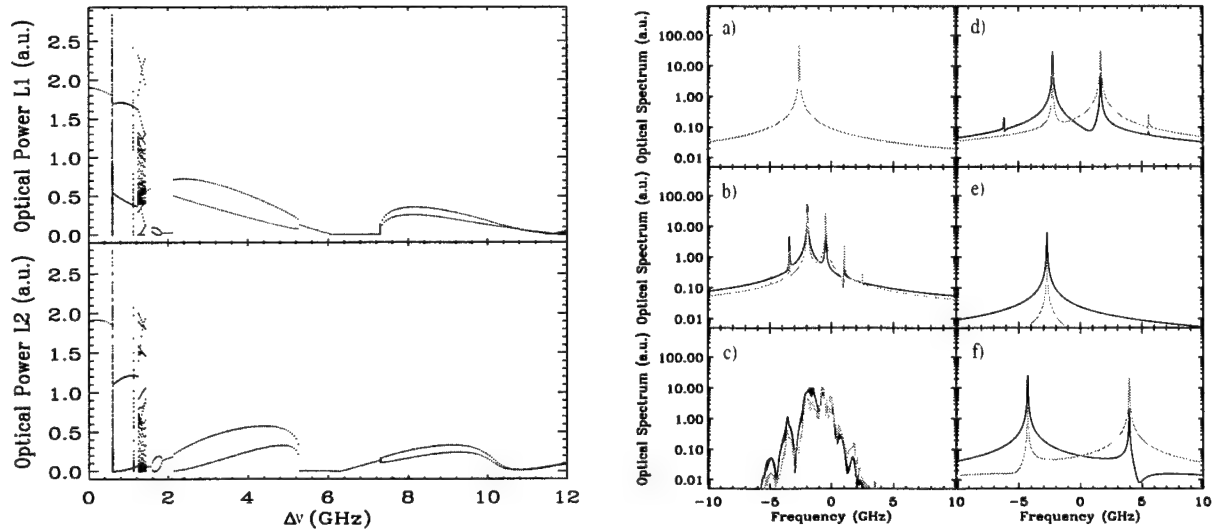


Figure 5. Left panel contains the bifurcation diagrams for the optical power of laser 1 and 2 against the detuning. Only extrema values are recorded. Right panel illustrates the optical spectra for: a) $\Delta\nu = 0.4$ GHz, b) $\Delta\nu = 0.8$ GHz, c) $\Delta\nu = 1.3$ GHz, d) $\Delta\nu = 4$ GHz, e) $\Delta\nu = 6$ GHz, and f) $\Delta\nu = 8$ GHz. Black and grey colors distinguish the laser 1, 2.

d) both lasers are unlocked and oscillate around separated fixed points located approximately at $\approx \pm\Delta/2$, e) the lasers lock again near the negative frequency state and f) the system comes back to an unlocked regime oscillating around different fixed points. It is worth noting that for the range of moderate values of detuning we have studied here ($\Delta < 12$ GHz), the number of steady-states decreases with the detuning until only two fixed points appear with frequencies close to $\approx \pm\Delta/2$.

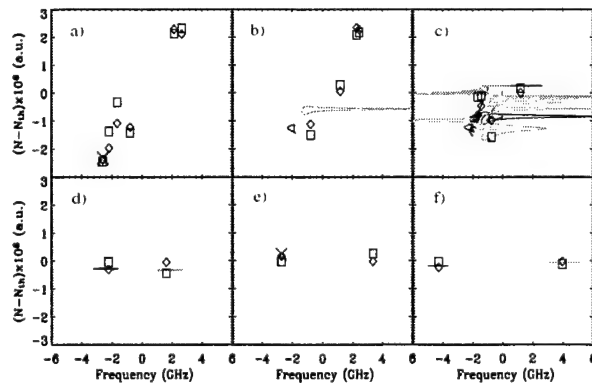


Figure 6. Fixed points and trajectories in the Inversion-Frequency plane for: a) $\Delta = 0.4$ GHz, b) $\Delta = 0.8$ GHz, c) $\Delta = 1.3$ GHz, d) $\Delta = 4$ GHz, e) $\Delta = 6$ GHz, and f) $\Delta = 8$ GHz. Diamonds and squares stand for the asymmetric fixed points of the laser 1 and 2, respectively. Crosses are used to identify the final states for the trajectories that reach a fixed point. Black and grey colors distinguish the laser 1 and 2.

In all the previous studies, the propagation phase has been fixed to zero, despite it may play an important role in the dynamics. Now, we fix the detuning and change the phase in order to investigate the dynamical dependence on this critical parameter. Figure 7 contains the bifurcation diagram of both lasers when varying

the phase for 0 GHz (top panel) and 6 GHz (bottom panel). In the non-detuned case, depending on the phase value chosen one can observe constant, periodic or even chaotic oscillations but always there exists a high degree of anticorrelation between the two laser outputs as it is shown in Figure 8. For larger detunings, the phase is only able to switch from stable to periodic behavior but no chaotic states can be achieved.

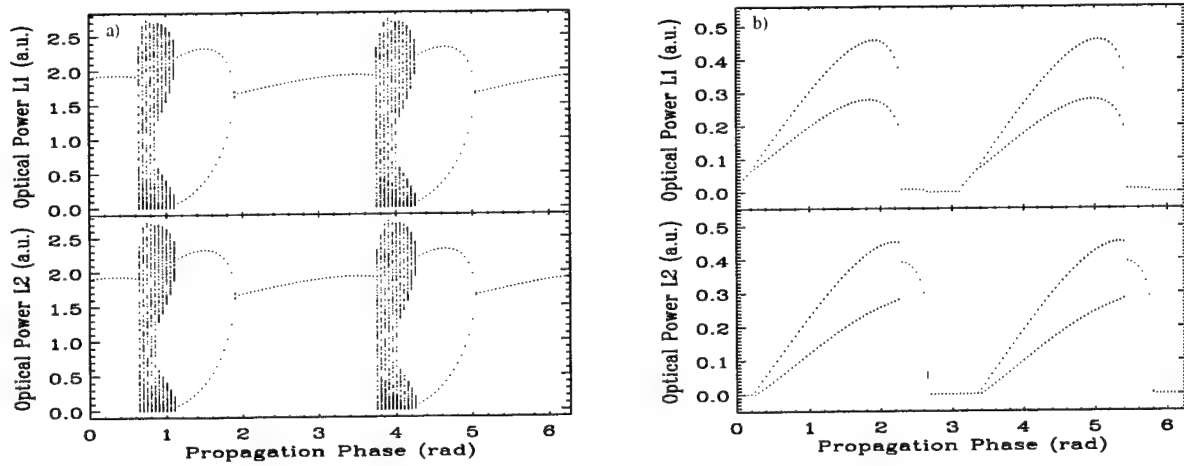


Figure 7. Bifurcation diagrams for the optical power of laser 1 and 2 against φ_0 . a) $\Delta = 0$ GHz. b) $\Delta = 6$ GHz.

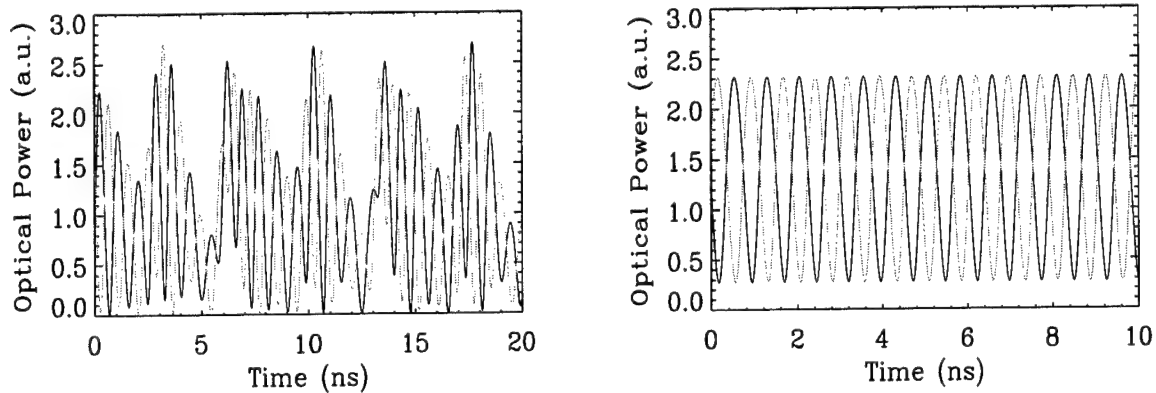


Figure 8. Temporal traces for the laser 1 and 2 showing anticorrelated dynamics for the non-detuned case. Left panel: $\varphi_0 = 0.8$ rad. Right panel: $\varphi_0 = 1.4$ rad. Black and grey colors distinguish the laser 1 and 2.

Now, we move to the long intercavity regime by increasing the distance between lasers up to $L = 120$ cm ($\tau = 4$ ns). Here, the role of the phase φ_0 is not so important as in the short delay time case. The rest of the coupling conditions are the same than those used in the study of the short injection delay time. However, for this situation both lasers are in the LFF regime, at least for the non-detuned case. We gradually increase the solitary frequency of the laser 2 with respect to the laser 1, and we analyze the modification of the steady-states. We find very different situations: solutions with nearly the same inversion for the two lasers giving rise to almost the same optical power and solutions with very asymmetric operation of the two lasers. For small detunings, $\Delta\nu = 0.5$ GHz (see Figure 9(a)) we observe two slightly distorted ellipses with a maximum deformation close to their edges. The separation between the upper and lower branch of the ellipses decreases for the lower (higher) inversion modes of the low (high) frequency laser. For a larger detuning, $\Delta\nu = 1.75$ GHz (see Figure 9(b)) we

observe that the two ellipses split, giving rise to two new banana-like-shaped ellipses with very different inversion levels. In this case, and depending on the initial conditions, one can have operation in different regions of the diagram. Increasing further the detuning, the number of steady-states decreases until the boundary for the existence of frequency locked solutions is reached.

For a fixed detuning, we have analyzed the modification in the distribution of steady states when the injection current is increased observing that the metamorphosis of steady-states become more and more complex. Even for small detuning ($\Delta\nu = 0.5$ GHz), increasing the pumping level we observe that both ellipses split in two new ellipses with different inversion levels.

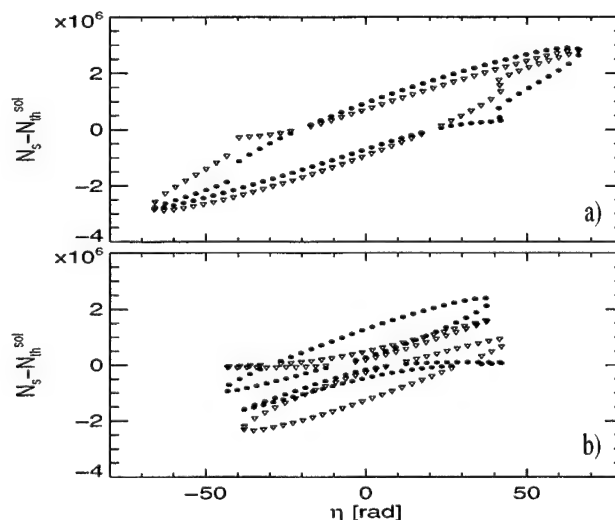


Figure 9. Steady-states in the Inversion-Frequency plane. Laser 2 (1) fixed points are represented by triangles (circles). a) $\Delta\nu = 0.5$ GHz. b) $\Delta\nu = 1.75$ GHz.

Regarding the temporal evolution of the system, we observed that for the zero-detuning case, the laser that drop first in the LFF regime seems to be randomly chosen, but as we discuss below this process becomes more regularized by increasing the detuning. Typical time traces of the intensity for different detunings are shown in Figure 10. Panel a) corresponds to $\Delta\nu = 1$ GHz. We observe power dropouts similar to those obtained in the resonant case but now appearing in a well defined leader-laggard sequence. The vertical lines in the figure indicate that the dropout of the higher frequency laser is followed by the dropout of the lower frequency one. The power dropouts become more periodic for $\Delta\nu = 6$ GHz as shown in the panel b). We note that, in this case, the shape of the power dropouts differs from the usually one obtained under resonant conditions. The time traces for the lower frequency laser resemble to a sawtooth signal, while for the higher frequency laser resemble to a square one. For larger detuning, $\Delta\nu = 8$ GHz, in panel c), the time traces consist of dominant high frequency pulses of the intensity displaying some degree of correlation between the two series. For detuning larger than 12 GHz the synchronization is lost.

5. CONCLUSIONS

We have derived a potential picture of the phase dynamics of two semiconductor lasers coupled in a face to face configuration. Numerical comparison between this reduced and the full model shows excellent agreement in the low coupling strength limit. From this potential framework, the effect of the spontaneous emission noise and detuning are clearly identified. In particular, mode hopping characteristics and locking borders have been

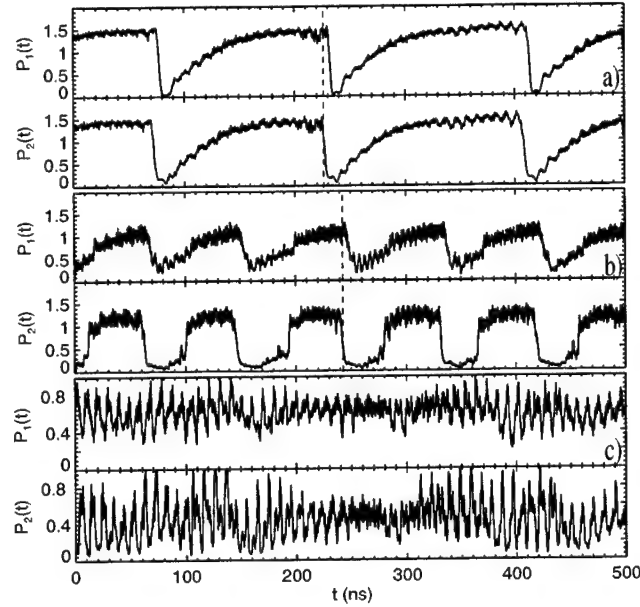


Figure 10. Typical time traces of the laser intensities under detuned operation. a) $\Delta\nu = 1$ GHz, b) $\Delta\nu = 6$ GHz, and c) $\Delta\nu = 8$ GHz.

predicted. Focusing on the short injection coupling time, the detuning-induced dynamics has been observed to pass through different stages. Interestingly, several islands of stable locking have been found to be located between regions of unlocking behavior. The role of the propagation phase have been also found to be critical in the short distance limit. Finally, in the long coupling delay time limit, we have studied how the LFF oscillations are modified in the presence of detuning. Rigorous study of the stability of the fixed points and limit cycles in the short intercavity regime, as well as a complete study of the relative dynamics between the lasers when parameters like the coupling strength or the coupling delay time are varied, are interesting subjects for future works.

APPENDIX A

The conditions to be imposed in order to obtain frequency-locked solutions are $E_1(t) = \sqrt{P_1}e^{i\Omega t}$ and $E_2(t) = \sqrt{P_2}e^{i(\Omega t + \phi)}$ allowing a relative phase ϕ between the two fields. Furthermore, $\dot{P}_1 = \dot{P}_2 = 0$ and $\dot{N}_1 = \dot{N}_2 = 0$ in a steady-state. Introducing these conditions into eqs. (1-2) and neglecting Langevin noise sources, we arrive to a set of non-linear equations that reads

$$\eta + \delta = -aC \sin(\eta + \varphi_0 + \arctan \alpha - \phi), \quad (\text{A1})$$

$$\eta - \delta = -\frac{1}{a}C \sin(\eta + \varphi_0 + \arctan \alpha - \phi), \quad (\text{A2})$$

$$0 = J_k - \gamma_e N_k - G_k P_k \quad k = 1, 2. \quad (\text{A3})$$

At this point, we have defined the following quantities: the compound system mode frequency $\eta = \Omega\tau$, the power ratio $a^2 = P_2/P_1$, the normalized detuning $\delta = \Delta\tau$, the injection phase $\varphi_0 = \Omega_0\tau$ and the effective coupling parameter $C = \kappa\tau\sqrt{1 + \alpha^2}$. A solution of the system of equations (A1-A3) determines a vector of six unknowns ($P_1, P_2, N_1, N_2, \eta, \phi$) that defines a frequency locked solution of the coupled system. Multiplying eq. (A1) by (A2) we find an expression for $y \equiv \sin(\phi)$,

$$y(\eta) = \pm \sqrt{\sin^2(\eta + \varphi_0 + \arctan \alpha) - (\eta^2 - \delta^2)/C^2}, \quad (\text{A4})$$

while dividing eq. (A1) by (A2) we can obtain an expression for $a(\eta, y)$ that reads

$$a^2 = \left[\frac{\eta + \delta}{\eta - \delta} \right] \left[\frac{\sqrt{1 - y^2} + y \cot(\eta + \varphi_0 + \arctan \alpha)}{\sqrt{1 - y^2} - y \cot(\eta + \varphi_0 + \arctan \alpha)} \right]. \quad (\text{A5})$$

Finally, extracting from eqs. (A3) the power ratio a^2 and combining with eqs. (A4) and (A5), we arrive at the following non-linear equation for the compound system mode η

$$a^2 [\rho_1 + aT_+] [a - bT_-] - [a\rho_2 + T_-] [1 - abT_+] = 0, \quad (\text{A6})$$

with $T_{\pm} = \sqrt{1 - y^2} \cos(\eta + \varphi_0) \pm y \sin(\eta - \varphi_0)$. In order to simplify notation we have introduced two additional parameters, $b = 2\kappa/\gamma$ and $\rho_{1,2} = \frac{g}{2\kappa\gamma_e}(p_{1,2} - 1)J_{th}^{sol}$.

After solving eq. (A6) for η_s and having avoided spurious solutions, we can use eqs. (A4) and (A5) to determinate the remaining unknowns y_s , a_s and the following quantities

$$\phi = \arcsin(y_s), \quad (\text{A7})$$

$$G_{1,2} = \gamma - 2\kappa a_s^{\pm 1} \cos(\eta_s + \varphi_0 \mp \phi), \quad (\text{A8})$$

$$P_{1,2} = \frac{(p_{1,2} - 1)J_{th}^{sol} - (\gamma_e/g)(G_{1,2} - \gamma)}{G_{1,2}(1 + s\gamma_2/g)}, \quad (\text{A9})$$

$$N_{1,2} - N_{th}^{sol} = \frac{1}{g} [G_{1,2} - \gamma] + sG_{1,2}P_{1,2}/g. \quad (\text{A10})$$

ACKNOWLEDGMENTS

R.V., J.M. and C.R.M. acknowledge financial support from the Ministerio de Ciencia y Tecnología (Spain) and FEDER and BFM2002-04369) and from the EC project IST-2000-29683 OCCULT. C.R.M. is also grateful for the hospitality and support of the Electrical Engineering Department, University of California, Los Angeles. C.R.M. is also funded by the Secretaría de Estado de Educación y Universidades, Ministerio de Educación, Cultura y Deporte, Spain. Marc Sciamanna is a Research Fellow from the Fonds National de la Recherche Scientifique (FNRS), Belgium.

REFERENCES

1. J. Mork and B. Tromborg, "The mechanism of mode selection for an external cavity laser," *IEEE Phot. Tech. Lett.* **2**, p. 21, 1990.
2. J. Mork, M. Semkow, and B. Tromborg, "Measurement and theory of mode hopping in external cavity lasers," *Electronics Lett.* **26**, p. 609, 1990.
3. D. Lenstra, "Statistical theory of the multistable external-feedback laser," *Optics Comm.* **81**, p. 209, 1991.
4. A. Glova, S. Kurchatov, V. Likhanskii, A. Lysikov, and A. Napartovich, "Coherent emission of a linear array of co₂ waveguide lasers with a spatial filter," *Quant. Electron.* **26**, p. 500, 1996.
5. H. Haken, J. Kelso, and H. Bunz, "A theoretical model of phase transitions in human hand movements," *Biol. Cybern.* **51**, p. 347, 1985.

6. A. Pikovsky, M. Rosenblum, and J. Kurths, *Synchronization: A Universal Concept Nonlinear Science*, Cambridge University Press, 2002.
7. A. Hohl, A. Gavrielides, and V. Erneux, T. Kovanis, "Localized synchronization in two coupled nonidentical semiconductor lasers," *Phys. Rev. Lett.* **78**, p. 4745, 1997.
8. H. T., I. Fischer, W. Elssser, J. Mulet, and C. Mirasso, "Chaos synchronization and spontaneous symmetry-breaking in symmetrically delay-coupled semiconductor lasers," *Phys. Rev. Lett.* **86**, p. 795, 2001.
9. J. Mulet, C. Masoller, and C. R. Mirasso, "Modeling bidirectionally coupled single-mode semiconductor lasers," *Phys. Rev. A* **65**, p. 063815, 2002.
10. J. M. Buldu, R. Vicente, T. Perez, C. R. Mirasso, M. C. Torrent, and J. Garcia-Ojalvo, "Periodic entrainment of power dropouts in mutually coupled semiconductor lasers," *Appl. Phys. Lett.* **81**, p. 5105, 2002.
11. J. Javaloyes, P. Mandel, and D. Pieroux, "Dynamical properties of lasers coupled face to face," *Phys. Rev. E* **67**, p. 036201, 2003.
12. R. Vicente, J. Mulet, C. R. Mirasso, S. Tang, and J. Liu, "Dynamical properties of two semiconductor lasers with bidirectional optoelectronic coupling," *Physics and Simulation of Optoelectronic Devices XI, SPIE Proceedings* **4986**, p. 440, 2003.
13. F. Rogister, A. Locquet, D. Pieroux, M. Sciamanna, O. Deparis, P. Megret, and M. Blondel, "Secure communication scheme using chaotic laser diodes subject to incoherent optical feedback and incoherent optical injection," *Optics Letters* **26**, p. 1486, 2001.
14. A. Hohl, A. Gavrielides, and V. Erneux, T. Kovanis, "Quasiperiodic synchronization for two delay-coupled semiconductor lasers," *Phys. Rev. A* **59**, p. 3941, 1999.
15. R. Lang and K. Kobayashi, "External optical feedback effects on semiconductor injection laser properties," *IEEE J. of Quantum Electron.* **16**, p. 347, 1980.
16. T. Saaty, *Modern Nonlinear Equations*, Dover, 1981.
17. J. Mulet, C. Mirasso, T. Heil, and I. Fischer, "Synchronization scenario of two distant mutually coupled semiconductor lasers," *J. Opt. B: Quantum Semiclass. Opt.* **6**, p. 97, 2004.
18. P. Hanggi, P. Talkner, and M. Borkovec, "Reaction-rate theory: Fifty years after kramers," *Rev. Mod. Phys.* **62**, p. 251, 1990.
19. G. Tartwijk and D. Lenstra, "Semiconductor lasers with optical injection and feedback," *J. Opt. B: Quantum Semiclass. Opt.* **7**, p. 87, 1995.

Experimentally Observed Dynamical Characteristics of Mutually Coupled Semiconductor Lasers With or Without Optoelectronic Feedback

S. Tang, M.C. Chiang, J.M. Liu, R. Vicente^a, and C.R. Mirasso^a

Electrical Engineering Department, University of California, Los Angeles, Los Angeles, CA 90095-1594, USA

^aOn leave from Departament de Fisica, Universitat de les Illes Balears, E-07122 Palma de Mallorca, Spain

ABSTRACT

Mutually-coupled semiconductor lasers are of great current interest because of the important insight they provide into coupled physical, chemical, and biological systems. Two semiconductor lasers either with or without optoelectronic feedback are mutually coupled together through optoelectronic paths. It is found that mutual coupling can significantly affect the dynamics of the semiconductor lasers, depending on the coupling delay time and the coupling strength. Interesting phenomena such as generation of chaos, quasiperiodic and period-doubling bifurcation to chaos, and death by delay are observed. Synchronization of the chaotic outputs from mutually coupled semiconductor lasers is also observed.

Keywords: Chaos, Semiconductor Lasers, Mutual Coupling, Optoelectronic Feedback

1. INTRODUCTION

Chaotic optical communications with messages encoded in chaotic optical waveforms and decoded through chaos synchronization have been widely investigated and demonstrated using semiconductor lasers.^{1,2} Nonlinear dynamics of semiconductor lasers are of great interests because of the important roles semiconductor lasers play in such chaotic optical communications. Chaotic dynamics can be induced in a semiconductor laser by increasing the dynamical dimension of the laser through a proper external perturbation, such as optical feedback, optical injection, or optoelectronic feedback. With optoelectronic feedback, a single-mode semiconductor laser can have chaotic dynamics in certain operating conditions. Either positive³ or negative⁴ optoelectronic feedback can be applied to a solitary single-mode semiconductor laser to generate chaotic dynamics. In both cases, the laser follows a quasiperiodicity route to chaotic pulsing.

While the dynamics of individual semiconductor lasers have been widely investigated, the effects of coupling between two semiconductor lasers have been of great interests recently. In unidirectionally coupled semiconductor lasers, chaos synchronization and chaotic communications have been demonstrated. Semiconductor lasers can also be mutually coupled.^{5,6} Leading and lagged synchronization has been observed in semiconductor lasers with mutual optical coupling. Mutual coupling also induces new nonlinear dynamical phenomena and significantly changes the dynamics of uncoupled semiconductor lasers. Uncoupled semiconductor lasers are independent nonlinear oscillators. Mutual coupling connects those nonlinear oscillators together. Mutual coupling has been observed to stabilize and quench the oscillation amplitude such as in the phenomenon of death by delay. Mutual coupling can also destabilize the nonlinear system to generate highly complex chaos.

In this paper, we study the nonlinear dynamics of two semiconductor lasers that are mutually coupled through optoelectronic paths. Three different system configurations with the presence or absence of feedback to the lasers are investigated. The effect of mutual coupling on the semiconductor laser dynamics is found to be significant. Stabilization of oscillation is observed due to mutual coupling. Highly complex chaos and the route to chaos are also demonstrated. Synchronization of the dynamical outputs from the lasers with mutual coupling is also

Further author information: (Send correspondence to J.M. Liu)

J.M. Liu: E-mail: liu@ee.ucla.edu, Telephone: 1-310-206-2097

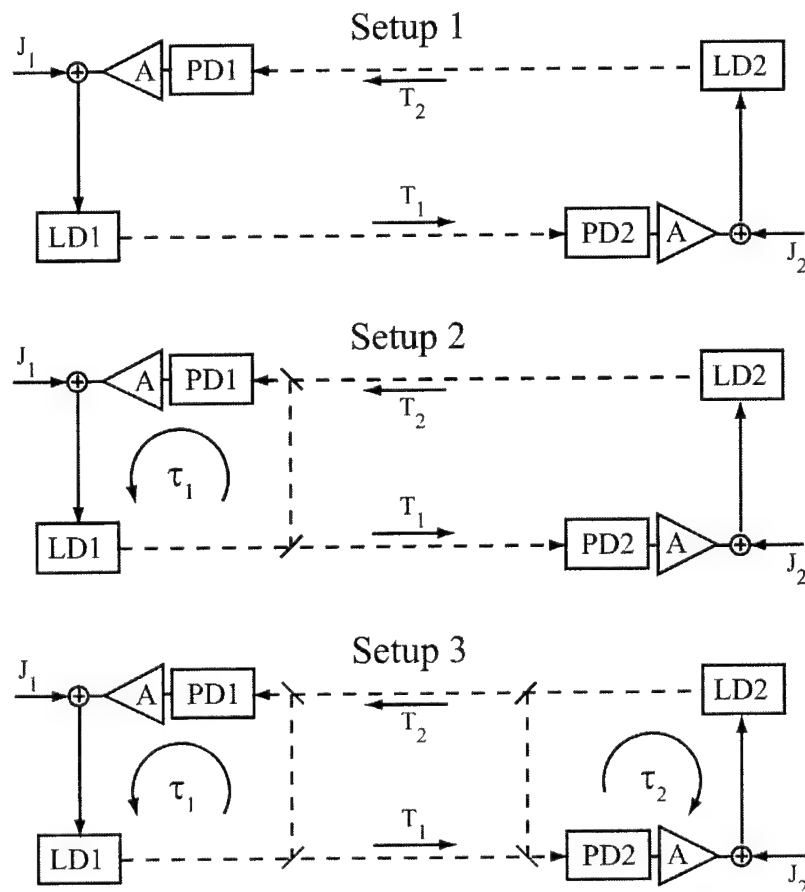


Figure 1. Schematics of mutually coupled semiconductor lasers. Setup 1, mutually coupled semiconductor lasers without optoelectronic feedback; Setup 2, mutually coupled semiconductor lasers with optoelectronic feedback for only one laser; Setup 3, mutually coupled semiconductor lasers with optoelectronic feedback for both lasers. LD: Laser diode; PD: Photodetector; A: Amplifier; τ : Feedback delay time; T : Mutual coupling delay time; J : Bias current.

studied. The organization of this paper is as follows: The system modeling and numerical results are given in Section 2. Sections 3, 4, and 5 cover the experimentally observed effects of mutual coupling for each of the three different system setups. Various dynamical states under different operation conditions for different coupling configurations are discussed in Section 6. A brief conclusion is given in Section 7.

2. SYSTEM CONFIGURATION AND MODELING

The schematics of semiconductor lasers with mutual optoelectronic coupling are shown in Fig. 1. Depending on the presence or absence of optoelectronic feedback to the lasers, the system can have three different configurations. In all three configurations, the two semiconductor lasers are mutually coupled. The output of laser diode 1 (LD1) is coupled to laser diode 2 (LD2) through an optoelectronic path which is consisted of photodetector 2 (PD2) and an amplifier. The detector PD2 converts the optical signal into an electronic signal. The electronic signal after PD2 and the amplifier is sent to LD2 through its current drive. Similarly, the output of LD2 is coupled to LD1 through another optoelectronic path consisting of photodetector 1 (PD1) and an amplifier. The differences in the setups are in the optoelectronic feedback. In Setup 1, no laser has any optoelectronic feedback. In Setup 2, only one laser has optoelectronic feedback. In Setup 3, both lasers have optoelectronic feedback. Under certain conditions, optoelectronic feedback can drive a semiconductor laser into nonlinear oscillation, such as regular pulsing, quasiperiodic pulsing, or chaotic pulsing. The rich nonlinear dynamics of semiconductor lasers with

optoelectronic feedback have been demonstrated.^{3,4} In this paper, we study the coupling effect on semiconductor lasers with mutual optoelectronic coupling.

The two semiconductor lasers can be modeled by the rate equations of the intracavity photon density, S , and the carrier density, N . LD1 can be modeled as

$$\frac{dS_1}{dt} = -\gamma_{c1}S_1 + \Gamma g_1(N_1, S_1)S_1 + 2\sqrt{S_0 S_1}F_{s1}, \quad (1)$$

$$\frac{dN_1}{dt} = \frac{J_1}{ed} [1 + \xi_{f1}y_{f1}(t - \tau_1) + \xi_{c1}y_{c1}(t - T_2)] - \gamma_{s1}N_1 - g_1(N_1, S_1)S_1, \quad (2)$$

$$y_{f1}(t) = \int_{-\infty}^t d\eta f_1(t - \eta)S_1(\eta)/S_0, \quad (3)$$

$$y_{c1}(t) = \int_{-\infty}^t d\eta f_1(t - \eta)S_2(\eta)/S_0. \quad (4)$$

The signal $\xi_{f1}y_{f1}(t - \tau_1)$ in Eq. (2) is the feedback signal of LD1, where ξ_{f1} is the feedback strength and τ_1 is the feedback delay time. As is shown in Eq. (3), $y_{f1}(t)$ is the convolution of $S_1(t)$ with the frequency response function $f_1(t)$ of the photodetector and the amplifier in the loop of LD1. Meanwhile, the signal $\xi_{c1}y_{c1}(t - T_2)$ is the coupling signal from LD2 to LD1, where ξ_{c1} is the coupling strength and T_2 is the coupling delay time. As is shown in Eq. (4), $y_{c1}(t)$ is the convolution of $S_2(t)$ with the frequency response function $f_1(t)$. The parameter ξ_{f1} or ξ_{c1} respectively goes to zero if there is no optoelectronic feedback or coupling to LD1. In the configuration of Fig. 1, both the feedback and the coupling signals are bandwidth-limited by the frequency response function $f_1(t)$ of the photodetector and the amplifier in the loop of LD1.

Similarly, LD2 can be modeled as

$$\frac{dS_2}{dt} = -\gamma_{c2}S_2 + \Gamma g_2(N_2, S_2)S_2 + 2\sqrt{S_0 S_2}F_{s2}, \quad (5)$$

$$\frac{dN_2}{dt} = \frac{J_2}{ed} [1 + \xi_{f2}y_{f2}(t - \tau_2) + \xi_{c2}y_{c2}(t - T_1)] - \gamma_{s2}N_2 - g_2(N_2, S_2)S_2, \quad (6)$$

$$y_{f2}(t) = \int_{-\infty}^t d\eta f_2(t - \eta)S_2(\eta)/S_0, \quad (7)$$

$$y_{c2}(t) = \int_{-\infty}^t d\eta f_2(t - \eta)S_1(\eta)/S_0. \quad (8)$$

The corresponding parameters in LD2 have the same meaning as those in LD1. The parameter ξ_{f2} or ξ_{c2} respectively goes to zero if there is no optoelectronic feedback or coupling to LD2. Other parameters in the rate equations are the free-running intracavity photon density S_0 when the laser is not subject to feedback, the optical gain coefficient $g(N, S)$ as a function of N and S , the bias current density J , the cavity photon decay rate γ_c , the spontaneous carrier decay rate γ_s , the confinement factor of the laser waveguide Γ , the electronic charge constant e , the active layer thickness d , and the stochastic noise term F_s .

The effect of coupling on the semiconductor lasers can be controlled by the four coupling parameters ξ_{c1} , T_1 , ξ_{c2} , and T_2 . Theoretical analysis and numerical simulations have been carried out, and rich nonlinear dynamics have been observed in the system modeled by Eqs. (1)–(8). Complex chaotic dynamics are found in the system. The characteristics of a typical chaotic state are shown in Fig. 2. As is seen from these characteristics, the time series and power spectra of both lasers are demonstrated to develop into a chaotic state. Many interesting phenomena such as generation of chaos, quasiperiodic and period-doubling bifurcation to chaos, and death by delay are observed in semiconductor lasers with mutual coupling. Details of these phenomena are discussed in the following sections with experimental results.

In the experiments described in the following sections, the lasers are InGaAsP/InP single-mode DFB lasers both at 1.299 μm wavelength. Both lasers are temperature stabilized at 21°C. The photodetectors are InGaAs photodetectors with a 6 GHz bandwidth, and the amplifiers are Avantek SSF86 amplifiers of 0.4 – 3 GHz

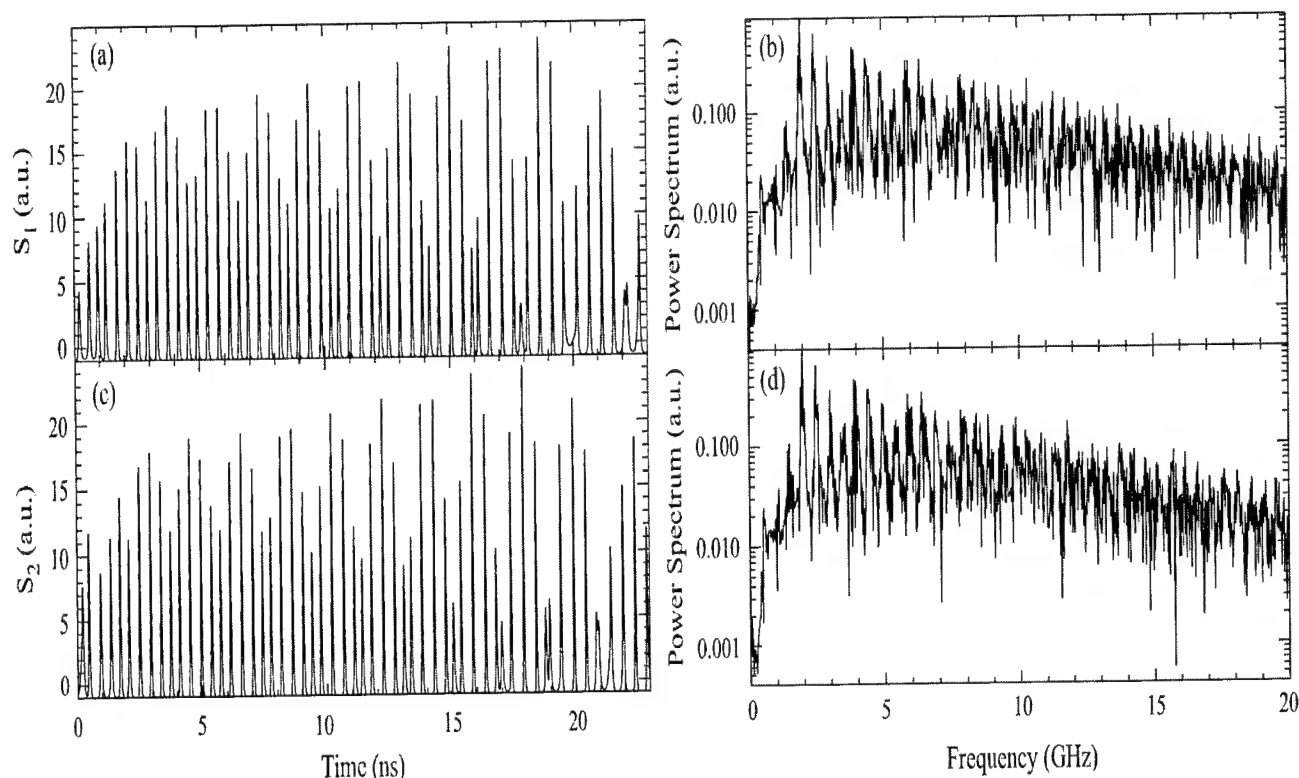


Figure 2. Numerically calculated time series of mutually coupled (a) LD1 and (c) LD2 showing fully developed chaotic oscillations. Corresponding power spectra are shown in (b) and (d).

bandpass. The intensity measured by photodetectors are recorded with a Tektronix TDS 694C digitizing sampling oscilloscope with a 3 GHz bandwidth and up to 1×10^{10} Samples/s sampling rate. Power spectra are measured with an HP E4407B RF spectrum analyzer that has a spectrum range from 9 kHz to 26.5 GHz.

3. MUTUAL COUPLING WITH NO FEEDBACK ON BOTH LASERS

Setup 1 in Fig. 1 indicates the situation where the two semiconductor lasers have mutual optoelectronic coupling but no optoelectronic feedback. Without mutual coupling, the two lasers are solitary lasers. No complex nonlinear dynamics are observed in such solitary lasers. However, with mutual coupling, complex dynamics are observed in the system because its dynamical dimension is much increased by this delayed coupling mechanism. With Setup 1, complex dynamics such as chaos are observed when one or both lasers are biased below threshold. When both lasers are biased above threshold, no chaotic pulsing is observed. One route to chaos in this system is shown to be quasiperiodicity. In addition, period-doubling bifurcation is also found in this system when the coupling delay time or the coupling strength is varied.

Chaotic dynamics and a quasiperiodic route to chaos are observed in this system. Figure 3 shows a sequence of three dynamical states which are regular pulsing (RP), two-frequency quasiperiodic pulsing (Q2), and chaotic pulsing (C), respectively, obtained by varying the coupling delay time T_2 . For each dynamical state, the time series, power spectrum, and phase portrait from the system output of PD2 are plotted as in the first, second, and third columns, respectively. The output of the system from PD1 is similar to that from PD2 for each dynamical state.

In Figs. 3(a)-(c), the system is in a regular pulsing state. The time series in Fig. 3(a) shows a train of regular pulses with a constant pulsing intensity and interval. The corresponding power spectrum Fig. 3(b) has only one fundamental pulsing frequency, f_1 , which is about 1 GHz. The phase portrait Fig. 3(c) is obtained by recording a

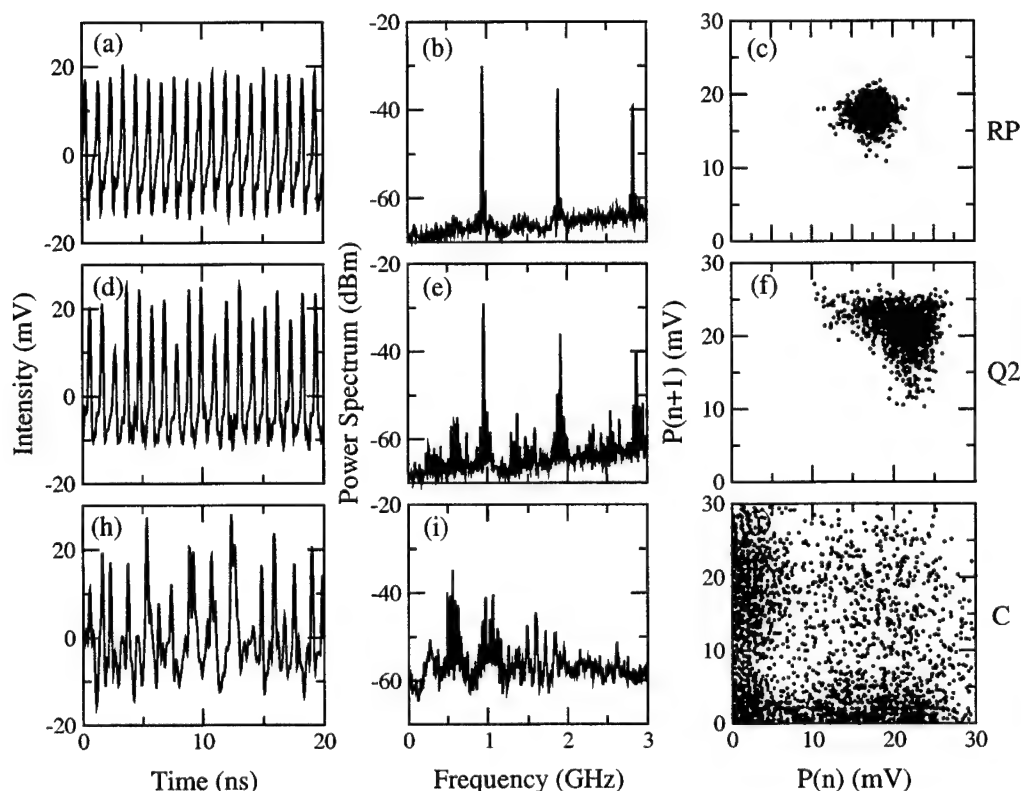


Figure 3. Quasiperiodic pulsing route to chaos for mutually coupled lasers with the configuration of Setup 1. RP: Regular pulsing state; Q2: Two-frequency quasiperiodic pulsing state; C: Chaotic pulsing state. First column, time series; Second column, power spectra; Third column, phase portraits.

peak sequence $P(n)$ at the local intensity maxima of a pulse train and further plotting $P(n)$ versus $P(n+1)$. In the regular pulsing state, the output has a constant peak intensity, and the phase portrait shows only one spot. The fluctuations in the time series and, consequently, the scattering in the phase portrait are mainly caused by the noise in the system and the sampling errors from the oscilloscope. When the coupling delay time T_2 is decreased, the system enters a two-frequency quasiperiodic pulsing state with the pulsing intensity modulated at a certain frequency f_2 as shown in Figs. 3(d)-(f). The time series clearly shows the modulation of the peak intensity. In the power spectrum, except the pulsing frequency f_1 , an incommensurate f_2 indicating the modulation of peak intensity shows up. This f_2 is related to the coupling delay time T_1 and T_2 of the mutual coupling loop because of the nonlinear interaction in this system. The appearance of two incommensurate frequencies, f_1 and f_2 , is the indication of quasiperiodicity. In the phase portrait, the data points are still scattered due to noise and sampling errors. However, we can see that the distribution in Fig. 3(f) is more scattered than that in Fig. 3(c) because of the modulation on the pulse intensity. In Figs. 3(h)-(j), when T_2 is further decreased, the system enters a chaotic pulsing state. From the time series, we find that both the pulse intensity and the pulsing interval vary chaotically. At the same time, the power spectrum of the chaotic pulsing state is broadened with a much increased background, indicating the onset of chaos. The phase portrait shows a highly scattered distribution in a large area. Therefore, the system is shown to enter a chaotic pulsing state through a quasiperiodic route.

4. MUTUAL COUPLING WITH FEEDBACK ON ONLY ONE LASER

In Setup 1, the two lasers have only mutual coupling but no feedback. This setup can be modified to include a feedback loop on one laser, as is shown in Setup 2 of Fig. 1. In Setup 2, the output from LD1 is split

into two parts. One is coupled to LD2, and the other is fed back to drive LD1 through an optoelectronic feedback loop that consists of PD1 and the corresponding amplifier. Therefore, even without mutual coupling, LD1 can have its own nonlinear dynamics due to the optoelectronic feedback. The dynamics of a semiconductor laser with optoelectronic feedback has been investigated, and a quasiperiodic route to chaos has been reported.^{3,4} Nevertheless, mutual coupling can further increase the complexity of both the system and its nonlinear dynamics.

Figure 4 shows a sequence of dynamical states obtained with Setup 2 by varying the coupling delay times T_1 and T_2 . From top to bottom, the total coupling delay time $T_1 + T_2$ is gradually increased. A mixed bifurcation of quasiperiodicity and period doubling showing the route to chaos is demonstrated. In Fig. 4, the five rows show five dynamical states, which are regular pulsing (RP), quasiperiodic pulsing (Q2), period-two pulsing (P2), mix of period-two and quasiperiodic pulsing (P2+Q2), and finally chaotic pulsing (C). For each dynamical state, the time series, power spectrum, and phase portrait from the system output of PD2 are plotted as in the first, second, and third columns, respectively. The output of the system from PD1 is similar to that from PD2 for each dynamical state.

The first two dynamical states are the RP and the Q2 states, which are similar to those in Fig. 3. The third state is a P2 state, where the pulse intensity has two distinct values which repeat one after another. In the power spectrum, besides the pulsing frequency f_1 , the subharmonic of $f_1/2$ also shows up. The other frequency peaks are the harmonics and combinations of f_1 and $f_1/2$. In the phase portrait, two scattered spots are clearly observed, which is the characteristic of a period-two state. From the P2 state, the system further evolves into a mixed state of P2 and Q2. In the time series, a modulation on the pulse intensity is observed. In the power spectrum, a second fundamental frequency f_2 shows up besides the frequency peaks of a typical P2 state. The phase portrait shows two spots with more scattering than those two spots in a simple P2 state due to the modulation on the peak intensity. Finally, the system enters a chaotic pulsing state. Therefore, it is demonstrated that a mixed bifurcation of quasiperiodicity and period-doubling coexists in this system.

With Setup 2 as shown in Fig. 1, besides the mutual coupling between the two lasers, one of the lasers also has an optoelectronic feedback loop. Without mutual coupling, one laser still has its own nonlinear dynamics. The mutual coupling further increases the dynamical dimension of the system which results in highly complex dynamics in the system. A mixed bifurcation of quasiperiodicity and period-doubling is demonstrated. The system can get into chaos through a quasiperiodic pulsing route or a period-doubling route or a mixture of these two. The system with Setup 2 is found to be prone to chaos, and such chaos is more complex than that found in the system with Setup 1. Since LD1 can have nonlinear dynamics before mutual coupling, an interesting phenomenon of death by delay is also observed in this setup. In the death by delay phenomenon, LD1 is operated in a pulsing state before mutual coupling. After mutual coupling, this oscillation is quenched to zero amplitude due to the delayed coupling. Details of death by delay are further discussed in the following section.

5. MUTUAL COUPLING WITH FEEDBACK ON BOTH LASERS

In Setup 3 as shown in Fig. 1, each of the two mutually coupled lasers also has an optoelectronic feedback loop of its own. Even without mutual coupling, both LD1 and LD2 can have their own nonlinear dynamics due to their optoelectronic feedback. The two lasers with their optoelectronic feedback are two nonlinear oscillators. With this setup, we can study the coupling effect between two nonlinear oscillators. The coupling effect is found to be very significant. Depending on the coupling delay time and coupling strength, the mutual coupling can either stabilize the nonlinear oscillation as in a death-by-delay phenomenon, or it can drive the nonlinear oscillation into more complex dynamical states such as highly chaotic oscillations.

Death by delay is a very interesting and important phenomenon where two limit-cycle oscillators suddenly stop oscillating due to a time-delayed coupling between the two oscillators. This phenomenon has been theoretically predicted in coupled oscillators and has been experimentally observed in coupled circuits and biological systems.⁷⁻⁹ The investigation on death by delay is important because the world is full of oscillators which are often coupled together. A sudden death of some oscillations can have serious consequences. Using Setup 3 in Fig. 1, we can conveniently study the effect of death by delay in semiconductor laser oscillators in particular and the effect in general. The mutual coupling strength and the coupling delay time can be adjusted by changing the attenuation on the coupled optical power and the optical path length in the coupling channel, respectively.

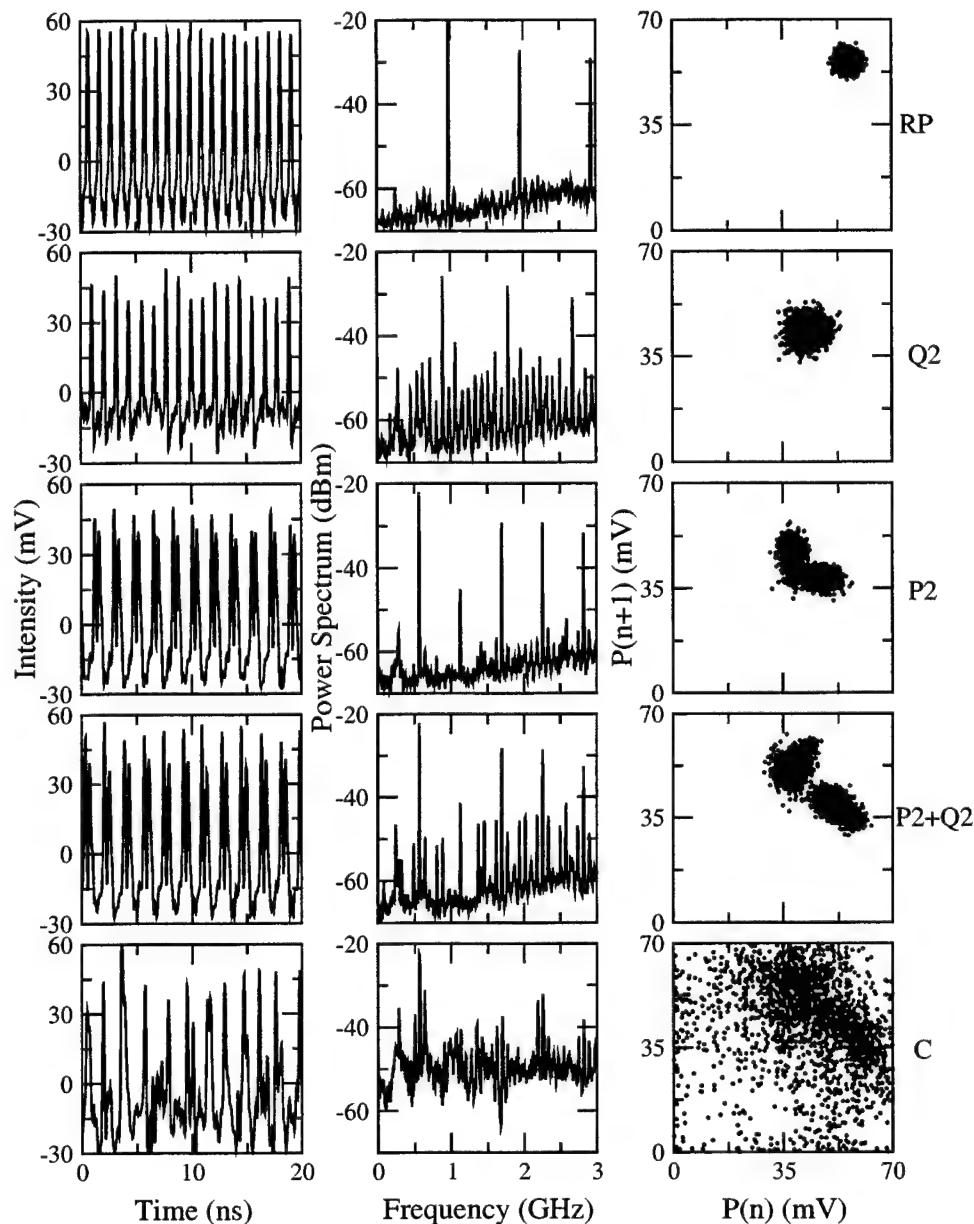


Figure 4. Mixed quasiperiodic and period-doubling bifurcation to chaos for mutually coupled lasers with the configuration of Setup 2. RP: Regular pulsing state; Q2: Two-frequency quasiperiodic pulsing state; P2: Period-doubling state; P2+Q2: Mixture of period-doubling and two-frequency quasiperiodic state; C: Chaotic pulsing state. First column, time series; Second column, power spectra; Third column, phase portraits.

The phenomenon of death by delay is observed in the coupled semiconductor lasers with very high frequency limit-cycle oscillations. Figure 5 shows the time series, power spectra, and correlation plots of the outputs from PD1 and PD2 in the setup before and after mutual coupling. Before mutual coupling, the two lasers are operated in independent limit-cycle oscillations. The time series and the power spectra of such oscillations are shown in Figs. 5(a) and (b), respectively. As is shown, the two lasers oscillate at regular pulsing states with almost the same fundamental frequency at 1 GHz. However, because the two oscillations are independent and their

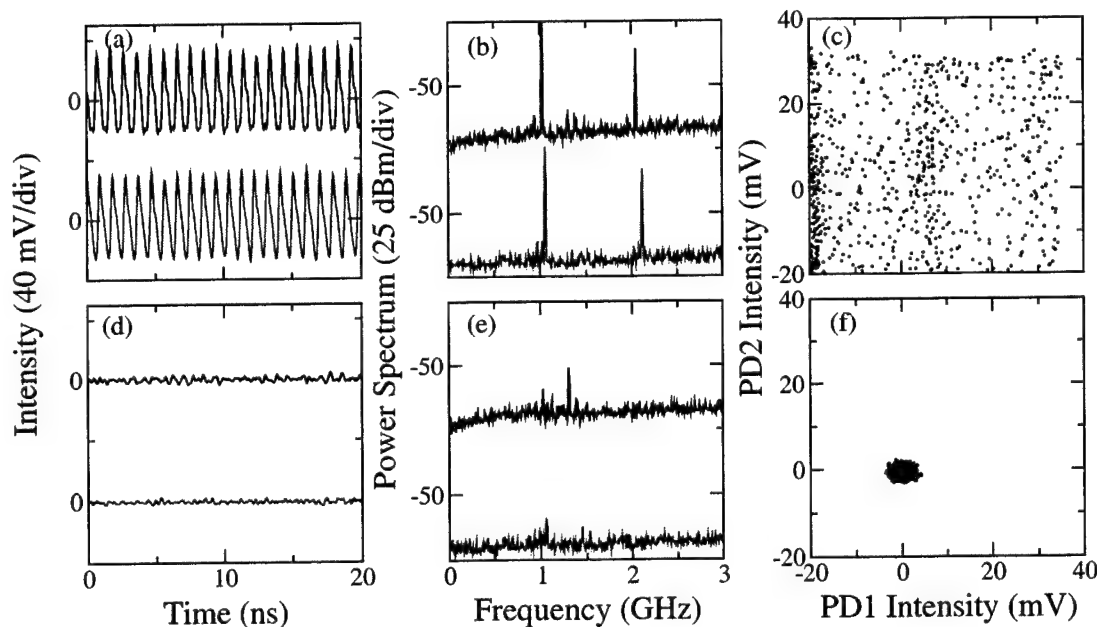


Figure 5. Phenomenon of death by delay for mutually coupled lasers with the configuration of Setup 3. (a)-(c), time series, power spectrum, and correlation plot of the outputs from PD1 and PD2 before mutual coupling. (d)-(f), corresponding plots after mutual coupling.

oscillation frequencies are not exactly the same, the output from the two lasers are not correlated. Figure 5(c) shows the correlation plot of the output from PD1 versus that from PD2. The correlation plot is scattered all over the place, which indicates that the two lasers oscillate with uncorrelated large amplitude variations. However, as soon as mutual coupling is applied to the two semiconductor lasers, the original large-amplitude oscillations are suddenly quenched to almost zero amplitudes. The time series and the power spectra of the outputs in this state of mutual coupling are shown in Figs. 5(d) and (e), respectively. As is shown, no oscillations exist anymore, and the amplitudes of both time series are almost zero. The flat spectra in Fig. 5(e) are close to the noise floor. The residual fluctuations in the two lasers after mutual coupling are caused by noise from the lasers and the electronic circuits in the system. Nevertheless, comparing the time series and the power spectra before and after mutual coupling, it is clear that the oscillations are almost completely quenched by the mutual coupling between the two oscillators. Figure 5(f) shows the correlation plot which is almost a single spot due to the quenched amplitude of the oscillations. In the plots of time series and power spectra, the output from PD2 is down shifted for clear comparison.

The phenomenon of death by delay happens only at certain coupling delay times. As the two lasers are mutually coupled to each other through separate paths, the mutual coupling delay times T_1 and T_2 can be adjusted separately. However, it is the total mutual coupling delay time $T_1 + T_2$ that determines the appearance of a death island. Multiple death islands are observed when the total mutual coupling delay time $T_1 + T_2$ is changed over a wide range. Figure 6 shows four death islands when $T_1 + T_2$ is varied. In Fig. 6, the circles with the connecting bars show the death islands when T_2 is changed first, and the squares with the connecting bars show the death islands when T_1 is changed first. When the total coupling delay time is increased, a sequence of death islands show up at multiple positions which have almost the same separations. In Fig. 6 the averaged separation between the islands is about 1 ns. This time separation matches with the inverse of the original oscillation frequency before coupling, which is about 1 GHz as shown in Fig. 5(b). When we either change T_1 first or T_2 first, the values of T_1 and T_2 are not the same for each death island. However, the total values of $T_1 + T_2$ are the same for each corresponding death island no matter whether T_1 or T_2 is changed. This observation confirms that the appearance of a death island really depends on the total $T_1 + T_2$ but not the separate values

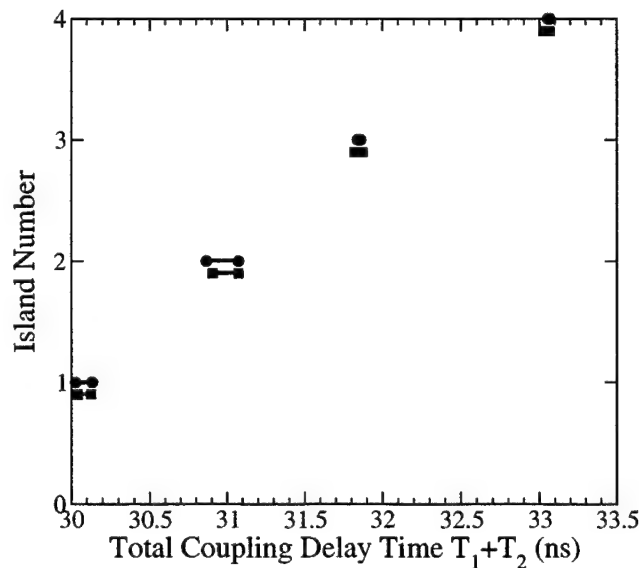


Figure 6. Total coupling delay time $T_1 + T_2$ for multiple death islands.

of T_1 or T_2 .

As we have discussed in Section 4, the phenomenon of death by delay is also observed in Setup 2 as shown in Fig. 1 where only one laser has optoelectronic feedback. Actually, the locations of the death islands for Setup 2 and Setup 3 are matched at the same values of $T_1 + T_2$. Based on our investigations, the phenomenon of death by delay is caused by a negative feedback loop from the mutual coupling to each oscillator, which quenches the original oscillation. The dependence of the death islands on the total mutual coupling delay time confirms our explanation because the total mutual coupling delay time is exactly the delay time in this negative feedback loop created by the mutual coupling. Since the phase shift repeats after every period of the oscillation, the death islands can be repeated when the total mutual coupling delay time is changed by a period of the oscillation. This is in good agreement with the experimental results presented in Fig. 6.

As is shown in Fig. 5, mutual coupling between two oscillators can quench the oscillation amplitude and stabilize the coupled semiconductor lasers. On the other hand, mutual coupling can also drive the coupled oscillators into chaotic states and destabilize the coupled semiconductor lasers. The chaotic state and the route to chaos are similar to those obtained with Setups 1 and 2. A mixed bifurcation of quasiperiodicity and period-doubling is observed.

6. DISCUSSIONS

From Setup 1 to Setup 3, the system gradually changes from mutually coupled semiconductor lasers without feedback, to one laser with feedback, and eventually to both lasers with feedback. We can also compare the dynamical states when such change in configuration evolves. The dynamics change significantly when the configuration is changed. With the complete Setup 3 in Fig. 1, we can conveniently block the mutual coupling, any one of the two feedback loops, or both of the feedback loops. Thus we can study changes in the dynamical states of the system with the same operating conditions but under different configurations with or without mutually coupling or feedback. Figure 7 shows a sequence of dynamical states when all the operating conditions are fixed but with the mutual coupling or feedback channel blocked in different ways. For each situation, the time series, correlation plot, and correlation coefficient are plotted in the first, second, and third columns, respectively.

In the first situation as shown in row (a), the two lasers both have their own optoelectronic feedback but with no mutual coupling. As is shown, the two lasers each oscillates at an independent regular pulsing state due

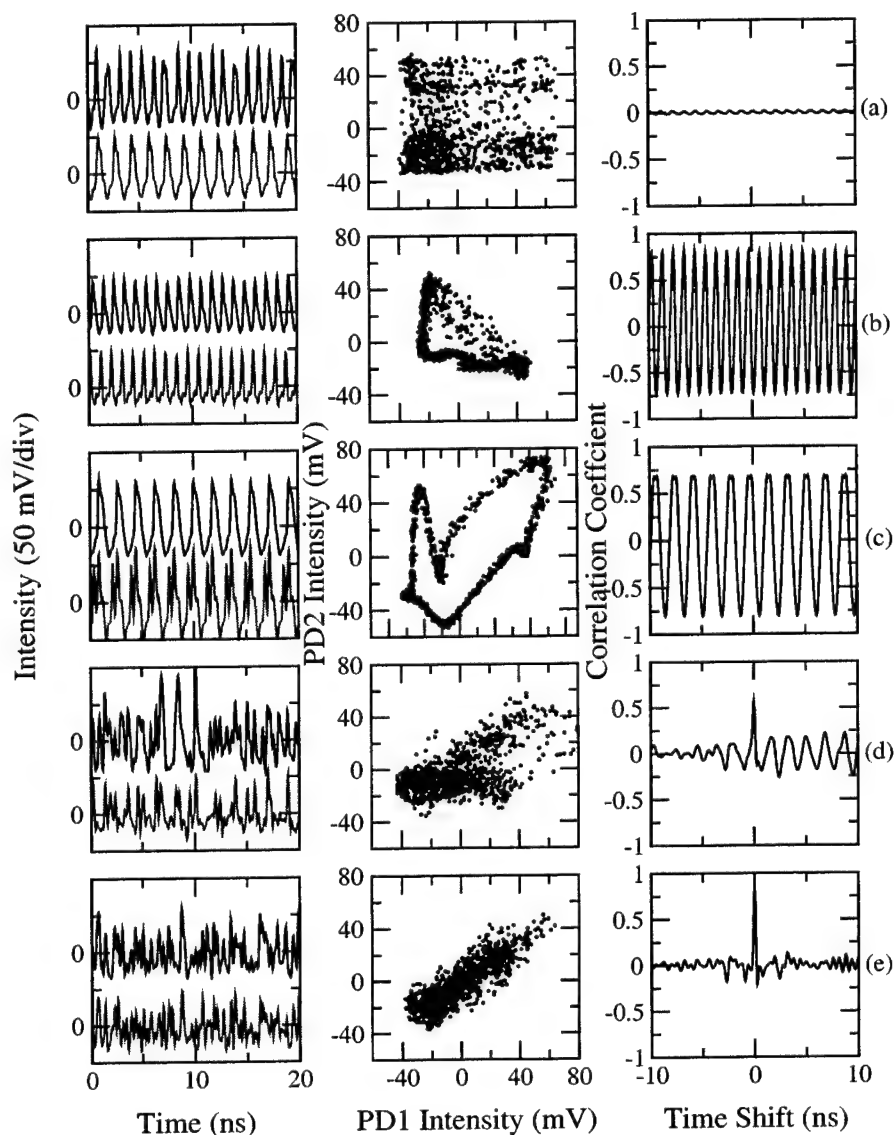


Figure 7. Different dynamical states under the same operating conditions but with different configurations in the setup. Row (a), LD1 and LD2 both have optoelectronic feedback but with no mutual coupling; Row (b), LD1 and LD2 have mutual coupling but with no optoelectronic feedback; Row (c), LD1 and LD2 have mutual coupling but only LD2 has optoelectronic feedback; Row (d), LD1 and LD2 have mutual coupling but only LD1 has optoelectronic feedback; Row (e), LD1 and LD2 have mutual coupling and both have optoelectronic feedback. First column, time series; Second column, correlation plot of output from PD1 vs. that from PD2; Third column: shifted correlation coefficient between the outputs from PD1 and PD2.

to the feedback effect. However, the two outputs are not correlated because there is no mutual coupling between them. Thus the correlation plot shows a very scattered distribution over the entire area. Shifted correlation coefficient is calculated between the outputs from PD1 and PD2 when the waveform from PD2 is time shifted gradually. As is shown, there is no correlation peak in the plot which indicates that indeed the two lasers are not correlated when they are not mutually coupled. In the second situation as shown in row (b), the two lasers are mutually coupled but none of them has a feedback loop. With mutual coupling only, the two lasers can

have some nonlinear dynamics due to the nonlinear effect from mutual coupling. Under the current operating conditions, the two lasers oscillate in regular pulsing states. Different from the first situation, now the two lasers are mutually coupled and thus their oscillations are correlated. As is shown, the two lasers oscillate at the same pulsing frequency. The correlation plot shows a simple pattern which indicates that the two outputs are correlated with some phase shift. In the shifted correlation coefficient, there are oscillating correlation peaks which means that the two waveforms are correlated regular pulsing waveforms. The correlation coefficient repeats when the waveform from PD2 is phase shifted by 2π every time. In the third situation as shown in row (c), the two lasers have mutual coupling between them but only LD2 has optoelectronic feedback. The two lasers are not symmetric under this situation because one laser has feedback while the other one does not. As a result, the outputs from PD1 and PD2 are not exactly the same but are phase correlated. The output from PD1 is a regular pulsing state, while that from PD2 is a period-two pulsing state. The correlation plot shows that the two waveforms are correlated with fixed phase shift. The correlation coefficient also has high peaks which oscillate due to the simple waveform pattern. In the fourth situation shown in row (d), the two lasers have mutual coupling between them but only LD1 has optoelectronic feedback. Although there are mutual coupling in both situations (c) and (d), the laser which has optoelectronic feedback is switched in those two situations. Since the two lasers can have slightly different intrinsic and operating feedback parameters, the dynamical states are different in (c) and (d). In row (d), the outputs from PD1 and PD2 are chaotic due to the combined effect of mutual coupling and feedback. The two waveforms are partially correlated because the lasers are mutually coupled. The shifted correlation coefficient also shows a correlation peak at the center. However, this correlation is not very high because the two lasers are not symmetric. Finally, in the fifth situation as shown in row (e), the two lasers have mutual coupling between them and they both have optoelectronic feedback also. Thus the two lasers are exactly symmetric in the configuration. As is shown, the outputs are highly complex chaotic waveforms due to the combined effect of mutual coupling and optoelectronic feedback. Furthermore, the two chaotic waveforms are highly correlated with a very nice distribution along the 45° diagonal, indicating that the two lasers are reliably synchronized. The shifted correlation coefficient also has a single peak at zero time shift which means that the two waveforms are synchronized in time. The high quality of synchronization between the two outputs are due to the mutual coupling and the symmetric configuration between the two lasers.

Thus in Fig. 7 from (a) to (e), the complexity of the system configuration is gradually increased as the dynamics evolve from simple regular pulsing state to chaotic pulsing state. Although the complexity of the dynamical states is increased, the correlation property between the two outputs is also increased due to the mutual coupling between the two lasers and also the increased symmetric configuration between them.

7. CONCLUSIONS

Mutually-coupled semiconductor lasers are investigated in order to study the effect of mutual coupling on semiconductor lasers in particular and such effect on mutually coupled systems in general. It is found that mutual coupling can significantly affect the dynamical states of the semiconductor lasers, depending on the coupling delay time and the coupling strength. Highly complex chaos can be generated in the mutually coupled lasers. A mixed bifurcation of quasiperiodicity and period-doubling is found in such lasers. Death by delay caused by the effect of mutual coupling is demonstrated. High quality of synchronization between the chaotic outputs from mutually coupled semiconductor lasers are also observed. From these experimental demonstrations, it is shown that mutual coupling plays very important roles in coupled dynamical systems.

ACKNOWLEDGMENTS

This work is supported by the U.S. Army Research Office under contract No. DAAG55-98-1-0269.

REFERENCES

1. "Special issue on applications of chaos in modern communication systems," *IEEE Trans. Circuits Syst. I*, vol. 48, Dec. 2001.
2. "Feature section on optical chaos and application to cryptography," *IEEE J. Quantum Electron.*, vol. 38, Sept. 2002.

3. S. Tang and J. M. Liu, "Chaotic pulsing and quasiperiodic route to chaos in a semiconductor laser with delayed optoelectronic feedback," *IEEE J. Quantum Electron.*, vol. 37, no. 3, pp. 329-336, Mar. 2001.
4. F.Y. Lin and J.M. Liu, "Nonlinear dynamics of a semiconductor laser with delayed negative optoelectronic feedback," *IEEE J. Quantum Electron.*, vol. 39, pp.562-568, Apr. 2003.
5. T. Heil, I. Fischer, W. Elsasser, J. Mulet, and C.R. Mirasso, "Chaos synchronization and spontaneous symmetry-breaking in symmetrically delay-coupled semiconductor lasers," *Phys. Rev. Lett.*, vol. 86, pp. 795-798, Jan. 2001.
6. J. Mulet, C. Masoller, and C.R. Mirasso, "Modeling bidirectionally coupled single-mode semiconductor lasers," *Phys. Rev. A*, vol. 65, Art. No. 063815, June 2002.
7. D.V.R. Reddy, A. Sen, and G.L. Johnston, "Experimental evidence of time-delay-induced death in coupled limit-cycle oscillators," *Phys. Rev. Lett.*, vol. 85, pp. 3381-3384, Oct. 2000.
8. A. Takamatsu, T. Fujii, and I. Endo, "Time delay effect in a living coupled oscillator system with the plasmodium of *Physarum polycephalum*," *Phys. Rev. Lett.*, vol. 85, pp. 2026-2029, Aug. 2000.
9. R. Herrero, M. Figueras, J. Rius, F. Pi, and G. Orriols, "Experimental observation of the amplitude death effect in two coupled nonlinear oscillators," *Phys. Rev. Lett.*, vol. 84, pp. 5312-5315, June 2000.

Dynamics of Mutually Coupled VCSEL's

Raúl Vicente^a and Claudio R. Mirasso^{a,b}

^aDepartament de Física, Universitat de les Illes Balears, Crta. Valldemossa Km 7.5,
E-07122, Palma de Mallorca, Spain;

^bElectrical Engineering Department, University of California, Los Angeles, Los Angeles, CA,
90095-1594, USA

ABSTRACT

We study the dynamics of two Vertical Cavity Surface Emitting Lasers (VCSEL's), when they are bidirectionally coupled through the mutual injection of their coherent optical fields. In the long distance limit between the lasers, we focus on the Low Frequency Fluctuations (LFF) regime and we investigate the polarization-resolved dynamics of each laser under the effect of detuning. In the short distance limit, the influence of the propagation phase parameter is also evaluated. For large spin-flip rates, it is found that a change in the propagation phase may induce a sudden switch in the polarization mode that becomes dominant. Extensive simulations scanning the Coupling-Detuning space are performed for both long and short injection delay times.

Keywords: Semiconductor Lasers, VCSEL, Delay, Bidirectional Coupling.

1. INTRODUCTION AND MODEL

The nonlinear dynamics of VCSEL's subject to external perturbations has been studied for a long time. Conventional optical feedback, polarization selected or rotated optical feedback and unidirectional optical injection¹⁻³ are among the most popular schemes for investigating the dynamical response of the VCSEL. High frequency polarization modulation and polarization switching has been achieved with the use of the former setups. Much less common in the literature are the works concerning to the mutual injection of two VCSEL's in a face to face configuration, where the experimental results obtained by Ohtsubo and collaborators⁴ demonstrated that chaotic synchronization between one mode (the \hat{x} -mode) of each laser could be attained. However, an exhaustive investigation of the synchronization properties of this system still lacks to be done. This work is indeed devoted to characterize the influence of several operating and internal parameters on the dynamics and synchronization of two mutually coupled VCSEL's.

The modeling of the setup is performed at the level of modified rate equations, under the framework of the Spin-Flip-Model (SFM)⁵ for the individual dynamics of each VCSEL. After the adiabatic elimination of the material polarization and considering moderate values of the coupling constant (in order to avoid higher order reflection terms), the equations governing the fields and carrier numbers inside each laser are

$$\dot{E}_{1\pm} = -i\Delta E_{1\pm} + \kappa(1 + i\alpha)[N_1 \pm n_1 - 1]E_{1\pm} - (\gamma_a + i\gamma_p)E_{1\mp} + \xi e^{-i\Omega\tau} E_{2\pm}(t - \tau) + F_{1\pm}(t), \quad (1)$$

$$\dot{N}_1 = -\gamma_e [N_1 - \mu + (N_1 + n_1)|E_{1+}|^2 + (N_1 - n_1)|E_{1-}|^2], \quad (2)$$

$$\dot{n}_1 = -\gamma_s n_1 - \gamma_e [(N_1 + n_1)|E_{1+}|^2 + (N_1 - n_1)|E_{1-}|^2], \quad (3)$$

$$\dot{E}_{2\pm} = i\Delta E_{2\pm} + \kappa(1 + i\alpha)[N_2 \pm n_2 - 1]E_{2\pm} - (\gamma_a + i\gamma_p)E_{2\mp} + \xi e^{-i\Omega\tau} E_{1\pm}(t - \tau) + F_{2\pm}(t), \quad (4)$$

$$\dot{N}_2 = -\gamma_e [N_2 - \mu + (N_2 + n_2)|E_{2+}|^2 + (N_2 - n_2)|E_{2-}|^2], \quad (5)$$

$$\dot{n}_2 = -\gamma_s n_2 - \gamma_e [(N_2 + n_2)|E_{2+}|^2 + (N_2 - n_2)|E_{2-}|^2]. \quad (6)$$

Further author information: (Send correspondence to R.V.)

R.V.: E-mail: raulv@imedea.uib.es, Telephone: 34 971172505

where the electrical fields E_{\pm} are written in the circular basis and both lasers are taken identical, except for a possible mismatch between their free-running optical frequencies ($\Delta = \frac{\omega_2 - \omega_1}{2}$, $\Omega = \frac{\omega_2 + \omega_1}{2}$). In order to simplify the model, the transverse mode structure has not been considered here. Another important assumption made in the equations, is the perfect alignment between both lasers with respect to their two preferred orthogonal orientations for the optical field, \hat{x} and \hat{y} . In the former equations, N represents the total inversion population while n is the difference in population inversions of the two spin channels associated to the emission of opposite circularly polarized photons in the SFM description. The last term in the field equations accounts for the Langevin noise sources associated to the spontaneous emission processes $F_{\pm}(t) = \sqrt{\beta\gamma_e(N \pm n)}\chi_{\pm}$, where for each noise realization χ_{\pm} are two independent complex random numbers with zero mean and δ -correlated. Typical values of the parameters appearing in (1-6) that will be used throughout this paper are collected in Table 1.

Parameter	Meaning	Value
α	Henry's linewidth enhancement factor	3
κ	field decay rate	300 ns ⁻¹
γ_e	total carrier number decay rate	1 ns ⁻¹
γ_s	spin-flip rate	50-400 ns ⁻¹
γ_a	amplitude anisotropy	-0.1 ns ⁻¹
γ_p	phase anisotropy	3 ns ⁻¹
μ	normalized pump	1-1.5
ξ	coupling strength	0-30 ns ⁻¹
τ	injection delay time	0.2-4 ns
$\Delta\nu$	frequency detuning	0-10 GHz
β	spontaneous emission factor	0-1 $\times 10^{-5}$

Table 1. Range of values used in this work for the parameters appearing in equations (1-6).

The rest of the paper is organized as follows. Section 2 deals with the modification of the LFF behavior displayed by both polarizations in the appropriate conditions, when a detuning is present in the system. Section 3 shows the effect of changing the propagation phase between the VCSEL's in the polarization resolved dynamics and how the spin-flip rate modifies these results. In Section 4 we discuss the possible dynamical states of the coupled system as function of the detuning and coupling coefficients. Finally, a brief summary and future perspectives are elucidated in the Conclusions section.

2. LOW FREQUENCY FLUCTUATIONS STATES

When two long-separated mutually coupled Edge Emitting Semiconductor Lasers (EESL) are both pumped close to their solitary threshold, they use to enter in the so-called Low Frequency Fluctuations regime. It is also known that the effect of the detuning on the system is to induce a leader-laggard synchronization between the two optical fields.⁶ However, in the present situation, it naturally arise the question of the role of each polarization in the synchronization process, which has not counterpart in the EESL case. So, in order to illustrate the polarization resolved contribution to the LFF dynamics, we plot in Figure 1 typical traces of the \hat{x} and \hat{y} polarized intensities for several values of the detuning parameter. All temporal series have been smoothened with a fifth-order Butterworth filter with a high cut-off frequency of 100 MHz.

In the case of low spin-flip rate, at zero detuning (a), only the high frequency mode of each laser (\hat{x} -mode) starts lasing, exhibiting the typical achronal synchronized LFF traces. As usual, the cross-correlation function $\sigma(\Delta t)$ shows two maximum peaks at $\pm\tau$ with a correlation coefficient of $\sigma(\pm\tau) \approx 0.87$. Increasing the detuning (b), we find that the low frequency mode starts to get active taking the principal role in the low frequency dynamics. Now, the \hat{x} -modes of both lasers show a worse lag synchronization quality than in the previous case $\sigma(\pm\tau) \approx 0.63$, while the \hat{y} -modes cross-correlation at $\pm\tau$ takes a value of 0.92. In the dropouts sequence, it is observed that is the dominant mode of the laser with higher frequency who drops first. Further increasing

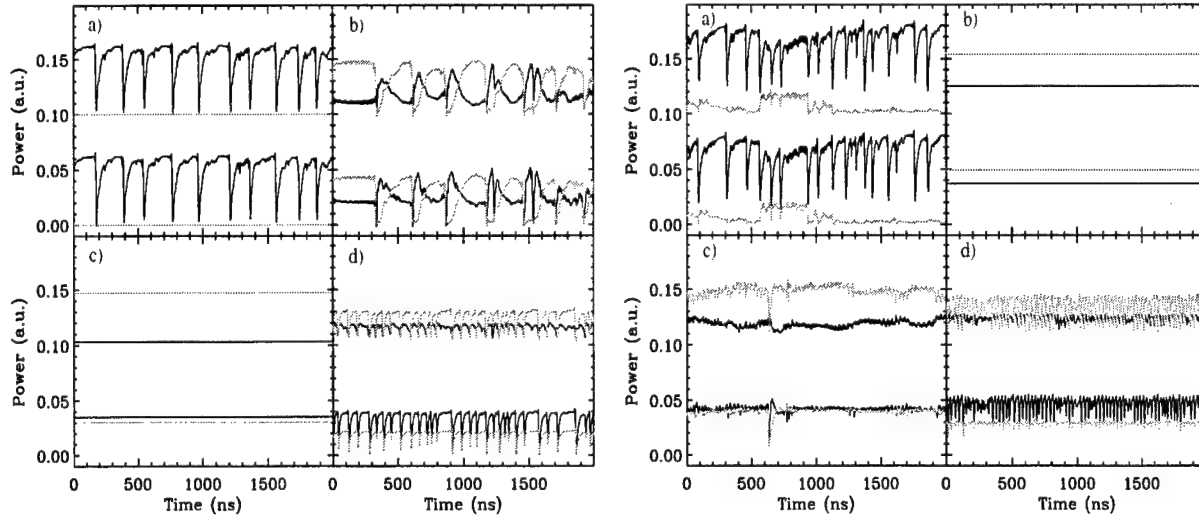


Figure 1. Detuning effect on the LFF. Time traces for the \hat{x} (\hat{y}) polarized intensities are plotted in black (grey). Series corresponding to the laser 1 has been vertically shifted for clearness reasons. The left panel contains simulations performed with $\gamma_s = 50 \text{ ns}^{-1}$ and $\mu = 1.01$, while in the right panel $\gamma_s = 400 \text{ ns}^{-1}$ and $\mu = 1.03$, have been used. a) $\Delta\nu = 0 \text{ GHz}$, b) $\Delta\nu = 3 \text{ GHz}$, c) $\Delta\nu = 6 \text{ GHz}$ and d) $\Delta\nu = 10 \text{ GHz}$. Other parameters are $\xi = 15 \text{ ns}^{-1}$ and $\tau = 4 \text{ ns}$.

the frequency mismatch (c), the system enters into a stable locking area where a constant output power is achieved for the different polarizations. In particular, it is noticed that for the laser 2 (higher frequency laser), the dominant mode is the \hat{x} -mode, whereas for the laser 1 (lower frequency laser) is the \hat{y} -mode the one that is extracting more optical power. For detunings as large as 10 GHz (d), it turns out that the dominant modes of each laser are nearly perfectly correlated with lag τ , what implies a synchronization between the \hat{y} -mode of the laser 1 with the orthogonally oriented \hat{x} -mode of the laser 2. Regarding the synchronization of \hat{x} and \hat{y} -modes belonging to the same VCSEL, it is worth to mention the excellent zero-lagged synchronization achieved by these two modes in the higher frequency laser ($\sigma(0) = 0.96$). A worse correlation value is obtained for \hat{x} and \hat{y} -modes associated to the lower frequency laser. It is also worth to mention the reduction of time between consecutive dropout events for large detuning values.

For the large spin-flip rate case, it was necessary to increase the pump value considered previously, in order to enter in the LFF regime. Nevertheless, the main features of the before-mentioned characteristics are also shared in this case. Now, the principal differences observed are that the locking state is reached for smaller values of the detuning and that some irregular oscillations appear for intermediate detunings.

Finally, we show in Figure 2 the optical spectra corresponding to the locking state observed in the left panel of Figure 1. Here, the mutual frequency pulling and pushing effects shift all the present polarization modes ($\hat{x}_1, \hat{y}_1, \hat{x}_2$ and \hat{y}_2) to lock to a relative optical frequency around -6 GHz , nearly coinciding with the original frequency mismatch $\Delta\nu$.

3. PHASE PROPAGATION INFLUENCE IN THE SHORT INTERCAVITY REGIME

When the injection delay time between two mutually coupled semiconductor lasers is much smaller than the relaxation oscillation period, the propagation phase $\varphi_0 = \Omega\tau \bmod 2\pi$ becomes a critical parameter in the system. In our case of mutually coupled VCSEL's, we study how this phase affects the dynamics of each polarization mode and what is the influence of the spin-flip rate. In Figure 3, we show the bifurcation diagrams of the optical power associated to the four polarization modes, when the propagation phase has been taken as the bifurcation parameter.

In this first case ($\gamma_s = 50 \text{ ns}^{-1}$), we observe how changing the propagation phase, chaotic, periodic and steady states can be selected for the dominant polarization (\hat{y} -modes) of each VCSEL, by just slightly modifying

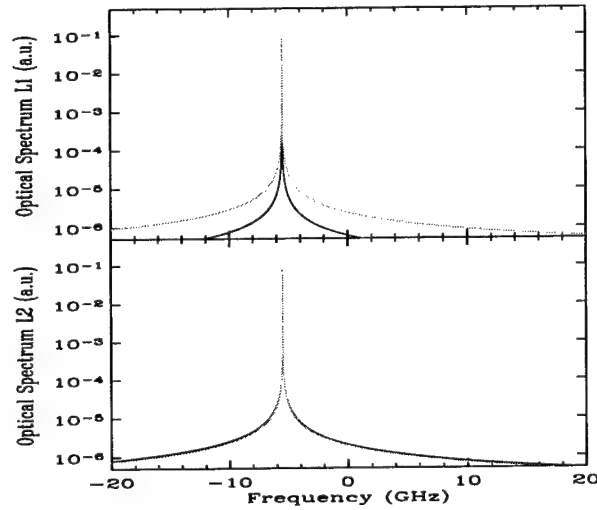


Figure 2. Optical spectra of the polarization modes under frequency locked operation. Black and grey distinguish the \hat{x} -modes from the \hat{y} -modes.

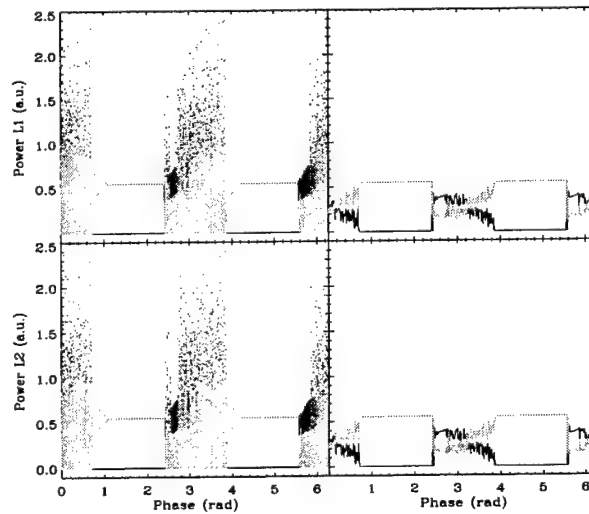


Figure 3. Left panel contains bifurcation diagrams for the optical power of the two polarization modes of both lasers. Right panel shows the mean value of the left panel series when averaged over 50 ns. Black and grey distinguish the \hat{x} -modes from the \hat{y} -modes. Other parameters are $\mu = 1.5$, $\kappa = 10 \text{ ns}^{-1}$, $\tau = 0.2 \text{ ns}$ and $\Delta = 0$. A low spin-flip rate is considered here, $\gamma_s = 50 \text{ ns}^{-1}$.

the distance between lasers. Regarding the less powerful \hat{x} -modes, it is clear that only at certain values of the phase they may become active, while for other regions they are strongly suppressed. It is also noticed that the polarization in both lasers behaves identically.

Increasing the spin-flip rate up to $\gamma_s = 400 \text{ ns}^{-1}$, we found a very different behavior from the analyzed in the previous case, as it can be observed in Figure 4. Now, a constant optical power of each polarization mode is found for almost all the phase values. Only narrow periodic windows are centered around selected values of

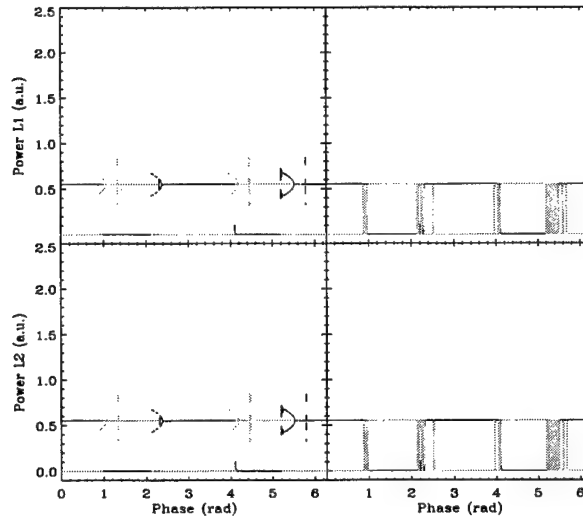


Figure 4. Left panel contain bifurcation diagrams for the optical power of the two polarization modes of both lasers. Right panel shows the mean value of the left panel series when averaged over 50 ns. Black and grey distinguish the \hat{x} -modes from the \hat{y} -modes. Same parameters than those used in Figure 3, except $\gamma_p = 400 \text{ ns}^{-1}$.

the propagation phase. However, one of the main differences is related to the fact that a change in the phase may induce a switching between the dominant modes, i.e., depending on the specific phase value, the dominant polarization can be the \hat{x} or the \hat{y} -mode. Several of these transitions are illustrated in the Figure 4. We also point out that generically, when a mode becomes dominant the other one hardly carries any optical power.

4. NUMERICAL STUDY OF THE POLARIZATION DYNAMICS IN THE COUPLING-DETUNING PLANE

Under this section, we collect some numerical simulations in order to characterize the behavior of the system in the two-parameter space defined by the coupling and detuning coefficients. The effect of the distance between lasers will be also discussed.

First of all, we focus our attention on the mean optical power extracted by each polarization mode, as function of the coupling and detuning values. Figure 5 shows the optical power averaged over 50 ns for the $\hat{x}_1, \hat{y}_1, \hat{x}_2$ and \hat{y}_2 , modes, when considering a short injection delay time $\tau = 0.2 \text{ ns}$ and a low spin-flip rate $\gamma_s = 50 \text{ ns}^{-1}$. Hereafter, the pumping current will be fixed to $\mu = 1.5$. When uncoupled, for the set of parameters chosen, each VCSEL is mainly emitting in its \hat{y} polarization mode. This situation, where the predominant mode is the \hat{y} one, is maintained in a neighborhood of the uncoupled zero-detuning state. However, as seen in the Figure 5, if we allow for a large detuning in the low coupling limit, then it is the \hat{x} -mode which becomes dominant in both lasers. As it can be observed, this phenomenon occurs for both signs of the detuning value. It is also noticed a kind of periodic structure when increasing the coupling strength while keeping the detuning at small values. So, repetitively the \hat{y} -mode pass through a serie of maxima and minima levels with a complementary behavior of its \hat{x} -polarized counterpart. Consequently, under the actual conditions, coexistence or strongly suppressed \hat{x} -mode polarization states can be obtained by changing the coupling coefficient.

In the case that the long distance limit between the VCSEL's is considered (see Figure 6), we find the same kind of detuning-induced change of the dominant mode for low coupling rates. However, now we observe a monotonic behavior of polarization optical powers when increasing the coupling, contrarily to what happens in the previous case where a periodic structure was revealed.

In order to illustrate the dynamics at some points of the former Coupling-Detuning plane, where only averaged powers were computed, we show in Figure 7 the temporal series and optical spectra corresponding to several

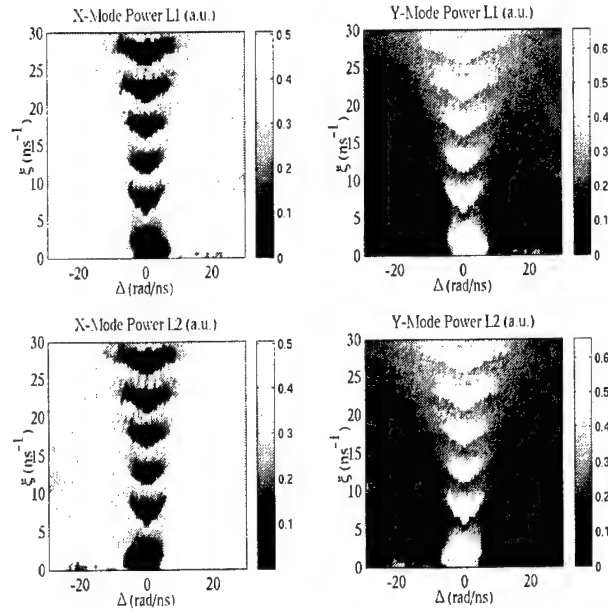


Figure 5. Mean optical polarization-resolved power in the Coupling-Detuning plane. The average has been taken over 100 ns of temporal evolution. Short distance limit ($\tau = 0.2$ ns). Other parameters are: $\mu = 1.5$, $\gamma_s = 50$ ns $^{-1}$ and $\varphi = 0$.

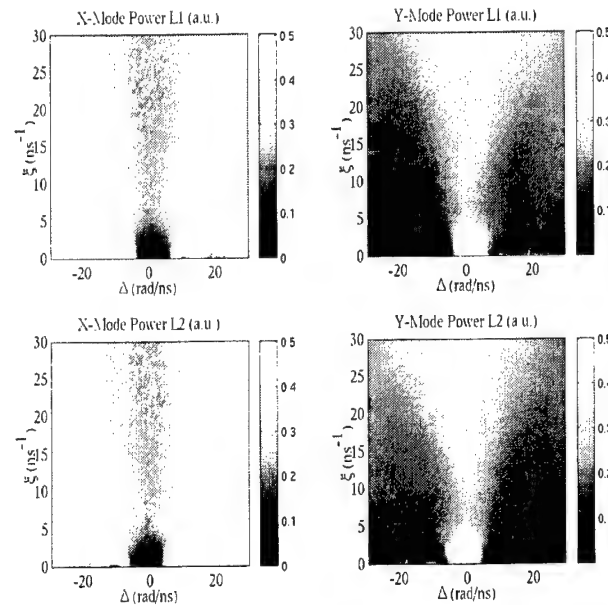


Figure 6. Mean optical polarization-resolved power in the Coupling-Detuning plane. The average has been taken over 100 ns of temporal evolution. Long distance limit ($\tau = 4$ ns). Other parameters are: $\mu = 1.5$, $\gamma_s = 50$ ns $^{-1}$ and $\varphi = 0$.

simulations in the short intercavity regime, where the detuning has been varied. Although a very low coupling was chosen ($\xi = 3$ ns $^{-1}$), aperiodic oscillations are found even in the absence of detuning for the \hat{y} -mode of each laser, while the \hat{x} -mode remained completely inactive in both VCSEL's. As the detuning is increased, the coexistence of both modes in each laser exhibiting irregular oscillations leads to a polarization state of the light, that is continuously moving over a large portion of the Poincare sphere surface (see Figure 8). Further increasing

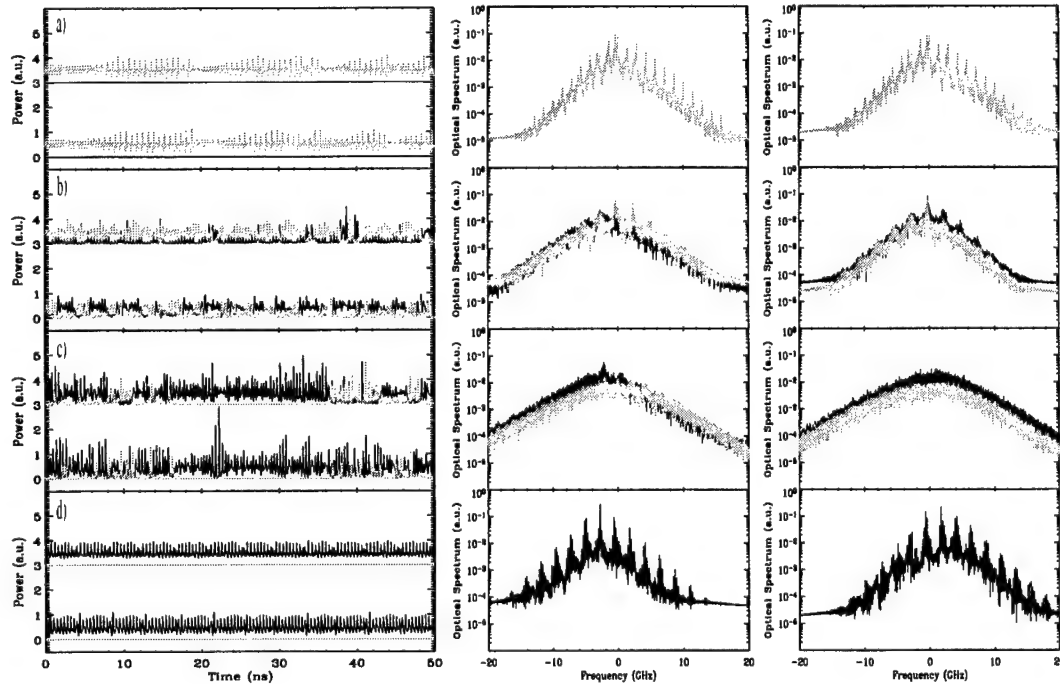


Figure 7. Left panel: temporal series of the \hat{x} and \hat{y} -modes for detunings a) $\Delta = 0$, b) 5, c) 10 and d) 15 rad/ns. VCSEL 1 traces have been vertically shifted for clearness reasons. Center panel: Optical spectra for the Laser 1 polarization modes. Right panel: Optical spectra for the Laser 2 polarization modes. The coupling strength have been fixed to $\kappa = 3 \text{ ns}^{-1}$. The rest of parameters are the same than those used in Figure 5.

the detuning, the \hat{y} -mode of each laser is switched-off while the \hat{x} -mode evolves in a quasiperiodic state.

5. CONCLUSIONS

In this paper, we have explored the polarization resolved dynamics of two mutually coupled VCSEL's. Focusing on the LFF regime, we have observed how detuning is able to switch the dominant polarization mode of the lower frequency VCSEL. Moreover, frequency locked states were also clearly identified for moderate values of detuning. Similar behavior was found for low and high spin-flip rates. Regarding the role of the propagation phase between the lasers in the dynamics of the system, we adjusted the injection delay time to a very short one and scanned the phase in a typical bifurcation diagram. The results pointed out that for high spin-flip rates, a sudden switch in the dominant polarization mode can be induced by slightly changing the intercavity phase. Finally, we performed extensive numerical simulations varying the coupling rate and the detuning. As future work, we consider the generalization of the present results to a situation in which the principal axis of both lasers are not perfectly aligned, i.e. when a VCSEL is rotated with respect to the other one.

ACKNOWLEDGMENTS

The authors acknowledge financial support from the Ministerio de Ciencia y Tecnología (Spain) and FEDER and BFM2002-04369) and from the EC project IST-2000-29683 OCCULT. C.R.M. is also grateful for the hospitality and support of the Electrical Engineering Department, University of California, Los Angeles. C.R.M is also funded by the Secretaría de Estado de Educación y Universidades, Ministerio de Educación, Cultura y Deporte, Spain.

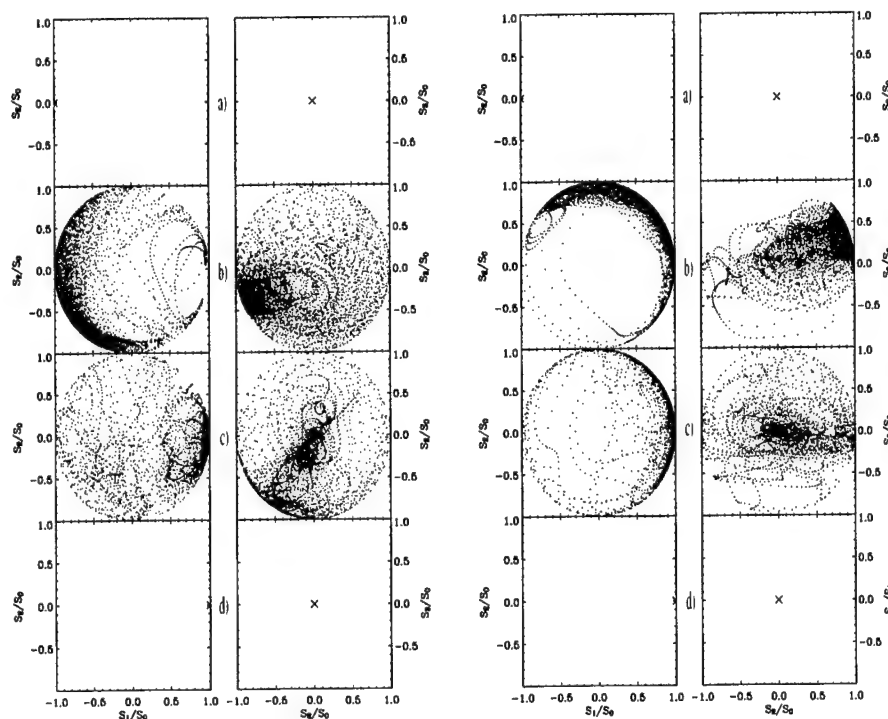


Figure 8. Evolution of the polarization in the Poincaré sphere projections corresponding to the temporal traces in Figure 7. Left and right panels collect the results for the laser 1 and 2, respectively.

REFERENCES

1. N. A. Loiko, A. V. Naumenko, and N. B. Abraham, "Complex polarization dynamics in a vcsel with external polarization-selective feedback," *J. Opt. B: Quantum Semiclass. Opt.* **3**, p. 100, 2001.
2. M. Sciamanna, F. Rogister, O. Deparis, P. Megret, and B. M., "Bifurcation to polarization self-modulation in vertical-cavity surface-emitting lasers," *Optics Lett.* **27**, p. 261, 2002.
3. P. Spencer, C. R. Mirasso, P. Colet, and A. Shore, "Modeling of optical synchronization of chaotic external-cavity vcsel's," *IEEE J. of Quantum Electron.* **34**, p. 1673, 1998.
4. N. Fujiwara, Y. Takiguchi, and J. Ohtsubo, "Observation of the synchronization of chaos in mutually injected vertical-cavity surface emitting semiconductor lasers," *Optics Lett.* **28**, p. 1677, 2003.
5. M. San Miguel and J. V. Feng, Q. Moloney, "Light polarization dynamics in surface emitting semiconductor lasers," *Phys. Rev. A* **52**, p. 1728, 1995.
6. H. T., I. Fischer, W. Elsser, J. Mulet, and C. Mirasso, "Chaos synchronization and spontaneous symmetry-breaking in symmetrically delay-coupled semiconductor lasers," *Phys. Rev. Lett.* **86**, p. 795, 2001.

Period-One Oscillations in Optically Injected Semiconductor Lasers

S.K. Hwang¹, J.M. Liu², and J.K. White³

¹ Graduate Institute of Opto-Mechatronics, National Chung Cheng University
Chia-Yi, Taiwan

² Department of Electrical Engineering, University of California, Los Angeles
Los Angeles, CA 90095, USA

³ Bookham Technology, 1-10 Brewer Hunt Way, Kanata, On, K2K 2B5 Canada

ABSTRACT

The characteristics of period-one oscillations in semiconductor lasers subject to optical injection is experimentally and quantitatively investigated. The changes in the frequency separation and in the magnitude difference between the principal oscillation and the sideband of the injected laser are studied as a function of experimentally accessible parameters, the detuning frequency and the injection strength of the injection signal. The frequency separation decreases as the injection strength and the detuning frequency decrease. The magnitude of the principal oscillation decreases with the decreasing injection strength and the increasing detuning frequency, while that of the sideband grows at the same time. At some operating conditions, these characteristics leads to a situation that the magnitude of the sideband becomes larger than that of the original principal oscillation, resulting in a frequency shift of the principal oscillation from the injection frequency to the sideband.

Keywords: Semiconductor laser; Injection locking; Nonlinear dynamics; Period-one oscillation

1. INTRODUCTION

The behavior of an optically injected semiconductor laser has attracted much attention over the past years because of its importance in the applications of optical communications and in the exploration of laser property. Under external optical injection, many modulation characteristics of a semiconductor laser can be modified. They include, for example, single-mode operation under high-speed modulation,^{1,2} frequency-chirp reduction,^{3,25,5} linewidth narrowing,⁶ optical frequency and phase modulation,^{7,8} modulation bandwidth enhancement,^{9,10} and noise reduction.^{25,11,12} These characteristics provide great improvements and advantages of the semiconductor laser system for advanced technological applications.

Depending on the operating conditions, an optically injected semiconductor laser can also undergo a rich variety of different dynamical states. They include stable injection locking, locking-unlocking bistability, periodic oscillations, deterministic chaos, and many other instabilities.¹³⁻¹⁵ A map was even experimentally obtained¹³ to show the regions of different dynamical states of an optically injected laser as a function of experimentally accessible parameters. The abundant dynamical behaviors in an optically injected semiconductor laser provide great opportunities for researchers to investigate either from the basic physics viewpoint or for possible technological applications.

A number of efforts have actually been made to understand the characteristics of stable injection locking,¹⁶⁻¹⁸ which include the stability of locking, the locking range as a function of experimentally accessible

Further author information: (Send correspondence to S.K. Hwang)

S.K. Hwang: E-mail: skhwang@ccu.edu.tw

J.M. Liu: E-mail: liu@ee.ucla.edu

parameters, and the relation between the relaxation oscillation and locking. As for the nonlinear dynamical behaviors, it was numerically predicted¹⁹ and experimentally demonstrated²⁰ that an optically injected semiconductor laser follows a period-doubling route to chaos. Lately, a number of efforts have been dedicated to understanding the mechanism of bifurcation^{21,22} and route to chaos^{23,24} of the laser system under different operating conditions. With the success in chaos synchronization, chaotic communication using optically injected semiconductor lasers has been demonstrated.²⁵ The effects of different modulation schemes on the laser systems in chaotic communication was also explored.²⁶ While many studies have been done to understand the characteristics and applications of deterministic chaos, there is little investigation on period-one oscillations.¹³ Therefore, in this study, an experiment is conducted to quantitatively explore the characteristics of period-one oscillations in optically injected semiconductor lasers.

2. EXPERIMENTAL SETUP

Figure 1 is a schematic of the experimental apparatus. One laser diode operating at the optical frequency ν_{ML} is used as the master laser. The output of the master laser is used to injection lock a second laser, the slave laser, initially oscillating at the free-running frequency ν_{SL} . The frequency difference, $f = \nu_{ML} - \nu_{SL}$, between the master and the slave lasers is named as the detuning frequency in the study. In the path of the injection, there consist of one half wave plate, one polarizing beam splitter, one Faraday rotator, and another half wave plate in sequence. The first half wave plate, HW1, is used to change the polarization state of the injection signal. This in turns determines the level of the injection that can be guided to the slave laser due to the polarization-dependent beam splitter following HW1. Therefore, the level of the injection from the master laser can be varied by either adjusting HW1 and/or the variable attenuator. The injection strength received by the slave laser is characterized by the injection parameter, ξ ,¹⁵ in the study. The injection parameter is proportional to the ratio of the electric fields between the injection signal and the free-running slave laser. The square of the injection parameter is proportional to the injection power actually received by the slave laser. The second half wave plate, HW2, is so adjusted that most of the output of the slave laser transmits through the polarizing beam splitter, and that, at the same time, the polarization state of the injection signal becomes the same as that of the slave laser output right before the lens. Note that the

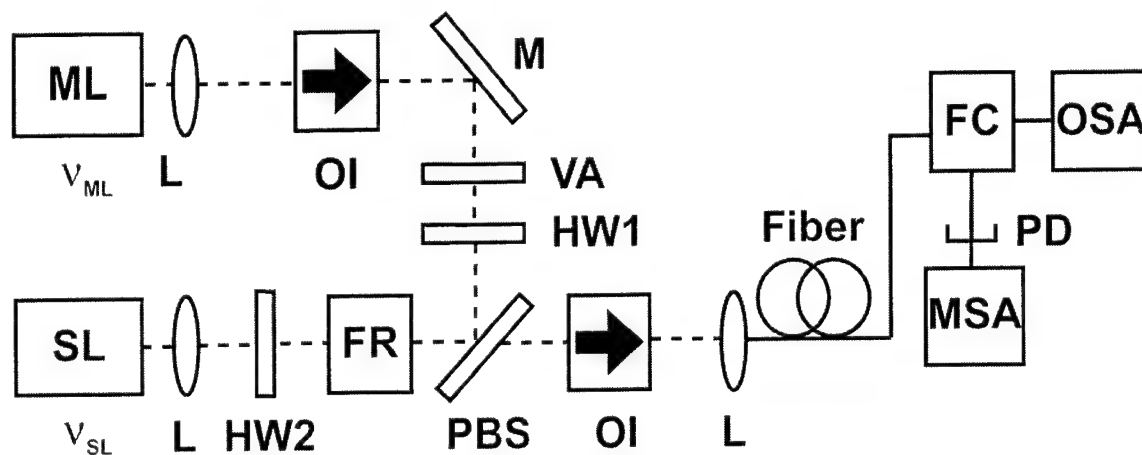


Figure 1. Schematic of the experimental apparatus. ML: master laser; SL: slave laser; L: lens; PBS: polarizing beam splitter; M: mirror; HW: half wave plate; FR: faraday rotator; VA: variable attenuator; OI: optical isolator; FC: fiber coupler; PD: photodiode; OSA: optical spectrum analyzer; MSA: microwave/RF spectrum analyzer.

Faraday rotator rotates linear polarization of an optical field by 45 degree along the same direct no matter which side of the rotator the optical field is incident into.

The output of the slave laser is coupled into a single-mode fiber, evenly split by an optical fiber coupler, and finally sent to a detection system to measure both optical and power spectra. Power spectra are obtained by first using a high-speed photodiode (Discovery Semiconductors DSC20S-3-FC) of 35-GHz frequency response to convert the optical signal to an electrical signal, next by amplifying the electrical signal through an RF amplifier (HP 83006A) that has a gain of 20 dB and a bandwidth of 26.5 GHz, and finally by displaying the amplified electrical signal on a microwave spectrum analyzer that has a bandwidth of 50 GHz (HP 8565E). Optical spectra are taken by using a scanning Fabry-Perot interferometer (Newport SR260C) with a free spectral range of 200 GHz and a Finesse of 8888, and also by using an Michelson-type optical spectrum analyzer (Advantest Q8347) with a wavelength resolution of around 0.01 nm at 1.55 μm . Optical isolators are used to avoid mutual injection and to reject back-reflection light from any component in the optical path.

The lasers used in this experiment are single-mode distributed feedback semiconductor lasers from Bookham Technology. The threshold current for the slave laser is approximately 18 mA. The bias current of the slave laser is fixed at 40 mA and the temperature is kept at 18° C throughout the study. This results in an output power of approximately 4.5 mW and an oscillating wavelength of around 1313.3 nm. The threshold current for the master laser is around 15 mA. The bias current is varied around 113 mA depending on the preferred operating condition, and the temperature is fixed at 15.5° C.

3. DYNAMICAL CHARACTERISTICS

At a given bias current level, the dynamical characteristics of a semiconductor laser subject to external optical injection depend on two operational parameters of the injection signal, the detuning frequency, f , and the injection parameter, ξ .¹⁵ Figure 2 shows the progression of the observed optical spectra and the corresponding power spectra from the optically injected laser system under consideration when the detuning frequency is fixed at $f = 7.55$ GHz and the injection strength is decreased from the highest level that can be achieved in the experiment. The optical and power spectra are shown in the columns on the left- and right-hand sides of Fig. 2, respectively. The optical spectra presented here are taken using the scanning Fabry-Perot interferometer with a frequency resolution of 22.5 MHz, which are also monitored and confirmed by using the Michelson-type optical spectrum analyzer. Note that, in the optical spectra, the frequency axis is relative to the free-running frequency of the slave laser. The dotted curve in each of the optical spectrum plot represents the optical spectrum of the free-running slave laser, which serves as a comparison with that of the optically injected slave laser.

In Fig. 2 (a-1), $\xi = 2.65 \times 10^{-1}$, the optical spectrum consists of a single very sharp line at the injection frequency, indicating that the slave laser is stably locked to the injection signal. The corresponding power spectrum, as depicted in Fig. 2 (a-2), shows no significant spectral feature but a small bump above the noise level of the system at around 28 GHz, which is not shown in the figure. This confirms the observation in the optical spectrum. The small bump observed in the power spectrum represents the relaxation resonance sidebands. Because the magnitude of relaxation resonance sidebands is very small, they are obscured in the optical spectrum by the system noise around -22 dB. The frequency difference between the relaxation resonance sidebands and the principal oscillation is commonly referred to as the relaxation resonance frequency. Therefore, the relaxation resonance frequency of the stably injected laser is around 28 GHz. Note that the relaxation resonance frequency of the free-running slave laser is around 10 GHz. This suggests a nearly 3 fold of enhancement in the resonance frequency for the injection-locked slave laser, implying a similar level of enhancement in modulation bandwidth.

As the injection level is slowly decreased from $\xi = 2.65 \times 10^{-1}$, the principal oscillation still locks at the injection frequency and the relaxation resonance sidebands shift toward the principal oscillation, thus reducing the relaxation resonance frequency from 28 GHz. Meanwhile, the magnitude of the relaxation sidebands increases. When the level of the optical injection is so reduced that the Hopf bifurcation boundary

is crossed, the locked laser becomes unstable. The Hopf bifurcation boundary is the upper boundary of the stable injection locking region.¹⁵ In Fig. 2 (b-1), $\xi = 2.34 \times 10^{-1}$, one sharp sideband emerges at the lower frequency of the spectrum, which is an experimental signature of a period-one oscillation.^{13,7} The feature of the period-one oscillation is also observed in the power spectrum as shown in Fig. 2 (b-2). The frequency separation between the principal oscillation and the emerging sideband is around 26 GHz. As also observed, the magnitude of the principal oscillation is 20 dB larger than that of the emerging sideband.

If we further decrease the injection strength from $\xi = 2.34 \times 10^{-1}$, the principal oscillation continues to oscillate at the injection frequency with a decreased magnitude. Moreover, the emerging sideband grows in magnitude, gradually approaching that of the principal oscillation. The sideband also moves toward the principal oscillation in frequency, reducing the frequency separation between them. Figure 2 (c-1), where

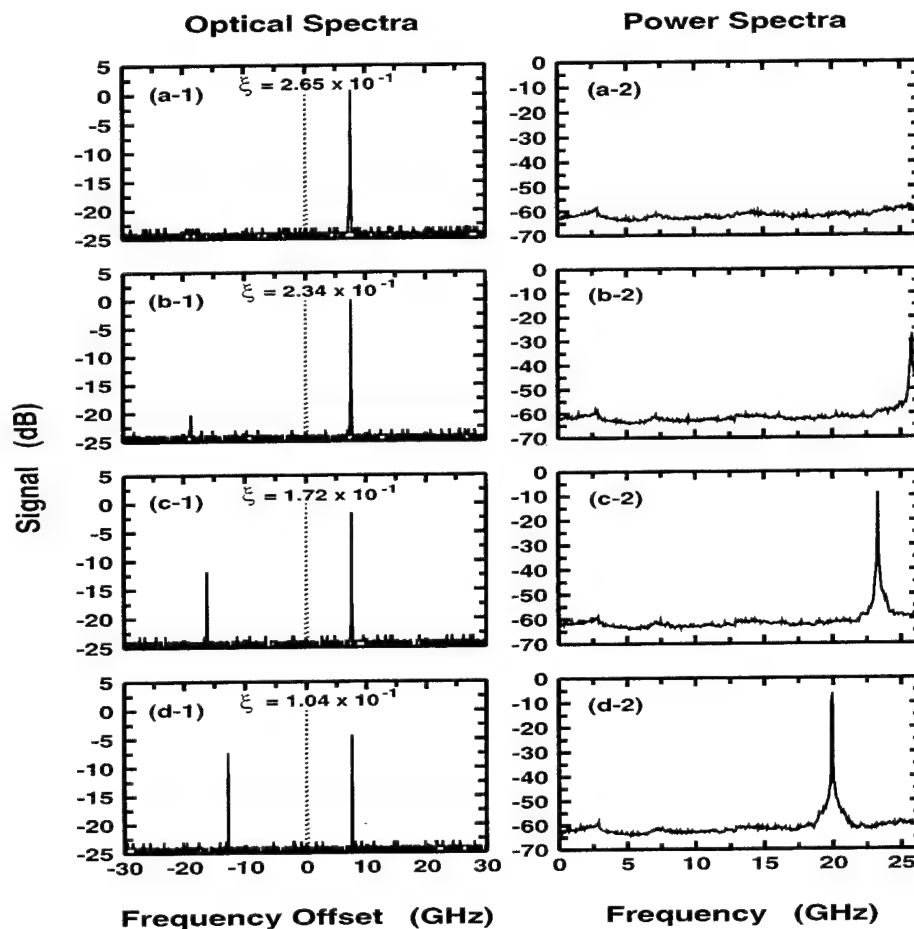


Figure 2. Measured optical spectra and the corresponding power spectra of the optically injected semiconductor laser at a fixed detuning frequency of 7.55 GHz as a function of the injection parameter. They are shown in the columns on the left- and right-hand sides, respectively. The dotted curve in each of the optical spectrum plot is the optical spectrum of the free-running slave laser.

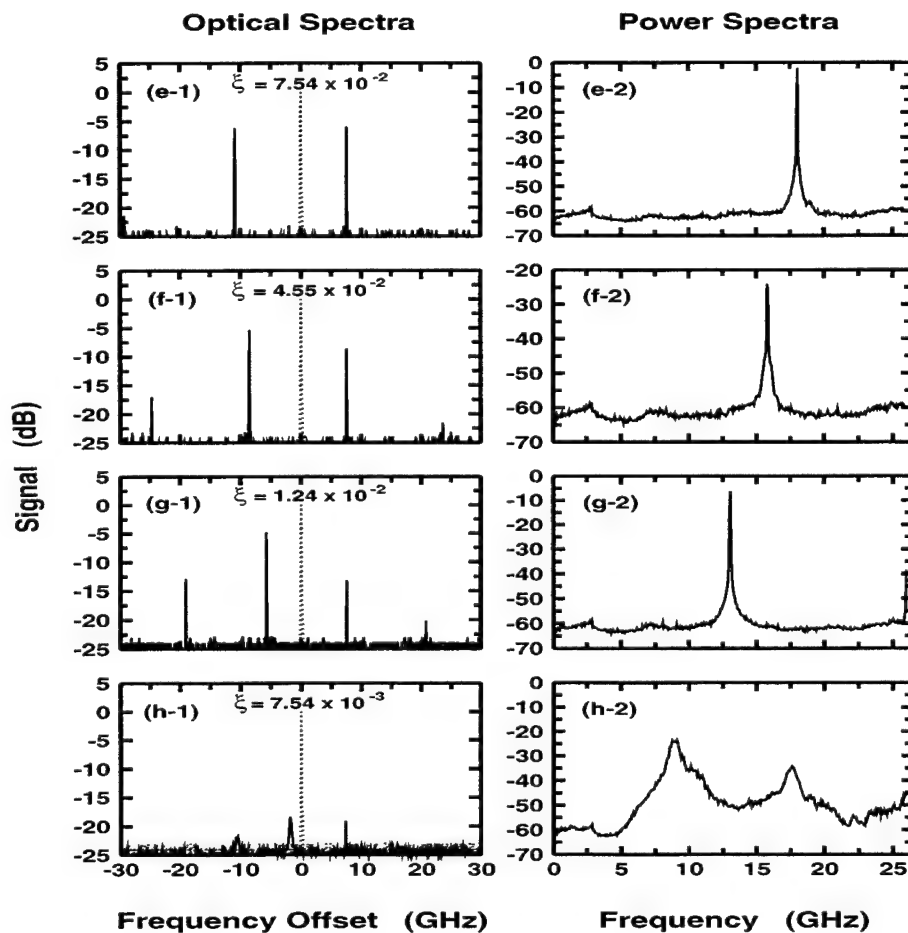


Figure 2 (Cont.). Measured optical spectra and the corresponding power spectra of the optically injected semiconductor laser at a fixed detuning frequency of 7.55 GHz as a function of the injection parameter. They are shown in the columns on the left- and right-hand sides, respectively. The dotted curve in each of the optical spectrum plot is the optical spectrum of the free-running slave laser.

$\xi = 1.72 \times 10^{-1}$, shows such observations. Now the frequency spacing between the principal oscillation and the emerging sideband decreases to around 23 GHz which can be more easily observed in Fig. 2 (c-2), and the magnitude of the principal oscillation is 10 dB larger than that of the sideband. Figure 2 (d-1), where $\xi = 1.04 \times 10^{-1}$, shows another such observations when the injection strength is further decreased. The frequency separation now becomes 20 GHz, and the magnitude of the principal oscillation is only 3 dB larger than that of the sideband.

If the injection level continues to reduce, the emerging sideband becomes the same magnitude as that of the oscillation at the injection frequency, as shown in Fig. 2 (e-1) where $\xi = 7.54 \times 10^{-2}$. As observed, the frequency separation between them now is around 18 GHz, smaller than that in Fig. 2 (d-1). Note that there is a second sideband appearing at a lower optical frequency that is two times the frequency separation away from the oscillation at the injection frequency. This is the harmonic signal of the first sideband due

to the inherent nonlinearity of the laser system. The corresponding power spectrum shown in Fig. 2 (e-2) does not show such a harmonic signal due to the limited bandwidth of the spectrum analyzer. As the injection level is further decreased, the first sideband becomes the principal oscillation as shown in Fig. 2 (f-1) where $\xi = 4.55 \times 10^{-2}$. Now the magnitude of the "original principal oscillation" is 3 dB smaller than that of the "emerging sideband". This indicates a frequency shift of the principal oscillation from the injection frequency to the period-one oscillation sideband, and the amount of the shift in frequency, under this operating condition, is round 16 GHz. It is observed that the amount of the shift in the optical frequency for the principal oscillation increases with the positively increasing detuning frequency. It is also found that the second sideband grows in magnitude. In addition, a new sideband emerges at the high frequency side of the spectrum. The frequency separation between the new sideband and the signal at the injection frequency is the same as that between the principal oscillation and the signal at the injection frequency.

In Fig. 2 (g-1), $\xi = 1.24 \times 10^{-2}$, the magnitude of the signal at the injection frequency keeps decreasing while the magnitude of other signals keeps increasing. In addition, the first sideband, which is now the principal oscillation, moves toward the signal at the injection frequency further, approaching the free-running frequency of the slave laser. Similar phenomena are observed if the injection strength keeps decreasing. At this fixed detuning frequency of 7.55 GHz, the magnitude difference between the principal oscillation (the first sideband) and the signal at the injection frequency can be as large as 12 dB. In addition, the frequency separation between the principal oscillation and the signal at the injection frequency reduces to around 13 GHz, which is very close to the relaxation resonance frequency of the free-running slave laser, due to the shift of the principal oscillation toward the high frequency side of the spectrum. As the injection level is further reduced, a broadened spectrum occurs which indicates a transition to chaotic dynamics, as that shown in Fig. 2 (h-1) where $\xi = 8.64 \times 10^{-3}$. Note that the optical power is spread over the spectrum so that the peaks are relatively small in magnitude. Nevertheless, the dynamical state for this operating condition shows some structure of periodicity, as suggested in Fig. 2 (h-2). The broadened spectrum continues as the injection level decreases.

4. ANALYSIS AND DISCUSSION

As discussed in Fig. 2 on period-one oscillations, the sideband shifts in frequency toward the signal at the injection frequency as the injection strength is decreased, thus reducing the frequency difference between them. In addition, the sideband gains more power as the injection level is reduced. Below a certain injection strength, the optical power of the sideband becomes so large that it dominates the signal at the injection frequency, thus becoming the principal oscillation. Similar observations are also found for other detuning frequencies as the injection level is varied. This suggests that the characteristics of the period-one oscillation follows a certain pattern as the injection strength changes.

Let us now first study how the frequency difference between the signal at the injection frequency and the first sideband varies with the detuning frequency and the injection strength. Figure 3 shows the frequency difference as a function of the detuning frequency for several magnitude differences. The same open symbol is used to indicate the operating conditions that have the same magnitude difference. A number is labeled next to each curve consisting of the same symbols to indicate the corresponding value of the magnitude difference. Note that the magnitude difference is defined by subtracting the magnitude of the signal at the injection frequency from that of the first sideband. For a fixed magnitude difference, it is observed that the frequency difference increases with the positively increasing detuning frequency. Therefore, if a certain power ratio of the principal oscillation to the sideband is required in applying period-one oscillation while the frequency separation between them needs to be varied, the detuning frequency is adjusted accordingly.

As also found in Fig. 3, if a detuning frequency is specified, the frequency difference increases with the decreasing magnitude difference. Note that the frequency shift of the principal oscillation from the signal at the injection frequency to the first sideband happens when the magnitude difference is above zero. It is then found that if a larger frequency shift in the principal oscillation is preferred for a fixed detuning frequency, a smaller power ratio of the principal oscillation, which is now the original first sideband, to the sideband,

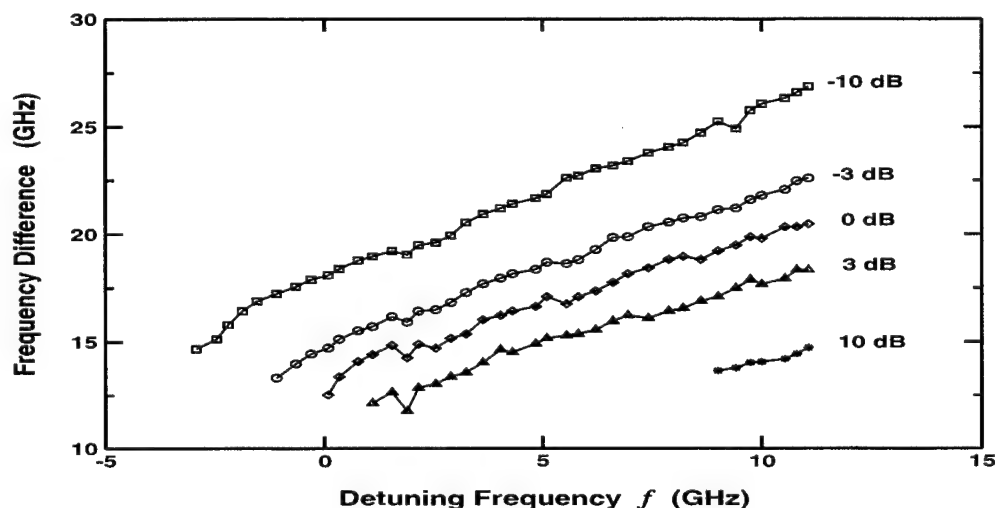


Figure 3. Frequency difference between the principal oscillation and the first sideband in period-one oscillations as a function of the detuning frequency for several magnitude differences. The same open symbol is used for a certain magnitude difference. A number is labeled next to each curve consisting of the same symbols to indicate the corresponding value of the magnitude difference.

which is now the signal at the injection frequency, is expected. In addition, it is found that the amount of the frequency shift in the principal oscillation increases with positively increasing detuning frequency. In Fig. 3, it is also found that for a fixed frequency difference, varying the detuning frequency can change the power ratio between the principal oscillation and the sideband.

Figure 4 shows the frequency difference as a function of the injection parameter for several magnitude differences. The same open symbol is used as in Fig. 3. It is found in Fig. 4 that for a fixed magnitude difference, the frequency separation between the principal oscillation and the sideband in period-one oscillation increases with the increasing injection strength. It is also observed that for a fixed injection strength, the frequency difference generally increases with the increasing magnitude difference. This suggests that if the injection power has to be fixed at a certain level, the frequency difference can be changed by varying the magnitude difference. As also found in Fig. 4, if the frequency difference is specified, the power ratio between the principal oscillation and the first sideband can be adjusted through the change in injection power. At certain weak injection levels, the frequency shift of the principal oscillation from the signal at the injection frequency to the first sideband would happen. By taking advantage of the observations in both Figs. 4 and 3, preferred characteristics of a period-one oscillation can be obtained by properly adjusting the injection strength and the detuning frequency.

5. CONCLUSION

The characteristics of period-one oscillations in an optically injected semiconductor laser as a function of the injection strength and the detuning frequency of the injection signal are experimentally and quantitatively studied. If the detuning frequency is fixed but the injection strength is varied, at high injection strength, the principal oscillation of the injected laser locks at the injection frequency and one side peak appears at a frequency below the injection frequency. As the injection strength decreases, the principal oscillation still

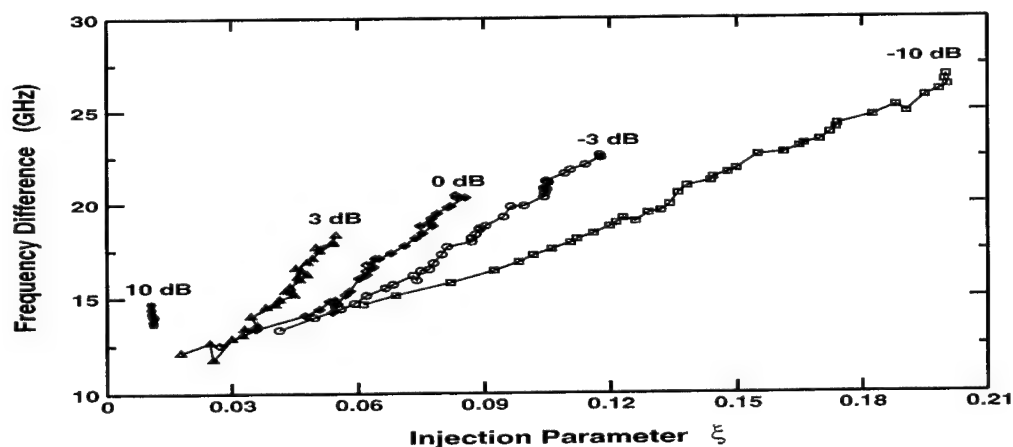


Figure 4. Frequency difference between the principal oscillation and the first sideband in period-one oscillation as a function of the injection parameter for several magnitude differences. The same open symbol is used as in Fig. 3 for a certain magnitude difference. A number is labeled next to each curve consisting of the same symbols to indicate the corresponding value of the magnitude difference.

locks at the injection frequency but the side peak moves toward the injection frequency, thus decreasing the frequency spacing between them. Moreover, the magnitude of the principal oscillation decreases while that of the side peak increases. This process continues as the injection strength continues to decrease. At some injection strength, both optical signals become the same in magnitude but still different in frequency. If the injection strength is further decreased, a frequency shift of the principal oscillation from the injection frequency to the "side peak" happens. Similar studies are conducted for different detuning frequencies. It is found that the frequency spacing increases with the detuning frequency and the injection strength. Moreover, it is observed that the magnitude difference decreases with the injection strength but increases with the detuning frequency.

REFERENCES

1. S. Kobayashi, J. Yamada, S. Machida, and T. Kimura, "Single-mode operation of 500 Mbit/s modulation AlGaAs semiconductor laser by injection locking," *Electron. Lett.*, vol. 16, pp. 746-748, 1980.
2. H. Nishimoto, H. Kuwahara, and M. Motegi, "Injection-locked 1.5 μm InGaAsP/InP lasers capable of 450 Mbit/s transmission over 106 km," *Electron. Lett.*, vol. 19, pp. 509-510, 1983.
3. S. Piazzolla, P. Spano, and M. Tamburrini, "Small signal analysis of frequency chirping in injection-locked semiconductor lasers," *IEEE J. Quantum Electron.*, vol. 22, no. 12, pp. 2219-2223, 1986.
4. H.F. Chen, J.M. Liu, and T.B. Simpson, "Response characteristics of direct current modulation on a bandwidth-enhanced semiconductor laser under strong injection locking," *Opt. Commun.*, vol. 173, pp. 349-355, 2000.
5. Y. Okajima, S.K. Hwang, and J.M. Liu, "Experimental observation of chirp reduction in bandwidth-enhanced semiconductor lasers subject to strong optical injection," *Opt. Commun.*, vol. 219, pp. 357-364, 2003.
6. P. Gallion, H. Nakajima, G. Debarge, and C. Chabran, "Contribution of spontaneous emission to the linewidth of an injection-locked semiconductor laser," *Electron. Lett.*, vol. 21, pp. 626-628, 1985.

7. R. Hui, "Optical PSK modulation using injection locked DFB semiconductor lasers," *IEEE Photon. Technol. Lett.*, vol. 2, pp. 743-746, 1990.
8. O. Lidoyne, P.B. Gallion, and D. Erasme, "Modulation properties of an injection-locked semiconductor laser," *IEEE J. Quantum Electron.*, vol. 27, pp. 344-351, 1991.
9. G. Yabre, "Effect of relatively strong light injection on the chirp-to-power ratio and the 3 dB bandwidth of directly modulated semiconductor lasers," *J. Lightwave Technol.*, vol. 14, no. 10, pp. 2367-2373, 1996.
10. T.B. Simpson and J.M. Liu, "Enhanced modulation bandwidth in injection-locked semiconductor lasers," *IEEE Photon. Technol. Lett.*, vol. 9, pp. 1322-1324, 1997.
11. T.B. Simpson, J.M. Liu, and A. Gavrielides, "Bandwidth enhancement and broadband noise reduction in injection-locked semiconductor lasers," *IEEE Photon. Technol. Lett.*, vol. 7, pp. 709-711, 1995.
12. J.M. Liu, H.F. Chen, X.J. Meng, and T.B. Simpson, "Modulation bandwidth, noise, and stability of a semiconductor laser subject to strong injection locking," *IEEE Photon. Technol. Lett.*, vol. 9, pp. 1325-1327, 1997.
13. T.B. Simpson, J.M. Liu, K.F. Huang, and K. Tai, "Nonlinear dynamics induced by external optical injection in semiconductor lasers," *Quantum Semiclass. Opt.*, vol. 9, pp. 765-784, 1997.
14. S.K. Hwang and J.M. Liu, "Attractors and basins of the locking-unlocking bistability in a semiconductor laser subject to strong optical injection," *Opt. Commun.*, vol. 169, pp. 167-176, 1999.
15. S.K. Hwang and J.M. Liu, "Dynamical characteristics of an optically injected semiconductor laser," *Opt. Commun.*, vol. 183, pp. 195-205, 2000.
16. F. Mogensen, H. Olesen, and G. Jacobsen, "Locking conditions and stability properties for a semiconductor laser with external light injection," *IEEE J. Quantum Electron.*, vol. 21, pp. 784-793, 1985.
17. C.H. Henry, N.A. Olsson, and N.K. Dutta, "Locking range and stability of injection locked $1.54\ \mu\text{m}$ InGaAsP semiconductor lasers," *IEEE J. Quantum Electron.*, vol. 21, pp. 1152-1156, 1985.
18. I. Petitbon, P. Gallion, G. Debarge, and C. Chabran, "Locking bandwidth and relaxation oscillation of an injection-locked semiconductor laser," *IEEE J. Quantum Electron.*, vol. 24, pp. 148-154, 1988.
19. J. Sacher, D. Baums, P. Panknin, W. Elsasser, e.O. Gobel, "Intensity instabilities semiconductor lasers under current modulation. external light injection, and delayed feedback," *Phys. Rev. A*, vol. 45, pp. 1893-1905, 1992.
20. T.B. Simpson, J.M. Liu, A. Gavrielides, V. Kovanis, P.M. Alsing, "Period-doubling route to chaos in a semiconductor laser subject to optical injection," *Appl. Phys. Lett.*, vol. 64, pp. 3539-3541, 1994.
21. T. Erneux, V. Kovanis, A. Gavrielides, V. Kovanis, P.M. Alsing, "Mechanism for period-doubling bifurcation in a semiconductor laser subject to optical injection," *Phys. Rev. A*, vol. 53, pp. 4372-4380, 1996.
22. S. Wieczorek, B. Krauskopf, and D. Lenstra, "A unifying view of bifurcations in a semiconductor laser subject to optical injection," *Opt. Commun.*, vol. 172, pp. 279-295, 1999.
23. E.K. Lee, H.S. Pang, J.D. Park, and H. Lee, "Bistability and chaos in an injection-locked semiconductor laser," *Phys. Rev. A*, vol. 47, pp. 736-739, 1993.
24. V. Annovazzi-Lodi, S. Donati, and M. Manna, "Chaos and locking in a semiconductor laser due to external injection," *IEEE J. Quantum Electron.*, vol. 30, pp. 1537-1541, 1994.
25. H.F. Chen and J.M. Liu, "Open-loop chaotic synchronization of injection-locked semiconductor lasers with gigahertz range modulation," *IEEE J. Quantum Electron.*, vol. 36, pp. 27-34, 2000.
26. S. Tang, H.F. Chen, S.K. Hwang, and J.M. Liu, "Message encoding and decoding through chaos modulation in chaotic optical communications," *IEEE Trans. Circuits Syst. I*, vol. 49, pp. 163-169, 2002.

Dynamics of lasers with ultra-short optical feedback

O. Ushakov^a, S. Bauer^b, O. Brox^b, H.-J. Wünsche^{a,b}, and F. Henneberger^a

^aHumboldt Universität zu Berlin, Institut für Physik, Newtonstr.15, 12489 Berlin, Germany

^bFraunhofer-Institut für Nachrichtentechnik, Heinrich-Hertz-Institut
Einsteinufer 37, 10587 Berlin, Germany

ABSTRACT

The dynamical behavior of a single-mode laser subject to optical feedback is investigated in the limit, when the delay time is much shorter than the period of the relaxation oscillations. Use of an integrated DFB device allows us to control the feedback phase. The system shows a very rich manifold of nonlinear phenomena. Among them are two kinds of Hopf bifurcations associated with regular self-pulsations of different frequencies as well as a fold and period doubling bifurcation.

Keywords: semiconductor laser, nonlinear dynamics, optical feedback, self-pulsations, mode-commutations

1. INTRODUCTION

The single-mode laser is a paradigm of self-organization in dissipative systems.¹ At threshold it undergoes a transition from incoherent to coherent emission. One optical mode becomes undamped here in a Hopf bifurcation. Its contribution to the optical field is harmonically oscillating and dominates beyond threshold, giving rise to high coherence. Distributed feedback (DFB) semiconductor lasers come close to this ideal.² They exhibit continuous wave (CW) single mode emission up to high pump currents. Upon a perturbation the intensity returns back to the stationary CW value with well damped relaxation oscillations (RO). Optical feedback can destabilize the CW state.³ Phenomena like self-sustaining intensity pulsations, coherence collapse,⁴ and others have been recently predicted and experimentally observed. Potential applications cover high-speed data transmission, cryptography,⁵ etc.



Figure 1. Scheme of the investigated DFB laser with integrated passive feedback section. The active zone ($\lambda_g = 1.55 \mu\text{m}$) is removed in the feedback section; the waveguide layer ($\lambda_g = 1.3 \mu\text{m}$) is common to both sections. I_{DFB} : pump current DFB section, I_P pump current in feedback section.

Optical feedback is usually achieved by combining the laser with an external mirror. The characteristic parameters are (i) the delay time τ through the round trip in the external cavity, (ii) the intensity fraction K^2 that re-enters the laser and (iii) the phase ϕ of the feedback field. The behavior in presence of feedback crucially depends on the number of modes that are of relevance in the compound device. This number grows when the feedback strength K increases. A second factor arises through the time-scales involved. Photon life-times in typical semiconductor lasers are $\tau_P \approx 1-10$ ps, while the period of the relaxation oscillations τ_R ranges between 0.1 and 1 ns. In the long-cavity limit, addressed in most previous studies, τ is much longer than τ_R . The solitary mode is hence transformed in a quasi-continuous spectrum of external cavity modes, even for modest K . The consequence is an irregular dynamical response with stochastic power dropouts. Studies on shorter cavities have yielded qualitatively different behavior.^{3, 15, 16} Here, the feedback phase begins to influence the field-inversion dynamics in the laser. Regular intensity pulsations have been reported already in early studies.³ However,

Send correspondence to ushakov@physik.hu-berlin.de

the multimode nature of the used Fabry-Perot lasers mixes with feedback effects.³ Using single mode lasers in a short feedback regime ($\tau/\tau_R \approx 0.3$ to 1), recently pulse packages have been observed that originate from a global trajectory along a limited number of modes in the phase-inversion space. The metamorphosis of this scenario with even shorter delay time was not subject to experiments yet. An exception are DFB lasers with active feedback used to generate self-pulsations of several ten GHz.¹⁰ The dynamics of these devices is however modified by coupling of the photons to two independent inversion ensembles.¹¹ Only the limit of feedback with zero delay is well known – the reflectivity from cleaved facets does not cause dynamic instabilities in DFB lasers.

In the present paper we consider structures, where laser and external cavity are monolithically integrated in a single device (Fig. 1). They enable to access the regime of very short cavities. Here, the length of both laser and feedback section is in the some 100- μm range resulting in $\tau/\tau_R \approx 0.01$. In this situation, two different pulsation phenomena are expected: mode-beating (MB) pulsations of mode-anti-mode pairs^{7,8} and undamped RO.^{9,13} Thus, the regime of pulse packages may be not the ultimate short-cavity limit with nontrivial dynamics.

The present paper summarizes the first experimental verification of these theoretical predictions. It is organized as follows: Device and experimental setup are described in Section 2. Section 3 reviews the observed dynamical scenarios. Phase tuning features are investigated in more detail in Sec. 4. A theoretical discussion of these experimental results in terms of optical modes and bifurcations is sketched in Sec. 5, followed by a detailed experimental verification of predicted bifurcations in Sec. 6. We finish with some conclusions.

2. DEVICE AND SETUP

The investigated device is sketched in Fig. 1. It is based on InGaAsP-InP material system and the optical wave is guided by a ridge waveguide structure. It consists of two sections: a $L_{\text{DFB}} = 220 \mu\text{m}$ long DFB laser is integrated with a passive feedback section of length $L_P = 200 \mu\text{m}$. The active bulk $\lambda_{\text{gap}} = 1.55 \mu\text{m}$ layer of the DFB laser is embedded in an asymmetric $\lambda_{\text{gap}} = 1.3 \mu\text{m}$ InGaAsP optical waveguide which has an index coupled grating without phase shifts. A coupling coefficient $\kappa = 130 \text{ cm}^{-1}$ was chosen in order to prevent mode switching between the two stop-band sides of the DFB laser. The short wavelength mode is supported by the resulting longitudinal hole burning. The facet of the DFB section is anti-reflection (AR) coated with a remaining power reflectivity of 10^{-4} .

In the feedback section the $1.55 \mu\text{m}$ layer is removed and the remaining layers do not directly couple to the emission of the laser. Its rear facet is cleaved, with a resulting power reflectivity $R \approx 0.3$. The feedback parameters are

$$\phi = -\frac{4\pi}{\lambda} n_{\text{eff}} L_P, \quad (1)$$

$$K = T_{\text{AP}} \exp(-\alpha_P L_P) \sqrt{R}, \quad (2)$$

$$\tau = 2L_P v_g^{-1}. \quad (3)$$

The phase shift ϕ is proportional to the effective refractive index n_{eff} which in turn is affected by the carriers injected into this section. Therefore, the current I_P can be used for phase tuning at fixed laser parameters in contrast to previous studies exploiting laser current³ (and references therein) or laser temperature.^{15,16} The measured phase tuning characteristics is shown in Fig. 2. More than 3 phase periods are accessible before the phase shift saturates beyond 80 mA. A secondary effect of I_P is induced free-carrier absorption. It degrades the feedback strength K by roughly a factor 3 in the considered range of currents. Comparing with transmission spectra of non-biased isolated feedback sections cut from the same wafer, we estimated about 10 cm^{-1} background losses in the feedback cavity and a transmissivity $T_{\text{AP}} \approx 0.7$ of the active-passive interface. The corresponding feedback amplitudes range from $K \approx 0.3$ down to $K \approx 0.1$. The measured group index $c/v_g \approx 3.5$ is nearly independent of the phase current, yielding a constant delay $\tau \approx 5 \text{ ps}$. The according round-trip frequency $\tau^{-1} \approx 200 \text{ GHz}$ is nearly two orders of magnitude larger than typical relaxation oscillation frequencies and, hence, the present device realizes the limit of very short feedback cavities.

In order to detect and to characterize self-pulsations, the experimental setup of Fig. 3 is used. The two section laser is connected to an oscilloscope, an optical spectrometer and an electrical spectrum analyzer by a single mode optical fiber (SM Patchcord 9/125) from the DFB facet. The sampling oscilloscope (HP 54120B

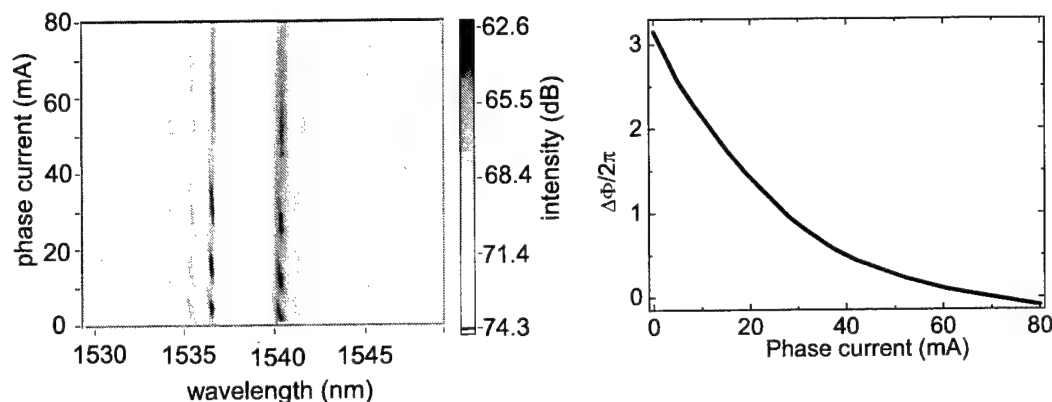


Figure 2. Phase tuning properties of the passive section. Left panel: movement of ASE ripples with the injection current of the feedback section (phase current). The intensity of the ASE spectra is coded with the given grey scale. Right panel: Phase shift versus phase current deduced from the ASE spectra.

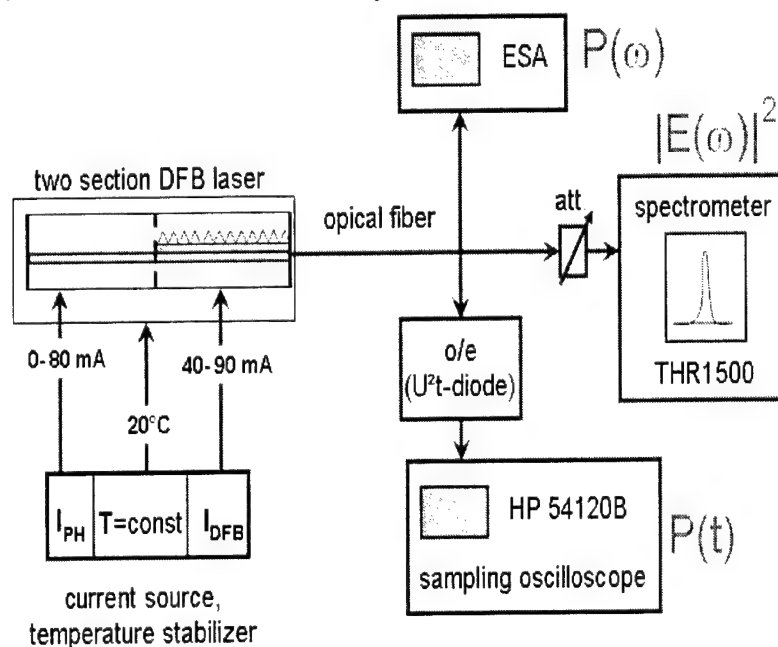


Figure 3. Experimental setup. The emission of the laser under investigation is analyzed with a power spectrometer R&S FSP 9, a digital 50 GHz sampling oscilloscope (HP 54120B), and a Czerny-Turner spectrometer (0.015 nm resolution) with an infrared camera as detector.

Digitize Oscilloscope) with an u2t photo diode is used to obtain time series. The bandwidth of the oscilloscope is 50 GHz. The optical spectra are measured by a Czerny-Turner spectrometer (THR 1500, grating 600 g/mm) with an IR camera as detector. An attenuator between the laser and the spectrometer is used to control the output intensity. Power spectra were measured by an electrical spectrum analyzer with a bandwidth of 40 GHz (R&S FSP 9/40GHz) using u2t photo diode. The time averaged mean power was measured by an optical powermeter (NOYES OPM 5), with averaging time of 5 s. The whole set of measurements are done at varying currents in the passive and active sections. Currents are controlled by the current source (Tektronix/Profile PRO 8000). Both sections of the laser are kept at a constant temperature $20\text{ }^{\circ}\text{C} \pm 0.05\text{ }^{\circ}\text{C}$.

3. REGIONS OF SELF-PULSATIONS

In order to find the theoretically predicted self-pulsations we map the two injection currents over a wide range. Depending on the point of operation, different types of RF and optical spectra are observed. Fig. 4 shows characteristic examples. A single line in the optical spectrum and a flat noise floor in the RF spectrum are

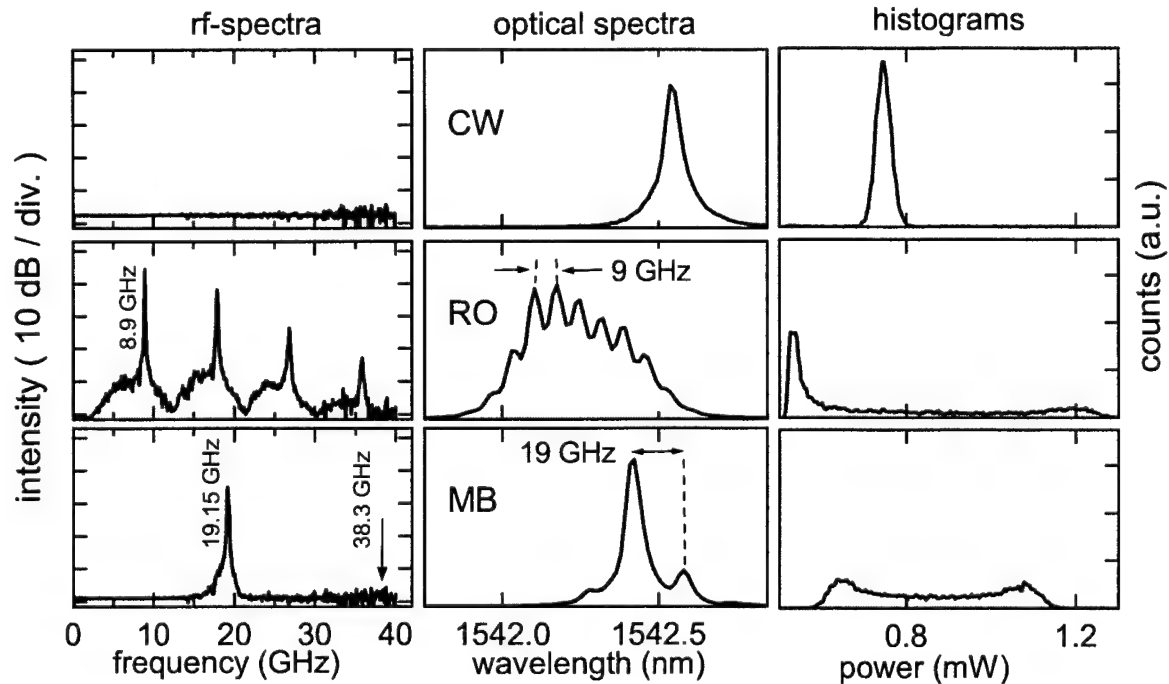


Figure 4. Characteristics of the most prominent types of laser emission. Left column: power spectra, middle column: optical spectra, right column: histograms. Upper row: CW emission (point CW of Fig. 5, $I_{\text{DFB}} = 65$ mA, $I_{\text{P}} = 45$ mA). Middle row: undamped RO pulsation (point RO of Fig. 5, $I_{\text{DFB}} = 50$ mA, $I_{\text{P}} = 28$ mA). Lower row: MB pulsation (point MB of Fig. 5, $I_{\text{DFB}} = 70$ mA, $I_{\text{P}} = 11$ mA).

attributes of CW emission. Sharp and strong RF peaks and a corresponding splitting of the optical emission line into several sublines are the fingerprints of self-pulsations. Fig. 5 shows the regions in the two-parameter plane $I_{\text{DFB}} - I_{\text{P}}$ where the major RF peak exceeds the noise floor by more than 5 dB.

Cycles of alternating SP and CW regimes appear in dependence on I_{P} due to the phase tuning property of this current. The injection level of the DFB section has only a small influence on the position of the SP islands. This influence is due to the change of the feedback phase with the emission wavelength. The SP islands of the different cycles are similar but not identical because I_{P} influences not only the phase but also the strength of feedback.

The frequencies of SP range from about 1 GHz up to 24 GHz. They increase sublinearly with I_{DFB} in the lower part of each SP island. This behavior is a fingerprint of relaxation oscillations. We can conclude that those parts of the SP-islands, which continuously evolve from these low frequency parts are regions of undamped RO. Below we shall give more evidence for this conclusion. We shall also prove that the high-frequency parts of the islands are not RO pulsations, in particular the upper parts within the first two phase cycles.

The right column in Fig. 4 shows how frequent a given optical power is detected by the oscilloscope within a persisted time. These histograms provide further statistical characteristics of the measured signals. The stationary state is represented by a single peak at the mean power. Its width is a measure for the noise induced intensity fluctuations. Regular pulsations are characterized by wide two-peak distributions. The peaks represent the mean minimum and maximum powers. Their heights measure how fast the intensity passes through the respective extrema. The RO histogram exhibits a high extinction ratio and a very distinct peak at the minimum

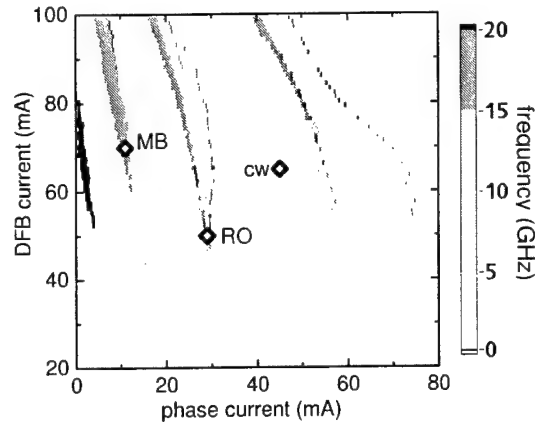


Figure 5. Self-pulsation regions in the plane of phase and DFB current. The gray levels code the frequency of the major peak in the RF spectrum. White: CW emission (major RF peak less than 5 dB above noise floor). Diamonds: points of operation presented in Fig. 4.

power. Thus, the RO pulsations are comparatively short pulses separated by relatively long valleys with minimum intensity. In contrast, the extinction of MB pulsations is smaller and the two similar peaks indicate a nearly sinusoidal behavior.

4. PHASE TUNING

So far we have identified the regions and frequencies of self-pulsations. The phase current appeared as main parameter for the bifurcations from CW to SP. Now we give a deeper characterization of the SP and of the bifurcations associated with the feedback phase. To these purposes we change the phase current in steps of 0.1 mA from 0 mA to 80 mA and reverse, keeping the DFB current at 50 mA. Mean intensity, modulation depth, and wavelength of the emission from the DFB facet are recorded in each point of operation. In Fig. 6, the data are plotted versus the phase parameter ϕ determined from I_P as described in Section 2.

Power and wavelength undergo cyclic variations with ϕ and exhibit distinct hysteresis effects due to the movement of external cavity modes across the fixed DFB resonance. The power becomes maximum when a mode coincides with the resonance. With changing ϕ from here, the threshold increases and the power decreases until a jump to the next better mode appears. The regions of nonzero modulation depth in Fig. 6c) are indications of self-pulsations. They appear for increasing phase (forward direction) in each period just before jumping to the next mode. Similar power and wavelength undulations were observed when changing the injection current of a semiconductor laser subject to external optical feedback.³

The different periods are not completely equivalent because I_P changes not only the phase of the feedback but also its strength K from ≈ 0.3 down to ≈ 0.1 in the investigated current range (see Section 2). Obviously, hysteresis and pulsation effects are most sensitive to this effect. They qualitatively change from region ii to region iii.

In regions i and ii pulsations occur only with small amplitude in a small interval in forward direction and the frequencies are around 20 GHz as expected for MB pulsations. In the other two periods, the SP have distinctly smaller frequencies, higher amplitudes, and show less hysteresis.

5. THEORETICAL ANALYSIS

The above observations reveal a specific scenario that is analyzed now more closely. The longitudinal modes of the compound cavity, comprising DFB and feedback section, follow from the round-trip condition

$$q(\Omega, N) \exp(-i\Omega\tau) = K \exp(-i\phi), \quad (4)$$

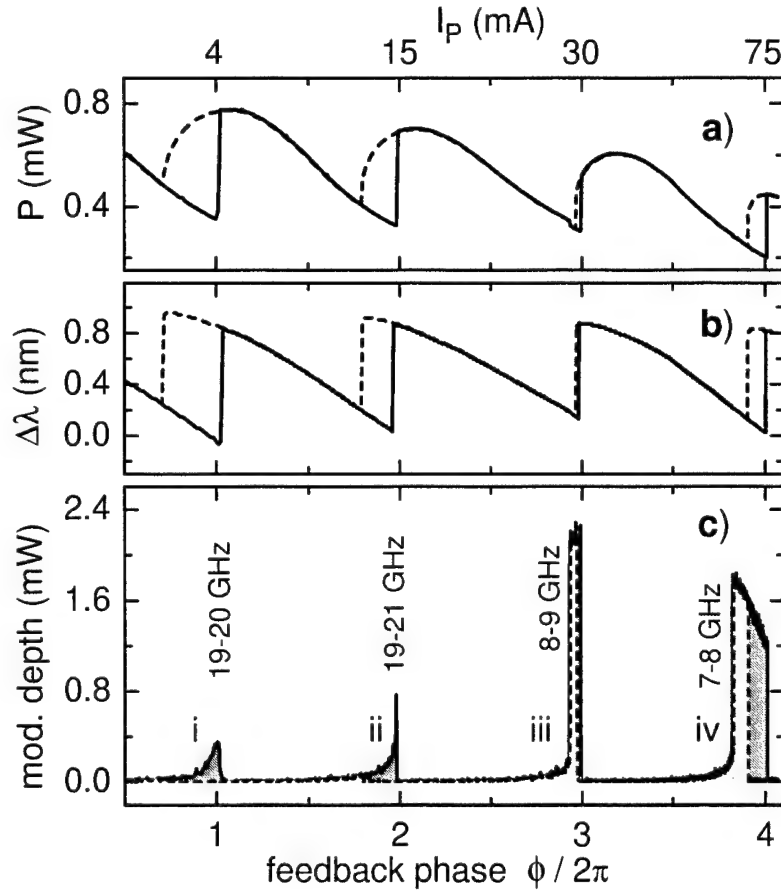


Figure 6. Control of the dynamics by feedback phase. Panel a) mean output power P . Panel b) shift $\Delta\lambda$ of the main peak in the optical spectrum Panel c) modulation depth M (difference between maximum and minimum on the sampling oscilloscope). Solid: increasing I_P . Dotted: decreasing I_P . The phase ϕ (bottom scale) is determined from the phase current (top scale) according to Fig. 2. The DFB current is kept at 50 mA.

where N is the average carrier density in the laser and Ω denotes the complex mode frequency, measured relative to the Bragg resonance at transparency. The DFB enters here by its inverse amplitude reflectivity²

$$q = \frac{i\gamma}{\kappa} \cot(\gamma L_{\text{DFB}}) - \frac{\beta}{\kappa} \quad (5)$$

with $\gamma^2 = \beta^2 - \kappa^2$ and the propagation constant

$$\beta(\Omega, N) = \frac{1}{2}[(i + \alpha_H)g'(N - N_{tr}) - \alpha_0] + \frac{\Omega}{v_g}. \quad (6)$$

The parameters involved ($\kappa = 130 \text{ cm}^{-1}$: coupling coefficient of index grating, $\alpha_H = -5$: linewidth enhancement factor, $\alpha_0 = 25 \text{ cm}^{-1}$: background absorption, $g' = 10^{-20} \text{ m}^2$: differential gain, including the transverse confinement factor, $N_{tr} = 10^{24} \text{ m}^{-3}$: carrier density at transparency level) have been deduced from independent measurements.

The solutions of the complex valued Eq. (4) are quite complex surfaces in the three dimensional space spanned by $\text{Re } \Omega$, $\text{Im } \Omega$, and N . Fig. 7 depicts these solutions by curves of constant K and constant ϕ in two different plane cuts through this space. The modes of the solitary laser ($K = 0$) are represented by vertices, where the equi-phase lines move together. The left panels shows the so-called external cavity modes. They belong to a fixed N , here the threshold density of the solitary laser. Obviously, the very short delay of our device has a

considerable impact on the mode structure. Without delay, curves of constant feedback strength $|q(\Omega, N)| = K$ are orbits around the mode of the solitary laser. Their extension is an increasing function of K . With delay, the factor $\exp(i\Omega\tau)$ in Eq. 4 gives rise to additional modes. At small $K = 0.1$, these new external cavity modes are highly damped and located on a separate line well above the orbit of the central laser mode. At the higher $K = 0.3$, this line has moved down and it merged with the central orbit forming a deep valley.

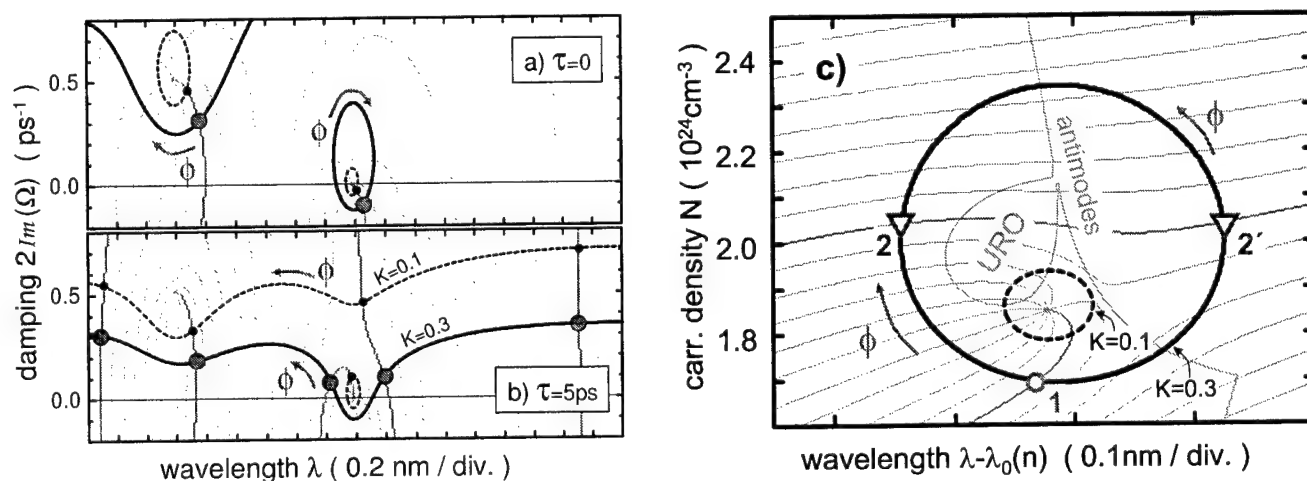


Figure 7. Modes calculated from Eqs. (4 to 6). Curves of constant feedback ($K = 0.1$ dashed, $K = 0.3$ solid) and curves of constant phase (thin grey, 10 lines per phase period) are drawn in all panels. Panels a) and b) External cavity modes in the damping-wavelength plane, carriers fixed to the threshold density of the solitary DFB laser. Panel c) Compound cavity modes in the wavelength-density plane $\text{Im}(\Omega)=0$. The carrier-induced shift $\lambda_0(N)$ is subtracted here for clarity. Gray area: regions of instability.

Fig. 7c shows the central part of the same scenario in terms of modes at threshold, often called compound cavity modes. Standard single-mode stability analysis⁶ of these modes yields two types of instabilities: saddles in the region labelled 'anti-modes' and undamped relaxation oscillations in the small island denoted by 'URO'. The grey borders of these islands represent saddle-node and Hopf bifurcations, respectively. The orbit $K = 0.1$ touches the 'URO' island but not the more extended orbit $K = 0.3$. This island topology explains, why RO pulsations are only found in higher phase periods of I_P (see Fig. 5), as K is sufficiently reduced here. It is also consistent with the observation of similar Hopf bifurcations for longer cavities.¹⁶ Undamped relaxation oscillations are hence a common feature of short and ultra-short cavities with weak feedback.

While the form of the orbit in the right panel is independent on τ , the delay controls the number of modes enclosed. For small K , $\exp(i\Omega\tau) \approx 1$ holds along the orbit. Only one mode exists that rotates with ϕ clockwise around the orbit. However, variation of $\Omega\tau$ along extended orbits is associated with a change of ϕ by more than one period, enabling thus several modes. It is this interrelation between feedback delay and strength that gives rise to new dynamics, even though $\tau/\tau_R \ll 1$. The variation of ϕ is not monotonous along the orbit. The equi-phase lines are tangential with the orbit, where it enters the anti-mode region. Pairs of modes appear or disappear here in saddle-node bifurcations. With increasing ϕ , the stable modes move up on the left part of the loop, while the unstable anti-modes do so on the right-hand side.

At a particular phase, mode and anti-mode arrive at comparable threshold densities (triangles). Here, both modes accommodate to each other at a common density and MB pulsations emerge in a Hopf bifurcation.^{7,9,13} This scenario is reminiscent of the bifurcation bridges predicted for long delay times.⁸ The peculiar feature of the ultra-short cavity regime is the existence of only one anti-mode, yielding regular dynamics, whereas the pulse-package scenario¹⁶ involves multiple anti-modes. The device output is therefore qualitatively different. Pulse packages are pulse sequences with a repetition rate exactly given by the external cavity frequency $1/\tau$, amplitude-modulated with a frequency below $1/\tau_R$. At variance, the MB pulsations are not modulated and their frequency is by about one order of magnitude smaller than $1/\tau$, due to pulling of the side-mode by the DFB

resonance. The transition between both regimes is an interesting subject of future research. We note finally that the instability above state 2 is also the source of the hysteresis observed experimentally. For decreasing ϕ , state 1 moves to longer wavelengths and, in contrast to forward phase, reaches the saddle-node bifurcation. Here, the laser switches to the only stable state of same ϕ on the left part of the orbit.

6. BIFURCATIONS

So far we have shown how two different types of SP can be generated by properly choosing the phase current. Theory predicts both types of SP to be born in a Hopf bifurcation,^{8,9,13} which is the classical scenario of temporal self-organization. Now we search for experimental evidence for this prediction.

Mathematically a Hopf bifurcation is characterized by a pair of complex conjugated eigenvalues of the dynamical matrix moving across the imaginary axis. What does it mean from physical point of view? Among many vibrational modes there is one oscillator whose damping approaches zero. In order to detect this process experimentally, we can profit from the noise in our real system, which is omnipresent e.g. due to spontaneous emission. Noise drives all possible oscillations. If the damping of one oscillator approaches zero, its oscillation amplitude increases. An increasing and narrowing line should appear in the power spectrum as a precursor of the Hopf bifurcation, whose position and width are a direct measure for the relevant complex eigenvalues.

6.1. Subcritical Hopf bifurcation

First we apply this concept to the SP region iii of Fig.6. The modulation depth re-plotted in a zoomed scale exceeds the noise level when approaching the pulsation region from left. This amplitude increase is already the fingerprint of an oscillator getting undamped. At the same time, a well resolvable line in the rf spectra appears (see of Fig.8). The distinct decay of its width gives evidence of a Hopf bifurcation at this boundary of the self-pulsation region.

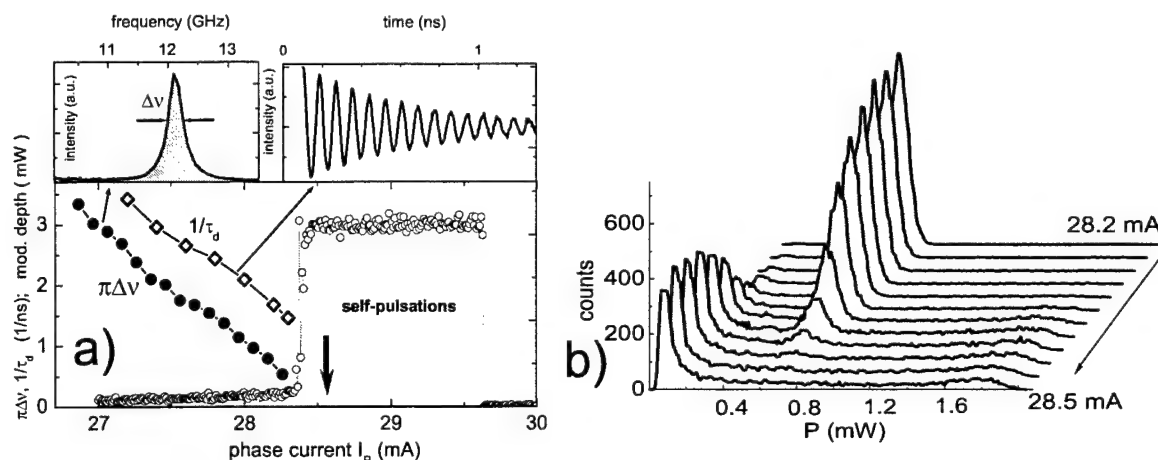


Figure 8. a) Characteristics of the Hopf-bifurcation of RO self-pulsations. DFB current at 50 mA. Small circles: modulation depth. Full circles: half-width $\pi\Delta\nu$ of the resonance line in the rf spectrum. Open circles: damping rate τ_d^{-1} of relaxation oscillations. Both linewidth and decay rate approach zero. The horizontal offset of the decay rates is possibly due to a change of the point of operation caused by the external excitation. b) Set of histograms with a change of the phase current.

In order to evaluate the physical nature of the undamped oscillator, the laser was excited by an external pulse and the decaying response was measured (see inset of Fig.8). The decay rates fall with the same slope as the rf linewidths. Thus, the oscillations undergoing the Hopf-bifurcation are relaxation oscillations. The small deviation between measured resonance widths and decay rates is possibly due to a small impact of the external excitation on the feedback phase.

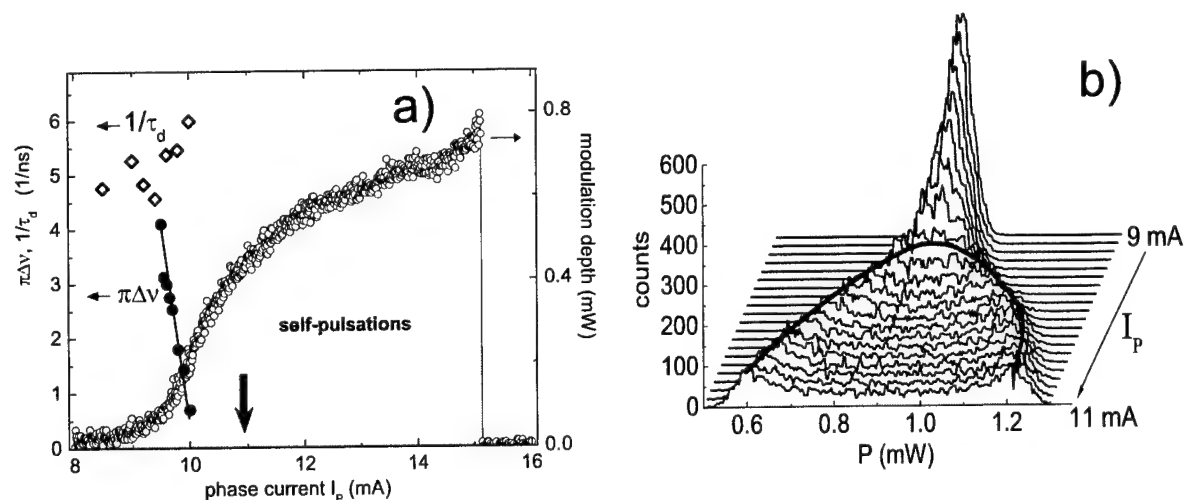


Figure 9. a) Characteristics of the Hopf-bifurcation of mode-beating self-pulsations. DFB current at 70 mA. Small circles: modulation depth. Full circles: half-width $\pi\Delta\nu$ of the resonance line in the rf spectrum. Open circles: damping rate τ_d^{-1} of relaxation oscillations. b) Evolution of histograms with phase current.

The frequency of the decaying oscillations is 12 GHz in agreement with the rf-peak positions, distinctly above the RO resonance of comparable DFB lasers without feedback. This finding is a typical effect of undamping by dispersive Q-switching which is accompanied by an increase of the effective differential gain.

The modulation depth suddenly blows up when crossing the bifurcation accompanied by a slowing down of the oscillations from 12 GHz to 9 GHz. However, no hysteresis is observable within the experimental resolution. We conclude, the investigated point of operation is very close to a codimension two degenerate Hopf bifurcation, where the Hopf changes its character from subcritical to supercritical.

The evolution of pulsations can also be observed in the histograms (Fig. 8b). The stationary state at 28.2 mA is represented by a single peak with about 0.8 mW mean power. At 28.5 mA, the histogram shows the typical features of RO pulsations. However, this transition is not sudden as might be concluded from panel a). In a finite intermediate range, the RO-peaks appear smoothly in the same manner as the single cw-peak drops down. We attribute this phenomenon to noise induced transitions between the two stable attractors close to the subcritical Hopf bifurcation. Obviously, the transitions from cw to RO and back appear with comparable probabilities within this range. This feature confirms the proximity to a degenerate Hopf.

6.2. Supercritical Hopf bifurcation

The same technique is applied now to the mode-beating pulsations on a horizontal cut crossing point MB in Fig. 5a). The spectra of the SP along the cut are similar to that in point MB (Fig. 4). They indicate nearly sinusoidal mode-beating pulsations with frequencies around 20 GHz. The left boundary of the pulsation region depicted in Fig. 9 is not sharp, the modulation depth raises smoothly here. However, the mode-beating line in the power spectrum emerges from a precursor whose width falls rapidly when approaching the pulsation region. Thus, the mode-beating pulsations are also born in a Hopf bifurcation as predicted theoretically.⁸ The measured decay rates of relaxation oscillations keep high along this bifurcation. Thus, the oscillator undergoing the Hopf bifurcation is not connected with the relaxation oscillations.

The evolution of the histograms in Fig. 9b exhibits similar tendencies as previously observed in the case of the subcritical Hopf bifurcation. The height of the main peak decreases and its width increases with the increase of the current. However, the two peaks of the pulsating state appear now in a smooth transitions which clearly resembles the features of a supercritical Hopf bifurcation.

7. CONCLUSION

A single-mode DFB laser with an biased passive feedback cavity has been investigated experimentally. Although the 5 ps feedback delay is shorter by two orders of magnitude compared to the period of relaxation oscillations, it is crucial for the dynamics of the device. Two different types of self-sustaining intensity-pulsations are detected depending on strength and phase of the feedback which are controlled by the bias to the passive section. One type of pulsations is emerging in a Hopf-bifurcation from relaxation oscillations. These oscillations become undamped due to dispersive self-Q switching. The second type of pulsations is a mode-anti-mode beating pulsation. It is also born in a Hopf bifurcation. These findings represent first experimental evidence for recent theoretical predictions.^{8,9} A supplementary mode and stability analysis agrees well with measurements and it is used to discuss the relations to intermediate-delay¹⁶ as well as zero-delay regimes.

REFERENCES

1. H. Haken, *Laser Theory* (Springer-Verlag, 1986).
2. John E. Carroll, J.E.A. Whiteaway and R.G.S. Plumb, *Distributed Feedback Semiconductor Lasers* (IEE Publishing, 1998).
3. R. Lang and K. Kobayshi, *IEEE J. of Quant. El.*, QE-16, 347-355 (1980).
4. I. Fischer, T. Heil, M. Munkel, and W. Elsässer, in *Proceedings of SPIE*, vol. 3283, pp. 571-579 (1998).
5. J. Ohtsubo, *IEEE J. of Quant. El.*, QE-38, 1141 (2002).
6. Vasile Z. Tronciu, H.-J. Wünsche, J. Sieber, K. Schneider and F. Henneberger, *Opt. Comm.* **182**, 221 (2000).
7. A. Tager and K. Petermann, *IEEE J. of Quant. El.*, QE-30, 1553-1561 (1994).
8. T. Erneux *et al.*, *Opt. Comm.* **183**, pp. 467-477 (2000)
9. J. Sieber, *SIAM J. of Appl. Dyn. Sys.* vol. **1**, 248 (2002).
10. S. Bauer *et al.* *Electron. Lett.*, vol. **38**, pp. 334-335 (2002)
11. S. Bauer *et al.*, *Phys. Rev. E* **69**, 016206 (2004)
12. H.-J. Wünsche, O. Brox, M. Radziunas and F. Henneberger, *Phys. Rev. Lett.* **88**, 023901 (2002).
13. M. Wolfrum and D. Turaev, *Opt. Comm.*, vol. **212**, pp. 127-138, 2002.
14. B. Sartorius, *et al.*, *IEEE Photonics Technol. Lett.*, vol. **7**, 1261 (1995)
15. T. Heil, I. Fischer, W. Elsässer, and A. Gavrielides, *Phys. Rev. Lett.*, vol. **87**, 243901 (2001)
16. T. Heil, I. Fischer, and W. Elsässer, B. Krauskopf and K. Green, A. Gavrielides, *Phys. Rew. E* **67**, 066214, 2003.

Instability and Dynamic Characteristics of Self-Pulsating Semiconductor Lasers with Optical Feedback

Hajime Koshio and Junji Ohtsubo

Faculty of Engineering, Shizuoka University, 3-5-1 Johoku, Hamamatsu, 432-8561 Japan

Abstract

Self-pulsating semiconductor lasers are devised to reduce optical feedback noises as light sources in optical data storage systems. However, they themselves include instabilities in their solitary oscillations without any optical feedback and they also show unstable behaviors induced by optical feedback. We experimentally investigate instabilities and dynamics of self-pulsating semiconductor lasers without and with optical feedback from a distant reflector on the order of several tens of centimeters to one meter.

Keywords: self-pulsating semiconductor lasers, instability, optical feedback, chaos

1. Introduction

Semiconductor lasers are used as light sources in various optical information processing and optical communications. Optical feedback from external optical components in semiconductor lasers causes serious problems in optical data handling and transmission, since semiconductor lasers are very sensitive to external optical feedback.^{1,2} For suppressing external optical feedback noises, a technique of high-frequency modulation to injection current of semiconductor lasers was frequently used in optical data storage systems. Self-pulsating lasers are devised and used in optical data storage systems as a robust light source for optical feedback. Self-pulsating semiconductor lasers can generate pulsating oscillations without any external modulations according to their unique device structures.³⁻⁶ Indeed, self-pulsating lasers are used for digital versatile disk (DVD) systems to reduce optical noises induced by optical feedback from disk surfaces. Although they are aimed to reduce optical feedback noises, noises are sometimes much enhanced under certain conditions of feedback configurations.

Though a large number of self-pulsating semiconductor lasers are currently used in optical data storage systems as light sources tolerant to optical feedback noises, their dynamic characteristics both for solitary oscillation and optical feedback have not sufficiently investigated. In optical data storage systems, feedback distance is usually a few centimeters. This length is short enough within a separation of successive pulses in self-pulsating lasers. The study for the dynamics in such systems is very important in a sense of practical applications of self-pulsating lasers. Even for such important characteristics, a little study for the dynamics induced by optical feedback has been reported.⁷ On the other hand, the dynamics of optical feedback from a distant reflector in self-pulsating lasers are also important for practical applications, such as the use of light sources in optical measurements. In this report, we conducted experimental study for the dynamics of self-pulsating lasers with optical feedback when an external reflector is located at several tens of centimeters to meter. We found various new dynamic characteristics of self-pulsating semiconductor lasers.

2. Experiments

Fig. 1 shows the experimental setup. The laser used in the experiment was a SONY SLD1134VL self-pulsating semiconductor laser of AlGaInP multi-quantum well (MQW) structure with oscillation wavelength of 655 nm and a maximum output power of 5 mW. The bias injection current of the laser was fixed by a stabilized current source driver and the temperature of the laser was controlled by an automatic temperature control circuit. The laser was developed for a light source of digital versatile disk systems. The emitted light from the laser is collimated and the part of the beam was fed back from an external reflector to the active area of the laser resonator or the substrate of the laser device. The feedback strength was adjusted by a neutral density (ND) filter inserted in the optical path. The external feedback fraction to the collimated lens in front of the laser facet was 12 % of the averaged intensity. But the actual amount of the

feedback to the active layer was much less than this fraction, since there were loss of light due to the coupling. The external cavity length was changed from ten centimeters to one and half meters.

The other beam divided by the beam splitter was fed into a high-speed photo-detector (NEW FOCUS 1537M-LF: bandwidth of 6.5 GHz) and an optical spectrum analyzer (ADVANTEST Q8344A, maximum resolution of 0.05 nm), and a wavelength meter (ADVANTEST QT8325, maximum resolution of 0.001 nm). The photo-current from the detector was fed into a fast digital oscilloscope (HP 54845A: bandwidth of 1.5 GHz) and a RF spectrum analyzer (HP 8595E: bandwidth of 6.5 GHz) to analyze chaotic time series and their Fourier components.

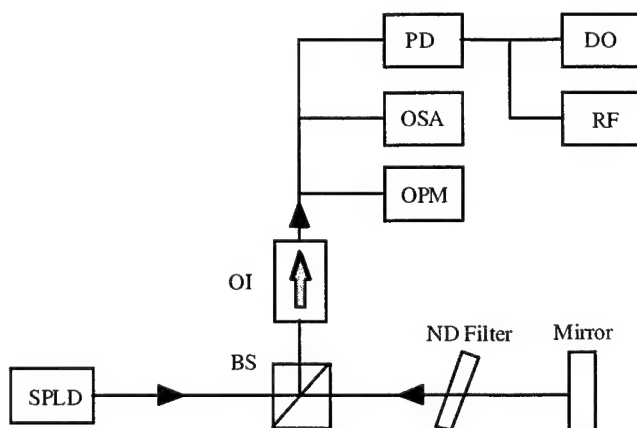


Fig. 1 Experimental setup. SPLD: self-pulsating laser, BS: beam splitter, OI: optical isolator, PD: photo -detector, OSA: optical spectrum analyzer, OPM: optical power meter, DO: digital oscilloscope, RF: radio frequency spectrum analyzer.

3. Results and discussion

3.1 L-I characteristics and dynamics of laser pulse

In this section, we present chaotic dynamics of laser outputs for the change of the bias injection current in self-pulsating semiconductor lasers with optical feedback. Fig. 2 shows experimental results of light-injection current (L-I) characteristics. The external mirror was positioned at $L=150$ cm. The laser threshold of the solitary oscillation was about 70 mA. Solid and long dashed lines are the results for solitary oscillation and optical feedback to the active layer, respectively. The L-I characteristics both for solitary oscillation and optical feedback to the active layer were almost the same. On the other hand, the output power is slightly larger than the L-I curve of the solitary oscillation when the light is fed back to the substrate. The region is a GaAs buffer layer in which carriers are generated by optical feedback. The laser shows stable and unstable operations depending on the bias injection current. The dynamic behaviors are divided into four regions for the bias injection current. In the injection current less than 74.5 mA but above the laser threshold (region I), the laser exhibited unstable oscillation. The region is clearly distinguished in the L-I characteristic curve. It is not easy to recognize but there is a kink around the bias injection current at 82.5 mA and the dynamics changed at the bias injection current. Above the injection current, the laser shows unstable oscillations (region III). The light output saturated for the injection current above 87.0 mA and the laser recovers its stability (region IV). We will see the details of the dynamics in the following.

Fig. 3 shows typical time series of pulsating oscillations for each region in Fig. 2 and the corresponding spectra are plotted in Fig. 4. In a lower bias injection level in region I, the laser shows unstable oscillations and pulse heights varied irregularly in time. For the solitary oscillation and feedback to the active layer, not only pulse heights but also pulse duration fluctuated, while jitter of pulses was very small as seen from the spectrum in Fig. 4(a). In region II, the laser shows regular pulsing even in the presence of optical feedback and we can see stabilized power spectra in Fig. 4(b). After the kink at the injection current of 82.5 mA, the laser shows unstable behaviors. At solitary oscillation in region III in Fig. 3(c), the laser behaved period-3 like oscillation as examined from the spectrum in Fig. 4(c) though it is not clear. On the other hand, the laser shows period-2 oscillation for optical feedback to the active layer and we can see two spectral components in the spectrum in Fig. 4(c). For optical feedback to the substrate, pulse heights of the laser oscillation fluctuate but the spectrum of the oscillation component still has a sharp peak. At saturated output power in region IV, the laser recovers its stability and shows regular pulsing states and clear spectral peaks are visible in Fig.

4(d). For the cases of the solitary oscillation and optical feedback to the active layer, peak frequencies of the power spectra are almost coincident with each other except in region III. However, the frequency of the laser pulsations for the feedback to the substrate differs from those of the other cases. This is related to a frequency-locking phenomenon discussed in later.

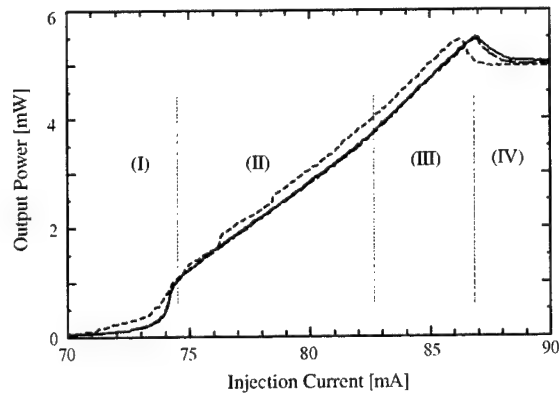


Fig. 2 L-I characteristics at $L=150$ cm. Solid line: solitary oscillation, long dashed line: optical feedback to active layer, dashed line: optical feedback to substrate.

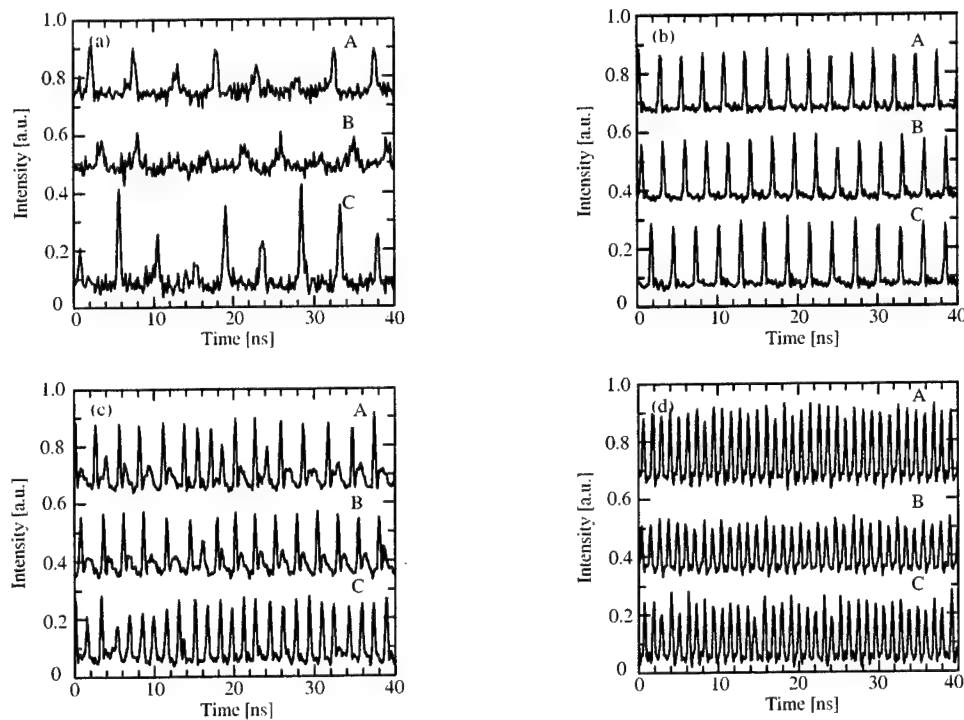


Fig. 3 Time series for four stable and unstable regions of the bias injection current. A: solitary oscillation, B: optical feedback to active layer, C: optical feedback to substrate. The injection currents are (a) 74.0 (region I), (b) 78.0 (region II), (c) 83.0 (region III), and (d) 88.0 mA (region IV).

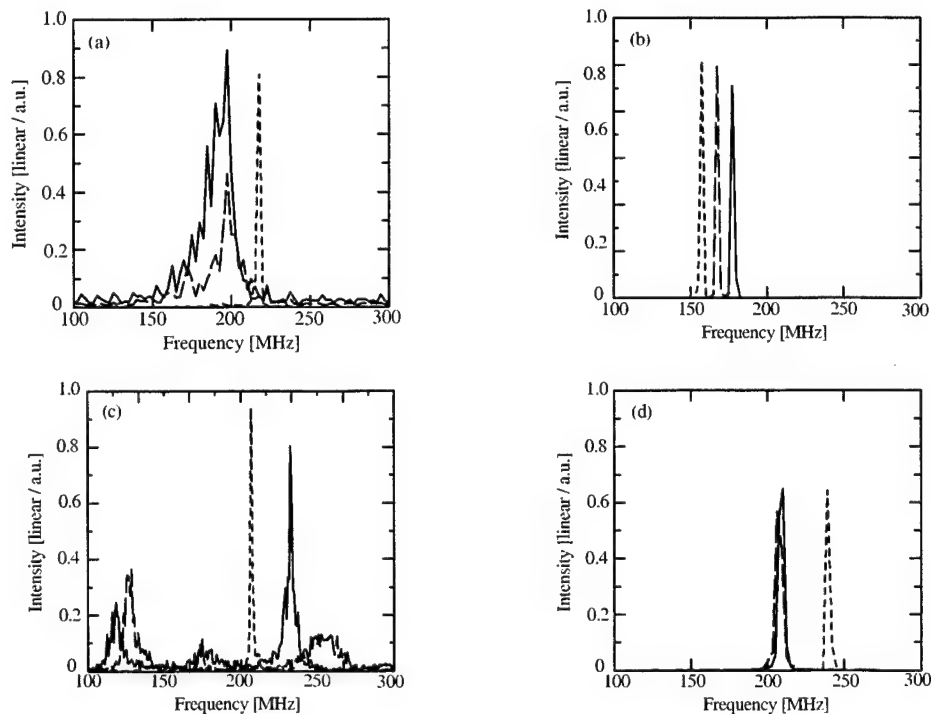


Fig. 4 Power spectra corresponding to Fig. 3. Solid line: solitary oscillation, long dashed line: feedback to active layer, dashed line: optical feedback to substrate.

3.2 Pulsing frequency and chaotic bifurcations

Fig. 5 is a plot of frequency of self-pulsating oscillations for the bias injection current. For the solitary oscillation (solid line), the oscillation frequency smoothly increases with the increase of the bias injection current. We can see kink around the bias injection current of 83 mA. For the case of optical feedback to the active layer (long dashed line), the frequency suddenly drops down to almost the half of the solitary state due to period-2 oscillation. Except for the region of this frequency drop, two cases showed the same trend of the change of frequency for the increase of the bias injection current. On the other hand, the change of the frequency for optical feedback to the substrate is completely different from two other cases. We can see frequency-locked states and stepwise frequency jumps for optical feedback to the substrate (dashed line). The jumps of the frequency occur periodically and the frequency of jumps is calculated to be 100 MHz. The frequency of jumps is exactly equal to a frequency calculated from the external cavity length of $L=150$ cm. Fig. 6 shows oscillation wavelength for the three cases with and without optical feedback. As a general trend, the oscillation wavelength increases with the increase of the bias injection current as expected. However, jumps of oscillation wavelength are visible corresponding to the frequency jumps for the case of optical feedback to the substrate. At higher bias injection current, we can see saturation of wavelength in accordance with saturated intensity.

We plot chaotic bifurcation diagrams of peak values of the laser output power for the change of the bias injection current in Fig. 7. Figs. 7(a), (b), and (c) are the diagrams for the solitary oscillation, optical feedback to the active layer, and optical feedback to the substrate, respectively. In region I, peak heights of the laser output fluctuate and the laser becomes chaotic oscillation. On the other hand, regular pulsing states are observed in region II. In region III, chaotic broadening of the oscillations are visible for all cases without and with optical feedback. However, chaotic states fully develop for the output powers at solitary laser oscillation in Fig. 7(a) and for optical feedback to the substrate in Fig. 7(c). Unstable oscillation in region III is also visible, but the state is very close to period-2 oscillation as we can see in Fig. 7(b). At saturated region IV of the laser output power, the laser again oscillate at regular pulsing state. In Fig. 7(c), some instabilities can be seen at positions of frequency jumps in Fig. 5.

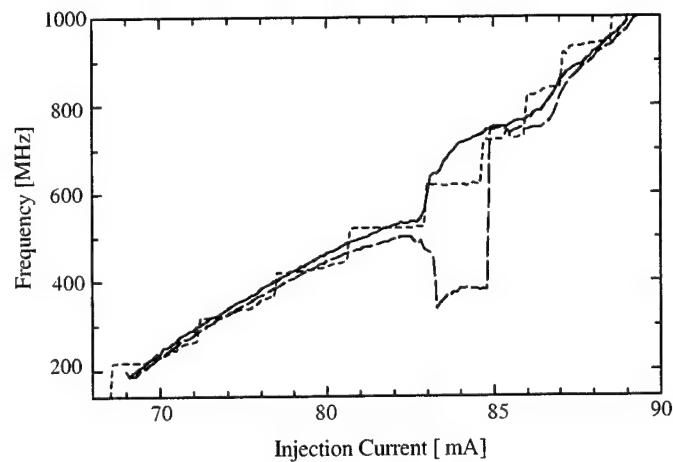


Fig. 5 Pulsing frequency at $L=150$ cm. Solid line: solitary oscillation, long dashed line: feedback to active layer, dashed line: optical feedback to substrate.

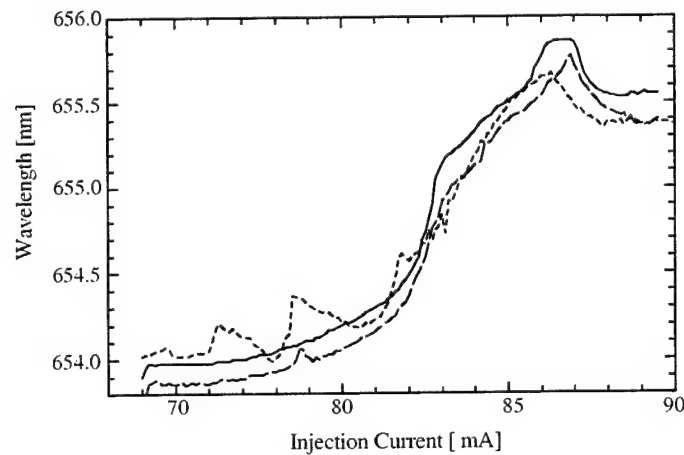


Fig. 6 Oscillation frequency corresponding to Fig. 5.

3.3 Frequency locking and dynamics for optical feedback to substrate

When the laser light once emitted from the active layer returns to the GaAs buffer layer in the substrate, we could observed frequency locked states of pulsations in the laser output power. We further investigated the dependence of the dynamics on the external cavity length. Fig. 8 is the result of pulsing frequency for different external mirror positions from $L=15$ to 75 cm. Solid line is the same result as already plotted in Fig. 5. Long dashed line is the result for the mirror position at $L=75$ cm. The calculated frequency of jumps is 200 MHz and is equal to the frequency corresponding to the external cavity length. Dashed line is the result for the position at $L=50$ cm and the frequency jump is read to be 300 MHz. Various dynamic features are observed as chaotic bifurcations for the change of the external mirror position as shown in Fig. 9. Chaotic bifurcations are strongly dependent on the external mirror position and the regions of stable and unstable oscillations also vary for the mirror position when the light is fed back into the GaAs buffer layer in the substrate. The origin of such variety of the dynamics is not clear at present and extensive experimental and theoretical studies are required to clarify such dynamic characteristics.

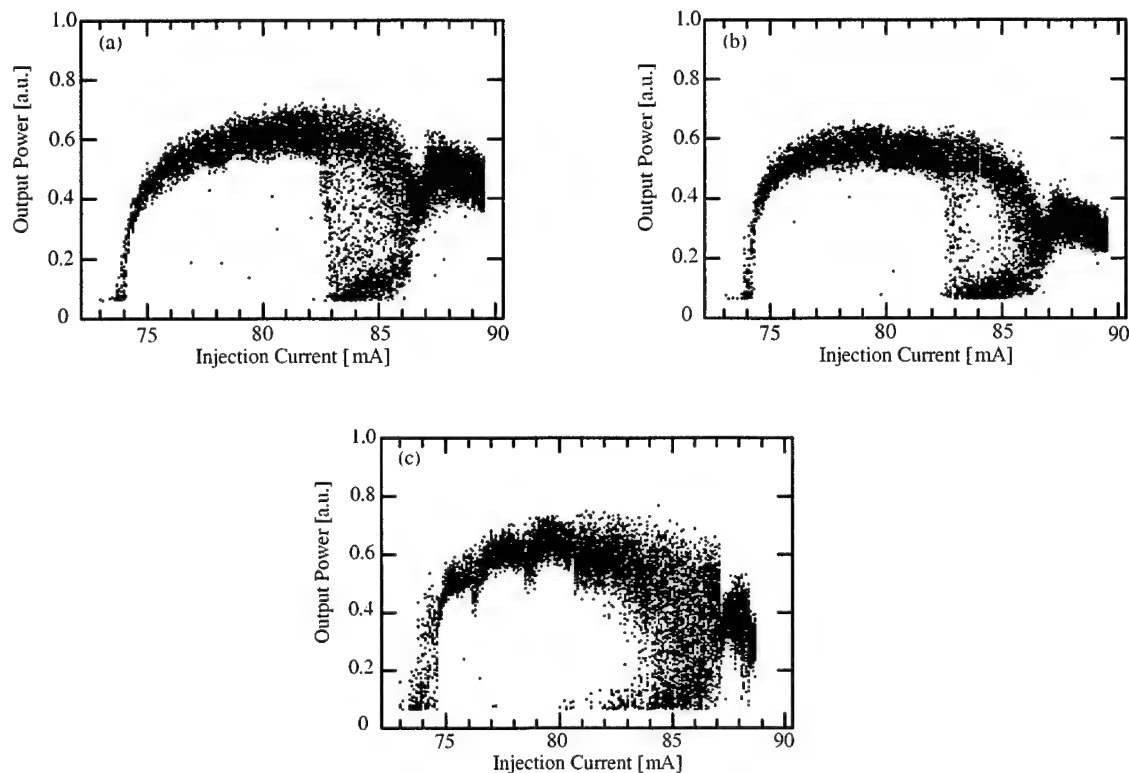


Fig. 7 Bifurcation diagrams at $L=150$ cm. (a) Solitary oscillation, (b) optical feedback to active layer, and (c) optical feedback to substrate.

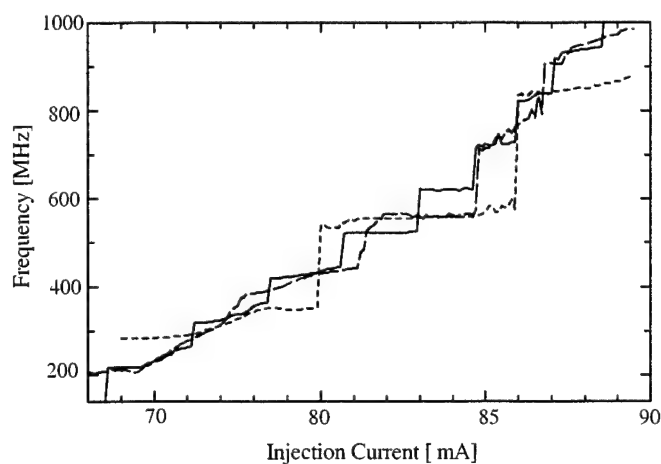


Fig. 8 Frequency locking and injection current dependence of pulsing frequency. Solid line: $L=150$ cm, long dashed line: $L=75$ cm, dashed line: $L=50$ cm.

4. Conclusion

We have experimentally examined dynamic characteristics of self-pulsating semiconductor lasers with optical feedback from a distant reflector. Even at solitary state, the laser showed stable and unstable oscillations depending on the bias

injection current. Four regions of unstable and stable oscillations have been identified. We have observed unstable chaotic oscillations for lower bias injection level and also the region of the bias injection well above the laser threshold. The dynamics for optical feedback to the active layer and also the GaAs buffer layer have investigated. Similar dependences of the dynamics on the bias injection current have been observed when optical feedback existed. But the laser showed period-2 oscillation in region III for optical feedback to the active layer, while it behaved chaotic oscillations at solitary mode. On the other hand, the laser showed rich variety of dynamics when the returned light was fed back into the GaAs buffer layer in the substrate. A typical feature of the feedback was a frequency-locking phenomenon of self-pulsation frequency. For the increase of the bias injection current, the pulsation frequency was locked for a certain range of the bias injection current and then jumped up at a certain current. The frequency of jumps was equal to that calculated from the cavity length of the external mirror. The origins of these phenomena are not fully clarified and further studies both for the experimental and theoretical research are required.

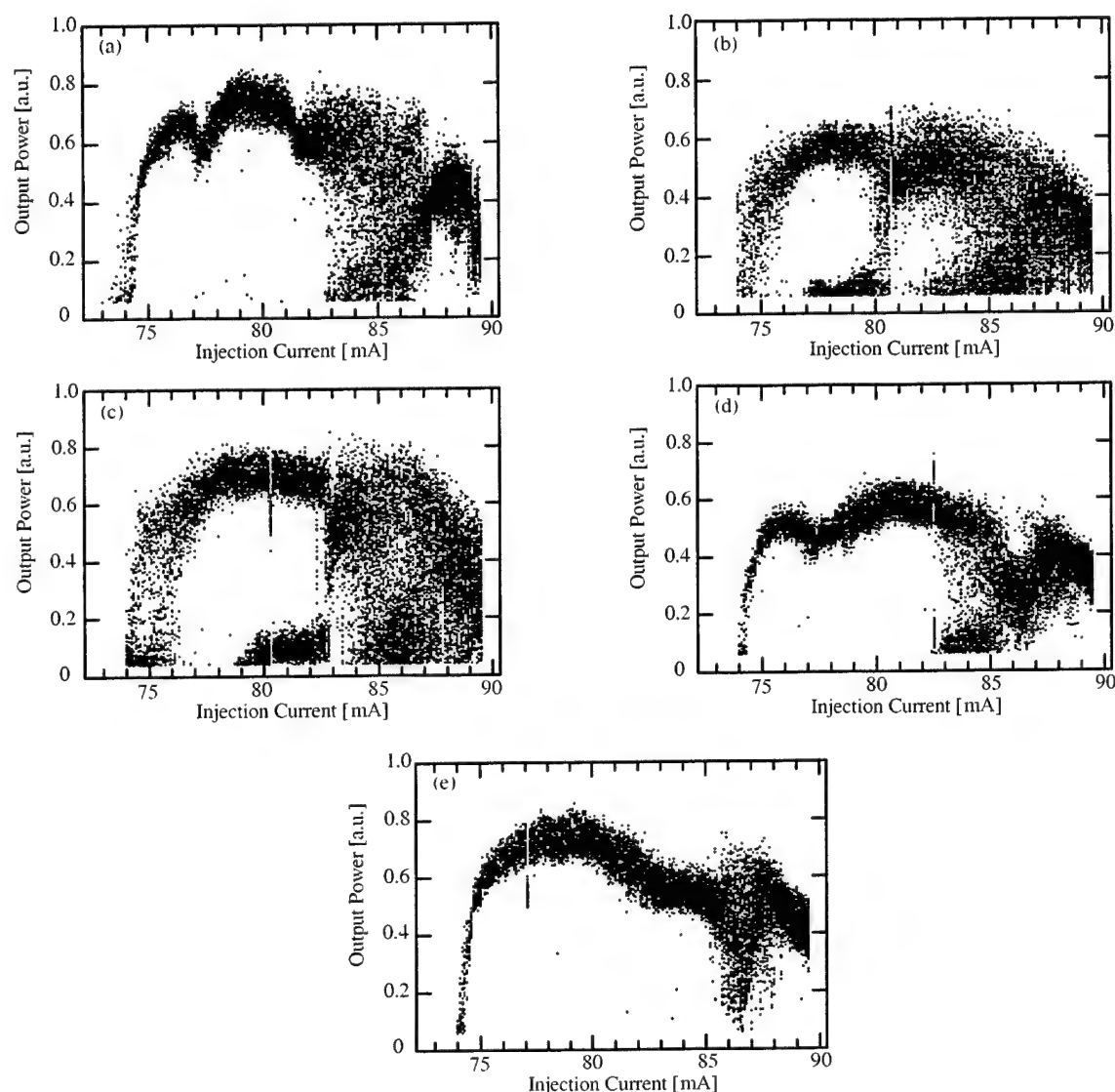


Fig. 9 Bifurcation diagrams for different external cavity lengths. The external cavity lengths are (a) $L=75$, (b) 50, (c) 40, (d) 30, and (e) 15 cm.

References

- [1] J. Ohtsubo, *Progress in Optics* **44**, Chapter 1, Ed. E. Wolf, (Elsevier Science B.V., Amsterdam, 2002).
- [2] G. H. M., van Tartwijk, and M. San Miguel, *IEEE J. Quantum. Electron.* **32**, 1191 (1996).
- [3] H. Adachi, S. Kamiyama, I. Kidoguchi, and T. Uenoyama, *IEEE Photon. Tech. Lett.* **7**, 1406 (1995).
- [4] A. Egan, M. Harley-Stead and P. Rees, S. Lynch, J. O'Gorman, and J. Hegarty, *IEEE Photon. Tech. Lett.* **8**, 758 (1996).
- [5] R. Mirasso, G. H. M. Van Tartwijk, E. Hernandez-Garcia, D. Lenstra, S. Lynch, P. Landais, P. Phelan, J. O'Gorman, M. San Miguel, and W. Elsaßer, *IEEE J. Quantum. Electron.* **35**, 764 (1999).
- [6] H. D. Summers, C. H. Molloy and P. M. Snowton, P. Rees, I. Pierce, and D. R. Jones, *IEEE J. Selected Topics Quantum Electron.* **5**, 745 (1999).
- [7] M. Yamada, Y. Ishikawa, S. Yamamura, M. Kidu, A. Kanamori, and Y. Aoki, *IEICE Trans. Electron.* **E82-C**, 2241 (1999).

J. Ohtsubo's e-mail address is tajohts@ipc.shizuoka.ac.jp.

High-power single-mode 1330 and 1550nm VCSELs bonded to silicon substrates

Virginia M. Robbins, Steven D. Lester, David Bour, Jeffrey N. Miller and Françoise Mertz

Agilent Technologies Laboratories, Communications and Optics Research Laboratory, Palo Alto, CA 94304

ABSTRACT

We demonstrate novel electrically driven 1330 and 1550 nm VCSELs using conventional InGaAsP active regions. The VCSELs employ two TiO₂/SiO₂ DBR mirrors and an InAlAs tunnel junction that converts electrons to holes, minimizing free carrier losses in the p-type material. The active layers are transferred onto Si wafers using wafer-scale Pd silicide bonding. We have obtained single-mode room-temperature output powers as high as 2.4mW at 1330nm and 2.7mW at 1550nm. At 80C we have obtained 0.6mW of single-mode power at 1330nm and over 1 mW at 1550nm. These are the highest power single-mode InP-based VCSELs reported in these wavelength ranges.

Keywords: Vertical Cavity Surface Emitting Lasers, InP-based material, wafer bonding

1. INTRODUCTION

Long wavelength VCSELs operating near 1300 or 1550 nm are attractive sources for fiber optic communication since they operate at low operating currents, produce beams that are easily coupled into fiber, and can be processed and tested using wafer-scale manufacturing. Although InP-based material is the conventional platform for fabricating edge-emitting laser diodes at these wavelengths, the performance of VCSELs has been hampered by the lack of a suitable monolithic DBR on InP substrates. Typically, InP-based DBRs based on InGaAsP/InP or AlInGaAs/AlInAs have a very small index contrast, ~ 0.2 . This means that large numbers of DBR pairs are required to achieve high reflectivity, and the stopbands of the mirrors are very narrow. This makes the manufacturing of long-wavelength VCSELs particularly challenging.

Several groups have demonstrated alternative mirror structures. The calculated reflectivity for a number of these structures is shown in Fig.1. AlGaAsSb DBRs can be grown epitaxially on InP but so far, MBE is the only material growth technology that has produced mirrors using this compound.¹ AlAs/GaAs DBRs have very attractive properties in terms of index contrast and thermal conductivity but these are not lattice-matched to InP. To combine an AlAs/GaAs DBR with an InGaAsP active region, it is necessary to resort to wafer bonding² or metamorphic growth.³

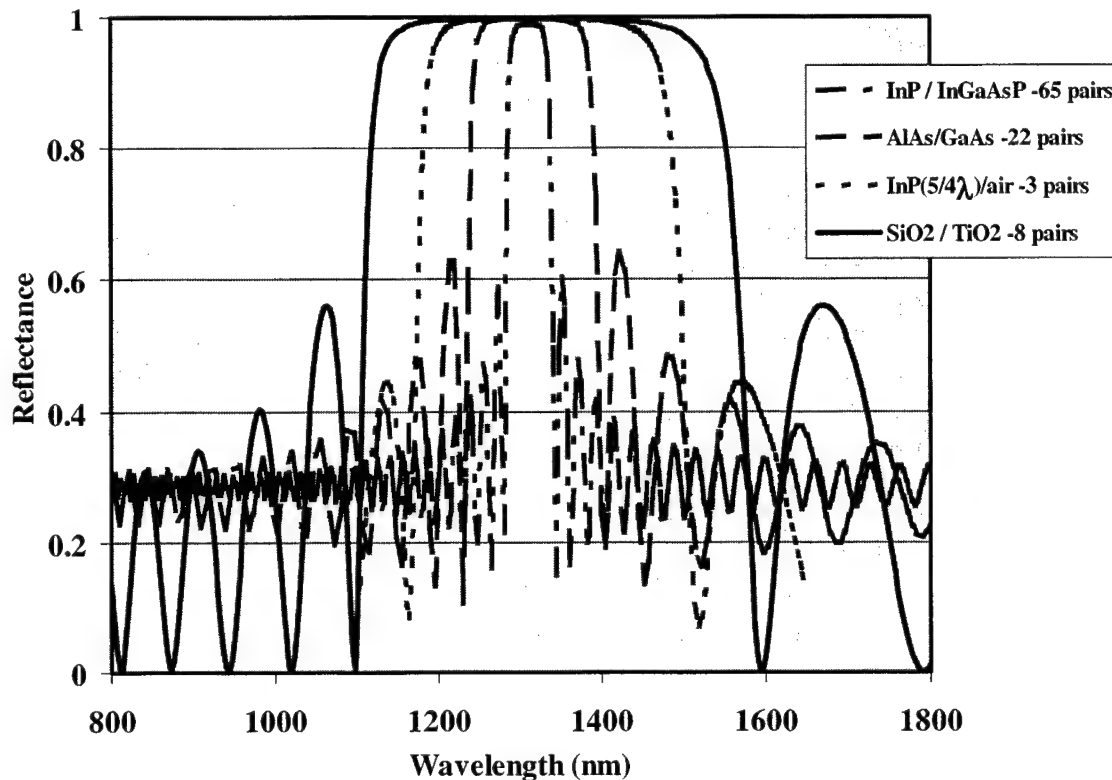


Fig.1 Mirror options for long wavelength VCSELs

The latter can only be used for the second mirror growth. VCSELs with monolithically grown InP/air mirrors were recently reported.⁴ These require sophisticated processing and a regrowth step to maintain structural integrity. Finally, a VCSEL structure with an AlO_x/Si metal bonded DBR on Si was reported⁵ but lasing was not reported. In this paper, we report on the design and performance of electrically driven 1330 and 1550nm VCSELs using a $\text{TiO}_2/\text{SiO}_2$ upper mirror and a $\text{TiO}_2/\text{SiO}_2/\text{Au}$ lower mirror bonded on a silicon substrate.

2. VCSEL FABRICATION

The InGaAsP active layer is grown on InP by MOCVD. It consists of either five or seven 80Å quantum wells (0.5% compression) separated by 60Å InGaAsP barriers (0.8% tension). These are surrounded by 200Å of lattice-matched InGaAsP with a bandgap $\sim 1.15 \mu\text{m}$. A tunnel junction to convert electrons to holes is grown after the active layer. It consists of an AlInAs p+ carbon-doped layer and an InP n+ selenium-doped layer. The tunnel junction is used so that free carrier loss from p-type material is minimized, and so that higher-mobility n-type material can be incorporated to spread the current. There is no bandedge absorption in either material at the VCSEL emission wavelength. The tunnel junction is placed at a first null (from the quantum wells) in the cavity standing wave. This minimizes the free-carrier loss in the heavily doped tunnel junction layers. Relatively thick InP layers are grown below the active layer and above

the tunnel junction to promote current spreading and heat flow. Overall, the semiconductor layers form an 8λ thick optical cavity.

Initially, an optically pumped VCSEL structure was used to optimize the optical cavity. A 980nm diode pump laser was used for excitation. Fig. 2a shows the reduction in the thermal impedance and the increase in the optical output power as the InP layer thickness is increased. As the thickness of the semiconductor portion of the cavity increased from 2λ to 8λ the thermal resistance was reduced by a factor of five. As a result the output power of the lasers increased by an order of magnitude. With further increases in cavity length, the lasers operated in multiple longitudinal modes. Based on these results an 8λ thick optical cavity was chosen for our device structure. It is also critical to optimize the quality of the mirror stacks, minimizing both scattering and absorption. Fig. 2b shows the improvement in output power as the mirror quality is improved. All of these structures have 8λ cavities and mirror stacks with the same calculated reflectivity. A multi-bounce reflectivity measurement showed that the initial mirrors had actual R-values $\sim 1\%$ below the ideal calculated value. Improvements in the materials and the deposition process resulted in measured reflectivity equal to the calculated value and a doubling of the maximum output power.

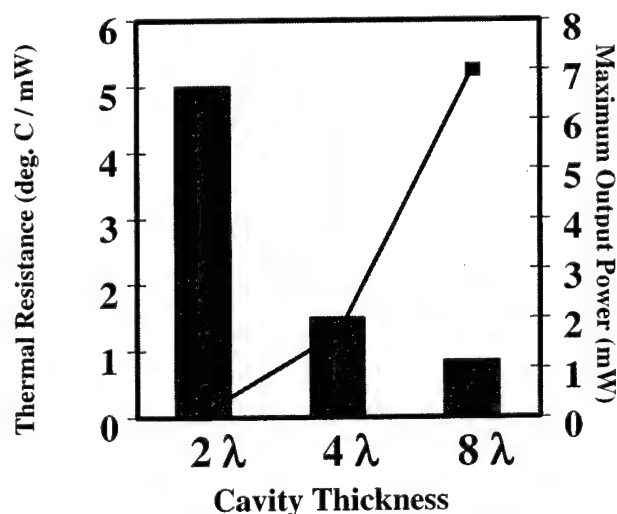


Fig. 2a Thermal effects of cavity thickness

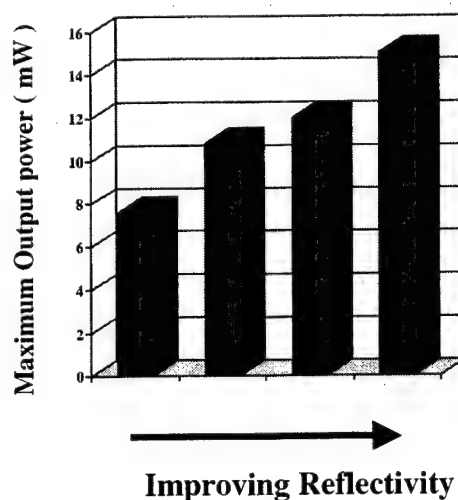


Fig. 2b Effect of reflectivity on output power

This optimized optical cavity was then incorporated into an electrically injected device structure. The process sequence used to fabricate the VCSELs is shown in Fig. 3. We first deposit a dielectric mirror onto the epitaxial layers consisting of $8\frac{1}{2}$ pairs of $\frac{1}{4}\lambda$ thick $\text{TiO}_2/\text{SiO}_2$ using ion-beam assisted sputtering. This is followed a gold layer that enhances the overall reflectivity.⁵ We calculate the reflectivity of this hybrid mirror to be greater than 99.99%. Next, Pt and Pd are deposited on top of the hybrid mirror. The Pd layer is used to form a metallic bond with a silicon wafer and the Pt prevents interdiffusion between the Pd and the Au portion of the mirror. The metallic bond to Si (to form palladium

silicide) is accomplished at 300C on full 2-inch wafers using a commercial wafer scale bonder in a process similar to that described by Tan, et al.⁶ The original InP substrate is then removed using HCl leaving the silicon as the host substrate, Fig. 3b.

Next a mesa is formed and the AlInAs side of the tunnel junction is undercut using a sulfuric acid based etch to create a current aperture, Fig. 3c. Finally, electrical contacts are made to the upper and lower n-InP layers and the output mirror consisting of 6, 7, or 8 pairs of SiO₂/TiO₂ is deposited. The completed device structure is shown in Fig. 3d.

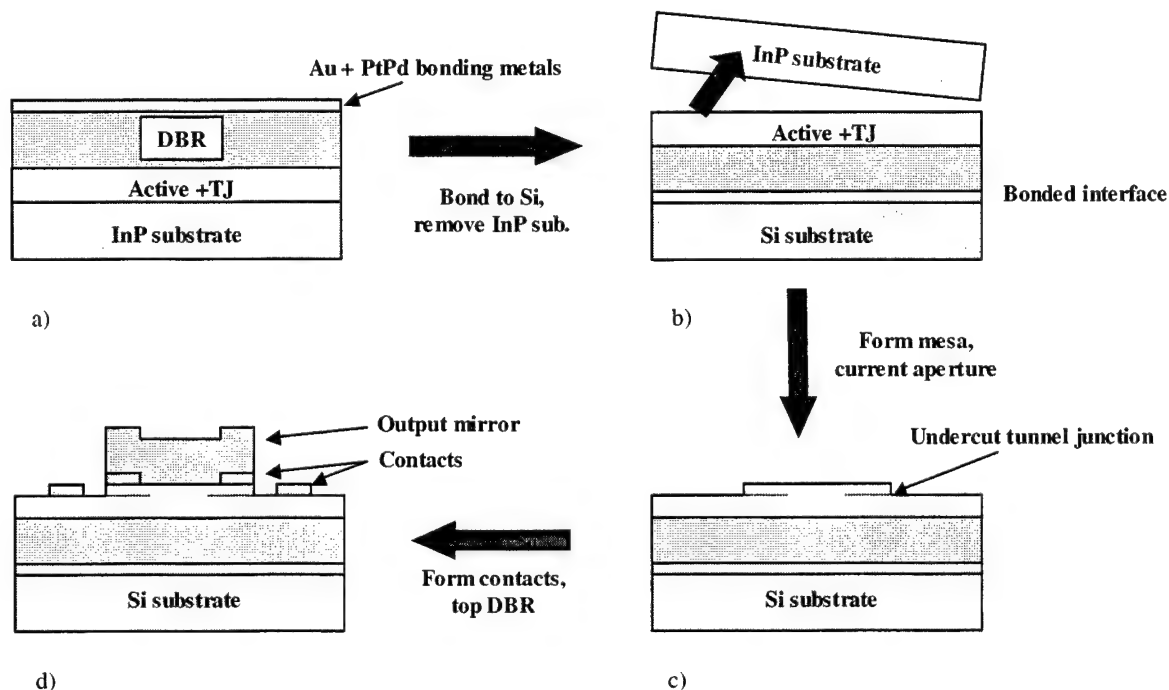


Fig. 3 Fabrication Process

3. DC PERFORMANCE OVER TEMPERATURE

The L-I-V characteristics of the VCSELs depend on the number of dielectric pairs used in the output mirror. Typically, the VCSELs can operate with output mirrors consisting of 6, 7, or 8 pairs, corresponding to reflectance values of 99.4, 99.7 and 99.9% respectively. Lower threshold current densities and higher operating temperatures are observed as the number of mirror pairs is increased. The differential quantum efficiency and overall output power are maximized with either 6 or 7 pairs.

The room-temperature L-I-V characteristics of single-mode VCSELs operating at 1330nm and 1550nm are shown in Figs. 4a,b for devices with 7 pairs in the output mirror. The 1330nm device has a threshold current of 0.69mA, a

differential quantum efficiency of 32.0%, and a maximum output power of 2.4mW. With 6 mirror pairs the threshold increases to 1.6mA and the differential quantum efficiency increases to 36.0% but there is no increase in maximum output power because thermal rollover occurs at a lower current. The 1550nm laser has a threshold current of 1.6mA, a differential quantum efficiency of 42.4%, and emits as much as 2.7mW. With six mirror pairs, the threshold increases to 3.3mA and the differential quantum efficiency increases to 56.5% but once again, there is no appreciable increase in the maximum output power. Lasers at both wavelengths remain single-mode with a side-mode suppression ratio of at least 30dB over the entire current range.

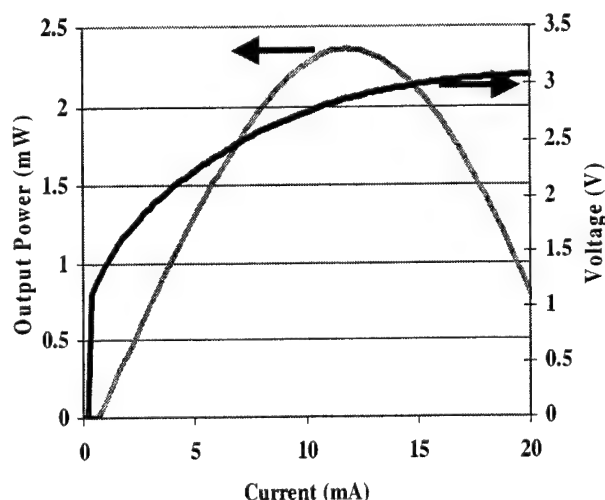


Fig. 4a Room temperature LIV at 1320nm

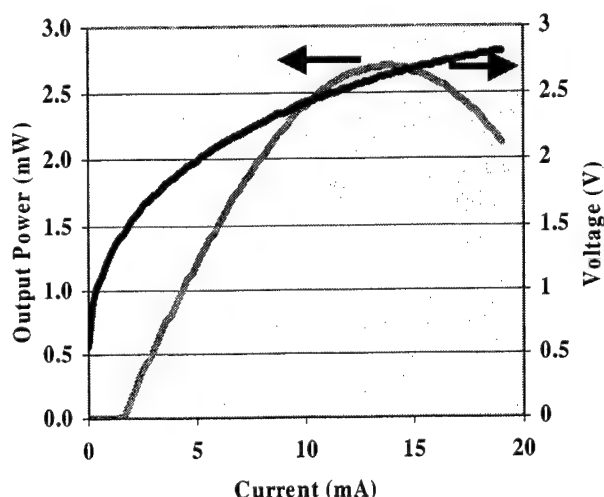


Fig. 4b Room temperature LIV at 1550nm

The voltage drop at the maximum output power is ~3V for each of the lasers. This voltage results from a combination of the tunnel junction, the active junction, the contact resistance and the lateral spreading resistance. A more recent design has an improved contact geometry and the voltage drop is reduced to ~1.8V at the maximum output power. The current aperture is approximately $7\mu\text{m} \times 7\mu\text{m}$ in single-mode devices. The thermal impedance of the electrically injected single-mode devices averages ~1550 C/W for both 1300nm and 1550nm devices. The thermal impedance does decrease with increasing aperture size but the devices become multimode. A large multimode device with a $16\mu\text{m} \times 16\mu\text{m}$ aperture has a thermal impedance of ~860 C/W.

These output powers and slope efficiencies are the highest yet reported for single-mode InP-based VCSELs in these wavelength ranges. We attribute the improved characteristics to the long-cavity design of the epitaxial layers that results in low thermal impedance, and to the low-loss dielectric DBRs used for both mirrors.

The maximum single-mode output power as a function of stage temperature is shown in Fig. 5. The 1300nm device emits as much as 2.6mW at 10C, diminishing to 0.6mW at 80C. Based on measurements of broad-area edge emitting lasers with similar active regions, we believe the performance at elevated temperatures of these devices results from insufficient carrier confinement. The 1550nm VCSELs perform better over temperature, emitting 2.95mW at 10C and over 1mW at 80C.

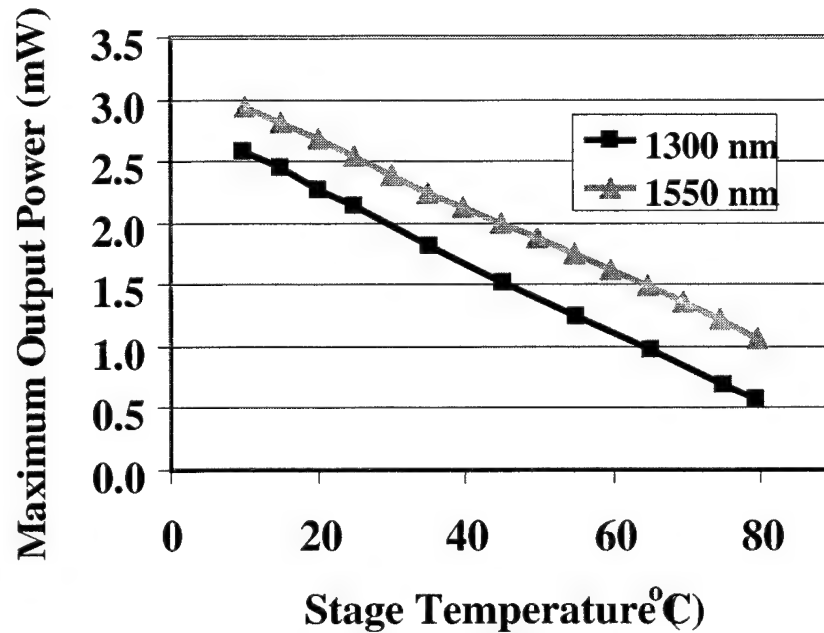


Fig. 5 Maximum output power as the stage temperature is varied

Figure 6a shows a typical output spectrum from a VCSEL operating at 1550nm. Laser emission from higher-order transverse modes can be seen in the series of spectral lines at shorter wavelengths than the fundamental peak. For

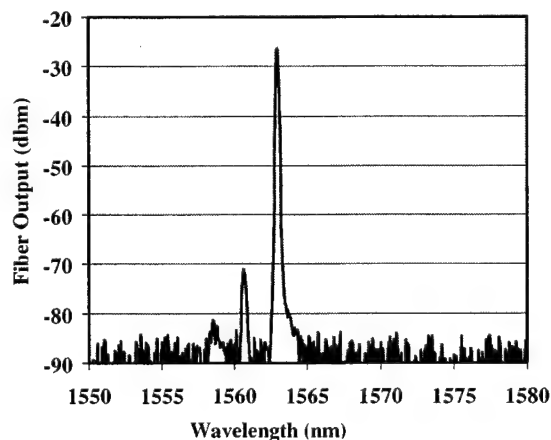


Fig. 6a Typical spectra of single-mode VCSEL

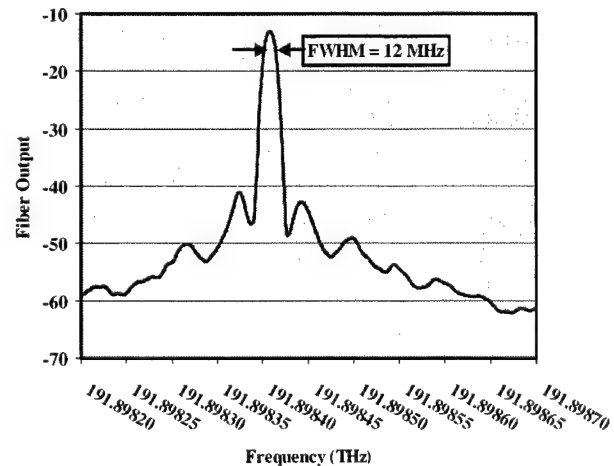


Fig. 6b High-resolution spectra of single-mode VCSEL

devices with aperture diameters less than $\sim 6\text{-}7\text{ }\mu\text{m}$, such as those reported here, these higher order peaks remain at least 30dB down from the fundamental line. The Fig. 6b shows a high-resolution scan of the fundamental mode. This measurement was taken with a high-resolution spectrometer that uses a heterodyne detection technique. The FWHM of the VCSEL is measured to be 12MHz. This linewidth is comparable to previous linewidth measurements taken on long-wavelength VCSELs with significantly lower output power.⁷

4. MODULATION CHARACTERISTICS

The results presented so far were obtained using a device designed for DC operation. A large parasitic capacitance limits the frequency response of these lasers. We recently processed devices using a high-speed design more suitable for modulation.

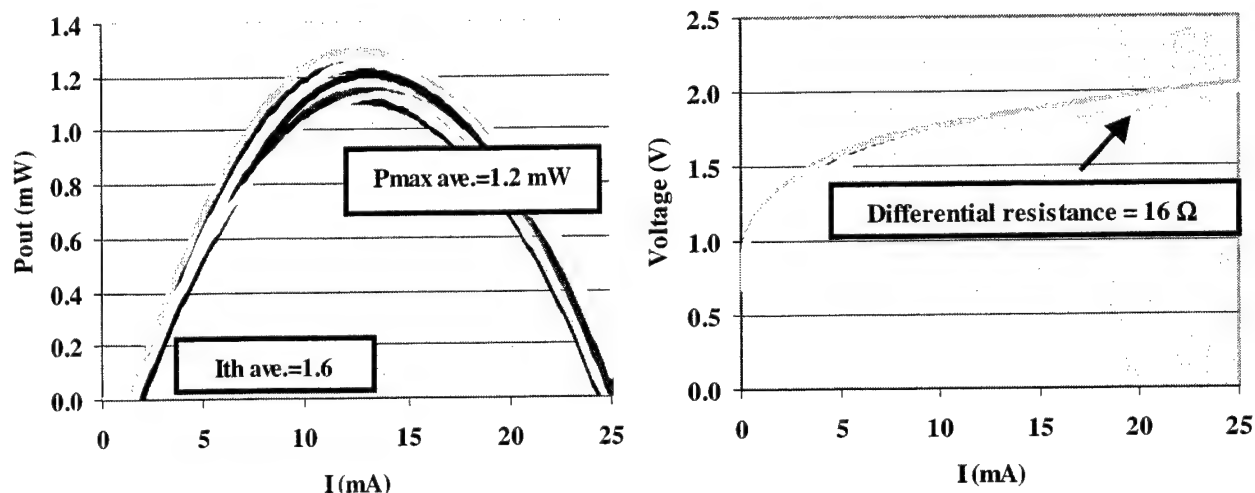


Fig. 7 a) L-I and b) I-V curves from array of 12 single-mode devices

The DC characteristics of 12 devices using the high-speed design are shown in Fig.7 above. The output mirror has seven mirror pairs. The average threshold current is 1.6mA, the average maximum room temperature output power is 1.2mW, and the differential quantum efficiency is 18%. These devices lase at 1305nm. The optical power emitted from these devices is less than that of the DC devices due to higher optical losses resulting from some processing issues. Their thermal impedance is 1510 C/W, comparable to our previous process so the performance is not compromised by thermal issues. The voltage drop at the peak output power is $\sim 1.8\text{V}$, a notable improvement over the previous design resulting from improved contact geometry.

Given that our devices have a long cavity and consequently a relatively large mode volume, modulation speed is a concern. The small-signal frequency response of the 1300nm devices was measured to determine the relaxation

oscillation frequency. The relaxation oscillation frequency is expected to be proportional to the square root of the drive current. This plot is shown in Fig. 8 for two devices. The behavior is linear for lower currents but is limited by thermal rollover at higher currents. For comparison to the high-speed design, we measured a $12\mu\text{m} \times 12\mu\text{m}$, multi-mode device fabricated using the DC design. The large area, DC device has a maximum relaxation oscillation frequency of 3.1 GHz and the high-speed, single-mode device has a maximum at 3.3GHz. However, it is possible to drive the large device to $\sim 15\times$ threshold before rollover while the smaller device is limited to $\sim 7\times$ threshold. A single-mode device in the DC design also did not rollover until $\sim 15\times$ threshold. When the processing of the high-speed structure is optimized and the devices can be run over a comparable current range, it should be possible to push the maximum f_R beyond 4 GHz. Significantly higher frequency performance will require further improvements to the device structure.

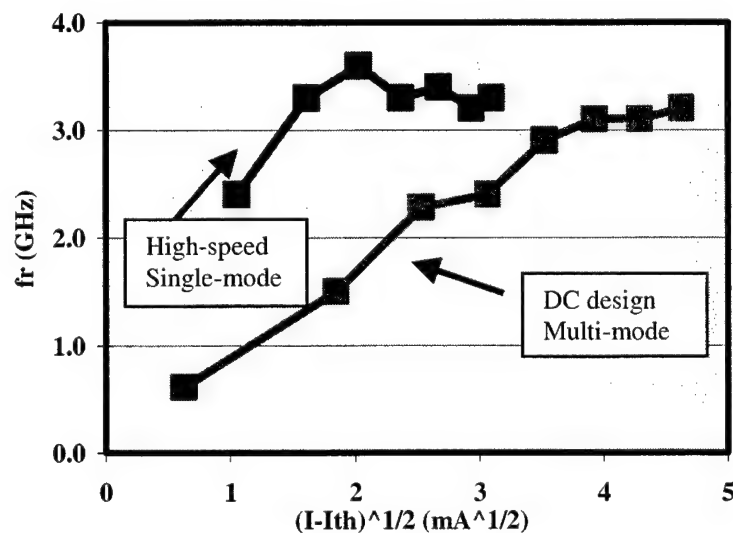


Fig. 8 Relaxation oscillation frequency as a function of the square of the current above threshold for both multi-mode and single-mode VCSELs

The large-signal modulation characteristics of the single-mode, high-speed device structure were also measured. The eye diagrams are shown in Fig. 9. The pattern degrades with increasing data rate but the eyes remain open up to 7Gbit/sec with an extinction ratio of 6dB.

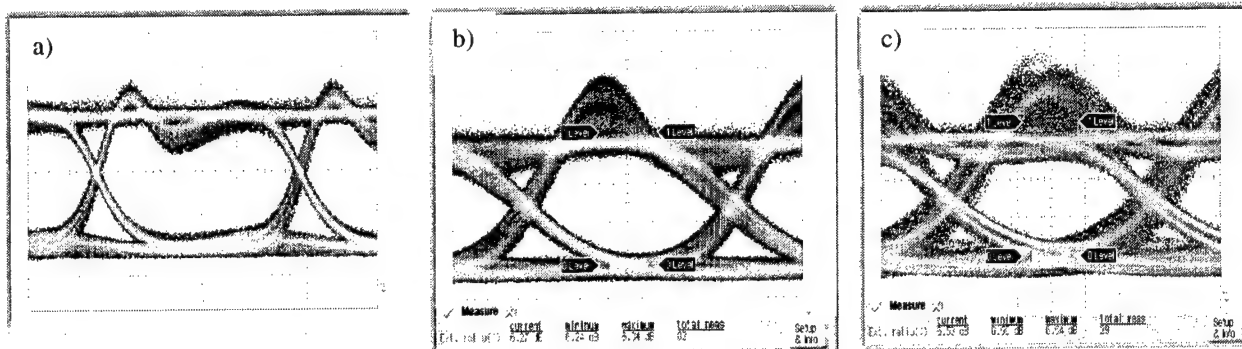


Fig. 9 Eye diagrams at a) 2.5 Gbit/sec. b) 5 Gbit/sec. and c) 7 Gbit/sec.

5. CONCLUSIONS

Long wavelength VCSELS at both 1300nm and 1550nm with high output powers have been fabricated in the traditional InGaAsP/InP material system using a process where the epitaxial layers are transferred to a Si substrate by means of palladium silicide bonding. Using a long laser cavity to facilitate heat transfer away from the active region and low loss dielectric mirrors, record dc output powers have been attained. Even with the large optical mode volume associated with the long cavity, modulation up to 7Gbit/sec can be achieved. Further optimization of the process and improvements in the thermal performance will lead to better performance at higher data rates.

5. REFERENCES

1. O. Blum, M. J. Hafich, J. F. Klem, K. L. Lear, and S. N. G. Chu, *Appl. Phys. Lett.* vol. 67, no. 22, pp. 3233-3235, 27 Nov 1995.
2. J. J. Dudley, D. I. Babic, R. P. Marin, L. Yang, B. I. Millers, R. J. Ram, T. E. Reynolds, E. L. Hu, and J. E. Bowers, *Appl. Phys. Lett.* vol. 64, no. 12, pp. 1463-1465, 21 Mar.1994.
3. J. Boucart, C. Starck, F. Gaborit, A. Plais, N. Bouche, E. Derouin, J. C. Remy, J. Bonnet-Gamard, L. Goldstein, C. Fortin, D. Carpentier, P. Salte, F. Brillouet, and J. Jacquet, *IEEE Jour of Selected Topics in Quantum Electronics*, vol. 5, no. 3, pp. 520-529, May/June 1999.
4. C.-K. Lin, D.P. Bour, J.Zhu, W.H. Perez, M.H. Leary, A. Tandon, S.W. Corzine, M.R.T. Tan, *Semiconductor Laser Conference, 2002. IEEE 18th International* , pp. 145-146, 29 Sept.-3 Oct. 2002.
5. H.C. Lin, K.L. Chang, K.C. Hsieh, K.Y. Cheng, and W.H. Wang, *Journal of Applied Physics*, vol. 92, no.7, pp 4132-4134, 1 Oct. 2002.
6. I.-H. Tan, C. Reaves, A.L. Holmes, Jr., E.L. Hu, J.E. Bowers, and S. DenBaars, *Electronics Letters*, vol. 31, no. 7, pp. 588-589, 30 March 1995.
7. P. Signoret, F. Marin, S. Viciani, G. Belleville, M. Myara, J.P. Turrenc, B. Orsal, A.Plais, F. Gaborit, and J. Jacquet, *IEEE Photonics Tech. Letters*, vol.13, no. 4, pp. 269-271, April 2001.

Design and Optimization of High-Performance 1.3 μm VCSELs

Joachim Piprek,^{*} Manish Mehta, and Vijay Jayaraman

Electrical and Computer Engineering Dept., University of California, Santa Barbara, CA 93106

ABSTRACT

This paper discusses the design and the internal device physics of novel high-performance vertical-cavity surface-emitting lasers (VCSELs) emitting at 1.32 μm wavelength. Our VCSEL design features intra-cavity ring contacts, strain-compensated AlGaInAs quantum wells, and an AlInAs/InP tunnel junction. The tunnel junction is laterally confined forming an aperture for current injection and wave guiding. Undoped AlGaAs/GaAs mirrors are bonded on both sides to the InP-based active region. These devices have recently demonstrated continuous-wave (CW) lasing at stage temperatures up to 134°C, the highest temperature reported thus far for any long-wavelength VCSEL. In order to increase the single mode output power at high temperatures, we simulate, analyze, and optimize our VCSEL using advanced numerical software tools. The two-dimensional model self-consistently combines electrical, optical, thermal and gain calculations. It gives good agreement with measurements after careful calibration of material parameters. Design optimization promises single mode output power of 2mW in CW operation at 80°C ambient temperature.

Keywords: long-wavelength vertical-cavity surface-emitting laser diode, VCSEL, tunnel junction, wafer bonding, numerical simulation

1. INTRODUCTION

Long-wavelength vertical-cavity surface-emitting lasers (VCSELs) are desired low-cost light sources for applications in fiberoptic communication. In contrast to the rapid development of GaAs-based VCSELs emitting at shorter wavelengths, the performance of InP-based long-wavelength devices is severely limited by disadvantageous material properties. With the lower bandgap of the InGaAsP active region, Auger recombination enhances non-radiative losses. With lower photon energy, free-carrier and intervalence band absorption (IVBA) lead to enhanced optical losses. Native InGaAsP/InP distributed Bragg reflectors (DBRs) only allow for a small variation of the refractive index that is about half the variation possible in AlGaAs. To obtain high DBR reflectances, a large number of mirror layers has to be grown causing significant diffraction losses. InGaAsP also exhibits low thermal conductivity due to disorder scattering of phonons. Thus, thick InGaAsP/InP DBRs block the thermal flux to the stage and lead to a strong increase of the active region temperature in continuous-wave (CW) operation. Therefore, several alternative material and design concepts for 1.3 μm VCSELs have been developed, including GaAs-based and hybrid approaches.

A main challenge with long-wavelength VCSELs is the *simultaneous* demonstration of high-temperature, high-speed, and high-power fundamental mode lasing. In order to achieve this goal, several design trade-offs need to be balanced carefully. For instance, large current apertures and thick InP cavity layers are advantageous for high-power and high-temperature operation, respectively. However, single mode lasing requires small apertures and high-speed modulation requires thin vertical cavities. Finding the optimum design by experimental methods is expensive and time-consuming. We here employ physics-based self-consistent VCSEL simulation software in order to analyze and optimize the internal device physics.¹ Carrier transport is simulated using a finite-element drift-diffusion model. The heat flux equation is included to address self-heating effects. Gain calculations are based on 4x4 kp bandstructure computations for the strained quantum wells. The transmission matrix method is employed for optical simulation in order to obtain the vertical optical intensity profile. The lateral optical modes are given by Bessel functions which are adjusted to measured VCSEL near fields. Further details of the model can be found elsewhere.² Material parameters are carefully calibrated in the simulation in order to achieve good agreement with the measurements.

^{*} Corresponding author, e-mail: piprek@ieee.org

2. VCSEL DESIGN

Our device design follows the hybrid approach by joining highly reflective GaAs-based mirrors and high-gain InP-based active layers in InP/GaAs wafer bonded VCSELs (Fig. 1, Tab. 1). Compared to our previous design of wafer-bonded 1.55 μm VCSELs³, this design of 1.3 μm VCSELs includes three main new features:

- (1) Strained AlGaInAs quantum wells (QWs) offering a larger conduction band offset than InGaAsP QWs which is essential to reduce electron leakage at high temperatures.
- (2) Intra-cavity contacts feed the current directly into highly conductive n-InP layers, without passing wafer-bonded interfaces, thereby reducing reliability risks.
- (3) A buried tunnel junction is located above the MQW region (Fig. 2). This junction has multiple advantages in our VCSEL, it reduces the intervalence-band absorption related to p-doping, it allows for lower threshold bias due to higher carrier mobility in n-InP, and it provides lateral electrical and optical confinement by selective etching.

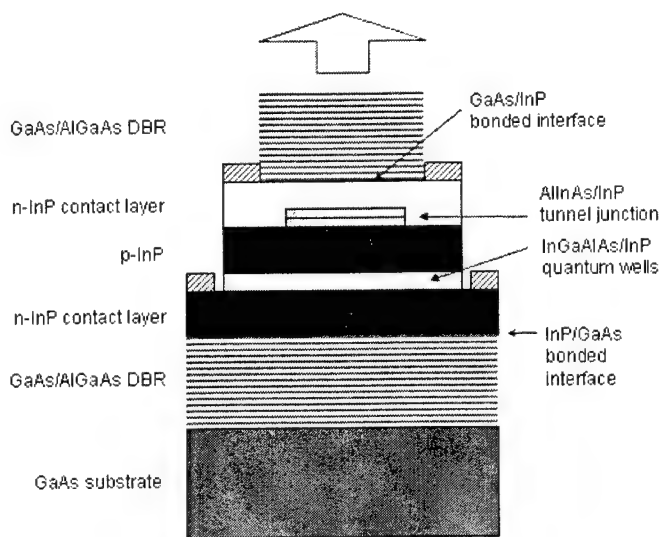


Fig. 1: Schematic structure of our vertical cavity laser.

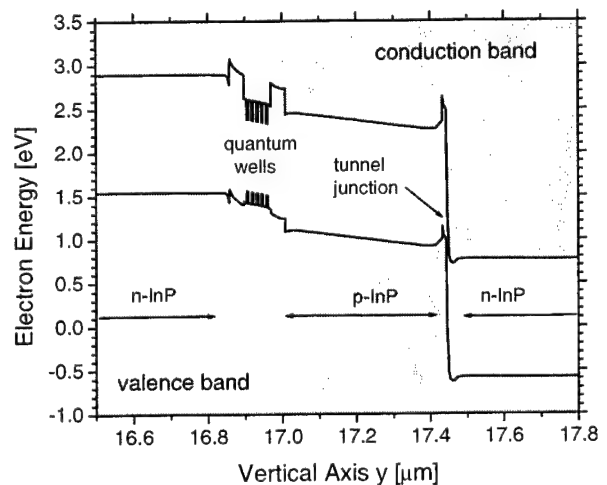


Fig. 2: Energy band diagram of the InP-based active region.

We have studied different design approaches for the lateral confinement. Our first device generation combined a tunnel junction with the commonly used lateral oxidation layer within the top DBR.⁴ However, the performance was mainly limited by lateral current leakage due to the high carrier (electron) mobility between aperture and tunnel junction. We therefore explored the lateral under etching of the MQW active region which promises better current confinement.⁵ The performance of this second device generation was poor due to misalignment of etched aperture and top DBR pillar. The third alternative investigated was patterned wafer bonding onto disk-shaped etched tunnel junctions.⁶ This approach allows for precise control of the aperture size which is not possible with lateral oxidation or etching. In order to accommodate intra-cavity contacts, our final design covers the etched tunnel junction by a re-grown n-InP contact layer before wafer bonding (Fig. 1).⁷ The etched tunnel junction introduces a step of about 30 nm in the top surface of the re-grown contact layer. This surface is sufficiently planar to permit wafer bonding of the top AlGaAs/GaAs mirror.

3. EXPERIMENTAL RESULTS

We here discuss experimental results for three VCSELs with different tunnel junction aperture size and different gain-mode offset.^{8,9} This offset is illustrated in Fig. 3 and it is a crucial VCSEL design parameter in order to achieve high-temperature operation. With increasing temperature, the gain spectrum moves to longer wavelength at a faster rate than

the wavelength of the lasing mode. With negative gain-mode offset, as shown in Fig. 3, the modal gain increases with higher temperature. Larger gain – mode offset allows for lasing at higher temperatures. However, larger offset also reduces the available gain at room temperature and the maximum output power. Thus, careful tuning of the gain – mode offset is required for optimum performance (see Sec. 5).

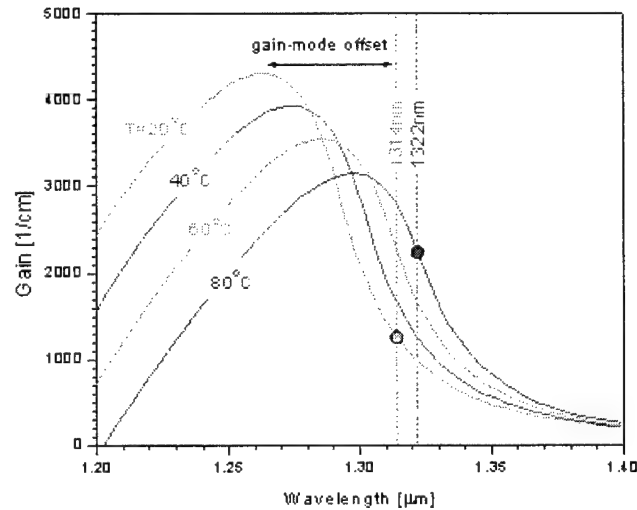


Fig. 3 Calculated gain spectra at different MQW temperatures (constant carrier density). The dashed vertical lines give the VCSEL emission wavelength at 20°C and 80°C, respectively, and the dots indicate the actual gain of the lasing mode.

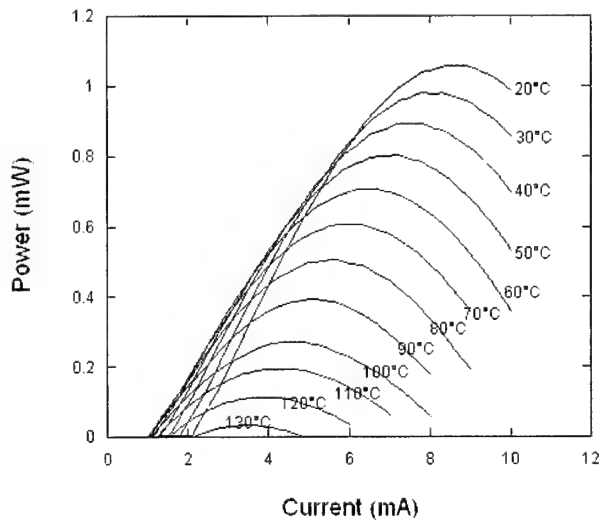


Fig. 4: Measured light-current characteristics in continuous-wave (CW) operation at different stage temperatures (8 μm aperture, 66 nm offset).

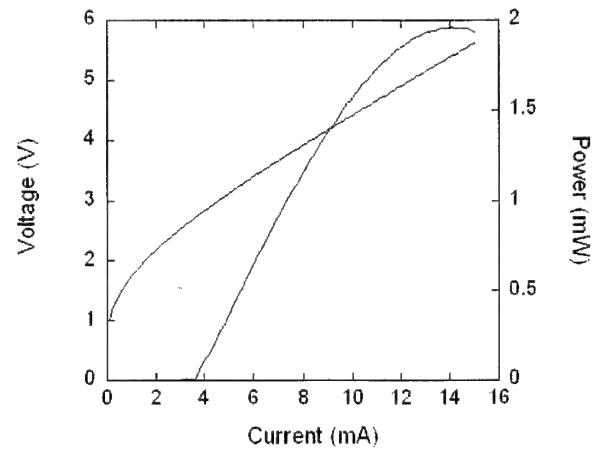


Fig. 5: CW light-current and current-voltage characteristics measured at room temperature (12 μm aperture, 51 nm offset).

All devices in this section employ 5 quantum wells, 25 top DBR periods and 31 bottom DBR periods. The exact position of the gain peak wavelength is unknown, however, it is close to the peak of the measured photoluminescence (PL) spectrum, which is used in the following to determine an offset parameter. Figure 4 gives light-current (LI) characteristics for 66 nm PL – mode offset and 8 micron aperture. This large offset results in lasing up to a maximum stage temperature of 134°C, the highest temperature ever achieved with any long-wavelength VCSEL. For this device, the maximum output power at room temperature is slightly above 1 mW.

Figure 5 gives the LI and current-voltage curve for a VCSEL with 12 micron aperture and with 51 nm PL - mode offset. Due to the larger spot size and the smaller offset, an enhanced differential efficiency of 30% and a larger output power of almost 2mW is achieved at room temperature. The threshold voltage of 2.7 V and the differential resistance of 245 Ω are relatively high. The maximum CW operating temperature of this device is 100°C. The larger aperture leads to multimode operation at higher temperatures. 66°C fundamental mode operation with almost 1 mW output power is observed with our third VCSEL that combines an 8 micron aperture with 51 nm PL - mode offset (Fig. 6). This device operates up to 123°C stage temperature.

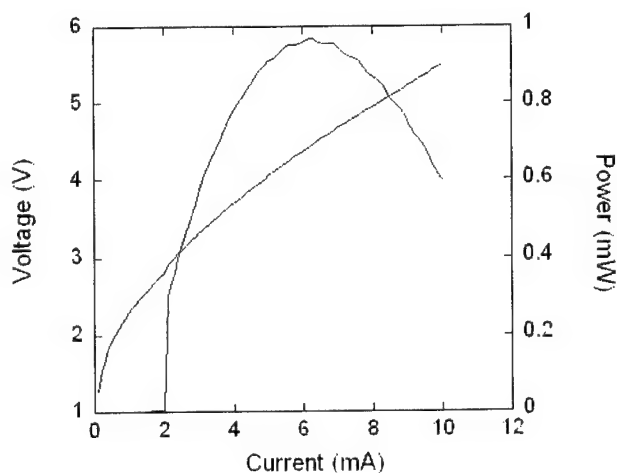


Fig. 6a: CW light-current and current-voltage characteristics measured at 66°C (8 μ m aperture, 51 nm offset).

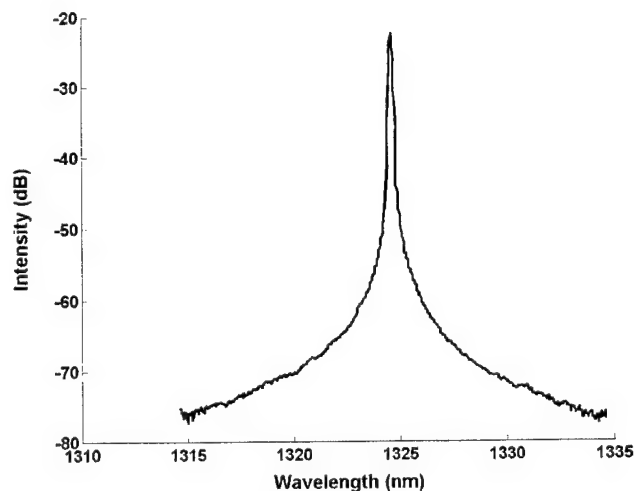


Fig. 6b: Modal spectrum at 66°C (8 μ m aperture, 51 nm offset).

4. SIMULATION AND ANALYSIS

In this section, we use advanced numerical simulation software¹ in order to analyze the internal physics and the performance limits of our VCSELs. The device model combines electrical, optical, thermal, and gain calculations self-consistently.² Such complex models include a large number of material parameters which need to be calibrated carefully for realistic simulation results. Table 1 lists key parameters for all the epitaxial layers of our VCSEL. The parameter calibration process is described in the following and it leads to good agreement between simulations and measurements as shown in Figs. 7 and 8. All measurements are for the same VCSEL with 8 μ m aperture. Nearfield measurements show a weak optical confinement with a fundamental mode diameter of about 13 μ m which is adopted in the following.

The peak of the calculated spontaneous emission spectrum coincides with the measured PL peak (Fig. 7) when quantum well bandgap renormalization is considered with

$$\Delta E_g = \xi \left(\frac{n + p}{2} \right)^{1/3} \quad (1)$$

and $\xi = -10^{-10}$ eV/m (n and p are respectively the densities of electrons and holes). Using a Lorentz broadening function with 50 fs scattering time gives good agreement with the important long-wavelength side of the spectrum (cf. Fig. 3). The short-wavelength side is not matched very well, i.e., LI simulation beyond the power roll-off is less reliable (cf. Fig. 8). The measured PL peak shifts at a rate of 0.45 nm/K with increasing temperature. This translates into a thermal bandgap shift of 0.334 meV/K, which is adopted for all layers in the simulation.

Parameter	d	N	μ	n	α	κ
Unit	μm	cm^{-3}	cm^2/Vs		cm^{-1}	$\text{W}/\text{cm K}$
i-Al _{0.92} Ga _{0.08} As (DBR, 27x)	0.111	nid	-	2.946	0.0	0.22
i-GaAs (DBR, 27x)	0.096	nid	-	3.411	0.0	0.22
n-InP (spacer, contact)	0.388	$5 \cdot 10^{17}$	2600	3.22	1.0	0.68
n-InP (tunnel junction)	0.020	$1.5 \cdot 10^{19}$	1100	3.22	30	0.68
p-In _{0.52} Al _{0.48} As (tun. junct.)	0.010	$1.5 \cdot 10^{20}$	10	3.24	1950	0.05
p-InP (spacer)	0.4325	$2 \cdot 10^{17}$	100	3.22	2.6	0.68
i-In _{0.52} Al _{0.48} As (stopper)	0.0382	nid	p:50	3.24	0.0	0.05
In _{0.68} Ga _{0.175} Al _{0.145} As (QW)	0.0044	nid	50	3.49	$\alpha(\text{n,p})$	0.05
In _{0.44} Ga _{0.326} Al _{0.234} As (bar.)	0.0084	nid	50	3.49	$\alpha(\text{n,p})$	0.05
i-In _{0.52} Al _{0.48} As (stopper)	0.0382	nid	n:4800	3.24	0.0	0.05
n-InP (spacer, contact)	0.4325	$1.2 \cdot 10^{18}$	2100	3.22	2.4	0.68
i-GaAs (DBR, 31x)	0.096	nid	-	3.411	0.0	0.22
i-Al _{0.92} Ga _{0.08} As (DBR, 31x)	0.111	nid	-	2.946	0.0	0.22
i-GaAs (substrate)	300	nid	-	3.411	0.0	0.44

Tab. 1: Epitaxial layer structure with key parameters at room temperature (d- thickness, N – doping, μ - majority carrier mobility, α - absorption, κ – thermal conductivity, nid – not intentionally doped, $\alpha(\text{n,p})$ – see Eq. 2).

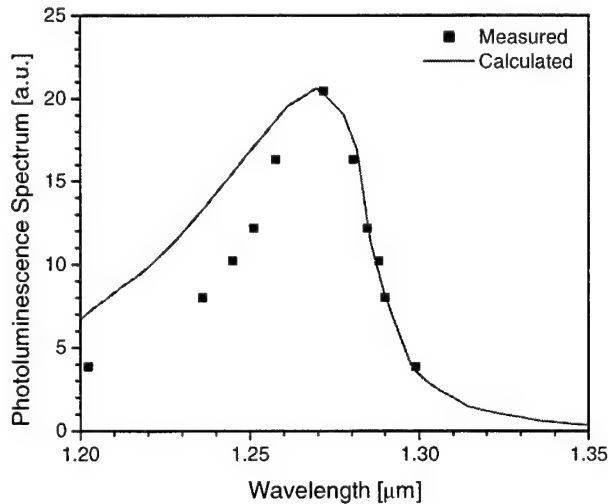


Fig. 7: Comparison of measured and simulated PL spectrum at room temperature.

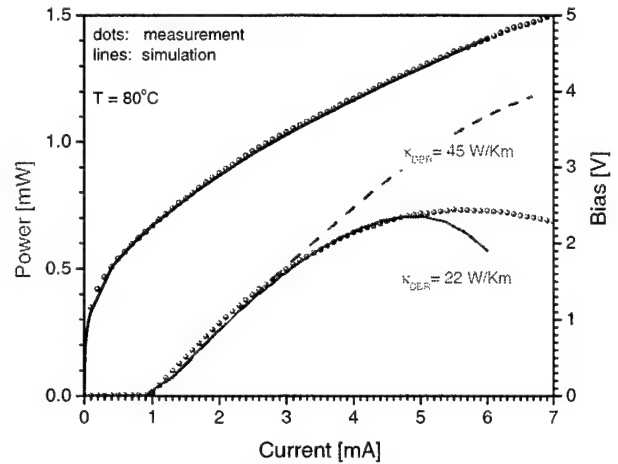


Fig. 8: Comparison of measured and simulated IV and LI characteristics at elevated temperature.

It is essential for the optical simulation of the laser diode to use accurate refractive index values for each material. The popular Sellmeier formulas for the refractive index¹⁰ are often inaccurate for photon energies near the band gap. Instead, we employ the Adachi model which was developed for energies close to the bandgap (Tab. 1).¹¹ The thermal change of the refractive index is assumed $2 \times 10^{-4}/\text{K}$ for InP-based layers and $3 \times 10^{-4}/\text{K}$ for GaAs-based layers,¹² which results in good agreement with the measured shift of the emission wavelength. Internal optical loss in 1.3 μm lasers is affected by free carriers (n,p) as well as by photon scattering (α_s) according to

$$\alpha(n,p) = \alpha_s + k_n n + k_p p. \quad (2)$$

It is expected to be mainly dominated by intervalenceband absorption ($k_p = 13 \times 10^{-22} \text{ m}^2$)¹³ and less by free electrons ($k_n = 2 \times 10^{-22} \text{ m}^2$). The scattering loss parameter is fitted to $\alpha_s = 3 / \text{cm}$ using the measured LI characteristic.

The drift-diffusion model of carrier transport considers Fermi statistics and thermionic emission at hetero-barriers. Thermionic emission is mainly controlled by the offset of conduction band (ΔE_c) and valence band (ΔE_v). For the AlGaInAs material system, a band offset ratio of $\Delta E_c / \Delta E_g = 0.72$ is commonly assumed. At the type-II interface of AlInAs and InP, we assume $\Delta E_c = 292 \text{ meV}$ and $\Delta E_v = 147 \text{ meV}$ (cf. Fig. 2). The Auger recombination rate is given by $(C_n n + C_p p)(n p - n_i^2)$ with the intrinsic carrier density n_i . Both the Auger coefficients are represented by a temperature dependent function

$$C(T) = C_0(T_0) \times \exp \left[\frac{E_A}{k} \left(\frac{1}{T_0} - \frac{1}{T} \right) \right] \quad (3)$$

with the Boltzmann constant k . The LI fit results in $C_0 = 1.15 \times 10^{-29} \text{ cm}^6 \text{ s}^{-1}$ at $T_0 = 298 \text{ K}$ and $E_A = 160 \text{ meV}$. This value of C_0 is in the middle of the range reported in the literature.² E_A is slightly larger than in previous investigations of $1.3 \mu\text{m}$ InGaAsP/InP lasers.¹⁴ The other quantum well recombination mechanisms are less important. The spontaneous recombination rate is obtained from the integration of the emission spectrum. The defect recombination lifetime is assumed as 10 ns within the quantum well and 100 ns elsewhere. The carrier mobility is a sophisticated function of composition, doping, local electric field, and temperature. Analytical functions are derived for binary materials.² Thus, some uncertainty remains with the mobilities in Tab. 1, especially for ternary and quaternary semiconductors. We here only adjust the hole mobility of the p-InP spacer layer which is considered the bottleneck for the carrier transport in our device. A value of $70 \text{ cm}^2/\text{Vs}$ gives good agreement with the IV characteristic measured at 80°C (Fig. 8).

This adjustment is especially important for CW simulations because the mobility also affects the Joule heat generated inside the device. Good agreement with the measured IV curve is a prerequisite to correctly simulate the generated heat power which affects the measured LI curve and causes the typical power roll-off at higher current (Fig. 8). The last remaining fit parameter is the thermal conductivity of the DBR. This number is affected by phonon scattering at the DBR interfaces and it cannot be deduced from bulk thermal conductivity data.¹⁵ A value of $\kappa_{\text{DBR}} = 22 \text{ W/mK}$ gives the best agreement with the measured power roll-off. For comparison, the simulated LI curve with $\kappa_{\text{DBR}} = 45 \text{ W/mK}$ is also shown in Fig. 8.

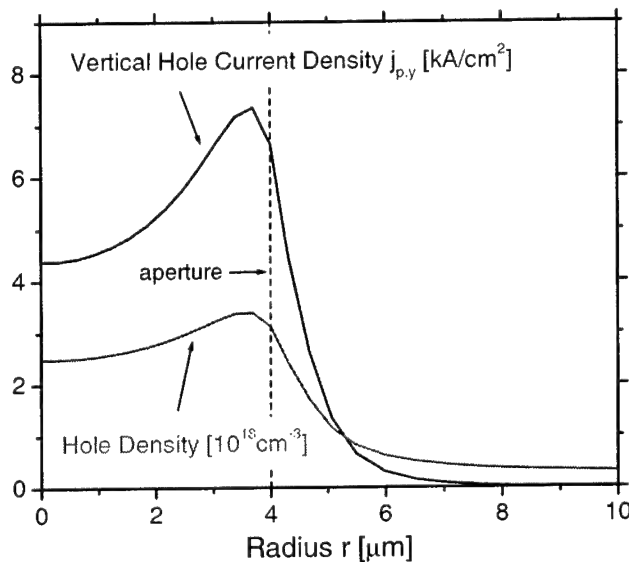


Fig. 9: Lateral profile of hole injection current density and hole density within the top quantum well ($I = 5 \text{ mA}$).

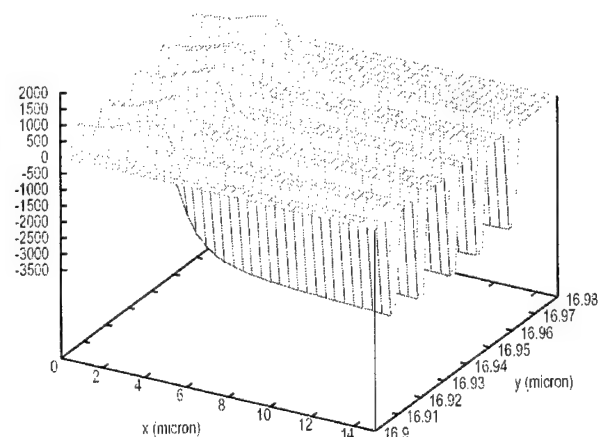


Fig. 10: 2D Surface plot of the optical gain within the MQW region ($I = 5 \text{ mA}$).

Based on this good agreement with measurements, we can now use the simulation to quantitatively analyze performance limitations of our VCSEL. First, we investigate the lateral quantum well carrier confinement as imposed by the tunnel junction aperture of 8 μm diameter. Figure 9 confirms relatively weak lateral current spreading in the p-InP layer leading to a good lateral carrier confinement within the quantum wells. The lateral gain profile is shown in Fig. 10 as surface plot for all five quantum wells. According to the carrier density minimum in the center of the device, the gain profile also exhibits a minimum in the center. Maximum gain occurs near the aperture where it potentially supports higher order transversal modes. Thus, the uniformity of the current injection through the tunnel junction aperture needs to be improved in order to better support the fundamental mode which has an intensity maximum in the center.

Figure 11 gives a 2D vector plot of the hole current indicating hole leakage from the MQW region into the n-doped InP spacer, where the holes recombine with electrons. This leakage is supported by the n-side AlInAs cladding layer underneath the MQW, which provides little hole confinement (cf. Fig. 2). In order to improve the VCSEL performance, this AlInAs layer should be removed since the InP layer gives a larger valence band offset.

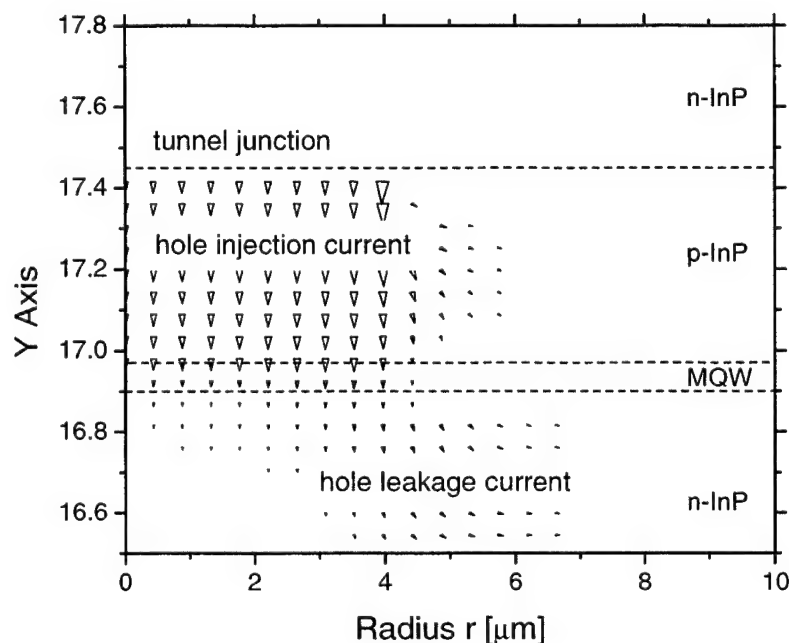


Fig. 11: 2D vector plot of the hole current density indicating hole leakage from the MQW region.

5. DESIGN OPTIMIZATION

1.3 μm VCSEL applications in telecommunication systems require single fundamental mode operation with more than 1 mW output power at 80°C ambient temperature. These performance goals need to be achieved simultaneously with the same device design. In the following, we optimize our device design using the insight gained in the previous section. A first step is the reduction of hole leakage by removing the lower AlInAs layer (Fig. 12). As a result, the hole leakage into the n-InP spacer layer is reduced by two orders of magnitude (Fig. 13). This restriction of carrier loss significantly enhances the internal quantum efficiency of the laser which leads to a larger slope efficiency as shown in Fig. 14. The internal bias is slightly lower which results in less self-heating.

Figure 15 shows the benefits of higher n-doping. The resistance of the top n-InP layer is reduced which results in less heating and more uniform current distribution within the aperture. However, the impact on the LI curve is relatively small. Much larger effect has an increased n-doping of the tunnel junction which reduces the junction bias by almost 1 V and gives a significant output power enhancement (solid curves).

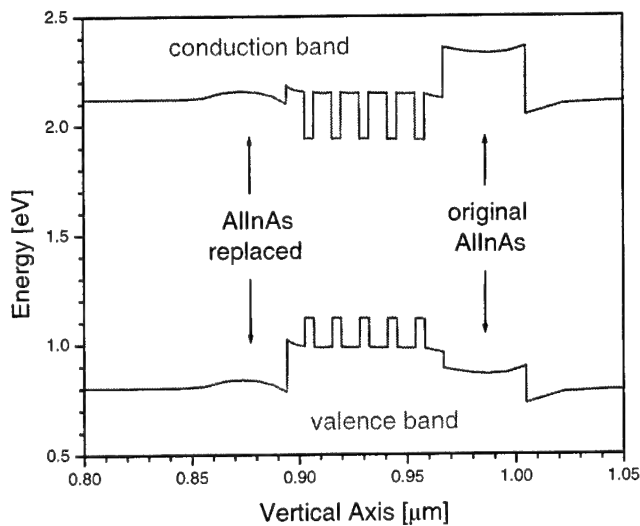


Fig. 12: Energy band diagram for device design without lower AllnAs layer.

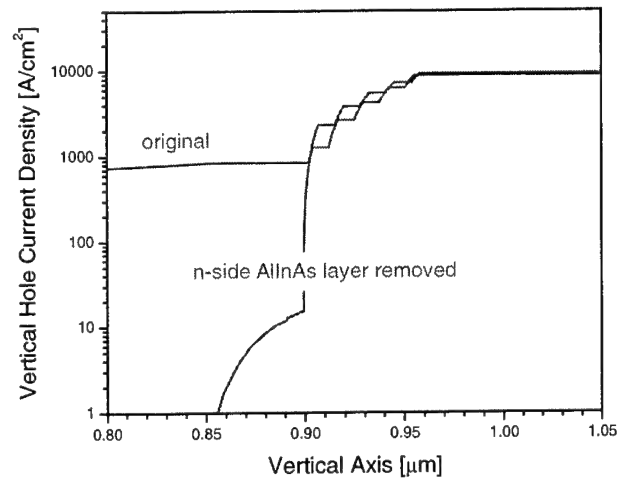


Fig. 13: Vertical hole current profile for device design without lower AllnAs layer.

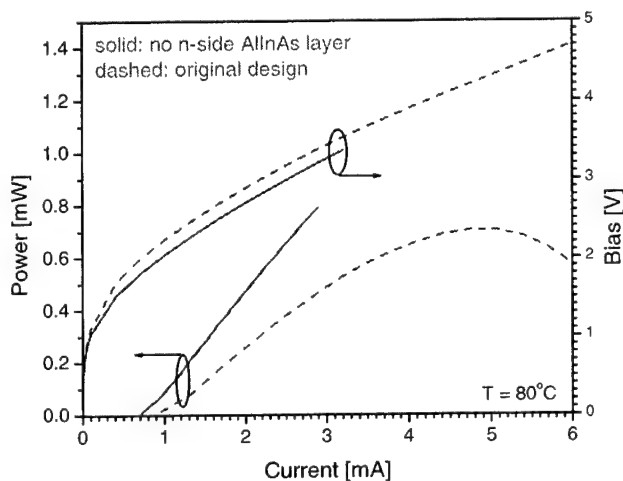


Fig. 14: Simulated LIV curves before (dashed) and after (solid) removal of the lower AllnAs layer (the solid line ends at about 3 mA since the simulation crashed at this point).

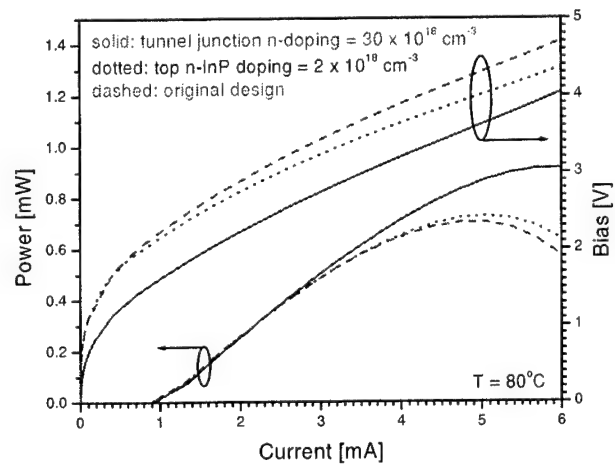


Fig. 15: Simulated LIV curves for increased n-doping of the top InP layer (dotted) and the tunnel junction (solid). The original design is represented by the dashed curves.

In order to reduce the bias and the intervalence band absorption, a thinner p-InP spacer layer above the MQW seems advantageous. We here simulate a reduction by half of the internal wavelength from 432.5 nm to 227.5 nm thickness. The resulting LIV curves are somewhat surprising (Fig. 16) as the bias is unchanged and the maximum output power is smaller than with the original design. An explanation can be derived from Fig. 17 which shows the lateral gain profile for both cases as well as compared to the fundamental mode profile. Obviously, the thinner p-InP restricts the lateral current spreading which gives the same overall bias and which reduces the area of positive gain. As a consequence, the

fundamental mode experiences stronger absorption in its tail regions which reduces the modal gain as well as the maximum output power.

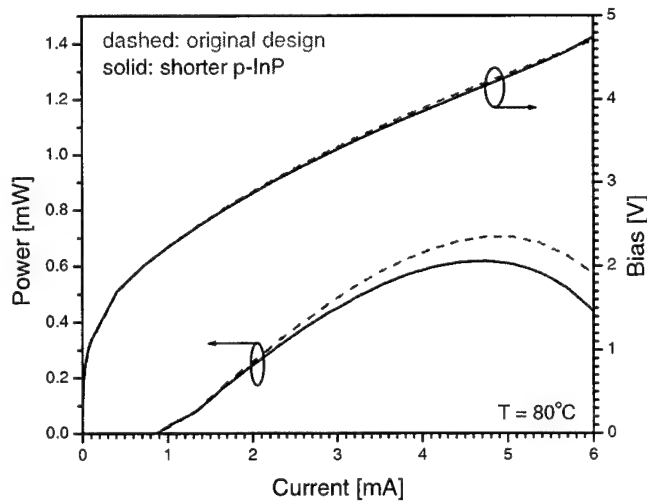


Fig. 16: Simulated LIV curves with shorter p-InP layer (solid) compared to the original (dashed).

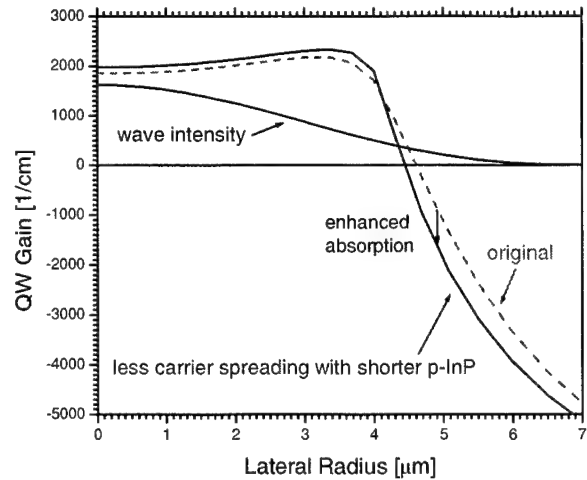


Fig. 17: Lateral gain profile within the top quantum well for the original design (dashed) and with thinner p-InP layer (solid). The intensity of the fundamental mode is plotted in the upper part.

Further design studies in search for a maximum output power lead to an optimized gain – mode offset of 32 nm, an optimized number of 28 top DBR periods, and a larger aperture of 10 μm . The original number of 5 quantum wells turns out to be optimum. Including the changes discussed above (except the thinner p-InP), the LIV characteristics for this optimized VCSEL design are shown in Fig. 18 with 0.6 mA threshold current, 1 V threshold bias, and a maximum fundamental mode power close to 2 mW.

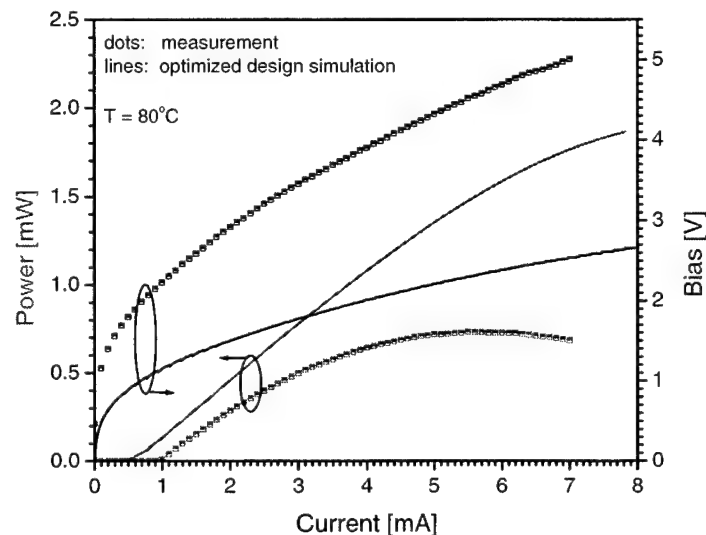


Fig. 18: Simulated LIV curves (lines) for the optimized VCSEL design compared to measurements on the original VCSEL (dots).

6. CONCLUSION

We have demonstrated by advanced numerical simulation that design optimization of our VCSEL can lead to simultaneous demonstration of high-temperature and high-power single mode lasing with the same device.

ACKNOWLEDGEMENT

This research was supported by Walsin USA, Sun Microsystems, and by an University of California Discovery grant (UC-SMART).

REFERENCES

- ¹ PICS3D by Crosslight Software, 2003.
- ² J. Piprek, *Semiconductor Optoelectronic Devices – Introduction to Physics and Simulation*, Academic Press, San Diego, 2003.
- ³ A. Karim, J. Piprek, P. Abraham, D. Lofgreen, Yi-Jen Chiu, and J. E. Bowers, "1.55 μm Vertical-Cavity Laser Arrays for Wavelength-Division Multiplexing", IEEE J. Sel. Topics Quantum Electron., Vol. 7, pp. 178-183, 2001.
- ⁴ J. Piprek, R. Glew, and Yi-Jen Chiu, "Wafer-Bonded 1.3-micron Vertical Cavity Laser", IEEE Semiconductor Laser Workshop, Long Beach, CA, 2002.
- ⁵ J. Piprek, A. Bregy, Y-J. Chiu, V. Jayaraman, and J. E. Bowers, "Lateral-Cavity Design for Long-Wavelength Vertical-Cavity Lasers," Proc. NanoTech Conf., San Francisco, 2003.
- ⁶ J. Piprek, "Advanced Analysis of Vertical Cavity Lasers", Proc. Int. Conf. Mixed Design MIXDES, Lodz, Poland, 2003.
- ⁷ V. Jayaraman, M. Mehta, A. W. Jackson, S. Wu, Y. Okuno, J. Piprek, and J.E. Bowers, "High power 1320 nm Wafer-Bonded VCSELs with Tunnel Junctions," IEEE Photonics Technology Letters, Vol. 15, No. 11, pp. 1495-1497, 2003.
- ⁸ M. Mehta, V. Jayaraman, A. Jackson, Y. Okuno, S. Wu, J. Piprek, and J. Bowers, "134°C continuous-wave operation of a 1.33 μm wafer-bonded VCSEL," CLEO Postdeadline Paper CThPDC10, Baltimore, June 2003.
- ⁹ Manish Mehta, Vijay Jayaraman, Andrew Jackson, Shaomin Wu, Yae Okuno, Joachim Piprek, and John E. Bowers, "Wafer-bonded Vertical-Cavity Lasers with Tunnel Junction," SPIE-ITCom Symp. *Semiconductor Optoelectronic Devices for Lightwave Communication*, Orlando, SPIE Proc. 5248-20, 2003.
- ¹⁰ M. J. Mondry, D. I. Babic, J. E. Bowers, L.A. Coldren, "Refractive indexes of (Al,Ga,In)As epilayers on InP for optoelectronic applications," IEEE Photonics Technology Letters, vol. 4, no. 6, pp.627-630, 1992.
- ¹¹ S. Adachi, *Physical Properties of III-V Semiconductor Compounds*, Wiley, New York, 1992.
- ¹² J. Piprek, D. I. Babic, and J. E. Bowers, "Simulation and analysis of 1.55-micron double-fused vertical-cavity lasers," Journal of Applied Physics, vol. 81, pp. 3382-3390, 1997.
- ¹³ C. H. Henry, R. A. Logan, F. R. Merritt, and J. P. Luongo, "The effect of intervalence band absorption on the thermal behavior of InGaAsP lasers," IEEE J. Quantum Electron., vol. 19, pp. 947-952, 1983.
- ¹⁴ S. Mogg and J. Piprek, "Optimization of the barrier height in 1.3-micron InGaAsP multiple-quantum-well active regions for high temperature operation," in: *Physics and Simulation of Optoelectronic Devices IX*, SPIE Proc. 4283-29, 2001.
- ¹⁵ J. Piprek, T. Troger, B. Schroter, J. Kolodzey, and C. S. Ih, "Thermal conductivity reduction in GaAs-AlAs distributed Bragg reflectors," IEEE Photonics Technology Letters, vol. 10, no. 1, pp. 81-83, 1998.

Resonant coupled-cavity effects in VCSELs with annular ring contacts

Gennady A. Smolyakov, Vladimir A. Smagley, Weiliang Chen, and Marek Osinski*

Center for High Technology Materials, University of New Mexico, 1313 Goddard SE,
Albuquerque, New Mexico 87106-4343

ABSTRACT

The role of metal apertures in the mechanism of lateral mode confinement in vertical-cavity surface-emitting lasers (VCSELs) is clarified by means of a detailed effective-frequency-method analysis of an oxide-confined VCSEL structure with the radius of the oxide window exceeding that of the metal aperture. Ring metal contact layer on top of the VCSEL structure is shown to be able to change the conditions for the lateral waveguiding in VCSELs by significantly modifying the local resonant properties of the VCSEL cavity. The resonant effects are demonstrated in the longitudinal coupled-cavity system consisting of the designed laser cavity, determined by the lower and top DBRs, and a very short cavity formed by the top DBR and semiconductor-metal interface. The conditions for higher-order lateral mode suppression using metal apertures are established.

Keywords: Numerical simulation, effective frequency method, semiconductor device modeling, semiconductor lasers, vertical-cavity surface-emitting lasers, oxide-confined VCSELs

1. INTRODUCTION

Many applications of vertical-cavity surface-emitting lasers (VCSELs) require operating in a fundamental lateral mode with sufficiently high power. Oxide apertures, commonly used for lateral mode control in VCSELs, provide very strong lateral mode confinement. With most of the mode volume effectively confined within the active region, determined by the oxide window, this technique introduces very little modal discrimination, which necessitates oxide apertures of very small diameters for single fundamental mode operation [Jung 1997]. In addition to being a factor that limits the output power of the device, very small oxide apertures are also very difficult to achieve from the technological point of view. The dynamics of the selective oxidation process is such that the oxidation rate depends strongly on the layer thickness and ambient temperature and varies with time as the oxidation process progresses, increasing enormously at the stage when the oxide aperture becomes very small [Osinski 2001]. Such behavior hampers the control over the oxidation process in VCSELs with very small oxide apertures.

The search goes on for other mechanisms of independent lateral mode control in oxide-confined VCSELs that would allow higher power from devices operating in a favored fundamental lateral mode. A number of different techniques have been employed with various degrees of success to achieve that goal, such as VCSELs with tapered oxide apertures [Choquette 1997], gain-apertured VCSELs [Choquette 2000], index anti-guided VCSELs [Wu 1995], [Zhang 1995], [Oh 1998], [Man 1998], VCSELs with an extended optical cavity [Unold 2000a], [Unold 2000b], [Unold 2001a], [Riyopoulos 2002], multi-oxide layer VCSEL structures [Nishiyama 2000], a hybrid ion implanted/selectively oxidized VCSEL structure [Young 2001], surface relief VCSEL structures [Dowd 1997], [Unold 1999], [Martinsson 2000], [Vukusic 2001], [Unold 2001b], [Unold 2001c], [Debernardi 2003], and microlensed VCSELs [Koch 1997], [Park 2002], [Park 2003].

Spatial filtering with metal aperture as a simple and effective method for lateral mode control has been successfully demonstrated in proton-implanted VCSELs with weak optical confinement [Morgan 1993] and recently revisited for oxide-confined VCSELs [Ueki 1999]. Improved single-mode behavior resulting from suppression of the higher-order lateral modes was experimentally observed in [Ueki 1999] for metal aperture sizes from less to equal or slightly larger than that of the oxide aperture. The lateral spatial modulation of reflectivity was named as the mechanism behind this

*Contact author: Email: osinski@chtm.unm.edu; Telephone: (505) 272-7812; Fax: (505) 272-7801; <http://www.chtm.unm.edu>

phenomenon in [Morgan 1993], where it was indicated that the reflectivity of the metal-semiconductor interface could be phase-mismatched to become smaller than that of semiconductor-air interface. Based on that assumption, the modal discrimination between zero- and first-order optical modes was estimated in [Ueki 1999] by calculating the round-trip losses for those modes as a function of the metal aperture size. Thus, the higher-order mode suppression was explained by a more significant overlap of those modes with the region under the metal contact.

While it has been realized that the metal apertures are not just spatial filters for the emission coming through the oxide aperture, but in some way modulate the waveguiding properties of VCSELs suppressing the higher-order lateral modes [Ueki 1999], their role in lateral mode competition may be more complicated than just increasing optical losses for higher-order modes. The lateral mode confinement in VCSELs is known to be governed by lateral changes in resonant wavelength as determined by local longitudinal resonances formed in VCSEL cavity [Hadley 1995]. Ring metal contact layer of quite high reflectivity can significantly modify the local resonant properties of the VCSEL cavity. In this paper we present, to our knowledge, the first detailed numerical analysis of the role of metal apertures in the mechanism of lateral mode confinement in VCSELs.

2. NUMERICAL APPROACH

For purely optical analysis of lateral waveguiding in an oxide-confined VCSEL structure, we used the effective frequency method (EFM) [Wenzel 1997], [Smolyakov 1999], [Biestman 2001] that will be briefly reviewed here. We search for eigenvalue solutions of the scalar wave equation linearized around the real-valued nominal angular frequency ω_0 , corresponding to designed periodicity of DBR mirrors:

$$\left[\Delta + k_0^2 n^2(\vec{r}, \omega_0) \right] E(\vec{r}, \omega) = v k_0^2 n(\vec{r}, \omega_0) n_g(\vec{r}, \omega_0) E(\vec{r}, \omega) \quad (1)$$

Here $k_0 = \omega_0/c$ is the vacuum wave number, $n(\vec{r}, \omega_0)$ and $n_g(\vec{r}, \omega_0)$ are the complex refractive phase and group indices evaluated at the nominal angular frequency ω_0 , and the dimensionless frequency parameter v , defined as

$$v = 2 \frac{\omega_0 - \omega}{\omega_0} = 2 \frac{\lambda - \lambda_0}{\lambda} - i \frac{2\omega''}{\omega_0} \quad (2)$$

plays the role of the eigenvalue of Eq. (1). The real part of v gives the relative wavelength shift from the nominal wavelength λ_0 , whereas its imaginary part is the relative decay constant of the corresponding mode. For circularly symmetric VCSELs, the spatially dependent field $E(\vec{r}, \omega)$ is approximately factorized as follows:

$$E(\vec{r}) = f(z; \rho) R_\ell(\rho) \exp(i\ell\phi), \quad \ell = 0, 1, \dots \quad (3)$$

where, for simplicity of notation, we have dropped the argument ω . The vertical part of the solution is normalized according to

$$\int_0^{L(\rho)} f^2(z; \rho) dz = 1 \quad (4)$$

with $L(\rho)$ corresponding to the length of the optical cavity at the radius ρ . $f(z; \rho)$ is given by Eq. (1) without in-plane derivatives

$$\left[\frac{d^2}{dz^2} + k_0^2 n^2(\rho, z) \right] f(z; \rho) = v_{\text{eff}}(\rho) k_0^2 n(\rho, z) n_g(\rho, z) f(z; \rho) \quad (5)$$

that is solved at each radial position ρ . We impose the “lasing” boundary conditions on $f(z;\rho)$, ensuring the outgoing plane waves at the bottom and top surfaces of the laser structure [Wenzel 1997], [Smolyakov 1999]. Thus, $f(z;\rho)$ and $v_{\text{eff}}(\rho)$ are the field distributions and frequency parameters describing local longitudinal resonances formed in the laser cavity at the different positions ρ .

The lateral profile of the effective frequency $v_{\text{eff}}(\rho)$ is then used in the equation for the radial part of the solution $R_\ell(\rho)$

$$\left[\frac{d^2}{d\rho^2} + \frac{1}{\rho} \frac{d}{d\rho} - \frac{\ell^2}{\rho^2} + v_{\text{eff}}(\rho) k_0^2 \langle nm_g \rangle_\rho \right] R_\ell(\rho) = v k_0^2 \langle nm_g \rangle_\rho R_\ell(\rho), \quad \ell = 0, 1, \dots \quad (6)$$

where

$$\langle nm_g \rangle_\rho = \int_0^{L(\rho)} n(z, \rho) n_g(z, \rho) f^2(z; \rho) dz \quad (7)$$

and $R_\ell(\rho)$ is assumed to satisfy the boundary condition ensuring a cylindrical outgoing wave at a sufficiently large value of $\rho = \rho_\infty$ [Wenzel 1997], [Smolyakov 1999]. Solutions of Eq. (6) are labeled as $\text{LP}_{\ell m}$ modes, $m = 1, 2, \dots$, and the corresponding complex eigenvalues $v_{\ell m}$ give the resonance wavelengths and decay constants of the modes of the entire VCSEL resonator. Under steady-state conditions, the imaginary part of $v_{\ell m}$ should satisfy the threshold condition

$$\text{Im}(v_{\ell m}) = 0 \quad (8)$$

As it follows from Eq.(6), it is the profile $v_{\text{eff}}(\rho)$ that determines lateral waveguiding in VCSELs. According to the definition of the frequency parameter (see Eq. (2)), radial blue-shift of the local cavity resonance would lead to cavity-induced guiding, while by red-shifting the local cavity resonance an anti-guiding condition can be realized. Gain-guiding effects are accounted for by the imaginary part of $v_{\text{eff}}(\rho)$, and are typically much weaker than those imposed by the real part of it. Thus, qualitative understanding of the mechanism of lateral mode confinement in VCSELs can be developed by following lateral changes in the local longitudinal cavity resonance.

3. DEVICE STRUCTURE AND PARAMETERS

We used the GaAs/AlGaAs oxide-confined 850-nm VCSEL structure of Fig. 1 in our calculations to illustrate the effect a metal aperture could have on lateral waveguiding in VCSELs. A basic diode design was used with a closely confined current aperture provided by two insulating oxide regions that define the window for vertical current flow. The top-emitting mesa laser has a ring contact at the top of the mesa, with the radius of the opening being smaller than the radius of the oxide window.

The design of the VCSEL structure illustrated in Fig. 1 is summarized in Table 1. The graded n -side and p -side distributed Bragg reflectors (DBRs) are composed of 35 and 25 $\text{Al}_{0.16}\text{Ga}_{0.84}\text{As}/\text{Al}_{0.92}\text{Ga}_{0.08}\text{As}$ pairs, respectively. Multiple-quantum-well (MQW) active region in Fig. 1 consists of three 7-nm-thick GaAs quantum wells separated by 7-nm-thick $\text{Al}_{0.3}\text{Ga}_{0.7}\text{As}$ barriers. The optical cavity between the DBRs is composed of n - and p -doped $\text{Al}_{0.98}\text{Ga}_{0.02}\text{As}$ (oxidation) and $\text{Al}_{0.92}\text{Ga}_{0.08}\text{As}$ layers and non-intentionally doped $\text{Al}_{0.47}\text{Ga}_{0.53}\text{As}$ and $\text{Al}_{0.3}\text{Ga}_{0.7}\text{As}$ layers, configured symmetrically on either side of the MQW.

The material parameters used in numerical calculations are given in Table 2. The phase and group refractive indices of AlGaAs material are extracted from [Adachi 1985]. The value for the refractive index of 30-nm-thick $\text{Al}_{0.98}\text{Ga}_{0.02}\text{As}$ oxidized layers is extracted from Fig. 1 of [Knopp 1998]. The refractive index data for the remaining materials are taken from [Palik 1985]. The values for the refractive indices shown in Table 2 are estimated at the designed resonant wavelength of 850 nm. Internal optical losses in different layers were estimated based on their doping levels (complete activation of the dopants was assumed) according to the well-known formula $\alpha \text{ (cm}^{-1}\text{)} = 3 \times 10^{-18} n \text{ (cm}^{-1}\text{)} + 7 \times 10^{-18} p \text{ (cm}^{-1}\text{)}$ [Casey 1978], which value was then converted to the imaginary part of the refractive index at 850 nm.

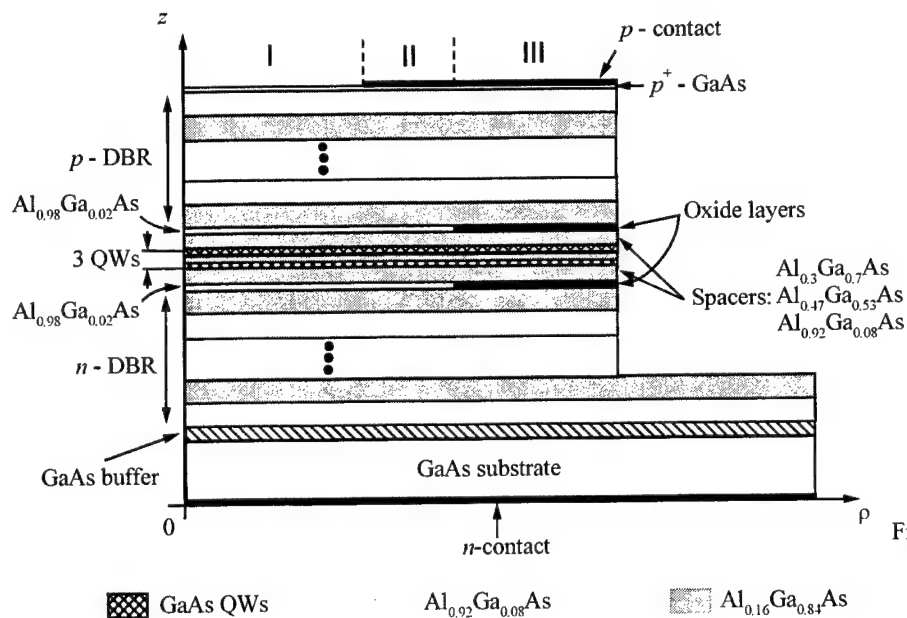


Fig.1. Schematic structure of cylindrically symmetric oxide-confined GaAs/AlGaAs VCSEL considered in this paper.

Table 1. Device design parameters used in calculations

Parameter	Units	Value	Comments
n -Al _{0.16} Ga _{0.84} As layer thickness	nm	41.7	n -DBR
n -AlGaAs graded layer thickness	nm	20	n -DBR
n -Al _{0.92} Ga _{0.08} As layer thickness	nm	48	n -DBR
Number of n -DBR pairs	-	35	-
$N(p)$ -Al _{0.98} Ga _{0.02} As layer thickness	nm	30	Oxidation layers
$N(p)$ -Al _{0.92} Ga _{0.08} As layer thickness	nm	36	$n(p)$ -spacers
nid -Al _{0.47} Ga _{0.53} As layer thickness	nm	47.5	nid -spacers
nid -Al _{0.3} Ga _{0.7} As layer thickness	nm	50	nid -spacers
nid -GaAs layer thickness	nm	7	Active QWs
Number of GaAs quantum wells	-	3	-
nid -Al _{0.3} Ga _{0.7} As layer thickness	nm	7	Barriers
Number of Al _{0.3} Ga _{0.7} As barrier layers	-	4	-
p -Al _{0.16} Ga _{0.84} As layer thickness	nm	41.7	p -DBR
p -AlGaAs graded layer thickness	nm	20	p -DBR
p -Al _{0.92} Ga _{0.08} As layer thickness	nm	48	p -DBR
Number of p -DBR pairs	-	25	-
P^+ -GaAs layer thickness	nm	10 ÷ 300	Cap layer
Au layer thickness	nm	210	Contact
Inner radius of p -contact, ρ_M	μm	8.5	-
Radius of oxide window, ρ_A	μm	13.5	-

For our purely optical analysis, we treated the VCSEL structure as consisting of three distinct sections in the lateral direction, shown schematically in Fig.1. Lateral uniformity of all material parameters, including material gain/absorption, was assumed within each section. Also, we neglected the temperature-induced waveguiding in our analysis as not essential for our purpose here.

Table 2. Material parameters used in calculations

Parameter	Material	Value	Comments
Phase refractive index	GaAs	3.67	at 850 nm, 300 K
Group index		4.58	
Phase refractive index	$\text{Al}_{0.16}\text{Ga}_{0.84}\text{As}$	3.52	at 850 nm, 300 K
Group index		4.42	
Phase refractive index	$\text{Al}_{0.3}\text{Ga}_{0.7}\text{As}$	3.43	at 850 nm, 300 K
Group index		4.02	
Phase refractive index	$\text{Al}_{0.47}\text{Ga}_{0.53}\text{As}$	3.32	at 850 nm, 300 K
Group index		3.76	
Phase refractive index	$\text{Al}_{0.92}\text{Ga}_{0.08}\text{As}$	3.05	at 850 nm, 300 K
Group index		3.35	
Phase refractive index	$\text{Al}_{0.98}\text{Ga}_{0.02}\text{As}$	3.01	at 850 nm, 300 K
Group index		3.3	
Phase refractive index	$(\text{Al}_{0.98}\text{Ga}_{0.02})_x\text{O}_y$	1.575	at 850 nm, 300 K
Group index		1.575	
Refractive index	Au	(0.195; -5.5)	at 850 nm, 300 K
Group index		(0.195; -5.5)	

4. RESULTS AND DISCUSSION

In order to get a qualitative understanding of lateral mode confinement in the VCSEL structure under consideration, we first calculate the lateral changes in the longitudinal cavity resonance. For that purpose, we perform one-dimensional longitudinal optical analysis by solving Eq. (5) in all three lateral sections of the device. The real part of the calculated value of $v_{\text{eff}}(\rho)$ (see Eq.(2) for the definition of the frequency parameter) gives us the local resonant wavelength λ , while its imaginary part tells us how lossy the local cavity resonance is, and can be directly converted into photon lifetime. To make the effect of the metal aperture on the local resonant properties of the cavity clearer, no material gain or resonance absorption in the active region was assumed in the calculations. The cap layer thickness was used as a parameter allowing us to phase-mismatch the reflection from the metal-semiconductor interface.

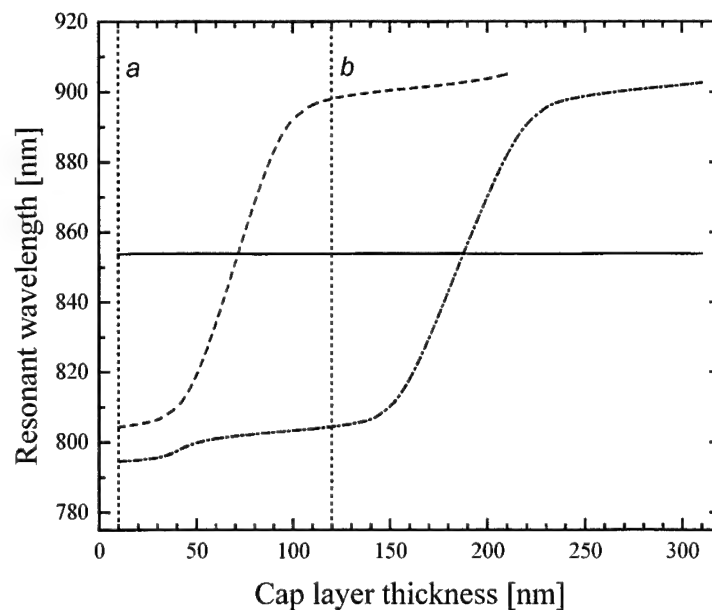


Fig. 2. The calculated system of three different longitudinal resonances for the first lateral section of the device. The dotted lines indicate the values of d_{cap} at which the longitudinal intensity distributions of Fig. 3 have been calculated.

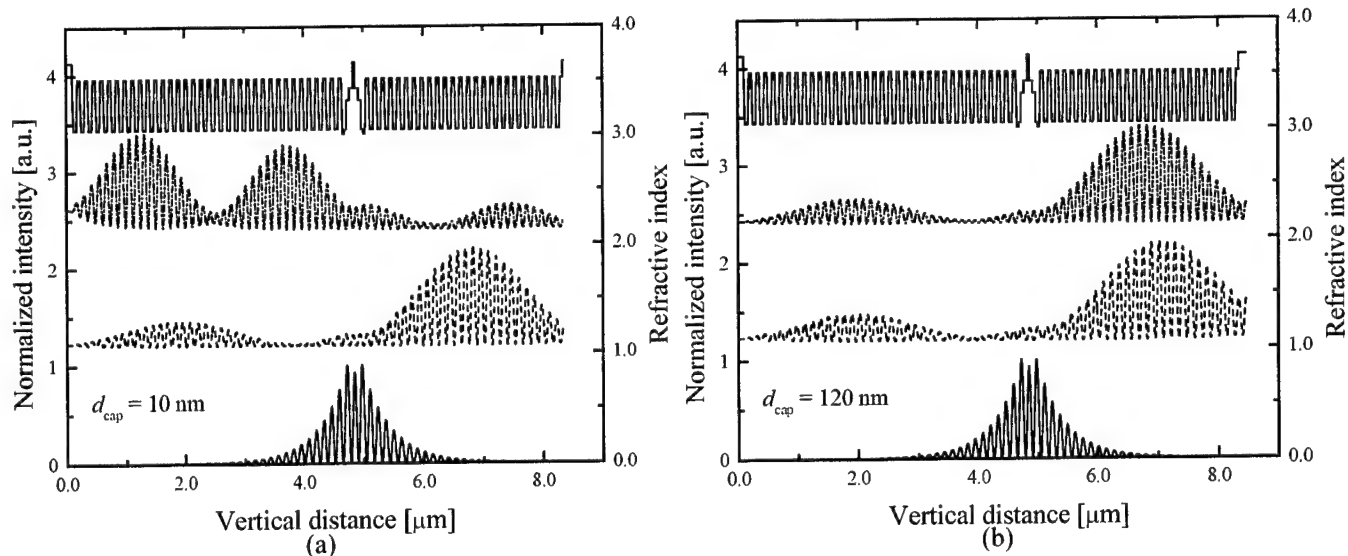


Fig. 3. The intensity distributions for three different longitudinal resonances of Fig. 2 calculated for particular cap layer thicknesses $d_{\text{cap}} = 10 \text{ nm}$ (a) and $d_{\text{cap}} = 120 \text{ nm}$ (b).

Fig. 2 shows the calculated resonant wavelength for a system of three different longitudinal resonances in the first (on-axis) lateral section of the device as a function of the cap layer thickness. The corresponding longitudinal intensity distributions are illustrated in Fig. 3a,b for particular cap layer thicknesses $d_{\text{cap}} = 10 \text{ nm}$ and $d_{\text{cap}} = 120 \text{ nm}$. As it follows from that Figure, the longitudinal resonance representing the cavity mode is given by solid curve in Fig.2. It should be noted here that we did not have a capability of dynamically readjusting the values for refractive indices with the wavelength in the calculations. Therefore, the parts of the solutions in Fig.1 that deviate significantly from the designed resonant DBR wavelength $\lambda_0 = 850 \text{ nm}$ (used as a reference wavelength in the EFM method) are only of qualitative value. However, the only important longitudinal resonance representing the cavity mode belongs to a very close vicinity of λ_0 , and thus can be trusted from the numerical point of view as well.

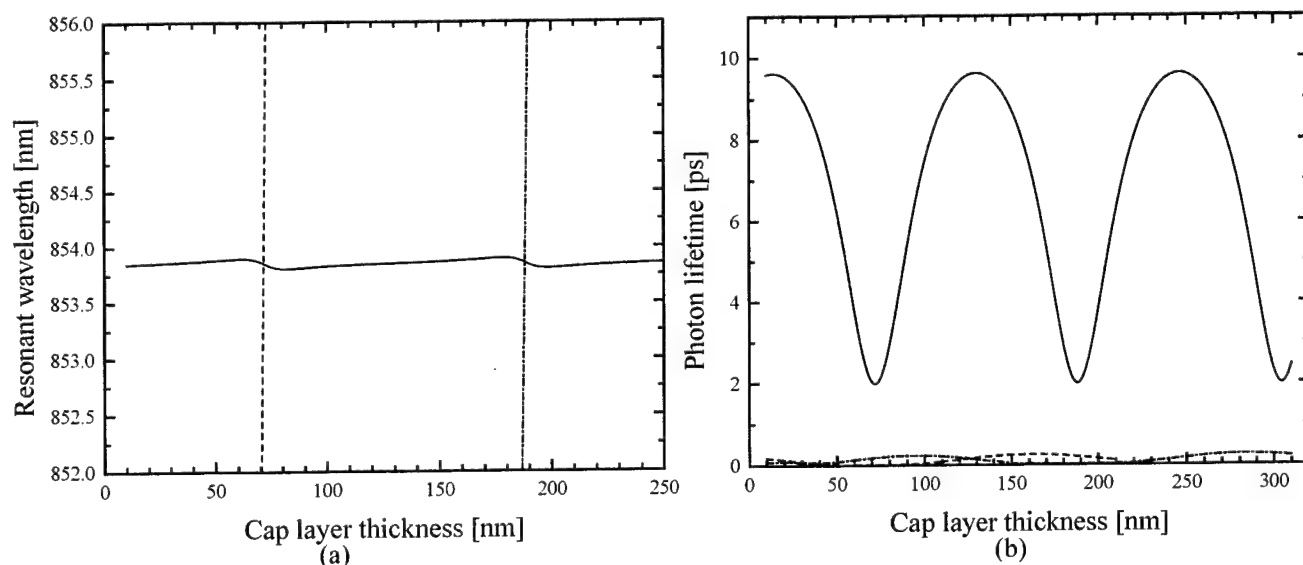


Fig. 4. The calculated system of three different longitudinal resonances for the first lateral section of the device (magnified) (a), and the corresponding photon lifetimes as a function of d_{cap} .

We show the details of that particular solution in Fig. 4a by magnifying the part of Fig.2 around $\lambda_0 = 850 \text{ nm}$. The corresponding photon lifetimes for different longitudinal resonances are shown in Fig. 4b. One can observe the minima

in photon lifetime occurring with the periodicity in cap layer thickness corresponding to $\lambda/2$ in the cap layer medium (GaAs). These minima correlate with the minima of reflection from the top DBR as determined by anti-resonant reflection condition from the semiconductor-air interface. With the reflectivity of that interface being quite small (~ 0.33 at $\lambda_0 = 850$ nm), we observe only a little disturbance in the local resonant wavelength around those points (Fig. 4a).

The situation, however, dramatically changes in the second lateral section, where the reflectivity of the top DBR is modified by the ring metal contact. The quite high reflectivity of the semiconductor-metal interface (~ 0.936 at $\lambda_0 = 850$ nm) leads to a system of longitudinal resonances demonstrating clear anti-crossing behavior (Fig. 5a), which means that the resonant wavelength corresponding to the cavity mode is now represented by two (or more, depending on the range of d_{cap}) different longitudinal solutions before and after the anti-crossing points. The points of anti-crossing correspond, as before, to the minima of reflection from the metal-modified top DBR (with the periodicity being the same as before, we show only the very first one). Those minima, however, are significantly shifted ($d_{\text{cap}} = 108.4$ nm as compared to $d_{\text{cap}} = 72$ nm for the on-axis solution), which is explained by a very large imaginary part of the refractive index of the metal layer resulting in an additional very significant phase shift in reflection from the semiconductor-metal interface.

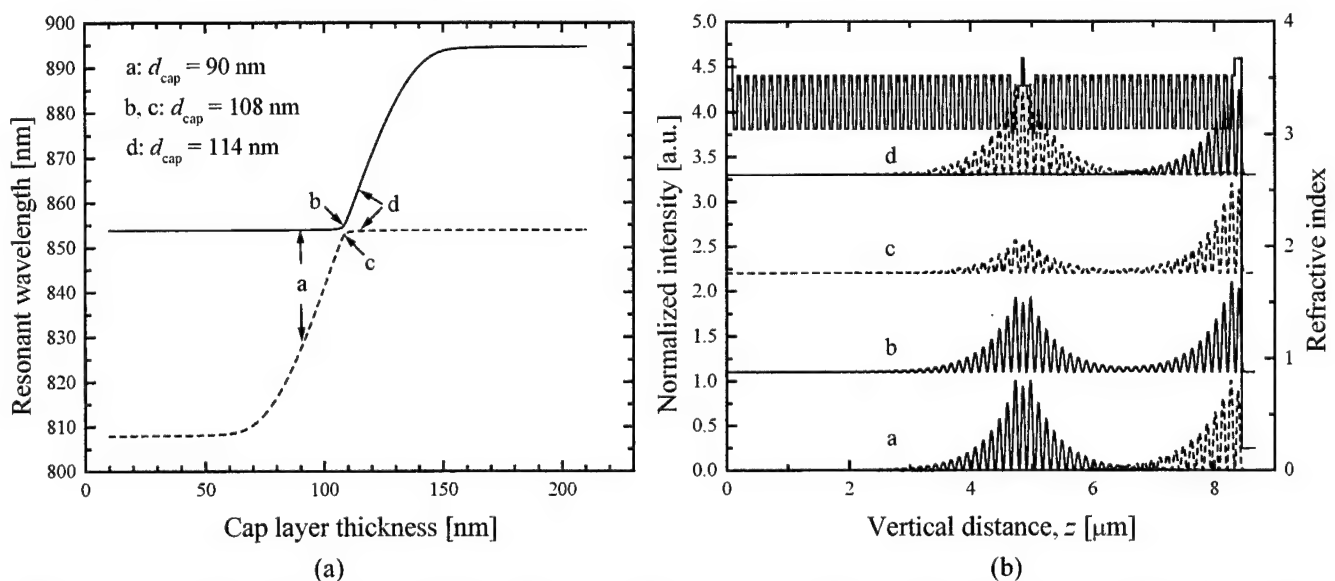


Fig. 5. The calculated system of two different longitudinal resonances for the second lateral section of the device (a), and the longitudinal intensity distributions calculated at the points indicated by arrows in Fig. 5a.

The position of anti-crossing in Fig. 5a corresponds to a resonance condition in the longitudinal coupled-cavity system consisted of the designed laser cavity, as determined by the lower and top DBRs, and a very short cavity formed by the top DBR and semiconductor-metal interface. Far from the resonance (curves a and d in Fig. 5b), the longitudinal solutions belong to either one of the cavities or the other. Close to the resonance, the longitudinal solutions acquire comparable intensity peaks in both of them (curves b and c in Fig. 5b). The much stronger anti-phase reflection from the semiconductor-metal interface at that point results in a dramatically reduced reflection from the metal-modified top DBR. The very significant part of the optical intensity is accumulated instead in the second short cavity and eventually strongly absorbed in the metal layer. The longitudinal cavity resonance in the second lateral section of the device is thus characterized by a very strong and quite narrow minimum in the photon lifetime seen in Fig. 6. For comparison purposes, the calculated photon lifetime for the on-axis solution (first lateral section of the device) is shown again in Fig. 6. As one can see from the Figure, the conditions for higher-order lateral mode suppression assumed in [Morgan 1993, Ueki 1999] exist in a very small range of cap layer thicknesses from $d_{\text{cap}} \sim 101.8$ nm to $d_{\text{cap}} \sim 116.2$ nm. If not carefully designed for precise phase-mismatched reflection, the ring metal contact on top of p -DBR would actually favor the higher-order mode generation by decreasing the optical losses for the part of emission extending under the metal contact. As the phase of the reflection from the metal-covered top DBR is significantly affected by the strong anti-phase reflection from the semiconductor-metal interface close to the anti-crossing, the tangible shift in the resonant wavelength is observed under close-to-resonance conditions in the coupled-cavity system (Fig. 5a).

A similar optical analysis performed for the third lateral section of the device revealed that both the wavelength of the longitudinal resonance and the position of the anti-crossing are shifted as compared to the other two sections by the presence of the oxide layers (Fig. 7a,b).

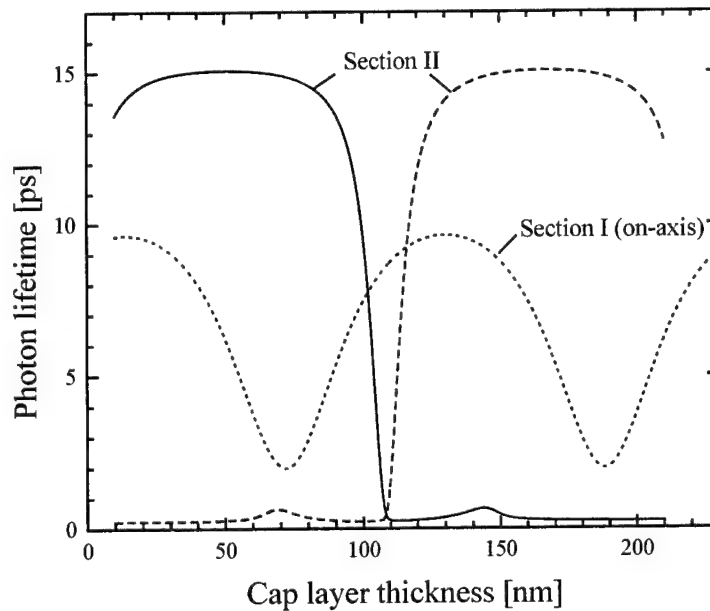


Fig. 6. The photon lifetimes as a function of d_{cap} , calculated for different longitudinal resonances in the first and second lateral sections of the device.

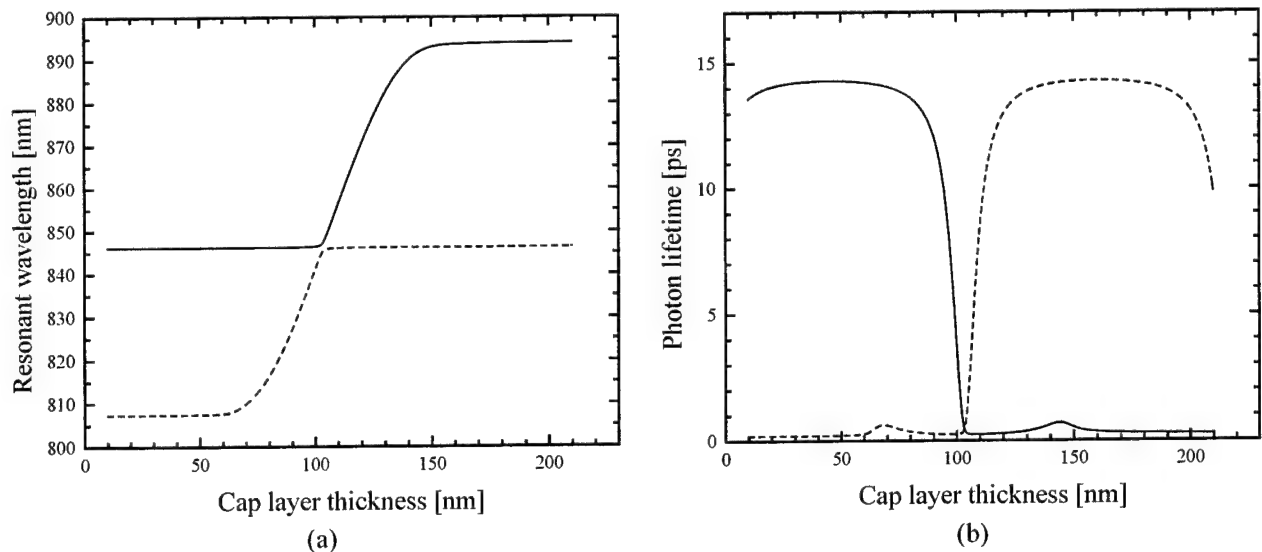


Fig. 7. The calculated system of two different longitudinal resonances for the third lateral section of the device (a), and the corresponding photon lifetimes as a function of d_{cap} .

We are now in a position to qualitatively understand the role of the metal aperture in the mechanism of lateral mode confinement by following the lateral changes in the longitudinal cavity resonance. The general picture is given in Fig. 8a where the calculated values for the local resonant wavelength for all three lateral sections of the device are summarized. The one immediate conclusion from that Figure is that the oxide section of the device (the third lateral section) is

strongly blue-shifted with respect to the other two lateral sections. That means that no matter what happens in the first two lateral sections of the device the lateral mode will always be very strongly confined within the aperture provided by the oxide window. Having established that, let us consider in more details the peculiarities of lateral mode formation in the first two sections. As revealed by Fig. 8b, the metal aperture provides additional lateral mode confinement by blue-shifting the local longitudinal resonance for all cap layer thicknesses up to the point of the first minimum in the top DBR reflection ($d_{\text{cap}} = 72$ nm) on the axis of the device. After that point the resonant wavelength on the axis of the device is shifted towards shorter wavelength, and the metal section (the second lateral section) turns out to be red-shifted with respect to the central part of the device. That red shift increases even more as the cap layer thickness approaches the point of anti-crossing for the second lateral section of the device. Significant lateral mode distortion should be expected in that range of cap layer thicknesses associated with the anti-guiding condition imposed by the red shift in the local longitudinal cavity resonance as discussed in Section 2 of this paper. After passing the resonant value of $d_{\text{cap}} = 108.4$ nm, the character of the mode confinement changes again as the longitudinal cavity resonance under the metal contact shifts to the shorter wavelengths, and that part of the device becomes blue-shifted again.

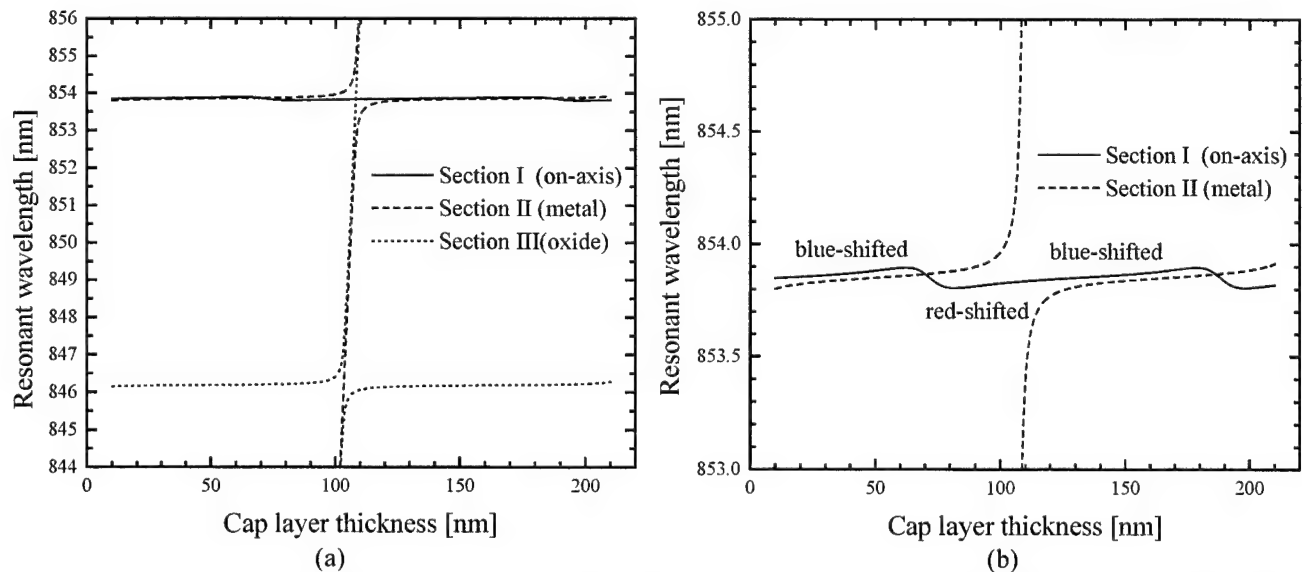


Fig. 8. The calculated longitudinal resonances for all three lateral sections of the device (a), and the calculated longitudinal resonances for the first two lateral sections of the device (b). The longitudinal resonances shown determine the cavity mode.

We support these predictions by showing the evolution of the fundamental LP_{01} lateral mode profile with the cap layer thickness, calculated at threshold for each value of d_{cap} . The lateral mode profiles are obtained by finally solving Eq.(6), based on the calculated profile of $v_{\text{eff}}(\rho)$. As expected, the initially well-behaved lateral mode is gradually pulled under the metal contact (Fig.9) just in the predicted range of the cap layer thicknesses.

For threshold calculations we assumed resonant absorption of 2000 cm^{-1} in the QWs everywhere outside the active region defined by the oxide window (the third lateral section) and constant material gain within the active region (the first two lateral sections). The threshold material gain is obtained by adjusting the value of the material gain until the threshold condition of Eq.(8) is satisfied. The calculated threshold material gain as a function of the cap layer thickness is shown in Fig. 10 for the first three lowest-order lateral modes. All three curves demonstrate a very similar behavior. The increase in the threshold around $d_{\text{cap}} = 72$ nm is explained by the minimum of reflection from the top DBR and hence the maximum of optical losses for the mode in the central on-axis part of the device (see Fig. 4b or Fig.6). The mode pulling under the metal contact does not automatically mean an increase in threshold, since the metal layer generally improves the resonator quality everywhere except for the very narrow range of the cap layer thicknesses around the resonant value of $d_{\text{cap}} = 108.4$ nm (see Fig. 6). It is in this very narrow range of d_{cap} that the threshold material gain first increases enormously for the laterally red-shifted VCSEL cavity, and then drops down as the corresponding blue-shift, after passing the resonance, changes the guiding condition again towards a well-behaved mode that has very little overlap with the metal region. By making the lasing generation impossible, this anomalous increase in the lasing threshold restricts even further the very small range of d_{cap} values suitable for higher-order mode suppression. Our

calculations show the higher threshold for higher-order modes in a very small range of cap layer thicknesses from $d_{\text{cap}} = 108.4$ nm to $d_{\text{cap}} = 116.2$ nm, while outside that very narrow region the metal aperture would favor the higher-order lateral mode generation.

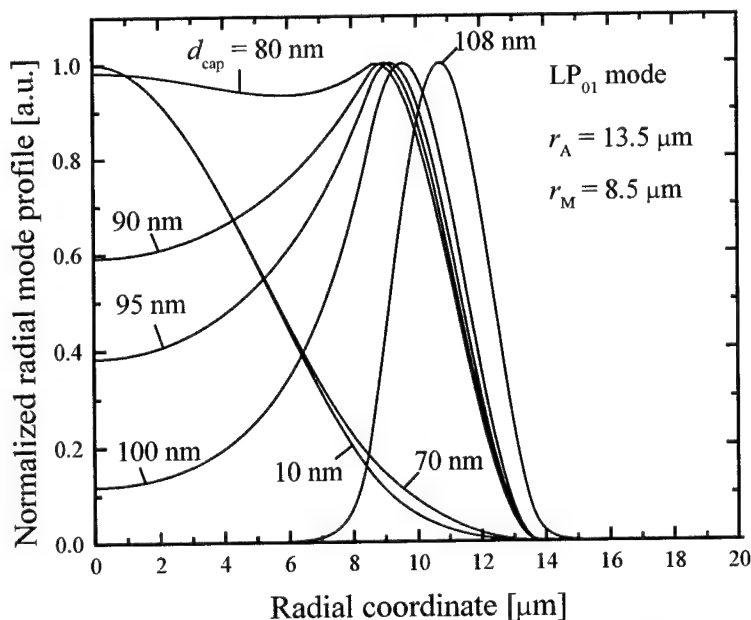


Fig. 9. The evolution of the fundamental LP_{01} lateral mode profile with the cap layer thickness. The lateral mode profiles are calculated at threshold for each value of d_{cap} .

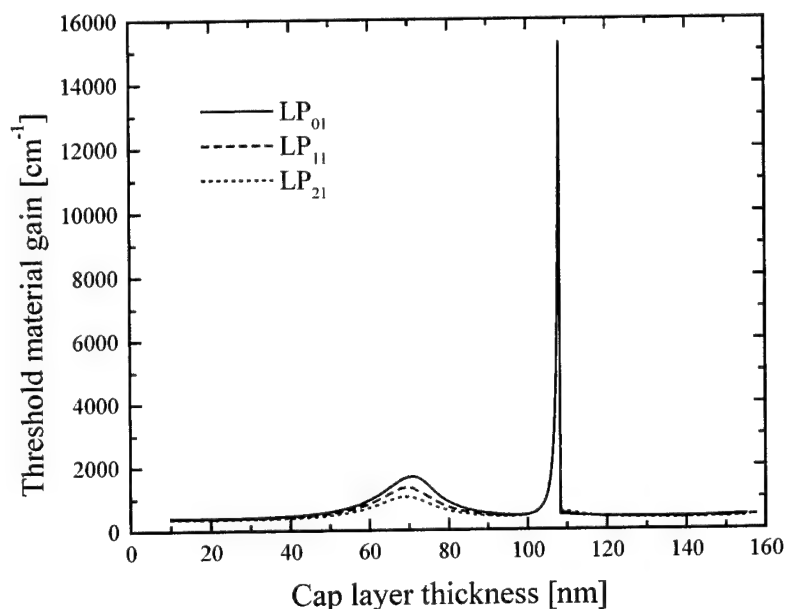


Fig. 10. The calculated threshold material gain for the first three lowest-order lateral modes as a function of the cap layer thickness.

CONCLUSIONS

In this paper the role of metal apertures in the mechanism of lateral mode confinement in VCSELs has been clarified by a detailed optical EFM analysis of an oxide-confined VCSEL structure with the radius of the oxide window exceeding that of the metal aperture. By significantly modifying the local resonant properties of the VCSEL cavity, metal contact layer can change the conditions for the lateral waveguiding in VCSELs. We have shown that ring metal contact layer on

top of the VCSEL structure does not necessarily provide the lateral mode confinement effect. Under certain conditions, it can impose "anti-guiding" condition in the VCSEL cavity resulting in severe distortion of the lateral mode configuration.

With the metal contact layer as an additional mirror, resonant coupled-cavity effects can be expected in VCSELs, provided the cap layer is thick enough to play the role of an additional cavity. The resonance in the coupled-cavity system can prevent lasing action in an "anti-guided" "red-shifted" device configuration as a result of severe modal gain suppression.

The conditions suitable for higher-order lateral mode suppression exist only in a very narrow range of the cap layer thicknesses in a dangerously close vicinity of the resonance in the coupled-cavity system. In order to use metal apertures for higher-order mode suppression, the cap layer thickness must be extremely carefully adjusted (1) to be close to the resonant values for the cap layer thickness and (2) to avoid "anti-guided" "red-shifted" cavity configurations.

ACKNOWLEDGMENTS

This work was supported by DARPA under the Optoelectronic Materials Center program, and by AFOSR under the Optoelectronics Research Center program.

REFERENCES

- [Adachi 1985] S. Adachi, "GaAs, AlAs, and $\text{Al}_x\text{Ga}_{1-x}\text{As}$: Material parameters for use in research and device applications", *J. Appl. Phys.*, vol. 58 (#3), pp. R1-R29, 1 Aug. 1985.
- [Bienstman 2001] P. Bienstman, R. Baets, J. Vukusic, A. Larsson, M. J. Noble, M. Brunner, K. Gulden, P. Debernardi, L. Fratta, G. P. Bava, H. Wenzel, B. Klein, O. Conradi, R. Pregla, S. A. Riyopoulos, J. P. P. Seurin, and S. L. Chuang, "Comparison of optical VCSEL models on the simulation of oxide-confined devices", *IEEE J. Quantum Electron.*, vol.37 (#12), pp.1618-1631, Dec. 2001.
- [Casey 1978] H. C. Casey, Jr. and M. B. Panish, *Heterostructure Lasers*, Academic Press, New York 1978.
- [Choquette 1997] K. D. Choquette, H. Q. Hou, G. R. Hadley, K. M. Geib, D. Mathes, and R. Hull, "High power single transverse mode selectively oxidized VCSELs", in *Dig. IEEE/LEOS Summer Topical Meeting*, 1997, pp.73-74.
- [Choquette 2000] K. D. Choquette, A. A. Allerman, K. M. Geib, and J. J. Hindi, "Lithographically-defined gain apertures within selectively oxidized VCSELs", in *CLEO Tech. Dig.*, 2000, pp. 232-233.
- [Debernardi 2003] P. Debernardi, H. J. Unold, J. Maehnss, R. Michalzik, G. P. Bava, and K. J. Ebeling, "Single-mode, single-polarization VCSELs via elliptical surface etching: Experiments and theory", *IEEE J. Select. Topics. Quantum Electron.*, vol.9 (#5), pp.1394-1405, Sep.-Oct. 2003.
- [Dowd 1997] P. Dowd, L. Raddatz, Y. Sumaila, M. Asghari, I. H. White, P. J. Heard, G. C. Allen, R. P. Schneider, M. R. T. Tan, and S. Y. Wang, "Mode control in vertical-cavity surface-emitting lasers by post-processing using focused ion-beam etching", *IEEE Photonics Technol. Lett.*, vol.9 (#9), pp.1193-1195, Sep. 1997.
- [Hadley 1995] G. R. Hadley, "Effective index method for vertical-cavity surface-emitting lasers", *Optics Lett.*, vol.20 (#13), pp.1483-1485, 1 Jul. 1995.
- [Jung 1997] C. Jung, R. Jäger, M. Grabherr, P. Schnitzer, R. Michalzik, B. Weigl, S. Müller, and K.J. Ebeling, "4.8 mW singlemode oxide confined top-surface emitting vertical-cavity laser diodes", *Electron. Lett.*, vol. 33 (#21), pp.1790-1791, 9 Oct. 1997.
- [Knopp 1998] K. J. Knopp, R. P. Mirin, D. H. Christensen, K. A. Bertness, A. Roshko, and R. A. Synowicki, "Optical constants of $(\text{Al}_{0.98}\text{Ga}_{0.02})_x\text{O}_y$ native oxides", *Appl. Phys. Lett.*, vol. 73 (#24), pp. 3512-3514, 14 Dec. 1998.
- [Koch 1997] B. J. Koch, J. R. Leger, A. Gopinath, and Z. Wang, "Single-mode vertical cavity surface emitting laser by graded-index lens spatial filtering", *Appl. Phys. Lett.*, vol.70 (#18), pp.2359-2361, 5 May 1997.
- [Man 1998] W. M. Man and S. F. Yu, "Comprehensive modeling of diffused quantum-well vertical-cavity surface-emitting lasers", *IEEE J. Select. Topics Quantum Electron.*, vol.4 (#4), pp.715-722, Jul.-Aug. 1998.
- [Martinsson 2000] H. Martinsson, J. A. Vukusic, and A. Larsson, "Single-mode power dependence on surface relief size for mode-stabilized oxide-confined vertical-cavity surface-emitting lasers", *IEEE Photonics Technol. Lett.*, vol.12 (#9), pp.1129-1131, Sep. 2000.
- [Morgan 1993] R. A. Morgan, G. D. Guth, M. W. Focht, M. T. Asom, K. Kojima, L. E. Rogers, and S. E. Callis, "Transverse mode control of vertical-cavity top-surface-emitting lasers", *IEEE Photonics Technol. Lett.*, vol.5 (#4), pp. 374-377, April 1993.

- [Nishiyama 2000] N. Nishiyama, M. Arai, S. Shinada, K. Suzuki, F. Koyama, and K. Iga, "Multi-oxide layer structure for single-mode operation in vertical-cavity surface-emitting lasers", *IEEE Photonics Technol. Lett.*, vol.12 (#6), pp.606-608, Jun. 2000.
- [Ueki 1999] N. Ueki, A. Sakamoto, T. Nakamura, H. Nakayama, J. Sakurai, H. Otoma, Y. Miyamoto, M. Yoshikawa, and M. Fuse, "Single-transverse-mode 3.4-mW emission of oxide-confined 780-nm VCSEL's", *IEEE Photonics Technol. Lett.*, vol.11 (#12), pp. 1539-1541, December 1999.
- [Oh 1998] T. H. Oh, M. R. McDaniel, D. L. Huffaker, and D. G. Deppe, "Cavity-induced antiguiding in a selectively oxidized vertical-cavity surface-emitting laser", *IEEE Photonics Technol. Lett.*, vol.10 (#1), pp.12-14, Jan. 1998.
- [Osiński 2001] M. Osiński, T. Svimonishvili, G. A. Smolyakov, V. A. Smagley, P. Maćkowiak, and W. Nakwaski, "Temperature and thickness dependence of steam oxidation of AlAs in Cylindrical Mesa Structures", *IEEE Photonics Technol. Lett.*, vol.13 (#7), pp. 687-689, July 2001.
- [Palik 1985] E. D. Palik, Ed., *Handbook of Optical Constants of Solids, I, II*, Academic Press, Orlando 1985.
- [Park 2002] S. H. Park, Y. Park, H. Kim, H. Jeon, S. M. Hwang, J. K. Lee, S. H. Nam, B. C. Koh, J. Y. Sohn, and D. S. Kim, "Microlensed vertical-cavity surface-emitting laser for stable single fundamental mode operation", *Appl. Phys. Lett.*, vol.80 (#2), pp.183-185, 14 Jan. 2002.
- [Park 2003] S. H. Park, Y. Park, and H. Jeon, "Theory of the mode stabilization mechanism in concave-micromirror-capped vertical-cavity surface-emitting lasers", *J. Appl. Phys.*, vol. 94 (#3), pp. 1312-1317, 1 Aug. 2003.
- [Riyopoulos 2002] S. Riyopoulos and H. Unold, "Theoretical interpretation of the enhanced single-mode stability in extended cavity VCSELs", *J. Lightwave Technol.*, vol.20 (#7), pp.1173-1181, Jul. 2002.
- [Smolyakov 1999] G. A. Smolyakov, V. A. Smagley, W. Nakwaski, P. G. Eliseev, and M. Osiński, "Design of InGaN/GaN/AlGaIn VCSELs using the effective frequency method", in *Physics and Simulation of Optoelectronic Devices VII* (P. Blood, A. Ishibashi, and M. Osiński, Eds.), Optoelectronics '99 - SPIE International Symp. on Integrated Devices and Applications, San Jose, CA, 25-29 Jan. 1999, *Proc. SPIE*, Vol. 3625, pp. 324-335.
- [Unold 1999] H. J. Unold, M. Grabherr, F. Eberhard, F. Mederer, R. Jager, M. Riedl, and K. J. Ebeling, "Increased-area oxidized single-fundamental mode VCSEL with self-aligned shallow etched surface relief", *Electron. Lett.*, vol.35 (#16), pp.1340-1341, 5 Aug. 1999.
- [Unold 2000a] H. Unold, S. W. Mahmoud, F. Eberhard, R. Jaeger, M. Kicherer, F. Mederer, M. C. Riedl, and K. J. Ebeling, "Large-area single-mode selectively oxidized VCSELs: Approaches and experimental", *Proc. SPIE*, vol. 3946, pp. 207-218, 2000.
- [Unold 2000b] H. J. Unold, S. W. Z. Mahmoud, R. Jager, M. Kicherer, M. C. Riedl, and K. J. Ebeling, "Improving single-mode VCSEL performance by introducing a long monolithic cavity", *IEEE Photonics Technol. Lett.*, vol.12 (#8), pp.939-941, Aug. 2000.
- [Unold 2001a] H. J. Unold, M. C. Riedl, S. W. Z. Mahmoud, R. Jager, and K. L. Ebeling, "Long monolithic cavity VCSELs for high singlemode output power", *Electron. Lett.*, vol. 37 (#3), pp.178-179, 1 Feb. 2001.
- [Unold 2001b] H. J. Unold, S. W. Z. Mahmoud, R. Jager, M. Grabherr, R. Michalzik, and K. J. Ebeling, "Large-area single-mode VCSELs and the self-aligned surface relief", *IEEE J. Select. Topics Quantum Electron.*, vol.7 (#2), pp.386-392, Mar.-Apr. 2001.
- [Unold 2001c] H. J. Unold, M. Golling, F. Mederer, R. Michalzik, D. Supper, and K. J. Ebeling, "Singlemode output power enhancement of InGaAs VCSELs by reduced spatial hole burning via surface etching", *Electron. Lett.*, vol.37 (#9), pp.570-572, 26 Apr. 2001.
- [Vukusic 2001] J. A. Vukusic, H. Martinsson, J. S. Gustavsson, and A. Larsson, "Numerical optimization of the single fundamental mode output from a surface modified vertical-cavity surface-emitting laser", *IEEE J. Quantum Electron.*, vol.37 (#1), pp.108-117, Jan. 2001.
- [Wenzel 1997] H. Wenzel and H.-J. Wünsche, "The effective frequency method in the analysis of vertical-cavity surface-emitting lasers", *IEEE J. Quantum Electron.*, vol. 33 (#7), pp. 1156-1162, July 1997.
- [Wu 1995] Y. A. Wu, G. S. Li, R. F. Nabiev, K. D. Choquette, C. Caneau, and C. J. Chang-Hasnain, "Single-mode, passive antiguide vertical-cavity surface-emitting laser", *IEEE J. Select. Topics Quantum Electron.*, vol.1 (#2), pp.629-637, June 1995.
- [Young 2001] E. W. Young, K. D. Choquette, S. L. Chuang, K. M. Geib, A. J. Fischer, and A. A. Allerman, "Single-transverse-mode vertical-cavity lasers under continuous and pulsed operation", *IEEE Photonics Technol. Lett.*, vol.13 (#9), pp.927-929, Sep. 2001.
- [Zhang 1995] J. P. Zhang, "Single mode power and modal behavior in buried vertical-cavity surface-emitting lasers", *Proc. Inst. Elect. Eng. - Optoelectron.*, vol.142 (#2), pp.87-93, Apr. 1995.

Molecular-beam epitaxy of III-N on novel ZrB_2 substrates

Jun Suda

Department of Electronic Science and Engineering, Kyoto University,
Katsura, Nishikyo-ku, Kyoto 615-8510, JAPAN

ABSTRACT

Electrically conductive zirconium diboride (ZrB_2) is a promising lattice-matched substrate for GaN-based nitride semiconductors. In this paper, important properties of ZrB_2 as a substrate for nitrides, such as, thermal expansion coefficient, thermal conductivity, optical reflectivity and cleavage, are reviewed. Then, heteroepitaxial growth of GaN and AlN on the substrate by molecular-beam epitaxy (MBE) are discussed. Direct growth and two-step growth using low-temperature GaN nucleation layers as well as characterization of the surface condition of ZrB_2 substrates by X-ray photoelectron spectroscopy (XPS) and the effect of surface treatment on grown layers are presented.

Keywords: GaN, ZrB_2 , Heteroepitaxy, Molecular-beam epitaxy, thermal expansion, lattice matching

1. INTRODUCTION

Gallium nitride (GaN)-based group-III nitrides (III-Ns) are the most promising materials for short wavelength light-emitting devices, high-frequency transistors and power switching devices owing to their material properties. Electrically and thermally conductive substrates are desirable for III-N devices with high-density vertical current flow, such as laser diodes (LDs) and vertical power transistors. In addition, of course, lattice matching is an important factors to realize high quality heteroepitaxial growth. Nitride researchers have tried various crystals as the substrate.

Kinoshita focused on zirconium diboride (ZrB_2), known as material for electrically conductive ceramic applications, as the substrate. Because the compound has a hexagonal structure with an in-plane lattice constant of 3.169 Å [1] which is very close to that of GaN and exactly the same as $\text{Al}_{0.25}\text{Ga}_{0.75}\text{N}$. However, due to its high melting point and strong violent evaporation at the melting point, growth of single crystal ZrB_2 was very difficult. Otani *et al.* had studied bulk growth of various metal borides by a floating-zone (FZ) method [2,3,4]. Based on the study, Kinoshita and Otani have started to develop the ZrB_2 bulk growth technique to obtain substrate-grade single crystals [5]. At the time, we started to assess the possibility of heteroepitaxial growth of GaN and AlN by molecular-beam epitaxy using ZrB_2 substrates provided by Kinoshita and Otani [6,7]. After confirmation of epitaxial growth of both GaN and AlN on the substrates by MBE, a metal-organic vapor phase epitaxy (MOVPE) study was started at Meijo University [8,9].

In this paper, properties of ZrB_2 as well as recent progress in bulk growth are reviewed. Some important properties as a substrate for III-N devices, such as thermal expansion coefficient, thermal conductivity, optical reflectivity and cleavage were described. Then, heteroepitaxial growth of GaN and AlN on the substrate by MBE is discussed. Direct growth and two-step growth using a low-temperature-grown GaN nucleation layer are presented. Characterization of surface condition of ZrB_2 substrates by X-ray photoelectron spectroscopy (XPS) and the effect of surface treatment on MBE growth of GaN layers are also mentioned.

2. PROPERTIES OF ZIRCONIUM DIBORIDE

2.1 Crystal structure

Metal diboride compounds (MB_2) have a hexagonal crystal structure as illustrated in Fig. 1 [10]. This structure is non-polar (space group $P6/mmm$). The metal and boron atoms are arranged in alternate planar layers along the c-axis. B atoms form a graphite-like two-dimensional hexagonal net structure. Metal atoms are arranged on a simple hexagonal lattice and its in-plane position is at the center of the hexagonal ring of B atoms. Both XPS and theoretical calculations suggest that the B atoms are bonded each other by graphite-like sp^2 bonding [11]. Due to the strong bonding, the melting point of MB_2 compounds is very high. For example, that of ZrB_2 is 3220°C.

2.2 Lattice constant

The in-plane (a-axis) lattice constant of MB_2 is dominated by covalent radii of boron. The standard covalent B-B bond length, 1.76 Å, gives an a-axis lattice constant of 3.05 Å. However, it has a small dependence on the metal atom, i.e., a larger metal atom increases the a-axis lattice constant slightly. Lattice constants for various metal borides are summarized in Table I. Among them, ZrB_2 has an in-plane lattice constant of 3.169 Å, which is between those of GaN (3.189 Å) and AlN (3.112 Å). Thus, the in-plane lattice constant of $\text{Al}_{0.25}\text{Ga}_{0.75}\text{N}$ is perfectly matched to that of ZrB_2 .

Hexagonal silicon carbide (SiC) and zinc oxide (ZnO) have been proposed as (nearly) lattice matched substrates for GaN-based materials. However, in the case of ZnO, to obtain perfect matching, ~20% incorporation of In is required. It is difficult to obtain homogenous InGaN films with such a high In content due to phase separation. In the case of SiC, where the in-plane lattice constant of SiC (3.081 Å) is 0.9% smaller than that of AlN, it is impossible to obtain lattice matching in the $\text{Al}_x\text{Ga}_{1-x}\text{N}$ system. Incorporation of B has been proposed to reduce the lattice constant of group-III nitrides. For example, $\text{B}_{0.17}\text{Ga}_{0.83}\text{N}$ is expected to be lattice matched to SiC. However, incorporation of B into the AlGaN system is still challenging. From the viewpoint of device applications, $\text{Al}_{0.25}\text{Ga}_{0.75}\text{N}$ lattice-matched to ZrB_2 is very suitable for the cladding layer in short-wavelength LDs. This makes the ZrB_2 substrate very attractive. It should be noted that c-axis lattice constant of ZrB_2 (3.530 Å) is much different from that of GaN (5.185 Å). Therefore, off-axis or other crystal faces of ZrB_2 are not suitable for epitaxy of III-nitrides.

2.3 Thermal expansion coefficient

Besides the lattice constant, the thermal expansion coefficient is another important physical property for substrates. The in-plane thermal expansion of single crystal ZrB_2 was measured from room temperature to 400°C [8]. Within the measured temperature range, the in-plane thermal expansion coefficient is $5.9 \times 10^{-6} \text{ K}^{-1}$, very close to that of GaN ($5.6 \times 10^{-6} \text{ K}^{-1}$). In GaN heteroepitaxy on substrates such as sapphire, SiC, and Si, wafer bending or cracking due to thermal expansion mismatch between the grown layer and substrate is a serious problem. In this regard, ZrB_2 is a superior substrate. The temperature dependence of the in-plane lattice constants of GaN and AlGaN was plotted in Figure 2 with those of ZrB_2 . Thanks to the similar thermal expansion coefficients, AlGaN maintains a good lattice match at 700°C, a typical MBE growth temperature.

Compound	a-axis	c-axis
MgB_2	3.084 Å	3.522 Å
AlB_2	3.009 Å	3.262 Å
TiB_2	3.028 Å	3.228 Å
YB_2	3.298 Å	3.843 Å
ZrB_2	3.169 Å	3.530 Å

Table I. Lattice constants of various metal diborides.

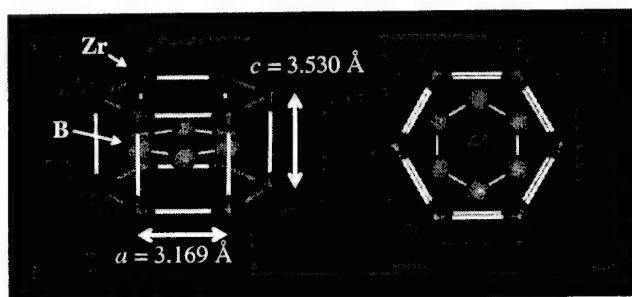


Figure 1. Crystal structure of ZrB_2 .

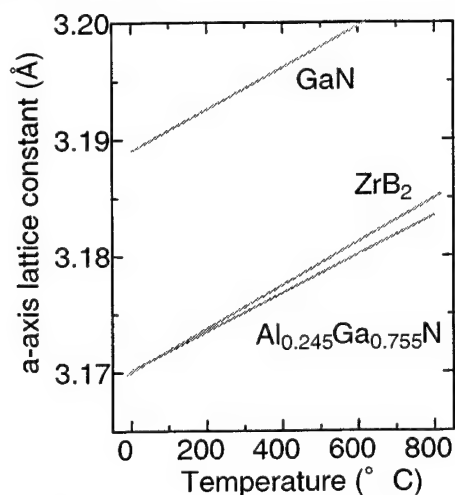


Figure 2. Temperature dependence of in-plane lattice constants of GaN, $\text{Al}_{0.25}\text{Ga}_{0.75}\text{N}$ and ZrB_2 .

2.4 Electrical and thermal conductivity

ZrB₂ is thought to be a semi-metal [12]. The electrical resistivity of single crystal ZrB₂ is on the order of $\mu\Omega\text{-cm}$ [13,14]. Thermal conductivities along the c-axis and a-axis were measured by Kinoshita *et al* by a laser flush method [Kinoshita1]. The value was 100 W/mK and 140 W/mK along the c-axis and a-axis, respectively. These values are almost three times larger than those of sapphire (30 W/mK, 50 W/mK). The values of ZrB₂ are comparable to that of silicon (150 W/mK). Compared to sapphire, ZrB₂ has a clear advantage in thermal dissipation. Of course, among possible substrates for III-nitrides, SiC has the highest thermal conductivity (300-490 W/mK).

2.5 Optical properties

To the eye the ZrB₂ substrate appears to be a good mirror, but the reflectivity for visible light is not 100%. Figure 3 shows reflectance spectra for a mirror-polished ZrB₂ (0001) substrate with an angle of incidence 5° off the normal. The reflectivity is around 60% for visible light, i.e., some light is absorbed by the substrate. Thus, unfortunately, high light-extraction efficiency structures utilizing multiple internal reflections (as reported for III-N/sapphire light-emitting diodes) can not be applied for III-N/ZrB₂. On the other hand, for LDs, optical light is confined within waveguide layers. Proper design of the laser structure can easily avoid the problem of absorption in the substrate.

Cleavage is a very effective way to fabricate the optical cavity for a LD. In the case of sapphire, the cleavage direction of the substrate is 30°-rotated against that of GaN. However, cleavage of thin ZrB₂ substrates was observed along the <11-20> direction with cleaving facets of {1-101} [15]. The direction is the same of that of GaN.

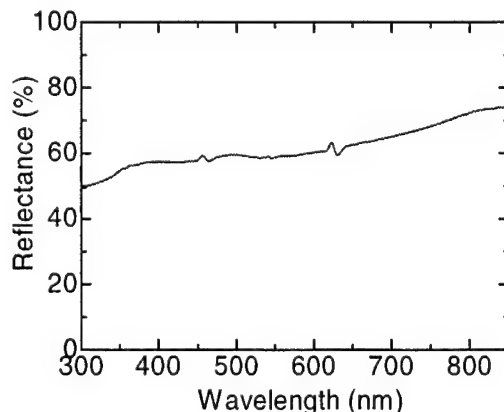


Figure 3. Reflectance from mirror-polished ZrB₂ (0001) surface. Angle of incidence is 5° off-normal.

2.6 ZrB₂ bulk growth

Otani *et al.* have studied RF heated floating zone method for TiB₂, HfB₂ and ZrB₂ [2,3,4]. Otani and Kinoshita developed the method for substrate-grade ZrB₂ bulk growth. Single crystals 10 mm in diameter and 60 mm long were successfully grown [5,8]. Thanks to melt growth, a high growth rate (moving rate of molten zone) of 20-30 mm/h can be obtained. Recently, Kinoshita reported a 20 mm-diameter and 40 mm-long single crystal [15]. Details of the bulk growth technique, crystalline quality and polishing process are given in the references listed above.

3. HETEROEPITAXIAL GROWTH

3.1 Challenges in heteroepitaxial growth of III-N on ZrB₂

As mentioned above, ZrB₂ is very attractive substrate for GaN-based nitrides. However, there are some problems to overcome. (1) Epitaxial relationship. In-plane lattice matching and cleavage direction matching described above is based on the assumption that $a\text{-axis}_{\text{GaN}}//a\text{-axis}_{\text{ZrB}_2}$. However, the chemical bonding in Zr-B and Ga-N are very different. Boron atoms form in-plane sp^2 bonding, but Ga and N atoms have tetrahedral bonding. There is a possibility that some other epitaxial relationship may be more stable than $a\text{-axis}_{\text{GaN}}//a\text{-axis}_{\text{ZrB}_2}$ due to the interface bonding between ZrB₂ and

GaN. If GaN were to grow on ZrB₂ with a 30° in-plane rotation, the presumed advantages of a-axis lattice matching and shared <11-20> cleavage direction would be completely lost. (2) Polarity. The ZrB₂ (0001) surface has no polarity, while the GaN (0001) surface has a polarity. Polarity control is very important to realize high-performance device. Interface control of GaN/ZrB₂ is essential to realize polarity control. Substrate surface treatments, polishing, etching and cleaning process, are also important.

	Crystal structure	Polarity	a-axis (Å)	Thermal Expansion (x10 ⁻⁶ /K)	Electrical Conductivity (Ω-cm)	Thermal Conductivity (W/m-K)
GaN	Hexagonal Wurtzite (2H)	Polar	3.189 Å	5.6	10 m	130
AlN	Hexagonal Wurtzite (2H)	Polar	3.112 Å -2.4%	4.2 (-1.4)	Insulator	285
Sapphire	Trigonal Corundum		2.747 Å* -16%	7.5 (+1.9)	Insulator	30-50
ZnO	Hexagonal Wurtzite (2H)	Polar	3.250 Å +1.8%	6.5 (+0.9)	40m	130
SiC	Hexagonal 4H or 6H	Polar	3.081 Å -3.5%	4.3 (-1.3)	10 m ~ S.I.	300-490
Si	Cubic Diamond		3.840 Å +17%	3.6 (-2.0)	0.1 m ~ 10 ⁴	150
Hf	Hexagonal h.c.p.		3.197 Å +2.5%	5.6 (~0)	35μ (metal)	23
ZrB ₂	Hexagonal AlB ₂		3.170 Å -0.5%	5.9 (0.3)	5 μ (semi-metal)	130

Table II. Comparison of various substrates for GaN-based nitrides. Lattice mismatch and thermal expansion difference are defined as $(a_{\text{sub}} - a_{\text{GaN}})/a_{\text{sub}} \times 100\%$ and $\Delta a/a_{\text{sub}} - \Delta a/a_{\text{GaN}}$, respectively. *The lattice constant of sapphire is the equivalent value by assuming epitaxial relationship between GaN and sapphire.

3.2 Direct growth

Direct growth of GaN and AlN were studied at the first stage. Because the lattice constant of the grown layer is nearly matched to the substrate, a buffer layer for relaxation of the lattice mismatch was thought to be not necessary. The source materials were elemental Ga and Al, and radio frequency (rf) plasma-excited active nitrogen (N*). Mirror-polished ZrB₂ (0001) crystals were used as substrates. It should be noted that growth temperature indicated in this paper is a direct reading of a thermocouple just behind the substrate, but the true substrate temperature may be lower than this. After thermal cleaning at 950~1000°C, the substrate temperature was decreased to 750°C (for GaN) or 850°C (for AlN). The nitrogen plasma cell was ignited and then the growth was initiated by supplying the group-III flux. The typical growth rates were 0.6 μm/h and 0.3 μm/h for GaN and AlN, respectively. The grown layers were characterized by X-ray diffraction (XRD) and atomic force microscopy (AFM) as well as *in situ* reflection high-energy electron diffraction (RHEED). The layer thickness was calculated from optical interference fringes using tabulated values for the refractive indices of GaN and AlN.

RHEED patterns from directly grown GaN layers were spotty all throughout the growth. The RHEED pattern after 3-h growth (thickness of 1.4 μm) is shown in Fig. 4. The pattern clearly indicates that hexagonal GaN was grown on the ZrB₂ substrate with a certain epitaxial relationship. However, the appearance of an arrow head-like spotty pattern suggests the surface is rough and faceted. Figure 5 shows XRD 2θ-scan measurement from the grown layer with an open detector slit condition. The GaN (0002) and (0004) diffraction peaks as well as the ZrB₂ (0001) and (0002) diffraction peaks were clearly observed. This result indicates the epitaxial relationship of c-axis_{GaN}//c-axis_{ZrB₂} ([0001]_{GaN}// [0001]_{ZrB₂}). High-resolution XRD measurement was also carried out to determine lattice constants. The c-

axis lattice constants of GaN and ZrB_2 were estimated to be $5.183 \pm 0.001 \text{ \AA}$ and $3.529 \pm 0.001 \text{ \AA}$, respectively. Since the c-axis lattice constant of bulk GaN is reported to be 5.185 \AA , the GaN layer grown on ZrB_2 is nearly strain-free. Assuming the GaN layer is fully relaxed at the growth temperature, a nearly strain-free condition at room temperature indicates good thermal expansion matching between GaN and ZrB_2 , as discussed above. Figure 6 shows XRD pole-figure measurements for (a) GaN (1-104) diffraction and (b) ZrB_2 (1-103) diffraction. The six-fold rotational symmetry peaks are clearly observed for both cases. The in-plane rotation angles (ϕ) for GaN (1-104) and ZrB_2 (1103) diffraction are the same. This clearly indicates the epitaxial relationship of a-axis_{GaN}//a-axis_{ZrB₂} ($[1-100]_{\text{GaN}} // [1-100]_{\text{ZrB}_2}$).

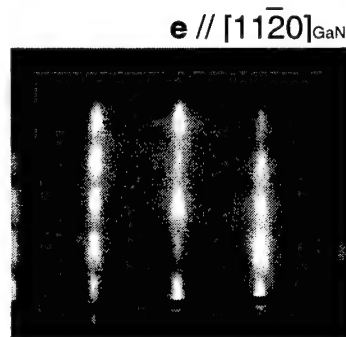


Figure 4. RHEED pattern from $1.4 \mu\text{m}$ -thick GaN layer grown on ZrB_2 (0001) substrate. Arrow head-like spot pattern for hexagonal GaN is observed, indicating rough and faceted surface.

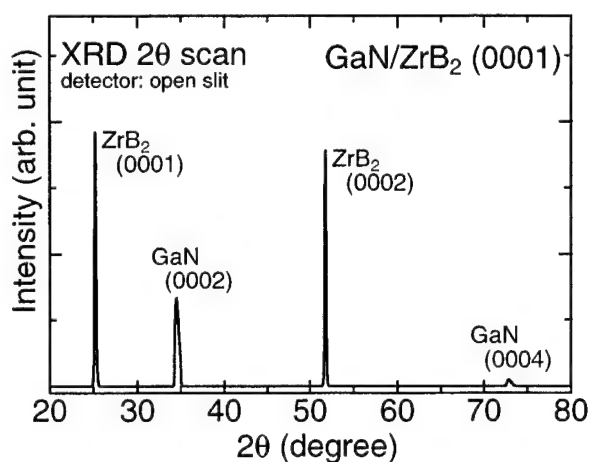


Figure 5. X-ray diffraction 2θ -scan of GaN/ ZrB_2 (0001) with open detector slit condition. FWHM of GaN diffraction is about 2-times larger than that of ZrB_2 .

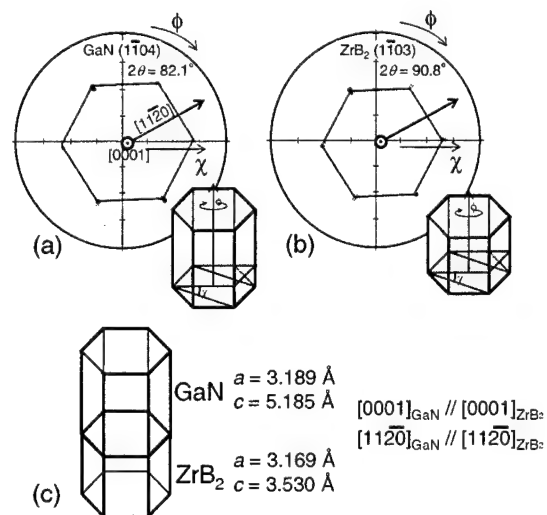


Figure 6. X-ray diffraction pole figure measurement of MBE-grown GaN on ZrB_2 (0001) substrate. (a) for GaN (1-104) diffraction and (b) for ZrB_2 (1-103) diffraction. The epitaxial relationship is illustrated in (c).

In the case of directly grown AlN, the RHEED pattern was spotty at the beginning of growth but changed to streaky gradually through the growth. After 3-h growth (thickness of $0.9 \mu\text{m}$), the RHEED pattern became sharp and streaky as shown in Fig. 7. XRD measurements revealed that the epitaxial relationship is the same as that of GaN/ ZrB_2 . Therefore, the same epitaxial relationship is expected for all $\text{Al}_x\text{Ga}_{1-x}\text{N}$ alloys regardless of composition.

GaN layers directly grown on ZrB_2 have a rough surface as shown in Fig. 8 (a) and poor crystal quality. For instance, the layer exhibits a broad and weak PL spectrum as shown in Fig. 9(a). The peak located at the highest energy, 3.471 eV , can be assigned to excitonic emission from hexagonal GaN (h-GaN). The emission located at 3.269 eV originates

from excitonic emission from cubic GaN (c-GaN)[16]. Broad emissions located at 3.42 eV and 3.34 eV are related to extended defects [17,18,19]. In addition, the commonly observed yellow luminescence is observed around 2.2 - 2.3 eV.

In an attempt to improve the crystal quality, direct growth of GaN at an elevated temperature was investigated. The growth was carried out at 850°C using various Ga fluxes with a fixed N* flux condition. In experiments on sapphire substrates at the same temperature, GaN growth was observed for all values of the Ga flux. However, for ZrB₂ substrates no growth was observed even under a slightly Ga-rich condition. Growth occurred only under a strongly Ga-rich condition. This indicates that nucleation of GaN on ZrB₂ is very difficult at this temperature.

The RHEED pattern from the layer grown under excess Ga supply was spotty all throughout the growth, which suggests three-dimensional growth of h-GaN. Each spot is diffuse and its intensity is much weaker than that of medium-temperature (750°C) growth mentioned previously. From SEM observations of this layer (not shown), pillar (or whisker)-like growth of GaN is observed. It is thought that too much excess Ga results in such an abnormal growth mode.

Figure 9 (b) shows a low-temperature PL spectrum from the layer grown at 850°C. Compared to the medium-temperature case shown in Fig. 9 (a), each emission peak becomes sharp and the peak intensity increases greatly. Two emissions, an excitonic emission from h-GaN located at 3.475 eV and a defect-related emission located at 3.418eV are dominant. The excitonic emission from c-GaN becomes much weaker.

The increase of growth temperature in the direct growth results in the improvement of optical quality but deterioration of surface morphology. These results indicate that it is impossible to obtain a high-quality GaN layer by the direct growth.

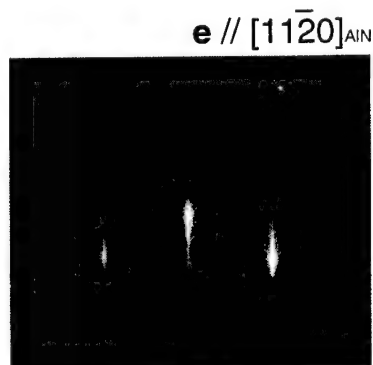


Figure 7. RHEED pattern from 0.9 μm-thick AlN layer grown on ZrB₂ (0001) substrate. Sharp streak pattern of AlN is observed, indicating smooth surface.

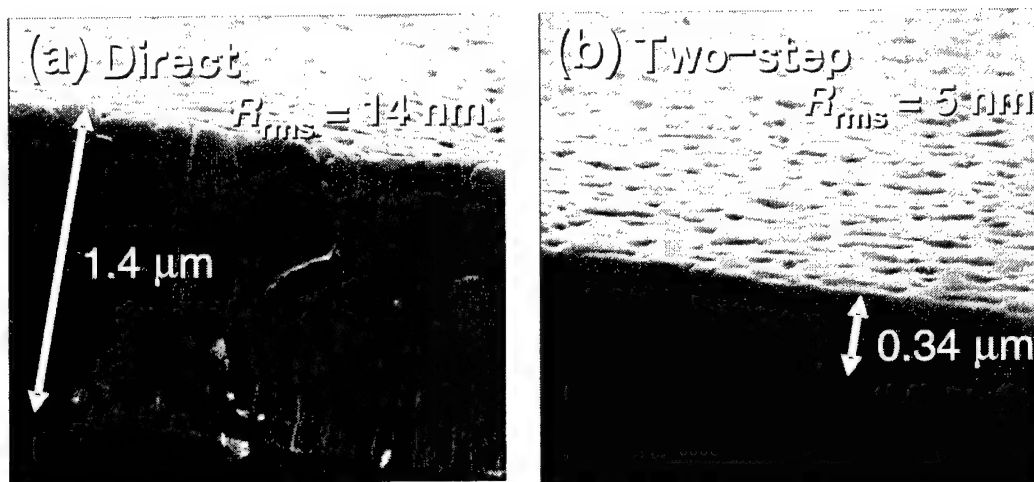


Figure 8. SEM images of GaN layers grown (a) directly on ZrB₂ substrate and (b) by two-step procedure.

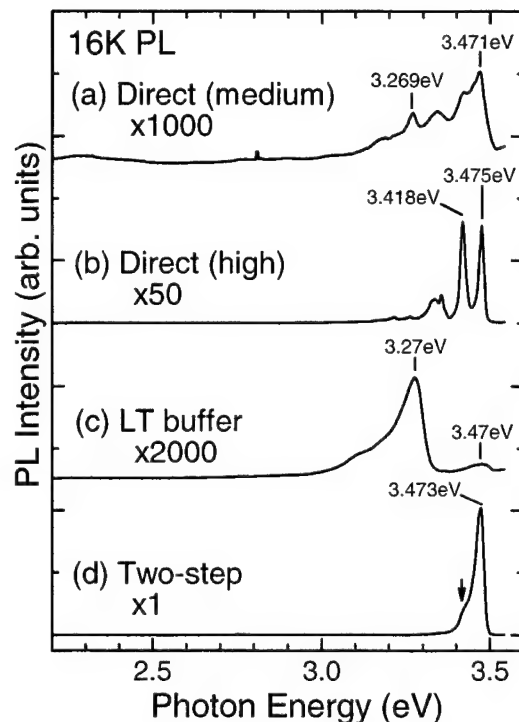


Figure 9. 16 K PL spectra for (a) direct growth at a medium temperature, (b) direct growth at a high temperature, (c) low-temperature grown buffer layer, and (d) two-step growth.

3.4 Two-step growth process

To control the initial nucleation, low-temperature (LT)-grown GaN buffer layers were investigated. Amorphous or poly-crystalline LT-grown layer should not be used in the case of ZrB_2 , because such highly defective nucleation layers would prevent transfer of the substrate lattice constants to the main epilayer. After thermal cleaning, a GaN layer was grown at 500°C for 3 min. Just after starting the growth, a sharp and intense streak pattern appeared, indicating epitaxial growth of a well-oriented crystalline layer with a flat surface. The thickness was around 30 nm. From SEM observations, most of surface is flat but some hillocks were observed, which may originate from defects (small bumps) on the as-received substrate. From AFM measurements, the root-mean-square (rms) roughness for the area without hillocks was evaluated to be less than 1 nm.

Figure 9 (c) shows low-temperature PL from the buffer layer. Due to the very low film thickness and a low growth temperature, the PL intensity is quite weak. Two broad peaks located at 3.27 eV and 3.47 eV are observed, indicating the LT-grown buffer layer is a mixture of c-GaN and h-GaN. It is consistent with an earlier study that found a low-temperature and Ga-rich growth condition resulted in the growth of c-GaN in plasma-assisted MBE [20].

A GaN layer was grown at 800°C on the buffer layer mentioned above. By optimizing the III/V ratio, a streaky RHEED pattern could be achieved all throughout the growth. The SEM images are shown in Fig. 8 (b). The GaN layer grew as a continuous film. The surface is still rather rough but the rms roughness measured by AFM was much improved compared to that of directly grown GaN. Figure 9 (d) shows a PL spectrum from the layer. The peak intensity is 50 times larger than that of the directly-grown layer. The defect-related emissions are strongly suppressed and only excitonic emission from h-GaN becomes dominant. It should be noted that the 3.418 eV emission still exists as a shoulder of the excitonic emission. Optimization of the growth conditions and the thickness of the buffer layer will be required to eliminate the shoulder.

Since nominally undoped GaN grown in our MBE system exhibited n-type conductivity, the origin of excitonic emission is thought to be donor-bound exciton transitions. The peak energy of the emission from the grown layer (3.473 eV for two-step growth) is larger than that of free-standing bulk GaN (3.471 eV) [21], but smaller than that of GaN

grown on sapphire (typically 3.480 eV for 1 μm -thick GaN). It indicates that the layer on ZrB_2 undergoes much weaker compressive stress compared to that grown on sapphire.

The polarity of the GaN layer was assessed by etching in KOH solution. Ga-polarity surface is resistant but the N-polarity surface is rapidly etched by this solution. SEM images after KOH etching are shown in Fig. 10. Ga-polarity and N-polarity GaN domains coexist together on a length scale of microns. This suggests that small fluctuations in the initial stage of growth and/or substrate surface inhomogeneity or contamination may affect the polarity of GaN grown on ZrB_2 . At the very least uniform polarity (and preferably Ga-polarity) is required for typical device applications. Control of the substrate surface and the initial stages of growth are essential.

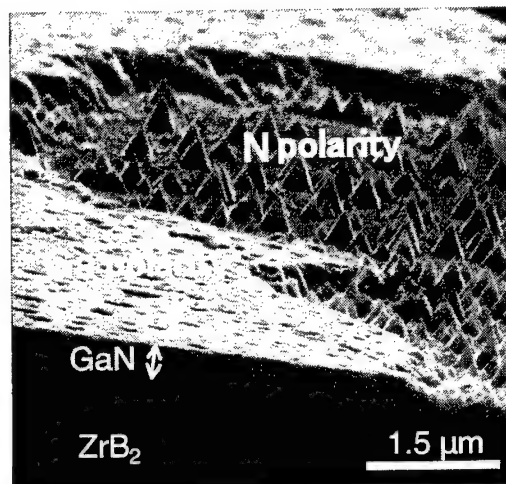


Figure 10. SEM image of GaN layer on ZrB_2 after KOH solution etching. Some parts of the surface were etched off, indicating coexistence of Ga-polar and N-polar GaN domains.

4. SURFACE TREATMENT OF SUBSTRATE

Heteroepitaxial growth of GaN and AlN were presented in the previous section. The epitaxial relationship and the effect of a two-step growth procedure using a LT-grown GaN nucleation layer were confirmed. However, the epilayer quality was insufficient for device applications. One possible reason for this is thought to be the presence of contaminants on the ZrB_2 surface prior to growth. In fact, the RHEED pattern from the ZrB_2 surface after thermal cleaning at 1000°C in the MBE chamber was faint compared to that from subsequently grown GaN layers, indicating insufficient cleaning. Although flash annealing at 1830°C was shown to yield a clean ZrB_2 surface [22,23], such high temperatures are not accessible in standard MBE systems. In this section, characterization of ZrB_2 surfaces by XPS and RHEED and various techniques for surface cleaning were discussed. MBE growth of GaN was also carried out to evaluate these new cleaning methods.

4.1 Characterization of as-received substrate

XPS spectra from an as-received substrate without thermal cleaning were measured. Besides Zr and B, C and O were also detected. After *in-situ* 500°C thermal cleaning the C signal disappeared, indicating that C exists mainly in the form of adsorbates such as hydrocarbons or carbon oxides. On the other hand, the O 1s peak remained even after thermal cleaning at 1000°C, indicating that O forms a stable compound after reaction with ZrB_2 . Figure 11 (a) shows the XPS spectra from ZrB_2 after *in-situ* 1000°C thermal cleaning of Zr 3d_{3/2}, Zr 3d_{5/2} and B 1s peaks. The Zr 3d_{5/2} peak split into two peaks, 178.5 eV and 182.7 eV. (The Zr 3d_{3/2} split into two, as well.) Reported values for metal Zr and ZrO_2 are 178.3 eV and 182.2 eV, respectively. The peak with larger binding energy (as indicated by arrows) agrees with the value expected for ZrO_2 .

Figure 12 (a) shows the RHEED pattern after thermal cleaning at 1000°C. A spotty pattern appeared superimposed on a faint streak pattern (the latter is difficult to see in the figure). Since the spacing (= in-plane lattice constant) of the faint streak pattern is almost the same as that of GaN, the faint streaks must correspond to the ZrB_2 crystal. The spotty pattern

corresponds to a twinned cubic crystal with calculated lattice constant $\sim 5.1 \text{ \AA}$ (14% smaller than that expected for ZrB_2), in agreement with values reported for cubic ZrO_2 . XPS and RHEED analysis clearly indicate the existence of a ZrO_2 surface layer.

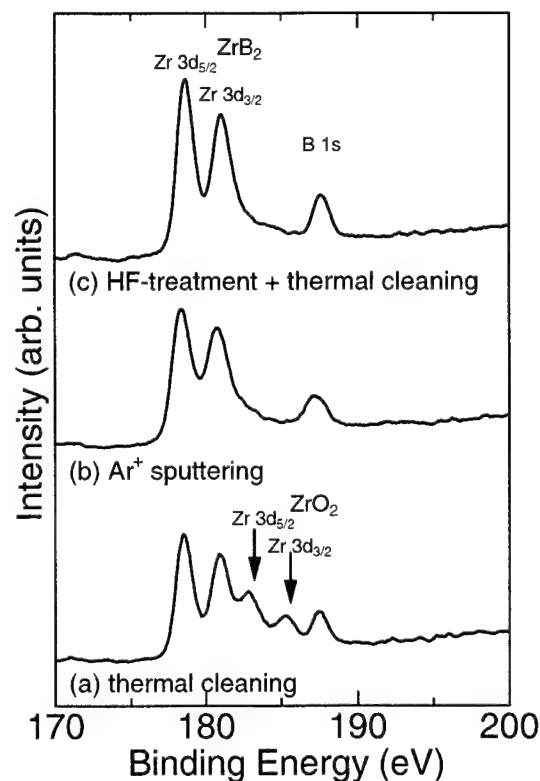


Figure 11. XPS from ZrB_2 substrates. (a) substrate with thermal cleaning, (b) with Ar^+ sputtering and (c) with HF-treatment and thermal cleaning. Zr 3d peaks split into two, indicating two different Zr compounds, ZrB_2 and ZrO_2 exist at the surface.

3.2 Ion sputtering cleaning

2 keV Ar^+ sputtering was carried out to remove the surface layer. After sputtering, the Zr 3d peaks associated with ZrO_2 disappeared as shown in Fig. 11 (b). The peaks with smaller binding energy can therefore be attributed to ZrB_2 . It should be noted that there is almost no chemical shift for Zr in ZrB_2 . The O 1s peak became much weaker but still exists even after prolonged sputtering. One possible explanation is re-oxidization due to insufficient XPS chamber background pressure and/or the purity of the sputtering gas. Figure 12 (b) shows the RHEED pattern after sputtering. The spotty pattern disappeared and a ZrB_2 streak pattern was clearly observed. Thermal annealing after sputtering did not significantly alter the RHEED pattern. Thus Ar^+ sputtering may be an effective surface treatment method. Surface damage due to ion bombardment is not obvious from the RHEED analysis, but nevertheless a gentler process such as wet chemical treatment might be preferable. Moreover, Ar^+ sputtering is not available in all MBE systems.

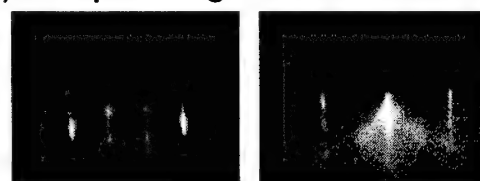
3.3 Chemical treatment

Three different solutions, KOH, H_2SO_4 , and HF were examined. Surface oxides comparable to those on as-received ZrB_2 were detected for the KOH- and H_2SO_4 -treated substrates. On the other hand, HF treatment had a significant effect. XPS analysis for HF-treated substrates was carried out. To remove surface adsorbates (mainly water vapor), the substrate was thermally cleaned before the measurement. The intensity of the O 1s peak after HF treatment was greatly

(a) thermal cleaning



(b) Ar^+ sputtering + thermal cleaning



(c) HF-treatment + thermal cleaning

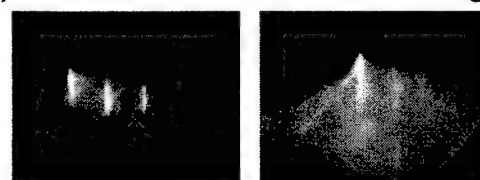


Figure 12. RHEED patterns from ZrB_2 substrates after thermal cleaning. (a) as-received, (b) Ar^+ sputtered and (c) HF-treated substrates.

reduced versus the as-received substrate, and was comparable to that of the Ar^+ sputtered substrate. As shown in Fig. 11 (c), no splitting was observed for the Zr 3d peak (only Zr 3d bounded to B was observed.) Judging from the XPS results, HF treatment has the almost same effect as Ar^+ sputtering. The RHEED pattern for the HF-treated substrate after thermal cleaning at 1000°C is shown in Fig. 12 (c). A sharp and intense streak pattern was evident. Compared to Ar^+ sputtering, wet processes are gentler and should result in better crystalline quality at the surface.

3.4 Growth of GaN on the treated ZrB_2 surface

To evaluate the effect of substrate treatment, GaN epilayers were grown on as-received and HF-treated substrates with the same growth parameters. For both substrates, thermal cleaning at 1000°C for 30 min was performed just before the growth. The epilayers were grown by a two-step procedure as described above. Figure 13 shows the 16 K photoluminescence spectra for two epilayers. GaN grown on the HF-treated substrate exhibited at least 20 times higher luminescence intensity and reduced defect-related emission, clearly indicating the better crystalline quality achieved with optimal substrate preparation. Note that the MBE growth conditions used in this experiment have been optimized using as-received substrates possessing significant native oxide layers. However when using HF-treated substrates the optimal growth conditions may be different, since suitably prepared substrates are largely free of oxides and have compositions approaching stoichiometric ZrB_2 . Further optimization of the MBE growth process is expected to yield superior GaN epilayers.

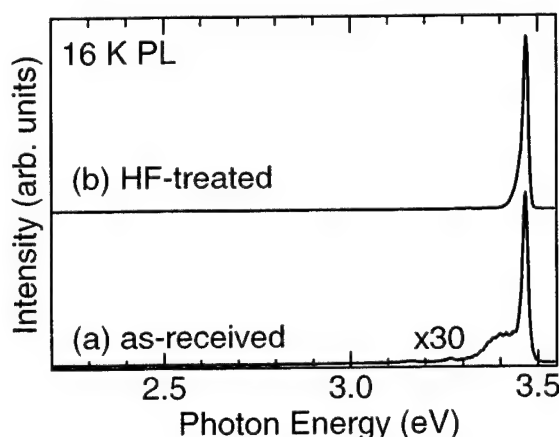


Figure 13. 16 K PL spectra of GaN layers grown by two-step procedure on (a) as-received substrate and (b) HF-treated substrate. GaN grown on HF-treated substrate exhibits at least 20 times more intense luminescence.

5. CONCLUSION

In this paper, properties of electrically conductive ZrB_2 were reviewed. Perfect lattice matching to $\text{Al}_{0.25}\text{Ga}_{0.75}\text{N}$ and thermal expansion coefficient matching, good thermal conductivity and cleavage make the compound very attractive as a substrate for GaN-based LDs. Heteroepitaxial growth of GaN and AlN on the substrate by MBE was described. The epitaxial relationship $a\text{-axis}_{\text{III-N}}/a\text{-axis}_{\text{ZrB}_2}$ assures that lattice matching is in fact achieved and that cleavage of ZrB_2 can be applied for cavity formation. However, it was also revealed that difficulties in initial nucleation of III-N on ZrB_2 resulted in a rough growth surface and inferior crystalline quality. A two-step growth procedure using epitaxial low-temperature-grown GaN as an initial nucleation layer was proposed. Characterization of the surface condition of the ZrB_2 substrate by XPS and RHEED suggests the existence of ZrO_2 at the surface. It was found that the native oxide can be removed by Ar^+ sputtering or etching in HF solution. The HF treatment resulted in improvement of the GaN crystalline quality.

However, the crystalline quality of GaN grown on ZrB_2 is still inferior compared to, for example, GaN grown on SiC using the same MBE system. In the case of heteroepitaxy of III-nitrides on SiC, precise control of the SiC surface is a

key to realize high quality epitaxial growth [24,25]. In this sense, surface control of ZrB_2 has much room for improvement. Recently, interesting theoretical calculations were reported by Iwata *et al* [26], which emphasized that precise control of the ZrB_2 surface and ZrB_2/GaN interface is essential to control the polarity of grown layers. III-N growth processes on ZrB_2 must still be further optimized to fully exploit the benefits of this novel substrate.

ACKNOWLEDGEMENT

ZrB_2 surface analysis was carried out by Mr. H. Yamashita and Dr. R. D. Armitage in the author's group. The author would like to thank Mr. Hiroyuki Kinoshita, Dr. Shigeki Otani, Mr. Shinji Inoue and Prof. H. Matsunami for valuable discussions. ZrB_2 substrates used in this study were provided from KYOCERA Corporation, Japan. XRD and SEM were carried out in the Kyoto University Venture Business Laboratory (KU-VBL). This work is partly supported by the Kyoto Nano-tech cluster project from the Ministry of Education of Japan.

REFERENCES

1. Power diffraction file, Joint Committee of Power Diffraction Standard (JCPDS) No. 34-423.
2. S. Otani, Y. Ishizawa, J. Crystal Growth 140 (1994) 451.
3. S. Otani and Y. Ishizawa, J. Crystal Growth 165 (1996) 319.
4. S. Otani, M.M. Korsukova and T. Mitsuhashi, J. Crystal Growth 186 (1998) 582.
5. S. Otani and H. Kinoshita, Abstr. 13th Int. Conf. Crystal Growth, Aug. 2001, 02a-K32-11.
6. J. Suda and H. Matsunami, Abstr. 13th Int. Conf. Crystal Growth, Aug. 2001, 02a-SB2-20.
7. J. Suda and H. Matsunami, J. Crystal Growth 237-239 (2002) 210.
8. H. Kinoshita, S. Otani, S. Kamiyama, H. Amano, I. Akasaki, J. Suda, and H. Matsunami, Jpn. J. Appl. Phys. 40 (2001) L1280.
9. R. Liu, A. Bell, F. A. Ponce, S. Kamiyama, H. Amano and I. Akasaki, Appl. Phys. Lett. 81 (2002) 17.
10. B. Post, *Boron, Metallo-Boron Compounds and Boranes*, Wiley, New York (1964).
11. H. Ihara, M. Hirabayashi and Hiroshi Nakagawa, Phys. Rev. B 16 (1977) 726.
12. T. Tanaka, Y. Ishizawa E. Bannai and S. Kawai, Solid. State. Commun. 26 (1978) 879.
13. J. Piper, J. Phys. Chem. Solids. 27 (1966) 1907.
14. W. Gordon Jr. and S. B. Soffer, J. Phys. Chem. Solids. 36 (1975) 627.
15. H. Kinoshita, S. Otani, S. Kamiyama, H. Amano, I. Akasaki, J. Suda and H. Matsunami, Jpn. J. Appl. Phys. 42
16. H. Okumura, K. Ohta, K. Ando, W. W. Rühle, T. Nagatomo, and S. Yoshida, Solid State Electron. 41 (1997) 201.
17. C. Wetzel, S. Fischer, J. Krüger, E. E. Haller, R. J. Molnar, T. D. Moustakas, E. N. Mokhov, and P. G. Baranov, Appl. Phys. Lett. 68 (1996) 2556.
18. Y. T. Rebane, Y. G. Shreter, and M. Albrecht, phys. stat. sol. (a) 164 (197) 141.
19. S. Strauf, P. Michler, J. Gutowski, H. Selke, U. Birkle, S. Einfeldt, and D. Hommel, J. Cryst.
20. H. Okumura, K. Balakrishnan, H. Hamaguchi, T. Koizumi, S. Chichibu, H. Nakanishi, T. Nagatomo, and S. Yoshida, J. Cryst. Growth 189/190, 264 (1998).
21. C. Kirchner, V. Schwegler, F. Eberhard, M. Kamp, K. J. Ebeling, K. Kornitzer, T. Ebner, K. Thonke, R. Sauer, P. Prystawko, M. Leszczynski, I. Grezegory, and S. Porowski, Appl. Phys. Lett. 75 (1999) 1098.
22. T. Aizawa, W. Hayami and S. Otani, Phys. Rev. B 65 (2001) 24303.
23. T. Aizawa, W. Hayami and S. Otani, J. Chem. Phys. 117 (2002) 11310.
24. J. Suda, K. Miura, M. Honaga, Y. Nishi, N. Onojima, and H. Matsunami, Appl. Phys. Lett. 81 (2002) 5141-5143.
25. N. Onojima, J. Suda and H. Matsunami, Jpn. J. Appl. Phys. 42 (2003) L445-L447.
26. J.-I. Iwata, K. Shiraishi and A. Oshiyama, phys. status sol. (c) 0 (2003) 2482.

Optical and electrical properties of interdigitated InGaN/GaN green light emitting diodes

Jinhyun Lee^a, Petr G. Eliseev^{a,b}, Marek Osinski^{a,*}, Dong-Seung Lee^c, Jeffrey C. Ramer^c,
Doru I. Florescu^c, and Eric A. Armour^c

^aCenter for High Technology Materials, University of New Mexico, 1313 Goddard SE,
Albuquerque, New Mexico 87106-4343

^bP. N. Lebedev Physics Institute, Russian Academy of Sciences, Moscow, Russia

^cVeeco TurboDisc Operations, 394 Elizabeth Avenue, Somerset, New Jersey 08873

ABSTRACT

Properties of InGaN/GaN multiple-quantum-well (MQW) light-emitting diodes (LEDs) grown by MOCVD on sapphire substrates are investigated over a temperature range from 290 to 340 K. Two types of wafers are used to fabricate the devices: one with Mg dopants in *p*-type epilayers pre-activated in N₂ ambient for 4 min at 800 °C, and the other as-grown, without any pre-activation of Mg acceptors. Measured specific resistances of *p*-side contacts are $1.49 \times 10^{-4} \Omega \text{cm}^2$ for contacts on pre-activated samples annealed at 650 °C for 4 min, and $1.55 \times 10^{-5} \Omega \text{cm}^2$ for contacts on as-grown samples annealed at 600 °C for 30 min. Based on the specific contact resistance experiments, interdigitated LEDs are fabricated using either the standard annealing procedures (separate annealings for *p*-type conduction activation and for ohmic contact formation) or a single-step annealing process (simultaneous annealing for activation of *p*-type conduction and for ohmic contact formation). In devices fabricated using the standard annealing procedures, the electroluminescence (EL) peak position at 300 K is at 2.379 eV (~521.3 nm) and the full width at half maximum (FWHM) is ~132 meV, while in devices fabricated using a single-step annealing, the EL peak position shows a red shift by ~10 meV without affecting the FWHM. Over the entire voltage range up to 4 V, tunneling is the dominant carrier transport mechanism. The operating voltage is comparable in both types of LEDs, and the output power of LEDs fabricated using the single-step annealing process is somewhat improved.

Keywords: Wide-bandgap group-III nitrides, green light emission, InGaN/GaN heterostructure, interdigitated LEDs

1. INTRODUCTION

Group-III nitrides are the most important materials for solid-state sources of UV and short-wavelength visible light. InGaN quantum wells are used as active medium in blue and green light emitting diodes (LEDs) and diode lasers [Nakamura 1995], [Nakamura 2000]. These light sources can be applied for color displays, traffic signals, indicators, *etc.* They are compact, effective and display high-speed performance. Commercial LEDs manufactured by the industry leader Nichia Chemical Industries demonstrate overall room-temperature efficiencies of 5-10 %. Most of these devices are fabricated by epitaxial growth on strongly lattice-mismatched sapphire substrates. Consequently, threading dislocation densities are extremely high ($10^8 - 10^{10} \text{ cm}^{-2}$). Nonetheless, this is not an obstacle for high external efficiency of emission, even though dislocations have been shown to act as nonradiative recombination centers in group-III nitride materials [Sugawara 1998], [Hino 2000]. For further progress in the application of nitride-based devices in lighting, illumination and communication, it will be important to improve the material quality and to overcome the limitation of relatively small emitting area in Nichia-type LEDs.

The surface-emitting design of LEDs implies light penetration through the electrode regions. In order to keep optical losses low, semi-transparent *p*-side electrodes are typically used. Such electrodes do not allow to scale up the emitting area because of associated increase in the lateral resistance for current spreading, resulting in significant current crowding. The latter phenomenon is known to be a contributing factor in the device degradation [Barton 1998]. An interdigitated configuration has been investigated as an alternative version of LED design [Guo 2001], [Kim 2002],

*Contact author: Email: osinski@chtm.unm.edu; Telephone (505) 272-7812; Fax (505) 272-7801; <http://www.chtm.unm.edu>

[Chitnis 2002]. Some power performance improvement was demonstrated [Kim 2002], and power saturation was observed to occur at higher driving currents [Chitnis 2002].

In this paper, we present results of fabrication and characterization of interdigitated LEDs with increased area of surface emission ($4 \times 0.443 \text{ mm}^2$), operating in green spectral region (peak wavelength $\sim 520 \text{ nm}$). We compare two types of structures fabricated using different activation and processing procedures. One type is fabricated using routine processing of pre-activated wafers (4-min-long thermal annealing at 800°C) and another type is processing of as-grown wafer with combined activation and contact annealing (30-min long annealing at 600°C). It will be shown that “one-step annealing” leads to satisfactory results; therefore, it is possible to exclude the preliminary acceptor activation step.

2. SAMPLE GROWTH AND FABRICATION

85-nm $p\text{-GaN}$ ($5 \times 10^{17} \text{ cm}^{-3}$)
25-nm $p\text{-Al}_x\text{Ga}_{1-x}\text{N}$ ($1 \times 10^{17} \text{ cm}^{-3}$, $x=0.15$)
4× 2-nm undoped InGaN 12.5-nm GaN:Si ($1 \times 10^{16} \text{ cm}^{-3}$)
1.5- μm $n\text{-GaN}$ ($3 \times 10^{18} \text{ cm}^{-3}$)
2- μm undoped GaN
30-nm GaN buffer
(0001) sapphire

Fig. 1. Structures of multiple quantum well wafers used for green-LED fabrication. The barrier was slightly doped with Si.

High resolution X-ray diffraction (HRXRD) was performed with a $K_{\alpha 1}$ radiation as an excitation line to estimate the alloy composition and to analyze the crystalline quality. PL mapping at RT was used to determine the bandgap of materials and the corresponding variation in composition. The indium and aluminum compositions were estimated based on the lattice constant and the bandgap energy measured using HRXRD and UV-PL. Atomic force microscopy (AFM) was used to verify the surface morphology and density of threading dislocations. RT Leighton and Hall measurements were performed to investigate the electrical properties of the layers.

InGaN/GaN heterostructures were grown on (0001) sapphire by MOCVD. TMGa, TMAI, TMIn, and NH_3 were used as the source precursors for Ga, Al, In, and N, respectively. SiH_4 was used for n -type doping and Cp_2Mg was used for p -type doping. First of all, 30-nm-thick GaN buffer layers were grown on sapphire at 525°C (500 Torr) followed by 2- μm -thick undoped GaN and 1.5- μm -thick heavily doped n -type GaN:Si at 1080°C (200 Torr), in which their electron concentration was $5 \times 10^{18} \text{ cm}^{-3}$. InGaN/GaN heterostructures were used for quantum wells and barriers. Four quantum wells consisted of with 2-nm-thick undoped $\text{In}_x\text{Ga}_{1-x}\text{N}$ ($x=28\%$) at 730°C (100 Torr) and 9-nm-thick slightly Si-doped GaN at 800°C (100 Torr), where its electron concentration was $1 \times 10^{16} \text{ cm}^{-3}$. Electron blocking layer of 25-nm $\text{Al}_x\text{Ga}_{1-x}\text{N}$:Mg layer ($x=15\%$) was grown at 980°C (200 Torr), and 85-nm-thick Mg-doped GaN contact layers for green sample were grown at 980°C (200 Torr), where their hole concentrations was $5 \times 10^{17} \text{ cm}^{-3}$. Schematic illustration of MQW diode structure is shown in Fig. 1.

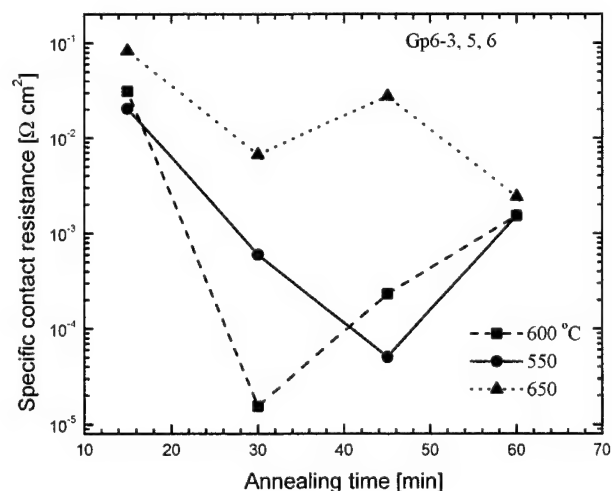


Fig. 2. Specific contact resistances as a function of annealing time for various temperatures. The samples were annealed in furnace in N_2 ambient.

Specific contact resistances were measured from activated and non-activated samples. 10-nm Ni/100-nm Au were deposited on both samples by e-beam evaporator. Specific contact resistance was obtained $1.49 \times 10^{-4} \Omega \text{ cm}^2$ at 650 °C for 4 min in N_2 ambient from the activated sample. The lowest value of specific contact resistance from one step annealing at 600 °C for 30 min in N_2 ambient is $1.55 \times 10^{-5} \Omega \text{ cm}^2$, which is about 10 times lower than that of the activated sample annealed at 650 °C for 4 min. Thus the optimal condition for the lowest specific contact resistance with one-step annealing process is at 600 °C for about 30 min, as shown in Fig. 2.

The Gp6-12-2 sample was prepared without pre-activation of Mg-dopant in *p*-type materials and interdigitated LEDs were fabricated with single-step annealing processes: activation of Mg dopant, and *n*- and *p*-side ohmic contact formation were all accomplished by a single annealing process at 600 °C in N_2 ambient. Prior to metal deposition, the Gp5-4-2 sample was pre-activated by annealing at 800 °C for 4 min in N_2 ambient in order to induce *p*-type conductivity. Subsequently, interdigitated LEDs were fabricated according to specific contact resistance experiments: *n*- and *p*-ohmic contacts annealed at 650 °C for 4 min in N_2 ambient. The basic dimensions of interdigitated devices are shown in Fig. 3.

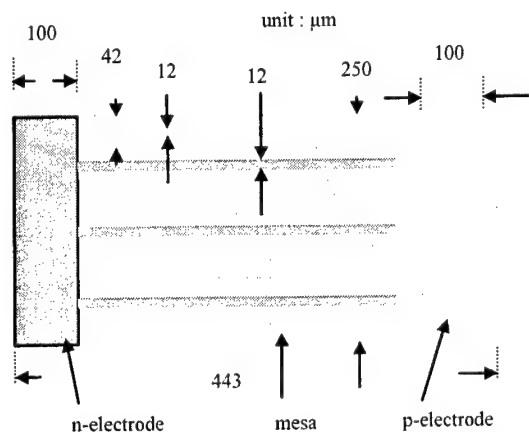


Fig. 3. Schematic drawing of an interdigitated LED. The Ni/Au contacts are deposited on the *p*-side mesas, while the Ti/Al/Pt/Au contacts are deposited on the *n*-side exposed by etching. The actual size of the interdigitated device is $443 \times 4000 \mu\text{m}^2$.

0.9-μm-deep mesas were etched using inductively coupled plasma (ICP) with Ar and Cl_2 gases. The Ni/Au *p*-side ohmic contact was then deposited on top of the mesa. Subsequently, Ti/Al/Pt/Au *n*-side ohmic contacts were deposited. The devices were then annealed at 650 °C for 4 min for Gp5-4-2 sample, and annealed at 600 °C for 30 min for Gp6-12-2 sample. Ti/Au pads were deposited for wire bonding. All metals were deposited in electron-beam evaporator.

The backside of sapphire in the samples was polished with diamond lapping films of particle sizes ranging from 3 μm to 0.5 μm. For the mirrors (for the reflection of light), 1-nm Cr/200-nm Al/50-nm Ni metal films were deposited on the sapphire. The samples were mounted on copper plates by soldering. Gold wire bonding was performed from Ti/Au *n*- and *p*-pads on the samples to Ti/Au coated semi-insulating GaAs pads on the copper plates. Electroluminescence (EL) spectra were measured from the edge of the green LEDs with a CVI spectrometer, DK 480, and a cooled GaAs photomultiplier. The output power of the green LEDs was detected from GaN topside with a Newport optical power-meter, model 1830-C. Current-voltage characteristics were measured by HP 4140B picoammeter.

3. EXPERIMENTAL RESULTS

EL spectra of 4 mm long, interdigitated LEDs between 290 and 340 K are shown in Fig. 4. Peak position of Gp5-4-2 is at $\sim 2.379 \text{ eV}$ ($\sim 521 \text{ nm}$), and full width at half maximum is $\sim 132 \text{ meV}$ at 300 K, respectively; while peak position of group Gp6-12-2 is at $\sim 2.388 \text{ eV}$ ($\sim 519 \text{ nm}$), and full width at half maximum is $\sim 134 \text{ meV}$ at 300 K. Peak position of LEDs annealed at 600 °C for 30 min is higher than those annealed at 650 °C for 4 min. This might be related to redistribution of indium during annealing process. The peak position of each LED is dependent on the dimension of *p*-contact area, which means peak position depends on the current density. As increase pumping rate, the peak position shift towards higher energy side.

As temperature increases from 290 to 340 K, the spectral peak of EL red-shifts monotonically, and the FWHM increases (see Fig. 5). The spectral shift is resulted by temperature-induced band-gap shrinkage. Notice that spectral peak position

of sample Gp6-12-2 remains larger by ~10 meV than that of sample Gp5-4-2 in whole temperature range. The difference between these samples is caused by different thermal treatment (there was a rapid high-temperature annealing in sample Gp5-4-2). Usually, thermal annealing of quantum-well structures leads to intermixing that accompanied with blue shift of spectral peak. It occurs due to some decrease of the average indium content during QW-intermixing. We see that it is not the case in sample Gp5-4-2. According to the band-tail model [Eliseev 1997a], the peak position in InGa_N depends not only on average alloy composition but also on the band-tail energy parameter σ . The latter is associated with fluctuations of indium content and correlated with average indium content. We have to emphasize that the thermal annealing in green-emitting InGa_N-based QW structures is a more complicated process than the QW intermixing in typical III-V alloys, such as InGaAs. The point is that annealing in the unstable alloy (in the immiscibility gap) is accompanied with segregation of alloy components rather than their intermixing. When segregation in the alloy occurs, some indium-rich clusters can accumulate more indium, and their energy position shifts to lower energy. This could be a tentative explanation of the observed spectral difference. Such a hypothesis should be verified by additional experiments. At this point, there is no other evidence for this explanation. The difference in the FWHM is rather small to compare (see Fig. 5). The bandwidth is dependent on temperature: therefore, it exceeds the inhomogeneous bandwidth, associated with the parameter σ . The temperature dependence of the bandwidth is produced by increase of the homogeneous component of broadening that is associated with collisional relaxation (due to involvement of optical phonons). Usually, this component is dominant at room and higher temperatures.

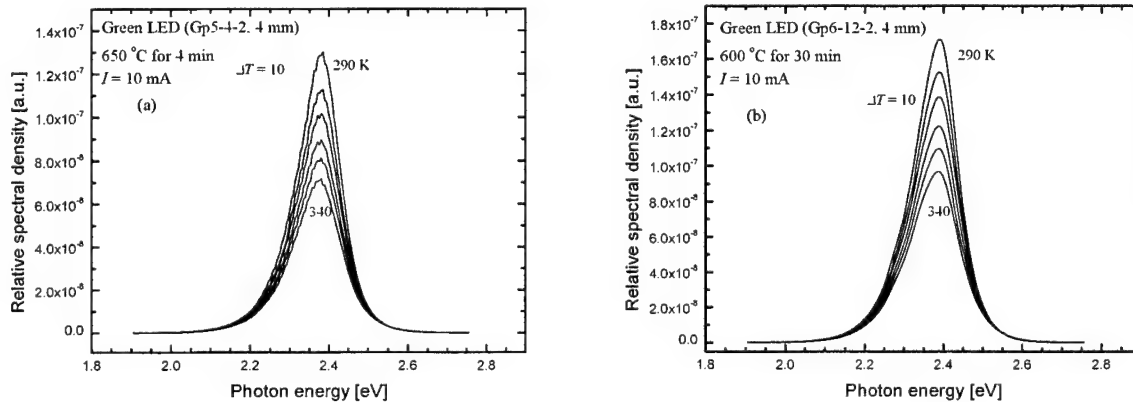


Fig. 4. EL spectra of 4 mm long-interdigitated green LEDs between 290 and 340 K.

The I - V curves illustrated in Fig. 6 can be interpreted in terms of two series resistors, with an ohmic series resistance of the diode R_s and a nonlinear resistance of the p - n junction (plus other possible depletion regions, if any). The latter can be represented by a simple expression

$$I(V_{pn}) = I_s \exp[eV_{pn}/E(T)] , \quad (1)$$

where V_{pn} is the junction voltage, I_s is the "saturation current" in traditional terminology, e is the electron charge, and $E(T)$ is the temperature-dependent energy parameter replacing the traditional term $nk_B T$ (where n is the ideality factor, k_B is the Boltzmann constant, and T is temperature).

The energy parameter E has different values in three regions: below 0.6 V, it is close to thermal diffusion transport with $n = 2$ ($E \approx 0.0517$ eV), and 0.6-1.7 V and above 1.7 V regions, it indicates tunneling ($E \gg 0.0517$ eV). Tunneling is the dominant transport mechanism in LEDs of group-III nitrides [Eliseev 1997b], [Franssen 2003], [Perlin 1996]. One feature of tunneling mechanism is that the slope of I - V curves is independent of temperature [Perlin 1996]. In the temperature range of 290-340 K, the slope indeed remains constant.

The reverse-bias current of 4-mm-long interdigitated green LEDs for both groups is shown in Fig. 7. The perimeter of interdigitated LEDs is larger than that of Nichia type LEDs. As the device size increases, its perimeter is proportional to

its size. Thus, in the case of interdigitated LEDs the role of sidewalls fabricated by dry or wet etching becomes more important. According to [Pernot 1998], under low voltage bias of different perimeters of devices, the leakage current on the etched surface of p - n junction GaN diodes is dominant compared to the current leakage through the volume of devices. However, based on band-to-band tunneling current in reverse bias [Forrest 1980], the following expression can be derived [Eliseev 1997b]:

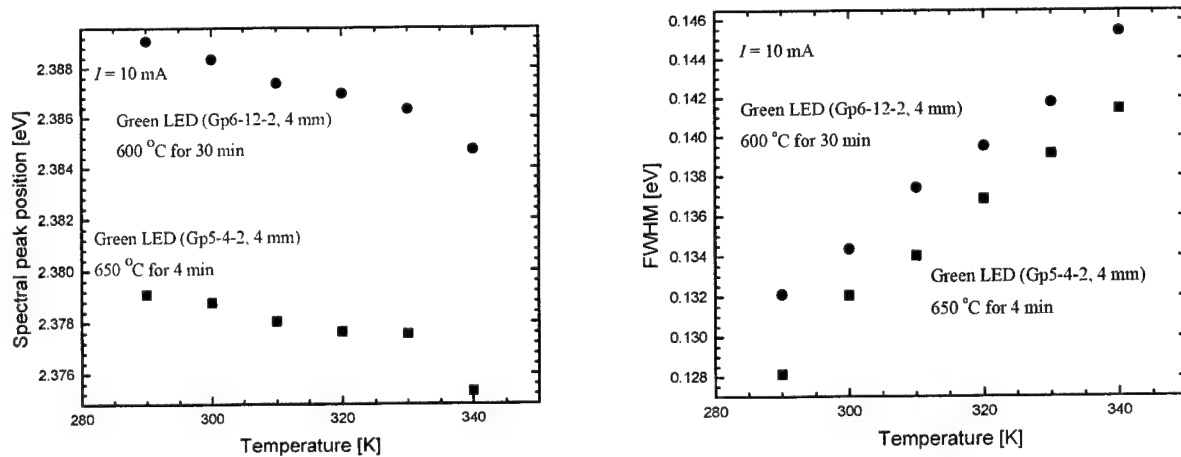


Fig.5. Spectral peak position and FWHM of 4-mm interdigitated green LEDs are calculated from the EL spectra between 290 and 340 K

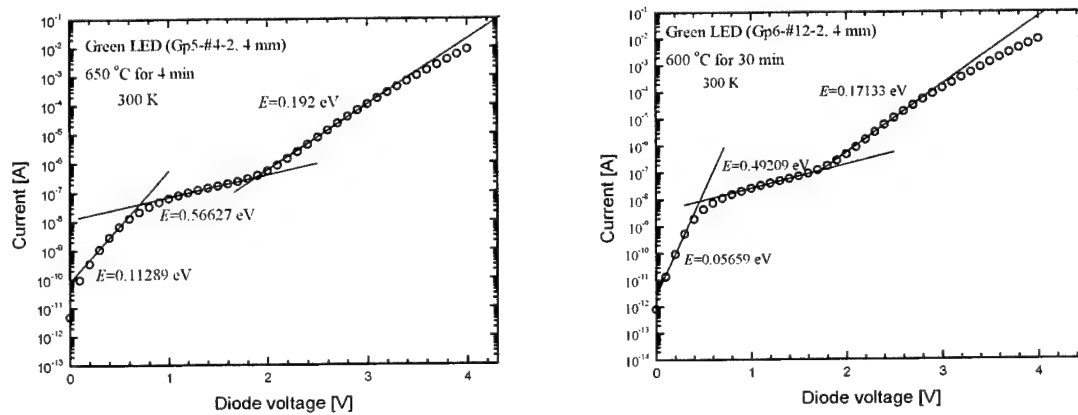


Fig. 6. Current-voltage characteristics of 4-mm interdigitated green LEDs at 300 K. I - V curves of group Gp5 (a) and I - V curves of group Gp6 (b).

$$I_{\text{rev}}(V) = a[(V + V_b)/V_b]^{3/2} \exp[-b(V + V_b)^{-1/2}], \quad (2)$$

where a and b are fitting parameters, and V_b is the built-in voltage. Even though the approximation is valid only above the built-in voltage, the I - V curves are well fitted over the entire range, which means that tunneling is also a dominant mechanism under the reverse bias. The built-in voltage V_b may be associated with the barrier when electrons tunnel into an impurity level on the p -side and recombine with holes nonradiatively [Eliseev 1997b]. The built-in voltages are 0.407 eV for Gp5-4-2 and 1.728 eV for Gp6-12-2, respectively.

Diode voltages in both LEDs are monotonically decreasing with temperature rise, as shown in Fig. 8, and significant sensitivity to temperature is observed. The turn-on voltages are ~ 3.25 V for Gp5-4-2 and ~ 3.24 V for Gp6-12-2, at 300 K. Diode voltage change from 290 to 340 K at dc driving current of 100 mA is from 4.847 to 4.4204 V (~ 91.2 %) for Gp5-4-2 and from 4.885 to 4.451 (~ 91.1 %) for Gp6-12-2.

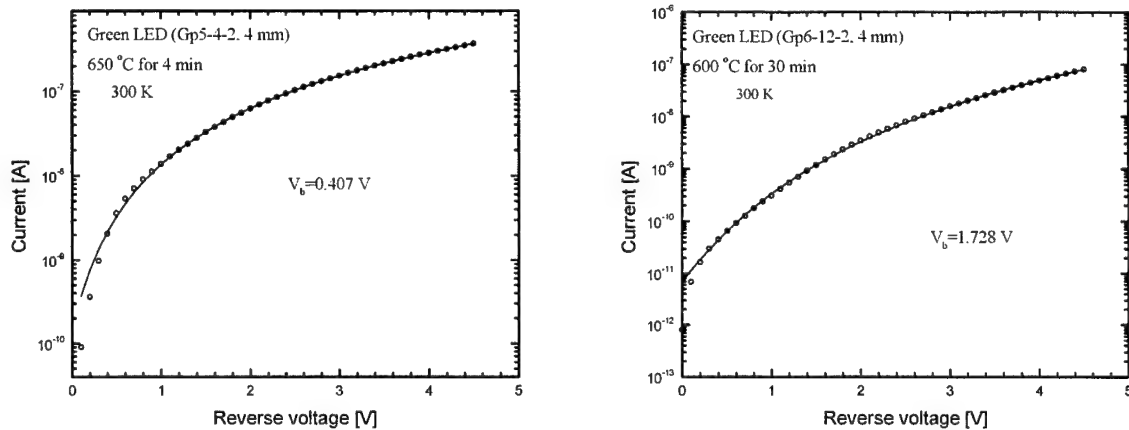


Fig. 7. Reverse bias-current characteristics of 4-mm long interdigitated green LEDs at 300 K.

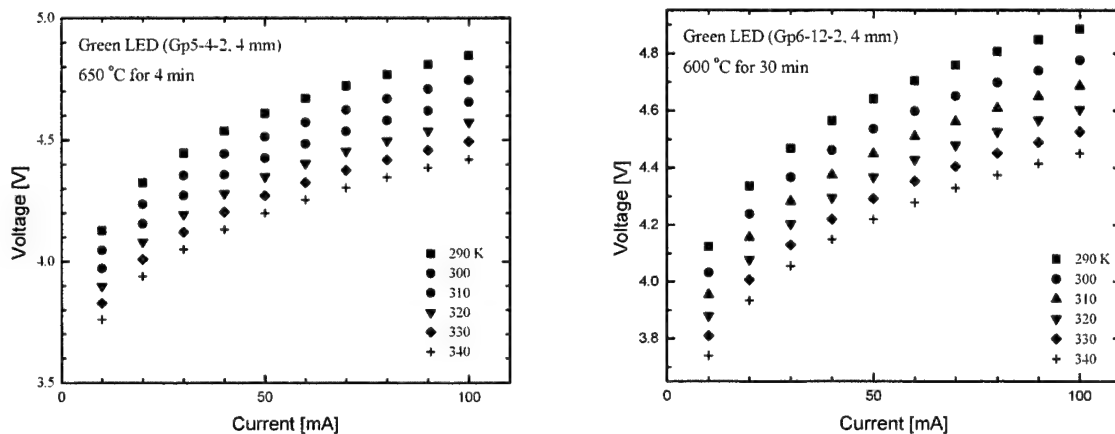


Fig. 8. Diode voltages of interdigitated green LEDs at various temperatures are drawn as a function of driving current.

The series resistances of each LED were calculated from I - V curves, *i.e.*, from plot of differential resistance of I - V curves versus inverse current, series resistance corresponds to the value of dV/dI when $1/I$ approaches to zero. As mentioned before, the specific contact resistance of p -side ohmic contact is dominant in series resistance, this result is insistent with previous experiments. The junction voltage of one-step annealed device is higher than that in regular fabricated one, compared with Figs. 8 and 9. This might be related to hole concentration on the p -side. When hole concentration is roughly calculated in one-step annealed sample (compared with a pre-activated sample), it is obtained about $2.7 \times 10^{17} \text{ cm}^{-3}$, which is almost half of that in activated sample. The screening effects may be involved with tunneling. Low concentration of holes results in a lower probability of tunneling, and thus causes a higher junction voltage.

Output powers of both LEDs are illustrated in Fig. 10. Output power of Gp6-12-2 is improved (~ 5.6 % at 290 K), compared with those of Gp5-4-2. In both LEDs, it shows superlinear below 50 mA and sublinear above 50 mA;

therefore, maximum external quantum efficiencies are at ~50 mA. With temperature rise, power changes from 290 to 340 K at driving current of 100 mA are 75.7 % for Gp5-4-2 and 74.4 % for Gp6-12-2, respectively.

4. CONCLUSIONS

Specific contact resistance of samples annealed at 600 °C for 30 min is almost 10 times lower than that of samples annealed at 650 °C for 4 min, in N₂ ambient. Based on this fact, 443×4000 μm² interdigitated green LEDs are fabricated. When characteristics of LEDs fabricated by one-step annealing process are compared to those of LEDs fabricated by the standard process, spectral peak position shifts ~ 10 meV towards low energy side and FWHM is comparable, diode and junction voltages are higher, output power is improved. Around room temperature, tunneling is dominant over the entire voltage range up to 4 V. The hole concentration can influence operating junction voltage.

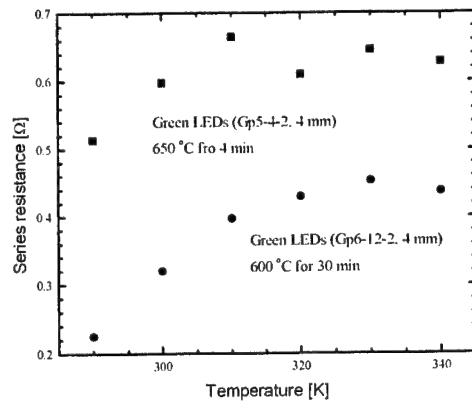


Fig. 9. Comparison of series resistances of 4-mm interdigitated LEDs.

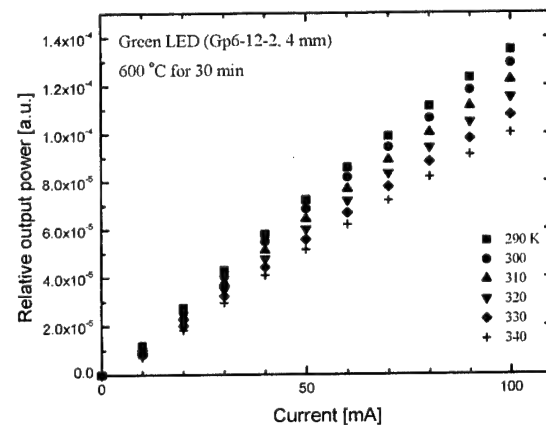
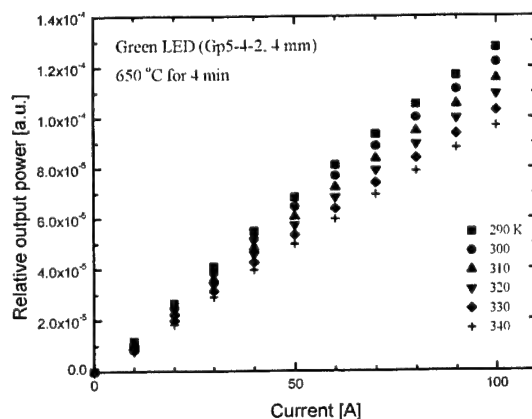


Fig. 10. Relative output power of 4-mm interdigitated green LEDs fabricated by two different annealing processes.

ACKNOWLEDGMENTS

The UNM portion of this work was supported by DARPA under the Optoelectronic Materials Center program and by AFOSR under the Optoelectronics Research Center program.

REFERENCES

- [Barton 1998] D. L. Barton, M. Osinski, P. Perlin, P. G. Eliseev, and J. Lee, "Degradation of single-quantum well InGa_N green light emitting diodes under high electrical stress", *1998 IEEE International Reliability Physics Symposium Proceedings 36th Annual*, pp. 119-123, 31 March-2 April 1998, Reno, NV, USA.
- [Chitnis 2002] A. Chitnis, V. Adivarahan, M. Shatalov, J. Zhang, M. Gaevski, W. Shuai, R. Pachipulusu, J. Sun, K. Simin, G. Simin, J. Yang, and M. A. Khan, "Submilliwatt operation of AlInGa_N based multifinger-design 315 nm light emitting diode (LED) over sapphire substrate", *Jpn. J. Appl. Phys.*, vol. 41 (Pt 2, #3B), pp. L320-L322, 2002.
- [Eliseev 1997a] P. G. Eliseev, P. Perlin, J. Lee, and M. Osinski, "Blue temperature-induced shift and band-tail emission in InGa_N-based light sources", *Appl. Phys. Lett.*, vol. 71 (#5), pp. 569-571, 1997.

- [Eliseev 1997b] P. G. Eliseev, P. Perlin, J. Furioli, P. Sartori, J. Mu, and M. Osiński, "Tunneling current and electroluminescence in InGaN: Zn, Si/AlGaIn/GaN blue light emitting diodes", *J. Electron. Mat.*, vol. 26 (#3), pp. 311-319, 1997.
- [Forrest 1980] S. R. Forrest, M. DiDomenico, Jr., R. G. Smith, and H. J. Stocker, "Evidence for tunneling in reverse-biased III-V photodetector diodes", *Appl. Phys. Lett.*, vol. 36 (#7), pp. 580-582, 1980.
- [Franssen 2003] G. Franssen, E. Litwin-Staszewska, R. Piotrkowski, T. Suski, and P. Perlin, "Optical and electrical properties of homoepitaxially grown multiquantum well InGaIn/GaN light-emitting diodes", *J. Appl. Phys.*, vol. 94 (#9), pp. 6122-6128, 2003.
- [Guo 2001] X. Guo, Y.-L. Li, and E. F. Schubert, "Efficiency of GaIn/GaN light-emitting diodes with interdigitated mesa geometry", *Appl. Phys. Lett.*, vol. 79 (#13), pp. 1936-1938, 2001.
- [Hino 2000] T. Hino, S. Tomiya, T. Miyajima, K. Yanashima, S. Hashimoto, and M. Ikeda, "Characterization of threading dislocations in GaIn epitaxial layers", *Appl. Phys. Lett.*, vol. 76 (#23), pp. 3421-3423, 2000.
- [Kim 2002] H. Kim, S.-J. Park, H. Hwang, and N.-M. Park, "Lateral current transport path, a model for GaIn-based light-emitting diodes: applications to practical device designs", *Appl. Phys. Lett.*, vol. 81 (#7), pp. 1326-1328, 2002.
- [Nakamura 1995] S. Nakamura, M. Senoh, N. Iwasa, S.-I. Nagahama, T. Yamada, and T. Mukai, "Superbright green InGaIn single-quantum-well-structure light-emitting diodes", *Jpn. J. Appl. Phys.*, vol. 34 (Pt 2, #10B), pp. L1332-L1335, 1995.
- [Nakamura 2000] S. Nakamura, M. Senoh, S.-I. Nagahama, N. Iwasa, T. Matsushita, and T. Mukai, "Blue InGaIn-based laser diodes with an emission wavelength of 450 nm", *Appl. Phys. Lett.*, vol. 76 (#1), pp. 22-24, 2000.
- [Perlin 1996] P. Perlin, M. Osiński, P. G. Eliseev, V. A. Smagley, J. Mu, M. Banas, and P. Sartori, "Low-temperature study of current and electroluminescence in InGaIn/AlGaIn/GaN double-heterostructure blue light-emitting diodes", *Appl. Phys. Lett.*, vol. 69 (#12), pp. 1680-1682, 1996.
- [Pernot 1998] C. Pernot, A. Hirano, H. Amano, and I. Akasaki, "Investigation of the leakage current in GaIn p-n junctions", *Jpn. J. Appl. Phys.*, vol. 37 (Pt 2, #10B), pp. L1202-L1204, 1998.
- [Sugahara 1998] T. Sugahara, H. Sato, M. Hao, Y. Naoi, S. Kurai, S. Tottori, K. Yamashita, K. Nishino, L. T. Romano, and S. Sakai, "Direct evidence that dislocations are non-radiative recombination centers in GaIn", *Jpn. J. Appl. Phys.*, vol. 37 (Pt 2, #4A), pp. L398-L400, 1998.

Color-dependent degradation of high-brightness AlGaInP LEDs

P. Altieri, A. Jaeger*, R. Windisch, N. Linder, P. Stauss, R. Oberschmid, K. Streubel
OSRAM Opto Semiconductors, Wernerwerkstr. 2, D-93049 Regensburg, Germany

ABSTRACT

Operation-induced degradation of internal quantum efficiency of high-brightness $(\text{Al}_x\text{Ga}_{1-x})_{0.5}\text{In}_{0.5}\text{P}$ light-emitting devices (LEDs) is analysed experimentally and theoretically. A test series of LEDs was grown by MOCVD with identical layer sequence but different Aluminum content x in the active AlGaInP layer resulting in devices emitting light between 644 nm and 560 nm. The analysis yields the wavelength dependence of both the nonradiative recombination constant A as well as the carrier leakage parameter C of devices before and after aging. While test devices with $\lambda > 615$ nm are very stable, LEDs with shorter emission wavelengths exhibit both an increase of A and a slight decrease of C upon aging. Possible degradation mechanisms are discussed.

Keywords: light-emitting devices, device reliability, AlGaInP, quantum efficiency, recombination mechanisms

1. INTRODUCTION

High-brightness visible light-emitting devices are attracting great interest for a number of applications that include automobile lighting, signs and liquid crystal display backlighting [1,2]. One of the main advantages of AlGaInP LEDs besides record high luminous efficiency in the red to yellowish-green spectral range is the considerably improved reliability compared to competing conventional incandescent bulbs. This fact was demonstrated by several groups [1,3,4]. By extrapolating long-term reliability data, lifetimes of more than 100.000 hours have been calculated. However, highly reliable LED operation requires a profound knowledge about epitaxial growth, chip processing and recombination processes occurring during operation of these devices. More specifically, a detailed understanding of the recombination processes such as nonradiative recombination or carrier losses owing to leakage and their change upon aging might allow a separation and identification of different degradation mechanisms.

Here we report on high-brightness AlGaInP LEDs having identical layer structure but different Aluminum content x in the active AlGaInP layers. The direct bandgap (Γ) and indirect bandgap (X) of AlGaInP lattice matched to GaAs at room temperature vary linearly with x [1].

$$E(\Gamma) = 1.900 + 0.61x \quad (\text{eV}) \quad (1)$$

$$E(X) = 2.204 + 0.085x \quad (\text{eV}) \quad (2)$$

The Γ -X crossover takes place for $x=0.58$ resulting in a useable wavelength range for light emission from AlGaInP LEDs between 550 nm and 650 nm. The aging behavior of a test series of LEDs covering this available wavelength range is found to be strongly wavelength-dependent. Red light emitting devices are very stable during operation. In contrast, LEDs with higher Aluminum content and orange luminescence show a pronounced light output degradation. Further increase of Aluminum content in the active region, however, reduces degradation in yellowish-green LEDs.

This result can be understood by comparing measurements of the external quantum efficiency of these LEDs as a function of operating current and junction temperature to an analytical model providing quantitative information on internal efficiency and loss mechanisms [5]. The model is based on a rate equation taking into account radiative and nonradiative recombinations as well as diffusive leakage of carriers into the confining layers. Photon recycling and its influence on the LED light extraction efficiency is self-consistently included in the model.

* arndt.jaeger@osram-os.com; www.osram-os.com

The analysis yields the wavelength dependence of both the nonradiative recombination constant A as well as the carrier leakage parameter C of devices before and after aging. LEDs with $\lambda > 615$ nm are stable during operation whereas LEDs with shorter emission wavelengths show an increase of A as well as a decrease of C upon aging. Since in fresh devices nonradiative recombination increases with increasing Aluminum content by about one order of magnitude from red to green LEDs, the calculation explains the strongest degradation of orange LEDs as due to the highest relative change of A .

2. EXPERIMENTAL

A test series of AlGaInP LEDs with emission wavelengths between 560 nm and 650 nm were grown by metal-organic vapor phase epitaxy on 6° misoriented (100) GaAs substrates. For the active region a multiple quantum well (MQW) structure sandwiched by doped AlInP confinement layers is used. The LED emission wavelength is adjusted by the Aluminum content in the quantum wells having a total active region thickness of 400 nm. Common LED structures are fabricated by a square die cut with a side length of 300 μm from the LED wafer with electrodes on the bottom and top side. At the p side we utilized a standard contact but not an additional surface texturing which would improve light extraction as shown in the past [6]. The LEDs are mounted on TO-18 headers and measured without encapsulation in an integrating sphere. Long-wavelength devices show excellent electro-optical characteristics with external quantum efficiency of 5% at a forward current $I_f = 20$ mA at room temperature (Fig.1). The drastic reduction of external quantum efficiency towards shorter wavelengths was previously ascribed to the transfer of electrons from the direct conduction band minimum at Γ point to the indirect conduction band minimum at X point [2,5,7,8].

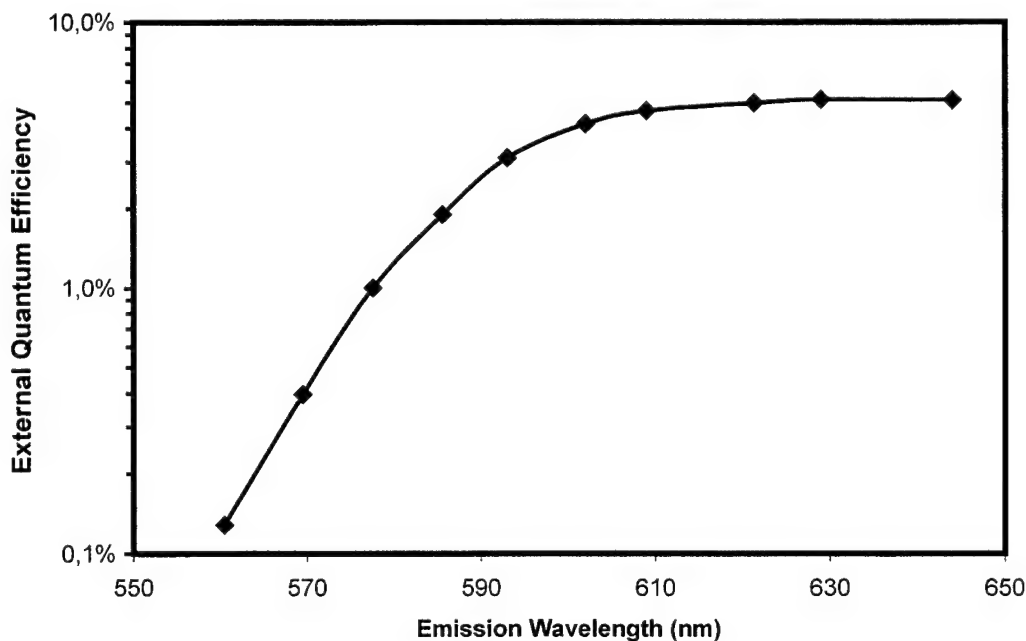


Fig. 1. External quantum efficiency of AlGaInP LEDs with different emission wavelengths measured at $I = 20$ mA.

For testing the color-dependent degradation the LEDs were operated for 88 hours under steady-state conditions ($I_f = 50$ mA at room temperature). The aging status is measured with improved sensitivity at currents smaller than the stress current such as 20 mA or even better at 1 mA. This fact was recently pointed out by Pursiainen et al. [9]. The resulting operation induced change of external quantum efficiency of AlGaInP LEDs is plotted in Fig.2 as a function of LED emission wavelength. Red LEDs with $\lambda > 615$ nm are very stable. However, LEDs with shorter emission wavelength exhibit the strongest degradation at 605 nm. Here the light output is reduced to about 20% at $I_f = 1$ mA. It is interesting to note that LEDs with shorter wavelength and higher x do show a lesser degree of degradation. Yellowish-green LEDs with $\lambda = 560$ nm emit at 1 mA more than 60% of the initial light intensity.

In the following sections these experimental findings are discussed in terms of a detailed model of the internal quantum efficiency. The analysis explains the impact of leakage effects as well as nonradiative recombination on the light output of LEDs during operation.

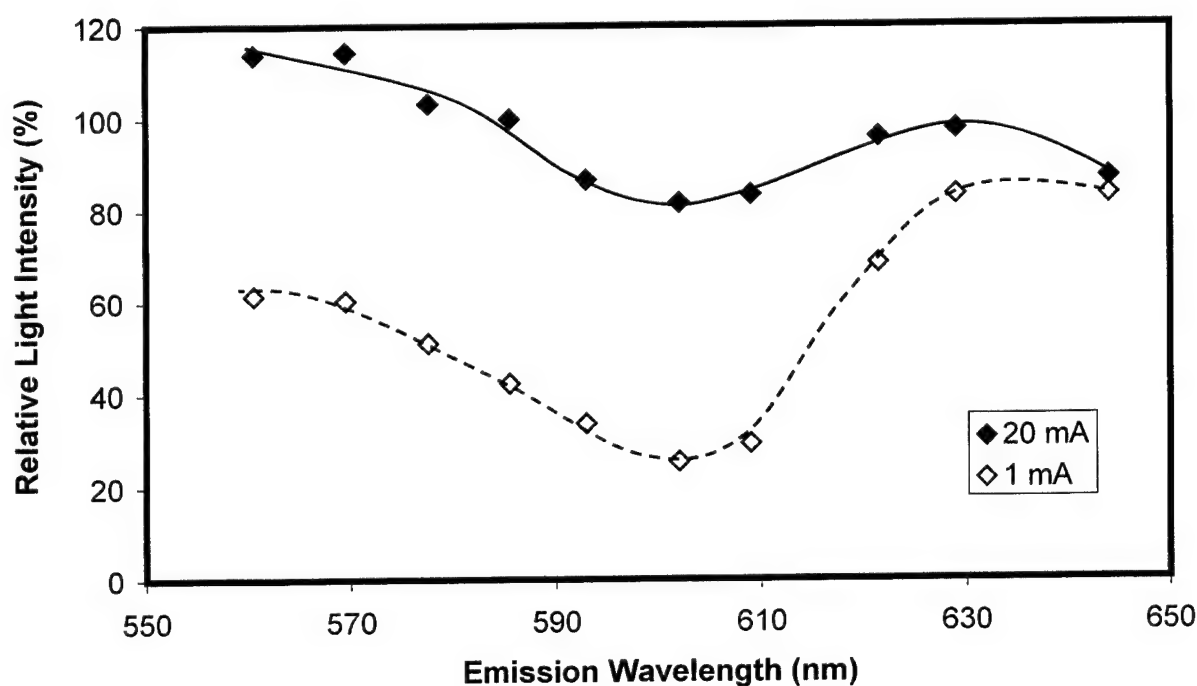


Fig. 2. Operation induced change of external quantum efficiency of AlGaInP LEDs as a function of emission wavelength.

3. THEORY OF INTERNAL QUANTUM EFFICIENCY

3.1. Rate equation model

The model to describe the internal quantum efficiency of fresh and aged LEDs as a function of current and temperature is based on the following rate equation [5]:

$$\frac{J}{qw} = R_R + R_{NR} + \frac{J_{Leak}}{qw} \quad (3)$$

Here J is the current density flowing in the device, q is the electron charge and w is the active layer thickness. The term on the left represents the carrier injection rate into the active region and is set equal to the different recombination mechanisms occurring in the device. The radiative rate R_R , the nonradiative rate R_{NR} and the carrier leakage current J_{Leak} are considered. In the case of a lowly doped active region ($n_0 = 1 \cdot 10^{15} \text{ cm}^{-3}$), the radiative recombination R_R changes quadratically with injected carrier concentration δn , while the nonradiative recombination R_{NR} depends linearly on δn :

$$R_R = B\delta n(\delta n + n_0) \quad (4)$$

$$R_{NR} = A\delta n$$

Here $B(T)$ is the radiative recombination parameter of AlGaInP material which is assumed to be identical to the GaAs value of $1.2 \cdot 10^{-10} \text{ cm}^3/\text{s}$ [10]. The radiative recombination parameter $B(T)$ is assumed to vary as $T^{-3.2}$ as resulting from the bulk density of states in the Boltzmann approximation. The nonradiative recombination parameter A is left a fitting parameter, depending on both emission wavelength and temperature.

The carrier leakage term also changes quadratically with δn and can be expressed as follows:

$$\frac{J_{Leak}}{qw} = C\delta n(\delta n + n_0) = C_0 \sqrt{T} e^{\frac{E_g^{QW} - E_g^{conf}}{kT}} \delta n(\delta n + n_0) \quad (5)$$

$$C_0^i \propto \frac{1}{(N_{eff}^i)^2} \sqrt{\frac{\mu_m^i}{\tau^i}} \quad i = p\text{-conf}, n\text{-conf} \quad (6)$$

where μ_m^i is the minority carrier mobility, $(N_{eff}^i)^2$ and τ^i are the effective doping density and the minority carrier lifetime, respectively, in the $\text{In}_{0.5}\text{Al}_{0.5}\text{P}$ confinement layers. E_g^{QW} and E_g^{conf} are the active region and confinement layer energy gaps, respectively. Due to lack of precise materials parameters the leakage prefactor C_0 is taken as a fitting parameter, independent of temperature and wavelength.

The external quantum efficiency is defined as the product of internal quantum efficiency and extraction efficiency which accounts for the probability that a generated photon escapes from the LED. The light extraction efficiency η_{extr} is calculated via a ray tracing simulation [5,11], in which the LED epitaxial structure and chip geometry is taken into account. The resulting extraction efficiency depends on the active region internal quantum efficiency. Using the extraction efficiency η_{extr} and solving equations (3)-(6) allows to calculate the external quantum efficiency:

$$\eta_{extQE} = \eta_{extr} \frac{B(\delta n + n_0)}{(B + C)(\delta n + n_0) + A} \quad (7)$$

This model provides the wavelength and temperature dependence of internal quantum efficiency of AlGaInP LEDs including the relative portion of the different recombination mechanisms. These results will be discussed in detail elsewhere [5] while we focus here on the application of the rate equation model to operation-induced changes in high-brightness AlGaInP LEDs with different emission wavelength.

3.2. Change of recombination rates

To illustrate the immense use of the rate equation model for LED aging analysis we calculated light output changes due to the main recombination mechanisms and plotted it as a function of current (Fig.3 and 4). The light output change is a parameter routinely measured during aging and exploited for LED quality control (cf. Fig.2). As we will see later on the presented analysis of these data by means of a sophisticated model will give new insights into degradation processes in AlGaInP LEDs.

By changing the values A and C the model is capable to reproduce the measured LED aging behavior. First the light output change is modeled for an LED with a nonradiative recombination rate $A=1\cdot 10^7\text{s}^{-1}$ and a carrier leakage parameter $C_0=7.5\cdot 10^{-10}\text{cm}^3/\text{s}$ (Fig.3). An increase of A by a factor of 1.5 results in a light output reduction (open symbols, solid line). This is very similar to what we usually observe in degrading LEDs due to its peculiar current dependence exhibiting an *enhanced* light output change at *lower* measuring currents [9]. On the other hand a decrease of A by a factor of 1.5 results in a light output increase again more pronounced at low currents.

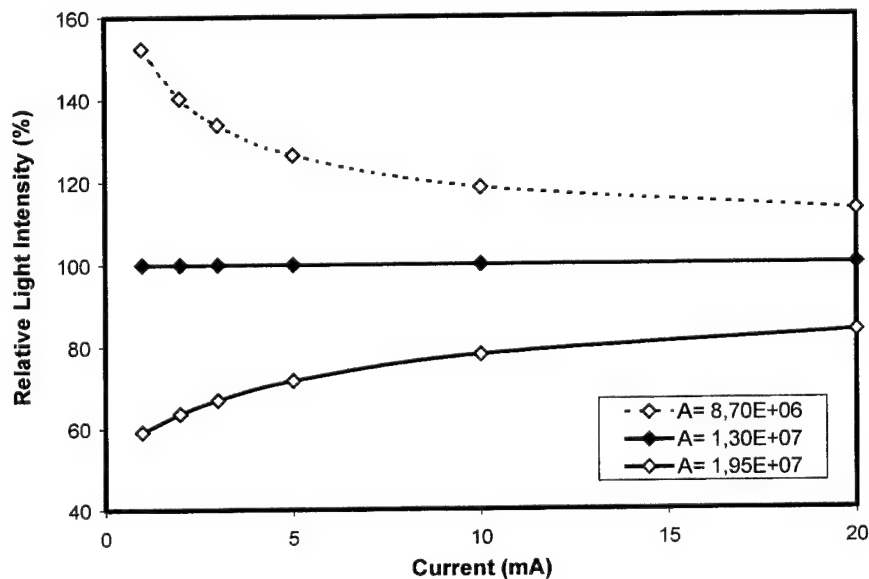


Fig.3. Calculated relative light intensity as a function of current demonstrating the effect of changes in the nonradiative constant A .

The light output change is now modeled for an LED with the same parameters $A=1\cdot 10^7\text{s}^{-1}$ and $C_0=7.5\cdot 10^{-10}\text{cm}^3/\text{s}$ (Fig.4) but varying carrier leakage parameter. An increase of C_0 by a factor of 1.5 causes a light output reduction. However, in contrast to the A increase the increase of C_0 results in a different current dependence with an *enhanced* light output change at *higher* measuring currents. A decrease of C_0 by a factor of 1.5 leads to a light output improvement especially at high currents (open symbols, dashed line). This case of decreasing C_0 seems to be similar to what occasionally was observed in previous studies [9].

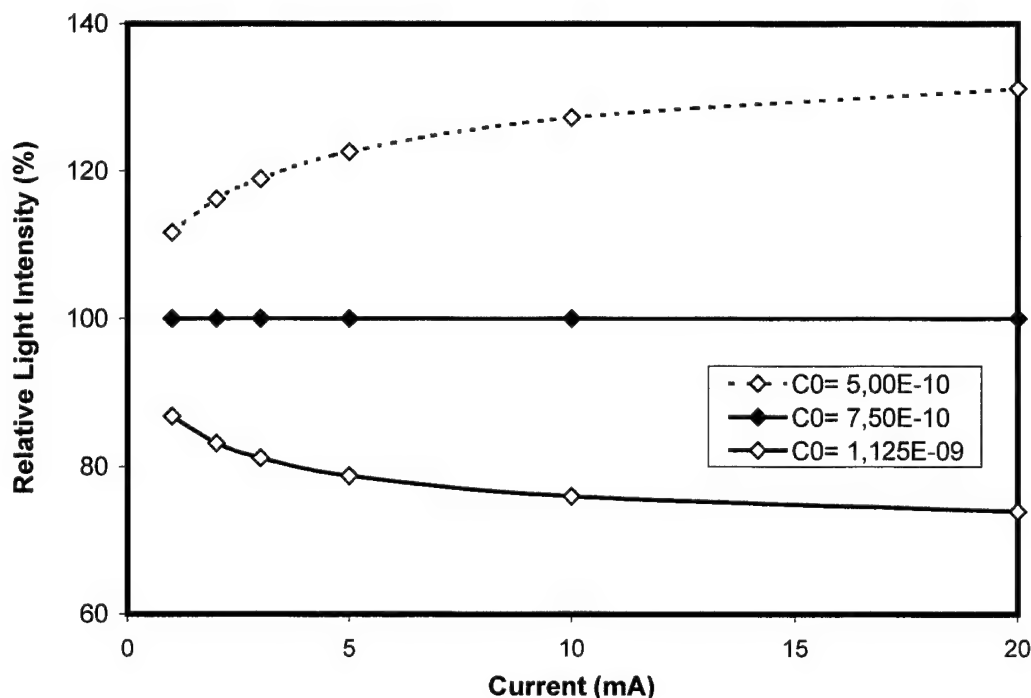


Fig.4. Calculated relative light intensity as a function of current demonstrating the effect of changes in the carrier leakage factor C .

In conclusion, these differences depending on the current range enable to differentiate between these aging effects. This is of great importance since it is very likely that in actual devices *both* parameters change during aging. In the following discussion the measured efficiency of LEDs of the color series will be compared to the calculation.

4. DISCUSSION

4.1. Current dependence of external quantum efficiency during aging

The external efficiency of a yellowish-green LED is measured before and after aging between 1 mA and 20 mA (Fig.5.a). The efficiency starts at a low level and increases rapidly towards a saturation level at high currents. This current dependence is the result of a saturation of nonradiative recombination centers at high carrier densities due to its linear dependence on the excess carrier density δn . The fitting procedure yields for both cases excellent agreement with the experimental data. The nonradiative recombination rate A and leakage factor C_0 are extracted from the fitting and it turns out that during aging A increased while C_0 decreased. The superposition of these degradation effects is more easily recognized in Fig. 5.b displaying the light intensity after aging relative to the fresh LED. Since carrier leakage is suppressed upon aging the LED increased its efficiency at high currents $I > 8$ mA. At low currents $I < 8$ mA the light output is decreased owing to operation-induced accumulation of defects acting as nonradiative recombination centers and hence increasing A . This degradation behavior of the yellowish-green LED is qualitatively found in all LEDs of the test series except from the stable red LEDs.

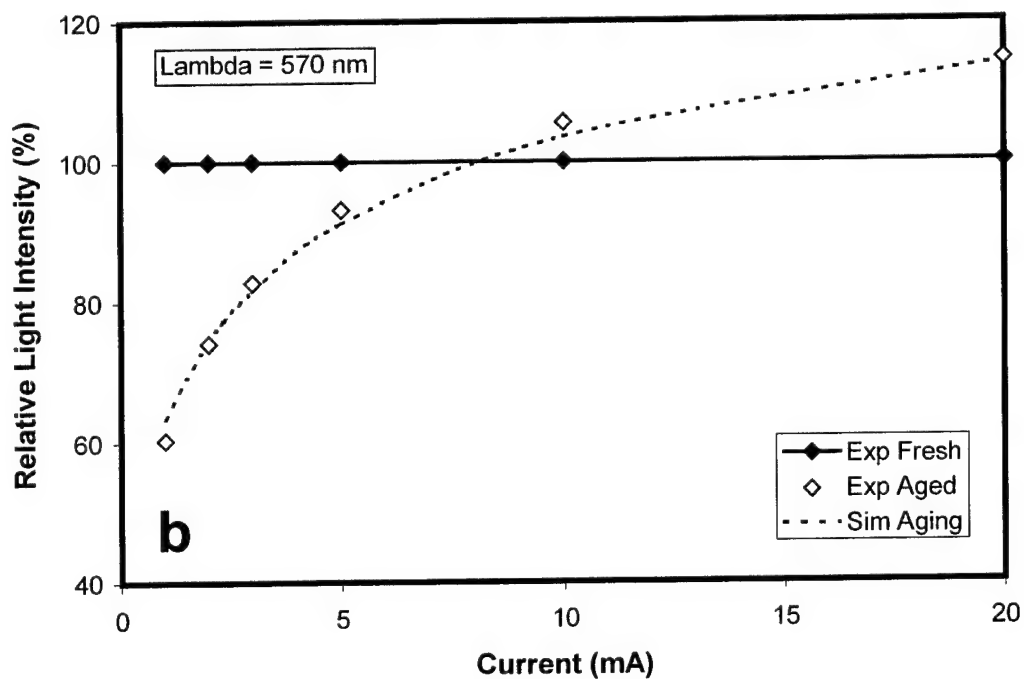
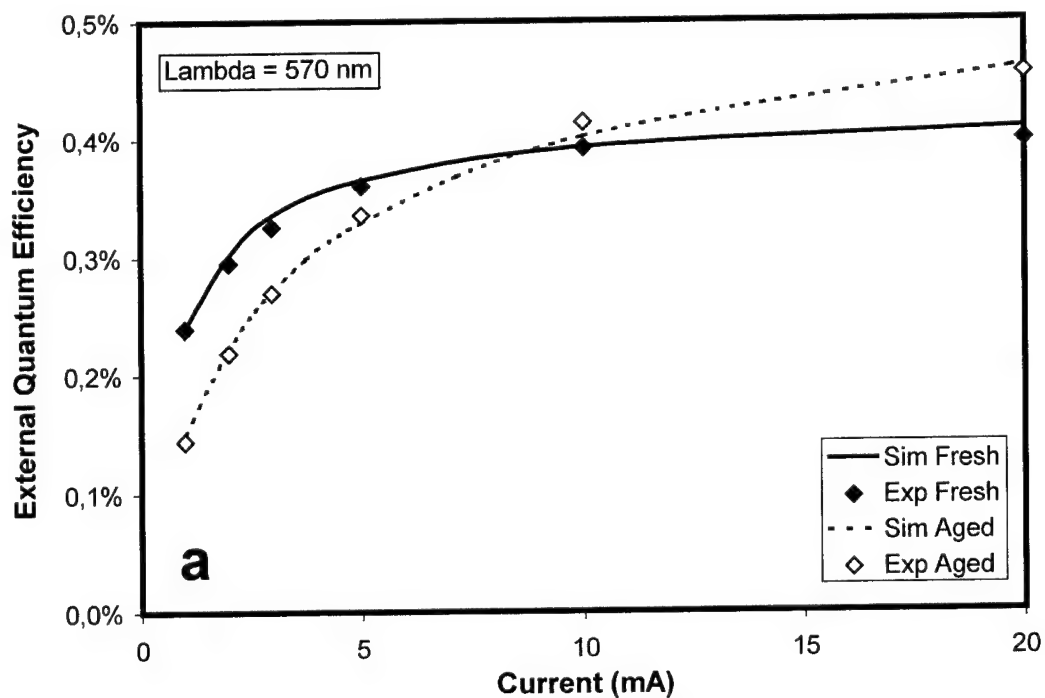


Fig.5. a. Measured and calculated external quantum efficiency as a function of current for a fresh and aged AlGaInP LED emitting in the yellowish-green spectral range.
 b. Measured and calculated relative light intensity as a function of current.

4.2. Wavelength dependence of electron leakage during aging

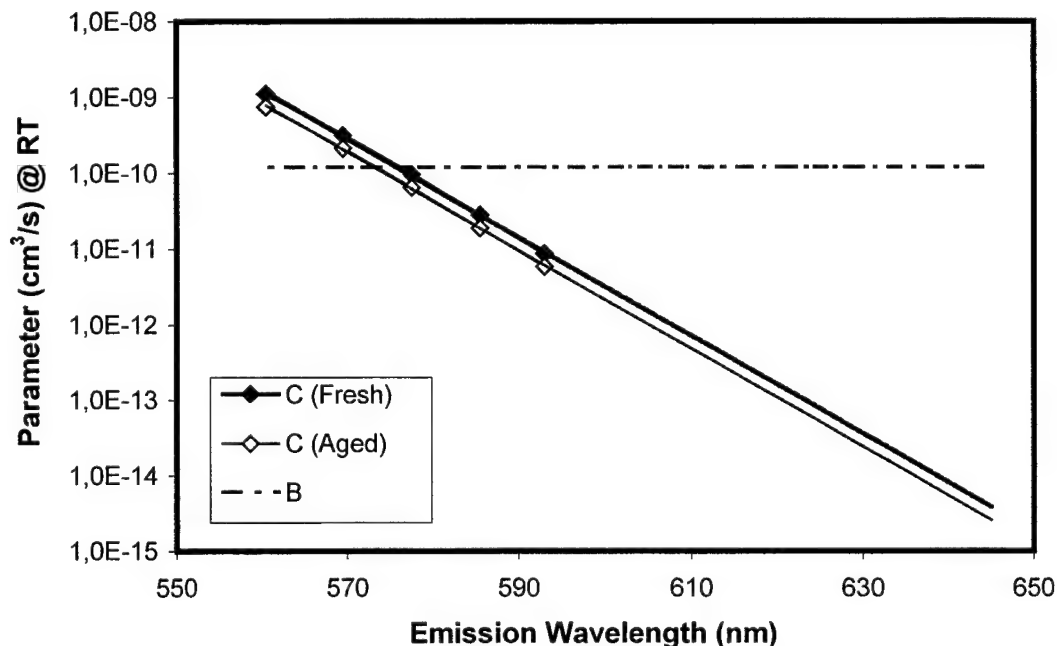


Fig. 6. Leakage parameter C as a function of the LED peak wavelength for fresh and aged devices. Radiative recombination rate B is assumed to be independent of wavelength and aging status.

The wavelength dependence of electron leakage parameter C as deduced from the current and temperature dependence of the external quantum efficiency of AlGaInP LEDs is plotted in Fig.6. In this wavelength range the thermal activation energy $\Delta E = E_g^{conf} - E_g^{QW}$ drops from 360 meV for red LEDs down to 70 meV for yellowish-green LEDs (cf. eq.(5)). Consequently the leakage current decreases exponentially by several orders of magnitude with increasing wavelength. Whereas at room temperature and $I_f = 20$ mA carrier leakage is the dominant loss mechanism for yellowish-green LEDs the leakage losses become negligible for orange-red LEDs with $\lambda > 600$ nm. For comparison the radiative recombination rate B is also shown in Fig.6.

From the fit to the measured external efficiency data the leakage parameters C_0 are obtained between 560 nm and 600 nm (squares in Fig.6). C_0 is found to be independent of wavelength which is reasonable since identical confinement layers are used in the LEDs of the test series. During aging the thermal activation energy ΔE is not altered, but the prefactor C_0 decreased by a factor 1.5. This can be interpreted as an increase of the effective doping density in one of the confinement layers during device operation. An other effect involved in the degradation might be an increase of minority carrier lifetime or a reduction of minority carrier mobility. Additional measurements to check these interpretations are currently under way.

4.3. Wavelength dependence of nonradiative recombination during aging

Calculations of external quantum efficiency before and after aging show that for long wavelength devices carrier leakage is extremely low and therefore changes in the carrier leakage parameters have only little effect. The dominating loss mechanism in these LEDs is the nonradiative recombination which can also be extracted by means of the model calculation from the current and temperature dependence of the external quantum efficiency. Fig. 7 shows the nonradiative recombination parameter A as a function of the LED peak wavelength for fresh and aged devices. The nonradiative parameter increases gradually with decreasing wavelength. This increase with Aluminum content could be

due to an enhanced transfer of electrons from Γ to X conduction band in the QW and/or barrier material [5,7,8] or due to an increased defect concentration [8]. During operation all LEDs with $\lambda < 615$ nm show an enhancement of nonradiative recombination constant A . LEDs with larger emission wavelength possess the smallest nonradiative recombination constant A which does not alter during operation. LEDs with emission at 605 nm exhibit the strongest light degradation because the relative change of A from aged to fresh devices is a maximum (see also Fig.2). The reduction of light output degradation for yellowish-green LEDs also becomes clear if one keeps in mind that carrier leakage being the dominant loss mechanism in the short-wavelength devices is reduced during aging which would actually result in a light output increase and thus partially compensates the light output decrease due to an increase of A .

These investigations allow us to develop AlGaInP LEDs having reduced light degradation during operation. Based on the simple model of internal quantum efficiency the effect of fundamental physical processes such as carrier leakage or Γ -X transfer during operation can be resolved as a function of LED emission wavelength.

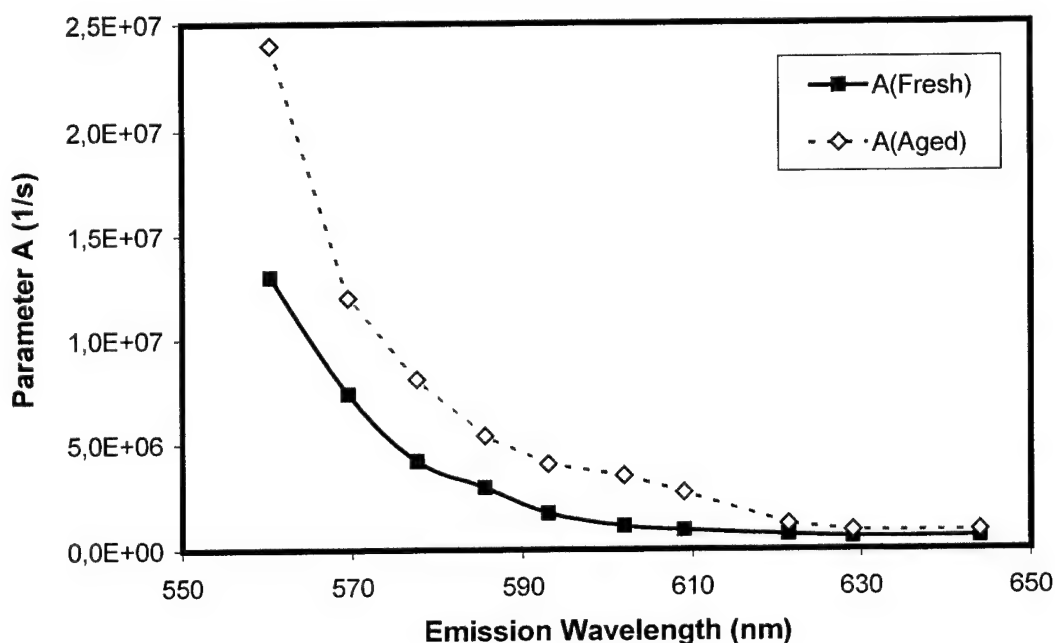


Fig. 7. Nonradiative constant A as a function of the LED peak wavelength for fresh and aged devices.

5. SUMMARY

The wavelength dependence of the external quantum efficiency of high-brightness AlGaInP LEDs is measured during operation and analysed by means of a rate equation model. The model accounts for radiative and nonradiative recombinations as well as carrier leakage effects and methods are demonstrated aiming for distinguishing these processes. The detailed theoretical and experimental analysis yields the wavelength dependence of these recombination processes. Red LEDs prove to be stable during operation whereas short wavelength LEDs suffer from light reduction upon aging due to enhanced nonradiative recombinations which is, however, partially compensated by a reduction of carrier leakage.

REFERENCES

1. F. A. Kish, R. M. Fletcher, Semiconductors and Semimetals 48, 149 (1997).

2. K. Streubel, N. Linder, R. Wirth, A. Jaeger, IEEE J. Sel. Top. Quant. Electr. 8, 321 (2002).
3. F. A. Kish, D. A. Vanderwater, D. C. DeFevere, D. A. Steigerwald, G. E. Hofler, K. G. Park, F. M. Steranka, Electronics Lett. 32, 132 (1996).
4. J. D. G. Lacey, D. V. Morgan, Y. H. Aliyu, H. Thomas, Qual. Reliab. Engng. Int. 16, 45 (2000).
5. P. Altieri, A. Jaeger, R. Windisch, N. Linder, P. Stauss, R. Oberschmid, K. Streubel, to be published
6. N. Linder, S. Kugler, P. Stauss, K. Streubel, R. Wirth, H. Zull, Proc. SPIE 4278, 19 (2001).
7. D. Patel, J. M. Pikal, C. S. Menoni, K. J. Thomas, F. A. Kish, M. R. Hueschen, Appl. Phys. Lett. 75, 3201 (1999).
8. P. C. Mogensen, P. Blood, G. Jones, S. W. Bland, N. J. Cain, D. W. Peggs, D. J. Mowbray, Proc. SPIE 3625, 485 (1999).
9. O. Pursiainen, N. Linder, A. Jaeger, R. Oberschmid, K. Streubel, Appl. Phys. Lett. 79, 2895 (2001).
10. K. Ikeda, S. Horiuchi, T. Tanaka, W. Susaki, IEEE Trans. Electr. Dev. 24, 1001 (1977).
11. R. Windisch, C. Rومان, B. Dutta, A. Knobloch, G. Borghs, G. H. Döhler, P. Heremans, IEEE J. Sel. Top. Quant. Electr. 8, 248 (2002).

Effect of oxygen on the electronic band structure of II-O-VI alloys

W. Shan^{*a}, W. Walukiewicz^a, K.M. Yu^a, J.W. Ager III^a, J. Wu^a, J. Beeman^a, M.A. Scapulla^{a,b}, O.D. Dubon^{a,b}, E. E. Haller^{a,b}, Y. Nabetani^c, and P. Becla^d

^aMaterials Sciences Division, Lawrence Berkeley National Laboratory, Berkeley, CA, 94720, USA;

^bDept. of Materials Science and Engineering, University of California, Berkeley, CA 94720, USA;

^cDepartment of Electrical Engineering, University of Yamanashi, Kofu 400-8511, Japan;

^dDepartment of Materials Science and Engineering, Massachusetts Institute of Technology, Cambridge, MA 02139, USA

ABSTRACT

We have studied the effects of composition and hydrostatic pressure on the direct optical transitions at the Γ point of the Brillouin zone in MBE-grown $\text{ZnO}_x\text{Se}_{1-x}$ and ion-implantation-synthesized $\text{Zn}_{1-y}\text{Mn}_y\text{O}_x\text{Te}_{1-x}$ alloys. We observe a large O-induced band-gap reduction and a change in the pressure dependence of the fundamental band gap of the II-O-VI alloys. The effects are similar to those previously observed and extensively studied in highly mismatched III-N-V alloys. Our results are well explained in terms of the band anticrossing model that considers an anticrossing interaction between the highly localized oxygen states and the extended states of the conduction band of II-VI compounds. The O-induced modification of the conduction band structure offers an interesting possibility of using small amounts of O to engineer the optoelectronic properties of group II-O-VI alloys.

Keywords: Oxygen, $\text{ZnO}_x\text{Se}_{1-x}$, $\text{Zn}_{1-y}\text{Mn}_y\text{O}_x\text{Te}_{1-x}$, II-VI compounds, band-anticrossing, highly mismatched alloys, band structure, pressure effect, photovoltaic

1. INTRODUCTION

Highly mismatched semiconductor alloys (HMAs) in which a small fraction of constituent anion elements is replaced by elements with highly dissimilar properties have recently attracted considerable attention. The most extensively studied HMAs to date are III-N-V alloys. It has been found that the substitution of the group V element in group III-V compounds with small amounts of nitrogen leads to dramatic changes of the electronic properties. These include a reduction of the fundamental band-gap energy [1,2], a significant increase in electron effective mass and a decrease in electron mobility [3-5]. Furthermore a new optical transition (E_+) appears from the valence band to the conduction band at the Γ point [6,7]. As one quantitative example, the incorporation of only one percent of nitrogen into GaAs induces a strikingly large reduction of 0.18 eV in the fundamental band-gap energy [8].

These dramatic changes of the electronic properties have recently been explained accurately by a band anticrossing (BAC) model [6,9]. The anticrossing interaction between the extended conduction-band states of a semiconductor matrix and the highly localized electronic states introduced by the isoelectronic substitutional atoms with high electronegativity can be expressed as [6,9]

$$E_{\pm}(k) = \frac{1}{2} \left\{ E_M(k) + E_O \pm \sqrt{(E_M(k) - E_O)^2 + 4V^2} \right\} \quad (1)$$

where $E_M(k)$ and E_O are, respectively, the energies of the unperturbed conduction band and of the localized states relative to the top of the valence band. The matrix element describing the interaction and hybridization between the localized states and the extended conduction-band states $V = C_{MO}x^{1/2}$, where C_{MO} is a constant describing the coupling between localized states and the extended states of the semiconductor matrix and x is the alloy composition.

* WShan@lbl.gov

Illustrated in Fig. 1 are schematic examples of the calculated band structure based on the BAC model. The interaction between the localized isoelectronic states and the extended conduction-band states has a pronounced effect on the dispersion relation of the two conduction subbands E_- and E_+ . If the localized state is located within the conduction band of the matrix, as depicted in Fig.1(a), the conduction-band states at the E_- edge retain mostly the extended E_M -like character and those at the E_+ edge are more of localized and E_D -like character. If the localized states lie below the conduction-band edge, as displayed in Fig.1(b), the conduction-subband edges E_- and E_+ switch their characters: the E_- subband states assume the highly localized nature and E_+ subband states possess the character of extended state. It is clear from the figure that the energy positions of the subband edges E_- and E_+ given by Eq.(1) depend on alloy concentration x and the coupling parameter C_{MO} , as well as the location of E_O with respect to the conduction band edge E_M .

In this work, we review our recent research on a new group of HMAs based on II-VI compounds. We show that partial replacement of group-VI anions with more electronegative O atoms in II-VI compounds does have the effect similar to incorporating nitrogen into III-V materials. The $\text{ZnO}_x\text{Se}_{1-x}$ and $\text{Zn}_{1-y}\text{Mn}_y\text{O}_x\text{Te}_{1-x}$ alloy systems are specifically chosen to represent the respective cases depicted in Fig.1. The observations of a significant band-gap reduction with increasing oxygen content in $\text{ZnO}_x\text{Se}_{1-x}$ and two well-resolved spectral features associated with the E_- and E_+ band edges in $\text{Zn}_{1-y}\text{Mn}_y\text{O}_x\text{Te}_{1-x}$, as well as the classical band-anticrossing behavior in the pressure dependence of the fundamental band gaps of these samples can all be quantitatively explained by the anticrossing interaction between the extended states of the conduction band of the host matrix materials and the highly localized oxygen states located at the vicinity of the conduction-band edge.

2. EXPERIMENTAL

The $\text{ZnO}_x\text{Se}_{1-x}$ samples used in this work were grown on GaAs (100) substrates by molecular beam epitaxy at a growth temperature of 350°C. Before the growth of ZnOSe epitaxial films, a 100-nm thick ZnSe buffer layer was deposited on the substrates. The O content in the alloy layers was controlled by varying the O_2 flow rate to a RF oxygen plasma source. The ZnOSe layer thickness is around 600 nm for all the samples. The oxygen concentration in the films was determined from Vegard's law using lattice constants determined from the double-crystal X-ray diffraction rocking

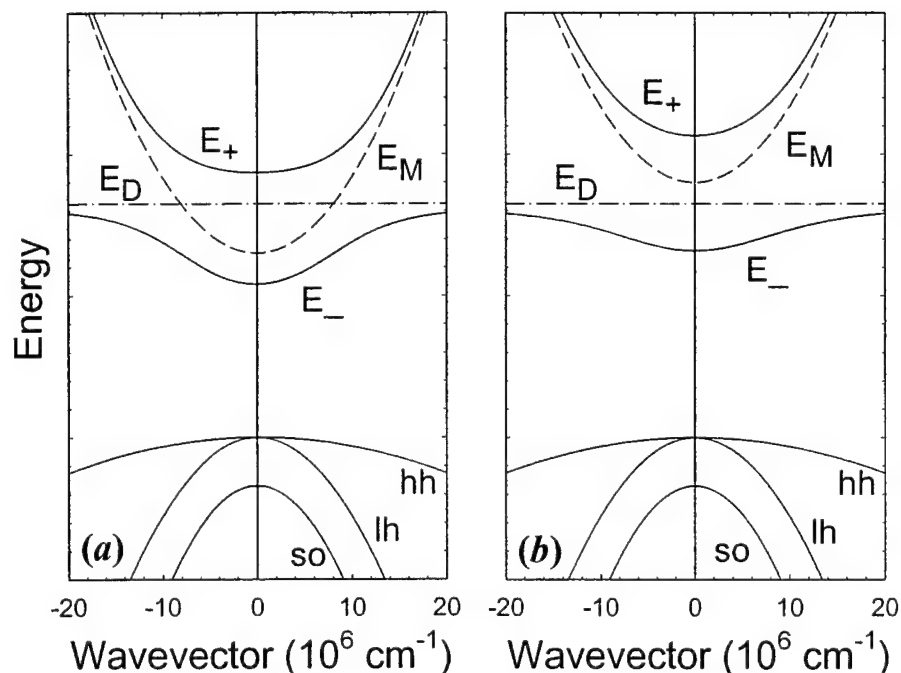


Fig.1. Illustration of the effects of band anticrossing on the Γ conduction band structure. (a) The highly electronegative isoelectronic impurity induced localized state resonant with the conduction band; (b) The localized state located below the conduction band. The solid lines are the restructured E_- and E_+ subbands resulting from the band anticrossing interaction between the localized states (dash-dotted line) and the extended states of the conduction band (broken line).

curves measured in the (400) and (511) planes [10]. The uncertainty in O concentration is about 20%.

The $\text{Zn}_{1-y}\text{Mn}_y\text{O}_x\text{Te}_{1-x}$ samples are synthesized using O ion implantation followed by pulsed laser melting (PLM). This approach is very effective in incorporating impurities into a crystal to levels well above the solubility limit due to the rapid recrystallization rate [11,12]. Synthesis of diluted $\text{GaN}_x\text{As}_{1-x}$ [13], as well as ferromagnetic $\text{Ga}_{1-x}\text{Mn}_x\text{As}$ [14] using ion implantation and the PLM process have recently been demonstrated. Multiple energy implantation using 30 and 90 keV O^+ ions was carried out into $\text{Zn}_{0.88}\text{Mn}_{0.12}\text{Te}$ single crystals to form $\sim 0.2 \mu\text{m}$ thick layers with the O concentration ranging from 0.0165 to 0.044. The reason for using ternary ZnMnTe as substrates is that the presence of Mn enhances and stabilizes the incorporation of O [15]. The O^+ -implanted samples were pulsed-laser melted in air using a KrF laser ($\lambda = 248 \text{ nm}$) with a pulse duration $\sim 38 \text{ ns}$. After passing through a multi-prism homogenizer, the fluence at the sample ranged between 0.020 and 0.3 J/cm^2 .

Photo-modulated reflection (PR), photo-modulated transmission (PT) and photoluminescence (PL) measurements were carried out to measure the band gap energy of the $\text{ZnO}_x\text{Se}_{1-x}$ and $\text{Zn}_{1-y}\text{Mn}_y\text{O}_x\text{Te}_{1-x}$ samples at room temperature (295 K). For the photo-modulation measurements, quasimonochromatic light from a Xenon arc or a tungsten halogen lamp dispersed by a 0.5-m monochromator was focused on the samples as a probe beam. A chopped HeCd laser beam (3250 or 4420 Å) provided the photomodulation. The PR or PT signals were detected by a Si photodiode using a phase-sensitive lock-in amplification system. For PL measurements, the 3250-Å HeCd laser line was used for excitation. Luminescence signals from the samples were dispersed by a 1-m double grating monochromator and detected by a photomultiplier tube. Application of hydrostatic pressure was accomplished by mounting small sample chips with sizes of $\sim 200 \times 200 \mu\text{m}^2$ into gasketed diamond anvil cells.

3. RESULTS AND DISCUSSIONS

3.1 $\text{ZnO}_x\text{Se}_{1-x}$

Figure 2 shows PR spectra measured on the $\text{ZnO}_x\text{Se}_{1-x}$ samples with different O content. In each case, the derivative-like spectral features correspond to the optical transitions from the valence-band edge to the conduction-band edge in the samples, and provide a direct measure of the band-gap energy. It is clear from Fig.2, the band gap of the samples shifts towards lower energy with increasing O concentration. The increasingly broadened PR spectral features are commonly observed in semiconductor alloys and can be partially attributed to the spatial alloy fluctuations of the O concentration in the sample.

Plotted in Fig. 3 are the band-gap energies of the $\text{ZnO}_x\text{Se}_{1-x}$ samples as a function of O concentration. The energy gap for each sample was determined by fitting the corresponding PR spectral curve associated with the transition from the top of valence band to the bottom of the conduction band to the lineshape functional form of three-dimensional interband transitions [16,17]. The band gap decreases at a rate of about 0.1 eV per atomic percent of oxygen. This large O-induced band-gap reduction indicates a large band-gap bowing that bears a close resemblance to the analogous effects that have been extensively studied in $\text{GaN}_x\text{As}_{1-x}$ and $\text{Ga}_{1-y}\text{In}_y\text{N}_x\text{As}_{1-x}$ HMA's ($x < 0.05$). The solid line in the figure is the best fit using Eq.(1) to the experimental data with C_{MO} and E_O as adjustable parameters. The fit to the data is excellent. The large reduction of the fundamental band gap in $\text{ZnO}_x\text{Se}_{1-x}$ with the increasing O

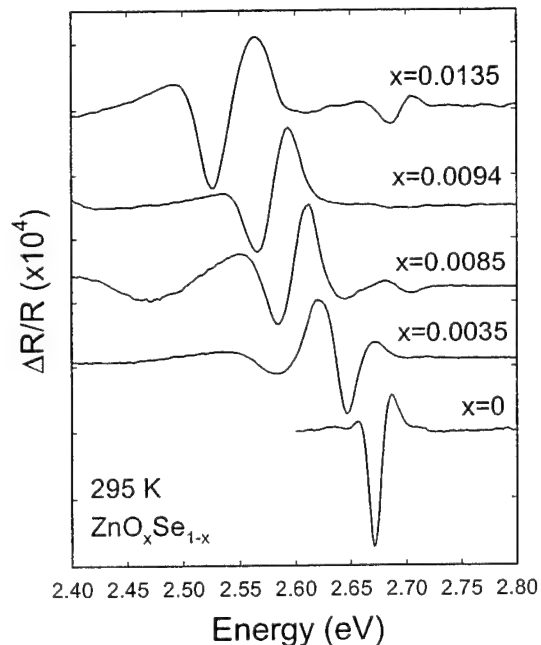


Fig. 2. PR spectra from $\text{ZnO}_x\text{Se}_{1-x}$ at 295K.

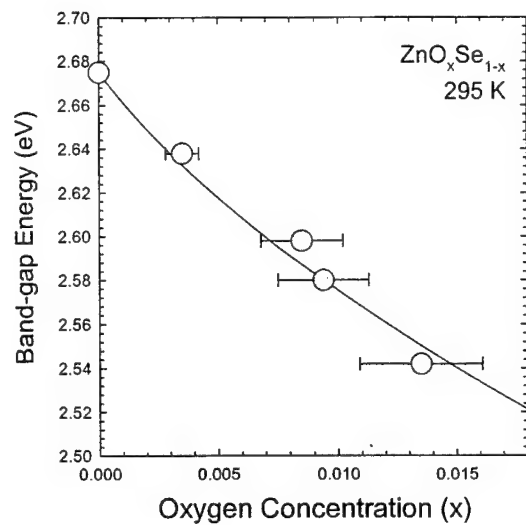


Fig. 3. Band-gap energies as a function of O concentration. The solid line is the best fit to the data using the BAC model.

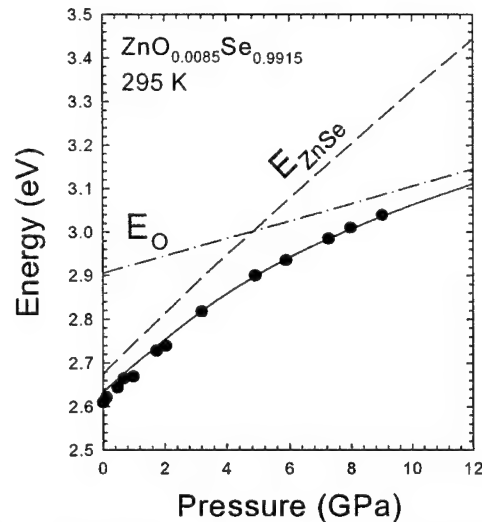


Fig. 4. The effect of pressure on PL transition energy associated with an $x=0.0085$ sample. The solid line is the calculated result using the BAC model.

concentration can be attributed to the downward shift of E_- relative to the valence band as a result of band anticrossing. The theoretical fitting results yield the energy position of O level $E_O = E_V + 2.90 \pm 0.02$ eV and the interaction parameter $C_{MO} = 1.8 \pm 0.3$ eV.

To further demonstrate that the band-gap reduction observed in the $\text{ZnO}_x\text{Se}_{1-x}$ samples results from band anticrossing, we have used PL to measure the energy positions of the optical transitions associated with the fundamental band gap in a $\text{ZnO}_{0.0085}\text{Se}_{0.9915}$ sample as a function of applied hydrostatic pressure. The results are shown in Fig. 4, along with the known pressure dependence of PL features from thick ZnSe epilayers grown on GaAs substrates [18]. The pressure-induced energy shift of the optical transition related to the direct band gap of the sample is weaker and much more nonlinear than in ZnSe. This indicates that the application of high pressure gradually changes the character of the conduction-band edge (E_-) from extended-like to localized-like. The solid line in the figure shows the pressure dependence of the PL transition energy that corresponds to the change of the band gap of the sample calculated using Eq.(1) with the same values of E_O and C_{MO} .

It is very interesting to note that the energy position of O level in ZnSe determined here can be used to evaluate band-edge offsets between ZnTe and ZnSe. It has been well established that the energy levels of highly localized states are independent of the host material. For example, the locations of the d-states of transition metals, have been used to determine the band edge offsets [19] and the band-edge deformation potentials in compound semiconductors [20]. The O level was previously found to be located at about 0.24 eV below the conduction-band edge in ZnTe [21]. Combining this with current result of 0.22 eV above the conduction band edge of ZnSe for the O level, it yields a value of $\Delta E_c \approx 0.46$ eV for the conduction-band offset and $\Delta E_v \approx 0.9$ eV for the valence-band offset for ZnTe/ZnSe system.

The absence of spectral features related to the optical transition associated with the conduction-band edge E_+ in the $\text{ZnO}_x\text{Se}_{1-x}$ samples used in this work is not inconsistent with the BAC model [6,9]. Note that the E_+ band edge has mostly localized-like character, and since the dipole interaction for optical transitions couples much more strongly to extended states than localized states, the transition related to E_+ is inherently weak. In addition, the energy separation between E_+ and E_- and the oscillator strength of the E_+ transition depend on the O content and the coupling parameter. In the case of $\text{GaN}_x\text{As}_{1-x}$, with $C_{MN} = 2.7$ eV, the E_+ transition can be spectrally observed only over the range of $x > 0.005 \sim 0.008$ [7,22,23]. This indicates that, with an almost two times smaller coupling parameter of $C_{MO} \approx 1.8$ eV in $\text{ZnO}_x\text{Se}_{1-x}$, it will certainly require an alloy composition of $x > 0.02$ to resolve the E_+ -transition related spectral feature.

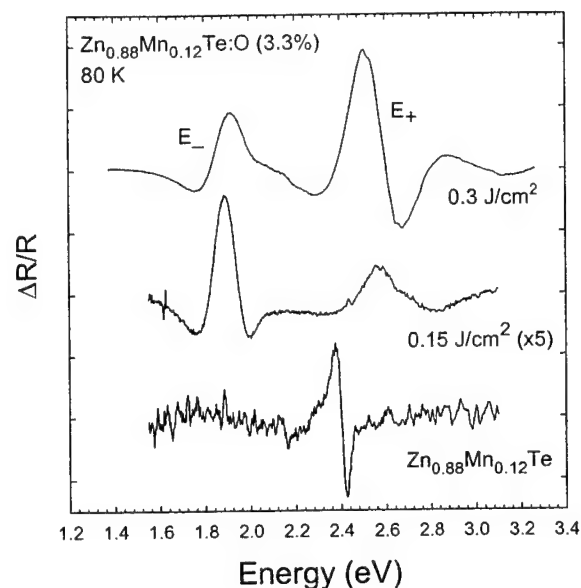


Fig. 5. PR spectra taken from $\text{Zn}_{0.88}\text{Mn}_{0.12}\text{Te}_{1-x}\text{O}_x$ samples at 80 K compared with the PR curve of $\text{Zn}_{0.88}\text{Mn}_{0.12}\text{Te}$ substrate.

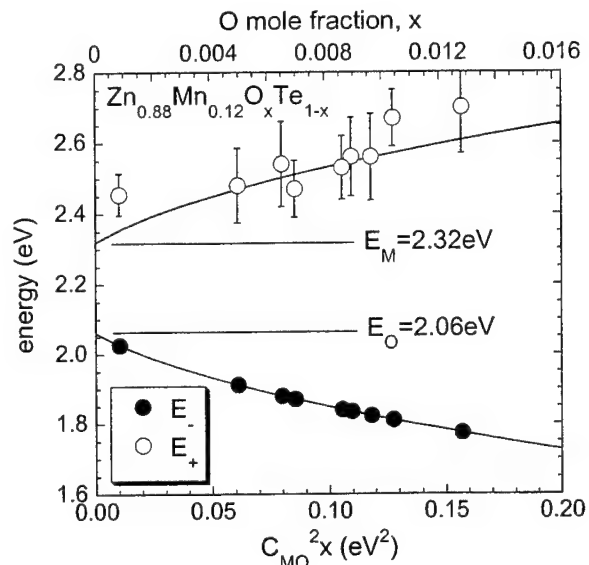


Fig. 6. The energy positions of E_- and E_+ for the $\text{Zn}_{0.88}\text{Mn}_{0.12}\text{O}_x\text{Te}_{1-x}$ alloys plotted against the O mole fractions x . The values of E_- and E_+ calculated according to the band anticrossing model are plotted as solid lines.

3.2 $\text{Zn}_{1-y}\text{Mn}_y\text{O}_x\text{Te}_{1-x}$

The relatively weak anticrossing interaction due to the relatively high location of the localized O level and small O mole fraction inhibits the observation of optical transitions associated with the E_+ band edge in the currently available $\text{ZnO}_x\text{Se}_{1-x}$ samples. To address the issue of E_+ transitions in II-O-VI alloys we have studied $\text{Zn}_{1-y}\text{Mn}_y\text{O}_x\text{Te}_{1-x}$ alloys. As discussed above, in the dilute limit ($x \rightarrow 0$) the O level is located below the conduction band of ZnTe. Because of a very small conduction band offset between ZnTe and ZnMnTe [24], the O level is expected to locate below the conduction band edge in ZnMnTe as well. Therefore, the E_- and E_+ band edges of $\text{Zn}_{1-y}\text{Mn}_y\text{O}_x\text{Te}_{1-x}$ formed by the band anticrossing interaction should possess a character opposite to that of $\text{ZnO}_x\text{Se}_{1-x}$, respectively, as described in Fig.1(b): E_- is of localized-like nature and E_+ is extended-like. The extended-like nature of the E_+ band edge of $\text{Zn}_{1-y}\text{Mn}_y\text{O}_x\text{Te}_{1-x}$ should have a relatively large oscillator strength to produce some detectable spectral response.

The PR spectra taken at 80 K from two $\text{Zn}_{0.88}\text{Mn}_{0.12}\text{O}_x\text{Te}_{1-x}$ samples implanted with 3.3% O^+ followed by PLM with a laser energy fluence of 0.15 and 0.3 J/cm^2 are shown in Fig. 5. The actual "active" O concentration (x) in the $\text{Zn}_{0.88}\text{Mn}_{0.12}\text{O}_x\text{Te}_{1-x}$ samples is estimated to be roughly around 1% by assuming a $C_{\text{MO}} = 3.5 \text{ eV}$ [25]. However, it should be noted that the precise value of the composition x is not very important in the discussion presented here. A PR spectrum taken from the $\text{Zn}_{0.88}\text{Mn}_{0.12}\text{Te}$ used as the substrate in this work is also plotted in the figure for comparison. The derivative-like spectral feature of the PR curve of $\text{Zn}_{0.88}\text{Mn}_{0.12}\text{Te}$ corresponds to the optical transition from the valence-band edge to the conduction-band edge. The band-gap energy is found to be 2.40 eV at 80 K for the $\text{Zn}_{0.88}\text{Mn}_{0.12}\text{Te}$ matrix. For the oxygen containing samples, the PR spectra exhibit two features with energies distinctly different from the fundamental band gap of $\text{Zn}_{0.88}\text{Mn}_{0.12}\text{Te}$ matrix. These two features can be attributed to the transitions from the top of the valence band to the two conduction subband edges, E_- ($\sim 1.85 \text{ eV}$) and E_+ ($\sim 2.6 \text{ eV}$), formed by the band anticrossing interaction between the localized O states and the extended conduction-band states of the ZnMnTe matrix. The strong photomodulation signals of both E_- and E_+ indicate the extended nature of the electronic states in E_- and E_+ subbands.

The energy positions of E_- and E_+ for the $\text{Zn}_{0.88}\text{Mn}_{0.12}\text{O}_x\text{Te}_{1-x}$ alloys with different x are plotted in Fig. 6. The data were taken at room temperature from samples implanted with different amounts of O (1.65, 2.2 and 4.4%) and PLM processed with different energy fluences. The energy positions of the two transitions predicted by the BAC model are plotted as

solid lines. Since, in this figure, the values of C_{MO}^2x were calculated from the energy of the E_- transition no error bars are given for E_- . Given the broad linewidth of the PR feature corresponding to the E_+ transitions, the data in Fig.6 are in reasonable agreement with the calculations based on the BAC model.

The effects of applied pressure on the E_- transition in the $Zn_{0.88}Mn_{0.12}O_xTe_{1-x}$ samples were studied in order to verify the origin of the E_- band. The energy positions of the E_- transition in the sample treated by PLM with a laser energy fluence of 0.3 J/cm^2 has been measured as a function of applied hydrostatic pressure at room temperature. The results are shown in Fig. 7, along with the measured pressure dependence of the band gap of the $Zn_{0.88}Mn_{0.12}Te$ matrix. The room-temperature energy position of the E_+ transition at atmospheric pressure is also shown in the figure. The inset shows a typical PT spectrum recorded at high pressures. The broad PT feature on the lower energy side corresponds to the E_- transition and the narrow PT feature (E_g^{ZnMnTe}) on the higher energy side is the transition associated with the fundamental band gap of $Zn_{0.88}Mn_{0.12}Te$ substrate.

A linear fitting to the experimental data that are shown by open circles in Fig.7 yields the value of $dE_g/dP=8.5 \text{ meV/kbar}$ for the pressure dependence of the $Zn_{0.88}Mn_{0.12}Te$ band gap. The pressure-induced energy shift of the E_- transition is much weaker with an initial slope $\approx 2 \text{ meV/kbar}$ than the pressure induced change of the direct band gap of $Zn_{0.88}Mn_{0.12}Te$ matrix. The weak pressure dependence of the E_- transition can be fully understood with the BAC model. The fact that E_- is located much closer to the energy level of the localized O states [Fig.1(b)] gives its wavefunction a pronounced O-like character. The solid lines through the experimental data in Fig. 7 are the calculated pressure dependencies of the E_- and E_+ transitions using Eq. (1). The best fits to the data yield the energy position of the O level (relative to the top of the valence band) $E_O=E_V+2.0\pm0.1 \text{ eV}$ at atmospheric pressure with a pressure dependence of $0.6\pm0.1 \text{ meV/kbar}$. It is clear from the figure that the pressure dependence of the E_- transition is slightly stronger than that of the O level as expected from the admixture of extended conduction-band Γ_C states of the matrix to the E_- band-edge states.

The present results have important inferences for the understanding of the origin of the unusual electronic structure of HMAs. They show very clearly that the BAC model provides a unifying description of the electronic structure of a large

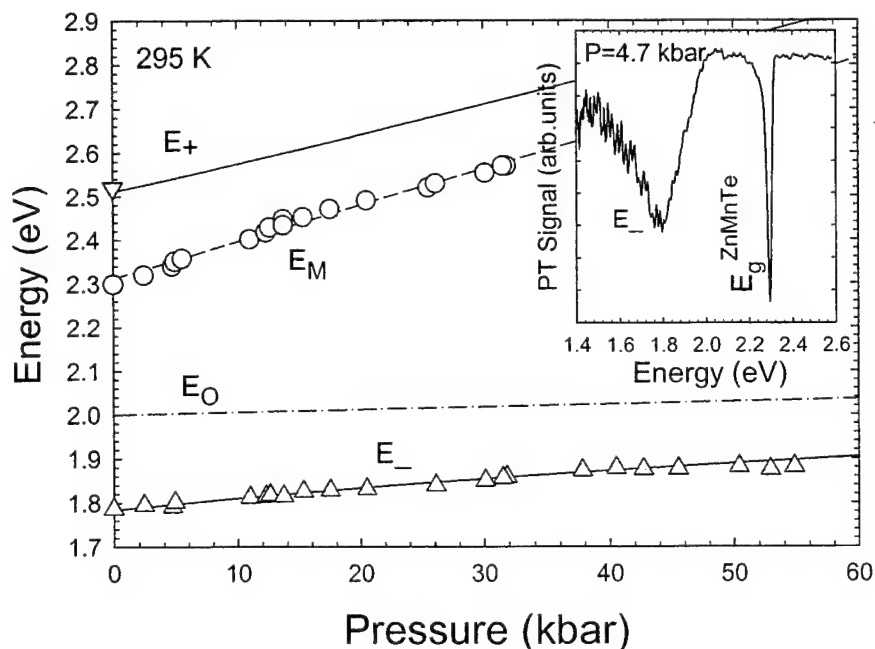


Fig. 7. Effect of pressure on the energy position of the E_- band edge of a $Zn_{0.88}Mn_{0.12}O_xTe_{1-x}$ sample (triangles). The change of the band gap of the $Zn_{0.88}Mn_{0.12}Te$ substrate with pressure is also displayed (open circles). The solid lines are theoretical fitting results. The dashed-dotted line is the location of E_O relative to the top of the valence band. The inset shows a typical PT spectrum of $Zn_{0.88}Mn_{0.12}O_xTe_{1-x}$ under pressure.

variety of different HMAs. They also provide strong arguments against other previously proposed models. It has been argued that the electronic structure of $\text{GaN}_x\text{As}_{1-x}$ alloys results from an interaction between the closely lying Γ_C , L_C , and X_C minima [26-28]. The interaction is caused by the perturbation potential resulting from the substitution of N atom on an As site. In these models the smaller and pressure-dependent pressure coefficient of the E_- transition observed in $\text{GaN}_x\text{As}_{1-x}$ alloys was attributed to the increasing contribution of the L_C and X_C minima whose pressure coefficients are much smaller than that of the Γ_C minimum. Apparently, these models cannot explain the results presented here. The large downward shift of 0.5 eV of the conduction band minimum (E_-) and the very weak pressure dependence of the band energy as shown in Fig.6 cannot be attributed to the influence from the conduction-band L and X edges because they are located far away from the Γ_C edge (>1.0 eV) in $\text{Zn}_{1-y}\text{Mn}_y\text{Te}$ [29]. Thus, our results directly confirm that the E_- transition together with the E_+ is the results of a band anticrossing interaction between the extended Γ conduction-band states and highly localized states in highly mismatched alloys.

3.3 Photovoltaic application

The O-induced modification of the conduction band structure offers an interesting possibility of using small amounts of O to engineer the optoelectronic properties of group II-O-VI alloys. One of the many technological potentials of II-O-VI HMAs is for photovoltaic applications. Efforts to improve the efficiency of solar cells have led to extensive experimental and theoretical studies of new materials and cell designs. To date, the highest power conversion efficiency of $\sim 33\%$ has been achieved with multi-junction solar cells based on standard semiconductor materials [30-32]. It was recognized over thirty years ago that the introduction of states in a semiconductor band gap presents an alternative to multi-junction designs for improving the power conversion efficiency of solar cells [33-35]. It was argued that deep impurity or defect states could play the role of the intermediate states for this purpose. Detailed theoretical calculations indicate that a single junction cell with one or two properly located bands of intermediate states could achieve power conversion efficiencies up to 62% [34] and 71.7% [35], respectively. However, difficulties in controlling the incorporation of high concentrations of impurity or defect states have thwarted prior efforts to realize such materials.

With the multiple band gaps that fall within the solar energy spectrum, $\text{Zn}_{1-y}\text{Mn}_y\text{O}_x\text{Te}_{1-x}$ provides a unique opportunity for the realization of the proposed multiband solar cell. The energy band structure and the density of states for the case of $\text{Zn}_{0.88}\text{Mn}_{0.12}\text{O}_x\text{Te}_{1-x}$ alloy (with $x \sim 0.01$) are shown in Fig. 8. An O derived narrow band of extended states E_- is separated from the upper subband E_+ by about 0.7 eV. Three types of optical transitions are possible in this band structure; (1) from the valence band to the E_+ subband, $E_{v+} = E_+(k=0) - E_v(k=0) = 2.56$ eV, (2) from the valence band to E_- subband, $E_{v-} = E_-(k=0) - E_v(k=0) = 1.83$ eV and (3) from E_- to E_+ , $E_{+-} = E_+(k=0) - E_-(k=0) = 0.73$ eV. These three absorption edges span much of the solar spectrum, indicating that these alloys could be good candidates for the multi-band semiconductors envisioned for high efficiency photovoltaic devices.

4. CONCLUSIONS

We have studied the effect of oxygen on the electronic band structure of $\text{ZnO}_x\text{Se}_{1-x}$ and $\text{Zn}_{1-y}\text{Mn}_y\text{O}_x\text{Te}_{1-x}$ alloys by investigating the optical transitions associated with the Γ point at the conduction-band and the valence-band edges, as well as the dependence of the transitions on applied pressure. A number of classical band-anticrossing behaviors

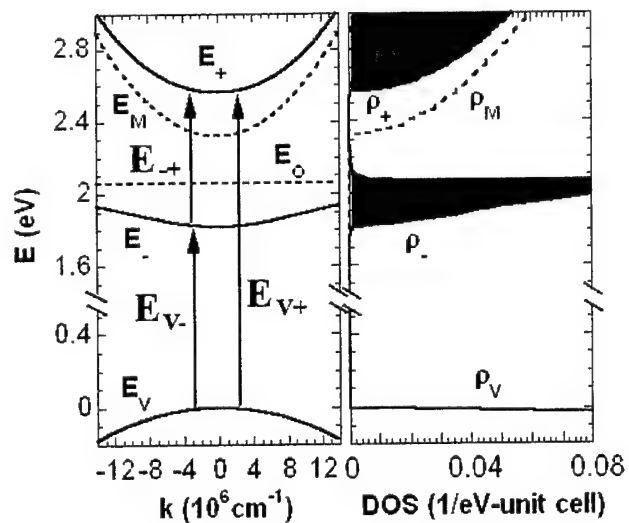


Fig. 8. The calculated energy band structure (left panel) and density of states (right panel) for $\text{Zn}_{0.88}\text{Mn}_{0.12}\text{O}_x\text{Te}_{1-x}$ with $x \sim 0.01$. The three possible optical transitions are indicated in the left panel.

resulting from the strong interaction between the localized O states and the extended conduction-band states of the host material matrix have been observed in the samples studied in this work: A significant band-gap reduction with increasing O concentration in $\text{ZnO}_x\text{Se}_{1-x}$ samples, optical transitions related to two conduction subbands E_- and E_+ in $\text{Zn}_{1-y}\text{Mn}_y\text{O}_x\text{Te}_{1-x}$ samples, and the demonstration of characteristic band-anticrossing behavior in the pressure dependence of the fundamental band gap in both alloy systems. These experimental results confirm that replacing group-VI anions in II-VI materials with isoelectronic but more electronegative O atoms does form highly mismatched II-O-VI alloy systems. The O-induced modification of the conduction band structure can be well described using the band anticrossing model that has been successfully applied to the III-N-V alloys. The O-induced modification of the conduction band structure offers the interesting possibility of using small amounts of O to engineer the optoelectronic properties of group II-O-VI alloys.

ACKNOWLEDGEMENTS

This work is supported by the Director, Office of Science, Office of Basic Energy Sciences, Division of Materials Sciences and Engineering, of the U.S. Department of Energy under Contract No. DE-AC03-76SF00098.

REFERENCES

1. M. Weyers, M. Sato, and H. Ando, *Jpn. J. Appl. Phys.* **31**, L853(1992).
2. M. Kondow, K. Uomi, K. Hosomi and T. Mozume, *Jpn. J. Appl. Phys.* **33**, L1056(1994).
3. C. Skierbiszewski, P. Perlin, P. Wisniewski, W. Knap, T. Suski, W. Walukiewicz, W. Shan, K.M. Yu, J.W. Ager, E.E. Haller, J.F. Geisz, and J.M. Olson, *Appl. Phys. Lett.* **76**, 2409(2000).
4. J.F. Geisz, D.J. Friedman, J.M. Olson, S.R. Kurtz, and M.B. Keyes, *J. Cryst. Growth*, **195**, 401(1998).
5. S.R. Kurtz, Allerman, C.H. Seager, R.M. Sieg, and E.D. Jones, *Appl. Phys. Lett.* **77**, 400(2000).
6. W. Shan, W. Walukiewicz, J. W. Ager III, E. E. Haller, J. F. Geisz, D. J. Friedman, J. M. Olson, and S. R. Kurtz, *Phys. Rev. Lett.* **82**, 1221(1999).
7. J. D. Perkins, A. Mascaranhas, Y. Zhang, J. F. Geisz, D. J. Friedman, J. M. Olson, and S. R. Kurtz, *Phys. Rev. Lett.* **82**, 3312(1999).
8. K. Uesugi, N. Marooka and I. Suemune, *Appl. Phys. Lett.* **74**, 1254 (1999).
9. W. Walukiewicz, W. Shan, J. W. Ager III, D. R. Chamberlin, E. E. Haller, J. F. Geisz, D. J. Friedman, J. M. Olson, and S. R. Kurtz, in *Photovoltaics for the 21st Century*, ed. V.K. Kapur, R.D. McDonnell, D. Carlson, G.P. Cesar, and A. Rohatgi, (The Electrochemical Society, Pennington, NJ, 1999), p.199.
10. Y. Nabetani, T. Mukawa, Y. Ito, and T. Matsumoto, *Appl. Phys. Lett.* **83**, 1148(2003).
11. C. W. White and P. S. Peercy, *Laser and Electron Beam Processing of Materials* (Academic Press, New York, 1980).
12. S. Williams, in *Laser Annealing of Semiconductors*, eds. J. M. Poate and J. W. Mayer, (Academic Press, New York, 1982) p. 385.
13. K. M. Yu, W. Walukiewicz, M. A. Scarpulla, O. D. Dubon, J. Jasinski, Z. Liliental-Weber, J. Wu, J. W. Beeman, M. R. Pillai, and M. J. Aziz, *J. Appl. Phys.* **94**, 1043(2003).
14. M. A. Scarpulla, K.M. Yu, O. Monteiro, M. Pillai, M.C. Ridgway, M.J. Aziz, and O.D. Dubon, *Appl. Phys. Lett.* **82**, 1251(2003).
15. K. M. Yu, W. Walukiewicz, J. Wu, J. W. Beeman, J. W. Ager III, E. E. Haller, I. Miotkowski, A. K. Ramdas, and P. Becla, *Appl. Phys. Lett.* **80**, 1571(2002).
16. D. E. Aspnes, in *Optical Properties of Solid*, ed. M. Balkanski (North-Holland, Amsterdam, 1980), Chap. 4A.
17. O. J. Glembocki, *SPIE Proc. Vol.1286*, 2(1990).
18. J.A. Tuchman, S. Kim, Z.F. Sui, and I.P. Herman, *Phys. Rev. B* **46**, 13371(1992).
19. J. M. Langer and H. Heinrich, *Phys. Rev. Lett.* **55**, 1414(1985).
20. D. D. Nolte, W. Walukiewicz, and E. E. Haller, *Phys. Rev. Lett.* **59**, 501(1987).
21. W. Walukiewicz, W. Shan, K.M. Yu, J.W. Ager III, E.E. Haller, I. Miotkowski, M.J. Seong, H. Alawadhi, and A.K. Ramdas, *Phys. Rev. Lett.* **85**, 1552(2000).
22. W. Shan, W. Walukiewicz, J. W. Ager, E. E. Haller, J. F. Geisz, D. J. Friedman, J. M. Olson, and S. R. Kurtz, *J. Appl. Phys.* **86**, 2349(1999).
23. P.J. Klar, *et al*, *Appl. Phys. Lett.* **76**, 3439(2000).
24. K.M. Yu, W. Walukiewicz, J. Wu, J.W. Beeman, J.W. Ager III, E.E. Haller, I. Miotkowski, A.K. Ramadas, and P.

- Becla, Appl. Phys. Lett. **80**, 1571(2002).
25. K. M. Yu, W. Walukiewicz, J. Wu, W. Shan, J. W. Beeman, M. A. Scarpulla, O. D. Dubon, and P. Becla, Phys. Rev. Lett. **91**, 246203(2003).
 26. E.D. Jones, N.A. Modine, A.A. Allerman, S.R. Kurtz, A.F. Wright, S.T. Tozer, and X. Wei, Phys. Rev. B**60**, 4430(1999).
 27. T. Mattila, S.H. Wei, and A. Zunger, Phys. Rev. B**60**, R11245(1999).
 28. N.G. Szewacki and P. Boguslawski, Phys. Rev. B**64**, 16201R(2001).
 29. *Landolt-Börnstein*, eds. O. Madelung and M. Schultz, New Series, Group 3, Vol.22, Part a, Springer-Verlag, Berlin, 1988.
 30. P.K. Chiang, J.H. Ermer, W.T. Nishikawa, D.D. Krut, D.E. Joslin, J.W. Eldredge, B.T. Cavicchi, and J.M. Olson, Proc. 25th IEEE Photovoltaic Specialists Conf. (IEEE New York, 1996) p. 183.
 31. S. R. Kurtz, D. Myers, and J. M Olson, Proc. 26th IEEE Photovoltaic Specialists Conf. (IEEE, New York, 1997) p. 875.
 32. R. R. King, P. C. Colter, D. E. Joslin, K. M. Edmondson, D. D. Krut, N. H. Karam, and Sarah Kurtz, Proc. 29th IEEE Photovoltaic Specialists Conf. New Orleans, 2002 (IEEE, New York, 2002) p. 852.
 33. M. Wolf, Proc. IRE, **48**, 1246(1960).
 34. A. Luque and A. Marti, Phys. Rev. Lett. **78**, 5014(1997).
 35. A. S. Brown, M. A. Green and R. P. Corkish, Physica, E**14**, 121(2002).
 36. W. Shockley and H. J. Queisser, J. Appl. Phys. **32**, 510(1961).

Essex distributed time domain model (eDTDM) for complex laser modeling

S. P. Higgins^a and A. J. Vickers^{*a}

^aUniversity of Essex, Wivenhoe Park, Colchester, Essex, CO4 3SQ, UK

ABSTRACT

We present a new distributed time domain model (DTDM) using Maxwell's wave equations with a time dependent polarization in the form of classical electron oscillators (CEO)s with randomly excited spontaneous emission using a virtual field. The model is based upon the neoclassical rate equations of A.E. Siegman¹ and includes effects such as chromatic dispersion, line-width enhancement, gain suppression, optically induced gratings, and excess noise. Although our equations were independently derived we have found that they do resemble the Maxwell-Bloch equations². However, most authors appear to favor the Ginzburg-Landau equations for their DTDM models³. We demonstrate that the model can reproduce results comparable with those of others, as well as new results.

Keywords: DTDM, CEO, dipole, Rabi flopping, Multimode, Mode locking

1. INTRODUCTION

This model was developed in an attempt to produce a more accurate mathematical description of the way that high speed optical signals interact with the carrier density, this is of particular importance in mode locked lasers devices, where the pulse duration is very small and hence wide bandwidth. The biggest improvement made in this work is that the power flow into or out of the carrier density in the gain medium or absorber comes from the optical polarization just as the gain does. This results in the power flow having the same frequency dependence as the incremental gain, which ensures that the stimulated emission rate varies by the same amount as the gain for any given optical mode. Whereas usually the power flow is taken as being equal to the square of the magnitude of the electric field times a carrier density dependant stimulated emission rate, which is not frequency dependant at all.

There are a large number of DTDM models in existence but to the best of our knowledge this is the first distributed dipole model to include spontaneous emission, especially by the use of a virtual electric field. Because it is different from other models we feel that a complete derivation is the best way to demonstrate how it works. The first stage in the derivation of this model is to apply the slowly varying envelope approximation (SVEA)¹ to Maxwell's wave equation for E , to reduce it from a single second order vector equation, to a pair of first order complex scalar equations. These represent light propagating to the right, and light propagating to the left. Next the gain is implemented using CEOs⁴ to represent the optical polarization; these too are approximated with the SVEA so that they become first order, resulting in a Lorentzian gain spectrum. Spontaneous emission is then included into these CEO's as a stimulated emission driven by a virtual electric field representing the vacuum fluctuations in the laser cavity.^{5, 6} Finally to complete the model, the boundary conditions are added along with a modification on the power flow to allow for optically induced refractive index gratings. These gratings are also implemented using CEO dipole techniques, and therefore have frequency and phase dependencies that are not accounted for using the usual product of forward and reverse field magnitude technique.

To verify that the mathematical model functions correctly a series of basic devices have been simulated, utilizing only parts of the model, before finally simulating more complicated structures with the entire model. Firstly we present the gain spectrum of a block of material using just the field propagation and dipole equations¹, and then we proceed to study the Rabi oscillations⁷ resulting from the application of a sudden large optical pulse to an absorbing material, using the field propagation, dipole equations, power flow equation⁸, and the carrier density equations. Next we examine the reflectance caused by the optically induced index grating effect^{9, 10} using counter propagating input pulses. Finally we demonstrate pulse compression using a saturable absorber¹¹. Having verified the correct functioning of the various attributes of the mathematical model we then proceed to numerically model a two section self-pulsating laser and a

* vicka@essex.ac.uk; phone 44 01206 872 876

compound cavity passively mode locked laser, and successfully produce both multimode self-pulsations and mode locked pulses.

2. THEORY

In the following section, all slowly varying variables are topped with tildes, and all vector quantities are topped with arrows, uni-directionally propagating fields use plus and minus superscripts to denote forwards and backwards propagation respectively. Sampled variables use n, k subscripts signifying position and time.

Table 1 Definition and values of variables used in the theory

Symbol	Value	Units	Meaning of symbol
a_g	2×10^{-20}	m^{-2}	Atomic cross section in gain section(s)
a_a	6×10^{-20}	m^{-2}	Atomic cross section in absorber section(s)
A_g	2×10^8	s^{-1}	Non radiative recombination in gain section(s)
A_a	5×10^{10}	s^{-1}	Non radiative recombination
B	1.25×10^{-4}	$m^3 s^{-1}$	Spontaneous recombination rate
D	6×10^{-8}	m	Depth of active layer
G		m^{-1}	Incremental absorption
\vec{E}		$Kg m s^{-2} c^{-1}$	Optical frequency electric field
J		$c s^{-1} m^{-2}$	Current density
K	4.12012×10^7	m^{-1}	Wave vector
L	2×10^{-4}	m	Length of laser diode
N		m^{-3}	Carrier density
N^r	1.2×10^{24}	m^{-3}	Transparency density
N_{dipole}		m^{-3}	Number of dipoles per volume of active medium
\vec{P}		$c m^{-2}$	Optical frequency Polarization
Q	1.60219×10^{-19}	c	Charge of one electron
\vec{r}		m	Position vector
R			Carrier generation rate per volume
$\tilde{V}_{n,k}^{\pm}$			Sampled slowly varying virtual electric field amplitude
Γ		s^{-1}	Atomic coefficient of damping
ϵ_r	16		Relative permittivity of material
ϵ_s	4.59742×10^{14}	$Kg^2 m s^{-4} c^{-2}$	Electric field saturation value
χ_E			Electric susceptibility
Ω	3.08795×10^{15}	s^{-1}	Optical frequency
$\tilde{\omega}$		s^{-1}	Detuning frequency relative to gain peak

2.1. Basic finite difference equations

Maxwell's wave equation for the electric field is

$$\nabla(\nabla \cdot \vec{E}(\vec{r}, t)) - \nabla^2 \vec{E}(\vec{r}, t) = -\sigma \mu_0 \frac{\partial \vec{E}(\vec{r}, t)}{\partial t} - \epsilon_0 \epsilon_r \mu_0 \frac{\partial^2 \vec{E}(\vec{r}, t)}{\partial t^2} - \mu_0 \frac{\partial^2 \vec{P}(\vec{r}, t)}{\partial t^2} \quad (1)$$

In the absence of charges and ohmic losses equation 1 simplifies to

$$\nabla^2 \vec{E}(\vec{r}, t) = \epsilon_0 \epsilon_r \mu_0 \frac{\partial^2 \vec{E}(\vec{r}, t)}{\partial t^2} + \mu_0 \frac{\partial^2 \vec{P}(\vec{r}, t)}{\partial t^2} \quad (2)$$

By considering only the component that lies parallel to the laser cavity, the wave equation becomes a one dimensional scalar equation, which with the aid of the SVEA, is reduced from second order to first order and down shifted from the optical frequency to zero frequency to give

$$\pm \frac{\partial \tilde{E}^{\pm}(z, t)}{\partial z} = -\sqrt{\epsilon_0 \epsilon_r \mu_0} \frac{\partial \tilde{E}^{\pm}(z, t)}{\partial t} + \frac{i\omega}{2} \sqrt{\frac{\mu_0}{\epsilon_0 \epsilon_r}} \tilde{P}^{\pm}(z, t) \quad (3)$$

The electric field now has two solutions, one with a plus superscript, indicating that it is traveling to the right and the other with a minus superscript meaning that it travels to the left. The tilde is chosen to indicate slowly varying complex amplitudes. Next the partial derivatives in equation 3 are converted to finite difference equations^{12, 13, 14} by using the equations 4, 5 and 6 to give equations 7 and 8.

$$\frac{\partial \tilde{E}^{\pm}(z, t)}{\partial z} = \lim_{\delta z \rightarrow 0} \frac{\tilde{E}^{\pm}(z + \delta z, t) - \tilde{E}^{\pm}(z, t)}{\delta z} \approx \frac{\tilde{E}_{n+1,k}^{\pm} - \tilde{E}_{n,k}^{\pm}}{\Delta z} \quad \frac{\partial \tilde{E}^{\pm}(z, t)}{\partial z} \gg \Delta z \frac{\partial^2 \tilde{E}^{\pm}(z, t)}{\partial z^2} \quad (4)$$

$$\frac{\partial \tilde{E}^{\pm}(z, t)}{\partial t} = \lim_{\delta t \rightarrow 0} \frac{\tilde{E}^{\pm}(z, t) - \tilde{E}^{\pm}(z, t - \delta t)}{\delta t} \approx \frac{\tilde{E}_{n,k}^{\pm} - \tilde{E}_{n,k-1}^{\pm}}{\Delta t} \quad \frac{\partial \tilde{E}^{\pm}(z, t)}{\partial t} \gg \Delta t \frac{\partial^2 \tilde{E}^{\pm}(z, t)}{\partial t^2} \quad (5)$$

The 'n' and 'k' subscripts in the difference equations represent position sample number and time sample number, where the continuous electric fields are sampled into discretised fields as follows

$$\tilde{E}_{n,k}^{\pm} = \tilde{E}^{\pm}(n\Delta z, k\Delta t) \quad (6)$$

From equations 3, 4, and 5 the difference equation for the right propagating wave is.

$$\tilde{E}_{n,k}^{+} = \tilde{E}_{n-1,k-1}^{+} + \frac{i\omega}{2} \sqrt{\frac{\mu_0}{\epsilon_0 \epsilon_r}} \Delta z \tilde{P}_{n-1,k}^{+} \quad (7)$$

And the difference equation for the left propagating wave is.

$$\tilde{E}_{n,k}^{-} = \tilde{E}_{n+1,k-1}^{-} + \frac{i\omega}{2} \sqrt{\frac{\mu_0}{\epsilon_0 \epsilon_r}} \Delta z \tilde{P}_{n+1,k}^{-} \quad (8)$$

2.2. Implementation of incremental gain and carrier generation using CEOs

The gain in this model results from resonant electric dipole transitions in the active medium, and appears as an imaginary part in the refractive index. Although the active medium in a semiconductor laser diode has bands of energy levels rather than discrete levels, the gain and absorption are both modeled as simple two level systems for simplicity. The atomic charge displacement is described by the following CEO equation

$$m_e \frac{\partial^2 \vec{x}_{atom}(\vec{r}, t)}{\partial t^2} = -q\vec{E}(\vec{r}, t) - m_e \gamma \frac{\partial \vec{x}_{atom}(\vec{r}, t)}{\partial t} - m_e \omega_0^2 \vec{x}_{atom}(\vec{r}, t) \quad (9)$$

The macroscopic dipole moment is made up of the sum of these atomic displacements times the charge q, and these displacements are all subject to de-phasing events such as phonon interactions which destroy the coherence between the individual atoms, thus reducing the sum dipole moment. So in fact the overall decay rate is greater than γ , and is written as $\Delta\omega$. The average electric dipole moment is defined as

$$\vec{\mu}(\vec{r}, t) = \sum_{i=1}^{N_{dipole}\Delta V} \vec{\mu}_i(\vec{r}, t) = \sum_{i=1}^{N_{dipole}\Delta V} q \vec{x}_i(\vec{r}, t) \quad (10)$$

The macroscopic polarization is thus given by the sum of the dipole moments¹⁵ in a small volume $\vec{\mu}(\vec{r}, t)$ divided by that volume ΔV .

$$\frac{\partial^2 \vec{P}(\vec{r}, t)}{\partial t^2} = \frac{-q^2 N_{dipole} \kappa \vec{E}(\vec{r}, t)}{m_e} - \Delta\omega \frac{\partial \vec{P}(\vec{r}, t)}{\partial t} - \omega_0^2 \vec{P}(\vec{r}, t) \quad (11)$$

Using the same simplifications used earlier in equation 2, the polarization simplifies to

$$\frac{\partial \tilde{P}^{\pm}(z, t)}{\partial t} = \frac{q^2 N_{dipole} \kappa}{i2\omega m_e} \tilde{E}^{\pm}(z, t) - \frac{\Delta\omega}{2} \tilde{P}^{\pm}(z, t) \quad (12)$$

In the numerical modeling the polarization is calculated using the sampled version of equation 12, in the following way

For the right propagating field

$$\tilde{P}_{n,k}^+ = \tilde{P}_{n,k-1}^+ + \left(\frac{q^2 N_{dipole} \kappa}{2i\omega m_e} \tilde{E}_{n,k-1}^+ - \frac{\Delta\omega}{2} \tilde{P}_{n,k-1}^+ \right) \Delta t \quad (13)$$

And for the left propagating field

$$\tilde{P}_{n,k}^- = \tilde{P}_{n,k-1}^- + \left(\frac{q^2 N_{dipole} \kappa}{2i\omega m_e} \tilde{E}_{n,k-1}^- - \frac{\Delta\omega}{2} \tilde{P}_{n,k-1}^- \right) \Delta t \quad (14)$$

The κ in equations 12, 13, and 14 is a carrier density dependent ratio that is responsible for determining the magnitude of the electric susceptibility, and thus the amount of incremental gain or absorption. This can be seen by solving equation 12 for steady state and rearranging to obtain an expression for the electric susceptibility

$$\chi_E(\tilde{\omega}) = \frac{\tilde{P}^\pm(z, t)}{\epsilon_0 \tilde{E}(z, t)} = \frac{q^2 N_{dipole} \kappa}{2i\omega \epsilon_0 m_e \left(i\tilde{\omega} + \frac{\Delta\omega}{2} \right)} \quad (15)$$

The resulting expression is clearly a complex Lorentzian function, the real part of which corresponds to phase shift per length and the imaginary part to the absorption. The electric susceptibility χ_E in equation 15 is related to the incremental electric field gain g and the carrier density in the active medium via the following equation

$$g(z, t) = -\frac{k}{2\epsilon_r} \text{Im}(\chi_E) = \frac{1}{2} \frac{a(z) [N(z, t) - N^r(z)]}{1 + \frac{1}{\epsilon_s} \left(|\tilde{E}^+(z, t)|^2 + |\tilde{E}^-(z, t)|^2 \right)} \quad (16)$$

And therefore κ is given by

$$\kappa_{n,k} = \frac{\omega \epsilon_0 \epsilon_r m_e \Delta\omega}{k q^2 N_{dipole}} \frac{a_n (N_{n,k} - N_n^r)}{1 + \frac{1}{\epsilon_s} \left(|\tilde{E}_{n,k}^+|^2 + |\tilde{E}_{n,k}^-|^2 \right)} \quad (17)$$

As well as the gain, the photon stimulated carrier generation and recombination processes are also calculated using the polarization, using the power density found by multiplying the electric field by the rate of change of polarization to give the absorption power density below

$$\text{Re} \left(\frac{\partial P^+(z, t)}{\partial t} E^+(z, t)^* + \frac{\partial P^-(z, t)}{\partial t} E^-(z, t)^* \right) \quad (18)$$

This gives a carrier density generation rate of

$$R_{n,k} = \frac{1}{\hbar\omega} \text{Re} \left(-i\omega \tilde{P}_{n,k}^+ \tilde{E}_{n,k}^{+*} - i\omega \tilde{P}_{n,k}^- \tilde{E}_{n,k}^{-*} \right) \quad (19)$$

The carrier density in this model is divided into sections, each of which has a pump term, a non radiative recombination, spontaneous emission recombination, and the carrier generation term quoted above.

$$\frac{\partial N(z, t)}{\partial t} = \frac{J(z, t)}{qd} - A(z, t)N(z, t) - B(z, t)N^2(z, t) + R(z, t) \quad (20)$$

When rearranged into integral form and sampled, the carrier density rate equation 20 becomes

$$N_{n,k+1} = N_{n,k} + \left(\frac{J_{n,k}}{qd} - A_n N_{n,k} - B_n N_{n,k}^2 + R_{n,k} \right) \Delta t \quad (21)$$

2.3. Adding spontaneous emission to the CEOs

In a purely classical description of atomic dipole transitions there is no spontaneous emission only stimulated emission and absorption, but a fully quantum mechanical treatment tells us that the upwards and downwards transition rates are not equal, and that even in the absence of a stimulating electric field, downward transitions still occur. Quantum

mechanics also predict that even at the ground state with no applied field present there exists half a photon of energy. The same is true of the field in the cavity. This residual half a quantum worth of energy is known as zero point energy¹⁶. In this model the zero point electromagnetic energy in the cavity is given as a virtual electric field which obeys the same propagation as the ordinary electric field but is not however subject to absorption or emission. The spontaneous emission is then modeled as if it were stimulated by the virtual field.

The slowly varying propagation equation for the virtual electric field is shown below

$$\pm \frac{\partial \tilde{V}^{\pm}(z, t)}{\partial z} = -\sqrt{\epsilon_0 \epsilon_r \mu_0} \frac{\partial \tilde{V}^{\pm}(z, t)}{\partial t} \quad (22)$$

This is sampled to give the following propagation equation

$$\tilde{V}_{n \pm 1, k}^{\pm} = \tilde{V}_{n, k-1}^{\pm} \quad (23)$$

To ensure that the absorption of virtual photons does not take place, the virtual electric field is applied only to the downward transition in the incremental gain function in equation 17 so that the polarization equations 13 and 14 can be written as

$$\tilde{P}_{n, k}^{\pm} = \tilde{P}_{n, k-1}^{\pm} + \left\{ \frac{1}{i\omega} \sqrt{\frac{\epsilon_0 \epsilon_r}{\mu_0}} \frac{a_n [N_{n, k} (\tilde{E}_{n, k-1}^{\pm} + \tilde{V}_{n, k-1}^{\pm}) - N_n'' \tilde{E}_{n, k-1}^{\pm}] - \tilde{P}_{n, k-1}^{\pm}}{1 + \frac{1}{\epsilon_s} (|\tilde{E}_{n, k}^+|^2 + |\tilde{E}_{n, k}^-|^2)} - \tilde{P}_{n, k-1}^{\pm} \right\} \frac{\Delta\omega}{2} \Delta t \quad (24)$$

2.4. Boundary conditions

When the electric field in the lasing cavity reaches the ends it is partially reflected back, and partially transmitted. We insert a source term at each of the end facets to allow for external light injection into the cavity. The electric field boundary conditions are as follows

For the left facet of the cavity the sampled propagation equation is

$$\tilde{E}_{1, k}^+ = t\tilde{E}_{in}^+ + r \left(\tilde{E}_{1, k-1}^- + \frac{i\omega}{2\epsilon_0 \epsilon_r} \Delta t \tilde{P}_{1, k-1}^- \right) \quad (25)$$

And for the right facet of the cavity the sampled propagation equation is

$$\tilde{E}_{m, k}^- = t\tilde{E}_{in}^- + r \left(\tilde{E}_{m, k-1}^+ + \frac{i\omega}{2\epsilon_0 \epsilon_r} \Delta t \tilde{P}_{m, k-1}^+ \right) \quad (26)$$

The equations for the virtual field are treated similarly except that the field source terms now represent the un-quantized zero point energy entering the cavity, instead of an optional applied field as before

$$\tilde{V}_{1, k}^+ = t\tilde{V}_{in}^+ + r\tilde{V}_{1, k-1}^- \quad (27)$$

$$\tilde{V}_{m, k}^- = t\tilde{V}_{in}^- + r\tilde{V}_{m, k-1}^+ \quad (28)$$

2.5. Induced grating effects

As the electric field propagating to the right passes through the field going to the left the intensity of the total field becomes corrugated along the cavity. Because the stimulated emission and absorption rates at any given point in the cavity are proportional to the light intensity at that point, a corresponding grating in the carrier density is created. So far in this paper, the spacing between sections have been set small enough that any curvature in the distribution caused by gain has negligible effect on the accuracy of the overall longitudinal carrier density, polarization and electric field. So the field profile is assumed to be constant in each section. But by assuming a constant distribution in each section, the induced grating effects are ignored. In order to increase the accuracy of the model the carrier density and polarization in a given section of the cavity are described by an average part plus a sinusoidal grating component.

$$P(z, t) = [\tilde{P}_{n, k}^{dc+} + \tilde{P}_{n, k}^{ac+} \cos(2kz + \phi)] e^{i(kz - \alpha t)} + [\tilde{P}_{n, k}^{dc-} + \tilde{P}_{n, k}^{ac-} \cos(2kz + \phi)] e^{i(-kz - \alpha t)} \quad (29)$$

$$N(\bar{z}, t) = N_{n,k}^{dc} + \text{Re}(N_{n,k}^{ac}) \cos(2kz) - \text{Im}(N_{n,k}^{ac}) \sin(2kz) \quad (30)$$

The ϕ in equation 29 is approximately given by the angle of the sinusoidal component of the carrier density in equation 30, and represents the fact that the position of the induced grating can move relative to the cavity. This relationship becomes approximate for fluctuating electric fields due to the finite response time of the polarization.

The new polarization equations are as follows.

$$\tilde{P}_{n,k}^{ac+} = \tilde{P}_{n,k-1}^{ac+} + \left\{ \frac{1}{i\omega} \sqrt{\frac{\epsilon_0 \epsilon_r}{\mu_0}} \frac{a_n N_{n,k}^{ac*} (\tilde{E}_{n,k-1}^+ + \tilde{V}_{n,k-1}^+)}{1 + \frac{1}{\epsilon_s} (|\tilde{E}_{n,k}^+|^2 + |\tilde{E}_{n,k}^-|^2)} - \tilde{P}_{n,k-1}^{ac+} \right\} \frac{\Delta\omega}{2} \Delta t \quad (31)$$

And for the left facing polarization

$$\tilde{P}_{n,k}^{ac-} = \tilde{P}_{n,k-1}^{ac-} + \left\{ \frac{1}{i\omega} \sqrt{\frac{\epsilon_0 \epsilon_r}{\mu_0}} \frac{a_n N_{n,k}^{ac} (\tilde{E}_{n,k-1}^- + \tilde{V}_{n,k-1}^-)}{1 + \frac{1}{\epsilon_s} (|\tilde{E}_{n,k}^+|^2 + |\tilde{E}_{n,k}^-|^2)} - \tilde{P}_{n,k-1}^{ac-} \right\} \frac{\Delta\omega}{2} \Delta t \quad (32)$$

The equations for the non corrugated parts of the polarization remain the same as they previously were in equation 24. However the electric field propagation equations now include an extra term.

$$\tilde{E}_{n,k}^{\pm} = \tilde{E}_{n-1,k-1}^{\pm} + \frac{i\omega}{2} \sqrt{\frac{\mu_0}{\epsilon_0 \epsilon_r}} \Delta z \left(\tilde{P}_{n,k}^{dc\pm} + \frac{\tilde{P}_{n,k}^{ac\mp}}{2} \right) \quad (33)$$

The first rounded bracket of equation 34 contains the usual averaged power flow terms of equation 19. While the second bracket contains the contribution of the grating to the average power, and remains zero unless there is both an induced grating present and an electric field propagating in both directions.

$$R_{n,k}^{dc} = \frac{1}{\hbar\omega} \text{Re} \left[i\omega (\tilde{P}_{n,k}^{dc-} \tilde{E}_{n,k}^+ - \tilde{P}_{n,k}^{dc+} \tilde{E}_{n,k}^-) + i\omega \frac{1}{2} (\tilde{P}_{n,k}^{ac+} \tilde{E}_{n,k}^- - \tilde{P}_{n,k}^{ac-} \tilde{E}_{n,k}^+) \right] \quad (34)$$

Equation 35, describes the carrier density generation rate of the grating itself, with the first rounded bracket containing the grating generation terms, and the second bracket the extinction terms.

$$R_{n,k}^{ac} = \frac{1}{\hbar\omega} \left[i\omega (\tilde{P}_{n,k}^{dc-} \tilde{E}_{n,k}^+ - \tilde{P}_{n,k}^{dc+} \tilde{E}_{n,k}^-) + i\omega (\tilde{P}_{n,k}^{ac+} \tilde{E}_{n,k}^- - \tilde{P}_{n,k}^{ac-} \tilde{E}_{n,k}^+) \right] \quad (35)$$

The upgraded rate equations are

$$N_{n,k+1}^{dc} = N_{n,k}^{dc} + \left[\frac{J_{n,k}}{qd} - A_n N_{n,k}^{dc} - B_n \left(N_{n,k}^{dc} + \frac{1}{2} |N_{n,k}^{ac}|^2 \right) + R_{n,k}^{dc} \right] \Delta t \quad (36)$$

$$N_{n,k+1}^{ac} = N_{n,k}^{ac} + \left(-A_n N_{n,k}^{ac} - 2N_{n,k}^{dc} B_n N_{n,k}^{ac} + R_{n,k}^{ac} \right) \Delta t \quad (37)$$

3. RESULTS

As was anticipated from equation 15, the gain resulting from the CEO dipole moment was found to produce Lorentzian gain and absorption spectra, shown below in figure 1, using equations 7 and 13 to model 200 μm of active medium with a fixed carrier density and no end reflectance. With a FWHM of 1THz, the model was found to be numerically stable from about 10 cavity sections onwards, and gave very consistent results for larger numbers of sections (50 and above). The graphs obtained compare favorably with other authors' findings.¹⁷

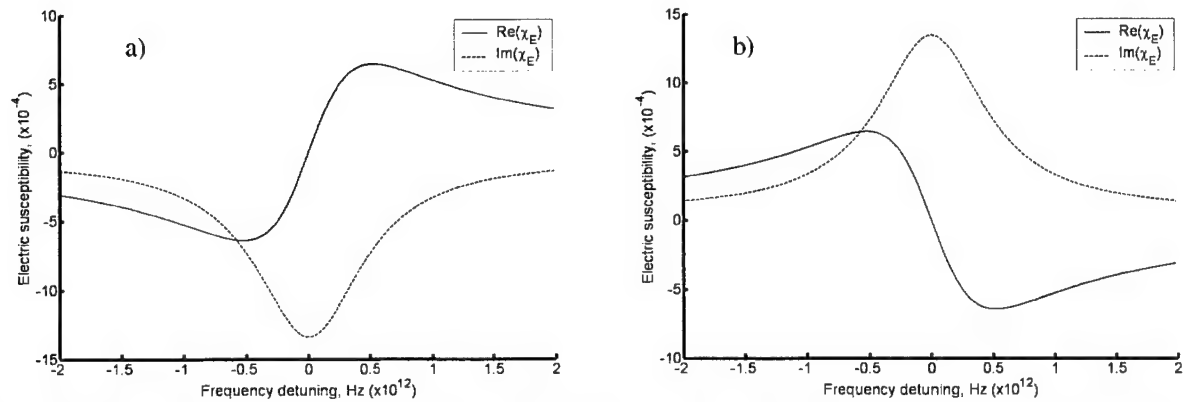


Fig 1 Numerically modeled electric susceptibility curves for 200 μ m of gain medium with a) a total gain of $\ln(2)$ and b) a total absorption of $\ln(2)$.

Using Equations 7, 13 and 21 it was found that when a pulse of sufficiently large magnitude was fed into an unbiased block of active medium, Rabi oscillations were observed¹⁸, see an example in figure 2. The frequency of these oscillations appeared to increase linearly with electric field amplitude, but display a square root dependence upon the spectral bandwidth of the CEO dipole in equation 13, see figure 3. This again is in keeping with expected theory⁷.

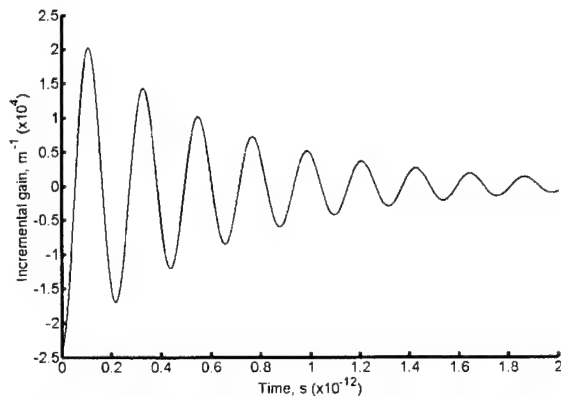


Fig 2. Rabi oscillations induced by a step function electric field of GV/m.

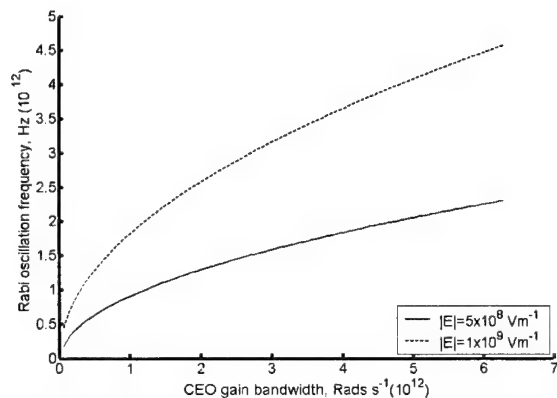


Fig 3 Rabi oscillation frequency from model, showing a linear dependence on electric field amplitude and a square root dependence on gain bandwidth.

To test the induced grating effect it was decided to numerically model the sending of a series of counter propagating Gaussian and rectangular pulses through a 200 μ m long block of antireflection coated gain medium, at a forward bias of 100mA, using the full set of equations. We began with a Gaussian pulse traveling to the right, followed by a bidirectional rectangular pulse of 1ns duration, which is sufficiently long to ensure the build up of the induced grating. A second Gaussian pulse was then inserted, also traveling to the right. As expected there was found to be no reflection from the first pulse since there was no induced grating present, but the second Gaussian pulse produced an easily detectable reflection shown in figure 4. It was observed that when the left and right components of the bidirectional pulse were at different frequencies, the carrier density grating was found to rotate in the complex domain at the difference between the frequencies, representing a moving grating rather than a stationary one. The magnitude of the grating was found to decrease as the difference between the frequencies was increased. Interestingly the spontaneous emission rate is greater when an induced grating is present. This can be explained by the AC dipole equations of 31 and 32 which produce no spontaneous emission unless a corrugation is present. This effect can also be understood by the fact that spontaneous emission rate is proportional to the mean square of the carrier density, which is larger when corrugated.

As a prelude to our mode locking work it was decided to prove that this model could demonstrate pulse shortening using a saturable absorber^{10, 11}. It was decided to numerically model a Gaussian pulse being transmitted through a reverse biased saturable absorber of 40 μ m length with antireflective coatings, as can be seen in figure 5. The pulse emerging from the far side of the absorber was indeed narrower than that which entered. And the degree of pulse shortening was found to improve with increasing non radiative decay rate. This implies that either ion implantation, or more likely an increased reverse bias could be used to improve pulse compression.

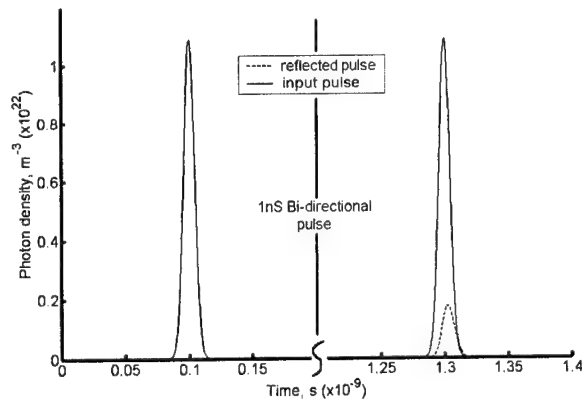


Fig 4. Reflection of an input pulse by an optically induced refractive index grating using 200 μ m of unbiased gain medium, showing the reflection before and after the application of a bi-directional pulse.

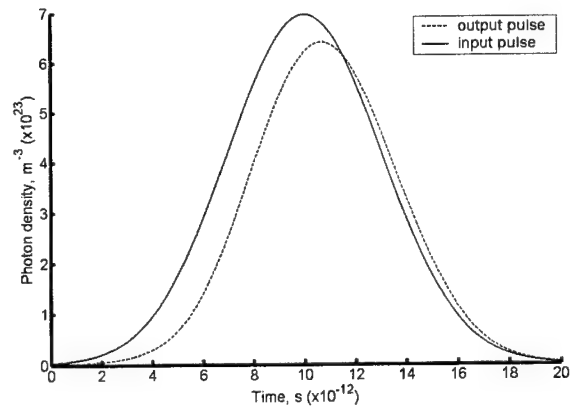


Fig 5 Single pass pulse compression using a 40 μ m reverse biased absorber section with antireflective facet coatings.

For the self-pulsation study a two section Fabry Perot laser diode was modeled with a 160 μ m gain section, and a 40 μ m reverse biased absorber. The non radiative decay rate in the absorber was set higher to account for the carrier sweep out effect of the reverse bias. Because the cavity was short and the absorber too slow for substantial pulse compression no mode locked pulses were observed. Instead a stream of fairly jittery pulses was produced. Each pulse having a Gaussian shape, seen in figure 6a, with a sequence of higher frequency ripples having a repetition rate consistent with the cavity round trip time shown in the inset of figure 6a. These ripples were shaped differently on every pulse indicating that the phase between each mode changes randomly between pulses. The random phase between the different modes seems to be the cause of the amplitude jitter. This randomness is present because each pulsation is seeded by the spontaneous emission, which is incoherent. The incoherent pulse seeding results in a spreading of the frequency spectrum of each mode, resulting in the spectrum shown in figure 6b.

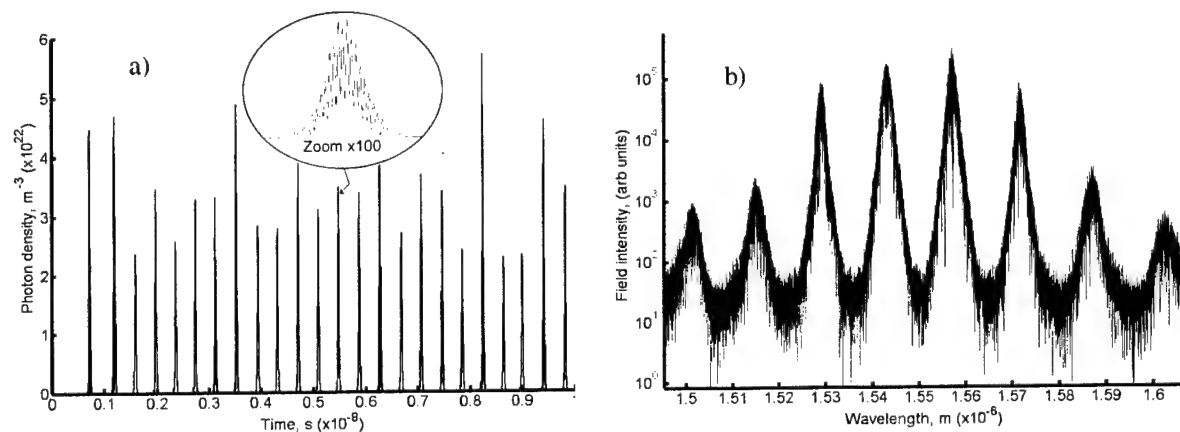


Fig 6 Self-pulsations in a 57.12mA asymmetrically pumped 200 μ m long Fabry Perot cavity containing a 40 μ m reverse biased saturable absorber, showing a) time domain, and b) frequency domain.

For mode locking the right hand facet was made anti reflective and a 6.7mm external cavity was formed with an external mirror. The mirror reflectivity was set the same as that of the left hand facet. The saturable absorber was placed on the left and the non radiative recombination rate in the absorber was increased to 1×10^{11} to increase the pulse compression ratio. The bias current was set to 100mA. The initial gain switched pulse contained many unsynchronized modes and so had a very jagged edge, but was not as intense as the mode locked pulses that followed because the energy was spread over a wider width. Immediately after the first pulse followed relaxation oscillations, containing rapidly narrowing pulses as all the modes became locked. This was followed by a stream of mode locked pulses with a slight amplitude modulation caused by weak self-pulsation, shown in figure 7a. These results are similar to ones shown in other publications^{19, 10}. The pulses themselves as shown in 7b appeared to be Gaussian in shape.

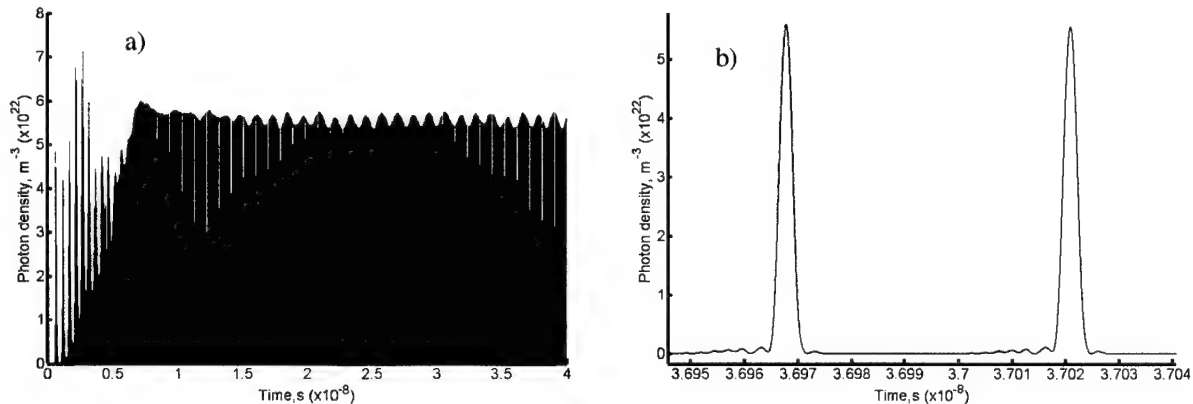


Fig 7 20GHz passively mode locked pulse generation from a 100mA asymmetrically pumped $200\mu\text{m}$ long laser diode with a 6.7mm external cavity, with a) showing the evolution from the transient response into steady state, and b) showing a close up of two of the steady state pulses.

4. CONCLUSION

At the time of writing this paper this model has been far from extensively studied, so there are likely to be many interesting and quite possibly unique results yet to be obtained, but already some interesting differences have come to light between this model and the usual techniques of others. Firstly in this model the presence of large pulses with fast rise times can result in Rabi oscillations, so one may well conclude that this will have an effect on the formation of mode locked pulses as we strive to create pulses ever closer to the transform limit. Secondly it is common practice to take the induced grating as being created by the product of the magnitude of the forwards and backwards propagating fields, times the average gain. This implies that a grating could be induced even if the left and right going fields have different frequencies. In this model however the use of dipolar power flow has necessitated a complex carrier density grating, resulting in a grating that actually moves along the cavity when the frequencies differ, and has magnitude related to not only the strength of the left and right fields but also to the temporal coherence between them.

ACKNOWLEDGEMENTS

Steven Higgins is grateful to the EPSRC for funding the initial work done on this paper.

REFERENCES

1. Anthony E. Siegman, *Lasers*, p 943-946, University Science Books, Sausalito, 1986.
2. Guido H. M. Tartwijk and Govind P. Agrawal, *Maxwell-Bloch dynamics and modulation instabilities in fiber lasers and amplifiers*, J Optical Society of America, Vol. 14, p 2618-2627, 1997.

3. C. S. Ng, and A. Battacharjee, *Ginzburg-Landau model for a free-electron laser: from single mode spikes*, Nuclear Instruments and Methods in Physics Research A, p 34-39, 1998.
4. Anthony E. Siegman, *Lasers*, p 80-96, University Science Books, Sausalito, 1986.
5. J. J. Sakurai, *Advanced Quantum Mechanics*, p 38-47, Addison-Westey Publishing Company, London, 1997.
6. Claude Cohen-Tannoud, *Quantum Mechanics Vol 1*, p 619, John Wiley & Sons, New York, 1997.
7. Anthony E. Siegman, *Lasers*, p 229-233, University Science Books, Sausalito, 1986.
8. Amnon Yariv, *Optoelectronics in Modern Communications*, 5th ed, p 10-11, Oxford University Press, New York & Oxford, 1997.
9. L. M. Zhang, and J. E. Carroll, "Dynamic response of colliding-pulse mode-locked quantum well lasers", *IEEE Journal of Quantum Electronics*, Vol.31, p 240-242, 1995.
10. D. J. Jones, L. M. Zhang, J. E. Carroll, and D. D. Marcenac, "Dynamics of monolithic passively mode-locked semiconductor lasers", *IEEE Journal of Quantum Electronics*, Vol.31, p 1051-1058, 1995.
11. D. J. Derickson, R. J. Helkey, A. Mar, J. R. Karen, J. G. Wasserbauer, and J. E. Bowers." Short pulse generation using multisegment mode-locked semiconductor lasers", *IEEE Journal of Quantum Electronics*, Vol. 28, p 2186-2202, 1992.
12. P. A. Morton, R. J. Helkey, and J. E. Bowers, "Dynamic detuning in actively mode-locked semiconductor lasers", *IEEE Journal of Quantum Electronics*, Vol. 25, p 2621-2633, 1989.
13. M. Schell, A. G. Weber, E. S. Scholl, and D. Bimberg, "Fundamental limits of sub-ps pulse generation by active mode locking of semiconductor lasers: the spectral gain width and the facet reflectivities", *IEEE Journal of Quantum Electronics*, Vol. 27, p 1661-1668, 1991.
14. A. G. Weber, M. Schell, G. Fischbeck, and D. Bimberg. "Generation of single femtosecond pulses by hybrid mode locking of semiconductor laser", *IEEE Journal of Quantum Electronics*, Vol. 28, p 2220-2229, 1992.
15. Anthony E. Siegman, *Lasers*, p 85, University Science Books, Sausalito 1986.
16. Leonard I. Schiff, *Quantum Mechanics*, 3rd ed, p 69, McGraw-Hill Book Company, New York, 1968.
17. Amnon Yariv, *Optoelectronics in Modern Communications*, 5th ed, p 196, Oxford University Press, New York & Oxford, 1997.
18. Anthony E. Siegman, *Lasers*, p 236-237, University Science Books, Sausalito. 1986.
19. A. E. Avrutin, J. H. Marsh, and E. L. Portnoi, "Monolithic and multi-Gigahertz mode-locked semiconductor lasers: Constructions, experiments, models and applications", *IEE Proc-Optoelectronics*, Vol. 147, p 251-278, 2000.

APPENDICES

SVEA approximations used in this paper

The one dimensional electric field is given by the sum of the left and right propagating fields thus.

$$E(z, t) = \tilde{E}^+(z, t)e^{i(kz - \omega t)} + \tilde{E}^-(z, t)e^{i(-kz - \omega t)}$$

The polarization is also given the same treatment.

$$P(z, t) = \tilde{P}^+(z, t)e^{i(kz - \omega t)} + \tilde{P}^-(z, t)e^{i(-kz - \omega t)}$$

The one dimensional wave equation is.

$$\frac{\partial^2 \tilde{E}^\pm(z, t)e^{i(\pm kz - \omega t)}}{\partial z^2} = \epsilon_0 \epsilon_r \mu_0 \frac{\partial^2 \tilde{E}^\pm(z, t)e^{i(\pm kz - \omega t)}}{\partial t^2} + \mu_0 \frac{\partial^2 \tilde{P}^\pm(z, t)e^{i(\pm kz - \omega t)}}{\partial t^2}$$

Expanding the above equation gives second order, first order, and zero order terms.

$$\begin{aligned} & \left[\frac{\partial^2 \tilde{E}^\pm(z, t)}{\partial z^2} \pm 2ik \frac{\partial \tilde{E}^\pm(z, t)}{\partial z} - k^2 \tilde{E}^\pm(z, t) \right] e^{i(\pm kz - \omega t)} \\ &= \epsilon_0 \epsilon_r \mu_0 \left[\frac{\partial^2 \tilde{E}^\pm(z, t)}{\partial t^2} - 2i\omega \frac{\partial \tilde{E}^\pm(z, t)}{\partial t} - \omega^2 \tilde{E}^\pm(z, t) \right] e^{i(\pm kz - \omega t)} \\ &+ \mu_0 \left[\frac{\partial^2 \tilde{P}^\pm(z, t)}{\partial t^2} - 2i\omega \frac{\partial \tilde{P}^\pm(z, t)}{\partial t} - \omega^2 \tilde{P}^\pm(z, t) \right] e^{i(\pm kz - \omega t)} \end{aligned}$$

The SVEA states that $\frac{\partial^2 \tilde{E}^\pm(z, t)}{\partial t^2} \ll \omega \frac{\partial \tilde{E}^\pm(z, t)}{\partial t} \ll \omega^2 \tilde{E}^\pm(z, t)$ and so the smallest terms from each side are ignored to give.

$$\pm \frac{\partial \tilde{E}^\pm(z, t)}{\partial z} = -\sqrt{\epsilon_0 \epsilon_r \mu_0} \frac{\partial \tilde{E}^\pm(z, t)}{\partial t} + \frac{i\omega}{2} \sqrt{\frac{\mu_0}{\epsilon_0 \epsilon_r}} \tilde{P}^\pm(z, t)$$

This process may also be repeated for the CEO.

$$\frac{\partial^2 \tilde{P}^\pm(\vec{r}, t)}{\partial t^2} = \frac{-q^2 N_{dipole} \kappa \tilde{E}^\pm(\vec{r}, t)}{m_e} - \gamma \frac{\partial \tilde{P}^\pm(\vec{r}, t)}{\partial t} - \omega_0^2 \tilde{P}^\pm(\vec{r}, t)$$

This may be expanded to give

$$\begin{aligned} & \frac{\partial^2 \tilde{P}^\pm(z, t)}{\partial t^2} - i2\omega_0 \frac{\partial \tilde{P}^\pm(z, t)}{\partial t} - \omega^2 \tilde{P}^\pm(z, t) \\ &= -\frac{q^2 N_{dipole} \kappa}{m_e} \tilde{E}^\pm(z, t) - \Delta\omega \frac{\partial \tilde{P}^\pm(z, t)}{\partial t} + i\omega\Delta\omega \tilde{P}^\pm(z, t) - \omega_0^2 \tilde{P}^\pm(z, t) \end{aligned}$$

Applying the SVEA to the above around the resonant frequency of the optical transition ω_0 gives

$$\frac{\partial \tilde{P}^\pm(z, t)}{\partial t} = \frac{q^2 N_{dipole} \kappa}{i2\omega m_e} \tilde{E}^\pm(z, t) - \frac{\Delta\omega}{2} \tilde{P}^\pm(z, t)$$

Optical gain

If we let the optical frequency electric field grow exponentially with respect to the z axis, with the gain part represented by an electric susceptibility as follows

$$E(z, t) = e^{i\omega(z\sqrt{\epsilon_0 \epsilon_r \mu_0} + \epsilon_0 \mu_0 \chi_E - t)}$$

Taking the derivative of this with respect to distance yields

$$\frac{\partial E(z, t)}{\partial z} = i\omega \left(\sqrt{\epsilon_0 \epsilon_r \mu_0} + \frac{\sqrt{\epsilon_0 \mu_0 \epsilon_r \chi_E}}{2\epsilon_r} \right) E(z, t) = ik \left(1 + \frac{\chi_E}{2\epsilon_r} \right) E(z, t)$$

The incremental electric field gain is thus given by the imaginary part of the electric susceptibility as follows

$$g(z, t) = -\frac{k}{2\epsilon_r} \text{Im}(\chi_E)$$

Design optimization of InGaAlAs/GaAs single and double quantum well lasers emitting at 808 nm

Mariusz Zbroszczyk*, Maciej Bugajski

Department of Physics and Technology of Low Dimensional Structures, Institute of Electron Technology, al. Lotników 32/46, 02-668 Warszawa; Poland

ABSTRACT

The laser diodes and laser bars with InGaAlAs/GaAs active region are attractive as high power devices operating at around 808 nm. The quaternary InGaAlAs active region seems to have distinctive advantages over the standard GaAs quantum well construction. The most important of them is that quantum wells, required to achieve desired wavelength can be wider, which provides better carrier confinement. Another advantage is better thermal conductivity of InGaAlAs as comparing to GaAs. We have modeled single and double quantum well separate confinement heterostructure lasers with various cavity lengths. The well thickness and indium content in the active region were optimized to obtain 808 nm wavelength with acceptable threshold current density. Numerical simulation based on the selfconsistent solution of drift diffusion equations, Schrödinger equation and photon rate equation has been used to optimize the high power lasers design. In this work we have used commercial simulation package PICS3D developed by Crosslight Soft. Inc.

Keywords: computer simulation, quantum wells, semiconductor-semiconductor heterostructures, InGaAlAs/GaAs

1. INTRODUCTION

High power laser diodes and laser bars have found wide spread applications as optical pumps for solid state lasers, in medicine and in material processing. InGaAlAs/GaAs diode lasers were recently reported^{1,2} as highly efficient and reliable light sources emitting at 808 nm. The quaternary InGaAlAs active region seems to have distinctive advantages over the standard GaAs quantum well construction. The chief of them is that we can use wider quantum wells, which provide better carrier confinement, to achieve desired emission wavelength. Although similar effect can be obtained with AlGaAs active region, the simultaneous addition of In stabilizes crystal lattice and makes InGaAlAs/GaAs lasers less prone to degradation. The another advantage of InGaAlAs/GaAs lasers is that they are natural extension of InGaAs/GaAs type lasers, which technology is very well developed³. High reliability of InGaAs/GaAs lasers, attributed to indium related *lattice hardening effect*, and their low threshold currents, resulting from strain related band structure modifications in the case of InGaAlAs/GaAs lasers have a chance to be augmented by their superior thermal properties⁴⁻⁶.

Since there is only a few experimental papers in the literature, dealing with this type of lasers and because the quaternary active regions offers more degrees, of freedom in manipulating its parameters it is important to evaluate theoretically possible designs and to optimize them with respect to the threshold current value. It has to be also mentioned that not all designs are equally feasible from technological point of view. The limitations are either of the pure materials origin, resulting from an excessive lattice mismatch between the layers, or they are directly related to the growth method, like for example the ones resulting from thermal lag of molecular fluxes and a consequent inability to change them rapidly in MBE technology. We have kept those limitations in mind while testing different laser constructions.

2. DETAILS OF MODELING

Numerical modeling is very important tool for optimization of semiconductor lasers and can significantly decrease the number of technological processes needed for particular device development. Optical and electrical parameters like

* mzbrosz@ite.waw.pl; phone:(+48 22) 5487931; fax: (+48 22) 5487925; www.ite.waw.pl

emitted wavelength and threshold current are the primary goal of theoretical analysis. In this work we have used PICS3D simulation package developed by Crosslight Soft. Inc.⁷. Transport of electrons and holes in a laser is described by the standard *drift-diffusion* model, consisting of three differential equations: Poisson's equation and continuity equations for electrons and holes, which govern the electrical behavior of a semiconductor laser and are solved selfconsistently with wave equation and photon conservation equation. The electron and hole confinement energies in the quantum well active region are obtained from the Schrödinger equation.

The model allows for including band nonparabolicity and valence band mixing effects as well as strain effects in the calculations. At the first step gain spectra are calculated and the wavelength range in which lasing is likely to occur is specified. At the next step bias is applied to the device and light-current characteristic is calculated together with the number of other characteristics of the laser. From the point of view of optimization of different laser designs the most important characteristics which are to be calculated are threshold current, differential (slope) efficiency and emission wavelength.

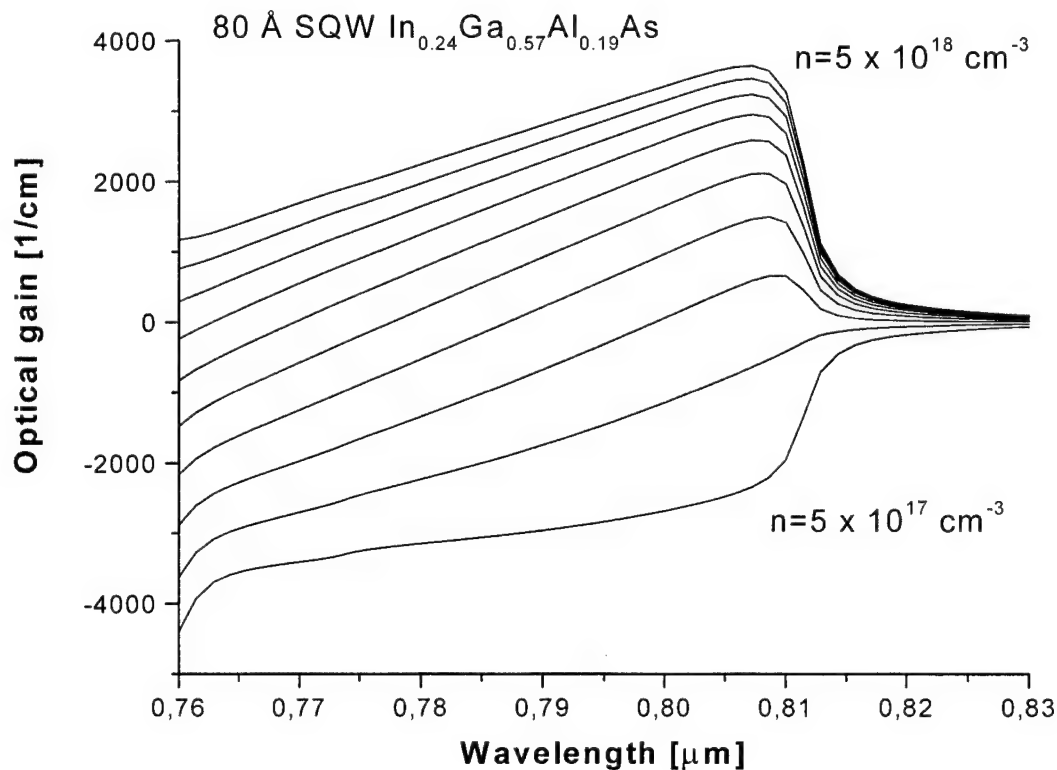


Fig. 1. Optical gain spectrum of 80 Å SQW $\text{In}_{0.24}\text{Ga}_{0.57}\text{Al}_{0.19}\text{As}$ laser.

3. RESULTS AND DISCUSSION

The lasers were designed for the operation at around 808 nm, suitable for pumping Nd-YAG solid state lasers. The laser structures investigated consisted of single (SQW) or double (DQW) $\text{In}_{0.24}\text{Ga}_{0.54}\text{Al}_{0.19}\text{As}/\text{Al}_{0.25}\text{Ga}_{0.75}\text{As}$ quantum well surrounded by $\text{Al}_{0.25}\text{Ga}_{0.75}\text{As}$ waveguide layers and $\text{Al}_{0.4}\text{Ga}_{0.6}\text{As}$ cladding layers. The total waveguide thickness was equal to 0.3 μm, the cladding layer thickness was 1.2 μm each. The thickness of well is equal 80 Å for SQW and DQW and the barrier is 100 Å thick (DQW). The length of the laser cavity varied from 400 μm to 1200 μm. The specific device which has been modeled was a broad contact $W = 100 \mu\text{m}$ laser. All calculation results refer to a constant temperature of 300 K.

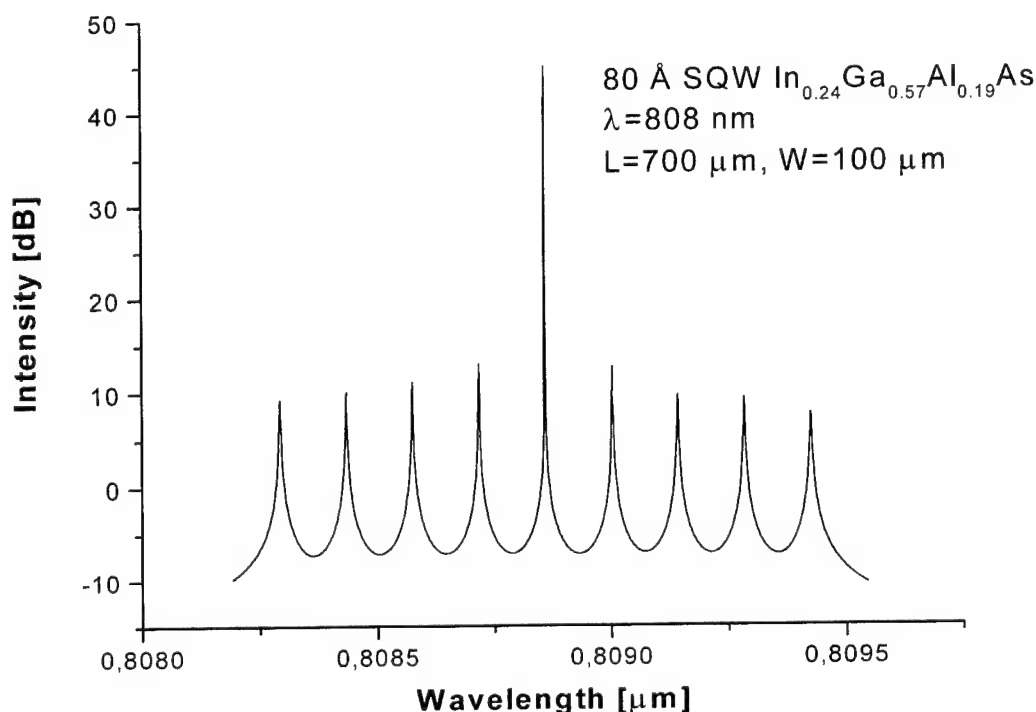


Fig. 2. Spectral characteristic of 80 Å SQW $\text{In}_{0.24}\text{Ga}_{0.57}\text{Al}_{0.19}\text{As}$ laser.

Indium content in the quantum well as well as the considered values of the quaternary active layer composition were technologically imposed. The first ones by the critical thickness of strained layer, the second by the specificity of MBE process. Higher than 29% indium content was not considered since in that case, the lattice mismatch between the well and barriers is such that it prevents a successful growth. Active region with $\text{In}_{0.24}\text{Ga}_{0.54}\text{Al}_{0.19}\text{As}/\text{Al}_{0.25}\text{Ga}_{0.75}\text{As}$ quantum well was chosen after theoretical optimization presented elsewhere⁸.

The optical gain spectrum for this laser is shown in Fig. 1. Lines are drawn for different concentrations of injected electrons from $5 \times 10^{17} \text{ cm}^{-3}$ to $5 \times 10^{18} \text{ cm}^{-3}$. Maximum gain indicates approximate wavelength of the lasing mode. Fig.2 presents spectral characteristic for the considered laser. The wavelength of the dominant longitudinal mode is almost exactly equal to 808 nm.

Fig. 3 shows calculated threshold current density for SQW and DQW lasers with different cavity lengths. For longer cavities threshold current density is higher for double quantum well but the difference between those lines decreases when cavity becomes shorter. The threshold current density is slightly bigger for SQW with the cavity length equal 500 μm or shorter.

Above threshold, the lasing power is given by the expression:

$$P(I) = \eta_d \frac{\hbar\omega}{q} (I - I_{th}) = \eta_i \frac{\alpha_m}{\alpha_m + \alpha_i} \frac{\hbar\omega}{q} (I - I_{th}) \quad (1)$$

and rises almost linearly with increasing injection current, which can be seen in Fig. 4ab, showing $P(I)$ characteristics for modeled SQW and MQW lasers with different resonator length. The $P(I)$ stands for total optical power emitted from

both facets of a symmetric Fabry-Perot laser. The slope efficiency is proportional to the differential quantum efficiency η_d , which depends on the internal optical loss α_i , on the mirror loss α_m and on the injection efficiency η_i , i.e., the fraction of total current increment that results in stimulated emission of photons. The differential quantum efficiency, determined from calculated P(I) characteristics is plotted versus cavity length for SQW and DQW lasers in Fig. 5. For both types of lasers we observe that the differential quantum efficiency increases when cavity length decreases. The maximum value of $\eta_d = 64\%$ and 54% for shortest ($L=400 \mu\text{m}$) SQW and DQW lasers, respectively. This is in agreement with the standard expression showing inverse slope efficiency as a function of cavity length⁹:

$$\frac{1}{\eta_d} = \frac{1}{\eta_i} \left(\frac{-2\alpha_i}{\ln(R_1 R_2)} L + 1 \right) \quad (2)$$

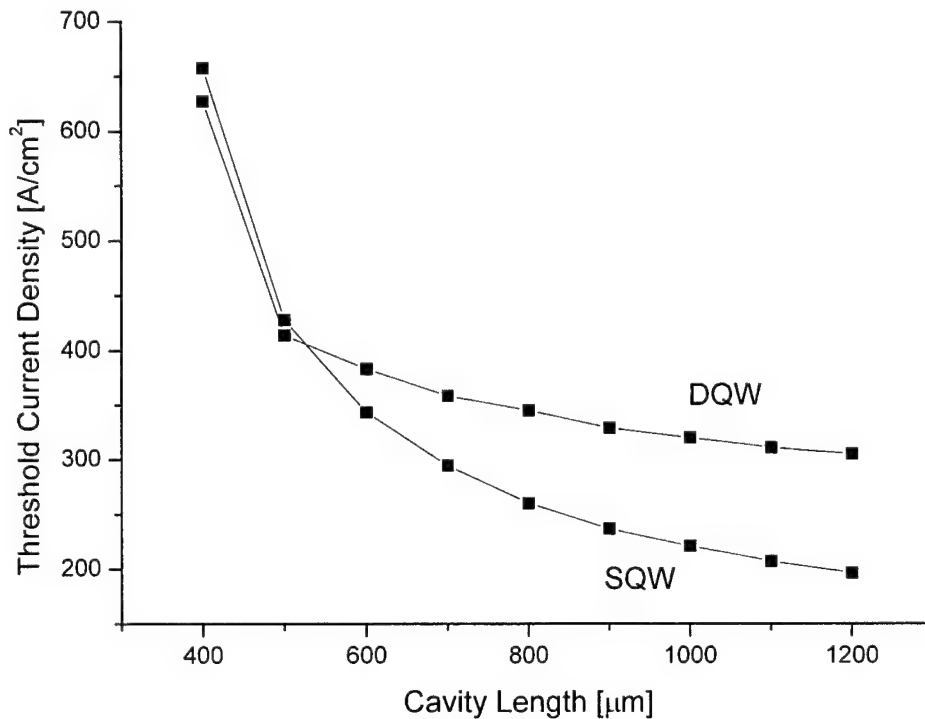


Fig. 3. Threshold current density versus cavity length for SQW and DQW lasers.

The eq.(2) is based on the assumption that η_i and α_i do not change with laser length. This assumption is questionable in very short cavity lasers, below certain critical length¹⁰. The main source of deterioration of differential efficiency in short cavity lasers is an increase of internal loss α_i caused free carrier absorption which rises proportionally to the carrier concentration. The mirror loss coefficient rises with shorter cavity lengths, requiring higher gain and consequently more carriers in the quantum well. In general this also causes higher leakage losses due to the escape of carriers from quantum well into waveguide layers. As it can be seen from our calculations this slope efficiency limitation mechanisms are negligible for the lasers with cavity length $L > 400 \mu\text{m}$.

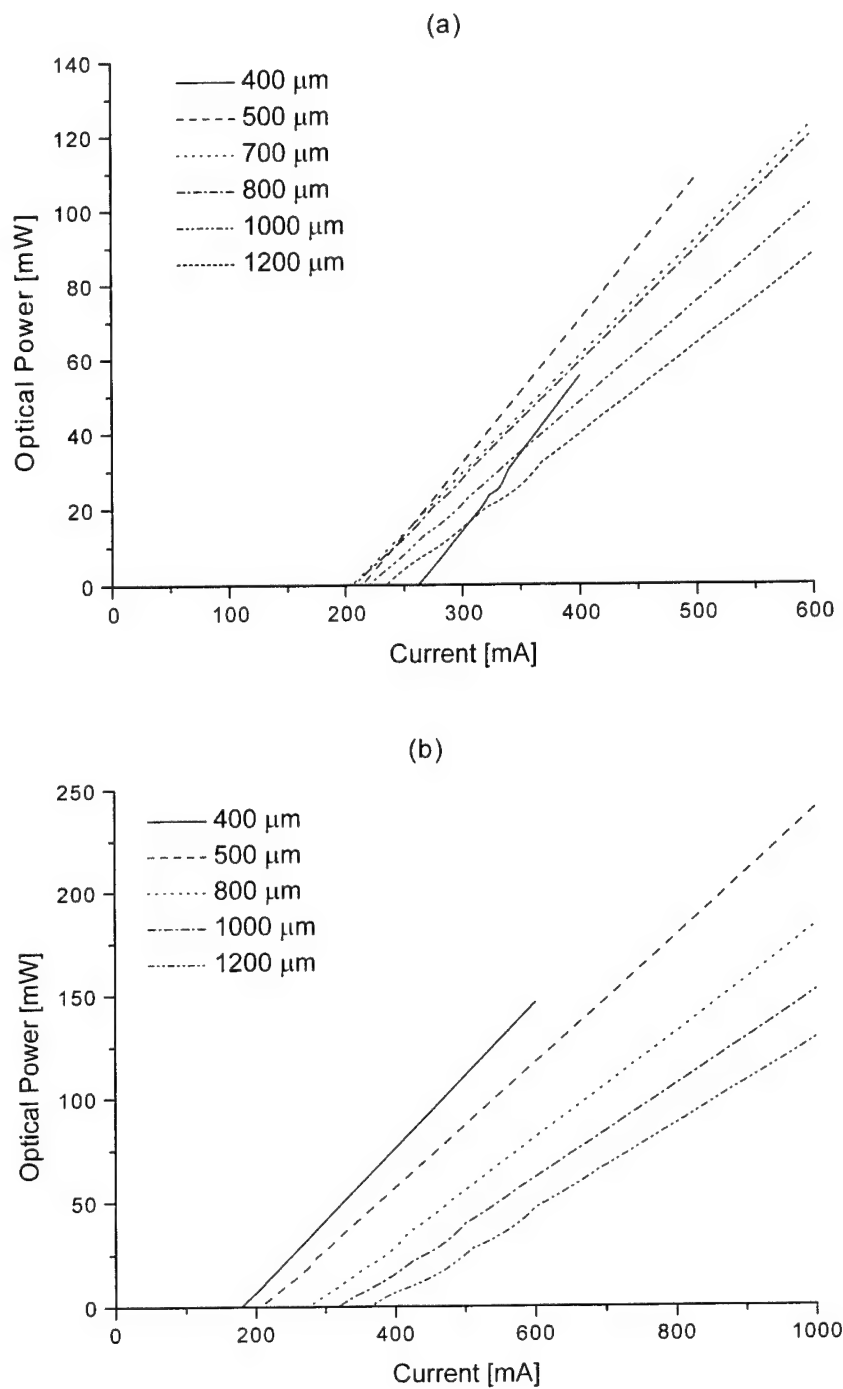


Fig. 4. Examples of P(I) characteristics calculated for SQW (a) and DQW (b) lasers with different cavity length.

Thermal phenomena are very important in high power application of lasers. The self-heating of the laser causes threshold current increase and slope efficiency decrease. One the major causes of these phenomena is optical gain reduction with temperature. We have studied that mechanism in details.

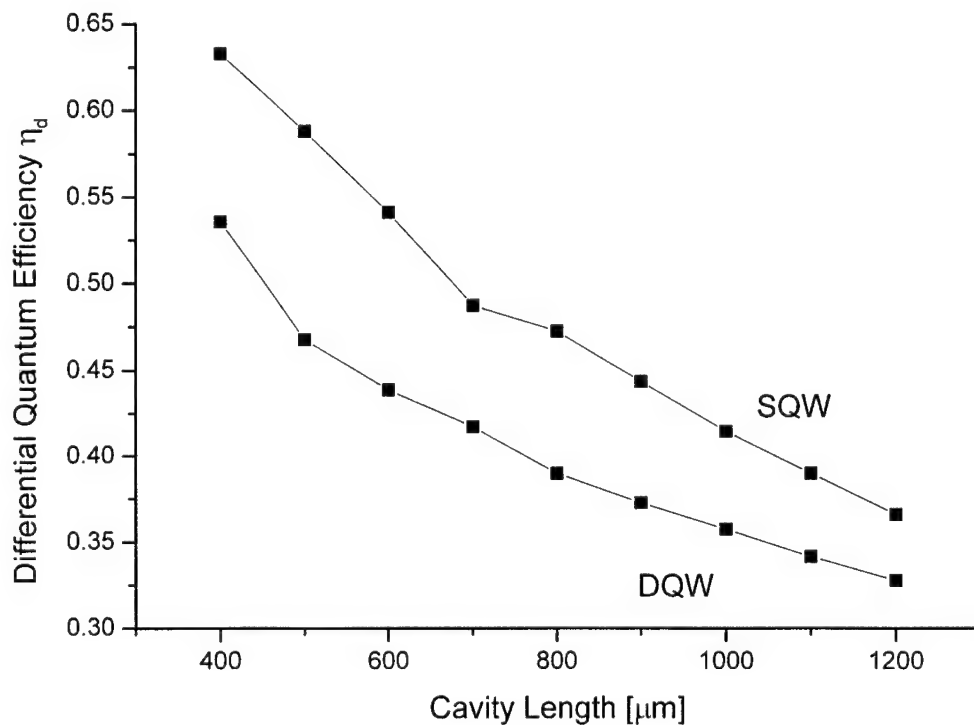


Fig. 5. Differential quantum efficiency versus cavity length for SQW and DQW lasers.

Fig. 6 shows peak material gain plotted versus recombination current density in the active region – equal to the spontaneous recombination rate times the active region thickness. Calculations were made for few temperatures from 300K to 380K. Peak material gain decreases considerably with temperature increase. The other effects, which might in this case contribute to the deterioration of laser performance with temperature are vertical and lateral carrier leakage.

4. CONCLUSIONS

The InGaAlAs/GaAs lasers are a novel construction, difficult from the technological point of view, but very promising as compared to standard GaAs lasers designed for operation at 808 nm. In order to get this wavelength with GaAs active region we need very thin active regions, which results in poor carrier confinement and an increased threshold. Additionally, due to the discrete nature of the layer thickness variation (the effect being more pronounced in thin wells comparing to thicker ones) it is difficult, if not impossible, to obtain specified wavelength, required by the applications. The use of InGaAlAs as an active region allows for obtaining 808 nm emission wavelength with a considerably thicker quantum wells than it is in the case of GaAs. Although similar effect can be obtained with AlGaAs active region, the simultaneous addition of In stabilizes crystal lattice and makes InGaAlAs/GaAs lasers less prone to degradation.

The numerical simulations performed allowed us to specify laser designs suitable for Nd:YAG pumping applications. The lasers with SQW and MQW active region were compared, showing slightly better performance of SQW lasers. The differential quantum efficiency of the lasers with different cavity length has been analyzed. The maximum value of $\eta_d = 64\%$ and 54% for shortest ($L=400 \mu\text{m}$) SQW and DQW lasers, respectively has been found. The well thickness and indium content in the active region were optimized to obtain 808 nm wavelength with acceptable threshold current density.

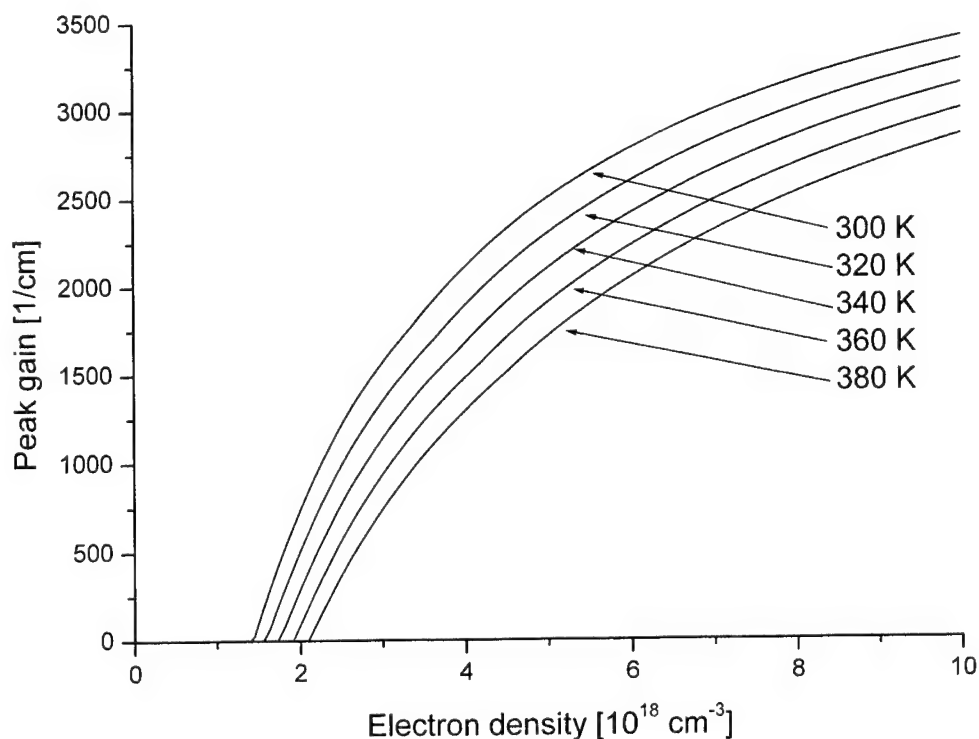


Fig. 6. Peak material gain plotted versus recombination current density in the active region.

ACKNOWLEDGMENTS

This work was partially supported by the State Committee for Scientific Research under grant number 7T11B02121.

REFERENCES

1. B. Acklin, M. Behringer, G. Herrman, J. Luft, C. Hanke, L. Korte, M. Marchiano, J. Wilhelmi, B. De Odorico, "200 W InGaAlAs-GaAs diode laser bars for pumping", *Advanced High-Power Lasers*, Proceedings of SPIE, vol. **3889**, pp. 128-33, 2001.
2. C. Hanke, L. Korte, B. Acklin, J. Luft, S. Grotsch, G. Herrmann, Z. Spika, M. Marciano, B. De Odorico, J. Wilhelmi, "Highly reliable 40 W CW InGaAlAs/GaAs 808 nm laser bars", *In-Plane Semiconductor Lasers III*, Editors: Hong K. Choi, Peter S. Zory, Proceedings of SPIE, vol. **3628**, pp. 64-70, 1999.
3. J. J. Coleman, "Strained-layer quantum well heterostructure lasers", *Thin Solid Films*, **216**, pp. 68-71, 1992.
4. E. W. Kreutz, N. Wiedmann, J. Jandeleit, D. Hoffmann, P. Loosen, R. Poprawe, "Reliability and degradation mechanisms of InGa(Al)As/GaAs DQW high-power diode lasers", *J. Crystal Growth*, **210**, pp. 313-17, 2000.
5. P. M. Smowton, P. Blood, P. C. Mogenssen, J. S. Roberts, "Al_xGa_yIn_{1-x-y}As/AlGaAs quantum well lasers at 670 to 750 nm", *In-Plane Semiconductor Lasers: from Ultraviolet to Midinfrared*, Editors: Hong K. Choi, Peter S. Zory, Proceedings of SPIE, vol. **3001**, pp. 153-62, 1997.
6. J.P. Sih, T.M. Chou, J.K. Kirk, J.K. Butler, G.A. Evans, A. Mantie, J. Kosciński, R. Defreez, Performance of ridge-guide AlGaInAs lasers", *In-Plane Semiconductor Lasers: from Ultraviolet to Midinfrared*, Editors: Hong K. Choi, Peter S. Zory, Proceedings of SPIE, vol. **3001**, pp. 235-42, 1997.
7. PICS3D, "Instruction Manual", Crosslight Software Inc., CA. 1998.

8. M. Zbroszczyk, M. Bugajski, "Design optimization of InGaAlAs/GaAs quantum well lasers", *7th International Conference on Nanometer-Scale Science and Technology and 21st European Conference on Surface Science*, Lund Univ., pp.2-4, 2002.
9. J. Piprek, *Semiconductor Optoelectronic Devices. Introduction to Physics and Simulation*, Academic Press, 2003.
10. B. Mroziewicz, M. Zbroszczyk, M. Bugajski, "Analysis of threshold current and wall-plug efficiency of diode lasers with asymmetric facet reflectivity", *Optical and Quantum Electronics*, in print.

Temperature dependence of photoluminescence in non-crystalline silicon

Ali Serpengüzel,* Temel Bilici,[†] Ibrahim Inanç,[‡] and Adnan Kurt
Koç University, Microphotonics Research Laboratory, Department of Physics,
Rumeli Feneri Yolu, Sariyer, Istanbul 34450 Turkey

Jim Carey and Eric Mazur
Harvard University, Department of Physics and Division of Engineering and Applied Sciences,
29 Oxford Street, Cambridge, Massachusetts 02138 USA

ABSTRACT

Crystalline silicon being ubiquitous throughout the microelectronics industry has an indirect bandgap, and therefore is incapable of light emission. However, strong room temperature visible and near-IR luminescence from non-crystalline silicon, e.g., amorphous silicon, porous silicon, and black silicon, has been observed. These silicon based materials are morphologically similar to each other, and have similar luminescence properties. We have studied the temperature dependence of the photoluminescence from these non-crystalline silicon to fully characterize and optimize these materials in the pursuit of obtaining novel optoelectronic devices.

Keywords: amorphous silicon, black silicon, non-crystalline silicon, porous silicon, plasma enhanced chemical vapor deposition, photoluminescence..

1. INTRODUCTION

Interest in silicon (Si) as a material for optoelectronics has increased recently. With modern process techniques, it will be possible to integrate lasers, photodetectors, and waveguides into optoelectronic silicon motherboards to route and modulate optical signals within such silicon motherboards. Integrated silicon optoelectronics is a rapidly developing field ¹. Discrete and integrated devices such as photodetectors, modulators, light emitters, resonant cavity enhanced (RCE) photodetectors, waveguides, photonic bandgap filters, optical amplifiers, optical interconnects, and optoelectronic integrated circuits are already being realized. However, most of these devices, with the exception of light emitters, are fabricated using crystalline silicon. Light emission requires the use of amorphous silicon, since crystalline silicon can not emit light due to its indirect bandgap. With modern process techniques, it will be possible to integrate lasers, photodetectors, and waveguides into Si motherboards ^{2,3} for wavelength division multiplexing (WDM) applications ⁴.

2. EXPERIMENTAL PHOTOLUMINESCENCE SETUP

The room temperature PL setup consists of a pump laser, a spectrometer, a lock-in amplifier, and a digital oscilloscope. The collected PL signal is imaged to the entrance slit of the spectrometer, whose output is fed to a sensitive photomultiplier tube (PMT). A lock-in-amplifier is providing the necessary electronic gain to the PMT output gain in phase with the laser pulse. The digital oscilloscope is used for monitoring and optimizing the PMT signal. All of the

* aserpenguzel@ku.edu.tr; phone: + 90 (212) 338-1312; fax: + 90 (212) 338-1547, <http://home.ku.edu.tr/~aserpenguzel>, <http://microphotonics.ku.edu.tr>. Koç University, Microphotonics Research Laboratory, Department of Physics, Rumeli Feneri Yolu, Sariyer, Istanbul 34450 Turkey. Ibrahim Inanç and Adnan Kurt are with Koç University, Microphotonics Research Laboratory, Department of Physics, Rumeli Feneri Yolu, Sariyer, Istanbul 34450 Turkey. [†] Temel Bilici is currently at Boston University, Department of Electrical and Computer Engineering, 8 St. Mary's Street, Boston, Massachusetts 02215 USA. [‡] Ibrahim Inanç is also with the Bogaziçi University, Physics Department, Bebek, Istanbul 34342 Turkey. Jim Carey and Eric Mazur are with Harvard University, Department of Physics, Cambridge, Massachusetts 02138 USA.

measurement and test devices are computer controlled and the data is acquired digitally. For the room temperature measurements at 300 K the samples are attached to a holder. For low temperature measurements the samples are placed in a closed cycle cryostat system. The closed cycle cryostat system is used to control the sample temperature from 10 K to 300 K.

3. AMORPHOUS SILICON

In the optoelectronics and microelectronics industry silicon is the most widely used semiconductor, not only in its crystalline, but also in its amorphous form. Being a direct band-gap material,⁵ unlike crystalline silicon,⁶ amorphous silicon is unmatched as a photoreceptor for laser printing, for switching elements in large area liquid crystal displays, for large photovoltaic panels, and any other application that calls for a high quality semiconductor that can be processed on large areas or on curved or flexible substrates. It is generally agreed that the terms amorphous solid, non-crystalline solid, disordered solid, glass, or liquid have no precise structural meaning beyond the description that, the structure is not crystalline on any significant scale. The principal structural order present is imposed by the approximately constant separation of nearest-neighbor atoms or molecules. Until the early 1970's, amorphous silicon prepared by evaporation or sputtering was not considered as one of the valuable semiconductor materials, because of high density of electronic states in the band gap related to a large density of structural defects.⁷ The discovery of an amorphous silicon material prepared by the glow discharge deposition of silane, which can be doped and whose conductivity can be changed by ten orders of magnitude marked a turning point and opened a new research area. Most interest focused on hydrogenated amorphous silicon and its alloys, since hydrogen by removing dangling bonds eliminates non-radiative recombination centers, that are responsible for reduced luminescence efficiency (and reduced photovoltaic efficiency) and allows doping.⁸ Hydrogenated amorphous silicon (a-Si:H) is already an established material in semiconductor technology.⁹ The major application of a-Si:H is photovoltaics, color detectors, and active matrix displays. The primary attribute of the technology is its large area capability, which is unavailable with other technologies. Another advantage of the hydrogenated amorphous silicon is that, it can be deposited by plasma enhanced chemical vapor deposition (PECVD) onto almost any substrate at temperatures below 500 K, which makes it compatible with the microelectronic technology. This property justifies the interest in a-Si:H as a potential optoelectronic material. Planar waveguides are already being realized from a-Si:H.¹⁰ The advantage of a-Si:H, as well as porous silicon (p-Si), is that, they attract interest as a potential optical gain medium, because of their room temperature visible electroluminescence (EL) and photoluminescence (PL). Recently, we have observed visible PL from a-Si:H, as well as its oxides (a-SiO_x:H) and nitrides (a-SiN_x:H) grown by low temperature PECVD.¹¹ While the exact mechanism of the occurrence of the PL in bulk a-SiN_x:H is still under discussion, the quantum confinement model is a widely accepted.¹² In the quantum confinement model the material consist of small a-Si clusters in a matrix of a-SiN_x:H. The regions with Si-H and Si-N, having larger energy gaps due to strong Si-H and Si-N bonds, isolate these a-Si clusters, and form barrier regions around them. The PL originates from the a-Si clusters. A-SiN_x:H can be grown both with and without ammonia (NH₃). The samples grown without NH₃ are referred to as the Si rich samples. The luminescence of these samples is in the red-near-infrared part of the optical spectrum. The samples grown with NH₃ and annealed at 800° C are referred to as the nitrogen rich samples. The luminescence of these samples is in the blue-green part of the optical spectrum.¹³

3.1. Temperature dependence of the amorphous silicon photoluminescence

Figure 3.1 shows the PL spectra of the a-SiN_x:H measured in the 550 - 900 nm wavelength and in the 12 - 298 K temperature range at a constant excitation laser intensity of 0.1 W cm⁻². A broad PL band centered at 710 nm ($E_p = 1.746$ eV) at 12 K is observed. The PL spectra have approximately a Gaussian lineshape modulated slightly by Fabry-Perot resonances. These resonances are due to the Fresnel reflections from the a-SiN_x:H film surfaces. The PL intensity decreases with increasing temperature. This feature is typical of the PL, which is due to donor-acceptor pair transitions observed in semiconductors. The variation of the PL peak with respect to temperature is plotted in the figure 3.2. In the 12 - 170 K range, the PL intensity decreases slowly. Above 170 K, however, the PL intensity decreases at a larger rate due to a thermal quenching process. The activation energy ΔE for this thermal quenching process can be derived in the 170 - 298 K temperature range using a nonlinear least squares fit to the following equation, $I = I_0 \exp(\Delta E/k_B T)$, where I is the PL intensity, I_0 a proportionality constant, and k_B the Boltzmann's constant. The semilog plot of the emission band intensity as a function of the reciprocal temperature gives a straight line in the 170 - 298 K region. An activation energy of $E_a = 0.027$ eV for the emission band is derived from the slope of the straight line fit. This activation energy is associated with a shallow level located at 0.027 eV from the band. This shallow level in undoped a-SiN_x:H may be associated with the presence of defects and unintentional impurities.

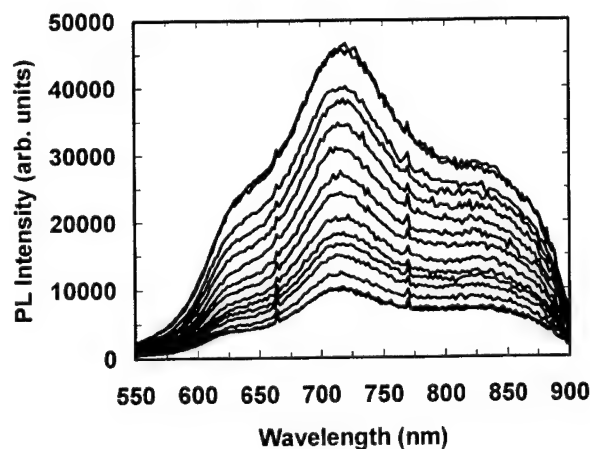


Figure 3.1. PL spectra of a-SiN_x:H in the 12 - 298 K temperature range.

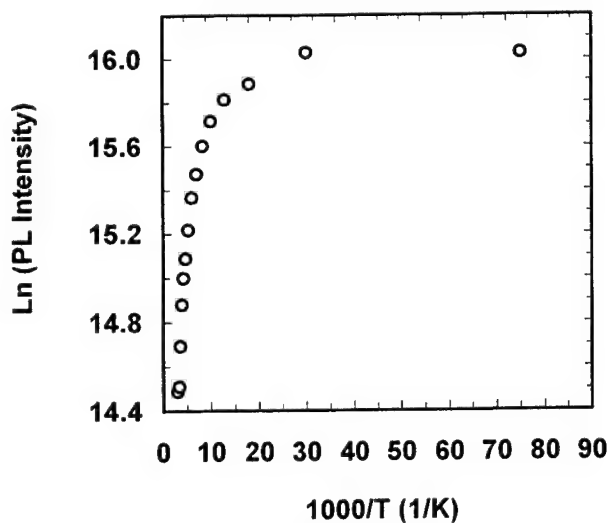


Figure 3.2. Temperature dependence of a-SiN_x:H PL intensity at the emission band maximum. Intensive quenching starts at 170 K.

3.2. Surface morphology of the amorphous silicon

Atomic force microscopy (AFM) has been performed on the a-SiN_x:H samples to characterize the morphology of the surface and to analyze origin of the luminescence. The surface of the a-SiN_x:H is optically flat and thus amenable for the growth of multiple layers. This is necessary condition for the realization of the one-dimensional PBG microcavity. The surface morphology of the a-SiN_x:H is quite uniform. The bulk of the material is composed of globules of a-SiN_x:H and is similar to -Si. Figure 3.3 shows the medium resolution AFM picture of the silicon rich a-SiN_x:H surface. Additionally, although the surface is flat optically, it is quite rough in the 100 nm range, which corresponds to the average globule size.

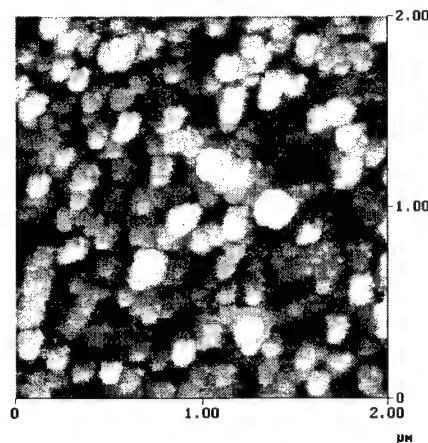


Figure 3.3. Medium resolution AFM of the silicon rich a-SiNx:H surface.

4. POROUS SILICON

Similar to hydrogenated amorphous silicon (a-Si:H), porous silicon (-Si) also exhibits room temperature visible PL¹⁴. Semiconductor microcavity effects have been applied to -Si , after the observation of room temperature visible PL¹⁵ made -Si a potential optical gain medium.¹⁶ Steady state^{17, 18, 19} and temporally resolved,²⁰ single and multiple²¹ microcavity controlled PL in -Si has been observed experimentally^{22, 23, 24} and calculated theoretically²⁵. The possibility of using -Si microcavities as chemical sensors has been investigated²⁶. In addition, microcavity controlled PL has been observed in -Si inorganic-organic structures,²⁷ as well as Si/SiO_x superlattices.^{28,29,30} SiO₂/TiO₂ microcavities,³¹ SiO_x/WO₃, and SiO_x/MO_y multilayers³² have been fabricated. Microcavity controlled electroluminescence (EL) of -Si has been reported.^{33, 34} Interference filters³⁵ and optical waveguides³⁶ have also formed from -Si . Two-dimensional (2-D) photonic crystals have been fabricated in -Si ³⁷ and silicon nitride (Si₃N₄)³⁸ waveguides.

4.1. Temperature dependence of the porous silicon photoluminescence

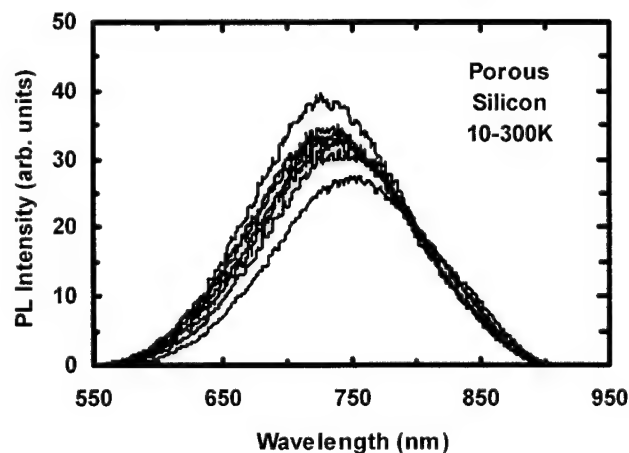


Figure 4.1. PL spectra of porous silicon in the 10 - 300 K temperature range.

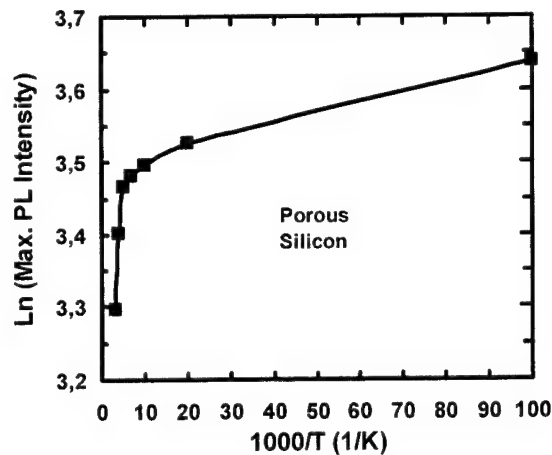


Figure 4.2. Temperature dependence of porous silicon PL intensity at the emission band maximum. Intensive quenching starts at 200 K.

Figure 4.1 shows the PL spectra of the porous silicon measured in the 550 - 900 nm wavelength and in the 10 - 300 K temperature range at a constant excitation laser intensity of 0.005 W cm^{-2} . A broad PL band centered at 750 nm ($E_p = 1.698 \text{ eV}$) at 10 K is observed. The PL spectra have approximately a Gaussian lineshape. The PL intensity decreases with increasing temperature. This feature is typical of the PL, which is due to donor-acceptor pair transitions observed in semiconductors. The variation of the PL peak with respect to temperature is plotted in the figure 4.2. In the 10 - 150 K range, the PL intensity decreases slowly. Above 200 K, however, the PL intensity decreases at a larger rate due to a thermal quenching process. The activation energy ΔE for this thermal quenching process can be derived in the 200 - 300 K temperature range using a nonlinear least squares fit to the following equation, $I = I_0 \exp(\Delta E/k_B T)$, where I is the PL intensity, I_0 a proportionality constant, and k_B the Boltzmann's constant. The semilog plot of the emission band intensity as a function of the reciprocal temperature gives a straight line in the 200 - 300 K region. An activation energy of $E_a = 0.009 \text{ eV}$ for the emission band is derived from the slope of the straight line fit. This activation energy is associated with a shallow level located at 0.009 eV from the band. This shallow level in porous silicon may be associated with the presence of defects and unintentional impurities.

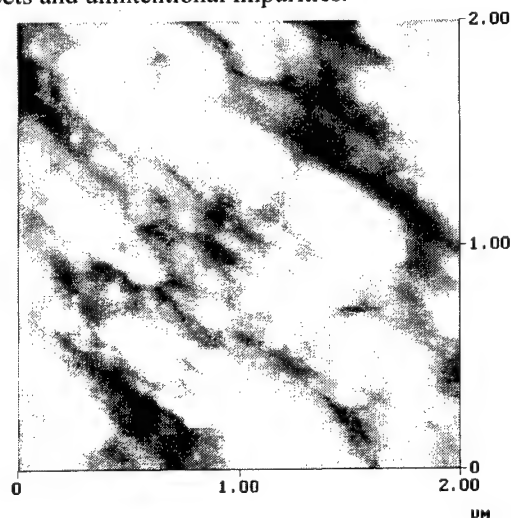


Figure 4.3. Medium resolution AFM of the porous silicon surface.

4.2. Surface morphology of the porous silicon

Atomic force microscopy (AFM) has been performed on the porous silicon samples to characterize the morphology of the surface and to analyze origin of the luminescence. The surface of the porous silicon is rather rough. The bulk of the material is composed of globules of as we have seen in porous silicon. Figure 4.3 shows the medium resolution AFM picture of the porous silicon surface.

5. BLACK SILICON

Ordinarily, silicon absorbs a moderate amount of visible light, but a substantial amount of visible light is reflected as well, and infrared and ultraviolet light are transmitted through silicon or reflected from it with very little absorption. Spiked silicon surfaces, in contrast, absorb nearly all light at wavelengths ranging from the ultraviolet to the infrared. This suggests it may be very useful in improving the performance of existing silicon devices, such as photodetectors and photovoltaics. Mazur group recently discovered that irradiation of silicon surfaces with femtosecond laser pulses in the presence of a halogen containing gas transforms the flat, mirror-like surface of a silicon wafer into a forest of microscopic spikes.^{39,40} The spiked surface is strongly light-absorbing: the surface of silicon, normally gray and shiny, turns deep black; hence the name black silicon.

5.1. Temperature dependence of the PL from the black silicon

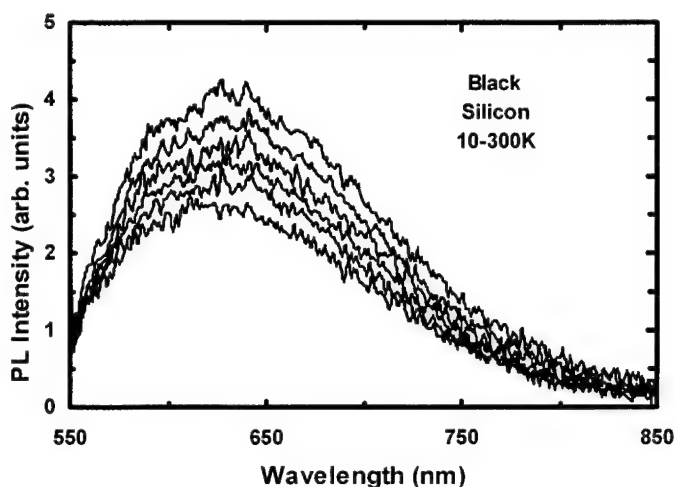


Figure 5.1. PL spectra of black silicon in the 10 - 300 K temperature range.

Figure 5.1 shows the PL spectra of the black silicon measured in the 550 - 850 nm wavelength and in the 10 - 300 K temperature range at a constant excitation laser intensity of 0.1 W cm^{-2} . A broad PL band centered at 630 nm ($E_p = 1.968 \text{ eV}$) at 10 K is observed. The PL spectra have approximately Gaussian lineshape. The PL intensity decreases with increasing temperature. The variation of the PL peak with respect to temperature is plotted in the figure 2. In the 10 - 120 K range, the PL intensity decreases slowly. Above 120 K, however, the PL intensity decreases at a larger rate due to a thermal quenching process. The activation energy ΔE for this thermal quenching process can be derived in the 120 - 300 K temperature range using a nonlinear least squares fit to the following equation, $I = I_0 \exp(-\Delta E/k_B T)$, where I is the PL intensity, I_0 a proportionality constant, and k_B the Boltzmann's constant. The semilog plot of the emission band intensity as a function of the reciprocal temperature gives a straight line in the 120 - 300 K region. An activation energy of $E_a = 0.006 \text{ eV}$ for the emission band is derived from the slope of the straight line fit. This activation energy is associated with a shallow level located at 0.006 eV from the band. This shallow level in black silicon may be associated with the presence of defects and unintentional impurities.

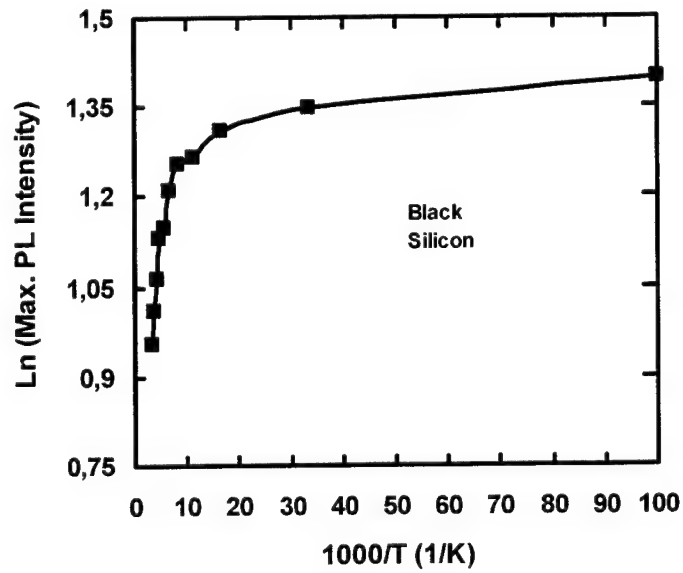


Figure 5.2. Temperature dependence of black silicon PL intensity at the emission band maximum. Intensive quenching starts at 120 K.

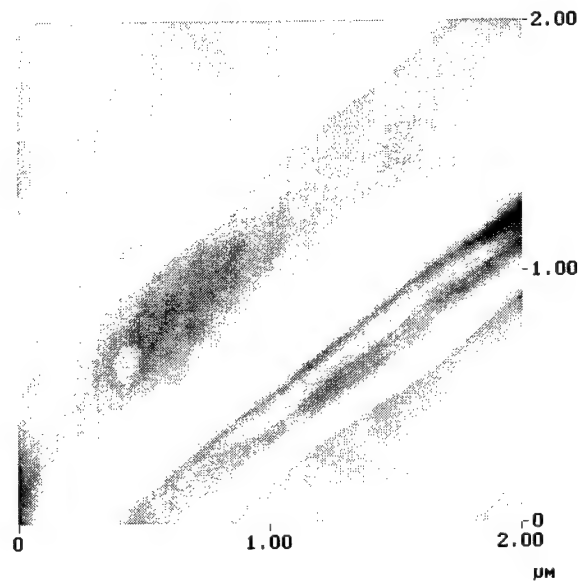


Figure 5.3. Medium resolution AFM of the black silicon surface.

5.2. Surface morphology of the black silicon

Atomic force microscopy (AFM) has been performed on the black silicon samples to characterize the morphology of the surface and to analyze origin of the luminescence. The surface of the black silicon is optically black and consists of conical layers. The bulk of the material is composed of globules of black silicon and is similar to α -Si. Figure 5.3 shows the medium resolution AFM picture of the black silicon surface.

6. CONCLUSIONS

Bulk luminescence properties of hydrogenated amorphous silicon nitride ($a\text{-SiN}_x\text{:H}$), porous silicon, and black silicon were studied at room temperature and at low temperatures. The PL emission intensity increases at low temperatures due to the lack of thermally excited phonons. The emission spectrum stays broad even at low temperatures. The broad luminescence spectrum even at low temperatures is a result of the heterogeneous size distribution of the amorphous silicon quantum dots. This heterogeneous size distribution is further confirmed by atomic force microscopy (AFM) measurements of the sample surface. The broad PL spectrum of the $a\text{-SiN}_x\text{:H}$, porous, and black silicon makes them suitable sources for wavelength division multiplexing (WDM) applications.

7. ACKNOWLEDGMENTS

We would like to acknowledge the partial support of this research by the Scientific and Technical Research Council of Turkey (TUBITAK) Grant No: TBAG-1952 and the European Office of Aerospace Research and Development (EOARD) Grants No: F61775-01-WE062 and FA8655-02-M-4086.

8. REFERENCES

- 1 H. Zimmermann, "Integrated Silicon Optoelectronics," (Springer Verlag, Berlin, 2000) pp. 1-352.
- 2 B. Jalali, S. Yegnanarayanan, T. Yoon, T. Yoshimoto, I. Rendina, and F. Copping, "Advances in Silicon on insulator Optoelectronics," IEEE J. Select. Topics in Quantum Electron. **4**, 938 (1998).
- 3 A. Kaneko, T. Goh, H. Yamada, T. Tanaka, and I. Ogawa "Design and applications of silica-based planar lightwave circuits," IEEE J. Select. Topics in Quantum Electron. **5**, 1227 (1999).
- 4 B. J. Offrein, R. Germann, F. Horst, H.W.M. Salemink, R. Beyerl, and G. L. Bona, "Resonant coupler-based tunable add-after-drop filter in silicon-oxynitride technology for WDM networks," IEEE J. Select. Topics in Quantum Electron. **5**, 1400 (1999).
- 5 J.D. Joannopoulos and G. Lucovsky, "The physics of hydrogenated amorphous silicon," (Springer Verlag, Berlin, 1984).
- 6 S. Perkowitz, "Optical Characterization of Semiconductors," (Academic Press, London, 1993), p.27.
- 7 P. Shaoqi and D. Xiaoning, "Properties of Sputtered Amorphous Silicon without Hydrogen", in "Proceedings of the International Workshop on Amorphous Semiconductors," H. Fritzsche, D. Han, C. C. Tsai, Eds. (World Scientific, Singapore, 1987).
- 8 J. I. Panvoke, "Luminescence in Hydrogenated Amorphous Silicon", in "Proceedings of the International Workshop on Amorphous Semiconductors," H. Fritzsche, D. Han, C. C. Tsai, Eds., (World Scientific, Singapore, 1987).
- 9 R. A. Street, Ed., "Technology and Applications of Amorphous Silicon," (Springer Verlag, Berlin, 2000), pp. 1-403.
- 10 A. M. Agarwal, L. Liao, J. S. Foresi, M. R. Black, X. Duan, and L.C. Kimerling, "Low-loss Polycrystalline Silicon Waveguides for Silicon Photonics," J. Appl. Phys. **80**, 6120 (1996).
- 11 A. Serpengüzel, A. Aydinli, and A. Bek, "Enhancement and inhibition of photoluminescence in hydrogenated amorphous silicon nitride microcavities," Optics Express **1**, 108 (1997).
- 12 M. H. Brodsky, "Quantum Well Model of the Hydrogenated Amorphous Silicon," Solid State Commun. **36**, 55 - 59 (1980).
- 13 A. Serpengüzel, A. Aydinli, A. Bek, and M. Güre, "Visible photoluminescence from planar amorphous silicon nitride microcavities," J. Opt. Soc. Am. B. **15**, 2706 (1998).
- 14 D. J. Wolford, B. A. Scoot, J. A. Reimer and J. A. Bradley, "Efficient visible luminescence from hydrogenated amorphous silicon," Physica **B 117**, 920 (1983).
- 15 T. Canham, "Silicon Quantum Wire Array Fabrication by Electrochemical and Chemical Dissolution of Wafers," Appl. Phys. Lett. **57**, 1046 (1990).
- 16 D. J. Lockwood, "Optical Properties of Porous Silicon," Solid State Commun. **92**, 101 (1994).
- 17 L. Pavesi, C. Mazolleni, A. Tredicucci, and V. Pellegrini, "Controlled photon emission in porous silicon microcavities," Appl. Phys. Lett. **67**, 3280 (1995).

- 18 L. Pavesi and V. Mulloni, "All porous silicon microcavities: growth and physics," *J. Lumin.* **80**, 43 (1999).
- 19 M. Araki, H. Koyama, and N. Koshida, "Precisely tuned emission from porous silicon vertical optical cavity in the visible region," *J. Appl. Phys.* **80**, 4841 (1996).
- 20 M. Cazzanelli and L. Pavesi, "Time-resolved photoluminescence of all porous silicon microcavities," *Phys. Rev. B* **56**, 15264 (1997).
- 21 E. K. Squire, P. A. Snow, P. St. J. Russell, L. T. Canham, A. J. Simmons, and C. L. Reeves, "Light emission from porous silicon single and multiple cavities," *J. Lumin.* **80**, 125 (1999).
- 22 M. Takahashi, Y. Toriumi, T. Matsumoto, Y. Masumoto, N. Koshida, "Significant photorefractive index change observed in porous silicon Fabry-Perot resonators," *Appl. Phys. Lett.* **76**, 1990 (2000).
- 23 S. Setzu, S. Letant, P. Solsona, R. Romestain, and J. C. Vial, "Improvement of luminescence in p-type as-prepared or dye impregnated porous silicon microcavities," *J. Lumin.* **80**, 129 (1999).
- 24 Z. H. Xiong, S. Yuan, Z. M. Jiang, J. Qin, C. W. Pei, L. S. Liao, X. M. Ding, X. Y. Hou, and X. Wang, "Photoluminescence studies of porous silicon microcavities," *J. Lumin.* **80**, 137 (1999).
- 25 E. K. Squire, P. St. J. Russell, and P. A. Snow, "Optimized light emission from layered porous silicon structures," *Appl. Opt.* **37**, 7107 (1998).
- 26 V. Mulloni and L. Pavesi, "Porous silicon microcavities as optical chemical sensors," *Appl. Phys. Lett.* **76**, 2523 (1999).
- 27 A. Arena, S. Patane, G. Saitta, S. Savasta, R. Girlanda, and R. Rinaldi, "Silicon based organic-inorganic microcavity and its dispersion curve from angle resolved photoluminescence," *Appl. Phys. Lett.* **72**, 2571 (1998).
- 28 B. T. Sullivan, D. J. Lockwood, H. J. Labbe, and Z.-H. Lu, "Photoluminescence in Amorphous Si/SiO_x Superlattices Fabricated by Magnetron Sputtering," *Appl. Phys. Lett.* **69**, 3149 (1996).
- 29 D. J. Lockwood, J.M. Baribeau, and B. T. Sullivan, "Visible light from Si/SiO_x superlattices in planar microcavities," *J. Vac. Sci. Technol. B* **16**, 1707 (1998).
- 30 D. J. Lockwood, B. T. Sullivan, and H. J. Labbe, "Visible light emission from Si/SiO_x superlattices in optical microcavities," *J. Lumin.* **80**, 75 (1999).
- 31 K. M. Cheng, A. W. Sparks, H.-C. Luan, D. R. Lim, K. Wada, and L. C. Kimerling, "SiO₂/TiO₂ omnidirectional reflector and resonator with sol-gel method," *Appl. Phys. Lett.* **75**, 3805 (1999).
- 32 F. Hamelmann, G. Haindl, J. Schmalhorst, A. Aschentrup, E. Majkova, U. Kleineberg, U. Heinzmann, A. Klipp, P. Jutzi, A. Anopchenko, M. Jergel, and S. Luby, "Metal oxide / silicon oxide multilayer with smooth interfaces produced by in situ controlled plasma enhanced MOCVD," *Thin Solid Films* **358**, 90 (2000).
- 33 L. Pavesi, R. Guardini, and C. Mazolleni, "Porous Silicon Resonant Cavity Light Emitting Diodes," *Solid State Commun.* **97**, 1051 (1996).
- 34 M. Araki, H. Koyama, and N. Koshida, "Controlled electroluminescence spectra of porous silicon diodes with vertical optical cavity," *Appl. Phys. Lett.* **69**, 2956 (1996).
- 35 D. Hunkel, R. Butz, R. Ares-Fisher, M. Marso, and H. Lüth, "Interference filters from porous silicon with laterally varying wavelength of reflection," *J. Lumin.* **80**, 133 (1999).
- 36 H. F. Arrand, T. M. Benson, P. Sewell, and A. Loni, "Optical waveguides in porous silicon pre-patterned by localized nitrogen implantation," *J. Lumin.* **80**, 199 (1999).
- 37 S. W. Leonard, H. M. van Driel, K. Busch, S. John, A. Birner, A.-P. Li, F. Müller, U. Gösele, and V. Lehmann, "Attenuation of optical transmission within the band gap of thin two-dimensional macroporous silicon photonic crystals," *Appl. Phys. Lett.* **75**, 3063 (1999).
- 38 M. C. Netti, M. D. B. Charlton, G. J. Parker, and J. J. Baumberg, "Visible photonic band gap engineering in silicon nitride waveguides," *Appl. Phys. Lett.* **76**, 991 (2000).
- 39 Tsing-Hua Her, Richard J. Finlay, Claudia Wu, and Eric Mazur, "Femtosecond laser-induced formation of spikes on silicon", *Appl. Phys. A* **70**, 383-385 (2000);
- 40 Tsing-Hua Her, Richard J. Finlay, Claudia Wu, Shrenik Deliwala, and Eric Mazur, "Microstructuring of silicon with femtosecond laser pulses", *Appl. Phys. Lett.* **73**, 1673-1675 (1998).

Multi-layered grating diffraction, graphical user interfaced simulation toolbox in the MATLAB® environment

Mark Auslender,* Avi Bergel, Nathan Pinhas and Shlomo Hava

Dept of Electrical and Computer Engineering, Ben-Gurion University of the Negev, POB 653,
84105 Beer-Sheba, Israel

ABSTRACT

Theoretical work of our group is placed in the general frame of efforts to improve numerical performance and efficiency of rigorous coupled-wave analysis of grating diffraction. Mathematical transformation of Maxwell equations for a multi-layered structure to evolution equations in functional space is presented. By-construction numerically stable symbolic algorithm to solve these equations using the notion of in-layer scattering operator is proposed. On the base of this algorithm a toolbox for simulation of diffraction from multi-layered grating structures, implemented by a graphical user interface is developed. An example of simulation using this in-house software is exposed.

Keywords: Diffraction theory, multi-layered structure, mode-matching methods, *S*-matrix algorithm, grating

1. INTRODUCTION

If smallest feature of diffractive optical element (DOE) scales down to operation wavelengths no approximate theory like scalar-diffraction or effective-medium still holds. Hence using of the full-vector electromagnetic diffraction theory to design and simulate performance of DOE in that resonance domain becomes unavoidable. Among various methods, rigorous coupled-wave analysis (RCWA) of grating diffraction is the most widely used technique. In different versions, it is nowadays well documented in the literature,¹ yet several comments seem to us worthwhile.

Due to employing the Fourier series, RCWA is compatible with the Fourier optics and the effective-medium theory, in their respective domains of validity and treats multi-layered gratings on equal footing with one-layer ones. In spite of this versatility, to the beginning of 1990's there emerged strong evidence that either for TM or conical diffraction from deep well gratings, large well number of grating layers and gratings made of highly reflective materials, the pre-existed RCWA algorithm proved numerically unstable and poorly convergent. Since then, RCWA was revised by using *S*-matrix algorithms^{2,3} and by changing the map of the propagation matrix for the conical⁴ and TM^{5,6} diffraction. This lead to the numerical stability⁷ and to dramatic, mathematically founded,⁸ improvement of the convergence. For the thus recast RCWA, the term Fourier modal method (FMM) is nowadays usable.

Our group faced those problems in the beginning of 1993, when started a project on optical and thermal-emission properties of gratings in silicon initiated by the group of Zemel.⁹ No in-depth discussion on the problems encountered in the grating-diffraction simulation algorithms was present to that time in the optics literature until the appearance of an analysis¹⁰ of the convergence in the RCWA context, and a study¹¹ of the numerical instability in the framework of eigen-function modal method (EMM). Independently of the latter study, present authors reported² on numerical instability they found in the RCWA-based simulations of the diffraction from one-layer gratings on silicon substrate. The both studies revealed the same cause of the numerical instability – the accumulation of large exponentials in the EM fields matching between layers, when propagating the solution from the top to the substrate – and developed two different modifications of the standard solution-propagation algorithm within EMM and RCWA, respectively. Li applied¹¹ an *R*-matrix algorithm borrowed¹² from chemical physics, which proved stable only conditionally.⁷ We considered² an *S*-matrix transformation, which lead to by-construction stable algorithm extended by us⁶ to multi-layered grating structure (MLGS).

* Send correspondence to M.A.: E-mail: marka@ee.bgu.ac.il

The solution-propagation algorithms are not specific for discretization, based it either upon the Fourier^{2,3} or the eigen-functions^{6,10} expansion series. But the question of convergence within RCWA can hardly be detached from that of overall simulation efficiency unless the algorithm made stable, since in this method the associated eigen-value problem changes at increasing the truncation order. Unluckily, power conservation test proved useless for testing the convergence since it holds in RCWA with a high accuracy, irrespective of the algorithm employed for solution propagation. Reformulation of RCWA with *S*-matrix algorithm² facilitated us,⁶ independently of other groups,^{4,5} to single out of all possible such map of the propagation matrix for the TM-polarization that provides the improved convergence.

The present paper is devoted to the conical diffraction from MLGS upon irradiation by elliptically polarized plane wave. In Section 2, Maxwell equations for general multi-layer structure are reduced to generalized wave equation, and an algorithm of the interlayer matching of its solution is developed. In Section 3, using recast Fourier-factorization rules⁸ for discretization, the developed is applied to the MLGS diffraction. In Section 4, a numerical realization of our method and an MLGS diffraction simulation toolbox implemented with graphical user interface (GUI), are presented.

2. BASIC EQUATIONS

2.1. Statement of the problem and reduction of Maxwell equations

Consider a structure of L plane layers, putting the coordinate system so that z -axis is perpendicular to the layers planes, which are assumed infinite both in the x - and y - direction. The layers are numbered by $p = 1, \dots, L$, while $p = 0, L + 1$ number the ambient media above and beneath the structure, respectively. In general, such a structure may be a two-dimensionally (2D) structured stack, in each layer of which the dielectric susceptibility $\epsilon^{(p)}$ depends both on x and y . An EM radiation, which impinges the structure from the top (see Fig.1), is partially reflected from and transmitted through it. Maxwell equations for the Cartesian components of the time-harmonic EM fields $\mathbf{E} = (E_x, E_y, E_z)$, $\mathbf{H} = (H_x, H_y, H_z)$, in the structure's part number p have the form

$$\begin{aligned} \partial_y E_z^{(p)} - \partial_z E_y^{(p)} &= ik H_x^{(p)}, \quad \partial_y H_z^{(p)} - \partial_z H_y^{(p)} = -ik \epsilon_x^{(p)} E_x^{(p)} \\ \partial_z E_x^{(p)} - \partial_x E_z^{(p)} &= ik H_y^{(p)}, \quad \partial_z H_x^{(p)} - \partial_x H_z^{(p)} = -ik \epsilon_y^{(p)} E_y^{(p)}, \\ \partial_x E_y^{(p)} - \partial_y E_x^{(p)} &= ik H_z^{(p)}, \quad \partial_x H_y^{(p)} - \partial_y H_x^{(p)} = -ik \epsilon_z^{(p)} E_z^{(p)} \end{aligned} \quad (1)$$

Here $k = 2\pi/\lambda$ and λ are the vacuum wave number and wavelength, respectively. Let $z = z_p$ is the equation of the lower interface of the layer number p (see Fig.1). Then in Eq.1, $z_p \leq z \leq z_{p+1}$ for $1 \leq p \leq L$, $0 \leq z < \infty$ for $p = 0$, and $-\infty < z \leq z_L$ for $p = L + 1$. The curl- \mathbf{H} subsystem of Eq.1 is intentionally written as if $\epsilon^{(p)}$ is a diagonal tensor with the different components along different axes. This will remind us that, even though $\epsilon^{(p)}$ is isotropic in the real space, its correct map onto the Fourier space may contain essential anisotropy (see below).

The z -components of \mathbf{E} and \mathbf{H} can easily be excluded using the bottom-line equations in Eq.1, after which it reduces to a 4×4 system of coupled differential equations for the electric and the magnetic wave functions, built of the remaining field components as follows

$$\Psi_E^{(p)} = \begin{bmatrix} E_x^{(p)} \\ E_y^{(p)} \end{bmatrix}, \quad \Psi_H^{(p)} = \begin{bmatrix} H_x^{(p)} \\ H_y^{(p)} \end{bmatrix}. \quad (2)$$

We write down the above system in the propagation-type form using shortened super-vector and super-matrix notations

$$\frac{\partial}{\partial z} \begin{bmatrix} \Psi_E^{(p)} \\ \Psi_H^{(p)} \end{bmatrix} = ik \begin{bmatrix} O & M_{EH}^{(p)} \\ M_{HE}^{(p)} & O \end{bmatrix} \begin{bmatrix} \Psi_E^{(p)} \\ \Psi_H^{(p)} \end{bmatrix}, \quad (3)$$

where O is the 2×2 zero matrix and

$$\mathcal{M}_{\text{EH}}^{(p)} = \frac{1}{k^2} \begin{bmatrix} -\partial_x \kappa_z^{(p)} \partial_y & k^2 + \partial_x \kappa_z^{(p)} \partial_x \\ -k^2 - \partial_y \kappa_z^{(p)} \partial_y & \partial_y \kappa_z^{(p)} \partial_x \end{bmatrix}, \quad \mathcal{M}_{\text{HE}}^{(p)} = \frac{1}{k^2} \begin{bmatrix} \partial_x \partial_y & -k^2 \varepsilon_y^{(p)} - \partial_x^2 \\ k^2 \varepsilon_x^{(p)} + \partial_y^2 & -\partial_x \partial_y \end{bmatrix}, \quad (4)$$

$\kappa_z^{(p)} = 1/\varepsilon_z^{(p)}$ is the inverse 'z-component' susceptibility. For surface-relief structures, of given by Eq.4 the 2x2 matrix operators, all the components of the first one are strongly singular due to emergence of the division between the ∂ operators, while the off-diagonal components of the second are only weakly singular due to emergence of multiplication by jumped susceptibility. For recorded (volume-holographic) structures, all the operators involved are smoothly regular.

For further basic-level discussion it is instructive to pass from Eq.3 to the second-order, with respect to z , differential equations for anyone of the two-component wave function

$$\partial_{zz}^2 \Psi_{\text{E(H)}}^{(p)} = -k^2 \mathcal{A}_{\text{E(H)}}^{(p)} \Psi_{\text{E(H)}}^{(p)}, \quad (5)$$

where

$$\mathcal{A}_{\text{E}}^{(p)} = \frac{1}{k^2} \begin{bmatrix} k^2 \varepsilon_x^{(p)} + \partial_{yy}^2 + \partial_x \kappa_z^{(p)} \partial_x \varepsilon_x^{(p)} & \partial_x \kappa_z^{(p)} \partial_y \varepsilon_y^{(p)} - \partial_{xy}^2 \\ \partial_y \kappa_z^{(p)} \partial_x \varepsilon_x^{(p)} - \partial_{xy}^2 & k^2 \varepsilon_y^{(p)} + \partial_{xx}^2 + \partial_y \kappa_z^{(p)} \partial_y \varepsilon_y^{(p)} \end{bmatrix}, \quad (6a)$$

$$\mathcal{A}_{\text{H}}^{(p)} = \frac{1}{k^2} \begin{bmatrix} k^2 \varepsilon_y^{(p)} + \partial_{xx}^2 + \varepsilon_y^{(p)} \partial_y \kappa_z^{(p)} \partial_y & \partial_{xy}^2 - \varepsilon_y^{(p)} \partial_y \kappa_z^{(p)} \partial_x \\ \partial_{xy}^2 - \varepsilon_x^{(p)} \partial_x \kappa_z^{(p)} \partial_y & k^2 \varepsilon_x^{(p)} + \partial_{yy}^2 + \varepsilon_x^{(p)} \partial_x \kappa_z^{(p)} \partial_x \end{bmatrix}. \quad (6b)$$

When obtaining Eqs.6 we performed operator multiplication formally, but detailed analysis shows that all cancellations emerged in that course are mathematically justified; the resulting operators prove more singular than the multipliers. In this section we ignore the singularity of the operators given by Eqs.4 and 6 and will return to this issue in Subsection 2.3. Treated as an evolution equation in an abstract vector space, where all the operators involved act, Eq.5 may be solved symbolically using the notions of square root and exponential operator-valued functions. Let us take the wave solution, omitting from now on the index of the wave function type, in the following form

$$\Psi^{(0)} = \exp\left(ikzQ^{(0)}\right) \cdot \xi^{(0)} + \exp\left(-ikzQ^{(0)}\right) \cdot \eta^{(0)} \quad (7a)$$

for z in the ambient top (here superstrate), and

$$\Psi^{(p)} = \exp\left(ik(z - z_{p-1})Q^{(p)}\right) \cdot \xi^{(p)} + \exp\left(-ik(z - z_{p-1})Q^{(p)}\right) \cdot \eta^{(p)} \quad (7b)$$

for z in the layers, $p=1, \dots, L$, and in the ambient medium beneath (here substrate), $p=L+1$; $Q^{(p)}$ is one of two operators $Q_{\text{E(H)}}^{(p)}$, which satisfy the operator 'square-root' equation

$$[Q^{(p)}]^2 = \mathcal{A}^{(p)}, \quad (8)$$

and $\xi^{(p)}$ and $\eta^{(p)}$ are yet unknown functions of x and y , i.e. independent of z vectors in the functional space considered, to be determined. Solution to Eq.8 is not unique so let us specify $Q^{(p)}$ more, namely to fix $Q^{(p)}$ be such that its spectrum would lie in the upper complex half-plane (including the real axis). By an analogy with scalar (one-channel) scattering two exponentials in the right-hand side of Eqs.7a, b may be considered as backward and forward scattered waves so that $\eta^{(0)}$, $\xi^{(0)}$ and $\eta^{(L+1)}$ are the wave amplitudes of incident, reflected and transmitted beams, respectively. The above analogy holds for modes of $Q^{(p)}$ with the spectrum lying in the upper-right complex plane quadrant that is true for homogeneous media, but may invert for structured layers. The $Q^{(p)}$ modes with both propagation directions possess *attenuation*, if any.

2.2. Matching of inlayer solutions and symbolic S-operator algorithm

To determine $\xi^{(p)}$ and $\eta^{(p)}$, the partial solutions of Eqs.7a, b should be matched at the layers interfaces using the EM boundary conditions, which express the continuity of the wave functions versus z

$$\Psi^{(p)} \Big|_{z=z_p+0} = \Psi^{(p+1)} \Big|_{z=z_p-0}, \quad [M^{(p)}]^{-1} \hat{c} \Psi^{(p)} \Big|_{z=z_p+0} = [M^{(p+1)}]^{-1} \hat{c} \Psi^{(p+1)} \Big|_{z=z_p-0} \quad (9)$$

Eqs.7a, b together with Eq.9 give the system of matching equations

$$\begin{aligned} [C^{(p)}]^{-1} \xi^{(p)} + C^{(p)} \eta^{(p)} &= \xi^{(p+1)} + \eta^{(p+1)} \\ \underline{Q}^{(p)} \{ [C^{(p)}]^{-1} \xi^{(p)} - C^{(p)} \eta^{(p)} \} &= \underline{Q}^{(p+1)} [\xi^{(p+1)} - \eta^{(p+1)}] \end{aligned} \quad (10)$$

where for $p=1, \dots, L$

$$C^{(p)} = \exp(ikh_p Q^{(p)}), \quad \underline{Q}^{(p)} = [M^{(p)}]^{-1} Q^{(p)}, \quad (11)$$

$h_p = z_{p-1} - z_p$ is the depth of p th layer and $C^{(0)} = I$ is the identity operator. The radiation conditions, stating that the only propagated forward at $z > 0$ is the incident wave with a given amplitude $\eta^{(0)}$ and no wave is scattered backward at $z < z_L$ so that the amplitude $\xi^{(L+1)}$ is put to the zero vector, formally close the system of Eq.10.

Any numerical approach to the problem considered employs discretization. It consists of either exact mapping of the abstract vectors and operators involved onto countable-component vectors and matrices with subsequent truncation, or of sampling $\Psi^{(p)}$ and $\varepsilon^{(p)}$ with replacing the derivatives by finite differences that approximates all the functions and operators by vectors and matrices of finite-dimension M (truncation order). Modal methods until 1993, whatever discretization they used, were dominated on the matching stage by so-called T -matrix algorithm, which propagates simultaneously $\xi^{(p)}$ and $\eta^{(p)}$ using system of Eq.10 and is, potentially, unstable numerically. Really, though $C^{(p)}$ is a bounded operator due to our choice of $Q^{(p)}$, $[C^{(p)}]^{-1}$ proves *unbounded* since $Q^{(p)}$ is certainly unbounded. So with every discretization, the matrix map of $[C^{(p)}]^{-1}$ will contain elements exponentially growing with the increase of h_p or/and M . Therefore, if M is large many factors with real positive exponents are met in Eq.10, their magnitudes being enormously large unless $kh_p \rightarrow 0$. Owing to the presence of growing exponentials matrix manipulations required for solving Eq.10 may fail numerically even for one layer. Otherwise, let L is large and M is not, but at least one attenuated mode is involved in each layer. Due to recurrence type of Eq.10, the exponential instability may develop readily when multiplying L times 2×2 block-matrices with $M \times M$ matrix blocks which contain real elements much larger than unity. With both M and L large enough the appearance of such instability is almost inevitable, on what really was reported in a number of papers.

Since it is the backward scattered amplitudes $\xi^{(p)}$ propagation that results in numerical instability, a transformation of Eq.10 to an equivalent system that doesn't contain $\xi^{(p)}$ at all would allow one to get rid of the instability problem prior to discretization. To this end, let us use the scattering-theory paradigm, according to which the out- and in-going wave amplitudes should be connected to each other linearly

$$\xi^{(p)} = S^{(p)} \eta^{(p)}, \quad (12)$$

where $S^{(p)}$ is scattering operator (S -operator). This transformation is consistent with Eq.10 and uncouples in two separate recurrence relations – the backward one for the S -operators

$$S^{(p)} = C^{(p)} [\underline{Q}^{(p)} + \underline{Q}^{(p+1)} \mathcal{D}^{(p+1)}]^{-1} \cdot [\underline{Q}^{(p)} - \underline{Q}^{(p+1)} \mathcal{D}^{(p+1)}] C^{(p)}, \quad (13a)$$

where $\mathcal{D}^{(p)} = [I + S^{(p)}]^{-1} [I - S^{(p)}]$, with the initial condition $S^{(L+1)} = O$, and the forward recurrence relations for the amplitudes $\eta^{(p)}$

$$\eta^{(p+1)} = 2[I + S^{(p+1)}]^{-1} [\underline{Q}^{(p)} + \underline{Q}^{(p+1)} \mathcal{D}^{(p+1)}]^{-1} \underline{Q}^{(p)} C^{(p)} \eta^{(p)}, \quad (13b)$$

Any discretization will map symbolic solution propagation procedure developed above to an executable by-construction unconditionally stable algorithm. This S -matrix propagation algorithm (SMPA)^{2,6} is generically different from those due to Cotter *et al.*³ and Li.⁷ In addition to apparent analogy with the S -parameters method in the theory of circuits, SMPA proved, incidentally, a matrix generalization of the Parratt algorithm¹³ for the X-rays reflection from multi-layer stacks.

3. DIFFRACTION FROM MLGS IN CONICAL MOUNTING

Here we apply the above results to the case of a one-dimensional (1D) MLGS, where independent of y $\varepsilon^{(p)}$ are periodic functions of x at most with the same period Λ (for homogeneous layer $\varepsilon^{(p)}$ is constant), postponing the diffraction analysis of 2D MLGS to separate consideration. Since in infinite medium every beam is presented as superposition of plane-wave beams, the present treatment is devoted to the irradiation by plane-wave; finite-beam cases will be considered elsewhere.

Let \mathbf{k}_i is the incidence wave vector. Due to Fig.1, and Eq.1 for $p = 0$, it is connected to the incidence angles ϑ, φ by

$$k_{ix} = -k^{(0)} \sin \vartheta \cos \varphi, k_{iy} = -k^{(0)} \sin \vartheta \sin \varphi, k_{iz} = -k^{(0)} \cos \vartheta; k^{(0)} = k \sqrt{\varepsilon^{(0)}}. \quad (14)$$

The presence of grating even in one layer dictates the quasi-periodicity (Floquet) condition for the EM field in every part of the structure, which may be satisfied by the Fourier (Fourier-Floquet, more correctly) modal series

$$\Psi^{(p)} = \sum_{n=-\infty}^{+\infty} \psi_n^{(p)}(z) e^{j(k_{nx}x + k_{iy}y)} \quad k_{nx} = k_{ix} + Kn, \quad K = \frac{2\pi}{\Lambda}, \quad (15)$$

where the Fourier components $\psi_n^{(p)}(z)$ represent a vector map of the wave function in $2 \times \infty$ dimensional Hilbert space. To realize actually executable SMPA in place of symbolic Eqs.13a, b, we should also map the operators $\mathcal{M}^{(p)}$ (Eq.4) and $\mathcal{A}^{(p)}$ (Eqs.6a, b) concordantly with Eq.15. To this end, the operators of partial differentiation and of multiplication by the susceptibility and its inverse should properly be mapped. To ∂_x and ∂_y correspond multiplying the components of a Hilbert-space vector by jk_{nx} and jk_{iy} , respectively. If $\varepsilon^{(p)}(x)$, and hence $\kappa^{(p)}(x)$, is continuous as with recorded gratings, to that multiplication correspond the Laurent-rule convolution, which in the Hilbert space is equivalent to multiplication by the infinite matrices $[\varepsilon^{(p)}]$ and $[\kappa^{(p)}]$ with the elements expressed via the corresponding Fourier coefficients by

$$[\varepsilon^{(p)}]_{nm} = \tilde{\varepsilon}_{n-m}^{(p)} = \frac{1}{\Lambda} \int_0^\Lambda \varepsilon^{(p)}(x) e^{jK(n-m)x} dx, \quad [\kappa^{(p)}]_{nm} = \tilde{\kappa}_{n-m}^{(p)} = \frac{1}{\Lambda} \int_0^\Lambda \frac{1}{\varepsilon^{(p)}(x)} e^{jK(n-m)x} dx \quad (16)$$

The above rule holds also for laminated/etched gratings in the case where the multiplied function is continuous, e.g. when Fourier factorizing $D_{yz} = \varepsilon^{(p)} E_{xy}$. Thus to $\varepsilon_{yz}^{(p)}$ there corresponds $[\varepsilon^{(p)}]$, and hence to $\kappa_z^{(p)}$ the *inverse* matrix $[\varepsilon^{(p)}]^{-1}$. At the same time, $D_x = \varepsilon^{(p)} E_x$ due to its continuity is better Fourier-factorized following the recast rule,⁸ in which the map of $\varepsilon_x^{(p)}$ proves the *inverse* matrix $[\kappa^{(p)}]^{-1}$; this is simply the second rule of Eq.16 applied to the inverted product $E_x = \kappa^{(p)} D_x$. Using these rules we readily calculate the required maps of Eqs.4 and 6, distinguishing them by hat above, to get

$$\hat{\mathcal{M}}_{EH}^{(p)} = \begin{bmatrix} \gamma_y [\gamma_x] \cdot [\varepsilon^{(p)}]^{-1} & [I] - [\gamma_x] \cdot [\varepsilon^{(p)}]^{-1} \cdot [\gamma_x] \\ -[I] + \gamma_y^2 [\varepsilon^{(p)}]^{-1} & -\gamma_y [\varepsilon^{(p)}]^{-1} [\gamma_x] \end{bmatrix}, \quad \hat{\mathcal{M}}_{HE}^{(p)} = \begin{bmatrix} -\gamma_y [\gamma_x] & -[\varepsilon^{(p)}] + [\gamma_x]^2 \\ -\gamma_y^2 [I] + [\kappa^{(p)}]^{-1} & \gamma_y [\gamma_x] \end{bmatrix}, \quad (17)$$

where $\gamma_y = k_{iy}/k$, $[\gamma_x]$ is the infinite diagonal matrix with the elements $\gamma_{nx} = k_{nx}/k$, and $[I]$ is the identity matrix. Further

$$\hat{\mathcal{A}}_E^{(p)} = \begin{bmatrix} \{[I] - [\gamma_x] \cdot [\varepsilon^{(p)}]^{-1} \cdot [\gamma_x]\} \cdot [\kappa^{(p)}]^{-1} - \gamma_y^2 [I] & [O] \\ \gamma_y \{[\varepsilon^{(p)}]^{-1} \cdot [\gamma_x] \cdot [\kappa^{(p)}]^{-1} - [\gamma_x]\} & [\varepsilon^{(p)}] - [\gamma_x]^2 - \gamma_y^2 [I] \end{bmatrix}, \quad (18a)$$

$$\hat{\mathcal{A}}_H^{(p)} = \begin{bmatrix} [\varepsilon^{(p)}] - [\gamma_x]^2 - \gamma_y^2 [I] & [O] \\ \gamma_y \{[\gamma_x] - [\kappa^{(p)}]^{-1} \cdot [\gamma_x] \cdot [\varepsilon^{(p)}]^{-1}\} & [\kappa^{(p)}]^{-1} \cdot \{[I] - [\gamma_x] \cdot [\varepsilon^{(p)}]^{-1} \cdot [\gamma_x]\} - \gamma_y^2 [I] \end{bmatrix}, \quad (18b)$$

where $[O]$ is the zero matrix. Then the infinite vectors and matrices should be truncated by cutting indices of the Fourier-components within finite, e.g. symmetric $|n| \leq N$, limits. The above mapping formulas were empirically found to provide good convergence at increasing $M = 2N + 1$.⁴⁻⁶ Two different rules used before 1996 mapping $\varepsilon^{(p)}(x)$ and $\kappa^{(p)}(x)$, whatever field component they multiply, onto matrices of Eq.16¹⁴ and another^{10,15} onto $[\varepsilon^{(p)}]$ and $[\varepsilon^{(p)}]^{-1}$, respectively, proved to result in slow¹⁰ or even poor⁶ convergence. Our reasoning⁶ was to match effective-medium limit that is exact at $\lambda/\Lambda \gg 1$, which lead to two rules, quite different from pre-existed ones. The correct rule resulting in Eqs.17, 18 was then singled out by numerical testing.⁶

The reduced form of matrices given by Eq.18 – with zero upper right angle sub-matrices – holds for all above rules of mapping. Due to this, the $2M \times 2M$ conical-diffraction eigen-value problem reduces to two independent $M \times M$ TE and TM planar-diffraction eigen-value problem (shifted by a unique constant), which make it possible to shorten the simulation time to only twice larger than that in the planar-diffraction cases.^{15,16} In the present study we consider the most general, elliptically polarized, plane wave described by geometric phases δ and α ;¹⁷ only linearly polarized beam incidence was considered in the RCWA framework to our knowledge (see^{15,16} and references therein).

4. NUMERICAL AND GRAPHICAL IMPLEMENTATIONS

4.1. MLGS diffraction toolbox in MATLAB

For numerical simulations we employed MATLAB®. This multi-profile software fits ideally our needs since its native objects are vectors and matrices and all linear-algebra manipulations (including matrix functions) with updated packages are available in MATLAB. In addition updated nonlinear programming packages are facilitated in Optimization Toolbox of MATLAB. Several other considerations motivated using MATLAB; among these are high programming efficiency – the performance of most MATLAB codes is only a bit lower than that of corresponding, say, C++ codes – and elegant graphical user interface (GUI) builder. Last, but not least, aspect of that convenience is that MATLAB is well supported by all PC and UNIX platforms.

The above toolbox contains program and design blocks. Program block contains main routine, which is user-defined MATLAB function (M-file) coding SMPA (Eqs.12, 13), M-files of objective functions calculating, using outputs of main routine, the EM fields in far-field zone, describing the diffraction, nearby and inside MLGS. Until discretization is not stated main routine looks like a symbolic record of Eqs.12, 13, which calls external routines for calculating the matrices required for actual execution. For FMM we actually use, M-files of the latter routines are also present in program block. Open architecture of our toolbox permits using any other method of discretization without changing main routine. Design block contains MATLAB scripts (run M-files) of optimal designs. According to optimal optical characteristic desired, suitable script calls appropriate routine of MATLAB Optimization Toolbox and directs specific objective function with such external parameters as grating period, filling factors, layers thicknesses etc. to be optimized.

4.2. Description of GUI

In order to automate the simulations of the previously described MLGS diffraction model with our toolbox for a custom user, we have developed a unique GUI we named Multi-Layer Grating Diffraction Simulator (MGDS). Fig.2 illustrates the hierarchical structure of the simulation platform. At the base is the “simulation model”, which performs the actual mathematical manipulation of the MLGS diffraction. Above it is the “simulation control block”, which comprises two parallel components: The “control data” which serves as the container of various data in the simulation,

this component was divided to the device structure parameters and to the EM source variables that have interaction with the device. The "control program" is a set of routines activating the simulation predefined by the "control data". The top layer in the figure is the GUI, with which the user can fulfil the whole simulation process, including data saving / loading / creating / editing, simulation starting / stopping and controlling the results output format (one / two / three dimensions and variable resolution).

We use the GUI-MATLAB® new sub-function for passing output arguments to the command line with the hObject and Handles structure, which handle the figure and user data. The usage of those sub-functions and formation of chaining array with reference cell point for each system variant, based on its structure location, enables us to maximize the simulation performance. On start-up the MGDS interface presents to the user with window that contain five data blocks as shown in Fig.3; this main frame was designed to enable the user minimum interaction with the MLGS diffraction toolbox software with maximum flexibility in the "Control Data" and the "Control Program" modules. The first three blocks include the system constants, MLGS characterization and MLGS substrate/superstrate characterization (all contained in the "Control Data" module).

System constants: User defines the EM beam and incidence parameters and coordination for the interaction as well as the device grating constants. The optical constants are input either manually or imported from the database available. MLGS characterization: Each MLGS may contain grating / homogeneous layers, excluding the substrate and superstrate. The latter are defining in MLGS Sub / Sup characterization block.

4.3. Simulation example

Let us consider, as demo example, simulation of grating-wave-guide resonance (GWR) reflection from MLGS containing three layers – a buffer polymer layer, 0.5 duty-cycle grating layer comprising polymer and silicon nitride, silicon nitride wave-guide layer – and a silicon dioxide substrate. The GWR phenomenon was described from both optical and physical viewpoints in detail (e.g.¹⁸ and references therein). Here we briefly consider the transformations of the reflectance peak upon introducing planar and conical angular offsets from the normal incidence. The results of simulation using our in-house software are shown on Fig.4.

REFERENCES

1. E.G. Loewen and E. Popov, *Diffraction Gratings and Applications*, Marcel Dekker, New York – Basel, 1997.
2. S. Hava, M. Auslender and D. Rabinovich, "Operator approach in electromagnetic coupled-wave calculations of lamellar gratings: Infrared optical properties of silicon gratings," *Appl. Opt.* **33**, 4807 – 4813 (1994).
3. N.P.K. Cotter, T.W. Preist and J.R. Sambles, "Scattering-matrix approach to multilayer diffraction," *J. Opt. Soc. Am. A* **12**, 1097 – 1103 (1995).
4. P. Lalanne and G.M. Morris, "Highly improved convergence of the coupled-wave method for TM polarization," *J. Opt. Soc. Am. A* **13**, 779 – 784 (1996).
5. G. Granet and B. Guizal, "Efficient implementation of the coupled-wave method for metallic lamellar gratings in TM polarization," *J. Opt. Soc. Am. A* **13**, 1019 – 1023 (1996).
6. M. Auslender and S. Hava, "Scattering-matrix propagation algorithm in full-vectorial optics of multiplayer grating structures," *Opt. Lett.* **21**, 1765 – 1767 (1996).
7. L. Li, "Formulation and comparison of two recursive matrix algorithms for modelling layered diffraction gratings," *J. Opt. Soc. Am. A* **13**, 1024 – 1035 (1996).
8. L. Li, "Use of Fourier series in the analysis of discontinuous periodic structures," *J. Opt. Soc. Am. A* **13**, 1870 – 1876 (1996).
9. Series of papers shared title "Polarized spectral emittance from periodic micromachined surfaces," subtitled: P. J. Hesketh, J. N. Zemel and B. Gebhart, "I. Doped silicon: the normal direction," *Phys. Rev. B* **37**, 10795 – 10802 (1988), "II. Doped silicon: angular variations," *ibid*, 10803 – 10813 (1988); T. K. Wang and J. N. Zemel, "III. Undoped silicon: the normal direction in shallow lamellar gratings," *Infrared Phys.* **32**, 477 – 488 (1991), "IV. Undoped silicon: the normal direction in deep lamellar gratings," *Appl. Opt.* **31**, 732 – 736 (1992), "V. Undoped silicon: angular measurement in shallow lamellar gratings," *ibid*, **32**, 2021 – 2027 (1993).
10. L. Li and W. Haggans, "On the convergence of the coupled-wave method for metallic lamellar diffraction gratings," *J. Opt. Soc. Am. A* **10**, 1184 – 1189 (1993).

11. L. Li, "Multilayer modal method for diffraction gratings of arbitrary profile, depth and permittivity," J. Opt. Soc. Am. A **10**, 2581 – 2591 (1993).
12. L.F. DeSandre and J.M. Elson, "Extinction-theorem analysis of diffraction anomalies in overcoated gratings," J. Opt. Soc. Am. A **8**, 763 – 777 (1991).
13. L.G. Parratt, "Surface studies of solids by total reflection of X-rays," Phys. Rev. **95**, 359 – 369 (1954).
14. K. Knop, Rigorous theory for transmission phase gratings with deep rectangular grooves," J. Opt.Soc.Am., **68**, 1206 – 1210 (1978).
15. M.G. Moharam, E.B. Grann, D.A. Pommet and T.K. Gaylord, "Formulation of stable and efficient implementation of the rigorous coupled-wave analysis for binary gratings," J. Opt. Soc. Am. A **12**, 1068 – 1076 (1995)
16. S. Peng and G.M. Morris, "Efficient implementation of rigorous coupled-wave analysis for surface-relief gratings," J. Opt. Soc. Am. A **12**, 1087 – 1096 (1995).
17. M. Born and E. Wolf, *Principles of Optics*, Sixth Edition, Pergamon Press, Oxford – New York, 1980.
18. S.S. Wang and R. Magnusson, "Multilayer waveguide-grating filters," Appl. Opt. **34**, 2414 – 2420 (1995).

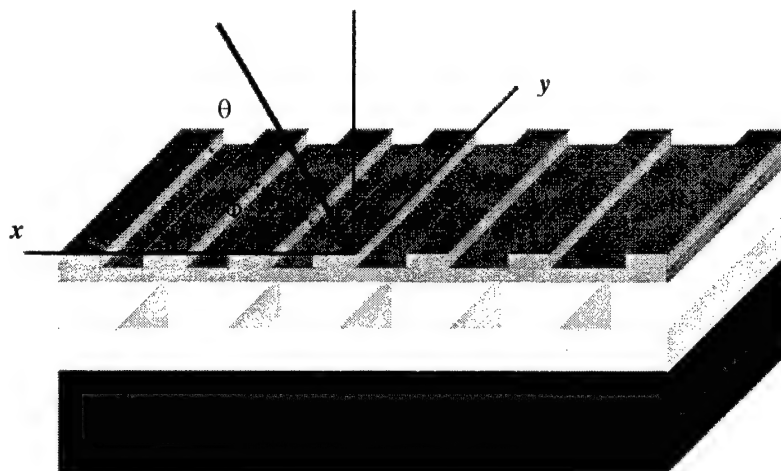


Figure 1. Multi-layered structure irradiated by an incident beam (arrow)

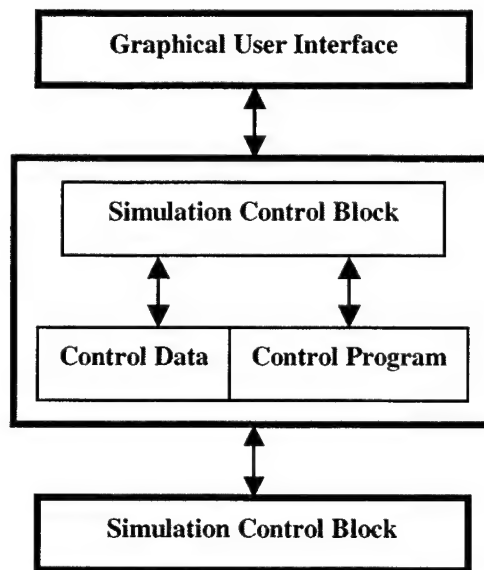


Figure 2. Hierarchical structure of the simulation platform

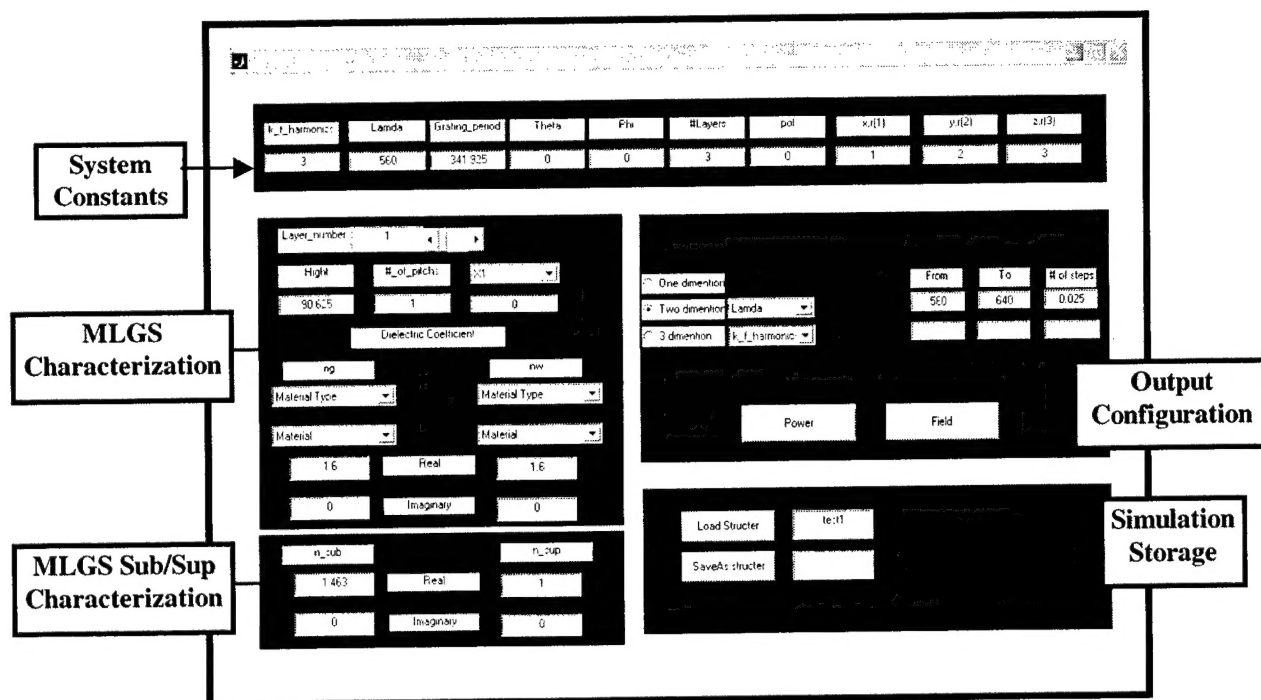


Figure 3. Front end of MGDS

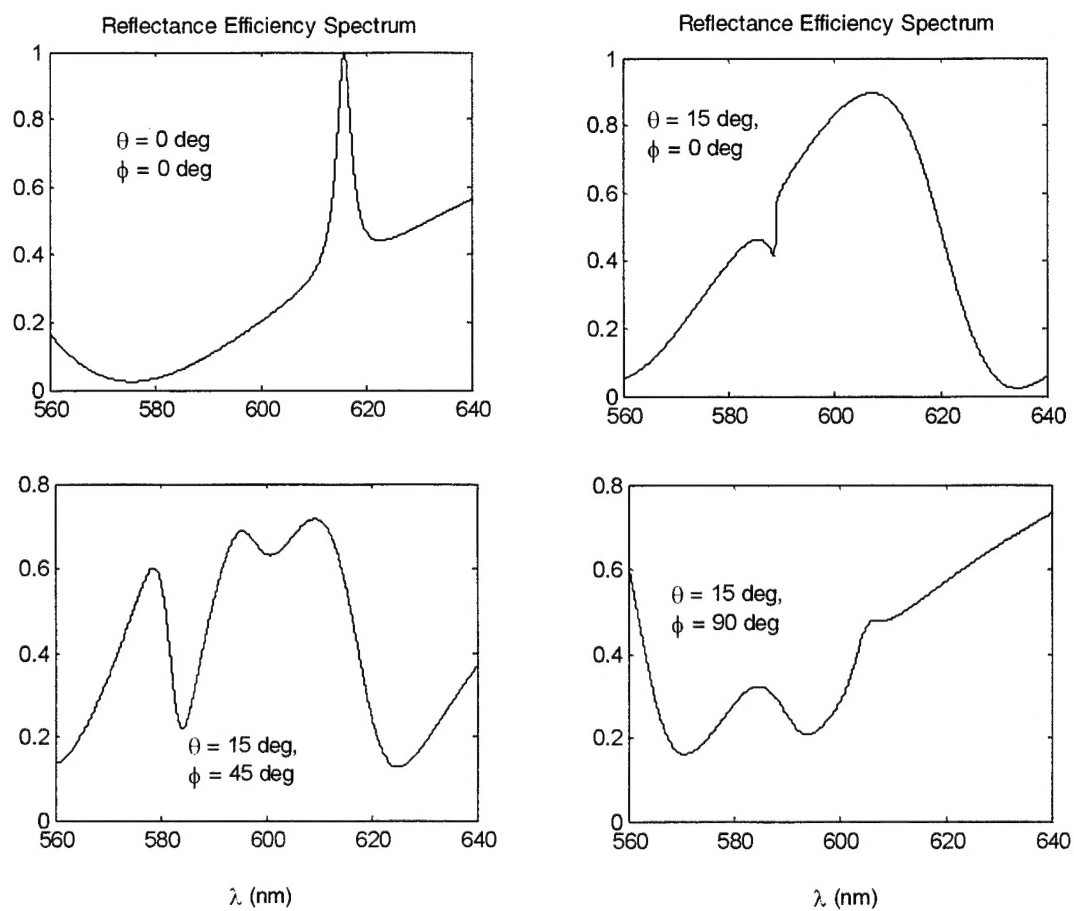


Figure 4. Degradation of GWR reflection performance of a MLGS

Author Index

- Ager, Joel W., III, 426
 Agrawal, Arti, 132, 151
 Alford, William J., 172
 Aliberti, Keith, 197
 Altieri, Paola, 416
 An, Chengwu, 112
 Ando, Tsuneya, 1
 Annovazzi-Lodi, Valerio, 290
 Armour, Eric A., 408
 Armstrong, Darrell J., 172
 Asryan, Levon V., 69
 Auslender, Mark, 463
 Baba, Kazutaka, 122
 Baba, Toshihiko, 103
 Barton, Jonathon S., 176
 Bauer, Stefan, 348
 Becla, Piotr, 426
 Beeman, Jeffrey, 426
 Benavidez, Marcita, 271
 Benedetti, Mauro, 290
 Bergel, Avi, 463
 Bergman, K., 228
 Bilici, Temel, 454
 Bimberg, Dieter, 31
 Blood, Peter, 63
 Blumenthal, Daniel J., 176
 Bour, David P., 206, 366
 Bowers, Mark S., 172
 Brox, Olaf, 348
 Bugajski, Maciej, 446
 Cao, Hongjun, 271
 Carey, Jim, 454
 Chang, Shu-Wei, 54
 Chang, Ying-lan, 206
 Chen, How Foo, 298
 Chen, Weiliang, 385
 Chen, Yi P., 11
 Chi, Jim, 31
 Chiang, Margaret C., 319
 Chong, Towchong, 112
 Chuang, Shun-Lien, 54, 90
 Coldren, Larry A., 176, 185
 Corzine, Scott W., 206
 Dong, Hao, 117, 255
 Duan, Guang-Hua, 262
 Dubon, O. D., 426
 Dutta, Niloy K., 117, 255
 Eliseev, Petr G., 46, 271, 408
 Florescu, Doru I., 408
 Fujiwara, Natsuki, 282
 Fukazawa, Tatsuhiko, 103
 Gadjiev, Igor M., 31
 Gallion, Philippe, 262
 Greiner, Christoph, 236
 Gubenko, Alexey E., 31
 Haller, Eugene E., 426
 Han, Jie, 11
 Hava, Shlomo, 463
 He, Wanxun, 112
 He, Yongzhi, 143
 Henneberger, Fritz, 348
 Henness, Jeffrey A., 176, 185
 Higgins, S. P., 435
 Hoffman, Erik H., 90
 Hoffmann, Stefan, 218
 Hofmann, Martin R., 218
 Holonyak, Nick, Jr., 54
 Huang, Chi-Chia, 247
 Huffaker, Diana, 63
 Hutchinson, John M., 176, 185
 Hwang, Sheng Kwang, 339
 Iazikov, Dmitri, 236
 Inanç, Ibrahim, 454
 Jaeger, Arndt, 416
 Jain, Geetika, 163
 Jayaraman, Vijay, 375
 Johansson, Leif A., 176
 Koshio, Hajime, 358
 Kovsh, Alexey R., 31
 Kurt, Adnan, 454
 Kutz, J. Nathan, 228
 Landais, Pascal, 262
 Ledentsov, Nikolai N., 31
 Lee, Dong-Seung, 408
 Lee, Jinhyun, 408
 Lester, Luke F., 63
 Lester, Steven D., 366
 Li, Jianzhong, 95
 Lin, Chao Kun, 206
 Lin, Ching-Fuh, 247
 Lin, Yi-Xiong, 247
 Linder, Norbert, 416
 Ling, Hai, 271
 Liu, Chiyu, 271
 Liu, Jia Ming, 298, 319, 339
 Liu, Mingyu, 112
 Livshits, Daniil A., 31
 Lott, James A., 31
 Lu, W., 228
 Luryi, Serge, 69
 Lutfi, Julie, 63
 Maleev, Nikolay A., 31
 Malloy, Kevin J., 46
 Mao, Aaron, 11
 Mašanović, Milan L., 176
 Maslov, Alex V., 24

Maximov, Mikhail V., 31
 Mazur, Eric, 454
 Mehandru, Rishabh, 197
 Mehta, Manish, 375
 Merlo, Sabina, 290
 Mertz, Françoise, 366
 Meyyappan, Meyya, 11
 Mikhlin, Sergei S., 31
 Miller, Jeffrey N., 366
 Mirasso, Claudio R., 307, 319, 331
 Miyagi, Mitsunobu, 122
 Mossberg, Thomas W., 236
 Mulet, Josep, 307
 Nabetani, Y., 426
 Newman, Peter G., 197
 Ng, Hou T., 11
 Ng, Lungtat, 112
 Nguyen, Pho, 11
 Ning, Cun-Zheng, 24, 95
 Norgia, Michele, 290
 Oberschmid, Raimund, 416
 Ohno, Fumiaki, 103
 Ohtsubo, Junji, 282, 358
 Osborne, Simon, 63
 Osipiński, Marek, 271, 385, 408
 Ouyang, Donald, 31
 Peake, Gregory M., 271
 Pinhas, Nathan, 463
 Piprek, Joachim, 185, 375
 Popescu, Dan P., 46
 Portnoi, Efim L., 31
 Ramer, Jeffrey C., 408
 Ren, Fan, 197
 Renaudier, Jeremie, 262
 Robbins, Virginia M., 366
 Scapulla, M. A., 426
 Sciamanna, Marc, 307
 Serpengüzel, Ali, 454
 Shan, W., 426
 Sharma, Anurag, 132, 151
 Sharma, Enakshi Khular, 163
 Shen, Paul Hongen, 197
 Shi, Frank G., 143
 Smagley, Vladimir A., 385
 Small, B., 228
 Smith, Arlee V., 172
 Smolyakov, Gennady A., 385
 Snowton, Peter, 63
 Sone, Yoshiaki, 122
 Stann, Barry, 197
 Stauss, Peter, 416
 Stintz, Andreas, 46, 63
 Streubel, Klaus, 416
 Su, Hui, 271
 Suda, Jun, 397
 Sysak, Matthew N., 176
 Tan, Michael R., 206
 Tandon, Ashish, 206
 Taneja, Ashmeet Kaur, 163
 Tang, Shuo, 319
 Torchynska, T. V., 46
 Trenado, Nicolas, 185
 Ushakov, Oleg, 348
 Uskov, Alexander V., 81
 Ustinov, Victor M., 31
 Vicente, Raúl, 307, 319, 331
 Vickers, Anthony J., 435
 Walukiewicz, W., 426
 Wang, Jyh Shyang, 31
 Wang, Qiang, 117, 255
 White, J. Kenton, 339
 Windisch, Reiner, 416
 Wu, Junqiao, 426
 Wünsche, Hans-Jürgen, 348
 Xin, Y. C., 63
 Xu, Baoxi, 112
 Yang, Peidong, 18
 Yu, Kin M., 426
 Yu, Yu-Chen, 247
 Yuan, Gaoqiang, 112
 Yuan, Hongxing, 112
 Zbroszczyk, Mariusz, 446
 Zhu, Guanghao, 117, 255
 Zhukov, Alexey E., 31